Sponsored by TRF

Sponsored by the Transducer Research Foundation, Inc.

TRF Catalog Number: 14TRF-0001 • ISBN Number: 9781940470016 • ISSN: 1539-204X (Electronic)
Library of Congress Control Number: 2014937764 • DOI 10.31438/trf.hh2014.0

Greetings from the General Chair

Welcome to the 30th Anniversary of the Solid State Sensors, Actuators, and Microsystems Workshop; the sixteenth in the biennial series of regional meetings that alternate with the International Transducers Conference. The goal of the Workshop - since its inception in 1984 - has been to provide a forum for presentation of new ideas and leading-edge research achievements, in a setting that facilitates exchange of ideas and community building.

Mark Allen has assembled and led an expert program committee in support of the Workshop's goal. Mind-expanding plenary presentations by leading academic and industry experts will kick-off each day, followed by oral and poster sessions of contributed papers. The Workshop schedule remains organized around single session oral and poster presentations. We have continued the tradition of significant unstructured time for informal discussions to support exchange of ideas and community building. Be sure to use these intervals for technical brainstorming and collaboration building, as well as career and business development.

All papers were selected on the basis of high-quality content and leading-edge contribution. Those deemed of broader interest to the attendees were designated as oral and those of special interest as poster. The "shotgun" format is used to inform the attendees of the content of the upcoming poster session of the day. Late News Oral and Poster papers selection process occurred in mid-March and bring the latest research to the attendees. In addition, we again have something new and exciting planned for the period formally known as the "Rump Session." A tremendous "thank you" goes to Mark Allen and the Technical Program Committee for putting together the technical content of the Workshop, which required studying, debating, ranking, and selecting from 217 submitted quality abstracts.

James Walker (Chair), Gary O'Brien, and Leland "Chip" Spangler worked tirelessly to create the commercial support and exhibition contributions of this meeting. A special thanks also goes to Sunil Bhave who worked on student travel support development, and the Transducers Research Foundation and Analog Devices for their travel grant support for the presenting student authors. The involvement of these individuals, and the financial support of the exhibitors and corporate sponsors are valuable and essential features of the Hilton Head Workshop, and I am most thankful to have had these outstanding people and companies participate in this 30th Anniversary celebration.

Katharine Cline and her team at Preferred Meeting Management, Inc., above all, deserve special recognition and thanks for all of their hard work and superb organization in pulling this meeting together and for making it run so smoothly. The work they do "behind the scenes" over the two years of preparation to make this meeting special is exceptional; our community and our meeting has been the beneficiary of their excellence and commitment.

This meeting belongs to all of you; thank you for your enthusiastic participation. My best wishes for a memorable gathering in Hilton Head Island this June 2014.

Mehran Mehregany
General Chair

Organizing Committee

General Chair	Mehran Mehregany, Case Western Reserve University
Technical Program Chair	Mark G. Allen, University of Pennsylvania, USA
Student Travel Grant Chair	Sunil Bhave, Cornell University, USA
Commercial Development Chair	James Walker, Kaplan Breyer Schwartz & Ottesen, LLP, USA
Commercial Development Vice-Chair	Gary O'Brien, Bosch, LLC, USA
Commercial Development Vice-Chair	Leland "Chip" Spangler, Aspen Microsystems, USA

Technical Program Committee Members

Mark G. Allen
University of Pennsylvania, USA

Oliver Brand
Georgia Institute of Technology, USA

Rob Candler
University of California, Los Angeles, USA

Alissa Fitzgerald
AM Fitzgerald & Associates, USA

Xiao-An "Sean" Fu
University of Louisville, USA

Michael Gaitan
National Institute of Standards & Technology, USA

Florian Herrault
HRL Laboratoties, USA

David Horsley
University of California, Davis, USA

Hal Jerman
Coherent, USA

Houri Johari Galle
InvenSense, USA

Hanseup Kim
University of Utah, USA

Jae Kwon
University of Missouri, USA

Tina Lamers
Avago Technologies, USA

Pete Loeppert
Knowles Electronics, Inc., USA

Mehran Mehregany
Case Western Reserve University, USA

Moses Noh
Drexel University, USA

Gianluca Piazza
Carnegie Mellon University, USA

Dennis Polla
ODNI, USA

Mina Rais-Zadeh
University of Michigan, USA

Swaminathan Rajaraman
Axion BioSystems, Inc., USA

Mark Sheplak
Univeristy of Florida, USA

George Skidmore
DRS Technologies, USA

Srinivas Tadigadapa
Pennsylvania State University, USA

Technical Program Committee

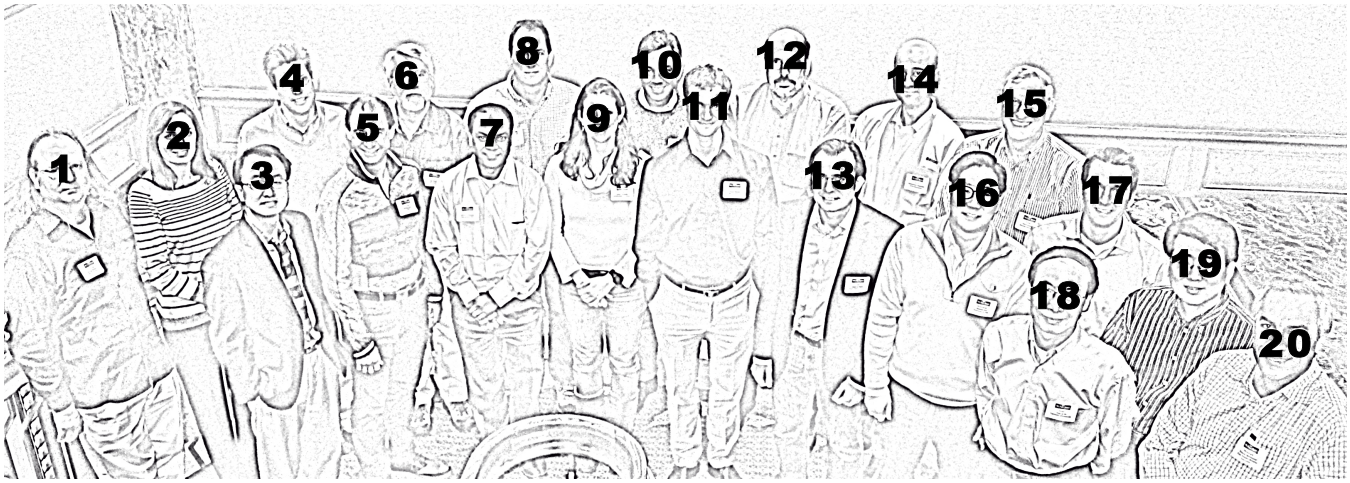

1 – George Skidmore
2 – Mina Rais-Zadeh
3 – Moses Noh
4 – Oliver Brand
5 – Michael Gaitan
6 – Hal Jerman
7 – Srinivas Tadigadapa
8 – Mark Sheplak
9 – Alissa Fitzgerald
10 – David Horsley
11 – Florian Herrault
12 – Mark G. Allen
13 – Gianluca Piazza
14 – Swaminathan Rajaraman
15 – Pete Loeppert
16 – Hanseup Kim
17 – Rob Candler
18 – Xiao-An “Sean” Fu
19 – Jae Kwon
20 – Mehran Mehregany

Not pictured: Houri Johari Galle, Tina Lamers, and Dennis Polla

Transducer Research Foundation

Officers

President G. Benjamin Hocker, *USA*

Vice-President Antonio J. Ricco, *Stanford University, USA*

Treasurer Mehran Mehregany, *Case Western Reserve University, USA*

Secretary Richard Muller, *University of California at Berkeley, USA*

Directors

Mark Allen
University of Pennsylvania, USA

G. Benjamin Hocker, *USA*

Tom Kenny
Stanford University, USA

Mehran Mehregany
Case Western Reserve University, USA

Dave Monk
Freescale Semiconductor, USA

Richard Muller
University of California, Berkeley, USA

Antonio J. Ricco
Stanford University, USA

Marty Schmidt
Massachusetts Institute of Technology, USA

Leland "Chip" Spangler
Aspen Microsystems, USA

Kimberly Turner
University of California, Santa Barbara, USA

Overseers

Luc Bousse
Bio-Rad Laboratories, Inc., USA

Joe Giachino, *USA*

Roger Howe
Stanford University, USA

Wen Ko, *USA*

Kurt Petersen, *USA*

Steve Senturia, *USA*

Ken Wise, *USA*

Executive Director

Katharine K. Cline
Preferred Meeting Management, USA

Acknowledgements

Special acknowledgement to the Transducer Research Foundation, Inc. and Analog Devices, Inc. for their educational grant funding support of this Workshop.

Exhibitors and Benefactors

We gratefully acknowledge the support of this Workshop from the following companies and institutions as of the printing of May 28, 2014:

Analog Devices, Inc.
Berkeley Sensor & Actuator Center (BSAC)
Case School of Engineering San Diego, Case Western Reserve University
Coventor, Inc.
EV Group
FemtoTools
Freescale
Heidelberg Instruments
ICSPI Corp.
IntelliSense
Kaplan Breyer Schwarz & Ottesen, LLP
Knowles
Lionix, BV
MEMS and Nanotechnology Exchange
MEMS Industry Group
MEMS Journal, Inc.
memsstar Ltd.
National Institute of Standards and Technology (NIST)
Oxford Instruments
Polytec, Inc.
Robert Bosch LLC
Silex Microsystems Inc.
Silicon Sensing Systems
SoftMEMS
SPTS Technologies
Tousimis
Ulvac Technologies, Inc.
University of Louisville Micro/Nano Technology Center
University of Pennsylvania

Table of Contents

Scroll to the title and select a **Blue** link to open a paper. After viewing the paper, use the bookmarks to the left to return to the beginning of the Table of Contents.

Sunday, June 8

6:00 p.m. - 9:00 p.m. **Registration and Welcome Reception**

Monday, June 9

7:00 am **Breakfast**

7:45 am **Welcome**
Mehran Mehregany, *Case Western Reserve University, USA*
Mark G. Allen, *University of Pennsylvania, USA*

Plenary Speaker I

Session Chair: O. Brand, *Georgia Institute of Technology, USA*

Session 1 - Biomedical & Cellular Devices

Session Chair: M. Noh, *Drexel University, USA*

10:05 am **Break and Tabletop Exhibits**

Session 2 - Bioassays
Session Chair: D. Horsley, *University of California, Davis, USA*

10:30 am **MEMS DEVICE INTEGRATED WITH VERTICALLY ALIGNED CARBON NANOTUBES FOR VIRUS CAPTURE AND DETECTION** 17
Y.-T. Yeh, N. Perea-Lopez, Y. Tang, B.U. McKellar, R. Harouaka, H. Lu, M. Terrones, and S.-Y. Zheng
Pennsylvania State University, USA

10:50 am **MULTIPLEXED PROTEOMICS USING TWO ORDERS OF MAGNITUDE ENHANCED DIELECTROPHORESIS: A COMPREHENSIVE ELECTRICAL AND ELECTROTHERMAL DESIGN METHODOLOGY** 21
S. Emaminejad, M.T. Barako, R.W. Davis, R.W. Dutton, K.E. Goodson, and M. Javanmard
Stanford University, USA

11:10 am **MICROFLUIDIC BARCODE ASSAY FOR MULTIPLEXED CLINICAL DIAGNOTICS** 24
R. Lin, A. Skandarajah, R.E. Gerver, D.A. Fletcher, and A.E. Herr
University of California, Berkeley, USA

11:30 am **Poster Preview Session 1**
Session Chair: H. Jerman, *Coherent, Inc., USA*

12:15 pm **Networking Lunch**

1:45 pm - 4:45 pm **Poster Session 1 – Contributed and Late News**
Session Chairs: X.-A. Fu, *University of Louisville, USA* and S. Tadigadapa, *Pennsylvania State University, USA*
See listing of posters for Session 1

4:45 pm **End of Day**

Tuesday, June 10

7:30 am Breakfast

Plenary Speaker II

Session Chair: M. Mehregany, *Case Western Reserve University, USA*

8:15 am **NEEDS AND OPPORTUNITIES FOR NANOTRIBOLOGY IN MEMS AND NEMS** 28
Robert W. Carpick, G.E. Wabiszewski, and F. Streller
University of Pennsylvania, USA

Session 3 - Materials & Surfaces

Session Chair: M. Gaitan, *National Institute of Standards & Technology, USA*

9:05 am **SILICON MIGRATION OF THROUGH-HOLES IN SINGLE- AND POLY-CRYSTALLINE SILICON MEMBRANES** 32
J. Stehle[1,2], V.A. Hong[3], A. Feyh[1], G.J. O'Brien[1], G. Yama[1], O. Ambacher[2], B. Kim[1], and T.W. Kenny[3]
[1]Robert Bosch Research and Technology Center, USA, [2]University of Freiburg, GERMANY, and [3]Stanford University, USA

9:25 am **IMAGE VALIDATION OF PARALLEL SCANNING TUNNELING MICROSCOPY WITH A CMOS MEMS PROBE ARRAY** 36
Y. Zhang, Y. Tang, L.R. Carley, and G.K. Fedder
Carnegie Mellon University, USA

9:45 am **Break and Tabletop Exhibits**

Session 4 - Fabrication & Materials

Session Chair: F. Herrault, *HRL Laboratories, USA*

10:10 am **RETAINING HIGH AREAL IN-PLANE MAGNETIC ENERGY DENSITY OVER LARGE MAGNETIC THICKNESS: A PERMANENT MAGNETIC MICROLAMINATION APPROACH BASED ON SEQUENTIAL MULTILAYER ELECTROPLATING** 40
Y. Li[1], J. Kim[2], M. Kim[2], A. Armutlulu[2], and M.G. Allen[1]
[1]University of Pennsylvania, USA and [2]Georgia Institute of Technology, USA

10:30 am **ATOMIC LAYER DEPOSITED PLATINUM AS A SENSOR MATERIAL: UNIFORMITY, 1/F NOISE, AND YOUNG'S MODULUS** 44
T.S. English[1], F. Purkl[2,3], A. Daus[2], J. Provine[1], Y. Won[1], G. Yama[2], A. Feyh[2], G. O'Brien[2], K.E. Goodson[1], O. Ambacher[3], and T.W. Kenny[1]
[1]Stanford University, USA, [2]Robert Bosch RTC, USA, and [3]University of Freiburg, GERMANY

10:50 am **STRAIN-MEDIATED ELECTRICAL CONTROL OF MAGNETIZATION IN MICRON-SCALE NICKEL RING ON PMN-PT** 48
H. Sohn[1], M.E. Nowakowski[2], J. Hockel[1], C. Liang[1], K. Wetzlar[1], M.A. Marcus[3], A. Doran[3], A.T. Young[3], M. Kläu[4], C.S. Lynch[1], G.P. Carmen[1], J. Bokor[2], and R.N. Candler[1,5]
[1]University of California, Los Angeles, USA, [2]University of California, Berkeley, USA, [3]Lawrence Berkeley National Lab, USA, [4]Johannes Gutenberg-Universität, Mainz, GERMANY, and [5]California NanoSystems Institute, USA

Session 5 - Magnetic Transducers

Session Chair: R. Candler, *University of California, Los Angeles, USA*

11:10 am **LORENTZ FORCE MAGNETOMETER WITH QUADRATURE FREQUENCY MODULATION** 52
M. Li[1], S. Sonmezoglu[1], E.J. Ng[2], V.A. Hong[2], C.H. Ahn[2], Y. Yang[2], T.W. Kenny[2], and D.A. Horsley[1]
[1]University of California, Davis, USA and [2]Stanford University, USA

11:30 am **HIGH SENSITIVITY MAGNETIC SENSOR CONCEPT BASED ON MAGNETOSTRICTIVELY INDUCED PERTURBATIONS IN PLATE RESONATOR CHARACTERISTICS** 56
G. Hatipoglu and S. Tadigadapa
Pennsylvania State University, USA

11:50 am **HIGH-GRADIENT MEMS ELECTROMAGNETS FOR PARTICLE BEAM MANIPULATION** 60
J. Harrison[1], J. Wu[1], O. Paydar[1], Y. Hwang[1], E. Threlkeld[1], J. Rosenzweig[1], P. Musumeci[1], and R. Candler[1,2]
[1]University of California, Los Angeles, USA and [2]California NanoSystems Institute, USA

12:10 pm - 1:40 pm **Networking Lunch**

7:00 pm - 10:00 pm **Banquet**

Wednesday, June 11

7:30 am Breakfast

Plenary Speaker III

Session Chair: M.G. Allen, *University of Pennsylvania, USA*

8:15 am **MEMS ENTREPRENEURIAL PERSPECTIVES** 64
Kurt Petersen
Band of Angels, USA

Session 6 - High-Q Resonators

Session Chair: M. Rais-Zadeh, *University of Michigan, USA*

9:05 am **1 MILLION Q-FACTOR DEMONSTRATED ON MICRO-GLASSBLOWN FUSED SILICA WINEGLASS RESONATORS WITH OUT-OF-PLANE ELECTROSTATIC TRANSDUCTION** 68
D. Senkal, M.J. Ahamed, S. Askari, and A.M. Shkel
University of California, Irvine, USA

9:25 am **GAN MEMS RESONATOR USING A FOLDED PHONONIC CRYSTAL STRUCTURE** 72
S. Wang, L.C. Popa, and D. Weinstein
Massachusetts Institute of Technology, USA

9:45 am **INVESTIGATION OF ENERGY DISSIPATION IN LOW FREQUENCY VIBRATORY MEMS DEMONSTRATING A RESONATOR WITH 25 MINUTES TIME CONSTANT** 76
S.A. Zotov, B.R. Simon, G. Sharma, J. Han, I.P. Prikhodko, A.A. Trusov, and A.M. Shkel
University of California, Irvine, USA

10:05 am **PHASE NOISE REDUCTION IN AN OSCILLATOR THROUGH COUPLING TO AN INTERNAL RESONANCE** 80
D.A. Czaplewski[1], B.S. Strachan[2], S.W. Shaw[2], M.I. Dykman[2], and D. Lopez[1]
[1]Argonne National Laboratory, USA and [2]Michigan State University, USA

10:25 am **Break and Tabletop Exhibits**

Session 7 - Resonant Systems

Session Chair: G. Piazza, *Carnegie Mellon University, USA*

10:50 am **A MEMS-BASED TUNABLE RF CHANNEL-SELECTING SUPER-REGENERATIVE TRANSCEIVER FOR WIRELESS SENSOR NODES** 83
T.O. Rocheleau, T.L. Naing, J.N. Nilchi, and C.T.-C. Nguyen
University of California, Berkeley, USA

11:10 am **DEVICE-LAYER OVENIZATION OF FUSED SILICA MICROMECHANICAL RESONATORS FOR TEMPERATURE-STABLE OPERATION** 87
Z. Wu, A. Pecsalski, and M. Rais-Zadeh
University of Michigan, USA

11:30 am **PHASE NOISE SQUEEZING BASED PARAMETRIC BIFURCATION TRACKING OF MIP-COATED MICROBEAM MEMS SENSOR FOR TNT EXPLOSIVE GAS SENSING** 91
L.L. Li[1], E.L. Holthoff[2], L.A. Shaw[1], C.B. Burgner[1], and K.L. Turner[1]
[1]*University of California, Santa Barbara, USA and* [2]*Army Research Laboratory, USA*

11:50 am **RESONANT M/NEMS PIEZORESISTORS FOR NARROW-BAND ELECTRONIC AMPLIFICATION** 95
A. Ramezany, M. Mahdavi, X. Guo, and S. Pourkamali
University of Texas, Dallas, USA

12:10 pm **Poster Preview Session 2**
Session Chair: M. Sheplak, *University of Florida, USA*

12:55 pm **Networking Lunch**

2:25 pm - 5:25 pm **Poster Session 2 - Contributed and Late News**
Session Chairs: H. Johari-Galle, *InvenSense, USA* and S. Rajaraman, *Axion Biosystems, USA*
See listing of posters for Session 2

6:30 pm - 8:00 pm **Poster Session 3 - Commercial & Open Posters**
Session Chairs: A. Fitzgerald, *AM Fitzgerald & Associates, USA* and P. Loeppert, *Knowles Electronics, USA*
Papers not included in the Technical Digest

8:00 pm - 10:30 pm **Rump Session**
Session Chairs: M. Allen, *University of Pennsylvania, USA*

10:30 pm **End of Day**

Thursday, June 12

7:30 am **Breakfast**

Session 8 Late News Papers Oral

Session Chair: T. Lamers, *Avago Technologies, USA*

8:15 am **AN ETCH HOLE-FREE PROCESS FOR TEMPERATURE-COMPENSATED, HIGH Q, ENCAPSULATED RESONATORS** 99
E.J. Ng, Y. Yang, Y. Chen, and T.W. Kenny
Stanford University, USA

8:30 am **ETCH-A-SKETCH RESONATOR** 101
R. Wang[1], S.A. Bhave[1], and K. Bhattacharjee[2]
[1]Cornell University, USA and [2]RF Micro Devices, Inc., USA

8:45 am **FUSED SILICA MICRO BIRDBATH SHELL RESONATORS WITH 1.2 MILLION Q AND 43 SECOND DECAY TIME CONSTANT** 103
J. Cho, T. Nagourney, A. Darvishian, B. Shiari, J.-K. Woo, and K. Najafi
University of Michigan, USA

9:00 am **LEVITATION OF UNTETHERED STRESS-ENGINEERED MICROFLYERS USING THERMOPHORETIC (KNUDSEN) FORCE** 105
V. Foroutan[1], R. Majumdar[1], O. Mahdavipour[1], S.P. Ward[2], and I. Paprotny[1]
[1]University of Illinois at Chicago, USA and [2]University of California, San Diego, USA

9:15 am **SELECTIVE WATER TRANSPORT ACROSS UNIFORM SUB-NANOMETER PORES IN MICROFABRICATED MEMBRANES** 107
T. Humplik[1], R. Raj[1], S.C. Maroo[1], T. Laoui[2], and E.N. Wang[1]
[1]Massachusetts Institute of Technology, USA and
[2]King Fahd University of Petroleum and Minerals, SAUDI ARABIA

9:30 am **TEMPERATURE-COMPENSATED TETHERLESS BULK ACOUSTIC PHONON TRAP FOR SELF-OVENIZED OSCILLATORS** 109
R. Tabrizian, A. Norouzpour-Shirazi, and F. Ayazi
Georgia Institute of Technology, USA

9:45 am **Break and Tabletop Exhibits**

Session 9 - Lab Chip & Microfluidics
Session Chair: H. Kim, *University of Utah, USA*

11:30 am - 1:00 pm **Networking Lunch and Workshop Adjourns**

POSTER SESSION 1
Contributed and Late News
Monday, June 9
1:45 pm - 4:45 pm

Actuators

Bio-Inspiration and Biomedical Devices

Biological Diagnostics, Systems, and Analysis

Characterization, Fabrication and Materials

Gas Sensors

Microfluidics

Physical and Optical Sensors and Devices

Power Generation and Management

Resonant Devices

POSTER SESSION 2
Contributed and Late News
Wednesday, June 11
2:25 pm - 5:25 pm

Actuators

Bio-Inspiration and Biomedical Devices

Biological Diagnostics, Systems, and Analysis

Physical and Optical Sensors and Devices

Late News

MEMS AND MORE FOR THE BRAIN: THE CLUSTER OF EXCELLENCE *BRAINLINKS-BRAINTOOLS* AT THE UNIVERSITY OF FREIBURG

O. Paul and P. Ruther*
Microsystem Materials Laboratory, Department of Microsystems Engineering (IMTEK),
University of Freiburg, Germany

ABSTRACT

In the fierce competition among German academic institutions in the national Excellence Initiative, the University of Freiburg has successfully defended the excellence cluster project *BRAINLINKS–BRAINTOOLS*. The cluster benefits of 28 Mio € of funding for the period from Nov. 2012 to Oct. 2017. Over 40 principal investigators of the University Clinic Freiburg and the Faculties of Biology and Engineering are teaming up, involving about a hundred young scientists. The cluster aims to bring the state of the art in bi-directional brain-machine interfaces to a new level. Its research program merges results on the neurocomputational foundations, novel MEMS tools, and computer science methods into platforms designed for clinically relevant applications. With Parkinson's disease, epilepsy, stroke, and paralysis, four major neurological disabilities are addressed.

INTRODUCTION

Whether the brain is the last frontier of science, as has been stated, may be questioned. However, without any doubt, its about 10^{11} neurons and their 10^{14} interconnections constitute a multiscale system of awe-inspiring complexity leaving much to discover.

Large project frameworks, such as the *Human Brain Project* (HBP) in Europe or the *Brain Initiative* in the USA have outlined steps to tackle this formidable challenge. HBP has been originally designed to trigger research investments at a level of about one euro-cent per neuron, while the *Brain Initiative* starts with an initial expenditure of 100 Mio US$ in 2014 and is planned for a duration of ten years.

Other leading centers of neurotechnology pursue more focused endeavors. Among them are the NSF Engineering Research Center for Sensorimotor Neural Engineering (CSNE) at the University of Washington, Seattle, emphasizing the development of neural control systems for prosthetic limbs; the Edmond and Lily Safra Center for Brain Sciences (ELSC) in Jerusalem, Israel, covering all aspects of neuroscience including computational neuroscience as well as motor BMI and DBS intervention; and thirdly, the Australian Bionic Vision Consortium (BVC) with its focus on visual prosthetics.

THE *BRAINLINKS-BRAINTOOLS* CLUSTER

Aims

The overall scientific goal of *BrainLinks-BrainTools* [1] is to to raise the bi-directional interaction between technical instruments and the brain to a new level by developing flexible yet stable, and adaptive yet robust hybrid brain-machine interfaces. With funds amounting to 28 M€ for five years, the cluster builds on the existing competence at the University of Freiburg and the University Clinic Freiburg in

- Neuroscience (Bernstein Center Freiburg; Department of Biology),
- MEMS engineering (Dept. of Microsystems Engineering [IMTEK], Faculty of Engineering),
- Artificial intelligence, machine learning, and robotics (Dept. of Computer Science [IIF], Faculty of Engineering),
- Clinical neuromedicine (University Clinic Freiburg), and
- Ethics of science and technology (Institute of Ethics and History of Medicine, Faculty of Medicine).

It combines the corresponding activities into a tightly knit research program. As a full-range university, the University of Freiburg thereby materializes its mission statement to contribute solutions to the pressing interdisciplinary challenges of our time. With *BRAINLINKS-BRAINTOOLS* it does so by establishing a strong link between engineering, the life sciences, and philosophy.

The cluster's scientific and technological activities are centered on clinical scenarios addressing four major neurological pathologies, namely Parkinson's disease, epilepsy, stroke, and paralysis. The approach to these disabilities is guided by two long-term visions for intelligent neuroprosthetic technology platforms. These are:

- Prosthetic limbs with Neural Control (LiNCs) defining brain-controlled assistive devices and prostheses to return movement capacity in paralyzed patients and amputees, and to improve the rehabilitation of patients suffering from stroke or brain trauma;
- Smart Energy-Autonomous Micronodes (SEAMs) targetting implantable, autonomous devices with closed-loop feedback through implanted recording and stimulation for the treatment of neurological disorders originating in pathological network structures and activity dynamics, such as epilepsy and Parkinson's disease, among others.

These two platforms will rely on far more than just novel MEMS devices. They will capitalize heavily on methods of computer science, especially in view of LiNCs with minimally invasive brain-machine interfaces, and of data evaluation and action planning needed for SEAMs.

Structure

The cluster is structured into three research areas and a central service and management unit. It relies on a relatively lean management and invests the dominant part of its funds directly into research and into strategic support measures ultimately benefiting research as well.

Research Area A 'Foundations' addresses the neurocomputational foundations, both in theory and experiment. The aim is to identify optimal strategies as to when, where, and how to interact with the brain, whether it is to read out information or induce intended changes in the activity of neural networks, from local circuit units to large-scale networks spreading across multiple brain areas. A range of techniques, from network modeling to functional magnetic resonance imaging (MRI), electrophysiology, and optogenetic tools, applied to in vitro and in vivo models, are used.

Research Area B 'Core Technologies' focuses on the development of multifunctional technical tools for interfacing with the brain, based on methods of microsystems engineering and computer science. Tailored for spatial resolutions from 30 µm to 5 mm, the tools are designed to be deployed in various brain regions, from the cortical surface to deep brain structures, both in view of monitoring neuronal activity and modulating, i.e., stimulating or inhibiting, it. The electrical, magnetic, and optical signal domains are being addressed. Advanced algorithms for signal processing and interpretation, data handling, and action planning turn the tools into stable, adaptive and robust neurotechnological interfaces.

9781940470016/HH2014/$25©2014TRF
DOI 10.31438/trf.hh2014.1

Solid-State Sensors, Actuators and Microsystems Workshop
Hilton Head Island, South Carolina, June 8-12, 2014

Thirdly *Research Area C 'Applications'* pursues the objective of developing therapies and paradigms transferring the results of Research Areas A and B into novel preclinical and clinical applications in the context of the above-mentioned neurological pathologies.

Strategic measures

BRAINLINKS-BRAINTOOLS has formed a strategic axis with the CSNE, the ELSC, and the BVC.

In addition, the cluster has already four out of five young research leader positions with candidates pursuing a research program of their design and endowed with funds for building up a small research teams for the duration of the cluster.

Three new professor positions have been defined and are currently being filled in the areas of

- Optophysiology (Faculty of Biology),
- Functional models and multi-scale networks (Faculty of Medicine), and
- Neurorobotics (Faculty of Engineering),

in order to round off the University of Freiburg's academic portfolio in neurotechnology and neuroscience.

Furthermore, the cluster has nationally and internationally teamed up with a large group of academic, clinical, and industrial application centers for training, dissemination, and transfer. It is open to further collaborations.

MEMS DEVELOPMENTS

Projects with durations of one year ('exploratory projects') and up to three years ('advanced projects') are funded based on periodic calls for proposal with a review-based selection process. In the following we outline currently funded projects. Further information is available online [1].

Current MEMS projects in *BRAINLINKS-BRAINTOOLS*

Project *AdvancedEDC* pushes the state of the art in highly integrated, electronically switchable, intracortical probe arrays for recording and stimulation. Advances over current electronic depth control (EDC) probes [2] aim at increasing (i) the reconfiguration flexibility and speed for switching between electrode configurations, (ii) the spatial resolution by using commercial 0.18 µm CMOS technology, (iii) the signal quality by the on-shaft cointegration of preamplifiers, filters, and analog-to-digital converters (ADC), and (iv) the number of simultaneously extracted neural signals up to 32 at least. Probes are tailored with respect to functionality and shaft dimensions to the needs of the neuroscientific experiments pursued by the cluster partners. Studies of mouse epilepsy for instance impose particularly severe restrictions on the probe dimensions.

The probe hardware will be complemented by dedicated in-situ microelectronic hardware for executing neurocomputational tasks, and by algorithms for the analysis and classification of neuronal signals, for data reduction and feedback policy learning.

Project *COLUMNS* addresses the development of non-invasive light sources for optogenetic experiments. Light beams shaped as Bessel beams [3] offer the property of beam self-reconstruction when penetrating diffractive media. Beam shaping is achieved by conical axicon elements [3] with thermally controlled focal lengths. Laser diodes will serve as light sources. A dense array of Bessel beams will allow one to generate the spatio-temporal patterns within the brain tissue required for a wide variety of optogenetic studies.

Similarly, project *WOLDOR* aims at the development of intracortical and epicortical optrodes, i.e., light sources for optogenetic experiments combined with recording electrodes. The approach is different, however, since the intracortical probes will be of the penetrating type, based on slender probe shafts [4], while the epicortical structures will capitalize on established fabrication techniques for PDMS rubber and polyimide (PI) based flexible epicortical grid (ECoG) arrays [5]. The project focuses on the development of fabrication, packaging, and testing techniques. Light sources with optogenetically relevant wavelengths, e.g., 450 nm, will be integrated into these multifunctional structures. The systems are electrically controlled and thus avoid the clumsy optical links via glass fibers of conventional optogenetic probes.

Project *MAGRITE* focuses on MEMS based micro-coils and culture chambers for in-situ high-resolution magnetic resonance imaging (MRI) studies of epileptogenesis in mouse brain slices. The studies aim at elucidating structural and molecular changes associated with the development of epileptic seizures. Micro-coil fabrication relies on wire-bonding and polymer micromachining [6]. Resolutions down into the 10 µm range have so far been achieved and further improvements by design optimization and implementation of novel spin hyperpolarization techniques [7] can be expected.

Compatibility with functional MRI (fMRI) is a definite advantage, if not a necessity, for any neural probe components. To support the development of fMRI compatible tools, project *NEUMARE* builds a database of MRI relevant properties of materials used for probe fabrication and identifies rules for judicious probe design. The materials include Al_2O_3, diamond-like carbon SiC, Si, IrO_x, Fe, Cu, Au, solder alloys, Mn, Mo, Pt, W, PDMS, PI, and teflon, among others [8]. In composite structures, magnetic susceptibility jumps between these materials in the ppm range can cause image distortions and artifacts, which require minimization by simulation and design optimization.

Project *SEAM-TEG* addresses the issue of in-situ energy scavenging for powering implanted neurotechnical components. It attempts to reach this goal by thermoelectric energy conversion using the temperature gradient between the body and the ambient to which subcutaneous tools may be exposed. Thermopiles based on electroplated Bi_2Te_3 and Sb_2Te_3 [9] are explored as a promising choice with acceptable energy conversion efficiencies.

New projects *NeuroTRACEIT*, *MAKE IT ReaL*, and *SEAM-WiT* propose to concentrate, respectively, on: the controlled release of fluorescent dies from polymer (PEDOT) electrodes for the precise post-mortem localization of neurons from which recordings were previously made; next-generation micro-ECoGs for the closed-loop recording and stimulation in an awake sheep model as a paradigm for the chronic functional testing of neural implants; the development of a powerful, versatile telemetry unit for energy and bi-directional data transfer with implantable neural probes.

Neurotechnology by the Microsystem Materials Laboratory

Probe fabrication approach

Silicon based neural probes for intracerebral recording have established themselves as valuable and reliable tool for acute and sub-chronic neuroscientific experiments. Probes by the pioneering groups at the University of Michigan [10] and University of Utah [11] have been used by many researchers and are being commercialized by *NeuroNexus* and *Blackrock Microsystems*, respectively. Fabrication of the Michigan probes has traditionally made use of heavily B-doped silicon shafts with thicknesses around 15 µm fixed on a thicker base and connected to the external instrumentation by ribbon cables based on the same highly doped material. In the case of the Utah probes the fabrication has proceeded by ion migration through thicker silicon substrates than standard wafers followed by trenching using dicing, and sharpening by isotropic etching [11].

A third approach benefiting of similar design degrees of freedom in view of the lateral shaft dimensions as the University of Michigan's, but at the same time offering design freedom regarding shaft thickness as well, has been proposed by the authors' team [12]. It is termed etch-before-grinding (EBG). After completion of the thin film deposition and structuring processes necessary for the definition of the recording sites and interconnection leads as well as their passivation, the probe shape is defined by deep reactive ion etching (DRIE) of the wafer front; the intended probe thickness is obtained by rear wafer grinding. Electrode metalizations apply either Pt or IrO_x combined with Ti/Au/Pt layer sandwiches used for interconnection leads along the slender probe shafts. Probes with shaft lengths between 1 and 40 mm, widths down to 30 µm, and thicknesses down to 25 µm have been demonstrated. Impedances for electrodes sites with areas of 962 μm^2 at 1 kHz are typically 1.2 MΩ and 140 kΩ for Pt and IrO_x electrodes, respectively [13][2]. Examples of probes are shown in Fig. 1.

Similarly fabricated probes with integrated fluidic channels [14] and biosensors [15] have been realized by dual-side DRIE of Si combined with additional Si micromachining, bonding processes, and integration of dedicated sensing layers.

Electronic depth control probes

Using the above techniques it is straightforward to realize probes with integrated microelectronic circuitry as well. To this end, before the EBG process, the substrates are processed using commercial CMOS technology. The advantage is that a vastly larger number of electrode sites can be integrated along the shafts, each site switchable to a given number of output lines. In shafts with 4 mm lengths realized in a 0.6 µm CMOS technology by X-FAB, Erfurt, Germany, 188 sites can each be switched to two among eight output lines. The switches are standard transmission gates controlled by D flip-flops linked as a shift register [2]. The switch arrangement allows any configuration of two tetrodes and a large number of configurations with eight sites scattered along the shaft to be selected. Combs with four such shafts are available as well. Since the microelectronic components are distributed along the shafts, the probe systems benefit of a relatively small base, which facilitates probe usage in sub-chronic experiments [16]. EDC probes are shown in Fig. 1(b).

In *AdvancedEDC* this state of the art is being pushed further by the use of 6-metal 0.18 µm technology by X-FAB. This technology node will enable significantly more smartness to be integrated into the probe shafts and bases.

Optrodes

Optogenetics has emerged as an extremely fruitful technique enabling experiments where neuronal activity is triggered or inhibited by optical signals rather than electrochemically [17]. This is achieved by viral transfection of neurons with optically sensitive

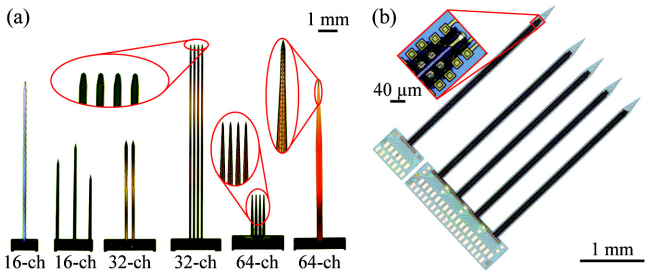

Fig. 1: Selected intracerebral neural probes: (a) passive probes with up to 64 channels (ch) and (b) active EDC probes with on-shaft circuitry for selecting eight out of 188 channels per shaft.

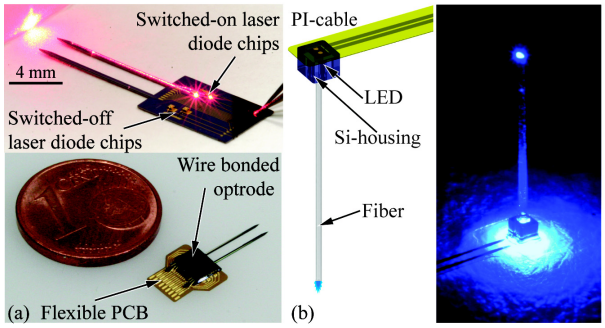

Fig. 2: Optrodes of (a) planar design with laser diodes and waveguides on slender Si probe shafts [4] and (b) miniaturized light source using LED chip mounted in Si housing and interfaced by polyimide (PI) cable (adapted from [18].

channel proteins, so-called opsins, variants of which can be expressed selectively in different types of neuronal cells. Optogenetic experiments require light of appropriate optical wavelengths to be dissipated in the neuronal network under study.

Traditionally this has been done using optical fibers connected to light sources external to the subject. In the absence of suitable optical couplers with rotational freedom, the relatively stiff connections severely restrict the freedom of motion of animals and thus are disturbing studies with freely behaving animals.

One idea to overcome this limitation has been to integrate the light sources directly onto the probes. Thereby the fiber connection is replaced by a purely electrical connection of the probe either to a telemetric headstage or through highly flexible PI cables. Figure 2 shows two examples of such systems [4][18]. In the first {Fig. 2(a)}, four laser diodes are integrated on the base of a two-shank probe, the light being guided to the vicinity of recording sites near the probe tip by SU-8 waveguides. In the second case {Fig. 2(b)}, a light emitting diode (LED) is mounted on a silicon platform carrying a short optical fiber.

Three-dimensional probes

In order to arrange stimulation and recording sites into even more powerful three-dimensional (3D) arrays we have explored successively refined assembly techniques. Probes of the planar type described above were inserted into dedicated platforms with micromachined bays for hosting probe bases. In a first generation, the challenge of the vertical-to-horizontal lead transfer from probe to base was addressed by electroplated Au contacts overhanging the bays [19]. Relaxing the severe geometrical tolerances of this approach, the bays were later enhanced by thermomechanical actuators pressing the bases against the contacts on a platform/cable assembly [20]. A third design relied on bridging the gaps between the contacts on the platform and the basis by electroplating [21].

Most recently, we have explored a modular system shown in Fig. 3 with spacer modules separating probe levels with a high angular accuracy better than 1°, both in the plane of the probe and in the out-of-plane direction [22].

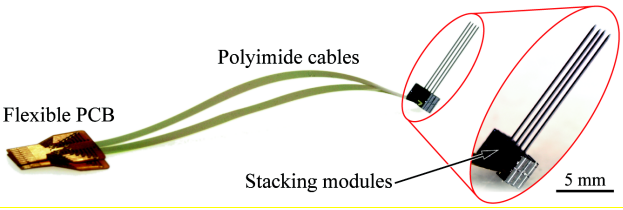

Fig. 3: 3D probe array based on stacking modules for probe alignment (adapted from [22]).

Probe assemblies and handling tools

In view of the widely varying methods and skills of experimental neuroscientists, a lesson well learnt is that there is no one-fits-all solution for handling the probes and interconnecting them to the experimentalist's preferred instrumentations. For this reason, customized interconnection solutions based on printed circuit boards for direct probe mounting or indirect connection via flexible PI cables with Pt lines have been custom-designed. We have realized assemblies compatible with vacuum chucks, micromanipulators, microdrives, and autonomous headstages, among others.

CONCLUSION AND OUTLOOK

BRAINLINKS-BRAINTOOLS is currently taking up speed through the projects outlined above. In the meantime a range of mature complementary neurotechnological projects independent of this funding source is being pursued at IMTEK, including the EC-funded projects *NeuroSeeker*, *LifeHand2*, and *BrainCon*. Spin-off activities are deployed by *CorTec* for the commercialization of ECoGs for human applications, and *Atlas Neuroengineering* for passive and active probes and assemblies. Overall these activities have created in Freiburg a hub of competence in neurotechnology embedded in a dense network of user groups.

In the early phase, most of the MEMS tools described in this paper are destined for acute and sub-chronic applications with animal models. Their transfer to human subjects will require a prolonged effort in order to ensure their minimal invasiveness and long-term reliability.

ACKNOWLEDGMENTS

Funding by the DFG through project no. EXC1086 *BRAINLINKS-BRAINTOOLS* is gratefully acknowledged.

REFERENCES

[1] www.brainlinks-braintools.uni-freiburg.de.

[2] K. Seidl, M. Schwaerzle, I. Ulbert, H.P. Neves, O. Paul, P. Ruther, "CMOS-Based High-Density Silicon Microprobe Arrays for Electronic Depth Control in Intracortical Neural Recording - Characterization and Application", J. Microelectromech. Syst., 21, 1426-1435 (2012).

[3] J. Brunne, U. Wallrabe, "Tunable MEMS Axicon Mirror Arrays", Optics Letters, 38 (11), 1939-1941 (2013).

[4] M. Schwaerzle, K. Seidl, U. Schwarz, O. Paul, P. Ruther, "Ultracompact Optrode With Integrated Laser Diode Chips and SU-8 Waveguides for Optogenetic Applications", Proc. IEEE MEMS Conf. 2013, Taipei, 2013, pp. 1029-1032.

[5] C. Henle, M. Schuettler, J. Rickert, T. Stieglitz, "Towards Electrocorticographic Electrodes for Chronic Use in BCI Applications", in: A. Brendan et al. (eds.) *Towards practical BCIs*, Springer, (2012) pp. 75-96.

[6] O.G. Gruschke, R. Kamberger, J. Hoefflin, J.G. Korvink, "Water-soluble sacrificial layer enables ultra low-cost integration of magnetic resonance microcoils with 100% filling factor", Dig. Tech. Papers Transducers 2013, Barcelona, Spain, 2013, pp. 132-134.

[7] J.-B. Hövener, N. Schwaderlapp, T. Lickert, S.B. Duckett, R.E. Mewis, L.A.R. Highton, S.M. Kenny, G.G.R. Green, D. Leibfritz, J.G. Korvink, J. Hennig, D. von Elverfeldt, "A hyperpolarized equilibrium for magnetic resonance", Nature Comm., 4, 2946 (2013).

[8] M.C. Wapler, J. Leupold, J. Dragonu, D. von Elverfeldt, M. Zaitsev, U. Wallrabe, "Magnetic Properties of Materials for MR Engineering, Micro-MR and Beyond", J. Magnetic Resonance (2014), in press.

[9] R. Rostek, J. Kottmeier, S. Urban, M. Kratschmer, J. Jaklin, M. Cichosz, V. Sklyarenko, P. Woias, "Thermoelectric Properties of Electrodeposited and Annealed Bi_2Te_3 and Sb_2Te_3", Proc. 32nd Intl. Conf. on Thermoelectrics (ICT2013), Kobe, Japan.

[10] K. Wise, A. Sodagar, Y. Yao, M. Gulari, G. Perlin, K. Najafi, "Microelectrodes, Microelectronics, and Implantable Neural Microsystems", Proc. IEEE, 96, 1184-1202 (2008).

[11] P. Campbell, K. Jones, R. Huber, K. Horch, R. Normann, "A Silicon-Based, Three-Dimensional Neural Interface: Manufacturing Processes for an Intracortical Electrode Array", IEEE Trans. Biomed. Eng., 38, 758-768 (1991).

[12] S. Herwik, O. Paul, P. Ruther, "Ultrathin Silicon Chips of Arbitrary Shape by Etching Before Grinding", J. Microelectromech. Syst., 20, 791-793 (2011).

[13] S. Herwik, S. Kisban, A.A.A. Aarts, K. Seidl, G. Girardeau, K. Benchenane, M.B. Zugaro, S.I. Wiener, O. Paul, H.P. Neves, P. Ruther, "Fabrication Technology for Silicon-based Microprobe Arrays Used in Acute and Sub-chronic Neural Recording", J. Micromech. Microeng., 19, 074008 (2009).

[14] S. Spieth, O. Brett, K. Seidl, A.A.A. Aarts, M.A. Erismis, S. Herwik, F. Trenkle, S. Tätzner, J. Auber, M. Daub, H.P. Neves, R. Puers, O. Paul, P. Ruther, R. Zengerle, "A Floating 3D Silicon Microprobe Array for Neural Drug Delivery Compatible with Electrical Recording", J. Micromech. Microeng., 21, 125001 (2011).

[15] O. Frey, T. Holtzman, R. McNamara, D. Theobald, P. van der Wal, N. de Rooij, J. Dalley, M. Koudelka-Hep, "Enzyme-based Choline and l-glutamate Biosensor Electrodes on Silicon Microprobe Arrays", Biosensors Bioelectronics, 26, 477-484 (2010).

[16] B. Dombovári, R. Fiáth, B.P. Kerekes, E. Tóth, L. Wittner, D. Horváth, K. Seidl, S. Herwik, T. Torfs, O. Paul, P. Ruther, H.P. Neves, I. Ulbert, "In Vivo Validation of the Electronic Depth Control Probes", Biomed. Tech, 11, 1-7 (2013).

[17] F. Zhang, A.M. Aravanis, A. Adamantidis, L. Lecea, K. Deisseroth, "Circuit-breakers: Optical Technologies for Probing Neural Signals and Systems", Nat. Rev. Neurosci., 8, 577-581, (2007).

[18] M Schwaerzle, P. Elmlinger, O. Paul, P. Ruther, "Miniaturized Tool for Optogenetics Based on an LED and an Optical Fiber Interfaced by a Silicon Housing", IEEE EMBC, 2014, Chicago, submitted.

[19] A.A.A. Aarts, H.P. Neves, R.P. Puers, C.V. Hoof, "An Interconnect for Out-of-plane Assembled Biomedical Probe Arrays", J. Micromech. Microeng., 18, 064004 (2008).

[20] S. Herwik, T. Holzhammer, O. Paul, P. Ruther, "Out-of-plane Assembly of 3D Neural Probe Arrays Using a Platform With SU-8-based Thermal Actuators", Dig. Tech. Papers Transducers Conf. 2011, Beijing, China (2011), pp. 2323-2326.

[21] F. Barz, T. Holzhammer, O. Paul, P. Ruther, "Novel Technology for the In-plane to Out-of-plane Transfer of Multiple Interconnection Lines in 3D Neural Probes", Dig. Tech. Papers Transducers 2013, Barcelona, Spain (2013), pp. 884-887.

[22] F. Barz, O. Paul, P. Ruther, "3D-Assemblierungsverfahren für intrakortikale Sondenarrays", Proc. Mikrosystemtechnik Kongress, Aachen, Germany (2013), pp. 131-134.

CONTACT

*O. Paul, phone: +49-761-2037191; paul@imtek.uni-freiburg.de

DEVELOPMENT AND *IN VIVO* TESTING OF RECONFIGURABLE NEURAL PROBES FOR CHRONIC ELECTRICAL RECORDING

Aalap Dighe[1], Ulrich P. Froriep[1], Michael Sunshine[2], Aiva Ievins[2], Polina Anikeeva[1], Chet Moritz[2], and Joel Voldman[1]*

[1]Massachusetts Institute of Technology, Cambridge, Massachusetts, USA

[2]University of Washington, Seattle, Washington, USA

ABSTRACT

We present the successful *in vivo* testing of a triggerable, reconfigurable neural probe designed to record neural activity in the central nervous system for extended periods of time. The probe consists of a thin polyimide-gold-polyimide sandwich structure that can be deflected prior to insertion to store mechanical energy. After inserting into the brain and waiting for the initial glial sheath to form, the device can be triggered, causing the recording tip of the device to penetrate into fresh tissue. Here we present the first *in vivo* triggering and acute electrical recordings from this device in the rodent motor cortex, demonstrating the essential device functionality.

INTRODUCTION

Electrical recording interfaces with the nervous system are critical for enabling neurally-controlled prostheses and better therapies for neurological disorders [1]. A major challenge with reliable chronic neural recording is tissue reaction, wherein a sheath of glial cells encapsulates the neural probe, electrically insulating the probe from the surrounding neurons [2]. This glial sheath arises both as a reaction to the initial surgical trauma and as a long-term reaction to the foreign body.

Various strategies have been tried to mitigate the glial reaction, including designing electrodes that are flexible [3], deliver immunosuppressants [3], or have bioactive coatings [4]. To-date, however, these approaches have not eliminated the chronic tissue response. Because of data suggesting that repositioning electrodes after the initial glial response has subsided can recover signals [5], and that small feature sizes reduce tissue response [6-8], researchers have started developing small reconfigurable probes, either using a Sandia surface-micromachined process [9] or a triggerable variant of the Michigan probes [10].

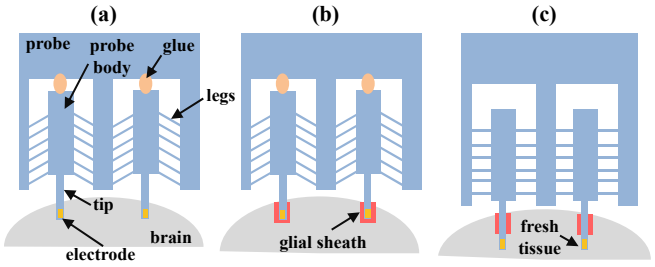

Figure 1: Device operation schematic. (a) The probe bodies are deflected and glued prior to insertion into the brain. (b) A glial sheath forms over time (~weeks) due to initial surgical trauma. (c) Dissolving the glue triggers the probe body to deflect the tips carrying recording electrodes into fresh tissue. Small tip dimensions prevent subsequent glial sheath formation.

Here we describe the first *in vivo* electrical recordings from a triggered reconfigurable probe with small dimensions. Our approach is to create a thin polymer probe whose body can be deflected and locked prior to insertion via a "glue", storing mechanical energy in the legs (Figure 1a). After inserting into the brain and waiting for the initial glial sheath to form (Figure 1b), the device can be triggered by dissolving the glue (Figure 1c), causing the recording tip of the device to penetrate into fresh tissue. Designing the tip dimensions to be small [8] (7-20 µm) should mitigate formation of an additional glial sheath post-triggering and thus improve chronic recording.

MODELING

Analytical models of the structural mechanics of the device body were developed to inform optimal device materials and dimensions, in order to balance device flexibility (to reduce elastic modulus mismatch with the brain), stiffness (to allow piercing through the glial sheath without buckling), energy storage in the device legs (to provide the > 1 mN force needed to pierce the glial sheath, based on similar triggered probes [9]) and adequate travel distance once deployed [11] (> 50 µm, to move the recording sites past the thickness of the glial sheath). Figure 2 shows example model results informing the appropriate lengths of the device legs, given the tradeoff between the mechanical stress induced in the deflected device legs and the total force that can be delivered by the device.

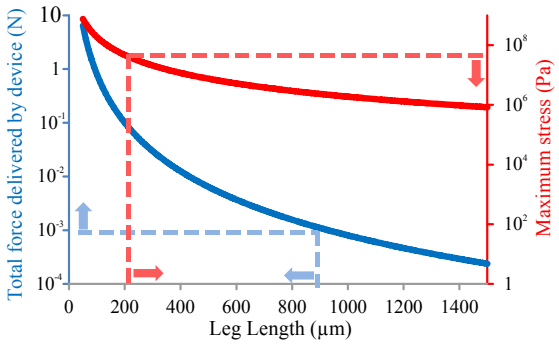

Figure 2: Plot of analytically calculated force delivered by the device (left) and the maximum stress in the device legs (right) as a function of leg length for a leg width of 20 µm, a leg thickness of 20 µm and a deflection distance of 50 µm. The requirement that the force delivered be ≥ 1 mN (design criteria) and the maximum stress be ≤ 70 MPa (yield stress of polyimide) informs a design space for the leg length (between 200 and 900 µm).

Mechanical buckling theory was used to ensure a tip geometry that should be able to pierce through the brain tissue and the glial sheath without buckling. Electrical models were also used to determine appropriate electrode materials, electrode site sizes, and trace widths. Additionally, the chosen device materials and dimensions needed to be biocompatible and compatible with available microfabrication facilities. All mechanical and electrical models were validated with laser-cut polyimide film prototypes as

9781940470016/HH2014/$25©2014TRF
DOI 10.31438/trf.hh2014.2

well as microfabricated short loop tests (data not shown) before microfabrication of the final devices.

Based on the above models and prototypes, the devices were chosen to have a 10 µm polyimide / 200 nm gold / 10 µm polyimide sandwich structure. The structural material was chosen to be polyimide because of its biocompatibility [12], its flexibility (reducing mechanical modulus mismatch with the brain and allowing for increased travel distance, compared to silicon probes) and its ability to store adequate energy when deflected despite being flexible. The device leg widths were varied between 20 – 40 µm, the leg lengths were varied between 200 – 500 µm, and leg spacing was varied between 20 – 40 µm. The device tips were designed to be 20 µm wide at the smallest point. The electrode site areas were varied between 450 – 5000 µm^2.

FABRICATION

The probe was fabricated using standard surface micromachining techniques, as shown in Figure 3.

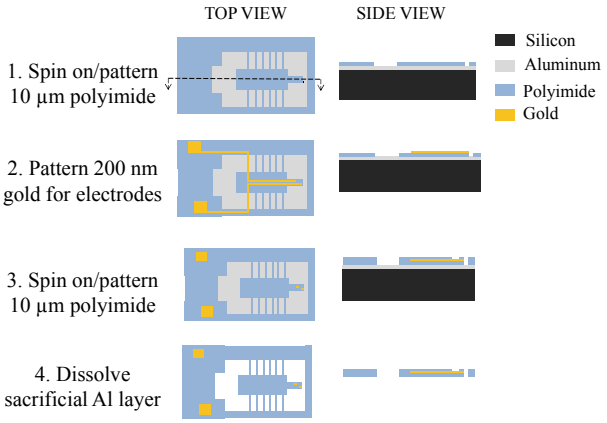

Figure 3: Fabrication process flow.

First, a 1-µm-thick sacrificial aluminum layer was sputter-deposited onto a 6-inch silicon wafer. Next, a 10-µm-thick base layer of photo-patternable polyimide (HD 4100) was spun onto the wafer and patterned using photolithographic masks (step 1). The polyimide was then partially cured (320^{o}C for 30 min) to create a stable surface for subsequent processing, while leaving some unterminated bonds for attaching to the top polyimide layer. Next, a 10-nm-thick titanium + 200-nm-thick gold layer was deposited using electron beam evaporation, and patterned using an acetone liftoff process (step 2). This gold layer forms the electrode sites and traces for the probe. The 10-µm-thick top layer of polyimide (HD 4100) was then spun onto the wafer and patterned. The wafer was hard baked (360^{o}C for 60 min) to complete the full cure of both polyimide layers (step 3). Finally, the polyimide sheet was removed from the silicon wafer by dissolving the sacrificial aluminum in aluminum etchant (Transene – type A) (step 4). All die geometries were designed so that the final dies could be easily separated by hand after peeling the polyimide film from the silicon wafer, thereby avoiding a final diesaw step. The fabricated device is shown in Figure 4.

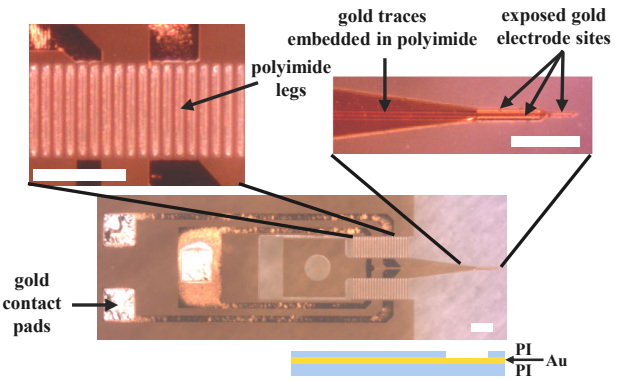

Figure 4: Optical images of the fabricated devices. The device consists of a 10 µm polyimide/ 200 nm gold/ 10 µm polyimide sandwich structure with the gold exposed at the electrode sites on the tip and at the contact pads. Scale bars = 300 µm.

RESULTS

The device was first characterized in benchtop tests in order to answer the following questions before *in vivo* testing: 1. Does the device tip pierce the brain tissue without buckling? 2. Does the device trigger mechanism work as designed? 3. Are the electrode sites functional?

Benchtop Mechanical and Electrical Characterization

The first critical component of the device is the probe tip, which is designed to be as flexible as possible while still being able to pierce through brain tissue. Insertion into freshly sacrificed rat pup brains demonstrated that the chosen dimensions could resist buckling (Figure 5). This validated the mechanical model used to design the tip geometry.

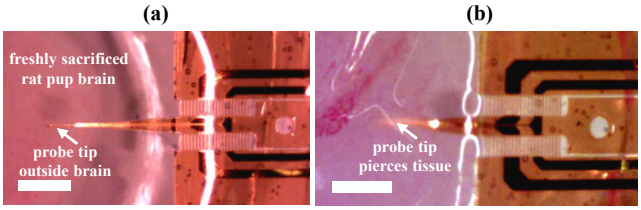

Figure 5: In vitro piercing tests to demonstrate that the probe tips can pierce brain tissue without buckling. (a) The probe tip lies just outside a rat pup brain. (b) As the probe is pushed in, the probe tip pierces the brain tissue without buckling. Scale bars = 1 mm.

The second critical component of the device is the trigger mechanism consisting of the device legs that are deflected to store energy prior to insertion. The legs are then held in place in this stored-energy configuration (Figure 6a) using a water- or thermally-soluble glue, which allows for triggering on-demand. Here we used a polyethylene glycol (PEG) hydrogel that dissolves acutely in saline. PEG was chosen because of its biocompatibility and tunable degradation times [12]. To demonstrate the triggering functionality, we applied saline to the PEG-glued probe, causing the glue to dissolve and the probe body to trigger and advance (Figure 6b). These tests validated the mechanical models used to design the trigger structure geometry.

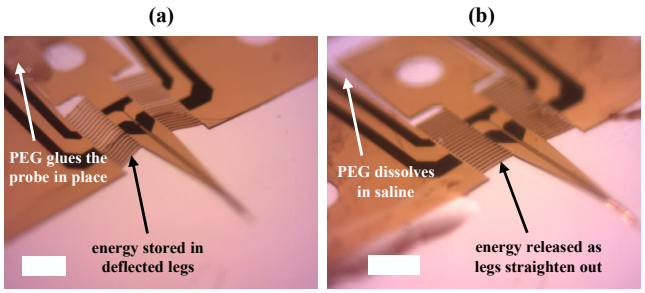

Figure 6: Benchtop triggering test. (a) The pulled-back probe body is held in place with PEG, storing energy in the deflected legs. (b) The PEG is dissolved by adding saline, thereby straightening the legs and pushing the tip forward by approximately 50 µm. Scale bars = 500 µm.

The third critical component of the device is the electrical functionality of the electrode sites. We measured the impedance of the electrode sites in saline (using an Agilent 4294A precision impedance analyzer) to be ~70-400 kΩ at 1 kHz, which is within the typical range for recording electrodes.

The benchtop tests above, thus, demonstrate successful mechanical and electrical characterization of the various critical components of the device.

In Vivo Testing – Electrical Functionality

To demonstrate electrical functionality of the electrodes in an *in vivo* setting, we inserted untriggered probes in the motor cortex of adult female Long Evans rats. Neural data were recorded intra-operatively under ketamine/xylazine anesthesia upon initial insertion of the device using a commercially available recording system (Tucker Davis Technologies) and single unit waveforms were discriminated using time-amplitude windows. Figure 7 shows a pile plot of the sorted waveform (action potentials) and the distribution of the inter-spike intervals recorded. These preliminary tests demonstrate the efficacy of the device in recording neural activity in an acute *in vivo* setting.

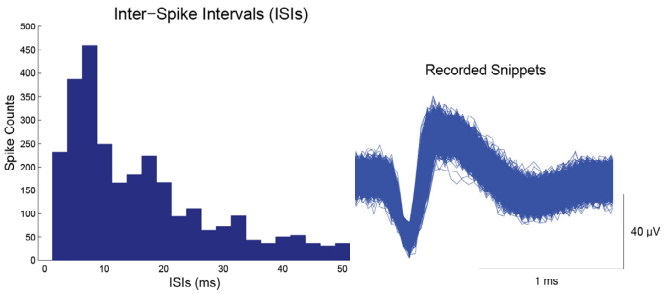

Figure 7: Inter-spike interval histogram (left) and time-amplitude sorted waveforms (right) recorded intra-operatively immediately following device insertion.

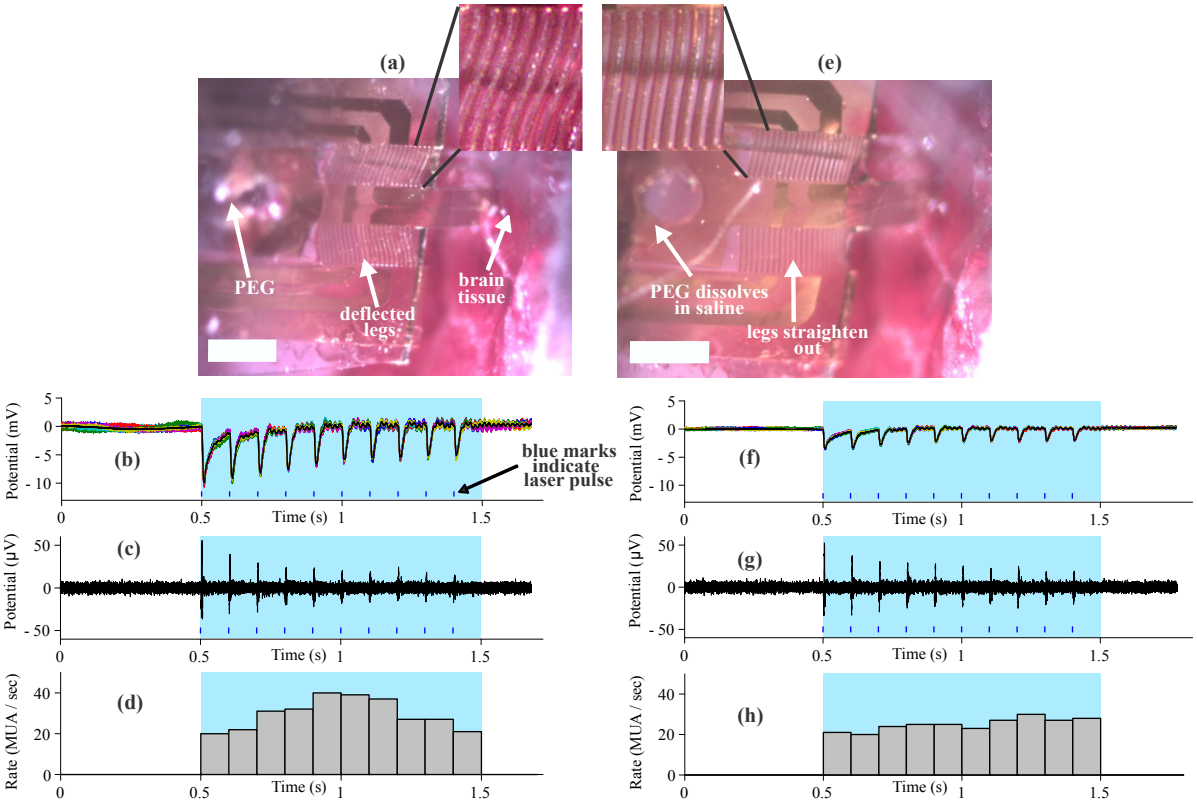

Figure 8: In vivo acute recordings of neural activity in the medial prefrontal cortex of a Thy1-ChR2-YFP *optogenetically active mouse.* ***(a)*** *The probe is inserted into the mouse brain in the deflected configuration (Scale bar = 500 µm).* ***(b)-(d)*** *Neural activity (Local Field Potentials (LFPs) and Multi-Unit Activity (MUA)) is then recorded closely following 20 laser stimulation trains (laser wavelength = 473 nm).* ***(e)*** *The probe is then triggered causing the tip to pierce ~50 µm deeper into the brain.* ***(f)-(h)*** *Neural activity is recorded again in response to the same laser stimulation as in (b)-(d). LFPs (**(b),(f)**), MUA (**(c),(g)**) and MUA histograms (**(d),(h)**) in response to the laser pulses all indicate successful electrical recording both before and after probe deployment.*

***In Vivo* Testing – Integrated Functionality**

Finally, we confirmed the integrated electrical and mechanical functionality of the probes under acute *in vivo* conditions in the medial prefrontal cortex of anesthetized (ketamine/xylazine) transgenic Thy1-ChR2-YFP mice. We inserted the probe in the deflected configuration (Figure 8a), and recorded neural activity (Figures 8b-d) closely following 20 laser stimulation trains (each train consisting of 10 pulses at 10 Hz with 5 ms pulse duration, and an inter-train interval of 5 s) delivered using a stationary optic fiber inserted adjacent to our probe. The probe was then triggered by applying saline to the PEG glue causing the tip to pierce ~50 µm deeper into the brain (Figure 8e). Neural activity was recorded again (Figures 8f-h) in response to similar laser stimulation as in Figures b-d. Local field potentials (LFPs, 1-1000 Hz filter settings, 3 kHz sampling frequency) (Figures 8b,f) indicate successful electrical recordings before and after deployment (colored lines indicate individual recordings from each of the 20 laser trains while the black line indicates the average of these 20 recordings). The LFP amplitude decreases after deployment in Figure 8f as expected since the probe tip moves deeper into the brain and further away from the stationary source of laser stimulation. Simultaneously with LFPs, we successfully recorded multi-unit activity (MUA) in response to laser pulses both before and after probe deployment (raw traces in Figures 8c,g, filter settings 0.3 - 8 kHz, ~50 kHz sampling frequency). Histograms for quantification across trials (Figures 8d,h) confirmed the reliability of the evoked activity over a total of the 20 laser stimulation trains. To ensure physiological origin of the recorded activity, we raised the stimulation frequency to 100 Hz resulting in loss of the correlation between stimulation and neural response as reported previously [13] (data not shown). We also performed a negative control experiment following the animal tests by immersing the probes in 0.9% sodium chloride solution and detected no response following optical stimulation (data not shown).

These tests demonstrate successful *in vivo* triggering and electrical recording of neural activity in acute conditions, paving the way for chronic triggering and recording tests using our device.

CONCLUSIONS

We present the development and successful testing of a new type of reconfigurable neural probe with small dimensions, designed to record neural activity for extended periods of time. Currently, technologies to do this are limited by both acute vascular injury and prolonged tissue reaction, the latter mediated by the body's immune reaction to foreign objects. The combination of these factors limits the reliability of single-unit recording from the brain. Our probe aims to advance beyond the tissue undergoing an immune reaction by changing shape at a time well after initial insertion into the brain, with sufficiently small tip dimensions so as not to trigger further reaction. We have demonstrated successful triggering and electrical recordings from this device in an acute setting in the rodent brain. This technology holds promise for creating chronic interfaces for recording stable neural activity.

ACKNOWLEDGEMENTS

This work was funded by the NSF Engineering Research Center on Sensorimotor Neural Engineering (NSF-1028725). All devices were fabricated in the Microsystems Technology Laboratories (MTL) at MIT. The authors would like to thank the MTL staff for their support, Dr. Thibault Honegger for providing the rat pup brains, Dr. Jorg Scholvin for polyimide fabrication process advice, Dennis Ward for help with the laser-cut polyimide prototypes, and Abubakar Abid for help with the post-fabrication device processing. Travel support has been generously provided by the Transducer Research Foundation.

REFERENCES

[1] D.R. Kipke, W. Shain, G. Buzsáki, E. Fetz, J. Henderson, J. Hetke, G. Schalk, "Advanced neurotechnologies for chronic neural interfaces: New horizons and clinical opportunities," *Journal of Neuroscience*, vol. 28, pp. 11830-11838, Nov 2008.

[2] V. S. Polikov, P. A. Tresco, W. M. Reichert, " Response of brain tissue to chronically implanted neural electrodes," *Journal of Neuroscience Methods*, vol. 184, pp. 1-18, Oct 2005.

[3] S. Takeuchi, D. Ziegler, Y. Yoshida, K. Mabuchi, T. Suzuki, "Parylene flexible probes integrated with microfluidic channels," *Lab on a Chip*, vol. 5, pp. 519-523, Apr 2005.

[4] L. Spataro, J. Dilgen, S. Retterer, A. J. Spence, M. Isaacson, J. N. Turner, W. Shain, "Dexamethasone treatment reduces astroglia responses to inserted neuroprosthetic devices in rat neocortex," *Experimental Neurology*, vol. 194, pp. 289-300, Apr 2005.

[5] P. Stice, J. Muthuswamy, "Assessment of gliosis around moveable implants in the brain," *J. Neural Eng.*, vol. 6, 2009.

[6] J. P. Seymour, D. R. Kipke, "Neural probe design for reduced tissue encapsulation in CNS," *Biomaterials,* vol. 28, pp. 3594-3607, 2007.

[7] P. Stice, A. Gilletti, A. Panitch, J. Muthuswamy, "Thin microelectrodes reduce GFAP expression in the implant site in rodent somatosensory cortex," *J. Neural. Eng*., vol. 4, pp.42-53, 2007.

[8] T. D. Y. Kozai, N. B. Langhals, P. R. Patel, X. Deng, H. Zhang, K. L. Smith, J. Lahann, N. A. Kotov, and D. R. Kipke, "Ultrasmall implantable composite microelectrodes with bioactive surfaces for chronic neural interfaces," *Nat Mater*, vol. 11, no. 12, pp. 1065–1073, Dec. 2012.

[9] J. Muthuswamy, M. Okandan, A. Gilletti, M. S. Baker, T. Jain, "An array of microactuated microelectrodes for monitoring single-neuronal activity in rodents," *IEEE Transactions on Biomedical Eng.,* vol. 52, no. 8, pp. 1470-77, Aug 2005.

[10] D. Engert, K. Najafi, "New class of chronic recording multichannel neural probes with post-implant self-deployed satellite recording sites," *IEEE Transducers*, 2011.

[11] D. H. Szarowski, M. D. Andersen, S. Retterer, A. J. Spence, M. Isaacson, H. G. Craighead, J. N. Turner, and W. Shain, "Brain responses to micro-machined silicon devices," *Brain Research*, vol. 983, no. 1–2, pp. 23–35, Sep. 2003.

[12] N. A. Peppas, J. Z. Hilt, A. Khademhosseini, R. Langer, "Hydrogels in biology and medicine: from molecular priciples to bionanotechnology," *Advanced Materials*, vol. 18, pp. 1345-1360, 2006.

[13] P. Anikeeva, A. S. Andalman, I. Witten, M. Warden, I. Goshen, L. Grosenick, L. A. Gunaydin, L. M. Frank, and K. Deisseroth, "Optetrode: a multichannel readout for optogenetic control in freely moving mice," *Nat Neurosci*, vol. 15, no. 1, pp. 163–170, Jan. 2012.

CONTACT

*Joel Voldman, tel: +1-617-253-2094; voldman@mit.edu

POLYMERIC MICRO-GRIPPER FOR APPLYING MECHANICAL STIMULATION ON THREE-DIMENSIONAL CELL AGGREGATES

Q. Wang, S. Zhao, J.K. Choi, X. He, and Y. Zhao[*]
Department of Biomedical Engineering, The Ohio State University, Ohio, USA

ABSTRACT

This work reports the development of a polymeric micromechanical device to provide mechanical stimulation to three-dimensional (3D) cell aggregates that are a few hundred of μm in size. Different from current loading technologies for 3D cultured cells, the device allows for the application of individually adjustable mechanical stimulation to a number of 3D cell aggregates, thus allowing parallel operation for in-depth investigation of loading parameter-dependent cell responses. Proof-of-concept experiments showed that the unique strain pattern generated by this device is able to guide the differentiation of embryonic stem cells towards a specific direction without the use of chemical inducing factors. This work indicates that 3D mechanical stimuli can be a promising inducing factor for regulating stem cell differentiation.

INTRODUCTION

Mechanical signal is universal in living tissues and organisms and is critical in regulating various physiological behaviors. The role of these mechanical signals on cell fate is often investigated by loading on *in vitro* cultured cell monolayers by engineered devices where the extracellular microenvironment is well controllable and the cells are shielded from undesired stimuli. The most prevalent method is to seed the cells on a substrate, and generate surface strain by deforming the substrate. Most commonly, an elastomeric membrane serves as the substrate. The membrane deformation can be induced by stretching the membrane directly by mechanical actuators or indirectly by deforming the connected elastomer structures using vacuum. Despite of its research popularity, the use of adherent cell monolayer for studying cell responses to mechanical signals is debatable due to the fact that the two-dimensional (2D) cell monolayer confines cell adhesion within a planar or a curved surface, in sharp contrast to those in natural tissues where the cells are allowed to reach out to a three-dimensional (3D) space. As such, for a cell in a 2D monolayer, nearly 50% of its surface is exposed to an artificial engineering substrate, while only a very small portion is in contact with other cells. This is substantially different from the natural environment where the entire surface area of a cell is often in contact with other cells through extracellular matrix. The lack of 3D structural architecture may lead to a totally different pattern of intracellular structures, intercellular mechanotransduction, signaling and in turn affect the overall cell function. Although the mechanism governing the difference between 2D and 3D cell culturing is still poorly understood, and whether the 3D culturing environments are superior over the 2D counterparts is arguable, there is a general consensus that the difference in morphological characteristics due to different culturing environment is likely to induce functional dissimilarities. This is backed up by many reports showing that 3D cultured cells by various methods exhibit distinct behaviors from the corresponding 2D models.

When the cells are cultured in 3D environments, the mechanical stimulation applied towards the cells is no longer in-plane. Current technologies for providing mechanical stimulation to 3D cultured cells include the use of a platen to press on cell-seeded hydrogels, electrospun matrix, or other 3D culturing substrates, stretching cell-seeded ring-shaped collagen gels to apply tensile strain; loading on microfluidic channels which is filled with cell-seeded collagen gel, just to name a few [7-11]. All these 3D loading methods have shown their effectiveness in applying tensile or compressive mechanical strain to cells (*i.e.* cell-embedded constructs or embryoid bodies). Nonetheless, the strain pattern that can be delivered is limited: in most cases only uni-axial strain can be applied. Numerous studies in 2D cell loading have reported that the cell response is often dependent on the strain pattern, *e.g.* uni-axial strain and equi-biaxial strain can result in very different effects on the mechanical regulation of stem cells [12]. It is plausible to infer that such effect also is valid for 3D loading, *i.e.* the response of 3D cultured cells exposed to uni-axial strain loading is different from those exposed to other strain pattern types. Moreover, since cell response to mechanical stimulation is often dependent on the loading parameters, parallel experimentation with simultaneous loading on multiple 3D samples is preferred.

In this work, we designed and fabricated a polymeric microdevice to apply compressive strain to an array of nine 3D cultured cell aggregates. Different from previous uni-axial loading, the cell aggregates were simultaneously loaded at four different spots, leading to a more complex strain distribution. The results showed that the device can successfully apply strains on alginate microbeads and cell-loaded microcapsules. Proof-of-concept cell loading test showed that 72-hour cyclic loading with the unique strain pattern delivered by this device was able to increase the expression of cardiac troponin I (cTnI) in the aggregates of undifferentiated R1 murine embryonic stem (ES) cells without the help of specific chemical inducing factors.

MATERIALS AND METHODS

Device Design

The device consists of multiple loading sites which can be individually actuated to simultaneously apply a differential pattern of mechanical compressive strains to a number of 3D cell aggregates. Each loading site consists of four microscale pillar-like structures on top of a thin circular membrane, and a microfluidic channel placed underneath (Figure 1a&b). The four pillars were arranged axially symmetrically on the circular membrane and their distance to the membrane center was adjusted to gain an enclosed space with the same diameter of the 3D cell aggregate to be loaded. Once the pressure in the microfluidic channel changes, a differential pressure occurs across the membrane and deforms the membrane, thus titling the pillars and changing the volume of space enclosed by them. In particular, once a positive pressure is applied, the circular membrane deflects upwards and the volume of the enclosed space increases (Figure 1c). The increased space is designed to be slightly greater than the size of the 3D cell aggregate so as for easy loading. Once the positive pressure is removed, the pillars returned to their vertical standings to hold the 3D cell aggregate in position. Once a negative pressure is applied, the circular membrane deflects downwards and the volume of the enclosed space decreases (Figure 1d). The four pillars thus press on the surface of the cell aggregate to apply mechanical stimulation. The strain magnitude and profile are functions of the applied differential pressure. To ensure good contact between the pillars and the cell aggregate and repeatability of the loading

9781940470016/HH2014/$25©2014TRF
DOI 10.31438/trf.hh2014.3

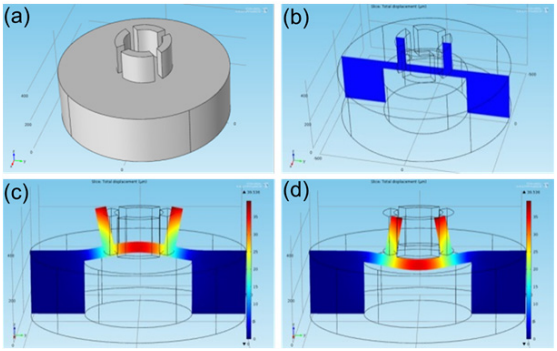

Figure 1: Schematic of the micro-gripper and the working principle of mechanical stimulation: (a) a micro-gripper consists of four fingers enclosing a cylindrical space; (b) cross-sectional view showing the micro-gripper on the top of a circular thin membrane. The micro-gripper deforms upon (c) a positive differential pressure to increase the enclosed volume or (d) a negative differential pressure to decrease the enclosed volume.

parameters, each pillar has a curved inner surface to match the surface of the spherical cell aggregate. The size of the circular membrane was determined to have the pillars gain the maximal tilting angle at a given pressure. The four-pillar assembly is referred to a micro-gripper and each pillar to a micro-gripper finger hereafter.

Given that the 3D cell aggregates used in this study has an average diameter of 225 μm, the inner diameter of the cylindrical space enclosed by the four fingers was set as 225 μm. The height of the fingers was determined in consideration of actuation range and operation reliability: if a finger is too tall, the tips of the four fingers may meet each other before a desired strain can be applied. If a finger is too short, the spherical cell aggregate tends to be unstable upon compression and has a high risk of escaping from the enclosed space especially under a large strain magnitude. After a trial-and-error experimental test assisted by finite element analysis, the height of the micro-gripper fingers was determined to be 180 μm for the cell aggregates with 225 μm in diameter. Each finger was 50 μm thick (the distance from the outer surface of the finger to its inner surface). Finite element analysis showed that with such a width and a height-to-width ratio, the micro-gripper finger itself does not yield significant deformation while pressing on the cell aggregate. According to the plate theory, the slope of deflection in a thin circular membrane along the radial direction reaches the maximal in the region 0.3R to 0.7R distant to the membrane center, where R is the membrane radius. The radius of the circular membrane was thus determined as 500 μm in diameter. The thickness was determined as 55 μm.

Device fabrication

The entire device was made of polydimethylsiloxane (PDMS). The thin circular membrane with micro-grippers was fabricated using a double-side replica molding process [13], in which the upper mold for creating the micro-gripper fingers and lower mold for creating the circular thin membrane were prepared separately (**Figure 2**). For the upper mold fabrication, extruded micro-gripper fingers (225 μm in inner diameter, 325 μm in outside diameter, and 180 μm in height; the gap between the adjacent fingers was 50 μm) were first created by patterning SU-8 negative photoresist (SU8 2100, Microchem, MA) on a silicon wafer by photolithography. PDMS prepolymer (10:1 w/w ratio) was dispensed on the wafer, cured and peeled off, forming complementary features of micro-gripper fingers in the PDMS

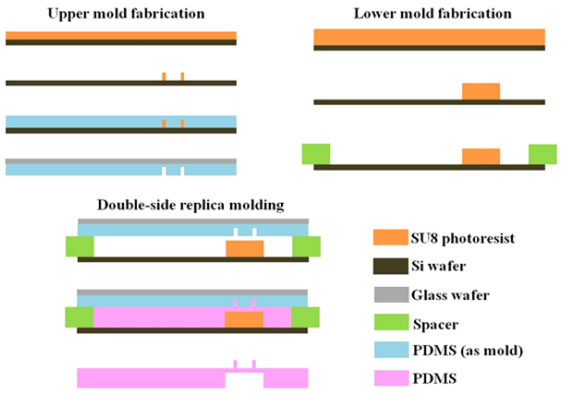

Figure 2: Fabrication process of the loading component. The PDMS substrate carrying the micro-gripper and the circular loading membrane was fabricated by double-side replica molding.

substrate. The outmost surface of the PDMS substrate was then treated with 0.1% Hydroxypropyl Methycellulose (HPMC) aqueous solution for 30 minutes in order to form a separation layer for easing subsequent mold releasing. For the lower mold fabrication, SU-8 microposts (500 μm in diameter and 245 μm in height) were patterned on a silicon wafer. Afterwards, the upper and lower molds were placed face-to-face, aligned and separated by spacers that were 300 μm thick. This left a 55 μm gap between the top surfaces of the upper and lower molds. While holding the two molds in position, PDMS prepolymer (10:1 w/w ratio) was filled into the gap, cured, and released from the two molds. The 55 μm thick PDMS circular membranes with micro-gripper fingers on their top surfaces were thus obtained, as shown in Figure 3.

After device fabrication, deionized water was pumped into the microfluidic channels underneath the membrane using a syringe pump for generating a hydraulic differential pressure across the loading membrane. The use of hydraulic instead of pneumatic actuation is in observation of possible air leaking and long-term strain drifting due to the gas permeability of PDMS. Once the channels are fully filled with water, the cell culturing surface of the device was cleaned by 1% Sodium dodecyl sulfate (SDS) solution for 1 hour, followed by rinsing with 70% ethanol, and exposed to UV light overnight. After sterilization, the cell culturing surface was rinsed twice with phosphate buffered saline (PBS), each for 5 minutes.

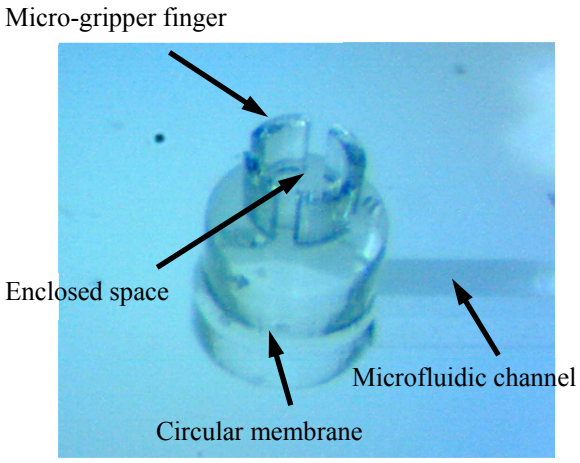

Figure 3: Optical micrograph showing a micro-gripper with four fingers and the underlying membrane.

In this study, microdevices with an array of nine microgrippers were fabricated for mechanical stimulation testing. Each micro-gripper was connected with an individual microfluidic channel and can thus be actuated independently.

Preparation of Solid Alginate Microbeads and Cell-Loaded Microcapsules

Solid alginate beads was prepared by electrospray using a previously reported method [14]. In brief, 2.0% (w/v) sodium alginate (Sigma) dissolved in 250 mM mannitol solution was pumped through a 30 gauge syringe needle at the flow rate of 27 µl/min and sprayed into 100mM calcium chloride as the gelling bath under a 1.8 kV open electric field. The solid alginate beads with the average diameter of 225 µm were then collected from the gelling solution and loaded to the devices.

R1 murine embryonic stem (ES) cells from ATCC were cultured in ES medium with Knockout® DMEM supplemented, 15% Knockout® serum, 1000 U/ml LIF, 4 mM *l*-glutamine, 0.1 M 2-mercaptoethanol, 10 µg/ml gentamicin, 100 U/ml penicillin, and 100 µg/ml streptomycin in gelatin coated tissue culture flasks with medium being changed daily. For the microcapsules loaded with cells, coaxial electrospray design was used to generate microcapsules with aqueous liquid core and alginate (hydrogel) shell, which is preferred for the embryonic cells to form single uniform aggregates. In general, the core solution containing $5x10^6$ per ml ES cells and 1% (w/v) sodium carboxymethyl cellulose in 250 mM mannitol solution and the shell solution of 2.0% alginate (w/v) were pumped through the concentric inner (28G) and outer lumen (21G) of a customized syringe needle respectively. Under the open electric field (~2.1kV), the core solution and the shell solution were sprayed into the gelling solution (100mM $CaCl_2$) at 40 µl/min and 60 µl/min, respectively. The encapsulated ES cells were then collected, washed with 0.5 M mannitol, and cultured in ES medium for 7 days, until spherical aggregates were formed in the liquid core of core-shell microcapsules.

Mechanical Stimulation and Immunostaining

Cyclic loading with the maximal differential pressure of -13 kPa was applied at 0.5 Hz for 72 hours. The un-loaded cell-loaded microcapsules were used at the control group. Both groups were maintained in regular DMEM with 10% FBS, 100 U/ml penicillin, and 100 mg/l streptomycin for the entire period of mechanical stimulation.

After mechanical stimulation, cTnI was examined by immunostainning. Encapsulated cell aggregates were collected and then released from capsules by incubating them in 75mM sodium citrate for 1 minute. Afterwards, cell aggregates were fixed by 4% PFA for 15 minutes, washed by PBS for three times and incubated in 3% bovine serum albumin (BSA) for 30 minutes to block non-specific binding at room temperature. The primary antibody of cTnI and corresponding secondary antibody were then applied. Before imaging, the nuclei of cell aggregates were further stained with 5 µM Hoechst 33342 for 15 minutes. The images were taken using an Olympus FV1000 confocal microscope and the intensity of each condition was analyzed using ImageJ (NIH).

RESULTS AND DISCUSSIONS

The solid alginate microbeads and ES cell-loaded microcapsules (both were 225 µm in diameters) were transferred into the micro-grippers, followed by cyclic application of negative differential pressure by the syringe pump. The deformation of the micro-gripper fingers and that of the solid alginate microbeads (or ES cell-loaded microcapsules) were measured using optical microscopy. Z-stack phase contrast images were obtained to show the boundaries of the microbeads as they deformed. A sequence of 90 images with 4 µm step distance was captured under each loading condition by scanning the microsphere from bottom to top. The image at the mid-plane of the microsphere was selected for deformation analyses, where the mid-plane before compression was determined from the image with the largest diameter; the corresponding mid-plane under compression was determined from its relative position to the top and the bottom of the micro-gripper fingers, assuming there was no slip between the microsphere and the micro-gripper fingers during mechanical stimulation.

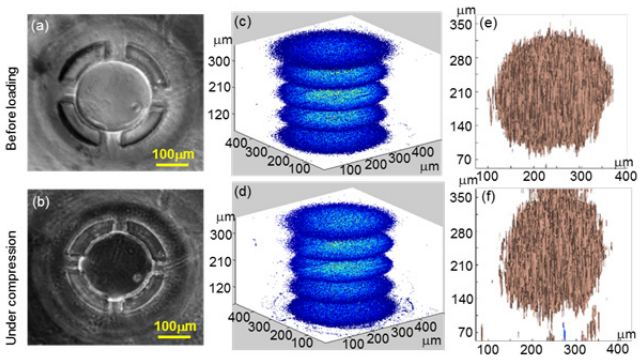

Figure 4. Deformation of solid alginate microbeads before and under mechanical stimulation: (a&b) phase contrast images; (c&d) z-stack fluorescent images of the microbead; (e&f) the 3D profile of the microbead reconstructed from the fluorescence images. The loading pressure was -13 kPa. The microbeads were with 2% alginate concentration.

Mechanical Loading on Solid Microbeads

The measurement in solid alginate microbeads showed that the deformation of all the microbeads increased with the differential pressure, while the microbeads with a higher alginate concentration yields a smaller deformation compared to that with a lower alginate concentration. Specifically, for microbeads with 1.2% alginate concentration, the mean diameter change at the mid-plane was 5.0 µm at -2.1 kPa. This number increased to 28.3 µm as the differential pressure changed to -13.0 kPa. For microbeads with 2.0% alginate concentration, the mean diameter change at the mid-plane was 3.5 µm at -2.1 kPa, and 20.7 µm at -13.0 kPa. For microbeads with 3.0% alginate concentration, the mean diameter change at the mid-plane was by 1.1 µm at -2.1 kPa and 5.4 µm at -13.0 kPa. The dependence of the diameter change with the alginate concentration is believed due to the different Young's moduli of the microbeads, which affects the maximal allowable strain range. FITC-dextran labelling was used to visualize the deformation of the microbeads. Z-stack phase contrast images were obtained to show the boundaries of the microbeads as they deformed. A representative deformation profile before and under compression was shown in Figure 4, with the alginate concentration of 2%.

Mechanical Loading on Cell-Loaded Microcapsules

The deformation of the microcapsules upon loading was also measured. The results showed that both the entire microcapsule and the cell core exhibited discernable deformation (Figure 5). For instance, for the microcapsules with the shell of 2.0% alginate concentration, the mid-plane of the entire microcapsule exhibited the mean diameter change of 3.7 µm at -2.1 kPa, and 23.4 µm at -13.0 kPa, and the mid-plane of the cell core exhibited the mean diameter change of 3.0 µm at -2.1 kPa, and 20.2 µm at -13.0 kPa. It was noted that the deformation of cell-loaded microcapsules

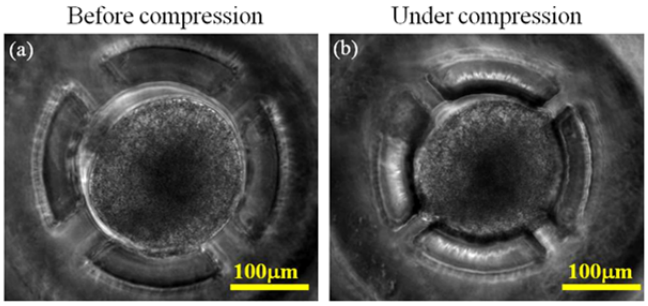

Figure 5: Deformation of a microcapsule (2% alginate concentration, with ES cell aggregates) upon loading: (a) microcapsule before compression; (b) microcapsule under compression. The differential pressure was -13.0 kPa.

were greater than that of the solid microbeads at the same alginate concentration. This indicated that the Young's modulus of the cell aggregates is lower than the alginate shell with 2% alginate concentration.

Mechanical Stimulation Regulated Stem Cell Differentiation

Immunostaining result after 72 hours of loading showed that the mechanical stimulation group exhibited significantly higher expression of cTnI comparing to those in the control group (Figure 6). This indicated that cyclic mechanical stimulation by the micro-grippers can promote the differentiation of 3D ES cell aggregates into cardiac like phenotypes without the help of chemical inducing factors. This may open up a new avenue for tailoring the multi-directional differentiation of ES cells. More systematical investigation of the relationship between the loading parameters, the strain pattern, and ES cell differentiation is underway.

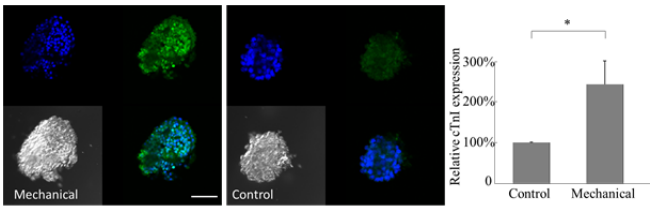

*Figure 6: Immunostaining of cTnI (green) in ES cell aggregates, Hoechst staining of cell nuclei (blue), and differential interference contrast (DIC) images showing the aggregates morphology. Scale bar: 100 μm. *: Statistically significant ($p < 0.05$).*

CONCLUSIONS

In this study, we develop a microdevice with an array of micro-grippers to apply mechanical strain towards 3D cell microaggregates encapsulated within an alginate shell. The results showed that the device can successfully load on both solid microbeads and cell-loaded microcapsules. The mechanical stimulation elevated the expression of cTnI, a cardiac marker, indicating the mechanical strain generated by the micro-grippers may regulate the differentiation of ES cells a specific phenotype. The microdevice also shows its compatibility with parallel operation, which is essential for investigating loading parameter-dependent cell responses to mechanical signals.

REFERENCES

[1] H. Lu, L. Y. Koo, W. M. Wang, D. A. Lauffenburger, L. G. Griffith, and K. F. Jensen, "Microfluidic shear devices for quantitative analysis of cell adhesion," *Analytical Chemistry,* vol. 76, pp. 5257-5264, 2011/10/17 2004.

[2] N. Watanabe, H. Kataoka, T. Yasuda, and S. Takatani, "Dynamic Deformation and Recovery Response of Red Blood Cells to a Cyclically Reversing Shear Flow: Effects of Frequency of Cyclically Reversing Shear Flow and Shear Stress Level," *Biophysical journal,* vol. 91, pp. 1984-1998, 2006.

[3] G. Keller, "Embryonic stem cell differentiation: emergence of a new era in biology and medicine," *Genes & Development,* vol. 19, pp. 1129-1155, 2005.

[4] M. Hata, K. Naruse, S. Ozawa, Y. Kobayashi, N. Nakamura, N. Kojima, *et al.*, "Mechanical Stretch Increases the Proliferation While Inhibiting the Osteogenic Differentiation in Dental Pulp Stem Cells," *Tissue Engineering Part A.,* vol. 19, pp. 625-633, 2013.

[5] S. Saha, L. Ji, J. J. de Pablo, and S. P. Palecek, "Inhibition of human embryonic stem cell differentiation by mechanical strain," *Journal of Cellular Physiology,* vol. 206, pp. 126-137, 2006.

[6] E. T. Pineda, R. M. Nerem, and T. Ahsan, "Differentiation patterns of embryonic stem cells in two- versus three-dimensional culture," *Cells, tissues, organs,* vol. 197, pp. 399-410, 2013.

[7] A. H. Huang, M. J. Farrell, M. Kim, and R. L. Mauck, "Long-term dynamic loading improves the mechanical properties of chondrogenic mesenchymal stem cell-laden hydrogel.," *European Cells and Materials,* vol. 19, pp. 72-85, 2010.

[8] K. L. Au-yeung, K. Y. Sze, M. H. Sham, and B. P. Chan, "Development of a Micromanipulator-Based Loading Device for Mechanoregulation Study of Human Mesenchymal Stem Cells in Three-Dimensional Collagen Constructs," *Tissue Engineering Part C: Methods. ,* vol. 16, pp. 93-107, 2010.

[9] V. F. Shimko and W. C. Claycomb, "Effect of Mechanical Loading on Three-Dimensional Cultures of Embryonic Stem Cell-Derived Cardiomyocytes," *Tissue Engineering Part A.,* vol. 14, pp. 49-58, 2008.

[10] C.-r. Wan, S. Chung, and R. Kamm, "Differentiation of Embryonic Stem Cells into Cardiomyocytes in a Compliant Microfluidic System," *Annals of Biomedical Engineering,* vol. 39, pp. 1840-1847, 2011.

[11] C. Moraes, G. Wang, Y. Sun, and C. A. Simmons, "A microfabricated platform for high-throughput unconfined compression of micropatterned biomaterial arrays," *Biomaterials,* vol. 31, pp. 577-584, 2010.

[12] J. S. Park, J. S. F. Chu, C. Cheng, F. Chen, D. Chen, and S. Li, "Differential effects of equiaxial and uniaxial strain on mesenchymal stem cells," *Biotechnology and Bioengineering,* vol. 88, pp. 359-368, 2004.

[13] Q. Wang, X. Zhang, and Y. Zhao, "Micromechanical stimulator for localized cell loading: fabrication and strain analysis," *Journal of Micromechanics and Microengineering,* vol. 23, p. 015002, 2013.

[14] W. Zhang, S. Zhao, W. Rao, J. Snyder, J. K. Choi, J. Wang, *et al.*, "A novel core-shell microcapsule for encapsulation and 3D culture of embryonic stem cells," *Journal of Materials Chemistry B,* vol. 1, pp. 1002-1009, 2013.

[15] Q. Wang, X. Zhang, and Y. Zhao, "A microscale mechanical stimulator for generating identical in-plane surface strains toward live cells on multiple loading sites," *Sensors and Actuators B: Chemical,* vol. 194, pp. 484-491, 2014.

CONTACT

*Y. Zhao, tel: +1-614-247-7424; zhao.178@osu.edu

NANOARRAY-ENHANCED IMPLANTABLE INTRAOCULAR PRESSURE SENSOR WITH REMOTE OPTICAL READOUT

Jeong Oen Lee[1], Kun Huang[1], Trong-Tuong Nguyen[2], David Sretavan[2], and Hyuck Choo[1]*
[1]California Institute of Technology, Pasadena, California, USA
[2]University of California, San Francisco, California, USA

ABSTRACT

We demonstrate a compact implantable intraocular pressure sensor with remote optical readout for glaucoma research and patient management. Using broadband white light between 780-1150nm, we excite the sensor's pressure-sensitive optomechanical cavity and detect the reflected light, whose optical signature changes as a function of intraocular pressure. When measured inside an artificial pressure chamber that emulates the anterior chamber of the eye, the sensor provided robust measurements of hydrostatic pressures between 10-60 mmHg with an accuracy of 0.15 mmHg and a linearity of 0.97.

INTRODUCTION

Glaucoma is a leading cause of blindness, affecting an estimated 4 million Americans and 70 million individuals globally [1]. As glaucoma typically affects the elderly, the aging demographic trends indicate that this disease will continue to be an ever-increasing socioeconomic burden to society [1-4]. Elevated intraocular pressure (IOP) is a major risk factor for glaucoma, and IOP monitoring is the single most important clinical management tool [2]. Despite the pervasive use of IOP readings for disease monitoring, and the clinically proven importance of the aggressive lowering of IOP [5-10], current clinical management is primarily based on only periodic snapshots of IOP in the doctor's office obtained every few months based on indirect measurements [11-12]. The inability of patients to easily monitor their own IOPs at different times of the day or during various daily activities, hinder the comprehensive understanding of the IOP profile of individual patients [13] and the possibility of custom-tailored IOP control. In addition to its use as a patient monitoring parameter, IOP is also the standard readout used in glaucoma research. However, achieving an acceptable level of accuracy and repeatability in animal-IOP measurements requires anesthesia and extreme care [14-15]. Conducting such time-consuming measurements in large populations of animals is a major hurdle in glaucoma drug discovery. The need for better IOP monitoring in clinical ophthalmology and in disease research has been widely appreciated, and a number of efforts have been made to develop MEMS-based implantable sensors [16-18]. However, these implants are too large (diameter: 1-3 mm) for use in rodent models (corneal diameter ~ 3.5 mm), which make up > 90% of the animal species used in glaucoma research. Sensor implants with such dimensions may also interfere with normal human ocular function and be cosmetically and psychologically unacceptable to patients.

We are developing a highly miniaturized IOP monitoring system using a nanophotonics-based implantable IOP sensor with remote optical readout that can be adapted for both patient and small animal research use. The device's operating principle and configuration are shown in Figures1 and Figure 2, respectively. A remote detector optically excites the pressure-sensitive nanophotonic structure of the IOP-sensing implant placed in the anterior chamber and detects the reflected light, whose optical signature changes as a function of IOP. Optical detection eliminates the need for large, complex inductive-coupling or capacitive-sensing (LC) structures [16-17] and simplifies sensor design. In addition, readout involves 780-1150nm light that is not sensed by the photosensitive neurons in the retina. The use of precisely engineered nanophotonic components improves the sensor's resolution and sensitivity, increases optical readout distance, and reduces its size by a factor of 10-30 (ultimately down to 50 μm in diameter and 25 μm in height) over previously reported implants. Its small size and convenient optical readout will allow more frequent and accurate self-tracking of IOP by patients in home settings. In addition, this technology can be adapted for use in automatically monitoring large cohorts of animals to support glaucoma research and drug discovery.

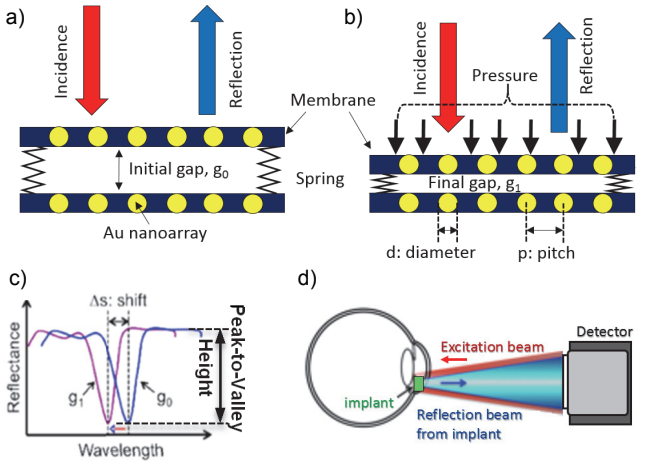

Figure 1: Schematic illustration of the IOP sensor operation. a) Disk-shaped optomechanical cavity whose optical resonance is enhanced by the presence of nanodot arrays. b) Flexible membrane deformation by ambient pressure. c) Resulting shift in resonance due to gap reduction. d) IOP sensor implanted in the anterior chamber and hand-held remote optical reader

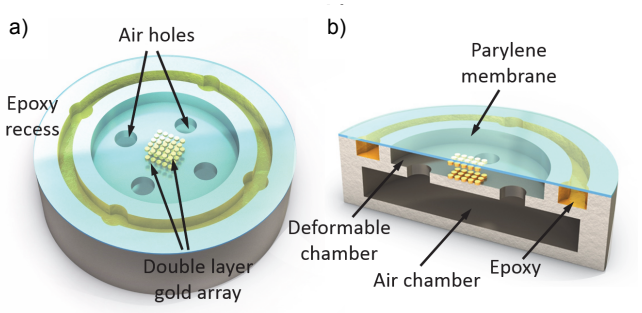

Figure 2: a) 3-D illustration of the sensor. b) Cross-sectional view. The sensor's diameter is 300 μm, which can be further reduced down to 50 μm. The size of the nanodot arrays, which determines the active area of the sensor, is 50 μm in width and length, and it can also be further reduced down to 25 μm.

DEVICE DESIGN

Operating Principle

The core of the device, the optomechanical cavity, is formed by a flexible 3-μm Parylene membrane with a diameter of 200 μm (the deformable part) [16-17] and a rigid silicon substrate on the bottom,

9781940470016/HH2014/$25©2014TRF
DOI 10.31438/trf.hh2014.4

as shown in Figure 2. Both the Parylene and silicon surfaces are embedded with resonance-enhancing 50×50-μm^2 gold nanodot arrays with the dot-to-dot pitch of 1000 nm and the nanodot diameter of 800 nm. These values were experimentally determined for the sensor's optimal performance and are discussed in more detail below. As the pressure increases from 1 atm, the initial 2-μm gap between the Parylene membrane and the silicon (Si) substrate decreases, and this decrease in the gap shifts the resonant wavelength of the cavity (Fig. 1).

Optomechanical Simulation and Design

To design a pressure sensor that exhibits highly linear mapping between spectral resonance shifts and pressure changes, we ran a series of optomechanical finite-element-method (FEM) and finite-difference-time-domain (FDTD) simulations using commercial programs (COMSOL and CST), in combination with experimental measurements.

We first determined the spectral range for pressure sensing. The wavelength range of interest is between 770 and 1100 nm because the light absorption in water and tissues would be minimal in this range, facilitating the penetration through the cornea and the aqueous humor. In addition, this wavelength range is not sensed by photoreceptor cells in the retina. We set the initial cavity gap at 2 μm, which is a gap value that can readily be microfabricated. Using FDTD simulation, we first identified a free spectral range of the sensor cavity for clear detection of the resonance shift, as shown in Figure 3.

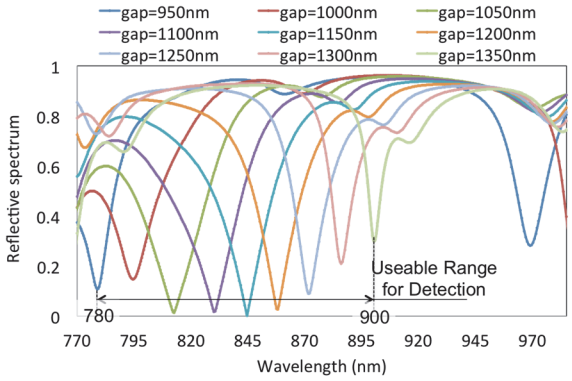

Figure 3: Simulated spectral shift of the cavity resonance as a function of the gap: The usable range is between 780 and 900 or total shift range of 120 nm.

The simulation results have indicated that the free spectral range exists between 780 and 900 nm, which would allow a shift range of 120 nm, when the gap decreases by 400 nm, from 2 µm to 1.6 µm. Next, using FEM simulation, we designed the Parylene membrane – its diameter and thickness – so that it would deflect 400 nm in response to the change in the ambient pressure (ie. IOP) of 40 mmHg between 10 and 50 mmHg. Based on our simulation results, the diameter and the thickness of the Parylene membrane were determined to be 100 µm and 3 µm.

Resonance-Enhancing Nanodot Arrays

The resonance strength and properties of a Fabry-Perot optical cavity are heavily influenced by the reflectivity at the cavity ends. If the reflectivity is high, the resonance becomes very narrow and sharp, and the quality factor of the resonance increases. However, in this case, the overall amplitude (peak-to-valley height) of the resonance, which directly translates to the signal-to-noise ratio for sensing application, significantly decreases. On the other hand, if the reflectivity is low, the resonance becomes very broad and its amplitude also becomes smaller, making it difficult to detect the resonance. This tradeoff is clearly illustrated by the blue line (from simulation) in Figure 5. Very high or low reflectivity results in low resonance amplitude or peak-to-valley height. An optimal reflectivity exists around 0.6 ± 0.2, where the peak-to-valley height is maximized.

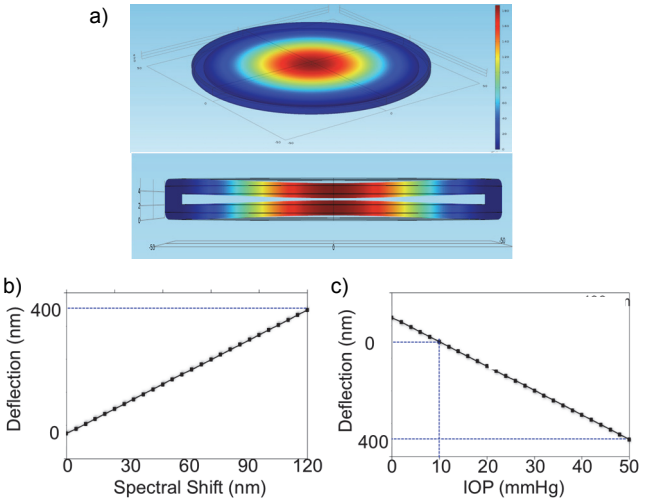

Figure 4: a) FEM simulation of a Parylene membrane deformation as a function of hydrostatic ambient pressure change. b) Linear mapping between "the membrane deflection vs. the spectral shift." c) Linear mapping between "the membrane deflection vs. the intraocular pressure change." For 1 mmHg change, the membrane deforms by 10 nm, and this results in 3nm shift in resonance or 3nm spectral shift per 1mmHg pressure change.

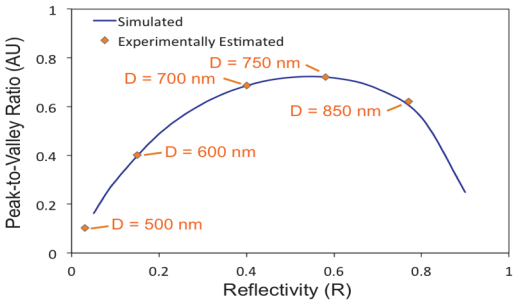

Figure 5: Measured P-V ratios vs. nanodot diameters: The optimal diameter ranges between 700 and 850 nm.

Hence, we use engineered gold nanodot arrays to optimize the reflectivity of the Parylene membrane surface and the silicon surface. In order to adjust reflectivity of a membrane using nanodot arrays, we only need to vary the diameter and pitch of the nanodots, which can be accomplished precisely and repeatedly using an electron-beam lithography system. Consequently, compared to using other coating techniques, the placement of gold nanodots allows us to control Parylene membrane reflectivity in a more reliable and repeatable manner. To find an optimal diameter, we fabricated a series of nanodot arrays with varying diameters from 500 to 850 nm while keeping the pitch at 1000 nm and experimentally measured their reflectivities. Fitting the experimentally obtained reflectivities onto the simulation curve as

shown in Figure 5, we found that the optimal nanodot diameter was 750 nm. To keep our nanofabrication parameters simple, we chose 800 nm for the nanodot diameter.

DEVICE FABRICATION

The proposed device is fabricated on a silicon wafer using microscale and nanoscale fabrication techniques. To fabricate the sensor, we first performed photolithography and deep reactive ion etching (DRIE) to create a 2-μm-deep cavity chamber and a recess (for adhesive) in the Si wafer (Figure 6a). Then, we patterned a 170-nm-thick gold nanodot array on the Si substrate using e-beam lithography, gold evaporation, and lift-off (Figure 6b). Next, using DRIE, we created four air holes on the front side of the wafer and on the air reserve chamber on the back of the wafer (Figure 6c). During the etching process, the air reserve chamber eventually reached the air holes, and they all become connected. Then we patterned another gold nanodot array on the Parylene membrane (Figure 6d) using e-beam lithography, gold evaporation, and lift-off. Next, using epoxy, we assembled the Parylene membrane and the Si substrate while keeping their nanodot arrays aligned to each other under the optical microscope (Figure 6e). Finally we completely sealed the air reserve chamber using epoxy and a Si chip (Figure 6f).

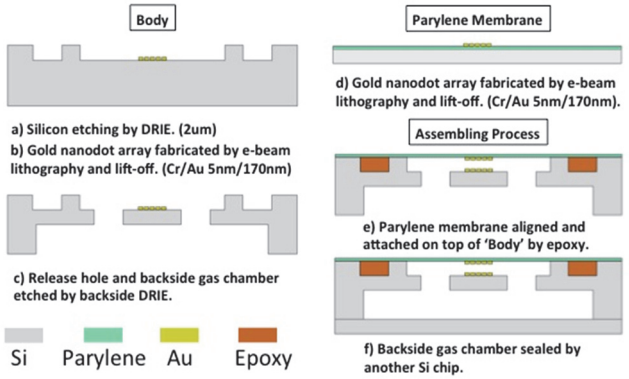

Figure 6: Fabrication process.

The photos of the completed device, including the SEM image of the gold nanodot, are shown in Figure 7. The requirement on alignment accuracy between the two gold nanodot arrays, one on the Parylene membrane and the other on the silicon substrate, is lenient. The maximum misalignment shown in Figure 7b is about 4 µm, and the size of the resulting active sensing area is 85% of the designed value, which can easily accommodate the probing beam and would not degrade the performance of the sensor.

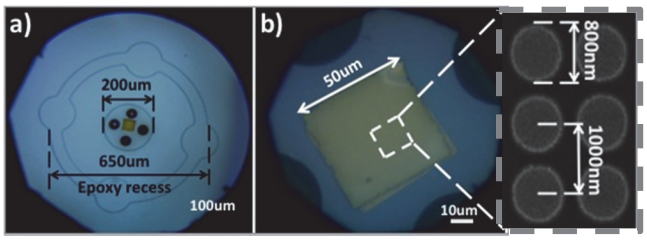

Figure 7: Images of the fabricated device: a) A photo of the entire device (top view). b) Two superimposed gold nanodot arrays. The SEM image shows the gold nanodot array on the Parylene membrane.

DEVICE MEASUREMENTS

We tested the completed devices inside a water-filled pressure chamber that emulated the anterior chamber of the human eyes (Figure 8). The artificial chamber has a transparent window on the top for optical measurements, and its internal pressure can be precisely adjusted using an external regulator and simultaneously monitored using a digital pressure gauge (model name: DPGWB-04; manufacturer: Dwyer Instruments, INC.; accuracy: ±0.5%; thermal effect: 0.05%).

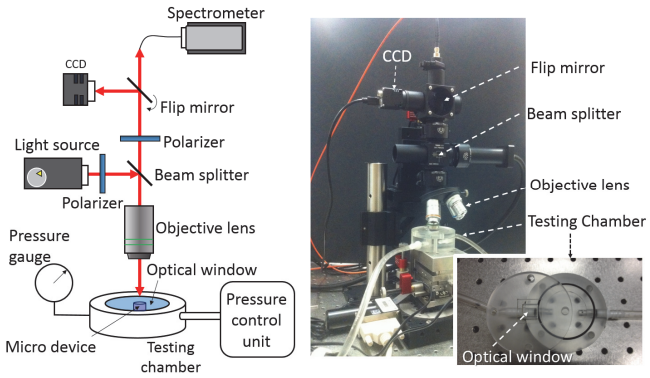

Figure 8: A schematic diagram and a photo of the measurement setup. The inset in the bottom-right corner shows the in-house built pressure chamber that emulates the environment of the anterior chamber.

Using a broadband source (model name: OSL1 High-Intensity Fiber Light Source; manufacturer: Thorlabs) and a commercially available mini-spectrometer (Maya 2000Pro by Ocean Optics; 0.22-nm spectral resolution), we remotely acquired the reflection spectra from the sensor in the chamber at a distance of 7 mm (Figure 8). As we linearly increased the chamber pressure from 10 to 60 mmHg and tracked the locations of the major peaks in the spectra, we observed that the spectra shifted to the shorter wavelengths, as shown in Figure 9. The average values and standard deviation of the peak locations were determined from over 300 measurements.

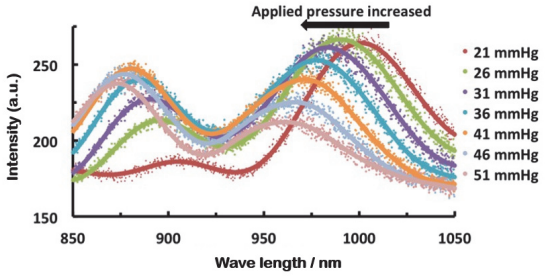

Figure 9: Reflective spectra showing resonance shift as a function of hydrostatic pressure between 21 and 51 mmHg.

The mapping between the pressure changes and the resonance shifts was highly linear as shown in Figure 10, with a linear fit of 0.966. The sensitivity and the accuracy of the pressure sensor were 1.53 nm/mmHg and 0.15 mmHg over the range of 10-60 mmHg. The mini-spectrophotometer with 0.22nm spectral resolution was used reliably to resolve 1.53nm change in resonance shift per 1 mmHg change in pressure. When compared to the sensor without gold nanodot arrays, the presence of the nanodot array significantly enhanced the signal-to-noise ratio of the sensor by a factor of seven and enabled more robust remote detection.

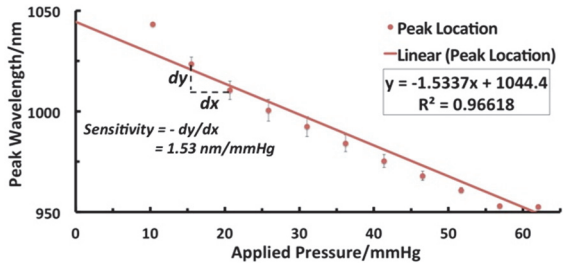

Figure 10: Linear mapping between the shift in peak locations and the ambient hydrostatic pressure: the linearity is 0.96618.

Following the successful measurements in the artificial pressure chamber, we pursued measurements in *ex-vivo* rabbit eyes. Figure 11 shows robust optical resonance captured remotely over a 7-mm distance from an earlier prototype device (consisting of two rigid membranes that do not flex) implanted in the anterior chamber of an *ex-vivo* rabbit eye and also in saline as a reference measurement. In both cases, we obtained consistent resonance peaks at identical locations.

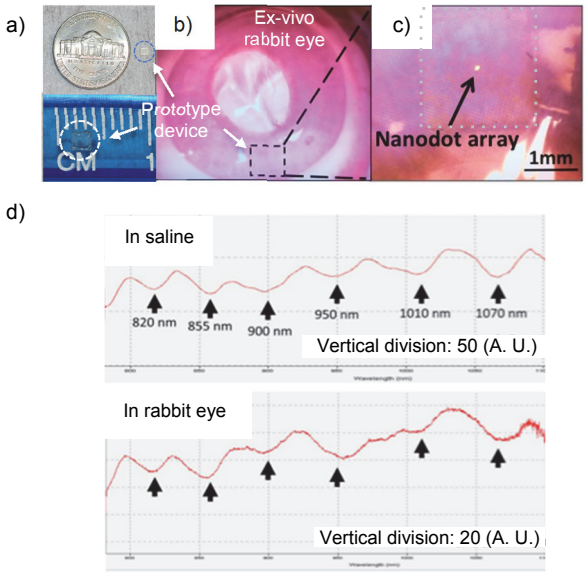

Figure 11: a) Earlier prototype device, ~ 2 mm by 2 mm. b) Prototype implanted in the anterior chamber of an ex-vivo rabbit eye. c) A zoom-in image of the implant in the ex-vivo rabbit eye – the gold nanodot array appears as a bright spot in the image, indicated by the arrow. d) A resonance spectrum captured from the prototype device implanted in ex-vivo rabbit eye and also in saline. The resonance dips appear exactly at the identical locations.

CONCLUSIONS

We have designed and fabricated a compact implantable IOP sensor with remote optical readout for glaucoma research and patient management. We have demonstrated its IOP-sensing capability between 10-60 mmHg in an artificial pressure chamber and captured the resonance spectrum from a prototype sensor implanted in the anterior chamber of an *ex-vivo* rabbit eye. We are presently working on (1) measurements in *ex-vivo* and *in-vivo* rabbit eyes; (2) further miniaturization of the implantable IOP sensors below 100 μm for use in rodent eyes; (3) a longer optical readout distance (theoretical limit ~ 20 cm); and (4) algorithms for automatic assignments of spectral shifts to pressure values.

REFERENCES

[1] www.glaucoma.org (Glaucoma Research Foundation)

[2] J. C. Morrison and I. P. Pollock, *Glaucoma: Science and Practice*, New York, New York: Thieme, 2002, Ch.1 & Ch.5.

[3] www.aoa.gov (Administration on Aging, Department of Health & Human Services)

[4] www.nei.nih.gov (National Eye Institute, NIH).

[5] B. L. Lee and M. R. Wilson, "Ocular Hypertension Treatment Study (OHTA) commentary," Current Opinion in Ophthalmology, vol. 14, no. 2, pp. 74-77, 2003.

[6] M. C. Leskea, A. Heijl, L. Hyman, B. Bengtsson, and E. Komaroff, "Factors for progression and glaucoma treatment: the Early Manifest Glaucoma Trial," Current Opinion in Ophthalmology, vol. 15, no. 2, pp. 102-106, Apr. 2004.

[7] J. T. Wilensky, "The role of diurnal pressure measurements in the management of open angle glaucoma," Current Opinion in Ophthalmology, vol. 15, no. 2, pp. 90-92, Apr. 2004.

[8] H. Bagga, J. H. Liu, and R. N. Weinreb, "Intraocular pressure measurements throughout the 24h," Current Opinion in Ophthalmology, vol. 20, no. 2, pp. 79-83, Mar. 2009.

[9] S. Asrani, R. Zeimer, J. Wilensky, D. Gieser, S. Vitale, and K. Lindenmuth, "Large diurnal fluctuations in intraocular pressure are an independent risk factor in patients with glaucoma," J. Glaucoma, vol. 9, no. 2, pp. 134-142, Apr. 2000.

[10] E. Hughes, P. Spry, and J. Diamond, "24-hour monitoring of intraocular pressure in glaucoma management: A retrospective review," J. Glaucoma, vol. 9, no. 2, pp. 232-236, Jun. 2003.

[11] C. R. Ethier, M. Johnson, and J. Ruberti, "Ocular biomechanics and biotransport," Annual Review of Biomedical Engineering, vol. 6, pp. 249-273, 2004.

[12] I. G. Pallikaris, G. D. Kyomionis, H. S. Ginis, G. A. Kounis, and M. K. Tsilimbaris, "Ocular rigidity in living human eyes," IOVS, vol. 46, no. 2, pp. 409-414, Feb. 2005.

[13] K. Singh and A. Shrivastava, "Intraocular pressure fluctuations: how much do they matter?" Current Opinion in Ophthalmology, vol. 20, no. 2, pp. 84-7, Mar. 2009.

[14] L. Jia, W. O. Cepurna, E. C. Johnson, and J. C. Morrison, "Effect of General Anesthetics on IOP in Rats with Experimental Aqueous Outflow Obstruction," IOVS, vol. 41, no. 11, pp. 3415-3419, Oct. 2000.

[15] J. Danias, A. I. Kontiola, T. Filippopoulos, and T. Mittag, "Method for the Noninvasive Measurement of Intraocular Pressure in Mice," IOVS, vol. 44, no. 3, pp. 1138-1141, Mar. 2003.

[16] P. J. Chen, D. C. Rodger, R. Agrawal, S. Saati, E. Meng, R. Varma, M. S. Humayun, and Y. C. Tai, "Implantable micromechanical parylene-based pressure sensors for unpowered intraocular pressure sensing," J. Micromechanics and Microengineering, vol. 17, pp.1931-1938, Oct. 2007.

[17] P. J. Chen, S. Saati, R. Varma, M. S. Humayun, and Y. C. Tai, "Wireless Intraocular Pressure Sensing Using Microfabricated Minimally Invasive Flexible-Coiled LC Sensor Implant," J. Microelectromechanical Systems, vol. 19, no. 4, pp. 721-734, Aug. 2010.

[18] D. Ha, W. N. de Vries, S. W. M John, P. P. Irazoqui, W. J. Chappell, "Polymer-based miniature flexible capacitive pressure sensor for intraocular pressure (IOP) monitoring inside a mouse eye," Bioemdical Microdevices, DOI 10.1007/s10544-011-9598-3, published online, Oct. 2011.

CONTACT

*J. O. Lee, tel: +1-626-395-8870; jolee@caltech.edu

MEMS DEVICE INTEGRATED WITH VERTICALLY ALIGNED CARBON NANOTUBES FOR VIRUS CAPTURE AND DETECTION

*Yin-Ting Yeh[1], Nestor Perea-Lopez[2], Yi Tang[3], Brian U. McKellar[1], Ramdane Harouaka[1], Huaguang Lu[3], Mauricio Terrones[2] and Si-Yang Zheng[1]**

[1] Department of Biomedical Engineering, [2]Department of Physics,
[3]Department of Veterinary and Biomedical Science, The Pennsylvania State University, U.S.A.

ABSTRACT

Point-of-care virus diagnosis is highly desirable in worldwide infectious disease control. Here we report a hand-held device for capturing viruses by applying physical size based exclusion inside a point-of-care device integrated with vertically aligned carbon nanotube (VACNT) nanostructures to achieve label-free and high throughput virus capture. The microfluidic device is constructed from a VACNT channel wall synthesized bottom-up via chemical vapor deposition (CVD). The VACNT has ~117nm average gap size and ~97% porosity. By bonding with a polydimethylsiloxane (PDMS) cover sealing the top, the aqueous sample containing virus particles filter through the VACNT channel wall under negative pressure applied at the outlet end. We have demonstrated that the device is capable of filtering 50µL of PBS containing ~6.3×10^4 counts of lentivirus particles in 10 minutes with 97% of capture efficiency, quantified by the cell infectious titration technique.

INTRODUCTION

Once a viral infectious disease breaks out, the detriment can grow exponentially without effective quarantine. In 1918, an influenza outbreak caused 50 million deaths globally. The HIV/AIDS pandemic has resulted in 36 million deaths thus far and the number is increasing [1]. The emergence of these pathogens and their subsequent spread have not only had a destructive impact on global health but have also caused economic losses and interruptions in trade and travel [2]. Therefore, rapid on-site detection and analysis are crucial. Viruses are small parasites and display in a variety of sizes and shapes. In general, most discovered viruses range from 20-300 nm in size and contain either an RNA or DNA genome surrounded by a protective protein coat or capsid [3]. Current diagnostic approaches include direct virus detection via isolation of the virus in cell culture, identification of viral nucleic acids or antigens, and serological tests detecting virus-specific antibodies. However, viral culture requires a minimum of two to ten days of enrichment to provide statistically relevant information [4]. Because immunological approaches depend on specific recognitions provided by antibodies or probes [5], it poses a challenge to target unknown viruses or unidentified strains.

In this paper, we integrate a hand-held device to achieve virus capture and enrichment by size-based filtration. The active material is a VACNT forest with 97% porosity and the ability to selectively isolate virus from aqueous suspensions at the nanoscale. Via bottom-up synthesis processing, VACNT selectively grow on patterned iron catalyst thin films. First, we characterized VACNT material synthesis by scanning electron microscopy (SEM), transmission electron microscopy (TEM), and Raman spectroscopy. Second, we studied VACNT filtration properties of gap size and porosity and fitted the results using Darcy's equation. Third, we integrated droplet-shaped VACNT pattern into a microfluidic device via a sealing PDMS cover on top. We characterized the device filtration performance using lentivirus and measured the capture efficiency by cell infectious titration.

FABRICATION AND FILTRATION MECHANISM

Bottom-up fabrication and device assembly

Starting from a 4" prime silicon wafer, the silicon substrate was cleaned by piranha solution followed by subsequent sonication in acetone, IPA and DI water. In Fig.1A, The iron catalyst thin film was deposited by e-beam evaporation and patterned by photoresist lift-off process. The ion thin film is approximately 6.5nm thick when measured by atomic force microscopy (AFM). Due to its better biocompatibility [6], nitrogen-doped CNTs were synthesized inside an aerosol based CVD by using benzylamine as the carbon source with nitrogen doping. The benzylamine mist was generated by an ultrasonic neubulizer and was carried by argon/hydrogen gas into two furnaces in series at 825℃ under a flow rate of 2.5 L/min. In Fig.1B, the VACNT selectively grew on a patterned catalyst thin film to form an enclosed droplet shape microfluidic chamber. The newly synthesized VACNT pattern was then sealed on top with s molded PDMS chamber via oxygen plasma enhanced bonding. We fabricated the PDMS cover by using an SU-8 mold and by puncturing two fluidic access ports, one inlet and one outlet. In Fig.1C, the inlet port is attached with a 100µL cylindrical reservoir made with silicone. The outlet port is connected to a flow-through collection tube and a vacuum source through a T-shaped adaptor. The negative pressure is regulated by a mechanical regulator and measured with a pressure gauge.

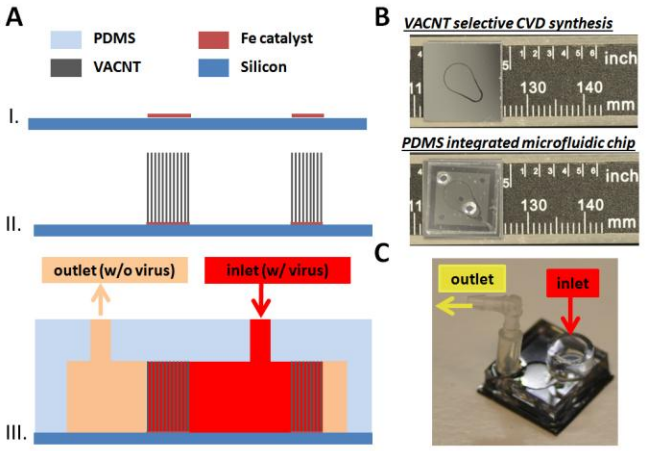

Figure 1. VACNT device fabrication and assembly process. A: Illustration of fabrication process flow. B: Top view of VACNT selective growth into droplet pattern (top), and device assembled with PDMS cover (bottom). C: Picture of hand-held virus capture device with fluidic access connections.

Filtration mechanism and operation

The test sample is loaded into the inlet reservoir by pipetting and actuated through the filtration device by negative pressure generated at the outlet end. The droplet-shaped porous wall was sealed on top by PDMS permanent bonding. Fig.2 illustrates that the device performs dead-end filtration through the VACNT forest with nanoscale gap size and high porosity. During the filtration process, the suspension mixture containing particles of different sizes is

9781940470016/HH2014/$25©2014TRF
DOI 10.31438/trf.hh2014.5

transported through the VACNT microfluidic channel wall by the pressure driven flow. The particles with a size range similar to the gap size are trapped inside the membrane. Any larger particles are blocked and remain confined within the enclosed droplet chamber, while smaller particles flow through the VACNT membrane and are collected at the outlet.

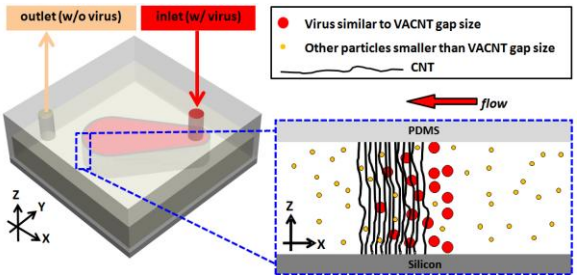

Figure 2. Schematic illustration of the virus isolation process inside the VACNT filtration device.

RESULTS

VACNT material characterization

We first characterized the newly synthesized VACNT by SEM, TEM and Raman spectroscopy. Fig.3A shows that multiwall carbon nanotubes (CNTs) selectively grow on the silicon substrate in a vertically aligned configuration with ~50µm in height after a 30-minute CVD synthesis. Through image analysis with ImageJ, we plotted diameter measurements into a histogram distribution, as shown in Fig.3B. The results show that the diameter of VACNT ranges from 4.2 to 71.2nm and is 25.3±11.8nm on average.

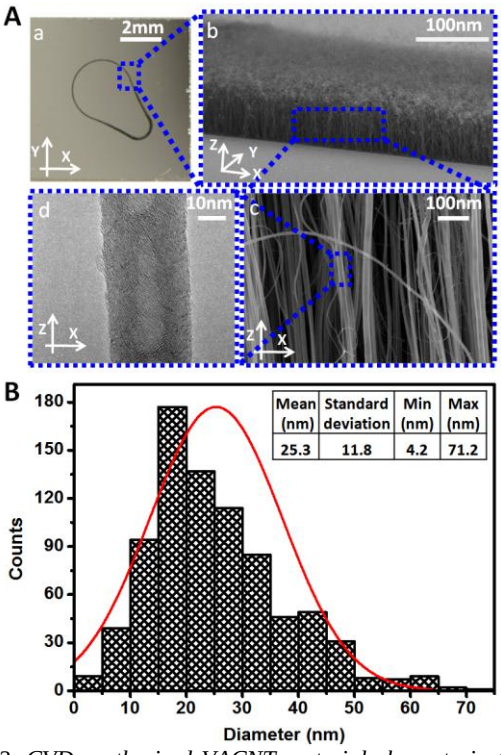

Figure 3. CVD synthesized VACNT material characterization. A: Images of VACNT synthesized in droplet shape pattern (a: bright field, b: SEM, c: SEM, and d: TEM images). B: Histogram of VACNT diameter and summary table of diameter distribution analysis.

Next, we used Raman microscopy (Renishaw, InVia Raman microscopy) to characterize the VACNT. We recorded the spectrum under 514nm laser excitation for 30 seconds under 50X magnification. The laser power to the sample was 10µW. As shown in Fig.4, the Raman spectrum indicates the VACNT has D, G and D* band peaks at 1352, 1578 and 2659 cm^{-1}, respectively. The results confirm that VACNT is multiple-wall with nitrogen doping [7].

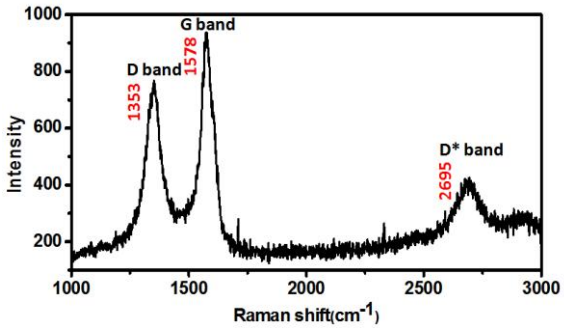

Figure 4, Raman spectrum of VACNT forest.

Filtration properties

Second, we studied the filtration properties (porosity and gap pore size) of VACNT. We synthesized VACNT on a 6.5nm iron catalyst film with an increasing synthesis time of 5, 10, 20, 30 and 40 minutes. Both diameter and density data were measured by image analysis of cross-sectional views of VACNT samples under SEM. For diameter analysis, the images were taken under 6×10^4 magnification and a total number of 200 focused CNTs were measured for each synthesis time. Fig.5A shows that the measurement results suggest the VACNT diameter can be considered independent of the synthesis time with 25.6±3.5µm on average. For density measurement, the images were taken under 2.5×10^4 magnification. By drawing a 1µm line perpendicular to VACNT growth direction on each image, we counted the numbers of focused CNTs that crossed with the drawing line. The results of the density measurement also indicate that density is independent of synthesis time after 10 minutes synthesis and the average density is ~3.19×10^9 counts/cm^2. For the conditions of short synthesis time, such as 5 minutes, the random growth nature of the CNT synthesis at the early stage results in unpredictable VACNT density characterization [8].

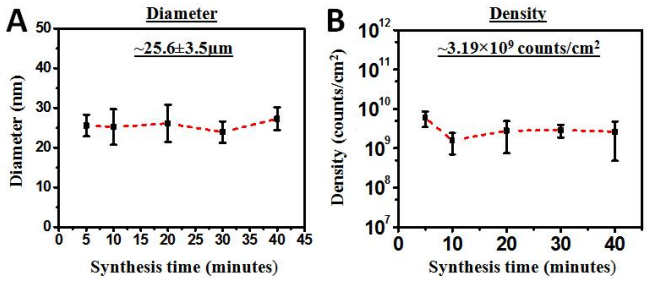

Figure 5. Results of VACNT characterization under different synthesis time by SEM image analysis (n=6). A: Plot of diameter measurement results. B: Plot of density measurement results.

Next, we studied VACNT forest filtration properties by using Darcy's porous flow equation assuming the orientation of the VACNT forest as a cylindrical model with a uniform density and diameter [9]. In Fig.6, for the case of cylindrical pillars, the bulk porosity of the cylindrical array is described as below

$$\emptyset = 1 - \frac{\pi}{4} \times \frac{D^2}{(P+D)^2} \quad (1)$$

where $\emptyset$ is the porosity, P is the gap pore size and D is the diameter of the cylindrical pillar [10]. As shown in Fig.6, the porosity is calculated by using density and diameter measurement obtained from Fig.4A and Fig.4B, respectively. The result shows the porosity of VACNT is approximately 97% on average.

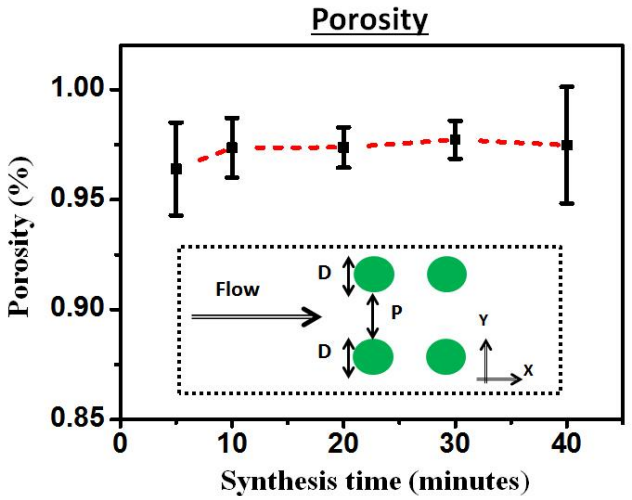

Figure 6. Results of VACNT porosity with illustration of cylindrical model assumption.

To calculated gap size (P), we plugged porosity (ϕ), obtained based on cylindrical model assumption and the VACNT diameter (D) from Fig.5B into equation (1). As seen in Fig.7, the VACNT forest has gap size in the range of 92~136nm with an average of 117.4±26.6nm.

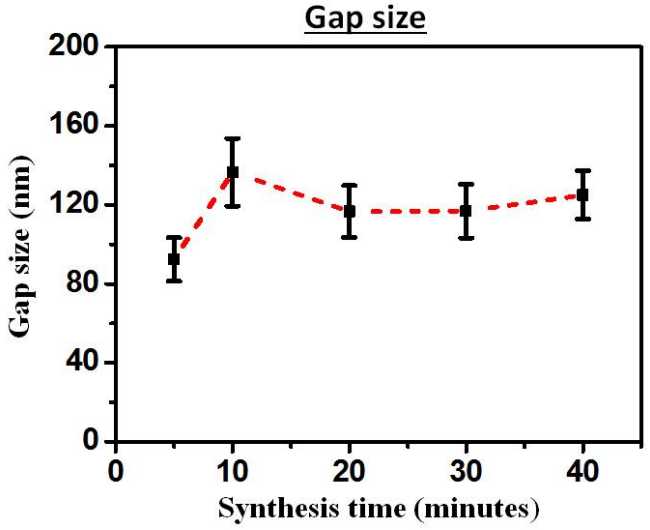

Figure 7. Calculated gap size of VACNT forest.

Feasibility study of virus capture

We tested the device feasibility of virus capture inside the VACNT integrated micro-device for lentivirus detection. We obtained lentivirus from HEK293 cell transfection [11]. The histogram plot of diameter distribution measured from SEM images shows that the lentivirus has dimensions of 128.5±24.1nm in diameter. The inset of Fig.8 shows a SEM image with lentivirus particles fixed on a glass-slide after negative staining [12].

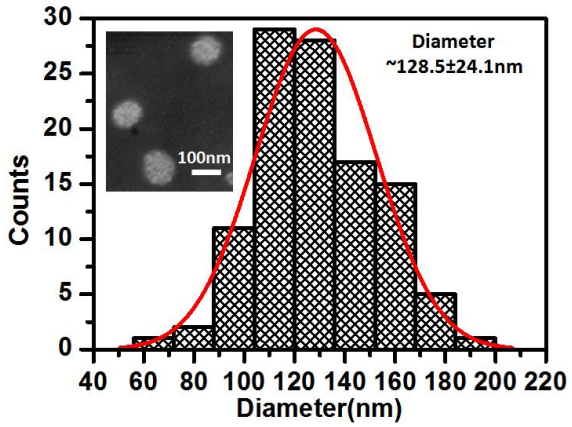

Figure 8, Histogram plot of lentivurs diameter measured via SEM images.

Prior to filtration testing, the virus sample was purified by ultracentrifugation, stained with the fluorophore Sybr Green (Invitrogen) and re-suspended in PBS with a final concentration of ~10^3/µL. The VACNT filtration device is prepared by flushing with 0.5% Tween-20 (50µL) and PBS (200µL), respectively. During the filtration process, 50µL of fluorescently labeled virus was loaded into the inlet reservoir, and 200µL PBS was used to flush and wash away the non-trapped virus particles inside the device. In Fig.9 A and B, a strong fluorescent signal is detected in the VACNT forest droplet shaped pattern, which indicates the presence of the virus. The trapped virus was confirmed by SEM, a seen in Fig.9 C and D.

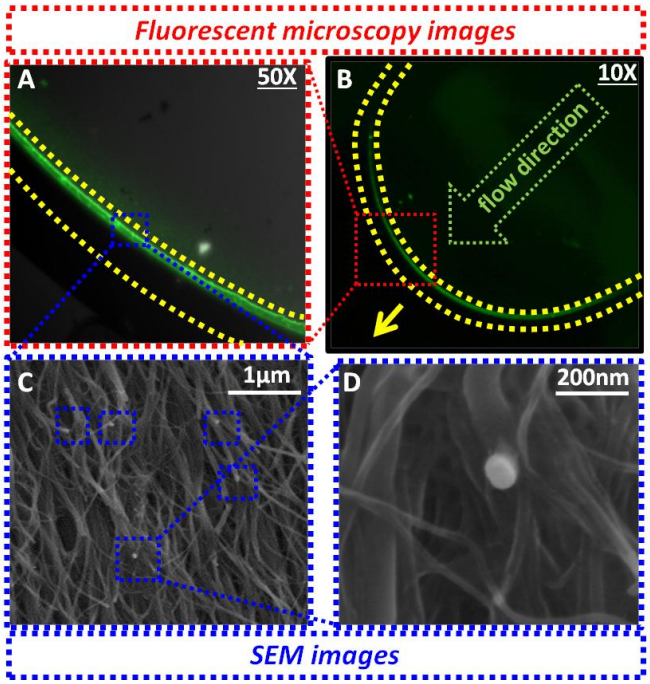

Figure 9. Fluorescently labeled virus captured inside VACNT filtration device. A,B: Fluorescent detection by fluorescence microscopy analysis (A: 50X magnification, B: 10X magnification). C,D: SEM image of captured virus particle

Virus capture efficiency

We further characterized the capture efficiency of the virus filtration device by counting the viral particles from sample flow-through collected at the outlet. We quantified the viral particle concentration by applying HEK293 cell infectious titration technique [13]. Cell culture plates containing HEK293 cell line with 100% confluence were infected by a series of dilutions of virus suspensions. As shown in Fig.10, the infected cells expressed green fluorescent protein (GFP). The fluorescent signal could be easily detected under fluorescence microscope. With the assumption of 100% infection efficiency of HEK293 cells by the lentivirus, we estimated virus particle concentration by multiplying the dilution factor to the counted number of infected cells. By loading a 50µL virus sample into the inlet of the device at a concentration of 6.3×10^4 counts (100%) of total viral particles, we detected 1.8×10^3 counts (3%) of viral particles inside flow-through to the outlet. Meanwhile, we tested two control experiments in parallel. The negative control experiment was to replace inlet virus sample with PBS and the positive control was to replace silicon substrate with VACNT forest into a prime silicon substrate without any pattern. We did not detect any virus for negative control experiment and 4.5×10^4 counts (71%) of virus particles for the positive control.

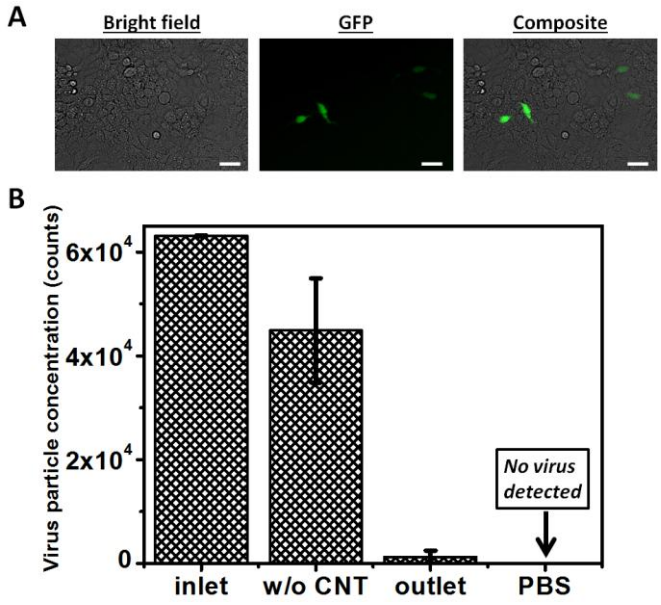

Figure 10, Capture efficiency characterization by HEK 293 cell infectious titration. A: Images of GFP protein expression detection via infected HEK 293 cell counting. B: Capture efficiency results characterized by virus concentration measurements.

CONCLUSION

We integrated a hand-held filtration device with ~120nm pore size, ~97% porosity and ~50µm high VACNT in a bottom-up synthesis process. We optimized the CVD synthesis process and characterized the filtration properties of the VACNT porous wall. We demonstrated that the lentivirus with ~128nm in diameter was captured inside the VACNT forest with capture efficiency of 97% by physical size exclusion. In point-of-care applications, the filtration process can be operated power-free if we replace the vacuum source with pipette suction. In addition, potential contaminations will be minimized since the trapped virus is contained inside the PDMS sealed device and is ready for further detection and manipulation. We believe that the device has potential in such point-of-care virus analysis applications.

ACKNOWLEDGEMENT

The authors appreciate assistance from the Penn State Material Characterization Lab (MCL). We would also like to thank Mr. Gene Gerber for his help with the experimental setup and also Dr. Yingwei Mao and Yijing Zhou for providing lentivirus particles. Travel support has been generously provided by the Transducer Research Foundation**.**

REFERENCES

[1] A. S. Fauci and D. M. Morens, "The perpetual challenge of infectious diseases," New England Journal of Medicine, vol. 366, pp. 454-461, (2012).

[2] M. S. Smolinski, M. A. Hamburg, and J. Lederberg, Microbial threats to health: emergence, detection, and response: National Academies Press, 2003.

[3] S. Baron and H. R. Gelderblom, "Structure and classification of viruses," in Medical Microbiology, ed Galveston, TX: University of Texas Medical Branch at Galveston, 1996.

[4] A. K. Shetty, E. Treynor, D. W. Hill, K. M. Gutierrez, A. Warford, and E. J. Baron, "Comparison of conventional viral cultures with direct fluorescent antibody stains for diagnosis of community-acquired respiratory virus infections in hospitalized children," The Pediatric infectious disease journal, vol. 22, pp. 789-794, (2003).

[5] I. M. Mackay, K. E. Arden, and A. Nitsche, "Real-time PCR in virology," Nucleic acids research, vol. 30, pp. 1292-1305, (2002).

[6] J. Carrero-Sanchez, A. Elias, R. Mancilla, G. Arrellin, H. Terrones, J. Laclette, et al., "Biocompatibility and toxicological studies of carbon nanotubes doped with nitrogen," Nano Letters, vol. 6, pp. 1609-1616, (2006).

[7] S. Webster, J. Maultzsch, C. Thomsen, J. Liu, R. Czerw, M. Terrones, et al., "Raman characterization of nitrogen doped multiwalled carbon nanotubes," in MATERIALS RESEARCH SOCIETY SYMPOSIUM PROCEEDINGS, 2003, pp. 129-134.

[8] M. Bedewy, E. R. Meshot, H. Guo, E. A. Verploegen, W. Lu, and A. J. Hart, "Collective Mechanism for the Evolution and Self-Termination of Vertically Aligned Carbon Nanotube Growth," The Journal of Physical Chemistry C, vol. 113, pp. 20576-20582, 2009/12/03 (2009).

[9] F. Fachin, G. D. Chen, M. Toner, and B. L. Wardle, "Integration of Bulk Nanoporous Elements in Microfluidic Devices With Application to Biomedical Diagnostics," Microelectromechanical Systems, Journal of, vol. 20, pp. 1428-1438, (2011).

[10] K. Vafai, Handbook of porous media: Crc Press, 2010.

[11] X. Wang and M. McManus, "Lentivirus Production," p. e1499, 2009/10/02/ (2009).

[12] M. Laue, "Electron microscopy of viruses," Methods in cell biology, vol. 96, pp. 1-20, (2010).

[13] L. Sastry, T. Johnson, M. Hobson, B. Smucker, and K. Cornetta, "Titering lentiviral vectors: comparison of DNA, RNA and marker expression methods," Gene therapy, vol. 9, (2002).

CONTACT

*S.Y. Zheng, tel: +1-814-865-8090; sxz10@psu.edu

MULTIPLEXED PROTEOMICS USING TWO ORDERS OF MAGNITUDE ENHANCED DIELECTROPHOREIS: A COMPREHENSIVE ELECTRICAL AND ELECTROTHERMAL DESIGN METHODOLOGY

Sam Emaminejad[1,2,3], Michael T. Barako[4], Ronald W. Davis[2,3], Robert W. Dutton[1], Kenneth E. Goodson[4], and Mehdi Javanmard[1,2,3]

[1]Electrical Engineering Department, Stanford University, Stanford, CA, USA
[2]Stanford School of Medicine, Stanford, CA, USA
[3]Stanford Genome Technology Center, Stanford University, Palo Alto, CA, USA
[4]Mechanical Engineering Department, Stanford University, Stanford, CA, USA

ABSTRACT

We present a methodological approach to analyze an enhanced dielectrophoresis (DEP) system from both a circuit analysis and an electrothermal view points. In our developed model, we have taken into account various phenomena and constraints such as voltage degradation (due to the presence of the protecting oxide layer), oxide breakdown, instrumentation limitations, and thermal effects. The results from this analysis are applicable generally to a wide variety of geometries and high voltage microsystems. Here, these design guidelines were applied to develop a robust electronic actuation system to perform a multiplexed bead-based protein assay. For proof of concept, we illustrated 16-plex actuation capability of our device to elute micron-sized beads that are bound to the surface through anti-IgG and IgG interaction which is on the same order of magnitude in strength as typical antibody-antigen interactions. In addition to its application in multiplexed protein analysis, our platform can be potentially utilized to statistically characterize the strength profile of biological bonds, since the multiplexed format allows for high throughput force spectroscopy using the array of uDEP devices, under the same buffer and assay preparation conditions.

INTRODUCTION

Using enhanced negative dielectrophoresis (nDEP), or ultra-DEP (uDEP), we demonstrate an electronic actuation system to perform a multiplexed bead-based protein assay (Figure 1). We pattern an array of proteins along a single microfluidic channel, where each element targets a specific secondary protein coated on micron-sized beads in the subsequently introduced sample. Below each element of the array, we have a pair of addressable interdigitated electrodes (IDE). By selectively applying voltage at the terminals of each IDE pair, the DEP force detaches protein-bound beads from each element of the array, one by one, without disturbing the bound beads in the neighboring regions. The detached beads can be quantified optically or electrically downstream. Here, we illustrate 16-plex actuation capability of our device to elute beads surface-bound through anti-IgG and IgG interaction which is on the same order of magnitude in strength as typical antibody-antigen interactions.

Previously, using nDEP force in conjunction with shear force and eluting agent, we demonstrated switch-like functionality to elute specifically bound beads from the surface [1]. The eluting agent was used to sufficiently weaken the bindings such that the inherently weak nDEP force would be able to push the bound beads off the surface. Generally, our ability to enhance DEP forces was limited by electrode corrosion when applying voltages beyond 10 V. We enhanced the DEP force by two orders of magnitude by fabricating high voltage tolerant electrodes, where we deposited a pinhole free nanometer-scale thin film oxide as a protective layer, using atomic layer deposition [2,3]. However, this approach imposed a number of challenges that needed to be resolved. From electrical modeling standpoint, deposition of oxide at the electrode-electrolyte interface and the resultant capacitance forms a voltage divider that causes an undesired voltage drop across the thin film, leading to degradation of the electric field (across the solution) and DEP force, and possibly, the breakdown of the oxide. Furthermore, in our high voltage system, the temperature in our channel may rise to the point that electrothermal effects may become dominant and outweigh the DEP effect; preventing DEP to act as a robust localized actuator.

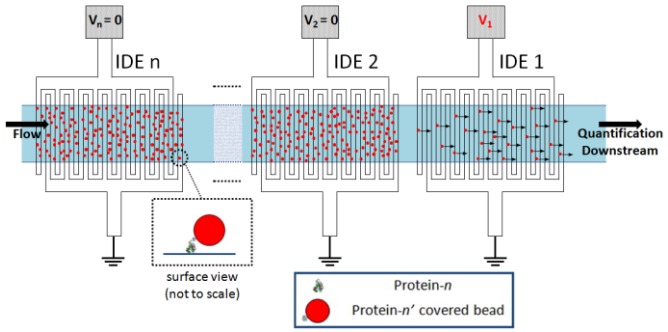

Figure 1: Bead-based multiplexed assay. Each element of array in the capture region is functionalized with a different protein, each targeting a specific protein that is coated on the micron-sized beads. Specifically bound beads on each element of the array are eluted selectively from the array and are quantified downstream (one element at a time). Here, applying voltage V_1 produces uDEP force, which in turn detaches the specifically bound beads from the surface of the 1st interdigitated electrode pair (i.e. IDE 1). With no voltage applied at the other IDEs, the protein-bound beads on the respective elements remain attached to the surface.

DESIGN METHODOLOGY

Following the nanometer-scale thin film oxide deposition, our approach focuses on maximizing the DEP force through maximizing the voltage that can be applied across the solution resistance, while meeting all the electrical and thermal constraints. From electrical modeling standpoint, our constraints are oxide breakdown and excitation circuitry's limitation in providing the high levels of voltage and current (required to establish the desired voltage level across the solution resistance). These constraints set an upper-bound on the maximum voltage that can be applied across the solution resistance i.e. $V_{R,\,max}$ as captured respectively by the equation below:

$$V_{R,max} = \min\left\{ 2E_{BR,ox}\pi\varepsilon_0\varepsilon_{ox}s_{el}\left(\frac{f}{\sigma}\right),\ \frac{V_{ac,max}}{\sqrt{1+\left[\left(\frac{1}{\pi\varepsilon_0\varepsilon_{ox}s_{el}}\right)\left(\frac{\sigma}{f}\right)t_{ox}\right]^2}},\ I_{ac,max}\left(\frac{s_{el}}{n\sigma A_{el}}\right)\right\}$$

9781940470016/HH2014/$25©2014TRF
DOI 10.31438/trf.hh2014.6

In this equation $E_{BR,ox}$ and ε_{ox} refer to electric field oxide breakdown and dielectric constant of our ALD thin film, s_{el} is the spacing between two electrodes, f is the frequency of excitation, σ is the solution conductivity, A_{el} is the area bound by the transverse width of the channel and width of a single electrode, and n is the number of electrode pairs in our interdigitated configuration. $V_{ac,max}$ and $I_{ac,max}$ refer to maximum voltage and current amplitude that can be delivered by the signal generator. To better visualize the design space, in Figures 2(a) we illustrated $V_{R,max}$ for t_{ox} = 10 nm while meeting the electrical constraints.

From thermal modeling standpoint, our main constraint is bubble formation due to the increase in the temperature upon applying higher voltages [4]. Assuming bubble formation takes place upon temperature increase of ΔT_{max}, $V_{R,max}$ constrained by thermal limitations can be derived as:

$$V_{R,max,th} \cong \sqrt{\beta \left(\frac{k_{sub}}{\sigma}\right) \Delta T_{max}}$$

In this equation k_{sub} refers to the thermal conductivity of the substrate (on which electrodes are patterned) and $\beta = 2\left(\frac{{s_{el}}^2}{t_{sub} w_{el}}\right)$ captures the role of geometrical dimensions (note in the expression for β, w_{el} refers to the width of the electrodes). For more precise analysis we can calibrate the value of β through simulation (Figure 2(b)).

To complete our design methodology, we need to take into account the effect of clausius mossotti factor f_{CM} (which is frequency- and conductivity-dependent) on DEP. As a result, in our design space to achieve maximum DEP force we need to operate in the region where $\mathrm{Re}\{f_{CM}\}\times V^2_{R,max}$ is maximized, as illustrated in Figure 3.

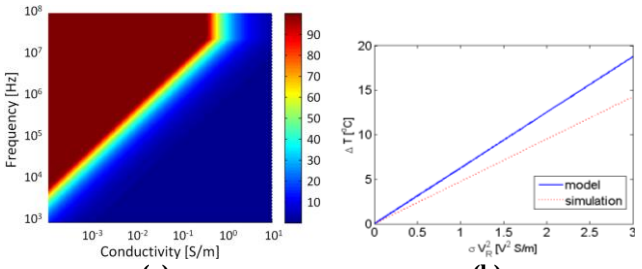

(a) **(b)**

*Figure 2: **(a)** Representative 'electrical' design space illustrating $V_{solution}$ for t_{ox} = 10 nm, while meeting the oxide breakdown criterion ($E_{BR,ox}$ = 1 V/nm) and instrumentation limitation (here assumed $V_{ac,max}$ = 100 V, $I_{ac,max}$ = 0.2 A) **(b)** Proportionality of the raise in temperature with the generated power density (setting an upper-bound on $\sigma V^2_{solution}$). Through calibration with simulation (in our case by ~30%) we can precisely model the 'thermal' behavior of the coplanar configuration.*

RESULTS AND DISCUSSION

We confirmed our developed model for electrical interface through impedance spectroscopy (similar to our approach in [2]). Also, through infrared microscopy characterization (Figure 4) we confirmed that DEP force stays dominant in the context of our high voltage microsystem and that electrothermal effects can be neglected.

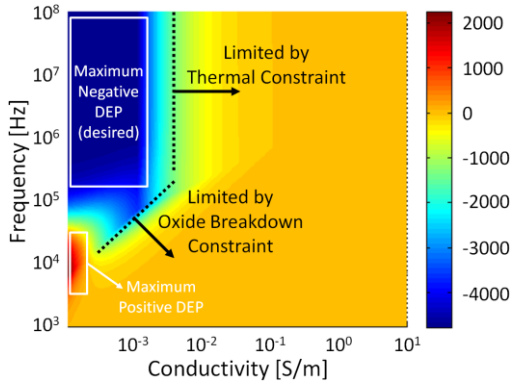

Figure 3: Representative 'electrothermal' design space illustrating relative maximum DEP force (proportional to $\mathrm{Re}\{f_{CM}\}\times V^2_{R,max}$) for a 10-nm deposited oxide that can be achieved for 7 µm wide and 7 µm spaced IDE pair geometry while meeting the design constraints. The limitations imposed by the dominant design constraints are annotated on the graph. -/+ values correspond to negative/positive DEP. For our application we prefer the most negative value.

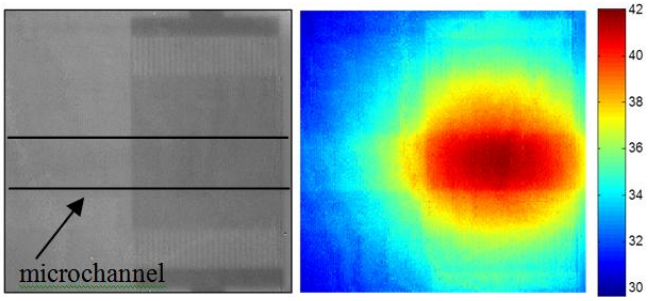

Figure 4: Representative infrared microscopy image of the device, providing a non-invasive measurement of the two-dimensional temperature map of the surface of the wafer. Here, the microchannel is filled with diluted phosphate-buffered saline and 50 V_{pp} is applied across the IDE pair. This technique provides a spatial resolution up to the diffraction limit (≈2 µm). In the left image the microchannel is outlined as it was not visible in the original captured image.

Upon characterization of the device's electrothermal behavior, we patterned an array of 16 uDEP IDEs along a single channel, and extended the enhanced and localized switch-like operation of the uDEP device to demonstrate the multiplexed actuation capability. Through a series of incubation and wash steps, 2.8 µm-diameter goat-anti-mouse-IgG covered beads were bound to mouse-IgG coated surface through specific interactions on each element of the array. We selectively detached immunobound beads from each element of the array, by applying voltage (turning uDEP on) at each IDE pair, one-by-one (Figure 5a). In addition to multiplexed protein analysis, our platform enhances the DEP capability in statistical characterization of the force spectrum of biological interactions, since the multiplexed format enables performing force spectroscopy on multiple devices independently (Figure 5b), with high dynamic range in a single channel; minimizing inter-experiment variations that originate from disparities in buffer conditions and assay preparation steps. We envision a plethora of possibilities for performing rapid and inexpensive multiplexed protein biomarker analysis using this localized electronic actuation method.

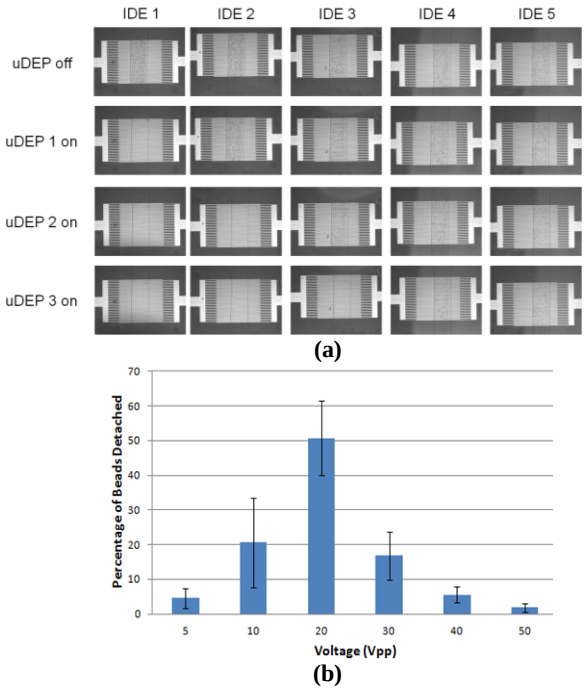

Figure 5: ***(a)*** *Five neighboring IDEs 1-5. Initially uDEP was off for all IDEs (row 1), and then uDEP was sequentially turned on by applying voltage at IDEs 1,2, and 3 (corresponding to rows 2,3, and 4).* ***(b)*** *Detachment percentage of protein-bound beads when ramping up the applied voltage at each of the IDE pairs one-by-one. The results represent the collective detachment profile when actuating anti-IgG-IgG bound beads using our 16-plex platform. The array format allows performing force spectroscopy multiple times while ensuring operation under the same buffer conditions and assay preparation steps (DEP force is proportional to the square of the applied voltage).*

ACKNOWLEDGEMENTS

This work was supported by the National Institutes of Health through grant PO1HG000205 and Natural Sciences and Engineering Research Council of Canada Scholarship through graduate tuition support. Fabrication of the devices was performed in the Stanford Nanofabrication Facility.

REFERENCES

[1] S. Emaminejad, M. Javanmmard, R.W. Dutton, and R.W. Davis, "Use of Negative Dielectrophoresis for Selective Elution of Protein-Bound Particles", Analytical Chemistry, 84 (3), pp 1432–1438 (2012).

[2] S. Emaminejad, M. Javanmmard, R.W. Dutton, and R.W. Davis, "Smart Surface for Elution of Protein–Protein Bound Particles: Nanonewton Dielectrophoretic Forces Using Atomic Layer Deposited Oxides", Analytical Chemistry, 84 (24), pp 10793–10801 (2012).

[3] M. Javanmmard, S. Emaminejad, C. Gupta, J. Provine, R.W. Davis, and R.T. Howe, "Depletion of Cells and Abundant Proteins from Biological Samples by Enhanced Dielectrophoresis", Sensors and Actuators B: Chemical, vol. 193, pp. 918-924 (2013).

[4] S. Emaminejad, M. Javanmmard, R.W. Dutton, and R.W. Davis, "Ultra Dielectrophoresis Using Atomic Layer Deposited Films: Electrothermal Analysis", ECS Transactions, 58 (10) 67-72 (2013)

CONTACT

*S. Emaminejad, same@stanford.edu

MICROFLUIDIC BARCODE ASSAY FOR MULTIPLEXED CLINICAL DIAGNOSTICS

Robert Lin[1], *Arunan Skandarajah*[1], *Rachel E. Gerver*[1], *Daniel A. Fletcher*[1], *and Amy E. Herr*[1]*
[1]University of California at Berkeley, USA

ABSTRACT

Here we present a novel method for creating three-dimensional, photocaptured protein patterns that can be completed with no additional linker molecules required. We utilized the photopatterned proteins to selectively capture antibodies and implemented a microfluidic sandwich assay. We demonstrate Hepatitis C virus (HCV) diagnostic device based on the technology and show that the device is capable of assaying human sera and can positively identify HCV+ human patient serum samples in 60 minutes. We also demonstrate a barcode assay using lectins to detect differences in prostate specific antigen (PSA) glycan structure. Additionally, we image the HCV diagnostic chip using a low-resource setting compatible imagining system – the fluorescence CellScope.

INTRODUCTION

Near-patient clinical diagnostics require simple-to-use assays. A powerful canonical format is the 'dipstick' lateral flow assay (e.g., home pregnancy test, HIV oral fluid screening test). These low or no power rapid dipstick tests provide only "yes/no" readouts for limited biomarkers. Nevertheless, to address 21st century challenges spanning from global health to skyrocketing costs in the developed world, new fast and simple – yet multiplexed and quantitative – tests are needed. Consequently, cell phones are emerging as feasible for diagnostic questions requiring sophisticated (beyond binary) readouts.[1-3] To yield a sophisticated diagnostic compatible with cell phone imaging, we introduce a simple and rapid microfluidic "barcode" immunoassay format, demonstrated for confirmatory diagnosis of Hepatitis C. The 60 minute, low-power (1mW) barcode assay advances telemedicine by eliminating the need for a centralized clinical laboratory.

In tandem with use of mobile technology in telemedicine,[4-7] healthcare delivery would benefit from reduced dependence on centralized laboratory facilities. For hepatitis C virus (HCV) confirmatory diagnosis after a positive rapid screening result, semi-quantitative measurement of reactivity against specific antigens or test of viral RNA presence comprises the gold-standard confirmation of infection. Current HCV confirmatory assays require a clinical lab facility. Taken together, we see assays that require no sophisticated hardware – e.g. pumps/valves – and mobile devices as potentially central to advancing towards new solutions to global health challenges.

The microfluidic format is uniquely suited to work with mobile imaging modalities. First, the small footprint of microfluidic devices along with the reduced bulk of smartphone-based imaging techniques lends to being adapted to the point-of-care setting. Second, materials used to fabricate microfluidic devices are usually optically clear – elastomers, glass and plastics – and are therefore compatible with the optical detection mechanism used for phone-based diagnostic systems. Lastly, the inherent small volumes leveraged in the microfluidic format are often difficult to be visualized with the naked eye. The ability to be combined with a low-cost mobile reader device greatly increases the utility of microfluidics in near-patient settings. A variety of microfluidic assays have been demonstrated to work with a mobile imaging device.[8-11]

The ability to define distinct regions in microfluidic devices serves as the basis for the creation of multiplexed analytical platforms. Of the more commonly employed methodologies, photopatterning has emerged as perhaps the most prominent techniques in creating complex patterns inside microfluidic devices.[12] Immobilization on bare channel surfaces suffers from the disadvantage of requiring grafting of reactive groups onto the surface and/or the use of linkers to attach proteins to the surface. Additionally, only a low percentage (as low as 0.01%) of proteins from the bulk solution can be captured onto the surface.[13] The low immobilization efficiency onto microchannel surfaces is largely due the extremely low surface area to volume ratio while operating in the microscale. Polymer monoliths occupy part of channel volume and provide increased surface area for the immobilization of proteins. However, the use of polymer monoliths still requires linker groups to be attached to the monoliths. Lastly, hydrogel matrices have been used as an immobilization matrix as well. However, as opposed to covalently immobilizing the proteins, the dense gel matrix physically traps the proteins.[14-17] In a recent implementation of immobilization inside hydrogel matrices, streptavidin-functionalized hydrogel was utilized. However, the technique involves a blocking step that lead to long processing times when creating complex patterns.[18]

In this manuscript we demonstrate a heterogeneous barcode immunoassay implemented in a microfluidic format (Figure 1a) that is capable of multiplexed detection against up to 5 distinct targets. We leverage a photopatternable gel substrate - light-activated volume-accessible gel (LAVAgel)[19] as the functional matrix. A multiplexed Hepatitis C virus (HCV) barcode assay on a microfluidic chip is used to test human serum samples to distinguish patients with and without HCV infection. We also demonstrate a barcode assay using lectins to detect differences in prostate specific antigen (PSA) glycan structure. Additionally, the HCV diagnostic chip can be imaged directly using the fluorescence CellScope (Figure 1b) – a low-resource setting imagining system based on a mobile phone.[7,20] Taken together, we believe the microfluidic barcode assay and fluorescence CellScope offers a robust and facile platform for implementing multiplexed heterogeneous immunoassays designed for point-of-care applications.

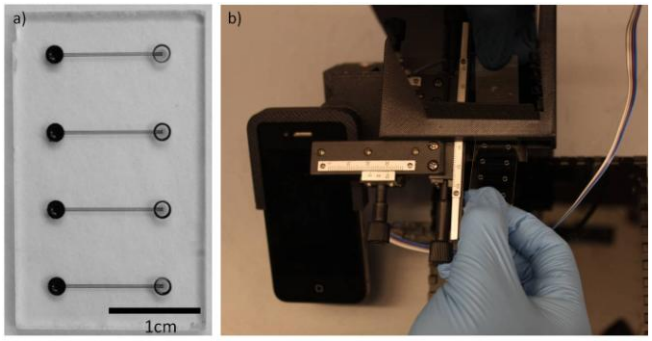

Figure 1 Microfluidic assay and imaging platform. a) Photograph of microfluidic chip with 4 (devices) well-pairs each connected by 3 microfluidic channels. The channels are filled with dye to facilitate visualization. b) Photograph of microfluidic chip being placed into the fluorescence CellScope.

9781940470016/HH2014/$25©2014TRF
DOI 10.31438/trf.hh2014.7

MATERIALS AND METHODS

Chemicals and Reagents

Aqueous solution of 30% (w/v) (29:1) acrylamide/bis-acrylamide, glacial acetic acid, ammonium persulfate (APS), N,N,N',N'-tetramethylethylenediamine (TEMED), methanol and 3-(trimethoxysilyl)-propyl methacrylate and sodium hydroxide (NaOH) were purchased from Sigma-Aldrich (St. Louis, MO). N-[3-[(4-benzoylphenyl) formamido-[propyl]-methacrylamide (BPMAC) was custom synthesized by PharmAgra Labs (Brevard, NC). AlexaFluor 488 (AF488) and AlexaFluor 555 (AF555) labeled Ovalbumin (OVA) and bovine serum albumin (BSA) were purchased from Life Technologies (Carlsbad, CA). FITC-labelled anti-BSA antibody was purchased from MyBiosource Inc. (San Diego, CA). Hepatitis-C Virus (HCV) positive serum, AF488 conjugated HCV Core(c22p), NS3(c33c) and NS4(c100p) antigens were provided by Norvartis Diagnostics (Emeryville, CA). HCV negative human sera were purchased from SeraCare Life Sciences (Oceanside, CA). AlexaFluor 568 (AF568) conjugated secondary goat anti-human antibody was purchased from Life Technologies (Carlsbad, CA). All antigen, antibody and serum samples were diluted into 1X Tris-Glycine buffer before introduction into the chip. 1X Tris-Glycine buffer was purchased at 10X concentration from Bio-Rad (Hercules, CA).

Image Acquisition, Control and Patterning Instrumentation

Fluorescence images were acquired on an Olympus IX-50 inverted microscope (Olympus USA, Center Valley, PA) with fluorescence illumination provided by X-cite exacte illumination system from Lumen Dynamics (Mississauga, Canada). Images were acquired through a 10X/0.3 NA objective (Olympus USA, Center Valley, PA) with filter cubes for GFP – Omega XF100-3 and Texas Red – XF102-2 (Omega Optical, Brattleboro, VT). Image analysis and stitching of multiple adjacent microscope images was performed using ImageJ from NIH (Bethesda, MD). Custom-built programmable high-voltage power supply (HVPS) was used for electrophoretic control with platinum electrodes directly inserted into the sample reservoir wells. UV for photopatterning was provided by a Hamamatsu Lightningcure LC5 unit (Bridgewater, NJ) through a Lumatec series 380 liquid light guide (Deisenhofen, Germany). Photomasks designs were created in-house and laser cut from 50µm thick stainless steel sheet using Universal Laser PLS6MW with a 30W fiber laser cartridge (Scottsdale, AZ).

Microfluidic chip preparation

Chip designs were performed in-house and fabrication was performed by Caliper Life Sciences (Hopkinton, MA). Standard wet etching and drilling methods were used followed by thermal bonding. Each device consists of three parallel microfluidic channel of 1.2mm length, 90µm width and 20µm depth connecting wells of 2mm in diameter and 1mm deep that serves as the sample reservoirs. Fig. 1a shows a photograph of a single device. One of the reagent wells is filled with dye to assist with visualization of the three microfluidic channels. Each chip contains 4 devices with 3 channels each.

Prior to introduction of polyacrylamide gel precursor solutions the glass channel surfaces were functionalized with acrylate-terminated self-assembled monolayer as previously described. Precursor solution with 1X TG, 4% wt/vol total acrylamide (4%T) with 2.6% of the total as cross-linker bisacrylamide (2.6%C) and 1.6nM BPMAC were mixed and degassed with sonication and vacuum. The BPMAC imparts photo-activatable capture capability to the polyacrylamide gel. Immediately prior to introduction into the device 0.08% (wt/vol) of APS and 0.08%(vol/vol) of TEMED were added to the precursor solution to initiate polymerization.

Barcode assay fabrication

Photopatterning of proteins bands (barcodes) inside the microfluidic channels are performed after completion of chip preparation. Briefly, proteins to be immobilized (labeled or unlabeled) are diluted into 1X TG buffer prior to pipetting into the sample wells (~6µL). The samples are then electrophoretically loaded into the microfluidic channel by applying a 200V electrical bias between the sample and sink wells. After loading, the photomask was placed on top of the channels and the light guide is placed directly on top of the opening and in contact with the mask. Subsequently, UV illumination is applied for five seconds at 20% diaphragm opening controlled through the instrument interface. After illumination the wells were each rinsed three times with 1X TG buffer and a reverse bias of 500V was applied for five minutes to electrophoretically wash out non-immobilized proteins. Successful protein band patterning was confirmed using fluorescence imaging.

Mobile Microscope Design

The CellScope fluorescence microscope used in this study consisted of a transmission light path capable of fluorescence and bright-field illumination and a finite conjugates imaging pathway built into a 3D printed casing designed to couple to an iPhone 4S. The collection optics included a 10x/0.25 NA objective (Edmund Optics, Barrington, NJ, #36-132) spaced 160mm from a 20x widefield eyepiece (#39-696) with a pair of silver turning mirrors (Thorlabs, Newton, NJ, CM1-P01) to make the design more compact. The casing, stage, and phone adapters were printed using thermally extruded ABS plastic utilizing a desktop 3D printer (Stratasys, Eden Prairie, MN, uPrint Plus). Illumination for the simultaneous dual-color fluorescence was provided by a mounted RebelNeutral White (4100K) LED purchased from Luxeon Star(MR-WN090-20S, Brantford, ON, CA) attached to a heat sink (Digikey, Thief River Falls, NY, 294-1111-ND). An aspheric lens (Newport, KPA031) with a diameter of 25 mm and 17 mm effective focal length was separated from the LED by its back focal length and used as a collector lens with a second asphere of the same type used as a condenser lens. The dual band-pass excitation filter (59022x, Chroma Technology) was placed after the collector to select two excitation bands centered at 470 nm and 570 nm from the collimated source. After the excitation filter, a coverslip set at 45° is used to couple in light from a standard 5mm green LED for bright-field imaging of the chip. An emission filter (59022m, Chroma Technology) is placed as close as practical to the back focal plane of the objective to select emission bands centered at 520 nm and 630 nm. A separate modular enclosure contains a rechargeable lithium ion battery (Astro Pro External Battery, Anker), a 700 BuckPuck DC Driver (3023-D-E-700, Luxeon Star), and a switch for selecting between fluorescence and bright-field illumination. Final separation of spatially overlaid fluorescent probes was done through the on-board Bayer Filter on the phone which, in combination with an on-board demosaicing algorithm, assigns a red, green, and blue value to each pixel. Imaging was done using the default camera application on the iPhone 4S with the exposure time and focus locked on a dark field to maximize sensitivity.

RESULTS AND DISCUSSION

HCV Diagnostic with Human Serum Sample

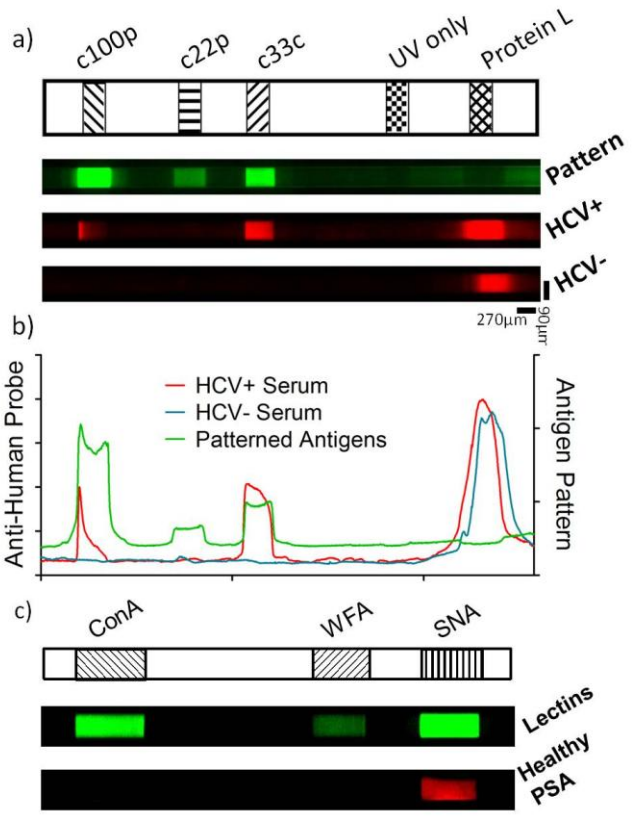

Figure 2 Microfluidic barcode assay testing biological samples. a) Fluorescence readout of Hepatitis C virus(HCV) assay examining human serum samples using an epi-fluorescence microscope with stitched images. HCV+ sample shows clear bands at 2 of the 3 HCV antigen locations. HCV- Sample shows only signal at the positive control location. b) Profile plots of the antigen patterns and blotted serum signals. c) Lectin-based barcode assay can be used to test for differences in prostate specific antigen glycan structure.

In order to demonstrate the platform's ability to make biologically relevant measurements, we move to implement a microfluidic barcode Hepatitis C virus (HCV) diagnostic assay. For the HCV diagnostic device a five band pattern was created (Fig. 6a) including three AF488-labeled HCV antigens, one negative control (UV only) and one positive control band patterned with protein L. Protein L is a bacterial protein that binds to human immunoglobulins and is used in the assay as positive control to verify the successful loading of serum samples. The first photograph – "Pattern" – in Fig. 2a shows a typical fluorescence image of the patterned proteins after patterning of all five bands. The three HCV antigens can be clearly visualized as three green bars on the left side of the microchannel, while the negative control band has no proteins immobilized and the positive control (Protein L) is unlabelled and shows no fluorescence.

To test the device's ability to identify HCV infection, serum samples are diluted 1:40 into 1X Tris-Glycine buffer and electrophoretically loaded into the HCV diagnostic device. The volume of human serum consumed per triplicate assay is approximately 150nl. After antibody washout the device is imaged using an inverted fluorescence microscope, the results are shown in Fig. 2a. The HCV+ serum sample shows secondary antibody signal at the c100p and c33c antigen locations in addition to the protein L band, suggesting the serum sample contains human antibodies that react with the patterned viral proteins – indicative of HCV infection. The HCV- sample shows only a single fluorescence band at the protein L location suggesting successful sample loading but no reactivity at any of the patterned antigen sites. Fig. 2b shows the electropherograms – patterned antigen in green line and secondary blotting results in red – for the HCV+ and HCV- sample. In the HCV+ case the blotting result peaks align perfectly with the patterned antigens at c100p and c33c, suggesting specific interactions of human antibodies with those antigens. The region with only UV illumination shows no signal indicating no nonspecific interaction with the activated gel. The HCV- sample device traces shows comparable levels of patterned antigens compared to the HCV+ sample device but no probed signal, suggesting the serum contains no HCV-reactive human IgGs. As non-infectious diseases, such as cancer become increasingly urgent in global settings, we also demonstrate a lectin-based barcode assay to assess differences in prostate specific antigen (PSA) glycan structure to potentially differentiate healthy vs. cancer-correlated PSA (Fig. 2c).

To further demonstrate the platform's potential to create diagnostic tools that are compatible with the point-of-care setting we imaged the HCV diagnostic device using a customized fluorescence-capable CellScope. It provides high resolution imaging in a portable form factor that takes advantage of the recent improvements in LED illumination and phone camera sensitivity.

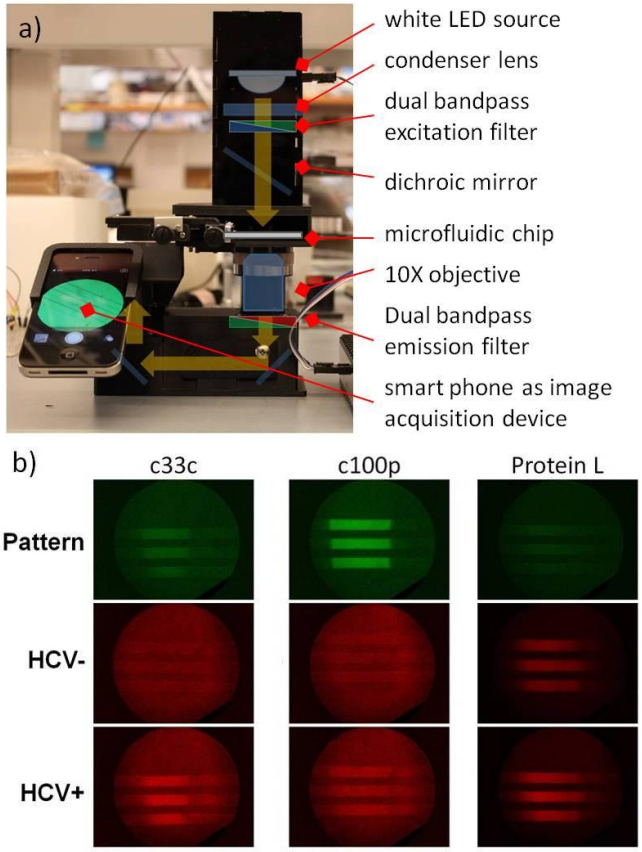

Figure 3 a) Photograph of the customized fluorescence CellScope. The light path used for imaging the microfluidic chip and the schematic of the optical components used is overlaid and labeled. b) Readout from microfluidic barcode assay device obtained using the fluorescence CellScope. Images were obtained by splitting the RGB image acquired from the smartphone into 3 separate channels/images. Only the green and red channel was used in the figure as no signal was present in the blue channel.

In the customized CellScope shown in Fig. 3a, a white light LED illumination source was paired with a dual band-pass filter set and the built-in Bayer Filter Array of the mobile phone to collect two channels of fluorescence data. Each photopatterned protein band in the barcode assay was imaged simultaneously in the green and red channels, enabling the correlation of the position of the antigen and captured antibodies. By utilizing this approach, there is no need to switch filters or illumination source during imaging of a given protein band location. This avoids the cost and complexity of the additional optics, electronics, and mechanical components that are used in multi-color fluorescence imaging with a scientific monochrome camera. Fig. 3b shows the set of images acquired using the CellScope that are analogous to those from Fig. 2a. The system was designed to capture the full field of view of the microscope, yielding a circular field of view inscribed on the rectangular sensor of the mobile phone. The first row shows each of the patterned protein bands with the second and third row showing the HCV- and HCV+ immunoblotting results respectively. As in Fig. 2a, the HCV+ and HCV- assays were performed in different devices with the identical pattern. In this case the pattern images were taken after the assay was complete. This allowed the images of the antigen pattern and the HCV+ probed results to be acquired simultaneously without the need to move the chip; resulting in perfect alignment of the imunnoblotted band and the patterned antigen.

CONCLUSION

We presented here a novel methodology for photopatterning complex patterns in microfluidic devices using a functionalized polyacrylamide gel matrix (LAVAgel). We then implemented a multiplexed microfluidic HCV diagnostic tool that is capable of detecting human anti-HCV antibodies from dilute human patient sera within 60 minutes. The microfluidic diagnostic assay was interfaced with a custom fluorescence CellScope and together demonstrates the platforms' potential to be used in a point-of-care setting. Taken together, we believe the microfluidic barcode assay and fluorescence CellScope offers a robust and facile platform for implementing multiplexed immunoassays for point-of-care applications.

REFERENCES

[1] P. Yager *et al.*, "Microfluidic Diagnostic Technologies for Global Public Health." *Nature* **442**, 412 (2006).

[2] C. D. Chin, V. Linder, S. K. Sia, "Commercialization of Microfluidic Point-of-Care Diagnostic Devices." *Lab Chip* **12**, 2118 (2012).

[3] G. S. Fiorini, D. T. Chiu, "Disposable Microfluidic Devices: Fabrication, Function, and Application." *Biotechniques* **38**, 429 (Mar, 2005).

[4] S. Vashist, O. Mudanyali, E. M. Schneider, R. Zengerle, A. Ozcan, "Cellphone-Based Devices for Bioanalytical Sciences." *Anal Bioanal Chem*, 1 (2013/11/28, 2013).

[5] D. Tseng *et al.*, "Lensfree Microscopy on a Cellphone." *Lab Chip* **10**, 1787 (2010).

[6] H. Zhu, O. Yaglidere, T.-W. Su, D. Tseng, A. Ozcan, "Cost-Effective and Compact Wide-Field Fluorescent Imaging on a Cell-Phone." *Lab Chip* **11**, 315 (2011).

[7] D. N. Breslauer, R. N. Maamari, N. A. Switz, W. A. Lam, D. A. Fletcher, "Mobile Phone Based Clinical Microscopy for Global Health Applications." *PLoS ONE* **4**, e6320 (2009).

[8] A. W. Martinez *et al.*, "Simple Telemedicine for Developing Regions: Camera Phones and Paper-Based Microfluidic Devices for Real-Time, Off-Site Diagnosis." *Anal Chem* **80**, 3699 (2008/05/01, 2008).

[9] Y. Lu, W. Shi, J. Qin, B. Lin, "Low Cost, Portable Detection of Gold Nanoparticle-Labeled Microfluidic Immunoassay with Camera Cell Phone." *Electrophoresis* **30**, 579 (2009).

[10] P. B. Lillehoj, M.-C. Huang, N. Truong, C.-M. Ho, "Rapid Electrochemical Detection on a Mobile Phone." *Lab Chip* **13**, 2950 (2013).

[11] S. Q. Wang *et al.*, "Integration of Cell Phone Imaging with Microchip Elisa to Detect Ovarian Cancer He4 Biomarker in Urine at the Point-of-Care." *Lab Chip* **11**, 3411 (2011).

[12] A. M. Tentori, A. E. Herr, "Photopatterned Materials in Bioanalytical Microfluidic Technology." *J Micromech Microeng* **21**, (May, 2011).

[13] R. A. O'Neill *et al.*, "Isoelectric Focusing Technology Quantifies Protein Signaling in 25 Cells." *P Natl Acad Sci USA* **103**, 16153 (Oct 31, 2006).

[14] W. Zhan, G. H. Seong, R. M. Crooks, "Hydrogel-Based Microreactors as a Functional Component of Microfluidic Systems." *Anal Chem* **74**, 4647 (Sep 15, 2002).

[15] S. Zimmermann, D. Fienbork, A. W. Flounders, D. Liepmann, "In-Device Enzyme Immobilization: Wafer-Level Fabrication of an Integrated Glucose Sensor." *Sensor Actuat B-Chem* **99**, 163 (Apr 15, 2004).

[16] J. Heo, R. M. Crooks, "Microfluidic Biosensor Based on an Array of Hydrogel-Entrapped Enzymes." *Anal Chem* **77**, 6843 (Nov 1, 2005).

[17] A. G. Lee, D. J. Beebe, S. P. Palecek, "Quantification of Kinase Activity in Cell Lysates Via Photopatterned Macroporous Poly(Ethylene Glycol) Hydrogel Arrays in Microfluidic Channels." *Biomed Microdevices* **14**, 247 (Apr, 2012).

[18] M. K. Araz, A. A. Apori, C. M. Salisbury, A. E. Herr, "Microfluidic Barcode Assay for Antibody-Based Confirmatory Diagnostics." *Lab Chip* **13**, 3910 (2013).

[19] A. J. Hughes, R. K. C. Lin, D. M. Peehl, A. E. Herr, "Microfluidic Integration for Automated Targeted Proteomic Assays." *P Natl Acad Sci USA* **109**, 5972 (Apr 17, 2012).

[20] A. Tapley *et al.*, "Mobile Digital Fluorescence Microscopy for Diagnosis of Tuberculosis." *Journal of Clinical Microbiology* **51**, 1774 (June 1, 2013, 2013).

CONTACT

*A.E. Herr, tel: +1-510-666-3396; aeh@berkeley.edu

ACKNOWLEDGEMENTS

The authors thank the Siebel Stem Cell Institute Postdoctoral Fellowship, NIH T32 training grant, as well as an NIH "New Innovator" Award to AEH. Thanks to members of the Herr lab for helpful discussion. We would also like to thank Dr. Jim Cheng for his generosity in assisting with the fabrication of the photomasks.

NEEDS AND OPPORTUNITIES FOR NANOTRIBOLOGY IN MEMS AND NEMS

R.W. Carpick [1], G.E. Wabiszewski[1], F. Streller[2]*
[1] Dept. of Mechanical Engineering and Applied Mechanics, U. Pennsylvania, Philadelphia, Pennsylvania, USA
[2] Dept. of Materials Science and Engineering, U. Pennsylvania, Philadelphia, Pennsylvania, USA

ABSTRACT

Nanoelectromechanical systems (NEMS) switches are a candidate "beyond CMOS" technology, with a key benefit being massively reduced power consumption. However, the reliability of the contact interface is a principal challenge, as the electrically conducting contacting surfaces need to be able to open and close up to a quadrillion times without excessive adhesion, wear, or contamination. Similar failure mechanisms occur in microelectromechanical systems (MEMS). These failure mechanisms are not well understood, and materials that can exhibit the needed performance have not yet been demonstrated. Here we highlight key challenges and opportunities for applying scientific insights from nanotribology to address these reliability challenges.

INTRODUCTION

Nanoelectromechanical systems (NEMS) switches have been identified as a potential next-generation transistor with far lower power consumption than existing electronic integrated circuits, a critical technological need. These switches are nanoscale moving devices that convert an electrical input signal into motion to close a conductive contact [1]. NEMS switches are thus a mechanical version of a transistor with topologies that often mimic larger microelectromechanical systems (MEMS) switches. However, NEMS switches require small dimensions for the fast, competitive switching speeds (<100 ns) desired in computer logic applications. The nanoscale dimensions and complex operating conditions at the electrical contact make NEMS logic switches susceptible to tribologically-mediated failure mechanisms. In particular, low contact and restoring forces may lead to device "stiction" (device permanently stuck closed), or intolerable increases in switch contact resistance due to the formation of insulating tribopolymer (TP) films. It may be possible to mitigate these failures with the use of low adhesion and catalytically inactive contact materials. This paper will review the opportunities presented by NEMS switch technology, and will discuss needs and approaches to address the technological barriers arising from tribological issues.

The Need for Low Power Computation

Sustained growth in computing power and decrease in computing cost has led to the proliferation of devices utilizing integrated processors in the last half century. These processors are overwhelmingly based on fully-electronic CMOS technology. While this technology has proven exceptional for decreasing transistor real estate and increasing speed [2], it is currently encountering a "power crises." Further scaling of CMOS leads to intractable increases in power loss per computation due to irreversible processes inherent to the physics controlling device operation [2]–[4]. The significant power requirements of computer processors, the power crisis of conventional CMOS, trends towards smart devices, the increasing penetration of home and laptop computers, the desire for long lasting battery-operated mobile devices, and power consumption requirements of CMOS outpacing battery capacities motivates the need to explore lower power transistors. Recognizing the physical limitations of existing CMOS technology, the International Technology Roadmap for Semiconductors (ITRS) has included nanoelectromechanical systems (NEMS) switches as a possible disruptive, low-power technology to cohabitate or usurp the conventional, fully electronic transistor.

NEMS Switches as an Alternative to the Transistor

Ohmic NEMS switches provide the same functionality as the conventional metal-oxide-semiconductor field-effect transistor (MOSFET). In both technologies, the application of a gate signal results in current transfer from the source to drain. However, CMOS relies on a fully-electronic, semiconductor junction to achieve this functionality whereas NEMS logic switches rely on the mating of conductive contacts (see Figure 1).

NEMS ohmic switches utilize mechanical motion to modulate the distance between two conductive contacts which serve as the source (S) and drain (D) electrodes. Figure 1(a) shows the topology and working principal of a NEMS switch prototype by Piazza and co-workers [5], [6]. The device is in an "off-state" when the source and drain electrodes are separated by a physical gap, and the "on-state" when the source and drain electrodes are closed with sufficient force to establish an electrical connection. The space separating the electrodes in the off-state is the switch gap. Ideally, closure of the source and drain electrodes results in current flow from the biased source to the drain, while contact release results in a near-infinitely resistive junction. Successful operation is dependent on reliably and repetitively making and breaking the source and drain electrodes while maintaining a conductive contact in the device on-state and a high resistance in the off-state.

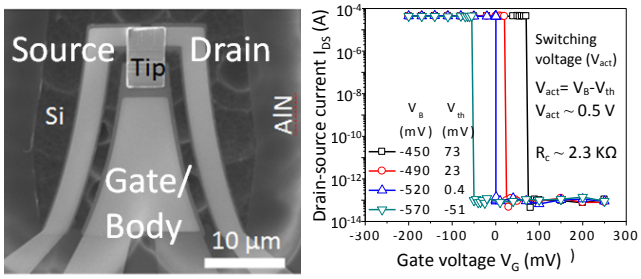

Figure 1. (a) SEM top view image of a working NEMS switch. (b) The device shows a steep subthreshold slope, low leakage current, and low switching voltage (V_B = switch body bias voltage, V_{th} = gate threshold voltage for switching, V_{act} = total actuation voltage, R_C = contact resistance). From [6].

An input voltage, the gate (G) signal, is converted to mechanical motion to modulate the gap. This motion can be achieved through various means of transduction using many topologies. Ohmic NEMS switches utilizing electrostatic [7]–[9] and piezoelectric [5], [6] actuation employing a range of geometries (see review in [10]) have been demonstrated. Regardless, all ohmic NEMS switches depend on reliable closure and separation of a conductive interface to achieve switching.

CMOS faces a scaling and power crisis. Continued Moore's Law scaling has contributed to increasing device leakage, resulting in significant power loses even when switching is not occurring [11]. Furthermore, a breakdown of Moore's law is predicted by approximately 2020 as critical MOSFET dimensions exceed physical limitations [2], [12]. Ohmic NEMS logic switches that reduce power draw per computation have been identified in the ITRS as a potential next-generation technology to cohabitate or usurp FETs [2]. Comparisons between NEMS relay-based logic to conventional CMOS revealed that energy savings of one to three orders of

9781940470016/HH2014/$25©2014TRF
DOI 10.31438/trf.hh2014.8

magnitude may be achieved with NEMS relays due to the low power consumption at the individual switch level [13]–[15] and design advantages unique to mechanical relays that reduce the number of switches necessary to perform logic operations [16]. The reduced power consumption is primarily a consequence of the physics underpinning device operation [17]. Figure 1(b) demonstrates the potential power savings via the steep on-off slope and the low gate voltage, as low as 0.4 mV through use of a body bias. The power consumption of a digital switch is characterized by power dissipated during both the off-state (V_G<0, sub-threshold leakage) and on-state (V_G>0, dynamic switching power). NEMS logic switches afford power savings both regimes [18], [19].

Off-state leakage in CMOS is dominated by source-drain and gate leakage that scales unfavorably with decreasing device dimensions [17]. This is seen as a current offset for voltages below the turn on threshold voltage. This leakage is due shorter and thinner oxide gate channels necessary to continue Moore's Law scaling. Sub-threshold leakage in CMOS currently represents ~50% of the total microprocessor power density [17] with standby leakage currents of 1 nA/transistor having been reported at 250 nm gate-width node. This leakage is dominated by gate leakage through the thin gate oxide and continues to increase with device downscaling. NEMS logic relays have already demonstrated leakage values five orders lower than MOSFET at the single device level [5]. These lower leakage values are due to the physical gap between the source and drain, eliminating source to drain leakage so long as the gap is >2 nm [2]. Unique to mechanical relays, physical gaps and low leakage gate materials (in the case of piezoelectrically-actuated devices) reduce gate leakage to effectively zero.

NEMS relays also offer far lower dynamic switching power than CMOS. The sub-threshold swing describes the inverse slope of the I-V curve and determines the voltage needed to attain a decade change in source to drain current [20]. Lower sub-threshold swings correspond to lower turn-on voltages, which confer lower active transistor power consumption. CMOS sub-threshold swing is thermodynamically limited by electron drift and diffusion to 60 mV/dec [11], with existing CMOS sub-threshold swings typically 70 – 100 mV/dec [17], [20]. This translates to turn on voltages of 0.3 – 1 V [21], several orders of magnitude larger than the minimum voltage (a few mV) necessary for communication. NEMS prototype logic relays offer the lowest sub-threshold slope of all potential transistor replacement devices [17] with sub-threshold slopes of 0.03 – 2 mV/dec already demonstrated [5], [6], [22], translating to threshold voltages of just a few mV [6].

In addition, NEMS logic relays are amenable to application spaces not accessible by CMOS. The functionality of CMOS relies critically on delicate doping levels that impose strict thermal budgets and minimization of heat generation due to device leakage. As NEMS logic does not rely on doping levels, these devices may be amenable to high temperature computing, allowing sensors in previously inaccessible, harsh environments such as temperatures up to 500 ˚C [23], [24]. Furthermore, co-integration of NEMS relays with CMOS –possible due to the low thermal budget of typical NEMS processing [2] – has led to the exploration of programmable gate array logic based on NEMS relays and traditional MOSFET [25], [26]. The presence of physical gaps in NEMS relays also confers robustness against electromagnetic shocks, which makes these transistors attractive in military applications where radiation-hard attributes are desired. Adhesion between the electrical contacts of NEMS relays may also be used for nonvolatile memory applications where the switch retains its last state (open or stuck closed) [27], [28]. NEMS relays are also amenable to three dimensional integration, which could increase functional density per given real-estate of a microchip to continue Moore's Law scaling.

CONTACT: NEMS' "ACHILLES' HEEL"

Despite the potential benefits of NEMS logic switches, tribological failure mechanisms at the electrical contact interface limit their viability [2]. Transistor functionality critically depends on maintaining high isolation in the off-state and low resistance in the on-state. Failure due to stiction that results in permanent welding of the switch interface, wear of contact materials, adsorbed layers of insulating contaminant films on free surfaces, and insulating tribopolymer (TP) formation of chemomechanical origin have been observed in microscale and nanoscale electrical contacts testing [10], [29]. The term tribopolymer (TP) is used in place of the more commonly used term "friction polymer". Friction polymers were first observed in sliding electrical contacts. However, it has since been observed that such polymer formation can be achieved under normal stresses (absence of significant shear stresses)[30].

The effects of stiction, insulating contaminant layers, and TP formation are expected to increase in severity as NEMS relays are scaled down in size. This is a consequence of the dominance of surface forces and the limited closure and separation forces available to NEMS relays. Figure 2(a) compares the closure and separation forces of micro- and nanoscale electrical switches and the necessary separation force for single (the fundamental unit of contact in nanoscale switches) to multiple contacting asperities indicative of multiasperity, microscale contacts. This approximation shows that the surface forces of NEMS relay contacts will outpace the relative generative force of the device. Microscale switches with soft, low hardness metallic electrical contacts (*e.g.* Au) have been particularly susceptible to stiction due to electromigration or softening that results in contact area growth [31]. Consequently, highly adhesive materials must be avoided to prevent stiction.

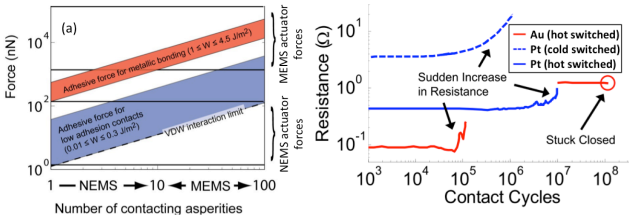

Figure 2. (a) Separation force of electrical contacts of various ranges of work of adhesion ranges, W, vs. the number of simultaneously interacting surface asperities. The asperity interactions are treated with adhesive contact mechanics. The adhesive force of nanoscale contacts can exceed the restoring force of typical NEMS actuators. (b) Contact resistance vs. make/break cycles for microscale electrical contacts of Au and Pt. TP formation causes dramatic increases in contact resistance.

Inhibiting the insulating TP formation may be the greatest challenge facing NEMS switches. It is affected by the gas environment, mechanical, electrical, and chemical properties of the contact materials, and the electrical power through the contacts. Figure 2(b) shows the effect of repetitive cycling of microscale noble metal contacts under both cold and hot cycling. Even for such non-reactive materials, contact resistance increases after 10^5 to 10^8 cycles, attributed to carbon and oxygen contaminants [29]. The origin of this effect appears to be mechanochemical – the presence of free surfaces, environmental contaminants, and pressure activate bond formation and chain lengthening. Even hermetically-sealed devices have demonstrated similar behavior [30]. Recent evidence suggests that operation of contacts in reducing environments such as oxygen can significantly reduce TP buildup [32] However, such device packaging can be costly to implement and limit the operation space of the device. Ultimately, conductive and non-reactive electrical contact materials must be sought.

NEMS SWITCH OPERATIONAL REQUIREMENTS

Since NEMS relay topologies and much work on electrical switch contact behavior borrows from MEMS switches, it is useful to identify how the local contact conditions vary between the two technologies. MEMS relays have been used for power savings and superior functionality in RF systems [33], are now considered a mature technology, and have been commercially deployed. Many lessons learned for the contact behavior of conventional switch materials (*i.e.* metals) can be attributed to work focused on microscale, multiasperity MEMS contacts. Table 1 compares the contact environment and needs of NEMS and MEMS relays.

The lifetime requirements for NEMS logic switches differ substantially from RF MEMS switches, which are designed as interrupts for RF transmission lines. While these contacts carry RF signals up to GHz frequencies, making and breaking of the contact happens far less frequently, usually on the order of kHz or less, requiring 10^8-10^{11} cycles before failure in commercial applications. NEMS logic relays carry a DC signal and the interruption of that signal determines the clock frequency of the device. Thus, NEMS relays must exhibit nanosecond closure times, which requires upwards of 10^{16} operating cycles without failure [2].

Requirement	MEMS RF Switches	NEMS Logic Switches
Lifetime (cycles)	10^8 – 10^{11} [33]	10^{15} - 10^{16} [2]
True contact area	10^{-8} - 10^{-12} m^2	10^{-17} - 10^{-18} m^2
Adhesion	Not explicitly treated	Major concern (energy use, reliability) [2]
Actuation force	µN – mN [33]	5 – 150 nN
Voltage across contact	2 – 70 V	Several mV to V
Current through contact	50 – 150 mA [33]	nA - µA
Current density	10^9 – 10^{14} A/m^2	10^5 - 10^{11} A/m^2
Power	<500 mW [33]	<1 mW
Max. contact resistance	0.5 – 2 Ω	<10^6 Ω
Main contact materials selection characteristics	High conductivity and non-fouling	Moderate conductivity, non-fouling, low adhesion

Table 1: Operational requirements of MEMS vs. NEMS switches.

The electrical constraints and power handling requirements of the electrical contacts of NEMS switches also differ substantially those of ohmic RF MEMS. Commercially viable ohmic RF MEMS switches demand contact resistances from 0.5 - 2 Ω [33, p. 5] in order to minimize insertion loses, which limits possible set of contact materials to high conductivity metals. Permissible NEMS logic relay contact resistances have a broader range – from several kΩ up to 100 kΩ, depending on device topology and the electrical time constants of the implementation – such that alternative, novel, and previously unconsidered materials could be implemented at the contact. Furthermore, the power across ohmic RF MEMS contacts often reaches 100+ mW with power being transferred across the contact after closure (cold switching). NEMS logic relays are expected to experience, at most, a few mW of power across the contact and operate in a hot-switched mode (bias applied across the contact during closure) with <1 V across the contacts during switching. These differing environments could change the degradation mechanisms. For instance, high voltages (>10 V) across MEMS contacts can lead to field evaporation, that may not be significant in nanoscale NEMS switch contacts.

HIGH-THROUGHPUT MATERIALS ASSESSMENT

We have developed a new high-throughput protocol developed for assessing the reliability of NEMS contact materials. An atomic force microscope (AFM) tip and a sample are each coated with the thin film materials of interest, using the same coating methods and conditions to be used for NEMS production. Tips are then imaged in scanning and transmission electron microscopes (SEM, TEM) to determine the quality of the coatings. TEM analysis requires no special sample preparation; the nano-scale tip diameter renders it sufficiently electron transparent (Figure 3). This approach has been tested by coating and characterizing tips with many different materials, *e.g.,* Pt, Au, Fe, amorphous carbon, diamond, and Pt_xSi (from annealing a Pt/Si coating). Typical deposition times are only a few minutes and multiple tips can be coated in a single run for reproducibility tests.

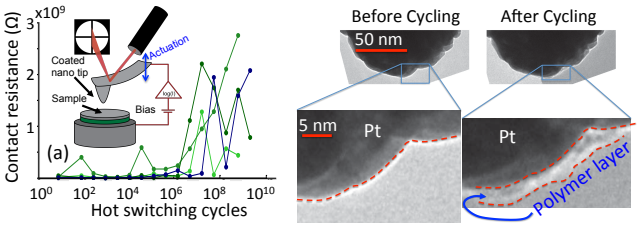

Figure 3: Left: High-throughput AFM test setup. High cycle testing of a series of Pt-Pt nanocontacts undergoing 5×10^9 test cycles in one day; failure (high resistance) is see at ~10^7 cycles. Inset: Dynamic AFM setup for high cycle testing. Right: TEM images of a Pt tip before and after 10^9 hot switching tests against a Pt surface.

The cantilever is then inserted in the AFM and oscillated at high frequency to simulate a dynamically-contacting asperity within a NEMS interface (Figure 3). Contacts can be cycled with our without bias. The state of the interface is probed *in situ* by regularly interrupting the cycling to acquire current- and force-displacement measurements. These measurements can reveal signatures of TP, the role of contact area, and the tip-sample adhesion force. At present, the cantilever is oscillated at its resonance frequency, typically ~50 kHz which corresponds to ~5×10^9 contact cycles in one day of testing. The right side of Figure 3 shows TEM images from before and after cycling a Pt tip against a Pt surface after 10^9 hot switching cycles. Interestingly, nanoscale TP buildup is evident, while plastic deformation is undetectable, consistent with the resistance increase observed for the contact. Significant resistance increases in these tests are observed to occur at similar cycle numbers as those seen in actual NEMS switches, suggesting the method has promise for screening candidate NEMS contact materials, and for developing scientific understanding of failure.

REFERENCES

[1] D. A. Czaplewski, G. A. Patrizi, G. M. Kraus, J. R. Wendt, C. D. Nordquist, S. L. Wolfley, M. S. Baker, and M. P. de Boer, "A nanomechanical switch for integration with CMOS logic," *J. Micromechanics Microengineering*, vol. 19, no. 8, p. 085003, Aug. 2009.

[2] "International technology roadmap for semiconductors (2011 edition)." 2011.

[3] S. Borkar, "Exponential challenges, exponential rewards - The future of moore's law," in *Proceedings of the VLSI-SOC*, Darmstadt, Germany, 2003.

[4] N. S. Kim, T. Austin, D. Baauw, T. Mudge, K. Flautner, J. S. Hu, M. J. Irwin, M. Kandemir, and V. Narayanan, "Leakage current: Moore's law meets static power," *Computer*, vol. 36, no. 12, pp. 68–75, 2003.

[5] N. Sinha, T. S. Jones, Z. Guo, and G. Piazza, "Body-biased complementary logic implemented using aln piezoelectric MEMS switches," *J. Microelectromechanical Syst.*, vol. 21,

no. 2, pp. 484–496, 2012.
[6] U. Zaghloul and G. Piazza, “10 - 25 nm piezoelectric nano-actuators and NEMS switches for millivolt computational logic,” in *IEEE 26th International Conference on Micro Electro Mechanical Systems (MEMS)*, Taipei, Taiwan, 2013, pp. 233–236.
[7] R. Nathanael, V. Pott, H. Kam, J. Jeon, and T.-J. King Liu, “4-terminal relay technology for complementary logic,” in *2009 IEEE International Electron Devices Meeting (IEDM 2009)*, Piscataway, NJ, USA, 2009.
[8] M. Tabib-Azar, S. R. Venumbaka, K. Alzoubi, and D. Saab, “1 volt, 1 GHz NEMS switches,” presented at the IEEE Sensors, 2010, pp. 1424–1426.
[9] W. W. Jang, J.-B. Yoon, M.-S. Kim, J.-M. Lee, S.-M. Kim, E.-J. Yoon, K. H. Cho, S.-Y. Lee, I.-H. Choi, D.-W. Kim, and D. Park, “NEMS switch with 30 nm-thick beam and 20 nm-thick air-gap for high density non-volatile memory applications,” *Solid-State Electron.*, vol. 52, no. 10, pp. 1578–1583, Oct. 2008.
[10] O. Y. Loh and H. D. Espinosa, “Nanoelectromechanical contact switches,” *Nat. Nanotechnol.*, vol. 7, no. 5, pp. 283–295, 2012.
[11] J. D. Meindl, Q. Chen, and J. A. Davis, “Limits on silicon nanoelectronics for terascale integration,” *Science*, vol. 293, no. 5537, pp. 2044–2049, Sep. 2001.
[12] J. A. . Hutchby, G. I. . Bourianoff, V. V. . Zhirnov, and J. E. . Brewer, “Extending the road beyond CMOS,” *IEEE Circuits Devices Mag.*, vol. 18, no. 2, pp. 28–41, Mar. 2002.
[13] F. Chen, H. Kam, D. Markovic, T. J. K. Liu, V. Stojanovic, and E. Alon, “Integrated circuit design with NEM relays,” in *Proceedings of the 2008 IEEE/ACM International Conference on Computer-Aided Design*, 2008, pp. 750–757.
[14] D. A. Czaplewski, G. M. Kraus, and C. D. Nordquist, “Nanomechanical switches for power saving in CMOS applications,” *Electron. Lett.*, vol. 45, no. 11, pp. 550–551, 2009.
[15] V. Pott, Hei Kam, R. Nathanael, Jaeseok Jeon, E. Alon, and Tsu-Jae King Liu, “Mechanical computing redux: Relays for integrated circuit applications,” *Proc. IEEE*, vol. 98, no. 12, pp. 2076–2094, Dec. 2010.
[16] M. Spencer, F. Chen, C. C. Wang, R. Nathanael, H. Fariborzi, A. Gupta, H. Kam, V. Pott, J. Jeon, T.-J. K. Liu, D. Markovic, E. Alon, and V. Stojanovic, “Demonstration of integrated micro-electro-mechanical relay circuits for VLSI applications,” *IEEE J. Solid-State Circuits*, vol. 46, no. 1, pp. 308–320, Jan. 2011.
[17] H. F. Dadgour and K. Banerjee, “Hybrid NEMS–CMOS integrated circuits: a novel strategy for energy-efficient designs,” *IET Comput. Digit. Tech.*, vol. 3, no. 6, p. 593, 2009.
[18] K. Akarvardar, D. Elata, R. Parsa, G. C. Wan, K. Yoo, J. Provine, P. Peumans, R. T. Howe, and H.-S. Wong, “Design considerations for complementary nanoelectromechanical logic gates,” in *Electron Devices Meeting, 2007. IEDM 2007. IEEE International*, 2007, pp. 299–302.
[19] A. M. Ionescu, V. Pott, R. Fritschi, K. Banerjee, M. J. Declercq, P. Renaud, C. Hibert, P. Fluckiger, and G. A. Racine, “Modeling and design of a low-voltage SOI suspended-gate MOSFET (SG-MOSFET) with a metal-over-gate architecture,” in *Quality Electronic Design, 2002. Proceedings. International Symposium on*, 2002, pp. 496–501.
[20] F. Fallah and M. Pedram, “Standby and active leakage current control and minimization in cmos vlsi circuits,” *IEICE Trans. Electron.*, vol. E88–C, no. 4, pp. 509–519, Apr. 2005.
[21] E. Yablonovitch, “There are orders-of-magnitude power advantages in complementing the transistor with a milli-volt switch,” presented at the MTO Symposium, San Jose, CA, USA, 07-Mar-2007.
[22] N. Abele, R. Fritschi, K. Boucart, F. Casset, P. Ancey, and A.-M. Ionescu, “Suspended-gate MOSFET: bringing new MEMS functionality into solid-state MOS transistor,” in *Electron Devices Meeting, 2005. IEDM Technical Digest. IEEE International*, 2005, pp. 479–481.
[23] S.-W. Lee, R. W. Johnstone, and A. M. Parameswaran, “MEMS mechanical logic units: characterization and improvements of devices fabricated with MicraGEM and PolyMUMPs,” 2005, p. 60371A–60371A–10.
[24] T.-H. Lee, S. Bhunia, and M. Mehregany, “Electromechanical computing at 500 C with silicon carbide,” *Science*, vol. 329, no. 5997, pp. 1316–1318, Sep. 2010.
[25] C. Chen, R. Parsa, N. Patil, S. Chong, K. Akarvardar, J. Provine, D. Lewis, J. Watt, R. T. Howe, H. S. P. Wong, and others, “Efficient FPGAs using nanoelectromechanical relays,” in *Proceedings of the 18th Annual Acm/Sigda International Symposium on Field Programmable Gate Arrays*, 2010, pp. 273–282.
[26] Y. Zhou, S. Thekkel, and S. Bhunia, “Low power FPGA design using hybrid CMOS-NEMS approach,” in *Proceedings of the 2007 international symposium on Low power electronics and design*, 2007, pp. 14–19.
[27] W. Y. Choi, Hei Kam, D. Lee, J. Lai, and T.-J. King Liu, “Compact nano-electro-mechanical non-volatile memory (NEMory) for 3D integration,” in *2007 IEEE International Electron Devices Meeting (IEDM 2007)*, Washington, DC, USA, 2007, pp. 603–6.
[28] S. Fujita, K. Nomura, K. Abe, and T. H. Lee, “3-d nanoarchitectures with carbon nanotube mechanical switches for future on-chip network beyond cmos architecture,” *IEEE Trans. Circuits Syst. Regul. Pap.*, vol. 54, no. 11, pp. 2472–2479, Nov. 2007.
[29] L. Chen, H. Lee, Z. J. Guo, N. E. McGruer, K. W. Gilbert, S. Mall, K. D. Leedy, and G. G. Adams, “Contact resistance study of noble metals and alloy films using a scanning probe microscope test station,” *J. Appl. Phys.*, vol. 102, no. 7, pp. 074910–1, Oct. 2007.
[30] D. A. Czaplewski, C. D. Nordquist, C. W. Dyck, G. A. Patrizi, G. M. Kraus, and W. D. Cowan, “Lifetime limitations of ohmic, contacting RF MEMS switches with Au, Pt and Ir contact materials due to accumulation of ‘friction polymer’ on the contacts,” *J. Micromechanics Microengineering*, vol. 22, no. 10, p. 105005, Oct. 2012.
[31] R. A. Coutu Jr., P. E. Kladitis, K. D. Leedy, and R. L. Crane, “Selecting metal alloy electric contact materials for MEMS switches,” *J. Micromechanics Microengineering*, vol. 14, no. 8, pp. 1157–1164, 2004.
[32] V. Brand, M. S. Baker, and M. P. de Boer, “Contamination Thresholds of Pt- and -Coated Ohmic Switches,” *J. Microelectromechanical Syst.*, vol. 22, no. 6, pp. 1248–1250, Dec. 2013.
[33] G. M. Rebeiz, *RF MEMS : theory, design, and technology*. Hoboken, NJ: J. Wiley, 2003.

CONTACT

*R.W. Carpick, tel: +1-215-898-4608; carpick@seas.upenn.edu

SILICON MIGRATION OF THROUGH-HOLES IN SINGLE- AND POLY-CRYSTALLINE SILICON MEMBRANES

J. Stehle[1,2], V.A. Hong[3], A. Feyh[1], G.J. O'Brien[1], G. Yama[1], O. Ambacher[2], B. Kim[1], and T.W. Kenny[3]*
[1]Robert Bosch Research and Technology Center, Palo Alto CA USA
[2]University of Freiburg, Freiburg, Germany
[3]Stanford University, Stanford CA USA

ABSTRACT

In this work we present migration phenomenon of through-holes in silicon membranes. The sealing of through-holes in hydrogen ambient at high temperature (1130°C) with various dimensions and annealing time durations was investigated in both single-crystalline silicon (sc-Si) and poly-crystalline silicon (poly-Si) membranes. The sealing process in silicon was observed as highly dependent on local crystal grain geometry, leading to more distributed, unpredictable migration rates and shape evolutions in poly-Si compared to holes in sc-Si. These findings can be leveraged in fabrication processes that require a balance between silicon migration and deposition.

INTRODUCTION

Silicon migration is a mass transportation effect that occurs even below the melting point of silicon. This effect is well-documented for single-crystalline silicon (sc-Si) by various groups at high temperatures and low-pressure deoxidizing ambient such as hydrogen (H_2) and at ultra high vacuum (UHV) [1,2]. The atomic-level smoothening of silicon transforms small features to minimize the surface energy [1,3,4]. Silicon migration is already utilized in instances such as the "silicon-on-nothing" developed by Mizushima et al [5].

The "epi-seal encapsulation" process developed by Robert Bosch GmbH and Stanford University, which utilizes epitaxially deposited silicon as the released membrane, has demonstrated promising results in diverse MEMS products such as resonators [6] and pressure sensors [7]. This process utilizes poly-crystalline silicon (poly-Si) membranes which function as encapsulation for resonators/inertial sensors and a diaphragm for pressure sensors. The membranes are patterned with through-holes and after removing silicon dioxide (SiO_2) with vapor-phase hydrofluoric acid (vHF), epitaxial poly-Si deposition is employed to seal these holes. This sealing deposition is conducted at a very high temperature (>1000°C) in hydrogen ambient, and as a by-product, silicon migration occurs around the through-holes.

The effect of release-hole migration during this sealing deposition can be an important factor for the sensor performance. For example, in case of pressure sensor applications, if these through-holes are not sealed at the bottom of the membrane, which is often the case of typical non-conformal deposition-based sealing, it makes the membrane softer, resulting in unpredictable sensitivity. In the case of inertial sensors, the topography in out-of-plane electrodes can become the source of noise during the in-plane movement. For such reasons, the effect of silicon migration on through-holes in the epitaxially deposited silicon membrane has to be further investigated and controlled.

Though the phenomenon of silicon migration of through-hole geometries in membranes has been preliminarily explored in previous works [5,3], these past studies limited their scope to only sc-Si and a few through-hole geometries. Therefore more research needs to be done to make it rather applicable for real MEMS device fabrication. Consequently this work extends our previous studies for better understanding with the following three primary focuses: 1) expansion to poly-Si for the comparison of migration behavior in sc-Si and poly-Si, 2) diverse through-hole geometries to investigate the effects of size/shape differences of etched through-holes, and 3) time-dependence evolution of the hole geometry migration aiming at three-dimensional hole geometry engineering.

For such purposes, through-holes with diverse shapes and dimensions were patterned in both sc-Si and poly-Si suspended membranes, and the shape evolution of those through-holes were observed and analyzed using a scanning electron microscope (SEM) after a high temperature anneal in low-pressure H_2 ambient for different time durations. The time dependence of through-hole shapes was also compared with the Matlab-based simulation results from the previous work in [8].

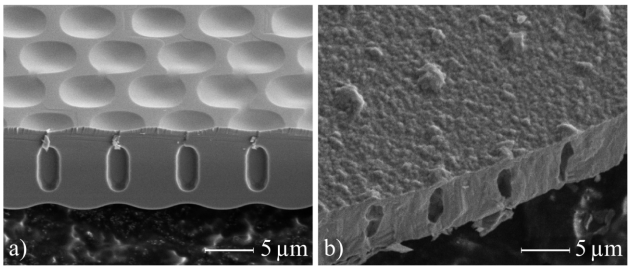

Figure 1: Image of direct comparison of single-crystalline and poly-crystalline through-holes after 10,000 s of annealing in hydrogen ambient

FABRICATION

Since most previous work on this topic was performed on sc-Si, two sets of samples were fabricated. This allowed comparison of the results to previous studies as well as a direct comparison between sc-Si and poly-Si (Figure 1).

Figure 2 shows the schematics of the fabricated devices. For the single-crystalline variant commercially produced 100 mm silicon-on-insulator (SOI) wafers were used with a 2-µm-thick buried silicon oxide (BOX) and a 10-µm-thick device layer with (100) orientation (p-type boron doped, 1-2 mΩcm). For the poly-crystalline samples, the process started on 100 mm silicon wafers (100) with a resistivity of 10-20 Ωcm, also p-type doped with boron. These wafers were then processed to become "poly silicon-on-insulator" (PSOI) wafers (Figure 2 a*) as a comparable starting point to the SOI wafers. Therefore a 2-µm-thick silicon dioxide (SiO_2) layer was thermally grown at 1000°C, followed by epitaxial deposition of a 12-µm-thick boron doped (p-type) poly-Si layer. The poly-Si deposition was performed in a reduced-pressure epitaxial reactor by Applied Materials (Centura EPI). The 12 µm of poly-Si were deposited in steps of 3 µm due to the tool limitations, including a seed layer before the first step. For the seed layer deposition, which is negligibly thin compared to the total thickness, silane (SiH_4) with H_2 as carrier was used as a precursor at 800°C and 600 Torr with a gas flow of 60 sccm for 90 s. For each 3 µm poly-Si deposition step the precursor was Dichlorosilane (DCS, SiH_2Cl_2) at 1080°C and 30 Torr with flow rate of 400 sccm in a H_2 carrier for 196 s; p-type dopant (1% diborane, B_2H_6) was simulta-

9781940470016/HH2014/$25©2014TRF
DOI 10.31438/trf.hh2014.9

neously flowed at 100 sccm. After the deposition the thickness was reduced to 10 µm and the surface was smoothened by chemical mechanical polishing (CMP). At this point the PSOI wafers had comparable properties to the chosen SOI wafers and therefore the following processing steps could be performed on both variants in parallel (Figure 2 a1/b1).

With optical lithography the wafers were patterned (Figure 3 and Table 1) and the device layer etched utilizing deep reactive ion etching (DRIE) to get high aspect ratio through-holes (Figure 2 a2/b2). Table 1 shows the different shapes and dimensions of the various structures. Due to constraints in lithography and etching 0.8 µm was chosen on the lower end as the limiting dimension. This width is constant for variants V2, V3, V6, and as diameter for V1. The length of each was varied from 0.8 µm to 5 µm. V4 and V5 have the same area as V2 but a different aspect ratio and therefore the width is wider than the limiting dimension. The through-holes were arranged in two patterns: One is rectangular, where all holes are equally distanced, and the other a circular one with alternating through-hole density due to the radial arrangement (Figure 3d). The circular version is used for a membrane in an actual device design by this group [7].

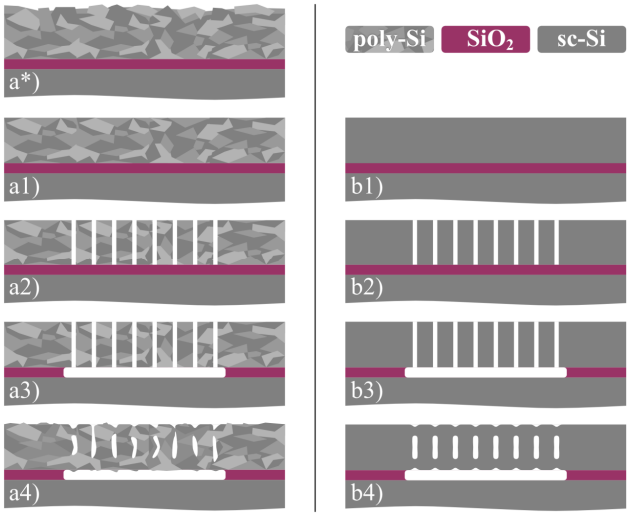

Figure 2: Process flow for a) poly-Si and b) sc-Si wafers. a) thermal SiO_2 grown on Si wafer and deposition of poly-Si in epitaxial reactor; a1) CMP to smoothen the surface; a2) through-hole patterning with DRIE a3) vHF etching to release membrane a4) annealing in H_2 ambient b1) SOI wafer b2) through-hole patterning with DRIE b3) vHF etching to release membrane b4) annealing in H_2 ambient*

Table 1: Overview of through-hole shape variations. These shapes were patterned using deep reactive ion etching (DRIE) through the 10-µm silicon device layer. The hole coverage is regarding to the rectangular membrane.

	V1	V2	V3	V4	V5	V6
Shape	●	▬	▮	■	▬	▬
	circular	rectangular	rect.	rect.	rect.	rect.
Dimensions	Ø 0.8 µm	0.8 µm × 5 µm	0.8 µm × 0.8 µm	2 µm × 2 µm	1.4 µm × 2.86 µm	0.8 µm × 2.5 µm
Area	0.503 µm²	4 µm²	0.64 µm²	4 µm²	4 µm²	2 µm²
Hole coverage	1.7 %	7.4 %	2.1 %	9.5 %	9.5 %	4.7 %

The underlying oxide was removed by vHF etching after reducing the moisture with a rapid thermal annealing (RTA) step (Figure 2 a3/b3). To confirm that the membranes are completely released, the samples were inspected with an infrared microscope.

The wafers were subsequently annealed in the epi process chamber (Figure 2 a4/b4) for varying time durations at 1130°C and 20 Torr in a H_2 ambient. For the poly-crystalline wafers the annealing time durations were chosen as 0 s (no annealing), 1000 s, 2000 s, 3000 s, 4000 s, and 10000 s and for the SOI wafers 0 s, 2000 s, 4000 s, and 10000 s.

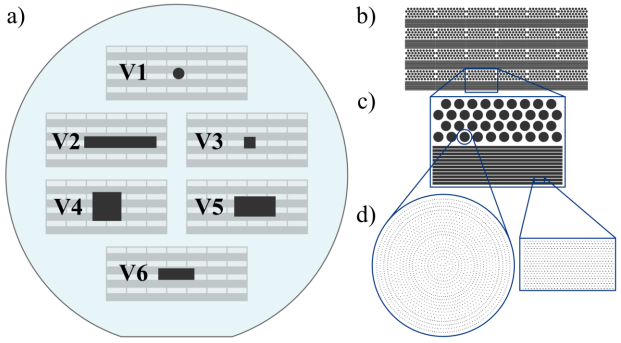

Figure 3: Mask layout for the through-holes a) arrangement on wafer of the various through-holes regions b) arrangement of the reticles for each through-hole variant, high number of repetition to raise chances for successful cleaving c) reticle layout d) left: circular membrane; right: rectangular membrane

CHARACTERIZATION AND DISCUSSION

The characterization was done on an SEM. Top-surface, bottom-surface, and cross-section images were taken of the membrane. For the cross-section images samples were mechanically cleaved. For the bottom-surface view of the membrane double coated conductive tabs were used; by attaching the tabs to the top surface and quickly removing, membranes were ripped out-of-plane, revealing the bottom side.

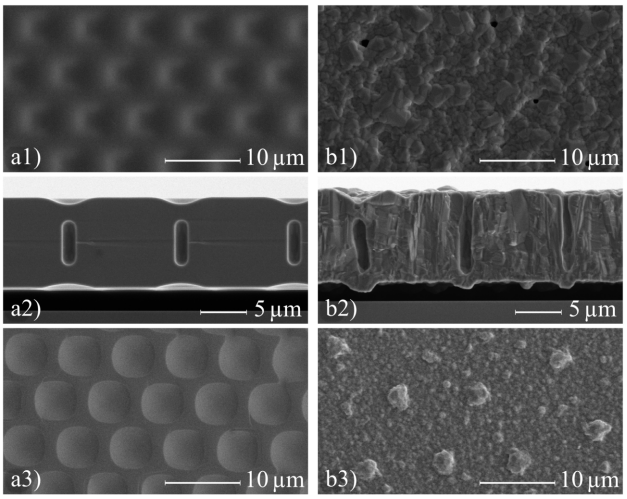

Figure 4: SEM images of sc-Si and poly-Si V6 through-holes after 10000 s of annealing. a1) sc-Si top view a2) sc-Si cross section a3) sc-Si bottom view b1) poly-Si top view b2) poly-Si cross section b3) poly-Si bottom view

These results are qualitatively consistent with the results from a silicon migration model developed by Kant [8] based on Mullins surface diffusion equation for sc-Si. Simulations with the same through-hole dimensions and similar conditions (temperature, pressure, ambient) were performed and are shown in Figure 5. The displayed progression towards closure can be compared with the cross-section shown in Figure 6.

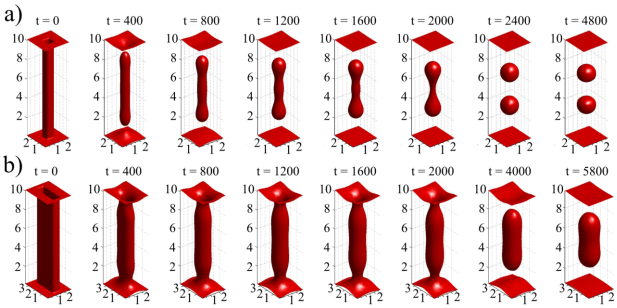

Figure 5: Simulation V3 based on Mullins surface diffusion equation (time units do not correspond to seconds)
a) V3 through hole b) V6 through-hole

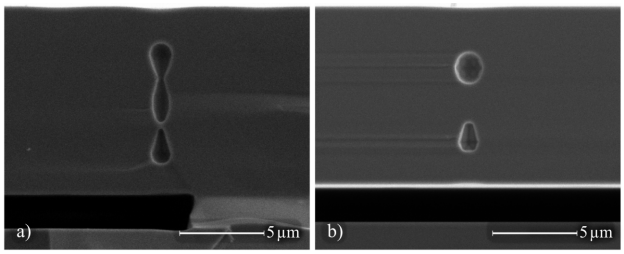

Figure 6: Cross section of single crystal Si V1 through-hole a) after 2,000 s b) after 10,000 s

The thickness of the membrane for SOI wafers stays approximately the same (measured to be about 9.9-10.1 µm for sc-Si after 10,000 s of annealing). A reduction in thickness due to volume conservation like witnessed by Provine et al [9] was not observed nor expected to be significant enough to notice. The volume of the through-holes is too small in relation to the pitch, so that the coverage of the through-holes is in the range of 1-10 % (Table 1).

Another finding in poly-Si is a clear distinction between the upper and the lower side of the membrane; nearly all patterned through-holes were closed on the bottom side after the 10,000 s anneal, while some holes remain open on the top side (Figure 4b). Additionally, the migration sealing of poly-Si through holes left 'lids' that grew out-of-plane (Figure 4b2), in contrast to the indented trench closures on the top side and in sc-Si samples shown in Figure 4a. This can be explained by the vertically oriented grain size gradient in the poly-Si membrane, which was also observed by Ng et al [10] using a similar fabrication process. The grain size increases from the base (~200 nm) towards the top (~3 µm). Therefore the diffusion mobility is higher at the bottom side leading to more active migration.

Figure 7 shows the evolution of the top-side openings for a) sc-Si and b) poly-Si. In Figure 7a3) the cross-section of the simulated V6 through-hole (0.8 µm x 2.5 µm) over 1000 time units is plotted. The qualitative transformation of the simulation correlates with the measured results. Both sc-Si and poly-Si morph from an elongated rectangular shape to a circular footprint. In the single-crystalline case the result is an almost perfect circle, for the poly-Si the trend towards a circular shape is clearly visible although it is more non-uniform (Figure 7b3).

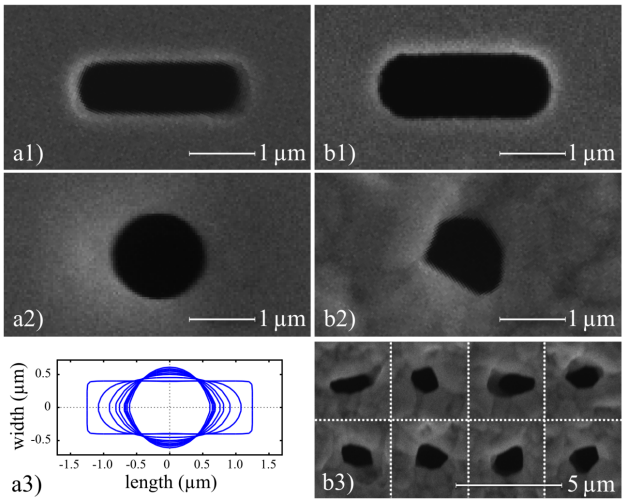

Figure 7: Transformation of a) sc-Si and b) poly-Si V6 through-holes from no annealing (a1,b1) to 2000 s (a2,b2/3). a3) shows the predicted evolution by the simulation for 1000 time units.

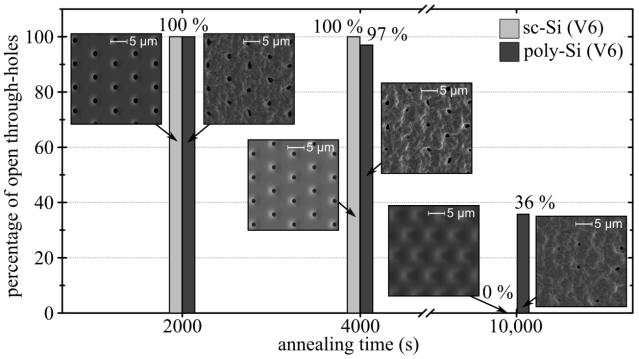

Figure 8: Comparison of V6 through-holes grown closed between sc-Si and poly-Si. All holes in sc-Si were in virtually the same sealing state: all open at 4,000 s and all closed at 10,000 s. In contrast, holes in poly-Si evolve gradually towards closure: some are already closed after 4,000 s while a few are still open even after 10,000s

Figure 8 compares the top side of the V6 membranes for sc-Si and poly-Si. Note that holes in sc-Si migrate at the same pace: all open at 4,000 s and all closed at 10,000 s. In contrast, through-holes in poly-Si evolve gradually towards closure; some are already closed after 4,000 s while a few still remain open even after 10,000 s indicating a high degree of non-uniformity across the device and the wafer.

The dependency of the through-hole orientation is displayed in Figure 9. In the case of sc-Si, there is an influence in the hole-sealing behavior clearly visible after 2,000 s and 4,000 s, but after 10,000 s all holes appear circular. This is explainable by the crystal orientation in the SOI wafers and the dependency of the migration rates on crystal orientation [8]. After a certain time changes in shape become slower (see Figure 5), and the differences in migration rate consequently even out. For the poly-Si samples the variation between through-holes has no correlation to the orientation on the wafer, since there is no global crystal orientation, and therefore the migration process is more non-uniform.

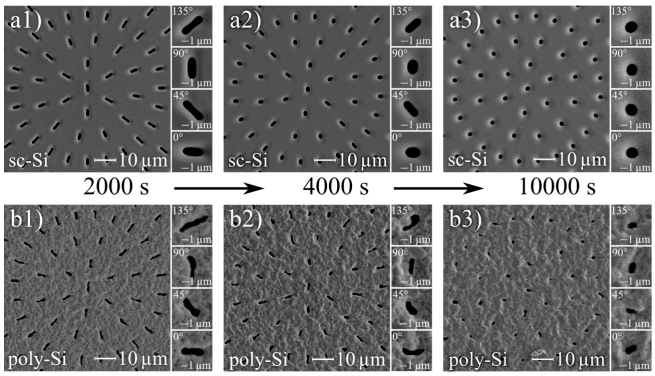

Figure 9: Top view SEM comparing the influence of crystal orientation on the example of through-hole V2; a) sc-Si; b) poly-Si. In the case of sc-Si, the crystal orientation dependence is clearly visible until 2,000-4,000 s, whereas holes in poly-Si migrate more non-uniformly.

CONCLUSION

The analysis of the samples and comparison with previous studies shows, that despite of the similarities, there are major differences in the evolution of the through-holes and the surface topology between sc-Si and poly-Si. Whereas the through-holes in sc-Si are generally uniform and homogeneous all over the membrane respectively the wafer, each through-hole in poly-Si evolves differently. The uniform behavior of the sc-Si makes the annealing process a reliable method for sealing, since after a specific time period all through-holes are closed. Migration of through-holes in poly-Si on the other hand is less predictable and gradual. While some holes are closed even earlier than in sc-Si, others take significantly longer than the average portion of the through-holes. It is more of a statistical process, which leaves the possibility of unclosed through-holes. Because a single open hole will compromise the hermeticity of the encapsulation, the exclusive use of migration in poly-Si is not an acceptable encapsulation technique on its own.

Also within the scope of a single through-hole, there are significant differences between the upper and lower side of the membrane, in contrast to the fairly symmetrical migration process in sc-Si. The bottom and top side of the closed off through-holes in the membrane are in the sc-Si scenario indented. In the case of poly-Si the vertical gradient in silicon grain size causes indented or quasi plane top surfaces but "out-of-plane lids" on the bottom side of the membrane.

In addition, there is a dependency in shape evolution visible for sc-Si. Due to the fact that there is no global crystal orientation in a poly-Si membrane, there is no such orientation dependent pattern noticeable.

Unlike the sealing with conformal deposition, the migration process is highly dependent on the through-hole geometry. For deposition, either the width or the length, the shorter one determines the critical dimension to seal the through-holes, which is not the case for migration sealing which depends more on the overall geometry such as shape, area, and perimeter of through holes. On the other hand it is difficult to seal the through-hole from bottom to top simultaneously with deposition methods, therefore insufficient sealing on the bottom side is usually observed.

To prevent the risk of possible unsealed release-holes and to minimize the annealing time, but also accomplish a satisfactory plane lower membrane side, a hybrid of migration sealing and deposition is proposed. The outcome of this study enables further investigation to find optimum release-hole geometry for poly-Si and is directly applicable to release-hole sealing in silicon film encapsulation technology such as "epi-seal encapsulation". It can be also directly applicable to other MEMS device fabrication such as micro-fluidic channels for lab-on-a-chips or chip coolers.

ACKNOWLEDGEMENTS

The fabrication work was done at the Stanford Nanotechnology Facility (SNF) and the characterization at the Stanford Nanocharacterization Laboratory (SNL). The authors would like to thank the staff at SNF and SNL for the support.

REFERENCES

[1] M.-C. M. Lee and M. C. Wu, "Thermal Annealing in Hydrogen for 3-D Profile Transformation on Silicon-on-Insulator and Sidewall Roughness Reduction", Journal of Microelectromechanical Systems, vol. 15, no. 2, pp. 338-343, April (2006).

[2] R. Kant et al., "Experimental investigation of silicon surface migration in low pressure nonreducing gas environments", Electrochemical and Solid-State Letters, vol. 12, no. 12, pp. H437-H440, (2009).

[3] H. Habuka et al., "Roughness of silicon surface heated in hydrogen ambient", Journal of the Electrochemical Society, vol. 142, no. 9, pp. 3092-3098, (1995).

[4] T. Sato et al., "Micro-structure Transformation Technology for Patterning Silicon Surfaces using the Surface Migration of Silicon Atoms by Hydrogen Annealing", Jpn. J. Appl. Phys., vol. 39, pp. 5033-5038, (2000).

[5] I. Mizushima et al., "Empty-space-in-silicon technique for fabricating a silicon-on-nothing structure", Applied Physics Letters, vol. 77, no. 20, pp. 3290-3292, (2000).

[6] B. Kim et al., "Frequency stability of wafer-scale film encapsulated silicon based MEMS resonators", Sensors and Actuators A: Physical, vol. 136, pp. 125-131, (2007).

[7] C.-F. Chiang et al., "Capacitive absolute pressure sensor with independent electrode and membrane sizes for improved fractional capacitance change", 16th International Solid-State Sensors, Actuators and Microsystems Conference, Transducers, Beijing, China, (2011), pp. 894-897.

[8] R. Kant, *Silicon Migration as a Process for Micro/Nanofabrication, PhD thesis*, Stanford University, Stanford, June 2009.

[9] J. Provine et al., "Time Evolution Of Released Hole Arrays Into Membranes Via Vacuum Silicon Migration", 14th Solid-State Sensors, Actuators, and Microsystems Workshop, Hilton Head, June (2010), pp. 344-347.

[10] E. J. Ng et al., "Ultra-stable epitaxial polysilicon resonators", Solid-State Sensors, Actuators, and Microsystems Workshop, Hilton Head, June (2012), pp. 273-174.

CONTACT

* J. Stehle; tel: +1-650-451-8391; jochen.stehle@us.bosch.com

IMAGE VALIDATION OF PARALLEL SCANNING TUNNELING MICROSCOPY WITH A CMOS MEMS PROBE ARRAY

Yang Zhang, Yingying Tang, L. Richard Carley and Gary K. Fedder
Department of Electrical and Computer Engineering
Carnegie Mellon University, Pittsburgh, Pennsylvania, USA

ABSTRACT

This paper reports on the design and test results from a dual-probe Scanning Tunneling Microscopy (STM) system, suitable for scaling to 1-D array parallel imaging with an eventual purpose for batch-nanofabrication. The 1-D array is fabricated using CMOS-MEMS technology. Each probe is individually addressable, equipped with an electrothermal (ET) microactuator for tip vertical deflection. A hierarchical dual servo system is tested to validate parallel STM operation with two probes on the chip. Dual STM images are obtained on a custom grating calibration sample. A second generation of probe array is being developed, where on-chip ET actuated micro-goniometers are designed for more scalable probe array-sample alignment.

INTRODUCTION

Scanning probe microscopy (SPM) is a powerful tool in surface science. SPM techniques make use of the interaction between the nano-scale sharp tip and the sample surface to study its local properties. Tip-based nanofabrication (TBN) extends the SPM functionalities where the tip is used for direct nanopatterning and modification on the surface [1]. While the minimum feature size has been scaled down to 14 nm using the current state-of-the-art photolithography technique, feature size down to sub-10 nm is achieved via TBN with little difficulty.

Unlike the sample-averaged techniques such as spectroscopy and crystallography, the probe of SPMs interacts with the materials' surface locally, point by point, and therefore provides direct information of material property at atomic and nano-scale that leads to the understanding of the materials in a different way. Yet it is also this nature of reliance on localized interaction of SPMs that make it a much slower surface characterization technique than the sample-averaged ones. It may require a few minutes to scan a few μm^2 areas while it may only take a couple of seconds in SEM.

To overcome the disadvantage of the intrinsic drawback of low-efficiency of SPM, probe arrays are developed. Multiple micro-probes work in parallel on multi-areas of a surface so the efficiency of surface characterization will be multiplied. A variety of 1D and 2D probe arrays have been developed and used in applications like "Millipede" probe-based data storage [2] and dip pen nanolithography [3]. Millimeter-scale parallel imaging in AFM constant force mode has been achieved using a 1 × 10 CMOS MEMS probe array [4]. In both imaging and fabrication, the array probes are in contact with the examined surface.

In our work, we have developed CMOS MEMS probe array technology intended for non-contact (NC) mode STM-based parallel imaging and nanofabrication. Compared to contact mode SPM operation, only NC mode SPM, like STM or NC AFM tapping mode, may achieve true atomic resolution because it relies on the short range tip-sample interactions that is comparable to the size of the atoms [5]. This indicates that the NC mode SPM may be able to produce an even smaller feature size than the contact mode SPM.

We previously demonstrated the parallel STM imaging via a dual CMOS-MEMS probe array system on a commercial calibration sample [6] along with establishing on-chip switched-capacitor transimpedance amplifier circuitry [7]. The alignment of the probe array and the sample surface was through an external macro goniometer [6]. In the present work, a custom calibration sample is designed and fabricated for the image validation of the dual probe system. A second generation of CMOS probe array is developed, where the spacing between adjacent probes is reduced by 20 times. On-chip active micro-goniometers are designed for this more scalable probe array-sample alignment.

A HIERARCHICAL DUAL-PROBE STM SYSTEM

The concept and configuration of a hierarchical dual-probe STM system was reported in [6]. The system block diagram is shown in Fig. 1. The CMOS MEMS probe array chip is mounted on the piezoscanner head of a Veeco Dim3000 conventional SPM system. A master servo controls position of the probe chip and its master STM tip relative to the sample and uses the piezoelectric actuator embedded in the conventional system. The second, slave servo controls the second tip relative to the sample while in the frame of reference of the master servo. Slave servo action is performed with the ET bimorph actuator embedded on the probe cantilever. In both servos, the tip current preamplifiers and PI controllers are implemented in custom off-chip analog electronics. For parallel STM image processing, the topography under the master tip is directly constructed from the piezo drive voltage. The topography under the slave tip is extracted by taking the weighted difference of the piezo and ET drive signals, as shown in Fig. 1 (b).

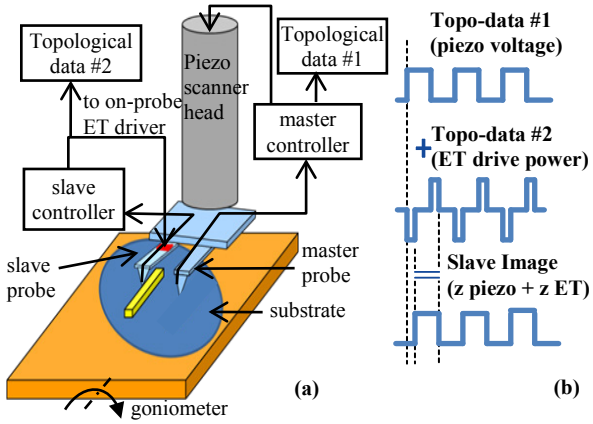

Figure 1: (a) Schematic of master-slave dual probe array system. (b) Slave image constructed by taking the weighted difference of two drive signals [6].

Fig. 2 shows the SEM images of the CMOS probe chip that is used in dual-probe STM system. An array of 5 identical active probes is arranged along one side of the chip, with each probe 329 µm in width. They are equipped with respective ET actuators for individual vertical deflection. The master probe is passive, without on-cantilever actuation mechanisms, and is located on the corner of the probe chip. One from the 5 active probes is used as the slave probe. In principle, the system can be extended to accommodate more active probes as slave probes with corresponding servo electronics. The platinum STM tip shown in the inset is prototyped with electron-beam induced deposition.

9781940470016/HH2014/$25©2014TRF
DOI 10.31438/trf.hh2014.10

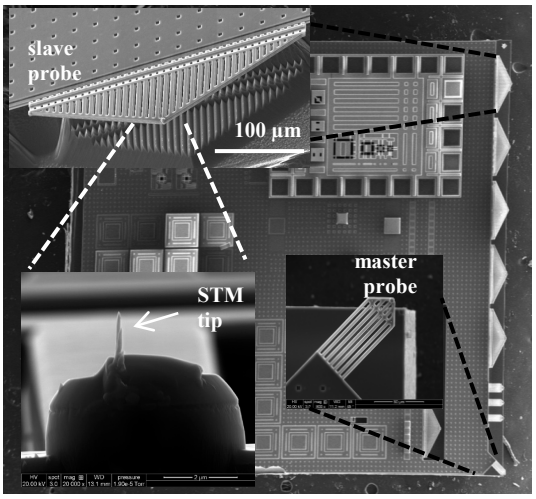

Figure 2: SEM images of CMOS probe chip, showing the two probes used in dual probe parallel imaging.

CUSTOM CALIBRATION SAMPLE

Previous characterization of the dual-probe STM system imaged a commercial grating calibration sample where all the gratings assume a same orientation, so the features under the master tip and the slave tip were essentially the same [6]. A custom calibration sample, following the schematic design in Fig. 3 (f) and the process steps in Fig. 3 (a) to (e), provides distinguishable images under different probes during the parallel operation. A series of grating patterns with different orientations and periods are fabricated on the substrate. Grating patterns are first made via e-beam lithography on 950 PMMA A4 resist spun on a 1" Si substrate. Next the patterns are transferred to the Si via anisotropic etch in a Plasma-Therm RIE 790 system. The resist is then washed off, and 5 nm-thick gold is deposited on the substrate bearing the patterns. Fig. 4 shows a representative optical image and an AFM image of the fabricated patterns. The patterns have periods ranging from 200 nm to 600 nm, with pitch depth of ~25 nm.

PARALLEL STM IMAGING OF DUAL-PROBES

In the parallel STM operation of the dual probes, the relationship between the piezo drive voltage and the slave drive power needs to be known for the construction of the image under the slave tip. The relationship is obtained through an *in situ* characterization using a piezo actuator-based STM servo. Fig. 5 describes the measurement method. The probe chip is mounted on the piezo-actuator of the conventional SPM system. One of the active array probes is used as a regular STM end-effector, relying on the piezo-actuator-driven feedback loop to perform the constant current mode STM scanning while the x- and y- direction movement is disabled. When operating in constant current mode, the separation between the tip and the sample surface is fixed at z_0 by the current set point. When using the on-cantilever ET actuator to drive the probe, it moves vertically and the tip-sample distance changes by Δz. To compensate for this distance change so as to maintain the constant current between the tip and the sample, the piezo actuator has to respond accordingly, *i.e.*, the piezo actuator has to drive the probe by Δz in the direction opposite to ET actuator's movement. Fig. 6 shows the obtained relationship, indicating that the travel distance caused by a change of 1 V of drive voltage on piezo scanner is equivalent to that caused by a change of 0.129 mW of drive power on ET actuator. The ET drive sensitivity is 131 nm/mW using the nominal piezo drive sensitivity of 17 nm/V.

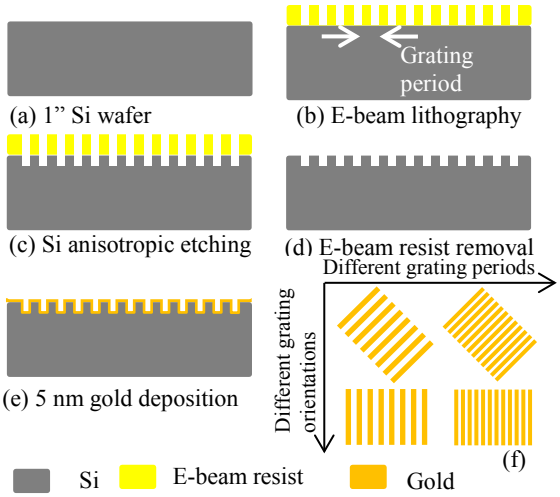

Figure 3: Process of fabricating STM calibration sample with custom gratings

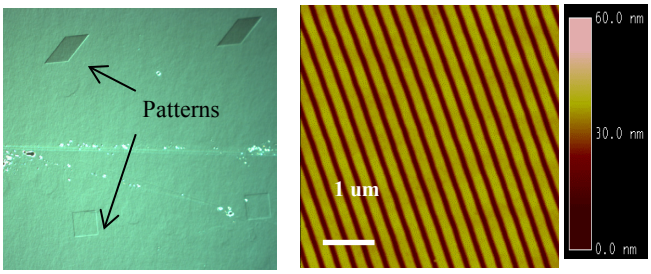

Figure 4: Optical and AFM images of the custom-made sample, showing the spacing and pitch of the gratings

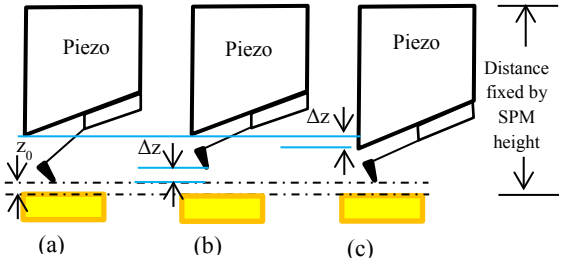

Figure 5: Schematic of the measurement of ET drive sensitivity via in situ STM scanning: (a) the tip is z_0 from the substrate, keeping a constant current; (b) the tip is lifted up by Δz from the substrate via ET actuation; (c) the piezo drive is extended by Δz to compensate for ET travel distance.

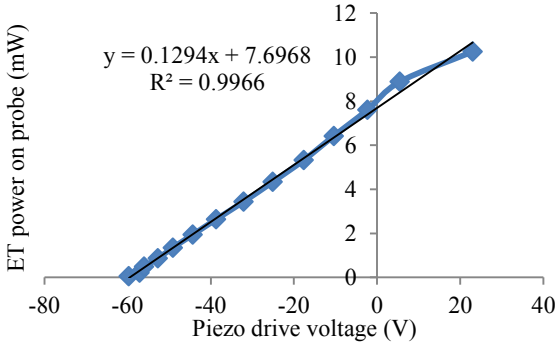

Figure 6: ET drive power vs piezoelectric drive voltage

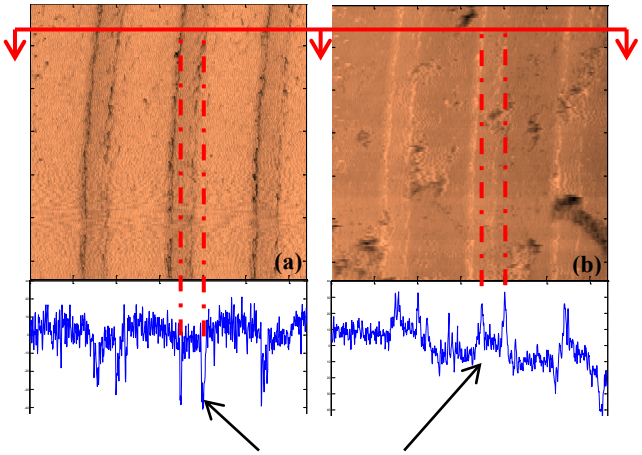

Representative line plot on the images. Peaks correspond to tips crossing steps of the grating

Figure 7: Dual images when the master probe is on the grating and the slave probe is not. (a) Image under the master tip; (b)Raw image from the slave tip; (c) Real image under the slave tip via the weighted addition of (a) and (b)

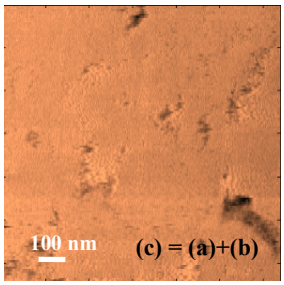

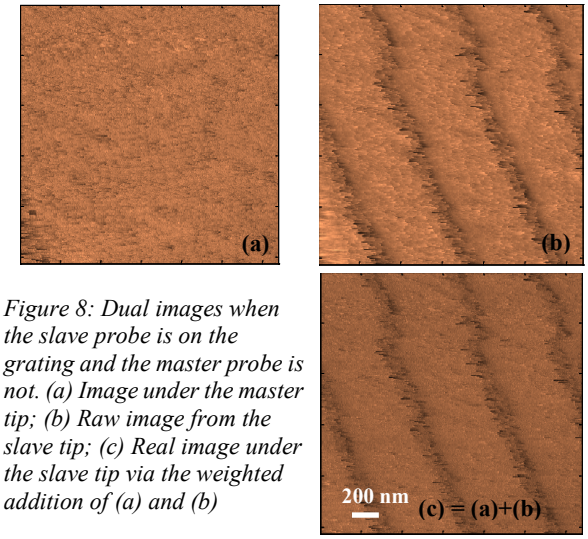

Figure 8: Dual images when the slave probe is on the grating and the master probe is not. (a) Image under the master tip; (b) Raw image from the slave tip; (c) Real image under the slave tip via the weighted addition of (a) and (b)

The dual probes are scanning on the custom calibration sample for parallel image acquisition. The custom gratings on the calibration sample can be manually moved under either the master probe or the slave probe. In one scenario, the master probe falls on the pattern while the slave probe is scanning on an unpatented area. Fig. 7 shows the obtained dual images. The image under the master tip shows the pattern with a period of around 282 nm. Although scanning on an area with no grating pattern, the slave image directly built from the ET drive power shows a grating that corresponds with that in the master image. Fig. 7 (c) shows the actual topographical image obtained from the weighted difference of the master piezo drive voltage signal and the slave ET power signal. The grating pattern disappears on this difference image, leaving behind only the real features under the slave probe.

In a second scenario, a grating is under the slave probe while the master probe is scanning on an area without gratings. Fig. 8 shows the obtained STM images. No grating patterns appear on the master image. Gratings are identified in the raw slave image and are preserved in the weighted difference image that removes the piezo drive signal.

MICRO-GONIOMETER

In the current version of CMOS-MEMS probe arrays, adjacent probes are spaced 340 µm apart. The lateral scanning range of a peizo-scanner on the commercial SPM system is generally 50 µm or less. It is desirable that the spacing between adjacent probes be smaller than this lateral scanning range so that the individual scanning areas will overlap and combine. When the spacing between array probes is scaled down to tens of microns, it is possible to build an on-chip micro-goniometer which offers a platform to hold an array of probes. It serves to provide the *in situ* fine adjustment of relative height among these probes above the sample surface. It will also facilitate the STM operation of probe arrays particularly in an ultra-high-vacuum (UHV) system where a macro-goniometer for tip-substrate parallelization is not easily implementable. To this end, a scaled generation of STM probe array is developed. Fig. 9 shows the SEM image of the STM probe array on a micro-goniometer. It consists of two separate "trunk cantilevers" which can be individually actuated, a leveling beam bridging the trunk cantilevers through two twist beams, and an array of active STM finger probes placed along the leveling beam, with a spacing of 15.1 µm between two neighboring finger probes. Similar to the widely-spaced array probes, the micro-goniometer and finger probes also adopt ET actuation as its driving approach. When the two trunk cantilevers are unevenly heated, *i.e.*, different drive powers are applied on the ET actuators of two trunks, they will have different vertical deflection, so one end of the leveling beam will be elevated higher than the other end, and the relative height among finger probes is therefore changed.

Different drive powers were applied on two trunk cantilevers to measure the tilt of the leveling beam. It is found that a critical power exists. Below the critical power, the tilt of the leveling beam has a linear dependence on drive powers, and the deformation is reversible, *i.e.*, the trunks of the goniometer recover their original shape. Above the critical power, the leveling beam is not straight anymore but bends. Furthermore, irreversible deformation occurs, *i.e.*, the leveling beam tilt remains after the power is removed.

The test started with a freshly released goniometer device. The drive power, which varied between 0 W and 32.2 mW but never went beyond this range, was applied on one trunk cantilever of the goniometer, while the other trunk was not powered. Fig. 10 shows the white light interferometric image when the goniometer is unevenly powered at 32.2 mW. Upon heating, the heated trunk bends downwards, and assumes a lower position than its counterpart on the other side. The leveling beam is tilted by 1.19°. The tilt angle is linearly dependent on the power and has a drive sensitivity of 0.038°/mW.

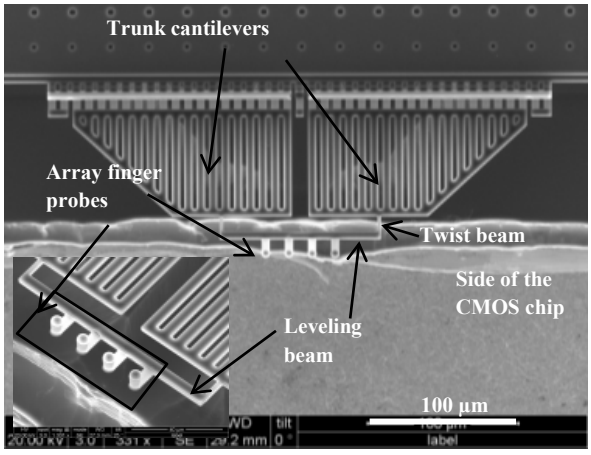

Figure 9: SEM image of the micro-goniometer showing its structure

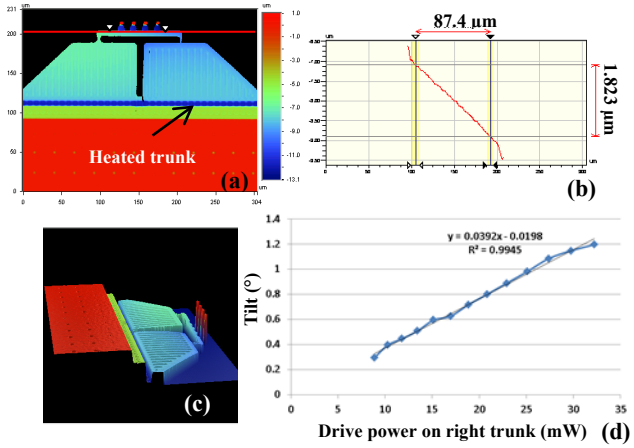

Figure 10: Tilt of the goniometer when a power of 32.2 mW is applied on the right trunk cantilever: (a) 2D contour. (b) The tilt of the leveling beam. (c) 3D contour. (d) Tilt dependence on the drive power below critical point.

Furthermore, irreversible deformation is introduced after a high enough drive power is applied and then removed from the trunk cantilever. To examine the time and power dependence of irreversible deformation, a freshly-released goniometer with no previous heating history and hence no irreversible deformation was tested. A fixed drive power was applied to its right trunk cantilever, maintained for different durations and the leftover deformation was measured after the power was removed. The process is akin to annealing, *i.e.,* heating the material to above a critical temperature, maintaining for a certain amount of time and then cooling. It is found that the heated trunk that experiences annealing restores to a higher position than its non-annealed counterpart after the removal of the power. Fig. 11 (a) shows the evolution of the tilt of the leveling beam with annealing time at three different drive powers. At a fixed power, the tilt angle increased with the annealing time, showing a logarithmic time response up to 1000 s. Fig. 11 (b) shows the tilt angle dependence on the power. Irreversible deformation occurs at around 28.4 mW, as extrapolated from the graph. No higher power than 66.7 mW was applied on the trunk cantilever during the test to avoid any possible damage from melting of the aluminum in the goniometer structure.

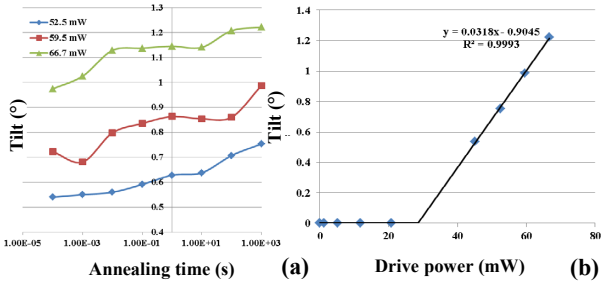

Figure 11: (a) Irreversible tilt angle vs. annealing time at different powers. (b) Irreversible tilt angle introduced by different powers. The annealing time is 1000 s for each power.

CONCLUSION

The custom grating calibration sample was successfully employed to verify the functionality of a hierarchically driven dual-STM servo system. Two simultaneous STM images were obtained, where the pseudo-features on the raw slave images introduced by the master servo are successfully removed by differencing the image signals. The measured drive sensitivity relationship between the ET actuator and the piezo actuator provides the weighting factor for this difference, validating the fundamental understanding of the system operation.

A second generation of scaled probe array is developed, which is placed on a micro-goniometer. That a permanent tilt angle can be introduced by asymmetrical annealing of the two trunk cantilevers indicates that continuous power is not needed to maintain a desired tilt angle, which is favorable in terms of power scaling for a large system. Besides, thermal coupling between the ET actuated goniometer and ET-actuated finger probes can also be avoided.

While operation of only two probes is demonstrated, the active probe technology is available to enable future multiple STM images obtained by a larger array of probes to be stitched together to make a large-area STM image. On-chip circuits such as in [7] will be desirable to scale the system to tens or even hundreds of probes.

REFERENCES

[1] A. A. Tseng, et al., "Recent developments in tip-based nanofabrication and its roadmap," *J. Nanosci. Nanotechnol.*, **8**, pp. 1 - 20, 2008.

[2] A. Pantazi, et al., "Probe-based ultrahigh-density storage technology," *IBM J. Res. & Dev.,* **11**, pp. 22 - 29, 2008.

[3] D. Bullen and C. Liu, "Electrostatically actuated dip pen nanolithography probe arrays," *Sensors and Actuators A*, **125**, pp. 504 - 511, 2006.

[4] H. Baltes, et al., "CMOS MEMS – Present and Future," MEMS'02, pp. 459 - 466.

[5] W. Hofer, et al., "Theories of scanning probe microscopes at the atomic scale," *Rev. Mod. Phys.*, **75**, pp. 1287 - 1331, 2003.

[6] Y. Zhang, Y. Tang, L. R. Carley, and G. K. Fedder, "Active CMOS-MEMS dual probe array for STM based parallel imaging and nanopatterning," MEMS'13, pp. 524 - 527.

[7] Y. Tang, Y. Zhang, G. K. Fedder and L.R. Carley, "A dual probe STM imaging system and a low noise switched-capacitor transimpedance amplifier," *IEEE Sensors Journal*, **13** (8), Aug. 2013, pp. 2984 - 2991.

CONTACT

*Y. Zhang, tel: +1-412-268-3059; yangz1@andrew.cmu.edu

RETAINING HIGH AREAL IN-PLANE MAGNETIC ENERGY DENSITY OVER LARGE MAGNETIC THICKNESS: A PERMANENT MAGNETIC MICROLAMINATION APPROACH BASED ON SEQUENTIAL MULTILAYER ELECTROPLATING

Yuan Li[1], Jooncheol Kim[2], Minsoo Kim[2], Andac Armutlulu[2] and Mark G. Allen[1]*
[1]University of Pennsylvania, Philadelphia, Pennsylvania, USA
[2]Georgia Institute of Technology, Atlanta, Georgia, USA

ABSTRACT

Many magnetic MEMS devices such as magnetic-based microscale energy harvesters rely on the availability of microscale permanent magnets capable of generating significant magnetic fluxes. Ideally, these magnets would be able to be integrated with MEMS in a batch-fabrication-compatible manner. A number of thin film permanent magnets possessing excellent intrinsic magnetic properties have been discussed in the literature. In order to achieve higher extrinsic properties such as magnetic flux, an intuitive approach is to simply increase the magnetic film thickness. However, it is observed that as the magnetic film thickness increases, the intrinsic magnetic properties (such as remanence and maximum energy product) often deteriorate, limiting the maximum achievable magnetic fluxes from these small-scale integrated magnets. In this work, we present a microfabricated permanent magnet with a multilayer structure that preserves the high magnetic energy density (and resultant magnetic flux density) of thinner magnetic films while simultaneously achieving a significant magnetic thickness and resultant extrinsic properties. The fabrication process relies on sequential multilayer electroplating: alternating layers of relatively thin (in microns) magnetic films and non-magnetic materials were electrodeposited in a multilayer fashion realizing a laminated permanent micromagnet up to a total magnetic thickness of 80 µm. A maximum energy product as high as 16.2kJ/m^3 (~ 70% of the value of a 1-µm-thick thin film) was retained in the laminated permanent micromagnet, and a 30% improvement over a CoNiP nonlaminated film with the same magnetic thickness has been successfully achieved. This fabrication approach could potentially be adapted to other permanent magnet materials systems.

INTRODUCTION

A key challenge in magnetic MEMS is the realization of large-volume, high-energy-product permanent micromagnets that can be deposited in a fully-integrated and CMOS-compatible manner. Such magnets are essential in applications ranging from biasing of magnetic sensors in a portable compass [1] to high force MEMS magnetic actuators [2] to energy harvesting [3]. As an example, the generation of voltage in a permanent magnet energy harvester depends on the rate of change of flux (rather than flux density) according to Faraday's law of induction [4]. For a vibration-based energy harvester operating at a given frequency, increasing the rate of change of the magnetic flux is achieved by increasing the total flux itself [4]. In an in-plane permanent magnet, magnetic flux can be increased by increasing the thickness of the magnet, as long as this thickness increase does not cause a concomitant decrease in intrinsic magnetic properties such as flux density or energy product. Although a number of thin films with high magnetic energy density have been shown [5-8], typically the energy density falls rapidly as the film thickness increases [2, 8-10], resulting in weakened permanent micromagnets which are of limited utility in the applications described above [11].

To address this issue, we propose laminated permanent micromagnets as illustrated in Figure 1. Since the magnetic properties of *thick* films degrade as film thickness increases, stacking multiple *thin* magnetic films with preserved properties can be an effective way to achieve considerable overall magnetic thickness while simultaneously retaining good magnetic properties. To achieve this structure, we exploited sequential multilayer electroplating [12], in which individual layers of relatively thin film magnets were electrodeposited in a multilayer fashion to achieve a laminated permanent magnetic structure in a stacked configuration as shown in Figure 1.

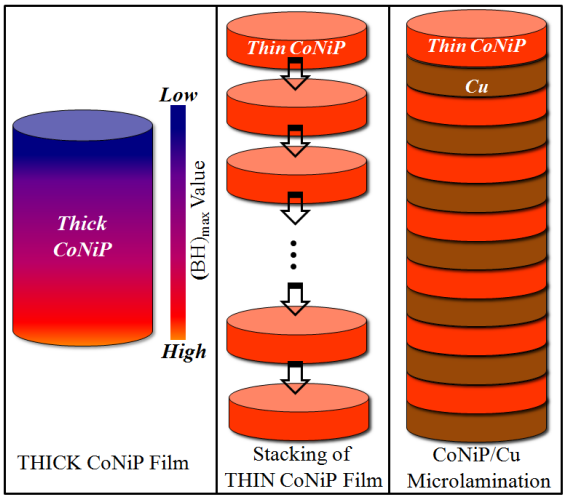

Figure 1: Illustration of the concept of laminated hard magnets (not drawn to scale). (Left) The intrinsic properties of thick electrodeposited magnetic films tend to decrease with thickness. (Center) Conceptually, stacking individual films can produce thick magnets with preserved properties. (Right) Implementation of stacking in-situ using sequential multilayer electrodeposition.

DESIGN AND FABRICATION

Material Selection

The laminated hard magnetic film is comprised of two types of component layers: a hard magnetic material to act as a functional layer and a nonmagnetic interlamination layer to act to 're-seed' the growth of high-energy-product magnetic films.

The candidate hard magnetic material for this work should be compatible with electrodeposition (due to the relative economy and large deposition rates achievable for films of substantial overall thickness) and should have a controllable direction of magnetic anisotropy. The multilayer structure of Figure 1 has magnetic films with a high aspect ratio of in-plane dimension to thickness, resulting in a high in-plane magnetic shape anisotropy. A magnetic material with controllable magnetocrystalline anisotropy could potentially

9781940470016/HH2014/$25©2014TRF
DOI 10.31438/trf.hh2014.11

be engineered to align the shape and crystalline anisotropy, thereby boosting overall magnetic performance.

The potential suitable hard magnetic materials include RE (rare earth) magnetic alloys (NdFeB and SmCo), equiatomic Pt-TM (Transition Metal) alloys (FePt $L1_0$ and CoPt $L1_0$), Co-rich hexagonal alloys (CoNiP, CoNiMnP, CoPt, CoPtP) and others [5, 6]. RE magnetic alloys often seen in bulk-scale applications could be integrated in MEMS [13] but with restrictive processing conditions [10]. Equiatomic Pt-TM alloys with attractive performance commonly require either a high temperature deposition environment or relatively high temperature post-process annealing. Among the Co-rich hexagonal alloys, CoNiP can not only be readily electroplated but also be conveniently tuned with bath compositions [14] and electroplating parameters [15] to yield in-plane magnetocrystalline anisotropy with significant in-plane maximum energy product.

In addition to being electrically conductive (to support the next deposition of magnetic material) and electrodepositable, it is hypothesized that the interlamination material should have excellent planarization properties such that the surface of the underlying magnetic material is fully reset for subsequent depositions. Cu plated from a commercial copper bath (Grobet, Clean Earth Cu-mirror solution) containing brighteners and levelers was chosen as the interlamination material for low surface roughness [16].

Magnetic Film Optimization

Park *et al.* [14] showed that the magnetic properties (in-plane/out-of-plane $(BH)_{max}$ and anisotropy) of CoNiP were strongly influenced by NaH_2PO_2 concentrations in the bath. Kirkwood *et al.* [15] demonstrated a strong correlation between applied current density and c-axis orientation (perpendicular/longitudinal) to the film plane. Based on these results, the plating bath and deposition parameters summarized in Table I were used in this work to achieve significant longitudinal (in-plane) magnetic anisotropy and energy density in the magnetic films. No agitation was applied and Ni sheet was used as an anode for Ni ion replenishment. Due to the lack of Co ion replenishment as plating continued, in order to ensure compositional uniformity of each magnetic film layer in the multilayer structure, the bath volume was adjusted such that the consumption of Co was less than 1% of total dissolved ions in the bath for every batch.

Table I: Bath composition for CoNiP thin films.

Chemicals	Concentration (g/L)
$NiCl_2 \bullet 6H_2O$	47.5
$CoCl_2 \bullet 6H_2O$	49.0
$NaH_2PO_2 \bullet H_2O$	3.0
NaCl	40.9
H_3BO_3	24.7
Saccharin	0.88
Current Density: 20 mA/cm^2, pH: 2.2	

Figure 2 shows typical in-plane and out-of plane magnetic hysteresis loops, measured by vibrating sample magnetometry, of a single layer 1-μm-thick CoNiP thin film deposited using the conditions discussed above. As desired, significant magnetic remanence in the longitudinal direction was observed. EDX results showed the 1 μm thin films had a composition (in Atomic %) of 78 Co%, 13%Ni and 9% P. Both the thin film composition and the magnetic performance are similar to literature values [14, 15].

Microlamination Fabrication

The fabrication sequence is summarized in Figure 3. An insulating layer of silicon dioxide was deposited on a silicon wafer by plasma enhanced chemical vapor deposition (PECVD). An electroplating seed layer structure (Ti/Cu/Ti) was then sputter-deposited (Figure 3(a), (b)). A thick photoresist (NR 21-20000P, Futurrex, Inc.) mold was then formed consisting of an array of circles, each 16mm^2 in area (Figure 3(c), (d)). To eliminate possible oxidation of the Cu seed layer in the sandwich Ti/Cu/Ti seed layer structure, the top layer of Ti was stripped in dilute hydrofluoric acid just before electroplating commenced (Figure 3(e)). Robotically-assisted sequential multilayer electrodeposition of CoNiP and Cu layers was then carried out in a dual bath system with the customized CoNiP bath (with plating conditions detailed in Table I) and the commercial Cu bath (at a current density of 20 mA/cm^2). Individual layer thicknesses of both the CoNiP and Cu layers were set to 1 μm by control of the deposition time (Figure 3(f)). After deposition, the photoresist mold was removed and the morphology of resultant micromagnets (Figure 3(g)) were characterized by a scanning electron microscope (SEM) equipped with energy-dispersive X-ray spectroscopy (EDX). The magnetic properties were characterized by vibrating sample magnetometery (VSM). No correction for demagnetization effects was applied to the data presented below.

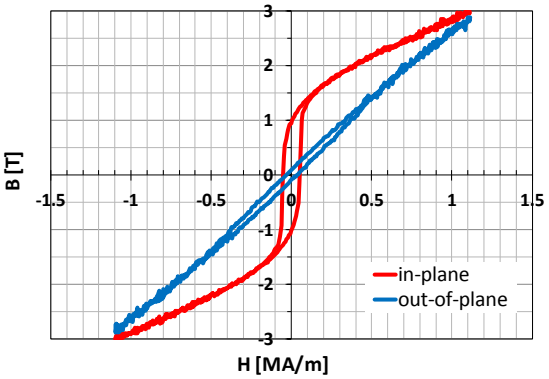

Figure 2: Typical in-plane and out-of-plane hysteresis loops of 1-μm-thick *CoNiP films.*

A cross-sectional SEM image of the fabricated magnetic microlamination is shown in Figure 4(a), comprising a 10-pair CoNiP(1 μm)/Cu(1 μm) laminated magnet. A short selective Cu wet etch was performed to create contrast between the layers; the brighter, protruding layer and darker, receding layer are CoNiP and Cu, respectively (see Figure 4(b)).

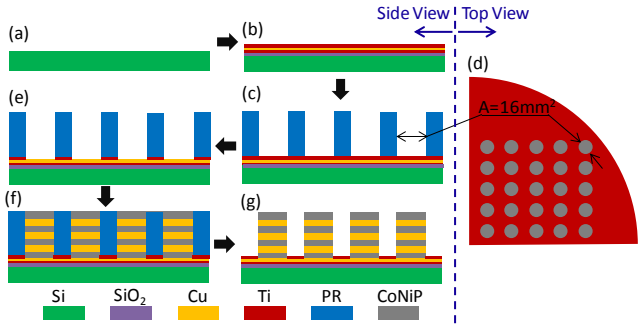

Figure 3: Fabrication process flow.

RESULTS AND DISCUSSION

Magnetic Characterization

In a multilayer structure such as the one fabricated here, the relevant thickness for comparing the magnetic properties of various structures is the total *magnetic* thickness (t_M): the sum of the thicknesses of the magnetic lamination layers. The magnetic thickness will always be less than or equal to the total thickness. For a single layer magnetic film, the magnetic thickness and the total thickness are equal.

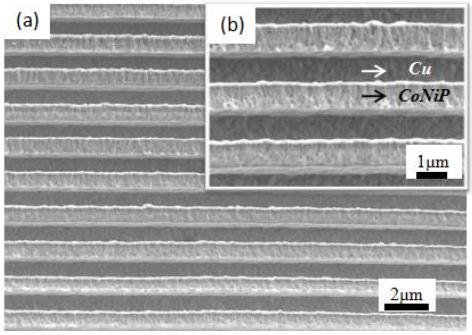

Figure 4: Cross-sectional SEM images of (a) a 10-pair CoNiP(1 μm)/Cu(1 μm) microlamination and (b) an enlarged view.

Figure 5 compares the dependence of various in-plane magnetic properties of CoNiP/Cu multilayer and CoNiP single layer films measured by VSM as a function of total magnetic thickness (t_M). Figure 5(a) shows the variation of in-plane maximum energy product ($(BH)_{max}$) versus t_M. It is evident that the $(BH)_{max}$ of the CoNiP was well-maintained in the microlamination configuration up to a total magnetic thickness of 80 μm, while a single 80 μm thick CoNiP film shows substantial degradation of $(BH)_{max}$. $(BH)_{max}$ as high as 16.2kJ/m^3 was achieved even at a large magnetic thickness of 80 μm, an approximately 30% improvement over nonlaminated CoNiP films of the same magnetic thickness.

Figures 5(b) and (c) compare the remanence and coercivity of single layer and multilayer films as a function of magnetic thickness. The deterioration of $(BH)_{max}$ in single layer thick CoNiP films can be primarily attributed to reduction of remanence rather than coercivity. The decrease in B_r with increasing film thickness in single layer films may originate from the randomization of crystallographic alignment (well-ordered in the case of thin films) as the film thickness increases [7, 17]. The coercivity of single layer CoNiP films exhibited a slight increase with increased magnetic thickness (a similar trend is also found in the CoNiMnP system [8]).

Figure of Merit

The utility of the microlamination technique can be further demonstrated by considering maximum areal magnetic energy density (maximum energy per unit area, or the product of $(BH)_{max}$ and t_M), as an appropriate figure of merit for integrated MEMS magnets. It is a manifestation of how much energy per unit area one can obtain from a microfabricated magnet given a MEMS-constrained footprint. Figure 6 compares the maximum areal energy densities of films with same magnetic thicknesses from this work and the literature [2, 8-10]. Figure 6 (a) shows all data collected for comparison. For better illustration, some data were selected and grouped into thickness ranges (Figure 6 (b)). As can be seen in Figure 6 (b), in the case of MEMS magnets deposited in a CMOS-compatible and fully integrated manner, the microlaminated magnets presented in this work can achieve the highest maximum areal energy density among the materials studied, due to their ability to maintain high $(BH)_{max}$ at very large total magnetic thicknesses.

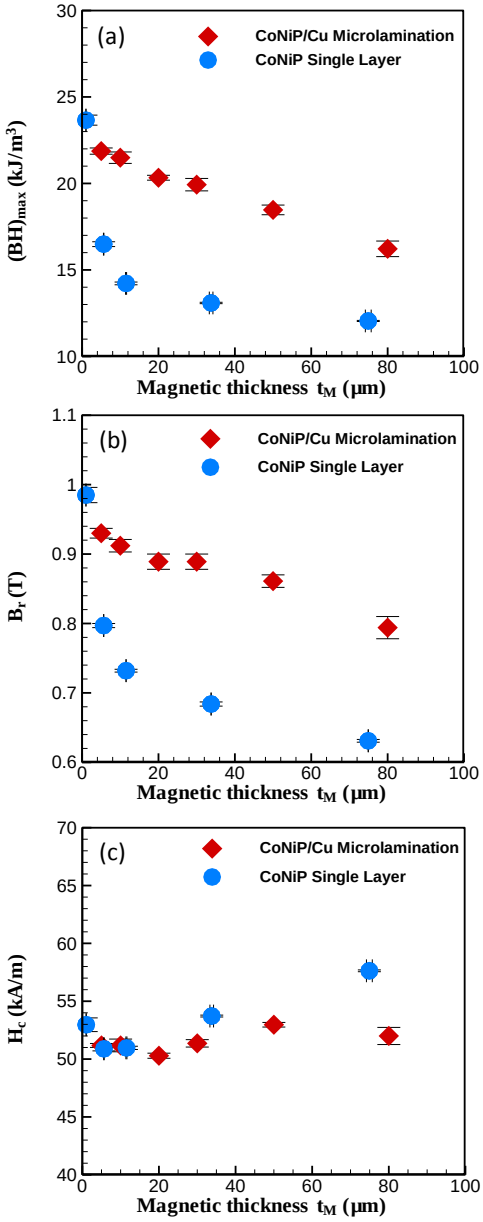

Figure 5: Comparison of the variation of in-plane magnetic properties: (a) maximum energy product, (b) remanence and (c) coercivity as a function of total magnetic film thickness (t_M) between CoNiP(1 μm)/Cu(1 μm) microlamination and CoNiP single layer films.

CONCLUSIONS

A large-volume, high-energy-product laminated hard micromagnet enabled by a fully-integrated, CMOS-compatible fabrication approach has been successfully demonstrated utilizing the technique of sequential multilayer electroplating. The resultant laminated micromagnets showed a 30% maximum energy density improvement at a large magnetic thickness of 80 μm over nonlaminated counterparts. Further, by comparison with the state of the art of the same kind, the proposed micromagnet with laminated structure possessed superior areal magnetic energy density with which the capability of magnetic MEMS devices such as actuators and energy harvesters could be further improved.

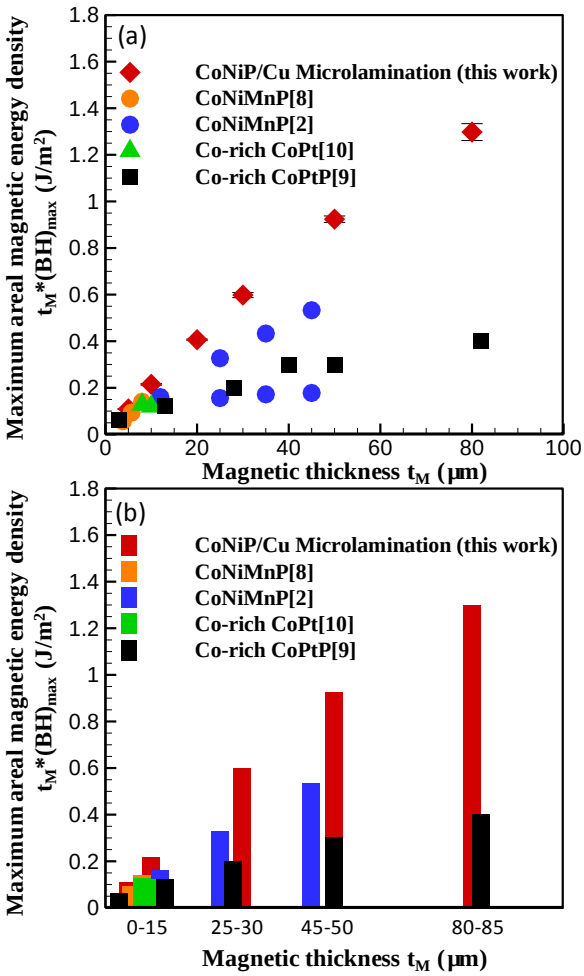

Figure 6: Comparison of film maximum areal magnetic energy density as a function of total magnetic film thickness (t_M) between this work and data reported in literature: (a) full data and (b) data groupings for selected thicknesses.

ACKNOWLEDGEMENTS

This work was supported in part by the DARPA AXiS program (Grant #N66001-11-1-4198). Travel support to the Hilton Head 2014 workshop has been generously provided by the Transducer Research Foundation. The authors would like to thank Dr. Jungkwun Kim for valuable discussions and Mr. Richard Shafer for helpful technical support on the electroplating robot.

REFERENCES

[1] D. Ettelt, P. Rey, M. Savoye, C. Coutier, M. Cartier, O. Redon, M. Audoin, A. Walther, P. Robert, and Y. Zhang, "A new low consumption 3D compass using integrated magnets and piezoresistive nano-gauges," in *IEEE TRANSDUCERS'2011*, pp. 40-43.

[2] T. Liakopoulos, W. Zhang, and C. H. Ahn, "Electroplated thick CoNiMnP permanent magnet arrays for micromachined magnetic device applications," in *IEEE MEMS'96, Proceedings*, pp. 79-84.

[3] M. Han, Q. Yuan, X. Sun, and H. Zhang, "Design and fabrication of integrated magnetic MEMS energy harvester for low frequency applications," *Microelectromechanical Systems, Journal of* vol. 23, pp. 204 - 212, 2013.

[4] P. Wang, K. Tanaka, S. Sugiyama, X. Dai, X. Zhao, and J. Liu, "A micro electromagnetic low level vibration energy harvester based on MEMS technology," *Microsystem technologies*, vol. 15, pp. 941-951, 2009.

[5] D. P. Arnold and N. Wang, "Permanent magnets for MEMS," *Microelectromechanical Systems, Journal of*, vol. 18, pp. 1255-1266, 2009.

[6] G. Pattanaik, D. M. Kirkwood, X. Xu, and G. Zangari, "Electrodeposition of hard magnetic films and microstructures," *Electrochimica acta*, vol. 52, pp. 2755-2764, 2007.

[7] S. Piramanayagam, M. Matsumoto, and A. Morisako, "Thickness dependence of magnetic properties of NdFeB thin films with perpendicular magnetic anisotropy," *Journal of magnetism and magnetic materials*, vol. 212, pp. 12-16, 2000.

[8] X.-M. Sun, Q. Yuan, D.-M. Fang, and H.-X. Zhang, "Electrodeposition and characterization of CoNiMnP-based permanent magnetic film for MEMS applications," in *IEEE NEMS' 2011*, pp. 367-371.

[9] S. Kulkarni and S. Roy, "Deposition of thick Co-rich CoPtP films with high energy product for magnetic microelectromechanical applications," *Journal of magnetism and magnetic materials*, vol. 322, pp. 1592-1596, 2010.

[10] N. Wang and D. P. Arnold, "Thick electroplated Co-rich Co-Pt micromagnet arrays for magnetic MEMS," *Magnetics, IEEE Transactions on*, vol. 44, pp. 3969-3972, 2008.

[11] D. P. Arnold, "Review of microscale magnetic power generation," *Magnetics, IEEE Transactions on*, vol. 43, pp. 3940-3951, 2007.

[12] F. Herrault, W. Galle, R. Shafer, and M. Allen, "Electroplatingbased approaches for volumetric nanomanufacturing," *Tech. Dig. Technologies for Future Micro-Nano Manufacturing*, pp. 1-4, 2011.

[13] B. Peterson, W. Patterson, F. Herrault, D. Arnold, and M. Allen, "Laser-micromachined permanent magnet arrays with spatially alternating magnetic field distribution," *Proceedings of PowerMEMS 2012, Atlanta, USA*, pp. 319-322, 2012.

[14] D.-Y. Park, N. Myung, M. Schwartz, and K. Nobe, "Nanostructured magnetic CoNiP electrodeposits: structure–property relationships," *Electrochimica acta*, vol. 47, pp. 2893-2900, 2002.

[15] D. M. Kirkwood, G. Pattanaik, and G. Zangari, "Electrodeposited CoNiP films with perpendicular magnetic anisotropy," *Journal of The Electrochemical Society*, vol. 154, pp. D363-D368, 2007.

[16] J. Kim, M. Kim, F. Herrault, R. Shafer, J. Park, and M. Allen, "Nanolaminated permalloy core for high-flux, high-frequency ultracompact power conversion," *Power Electronics, IEEE Transactions on*, vol. 28, pp. 4376 - 4383, 2013.

[17] Q. Yao, W. Liu, W. B. Cui, F. Yang, X. G. Zhao, and Z. D. Zhang, "Growth mechanism and magnetic properties for the out-of-plane–oriented Nd–Fe–B films," *Journal of Materials Research*, vol. 24, pp. 2802-2812, 2009.

CONTACT

*Yuan Li, tel: +1-404-644-7238; yuanli1@seas.upenn.edu

ATOMIC LAYER DEPOSITED PLATINUM AS A SENSOR MATERIAL: UNIFORMITY, 1/F NOISE, AND YOUNG'S MODULUS

T.S. English[1], F. Purkl[2,3], A. Daus[2], J Provine[1], Y. Won[1], G. Yama[2], A. Feyh[2], G. O'Brien[2], K.E. Goodson[1], O. Ambacher[3], and T.W. Kenny[1]*

[1]Stanford University, Stanford, California, USA

[2]Robert Bosch RTC, Palo Alto, California, USA

[3]University of Freiburg, Freiburg, Germany

ABSTRACT

This paper examines previously unmeasured properties of atomic layer deposited Pt films relevant to sensor design, including wafer-scale uniformity, 1/f noise, Young's modulus, and the dependence of all these parameters on ALD processing. We observe an increase in the 1/f noise Hooge parameter of nearly two orders of magnitude with decreasing thickness, which introduces constraints on the design of ALD Pt sensors with low noise requirements. Additionally, we measure the variation in wafer-scale electrical uniformity and Young's modulus with thickness, highlighting tradeoffs associated with integrating ALD Pt films into wafer-scale processing to achieve freestanding structures with high yield.

INTRODUCTION

Atomic layer deposition (ALD) provides several advantages in the fabrication of thin films, including the ability to deposit highly conformal and dense polycrystalline metals with low impurity concentrations and digital thickness control between the limits of nucleation and ~ 50 nm in thickness [1]. The upper thickness limit is generally determined by practical considerations, such as precursor cost and deposition time. Within this regime, ALD provides a unique opportunity to engineer and broadly tune material properties at the atomic scale.

Plasma-enhanced atomic layer deposition (PEALD) of Pt is of particular interest in sensor applications for several reasons. First, Pt has desirable thermistor properties, including a high temperature coefficient of resistance (TCR), low 1/f noise, and corrosion resistance [2]. These qualities have led to the adoption of resistive platinum thermometers in numerous sensor applications spanning a wide range of temperatures and operating environments. Second, the ratio of heat capacity (C_{th}) to thermal conductance (G_{th}) in freestanding PEALD Pt films can be tuned due to increased scattering of energy carriers contributing to G_{th} on grain boundaries and surfaces [3], providing an avenue to engineer small thermal time constants ($\tau_{th} = C_{th}/G_{th}$) below 100 µs. This enables higher bandwidth sensors in applications which were formerly limited by the thermistor thermal time constant. Third, by using plasma-enhanced recipes and seed layers optimized for nucleation, sub-20 nm Pt films can be deposited whose Young's modulus and density are within 15 and 5 percent of bulk values, respectively. These robust mechanical properties allow for freestanding structures with aspect ratios as large as 10,000:1 to be integrated with traditional batch wafer-scale processing [4].

In recent years, we've reported the fabrication of uncooled infrared detectors (bolometers) whose performance benefits from these unique characteristics of atomic layer deposited Pt [4,5]. However, practical questions remain, including, at what lower limit of Pt thickness do these beneficial characteristics begin to degrade? In the regime above ~ 12 nm, sheet resistance of PEALD Pt films scale linearly with film thickness. However, below this thickness, sheet resistance scales non-linearly in the regime where nucleation effects and Volmer-Weber style growth occur before a continuous and fully dense polycrystalline film is formed. Nucleation strongly influences the evolution of film properties beyond the formation of a conducting film. As a result, many properties of Pt pertinent to sensor design evolve gradually with a dependence on the film nucleation history. This introduces practical design tradeoffs to ensure not only that material properties are reliably obtained, but also that the films have both sufficient mechanical robustness to survive processing and uniformity to meet design specifications with high yield.

To obtain a more complete understanding of PEALD Pt as a sensor material in the sub-20 nm regime, we characterize the evolution of wafer-scale uniformity, 1/f noise, and Young's modulus through the transition from contiguous nucleation islands to continuous and dense films.

FABRICATION

300, 200, 150, 125, and 100 cycle PEALD Pt films are co-deposited in a Cambridge Nanotech Fiji reactor onto oxidized 4-inch silicon wafers coated with 5 nm PEALD Al_2O_3 and die containing polysilicon cantilever arrays. Following Pt deposition, the sheet resistance of each ALD film is measured at 49 equally spaced locations using an automated wafer probing station. Measurements are performed using a blunt ruthenium tipped probe and care is taken to ensure that the measurement locations do not coincide with the regions of Pt subsequently patterned to form 1/f noise test structures. Center tapped 4-point probe tests structures (also referred to as 5-point probes) are patterned by ion milling to form matched resistors for insertion into the lower half of a Wheatstone bridge. A scanning electron microscopy (SEM) image of a test structure is shown in Fig. 1. Each die contains arrays of 5-point probe test structures with nominal resistances spanning from ~ 100 Ω to more than 100k Ω. Following ion milling, 10 nm of Cr and 100 nm of Pt are evaporated to form an adhesion layer and bond pads for electrical contact.

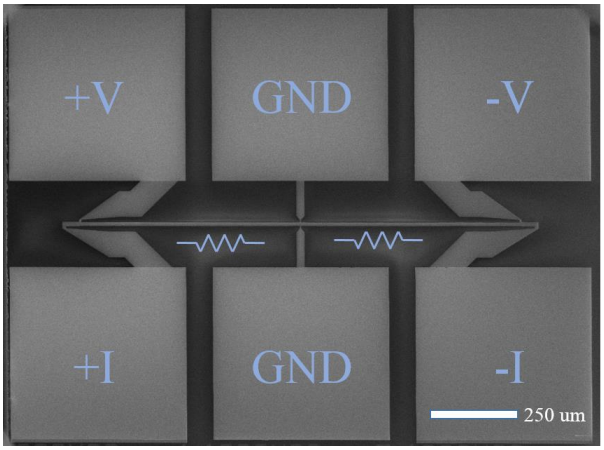

Figure 1: SEM of a 5-point probe 1/f noise test structure.

9781940470016/HH2014/$25©2014TRF
DOI 10.31438/trf.hh2014.12

The Young's modulus is determined by measuring the resonant frequency shift of cantilevers before and after conformal ALD coating using a laser doppler vibrometer. The details of the experimental setup [6] and analysis are outlined elsewhere [7].

Materials Characterization

Each film is characterized using high-resolution transmission electron microscopy (TEM) in both cross-section and plan-view configurations. Figure 2 shows TEM characterization of a subset of PEALD Pt films which span thicknesses > 15 nm (continuous & fully dense) down to < 7 nm (discontinuous) which exhibit Volmer-Weber island growth (Figures 1a,b). A subset of thinner films are characterized using Rutherford backscattering spectrometry (RBS) to provide complementary information to deconvolve thickness, density, and roughness in order to normalize the thickness of discontinuous films to an equivalent thickness at bulk density. This facilitates the comparison of 1/f noise in both continuous and discontinuous films using Hooge's empirical formulation, which depends upon the number of charge carriers and was originally intended to describe homogenous films. It is otherwise challenging to independently quantify the thickness, density, and roughness of such films because TEM characterization is strongly influenced by sample preparation and imaging conditions. Specifically, contrast from transmission through multiple grains of a discontinuous film in cross-section can cause films to appear thicker and/or denser then they truly are.

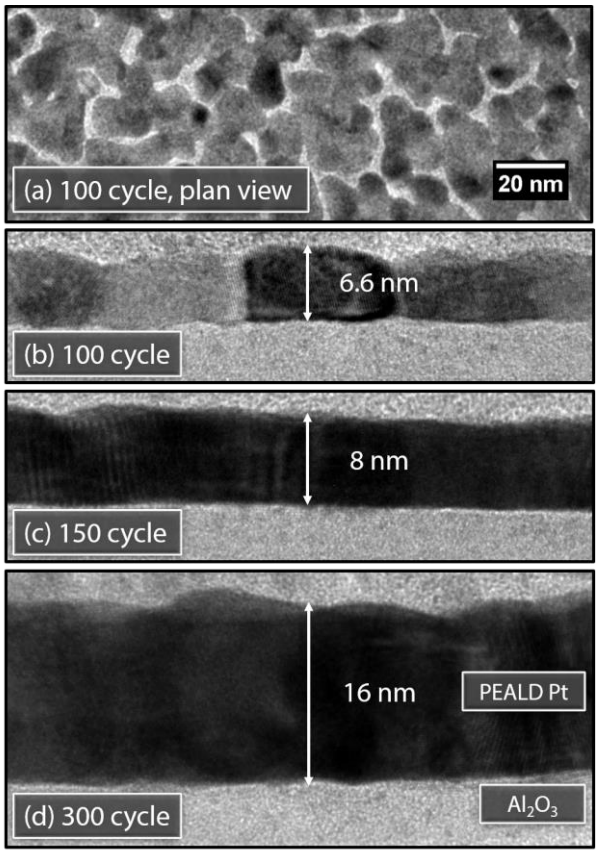

Figure 2: Transmission electron microscopy characterization of a subset of PEALD Pt films showing (c) fully dense and (a,b) non-dense films.

1/F NOISE

Theory

While the origins of 1/f noise continue to be debated to this day, there is broad experimental evidence and consensus that 1/f noise in metals originates from defects and therefore serves as a metric for the quality of a metal film [8]. The following empirical description of 1/f noise was postulated by Hooge

$$S_v(f) = \frac{\gamma V^2}{f^\alpha N} \qquad (1)$$

where Sv is the power spectral density (PSD) in units of V^2/Hz, N is the number of charge carriers, V is the bias across the sample, γ is an empirical noise parameter (Hooge constant), f is frequency, and $\alpha \approx 1$. The PSD dependence on the number of charge carriers suggests that 1/f noise originates from a bulk or volumetric effect, and furthermore, that 1/f noise increases with decreasing film thickness. This has motivated a great number of experimental studies with the objective of measuring 1/f noise in thin films common in micro- and nanofabrication [9]. However, the limited accuracy of experiments and control in fabrication has precluded systematic studies of 1/f noise in polycrystalline metals deposited on substrates where the effects of nucleation on 1/f noise can be measured. Furthermore, in the case of Pt, we might expect significant deviations in 1/f noise behavior during Volmer-Weber nucleation due to the accompanying transformation of grain structure, defect densities, and electron scattering dynamics.

We have addressed the former limitations by fabricating ALD Pt test structures optimized for 1/f noise measurements [10] and by extending recent advances in the design of noise spectroscopy experiments utilizing digital signal processing to remove errors which typically plague the measurement and interpretation of 1/f noise measurements in low-noise materials such as Pt [11,12].

Experimental Setup

Direct current (DC) measurements are challenging to apply to low-noise samples due to the 1/f noise within the first preamplifier stage itself. Additionally, low frequency temperature and biasing drifts can corrupt the 1/f noise measurements and prevent accurate determination of the experimental noise floor. Surrounding this challenge is the question of whether one is measuring the noise of the actual DUT, as desired, or the 1/f noise of the instrumentation in the signal path and interference from other sources. Alternating current (AC) measurements with a Wheatstone bridge provide a means of modulating the 1/f voltage fluctuations as noise sidebands at a frequency chosen such that the preamplifier 1/f noise is negligible (i.e., typically 250 Hz < f <1000 Hz). A dual channel commercial DSP lock-in amplifier (Zurich Instruments) is used to provide synchronous modulation of the 1/f noise, phase-sensitive detection, and direct digital acquisition of the voltage time series at the output filter of the lock-in. Furthermore, phase sensitive detection allows the background experimental noise floor to be measured simultaneously during data acquisition. By subtracting the in-phase signal (1/f noise + background) from the out-of-phase signal (background), a differential measurement is made in the frequency domain, providing further rejection of external noise sources along with a direct assessment of the noise floor of the experiment. Figure 3 shows a schematic highlighting key features of the experimental setup. A typical set of PSD measurements from a 125 cycle PEALD Pt film are shown in Fig. 4 for several applied voltages and a summary of 1/f noise measurements performed at 40 °C appear in Table I.

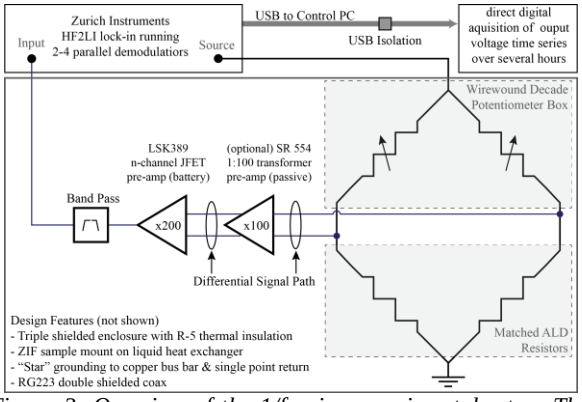

Figure 3: Overview of the 1/f noise experimental setup. The front end signal path is reconfigurable to allow for optimal matching to the sample impedance using a step up transformer pre-amplifier (no power gain) and high input impedance, low-noise differential JFET pre-amplifier. Conducting thermal paint is used to attach die to leadless chip carriers which are mounted to a copper liquid heat exchanger using a zero insertion force holder. A temperature controlled thermal bath provides long-term temperature stability without the noise of active temperature control elements.

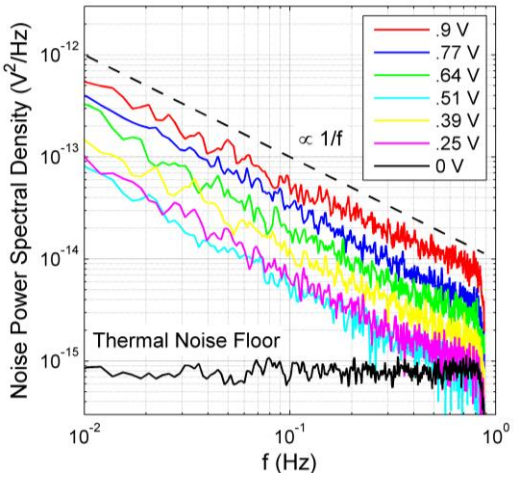

Figure 4: Noise power spectral density of a 125 cycle Pt film measured at several voltages.

Table 1: Summary of measured 1/f noise properties.

PEALD Pt Cycles	*100*	*125*	*150*	*200*	*300*
Thickness (nm) @ bulk density	4.6	6.6	8	10.7	16
1/f Hooge Parameter	1E-2	1.5E-3	2.8E-4	2.4E-4	2.4E-4
1/f exponent	1.13	1.16	1.16	1.15	1.16

After acquiring the voltage fluctuation time series directly from the lock-in, all subsequent data reduction is performed in the digital domain using digital signal processing. The voltage time series output at the lock-in is oversampled and decimated by a factor of 32 using finite impulse response filters to achieve fast roll off with a narrow transition band. This reduces the equivalent noise bandwidth while improving rejection of out-of-band noise.

EXPERIMENTAL RESULTS

The scaling of resistivity, TCR, 1/f noise Hooge parameter, and Young's modulus with number of ALD cycles is shown in Fig. 5. We observe an increase in the 1/f noise Hooge parameter of nearly two orders of magnitude below 10 nm as the film approaches nucleation. However, above this transition, PEALD Pt films display low 1/f noise for which Pt is known. In thermistor applications, the ratio of TCR to 1/f noise constant is a metric of interest that relates the sensitivity (thermal to electrical transduction) with the noise performance of the thermistor itself. In this context, it is interesting to note that the overall thermistor performance is reduced, not only by increasing 1/f noise below 10 nm (150 cycles) , but also by a reduction in the magnitude of the transduced signal due to reduced TCR. An average Young's modulus of 146 GPa was measured for continuous films in the 10-16 nm regime (figure 5d), between 85-90% of the bulk Pt value. Collectively, the trends in figures 5a-d highlight two important regimes surrounding the formation of continuous and dense films, below which the desirable properties of PEALD Pt degrade.

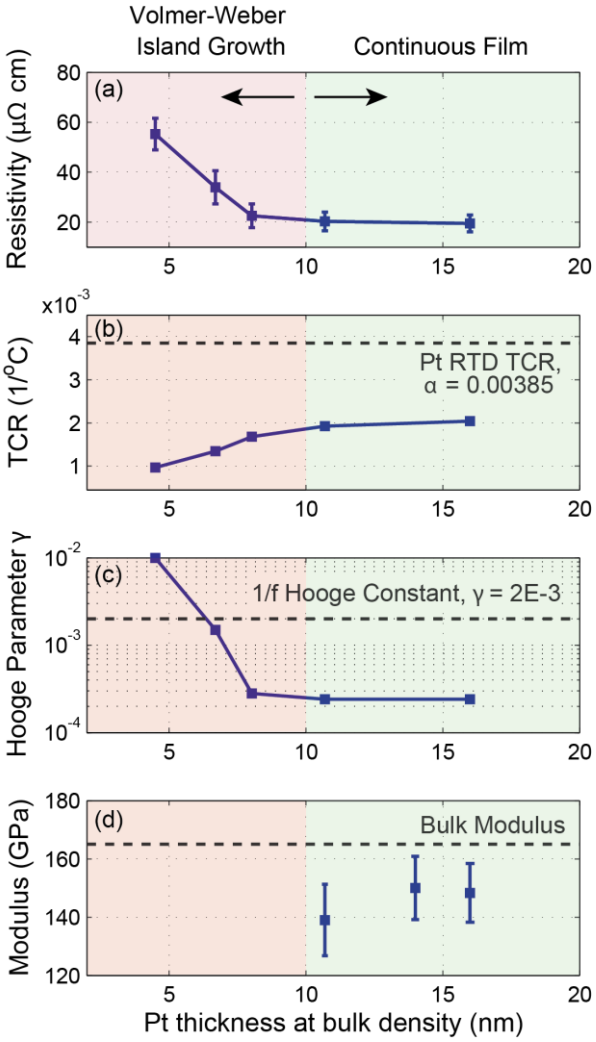

Figure 5: Measured resistivity with error bars reflecting uniformity, TCR, 1/f noise Hooge parameter, and Young's modulus as a function of PEALD Pt thickness normalized to bulk density.

Increasing non-uniformity with fewer ALD cycles may lead to portions of a wafer containing severely degraded thermistor properties (i.e., higher 1/f noise, lower TCR) and heightened sensitivity to processing conditions. While this presents challenges in fabricating devices close to the transition point, it also presents an opportunity to develop tuned recipes which may improve nucleation and wafer-scale uniformity. For example, three PEALD Pt recipe variations are evaluated to improve uniformity and quality of 100 cycle films by altering carrier gas dynamics during deposition. Sheet resistance was measured at 225 points per wafer and binned to form the histograms shown in Fig. 6. We observe that recipes tuned for the Pt precursor chemistry dynamics can reduce sheet resistance by nearly 35% due to improved grain nucleation and morphology while reducing the non-uniformity (standard deviation/average) to between 1 and 2%. An assessment of film thickness and density by TEM and RBS measurements indicate a corresponding reduction in resistivity. Figure 7 shows the improved spatial distribution of non-uniformity achieved with a tuned recipe.

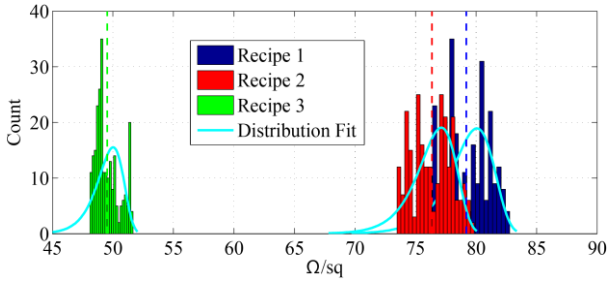

Figure 6: Sheet resistance histograms constructed from 225 wafer-scale measurements of 100 cycle films demonstrating an ability to tune electrical properties and uniformity via ALD recipe. Thickness & density were independently measured by TEM and Rutherford Backscattering spectrometry.

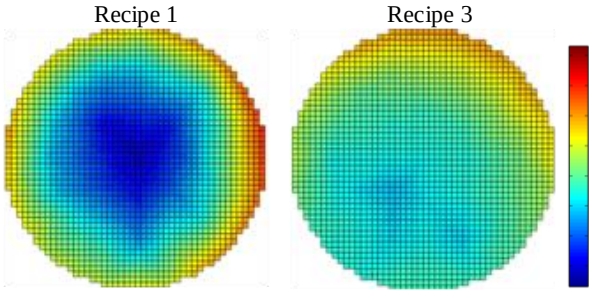

Figure 7: 4" wafer sheet resistance maps plotted with a constant color scale centered on the mean sheet resistance of each wafer.

CONCLUSIONS

At the lower thickness limit approaching nucleation, the ideal thermistor properties of PEALD Pt are found to degrade due to increasing 1/f noise and a corresponding reduction in TCR. This may drive tradeoffs and practical lower limits to thickness in the design of ultrathin PEALD Pt sensors. In contrast, we observe that PEALD Pt films retain their excellent thermistor and mechanical properties with increasing thickness above a transition point corresponding to the formation of dense and continuous films with a mature grain structure. The interplay between material properties, ALD recipes, and wafer-scale uniformity highlight the challenges of using PEALD Pt as a sensor material near the observed transition. Future work in this area includes the development of tuned ALD recipes targeting improved electrical, thermal, and mechanical properties of ALD Pt films for emerging sensor applications.

ACKNOWLEDGMENTS

Fabrication was carried out at the Stanford Nanofabrication Facility and was supported by the Defense Advanced Research Projects Agency through the N/MEMS S&T Fundamentals Program managed by Dr. Dennis Polla and Dr. Tayo Akinwande. T.S.E. is appreciative for funding support from the National Science Foundation through the Graduate Research Fellowship Program and from the Department of Defense through the National Defense Science & Engineering Graduate Fellowship Program.

REFERENCES

[1] T. Aaltonen, M. Ritala, T. Sajavaara, J. Keinonen, and M. Leskel, "Atomic Layer Deposition of Platinum Thin Films", Chemistry of Materials, **15**(9), 1924 (2003).

[2] R.F. Vines, *The Platinum Metals and Their Alloys*, The International Nickel Company, New York, 1941.

[3] S. Yoneoka, J. Lee, M. Liger, G. Yama, T. Kodama, M. Gunji, J. Provine, R.T. Howe, K.E. Goodson, and T.W. Kenny, "Electrical and Thermal Conduction in Atomic Layer Deposition Nanobridges Down to 7 nm Thickness," Nano Letters, 12(2), 683 (2012).

[4] F. Purkl, T.S. English, G. Yama, J Provine, A.K. Samarao, A. Feyh, B. Kim, G. O'Brien, O. Ambacher, R.T. Howe, and T.W. Kenny. "Serpentine Geometry for Enhanced Performance of Nanometer-thin Platinum Bolometers". Technical digest of Solid-State Sensors, Actuators and Microsystems (TRANSDUCERS & EUROSENSORS XXVII), (2013), pp. 1507-1510.

[5] F. Purkl, T.S. English, G. Yama, J. Provine, A.K. Samarao, A. Feyh, G. O'Brien, O. Ambacher, R.T. Howe, and T.W. Kenny, "Sub-10 Nanometer Uncooled Platinum Bolometers via Plasma Enhanced Atomic Layer Deposition," in Micro Electro Mechanical Systems (MEMS), IEEE 26th International Conference on. IEEE, Jan. (2013), pp. 185 - 188.

[6] Y. Won, Y. Gao, M.A. Panzer, S. Dogbe, L. Pan, T.W. Kenny, and K.E. Goodson, "Mechanical Characterization of Aligned Multi-walled Carbon Nanotube Films Using Microfabricated Resonators", Carbon, 50, 347 (2012).

[7] B. Ilic, S. Krylov, and H.G. Craighead, "Young's Modulus and Density Measurements of Thin Atomic Layer Deposited Films Using Resonant Nanomechanics", Journal of Applied Physics,108, 044317 (2010).

[8] P. Dutta and P.M. Horn, "Low-frequency Fluctuations in Solids: 1/f Noise", Reviews of Modern Physics, 53(3), 497 (1981).

[9] D.M. Fleetwood and N. Giordano, "Resistivity Dependence of 1/f Noise in Metal Films", Phys. Rev. B, 27(2), 667 (1983).

[10] J.H. Scofield, "AC Method for Measuring Low Frequency Resistance Fluctuation Spectra", Review of Scientific Instruments, 58(6), 985 (1987).

[11] D.M. Fleetwood, J.T. Masden, and N. Giordano, "1/f Noise in Platinum Films and Ultrathin Platinum Wires: Evidence for a Common, Bulk Origin", Phys. Rev. Lett., 50(6), 450 (1983).

[12] A. Ghosh, S. Kar, A. Bid, and A.K. Raychaudhuri, "A Set-up for Measurement of Low Frequency Conductance Fluctuation (Noise) Using Digital Signal Processing Techniques", condmat, arXiv:cond-mat/0402130 vi, (2004).

CONTACT

*T.S. English; englisht@stanford.edu

STRAIN-MEDIATED ELECTRICAL CONTROL OF MAGNETIZATION IN MICRON-SCALE NICKEL RING ON PMN-PT

H. Sohn[1], M.E. Nowakowski[2], J. Hockel[1], C. Liang[1], K. Wetzlar[1], M. A. Marcus[3], A. Doran[3], and A. T. Young[3], M. Kläu[4], C. S. Lynch[1], G. P. Carman[1], J. Bokor[2] and R.N. Candler[1 5]*

[1] University of California, Los Angeles, USA

[2] University of California, Berkeley, USA

[3] Lawrence Berkeley National Lab, Berkeley, USA

[4] Johannes Gutenberg-Universität, Mainz, Germany

[5] California NanoSystems Institute, Los Angeles, USA

ABSTRACT

The magnetic "onion" state in a micron-scale ferromagnetic ring on a piezoelectric substrate is controlled with electrically induced anisotropic strains. Two perpendicular ferroelectric strains imposed on the ring produce magnetoelastic energy sufficient to overcome the magnetic energy barrier and reorient the magnetic state along the new easy axis of magnetization. A 45° rotation of the magnetic onion state is achieved and is measured by Photo-Emission Electron Microscopy (PEEM), marking the first demonstration of deterministic control of magnetization using multiferroic rings.

INTRODUCTION

Recent resurgence of interest in multiferroics has focused on the potential of maximizing the magnetoelectric effect [1-4], where electrostatic fields can be used to control magnetization at the nanoscale. One method to achieve strong multiferroic properties is to develop laminate structures of pieozoelectric and magnetostrictive materials, coupling via strain (Figure 1). Electrically induced strain in an electrostrictive material is transferred to a magnetostrictive material, which changes magnetoelastic energy. As such, the laminate structure (Figure 2 (a)) enables magnetic control of devices ~1 μm or smaller, a size range where typical micro electromagnets face issues with power dissipation due to scaling of coil resistance.

More recently, ferromagnetic ring elements have been studied for their symmetric shape (yielding well-defined and stable magnetic states), as well as their varied magnetic states [5]. One interesting magnetic state available to the ring geometry is the magnetic "onion" state, which is observed at the micron- or submicron-scale (Figure 2 (b)). A remnant onion state can be formed under certain geometric and material constraints by applying a saturating magnetic field along an in-plane direction and then releasing the applied field [6]. The onion state possesses two opposite circular magnetizations, and their direction depends on the previous magnetization process. Due to its ability to maintain a magnetic state with no applied field, a few studies have attempted to manipulate the onion state for possible application in magnetic memory [7]. Reorientation of the onion state requires energy to overcome an energy barrier at its energy minimum [8].

Previously, feasibility of manipulating magnetic onion states was demonstrated in 2 μm ferromagnetic Ni rings on a piezoelectric PMN-PT substrate. The rings were initialized by a magnetic field applied in the [011] direction on the PMN-PT substrate, and 90° rotation of the onion state measured by Magnetic Force Microscopy (MFM) when electric field was applied [8].

In this study, we deposit the 2 μm Ni ring structures on an unpoled PMN-PT substrate, pole the PMN-PT, and then initialize the onion state at 45° to the [011] direction and demonstrate 45° rotation of the magnetic onion state to the [100] direction. Unlike

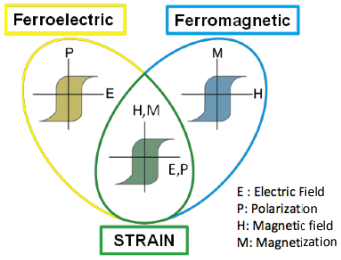

Figure 1. Concept of strain-coupled magnetoelectric structure [9].

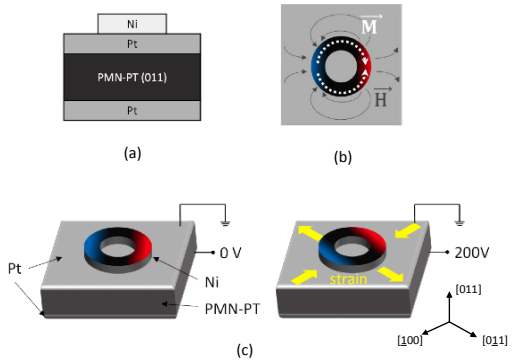

Figure 2. (a) Schematic of a Ni ring/PMN-PT heterostructure (b) Representaion of the maganetic onion state. (The white and gray arrows indicate the magnetization and the stay magnetic field, respectively.) (c) Rotation of the onion state. Left: initial onion state before applying E-field. Right: Rotated onion state after applying the E-field

the un-poled PMN-PT of the prior work, the strain on the poled PMN-PT is deterministically controllable, and the direction of the rotation is predictable. The measurement of the magnetic states is performed with PEEM.

Both MFM and PEEM are experimental methods to measure magnetization (Figure 3). MFM utilizes a magnetized scanning-probe and measures the magnetic interaction (repulsion and attraction) between the probe and the sample. Therefore, MFM is an indirect measurement of straying magnetic field from the sample. The magnetized tip may disturb magnetization in the sample. On the contrary, PEEM utilizes right and left circularly polarized x-rays, emitting secondary electrons from the sample. The emitted secondary electrons are collected and analyzed by electron microscopy to determine their spin and orbital magnetic moment. PEEM provides a direct measurement of magnetization and as a non-invasive technique has no potential to generate magnetic disturbance. PEEM can resolve magnetization to ~30 nm of magnetization, which makes it suitable for characterization of sub-micron magnetic structures.

9781940470016/HH2014/$25©2014TRF
DOI 10.31438/trf.hh2014.13

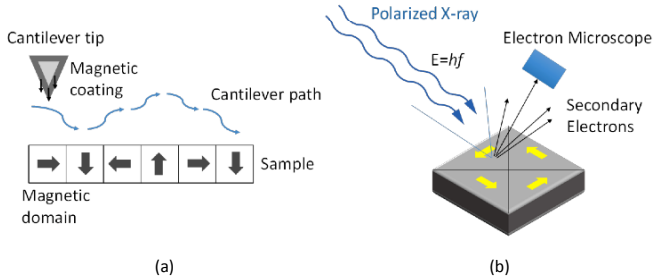

Figure 3. (a) Magnetic force microscopy and (b) photoemission electron microscopy

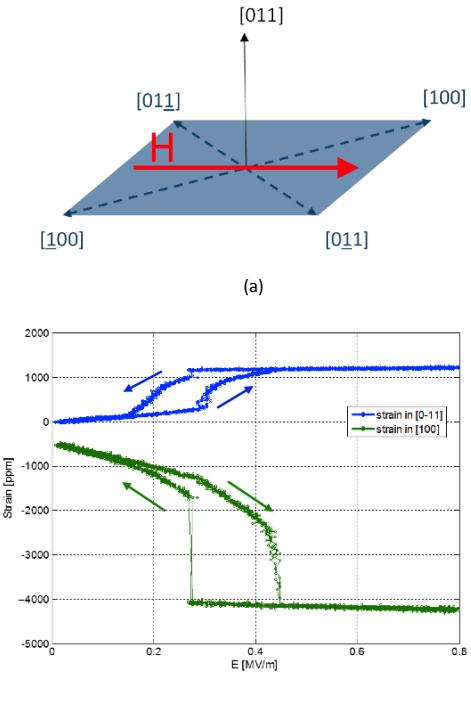

Figure 4. (a) Orientation of PMN-PT (The red arrow indicates the initialization direction of the magnetic field (H-field)) (b) PMN-PT strain curve with electric field

THEORY

PMN-PT

A single crystal piezoelectric material, (011) $Pb(Mg_{1/3}Nb_{2/3})O_3]_{(1-x)}$-$[PbTiO_3]_x$ x≈0.34 (PMN-PT), is chosen to generate anisotropic strains. The (011) PMN-PT produces tensile and compressive strains in two perpendicular in-plane directions [10], [0$\underline{1}$1] and [100], respectively, in response to application of an out-of-plane electric field in the polarization direction ([011] direction). An out-of-plane strain is also generated with application of this electric field, but it is not transferred to the ring. The orientation and strain curve of a PMN-PT substrate are shown in Figure 4. The strain jump in Figure 4 (b) is associated with an electric field induced phase transition.

Magnetic Energy Minimization Process

The magnetic onion state is a domain structure that minimizes magnetic energy.. The total magnetic energy density is the sum of

$$E_{tot} = E_{demag} + E_{exch} + E_{aniso} + E_{Zeeman} + E_{me} \quad (1)$$

where E_{demag}, E_{exch}, E_{aniso}, E_{Zeeman}, and E_{me} are demagnetization energy, exchange energy, magneto-crystalline anisotropy energy, Zeeman energy and magnetoelastic energy, respectively.

After removal of the external magnetic field, the uniformly magnetized ring carries an excess of demagnetization energy resulting from the stray field generated the magnetization that is not parallel to the ring perimeter. As a result, the demagnetization energy decreases by reorienting the magnetization and forming domains at the expense of exchange energy. Rebalancing between energy terms continues until the total energy is minimized, resulting in the onion state with two domain walls. It should be noted that there exist multiple magnetic states other than the magnetic onion state, such as the vortex state and further multi-domain states [11]. The width and thickness of the ring largely determine its magnetic state at the micron-scale and nanoscale [6, 11]. Crystal anisotropy energy and Zeeman energy are assumed to be zero because (1) the evaporated Ni structure used for experiments is polycrystalline, and (2) no external magnetic field exists after the first initialization of the magnetic onion state [12]. Demagnetization energy is determined by the interaction of magnetization elements and the geometry of the ring. Exchange energy depends on neighbor magnetizations and favors uniformly aligned magnetization. Magnetoelastic energy from an external strain is given as [12]

$$E_{me} = -\frac{3}{2}\lambda_s E \varepsilon_{ext}\left(\cos^2\theta - \frac{1}{3}\right) \quad (2)$$

where λ_S and E are saturation magnetostriction and Young's modulus, respectively. θ is the angle between magnetization and strain. For polycrystalline Ni, λ_S = -34 ppm, and E = 200 GPa and this was recently confirmed to hold for thin films [13]. A PMN-PT substrate with electric field along [011] direction generates two perpendicular anisotropic strains: tensile strain in [0$\underline{1}$1] and compressive strain [100]. Total magnetoelastic energy can be expressed as

$$E_{me} = -\frac{3}{2}\lambda_s E\left\{\varepsilon_{[100]}\left(\cos^2\theta - \frac{1}{3}\right) + \varepsilon_{[0-11]}\left(\sin^2\theta - \frac{1}{3}\right)\right\} \quad (3)$$

Since nickel has a negative magnetostriction, magnetic energy has a minimum along a compressive direction. In other words, anisotropic strains induce a new easy axis along the compressive direction. Reorientation of the magnetic state occurs if magnetoelastic energy from external strains produces enough energy to break the balance between energy terms, or overcome the energy barrier at the current energy minimum.

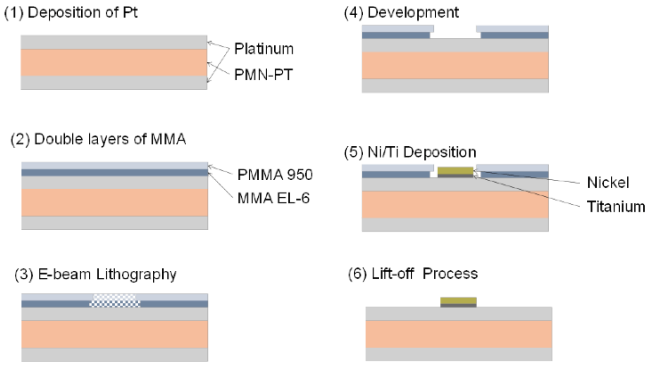

Figure 5. Process flow of Ni ring / PMN-PT magnetoelectric heterostructure fabrication

EXPERIMENTAL DETAIL

Fabrication

To investigate the strain-mediated magnetoelectric effect, we fabricated a nickel ring structure on a single crystal (011) PMN-PT substrate, where nickel is magnetoelastic and PMN-PT is piezoelectric. 5 nm Ti / 50 nm Pt is deposited on the top and bottom surface of the 8.0 x 8.0 x 0.5 mm^3 PMN-PT as an adhesion layer/electrode. On the top (011) PMN-PT surface, double layers of methyl methacrylate (MMA) for a lift-off process are spin-coated and patterned via electron beam lithography. After the pattern development in a methyl isobutyl ketone (MIBK) solution, 5 nm Ti/ 30 nm Ni as an adhesion/ferromagnetic layer is deposited by electron beam evaporation. A lift-off process is performed to define the Ni ring structures on the substrate. The dimensions of rings in this work are 2 μm/ 1.6 μm and 2 μm/ 1.4 μm (outer diameter/ inner diameter). The SEM images of the rings are shown in Figure 6.

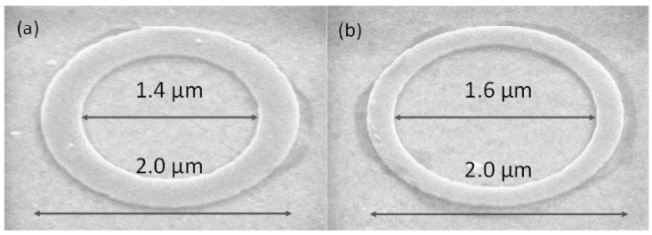

Figure 6. SEM images of nickel rings. (a) 2um/ 1.6 μm (b) 2um/ 1.4 μm. Note the images was taken under a tilt angle leading to the seemingly asymmetric shape.

Measurement

Polarization of intrinsic PMN-PT is randomly ordered. By applying an electric field across the PMN-PT, we pole, or align, the polarization to initialize in-plane strains as shown in Figure 4 (b).

After initializing the remnant strain, the onion states in the rings were formed through application of a 3 kOe magnetic field oriented 45° from the [100] and [0$\underline{1}$1] directions to obtain deterministic control of magnetization. PEEM in the Lawrence Berkeley National Lab was used to measure the magnetic state of the rings. The top electrode was grounded to avoid affecting the trajectory of emitted electrons. The voltage was applied to the bottom electrode to create electric field across the PMN-PT substrate through the in-situ voltage setup in the PEEM chamber. A schematic of the device to be tested is shown in Figure 2 (c). The magnetic state in the rings was imaged as the electric field was increased.

RESULTS

After the external magnetic field of 3 kOe was removed, the initial magnetic onion state in the rings was created (first column in Figure 7). The onion states exhibit two opposite circular magnetizations heading toward the +x axis and magnetic domains emerging from the ring where at the left and right sides.

At an electric field of 0.20 MV/m (second column in Figure 7), the PMN-PT has a strain of -1000 ppm in [100] and +150 ppm in [0$\underline{1}$1]. The result does not yet show appreciable magnetic change, indicating that magnetoelastic energy from anisotropic strains is not yet enough to overcome the energy barrier at its current energy minimum.

The onion state started to change at 0.40 MV/m (third column in Figure 7). The ring of 2.0 μm/ 1.4 μm exhibited a more significant change than the ring of 2.0 μm/ 1.6 μm, which started reorienting at 0.44 MV/m. The difference in magnetization between the two rings was attributed to the difference in demagnetization energy. The ring with a wider width has a smaller in-plane demagnetization factor than one with a thinner width (where ring width is defined as half the difference between inner and outer diameter). Furthermore in narrower rings the domain wall pinning is stronger due to a stronger interaction with edge roughness that plays a relatively larger role compared to the width. Thus it is easier to reorient magnetization in the wider ring, requiring less energy.

At an electric field of 0.52 MV/m, rotation of the onion states was accomplished. The onion states were reoriented, or rotated, along the new easy axis, the [100] direction, which had a compressive strain. The tensile and compressive strains produced anisotropic magnetoelastic energy gradient minimizing magnetic energy in the compressive direction and magnetization was reoriented in that direction. Evidence of anisotropic strain energy creates a new easy axis of magnetization, allowing for rotation of the onion state. No further change was observed at higher voltages.

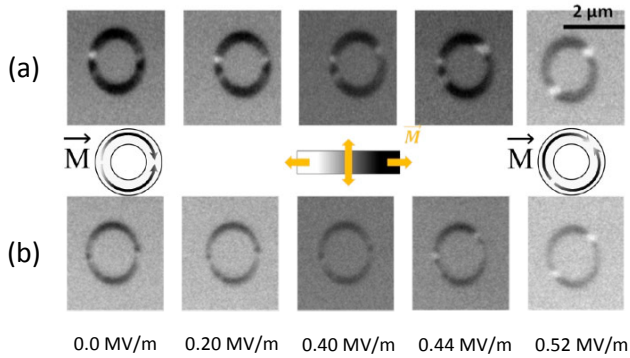

Figure 7. PEEM images of nickel rings with different E-fields. (a) 2 μm/ 1.6 μm (b) 2 μm/ 1.4 μm

CONCLUSION

We demonstrated that electrically induced anisotropic strain from a piezoelectric substrate can be used to reliably rotate the magnetic onion states in magnetoleastic rings. Since only electrostatically induced strains were required to reorient magnetic states, applications requiring low power and non-volatile control of magnetization, such as magnetic memory, become possible. With further development of full 360° rotation, magnetoelectric heterostructures could be used to build miniature motor systems with extremely high power densities.

ACKNOWLEDGMENTS

This project was supported by the National Science Foundation through the Cooperative Agreement Award EEC-1160504. The award, managed by Dr. Deborah J. Jackson, is for the Engineering Research Center on Translational Applications of Nanoscale Multiferroic Systems (TANMS). Fabrication was performed in Integrated Systems Nanofabrication Cleanroom (ISNC) and Nanoelectronics Research Facility (NRF) at UCLA.

REFERENCES

[1] S.-W. Cheong and M. Mostovoy, "Multiferroics: a magnetic twist for ferroelectricity," *Nature materials,* vol. 6, pp. 13-20, 2007.

[2] W. Eerenstein, N. D. Mathur, and J. F. Scott, "Multiferroic and magnetoelectric materials," *Nature,* vol. 442, pp. 759-65, Aug 17 2006.
[3] R. Ramesh and N. A. Spaldin, "Multiferroics: progress and prospects in thin films," *Nature materials,* vol. 6, pp. 21-29, 2007.
[4] C.-W. Nan, M. I. Bichurin, S. Dong, D. Viehland, and G. Srinivasan, "Multiferroic magnetoelectric composites: Historical perspective, status, and future directions," *Journal of Applied Physics,* vol. 103, p. 031101, 2008.
[5] S. Li, D. Peyrade, M. Natali, A. Lebib, Y. Chen, U. Ebels*, et al.*, "Flux closure structures in cobalt rings," *Physical Review Letters,* vol. 86, p. 1102, 2001.
[6] C. A. F. Vaz, T. J. Hayward, J. Llandro, F. Schackert, D. Morecroft, J. A. C. Bland*, et al.*, "Ferromagnetic nanorings," *Journal of Physics: Condensed Matter,* vol. 19, p. 255207, 2007.
[7] M. Hara, T. Kimura, and Y. Otani, "Controlled depinning of domain walls in a ferromagnetic ring circuit," *Applied physics letters,* vol. 90, p. 242504, 2007.
[8] J. L. Hockel, A. Bur, T. Wu, K. P. Wetzlar, and G. P. Carman, "Electric field induced magnetization rotation in patterned Ni ring/Pb (Mg1/3Nb2/3) O3](1− 0.32)-[PbTiO3] 0.32 heterostructures," *Applied Physics Letters,* vol. 100, p. 022401, 2012.
[9] D. Khomskii, "Classifying multiferroics: Mechanisms and effects," *Physics,* vol. 2, pp. 1-8, 2009.
[10] T. Wu, P. Zhao, M. Bao, A. Bur, J. L. Hockel, K. Wong*, et al.*, "Domain engineered switchable strain states in ferroelectric (011) [Pb(Mg1/3Nb2/3)O3](1−x)-[PbTiO3]x (PMN-PT, x≈0.32) single crystals," *Journal of Applied Physics,* vol. 109, p. 124101, 2011.
[11] M. Kläui, "Head-to-head domain walls in magnetic nanostructures," *Journal of Physics: Condensed Matter,* vol. 20, p. 313001, 2008.
[12] M. Weiler, A. Brandlmaier, S. Geprägs, M. Althammer, M. Opel, C. Bihler*, et al.*, "Voltage controlled inversion of magnetic anisotropy in a ferromagnetic thin film at room temperature," *New Journal of Physics,* vol. 11, p. 013021, 2009.
[13] S. Finizio, M. Foerster, M. Buzzi, B. Krüger, M. Jourdan, C. Vaz*, et al.*, "Magnetic Anisotropy Engineering in Thin Film Ni Nanostructures by Magnetoelastic Coupling," *Physical Review Applied,* vol. 1, p. 021001, 2014.

CONTACT

*H. Sohn, tel: +1-310-890-7175; son0913@ucla.edu

LORENTZ FORCE MAGNETOMETER WITH QUADRATURE FREQUENCY MODULATION

M. Li[1], S. Sonmezoglu[1], E.J. Ng[2], V.A. Hong[2], C. H. Ahn[2], Y. Yang[2], T.W. Kenny[2] and D.A. Horsley[1]*
[1]Univeristy of California, Davis, California, USA
[2]Stanford University, Stanford, California, USA

ABSTRACT

In this paper, a Lorentz force magnetometer demonstrates quadrature frequency modulation (QFM) operation. The Lorentz force magnetometer consists of a conventional 3-port resonator, which is put into oscillation by electrostatic driving and sensing. The bias current flowing through the resonator is proportional to the displacement, and generates Lorentz force in quadrature with the electrostatic force. As a result, the Lorentz force acts as an equivalent spring and the magnetic field can be measured by reading the change in oscillation frequency. The sensor has a sensitivity of 500 Hz/T with a short-term noise floor of 500 nT/√Hz. The bandwidth of the sensor is increased to 50 Hz, a factor of 12 greater than that of the same resonator operating in amplitude-modulated (AM) mode.

INTRODUCTION

Many Lorentz force magnetometers have been proposed in recent years [1-3]. The MEMS magnetometer is entirely silicon, sharing the same fabrication process as commercially available accelerometers and gyroscopes. A single-structure 3-axis magnetometer has also been reported [3], giving it great potential to be used as an electronic compass in smart phones. Compared to the commercially available Hall-Effect sensors currently used in smart phones [4], MEMS magnetometers do not require flux-concentrators for 3-axis measurement and are free from magnetic hysteresis.

This work demonstrates a resonant Lorentz force magnetometer with quadrature frequency modulation (QFM) readout. Readout control electronics based on amplitude modulation (AM) and fabrication of the device were reported in [1]. A conventional AM magnetometer modulates low frequency magnetic field to a frequency near the device's resonance frequency. The motion resulting from the Lorentz force is therefore amplified by the mechanical quality factor (Q) of the sensor, and the motion's amplitude is used as a measure of the input magnetic field. Although Brownian-limited noise floor can be achieved, AM magnetometers suffer from small bandwidth and large temperature sensitivity. In an FM magnetometer, input magnetic field results in a change in the oscillation frequency by varying the stiffness (k) of the sensor. Two different methods for FM modulation have been reported in the literature. A straightforward method is to use Lorentz force to generate axial stress [5] which results in a change in k of the oscillator and therefore the resonance frequency of the oscillator changes. The other method is to use quadrature frequency modulation (QFM), where an external force having the same frequency as, but in quadrature with, the self-sustaining force creates a phase shift in the oscillation loop. This phase shift results in a change in the oscillation frequency, since oscillation always occurs at the frequency that satisfies 0° phase shift around the loop. MEMS QFM gyroscopes (having Coriolis force as the external force) [6] and magnetometers (having Lorentz force as the external force) [7] were demonstrated. Using the same MEMS magnetometer structure, magnetic field can be either amplitude modulated (AM) or frequency modulated (FM) by controlling the phase difference between the Lorentz force and electrostatic force. Relative to earlier AM magnetometers, QFM operation extends the sensor's bandwidth from a few Hz to 50 Hz, which is independent from the sensor's mechanical bandwidth. QFM operation also significantly increases the dynamic range.

THEORY

System Dynamics

The MEMS Lorentz force magnetometer is based on a traditional three-port MEMS resonator operating as an oscillator. The resonance frequency serves as the system reference clock for the bias current generation.

The system dynamics of the Lorentz force magnetometer can be modeled as a second order mass-spring-damper system:

$$m\ddot{x} + b\dot{x} + kx = F_E + F_L \quad (1)$$

where m is the effective mass, b is the damping coefficient, k is the spring constant, F_E is the electrostatic driving force and F_L is the Lorentz force. In the operation of a QFM magnetometer, F_L is always in phase with the displacement x:

$$F_L = BIL = BA_I xL \quad (2)$$

where the bias current gain A_I is used here to represent the bias current to displacement ratio, $A_I = I/x$, which is controlled by the electronics. By replacing the Lorentz force F_L according (2), the equation of motion (1) can be written as

$$m\ddot{x} + b\dot{x} + \underbrace{(k - BA_I L)}_{k_{eff}} x = F_E \quad (3)$$

It is clearly seen from (3) that the magnetic field modifies the effective spring constant of the device, k_{eff}. Therefore, when the resonator operates in closed-loop, the magnetic field signal can be observed through a change in oscillation frequency.

To demonstrate the principle of operation, the open-loop force-to-displacement frequency response of the QFM magnetometer is measured. Figure 2 shows the amplitude (top) and phase (bottom) characteristics. In this measurement, the bias current gain is set to A_I = -3200 A/m. The black trace in Figure 2 shows the response of the magnetometer in the absence of an external magnetic field, whereas the blue and red traces show the

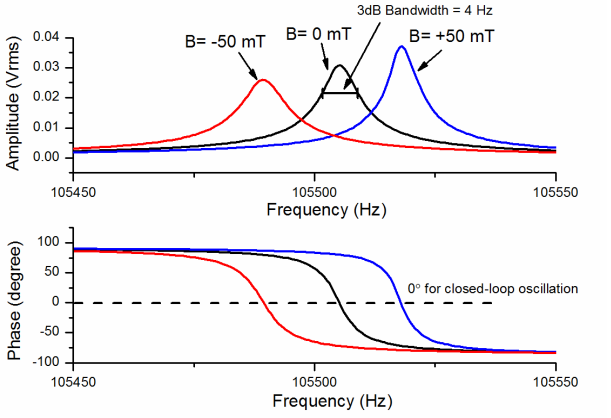

Figure 1: Amplitude (top) and phase (bottom) characteristics of the QFM magnetometer with no external magnetic field applied (black trace) and ±50 mT magnetic field (blue and red traces) applied.

9781940470016/HH2014/$25©2014TRF
DOI 10.31438/trf.hh2014.14

response in the presence of 50 mT and -50 mT magnetic field, respectively. In closed-loop operation, the phase around the oscillation loop is always 0°, as indicated by the black dashed line in the phase characteristic, and changes in magnetic field result in changes in the oscillation frequency. A change in the peak amplitude is also observed when magnetic field is applied, mainly due to the phase error introduced by the detection electronics and bias current generation. If the bias current is not exactly in quadrature with the velocity of the resonator, some part of the Lorentz force will be in phase with the damping term, thus changing the oscillation amplitude and the effective Q of the resonator. This effect can be suppressed by improving the electronics design.

Sensitivity

At resonance, the electrostatic force, F_E, is in phase with the velocity $\dot{x}$, but in quadrature with the Lorentz force, F_L. Using the effective spring constant, $k_{eff} = (k - BA_I L)$, the resonance frequency can be represented by

$$f_n = \frac{1}{2\pi}\sqrt{\frac{k_{eff}}{m}} \quad (4)$$

Taking the derivative of (4) with respect to magnetic field B, the sensitivity, in units of Hz/T, can be derived as

$$S_B = \frac{\partial f_n}{\partial B} = \frac{-A_I L}{4\pi\sqrt{m(k_{eff})}} \approx -\frac{f_n IL}{2kx} = -\frac{f_n L}{2k} A_I \quad (5)$$

Here, it is assumed that $k \gg BA_I L$. It can be observed that the fractional frequency change, $\Delta f_n / f_n = BIL/2kx$, is the ratio of the Lorentz force (BIL) over the recovering spring force (kx). Therefore, to maximize the sensitivity of the QFM magnetometer, the Lorentz force needs to be increased whereas the spring force needs to be decreased.

The FM magnetometer has low temperature sensitivity. From (5), the sensitivity S_B can be rewritten as:

$$S_B = -\frac{L}{4\pi\sqrt{km}} A_I \quad (6)$$

Changes in Q do not directly affect the sensor's frequency output because the sensitivity is independent of Q. Only the stiffness k has significant temperature dependence since the resonator's mass m is temperature invariant, the length L varies based on Silicon's thermal coefficient of expansion (2.6 ppm/K), and the amplifier's gain A_I is based on a resistance ratio and is temperature invariant to first-order. Typical temperature dependence of $\sqrt{k}$ for single-crystalline Silicon is 30 ppm/K. The temperature sensitivity of the QFM magnetometer is therefore 10 times smaller than that of a commercially-available AMR compass, which has a temperature sensitivity of 300 ppm/K compensated by a temperature sensor [8].

LORENTZ FORCE MAGNEMETER

The magnetometer was fabricated in the epi-seal encapsulation process [9]. The epi-seal encapsulation process was proposed by researchers at the Robert Bosch Research and Technology Center in Palo Alto and then demonstrated in a close collaboration with Stanford University. This collaboration is continuing to develop improvements and extensions to this process for many applications, while the baseline process has been brought into commercial production by SiTime Inc.

Figure 2 shows the Lorentz force magnetometer, a three-port MEMS resonator with electrodes DR for electrostatic driving and electrodes S for capacitive sensing. The 370 µm by 230 µm resonator is made out of 40-µm thick <100> single crystalline silicon. The suspended MEMS resonator is anchored at the *IB* electrodes. Bias current I is applied between the *IB*+ and *IB*- electrodes, out of phase with the electrostatic force F_E. Table I shows the device parameters.

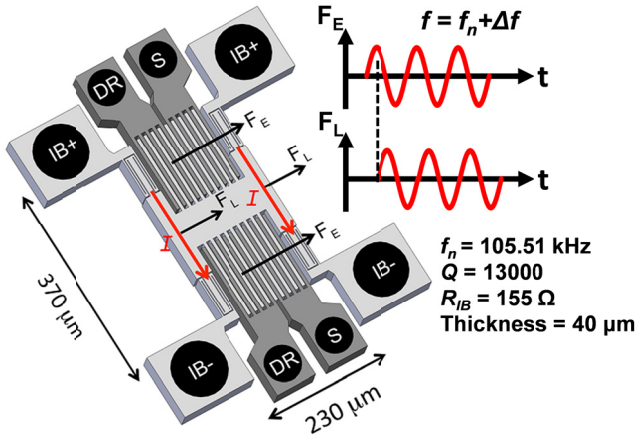

Figure 2: Lorentz force magnetometer.

TABLE I
DEVICE PARAMETERS

Parameter	Value
Device Thickness, t	40 µm
Device Area	0.08 mm^2
Proof mass	4 µg
Spring Constant, k	1800 N/m
Quality Factor, Q	13000
Drive Capacitance, C_d	660 fF
Sense Capacitance, C_s	660 fF
Capacitance Gap	0.95 µm
Resonance Frequency, f_n	105.51 kHz
Resistance	155 Ω
Effective Length, L	250 µm

IMPLEMENTATION

The MEMS resonator needs to be first put into a self-sustained oscillation loop, such that the change in the spring constant can be measured by the change in oscillation frequency. Figure 3 shows the block diagram of QFM operation. Here, we use a digital PLL to close the oscillation loop and the phase detector provides an output voltage that is proportional to the change in the oscillation frequency, $\Delta f(B)$. Alternatively, if a hard-limiting amplifier or automatic level control (ALC) are used to close the loop, a frequency counter or one-shot detector can be used to measure

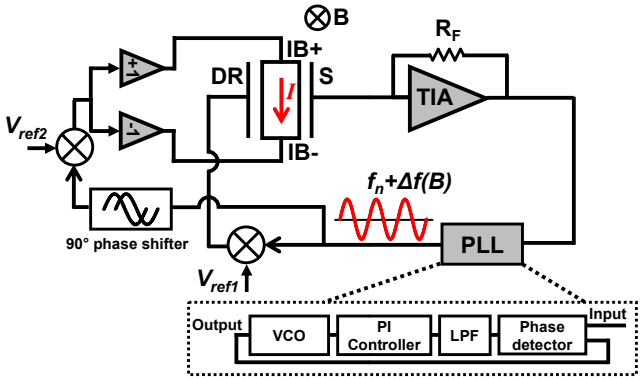

Figure 3: Block diagram of the Lorentz force magnetometer with quadrature FM. Reference voltages V_{ref1} and V_{ref2} are used to set the amplitude of the electrostatic and Lorentz force components, respectively.

frequency change.

The bias current driving through the proof-mass to produce Lorentz force ($F=BIL$) is generated using the electrostatic oscillation signal with a 90° phase shift. Thus, at resonance, the Lorentz force is always in quadrature with the electrostatic force. The AM and QFM modes can be implemented using the same resonator design with different phase shift (0° or 90°) between the electrostatic drive and bias current signals.

RESULTS

Figure 4 shows the output frequency versus input magnetic field of the magnetometer. The magnetometer is driven at a fixed oscillation amplitude of 19 nm. During all measurements, a 0.9 mA_{rms} bias current driven through the 155 Ω proof-mass results in 125 µW power consumption in the MEMS resonator. The bias current gain is A_I = -6700 A/m. The measured sensitivity is 500 Hz/T, close to the theoretical value of 493 Hz/T. We use customized Helmholtz coils to generate magnetic field for testing. The maximum field is limited to 3.6 mT by the power limit of the coil. The nonlinearity of the sensor is negligible in this range, and the theoretical linear operating range is 2.36T (assuming 1% non-linearity). The inset shows a real-time measurement in response to a 400 µT magnetic field input with a frequency of 20 Hz.

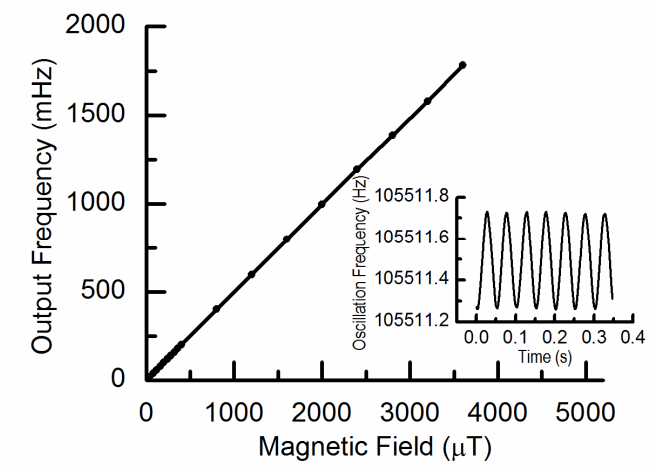

Figure 4. Output frequency vs. input magnetic field of the magnetometer. The measured sensitivity is 500 Hz/T. Inset: Measured output for 20 Hz 400 µT field input.

Figure 5 shows the frequency response of the magnetometer. Theoretically, the mechanical sensor in FM operation has unlimited bandwidth. Here, to reduce the total noise at the PLL output, the transfer function of the PLL limits the system bandwidth to 50 Hz. The measured sensor response matches well with the predicted transfer function of the digital PLL. The 3 dB bandwidths for QFM and AM operation are illustrated by the red dotted line. The bandwidth of the magnetometer is extended to 50 Hz in QFM operation compared to AM operation, in which the bandwidth is only 4 Hz. It has been experimentally shown that the bandwdith is improved by 12X in the QFM operation compared to the AM operation, independently from the mechanical sensor bandwidth.

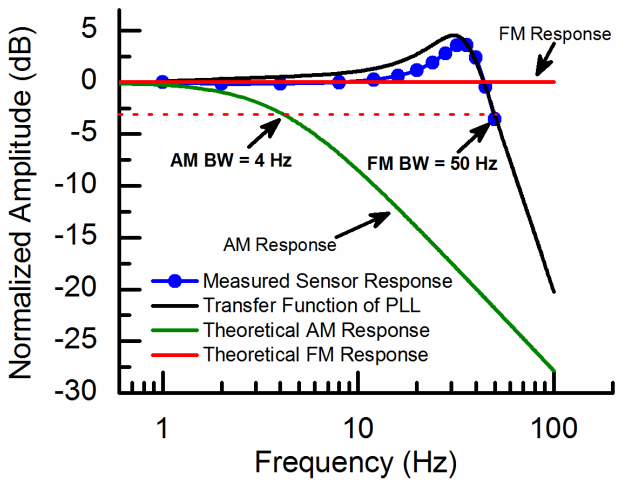

Figure 5. Frequency response of the magnetometer showing QFM achieves 12x greater BW than AM operation. The measured frequency response of the sensor output is shaped by the transfer function of the PLL.

Figure 6 shows the measured oscillator output spectrum in response to input magnetic field (40 µT) at 10 Hz, 20 Hz, 30 Hz and 40 Hz. The magnetic field appears as double-sided FM sidebands, which is consistent with narrowband frequency modulation. A nearly constant sensitivity over the frequency range is also observed. The slight amplitude difference observed at 30 Hz and 40 Hz is due to the frequency response of the PLL which exhibits some gain peaking at these frequencies.

Figure 7 shows the measured noise floor of the magnetometer. Although QFM operation provides constant sensitivity, in a wide sensor bandwidth the noise floor increases as the modulation index decreases. The long-term noise is dominated by the close-to-carrier phase noise of the oscillator, whereas the short-term noise is dominated by the far-from-carrier phase noise. A fitting of the sensor's noise floor shows a -10 dB/decade region close-to-carrier, followed by a flat region, and finally a +20 dB/decade region far-from-carrier. These three regions correspond to the $1/f^3$, $1/f^2$ and white noise components of the phase noise. The loop filter in the

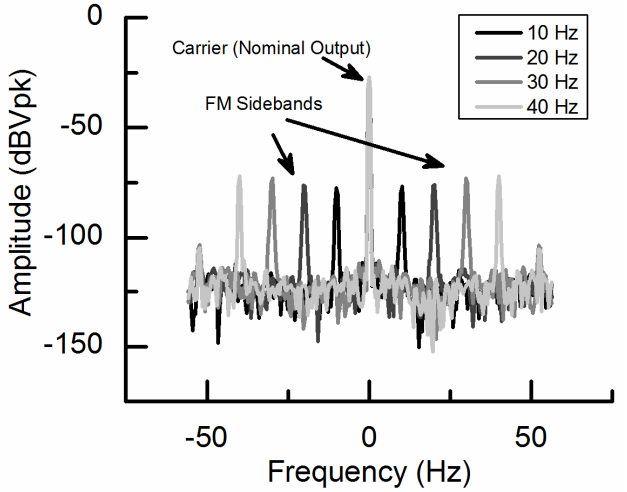

Figure 6. Measured oscillator output spectrum for 10 Hz, 20 Hz, 30 Hz and 40 Hz magnetic field (40 µT).

PLL will also affect the far-from-carrier phase noise. The noise floor is 500 nT/√Hz at frequencies from 3 Hz to 20 Hz, which is comparable to the Brownian-limited noise floor for the same magnetometer operating in AM mode. The dynamic range is expected to be 133 dB. The phase noise is measured as -92 dBc/Hz at 10 Hz. When normalized to GSM's 13 MHz [10], the phase noise is -50 dBc/Hz at 10 Hz. Table II compares Lorentz force magnetometers with different operation methods.

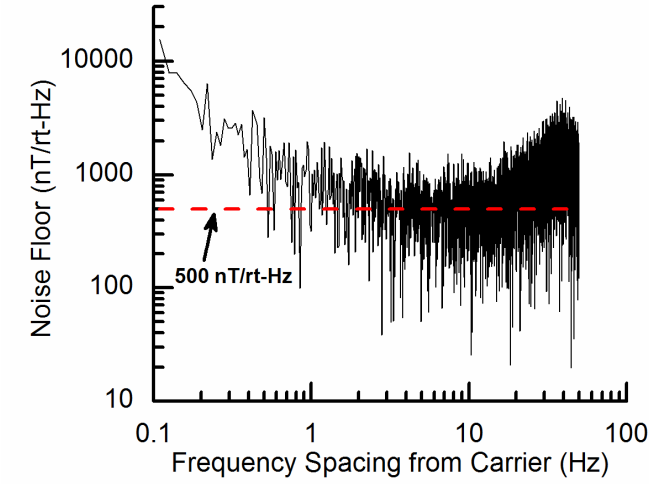

Figure 7. Measured noise floor showing Brownian limited noise from 3 Hz to 20 Hz.

TABLE II
COMPARISON OF LORENTZ FORCE MAGNETOMETERS

Parameter	Operation Methods		
	AM	Axial Stress FM	Quadrature FM
Readout	Amplitude	Frequency	Frequency
Sensitivity	ILQ/k	Af_nIL/k *	$f_nIL/(2kx)$
Bandwidth	$f_n/2Q$	Unlimited	Unlimited
Bias Current	In phase	DC current	Quadrature
Brownian-limited Resolution	$\frac{\sqrt{4k_bTb}}{IL}$	$\frac{\sqrt{4k_bTb}}{IL}$	$\frac{\sqrt{4k_bTb}}{IL}$

*A is a coupling coefficient that depends on the device geometry.

CONCLUSION

In conclusion, we demonstrate the QFM operation of a Lorentz force magnetometer based on a 105.5 kHz MEMS oscillator. The magnetometer achieves a sensitivity of 500 Hz/T for 0.9 mA_{rms} bias current. A Brownian limited noise floor of 500 nT/√Hz is also measured. Compared to the conventional AM magnetometer, QFM mode provides lower temperature sensitivity, larger sensor bandwidth (50 Hz vs. 4 Hz) and larger dynamic range (2.36 T vs. 10 mT), demonstrating great potential for electronic compass applications.

ACKNOWLEDGEMENTS

This work was supported by the Defense Advanced Research Projects Agency (DARPA) Precision Navigation and Timing program (PNT) managed by Dr. Andrei Shkel and Dr. Robert Lutwak under contract # N66001-12-1-4260 and the National Science Foundation under award number CMMI-0846379. The work was performed in part at the Stanford Nanofabrication Facility (SNF) which is supported by National Science Foundation through the NNIN under Grant ECS-9731293. The authors would also like to thank the SNF staff, particularly M. M. Stevens for the timely assistance with the epitaxial reactor.

REFERENCES

[1] M. Li, E. J. Ng, V. A. Hong, C. H. Ahn, Y. Yang, T. W. Kenny, and D. A. Horsley, "Lorentz force magnetometer using a micromechanical oscillator," *Applied Physics Letters,* vol. 103(173504), 2013.

[2] W. Zhang and J. E. Y. Lee, "Characterization and model validation of a micromechanical resonant magnetic field sensor," in *Proc. Transducers*, 2013, pp. 1859-1862.

[3] M. Li, E. J. Ng, V. A. Hong, C. H. Ahn, Y. Yang, T. W. Kenny, and D. A. Horsley, "Single-structure 3-axis Lorentz force magnetometer with sub-30 nT/√HZ resolution," in *Proc. MEMS 2014*, pp. 80-83.

[4] *AK8975 3-Axis Electronic Compass,* Asahi Kasei Microdevices Semiconductor Inc, Tokyo, Japan. 2010.

[5] W. Zhang and J. E. Y. Lee, "Frequency-based magnetic field sensing using Lorentz force axial strain modulation in a double-ended tuning fork," *Sensors and Actuators A: Physical,* to be published.

[6] M. H. Kline, Y. Yeh, B. Eminoglu, H. Najar, M. Daneman, D. A. Horsley, and B. E. Boser, "Quadrature FM gyroscope," in *Proc. MEMS 2013*, pp. 604-608.

[7] R. Sunier, T. Vancura, Y. Li, K. U. Kirstein, H. Baltes, and O. Brand, "Resonant Magnetic Field Sensor With Frequency Output," *Journal of Microelectromechanical Systems,* vol. 15, pp. 1098-1107, 2006.

[8] *3-Axis Digital Compass IC HMC5983* Honeywell Inc., Plymouth, MN, 2012.

[9] R. N. Candler, M. A. Hopcroft, B. Kim, W.-T. Park, R. Melamud, M. Agarwal, G. Yama, A. Partridge, M. Lutz, and T. W. Kenny, "Long-Term and Accelerated Life Testing of a Novel Single-Wafer Vacuum Encapsulation for MEMS Resonators," *Journal of Microelectromechanical Systems,* vol. 15, pp. 1446-1456, 2006.

[10] T. L. Naing, T. O. Rocheleau, E. Alon, and C. T. C. Nguyen, "A 78-microwatt GSM phase noise-compliant pierce oscillator referenced to a 61-MHz wine-glass disk resonator," in *European Frequency and Time Forum & International Frequency Control Symposium (EFTF/IFC)*, 2013, pp. 562-565.

CONTACT

*Mo Li, tel: +1-530-752-5180; moxli@ucdavis.edu

HIGH SENSITIVITY MAGNETIC SENSOR CONCEPT BASED ON MAGNETOSTRICTIVELY INDUCED PERTURBATIONS IN PLATE RESONATOR CHARACTERISTICS

Gokhan Hatipoglu and Srinivas Tadigadapa
Department of Electrical Engineering, The Pennsylvania State University, University Park, USA

ABSTRACT

Integrated, micromachined, room temperature magnetic sensors and sensor arrays with high sensitivity are highly desirable for several applications including magnetoencephalography, magnetic resonance imaging etc. In this work, we propose a sensor consisting of a micromachined AT-cut quartz bulk-acoustic wave cantilever resonator (500 x 45 x 22 μm) with one of the electrodes having 300 nm thick magnetostrictive Metglas® layer. The perturbations induced in the quartz resonator due to magnetically induced deformation in the quartz-Metglas® unimorph structure results a shift in the fundamental thickness-shear frequency and the at resonance impedance characteristics of the resonator. Using this configuration we have been able to achieve magnetic field sensitivity in the microTesla range with the possibility of extending the sensitivity into nanoTesla levels. This paper explores the concept using magnetostrictively induced perturbations in the plate resonator characteristics for magnetic sensing applications.

INTRODUCTION

A variety of chip scale magnetic sensors covering several orders of magnitude of sensitivity from milliTesla to femtoTesla fields have been developed and demonstrated [1-4]. However, sensors that can measure the picoTesla and femtoTesla range magnetic fields either operate at cryogenic temperatures such as SQUID sensors [5, 6] or use alkali atom vapors and optical detection [7]. For biomedical imaging applications such as magnetoencephalography, magnetic sensors with sensitivity better than the pico-Tesla range are required [6, 8]. Thus there is a clear opportunity to develop competing sensor technology that is compact, operates at room temperature, has the required high-sensitivity and a good price-to-performance ratio [9]. Therefore, integrated and micromachined, room temperature magnetic sensors and sensor arrays with high sensitivity are highly desirable for these kind of applications. Previously, we have reported two different magnetic sensor technologies: i) magnetoelectric flexural gate transistors with DC magnetic field sensitivity of 60 nT/√Hz [10] ii) quartz crystal/ferrofluid magnetic sensors employing magnetoviscous effect with DC magnetic field sensitivity of 15 nT√Hz [11]. Here, we investigate a promising magnetoelectric magnetic sensor concept consisting of quartz crystal micro-cantilever resonator coupled to a Metglas® magnetostrictive thin film.

Many ferromagnetic materials experience structural/shape change under applied magnetic fields – the phenomenon is known as magnetostriction. When such a thin film is placed on a piezoelectric film, the resulting strain due to magnetostriction is readily transduced into a charge by the piezoelectric material which can then be readout as a signal. This approach allows for the combination of high performance piezoelectric and magnetostrictive films to form high performance magnetoelectric magnetic sensing and has recently been extensively investigated [12-15]. However, until now these sensing modalities have not explicitly tried to exploit the effect of magnetostrictive strain on the resonance characteristics of piezoelectric crystal resonators. One can find reports on early stability studies on quartz resonators where sensitivity to magnetic fields was observed in resonators packaged and harnessed using ferromagnetic clamps. However, the overall sensitivity in these cases was extremely small ~15 mHz/mT [16]. Of course in precision frequency applications the focus of these studies was to minimize any such magnetic field related effects. In this work, however, instead of considering frequency shift due to magnetostriction as a source of instability, the authors aim to exploit the phenomenon as a very sensitive magnetometer concept. This is achieved by combining a mechanically compliant, high frequency quartz cantilever resonator with a highly magnetostrictive material, Metglas®, as one of the electrodes.

MAGNETOSTRICTION & MAGNETIC THIN FILMS

Application of magnetic fields to magnetostrictive materials causes strain and stress along the material due to a change in the magnetization, which is known as the Joule (Direct) effect. It is also known that application of stresses to magnetostrictive materials induces domain magnetization changes, which is known as the Villari (Converse) effect. The constitutive equations for direct and converse magnetostrictive effects are given by [17]:

$$\{\varepsilon\} = [S^H]\{\sigma\} + [d]^T\{H\} \quad (1)$$

$$\{B\} = [\mu^\sigma]\{H\} + [d]\{\sigma\} \quad (2)$$

where $\{\varepsilon\}$ and $\{\sigma\}$ are strain and stress respectively. $[S^H]$ is the elastic compliance under constant magnetic field and $[\mu^\sigma]$ is the permeability under constant stress. $[d]$ represents the magnetomechanical coupling coefficient. Equation 1 is the direct effect and Equation 2 is the converse effect.

For magnetoelectric sensor applications, a soft ferromagnetic material, with low hysteresis loss and steep slope in the B-H curve is desired since the material magnetization can be sensitively switched using application of low magnetic field amplitudes. Most commonly used and studied magnetostrictive materials are Terfenol-D [18], Galfenol [19] and Metglas®. Terfenol-D exhibits the highest magnetostriction (> 800 ppm) and the largest saturation field (~ 4 kOe) among these materials. Galfenol shows lower magnetostriction compared to Terfenol-D, however, it has a much higher permittivity. Metglas® shows the lowest magnetostriction (~ 27 ppm), the smallest saturation field (20 ~ 100 Oe) and the highest permeability (μ_r > 45,000). In this work, amorphous Metglas® 2605SA1 has been used as the magnetostrictive layer. Metglas® is an iron, silicon and boron alloy ($Fe_{85}B_5Si_{10}$) and has high bulk magnetostriction strain compared to similar materials, which is measured to be around 27 ppm. It is a good soft ferromagnetic material and has a high relative permeability that is around 45000 as cast [20].

The foremost challenge is the optimization of the deposition parameters of thin films of Metglas® since these have a significant impact on the magnetic properties of the thin film. To achieve this objective, a four gun ion beam deposition system has been designed and developed. The system consists of a vacuum chamber pumped using a turbomolecular pump and four ion guns from South Bay Technology Inc directed at the Metglas® target for deposition. Metglas® target was prepared by attaching three 25 μm

9781940470016/HH2014/$25©2014TRF
DOI 10.31438/trf.hh2014.15

thick Metglas® sheets on an aluminum substrate. The sample was place a distance of 10 cm from the source. The deposition of the film was performed at a pressure of 60 μTorr and deposition rate of ~1 nm/min.

300 nm thick films were deposited and characterized for their B-H loops. Quantum Design 1802 SQUID magnetometer with a field sweep range of 5T at 305 K was used for these measurements. The samples are digitally imaged to extract the sample area and then sewn onto SQUID straws in order to obtain the B-H characteristics. Figure 1 shows the in-plane B-H loop of two different Metglas® 2605SA1 films, deposited on 2 x 2 x 1 mm glass slides using the same target under different ion-beam deposition conditions as described above. As it is observed from the figure, the hysteresis loss as well as the saturation magnetization can be controlled by applying in-plane magnetic field during the deposition. The relative permeability of the films are around 6500-7000, which is lower than the bulk values, but still shows reasonably high permeability. The coercive fields are 15 Oe and 5 Oe for film 1 and film 2 respectively. The saturation of magnetization of two films are ~1 T.

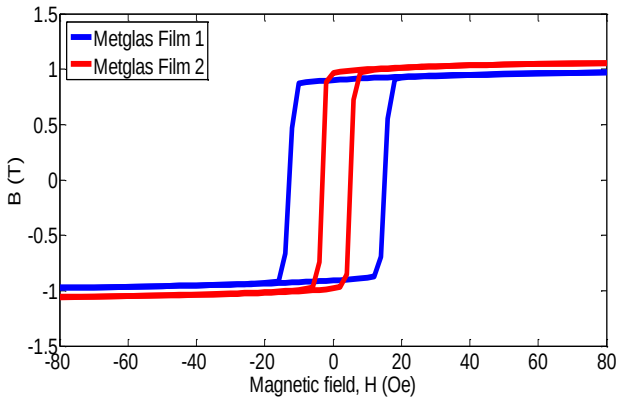

Figure 1: The BH curve of two different Metglas thin films. The film thicknesses are around 150 nm.

STRESS AND STRAIN SENSITIVITY OF QUARTZ

It has been unambiguously observed that AT-cut quartz bulk acoustic wave resonators are highly sensitive to applied stresses and acceleration. As a result of applied transverse loading, both the thickness shear mode resonance frequency as well as the quality factor of the resonators change. The normalized frequency shift is denoted by $\Delta f/f_0$ where Δf is the frequency shift due to applied stress, and f_0 is the fundamental resonance frequency of the quartz resonator. In literature, the resonance frequency shifts of circular AT-cut crystal plates subjected to transverse loading and radial loading are extensively studied by Lee [21] and Ballato [22]. A point load is applied to one end of the disk and resonance frequency shifts are measured experimentally as well as analytically modeled. As discussed in [23], the stress field in the quartz is very complex even though the plate is isotropic and rectangular. In the stress-strain relationship, the non-linear terms associated with the third-order elastic coefficients need to be included to solve for the exact frequency change. These assumptions will not be discussed within this paper, but a simplified equation estimating the frequency shift can be given by [23]:

$$\frac{\Delta f}{f_0} = \frac{1}{2C_{66}}\left(2E_1^{(0)} + C_{661}E_1^{(0)} + C_{662}E_2^{(0)} + C_{663}E_3^{(0)} + C_{664}E_4^{(0)}\right) - \left(\frac{b^2/(3)^{1/2}}{\pi C_{66}}\left(C_{165}E_{5,1}^{(1)} + C_{561}E_{1,3}^{(1)} + C_{563}E_{3,3}^{(1)}\right)\right) \quad (3)$$

where $E_i^{(0)}$ and $E_i^{(1)}$ are the zero order and first order strains respectively (i=1,2,…,6), C_{ij} and C_{ijk} are the second order and third order elastic stiffness coefficients respectively, and 2*b* is the thickness of the plate. A sensitivity of ~166 Hz/N for a 1 inch diameter crystal of AT-cut quartz has been reported [23]. As we will demonstrate in this work, that a much higher sensitivity can be achieved by micromachining quartz making it possible to achieve high magnetic field sensitivity.

SENSOR FABRICATION

An inverted mesa design circular quartz resonator with 350 μm diameter front electrode and 22 μm thickness was fabricated by dry etching of 100 μm thick AT-cut quartz substrates. The details of the fabrication process can be found in reference [24]. This was followed by the deposition of an unpatterned 300 nm thick Metglas® film on the unetched side of the resonator using 4-gun ion beam deposition system at a rate of ~1 nm/min. The deposited film has B-H loop characteristics similar to that of film 2 shown in Fig. 1. However, the circular shape of the resonator makes it mechanically stiff and difficult to strain the resonator either extensionally or flexurally. In order to increase the flexural bending sensitivity, a cantilever structure 500 μm in length and 45 μm in width was ion-milled out of the circular resonator structure to result in a more compliant structure. In order to form and release the cantilever, Focused Ion Beam (FIB) milling was used. The FIB parameters are given in Table 1. Since the cut time is ~10 hours, the quartz substrate showed considerable charge accumulation which resulted in the beam to vibrate sinusoidally. This has a negative effect on the dimension control of the cantilever. To avoid this problem, an electrically conductive probe is used to contact on the quartz surface. The final micromachined quartz cantilever resonator is shown in Fig. 2. As a result, a unimorph cantilever structure consisting of 22 μm thick quartz and a 300 nm thick Metglas® is formed. The 22 μm thickness of the quartz results in a fundamental thickness shear frequency of ~76.5 MHz. Governed by equation 1, the induced strain due to magnetostriction is now expected to result in the shift of the resonance frequency as a function of the magnitude of the applied magnetic field and at a much higher sensitivity.

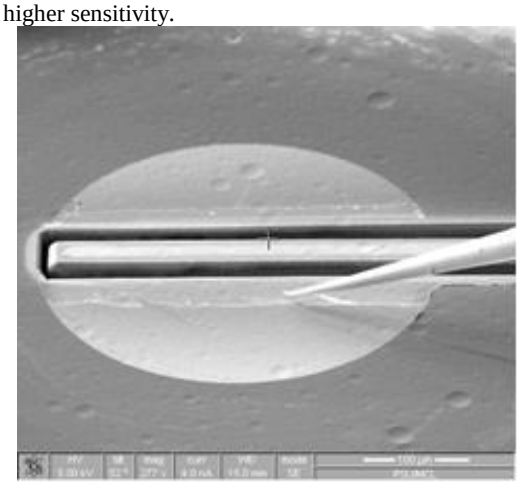

Figure 2: SEM picture while milling out the cantilever. The Omni probe is used in order to avoid charging.

Table 1: Focused Ion beam cut parameters

	Focused Ion beam cut parameters		
Cut time	*Beam energy*	*Beam current*	*Dwell Time*
10 hours	30 kV	20 nA	1 μs

EXPERIMENTAL

Flexural Sensitivity: Thermal Test

In order to determine the sensitivity of the quartz resonator to strain input we performed a thermal unimorph test. Since the sensor cantilever is a bilayer structure consisting of quartz and Metglas® layers, the temperature coefficient of expansion mismatch between the two layers will result in net out of plane moment. Furthermore, for small temperature excursions of less than 10 °C, the shift in AT cut quartz is very minimal. In fact, the frequency shift is on the order of ppm [25]. Thus, any resulting frequency change can be attributed to the resulting thermal strain in the device structure. Since, thermal actuation is theoretically very well understood and thermal expansion coefficients of the two materials are well characterized and known, the experimentally measured frequency shift in the resonance frequency can be easily related to the theoretical deflection from the bilayer microactuator. The bilayer cantilever curvature due to a temperature difference ΔT is given by [26]:

$$k = \frac{6b_1b_2E_1E_2t_1t_2(t_1+t_2)(\alpha_2-\alpha_1)\Delta T}{\left(b_1E_1t_1^2\right)^2+\left(b_2E_2t_2^2\right)^2+2b_1b_2E_1E_2t_1t_2\left(2t_1^2+3t_1t_2+2t_2^2\right)} \quad (4)$$

where subscript 1 and 2 refer to material properties of quartz and Metglas® layers respectively. The parameters b, E, t are the width, elastic modulus, and thickness respectively. α is the thermal expansion coefficient and ΔT is the temperature difference. The curvature is related to tip deflection, d as $d=kL^2/2$, where L is the length of the cantilever. Figure 3 plots the experimentally measured frequency shift vs the associated phase shift (y-axis1) of the cantilever resonator for five ΔT values. The right hand side axis is the corresponding calculated tip deflection. The sensitivity is the slope of Fig. 3, which indicates 78 pm/Hz. This sensitivity is encouraging to detect extremely small perturbations occurring within the quartz as a result of magnetostrictive bending of the unimorph.

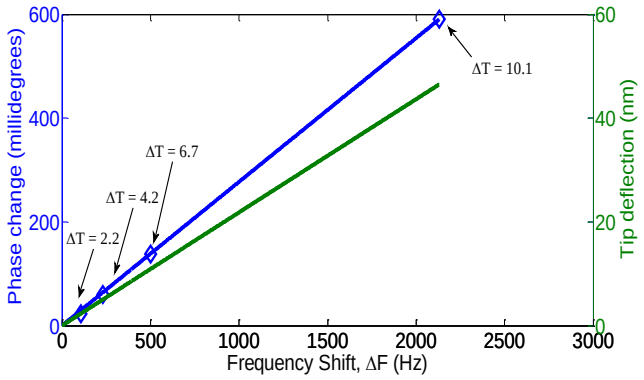

Figure 3: The peak to peak phase change and calculated tip deflection vs. the frequency shift, ΔF.

Magnetic Tests

The magnetic experimental setup consists of a Helmholtz coil with a diameter of 15 cm and 140 turns (N=140). Applied magnetic field is precisely controlled via the current through the coil. Quartz microcantilever impedance characteristics were monitored in real-time using an Agilent E5061B network analyzer. The S-parameters are converted into impedance parameters using a Labview® program. The phase of the resonator was measured at a fixed frequency corresponding to the maximum slope of the phase-frequency curve and recorded as a function of the applied magnetic field.

The first cantilever resonator we tested was an AT-cut quartz resonator with a thickness of ~37 μm, length of 200 μm and a width of 50 μm. The Metglas® was 150 nm thick. The device was placed in the middle of the Helmholz coil set-up and a square wave magnetic field with a frequency of 0.075 Hz corresponding to a cycle time of 13.33 s was applied. The peak-to-peak change in the susceptance of the resonator at resonance in response to the applied magnetic field was measured and is shown in Fig. 4. From the slope of the curve the sensitivity of the device can be given to be 0.095 μS/μT.

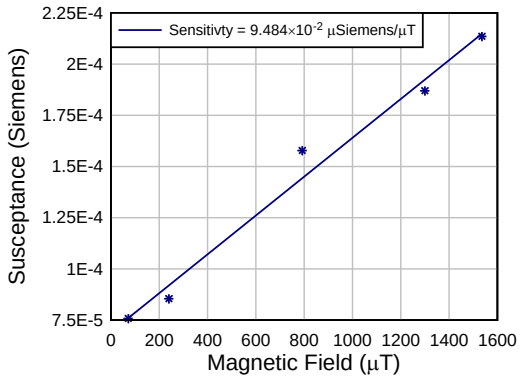

Figure 4: Sensitivity of quartz resonator susceptance at resonance to magnetic field is measured and shows a linear dependence.

Figure 5 shows the response of the 76 MHz, 500 μm long cantilever sensor to an applied square-wave, peak-to-peak magnetic field of 1.5 μT. The *x*-axis is time and the *y*-axis corresponds to phase shift of the resonator. For the resonator any of the impedance and admittance characteristics at resonance can be monitored as a function of the applied magnetic field. To ensure maximum sensitivity the frequency needs to be set at the maximum of the slope of the frequency vs quantity of measurement. Based on the signal-to-noise ratio performance nT range of sensitivity can be obtained.

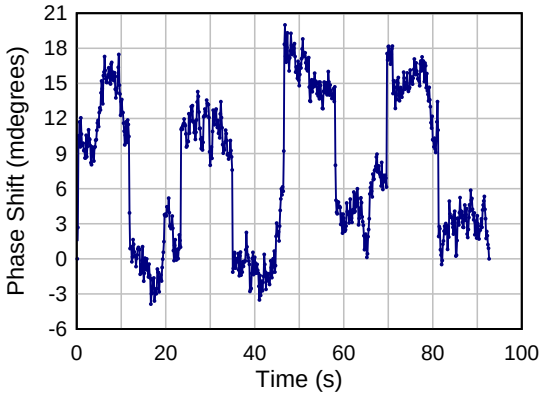

Figure 5: The phase change as a result of the applied ac magnetic field of 1.5 μT.

DISCUSSION

In this paper, the concept detecting magnetic fields by monitoring the induced changes in the at-resonance impedance and admittance characteristics of AT-cut quartz resonators has been explored. It is observed that the bending of the cantilever due to magnetostrictive strain of the magnetic layer affects the at-

resonance impedance and admittance characteristics of the resonator very sensitively. Using thermal unimorph bending performance of the device a sensitivity of 78 pm/Hz was experimentally determined. The response of the resonator phase to an applied field of 1.5 μT was obtained and the signal-to-nose sensitivity of the device shows that nanoTesla range sensitivity can be obtained by further optimizing the thicknesses, dimensions, and the cut of the quartz crystal. Optimization of the deposited Metglas® films are also expected improve the sensitivity of the device further.

ACKNOWLEDGEMENTS

This work was supported in part by National Science Foundation (NSF) under the grant # 1305653 The use of facilities at the PSU Site of the NSF National Nanotechnology Infrastructure Network (NNIN) under Agreement 0335765 is acknowledged. GH acknowledges partial support from Scientific and Technical Research Council of Turkey (TUBITAK) for a 2213-International PhD. Fellowship Program. GH also thanks to Transducers Research Foundation for the travel support.

REFERENCES

[1] P. Ripka, Ed., *Magnetic Sensors and Magnetometers*. Boston: Artech House Publishers, 2001, p.^pp. Pages.

[2] S. Dong, "Ultrahigh magnetic field sensitivity in laminates of TERFENOL-D and Pb(Mg1/3Nb2/3)O3?PbTiO3 crystals," *Appl. Phys. Lett.*, vol. 83, p. 2265, 2003.

[3] J. Zhai, Z. Xing, S. Dong, J. Li, and D. Viehland, "Detection of pico-Tesla magnetic fields using magneto-electric sensors at room temperature," *Applied Physics Letters*, vol. 88, p. 062510, 2006.

[4] J. Lenz and S. Edelstein, "Magnetic sensors and their applications," *Sensors Journal, IEEE*, vol. 6, pp. 631-649, 2006.

[5] R. L. Fagaly, "Superconducting quantum interference device instruments and applications," *Review of Scientific Instruments*, vol. 77, p. 101101, 2006.

[6] J. P. Wikswo, Jr., "SQUID magnetometers for biomagnetism and nondestructive testing: important questions and initial answers," *Applied Superconductivity, IEEE Transactions on*, vol. 5, pp. 74-120, 1995.

[7] I. K. Kominis, T. W. Kornack, J. C. Allred, and M. V. Romalis, "A subfemtotesla multichannel atomic magnetometer," *Nature*, vol. 422, pp. 596-599, 2003.

[8] I. M. Savukov and M. V. Romalis, "NMR Detection with an Atomic Magnetometer," *Physical Review Letters*, vol. 94, p. 123001, 2005.

[9] J. E. Lenz, "A review of magnetic sensors," *Proceedings of the IEEE*, vol. 78, pp. 973-989, 1990.

[10] F. Li, R. Misra, F. Zhao, Y. Wu, P. Schiffer, Q. M. Zhang, S. Tadigadapa, and S. Datta, "Magnetoelectric Resonant Gate Transistor with NanoTesla Sensitivity," *Journal of Microelectromechanical Systems*, vol. In preparation, 2012.

[11] H. Gokhan, "A novel magnetometer employing magnetoviscous effect of ferrofluids," *Hilton Head Technical Digest*, pp. 42-45, 2012 2012.

[12] S. Dong, "Giant magnetoelectric effect (under a dc magnetic bias of 2?Oe) in laminate composites of FeBSiC alloy ribbons and Pb(Zn1/3,Nb2/3)O3?7%PbTiO3 fibers," *Appl. Phys. Lett.*, vol. 91, p. 022915, 2007.

[13] S. Dong, J. Zhai, J. Li, and D. Viehland, "Near-ideal magnetoelectricity in high-permeability magnetostrictive/piezofiber laminates with a (2-1) connectivity," *Applied Physics Letters*, vol. 89, p. 252904, 2006.

[14] C.-W. Nan, M. I. Bichurin, S. Dong, D. Viehland, and G. Srinivasan, "Multiferroic magnetoelectric composites: Historical perspective, status, and future directions," *Journal of Applied Physics*, vol. 103, p. 031101, 2008.

[15] F. Zhao, N. Mokhariwale, L. Feng, S. Datta, and Q. M. Zhang, "Magnetoelectric Sensors With Directly Integrated Charge Sensitive Readout Circuit—Improved Field Sensitivity and Signal-to-Noise Ratio," *Sensors Journal, IEEE*, vol. 11, pp. 2260-2265, 2011.

[16] R. Brendel, "Influence of a magnetic field on quartz crystal resonators," *Ultrasonics, Ferroelectrics and Frequency Control, IEEE Transactions on*, vol. 43, pp. 818-831, 1996.

[17] M. J. Dapino, R. C. Smith, and A. B. Flatau, "Model for the ΔE effect in magnetostrictive transducers," 2000, pp. 174-185.

[18] A. E. Clark and D. Crowder, "High temperature magnetostriction of TbFe<inf>2</inf>and Tb<inf>.27</inf>Dy<inf>.73</inf>Fe<inf>2</inf>," *Magnetics, IEEE Transactions on*, vol. 21, pp. 1945-1947, 1985.

[19] T. Takahashi, T. Okazaki, and Y. Furuya, "Improvement in the mechanical strength of magnetostrictive (Fe–Ga–Al)–X–C (X = Zr, Nb and Mo) alloys by carbide precipitation," *Scripta Materialia*, vol. 61, pp. 5-7, 2009.

[20] M. C. Products. (2014, 03/25/2014). *Metglas® 2605SA1 & 2605HB1M Magnetic Alloy properties*. Available: http://www.metglas.com/products/magnetic_materials/2605SA1.asp

[21] P. C. Y. Lee, Y. S. Wang, and X. Markenscoff, "Effects of Initial Bending on the Resonance Frequencies of Crystal Plates," in *28th Annual Symposium on Frequency Control. 1974*, 1974, pp. 14-18.

[22] A. D. Ballato, "Effects of Initial Stress on Quartz Plates Vibrating in Thickness Modes," in *14th Annual Symposium on Frequency Control. 1960*, 1960, pp. 89-114.

[23] P. C. Y. Lee, Y. S. Wang, and X. Markenscoff, "Nonlinear effects of initial bending on the vibrations of crystal plates," *The Journal of the Acoustical Society of America*, vol. 59, pp. 90-96, 1976.

[24] P. Kao, D. Allara, and S. Tadigadapa, "Characterization of viscoelastic properties of adsorbed biomolecules and biomolecular assemblies with high frequency micromachined quartz resonators," *Sensors and Actuators B: Chemical*, vol. 142, pp. 406-411, November 5, 2009 2009.

[25] "Basic Technology of Quartz resonators," ed, 2014.

[26] W.-H. Chu, M. Mehregany, and R. L. Mullen, "Analysis of tip deflection and force of a bimetallic cantilever microactuator," *Journal of Micromechanics and Microengineering*, vol. 3, p. 4, 1993.

CONTACT

*Srinivas Tadigadapa, Tel: +1-814-865-2730; sat10@psu.edu

HIGH-GRADIENT MEMS ELECTROMAGNETS FOR PARTICLE BEAM MANIPULATION

J. Harrison[1], J. Wu[1], O. Paydar[1], Y. Hwang[1], E. Threlkeld[1], J. Rosenzweig[1], P. Musumeci[1], and R. Candler[1,2]*
[1]University of California, Los Angeles, California, USA
[2]California NanoSystems Institute, Los Angeles, California, USA

ABSTRACT

We present the first experimental demonstration of MEMS-based magnetic optics for control of charged particle beams. Combined function (steering and focusing) 4-pole electromagnets with a 600-µm bore and 55-µm yoke thickness (686-µm magnetic length) have been fabricated with a novel MEMS process. These 3D solenoidal multi-pole electromagnets have demonstrated hysteresis-free adjustable 2D steering and focusing of a pC-charge 34-keV electron beam with 24-mT field intensity, 220-T/m field gradient, and potential for pulsed operation beyond 100 kHz. Simple geometric optimizations promise a 4-fold improvement in both field intensity and gradient without further scaling.

INTRODUCTION

Favorable scaling of magnetic field intensity [1] and mature technology from the magnetic recording industry have made magnetic MEMS inductors, actuators, and relays a common application of microfabrication. These have enabled technologies from miniaturized magnetometers and high-density CMOS passives to high-force actuators and low-insertion-loss RF switches. Applications that use the magnetic field to interact with particles [2,3] are less mature, but can take advantage of the linear scaling of magnetic field gradient with miniaturization of the magnet geometry. One such application is the optical elements used to control charged particle beams: dipole, quadrupole, and higher order fields (Fig. 1). Because the Lorentz force is proportional to particle velocity, forces due to practical magnetic fields dominate Coulomb forces, well before the particles become relativistic (Eq. 1). As a result, strong magnetic optics are necessary in place of electric field optics.

$$F = \gamma ma = q(E + v \times B) \quad (1)$$

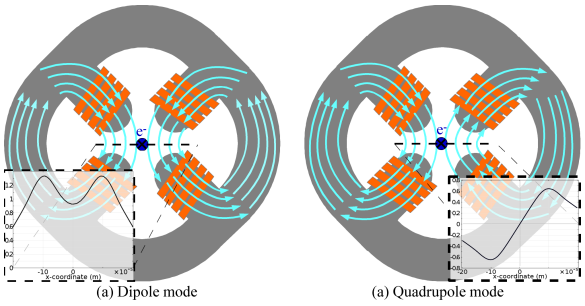

Figure 2. Illustration of a 4-pole MEMS electromagnet operating in dipole field beam steering configuration (left) and quadrupole field beam focusing configuration (right). Inset graphs show magnetic field across the dashed lines.

Multi-pole field scaling

Modern low-emittance electron and proton beams have transverse dimensions in the µm-scale and require intense dipole magnetic fields to steer charged particle beams and strong quadrupole magnetic gradients to maintain focus the beams. As the geometry of a multi-pole electromagnet is scaled down, both steering strength and focusing strength improve. Steering is accomplished with Lorentz force, where the dipole field of an electromagnet can be approximated by $B = \mu nI/2r$: μ is the electromagnet yoke permeability, n is the number of turns in the electromagnet winding, I is the current in the winding, and $2r$ is the separation between the electromagnet pole tips. For focusing, the focal length of a magnetic lens can be expressed by $f^{-1} = qgl/p$: q is the particle charge, g is the quadrupole field gradient, l is the magnetic length, and p is the particle momentum. The magnetic length, l, is the normalized interaction length between particles and the magnetic field and requires that the electromagnet yoke be a thick enough film (50+µm) to change the momentum of the beam. The gradient can be approximated by $g = 2\mu nI/r^2$, scaling inversely with the square of the magnet bore.

The reduced inductance of miniaturized electromagnets provides further scaling advantages, allowing the electromagnet to operate pulsed with a reduced duty cycle and at higher frequencies.

Background

Many groups have pursued scaling magnetic optics and systems, primarily using machined permanent magnet technology. Tatchin et al. led early efforts with the goal of a miniaturized undulator, using high-precision machining to scale periodic NdFeB magnets down to 353-µm size [4]; however, device quality was inadequate to realize the promised performance. A more modern effort by Oniku et al. used laser-machined SmCo with 50-mT_{peak} periodic fields in a 200-µm gap [5]. A recent 5 mm bore NdFeB Halbach quadrupole now holds the focusing strength record with a field gradient of 560 T/m [6], though the machining method resulted in a device size 10x greater than the magnetic optics described here. Our method differs from prior work by using actively powered MEMS electromagnets, enabling powerful and rapidly tunable dipole and quadrupole magnetic fields.

FABRICATION

The fabrication process for these 4-pole electromagnets was inspired by the UCLA switch [7]. The process was redesigned for multi-pole electromagnets with 55-µm thick electromagnet yokes (5x thicker than previous devices) and 2500-μm^2 cross-section windings for high-current electromagnets [8] (Fig. 2).

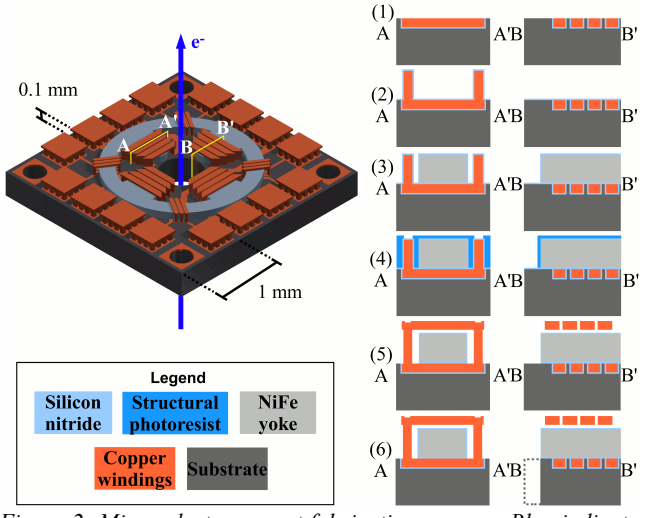

Figure 2: Micro-electromagnet fabrication process. Blue indicates the electron beam path through the device.

9781940470016/HH2014/$25©2014TRF
DOI 10.31438/trf.hh2014.16

(1) Bottom-winding layer

The pattern for the winding's bottom layer is photolithographically defined on a Si wafer using KMPR 1005 photoresist and an aligner (Karl Süss MA6). Trenches are etched 20-µm into the Si through this soft mask using a deep reactive ion etcher (Plasma-Therm SLR-770). The photoresist is stripped in ALEG-380 and 5:1 Piranha. A 500-nm SiO_2 film is grown by thermal oxidation (Tystar Mini 3600) to isolate the bottom windings from the wafer. An electroforming seed is deposited on the SiO_2 by RF sputtering (CVC 601). The seed layer consists of 30-nm Ti for adhesion to the substrate and 300-nm Cu to carry the electroplating current. A 25-µm Cu film is electroplated onto the seed layer from a phosphorized Cu anode in a sulfate based solution (Technic Elevate 6320) through a woven polypropylene filter at 5 mA/cm^2. The wafer is polished to Si with chemical mechanical polishing, CMP, (Logitech PM5) using 100-nm alumina slurry, yielding the winding's bottom layer inlayed in the substrate. Fig. 3 shows the first layer of a 4-pole electromagnet after CMP.

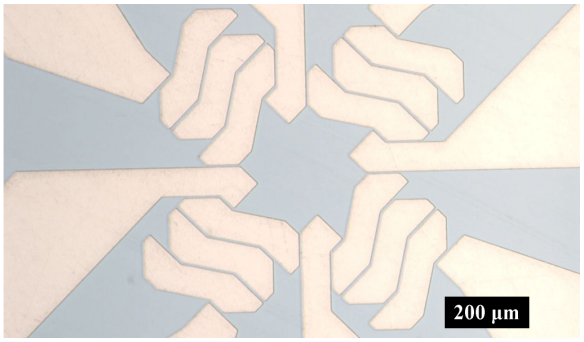

Figure 3: Photograph of Cu inlaid in a Si wafer, forming the winding's bottom layer of the 4-pole electromagnet.

(2) Winding vias

Another electroforming seed is sputter deposited, with an additional 30-nm layer of Ti for adhesion between the seed and electroplating mold (i.e., Ti/Cu/Ti layer). A 100-µm negative photoresist (KMPR 1025) film is patterned to define the electromagnet winding's interconnect geometry. The seed exposed by the pattern is etched to Cu in 1% HF, and 100 µm of Cu is electroplated through the mold. The features are planarized by CMP. The mold is removed by plasma etching with 4:1 O_2:CF_4 plasma (STS AOE). The electroplating seed is stripped with a sputter etch and dips in 5% $C_2H_4O_2$ and 1% HF. Finally, a 2-µm insulating Si_3N_4 film is deposited by plasma enhanced chemical vapor deposition, PECVD, (STS Multiplex CVD) to isolate the windings from the magnetic yoke.

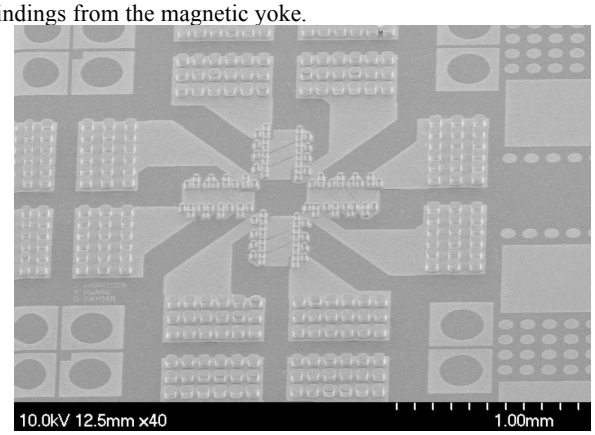

Figure 4: SEM of Cu vias after stripping the electroplating mold.

(3) Magnetic yoke

An electroforming seed is deposited as described in step 2. A 100-µm film of KMPR photoresist is patterned into the geometry of the magnet yoke. Between pouring the photoresist and spinning, the film is de-gassed in a vacuum oven at 30 Torr for 30 sec. The exposed Ti is etched to Cu in 1% HF, and a $Ni_{80}Fe_{20}$ electromagnet yoke (B_{sat} = 1.1 T, μ_r = 8000) is plated through the mold using the process detailed by Glickman et al. [8]. Planarization, mold stripping, seed stripping, and isolation proceed as described in step 2. Fig. 5 shows an electromagnet after step 3.

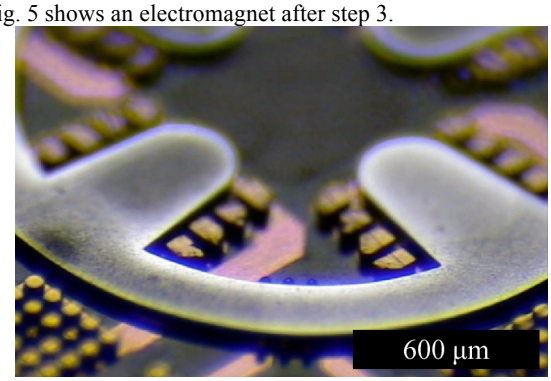

Figure 5: Photograph of NiFe yoke and pole tips after stripping the electroplating mold.

(4) Planarization layer

A 100-µm film of photoresist (SU-8 2025) is used to provide a planar surface for defining the top of the coil windings. The photoresist is de-gassed in the same manner as in the previous step, and patterned to expose the winding vias. The photoresist planarized to 10 µm above the yoke by CMP between the post exposure bake and development to improve thickness uniformity. The film is annealed in vacuum for 8 hours at 200 °C. Fig. 6 shows multi-pole electromagnets after step 4.

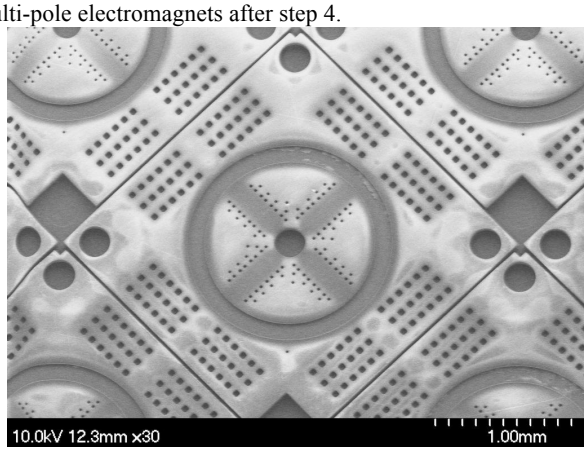

Figure 6: SEM of a 4-pole electromagnet after CMP of the planarization layer.

(5) Top winding layer

The Cu in the vias is exposed by etching the Si_3N_4 with C_4F_8 plasma (STS AOE). A seed layer is sputtered on the surface as described in step 2. A 25-µm KMPR layer is patterned into the geometry of the top winding layer, and 20-µm Cu is electroplated through the mold. The mold and seed are stripped using the process described in step 2, completing the 4-pole electromagnets. The SU-8 is etched using the mold stripping process described in step 2 to avoid problems from thermal expansion mismatch during operation. Fig. 7 shows an electromagnet after step 5.

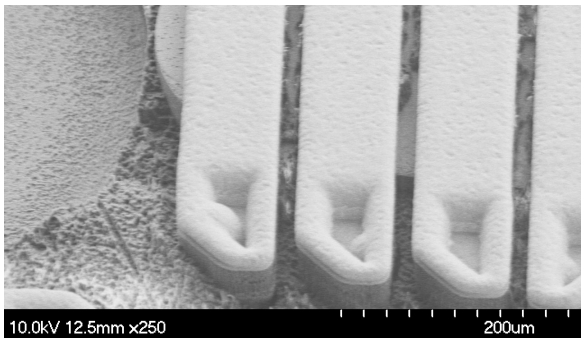

Figure 7: SEM of a 4-pole electromagnet after etching the planarization layer back.

(6) Through wafer etch

Through-wafer holes are necessary for the particle beam. An etch pattern is defined with KMPR 1005 photoresist on the back-side of the wafer and aligned to the front using a contact aligner. Holes and trenches are etched from the back of the substrate to the front using a post-process Bosch etch (Oerlikon FDSE II), defining the electromagnet gap and singulating the devices. Fig. 8 shows an electromagnet after step 6.

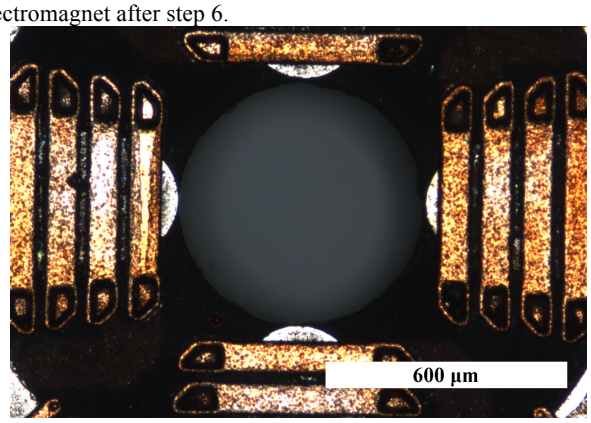

Figure 8: Photograph of a 4–pole electromagnet after through-wafer etching the electron beam path.

(7) Packaging

The 4-pole electromagnet is mounted in a conventionally machined Cu fixture and wirebonded to an integrated PCB (Rogers Duroid 6002) with 15-µm Al wires. The unpackaged electromagnet die has withstood 70-A pulses on a probe station without failure, but the 15-µm Al wirebonds in the package fail at 5.5 A. Figure 9 shows an electromagnet after step 7.

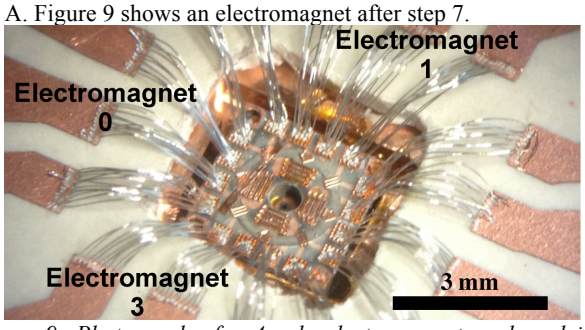

Figure 9: Photograph of a 4-pole electromagnet packaged in a copper beam-testing fixture.

CHARACTERIZATION & SIMULATION

Each winding of the electromagnet is measured using an impedance analyzer (Agilent 4294A) with a set of coaxial probes (APT 740CJ) in a four-terminal pair configuration. Before packaging, the windings have 58.2±1.2-mΩ resistance and 30.4±1.9-nH inductance at 100 kHz. Fig. 10 shows the electromagnet resistance and inductance vs. frequency after rework and packaging.

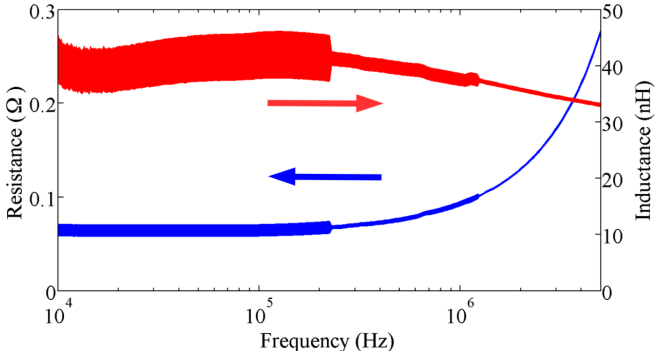

Figure 10: Measured resistance and inductance of the quadrupole shown in Fig. 9. Line thickness denotes measurement precision.

The field produced by -1.0 A in each coil of the multi-pole electromagnet was simulated using the finite element method multiphysics software COMSOL. Fig. 10 shows the simulated field profile. The inductance calculated by integrating the stored magnetic energy ($E=\int B^2/2\mu\ dv$) matched the measured inductance within 6% before packaging and 25% after packaging. Post-packaging measurements were through 20 wire bonds reworked with a chlorine plasma etch, potentially explaining the measurement variation.

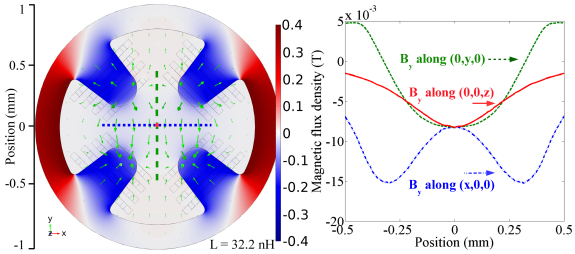

Figure 10: Simulated transverse magnetic dipole field profile for I = -1.0-A drive current along x-, y-, and z-axes. Integration across the model volume yields a 32.2-nH inductance. Dividing the z-integrated field by the peak field yields a 686-µm magnetic length, which is the normalized interaction distance of a charged particle.

Simulations show that the electromagnet yoke fully saturates for I > 2.0-A dipole current, with the poles only 25% saturated. The yoke width in these devices was limited by a 3-mm die size; however, a 4x field strength improvement could be realized by widening the yoke without further optimization. Optimized simulations with a 200-µm gap rather than 600-µm gap exceed 300-mT field and 3-kT/m field gradient, and 600 mT and 6000 T/m with a higher-saturation yoke (B_{sat} = 2.1 T for CoNiFe).

EXPERIMENT

The MEMS electromagnet was mounted in the path of an electron beam following a translatable iris and powered in dipole or quadrupole configuration to demonstrate beam steering and focusing. By varying the electrical current in each coil, the electron beam was steered across an imaging system. The magnetic field could then be calculated from the centroid on the image using Lorentz force and the magnetic length from FEM simulation. By translating the beam iris with the electromagnet field constant, the spatial distribution of the magnetic field was mapped.

The experiment uses an electron beam generated by photoelectric effect with a UV laser and Cu cathode accelerated with an electric field. A solenoid electromagnet adjusts beam focus

exiting the electron gun, and a set of steering electromagnets adjusts position and angle. After a drift length, a chamber houses the MEMS electromagnet, and after another drift length, an imaging system composed of a Z-stack micro-channel plate (MCP) intensifier, phosphor screen, and cooled CCD camera (Hamamatsu Flash 2.8) images the beam position and shape. The MEMS electromagnet is mounted behind a pair of micrometer-mounted orthogonal 20-μm slits (Thorlabs S20R) that have been stripped of anodizing and iron oxide coatings with 10% HCl and 10% NaOH.

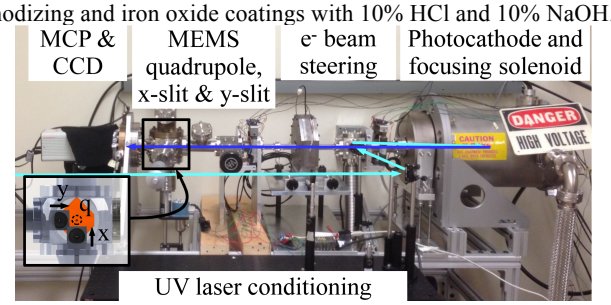

Figure 11. Photograph of the steering and focusing experiment. Cyan is the laser used to extract electrons from the photocathode and blue is the electron path. The beam is imaged using a micro-channel plate intensifier and cooled CCD. The inset shows the inside of the experiment chamber, with the MEMS quadrupole 'q' entering from above, and the horizontal and vertical slits that form the beam iris, 'y' and 'x', entering from the left and below.

All beam measurements were calibrated by subtracting an image of the MCP with the electron beam off. The electron beam was slightly under-focused, 34 keV, sub-pC, and pulsed at 1 kHz. Iris centering was accomplished by switching the electromagnet on and off in quadrupole configuration and translating the iris until there was no movement of the beam on MCP. Each measurement consisted of 25 images taken with 100 ms exposure time.

Electromagnet current was stepped from -1.5 A to +1.5 A, and back to -1.5 A in x- and y-deflecting configurations. Fig. 8 shows the beam centroid deflection. The measurements demonstrated less than 0.7% electromagnet hysteresis throughout all electromagnets, a value within the experimental error.

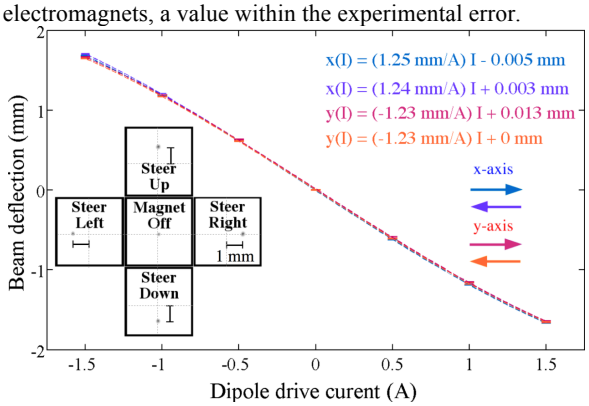

Figure 12. . Deflection measurement of a 34 keV electron beam using the electromagnet in Figure 3 powered in dipole configuration. Measured hysteresis is within the experiment error.

Electromagnet current was fixed at -1 A in an x-focusing quadrupole configuration while the iris slit was translated across the x-axis of the electromagnet bore to map the field distribution. The beam centroid was measured with the electromagnet on and off to provide a differential measurement of the beam translation. Fig. 13 shows the measured field across the electromagnet bore. The inset image in Fig. 13 shows the normalized intensity profile of the electron beam with different focusing currents.

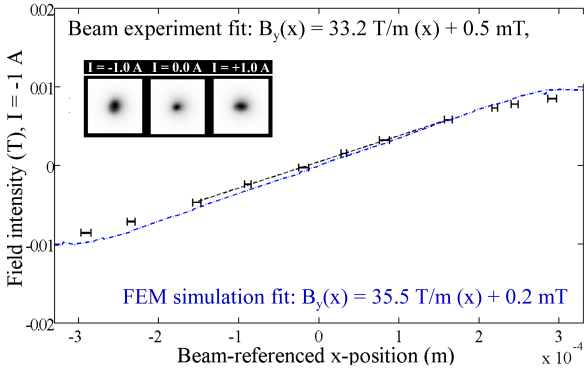

Figure 13. Field measurement and simulation of the electromagnet powered in quadrupole configuration. The inset images show normalized beam shape under x- and y-focusing currents.

CONCLUSION

We have fabricated 4-pole electromagnets with 600-μm bore and 55-μm thickness using a novel process. Hysteresis-free 24-mT fields and linear 33-T/m field gradients have been measured with a 34-keV electron beam, marking the first demonstration of 3D micro-electromagnets for particle beam manipulation. At saturating currents, 220 T/m is produced, and gradients exceeding 3 kT/m are possible by scaling the design to a 200-μm gap.

ACKNOWLEDGEMENT

The authors would like to thank the UCLA Nanolab and ISNC for use of their fabrication facilities and gratefully acknowledge support from DARPA #N66001-12-1-4209 and NSF #1350034.

REFERENCES

[1] J.W. Judy, "Microelectromechanical systems (MEMS): fabrication, design and applications," Smart Mater. Struct., 10, 6, (2001).

[2] P. Tseng, J.W. Judy, D. Di Carlo, "Magnetic nanoparticle–mediated massively parallel mechanical modulation of single-cell behavior," Nat. Methods, 9, (2012).

[3] N. Pamme and C. Wilhelm, "Continuous sorting of magnetic cells via on-chip free-flow magnetophoresis", Lab Chip, 6 (2006).

[4] R. Tatchyn and P. Csonka, "Attainment of submillimeter periods and a 0.3□T peak field in a novel micropole undulator device", App. Phys. Lett., 50, 377 (1987)

[5] O.D. Oniku, B. Peterson, W.C. Patterson, A. Garraud, F. Herrault, M.G. Allen, and D.P. Arnold, "Progress toward mini and micro magnetic undulators", Proceedings of the 2013 workshop on Physics and Applications of High Brightness Beams, San Juan, PR, 3/25-28/13, ICFA, Batavia (in print).

[6] J.K. Lim P. Frigola, G. Travish, J.B. Rosenzweig, S.G. Anderson, W.J. Brown, J.S. Jacob, C.L. Robbins, and A.M. Tremaine, "Adjustable, short focal length permanent-magnet quadrupole based electron beam final focus system", Phys. Rev. STAB, 8, 072401 (2005).

[7] M. Glickman, P. Tseng, J. Harrison, T. Niblock, I.B. Goldberg, and J. W. Judy, "High-Performance Lateral-Actuating Magnetic MEMS Switch", JMM, 20, 842 (2011)

[8] J. Harrison, O. Paydar, Y. Hwang, J. Wu, E. Threlkeld, P. Musueci, andn R. Candler, "Fabrication process for thick-film micromachined multi-pole electromagnets", JMEMS(in print)

CONTACT

*J.Harrison, tel: +1-623-695-0417; jere.harrison@ucla.edu

MEMS ENTREPRENEURIAL PERSPECTIVES

Kurt Petersen, PhD
Band of Angels, Menlo Park, California, USA

ABSTRACT

Being involved in the founding of a successful start-up company is one of the most exhilarating and satisfying experiences a person can have. Inventing, developing, and bringing to market a new product or a new technology, which provides a service that thousands or even millions of people will actually PAY to enjoy, is almost mind numbing. I have started six companies. TDI, NovaSensor, and Verreon were eventually acquired. Cepheid did an IPO in 2000. SiTime and Profusa are still private, but both have the potential to do an IPO. Looking back, you realize how luck can also be involved in such successes. To a large extent, people do make their own luck, but large success stories are often dependent on a substantial degree of good fortune. This paper is intended to discuss various stories of some of my start-up companies, how we overcame crucial hurdles, start-up advice, and how today's entrepreneurs might help themselves "make their own luck".

THE TEAM

When investors evaluate new start-up companies for potential funding, the first thing they consider is "the team". Ideally, they look for experienced, been-there-done-that people, who have had previous involvement with successful start-up companies. This experienced team is somewhat more crucial when a (rare) Series A financing of $5M to $10M is involved. Investors today are much more risk averse than those hey-days around 2000 and again around 2007. It is extremely difficult, in 2014, for hardware start-ups to obtain Series A investments. Today, hard-ware start-ups are often seed-funded by angel investors, such as the Band of Angels in Silicon Valley. In this case, teams can be much more junior, as long as there is an understanding among the founders that more senior, seasoned executives may replace founders in CEO and President roles at a later date. Founders, please do not be offended by this possibility. It is important to realize that all successful companies require a wide variety of necessary skills, from inventors, to engineers, to operations people, to marketing and sales people, to financial experts, to skilled business people. It is the rare founder who is expert in 2 or more of such skills.

So, put a lot of thought and energy into the design of the team. As we founded Verreon, we specifically designed the entire company to be acquired by Qualcomm. Since Qualcomm is so obsessed with IP, we hired a patent agent who was experienced with MEMS. And we also hired an operations expert who would bring more to the team than just a bunch of inventors. Qualcomm loved our team and the acquisition happened within 9 months of engaging with them. After this team was eventually acquired by Qualcomm, the yearly Qualcomm employee ranking system rated the Verreon employees at the very top of their engineering population.

When we founded Cepheid, one of the first tasks I undertook was the recruitment of a biomedical-experienced CEO, from my network. All the other founders were technical people, one biologist, one micro-fluidics engineer, one electrical engineer, and one mechanical engineer. Very shortly after getting funding, we hired an experienced industrial design engineer. It's always the Team that makes a company successful.

By the way, it is your network which makes it possible to connect with potential partners and potential employees for your start-up. Always look for any occasion to enhance your network. The wider your network, the more opportunities you will have for potential employees and/or partners and/or new prospective start-up companies. It is never too early to start putting your network together and you never stop expanding your network.

Besides the composition of the team, one of the biggest issues you will deal with when organizing a new start-up company is the distribution of stock. Be as fair and as generous as you can. But, please do not waste countless hours quibbling about a few percentage points here and there, which I have seen too many times. Keep in mind that business experience is just as important, if not more so, than engineers and inventors. It is also critical, of course, to set aside stock for additional potential employees.

THE VISION

It is critical that your company have a "Vision", which you can articulate to anyone within 60 seconds. A simple technical idea is critical, of course, but it is not enough for a truly transformative new company. The Vision must capture the long-term goals of the company and why the company's products will transform the intended marketplace. At Cepheid, we had the vision of transforming the diagnostics industry by providing rapid DNA diagnostics totally automatically in less than an hour. At SiTime, we had the vision of creating a timing-chip company, where customers who bought SiTime timing chips, would not have to buy a quartz crystal, because the MEMS replacement for the quartz crystal was already inside the same package with the timing chip. At Profusa, we have the vision of finally solving the problem of implantable chemical sensors.

Technical ideas can come from many different sources. Obviously, the most important issue is that the idea must become a product which people will want to purchase. Less obvious is that the product(s) or product line should also have the capability to grow dramatically in customer demand. That is, try not to be a one-trick pony. At NovaSensor, we wanted to create a "MEMS" company, but we did not have a specific first product in mind. Our funded sponsor, Schlumberger, had contracted with us to develop three very high performance pressure sensors, but no one knew how long it would take to get these very advanced devices into production, actually generating revenue. Fortunately, within a few months of starting NovaSensor, a company approached us to manufacture disposable blood pressure sensor chips for them because their current supplier was unreliable. So, our first product was the second source to replace another supplier. The first shipment (50K of these disposable pressure sensor chips) was made when the company was only about 6 months old. This was actually NovaSensor's financially most successful product for several years and set the company up for acquisition 4 years later. Even if the first product is not the ultimate best product, the ability to be in production as soon as possible is incredibly important, because you will have sales revenue coming in the door.

In 1996, two new ideas started Cepheid; the ability to perform rapid PCR for diagnostic identification of DNA or RNA segments, and automatic sample preparation (extracting and purifying DNA or RNA from a raw biological sample). When these two capabilities are completely developed, a disposable cartridge could perform a complete diagnostic assay totally inside the cartridge. However, creating the complete diagnostic platform, as well as the

9781940470016/HH2014/$25©2014TRF
DOI 10.31438/trf.hh2014.17

PCR-based assays, would require MANY years of development and FDA approvals, while not generating any revenues. So, we developed the rapid PCR capability first and built a life sciences research product to start (which does not require FDA approval). First shipments of this relatively simple product occurred 3 years after founding Cepheid. Sales of the SmartCycler helped to subsidize development of the fully integrated product, the GeneXpert, which came on the market 2½ years later. Again, a not-perfect first product came to market first and subsidized the product which was the ultimate goal of the company.

At SiTime, the process for the creation of the MEMS-first oscillators was actually developed at Robert Bosch to reduce the packaging complexity of gyroscopes. When it was discovered that a resonator inside the epi-sealed cavity could exhibit a Q of over 100K, the idea for a MEMS-based oscillator evolved. When the idea was developed to compensate the inherent temperature drift of these single crystal silicon resonators using circuitry, the basic concept was in place to create a product and a company to compete with the quartz crystal. The first 100K parts were shipped to a customer within 32 months after receiving funding. However, it took another 5 years to demonstrate MEMS oscillators which were better than quartz in every way measurable, cost, noise, temperature performance, size, power, and reliability. The company is now poised to dominate the timing marketplace.

THE MARKET

Clearly the potential market for your device must be huge; multiple $100M, preferably over $1B. If it is not huge, investors will not write their checks. Why does the market need to be so large? Simple math. High risk investors, like venture capitalists and angels, expect to return at least 20%/year on their investments. If it takes $50M and 4 years to bring your idea into volume production, and you are fortunate enough to capture a very optimistic market share of 20% in another 2 years, this is $20M/year in sales for a market size of $100M. If you exit after 6 years, the investors need to return $150M, more than the entire size of the market! In this scenario, it will be impossible for the investors to make a reasonable return.

Less obvious is the fact that the founders have to anticipate what customers will want, not today or tomorrow, but 5 or more years from today, because that is how long it will take to bring the new idea into real production. Convincing investors that your idea will be wanted by millions of people, 5 years or more from now, can be a challenge.

We had this problem big-time at Cepheid. In the late 90‘s, MANY people were doing microfluidics. At the time, most microfluidic companies (Caliper, ACLARA, for example), were targeting drug development markets and applications, requiring thousands to millions of very small fluidic samples (nano-liters to pico-liters). Cepheid was somewhat of an outlier, targeting unproven diagnostic applications with milli-liter volumes. I’m pretty sure that investors thought nano-liters were sexier than milli-liters. However, Cepheid *was* actually targeting an enormous market, which was being made possible by the huge progress in DNA sequencing going on at the time. Cepheid was founded in 1996. The first draft of the human genome was not published until 2000. Since then, virtually every organism has now been sequenced. How is this wealth of new information being used? It has revolutionized the field of molecular diagnostics, exactly where Cepheid is positioned as the leader. While not the case in 1996, molecular diagnostics today is a multi-billion dollar industry and is the fastest growing field in medical diagnostics.

Over 12 billion quartz crystal oscillators are shipped to the world’s electronic companies every year. It is a $5B+ market. Yet, quartz is a terrible, old-fashioned technology with inefficient production, high failure rates, and no possibility of integration with circuitry. So, when Markus Lutz, from Robert Bosch showed me his MEMS oscillator and how it could be controlled to compete with quartz crystals, I immediately began working on a business plan for a new company, SiTime. We had no trouble getting funding, because the market is enormous. However, competing with the quartz incumbent has been no easy task. While SiTime’s oscillators are better than quartz in every way (as mentioned above), convincing the market to abandon a 50 year-old standard technology which only costs about 25 cents, has been challenging.

THE DEMO

While there are clearly exceptions, today it is basically not possible to generate serious interest from potential investors, without a significant demonstration of the technology and product. (BTW, venture capital folks are always “very interested” and polite and seldom to never say, “no, we are not interested”. But getting a check from them is a different matter.) To maximize acceptance, the demonstration should be as complete as possible. When Cepheid was founded, we had demonstrated virtually nothing. However, I would be embarrassed to give the 1997 Cepheid presentation to today’s much more sophisticated, selective, and risk averse, potential investors. Demonstrations should be focused around a targeted product, with the packaging and software to fully illustrate the advantages of the product. The importance of a demo in today’s financing environment cannot be overestimated. It engages the audience, it proves the device can be built, it clarifies the use case, and it gives them more confidence that full scale production may not be that far away and may not be too difficult.

INTELLECTUAL PROPERTY

For hardware start-ups, there cannot be anything more important that IP. Investors will expect an extensive and comprehensive IP plan, and even filed provisionals or patents. They will review your patents and patent applications. They may even have experts evaluate your patents. Depending on the Vision and the Idea, investors may want to see a legal opinion on the company’s Freedom to Operate (FTO). Basically, they are hoping to reduce the risk of competitors damaging the value of your company and the value of their investment, as well as evaluating the potential for future lawsuits. Work with experienced patent attorneys to put your portfolio together.

EARLY FUNDING

Hardware start-ups can require a lot of capital (maybe even as high as $100M) and long periods of time (I always tell potential employees “at least 7 years”) to become a convincing, money-making success. Investors’ expectations today, even for early seed financing, is extremely high, especially for hardware companies (as opposed to software/internet, which we are not considering here). More and more early stage start-ups today are relying on small amounts of angel financing, as much government contracts they can get, and partnerships with large companies; then working very frugally to get the product close to volume production and getting interested potential customers. Funding from government agencies, such as DARPA and NIH, can be incredibly important today for getting a new company off the ground. At Profusa, which is developing an entirely new class of implantable chemical sensors, the company survived its first 4 *years* on small amounts of money from friends and family and small DARPA and NIH grants. Eventually these small DARPA and NIH grants became large DARPA and NIH grants. There are two other huge benefits to such grants. First, they add a huge degree of validation for future

investors, and secondly, they are a form of non-dilutive funding, which is very advantageous to equity investors, like angels and VCs. After nearly 5 years of small scale funding, but a back-log of over $7M in government grants, Profusa raised a $1M angel round, then a $3.5M Series A round, all from HNW individual investors.

At Cepheid, a key part of our pitch for our Series A was, "we have a license agreement for a key patent from Lawrence Livermore Labs, and we have a $3M contract from the US Army". The grant was THE deciding factor for many Series A investors.

However, there is another side to government money of which you need to be cognizant. I have a friend who calls government money "cocaine". Without discipline, the company can easily turn into "an SBIR factory," relying on new BAAs to get more money, which then distracts the company from its real, commercial product. At Cepheid, as well as at Profusa, we had a firm rule that any government money would not distract us from the real product and, in fact, would *only* be spent on product development, or we would not take the money.

CHAMPIONS

Your chances of getting funding increases dramatically when you have real outside "champions" for your technology/product or company. Investors rely heavily on such champions to vet your company and to assess your likelihood for financial success. At Cepheid, we had several eminent doctors on our Technical Advisory Board (TAB). One was Nobel Prize winner, Stanley Falkow. Another was David Relman, president of the Infectious Disease Society of America. At SiTime, we were lucky to get a huge endorsement from John Vig, the reputed expert on quartz crystal oscillators. John joined the SiTime TAB. Again, use your network to attract these folks. They can be incredibly influential.

INCORPORATING THE COMPANY

Seemingly a mundane and obvious procedure, incorporating the company *properly* is critical. An improper incorporation can have severe consequences later in the history of the company. Both experienced investors as well as potential acquirers, who might like the company, have stringent legal requirements on investments/acquisitions. Don't go to your cousin's friend who is an attorney, for legal work. Talk to veteran entrepreneurs (your network!) and get recommendations on credible law-firms, experienced with the unique requirements of high-tech start-ups. I have lived through one such situation. We got an acquisition interest from a larger company and began negotiations. However, the legal structure of the start-up was a mess. It took an enormous effort, and almost collapsed the deal, to resolve all the issues.

GETTING REAL MONEY

Timing for VC funding is critical. We closed our Series B and C rounds for Cepheid, partly funded by VCs, in 1998 and 2000, during the up-slope of the dot-com boom. We closed our Series A, B, and C rounds for SiTime in 2004, 2006, and 2007 just on the up-slope of the financial recovery after the crash of 2000. Only one of my six companies, SiTime, was fully funded with "traditional" venture capital money. It is supremely difficult to raise traditional VC funding in a down cycle for the economy and for several years later. It is important that you consider the existing economic conditions related to the timing of the founding of your company, because this will impact how you get funding.

One of the most important moves of my career was when my co-founder, Bill McMillan, and I recruited Tom Gutshall and asked him to be CEO of Cepheid. Tom had been a senior VP at Syntex and president of their diagnostic division, Syva. He had just headed the sale of Syntex to Roche for $5.3B, so he completely understood the biomedical industry. Critical for Cepheid is that Tom had an amazing "rolodex". His list of high net worth (HNW) individuals was phenomenal. We raised our Series A, $3.2M, mostly from Tom's rolodex and from the Band of Angels. BTW, in a start-up, you *never* stop trying to raise money until you are profitable. It is a constant issue for every start-up and is the CEO's most important occupation and responsibility.

Where you get your funding can be just as important as getting money at all. I was associated with one Silicon Valley start-up whose largest share-holder was a multi-billion-dollar conglomerate run by a "visionary" individual. Unfortunately, just when the start-up was transitioning into production, the FBI discovered that the true vision of this character was to operate a Ponzi scheme. When the FBI raided his headquarters, all of the assets of the conglomerate were placed in the hands of the court, the monthly funding to the start-up stopped, and 25 people at the start-up were suddenly out of a job. Even the 22 patents from the start-up were held by the court!! Customers were frantic to get more parts, which was impossible. Fortunately, the story does have a happy ending. After 2 years, the start-up CEO was eventually able to purchase the 22 patents from the court, then sold them to a large electronics company, which is now putting the product back into production with most of the original team.

OPERATIONS

This is one of my pet peeves. Many entrepreneurs make the *big* mistake of thinking that "the most difficult and most important part of any new product is inventing it". WRONG ! The real magic to create a viable, successful new company is operations. Good operations people have a different mind-set than inventors. Inventors are great at building "one" part. Operations people want to build "thousands" or "millions" of parts which are exactly identical. Good operations people speak about Design for Manufacturability, Design for Test, Cpk (process capability index), SPC (statistical process control), six-sigma, on-time delivery, and are very deliberate and organized. The operations person at SiTime would drive the engineers crazy by worrying about seemingly miniscule process issues. However, the company was moving into markets which required absolutely on-time deliveries and failure rates in the few ppm. Such discipline and rigor in manufacturing is absolutely essential. At Cepheid, I hired an operations person to ramp up production on the SmartCycler. Every month for the following 4 months, he would come to me and say, "I *think* I can make all the deliveries this month". We had just done an IPO! If we missed our numbers for the quarter, the stock would crash. I fired him and hired an experienced operations person who told me, "I know how to do this. This is what I like to do." She never missed a shipment for the next 4 years.

Similarly, the design of production-ready instrumentation, such as the Cepheid SmartCyler and GeneXpert systems, require *experienced* industrial design engineers with a focus on design for manufacturability. I have seen SO many "tinker-toy" instruments at start-ups, built by the inventors, which NEVER made it to production. Early at Cepheid, we had 2 competing design concepts for the flag-ship GeneXpert system. One concept was championed by a brilliant PhD engineer from Berkeley, the other was championed by 2 very experienced, but junior, engineers with no degrees. However, the junior engineers had already designed successfully-manufactured, cost-effective instruments at previous companies. When it came time to make a decision about which design concept to continue into development, I chose the version championed by the 2 junior engineers, despite the fact that either concept would have done the job well. I know this decision would

inspire the junior engineers to do an outstanding job, using all their DFM experience. Twelve years later, this design represents 95% of the $450M run-rate at Cepheid and its performance is unmatched by any other competitor.

THE EXIT

Give a lot of thought to your exit from the day you form the company, because I guarantee you, potential investors will ask your thoughts about this. What I mean by "exit" is the point where founders and investors are paid for their stock. Of course, the two most common exits are an IPO, and an acquisition. Be realistic and truthful to yourself during this analysis. Besides the fact that an IPO for a hardware company is extremely rare, the time it can take to achieve an IPO can be extremely long. InvenSense took 8 years. SiTime has entered its 9th year - no IPO yet. While Cepheid did its IPO in 2000 (its 4th year) this was during the unusual dot-com boom when IPOs were the norm. Those days are long gone. So, maintain in your mind the option of an acquisition. Encourage and continually reinforce relationships with potential acquirers. In early 1990, NovaSensor was having trouble raising needed capital from investors. However, we knew that the MEMS products we were shipping and the technology we had developed was valuable. One of my partners, Janusz Bryzek, had a lot of contacts (his network) in the nascent MEMS industry. He knew of a company, Lucas Industries, which had tried and failed to purchase a competitor pressure sensor manufacturer. He contacted Lucas and they immediately engaged with us to acquire NovaSensor. The sale was completed in May of 1990, to the benefit of the founders.

Even though an acquisition is statistically much more likely than an IPO, your company is MUCH more valuable to the acquirer if it is organized and operated as a professional, stand-alone company, ready for an IPO. For this reason, quality systems, HR, finance, legal, operations, all need to be established and maintained at the highest possible levels, even if you are planning for an acquisition. Get those experienced business people in place.

FINAL THOUGHTS

While I have always thought of myself as a research person, I am passionate that the fruits of my research become products which help people in some way. This is the reason I originally began my career as an entrepreneur. However, a start-up is not for the faint of heart. Be prepared, it is a huge emotional roller-coaster ride, with enormous highs and lows. The pressures and the uncertainties can be intense.

If you want to be involved with start-up companies, your network is your best friend. Don't be shy about asking accomplished entrepreneurs for advice and mentoring. Even a modestly successful start-up company is incredibly exhilarating and satisfying. Remember, for investors, the Team is first, the Market is second, and the Technology is third. Even though Series A financings are very difficult to achieve today, there are still MANY opportunities for start-up companies, especially from the angel community. Also, the proliferation of incubators and hardware development labs/companies is a *huge* benefit for new entrepreneurs. Go ahead, don't be afraid to change the world !!

1 MILLION Q-FACTOR DEMONSTRATED ON MICRO-GLASSBLOWN FUSED SILICA WINEGLASS RESONATORS WITH OUT-OF-PLANE ELECTROSTATIC TRANSDUCTION

D. Senkal, M.J. Ahamed, S. Askari, and A.M. Shkel*
MicroSystems Laboratory, University of California, Irvine, CA, USA

ABSTRACT

In this paper, for the first time, we report Q-factor over 1 million, on both modes, and high frequency symmetry ($\Delta f/f$) of 132 ppm on wafer-level micro-glassblown 3-D fused silica wineglass resonators at a compact size of 7 mm diameter and center frequency of 105 kHz. In addition, we demonstrate for the first time, out-of-plane capacitive transduction on MEMS wineglass resonators. High Q-factor is enabled by a high aspect ratio, self-aligned glassblown stem structure, careful surface treatment of the perimeter area, and low internal loss fused silica material. Electrostatic transduction is enabled by detecting the spatial deformation of the 3-D wineglass structure using a new out-of-plane electrode architecture. To the best of our knowledge, work presented in this paper is the highest reported Q-factor on a degenerate mode device at 7 mm diameter or smaller. Micro-glassblowing may enable batch-fabrication of high performance fused silica wineglass gyroscopes at a significantly lower cost than their precision-machined macro-scale counterparts.

INTRODUCTION

Recently, there has been a growing interest in 3-D MEMS wineglass resonator architectures for use in inertial sensing applications due to potential advantages in symmetry, minimization of energy losses, and immunity to external vibrations [1]–[5].

Q-factor and frequency symmetry are key parameters for high performance degenerate mode Coriolis Vibratory Gyroscope (CVG) operation, as they directly relate to gyro performance metrics such as rate sensitivity, noise performance, and power consumption. However, obtaining high-Q factor and the required symmetry on 3-D MEMS devices remains to be a challenge due to factors such as thermoelastic dissipation, granularity of thin films, intrinsic material losses, high surface roughness, lack of a functional stem structure, and the associated anchor losses. Primarily, two main methods are employed in fabrication of MEMS wineglass structures: (1) deposition of thin-films on pre-defined molds, (2) blow molding the device layer into a pre-defined cavities. For example, Q-factor of 19.1k have been demonstrated on poly-silicon shell structures deposited in pre-etched cavities [1]. Q-factors up to 6.3k [2] were measured on poly-diamond wineglass shells deposited in pre-etched cavities and up to 20k were measured on sputtered ultra low expansion (ULE) glass shells deposited on precision ball lenses [3]. Blow molding was used to demonstrate Q-factors as high as 7.8k on bulk metallic glass shells [4] and 300k on fused silica shells [5].

In this paper, we explore an alternative fabrication paradigm under the hypothesis that surface tension and pressure driven micro-glassblowing process may serve as an enabling mechanism for wafer-scale fabrication of extremely symmetric and atomically smooth wineglass resonators. Micro-glassblowing process relies on viscous deformation of the device layer under the influence of surface tension and pressure forces to define the 3-D shell structure as opposed to conventional deposition, molding, or etching techniques. During the brief duration, while the device layer is still viscous, surface tension forces act on the 3-D shell structure, at an atomic level, to minimize surface roughness and structural imperfections; this leads to levels of smoothness and structural symmetry that is not available through conventional fabrication techniques. In addition, current MEMS fabrication techniques restrict the material choice to a few materials limiting the maximum achievable Q-factor. Available materials such as single-crystal silicon, have relatively high coefficient of thermal expansion (CTE) and consequently high thermoelastic dissipation (TED). Materials with low CTE, such as fused silica (0.5 ppm/°C) or ultra low expansion titania silicate glass, provide a dramatic increase in fundamental Q_{TED} limit (ULE TSG is a glass that consists of SiO_2 & TiO_2; this engineered material has the lowest known isotropic CTE of 0.03 ppm/°C). However, when compared to silicon, titania silicate glass and fused silica dry etching suffers from an order of magnitude higher surface roughness, lower mask selectivity (1:1 for KMPR photoresist), and lower aspect ratio, $<$ 6:1 [6]. Micro-glassblowing allows the use of fused silica material on a wafer-level without the need for these challenging dry etching techniques.

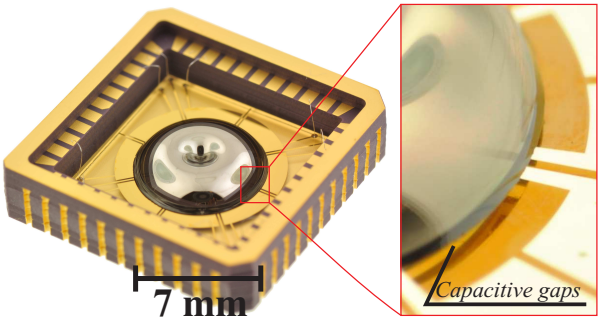

Figure 1: 1 million Q-factor fused silica wineglass structure presented in this paper (left), close-up of capacitive gaps (right).

Micro-glassblowing of borosilicate glass spherical shell structures has been demonstrated for nuclear magnetic resonance applications [7]. Later, fused silica and ultra low expansion glass micro-glassblowing of inverted-wineglass structures has been demonstrated at temperatures as high as 1700 °C [8]. Assembled electrode structures and a piezo-pinger setup were developed in [9] for electrostatic and mechanical excitation of micro-glassblown structures. Finite element analysis of the micro-glassblowing process [10], and further improvement in the fabrication process led to frequency splits (Δf) as low as $<$ 1 Hz on borosilicate glass wineglass structures [11].

In this work, we report the most recent developments in the wafer-level, micro-glassblowing paradigm for fabrication of 1 million Q-factor, highly symmetric ($\Delta f/f$ = 132 ppm) fused silica wineglass resonators at 7 mm diameter and first demonstration of out-of-plane electrostatic transduction on MEMS wineglass resonators, Fig 1.

9781940470016/HH2014/$25©2014TRF
DOI 10.31438/trf.hh2014.18

Solid-State Sensors, Actuators and Microsystems Workshop
Hilton Head Island, South Carolina, June 8-12, 2014

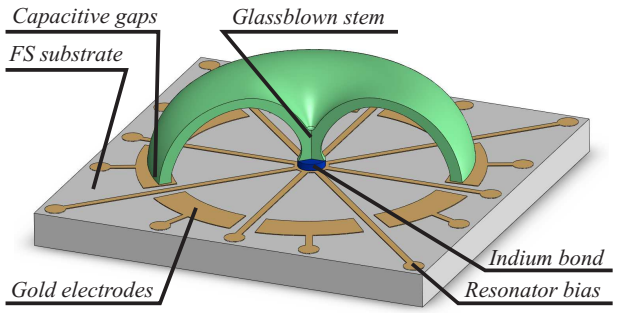

Figure 2: Out-of-plane electrode architecture consists of a micro-glassblown fused silica wineglass resonator and planar Cr/Au electrodes defined on fused silica, enabling batch-fabrication.

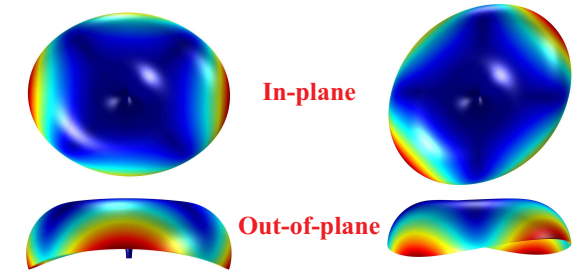

a) 1st n=2 wineglass mode *b) 2nd n=2 wineglass mode*

Figure 3: Out-of-plane transduction scheme utilizes out-of-plane component of wineglass modes to drive and sense in-plane motion.

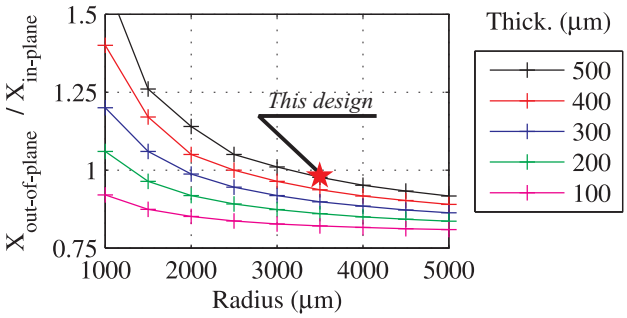

Figure 4: Out-of-plane to in-plane displacement ratio for mushroom resonators: Due to the 3-D nature of the resonator, the ratio is close to 1:1. Star marks the design presented in this paper.

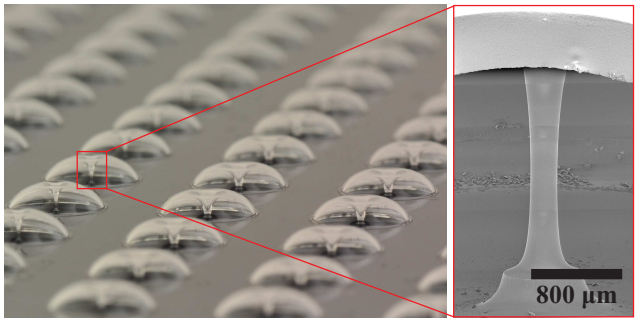

Figure 5: Array of micro-glassblown wineglass structures (left), glassblown self-aligned stem structure (right).

DESIGN

Out-of-plane electrode architecture and parameters affecting Q-factor are discussed in this section.

Out-of-plane electrode architecture

Wineglass coriolis vibratory gyroscopes typically utilize 8 or more electrodes to drive and sense the primary wineglass modes. One of the main challenges of fabricating micro-wineglass resonators is the definition of the electrode structures in a manner compatible with batch-fabrication. 3-D side-walls of the wineglass geometry makes it challenging to fabricate radial electrodes with small capacitive gaps and to keep the gap uniform across the height of the structure. Even though post-fabrication assembly techniques have been successfully demonstrated [9], these approaches create a bottle-neck in batch-fabrication of the devices at wafer level.

In this paper, we explore an alternative transduction paradigm based on out-of-plane electrode architecture. Out-of-plane electrode architecture consists of a micro-glassblown fused silica wineglass resonator and planar Cr/Au electrodes defined on a fused silica substrate, Fig. 2. Out-of-plane capacitive gaps are formed between the Cr/Au metal traces and the perimeter of the wineglass resonator. Electrostatic transduction is made possible by the 3-D mode shape of the wineglass resonator: in-plane deformation of wineglass modes is accompanied by an out-of-plane deformation, Fig. 3. This permits the use of out-of-plane transduction to drive and sense the in-plane oscillations, which are sensitive to coriolis forces along the z-axis of the structure [12]. This kind of electrode structure has several advantages over radial electrode structures:

- Even though a smaller surface area is utilized for capacitive gaps compared to radial electrodes, planar nature of the electrode structure makes it easier to obtain smaller capacitive gaps, which helps compensate for the loss of surface area.
- Sacrificial layers and wafer-to-wafer bonding techniques can be used to define the capacitive gaps, which makes the process very robust to alignment errors, as the gap uniformity is defined by the thickness of the sacrificial layer and not the wafer to resonator alignment accuracy.
- The metal traces for the electrodes can be defined on the same material used for the resonator (i.e. fused silica), providing uniform coefficient of thermal expansion between the electrode die and the resonator.
- For mushroom type geometries the ratio of out-of-plane motion to in-plane motion is close to 1:1, leading to very efficient out-of-plane transduction, Fig. 4.

Optimization of Q-factor

Total Q-factor of the vibratory structure can be calculated from contribution of individual dissipation mechanisms in a manner analogous to solving a parallel resistor network, Eq. 1. For this reason the total Q-factor is dominated by the dissipation mechanism with the lowest Q-factor (weakest link).

$$Q_{total}^{-1} = Q_{visc}^{-1} + Q_{anchor}^{-1} + Q_{mat}^{-1} + Q_{surf}^{-1} + Q_{etc}^{-1} \,. \quad (1)$$

In order to optimize the Q-factor all loss mechanisms affecting the system need to be individually addressed:

- Viscous damping, Q_{visc}, is the most dominant affect with Q-factor of several thousands at atmospheric conditions.

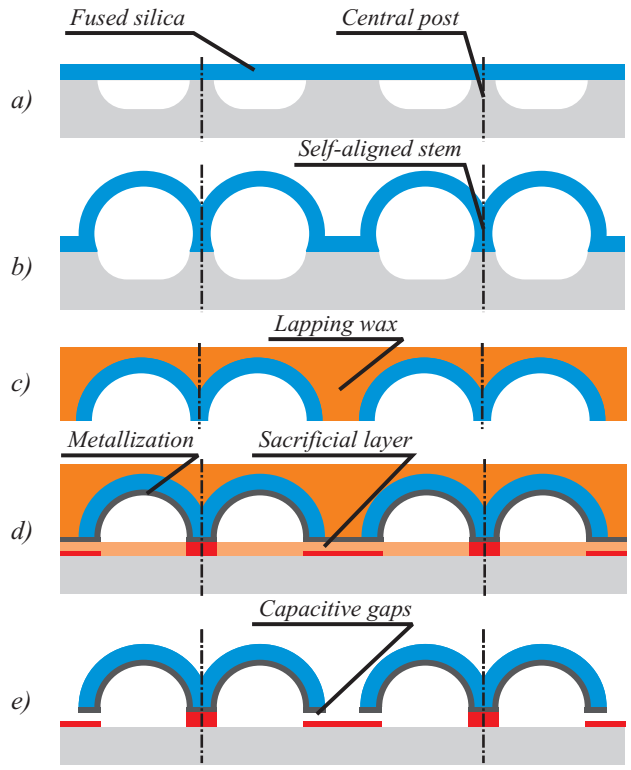

Figure 6: Wafer-level fabrication process for fused silica micro-wineglass structures.

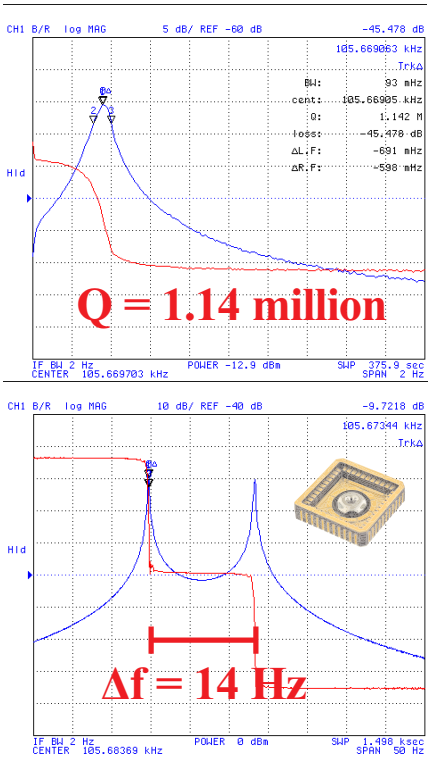

Figure 7: Frequency sweep revealed a Q-factor of 1.14 million and as fabricated freq. split (Δf) of 14 Hz at 105 kHz center freq.

However, it can easily be eliminated by operating the device in moderate to high vacuum.

- Anchor losses, Q_{anchor}, are caused by acoustic losses into the substrate and are minimized by decoupling the resonator and the substrate through a self-aligned, solid stem structure, Fig. 5.
- Material losses, Q_{mat}, can be divided into several individual loss mechanisms. Thermoelastic dissipation is caused by an interaction between the thermal fluctuations and mechanical oscillations and is minimized by using materials with low coefficient of thermal expansion (CTE), such as fused silica (0.5 ppm/°C). Additional material losses are caused by microscopic effects, such as presence of foreign materials within the matrix of the resonator material and lattice defects at grain boundaries [13]. These effects are minimized by using a high purity, isotropic fused silica material.
- Surface losses, Q_{surf}, are mainly caused by high surface roughness and metallization losses [13]. These effects are minimized through atomically smooth surfaces of micro-glassblown structures [8] and keeping the thickness of the metal layer very small with respect to the resonator shell thickness (50 nm of sputtered Iridium).
- Additional loss mechanisms, Q_{etc}, such as Akheiser dissipation have typically very high Q-factors at kHz range and are not taken into account [14].

FABRICATION

Micro-glassblowing is a wafer-level process, Fig. 5, which utilizes surface tension and pressure forces to minimize surface roughness and structural asymmetries (Δf) [11]. Fabrication process starts with $\sim 2\ \mu$m thick LPCVD poly-silicon deposition on 1 mm thick fused silica wafers. The poly-silicon mask is used to etch hemi-toroidal cavities into fused silica wafers down to $\sim 300\ \mu$m depth. The next step of the fabrication process is plasma assisted fusion bonding of a 500 μm thick fused silica device layer (Corning 7980), Fig 6(a) [8]. The wafer stack is later glassblown at $> 1600\ ^{\circ}C$ for ~ 2 minutes and rapidly cooled to room temperature, Fig 6(b). During glassblowing the device layer at the central post merges to create a solid, self-aligned stem structure, critical for high-Q operation, Fig. 5. This is followed by back-lapping the wafer stack to release the inverted wineglass structures using an Allied Multiprep 12" lapping system, Fig 6(c). A series of diamond lapping films with descending grit size of $30\ \mu\text{m} \Rightarrow 6\ \mu\text{m} \Rightarrow 3\ \mu\text{m} \Rightarrow 1\ \mu\text{m} \Rightarrow 0.5\ \mu\text{m} \Rightarrow 0.1\ \mu\text{m}$ are used for lapping, final polish is done using polishing cloth and 50 nm colloidal suspension to obtain optical polish at the perimeter of the shell structure.

Interior surface of the wineglasses is metallized with 50 nm thick sputtered Iridium on a two axis planetary stage for film uniformity. For the out-of-plane electrode structures, separate fused silica wafers are patterned with Cr/Au (100 nm / 500 nm) electrodes and coated with a thin layer of photo-resist sacrificial layer. Subsequently, lapped and metalized wineglass wafer is bonded to the out-of-plane electrode wafer at the stem of each wineglass using low out-gassing epoxy, Ablebond JM7000, Fig 6(d). Once the bonding is complete, the sacrificial layer is removed to release the inverted wineglass structures around their perimeter, creating capacitive gaps between the metalized inverted wineglass structures and the Cr/Au electrodes, Fig 6(e).

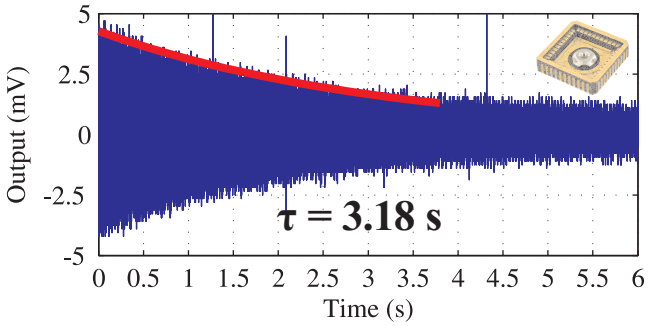

Figure 8: Ring-down experiment at 19 μTorr shows τ = 3.18 s, giving 1.05 million Q-factor at 105 kHz, confirming the sweep.

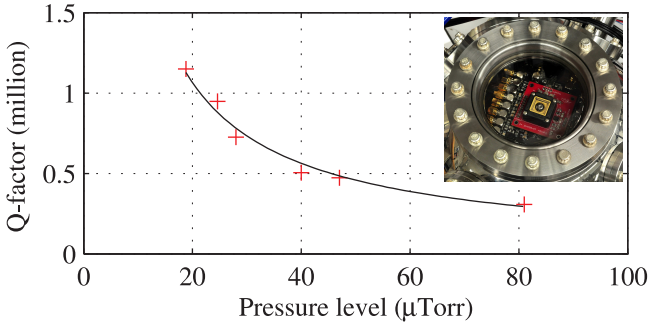

Figure 9: Q-factor vs pressure level experiment. Q-factors above 1 million were obtained after pumping down to 20 μTorr.

EXPERIMENTAL RESULTS

Frequency sweep using out-of-plane electrodes revealed Q-factor of 1.14 million and frequency split of 14 Hz at a center frequency of 105 kHz ($\Delta f/f$ = 132 ppm), Fig. 7. A separate ring down experiment was performed where the device was excited with a narrow bandwidth swept sine-wave impulse and resonator output during free vibration was recorded. Ring down experiment demonstrated a time constant of 3.18 seconds and Q-factor of 1.05 million, confirming the frequency sweeps, Fig. 8. In order to observe the effect of viscous damping on the overall Q-factor, the frequency sweep was repeated at different pressure levels. Q-factor of 1 million was obtained below < 20 μTorr, Fig. 9. No further improvement in Q-factor was observed below < 20 μTorr.

CONCLUSIONS

Micro-glassblown fused silica wineglass resonators with out-of-plane electrode structures have been fabricated. Q-factor over 1 million, on both modes, and high frequency symmetry ($\Delta f/f$) of 132 ppm have been experimentally demonstrated at a compact size of 7 mm diameter. In addition, out-of-plane capacitive transduction on MEMS wineglass resonators have been demonstrated for the first time.

To the best of our knowledge, work presented in this paper is the highest reported Q-factor on a degenerate mode device at 7 mm diameter or smaller. Low internal dissipation of fused silica combined with high structural symmetry of MEMS micro-glassblowing paradigm may enable batch-fabrication of high performance fused silica wineglass gyroscopes on a wafer surface at a significantly lower cost than their precision-machined macro-scale counterparts.

ACKNOWLEDGEMENTS

This material is based upon work supported by DARPA grant W31P4Q-11-1-0006 (Program Manager Dr. Robert Lutwak).

REFERENCES

[1] P. Shao, V. Tavassoli, L. Chang-Shun, L. Sorenson, and F. Ayazi, "Electrical characterization of ALD-coated silicon dioxide micro-hemispherical shell resonators," in *IEEE MEMS*, San Francisco, CA, USA, 2014, pp. 612–615.

[2] A. Heidari, M. Chan, H.-A. Yang, G. Jaramillo, P. Taheri-Tehrani, P. Fonda, H. Najar, K. Yamazaki, L. Lin, and D. A. Horsley, "Micromachined polycrystalline diamond hemispherical shell resonators," in *Solid-State Sensors, Actuators, and Microsystems Workshop (TRANSDUCERS)*, Barcelona Spain, 2013, pp. 2415–2418.

[3] Y. Xie, H. C. Hsieh, P. Pai, H. Kim, M. Tabib-Azar, and C. H. Mastrangelo, "Precision curved micro hemispherical resonator shells fabricated by poached-egg micro-molding," in *IEEE Sensors*, Taipei, Taiwan, 2012, pp. 279–283.

[4] M. Kanik, P. Bordeenithikasem, J. Schroers, D. Kim, and R. T. M'Closkey, "Microscale Three-Dimensional Hemispherical Shell Resonators Fabricated from Metallic Glass," in *IEEE ISISS*, Laguna Beach, CA, 2014, pp. 9–12.

[5] J. Cho, J. Yan, J. A. Gregory, H. Eberhart, R. L. Peterson, and K. Najafi, "High-Q fused silica birdbath and hemispherical 3-D resonators made by blow torch molding," in *IEEE MEMS*, Taipei, Taiwan, 2013, pp. 177–180.

[6] M. J. Ahamed, D. Senkal, A. A. Trusov, and A. M. Shkel, "Deep NLD plasma etching of fused silica and borosilicate glass," in *IEEE Sensors*, Baltimore, Maryland, USA, 2013, pp. 1767–1770.

[7] E. J. Eklund and A. M. Shkel, "Self-inflated micro-glass blowing," *US Patent 8,151,600*, 2012.

[8] D. Senkal, M. J. Ahamed, A. A. Trusov, and A. M. Shkel, "High temperature micro-glassblowing process demonstrated on fused quartz and ULE TSG," *Sensors and Actuators A: Physical*, vol. 201, pp. 525–531, Dec. 2012.

[9] D. Senkal, M. J. Ahamed, A. A. Trusov, and A. M. Shkel, "Adaptable test-bed for characterization of micro-wineglass resonators," in *IEEE MEMS*, Taipei, Taiwan, 2013.

[10] D. Senkal, M. J. Ahamed, and A. M. Shkel, "Design and Modeling of Micro-glassblown Inverted-wineglass Structures," in *IEEE ISISS*, Laguna Beach, CA, 2014, pp. 13–16.

[11] D. Senkal, M. J. Ahamed, A. Trusov, and A. M. Shkel, "Achieving Sub-Hz Frequency Symmetry in Micro-Glassblown Wineglass Resonators," *Journal of Microelectromechanical Systems*, vol. 23, no. 1, pp. 30–38, 2014.

[12] A. Renault and P. Vandebeuque, "Hemispherical resonator with divided shield electrode," *US Patent 6,945,109*, 2005.

[13] B. S. Lunin, "Physical and chemical bases for the development of hemispherical resonators for solid-state gyroscopes," *Moscow Aviation Institute, Moscow*, 2005.

[14] S. Chandorkar, M. Agarwal, R. Melamud, R. N. Candler, K. E. Goodson, and T. W. Kenny, "Limits of quality factor in bulk-mode micromechanical resonators," in *IEEE MEMS*, Tucson, AZ, USA, 2008, pp. 74–77.

CONTACT

* D. Senkal, tel: +1-949-945-0858; doruksenkal@gmail.com

GAN MEMS RESONATOR USING A FOLDED PHONONIC CRYSTAL STRUCTURE

Siping Wang[*]*, Laura C. Popa, and Dana Weinstein*
Department of Electrical Engineering and Computer Science
Massachusetts Institute of Technology, Cambridge, MA

ABSTRACT

We present a Gallium Nitride (GaN) Lamb Wave resonator using a Phononic Crystal (PnC) to selectively confine elastic vibrations with wide-band spurious mode suppression. A unique feature of the design demonstrated here is a folded PnC structure to relax energy confinement in the non-resonant dimension and to enable routing access of piezoelectric transducers inside the resonant cavity. This provides a clean spectrum over a wide frequency range and improves series resistance relative to transmission line or tethered resonators by allowing a low-impedance path for drive and sense electrodes. GaN resonators are demonstrated with wide-band suppression of spurious modes, $f.Q$ product up to 3.06×10^{12}, and resonator coupling coefficient k_{eff}^2 up to 0.23% (filter BW up to 0.46%). Furthermore, these PnC GaN resonators exhibit record-breaking power handling, with IIP3 of +27.2dBm demonstrated at 993MHz.

INTRODUCTION

High Q, small footprint MEMS resonators are very promising for building blocks in RF wireless communication, timing, inertial navigation, and sensing applications. Their potential for monolithic integration with circuits provides critical benefits such as the elimination of parasitic capacitance and inductance from bond pads and off-chip routing, size, weight, and power scaling, and simplification of fabrication and packaging. Recent advances in GaN Monolithic Microwave IC (MMIC) technology have made it an attractive platform for the realization of high performance MEMS resonators. With GaN's wide band gap (3.4 eV), high 2DEG mobility, and high piezoelectric coefficients, integration of GaN MEMS with High Electron Mobility Transistors (HEMTs) presents many opportunities for high power, high frequency applications.

This work focuses on the development of MEMS resonators for channel-select filtering in RF receiver front ends. For a MEMS band pass filter, the presence of spurious modes in the constituent resonators strongly impacts filter performance. Resonators with a clean frequency spectrum help reduce ripples in the pass-band and prevent interference from unwanted signals outside the pass-band. Conventional MEMS resonator designs with free mechanical boundaries are inherently prone to spurious modes, since free boundaries act as acoustic reflectors over all frequencies. To resolve this issue, the resonator boundary needs to be frequency selective.

One way to define the MEMS resonator cavity with frequency selective confinement is by using Phononic Crystals (PnCs), which involve periodic scatters to achieve highly reflective boundary conditions only for frequencies in a specific range. This acoustic band gap can be engineered based on the unit cell size and material configuration. Research in micro-scale PnCs has progressed rapidly in the past decade with band gap optimization at GHz frequencies in Si and SiC [1,2] and high-Q resonators in Si, AlN and ZnO [3,4,5]. High-Q resonant cavities using PnCs have been previously defined either as defect modes in a uniform 2D PnC (Fig. 1(a)) or as a suspended slab with free boundaries in the non-resonant dimension (Fig. 1(b)). While the acoustic band gap of these PnCs helps reduce resonance outside the band gap, these structures provide no spurious mode suppression inside the band gap. Furthermore, transducers must be routed through the PnC in these configurations, leading to resistive loading of Q. In this work, we demonstrate a new resonant structure leveraging both PnC acoustic confinement and the electromechanical benefits of GaN. The proposed GaN folded PnC structure (Fig. 1(c)) provides several important benefits:

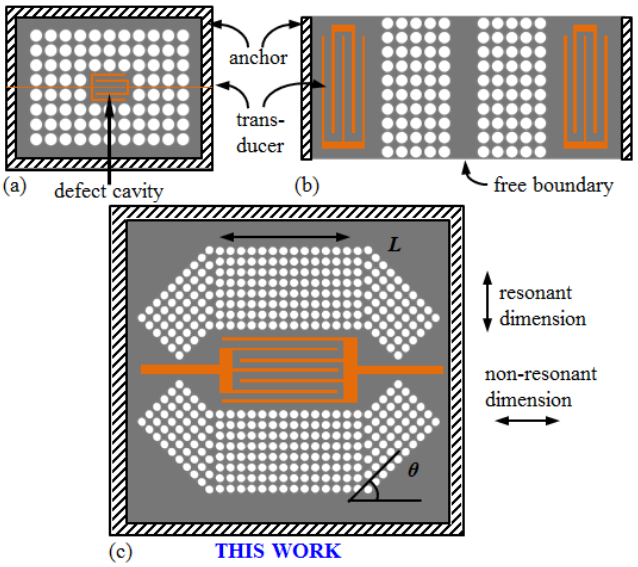

Figure 1: (a) Defect cavity in 2D PnC. Transducer routes through PnC to cavity. (b) Transmission line PnC resonator, with transducers external to the resonance cavity (c) This work: Folded PnC resonator enabling transducer inside resonant cavity with spurious mode suppression, high-Q mode, and large power handling.

- wide-band spurious mode suppression, both outside and inside the PnC band gap, through relaxed confinement in the non-resonant dimension,
- low-loss electrical routing to the resonant cavity to incorporate drive and sense transducers inside the resonator,
- improved heat dissipation relative to other PnC or tethered resonators, and
- robust design that is immune to residual stress and handling.

Using the folded PnC design, these improvements can be achieved while maintaining quality factor and transducer coupling comparable to traditional tethered resonators.

DESIGN AND SIMULATION

A square lattice PnC was chosen to define the resonant cavity of the folded PnC resonator. The PnC unit cell is a square block with a finite thickness defined by the GaN layer thickness, and a circular hole at the center as illustrated in Fig. 2(a). For the irreducible Brillouin zone (IBZ) in Fig. 2(b), the PnC band structure of the 537 MHz (unit cell a = 5.6 μm) resonators in this work is given in Fig. 2(c). It should be noted that the PnC does not have a complete band gap. Rather, there are only band gaps from O to X and from X to M but not from O to M. This partial band gap is sufficient for the designed resonator since the PnC needs to be reflective only in the resonant dimension.

While the PnC resonator inherently suppresses spurious modes *outside* the band gap, it was found that the majority of spurious modes found *inside* the band gap are due to harmonics established in the non-resonant dimension. Energy confinement along the non-resonant dimension must therefore be relaxed while

9781940470016/HH2014/$25©2014TRF
DOI 10.31438/trf.hh2014.19

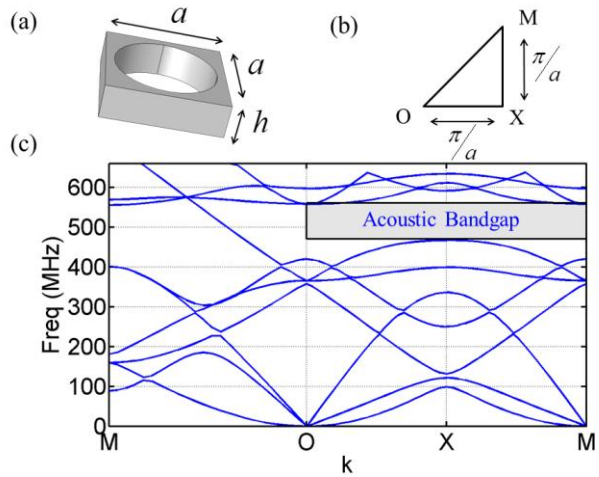

Figure 2: (a) Unit cell of the PnC structure. (b) Irreducible Brillouin zone in k space. (c) PnC band structure, showing a partial band gap along edges of unit cell (O to X to M).

maintaining high Q for the fundamental mode. These design considerations motivated the folded-PnC structure, in which square lattice PnC segments are designed at a folding angle θ relative to the main PnC to provide good confinement for the desired mode while minimizing standing waves formed in the non-resonant dimension.

A. Performance dependence on folding angle θ

Using 3D finite element method (FEM) simulations in COMSOL, folded PnC resonators with varying folding angle θ were investigated for their quality factor and spurious-free frequency range (SFFR). In these devices, Q is limited by acoustic losses to the substrate. To capture this loss in the FEM simulation, Perfectly Matched Layers (PMLs) were implemented on the perimeter of the device beyond the PnC. Simulations included Multiphysics piezoelectric transduction to determine the 1-port response of the resonator. Q and SFFR were then extracted from a multi-pole fit to the 1-port admittance of the resonator. Simulated results of the angular dependence of Q and SFFR are shown in Fig. 3(a), where the angle θ = N/A corresponds to a PnC resonator of length L with completely open boundaries in the non-resonant dimension (no folded PnC segments). The simulated GaN resonator with interdigitated transducer (IDT) has a 7th harmonic S_0 Lamb mode around 537 MHz, using a PnC unit cell length of a = 5.6 µm. A constant folded segment length of 5 unit cells was chosen for this design. The PnC band gap is established between 467 and 562 MHz.

As can be seen in Fig. 3(a), the presence of the folded PnC improves Q by a factor of over 2 above a critical angle between 30-45°, but tends to introduce spurious modes near the desired resonance. This can be explained by the role of the folded PnC segments in reflecting some radiated energy from the openings for all frequencies within the band gap, providing high Q for the fundamental mode but enabling standing waves orthogonal to the resonance which result in additional modes within the band gap.

At all angles of the folded PnC segments, and even in the limiting case where no folded segments exist (θ = N/A), undesired harmonic modes along the non-resonant dimension are established due to the finite length of the PnC and driving electrodes which results in a break in translational symmetry. Fig. 4 plots the 1-port frequency response of a simulated folded PnC resonator and the mode shapes of its main resonance and spurious modes. A device with longer cavity length (L/a = 28) is chosen for better illustration

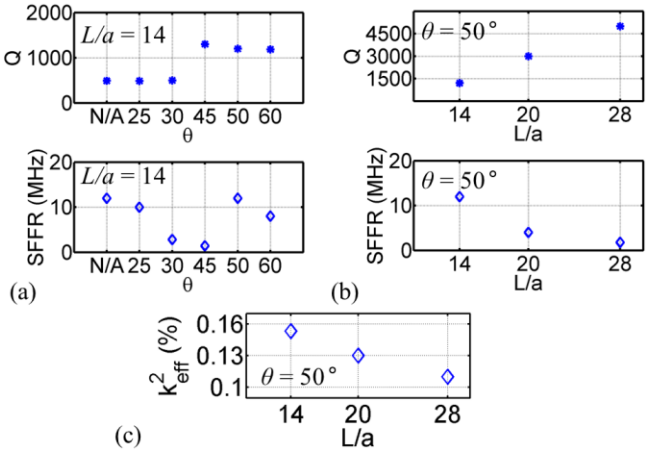

Figure 3: COMSOL simulated resonator performance, including Q, spurious-free frequency range (SFFR), and resonator coupling coefficient k_{eff}^2 for varying PnC folding angle θ and cavity length L, normalized to the PnC unit cell length (a = 5.6 µm at 537 MHz).

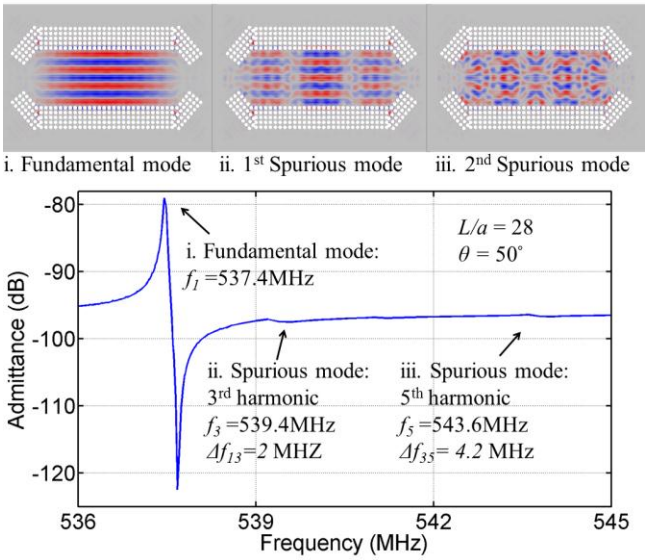

Figure 4: Simulated resonator mode shape and frequency spectrum. Compressive strain field along the resonant dimension is plotted.

of harmonics in the non-resonant dimension and the two spurious modes established within the band gap correspond to the 3rd and 5th harmonics. Even harmonics are suppressed due to symmetry of the driving and sensing electrodes. For a fundamental mode frequency f_1 centered in the band gap, the frequency of the nth harmonic spurious mode can be approximated to first order by

$$f_n = \sqrt{f_0^2 + \left(\frac{nv}{L}\right)^2} \quad (1)$$

where v is the wave velocity along the non-resonant dimension and f_0 is the resonance frequency of the S_0 Lamb mode in the case when cavity length L is infinite. As can be seen in Fig. 4, these harmonics are significantly attenuated relative to the fundamental mode. This attenuation is attributed to signal cancellation in the IDT and to the openings designed on the central axis of the folded PnC structure, which not only route the transducer signal to the resonant cavity, but also relax energy confinement for waves traveling in the non-resonant dimension.

At certain folding angles, additional anharmonic spurious modes not predicted by Eqn. 1 arise due to scattering off the "defect" at the folding point of the PnC. It is found from FEM simulation that at θ = 50°, these spurious modes are entirely suppressed, achieving SFFR comparable to the case of no folded segments (θ = N/A). Moreover, at θ = 50° resonator Q is twice as high as that of the resonator without folded segments. Hence, this folding angle was selected for all designs in this work.

B. *Performance dependence on cavity length L*

A similar trade-off exists between Q and SFFR as a function of cavity length L, which also strongly affects resonator k_{eff}^2. Simulation results of this dependence are presented in Fig. 3(b) and (c). As L increases, resonator volume and therefore total stored energy increase. Meanwhile, energy loss is dominated by radiative losses at the PnC openings on the resonator's central axis. For a given folding angle and folded PnC aperture at the openings, the ratio between stored energy and energy loss increases with L leading to a higher Q. A larger L also leads to smaller SFFR since increasing L brings spurious modes closer to the main peak, consistent with Eqn. 1. On the other hand, shorter resonators will have spurious modes pushed to higher frequencies, causing those modes to be more attenuated as they are closer to the PnC band edge. For a short enough cavity, spurious modes can even be pushed outside the PnC band gap and become significantly attenuated, potentially eliminating all spurious modes inside the band gap. However, such design requires very small L, resulting in a reduced Q of the fundamental mode and increased motional impedance.

The decrease in k_{eff}^2 with increasing L (Fig. 3(c)) is mainly a side-effect of the increase in Q. For the same IDT transducer configuration, scaling the cavity length L does not affect C_m/C_o, where C_m is the motional capacitance of the resonator and C_o is the nominal capacitance of the transducer, since both the mode and electrodes extend equally with L in the non-resonant dimension. When $Q \sim C_o/C_m$, the series and parallel resonance of the mode shift apart, making k_{eff}^2 larger than C_m/C_o. As Q increases, the two resonances move closer together, decreasing k_{eff}^2, which approaches C_m/C_o when $Q(C_m/C_o) >> 1$ [6]. For the devices in this work, $Q(C_m/C_o) \sim$ 0.5-1, a regime where the trade-off between Q and k_{eff}^2 still exists. Consequently, the increase in Q corresponding to increased cavity length L leads to a drop in k_{eff}^2, as observed in simulation.

FABRICATION

Folded PnC resonators were fabricated in MIT's Microsystems Technology Lab using Raytheon's MMIC GaN-on-Si heterostructure, comprised of AlGaN(25 nm)/GaN(1.7 um) grown on (111)-Si using Molecular Beam Epitaxy (MBE). A shallow AlGaN etch was used to remove the 2D electron gas (2DEG) between the AlGaN/GaN layers and allow for transduction in the GaN layer. A 100 nm layer of Ni (used as the gate metal for GaN HEMTs) was then deposited and patterned to define piezoelectric IDTs. The choice of Ni for the electrodes is a departure from conventional Au electrodes found in GaN MMICs, as Au is mechanically lossy and is known to reduce resonator Q. Since these devices are processed side by side with GaN HEMTs, a PECVD Si_3N_4 layer (150 nm) was deposited to passivate the surface and protect the 2DEG channel. A deep Cl_2

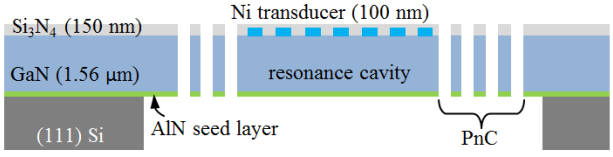

Figure 5: Cross section of MBE GaN resonator on Si.

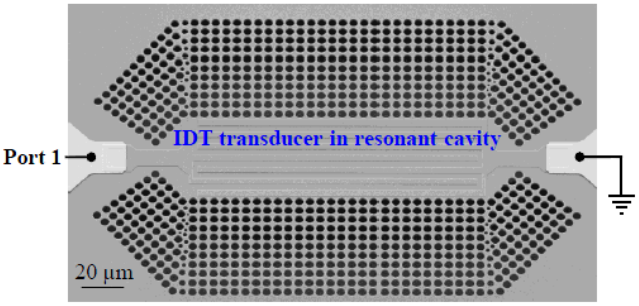

Figure 6: SEM of Device 1. IDT transducers (Ni) are routed into the resonant cavity through the openings. It is connected through vias to the probe pads, which are made of Au/Ti.

GaN etch then defined the PnCs and acoustic cavities. Metal pads (50 nm Ti/300 nm Au) were then connected to the gate electrodes through vias in the passivation layer. Finally, a XeF_2 etch released the resonators from the Si substrate. Fig. 5 depicts the cross section of the final suspended resonator. An SEM of one of the fabricated PnC resonators (Device 1) is shown in Fig. 6, with cavity length L of 157 µm, folding angle θ = 50° and resonance at 516 MHz. This fabrication process is compatible with GaN HEMT technology [7].

EXPERIMENTAL RESULTS AND ANALYSIS

Devices were tested under vacuum in a Cascade PMC200 RF probe system. A standard 1-port S-parameter measurement was performed using an Agilent 5225A Network Analyzer with on-chip open de-embedding structure up to the routing electrodes outside the cavity. The measured 1-port device admittance was fitted to a modified Butterworth-Van Dyke circuit to extract resonance parameters, with a shunt capacitor and resistor used to model the feed-through.

We compare the performance of two devices with resonant dimension defined based on the structure in the simulation in Fig. 3 to demonstrate the behavior and design trade-offs of the folded PnC resonator. Labeled 'Device 1' and 'Device 2', the parameters of these resonators are provided in Table 1. Fig. 7 shows the wide-band and zoomed in (inset) frequency response of Device 1, exhibiting a clean spectrum over >500 MHz range.

Device 2 is identical apart from its cavity length, which is half that of Device 1. The 1-port frequency response of Device 2 is shown in Fig. 8. Reducing the cavity length by 2× decreases Q by 2.5× but improves k_{eff}^2 by 2.3×. This trend is in accordance with simulation (Fig. 3) in which a 4× decrease and 1.6× increase are expected for the same length scaling for Q and k_{eff}^2, respectively.

Table 1: Measured performance comparison of GaN folded PnC resonators.

	θ	a (µm)	L/a	f_o (MHz)	R_m (kΩ)	Q	k_{eff}^2
Dev. 1	50°	5.6	28	516	10	2924	0.10%
Dev. 2	50°	5.6	14	528	30	1160	0.23%

In the interest of scaling to higher frequency, a third folded PnC resonator (Device 3) was demonstrated at 993 MHz, achieving an $f.Q$ product of 3.06×10^{12}. The PnC used for Device 3 has a band gap of from 940 to 1040 MHz. The SEM, frequency response, and fitted parameters for this structure are shown in Fig. 9. The harmonic spurious modes described by Eqn. 1 can be seen more clearly in Device 3, since the frequency difference between the fundamental mode and the first spurious mode is the same as in the case of Devices 1 and 2, but at 993 MHz the fractional difference is smaller.

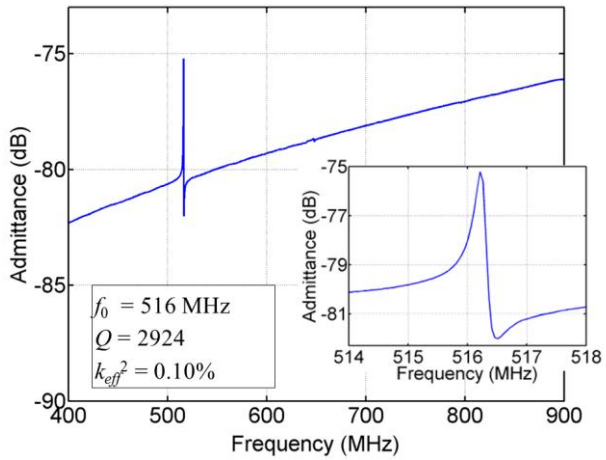

Figure 7: Measured frequency response of Device 1 with wide and narrow sweeps showing spurious-free spectrum.

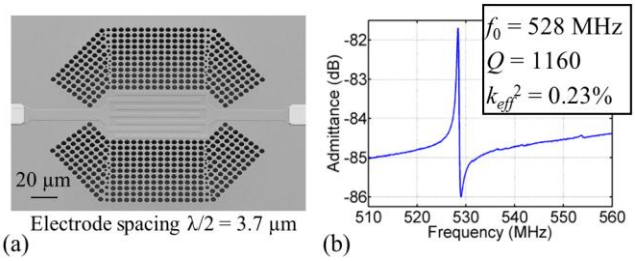

Figure 8: (a) SEM of Device 2, with L/a = 14. (b) Measured 1-port frequency response and fitted resonator parameters.

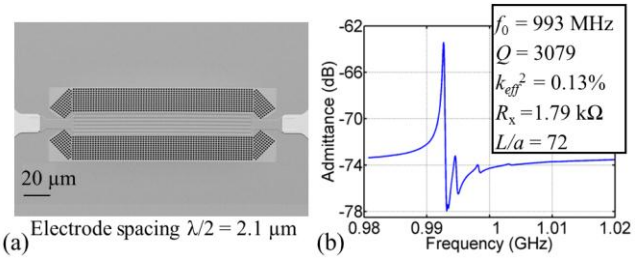

Figure 9: (a) SEM of Device 3 at 993 MHz (a=2.3µm) (b) Measured 1-port frequency response and fitted resonator parameters.

Table 2 lists fundamental resonance frequency, spurious frequencies and their spacings. It can be seen that $\Delta f_{23} = 2\,\Delta f_{12}$ and $\Delta f_{35} = 2\,\Delta f_{13}$, consistent with the prediction based on Eqn. 1. The 2nd harmonic spurious mode in this device appears due to slight misalignment of the IDT electrodes.

Table 2: Spurious modes frequencies and spacings in Device 3.

f_1	f_2	f_3	f_5	f_7
992.7	993.3	994.5	998.1	1003.1
Δf_{12}	Δf_{23}	Δf_{13}	Δf_{35}	Δf_{57}
0.6	1.2	1.8	3.6	5.0

Finally, an IP3 measurement was performed on Device 3 to characterize the device's power handling capability, a critical metric for filter applications. Two interfering tones with same power, spaced at 300 kHz and 600 kHz, were combined to drive the resonator. At the output, the signal at the resonant frequency was detected due the 3rd order nonlinearity of the device. Measurement results and calculated IIP3 are shown in Fig. 10. Input power has been calibrated to represent the power incident onto the device input port. The folded structure PnC resonator exhibits IIP3 of +27.2 dBm, the highest reported in a GaN resonator to date. This is attributed to improved thermal conductance offered by the PnC boundaries relative to tethered structures.

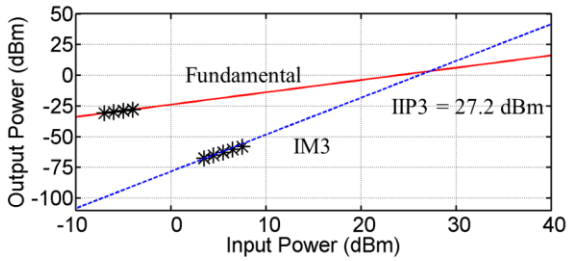

Figure 10: Power handling measurement of Device 3 at 993 MHz, using input tones spaced at 300 kHz and 600 kHz. The IIP3 of +27.2 dBm is the highest reported in GaN resonators to date.

CONCLUSION

We introduce a new RF MEMS resonator using a folded PnC structure to achieve wide band spurious mode suppression. Devices show clean frequency response over a wide bandwidth (>500MHz). At 993 MHz, high *f.Q* product of 3.06×10^{12} was demonstrated, on par with the best results in GaN to date. Furthermore, the device exhibited large power handling of over +27 dBm afforded by improved thermal dissipation in the large-perimeter PnC. This design leverages GaN MMIC technology, providing a low barrier-to-entry solution for monolithic timing and RF wireless communication applications including GHz MEMS front end band pass filters with excellent spurious mode suppression, linearity, and frequency selectivity.

ACKNOWLEDGMENT

The authors thank Brian Schultz and Thomas Kazior at Raytheon for GaN growth and process discussions, and Prof. Steven Johnson at MIT for helpful discussion. This work was funded by DRAPA DAHI Foundry N66001-13-1-4022 and NSF Career EECS-1150493.

REFERENCES

[1] M.F. Su, R. Olsson, Z. Leseman, El-Kady, "Realization of a phononic crystal operating at gigahertz frequencies," *Applied Physics Letters*, 96, 053111 (2010).

[2] N. Kuo, S. Gong, G. Piazza, "Ultra high frequency phononic crystal in silicon carbide," *Solid-State Sensors, Actuators and Microsystems Conference (TRANSDUCERS'11)*, 2486-2489, (2011).

[3] S. Mohammadi, A. Adibi, et al., "High-Q micromechanical resonators in a two-dimensional phononic crystal slab," *Applied Physics Letters*, 94, 051906, (2009).

[4] S. Mohammadi, A. Adibi, "Waveguide-based phononic crystal micro/nanomechanical high-Q resonators," *J. Microelectromechanical Systems*, 21, 379-384, (2012).

[5] C.-Y. Huang, J.-H. Sun, T.-T. Wu, "A two-port ZnO/Silicon Lamb wave resonator using phononic crystals," *Applied Physics Letters*, 97, 031913, (2010).

[6] R. Ruby, et al., "After 60 years: A new formula for computing quality fact or is warranted," Ultrasonics 2008, pp. 431-436.

[7] L.C. Popa, D. Weinstein, "Switchable piezoelectric transduction in AlGaN/GaN MEMS resonators," *Solid-State Sensors, Actuators and Microsystems (TRANSDUCERS'13)*,2461-64, (2013).

CONTACT Siping Wang; spinwang@mit.edu

INVESTIGATION OF ENERGY DISSIPATION IN LOW FREQUENCY VIBRATORY MEMS DEMONSTRATING A RESONATOR WITH 25 MINUTES TIME CONSTANT

S.A. Zotov, B.R. Simon, G. Sharma, J. Han, I.P. Prikhodko, A.A. Trusov, A.M. Shkel
MicroSystems Laboratory, University of California, Irvine, CA, USA

ABSTRACT

We report a conventionally batch micromachined silicon tuning fork MEMS resonator, with ultra-low energy dissipation. The dissipation time constant of 25 minutes was experimentally achieved by using a test device with natural frequency of 570 Hz and Quality factor of 2.7 million. This low level of energy dissipation was accomplished through identification and minimization of the dominating dissipation mechanisms. Results of the experimental investigation lead to the formulation of practical design guidelines and tradeoffs for low frequency resonant devices.

INTRODUCTION

Dissipation of energy is a fundamental characteristic of a resonance system which defines a limit of performance. For some devices, such as 1-D oscillators, frequency multiplied by Q-factor, f×Q, is the figure of merit [1]. For others, such as Coriolis Vibratory Gyroscopes (CVG), the dissipation time constant, τ, is a parameter of interest. Macro-scale CVGs with size on the order of several inches can achieve a dissipation time constant of tens of minutes and Q-factor in the tens of millions, with bias instability on the order of 10^{-5} deg/hr [2]. Additionally, a high dissipation time constant provides advantageous mechanizations, such as continuous whole angle operation uninterrupted by power failures (i.e., electromagnetic impulse), which is not possible using optical devices, such as Fiber Optic Gyroscopes (FOGs) and Ring Laser Gyroscopes (RLGs).

Low dissipation vibratory systems, especially systems with a high time constant, are generally associated with large spatial dimensions. It is often assumed that conventionally batch fabricated silicon MEMS resonators are not suitable for applications where large dissipation time is necessary due to their small mobile masses. However, state of the art MEMS devices have demonstrated time constants up to three minutes in recent reports, [3], [4].

Unlike mature RF resonators, there is a gap in the literature in the field of low dissipation micromachined vibratory gyroscopes. In this paper, an ultra-low dissipation resonator is reported and used in an experimental study of design trade-offs and formulation of practical design guidelines. The fabricated prototype has demonstrated a time constant of ~ 1/2 hour and Q-factor of 2.7 million at a natural frequency of 570 Hz, Fig. 1, as well as a high dissipation time constant and high value of Q-factor throughout a wide temperature range, from -40 °C to 100 °C.

For low frequency resonators there are five primary energy loss mechanisms. In order of importance, these are: viscous damping, support (anchor) loss, loss due to structural asymmetry, ThermoElastic Damping (TED), and electrical damping. These mechanisms comprise the total Q-factor of the device [5]:

$$\frac{1}{Q_{total}} = \frac{1}{Q_{Viscous}} + \frac{1}{Q_{Anchor}} + \frac{1}{Q_{Asym}} + \frac{1}{Q_{TED}} + \frac{1}{Q_{El}} + \frac{1}{Q_{Other}}. \quad (1)$$

Throughout this paper, each of these five dissipation mechanisms are systematically investigated, and the impact of each is quantitatively assessed. It is also experimentally validated that any additional damping mechanisms, Q_{Other}, are negligibly small for low frequency resonators.

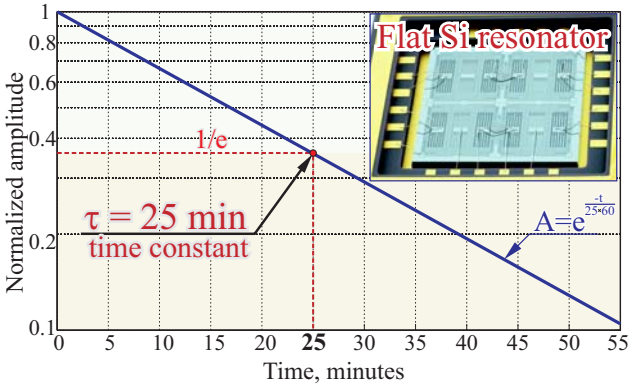

Figure 1: Experimental characterization of vacuum-sealed Si resonator using the amplitude decay method, revealing a dissipation time constant of 25 minutes (Q-factor of 2.7 million at 570 Hz natural frequency).

TEST-BED RESONATOR

To support this theoretical investigation, a specially designed resonator was fabricated. This resonator was designed to minimize energy dissipation from viscous damping, thermoelastic damping, and support loss. With these three mechanisms sufficiently reduced, a detailed investigation into electrical damping of the detection system is conducted.

To alleviate support losses, a tuning fork architecture was employed. The proposed tuning fork resonator comprises of two coupled tines (4 mm by 4 mm each), each driven in opposite directions, or anti-phase resonance. Each tine includes differential lateral comb electrodes for capacitive detection, and differential lateral comb electrodes for electrostatic excitation of the anti-phase mode. The anti-phase mode of resonator minimizes the net reaction force applied to the substrate, providing both rejection of common-mode external accelerations, and reduction of energy dissipation from the vibrating structure. Any in-phase component of motion is due to fabrication imperfection and is considered parasitic; to reduce undesirable in-phase motion the design includes non-differential parallel plate capacitors for dynamic balancing by modulation of stiffness through the negative electrostatic spring effect, Fig. 2. Also, the parallel plate electrodes allow for the simultaneous and independent tuning of operational (resonance) frequency and Q-factor through electrical damping. The fabrication of the prototype was performed using an in-house, wafer-level, single-mask process. Devices were fabricated using Silicon-on-Insulator (SOI) wafers with a 100 µm single crystalline silicon device layer, a 5 µm buried oxide layer, and a 500 µm handle wafer, Fig. 2. After wafer fabrication and dicing, sensors were attached to a ceramic DIP-24 package through the use of a UniTemp RSS-160 solder reflow system, and a low-stress die attachment procedure. The attachment was made using an eutectic solder comprised of 80 % gold and 20 % tin. Eutectic Au/Sn solder was used in this process for three main reasons: 1) it is a low out-gassing material, well suited for vacuum sealing with getter, 2) it creates a strong, rigid attachment to the package, preventing spurious degrees of freedom, and 3) it is capable of surviving high temperatures. Due to mismatches in the thermal properties between

9781940470016/HH2014/$25©2014TRF
DOI 10.31438/trf.hh2014.20

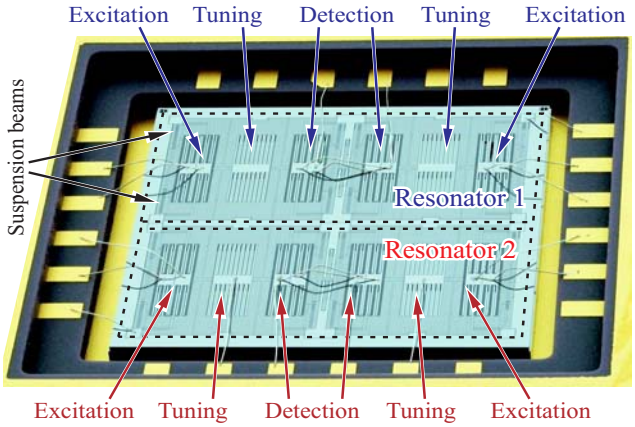

Figure 2: Optical photograph of the test-bed resonator, before vacuum sealing with getter material.

the package and die, changes in temperature can induce stress within the die, creating structural asymmetry and increasing the dissipation of energy through the substrate, [4]. This effect is minimized by reducing the die attachment area, as described in [6].

We demonstrated a tuning fork design with a time constant of 2 minutes, in [4]. The prototype was fabricated without reduction of the die attachment area, leading to energy dissipation through the substrate. Evidence is shown in Fig. 5a, where electrical tuning is able to increase the Q-factor of the device by increasing the structural symmetry, [4]. In contrast, the design of the tuning fork proposed in this paper took full advantage of the reduction of the die attachment area. As shown in Fig. 5b, any tuning voltage applied to the resonant masses increase the asymmetry, resulting in a reduction of Q-factor.

VISCOUS DAMPING

Viscous damping is a first major contributor to energy loss in MEMS devices, especially for low frequency resonators. For the tuning fork demonstrated in this work, the device has a Q-factor of 4 in air, before vacuum sealing. The first step to raising the Q-factor is to provide vacuum, and ensure a stable pressure environment through the life of the sensor. To achieve this, the package of the device was sealed under high vacuum (1 μTorr). A thin-film getter material was sealed inside the packaged cavity in order to absorb any residual gases that may be present after the vacuum packaging process, compensating for out-gassing.

Glass lids were prepared using 4 inch wafers of D263 glass, specifically chosen to match the coefficient of thermal expansion of the ceramic package, 7.1 ppm/K. These wafers were patterned with a thin layer of chrome and gold, 50 nm and 500 nm, respectively.

The vacuum-sealing process was completed using a model 3150, high vacuum furnace from SST International. Before sealing, a solder preform in the shape of a frame was tacked to each package at the interface of package and lid. The material of the solder frame was identical to the die attachment process: 80/20 Au/Sn solder. Both package and lid were then separately loaded into the vacuum furnace, and vacuum sealed after several hours of prebaking, using the procedure as described in [6].

THERMOELASTIC DAMPING

Thermoelastic damping is a fundamental source of damping for any vibratory structure. It is a material-dependent loss mechanism that arises from the coupling of internal stress to the thermal domain through the coefficient of thermal expansion.

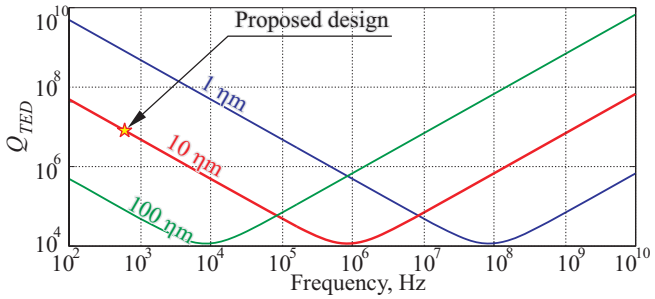

Figure 3: Thermoelastic Q-factor versus frequency for silicon springs of three different widths (1, 10, and 100 μm).

Vibrations of flexing suspension elements create a stress gradient across its cross-section, which in turn induces a thermal gradient.

After this thermal gradient is equalized, resonant energy is reduced in the system, converting to entropy, [5]. Given a suspension beam that is experiencing sinusoidal flexing, energy loss is maximized (or Q-factor minimized), when choosing a mechanical resonance frequency with period that matches the time required for energy to flow from one side of the suspension beam to the other. This phenomenon can be analytically described by Zener's equation [7], which is plotted in Fig. 3 for silicon beams of various widths (1-100 μm). Through choice of beam width, a trade-off exists between thermoelastic damping and structural asymmetry; thin beams increase thermoelastic Q-factor, but reduce structural symmetry, which directly influences losses through the substrate, as detailed in the following sections. In this work, a suspension beam element of 10 μm in width is used.

The mechanical frequency that maximizes thermoelastic energy loss for beam widths of 10 μm for silicon is roughly 900 kHz, Fig. 3. To minimize the thermoelastic damping effect, the period of the mechanical resonance must be separated from the thermal period as far as possible. This can be accomplished by changing the material or physical dimensions of the resonator.

While the above model is valid for a simple beam, it can only serve as an approximation for complex structures. For this reason, finite element modeling was conducted for the design using COMSOL Multiphysics, revealing a thermoelastic Q-factor of 5.7 million at a low operational frequency of 570 Hz.

SUPPORT LOSS

Support loss, or anchor loss, is a form of energy loss due to stress waves propagating away from the resonant structure, though the anchors and into the substrate and package of the device. Designing devices that consist of two or more separate proof masses operating in an anti-phase mode shape is one method of reducing this effect, assuring the effective reaction forces to be equal to zero. While this can greatly reduce the effects of support loss, it does not eliminate it completely.

To gauge the effects of anchor loss for the given design, a 3-D FEA model was created containing the device, substrate, and a Perfectly Matched Layer (PML). The PML represents an infinite boundary, behaving as an acoustic absorption layer. Acoustic waves that enter the PML attenuate before they can be reflected back into the model, Fig. 4(a). The footprint of the substrate is 4.1 x 8.1 mm. In this study, a PML beneath the substrate is chosen to absorb one wavelength of stress, transmitted at the resonant frequency of the vibratory modes. The Q-factor of the anti-phase mode is calculated to be $Q_{Anchor}=5.67\times10^6$. Mesh elements, varied from 114×10^3 to 218×10^3, confirm the convergence of the model with a tolerance of 1 %, Fig. 4 (b).

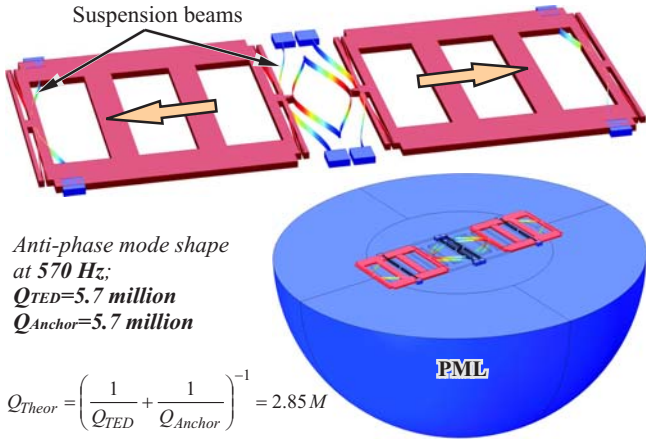

a) 3-D anchor loss model, highlighting tuning fork and PML layer.

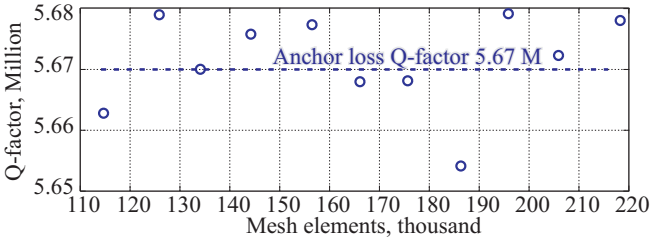

b) Dependence of Q-factor for anti-phase mode on the number of elements.

Figure 4: Finite element modeling of energy dissipation through the substrate (anchor loss) reveals a Q-factor of the anti-phase mode of 5.67×10^6, illustrating the theoretical Q-factor limit of 2.85 million for the anti-phase vibratory mode of the tuning fork.

LOSS DUE TO STRUCTURAL ASYMMETRY

In the previous section, the calculated support loss is for an ideal anti-phase vibratory mode. While this result offers the minimum support loss, it does not account for any fabrication imperfections within the structure that create variances in the nominal mass and stiffness values. Any asymmetry between the two resonant masses has the potential to induce additional energy loss through the anchor due to unbalanced motion. Despite driving the resonator in anti-phase motion, this structural asymmetry couples the anti-phase motion into in-phase motion. This mechanism, as well as a technique of dynamically balancing tuning forks to alleviate substrate losses, is theoretically and experimentally studied in [4].

A voltage applied to the tuning electrode of each tine was used to tune the dissipation time constant and quality factor of the resonator by disturbing the dynamic balance of the structure, Fig 5. While the design presented previously in [4] required additional tuning to achieve dynamic balance, Fig 5a, the proposed design is initially well balanced, Fig 5b. For the design studied in this paper, the experiment reveals that any tuning of stiffness in the left or right tines results in additional misbalance, reducing the Q-factor and dissipation time constant, Fig 5b.

ELECTRICAL DAMPING

Electrical damping can occur as a result of interference between electrical components when using electrostatic detection. Usually, this affect is minimal, which allows other energy loss mechanisms to dominate. However, for low dissipation resonators, it can be beneficial for independent tuning of Q-factor. Existing methods of Q-factor tuning couple inseparably Q-factor and

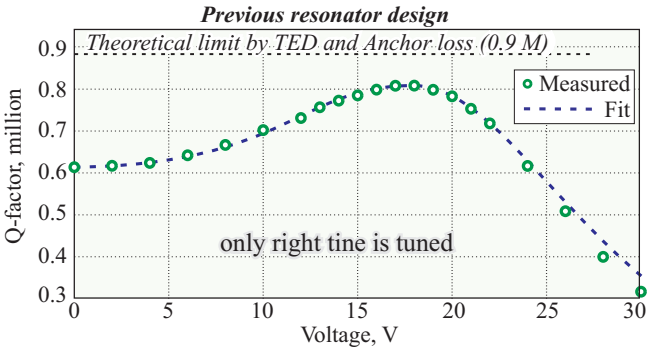

a) First generation resonator reveals a stiffness misbalance between the right and left tines of 1.5 % before tuning (see [4] for details).

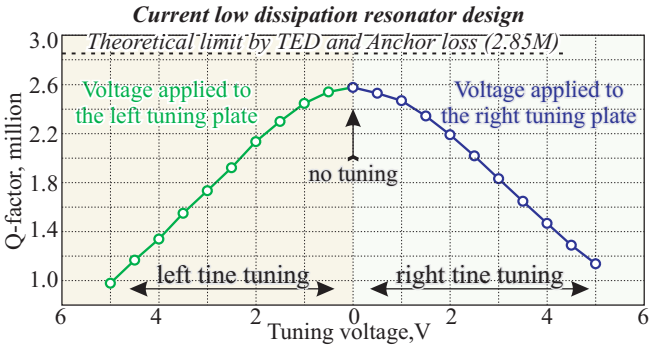

b) The low dissipation resonator, as-built, is a well balanced device, measured with a precision of less than 20 ppm.

Figure 5: Characterization of the stiffness matching effect on the resonator's Q-factor by measuring Q-factor of the anti-phase mode versus tuning voltage applied to the left and right tines.

frequency through the use of an electrostatic spring, inducing a momentum imbalance [4]. In contrast, when electrical damping is introduced, only the Q-factor is affected. This technique is useful for gyroscopes, especially when operated in whole-angle mode, where independent tuning of frequency and Q-factor is critical. However, this phenomenon imposes additional restrictions on the parameters of the detection system, specifically the electrical gain of the detection pick-off. A trade-off exists between the pick-off gain and Q-factor tuning ability, which is experimentally demonstrated in this section.

To demonstrate the phenomena, the packaged resonator was mounted on a two stage PCB, Fig. 6. The top stage of the electronics is comprised of front-end transimpedance amplifiers, while the bottom stage stabilizes input voltages and creates the device excitation signals. Electrostatic actuation and capacitive detection were employed along with the ElectroMechanical Amplitude Modulation (EAM) technique to eliminate parasitic feed-through. Instead of a DC bias, an AC carrier voltage with variable amplitude at 52 kHz frequency was applied to the mobile masses. The anchored differential sense-mode comb-electrodes were connected to the inputs of a two-stage differential transimpedance amplification circuit implemented on the PCB, Fig. 6. All signal processing is performed in real-time using an FPGA-based lock-in amplifier from Zurich Instruments.

To show the influence of the detection system on the Q-factor of the tuning fork, Q-factor was measured versus carrier amplitude from 0.3 V to 6 V for four different feedback resistors (24, 46, 91, and 196 kOhm), along with feedback capacitors of 10 pF. The experimental results demonstrate that Q-factor is reduced as carrier

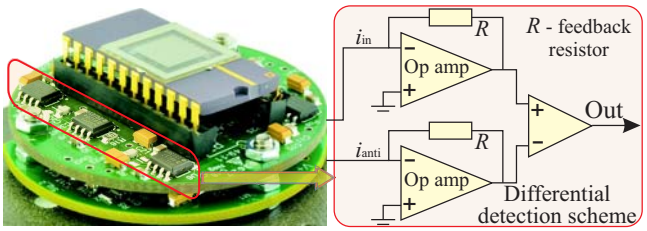

Figure 6: Photograph of a packaged differential tuning fork assembled with signal conditioning PCBs, realized with signal transimpedance detection. The feedback capacitor is not shown.

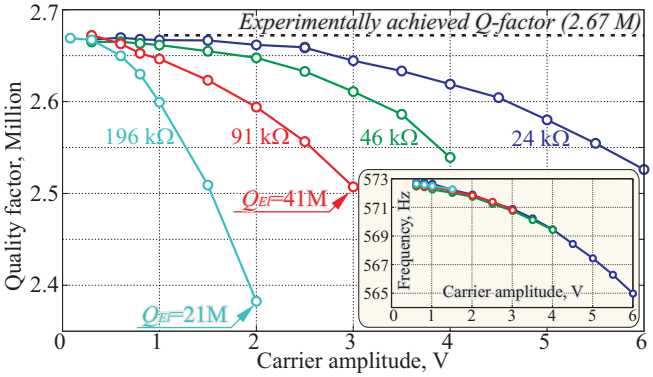

Figure 7: Experimentally measured Q-factor vs. carrier amplitude for various feedback resistors. Q-factor lowers as carrier amplitude increases. (Inset: natural frequency vs. carrier amplitude for the same experiment).

amplitude is increased, and this effect is more pronounced for large values of feedback resistance. Considering feedback resistance is directly correlated to electronic gain, increasing this gain has the potential to be a limiting mechanism of Q-factor. This effect is demonstrated in Fig. 7, which also displays the natural frequency of the resonator for each data point. While the natural frequency is influenced by the amplitude of the carrier voltage, there is no influence from changes in the feedback resistance. By using formula (1), electrical Q-factor, Q_{El}, was estimated for different feedback resistors, R, and carrier voltage, V. For R=196 kOhm and V=2 Volts, Q_{El}=22 million. For R=91 kOhm and V=3 Volts, $Q_{El.}$=41 million, Fig. 7. This phenomenon provides a mechanism for an independent tuning of frequency and Q-factor.

Characterization of Q-factor and dissipation time constant at different temperatures, over a range from −40 °C to +100 °C, reveals a time constant of over 14 minutes (Q-factor = 1.65 million), with maximum value of over 25 minutes (Q-factor = 2.67 million) for temperatures below 20 °C, Fig. 8. In addition, using the same balancing technique as described in section "Loss due to structural asymmetry" and in [4], it was confirmed that across various temperatures, ranging from −40 °C to +100 °C, the resonator remained dynamically balanced.

The experimentally measured maximum Q-factor of 2.67 million was achieved using a low electrical dissipation setup of a 24 kΩ feedback resistor and carrier amplitude of 0.3 Volts, Fig. 7. At the same time, the contribution of both TED and anchor loss equally limit the Q-factor to 5.7 million, providing the theoretical limit of 2.85 million, which is 9% larger than the experimentally measured value. This discrepancy can be attributed to additional, unaccounted for damping mechanisms: residual viscous damping, electrical damping, surface loss, loss due to structural asymmetry, and other energy loss mechanisms, described in [5]. Using formula (1), with Q_{total} = 2.67 million and Q_{anchor} = Q_{TED} = 5.7 million, the unaccounted for Q-factor can be calculated to be 43 million.

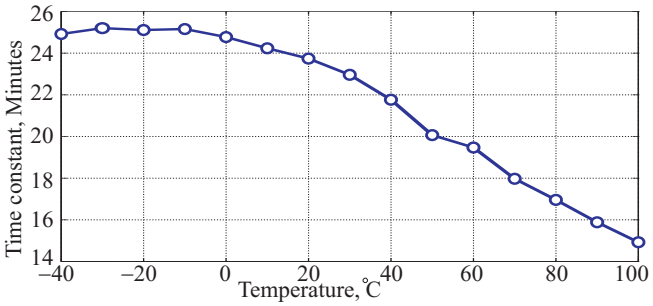

Figure 8: Measured dissipation time constraint versus temperature for a vacuum sealed tuning fork resonator.

CONCLUSION

This paper presents a conventionally batch-fabricated, vacuum-packaged, silicon MEMS resonant device with a time constant of 25 minutes and a quality factor of 2.67 million at a natural frequency of 570 Hz. The reported time constant is comparable to that of the macro-scale hemispherical resonator gyroscope, bridging the gap between flat MEMS and 3-D quartz devices. The resonator demonstrates a high dissipation time constant and a high Q-factor throughout a wide temperature range, from −40 °C to +100 °C. These results are achieved by specifically targeting and minimizing influences of the five primary sources of damping: viscous damping, support (anchor) loss, loss due to structural asymmetry, ThermoElastic Damping (TED), and electrical damping. We also experimentally validated that the detection system can be a measurable source of energy dissipation. Finally, we demonstrated that the Q-factor can be tuned independently of other system parameters, such as frequency.

ACKNOWLEDGMENT

This work was supported by DARPA under grant N66001-12-C-4035. Authors would like to thank Dr. Flavio Heer of Zurich Instruments AG as well as David Muhs, Pierino Zappella of SST International. The devices were designed and tested at the MicroSystems Laboratory, UC Irvine.

REFERENCES

[1] J.E-Y. Lee and A.A. Seshia, "Square wine-glass mode resonator with a Q-Factor of 4 million," IEEE Sensors, Lecce, Italy, 2008, pp. 1257 – 1260.

[2] D.M. Rozelle, "The hemispherical resonator gyro: from wineglass to the planets," in: Proc. of the 19th AAS/AIAA Space Flight Mechanics Meeting, Feb. 2009, pp. 1157 – 1178.

[3] S.A. Zotov, A.A. Trusov, and A.M. Shkel, "Experimental demonstration of a wide dynamic range angular rate sensor based on frequency modulation," IEEE Sensors, Limerick, Ireland, 2011, pp. 577 – 580.

[4] A.A. Trusov, S.A. Zotov, and A.M. Shkel, "Electrostatic Regulation of Quality Factor in Tuning Fork MEMS," IEEE Sensors, Limerick, Ireland, 2011, pp. 20 – 23.

[5] V.B. Braginsky, V.P. Mitrofanov, and V.I. Panov, "Systems with small dissipation," Univ. Chicago Press, 1985, p. 145.

[6] I.P. Prikhodko, B.R. Simon, G. Sharma, S.A. Zotov, A.A. Trusov, and A.M. Shkel, "High and Moderate Level Vacuum Packaging of Vibratory MEMS," IMAPS, Orlando, FL, 2013, pp. 705–710.

[7] C. Zener, "Internal friction in solids I: Theory of internal friction in reeds," Phys. Rev., vol. 52, no. 3, pp. 230 – 235.

CONTACT

*S.A. Zotov, email: zotov.sergei@gmail.com

PHASE NOISE REDUCTION IN AN OSCILLATOR THROUGH COUPLING TO AN INTERNAL RESONANCE

D.A. Czaplewski[1], B.S. Strachan[2], S.W. Shaw[2], M.I. Dykman[2] and D. Lopez[1]*
[1]Argonne National Laboratory, Argonne, Illinois, USA
[2]Michigan State University, East Lansing, Michigan, USA

ABSTRACT

In this paper, we describe an oscillator, operating at room temperature that can be operated in a condition of internal resonance, where a driven, in-plane mode of the MEMS frequency selective resonator interacts with a torsional mode, resulting in 70 dB decrease in phase noise at a 1 Hz offset as compared to the oscillator operating in driven mode alone. The resonator element is a clamped-clamped beam where the primary mode of oscillation is an in-plane flexural mode, which can be driven at a frequency where vibrational energy is coupled to a higher frequency torsional mode. The coupling to the torsional mode stabilizes the vibrational frequency of the primary mode, resulting in a measured phase noise of -90 dBc at 1 Hz offset and an Allan deviation of 4×10^{-9}. These oscillators show similar behavior to quartz crystals and could be explored for use in timing applications where, currently, single mode resonator micro- and nano-mechanical oscillators are being used in applications such as clocks and frequency standards. We present a theoretical model that qualitatively explains the behavior and demonstrates that phase noise can be greatly reduced at the internal resonance condition.

INTRODUCTION

Oscillators are a key component in practically all electronic devices, serving as clocks for logic circuits, frequency standards for heterodyning communication signals, timing applications, and as sensors [1-3]. Currently, most commercial oscillators are fabricated from quartz crystals, which are macro-scale, cannot be integrated with the CMOS circuitry, and consume a relatively large amount of power. Microelectromechanical (MEMS) oscillators are being produced as alternatives to quartz oscillators primarily because they offer a path to create a monolithic structure with all circuit elements fabricated on a single silicon chip using fabrication techniques that are compatible with CMOS processing [4]. Commercial MEMS oscillators are starting to show up in uses such as gyroscopes and timing applications. Most MEMS oscillators operate in the linear regime of the resonator element; however, as the dimensions of the MEMS are reduced to keep in step with the CMOS circuitry, the linear operating range is reduced [5]. MEMS oscillators have typically not operated in the non-linear regime because non-linear oscillators experience increased frequency noise due to amplitude-frequency noise conversion through the amplitude dependence of frequency, generically modeled by a cubic (Duffing) restoring force [6]. In spite of these detrimental effects, it has been recently demonstrated that non-linear resonator dynamics can be used to reduce phase noise in oscillators [7-9]. We have previously showed that a non-linear oscillator operating at an internal resonance condition shows improvement in frequency stability by a factor of over 300 [9]. In this paper, we present a detailed study of the phase noise reduction achievable in the current MEMS devices and we introduce a model to describe the mechanism responsible for this reduction in phase noise.

DESIGN, FABRICATION AND OPERATION

The resonators are fabricated using the SOIMUMPS process from MEMSCAP with a 10 μm thick silicon layer. The resonator consists of 500 μm long, parallel, doubly clamped beams attached at their center to ensure that the three beams move together as a single element (Fig. 1).

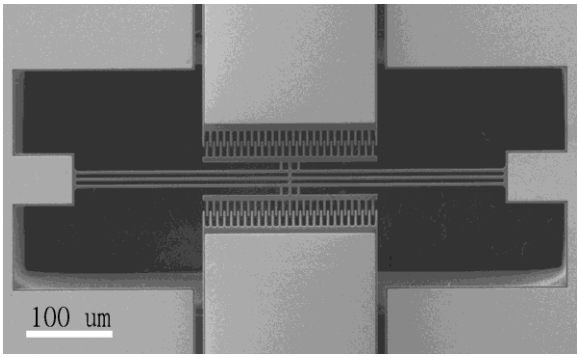

Figure 1: Scanning electron micrograph of the oscillator showing the comb drives for actuation and signal transduction.

Attached to the center of the beam are two comb drives. One comb drive is used for driving the resonator while the other comb drive is used to transduce its response. The total capacitance of each comb drive is calculated to be 50 fF. The primary mode of oscillation is an in-plane flexural mode with a linear response at a frequency of approximately 65 kHz. The second and third order modes are a flexural out-of-plane and torsional mode respectively, both with a modal frequency of approximately 200 kHz [9]. The electronic operation of the device has been described previously [9] and will be summarized briefly. An AC voltage is applied to one of the comb drives, which causes the beam to vibrate at the frequency of the AC voltage. The motion of the beam causes a changing capacitance in the other comb drive, which generates an AC current at the output of the comb drive. The current is passed through a current preamplifier, where it is filtered by a band pass filter between 10 kHz and 1 MHz. The output of the preamplifier is sent through a transimpedance amplifier to convert the current into a voltage. The voltage output is phase shifted and used as the reference in a phase feedback oscillator [3], where the drive voltage amplitude is held constant, independent of the oscillator amplitude. The output from the transimpedance amplifier is also used to measure the phase noise and the Allan deviation of the oscillator through a Zurich UHFLI lock-in amplifier. The phase noise is measured by the power spectral density (PSD) of the in-phase and quadrature components of the voltage signal at a specified frequency. Experimentally, the reference frequency of the lock-in amplifier is set so that the phase of the measured signal does not deviate for a short period of time. Then the PSD is acquired over a period of time, the inverse of which, defines the frequency resolution of the spectrum. In a second experiment, the Allan deviation is calculated using a running average of the frequency data recorded as a function of time.

9781940470016/HH2014/$25©2014TRF
DOI 10.31438/trf.hh2014.21

From an experimental perspective, to achieve oscillation, the oscillator needs to be entrained by sweeping the drive voltage from a start frequency to the desired frequency where the drive can be switched to the phase feedback circuit. Without sweeping the applied voltage, the oscillator will not be entrained. Once in oscillation, the drive amplitude and phase are used to tune the frequency of the oscillator.

In our system, an internal resonance occurs when the frequency of the primary mode equals 1/3 of the frequency of the torsional mode (1:3 mode coupling). In this situation the coupling between modes acts as a *mechanical negative feedback* responsible for stabilizing the frequency of the resonator [9].

RESULTS

Over a range of operating parameters the system is bi-stable, with one operating condition dominated by the primary mode and the other having two modes active via the internal resonance. To determine the stabilization effect the internal resonance condition has on the oscillator, the phase noise of the oscillator outside and inside the internal resonance condition is measured. The oscillator is set to operate with a 100 mV AC signal and the phase noise of the oscillator is measured using the lock-in amplifier. The phase noise performance of the self-sustained oscillator in and out of the internal resonance condition can be seen in Fig. 2a. When the oscillator is operating outside internal resonance, the phase noise at 1 Hz offset is approximately -20 dBc (using an 8th order, low pass filter and 100 Hz bandwidth for the lock-in). The phase noise shows 1/f^4 behavior, indicative of frequency random walk. This result is the typical response from a non-linear oscillator where the spectrum is dominated by amplitude-frequency noise resulting from the cubic term in the restoring force.

To measure the effect of the internal resonance condition, the frequency of the oscillator is changed so that the internal resonance condition is met, for this oscillator, at 66520 Hz. The phase noise of the oscillator working at internal resonance is shown in Figure 2a. The phase noise at a 1 Hz offset is approximately -90 dBc (using an 8th order, low pass filter and 10 Hz bandwidth for the lock-in), a reduction of 70 dB over the noise measured outside of internal resonance. The data shows slopes of 1/f^2 and 1/f^6. The slope of 1/f^2 is from the Leeson effect suggesting that the oscillator noise is limited by the noise of one of the amplifiers in the feedback circuitry [10], which indicates that by improving the experimental setup the noise can be reduced even further. From measurements of frequency data as a function of time, the Allan variance was calculated inside and outside the internal resonance condition (Fig. 2b). Frequency stability of 4×10^{-9} at a characteristic time of 10 s can be easily achieved with the device. For timescales above this, the data is limited by the random walk of the oscillator.

THEORY

A fundamental understanding of the oscillator phase noise is the key to identifying the ultimate frequency stabilization achievable by coupling resonator modes through an internal resonance. We have developed a non-linear model to describe the mechanism that reduces the phase noise of the primary mode of the oscillator when it couples to the higher frequency mode. The model is a standard closed-loop oscillator with a frequency selective element consisting of two electro-mechanical vibration modes with a 1:3 frequency ratio between the driven and secondary modes, and these modes are coupled through nonlinear electromechanical effects that arise from finite mechanical deformations.

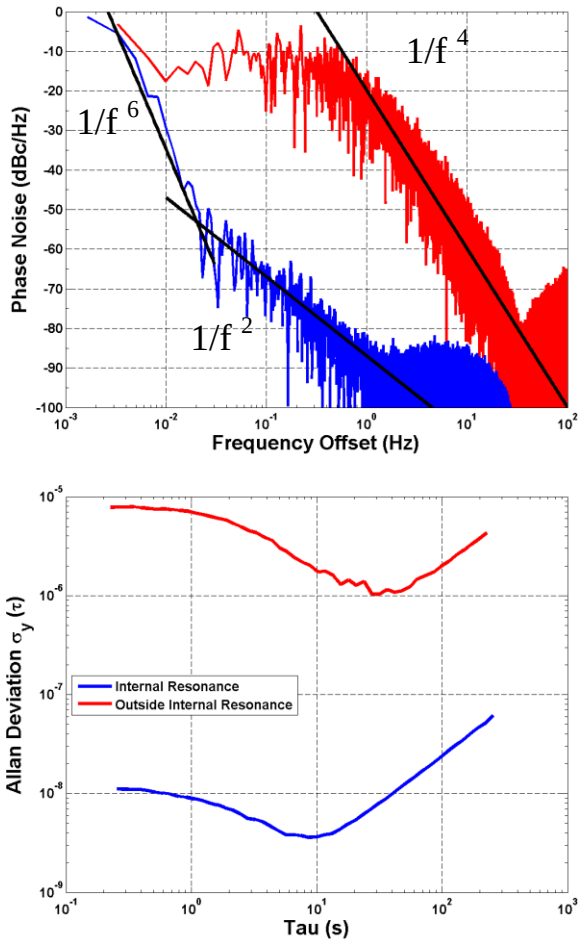

Figure 2: a) Phase noise data from the oscillator operating both outside and inside the internal resonance condition. The change in phase noise is expected from the model of the system. b) A plot of the Allan Deviation away from internal resonance and at internal resonance for different characteristic times, τ. At internal resonance, the minimum Allan Deviation, 4x10^{-9}, occurs at a characteristic time of 10s. For greater times, the random walk of the oscillator dominates.

The resulting model can be understood as a specific case of a generic two-mode system with non-linear coupling that promotes energy transfer between modes [5]. Additive and multiplicative noise sources are included for both modes, and the feedback loop is modeled using a phase shifter and an amplifier operating in its saturated regime. Using standard perturbation methods, one can derive expressions for the dynamics of the slowly varying amplitudes and phases of the two modes in the closed loop system. Solution of the steady-state operating conditions shows a parameter range where the response is bi-stable, with one stable operating condition dominated by the primary mode and the other involving both internally resonant modes. By linearizing the model about these steady states we can compute and compare the spectrum of the oscillator phase fluctuations and investigate the manner in which system parameters and various noise sources contribute to the phase noise of the oscillator.

For numerical investigations of the model, we employ generic parameters that demonstrate the behavior of interest, since the full set of device system parameters is yet to be determined. White noise with a constant intensity is assumed for all sources, and the intensity for the primary mode is taken to be two orders of magnitude larger than that for the second mode, due to effects of the amplifier, which acts directly on the primary mode. Figure 3a shows the oscillator frequency ω_0, normalized by 1/3 of the second mode frequency, versus the amplifier saturation amplitude *F* (proportional to the driving voltage). As *F* is increased, ω_0 initially increases until it becomes close to 1/3 of the secondary mode frequency ω_2, initiating the internal resonance. Through the internal resonance region, the oscillator frequency remains entrained close to this value (red curve), while the frequency of an oscillator operating without internal resonance would continue its upward trend, in the bi-stable region and beyond (black curve). Note that hysteresis is observed when F is swept up and down.

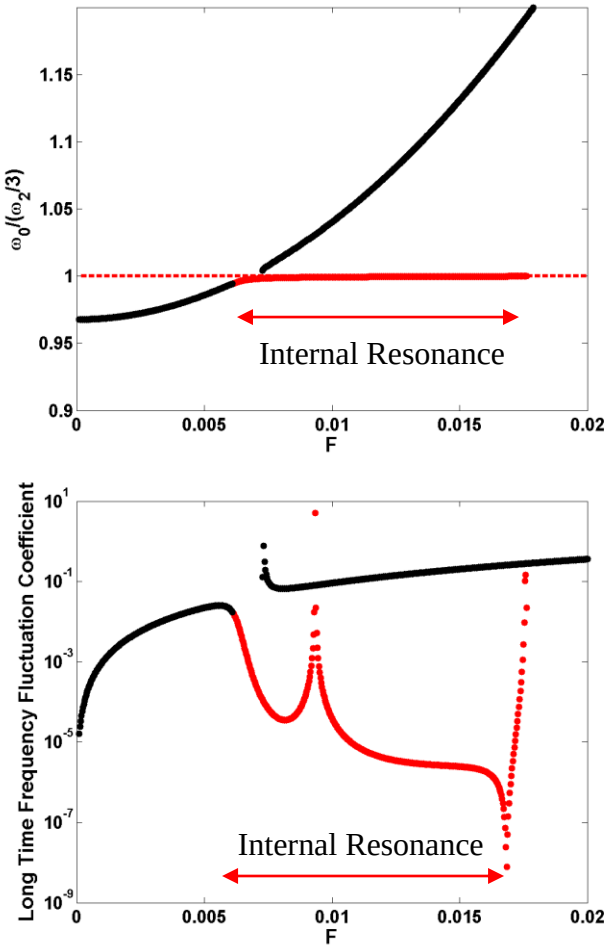

Figure 3: Results obtained from the two-mode oscillator model. a) Normalized oscillator frequency vs. the amplifier saturation amplitude F. As F increases the oscillator frequency increases monotonically along the single mode response (black curve), and remains very close to 1/3 that of the secondary mode when operating with internal resonance (red curve). b) Magnitude of the long term phase diffusion coefficient vs. F. The red curve corresponds to the internally resonant operating condition, while the black curve is from the single mode operating condition. The observed reduction in phase noise due to the internal resonance is consistent with the experimental results reported in [9].

Figure 3b shows the computed magnitude of the long term phase diffusion coefficient versus *F* over the relevant parameter range. In the range of bi-stability, aside from a narrow peak, the phase noise is reduced by several orders of magnitude when operating with internal resonance, as compared to that without internal resonance. These results are consistent with experimental results presented in [9].

The analysis indicates that the oscillator phase noise is not limited by the phase noise of the primary mode, as is the case with single mode oscillators. In order to utilize this predictive analysis for a given device, one must have values for the system parameters and information about the spectrum of various noise sources, work that is underway for the present device.

CONCLUSION

We present data showing that by operating an oscillator at a frequency where the primary mode of the resonator couples to a higher frequency mode (internal resonance condition), the phase noise of the oscillator can be reduced by orders of magnitude. Characterization of the oscillator shows behavior consistent with a nonlinear two-mode resonator as the frequency selective element. A coupled-mode oscillator model using Duffing-like behavior qualitatively predicts this behavior. We envision this approach being expanded to other oscillator types and modes to provide a means to stabilize the frequency response of oscillators.

ACKNOWLEDGEMENTS

The authors would like to thank Dario Antonio for helpful discussions. This work was performed in part at the Center for Nanoscale Materials, a U.S. Department of Energy, Office of Science, Office of Basic Energy Sciences User Facility under Contract No. DE-AC02-06CH11357. The submitted manuscript has been created by UChicago Argonne, LLC, Operator of Argonne National Laboratory ("Argonne"). Argonne, a U.S. Department of Energy Office of Science laboratory, is operated under Contract No. DE-AC02-06CH11357. The U.S. Government retains for itself, and others acting on its behalf, a paid-up nonexclusive, irrevocable worldwide license in said article to reproduce, prepare derivative works, distribute copies to the public, and perform publicly and display publicly, by or on behalf of the Government. The MSU work on this topic is supported by the DARPA MTO DEFYS program and by NSF grant 1234067.

REFERENCES:

[1] J. T. M. van Beek and R. Puers, *J. Micromech. Microeng.* **22** 013001 (2012).
[2] Y. T. S. Yang, X. L. Feng, K. L. Ekinci, & M. L. Roukes, *Nano Lett.* **6** 583 (2006).
[3] R. S. Decca, et al. *Phys. Rev. Lett.* **94** 240401 (2005).
[4] G. Piazza, V. Felmetsger, P. Muralt, R. H. Olsson and R. Ruby, *MRS Bull.* **37** 1051 (2012).
[5] L. G. Villanueva, et al., *Phys. Rev. Lett.* **110** 177208 (2013).
[6] H. K. Lee, et al., Transducers 2011 510-13 (2011)
[7] D. K. Agrawal, J. Woodhouse, and A. A. Seshi, Phys. Rev. Lett. **111** 084101 (2013)
[8] M. H. Matheny, et al., Phys. Rev. Lett. **112** 014101 (2014).
[9] D. Antonio, et al., Nature Comm. **3** 806 (2012).
[10] E. Rubiola, *Phase Noise and Frequency Stability in Oscillators*, Cambridge University Press, New York, 2009.

CONTACT

*David A. Czaplewski, tel: +1-630-252-3258;
dczaplewski(at)anl.gov

A MEMS-BASED TUNABLE RF CHANNEL-SELECTING SUPER-REGENERATIVE TRANSCEIVER FOR WIRELESS SENSOR NODES

Tristan O. Rocheleau, Thura Lin Naing, Jalal Naghsh Nilchi, and Clark T.-C. Nguyen
University of California, Berkeley, USA

ABSTRACT

An electromechanical circuit comprising a capacitive-gap RF MEMS resonator embedded in a positive feedback loop with an ASIC transimpedance amplifier has demonstrated a first fully-functional MEMS-based tunable RF channel-selecting radio transceiver employing a super-regenerative reception scheme. Unlike previous super-regenerative receivers, this rendition harnesses the exceptionally high Q around 100,000 and voltage-controlled frequency tuning of its capacitive-gap transduced disk resonator to enable selection of any one of among twenty 1-kHz-wide RF channels over an 80-kHz range, while rejecting adjacent channels and consuming under 490 µW. These are well suited to the target wireless sensor node application, for which low-power and simplicity trump transmission rate. Electrical stiffness-based frequency tuning also allows this same device to operate as an FSK transmitter, making it a complete transceiver in one simple device. Finally, the geometric flexibility of capacitive-gap transduced resonator design should permit a large range of usable RF frequencies, from the presently demonstrated 60.6-MHz VHF, all the way up to UHF.

INTRODUCTON

The field of RF-MEMS has thus far improved many aspects of wireless communication, with commercially available products ranging from on-chip MEMS devices providing compact and low phase-noise reference oscillators [1, 2], to band-selecting RF front-end duplexers [3]. Greater potential remains, however, if the high quality factor and CAD-definable frequency possible in capacitive-gap MEMS can be harnessed to achieve a true channel-selection scheme.

In particular, MEMS-based communication offers a viable path towards meeting the ultra-low-power requirements demanded by wireless sensor networks. Tiny, low-cost wireless motes, where on-board sensors collect and transmit data through a mesh network while operating only on scavenged or battery power, stand to revolutionize data collection in applications ranging from industrial or environmental monitoring to biomedical imaging. While significant advances have been made towards such goals [4], the power consumption of current conventional-technology efforts are still in the milliwatt range, in excess of that needed for true set-and-forget sensor nodes.

Capacitive-gap MEMS devices have emerged as one option that provides the high quality factors (Q) that make possible the narrow bands required to greatly lower power. With $Q > 40{,}000$ even at GHz frequencies [5], such resonators easily allow for the tightly-spaced kHz-frequency bands ideal for sensor nodes, without requiring the processing and power-hungry spread-spectrum approaches currently used. Indeed, power consumption of oscillators constructed from such resonators has been demonstrated below 100 µW [1], even in the face of modest resonator impedance in the kΩ-range. These are ideally suited to the target wireless sensor node application, for which low-power and simplicity trump transmission rate.

In this paper, one such electromechanical circuit comprising a capacitive-gap RF MEMS resonator (*cf.* Fig.1) embedded in a positive feedback loop with an Application-Specific Integrated Circuit (ASIC) Trans-Impedance Amplifier (TIA) has demonstrated a fully-functional MEMS-based tunable RF channel-selecting radio transceiver employing a super-regenerative reception scheme.

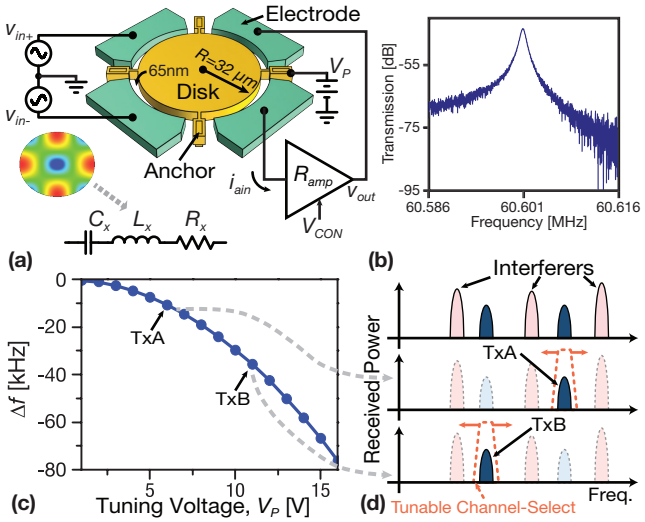

Figure 1. Perspective-view schematic (a) of the micromechanical disk resonator circuit used in this work. (b) presents the high Q~100,000 resonator frequency response, which may be tuned as in (c) via negative electrical stiffness with applied voltage to select one of several communication channels as illustrated in (d).

Unlike previous super-regenerative receivers [6, 7], this rendition harnesses the high Q filtering and voltage-controlled frequency tuning [8] of its capacitive-gap transduced disk resonator to enable selection of 1-kHz-wide RF channels across a 80-kHz range, as in Fig. 1(c,d). Furthermore, the split electrode resonator design made possible here isolates the loop amplifier from the antenna, greatly relaxing circuit linearity requirements and eliminating the need for an isolation amplifier, thus saving considerable power.

This electrical stiffness-based tuning additionally allows the same MEMS-ASIC system to operate as an FSK transmitter, enabling a complete transceiver in one simple device. Operated as a closed-loop oscillator with FSK modulation enabled via an applied voltage on the MEMS input electrodes, this transmitter offers direct carrier generation at the RF frequency of interest without the power-hungry complexity of previous PLL-based MEMS transmitters [9].

THE REGENERATIVE TRANSCEIVER

Fig. 2 presents the system-level design used for the super-regenerative receiver in this work, while Fig. 3 illustrates typical operation. This super-regenerative system identifies an incoming '1' or '0' by measuring the rate at which oscillation grows in a positive feedback circuit. In this rendition, the absence of received antenna signal power in the resonance passband results in a slow rise in oscillation amplitude, which indicates a '0'. On the other hand, with received power on resonance, signal couples into the positive feedback loop, speeding up rise time to indicate a '1'. Operated in such a fashion, this regenerative receiver forms a Binary Frequency-Shift Keying (BFSK) demodulator, where the FSK 'mark' and 'space' correspond to on and off-resonance signals, respectively.

To generate a stream of received bits, a periodic quench signal V_{CON} restarts oscillation, allowing each bit to be decoded in a separate, short oscillation growth as seen in Fig. 3(b). Fig. 3(c)

9781940470016/HH2014/$25©2014TRF
DOI 10.31438/trf.hh2014.22

Solid-State Sensors, Actuators and Microsystems Workshop
Hilton Head Island, South Carolina, June 8-12, 2014

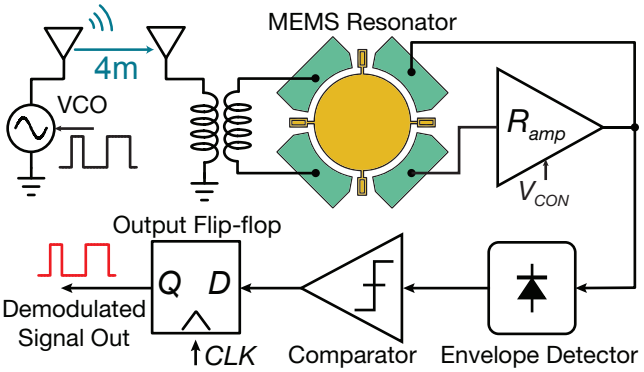

Figure 2. Schematic of the regenerative MEMS radio transceiver configured in receive-mode. Here, the MEMS resonator applies the needed channel-selecting filter to RF signals picked up by the antenna. The ASIC amplifier regeneratively amplifies this weak received in-band signal to produce a growing oscillation output, periodically quenched via V_{CON}. An envelope detector, comparator and flop-flop latch recovers the original transmitted digital data.

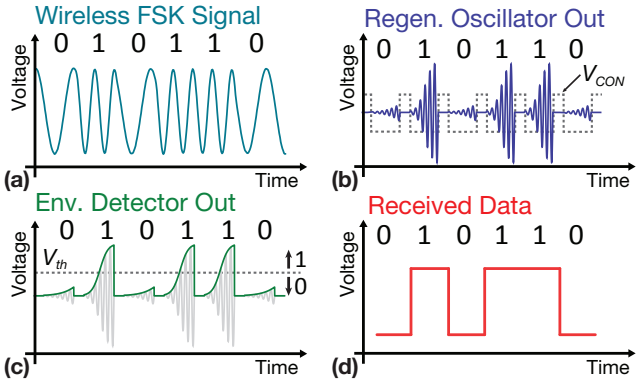

Figure 3. Conceptual operation of the regenerative receiver. The BFSK modulated and transmitted waveform of (a) gives rise to the periodically restarted oscillation of (b), where the on-resonance signal generates faster oscillation growth. Here, amplifier output drops to zero when V_{con} is raised, though resonator motion decays with a time constant based on resonator Q. Finally, envelope amplitudes which exceed V_{th} in (c) allow discrimination of '0's and '1's, recovering the original data in (d).

presents the envelope of the periodic oscillation growth produced by the envelope detector of Fig. 2. The output of this envelope detector feeds a comparator, the output of which in turn is latched into a flip-flop to recover the original transmitted data (Fig. 3(d)).

With the high *Q* of the MEMS resonators, this receiver isolates a single narrow channel while rejecting signals in nearby channels, spaced here at 4 kHz apart. Because the amplifier in such a design is isolated from the input antenna with only on-resonance signals passed through the MEMS resonator, out-of-channel interferers are blocked. This marks a significant improvement over previous regenerative receiver architectures [6], where loop amplifiers must handle any spurious signal received by the antenna without causing excess intermodulation. Here, the filtering of any such interferers greatly relaxes the linearity, and hence power consumption, of the amplifier.

Meanwhile, with voltage tunable via electrical-stiffness, such MEMS oscillators may also be configured as frequency-modulated elements, offering a uniquely simple, continuous-phase Frequency-Shift Keying transmitter. Such operation can be enabled using the same circuit as used for receive-mode, but with amplifier gain held

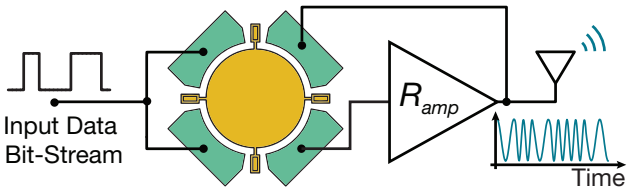

Figure 4. Schematic of the MEMS radio transceiver configured in transmit-mode where demodulating circuitry is switched out for an FSK modulating input to the capacitive-gap disk. With TIA gain no longer quenched, a continuous RF carrier is generated.

constant to generate a continuous RF carrier as shown in Fig. 4. Data to be transmitted may be applied to the input MEMS electrodes to generate FSK modulation, while the output of the amplifier is wired to the antenna.

Sustaining Amplifier Design

Fig. 5 presents the transimpedance amplifier ASIC used to achieve regenerative amplification (in receive mode, *cf.* Fig. 2) and the FSK modulated carrier (in transmit mode, *cf.* Fig 4). This circuit, fabricated in a 0.35 µm CMOS process, consists of a differential CMOS amplifier with output taken from one side, with the other side connected in shunt-shunt feedback to achieve a 0° phase shift from input to output while realizing controllable gain via a feedback resistance. Transistors M_1-M_4 comprise the basic differential pair biased by a Common-Mode FeedBack (CMFB) circuit; M_{RF} serves as the voltage controllable feedback resistor to allow control of the total transimpedance gain via input bias voltage V_{CON}.

With transresistance gain R_{amp} sufficient to overcome resonator losses, the oscillator loop amplitude rises exponentially with time constant given by

$$\tau = \frac{2L_x}{R_{amp} + R_x} \qquad (1)$$

where R_x and L_x are the equivalent circuit model elements for the MEMS resonator tank shown in Fig. 1(a). An on-resonance signal reduces the time required to rise to the '1'-bit threshold amplitude in two ways: first, the drive signal is resonantly enhanced to produce a resonator starting amplitude at the beginning of each oscillation cycle much larger than the background thermal noise, and second, this input signal continues to drive the resonator to increased amplitude during oscillation startup.

As with any filter, the bandwidth of the filter limits the possible data transmission rate. Here, such a limit is enacted by the decay time required for the resonator to reach a low amplitude of motion following a '1'. If the amplifier quench time falls short of the decay time of the resonator (here a long 0.5 ms due the high resonator *Q*), oscillation will restart quickly even in the absence of an input signal, preventing detection of subsequent '0's.

MEMS Resonator

To meet the filtering requirements of channel-select radio applications, the MEMS resonators used must possess both a useful RF operating frequency and sufficient *Q* to achieve the narrow ~1 kHz bandwidths desired for the sensor node application. To this end, the disk resonators depicted in Fig. 1(a) and Fig. 2 are quite suitable, with the added capability to accurately define multiple unique frequencies on the same die via only CAD layout, thus expanding possible operating frequency beyond that achievable from electrical stiffness tuning alone. The base device comprises a 2 µm-thick polysilicon disk supported by beams at quasi-nodal points and coupled along its sidewalls to input-output electrodes by tiny

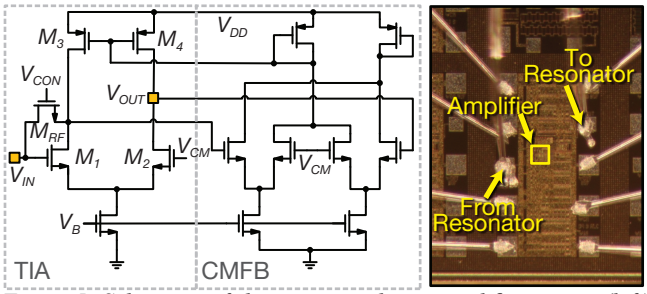

Figure 5. Schematic of the transimpedance amplifier circuit (left) and die photo (right). Bondwires connect the MEMS resonator between nodes V_{in} and V_{out} as in Fig. 2 to generate a closed oscillator loop with loop gain controlled by voltage applied to V_{CON}.

65 nm capacitive gaps. To drive the resonator into motion, a bias voltage V_P on the disk structure combines with a differential ac drive voltage applied to input electrodes to produce forces across the input electrode-to-resonator gaps that, at resonance, excite the compound (2, 1) mode shape, shown in the inset of Fig. 1(a). The frequency of resonance is given by [10]:

$$f_{nom} = \frac{K}{R}\sqrt{\frac{E}{\rho(2+2\sigma)}} \qquad (2)$$

where R is the disk radius, K a material-dependent constant equal to 0.373 for polysilicon, and E, σ, and ρ are the Young's modulus, Poisson ratio, and density of the polysilicon material, respectively.

In such resonators, a position-dependent electrical force across the capacitive gap additionally gives rise to the required electrical stiffness effect and resultant resonance frequency shift [10], given by:

$$k_e = -\alpha\frac{\varepsilon_0 A V_P^2}{d^3}; \quad f_0 = f_{nom}\left[1+\frac{k_e}{k_m}\right]^{\frac{1}{2}} \qquad (3)$$

where ε_o is the vacuum permittivity, A is the resonator-electrode overlap area, V_P is the voltage placed across the gap, d is gap width, and α is a dimensionless constant based on mode and electrode shape, equal to 0.637 for the design used here.

EXPERIMENTAL REALIZATION

Using Eqn. (3), MEMS resonators were designed for operation at 60.6 MHz with a disk radius of 32 µm. Fig. 6 summarizes the surface micromachining process used for fabrication, based on the same process as [11]. Here, phosphorus-doped polysilicon deposited via low-pressure chemical-vapor deposition (LPCVD) at 615 ºC provided all resonator structure, electrode and electrical interconnect material. A high-temperature oxide (HTO) sidewall sacrificial deposition defined the 65 nm resonator-to-electrode gaps. Two chemical-mechanical polishing (CMP) steps, one before structural polysilicon deposition and patterning and the other after the electrode polysilicon deposition, provided planar surfaces desired for precise lithography, as well as removed electrode-disk overhangs that can otherwise cause pull-in and device failure at low bias voltages. Following fabrication, structures were released in 49% HF to yield the final device imaged in the SEM of Fig. 6.

To construct a complete radio transceiver, released MEMS resonators are bondwired together with the CMOS ASIC described above and affixed to PCB circuits that provided all needed bias voltages as well as the simple off-chip RF diode detector and flip-flop circuit used for data recovery. Fig. 7 presents this assembled MEMS transceiver mounted in a custom bell-jar setup to allow measurement in a µtorr vacuum. The hermetic feedthroughs seen on the right connect the radio to a simple antenna formed frome

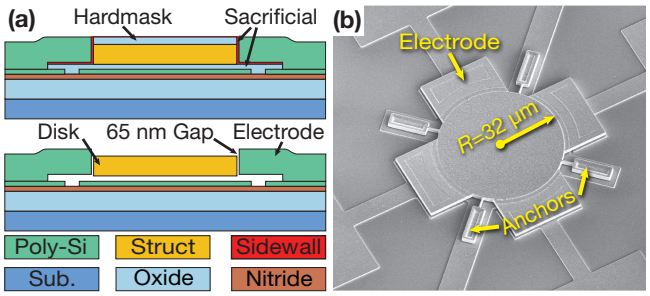

Figure 6. Cross sections (a) illustrating the MEMS resonators before (top) and after release in 49% HF (bottom). (b) presents an SEM of one completed device used in this work.

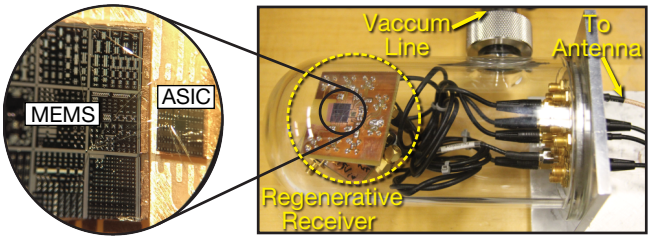

Figure 7. Measurement setup consisting of the regenerative transceiver dies mounted on a Printed Circuit Board (PCB) and measured in a bell-jar vacuum environment. The inset displays the MEMS and ASIC dies, both fabricated with many devices on a single die, one each of which is bondwired to the PCB.

~20 cm of wire. A bench-top frequency-synthesizer connected to a 2nd antenna positioned 4 m from the receive antenna provided wirelessly transmitted test signals.

Measurements

Fig. 8 presents measured time-traces illustrating operation of the receiver circuit of Fig. 2. Here, a frequency synthesizer transmits the -17 dBm (20 µW) test signal modulated with the bit-stream of Fig. 8(a) using 1-kHz mark-space separation FSK at a data rate of 1 kbps. Gating the regenerative amplifier gain control V_{CON} at the receive data rate to periodically grow and quench oscillation produces the oscillation envelope of Fig. 8(c), generated from a receive antenna located at a distance of 4 m from the transmitter. Here, small in-band signals are regeneratively amplified to create the observed speed-up in oscillation amplitude growth, clearly distinguishing mark vs. space frequency of the transmitted signal. Fig. 8(d) presents the output of the comparator following the envelope detector, while Fig. 8(e) shows the final data latched into the output flip-flop, clearly recovering the original transmitted data from Fig. 8(a).

Despite the use of make-shift antennas, the performance is remarkable and demonstrates the sensitivity and selectivity of this capacitive-gap MEMS-based receiver, even in the face of typical interferers in an unshielded environment. To further gauge this ability to reject interference, Fig. 9 presents the measured receiver output with the transmitter detuned by 4 kHz to a nearby channel and increased by 30 dB, showing no detected signal, as it should.

Meanwhile, Fig. 10 demonstrates the BFSK-modulated output of the transmit-mode configuration in Fig. 4, where the TIA gain is no longer gated and the transmit data-stream is applied to the input electrodes. With the input data encoded in the 200 mV swing seen in Fig. 10(a), the oscillation output (Fig. 10(b)) is seen to undergo a fast-response, continuous-phase FSK modulation, well-suited to the desired transmit function.

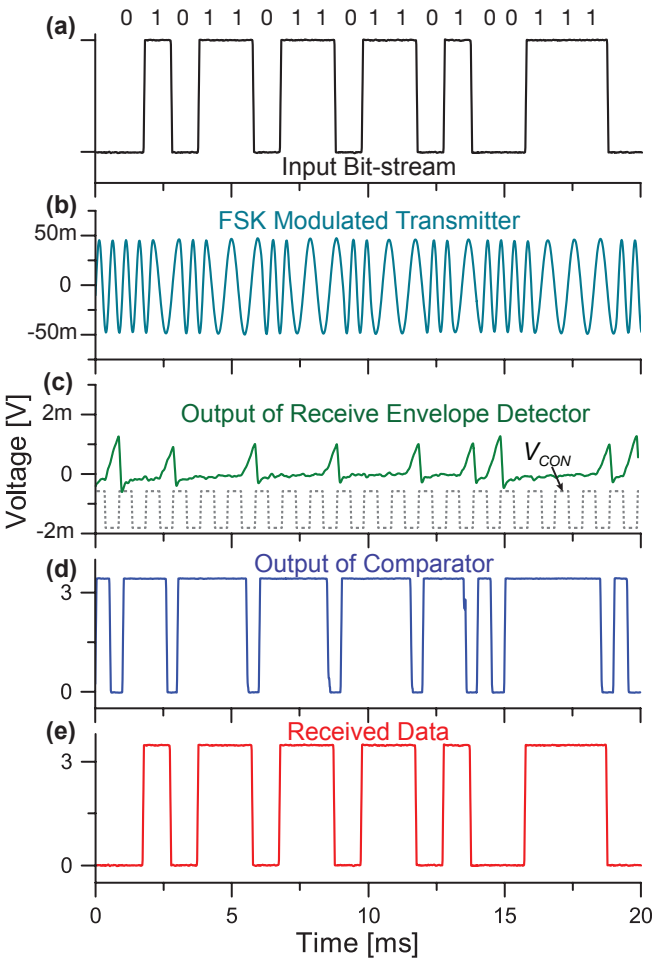

Figure 8. Measured receiver operation for a 1 kbps bit-stream transmitted across a distance of 4 m as in Fig. 2 using a Binary-FSK modulated transmitter with 1kHz shift and output power of -17dBm (20μW). The transmitted data-stream (a) is BFSK encoded and transmitted on a 60.6 MHz RF carrier (b) using a bench-top signal generator (shown mixed down to 2 kHz). Regenerative detection yields (c) amplitude following envelope detection; (d) shows resultant signal following comparator; and (e) presents the final recovered data-stream clocked by the output flip-flop. Here, the MEMS resonator is biased with 10.3 V, and the ASIC is operated on a 2.1 V supply drawing ~233 μA.

CONCLUSIONS

Using a periodically quenched transimpedance amplifier ASIC, the demonstrated MEMS-based circuit provides not only reliable selection and detection of individual narrow-band channels, but also FSK generation for transmission, and marks a first demonstration of an RF channel-select-capable MEMS radio transceiver. Additionally, a separate set of MEMS resonator electrodes for the antenna input and the amplifier loop shield the amplifier from out of band interferers. This greatly relaxes the amplifier linearity spec, which lowers its power consumption to enable a significant improvement over previous regenerative MEMS receiver topologies.

The demonstrated transceiver now offers a compelling new option for wireless sensor node devices. The power consumption here already offers significant improvement over previous sensor node systems [4], while the use of capacitive-gap MEMS devices provide extremely small size. Of course, transmit power above a few μW will require an additional power amplifier. For this, the narrow band and constant envelope of the FSK signal encourage the use of efficient RF amplifier topologies, and even opens the possibility of using the MEMS device itself as an efficient Class E amplifier [12]. If expectations for lowering power consumption to less than 100 μW (such as has already been demonstrated in a similar MEMS oscillator design [1]) are on target, then true set-and-forget nodes may soon become possible, capable of operating for long periods on tiny on-board batteries or even just scavenged power.

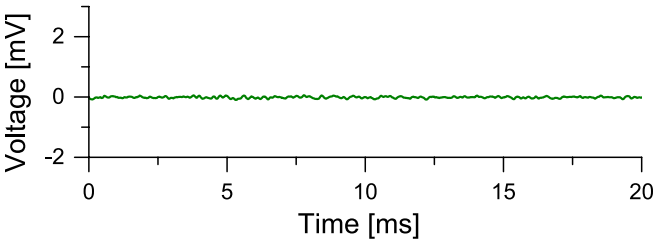

Figure 9. Measured regenerative receiver signal when transmitter is shifted by 4 kHz to a near-by channel and increased 30dB in power.

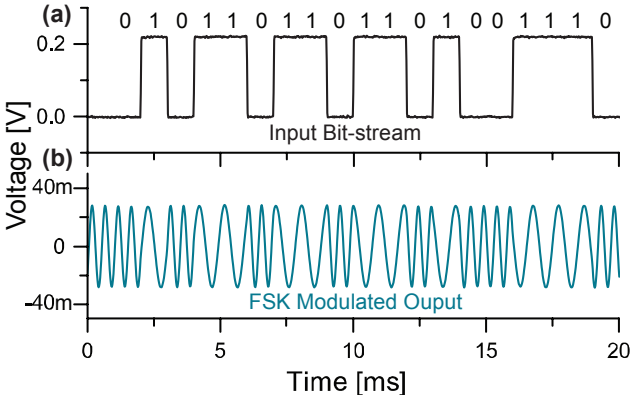

Figure 10. Measured FSK modulation at a 1kHz mark-space frequency separation generated using the transmit-mode configuration of Fig. 3. With the applied modulation signal (a), a continuous-phase output modulation is produced (b), shown here mixed down to ~2kHz for presentation.

Acknowledgment: This work was supported by DARPA.

REFERENCES

[1] T. L. Naing, *et al.*, *Proceedings, IFCS*, 2013, pp. 562-565.
[2] H. Lee, *et al.*, "Low Jitter and Temperature Stable MEMS Oscillators," *Proceedings, IFCS*, 2012, pp. 271-275.
[3] Avago, LTE Band 7 Duplexer, Part No. ACMD-6007
[4] J. M. Rabaey, *et al.*, *Computer,* vol. 33, pp. 42-48, 2000.
[5] T. L. Naing, *et al.*, *Proceedings, IFCS*, 2012, pp. 276-281.
[6] B. Otis, *et al.*, *Proceedings, ISSCC*, 2005, pp. 396-606 Vol. 1.
[7] A. Vouilloz, *et al.*, *JSSC,* vol. 36, pp. 440-451, 2001.
[8] H. C. Nathanson, *et al.*, *IEEE Trans. on Electron Devices,* vol. 14, pp. 117-133, 1967.
[9] W.-T. Hsu, *et al.*, *Proceedings, ISSCC*, 2006, pp. 1111-1120.
[10] M. Akgul, *et al.*, "A Negative Capacitance Equivalent Circuit Model for Parallel-Plate...", *IEEE Trans. on UFFC,* In Press.
[11] T. O. Rocheleau, *et al.*, *Proceedings, IEEE Int. Conf. on MEMS*, 2014, pp. 210-213.
[12] W.-C. Li, *et al.*, *Proceedings, Transducers*, 2013, pp. 2469-2472.

Contact: Tristan O. Rocheleau, tel:+1-607-232-2162; tristan@eecs.berkeley.edu

DEVICE-LAYER OVENIZATION OF FUSED SILICA MICROMECHANICAL RESONATORS FOR TEMPERATURE-STABLE OPERATION

Zhengzheng Wu[*], *Adam Peczalski, and Mina Rais-Zadeh*
University of Michigan, Ann Arbor, MI 48109, USA

ABSTRACT

In this paper, we report on temperature-stable operation of multiple MEMS silica resonators on an ovenized fused silica device-layer. Temperature servo-control circuits are implemented for compensating the resonator frequency drift using an on-chip RTD-based temperature sensor. A wide linear range analog controller has been implemented to reduce the effective TCF of fused silica resonator by an order of magnitude. Digital calibration method is further proposed and characterized to mitigate the offset errors induced from the non-ideal temperature sensing. Calibration reduces the resonator frequency drift to within 5 ppm across 105 °C of external temperature change. The power consumption of the ovenized device-layer is lower than 16.2 mW.

INTRODUCTION

Towards the ultimate goal of realizing a silica-based integrated timing and inertial measurement unit (TIMU), high-performance micro-electromechanical resonators [1], silica packaging processes, and multi-layer vertically stacked fused silica microsystems [2] have been demonstrated. Such technologies leverage material properties of fused silica to realize both resonant MEMS devices and hermetic packages for multi-sensor platforms. In terms of thermal properties of fused silica, a distinctive feature is its extremely low thermal conductivity of 1.3 W/m•K. However, due to a high temperature coefficient of elasticity (TCE) of ~+180ppm/K, fused silica TIMU requires temperature compensation techniques for stable operation. In this work, we take advantage of the low thermal conductivity to ovenize a large silica device layer with multiple micro-devices at low power levels. We further analyze the thermal design of the fused silica platform and present circuits for realizing closed-loop temperature control. The ovenized silica platform drastically improves temperature stability of silica MEMS resonators in the device fusion platform.

OVENIZED FUSED SILICA DEVICE-LAYER

It has been reported that fused silica MEMS resonators exhibit a high temperature coefficient of frequency (TCF) of ~ +89 ppm/K [1]. The high TCF is mostly attributed to the high temperature TCE of the fused silica material. While passive material compensation has been employed to reduce the TCF of MEMS resonators [3], the high TCE of fused silica makes passive compensation difficult. On the other hand, ovenization is known to offer excellent thermal stability. Ovenized quartz crystal oscillators (OCXOs) are known to deliver best stability among crystal timing references. Moreover, ovenized MEMS resonators have been demonstrated with power consumption as low as tens of milli-Watts [4]. However, most reported approaches are specific to a single resonator and are not directly applicable to a multi-device system such as the TIMU sensor fusion platform.

In this work, we demonstrate an ovenized fused silica layer (or platform) that can stabilize multiple MEMS devices over a wide external temperature range. The platform active area is 3.5 mm× 3.5 mm and includes four MEMS resonators. A scanning electron microscope (SEM) image of the fabricated fused silica platform is shown in Fig. 1. A resistance temperature detector (RTD) is co-fabricated on the silica device-layer using a 1000 Å-thick platinum (Pt). The RTD has a nominal resistance of 7 kΩ. A Pt heater ring is placed on the edge of the active area and can be used to heat the platform to a fixed oven set temperature.

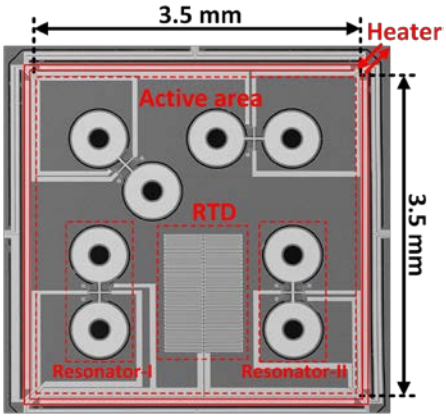

Figure 1: SEM image of a fused silica platform consisting of four resonators, an integrated RTD, a heater, and thermal isolation legs.

In order to reduce the power consumption, it is critical to thermally isolate the active area from the external environment. Heat transfer mechanisms from a MEMS device to external environment include heat conduction, heat convection, and radiation heat transfer. For minimizing heat conduction transfer, design of thermal isolation structures is critical. As shown in Fig. 1, the active area is connected to the external boundary using thermal isolation legs. With the low thermal conductivity provided by fused silica, eight thermal isolation legs with relatively large width (100 μm) are used. Such a design improves robustness by avoiding long and meandered supporting legs used in silicon MEMS [4], while good thermal isolation is still maintained. Also, the wide legs allow wiring of multiple low-resistance electrical connections to external pads using a thin-film metal layer, which favor integrating multiple devices on the platform. Using COMSOL FEM simulation, the thermal resistance of the designed isolation structure is extracted to be 28 K/W if heat conduction through solid structures dominates heat transfer (Fig. 2). Additional challenges arise in developing a large ovenized MEMS device-layer as compared to an individual MEMS device. Due to a larger surface area, the heat loss is more susceptible to convection and radiation heat transfer. When a high vacuum condition (pressure lower than 1 mTorr) cannot be obtained, the assumption that heat conduction dominates heat transfer is no longer valid. As a result, the effective thermal resistance decreases. Heat losses from convection and radiation are further included in the FEM simulation studies. To take into account for typical vacuum condition in a hermetic MEMS package, a heat transfer coefficient (h) of 0.05 W/m2•K is assumed for modeling the convection heat loss, which amounts to mTorr pressure level typically seen in a MEMS package. The radiation effect is simulated as surface-to-ambient radiation with surface emissivity of 0.9, accounting for the material property of fused silica. With an ambient temperature of 233 K (-40 °C), the temperature increase at the center of the silica active area relative to ambient is simulated as a function of the heating power, and results are also plotted in Fig. 2. It can be seen that the effective thermal resistance is reduced

9781940470016/HH2014/$25©2014TRF
DOI 10.31438/trf.hh2014.23

(indicating worse thermal isolation) by more than four times compared to the results that only consider conduction heat transfer.

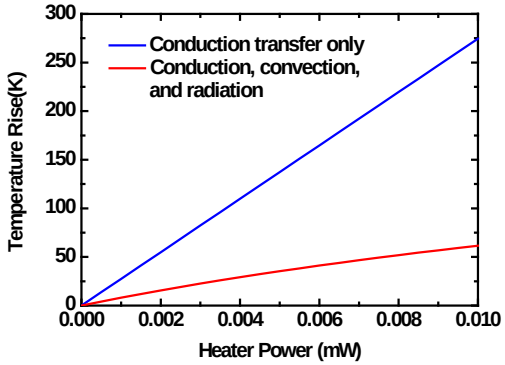

Figure 2: Temperature rise of the fused silica device-layer versus heater power from COMSOL FEM simulation.

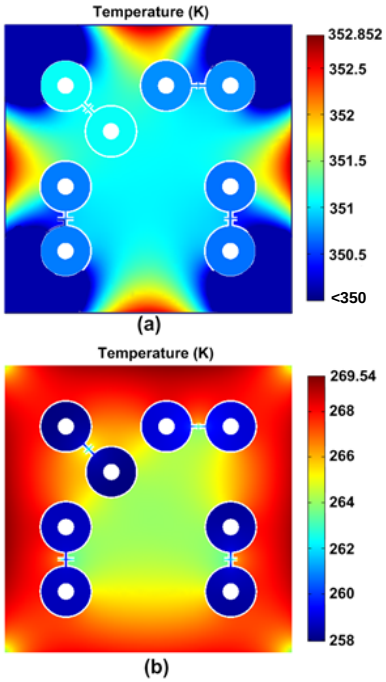

Figure 3: Temperature distribution within the active area when 4.3 mW of power is applied to the heater at an external temperature of 233 K: (a) only considering conduction heat transfer; (b) considering heat conduction, convection, and radiation.

Moreover, there exists larger temperature non-uniformity across the active area due to heat loss from heat convection and radiation. Figure 3 shows the temperature distribution within the fused silica active area when a heater power of 4.3 mW is applied to heat up the device to oppose an external temperature of 233 K (-40 °C). Figure 3(a) only considers conduction heat transfer. It can be observed that temperature across the large active area is quite uniform. The four devices on the platform show less than 1 K of temperature difference. Figure 3(b) includes the effect of convection and radiation heat transfer. It can be found that a much larger temperature gradient exists inside the active area. As high-*Q* MEMS resonators typically use long and narrow tethers to reduce anchor loss [1]; the large thermal resistance inherent in these tethers causes a large temperature gradient from the resonator bodies to the anchor area when the resonator bodies loose heat due to convection and radiation. As a result, the resonators experience large temperature offsets compared to the region where the RTD is placed. Therefore, it is very challenging for the RTD to accurately sense the real temperature of MEMS devices.

TEMPERATURE CONTROLLER DESIGN

High Gain Analog Controller

An analog servo-control system is implemented for monitoring the RTD response and generating a feedback power control signal. As shown in the circuit schematic in Fig. 4, the RTD is connected in a Wheatstone bridge configuration along with three other low-TCR and precision resistors. The Wheatstone bridge is interfaced to an instrumentation amplifier (IA) for pre-amplification. The IA provides a high voltage gain of 10,000 and ensures that temperature is measured with a low offset error. The signal generated from the IA is filtered and fed to a heater driver stage. The heater driver is implemented using an analog square-root generator based on BJT translinear circuits [5]. The square-root generator linearizes the transfer function from the input control voltage to the output heater power. Figure 5 plots the normalized power gain versus input voltage of the square-root generator extracted from measurement. Compared to an earlier work that employed a linear amplifier to generate a heater current proportional to the sensor signal [6], the heater driver design in this work performs linearization and ensures a near constant thermal loop gain across a wide input range (Fig. 5). Therefore, a sufficient power gain can be ensured even at low heater power levels. Using this heater driver, the oven temperature can be set close to the maximum device working temperature without degrading the control performance, thus minimizing the power consumption of ovenization.

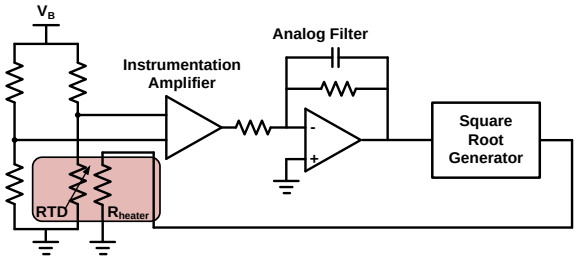

Figure 4: Circuit schematic of the resistive temperature detector (RTD) interface and analog oven-control system.

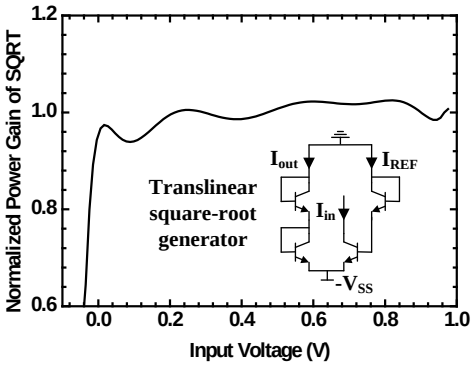

Figure 5: Normalized power gain versus input voltage of the square-root generator (with translinear square-root circuit schematic inset).

The temperature stability of a MEMS resonator inside the active area is measured over external temperature changes. Before taking measurements, the bulk micromachined fused silica die is mounted on a silicon carrier attached to a ceramic package (Fig. 6). The signal pads are bondwired to the ceramic package for external electrical connections. Thermal conductive glue is used to ensure good thermal conductivity between interfaces. During temperature measurements, the whole package is placed in a vacuum chamber. The vacuum chamber maintains a vacuum level of less than 10 mTorr, and the temperature can be set to different values with +/-0.1 K of accuracy. While the analog temperature controller is used to provide a servo-control, the frequency drift of the MEMS resonator is monitored using a network analyzer. The frequency drift of Resonator I (in Fig. 1) over a chamber temperature from -40 °C to +75 °C is plotted in Fig. 7. Using oven-control, the effective TCF of the fused silica resonator has been reduced to +10 ppm/K, as compared to +89 ppm/K for an uncompensated silica resonator.

The effective thermal loop gain of the analog controller has been extracted to be as high as ~1900. Although the active compensation has reduced the uncompensated TCF of a fused silica resonator by almost an order of magnitude, a significantly smaller drift is expected due to a large thermal loop gain provided by the servo-control system. Yet, there is overall frequency drift of 1163 ppm over -40 °C to +75 °C. This is mainly due to the temperature gradient within the active area as analyzed in the previous section. Since the temperature sensor (RTD) is not sensing the true resonator temperature, further increasing the thermal loop gain is ineffective in improving the temperature control accuracy, as demonstrated with a loop gain of ~5,000 in Fig. 7. Such non-ideal property of resistive temperature sensor is especially pronounced for an ovenized fused silica active device-layer.

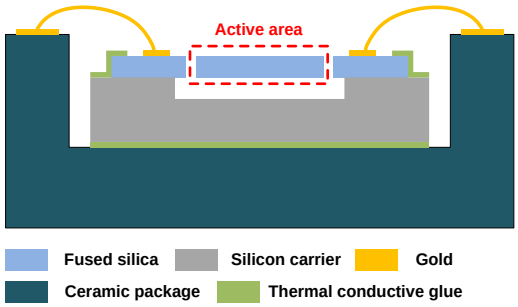

Figure 6: Cross-sectional view showing the fused silica die mounted in a ceramic package for temperature stability measurement.

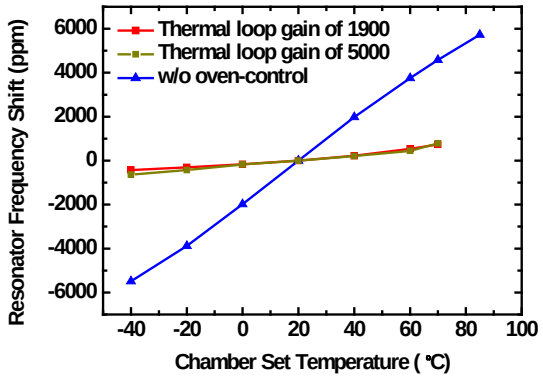

Figure 7: Measured frequency drift of Resonator I with analog control and TCF of a similar but uncompensated silica resonator.

Stability Improvement with Digital Calibration

In order to improve the temperature sensing accuracy, it is desirable to place the RTD sensor very close to the MEMS resonator or even on the resonator body. In this scenario, the temperature sensor readout will reflect the real device temperature with better fidelity. However, in order to design an RTD with sufficiently strong voltage output and minimal self-heating in a Wheatstone bridge configuration, an RTD needs to have large enough nominal resistance (typically kΩ range). To satisfy these requirements, the on-chip integrated RTD in this work occupies an area of approximately 1 mm^2. Although there is still room to shrink the footprint of the RTD, it is in general very difficult to place the RTD on the body of a MEMS resonator or a resonant sensor. Moreover, temperature compensation needs to be performed for all the devices in the device fusion platform, further complicating the design.

Considering the adverse effect of temperature gradient across the active area discussed in the previous section, the RTD-based temperature compensation method mainly suffers from offset errors due to a non-uniform temperature distribution. The offset error can be compensated using digital calibration in the temperature controller design. As plotted in Fig. 8, after the RTD sensor response is pre-amplified and filtered, the output voltage can be digitized for further processing. A digital calibration table is used to store the offset errors across the RTD sensor output range. After the data is converted back to analog domain to generate a heater control signal, the offset errors are effectively removed in the servo-control system. In order to maintain a constant loop gain, the square root function from control voltage to heater driver voltage can also be performed in a digital calibration look-up table to simplify the analog implementation.

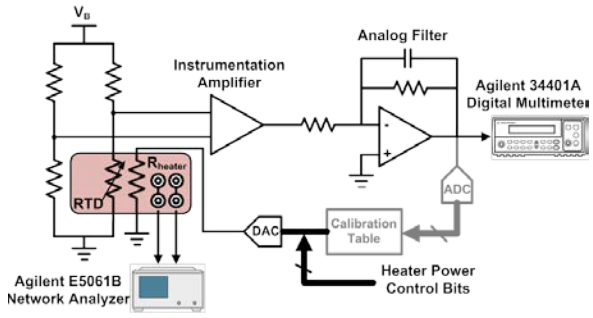

Figure 8: Circuit schematic of the RTD interface and oven-control system with digital calibration to reduce sensor offset.

To study the effectiveness of digital calibration in this work, the temperature control system is characterized by setting the control bits (instead of using a closed-loop operation) to control heater power according to different conditions. In the meantime, the output voltage from the RTD front-end (RTD with an IA and an analog filter) is monitored using a digital multimeter (Fig. 8). From the sensor output voltage measurement, the resistance change of the RTD can be back calculated. The frequencies of two MEMS resonators (Resonator I and Resonator II in Fig. 1) in the fused silica platform are also monitored using a Network Analyzer. The oven set temperature point is ~ 70 °C. At this oven set point, the RTD sensor front-end voltage output is adjusted to near zero.

In the first measurement setup, the RTD voltage output is maintained at zero output (constant RTD resistance) by the system across the chamber set temperature range. This is comparable to an analog controller with an integrator in the loop that keeps the RTD at a constant temperature. The frequency shift of two resonators are measured and plotted in Fig. 9. It is shown that although the RTD

sensor maintains a near constant temperature (within 0.04% of resistance change) through controlled heater power, the two resonators still exhibit obvious residue frequency shift. Resonator I experiences a total shift of 944 ppm, whereas resonator II shows a total shift of 697 ppm across a chamber set temperature range of -40 °C to +65 °C. It can be observed that Resonator I exhibits larger frequency drift than Resonator II. This is believed to mainly arise from the difference in the tether length of these two fused silica resonators. The support tethers of Resonator I is 90 μm in length as whereas Resonator II has 65 μm-long tethers. A longer tether will introduce a larger thermal resistance from the resonator body to the outer fused silica active area, making it harder to equalize the temperature with the external boundary. Placement of two resonators also slightly affects their temperature drifts.

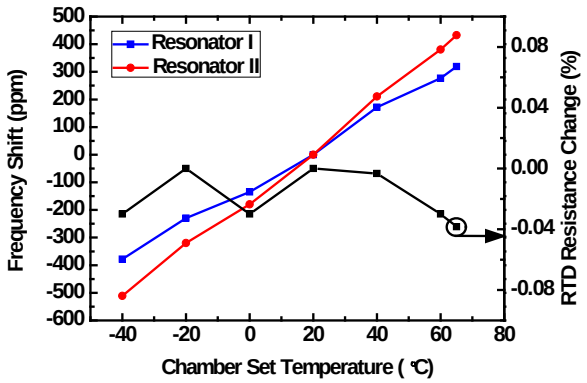

Figure 9: Frequency drift of two resonators with digitally controlled heater power to maintain a near constant RTD resistance (RTD resistance is included).

In the second measurement, the heater power is calibrated to stabilize the frequency of Resonator I. In this case, the frequency shift of two resonators are measured and plotted in Fig. 10. Benefited from calibration, the total frequency drift of Resonator I is less than 5 ppm. The total frequency drift of Resonator II is also improved to be within 264 ppm over the chamber set temperature of -20 °C to +65 °C. The output voltage from the RTD front-end is also monitored, and the extracted RTD resistance change is plotted in Fig. 10. It can be observed that the RTD is experiencing temperature increase at lower chamber temperatures if the system tries to stabilize the resonator frequency.

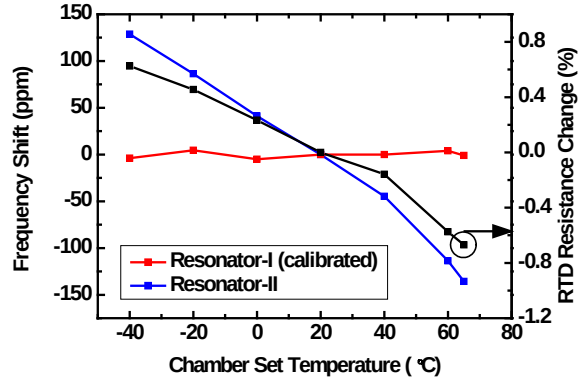

Figure 10: Frequency drift of two resonators with digitally controlled heater power to maintain a stable frequency for Resonator I (RTD resistance is included).

The power consumption of the heater is plotted and compared in Fig. 11 for the above two calibration settings. Due to the temperature difference between Resonator I and the RTD, a small amount of excessive heater power is needed to stabilize the frequency of resonators compared to maintaining a constant RTD resistance. The digital calibration method mentioned above can set the offset to achieve a constant frequency output. Benefited from low thermal conductivity of fused silica material, the power consumption of the ovenized device is less 16.2 mW across a wide external temperature range.

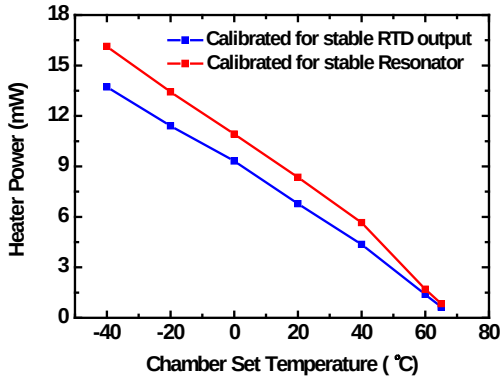

Figure 11: Extracted power consumption of the heater vs. chamber temperature.

CONCLUSION

In this work, a fused silica platform is implemented for integrating multiple MEMS devices on a single die. Thermal properties of the platform are analyzed, showing that the temperature of devices can be stabilized at low oven power levels. Temperature sensing and closed-loop servo-control is demonstrated as an effective active compensation method. Nnon-ideal properties of RTD-based temperature sensing are also studied, and digital calibration method is introduced to reduce offset errors in the servo-control.

REFERENCES

[1] Z. Wu, A. Peczalski, V. A. Thakar, Z. Cao, Y. Yuan, G. He, R. L. Peterson, K. Najafi, and M. Rais-Zadeh, "Piezoelectrically transduced high-Q silica micro resonators," *Proc. IEEE MEMS*, Jan. 2013.

[2] Z. Cao, Y. Yuan, G. He, R. L. Peterson, and K. Najafi, "Fabrication of multi-layer vertically stacked fused silica microsystems," *Proc. TRANSDUCERS*, June 2013.

[3] V. A. Thakar, Z. Wu, A. Peczalski, and M. Rais-Zadeh, "Piezoelectrically transduced temperature-compensated flexural-mode silicon resonators," *J. Microelectromechanical Systems*, vol. 22, pp. 815, 2013.

[4] C. M. Jha, M. A. Hopcroft, S. A. Chandorkar, *et al.*, "Thermal isolation of encapsulated MEMS resonators," *J. Microelectromechanical Systems*, vol. 17, pp. 175, 2008.

[5] B. Gilbert, "Translinear circuits: a proposed classification," *Electronics Letters*, vol. 11, pp. 4, 1975.

[6] J. C. Salvia, R. Melamud, S. A. Chandorkar, *et al.*, "Real-Time Temperature Compensation of MEMS Oscillators Using an Integrated Micro-Oven and a Phase-Locked Loop," *J. Microelectromechanical Systems*, vol. 19, pp. 192, 2010.

CONTACT

*Z. Wu, tel: +1-734-389-9507; zzwu@umich.edu

PHASE NOISE SQUEEZING BASED PARAMETRIC BIFURCATION TRACKING OF MIP-COATED MICROBEAM MEMS SENSOR FOR TNT EXPLOSIVE GAS SENSING

L. L. Li[1], E. L. Holthoff[2], L. A. Shaw[1], C.B. Burgner[1] and K.L. Turner[1]*
[1]University of California, Santa Barbara, California, USA
[2]Army Research Laboratory, Sensors and Devices Directorate, Adelphi, MD, USA

ABSTRACT

This paper reports real time explosive gas sensing (DNT) in atmospheric pressure utilizing the noise squeezing effect that occurs prior to a bifurcation event. A noise-squeezing controller based on the statistics of phase noise is implemented using high speed LabVIEW™ field programmable gated array (FPGA). A high frequency TNT-molecularly imprinted fixed-fixed microbeam sensor utilizes this nontraditional sensing strategy and performs DNT sensing at various concentrations. Experiments are conducted using both noise-based and sweep-based bifurcation tracking for a direct comparison. Results demonstrate noise-based bifurcation tracking is not only capable of performing reliable frequency tracking, but also shows the method is superior to the bifurcation sweep-based tracking. Over three orders of magnitude improvement in acquisition rate is achieved, and, as a result, confidence and precision on bifurcation frequency estimation is significantly improved over the bifurcation sweep tracking method, enabling DNT sensing at concentrations much below sub-ppb (parts-per billion) level.

INTRODUCTION

High sensitivity and selectivity and low cost are key considerations for sensors designed for trace explosive detection [1]. Low mass, high frequency and low cost micro/nano sensors utilizing mass loading of microcantilevers have drawn increasing attention in the area of mass sensing in recent years [2,3]. Molecular imprinted polymers (MIPs) have become an attractive thin-film coating for many MEMS sensors and a deeper understanding of binding sites in MIPs has been achieved [4, 5]. In this work, 15 nm films of sol-gel-derived xerogels molecularly imprinted for tri-nitro toluene (TNT) have demonstrated selectivity and stability in combination with a fixed-fixed beam MEMS sensor [6-7]. The sensor was characterized by parametric bifurcation sweep-based tracking [6]. Traditionally, mass sensing using MEMS has been achieved based on the natural frequency shift due to an increase of resonator mass. However, noise has set the limit of detection for linear sensing [8]. The ability to track the minimum shift of the natural frequency is determined by both the intrinsic and extrinsic noise of the system. Dynamics of parametrically excited oscillators and their applications have been studied extensively [9-11] as well as successful attempts to improve the effective quality factor of microcantilever arrays operating in the linear regime utilizing parametric amplification have been made [12,13,15]. However, bifurcation mass sensing has demonstrated superior sensitivity in the presence of measurement noise when compared to linear sensing in air [14]. As shown in figure 1, the critical location of the bifurcation mass tracking is recorded by repeatedly sweeping the frequency towards the critical point until large amplitude occurs. A system reset is required after each sweep cycle due to hysteresis. This sensing method offers higher sensitivity and noise resistivity over the harmonic resonant tracking [14], however, the long settling time and its high dependency on sweep rate to noise ratio [16-17] make it less desirable. In this work, we investigate a different sensing approach based on noise squeezing effect in parametric systems [15, 18-20] that occurs prior to the critical point. A LabVIEW™ FPGA controller is implemented to keep the device operating close to the edge of instability and inhibiting large amplitude grows (Fig. 1). As a result, close to three order of magnitude of improvement in acquisition rate is achieved.

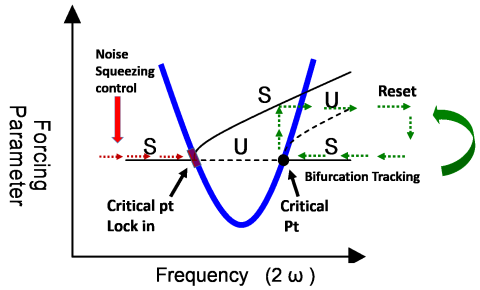

Figure 1: Schematic of both noise squeezing-based tracking (left) and bifurcation sweep-based tracking methods (right). The bifurcation sweep based tracking method tracks the bifurcation locations by repeatedly performing frequency sweeps towards critical point until large amplitude results. Then the device is relaxed to a zero stable state before the next sweep starts. However, in the noise squeezing control tracking method, the device approaches the critical point until the noise squeezes below some threshold, then feedback control keeps the device close to the edge of instability while maintaining small a response amplitude.

THEORY

In this work, parametric resonance is achieved by applying periodic axial forcing to a fixed-fixed microbeam through an external shear piezo, and the resulting dynamic is governed by the Matehieu-Hill equation with noise term, and the analysis can be found in [21]. As shown in figure 2, far away from the critical point where zero solution is stable, the phase appears to be random ranging from $-\pi$ to π due to thermomechanical noise. As it gets closer to the critical point, phase noise squeezes onto the slow manifold that corresponds to the eigenvector direction associated with eigenvalue with the smallest magnitude. If it keeps going, the phase noise squeezes more and zero solution becomes unstable, large amplitude results. The large phase variance where phase starts to squeeze makes it a perfect location for a feedback controller operation to stay close to the edge of bifurcation (Figure 1).

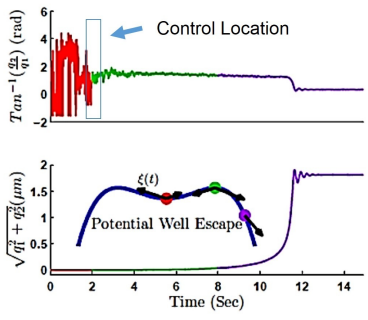

9781940470016/HH2014/$25©2014TRF
DOI 10.31438/trf.hh2014.24

Figure 2: Transient Response of a parametrically excited gyro before and after the critical bifurcation point. A coordinate transformation of (q_1, q_2) into a frame rotating at half the drive frequency is used. The system undergoes a supercritical/subcritical pitchfork bifurcation. Far away from the critical point, the phase (in red) alternates randomly with a large variance. As the device approaches the critical point, indicated by the transition from red to green, the dynamics collapse onto a one dimensional slow manifold, where the phase variance drops dramatically, making it an ideal location for control. As a consequence, the phase noise correlates and the amplitude starts to grow. Escape to a large amplitude (in purple) occurs as the parameters cross the instability boundary.

DEVICE AND EXPERIMENTAL SETUP

The device under testing is comprised of a fixed-fixed microbeam with a natural frequency of 49.33 kHz, as shown figure 3. The sensor was spin-coated with xerogel-based molecularly imprinted polymers (MIPs) that is highly selective to TNT. However, 2-4 di-nitro toluene (DNT) is used for mass sensing experiment, the results can be inferred to the sensing of TNT as they are structurally similar.

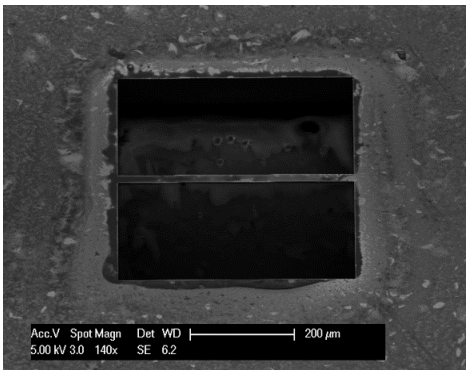

Figure 3: SEM image of a 450 µm x 20 µm x 2 µm sensor coated with MIPs. The device used in this paper is 600 µm x 20 µm x 2 µm.

Shown in Figure 4, experiment is conducted at atmospheric pressure and room temperature. The sensor was mounted on a shear piezo, driven by the function generator at nearly twice the resonant frequency (to drive parametric resonance) at a fixed voltage of 32 Volts. DNT vapor was generated in a permeation oven by heating 2-4 DNT permeation tube at constant temperature mixed with N_2. The flow rates were controlled by mass flow controllers (MFC). The concentration of the DNT/N_2 mixture in parts per billion (ppb) can be calculated based on the flow rate and oven temperature for a specific permeation tube. The sensor response is detected by an optical laser vibrometer and the signal is analyzed in the phase lock amplifier, which outputs the amplitude and phase in reference to the reference signal at half the drive frequency. The FPGA controller samples the phase data and is dedicated to the calculation of phase variance. Based on the statistics of the phase variance, a feedback control is implemented to adjust the corresponding frequency change to keep the device close to the edge of instability. Any change of frequency due to mass loading is followed by the noise squeezing controller immediately.

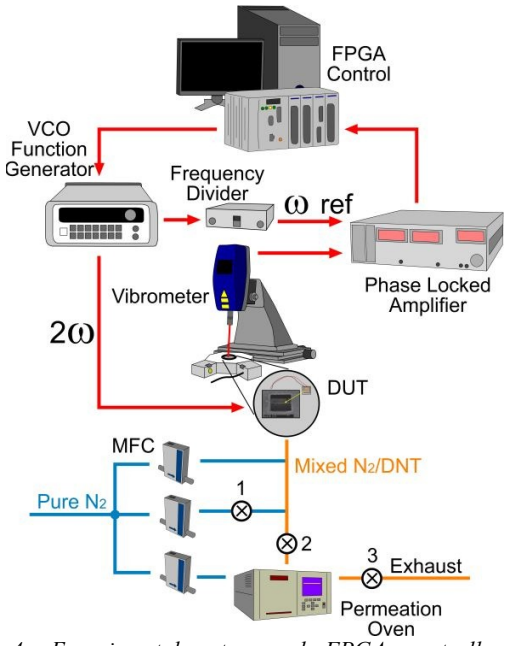

Figure 4: Experimental setup and FPGA controller design schematics. The device is mounted onto a shear piezo and is driven at ~ twice its natural frequency. The sensor velocity response coupled by a laser vibrometer through an optical microscope. The vibrometer signal and the reference square wave at half the drive frequency are fed into a phase lock amplifier (PLA). The FPGA samples the outputs of the PLA and provides feedback control to hold response close to the edge of bifurcation. The 2-4 DNT/N_2 gas test experiment is conducted in a closed chamber at atmospheric pressure and room temperature. DNT/N_2 is generated by heating the 2-4 DNT permeation tube in a permeation oven at constant temperature. DNT vapor is carried by N_2 and the mixture is fed into the test chamber at constant flow rate controlled by mass flow controllers. When the device is not under active DNT test, only N_2 is used.

RESULTS

DNT gas sensing experiment was performed with the noise-squeezing controller at a low concentration of 0.93 ppb DNT/N_2 mixture. In this experiment, nine repeated tests of 15 minutes of pure N_2 followed by 10 minutes of DNT/N_2 were conducted, as shown in Figure 5.

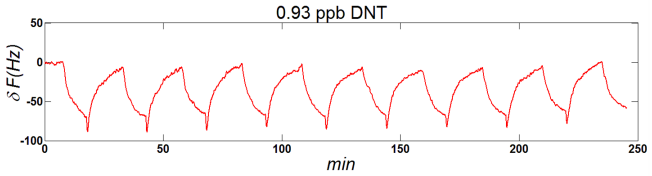

Figure 5: Figure shows a constant concentration of 0.93 ppb DNT/N_2 gas experiment. Pure N_2 was first introduced for 15 minutes and was followed 10 minutes of DNT/N_2. The parametric drive frequency was lowered by 67 ± 3 Hz due to the polymer absorption of DNT. The same process was repeated 9 times. The linear frequency drift of 0.05 Hz/min was accounted for in the post processing.

Higher concentration DNT gas experiments were also conducted. These experiments were carried out by the noise squeezing bifurcation sensing method and the bifurcation sweep tracking method described in [7] for comparison. Reversibility

was not able to obtained due to the stiction of DNT at high concentrations, hence, instead of introducing N_2 purging cycle after each DNT testing, higher concentration DNT experiment were conducted after the previous concentration reached its saturation level. Calibration curve of frequency shift as a function of the concentration in parts per billion (ppb) shown in Figure 8 is used to find the sensitivity of the MIPs. Frequency stability is quantified by Allan Variance [22] of data highlighted in red in Figure 6 and Figure 7. The sensitivity of frequency shift to concentration is characterized by the slope of the calibration curve in Figure 8. A summary of the comparison of the two tracking method is shown in table 1.

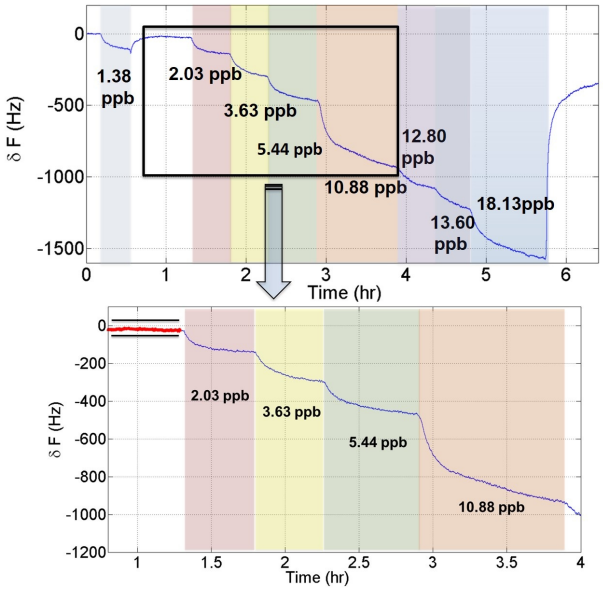

Figure 6: DNT gas sensing using a noise squeezing controller. (a) shows the gas experiment with lowest concentration of 1.38 ppb and highest concentration of 18.13 ppb. (b) is a zoom in figure of the portion inside the square window in (a). The highlighted portion corresponds to pure N_2 purging after the 1.38 ppb DNT/N_2 gas test. However, absorbed DNT did not completely come off, and the frequency did not fully recover initial starting frequency. Hence, this explains why the highlighted data in red does not start at zero. (b) is used to make direct comparison with the data collected from the bifurcation sweep method (Figure 7) at the same concentration.

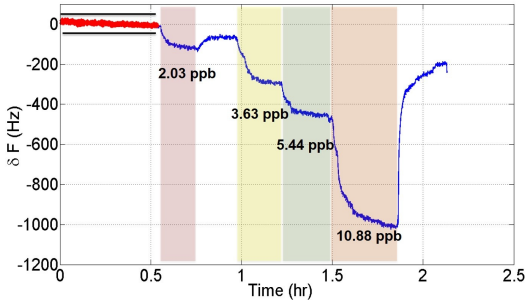

Figure 7: DNT gas sensing using the bifurcation sweep method. Pure Ns was introduced after the first and last DNT gas test (2.03 ppb and 10.88 ppb). Absorption phenomenon persisted, and the following higher concentration DNT/N_2 experiments were conducted after the steady state of lower concentration was reached.

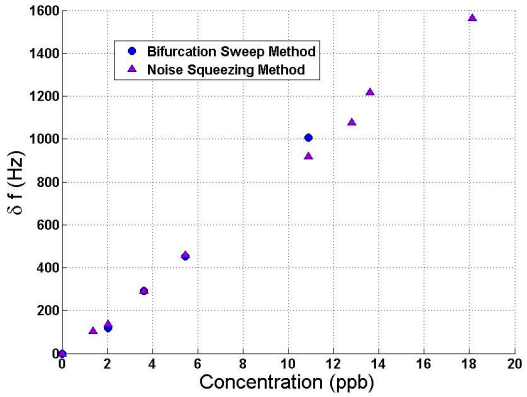

Figure 8: Calibration curve for both the noise squeezing tracking and bifurcation sweep tracking method. The slope of linear curve fit for each corresponds to its sensitivity.

Table 1: This table summarizes the results of both the noise squeezing method and the bifurcation method. Minimum frequency corresponds to the Allan variance for each method and sensitivity corresponds to the slopes of the calibration curve. LOD is the ratio between minimum frequency and the sensitivity of natural frequency.

	Noise Squeezing Method	**Bifurcation Sweep Method**
Minimum Frequency (Hz)	0.045	5.43
Sensitivity (Hz/ppb)	87.62 ±3	94.7±13.5
LOD (ppb)	0.0005	0.06

DISCUSSION

Experimental results demonstrate that noise-squeezing control bifurcation tracking is capable of tracking frequency change due to mass loading. The lowest concentration tested is 0.93 ppb, and good reversibility is demonstrated at low concentration (Figure 5). The noise squeezing controller estimates the critical location at less than 10 ms, while the average time for a bifurcation sweeps take up to 15-20 s. Hence, acquisition rate is increased by close to three orders of magnitude. The noise squeezing controlled tracking offers better frequency stability over the bifurcation sweep tracking method, leading to two orders of magnitude smaller in lowest order of detection (LOD). The DNT response time is found to be around 90 sec, which is much longer than the reported time in [7]. This can be attribute to the degradation of the polymer, since it was over two years old when the experiments were conducted for this paper. This issue is also reflected in the sensor's inability to recover to its original state at high concentration shown in Figure 6 and Figure 7. However, the DNT response sensitivity is directly related to the sensitivity of the polymer. Hence, confidence of the noise squeezing controlled bifurcation tracking ability can still be assured.

CONCLUSION

Experiments successfully demonstrate that the noise squeezing based sensing is a superior sensing strategy over the sweep-based bifurcation tracking method for real time DNT explosive sensing at atmospheric pressure. Three orders of magnitude improvement in

acquisition rate leads to faster, more confident and more precise estimation over the compared sensing method [23]. Even though the sensor response to the TNT is slow due to the degrading of the MIPs, it does not question the sensitivity of the noise-squeezing controller, since the TNT/DNT sensitivity of the sensor is highly depended on the sensitivity of the coating. This issue is expected to be resolved with better coating material and is currently underway.

ACKNOWLEDGEMENT

This work was supported by the Institute for Collaborative Biotechnologies through grant W911NF-09-0001 from the U.S. Army Research Office. The content of the information does not necessary reflect the position or the policy of the Government and no official endorsement should be inferred. Travel support has been generously provided by the Transducer Research Foundation.

REFERENCES

[1] Senesac, L., & Thundat, T. G. (2008). Nanosensors for trace explosive detection. Materials Today, 11(3), 28–36. doi:10.1016/S1369- 7021(08)70017-8

[2] Lang, H. P., Berger, R., Battiston, F., Ramseyer, J.-P., Meyer, E., Andreoli, C., … Gimzewski, J. K. (1998). A chemical sensor based on a micromechanical cantilever array for the identification of gases and vapors. Applied Physics A: Materials Science & Processing, 66(7), S61–S64. doi:10.1007/s00339005110

[3] Battiston, F. ., Ramseyer, J.-P., Lang, H. ., Baller, M. ., Gerber, C., Gimzewski, J. ., … Güntherodt, H.-J. (2001). A chemical sensor based on a microfabricated cantilever array with simultaneous resonance-frequency and bending readout. Sensors and Actuators B: Chemical, 77(1-2), 122–131. doi:10.1016/S0925-4005(01)00683-9

[4] Ayela, C., Vandevelde, F., Lagrange, D., Haupt, K., & Nicu, L. (2007). Combining resonant piezoelectric micromembranes with molecularly imprinted polymers. Angewandte Chemie (International ed. in English), 46(48), 9271–4. doi:10.1002/anie.200703881

[5] García-Calzón, J. a., & Díaz-García, M. E. (2007). Characterization of binding sites in molecularly imprinted polymers. Sensors and Actuators B: Chemical, 123(2), 1180–1194. doi:10.1016/j.snb.2006.10.068

[6] Holthoff, E. L., Stratis-Cullum, D. N., & Hankus, M. E. (2011). A nanosensor for TNT detection based on molecularly imprinted polymers and surface enhanced Raman scattering. Sensors (Basel, Switzerland), 11(3), 2700–14. doi:10.3390/s110302700

[7] Turner, K. L., Burgner, C. B., Yie, Z., & Holtoff, E. (2012). Using nonlinearity to enhance micro/nanosensor performance. In 2012 IEEE Sensors (pp. 1–4). IEEE. doi:10.1109/ICSENS.2012.6411564

[8] Ekinci K L, Yang Y T and Roukes M L 2004 *J. Appl. Phys* 95 2682–9

[9] Rhoads, J. F., Shaw, S. W., & Turner, K. L. (2006). The nonlinear response of resonant microbeam systems with purely-parametric electrostatic actuation. Journal of Micromechanics and Microengineering, 16(5), 890–899. doi:10.1088/0960-1317/16/5/003

[10] Rhoads, J. F., Shaw, S. W., Turner, K. L., Moehlis, J., DeMartini, B. E., & Zhang, W. (2006). Generalized parametric resonance in electrostatically actuated microelectromechanical oscillators. Journal of Sound and Vibration, 296(4-5), 797–829. doi:10.1016/j.jsv.2006.03.009

[11] Rhoads, J. F., Shaw, S. W., & Turner, K. L. (2010). Nonlinear Dynamics and Its Applications in Micro- and Nanoresonators. Journal of Dynamic Sy20-222stems, Measurement, and Control, 132(3), 034001. doi:10.1115/1.4001333

[12] Yie, Z., Miller, N. J., Shaw, S. W., & Turner, K. L. (2012). Parametric amplification in a resonant sensing array. Journal of Micromechanics and Microengineering, 22(3), 035004. doi:10.1088/0960-1317/22/3/035004

[13] Cleland, A. N. (2005). Thermomechanical noise limits on parametric sensing with nanomechanical resonators. New Journal of Physics, 7(1), 235–235. doi:10.1088/1367-2630/7/1/235

[14] Yie, Z., Zielke, M. a, Burgner, C. B., & Turner, K. L. (2011). Comparison of parametric and linear mass detection in the presence of detection noise. Journal of Micromechanics and Microengineering, 21(2), 025027. doi:10.1088/0960-1317/21/2/025027

[15] D. Rugar & P. Grutter. Mechanical Parametric Amplification and Thermomechanical Noise Squeezing. Physics Review Letters. Vol. 67, Number 6. August 1991.

[16] Evstigneev, M. (2008). Statistics of forced thermally activated escape events out of a metastable state: most probable escape force and escape-force moments. Physical review. E, Statistical, nonlinear, and soft matter physics, 78(1 Pt 1), 011118. Retrieved from http://www.ncbi.nlm.nih.gov/pubmed/18763930

[17] Mandel, P., & Erneux, T. (1987). The slow passage through a steady bifurcation: Delay and memory effects. Journal of Statistical Physics, 48(5-6), 1059–1070. doi:10.1007/BF01009533

[18] G. Prakah,et al. (2012) Parametric Noise Squeezing and Parametric Resonance of Microcantilevers in Air and Liquid Environments. Review of Scientific Instruments.

[19] Nicholas Miller, Chris Burgner, Mark Dykman, Steven Shaw, Kimberly Turner, Fast estimation of bifurcation conditions using noisy response data, 2010/3/25, SPIE Smart Structures and Materials+ Nondestructive Evaluation and Health Monitoring, Pages76470O-76470O-12

[20] Christopher Burgner, William Snyders, & Kimberly Turner, Control of MEMS on the Edge of Instability, IEEE Transducers, Beijing, China June 2011

[21] Ph.D. dissertation of Nicholas J. Miller. "*NOISE IN NONLINEAR MICRO-RESONATORS"*.

[22] D.W. Allan. Statistics of atomic frequency standards. Proc. IEEE, 54:221– 231, 1966.

[23] Li, L. L.,Holthoff, E. L, Shaw, A. L., Burgner, B. C & Turner, K. L. " Noise Squeezing Controlled Parametric Bifurcation Tracking of MIP-Coated Microbeam MEMS sensor for TNT Explosive Gas Sensing", JMEMS, in press.

CONTACT

*L.L. Li, lily@engr.ucsb.edu

RESONANT M/NEMS PIEZORESISTORS FOR NARROW-BAND ELECTRONIC AMPLIFICATION

A. Ramezany, M. Mahdavi, X. Guo, and S. Pourkamali
Department of Electrical Engineering, University of Texas at Dallas, Texas, USA

ABSTRACT

This work demonstrates amplification of electronic signals using a bare silicon electromechanical resonant micro-device. The structure consists of a narrow piezoresistor connecting two plates that can vibrate in an in-plane resonant mode. It is shown that vibration amplitude amplification by a combination of mechanical quality factor and thermal-piezoresistive "energy pumping" can turn the relatively weak piezoresistivity of silicon into a viable amplification mechanism. The energy pump is a result of interactions between electro-thermal forces in the piezoresistor and its piezoresistivity leading to a negative electrical equivalent resistance for the device (i.e. an active element). Tunable voltage gains up to 16dB for a 50Ω load have been demonstrated at 4.8MHz. The thermal-piezoresistive coupling also significantly enhances the effective quality factor (Q) of the resonator showing Q of up to 204,000 for a structure with intrinsic mechanical Q of less than 15,000 in air. Such narrow band amplifiers can potentially be used as channel selective low-noise amplifiers in wireless communications eliminating the need for multiple off-chip filtering steps.

INTRODUCTION

Transistors have been the basis of modern electronics propelling the microelectronics industry towards unimaginable triumphs over the past few decades. Although the solid state transistor technology has been an effective and reliable power-house leading the human civilization into the electronics age, it seems to have reached its fundamental limits while the quest for more versatile next generation technologies continues. One of the needs not addressable using the semiconductor based technologies is the need for ultra-narrow band filtering along with amplification of small signals in wireless communications and some sensory applications. Due to the relatively low quality factor of on-chip inductors and capacitors, accurate and narrow-band frequency selection still relies on off-chip mechanical resonators. Even such mechanical components cannot offer high enough selectivity for most wireless applications necessitating further filtering for selection of individual channels after frequency down-conversion.

MEMS resonators have been the center of attention over the past two decades in hopes of enabling on-chip frequency selection. The "Resonant Gate Transistor" demonstrated in 1967 [1], known to be the very first MEMS resonator, was an active device integrating high mechanical Q of a suspended metallic cantilever within a field effect transistor. However, the main bulk of recent research on micromechanical resonant devices has been focused on piezoelectric and capacitive resonators that are passive components. Such devices have not been able to meet the selectivity and pass-band loss requirements for wireless communications leading some researchers to turn the focus back to active on-chip resonant components. Examples of such include the resonant amplifier utilizing capacitive actuation and piezoresistive readout [2], and the resonant beam selectively doped for field effect transduction (similar to a FET) [3]. This work takes such efforts one step further by taking advantage of the previously demonstrated internal thermal-piezoresistive energy pumping [4,5] to reach significantly higher amplification factors using extremely simple devices. In addition to frequency selection capability, such devices can be aggressively scaled down into the deep nano-scale range without hitting some of the fundamental road blocks that the semiconductor industry is facing.

CONCEPT AND THEORETICAL ANALYSIS

A piezoresistor is an active transducer by nature as it can absorb electrical power from a DC source and transfer a modulated power to a load. Similar to the current flow in a transistor channel that is controlled by an input gate or base voltage, current in a piezoresistor is controlled by its mechanical stress. Therefore, an electrical component very similar to a transistor can be realized by combining a piezoresistor with an electromechanical actuator turning the input voltage into a mechanical force. The piezoresistive effect, however, is generally far too weak for such "transistor" to be able to offer a useful amplification factor (gain > 1). For example, while the current in a solid state transistor can be modulated over its full range by only a fraction of a volt change in its input voltage, 1MPa of mechanical stress changes the current in a silicon piezoresistor by less than 0.1%.

One solution to make up for this weakness is to use mechanical resonance to multiply vibration amplitude and therefore mechanical stress resulting from the input force by Q times. In this manner, a piezoresistor embedded within a high-Q resonant system can offer significantly improved electrical amplification behavior. Voltage gain as high as 4.6 dB has been demonstrated in [2] using this approach. This work takes this one major step further by adding the thermal-piezoresistive internal amplification effect [4,5] that can further amplify the resonator vibration amplitude and consequently the piezoresistor amplification factor at resonance. For this purpose, instead of using an electrostatic actuator to turn the input voltage to mechanical strain, the piezoresistor itself is used as a thermal actuator. Figure 1 schematically shows how such device operates as a self-amplifying resonator by coupling of thermal actuation forces with piezoresistivity of the actuator. The combination of DC bias current and input AC signal leads to slight temperature fluctuations (via Joule heating) and therefore thermal stress at the same frequency as the input signal within the in the piezoresistor. If the input signal frequency is close to the natural resonant frequency of the vibration mode of interest, the mode is excited leading to a significant vibration amplitude and therefore fluctuating strain in the same piezoresistor. The resulting strain in turn modulates the electrical resistance of the piezoresistor that along with the DC bias current leads to an additional fluctuating ohmic heating component. Depending on the sign of the piezoresistive coefficient of the structural material this additional heat (and therefore force/stress) component can be in phase or out of phase with respect to the main heat component resulting from the input signal. It can be demonstrated that for n-type silicon, where the piezoresistive coefficient is negative, the piezoresistive heat component will be in phase with the input signal heat component and therefore can add to the resonator vibration amplitude [5]. In this manner, the piezoresistor absorbs more energy from the DC bias source and amplifies the mechanical vibration amplitude and along with it the stress and therefore voltage fluctuations across the piezoresistor (resonant amplifier output voltage).

9781940470016/HH2014/$25©2014TRF
DOI 10.31438/trf.hh2014.25

Solid-State Sensors, Actuators and Microsystems Workshop
Hilton Head Island, South Carolina, June 8-12, 2014

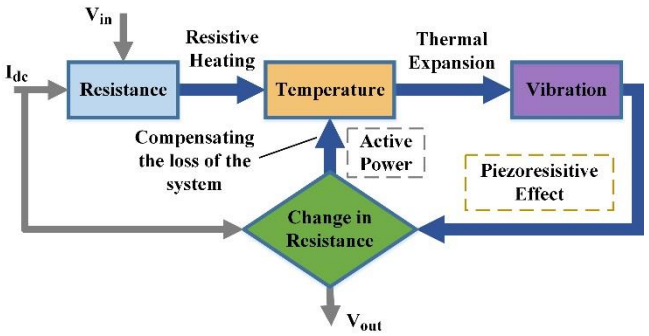

Figure 1. Schematic diagram of an amplifying resonant piezoresistor showing the internal thermo-electromechanical amplification loop, also known as the internal energy pump [5].

Figure 2 shows the SEM view of the silicon structure used in this work. The device consists of a narrow piezoresistor in the middle connecting two plates that can vibrate in-plane in opposite directions in the resonant mode of interest.

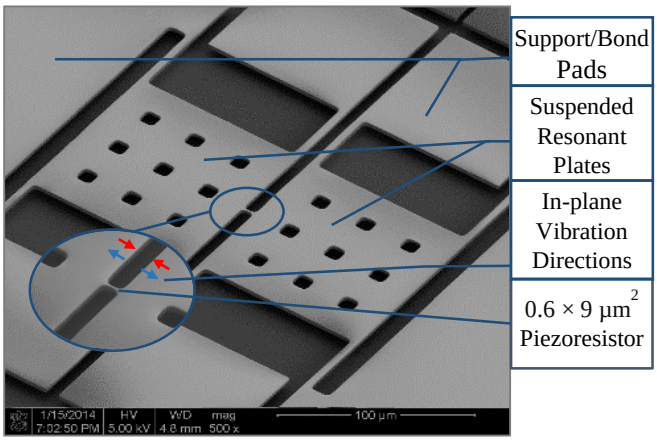

Figure 2. SEM view of the silicon microstructure used as an electronic amplifier consisting of a 9µm×600nm piezoresistor and two resonating plates. The structure is 4µm thick.

The amplitude of the pumped energy can be tuned by changing the bias current of the resonator. When the pumped energy is smaller than the energy lost due to mechanical losses compensating only a portion of resonator mechanical loss, the resulting effective Q of the resonator increases and can reach values much higher than the intrinsic mechanical Q of the device. This is referred to as thermal-piezoresistive Q-amplification [5]. By further increasing the feedback loop gain at some point the pumped energy can compensate all the mechanical energy loss in the system leading to self-sustained oscillation [5].

Fig. 3a shows the equivalent electrical circuit of such thermally actuated resonant piezoresistor [6]. R_A represents the physical resistance of the piezoresistor at rest, which is in parallel with a series RLC representing the resonance behavior of the device. The current passing through the RLC represents the motional current of the resonant structure, i.e. the modulated bias current due to vibration induced piezoresistor fluctuations. The motional conductance of the device, which is the ratio of motional current to the actuation voltage is given by Eq. (1), where α, E, and π_l are the thermal expansion coefficient, young's Modulus, and longitudinal piezoresistive coefficient of the structural material respectively, C_{th} is the thermal capacitance of the thermal actuator (piezoresistor), ω_0 is the mechanical resonance frequency, and I_{dc} is the bias current. [6]

$$g_m = \frac{\alpha E \pi_l Q I_{dc}^2}{C_{th}\omega_0} \quad (1)$$

Figure 3b shows a simplified version of the same circuit at resonance frequency consisting of the physical resistance (R_A or the passive resistance) in parallel to a current source. The direction of the current from the current source can be the same or the opposite of the direction of the current in the resistor depending on the sign of the piezoresistive coefficient. An opposing current source can be interpreted as a negative resistor with value of $1/g_m$.

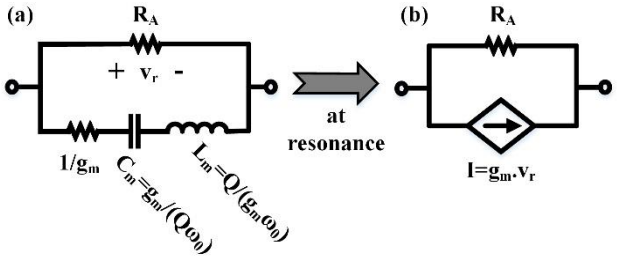

Figure 3. Small signal equivalent circuit of the a resonant piezoresistive amplifier: (a) the RLC combination representing resonant behavior of the device, (b) the RLC simplified to a dependent current source (potentially negative resistance) at resonance frequency.

Operation of such devices in both Q-amplification and self-oscillation modes have previously been demonstrated and analyzed [5]. This work demonstrates that such devices can in fact have three distinct modes of operation when a significant resistive load is added to the output of the device. The resistive load adds an electrical loss component to the equation delaying the inset of self-oscillation. It can be shown that in this case in the interval between full compensation of resonator losses and the inset of self-oscillation, electrical amplification occurs delivering the amplified input signal to the load. Therefore, depending on the value of bias current, the piezoresistor can operate in three different regimes: attenuation, amplification, and self-sustained oscillation. At small bias currents g_m has a very small negative value, therefore the $1/g_m$ resistor is very large and the overall resistance of the device R_D (where $R_D = R_A||1/g_m$) is positive acting as a passive resistance consuming a part of the input power and attenuating the input signal.

As the bias current is increased, absolute value of g_m increases, which in turn decreases the absolute value of the active resistance. When the value of the active resistance matches the value of the passive resistance, R_D is no longer positive. In this case the resonator acts as an overall negative resistance in series with the load and no longer attenuates the input signal by consuming power, but rather adds power to the system increasing the power delivered to the load. Gain of the system in this case can be calculated by:

$$Gain = \frac{R_L(1 + g_m R_A)}{R_A + R_L(1 + g_m R_A)} \quad (2)$$

where $R_L$is the load resistance. This gain is only valid for bias currents at which the self-sustained oscillation has not yet occurred. Once the self-oscillation starts, the output signal will no longer depend on the input signal and input to output gain becomes meaningless.

Finally, self-sustained oscillation starts when the value of $\boldsymbol{g_m}$ becomes so high that the overall combined device and load resistance becomes negative. In other words, this occur when the

absolute value of g_m reaches the conductance of the parallel combination of the load and piezoresistor physical conductance ($R_L^{-1}+R_A^{-1}$), and therefore, the gain from Eq. (2) goes to infinity. With larger load resistance values, the transition from amplification to self-sustained oscillation occurs at lower bias currents. Therefore, for general application of such amplifier, the matched value of the load resistance must be chosen wisely and according to the maximum gain requirements.

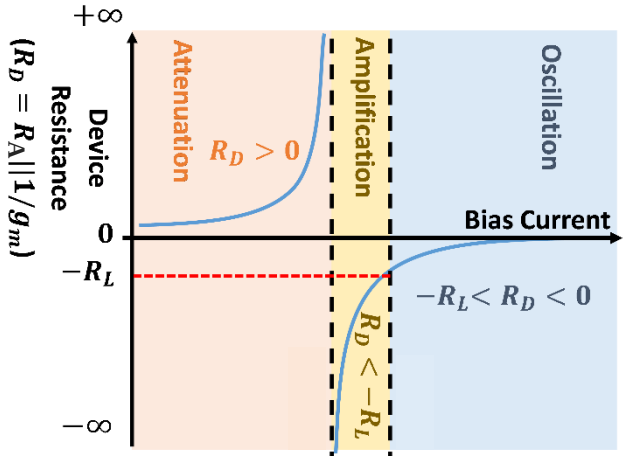

Figure 4. Qualitative representation of overall resistance of the device (R_D) versus bias current, showing three different working regions and transition points between them.

EXPERIMENTAL RESULTS

The themal-piezoresistive resonator shown in Fig. 2 was fabricated through a single mask fabrication process on an N-type SOI substrate with device layer thickness of 4µm. Submicron piezoresistor width was achieved by thinning down the lithography defined beam via oxidation and oxide removal. The measurement configuration used for characterization of the device is shown in Fig. 5. The 50Ω resistors are network analyzer port input resistances that need to be considered in gain calculations. R_1 and R_2 were included in the measurement circuit so that input and output termination resistance of the device can be controlled.

Fig. 6 shows the measured frequency responses taken from the Network Analyzer that show the gain at resonance frequency as a function of bias voltage, with R_1 and R_2 set to zero, and the input power set to -45dBm. As discussed in the previous section, by increasing the bias current the resonator effective quality factor increases, making the peak sharper and taller. By passing the attenuation region the peak's value, which is the voltage gain at resonance, becomes positive. As the current is increased, Joule heating also increases, and the resulting temperature increase will cause a resonance frequency shift due to changes in the piezoresistor stiffness [7].

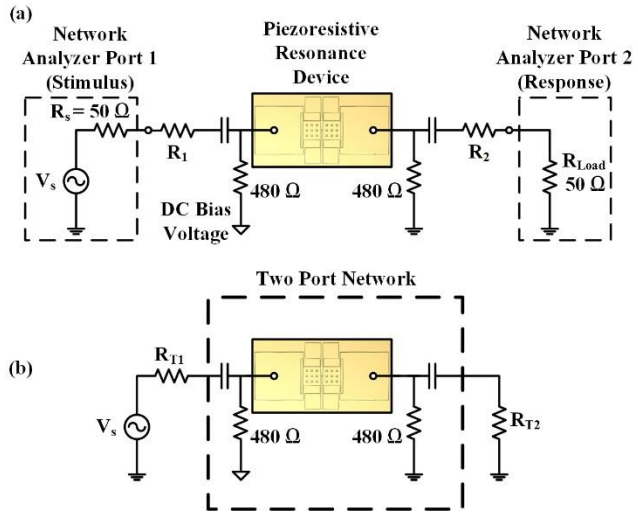

Figure 5. (a)Test circuit configuration showing bias resistors and coupling capacitors. Effectively, the MEMS device is connected in series with the input resistance of the network analyzer acting as a 50Ω load. (b) Combining the effects of Network Analyzer impedances with the circuit resistances to treat the whole device and its supporting elements as a two port network.

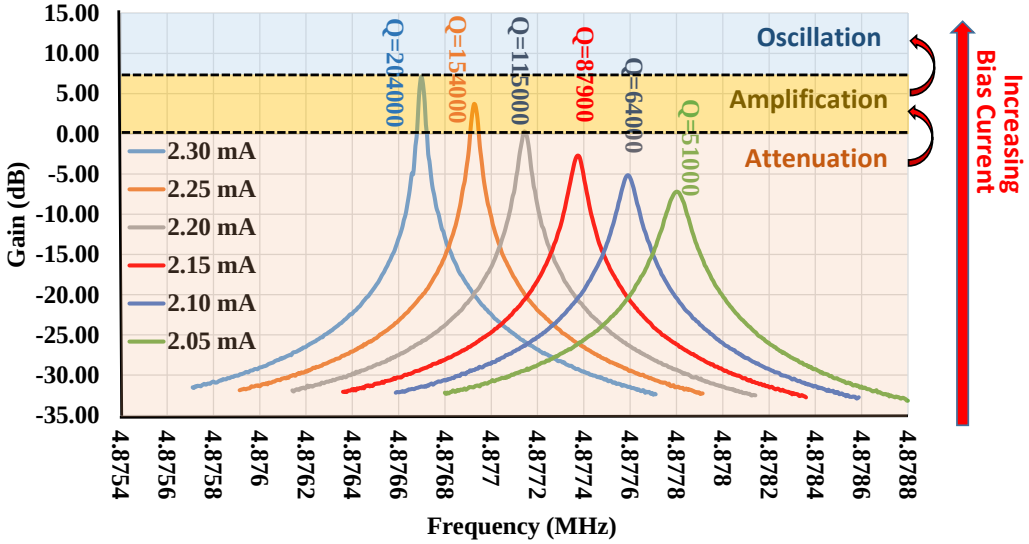

Figure6. Measured frequency responses of the device with different DC bias values. As the bias voltage (and current) increases the peak amplitude increases while sharpening (Q enhancement) and the device goes from an attenuator to an amplifier, and eventually self-sustained oscillation occurs.

With a constant input termination resistance, i.e. the same input power, according to Eq. (2), increasing the load resistance should increase both gain and voltage swing. However, since higher gain takes the device closer to mechanical saturation, the input power needs to decrease, which results in reducing the output voltage swing. By choosing the right values for R_1 and R_2 one can control both gain and voltage swing. The experimental results showing the relationship between gain, voltage swing, and input/output termination resistances ($R_{T1}=R_1+50$ and $R_{T2}=R_2+50$) are graphed in Figures 7 and 8. Therefore, voltage gain and swing of the amplifier, can be tuned by changing the values of R_1 and R_2 and bias current. It should be noted that all the measurements have been performed under atmospheric pressure and therefore vacuum packaging would not be required in a real application.

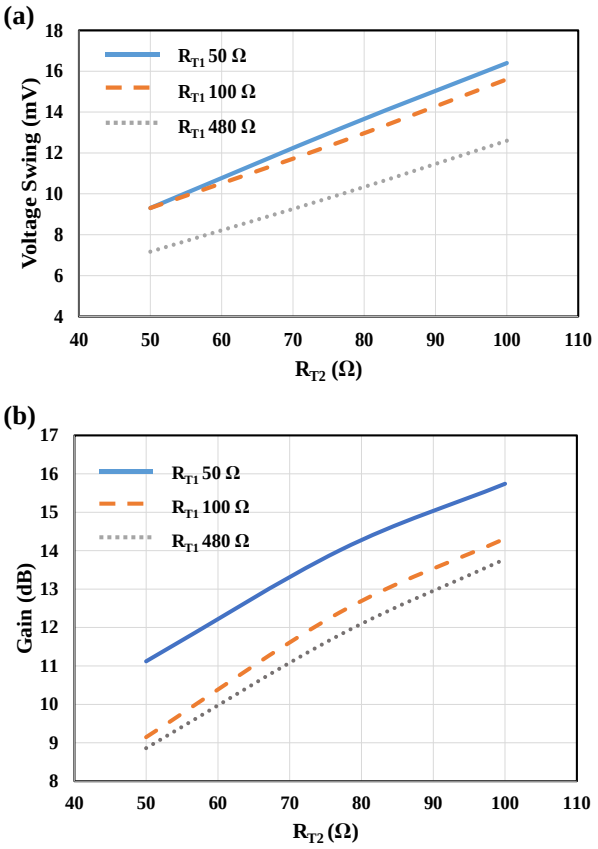

Figure 7. (a) Measured voltage gain with different input and output termination resistances, (b) measured output voltage swing with different input and output resistances.

CONCLUSION

Amplification of electronic signals using a bare silicon electromechanical resonant micro-device with tunable gain, swing and frequency was demonstrated. It was demonstrated that thermal piezoresistive resonators in combination with resistive loads can work in three different regimes of attenuation, amplification, and self-sustained oscillation.

Such devices can potentially address the need for low loss highly selective on-chip frequency selection in communication systems.

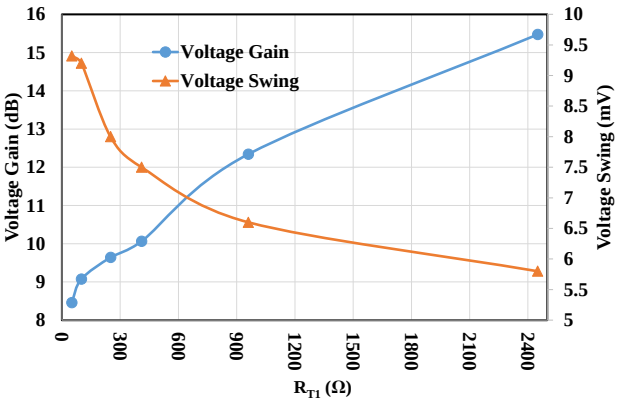

Figure 8. Output voltage and swing as a function of input termination resistance with a constant output termination resistance, showing the tunability of the gain and output swing of the MEMS resonant amplifier (R_{T2} = 50 Ω).

Future work includes better understanding and improvement of the device gain and power handling (output voltage swing) limitations.

ACKNOWLEDGEMENT

This work was supported by National Science Foundation CAREER grant #1056068.

REFERENCES:

[1]. H. C. Nathanson, W. E. Newell, R. A. Wickstrom, and J. R. Davis, Jr.,"The resonant gate transistor," *IEEE Trans. Electron Devices*, vol. ED-14,no. 3, pp. 117–133, Mar. 1967.

[2]. J.T.M. van Beek, K.L. Phan, G.J.A.M. Verheijden, G.E.J. Koops, C. van der Avoort, J. van Wingerden, D. Ernur Badaroglu, J.J.M. Bontemps, R. Puers, "A piezo-resistive resonant MEMS amplifier", Electron Devices Meeting, 2008. IEDM 2008. IEEE International, pp. 1 – 2.

[3]. D. Grogg, A.M. Ionescu, "The Vibrating Body Transistors", IEEE Transactions on Electron Devices (Volume: 58, Issue: 7), pp. 2113 – 2121 (2011)

[4]. K. L. Phan, P. G. Steeneken, M. J. Goossens, G. E. J. Koops, G. J. A. M. Verheijden, and J. T. M. van Beek, Spontaneous Mechanical Oscillation of a DC Driven Single Crystal, 2009, ArXiv 0904.3748

[5]. A. Rahafrooz, and S. Pourkamali, "Thermal-piezoresistive energy pumps in micromechanical resonant structures," IEEE Transactions on Electron Devices, 59, 3587 (2012)

[6]. A. Rahafrooz and S. Pourkamali, "High-frequency thermally actuated electromechanical resonators with piezoresistive readout," IEEETrans. Electron Devices, vol. 58, no. 4, pp. 1205–1214, Apr. 2011

[7]. A. Hajjam, A. Logan, and S. Pourkamali, "Doping induced temperature compensation of thermally actuated high frequency silicon micromechanical resonators," in IEEE MEMS Journal, vol.21, issue. 3, pp. 681-687, Jun. 2012.

CONTACT:

A.Ramezany, Email: axr134530@utdallas.edu
M.Mahdavi, Email: mxm130730@utdallas.edu

AN ETCH HOLE-FREE PROCESS FOR TEMPERATURE-COMPENSATED, HIGH Q, ENCAPSULATED RESONATORS

Eldwin J. Ng[*], *Yushi Yang, Yunhan Chen, and Thomas W. Kenny*
Stanford University, Stanford, California, USA

ABSTRACT

A process is presented for the fabrication of high quality factor (Q), temperature-compensated silicon resonators without release-etch perforations within the epitaxial polysilicon encapsulation (*epi-seal*). Electrostatically actuated Lamé-mode square resonators up to 400 µm wide with frequencies from 8 to 107 MHz are released with no etch perforations, resulting in high f-Q products of up to 2e13 Hz. Temperature compensation with a turnover point is achieved using an epitaxially grown, highly boron-doped device layer.

INTRODUCTION

Silicon resonators have been shown to have excellent stability when properly encapsulated [1] and also very high quality factors. Lamé-mode resonators have near-zero thermoelastic dissipation (TED) losses and are known for their high f-Q products of ~1.5e13, believed to be limited by the Akhieser effect [2]. Holes in the device layer for oxide temperature compensation [3] or for device release are generally seen to cause a degradation in the quality factor through TED [4].

To maintain a high f-Q product together with passive temperature compensation, the device silicon can be highly doped. Doping with either p- or n-type dopants has been seen to cause a reduction in the frequency-temperature dependence [5-8], with temperature turnover points previously demonstrated with n-type dopants. This paper demonstrates a similar turnover in highly boron-doped silicon, with a smaller second order temperature coefficient than typically achieved with n-type dopants. High f-Q products are preserved using a process that leaves no etch perforations within the Lamé-mode resonator, and is compatible with the clean, wafer-level *epi-seal* encapsulation process [9].

FABRICATION

Good control of the doping concentration for a thick (tens of µm) device layer is desirable for manufacturable temperature compensated devices, and can be achieved by growing doped silicon epitaxially on a silicon-on-insulator wafer with a thin device layer. However, significant tensile stress is induced in the crystal for high doping concentrations as a result of the substitution of silicon atoms for smaller boron atoms, which translates to severe wafer bow and unprocessable wafers. To reduce the stress, it is key to note that the stress here arises from the mismatch of the average lattice constant between the seed and the grown layer. Hence, instead of starting with a lightly doped silicon-on-insulator (SOI) device layer and growing highly doped (p++) silicon epitaxially, it is important to first start with a highly doped device layer. This was achieved by first growing a thin (2.5 µm), p++ (~2e20cm^{-3}) device layer on a sacrificial wafer and fusion bonding to create an SOI wafer with a 2 µm p++ device layer atop a 2 µm layer of buried oxide (Fig. 1a). Vent holes (⌀ 0.6 µm) are defined in this thin layer, and vapor HF is then used to release the buried oxide under large devices (Fig. 1b). Silicon migration and a thick (18 µm) p++ epitaxial silicon deposition at 1130°C and 30 torr is used to seal the vent holes and build up the device layer (Fig. 1c). This is followed with the standard *epi-seal* process, where devices are then patterned into the p++ device layer. 2 µm of oxide is deposited over the trenches (Fig. 1d), electrical contact holes are etched into the oxide. A first epitaxial polysilicon cap (5 µm) is put on, and after etching vents (⌀ 0.8 µm) (Fig. 1e) and releasing the oxide around the device, a second thick layer of polysilicon (20 µm) is deposited (Fig. 1f). Electrical contacts vias are then patterned in the cap, and the cavity pressure is lowered to <1 Pa by diffusing residual hydrogen out of the cavity (Fig. 1g). The device layer resistivity was measured post-process to be 0.739 mΩ-cm.

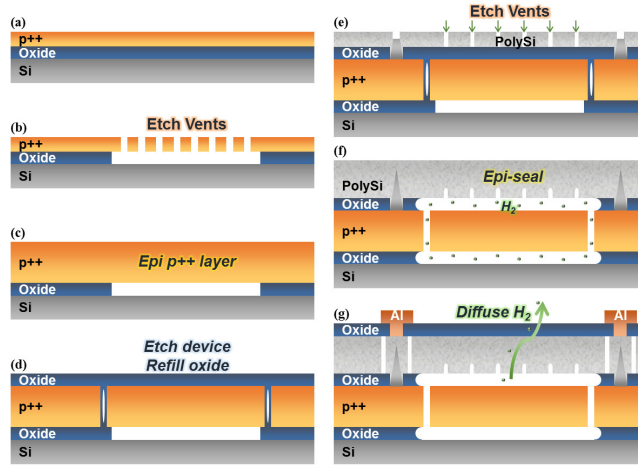

Figure 1. Process for releasing large device areas without etch holes and controlling the doping concentration via epitaxial deposition, with epi-seal encapsulation.

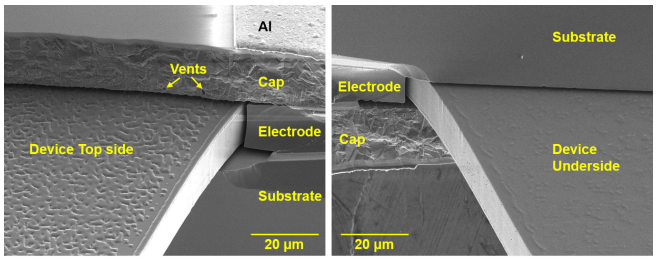

(a) **(b)**

Figure 2. 45° SEM images of an encapsulated device free from etch perforations, from (a) the top side and (b) the underside.

45°-view SEM images of the top and bottom surfaces of the encapsulated device (Fig. 2) show no traces of the etched device-layer vent holes in Fig. 1b. Surface roughness is observed, especially on the top surface of the device and is likely a result of the silicon deposition through the vent holes during the sealing of the cap (Fig. 1f).

RESULTS

Quality factors

Fundamental and higher order Lamé-mode resonators oriented in the <100> and <110> directions, with and without device-layer etch holes (⌀ 2 µm), were characterized in linear operation and are summarized in Table 1. For higher order modes, pull-in (PI) electrodes [10] were used to narrow the transduction gap to reduce the bias voltage required for operation. Frequency sweeps were performed using an Agilent 8753ES network analyzer at room temperature (~24°C), and f-Q products of between 1e13

9781940470016/HH2014/$25©2014TRF
DOI 10.31438/trf.hh2014.26

Table 1: Lamé-mode resonator designs and test results.

Edge length (μm), design features	Crystal Orientation	Bias voltage, input power	Frequency (MHz)	Quality Factor	f-Q (Hz)
400	<100>	15 V, -15 dBm	8.1	1.7 M	1.4e13
400	<110>	15 V, -15 dBm	10.0	1.7 M	1.7e13
300 Pull-in	<110>	30 V, -40 dBm	13.4	1.2 M	1.6e13
250	<100>	25 V, -15 dBm	13.0	1.5 M	2.0 e13
250	<110>	35 V, -15 dBm	16.1	1.0 M	1.6e13
300 Pull-in (3rd order)	<110>	35 V, -15 dBm	40.3	370 k	1.5e13
300 Pull-in (4th order)	<110>	35 V, -15 dBm	53.7	380 k	2.0e13
300 Pull-in (8th order)	<110>	70 V, -15 dBm	107.3	100 k	1.1e13
400 Etch holes	<100>	35 V, -10 dBm	9.7	80 k	7.8e11
400 Etch holes	<110>	35 V, -10 dBm	7.8	120 k	1.1.e12

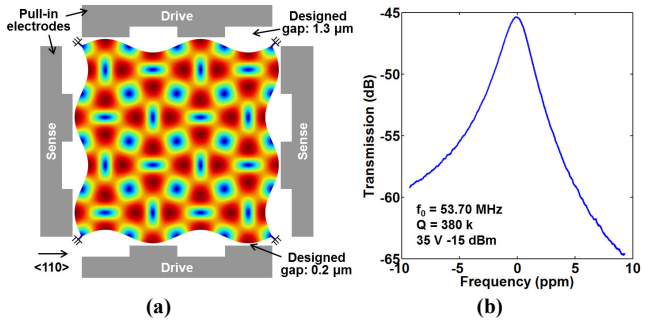

Figure 3. (a) 4th order resonant Lamé mode shape in the <110> direction with 300 μm edge length, actuated using pull-in electrodes. (b) Frequency sweep with an f-Q product of 2.0e13 Hz.

and 2e13 Hz were consistently observed for the resonators without etch holes. A frequency sweep of the 4th order Lamé mode is shown in Fig. 3. This f-Q of 2.0e13 Hz is about three times as high as achieved in the *epi-seal* process with limited release areas [11].

Temperature Compensation

It is seen that highly boron-doped Lamé resonators in the <100> and <110> directions show different frequency-temperature dependences (Fig. 4). Notably, the <110> Lamé resonators have temperature turnover points, with smaller second order temperature coefficients of ~-22 ppb/°C^2 as compared to the typical -65 ppb/°C^2 for temperature-compensated n-type resonators [12].

CONCLUSION

Demonstrated is a process for achieving high quality factor resonators in conjunction with temperature-compensation within an ultra-clean encapsulation process. No residual etch holes are present in the device, allowing for high quality factors. For temperature compensation, epitaxial deposition was used to achieve good control of the device boron doping. Stress effects from the high dopant concentration are mitigated by starting with a highly doped seed. Resonators with f-Q products of up to 2.0e13 Hz are demonstrated with temperature turnover points.

ACKNOWLEDGEMENTS

This work was supported by DARPA grant N66001-12-1-4260, "Precision Navigation and Timing program (PNT)," managed by Dr. Robert Lutwak, and DARPA grant FA8650-13-1-7301, "Mesodynamic Architectures (MESO)," managed by Dr. Jeff Rogers. The fabrication work was performed at the Stanford Nanofabrication Facility (SNF) which is supported by National Science Foundation through the NNIN under Grant ECS-9731293.

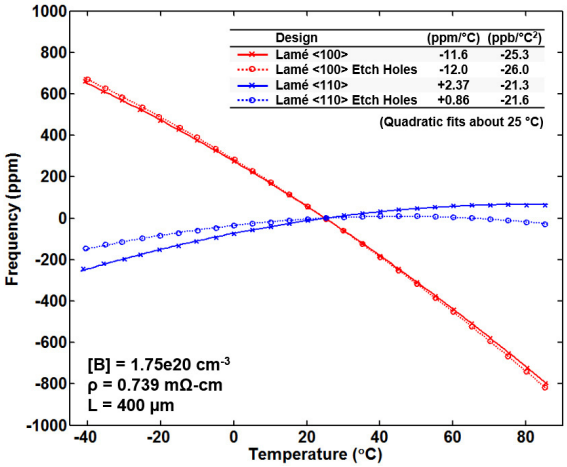

Figure 4. Frequency-temperature dependence of highly boron-doped Lamé resonators with fitted temperature coefficients.

REFERENCES

[1] B. Kim *et al.*, "Frequency Stability of Wafer-Scale Film Encapsulated Silicon Based MEMS Resonators," *Sensors and Actuators A,* vol. 136, pp. 125-131, May 2007.

[2] S. A. Chandorkar *et al.*, "Limits of Quality Factor in Bulk-Mode Micromechanical Resonators," *IEEE MEMS 2008,* pp. 74-77, 2008.

[3] V. Thakar and M. Rais-Zadeh, "Temperature-compensated Piezoelectrically Actuated Lamé-mode Resonators," *IEEE MEMS 2014,* pp. 214-217, Jan 2014.

[4] C. Tu and J. E.-Y. Lee, "Study on Thermoelastic Dissipation in Bulk Mode Resonators with Etch Holes," *IEEE NEMS 2012,* pp. 478-482, 2012.

[5] J. S. Wang, K. M. Lakin, and A. R. Landin, "Sputtered C-Axis Inclined Piezoelectric Films and Shear Wave Resonators," *IEEE Freq. Ctrl. Sym. 1983*, pp. 144-150, 1983.

[6] A. K. Samarao and F. Ayazi, "Temperature Compensation of Silicon Micromechanical Resonators via Degenerate Doping," *IEEE IEDM 2009,* pp. 737-740, 2009.

[7] M. Shahmohammadi, B. P. Harrington, and R. Abdolvand, "Turnover Temperature Point in Extensional-Mode Highly Doped Silicon Microresonators," *IEEE Trans. Elec. Dev.,* vol. 60, pp. 1213-1220, Mar 2013.

[8] T. Pensala, A. Jaakkola, M. Prunnila, and J. Dekker, "Temperature Compensation of Silicon MEMS Resonators by Heavy Doping," *IEEE Intl. Ultrasonics Symposium 2011,* pp. 1952-1955, 2011.

[9] R. N. Candler *et al.*, "Long-Term and Accelerated Life Testing of a Novel Single-Wafer Vacuum Encapsulation for MEMS Resonators," *JMEMS,* vol. 15, pp. 1446-1456, Dec 2006.

[10] E. J. Ng *et al.*, "Stable Pull-in Electrodes for Narrow Gap Actuation," *IEEE MEMS 2014,* pp. 1281-1284, 2014.

[11] R. Melamud *et al.*, "MEMS Enables Oscillators with sub-ppm Frequency Stability and sub-ps Jitter," *Hilton Head 2012,* pp. 66-69, 2012.

[12] A. Jaakkola, M. Prunnila, T. Pensala, J. Dekker, and P. Pekko, "Determination of Doping and Temperature Dependent Elastic Constants of Degenerately Doped Silicon from MEMS Resonators," *arXiv: 1401.1363 [cond-mat.mtrl-sci],* 2014.

CONTACT

*E.J. Ng; eldwin@mems.stanford.edu

ETCH-A-SKETCH RESONATOR

[1]R. Wang, [1]S. A. Bhave and [2]K. Bhattacharjee
[1]Cornell University, Ithaca, NY, USA
[2]RF Micro Devices Inc., Greensboro, NC, USA

ABSTRACT

This paper demonstrates AFM-based post-release piezoelectric domain engineering [1] on a Lithium Niobate (LN) MEMS resonator. We "Etch-A-Sketch" a poling pattern on the membrane resonator that redefines the electro-mechanical coupling of the mechanical vibration modes. This technique introduces a new resonance peak at 681 MHz to the original un-poled admittance spectrum of the resonator. In addition, this method only requires 80V (magnitude) to achieve domain inversion, which is over 100× lower than the poling voltage required for bulk LN.

FABRICATION PROCESS AND DEVICE CONCEPT

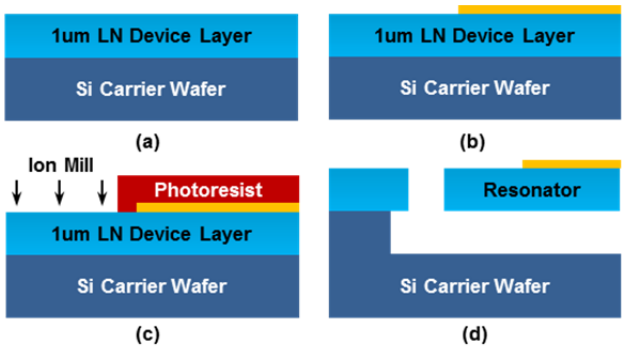

Figure 1. Fabrication of Etch-a-Sketch resonator: (a) Lithium Niobate thin-film bonded to Si substrate. (b) Top gold electrodes are defined by lift-off, (c) ion milling etches the LN to define device geometry, and (d) XeF_2 is used to release the resonator.

Fabrication of the Etch-a-Sketch resonator begins with a 1µm thin[2] white LN thin film directly bonded on a Si substrate, with crystal z-axis normal to plane of the wafer. Z-cut LN does not provide modes with high coupling coefficient, k_{eff}^2, that can be easily excited using interdigitated transducers (IDT). However, we chose this cut for a proof-of-concept demonstration as domain inversion is well-studied on z-axis LN [1]. Top electrodes are defined by lift-off, followed by ion milling through the LN film with a photoresist mask to define the resonator geometry [3]. Finally, the membrane resonator is released from the substrate using XeF_2 (Fig. 1). Fig. 2 shows an SEM of the released device, where the IDT fingers oriented perpendicular to the crystal y-axis

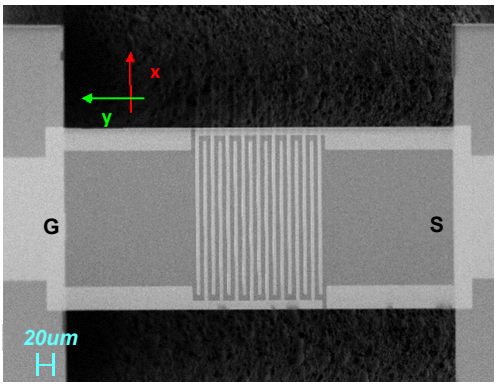

Figure 2. SEM of the z-cut LN Etch-A-Sketch resonator.

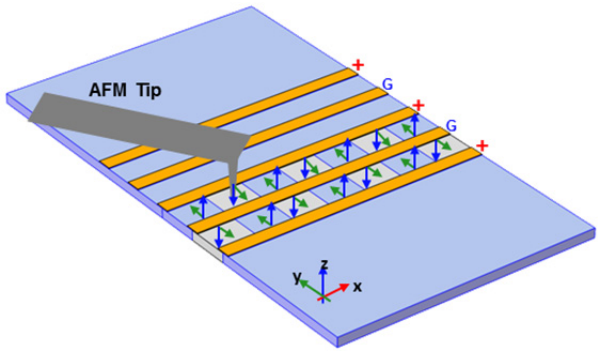

Figure 3. "Writing" the resonator frequency by AFM tip poling checkerboard patterns on the LN resonator. Green and blue arrows mark +y-axis and +z-axis domain directions respectively.

are spaced by 4.5µm. The width (x-direction) of the resonator is 72µm. Before performing domain patterning, the admittance of the resonator is measured as baseline for comparison with the admittance after poling.

An Asylum AFM system was used to perform the domain patterning of the resonator. The membrane was scanned continuously between the IDT electrodes in contact mode while applying periodic voltage to the AFM tip to invert the domain direction of the membrane in a checkerboard pattern (Fig. 3). A low spring constant (8N/m) solid platinum AFM tip (Model No.: 25Pt400B, Rocky Mountain Nanotech.) was used to minimize the stress on the membrane during domain writing, while providing good electrical contact.

In addition to excellent spatial control (25nm resolution), a key benefit of Etch-a-Sketch poling is the focused E-field from the sharp AFM tip which penetrates the thin film LN. This reduces the voltage required to achieve domain inversion relative to bulk LN poling by over 100×. In this work, 80V (magnitude) was sufficient to surpass the coercive field of LN [4], and ensured high contrast domain inversion. The poled domain pattern was verified by piezo-response force microscopy (PFM). Fig. 4 shows the phase of the piezo-response which exhibits a clear checkerboard pattern.

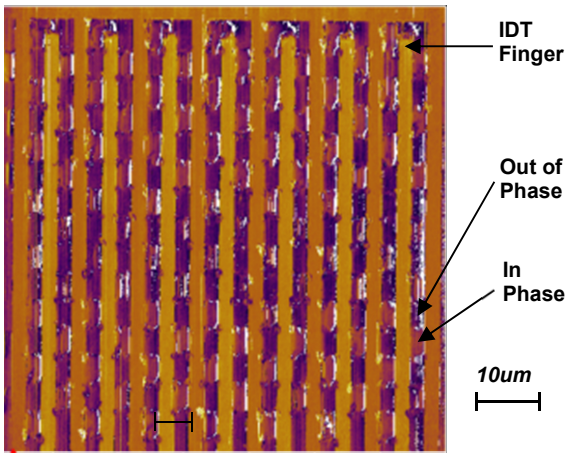

Figure 4. Phase response of the PFM after domain poling.

9781940470016/HH2014/$25©2014TRF
DOI 10.31438/trf.hh2014.27

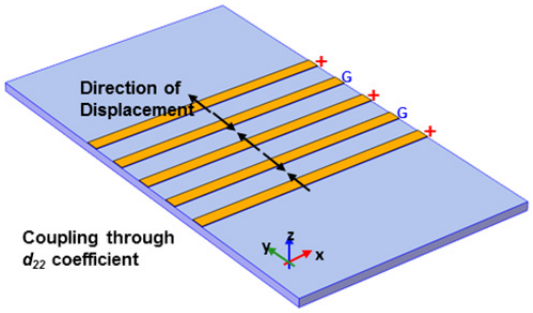

Figure 5. Without poling, E-field couples to mechanical motion in y direction through d_{22} coefficient.

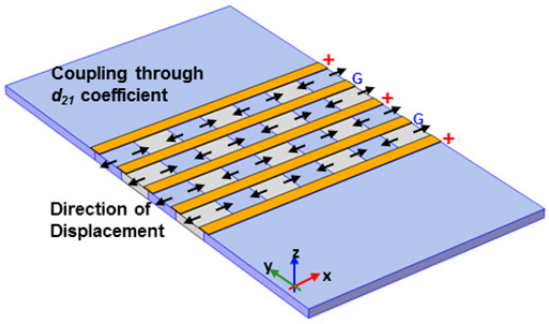

Figure 6. After poling, E-field couples to motion in x direction through d_{21} coefficient.

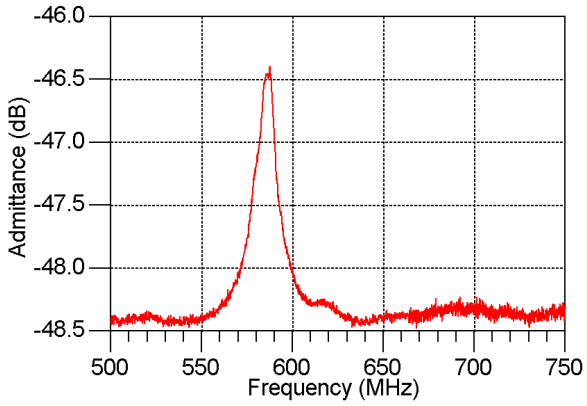

Figure 7. Admittance of the resonator before poling.

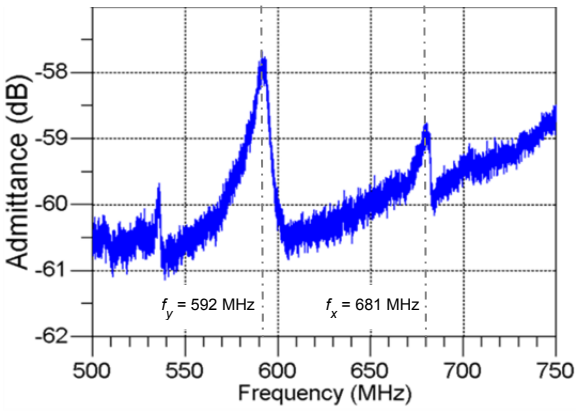

Figure 8. Admittance of the resonator after poling.

The poled pattern has a period of 4μm in the x-direction. The dark violet color indicates the thin film moves out of phase with the PFM excitation, and orange indicates in phase motion (opposite polarity). Metal electrode fingers appear in light yellow. It should be noted that as the domain inversion happens, both the y-axis and z-axis of the domain are inverted, while the x-axis remains unchanged [5].

In the absence of the periodically poled pattern, the primary resonance frequency is defined by finger spacing. The acoustic wave is excited through the d_{22} coefficient, and travels parallel to the crystal y-axis. Therefore, this device behaves like a traditional contour mode resonator without periodical poling (Fig. 5). After we Etch-A-Sketch the checkerboard pattern in the LN, the two domains with opposite crystal orientation bounded by two adjacent fingers are excited out-of phase in the x-direction through the d_{21} coefficient. Simultaneously, the two adjacent domains separated by electrode finger move in phase (Fig. 6) because both the E-field and crystal axis have opposite polarizations. As a result, all the domains move collectively as a high-order contour mode vibrating in the x-direction. In this case, the frequency is determined by the periodicity of the domain pattern. By writing domain patterns with different period, we can control the resonance frequency of the resonator.

EXPERIMENTAL RESULTS

RF characterization was performed in air using a standard 1-port measurement with signal configuration as indicated in Figs. 5 and 6. No de-embedding was performed. Fig. 7 shows the admittance of the device before poling, with a 592 MHz peak corresponding to the y-axis contour mode. This resonance matches well with analytical derivation for 4.5μm IDT spacing. Since the Etch-a-Sketch poling does not affect this mode, the 592 MHz resonance serves as a reference for mapping the frequency and wavelength of the resonance generated by domain patterning. Fig. 8 shows the admittance after domain patterning (4μm period in x-direction) which generates a new resonance at 681 MHz, next to the y-axis mode. As expected, the measured frequency ratio $f_x/f_y = 1.14$ between the two peaks is almost identical to the ratio of the IDT spacing and poling pattern (4.5μm/4μm = 1.125), validating the Etch-A-Sketch concept.

In conclusion, we demonstrated an Etch-A-Sketch resonator, in which resonance frequency can be programmed by "writing" periodic domains on the resonator with an AFM tip. Initial results from this device demonstrate targeted generation of x-axis resonance with predictable and controllable frequency. Integrated with AFM tip arrays (e.g. [6] by Intel), such devices can achieve wide range in-field tuning of the resonance frequency, and facilitate the realization of reconfigurable RF MEMS front-ends.

REFERENCES

[1] B. Rodriguez, et al., "Domain growth kinetics in Lithium Niobate single crystals studied by piezoresponse force microscopy," APL 86, 012906 (2005).

[2] S. Gong and G. Piazza, "High electromechanical coupling resonators using ion sliced X-cut LiNbO3 thin film," IEEE Microwave Symposium, pp. 1-3, 2012.

[3] R. Wang, et al., "High $k_t^2 \times Q$, multi-frequency Lithium Niobate resonators," MEMS 2013, pp.165-168, 2013.

[4] S. Kim, et al., "Coercive fields in ferroelectrics: a case study in Lithium Niobate and Lithium Tantalate," APL 80, 2740 (2002).

[5] T. Sono, et al., "Reflection second harmonic generation on a z-cut congruent lithium niobate crystal," PRB 74, 205424 (2006).

[6] S. Severi, et al., "CMOS-integrated poly-SiGe cantilevers with read/write system for probe storage device," Transducers'09, pp. 2409-2412, 2009.

FUSED SILICA MICRO BIRDBATH SHELL RESONATORS WITH 1.2 MILLION Q AND 43 SECOND DECAY TIME CONSTANT

J. Cho, T. Nagourney, A. Darvishian, B. Shiari, J.-K. Woo, and K. Najafi
Center for Wireless Integrated MicroSensing and Systems, University of Michigan, USA

ABSTRACT

We report a micro-scale fused silica (FS) birdbath (BB) shell resonator with a high mechanical quality factor (Q = 1.2 million), long decay time constant (τ = 43.6 s), a resonant frequency of 8.8 kHz for wineglass modes, and excellent symmetry resulting in a frequency split of only 6.7 Hz between two wineglass modes. The resonator has a volume of 41 mm^3 (radius = 2.5 mm, anchor radius = 0.5 mm, height ~ 2.1 mm). The resonator is useful in a wide range of applications, including inertial sensors, timing devices, and chemical and biological sensors.

INTRODUCTION

A high Q and long decay time constant (τ) are desired in many sensing applications, because they reduce mechanical noise and bias drift. A silicon gyroscope with f ~ 2 kHz and Q of 1.16 million has been reported [1]. Macro-scale FS wineglass resonators with Q of tens of millions at 3 kHz [2] or 1 million at >70 kHz have been reported [3]. For micro vibratory gyroscopes, an f of ~10 kHz is preferred, because the sensor 1) can operate above the f of environmental noises, 2) has good flexibility, which results in a large scale factor, and 3) and has a long decay time constant (τ) leading to good bias stability. On the micro scale, there has been a lack of materials and fabrication techniques to achieve an ultra-high Q and a long τ in this frequency range. It is difficult to achieve >1 million Q with Si in the ~10 kHz frequency range due to high thermoelastic damping (TED). FS suffers less TED than Si; however, it is difficult to etch or form complicated FS structures using conventional fabrication processes. We overcame these challenges and achieved both very high Q, long τ, and very small frequency split (Δf) in our birdbath shell resonators.

FABRICATION

We fabricated our shells using a 3D micro blowtorching process (Figure 1) [4]. A thin FS substrate (thickness ~ 100 µm) is placed on top of a graphite mold and is controllably heated by a propane-oxygen blowtorch at >1600 °C while applying vacuum from the bottom of the mold. The shells were released using conventional lapping and CMP processes. The devices have a 2.5 mm radius, 0.5 mm anchor radius, ~2.1 mm height (Fig. 2), and ~60 µm rim thickness (Figure 2).

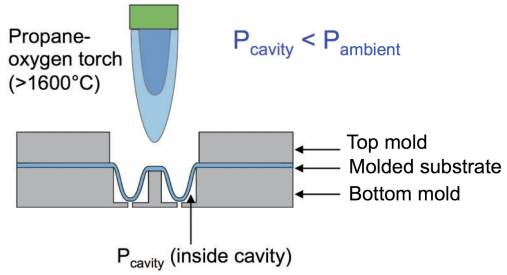

Figure 1: Three dimensional micro blowtorch molding process

DEVICE CHARACTERIZATION

The f and τ of an uncoated BB resonator were measured by AS&T using conformal Laser Doppler Vibrometry [5] while driving it with a PZT actuator. We tested a metal-coated BB resonator (sputtered Cr/Au = 15/50 Å) using a capacitive measurement method. Both tests were done at <1 mTorr pressure at room temperature. Both samples were cleaned using BHF for 3–30 s before testing. The uncoated BB resonator has n = 2 wineglass modes at 8.718 kHz with τ = 42.18 s (Q = 1.16 million) and 8.725 kHz with τ = 43.58 s (Q = 1.19 million) (Figure 3). These time constants are the longest reported for small wineglass structures. The coated BB resonator has wineglass modes at 10.163 kHz with τ = 15.24 s (Q = 486k) and 10.188 kHz with τ = 9.70 s (Q = 310k) (Figure 4). We believe that a combination of large device height, BHF etching, and a thinner metal layer led to the improvement of τ. Figure 5 shows the dependency of τ on the BHF etching duration as well as the thicknesses of the metal coating on six different devices. We found ~2× improvement in τ due to the reduced metal thickness and 30 s BHF etching. However, after longer BHF etching (95 s), we found a reduction in τ even with the same metal thickness, likely due to increase in surface roughness.

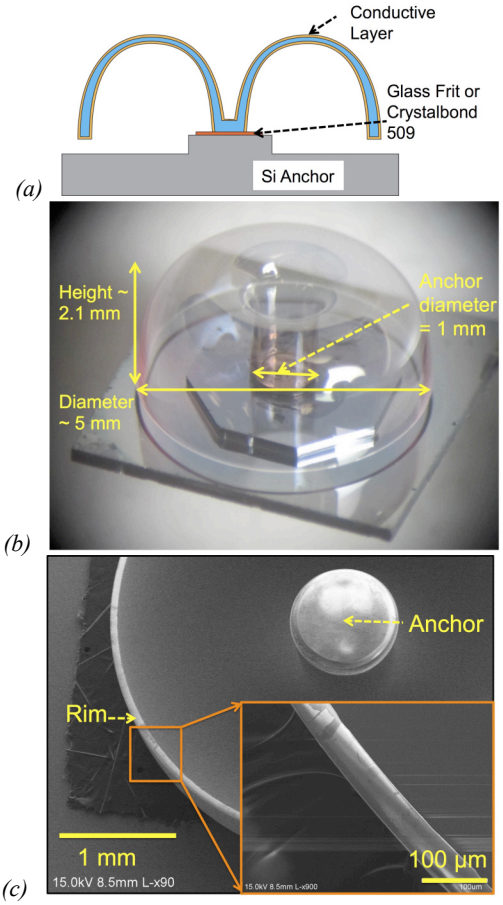

Figure 2: (a) Illustration, (b) photograph, and (c) SEM image of fused silica micro birdbath shell resonator. The shell is coated with Cr/Au = 15/50 Å. Device dimensions: radius ~ 2.5 mm, anchor radius = 0.5 mm, height ~ 2.1 mm, rim thickness ~ 60 µm.

9781940470016/HH2014/$25©2014TRF
DOI 10.31438/trf.hh2014.28

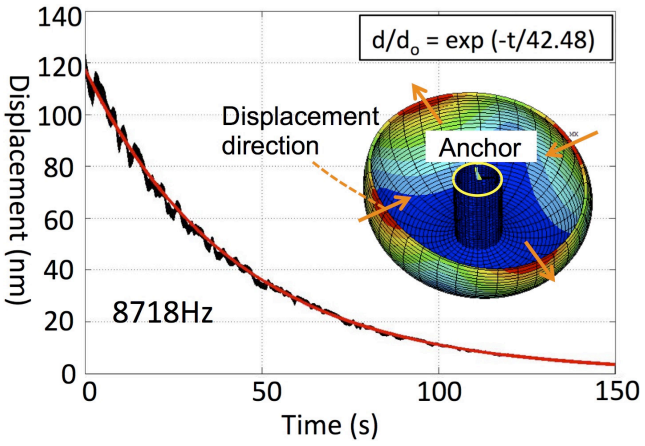

(a)

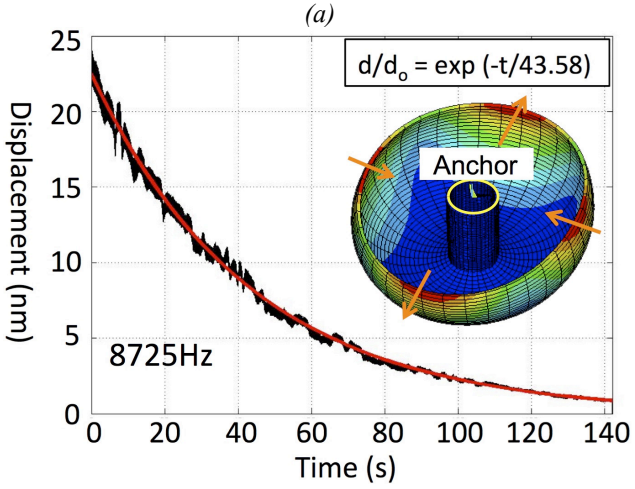

(b)

Figure 3: Ring-down time plot of n = 2 wineglass modes of uncoated BB resonator using conformal Laser Doppler Vibrometry: (a) f = 8.718 kHz and τ = 42.18 s (Q = 1.16 million). (b) f = 8.725 kHz and τ = 43.58 s (Q = 1.19 million) [5].

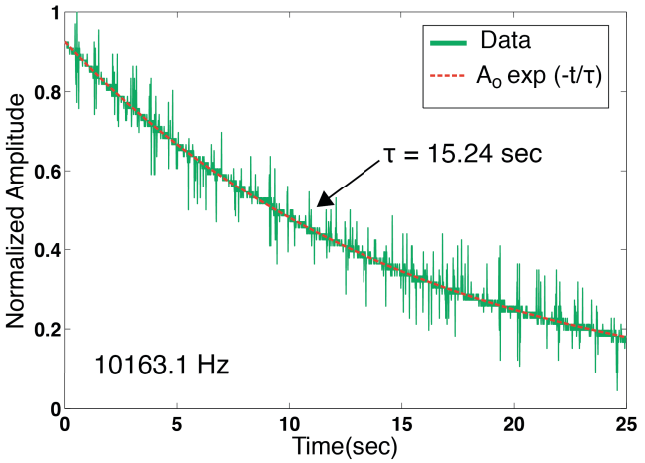

Figure 4: Ring-down time plot of n = 2 wineglass modes of coated BB resonator using capacitive measurement method: f = 10.163 kHz and τ = 15.24 s (Q = 486k). Another mode has f = 10.188 kHz and τ = 9.70 s (Q = 310k).

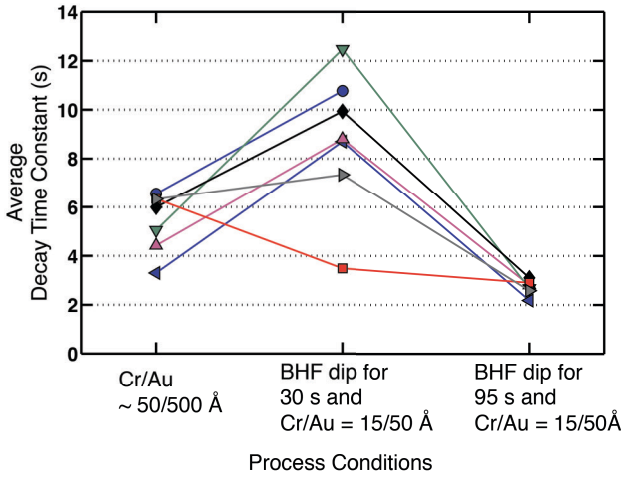

Figure 5: Dependency of τ on metal coating and BHF etching for six different samples. These devices have resonant frequencies at 9.5 ~ 11 kHz.

CONCLUSION

We report a micro BB resonator with a small volume (~41 mm^3) with one of the best *Q*s (= 1.2 million), τs (= 43.58 s), and structural symmetries (*Δf* = 7 Hz). The good resonance characteristics are due to the low TED and ultra-low surface roughness (< 1 nm) achieved using the 3-D micro blowtorch molding process. The process can be adopted to fabricate a wider variety of high-performance micro sensors and actuators. We found strong dependency of τ on the conductive metal coating and surface cleaning.

ACKNOWLEGEMENTS

This work is supported by DARPA MRIG award #W31P4Q-11-1-0002. We thank Jim Kilpatrick, Adela Apostol, and Vladimir Markov of Advanced Systems and Technologies, Inc., Irvine, CA for measurements with the conformal imaging vibrometry. We thank Dr. Radheshyam Tewari and Professor Craig Friedrich at Michigan Technological University for machining graphite molds. Portions of this work were done in the Lurie Nanofabrication Facility (LNF), a site of the National Nanotechnology Infrastructure Network (NNIN), which is supported in part by the National Science Foundation (NSF).

REFERENCES

[1] S.A. Zotov, A. A. Trusov, A. M. Shkel, "High-Range Angular Rate Sensor Based on Mechanical Frequency Modulation", J. Microelectromech. Sys., 22, 398 (2012).

[2] E. J. Loper and D. D. Lynch, "Projected System Performance Based on Recent HRG Test Results", Proc. IEEE/AIAA 5th Digital Avionics System Conference, Seattle, WA (1983), pp. 18.1.1 – 18.1.6.

[3] M. J. Ahamed, D. Senkal, and A. M. Shkel, "Effect of Annealing on Mechanical Quality Factor of Fused Quartz Hemispherical Resonator", Proc. IEEE ISSIS 2014, Laguna Beach, CA (2014), pp. 59-62.

[4] J. Cho, J. Yan, J. A. Gregory, H. Eberhart, R. L. Peterson, and K. Najafi, "3-Dimensional Blow Torch-Molding of Fused Silica Microstructures", J. Microelectromech. Sys., 22, 1276 (2013).

[5] J. Kilpatrick, A. Apostol, and V. Markov, "MEMS characterization with Conformal Imaging Vibrometry", Proc. IEEE ISISS 2014, Laguna Beach, CA (2014), pp. 86-88.

LEVITATION OF UNTETHERED STRESS-ENGINEERED MICROFLYERS USING THERMOPHORETIC (KNUDSEN) FORCE

V. Foroutan[1], R. Majumdar[1], O. Mahdavipour[1], S. P. Ward[2], and I. Paprotny[1]*
[1]Department of Electrical and Computer Engineering University of Illinois, Chicago, USA
[2] Department of Electrical and Computer Engineering University of California, San Diego, USA

ABSTRACT

In this paper we present the theory and initial successful levitation experiments of untethered microscale structures (microflyers) using thermophoretic force. The microflyers consist of a 300 µm × 300 µm sized chassis fabricated from polycrystalline silicon using a surface micromachining process. The devices are levitated using microfabricated heaters attached to an underlying substrate. A novel *in-situ* masked post-release stress-engineering process is used to generate a concave upwards curvature of the flyers chassis, resulting in increased pitch and roll stability during flight, take-off, and landing.

INTRODUCTION

Several novel microscale mobile robotic systems have been developed in last decade, such as electrostatically driven stress-engineered microrobots (MicroStressBots) [1], resonating stepping robots, stick-slip magnetic walkers and microscrew-based swimmers. Although flying microscale robots have not been previously demonstrated, levitation of untethered microstructures using the thermophoretic force has been previously proposed in [2].

In this paper we present the ***first experimental validation*** of successful untethered levitation of 300 µm × 300 µm sized microscale structures (microflyers). The device is actuated (levitated) by Knudsen force generated by an underlying microfabricated heater. This is the first validation of potentially a new type of actuation mechanism for MEMS structures, which may pave way for new class of free-flying microscale robots.

The microflyer chassis was fabricated using a surface micromachining process. To stabilize the device during flight, the chassis was curved out-of-plane using an *in-situ* masked MEMS stress-engineering process.

KNUDSEN FORCE

When two separate objects at different temperatures are surrounded by a gas there is a force experienced by each of the objects known as the Knudsen force. The underlying mechanism for this force is the momentum imparted from the heated gas molecules onto the lower temperature object is greater than the momentum from the slower molecules striking the opposite side of the object. This force is strongest when the distance between intermolecular collisions and the separation distance are comparable i.e. their ratio is close to one. A relationship for the force between the temperature of the heated surface and a microcantilever was found by Passian [3] to be:

$$F_{th} = \frac{A_c P_r}{2}\left[\sqrt{\frac{T_s'}{T_r}} + \sqrt{\frac{T_{cb}'}{T_r}} + \sqrt{\frac{T_{ct}'}{T_r}} - 1\right] \quad (1)$$

where A_c is the surface area of the microflyer, P_r is the pressure of the surrounding gas, Tr is the temperature of the surrounding gas, and T_s', T_{cb}', and T_{ct}' are the temperatures of the reflected gas molecules after colliding with the substrate (heater), carrier bottom (bottom of the microflyer), and carrier top (top of the microflyer) respectively.

DEVICE DESIGN

The initially planar microrobot chassis was fabricated from polycrystalline silicon (polysilicon) using a multi-user MEMS fabrication process. The flyers and the heaters were released in hydrofluoric acid (49% HF), and out-of-plane curvature was generated using a novel post-release stress engineering process. Figure 1 shows a scanning-electron micrograph of two of the stress-engineered microflyers that were successfully levitated during our experiments.

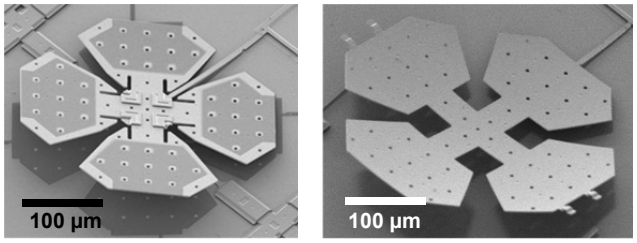

(a) *(b)*

Figure 1: Scanning-electron micrograph of two types of stress-engineered microflyers.

Figure 2 shows the curvature profile of five cantilevered test structures (SEM of the cantilevers is shown in the inset) exposed to 75 nm of thermally evaporated Chromium (Cr) with an intrinsic compressive stress of 1.42 $\times 10^9$ Pa. The curvature can be controlled by varying the cross section (between cantilevers ii, iii, and iv), attaching fixed shadow masks (cantilever v), or using reconfigurable in-situ fabricated shadow masks (cantilever i). Sacrificial shadow-masks were also used to limit the curvature of the microflyer in Figure 1(a).

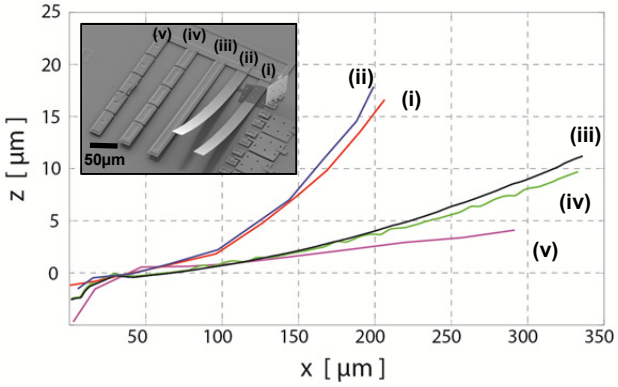

Figure 2: Height profiles for cantilevers (i-v) curved using in-situ masked stress engineering. Inset shows scanning-electron micrograph of the curved cantilevers.

The microflyers are fabricated attached to the transfer frames to enable successful transfer and placement on the heater prior to levitation. Figure 3 shows an optical micrograph of a transfer frame [1]. Microprobes inserted into the hinges of the transfer

9781940470016/HH2014/$25©2014TRF
DOI 10.31438/trf.hh2014.29

frame can be used to transport the microflyers between their location on the die and the fabricated heater.

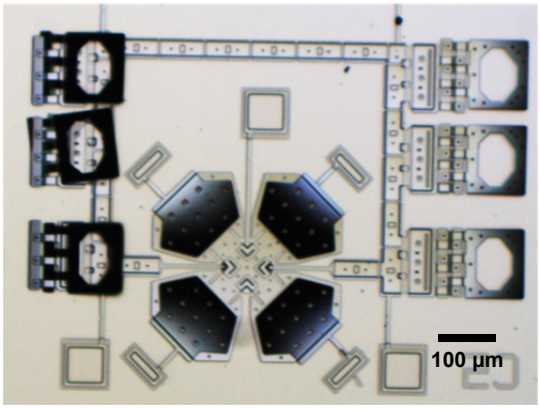

Figure 3: Optical micrograph of a stress-engineered microflyer attached to a transfer frame [1], which allows the flyer to be transported and deposited onto the heater. The frame chassis contains attached shadow masks, which protects it during the deposition of the stressor layer.

EXPERIMENTAL RESULTS AND DISCUSSION

We demonstrated both the actuation of microfabricated test structures using the Knudsen force, as well as the levitation of the untethered microrobot. Figure 4 shows the elevation of a tethered hinged test structure (as shown in the inset optical micrographs) using thermophoretic force generated by an underlying heater. These experimental results confirm our theoretical modeling of the thermophoretic force. Figure 5 shows images of microflyers prior to take-off, mid-flight, and after landing, in two separate levitation experiments. Because the heater was approximately the same size as the microflyer, the device would always translate towards its periphery. As expected, landing would occur as soon as significant part of the microflyer chassis would transit outside of the heated area.

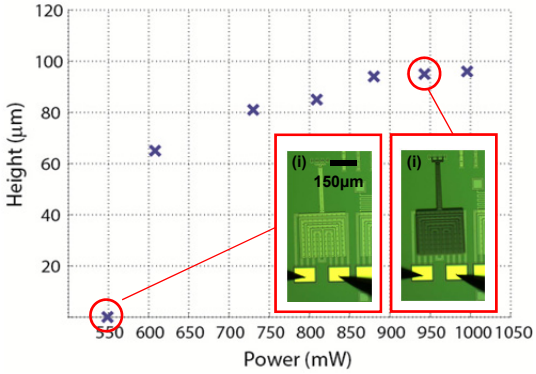

Figure 4: Tip height of a tethered hinged (i) test structure during the activation of an underlying heater. Inset shows the test structure before (left) and after (right) elevation close to its maximum height.

The results from repeated levitation experiments using both stress-engineered and flat (not stress-engineered) microflyers are shown in Table 1. Successful microflyer levitation occurred in 85% of experiments using stress-engineered devices compared to 0% in the case of flat devices of otherwise similar geometry. In both cases, identical take-off power was applied to the heater. The experiments show that the stress-engineering process is instrumental in increasing the in-flight stability of the levitated microstructures.

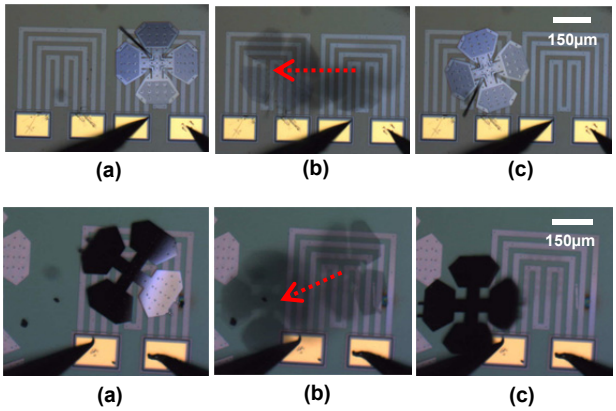

Figure 5: Two separate successful levitation experiments using two different types of microflyers (top and bottom). The optical micrographs show the flyers before (a), during (b) and after (c) levitation. Red arrow indicates the displacement of the flyers during the experiment.

Table 1: Results from levitation experiments using both stress-engineered and flat microflyers.

	Stress-Engineered	Flat
Number of Trials	7	5
Success Rate[%]	85%	0%

CONCLUSION

We present the theory and experimental results demonstrating that concave stress-engineered structures are capable of achieving reliable untethered levitation using thermophoretic forces. Levitating microstructures present a novel mechanism for microrobot actuation, and enable many future applications in areas such as assembly, micromanipulation, and surveillance. As the thermophoretic force can be generated by heating the wings of the flyers rather than by using underlying heaters, the levitation mechanism demonstrated in this work may enable the development of future untethered aerial microscale robots.

REFERENCES

[1] B. R. Donald, C. G. Levey and I. Paprotny. "Planar Microassembly by Parallel Actuation of MEMS Microrobots." Journal of Microelectromechanical Systems (JMEMS) 17, 4 (2008), pp. 789-808.

[2] B. Gotsmann, D. Michel, and U. Duerig. "Controlled Thermophoresis as an Actuation Mechanism for Noncantilevered MEMS Devices." Journal of Microelectromechanical Systems (JMEMS) 17, 6 (2008), pp. 1287-1293.

[3] A. Passian, A. Wig, F. Meriaudeau, T.L. Ferrell and T. Thundat "Knudsen forces on microcantilevers." Journal of applied physics 92, 10 (2002), pp. 6326-6333.

CONTACT

*I. Paprotny, paprotny@uic.edu

SELECTIVE WATER TRANSPORT ACROSS UNIFORM SUB-NANOMETER PORES IN MICROFABRICATED MEMBRANES

T. Humplik[1], R. Raj[1,2], S. C. Maroo[1,3], T. Laoui[4], and E.N. Wang[1]*
[1]Massachusetts Institute of Technology, Cambridge, MA, USA
[2]Currently with: Indian Institute of Technology Patna, Bihar, India
[3]Currently with: Syracuse University, Syracuse, NY, USA
[4]King Fahd University of Petroleum and Minerals, Dhahran, Saudi Arabia

ABSTRACT

We demonstrate selective water transport through uniform sub-nanometer pores using microfabricated zeolite membranes. Despite advances in micro/nanoscale manipulation, creating well-defined sub-nanometer pores for transport studies is challenging. We fabricated the first model platform to characterize and measure water transport limited to ≈5.5 Å pores over >20 mm^2 areas. Furthermore, with these membranes, we elucidated the effect of surface chemistry and pore confinement on water permeability. Using a custom-built flow cell, we showed osmotically-driven water transport where a more hydrophobic interface allows for an ≈10x increase in water flux. These insights will help tailor high performance desalination membranes, and can be extended to gas separation, sensing, and energy storage systems.

INTRODUCTION

Membrane-based water desalination has received significant interest due to limited clean water resources [1]. However, current membranes are limited by diffusive transport through tortuous polymeric active layers [1]. By using oriented sub-nanometer pores, water permeability and salt rejection across membranes promise to be substantially increased [2]. Yet, significant challenges in creating such small pores exist, and improved understanding of water transport in sub-nanometer pores is also necessary.

This paper presents a zeolite-based microfabricated membrane to experimentally quantify the water flux and demonstrate size-selective transport. Synthetic MFI zeolites with uniform three-dimensional structures of ≈5.5 Å pores, ideal for water transport (≈3 Å) and rejection of hydrated salt ions (>7 Å), were used. Furthermore, the pore surface chemistry was modified to create more hydrophobic/hydrophilic interfaces.

EXPERIMENTAL APPROACH AND RESULTS

We prepared two different MFI-type zeolites using hydrothermal synthesis [3]: a hydrophobic (H-MFI) and a more hydrophilic form infused with extra framework sodium cations (Na-MFI). We oriented the zeolites on a commercial anodized aluminum oxide (AAO) membrane (d=150 nm, Synkera) using manual direct assembly [4] and evaporated 40 nm of gold to mask the zeolites during fabrication (Figure 1a). To limit the transport to the sub-nanometer zeolite pores, we utilized the conformality of atomic layer deposition with hafnia to fill the exposed AAO not covered by zeolites (Figure 1b). To expose the zeolites for transport, both reactive ion etching (Figure 1c) and wet etching (Figure 1d) were used. This technique can create membranes >20 mm^2, which allows for the measurement of water transport across >10^{13} sub-nanometer pores (Figure 2).

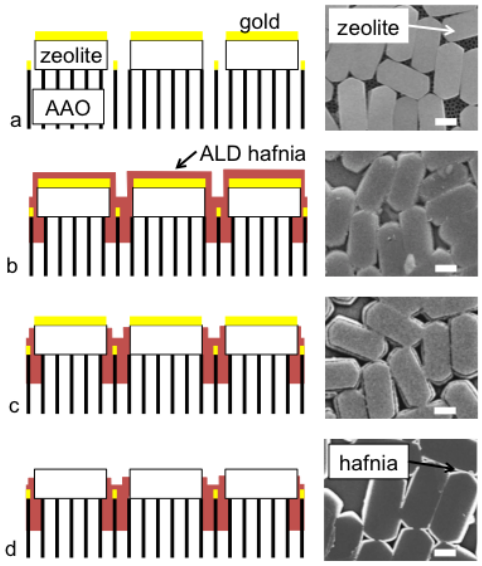

Figure 1: Fabrication schematic (shown with H-MFI zeolites) with corresponding SEM images. (a) Following the zeolite orientation onto the AAO, 40 nm of gold was thermally evaporated (Sharon Vacuum) onto the membrane to mask the zeolites during processing. (b) The remaining exposed AAO pore structure was filled by depositing hafnia (red in schematic) via atomic layer deposition (Savannah 100, Cambridge NanoTech). (c) Any hafnia that covered the zeolite crystals was dry etched using a CF_4/O_2 chemistry (Cirrus 150, Nexx Systems). (d) The gold was wet etched (Gold Etchant, Sigma Aldrich) to expose the underlying sub-nanometer pore structure and remove any residual hafnia covering the crystals. The scale bar for all images is 1 μm.

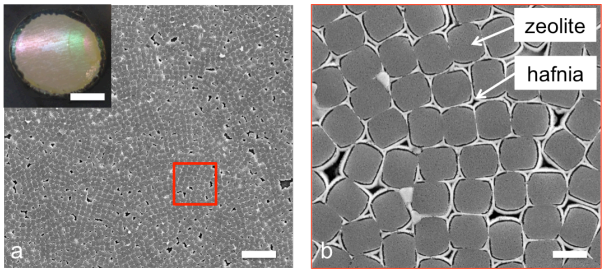

Figure 2: Images of fabricated Na-MFI membranes. (a) Low magnification image demonstrating zeolite orientation over a large area (scale bar is 10 μm). Inset: Image of fabricated membrane on AAO (scale bar is 5 mm) (b) Higher magnification image of red boxed region in (a) highlighting both the zeolite (darker cubes) and surrounding ALD hafnia (white regions) (scale bar is 1 μm).

9781940470016/HH2014/$25©2014TRF
DOI 10.31438/trf.hh2014.30

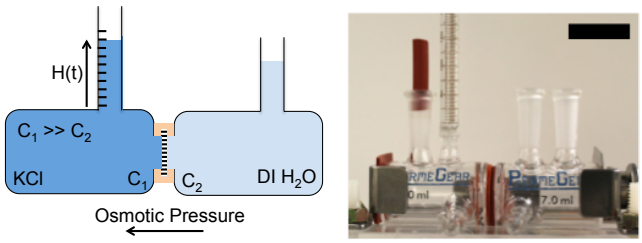

Figure 3: (a) Schematic and (b) image of flow cell used to study water transport across microfabricated zeolite membranes (scale bar is 2 cm). Various molar concentrations (0.5 M – 4 M) of potassium chloride was used to generate osmotic pressures of ≈2.5 MPa to ≈20 MPa to drive the water flux across the membranes. The change in volume (corresponding to a change in height in the graduated cylinder) was monitored as a function of time to quantify the water flux.

We used a custom-built flow cell to investigate water transport using pure water and KCl (Figure 3). Since the sub-nanometer zeolite pore structure can exclude the transport of hydrated salt ions [2,5], a selective water flow was generated by a difference in salt concentration (*i.e.,* osmotic pressure).

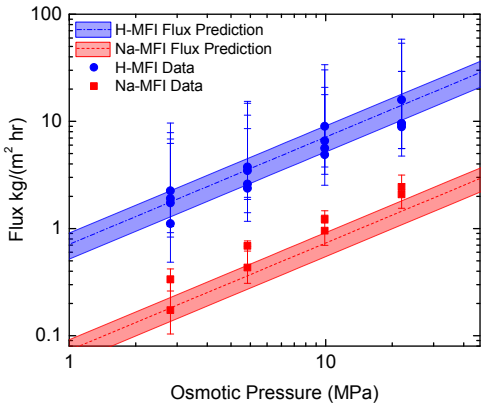

Figure 4: Comparison between experimental data (symbols) and flux prediction (shaded regions) made using transient uptake and desorption analysis (for more details on the model, see [6]). The error bars are associated with the uncertainty in the flux measurements and variation in membrane active area. The linear increase in the flux as a function of the osmotic pressure indicates that water is selectively transporting through the zeolite pores while salt ions are being rejected. The hydrophobic H-MFI zeolites (blue symbols) exhibit ≈10x higher water flux than the more hydrophilic Na-MFI zeolites. The decrease in flux associated with the more hydrophilic zeolites is associated with the stronger attraction to the pore interface, which effectively decreases the water diffusivity compared to the hydrophobic interface of the H-MFI zeolites. This insight leads to the possibility of further increasing the flux by up to an order of magnitude by utilizing zeolites that are more hydrophobic than H-MFI.

Figure 4 shows the measured water flux through the membranes compared to our developed model which accounts for the solution-diffusion based transport through the pores [6]. The linear trend of the flux as a function of the osmotic pressure indicates osmotically-driven flow (*i.e.,* the zeolite pores selectively transported water). Furthermore, the flux through the more hydrophobic H-MFI zeolites was ≈10x higher than that of the Na-MFI zeolites, contrary to previous zeolite studies [7], and is attributed to the decreased water attraction to the pore surface. Finally, our good agreement between the experiments and model indicate that the water transport is diffusion-limited, and can be increased further (possibly by an order of magnitude) by enhancing the hydrophobicity of the zeolites.

CONCLUSIONS

We demonstrated the first device that limits transport to well-defined and oriented sub-nanometer pores over areas >20 mm^2 and showed that pores with a more hydrophobic internal surface facilitate faster water transport. The experimental results from this study can be utilized to provide detailed physical insights into the transport mechanisms, which can guide the design of high permeability membranes in various water-based separation applications.

ACKNOWLEDGEMENTS

We thank Prof. Michael Tsapatsis (University of Minnesota) and Prof. Rohit Karnik (MIT) for helpful discussions and advice. This work was performed in part at the Center for Nanoscale Systems (CNS), a member of the National Nanotechnology Infrastructure Network (NNIN), which is supported by the National Science Foundation under NSF award no. ECS-0335765. CNS is part of Harvard University. This work was funded by the King Fahd University of Petroleum and Minerals in Dhahran, Saudi Arabia through the Center for Clean Water and Clean Energy at MIT and KFUPM under Project No. R10-CW-09. R.R. acknowledges fellowship support from Battelle's National Security Global Business.

REFERENCES

[1] T. Humplik, J. Lee, S. C. O'Hern, B. A. Fellman, M. A. Baig, S. F. Hassan, M. A. Atieh, F. Rahman, T. Laoui, R. Karnik, and E. N. Wang, "Nanostructured materials for water desalination," *Nanotechnology*, vol. 22, no. 29, p. 292001, Jun. 2011.

[2] Y. Liu and X. Chen, "High permeability and salt rejection reverse osmosis by a zeolite nano-membrane," *Phys Chem Chem Phys*, vol. 15, no. 18, pp. 6817–6824, 2013.

[3] T. Humplik, R. Raj, S. C. Maroo, T. Laoui, and E. N. Wang, "Framework Water Capacity and Infiltration Pressure of MFI Zeolites," *Microporous and Mesoporous Materials*, 2014.

[4] J. S. Lee, J. H. Kim, Y. J. Lee, N. C. Jeong, and K. B. Yoon, "Manual assembly of microcrystal monolayers on substrates," *Angew Chem Int Edit*, vol. 46, no. 17, pp. 3087–3090, 2007.

[5] S. Murad, K. Oder, and J. Lin, "Molecular simulation of osmosis, reverse osmosis, and electro-osmosis in aqueous and methanolic electrolyte solutions," *Molecular Physics*, vol. 95, no. 3, pp. 401–408, 1998.

[6] T. Humplik, R. Raj, S. C. Maroo, T. Laoui, and E. N. Wang, "Effect of Hydrophilic Defects on Water Transport in MFI Zeolites," *Langmuir, (submitted)*

[7] L. Li, N. Liu, B. McPherson, and R. Lee, "Enhanced water permeation of reverse osmosis through MFI-type zeolite membranes with high aluminum contents," *Ind. Eng. Chem. Res*, vol. 46, no. 5, pp. 1584–1589, 2007.

CONTACT

*E.N. Wang, tel: +1-617-324-3311; enwang@mit.edu

TEMPERATURE-COMPENSATED TETHERLESS BULK ACOUSTIC PHONON TRAP FOR SELF-OVENIZED OSCILLATORS

R. Tabrizian, A.Norouzpour-Shirazi and F. Ayazi
Georgia Institute of Technology, Atlanta, Georgia, USA

ABSTRACT

This paper reports on a novel temperature-compensated single-crystal silicon resonator that has a quadratic temperature characteristic with a high turn-over temperature. An energy-trapped resonance mode is synthesized from acoustic coupling of evanescent and propagating phonons with opposite temperature sensitivity trends in a <100>-aligned engineered waveguide (phonon trap). A 77MHz device implemented in AlN-on-silicon platform shows a *Q* of 13,000 and a turn-over temperature of 87°C facilitating implementation of an oven-controlled frequency reference. An oscillator implemented using this device, while self-ovenized by a DC current passing through its body, exhibits a consistent phase-noise of -106 dBc/Hz at 1kHz offset from carrier.

INTRODUCTION

For the past decade, MEMS resonators have been promising realization of highly-stable frequency references as an integrated alternative to replace their Quartz-based discrete counterparts. Although MEMS oscillators have been successful in surpassing Quartz references in several performance metrics including phase-noise and long-term stability [1], however large temperature sensitivity of these devices has remained a big challenge, especially as MEMS oscillators are targeting TCXO and OCXO markets with sub-ppm and sub-ppb instability requirements respectively. To address this challenge, a large variety of device-level [2, 3] and circuit/system-level [4] temperature compensation techniques have been proposed. However, these techniques usually impose large deviation from resonator design and implementation baseline, including excessive power consumption or manufacturing complexities.

In this paper we leverage single-crystal silicon as a designable and controllable thermo-mechanical platform to realize flexible, yet accurate, control on the temperature characteristic of the resonator frequency. Evanescent phonons with highly-positive temperature coefficient of frequency (*TCF)* are acoustically coupled to propagating phonons with negative *TCF* to create a temperature-stable resonance mode in a geometrically-engineered acoustic waveguide. Proper distribution of acoustic energy in propagating and evanescent fields in such structure not only provides compensation of the linear *TCF*, but also substantially eliminates support-loss through trapping propagating phonons in the central region of the acoustic cavity and far from anchoring regions (hence the name phonon trap). This, in turn, obviates the need for narrow tethers to anchor the device to the substrate and facilitates self-ovenization of the device by passing a DC current uniformly distributed across the cross-section of the cavity.

TEMPERATURE-COMPENSATED PHONON TRAP

Proper cascading and geometry engineering of multiple waveguides complying with displacement and strain continuity conditions at transition boundaries facilitate realization of synthesized modes in a phonon trap [5]. While a central waveguide supports propagating phonons, waveguides in flank regions can only support evanescent phonons with exponentially decaying energy as moving towards the substrate. Figure 1 demonstrates the concept of phonon trap through dispersion characteristics of guided waves in rectangular waveguides. The synthesized mode is highlighted with stars on different branches.

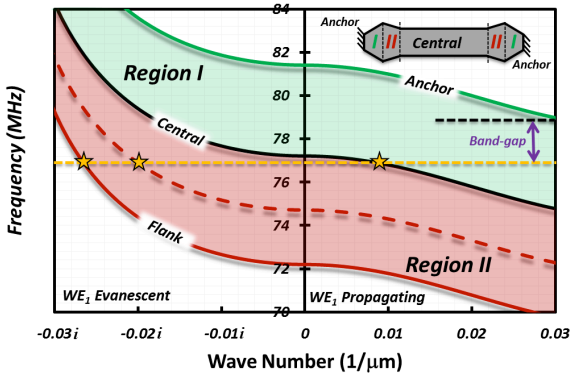

Figure 1: Dispersion characteristic of the first width-extensional (WE_1) phonon branch for different regions of the <100> phonon trap. Proper engineering of flanks and anchors facilitate acoustic energy trapping in the center of cavity and far from substrate.

Since the device is engineered to exclusively trap the energy of a single phonon-type, various spurious modes which are commonly excited in piezoelectrically-transduced resonators are efficiently suppressed as their energy leaks to the substrate through wide anchors of the structure.

Figure 2 shows the *TCF* behavior of different phonon branches of a single waveguide, exhibiting highly different characteristics for different phonon types, as well as opposite trends in evanescent and propagating portions of each branch.

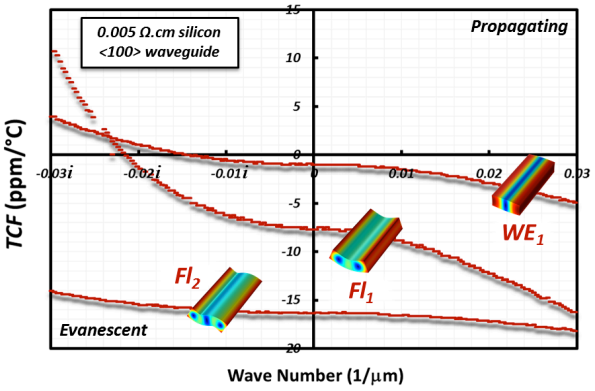

Figure 2: COMSOL-simulated TCF behavior of propagating and evanescent phonons for different branches of a rectangular waveguide aligned in <100> direction of N-doped (100) SOI substrate with a resistivity of 0.005 Ω.cm.

DEVICE CHARACTERIZATION AND DISCUSSION

Figure 3 shows the SEM image of the <100>-aligned phonon trap implemented on the same chip with two conventional silicon bulk acoustic resonators (SiBAR) aligned to <100> and <110> directions to highlight the efficiency of temperature compensation by comparing their temperature behavior.

9781940470016/HH2014/$25©2014TRF
DOI 10.31438/trf.hh2014.31

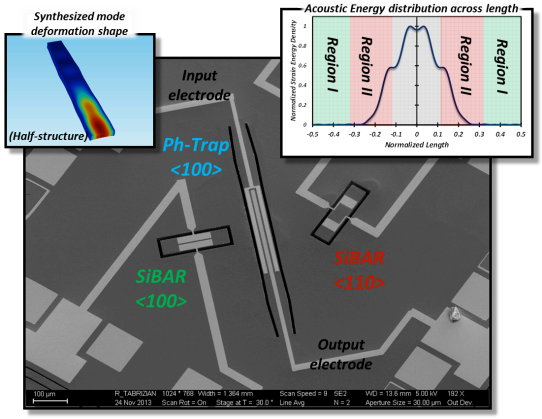

Figure 3: SEM image of <100>-aligned phonon trap adjacent to two conventional SiBARs aligned in <100> and <110> crystallographic directions. The insets show the synthesized mode-shape and its energy distribution across device length.

Figure 4 shows the large-span frequency response of the phonon trap. Spurious modes are efficiently suppressed as a result of selective energy trapping and tether elimination.

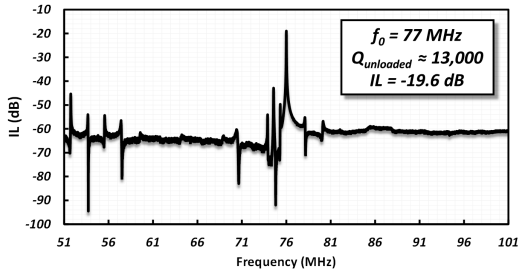

Figure 4: Large-span frequency response of the phonon trap.

Figure 5 compares the temperature characteristic of resonance frequency for the trap and SiBARs of Figure 3, showing the effectiveness of temperature compensation technique.

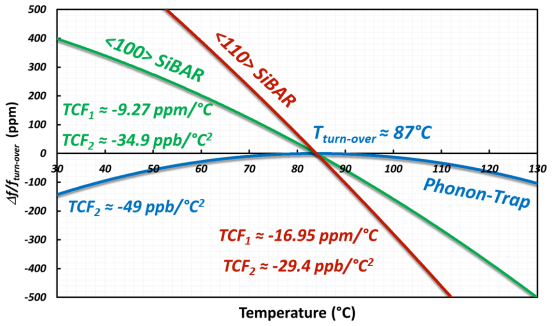

Figure 5: Temperature characteristic of the <100> phonon trap in comparison with conventional SiBARs aligned to <100> and <110> crystallographic directions of silicon, all on the same die.

While <100> and <110> SiBARs show linear *TCF*s of -10 and -17 ppm/°C respectively, the phonon trap shows a quadratic temperature characteristic with a turn-over temperature of 87°C. This is the highest turn-over temperature reported to date for a single crystal silicon resonator realized without the need for ultra-low resistivity substrate. Exceeding the industrial temperature range for frequency references, an oven-controlled MEMS oscillator can be implemented by ovenizing this device at the temperature-insensitive turn-over point. Such ovenization, if only provides a temperature control of ±0.1°C, will be sufficient for realization of references with sub-ppb instability.

SELF-OVENIZED MEMS OSCILLATOR

An oven-controlled MEMS oscillator is implemented using the 77MHz phonon trap. Figure 6 shows the frequency behavior of the oscillator for different self-ovenizing DC currents passing through the device body.

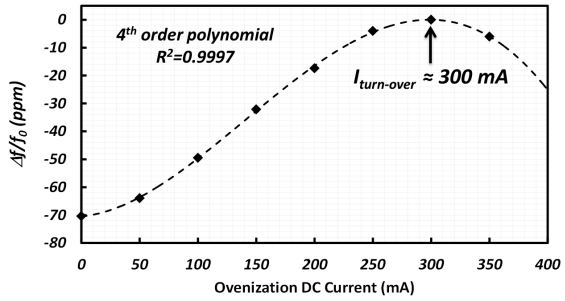

Figure 6: Frequency behavior of oscillator for different self-ovenizing DC currents. Ovenization currents can be significantly reduced by proper die layout and vacuum-encapsulation.

A consistent phase-noise of -106 dBc/Hz at 1kHz offset from carrier has been measured from the oscillator for different ovenization currents, including the current required to have the device operating at turn-over point in room-temperature (Figure 7). Such performance demonstrates the potential of the device for realization of highly-stable oven-controlled MEMS oscillators.

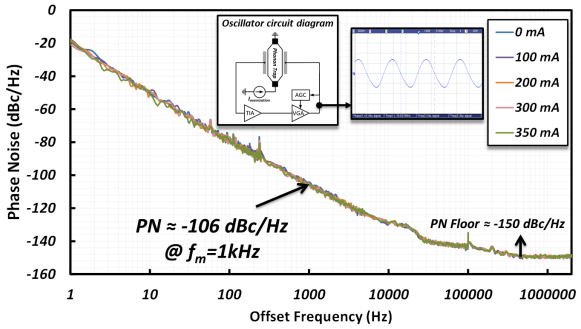

Figure 7: Phase-noise performance of the oscillator for different ovenization DC currents passing through the device body.

REFERENCES

[1] H. Bhugra, et al, "Commercialization of World's First PiezoMEMS Resonators for High Performance Timing Applications," *IEEE MEMS 2014*.

[2] R. Tabrizian, et al, "Temperature-Stable Silicon Oxide (SilOx) Micromechanical Resonators," *IEEE TED*, 2013.

[3] M. Shahmohammadi, et al, "Turnover Temperature Point in Extensional-Mode Highly Doped Si Microresonators," *IEEE TED*, 2013.

[4] H. M. Lavasani, et al, "Electronic Temperature Compensation of Lateral Bulk Acoustic Resonator Reference Oscillators using Enhanced Series Tuning Technique," *IEEE JSSC*, 2012.

[5] R. Tabrizian and F. Ayazi, "Acoustically-Engineered Multi-Port AlN-on-Silicon Resonators for Accurate Temperature Sensing," *IEEE IEDM 2013*.

ACKNOWLEDGEMENT

This work was supported by Integrated Device Technology (IDT), and in part by DARPA TIMU program through SSC pacific contract # N66001-11-C-4176.

CONTACT

*R. Tabrizian, tel: +1-404-259-7322; roozbeh@gatech.edu

SPORESAT: A NANOSATELLITE PLATFORM LAB-ON-A-CHIP SYSTEM FOR INVESTIGATING GRAVITY THRESHOLD OF FERN-SPORE SINGLE-CELL CALCIUM ION CURRENTS

W.W.A. Wan Salim[1], J. Park[1], J.L. Rickus[1], A. Rademacher[2], A.J. Ricco[2], A. Schooley[2], J. Benton[2], B. Wickizer[2], A. Martinez[2], N. Mai[2], M. Rasay[3], D.M. Porterfield[1], L. Brownston[2], M. Cote[2], G. Defouw[2], M. Henschke[2], C. Kitts[3], E. Luzzi[2], M. Perez[2], S. Roux[4], M. Salmi[4], and A. Sweet[2]*

[1]Purdue University, West Lafayette, IN, USA

[2]NASA Ames Research Center, Moffett Field, CA, USA

[3]Santa Clara University, Santa Clara, CA, USA

[4]University of Texas, Austin, TX, USA

ABSTRACT

SporeSat – a lab-on-a-chip (LOC) centrifuge platform designed for integration as the payload of a small (5.5 kg), free-flying satellite – has been developed to determine the gravitational thresholds for calcium-ion channel activation of a single-cell spore from the fern *Ceratopteris richardii*. This fern is an important model system for gravity-directed plant-cell development during variable-gravity conditions attainable only in space flight. Calcium-ion channel activity is measured by photolithographically defined calcium ion–selective electrodes (ISEs) at opposite ends of each spore. Artificial gravity is created by rotating a disk-like platform that contains the spores in wells along with the calcium ISEs. Ground experiments reveal a maximum calcium concentration ratio at 2.2x*g*, between micro-ion-selective electrodes near the "top" and "bottom" ends of the spore, indicating an increasing calcium concentration at one "end" of the fern spore with respect to the other. Confocal micrographs of rhizoid formation confirm the light-induced germination. SporeSat is a spaceflight experiment that will take ~ 4 days; data will be telemetered to Earth over ~ 100 days.

INTRODUCTION

Plants and plant cells are known to have sensors for external cues, but the molecular mechanism by which they sense gravity remains to be determined. Plants have no ambulatory function, but possess a basic capability to sense the intensity of the *g*-force [1]. To understand plant gravisensing, researchers have utilized spores of the fern *Ceratopteris richardii* as a gravitational plant model system, because the spore is unicellular, has a short life span, and is easily handled and cultured [2].

Previous studies using self-referencing ion-selective (SERIS) electrodes and cell-electrophysiology-lab-on-a-chip (CEL-C) technologies have found that calcium ions play a role in gravity-directed polarity development of the *C. richardii* fern spore. Calcium channel and pump activity appear to be influenced by gravity [3]. Polarity of calcium transport was observed in ground studies with a SERIS electrode: a strong efflux of Ca^{2+} at the top and a strong influx at the bottom of the spore. This polar ion flux was found to occur at 6-12 hours from the onset of germination initiated by light. However, studies on fern spores utilizing the SERIS electrode lack temporal resolution. The CEL-C biochip developed later has the desired temporal resolution while serving as a template for simultaneous measurements of Ca^{2+} concentration on 16 spores [4]. However, the CEL-C is stationary. When flown on parabolic flights the CEL-C was used to observe the effect of micro-*g* and hyper-*g* levels on spore calcium flux. In these experiments, the magnitude of the Ca^{2+} ratio between the two "ends" of a spore was highest at 2x*g*, and this concentration ratio decreased at 0.01x*g*. There was a lag of 10-15 seconds before a change in Ca^{2+} concentration was observed in the fern spores when going from hyper-*g* to micro-*g*, whereas the lag was only 2 seconds from micro-*g* to hyper-*g* [5]. From these initial results, it was hypothesized that calcium-ion channels and pumps are activated at gravity levels in between these two extreme *g*-values.

To determine the onset of the calcium-channel and pump activation that produces the Ca^{2+} current polarity, we are developing a cell-electrophysiology-lab-on-a-chip (CEL-C) advanced bioCD, or in short, the bioCD. The bioCD aims to investigate the gravitational threshold for calcium-ion channel and pump activation in the single-cell spore of the fern *Ceratopteris richardii*. The bioCD enables finer investigation of *C-richardii* gravisensing; it has a rotating centrifuge format that provides varying artificial gravity levels in microgravity, with capability for simultaneous Ca^{2+} current measurements.

SPORESAT PAYLOAD

Payload Design

SporeSat [6] is a nanosatellite (10x10x34 cm, 5.5 kg), the payload of which integrates motors, thermal control, measurement electronics, and various sensors with three bioCDs, all housed in a container with an internal pressure of 1 atm (Fig. 1). Two bioCDs rotate; the third remains stationary as a control. A bioCD, fabricated on 2-inch fused-silica substrate (Fig. 2), includes thirty-two 126-µm-diameter cylindrical SU-8 wells (1:1 aspect ratio), each housing one fern spore. Four Pt resistance-temperature devices (RTDs) per bioCD provide closed-loop thermal control. A pair of ion-selective electrodes (ISEs) measures the ratio of Ca^{2+} concentrations at either "end" of each fern spore. When the bioCD rotates, spores are subject to different gravitation magnitudes based on their distance from the rotational axis (8 wells at each of 4 distances) and rotational velocity (Table 1).

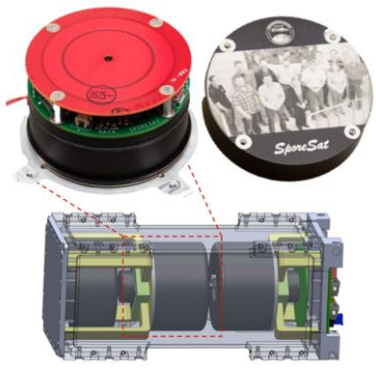

Figure 1: SporeSat payload showing location of 3 bioCD assemblies inside a 1-atm container. Each bioCD rotating assembly measures differential calcium-ion concentrations from germinating fern spores.

9781940470016/HH2014/$25©2014TRF
DOI 10.31438/trf.hh2014.32

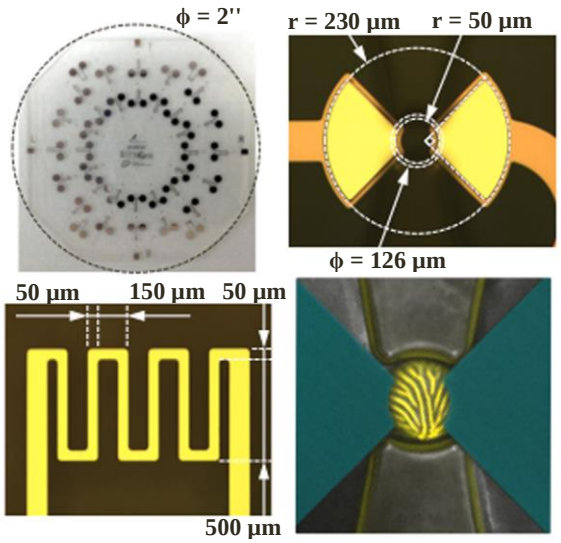

Figure 2: BioCD design showing 32 wells on a 2-inch-diameter area (photo, top left). Eight wells are located at each of four radial distances from the rotational axis. Each well has a pair of wedge-shaped ISEs (top right) on either side of a single fern spore (bottom right, held between SU-8 "pincers"). Four thin-film RTDs (bottom left) are located near the outer wells.

Table 1: Artificial gravity generated from rotation at wells located at various radial distances. The g levels vary from 2xg to 0.06xg.

Rotation rate		Gravity at R (mm)			
(rpm)	(Hz)	R_1=9	R_2=12	R_3=15	R_4=18
80	1.38	0.06x*g*	0.09x*g*	0.11x*g*	0.13x*g*
112	1.87	0.13x*g*	0.17x*g*	0.21x*g*	0.25x*g*
158	2.63	0.25x*g*	0.34x*g*	0.42x*g*	0.50x*g*
223	3.72	0.50x*g*	0.67x*g*	0.83x*g*	1.00x*g*
315	5.25	1.00x*g*	1.33x*g*	1.66x*g*	2.00x*g*

bioCD Fabrication and Spore Localization

The bioCD is fabricated via a four-mask process. Mask one is for electrical connection and RTD definition, mask two is for exposing the conductive active electrode by etching away the oxide passivation layer, mask three is for Ag deposition on active electrode areas, and mask four is for SU-8 spore-well fabrication. Afterwards, the bioCD Ag electrodes are chlorided in sodium hypochlorite (NaClO), resulting in Ag/AgCl electrodes, and subsequently spin-coated with an ion-selective membrane (ISM) specific for Ca^{2+}. The Pt-Ag/AgCl-ISM layer is called an ion-selective electrode (ISE). Figure 3 shows the fabricated cross-sectional schematic at the final stage of each mask process, and the surface functionalization of the electrodes.

Each ISE operates based on the potentiometric electrochemical principle. The ISE reacts with Ca^{2+} and outputs an electrical signal that is proportional to the Ca^{2+} concentration. The Nernst equation defines the concentration of Ca^{2+} at equilibrium; the potential difference, which exists at both "ends" of a spore, is translated into a voltage value. A plot of measured potential vs Ca^{2+} concentration is linear if the ISM is perfectly selective. Calibration of the ISE for Ca^{2+} reveals an average Nernstian slope of ~30 mV/decade change in Ca^{2+} concentration.

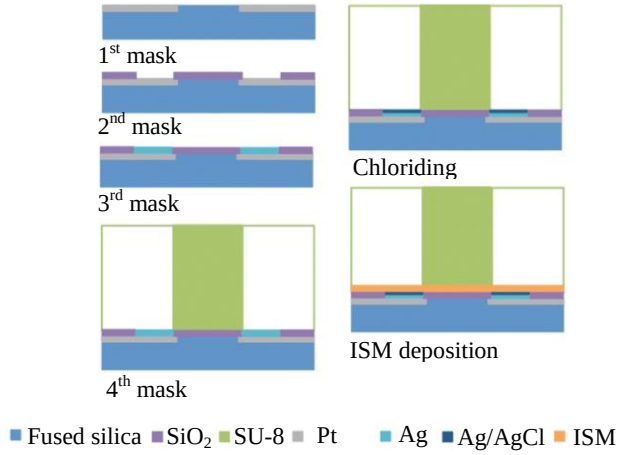

Figure 3: bioCD electrode fabrication and surface-functionalization process cross-sectional schematic.

After Ag/AgCl electrode preparation and ion-selective membrane deposition, bioCDs are conditioned for ~ 24 hr (1 µM $CaCl_2$ / 10 µM KNO_3) before loading one spore (126 µm diameter) per well. Figure 4 shows the cross-sectional schematic of a spore in a well.

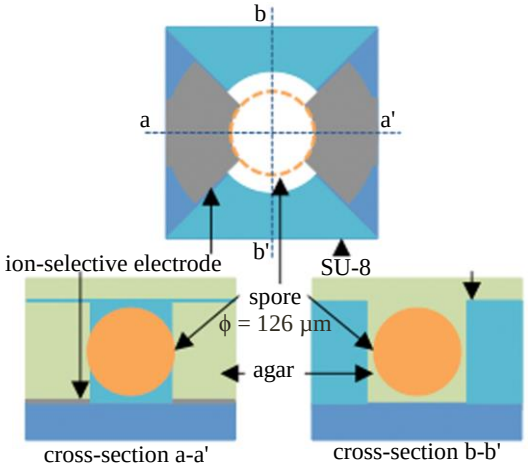

Figure 4: Cross-sectional schematic of a spore in a bioCD well. The SU-8 epoxy features along b-b' form a "pincer" that, along with agar gel, holds the spore in place. ISEs are located beneath the "ends" of the spore closest to and furthest from the center of rotation.

Each bioCD is housed in a sealed assembly (Fig. 5) containing two layers of agar gel – 0.5% to provide high ionic mobility in a hydrated environment between two ISEs, and 2.0% to immobilize the spore and preventing it from dislodging during shock and vibration. Integral co-rotating circuit boards with local batteries, contacting each bioCD via pogo-pin arrays, include 32 differential amplifiers to measure and digitize Ca^{2+} concentration ratios, as well as controlling a lighting system (red OLED disk) that germinates the spores through the bottom of the transparent bioCD. Digital signals are transmitted capacitively across a sub-mm gap to a mating stationary PC board.

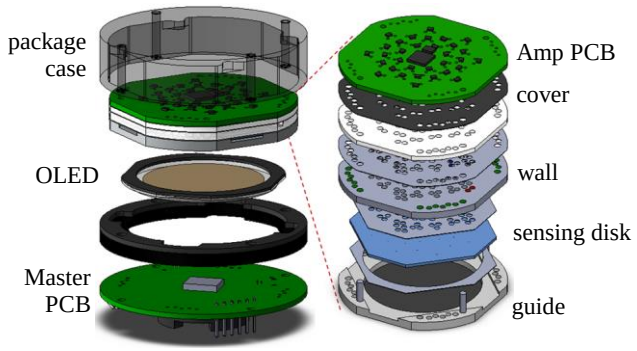

Figure 5: Exploded-view schematic of the bioCD rotating assembly. The bioCD package consists of the enclosed assembly (EA) unit, which seals the agar that surrounds the spores in the wells to prevent drying out and maintain spore viability for as long as 90 days.

GROUND EXPERIMENTS AND DISCUSSION

Experiments were conducted on the ground to test the system. Fern spores were sterilized in 20% Clorox® bleach, and loaded into the bioCD in the dark under green safety light; the bioCD was then sealed into the container and stored to simulate pre-spaceflight stasis during launch-vehicle integration. Zero-day tests were conducted: spores were exposed to 2 hours of red light at 620 nm peak wavelength and rotation at 290 rpm (simulated gravity levels at 1.1, 1.5, 1.8, and 2.2xg from inner to outer radii).

In these tests, spores were stored for 3 weeks and five days in agar medium before exposure to light and rotation. Furthermore, the bioCD also contains negative controls; these are wells filled with agar or a glass bead at all *g*-levels. Figure 6 shows the calcium concentration ratio of representative ISE pairs for fern spores at 2.2, 1.8, 1.5, and 1.1xg, a glass bead, and an empty agar well. A higher differential ratio indicates increasing $[Ca^{2+}]_{outer}/[Ca^{2+}]_{inner}$ on either "end" of the fern spore. A higher differential ratio implies larger $[Ca^{2+}]$ differences between the two "ends" of the fern spore.

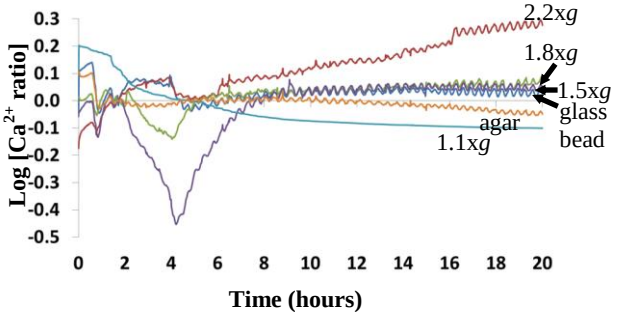

Figure 6: Calcium concentration differential measured during ground experiments for an ISE pair at either "end" of a germinating fern spore under rotation (f = 290 rpm) after a 2-hr red-light exposure, for wells experiencing 2.2, 1.8, 1.5, and 1.1xg, in comparison to wells that contain empty agar or agar with a glass bead.

From Figure 6, we can state the following: the magnitude of the $[Ca^{2+}]$ ratio is highest at 2.2xg; the $[Ca^{2+}]$ ratio of fern spores at the other *g*-levels does not significantly differ from that of the glass bead and empty agar. From these results, we can say that the signals from germinating spores at the highest *g*-level differ significantly from those from an empty well or a glass bead. It is important to note that ground studies do not emulate what the spores will experience at microgravity since the spore is being subject to the vector sum of both Earth and centrifugal gravities, where the resultant force vector is not well aligned with the axis of the two ISEs. Since the $[Ca^{2+}]$ ratio is between the two ends of a spore, one end having an efflux of $[Ca^{2+}]$ and the other end having an influx of [Ca2+], the ISE location would be at the wrong place to measure the efflux, especially for the lower *g* levels. At the highest *g*-level, the vector sum shifts to being more at the plane of the bioCD, which will bring one "top " of a spore closer to one of the ISEs.

To understand electrical signals obtained from the system, we conducted confocal imaging immediately after the zero-day tests, to visualize spore physical development. Spore development begins with the cracking of a trilete marking on the spore coat, followed by emergence of the primary rhizoid from this opening in the spore coat. In these studies, spore germination is defined as visible rhizoid emergence from the spore. Figure 7 shows a confocal micrograph of a germinated spore in a zero-day test bioCD after rhizoid formation. The germinated fern spores in the bioCD confirm that the lighting and environmental conditions are sufficient for spores to germinate.

Figure 7: Representative confocal micrograph image of a spore with primary rhizoid in a well.

Previous studies using CEL-C have confirmed that the Ca^{2+} current polarity in a single-cell fern spore is directed by gravity. SporeSat provides a variety of artificial gravities to determine the gravity threshold of polarity development. SporeSat inherits the dual-electrode-differential-coupling (DEDC) measurement method of the CEL-C [4], where the Ca^{2+} concentration ratio between two "ends" of a spore is measured instead of absolute concentration. In DEDC, two electrodes reference each other; perfectly matched electrodes will give a voltage reading of 0 V. Subtle changes in one electrode will give a large signal amplification.

CEL-C differs from SporeSat in overall biochip design, most significantly in the electrode geometry. The CEL-C had an active electrode area of 1660 μm^2; one electrode was located on each of the four sides of an etched pyramidal silicon well (150 μm^2), with a spore located inside the well. All poles of a spore were within ~10 µm of the electrodes. The bioCD wedge-shaped active electrode area is 35909 $\mu m^{2,}$ but only 10537 μm^2 touch the spore at

each "end." The spore is contained in an etched SU-8 well. The distance of an ISE to a spore for both systems is limited to less than 10 µm in order to minimize the diffusion distance of the Ca^{2+} ions to the ISE and to prevent signal loss.

Conditions relating to the spore also differ between the two systems in terms of lighting for germination. The CEL-C system had no integrated lighting system, spores being exposed to ambient light continuously before and during measurements, whereas the bioCD system is kept in the dark and spores are simply exposed to red light (peak λ = 620 nm) for 2 hours to initiate germination. Thanks to the transparent bioCD substrate, uniform lighting and time of exposure to the spores are attainable. The CEL-C could not achieve this because of its opaque substrate.

Owing to the differences in electrode geometry and lighting system between the CEL-C and SporeSat systems, results are not parallel. It can be expected that the $[Ca^{2+}]$ ratio is less in the SporeSat owing to the smaller electrode area touching the spore and the larger total electrode area. Furthermore, spores experience only 2 hours of lighting in the bioCD, in comparison to the continuous lighting in the CEL-C.

Although these are not parallel systems, both the CEL-C and the SporeSat are viable tools to study fern-spore electrophysiology: they utilize a similar electrochemical measurement method; both systems measure the differential voltage that are translated to a ratio of Ca^{2+} concentration on both sides of the spore. A 24-hour germination experiment on the ground can be correlated with previous SERIS experiments, but with tremendously enhanced throughput.

CONCLUSIONS

Previous CEL-C experiments in microgravity reveal that gravity is locally affecting transcellular Ca^{2+} with mechanosensory Ca^{2+} ion channels as the major player in the mechanism. The transcellular Ca^{2+} flux closely follows the rapidly changing gravity force, with hyper-*g* polarizing the current while micro-*g* results in a zero magnitude of calcium current. However, what we still do not know is the gravity threshold of fern-spore polarity development from Ca^{2+} ions. The SporeSat system aims to provide the answer, by providing several artificial gravity levels to the spore in microgravity. Ground studies with the bioCD reveal a significant $[Ca^{2+}]$ ratio for fern spores at 2.2x*g* in comparison to glass bead and agar-only wells, while at lower *g*-levels the ratios trend more closely to the glass bead and empty wells. Confocal imaging has proved that spores do germinate (formation of rhizoid) in the bioCD wells under the lighting and storage conditions, but more studies are needed to find the optimal lighting condition for the spores.

The platforms can easily be tailored to fit other cell types by changing the well or electrode design, making the CEL-C and SporeSat systems especially suitable for single-cell electrophysiological measurements. From a microfabrication standpoint, changing well size and electrode geometry is simply changing the masks that are used to pattern the features on the substrate. Furthermore, to modify the applications of the system, one can always change the surface functionalization process.

Under the requirements of spaceflight research, such as payload constraints and limited crew time, electrochemical sensor use is especially attractive. Furthermore, electrochemical sensors are also easily packaged and integrated with spaceflight hardware systems, allowing for sensor operation to be made autonomous. The SporeSat will be the first electrochemical sensor system in a LOC format whose functionality will be demonstrated in Space.

REFERENCES

[1] A.H. Brown, "The Influence of Gravity on the Structure and Functions of Plant Material", Advances in Space Research, 4, 12 (1984).

[2] A. Chatterjee, and S. J. Roux, "Ceratopteris richardii: A Productive Model for Revealing Secrets of Signaling and Development", Journal of Plant Growth Regulation, 19, 3 (2000).

[3] A. Chatterjee, D. M. Porterfield, P.S. Smith, and S. J. Roux, "Gravity-directed Calcium Current in Germinating Spores of Ceratopteris richardii," Planta, 210, 4 (2000).

[4] A. Ul Haque, M. Rokkam, A. R. Decarlo, S. T. Wereley, S. J. Roux, P. P. Irazoqui, and D. M. Porterfield, "A MEMS Fabricated Cell Electrophysiology Biochip for In Silico Calcium Measurements", Sensors and Actuators B: Chemical, 123, 1 (2007).

[5] M. L. Salmi, A. Ul Haque, T. J. Bushart, S. C. Stout, S. J. Roux, and D. M. Porterfield, "Changes in Gravity Rapidly Alter the Magnitude and Direction of a Cellular Calcium Current", Planta 233, 5 (2011).

[6] The SporeSat Mission is a Mission of Opportunity ("MoO-2") funded by the NASA Human Exploration and Operations Mission Directorate (HEOMD).

CONTACT

*W.W.A. Wan Salim, amanisalim6@gmail.com

A PAPER-BASED MICROBIAL SENSOR ARRAY FOR RAPID SCREENING OF ELECTRICITY-PRODUCING BACTERIA

A. Fraiwan[1], C. Dai[1], D. J. Hassett[2], and S. Choi[1]*
[1]Bioelectronics and Microsystems Laboratory, Department of Electrical and Computer Engineering, State University of New York at Binghamton, New York, USA
[2]Department of Molecular Genetics, Biochemistry and Microbiology, University of Cincinnati, Ohio, USA

ABSTRACT

We demonstrate the use of paper-based test platforms for rapid characterization of electricity-generating bacteria. The presented device contains vertically stacked anode/cathode paper chambers (or reservoirs) separated by a proton exchange membrane (PEM), and gold anode/cathode interface pads with through-holes in the center to introduce anolyte/catholyte. The paper-based sensor exploits the paper's ability to quickly wick fluid and promote bacterial attachment to the gold anode pads, resulting in instant current generation upon loading of the bacterial inoculum and catholyte. Within just 50 minutes, we successfully determined the electricity generation capacity of two known bacterial electrogens and another metabolically more voracious organism with four isogenic mutants. This paper-based microbial screening tool does not require external pumps/tubings and represents the most rapid test platform (<50 min) compared with the time needed by using traditional screening tools (up to 103 days) and even recently proposed MEMS arrays (< 2 days).

INTRODUCTION

Microbial fuel cells (MFCs) have recently emerged as a clean power source with the potential of generating sustainable electricity using bacterial metabolism [1]. This technology has found applications in wastewater treatment and as a power source for low-power electronics. However, the commercialization of MFCs has not yet been realized owing to many factors governing their performance in terms of the current/power levels they generate. One of the most important issues limiting the power generation levels is the electricity generation capabilities of the microorganism used and the success of the cell architecture modifications aiming at lowering the cell's resistance and improving the microorganisms' reaction with the electrode which will eventually lead to higher current levels [2].

Only a few of the bacterial species believed to be capable of extracellular electron transfer have been discovered, among those primarily *Geobacter sulfurreducens* and *Shewanella oneidensis* have been the focus of intensive research to fully understand the mechanisms used for electron transfer. The electron transfer mechanisms by which the bacterial cells are able to transfer electrons to electrodes surfaces unveiled so far include: (i) direct electron transfer through the bacterial cell membranes, and conductive nanowires that some species can develop, as well as (ii) indirect electron transfer using soluble electron shuttling compounds. The rate of electron transfer in the bacterial species is evidently the limiting factor for current generation. However, to date these mechanisms have not yet been fully explored to determine which of these mechanisms prevails in each electrogenic species, and is responsible for the major part of the generated current due to the lack of devices that allow parallel analyses or high throughput screening of microorganisms with electrochemical activities [3].

Research on screening and characterization of electrochemically active microbes has been carried out by operating multiple MFCs in series or in parallel. These methods can be very slow due to the time required to run multiple experiments in sequence; they also require large space and significant amounts of materials [4]. These constraints lead to the development of microbial fuel cell arrays. The pioneer MFC array was developed by Biffinger and coworkers [4]. They were able to develop a multi anode/cathode array that was used to monitor the growth cycles of *Shewanella oneidensis* MR-1 species, and compare its current generation responses to different nutrients [4]. Subsequently, Hou et al. proposed several microfabricated MFC arrays for the identification and characterization of electrochemically active microbes in addition to the screening of environmental microbes [5-8]. We previously reported an array of six MEMS MFCs with six independent fluidic accesses and successfully determined the electrical characteristics of six bacterial strains [9, 10]. More recently, we introduced a nine-well MEMS based parallel analyses platform for testing the current generation of eight microbial consortia [11].

The MFC arrays have been proven to be an invaluable tool that supports parallel analyses and allows for high throughput screening and characterization of electrochemically active microbes. The devices developed so far are fabricated from polymer based substrates such as polydimethylsiloxane (PDMS) and they are fabricated using conventional lithography and photolithography techniques, which add to the complexity and the cost of building such devices. Also, most of these devices have large individual chamber volumes in the ranges of a few hundred microliters, have large startup times in the range of a few hours and need a relatively long periods of times (< 2 days) to complete the screening processes, which in turn requires bulky pumps and large amounts of inoculum and oxidant to maintain continuous operation [10].

Recently, paper has been utilized as a substrate for electronic devices instead of conventional rigid materials such as silicon, glass and plastics [12]. This is because paper offers a number of useful advantages; (i) the low cost and combustibility for single-use measurements, (ii) the easy/rapid/low cost patterning and processing of the paper, (iii) high surface area for reagents to be stored, (iv) porosity and biocompatibility, and (v) light weight and flexibility [12]. Moreover, paper is attractive because it has the ability to wick fluids via capillary action. Due to these advantages, paper-based devices have attracted high recent interest and have shown remarkable potential applications in many areas. Recently, our group reported, for the first time, a paper-based microbial fuel cell (MFC) requiring only a drop of bacterial inoculum onto the anode for power generation [13]. This paper MFC showed rapid electricity generation while conventional MFCs require long start-up time which is attributed to the accumulation and acclimation of bacteria on the anode of the MFCs [10]. This is because the hydrophilic paper reservoir rapidly absorbs the anolyte and immediately promotes the attachment of a number of bacteria cells to the anode. This prominent feature of the paper-based MFC has motivated us to develop a paper-based microbial sensor array for rapid screening of electrogenic bacteria. We expect that this work exposes the potential realization of a practical tool for efficient high-throughput bacterial screening and fundamental MFC

9781940470016/HH2014/$25©2014TRF
DOI 10.31438/trf.hh2014.33

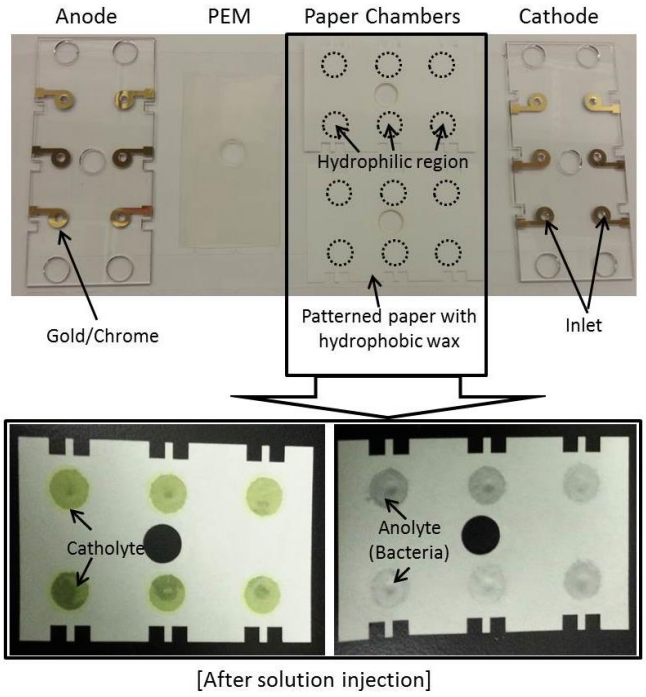

Figure 1. Individual layers of the array and paper chambers after loading the inoculum and catholyte. Hydrophobic wax boundaries were made by heat pressing wax paper onto filter paper.

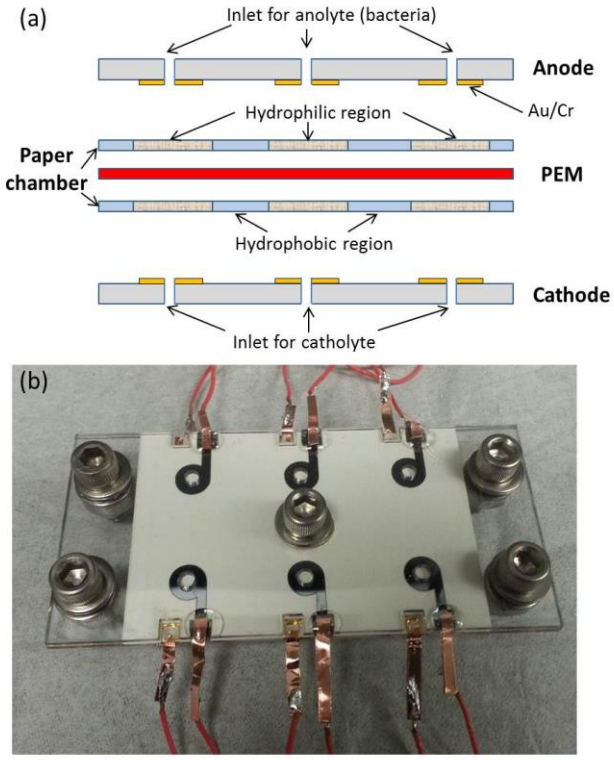

Figure 2. (a) Schematic and (b) photo-image of the paper-based microbial sensor array. The array consisted of five functional layers; an anode layer, a paper reservoir layer for anolyte, a proton exchange membrane, a paper reservoir layer for catholyte and a cathode layer. Copper tapes were attached to the gold pads for electrical contacts.

understanding, which may further improve power extraction in MFCs.

EXPERIMENTAL SET-UP

Device Fabrication

The six-well sensor array consisted of five functional layers as shown in Fig. 1; an anode layer (Au/Cr on PMMA), a paper anode reservoir layer, a PEM, a paper cathode reservoir layer, and a cathode layer (Au/Cr on PMMA). Each layer except for the PEM was first micro-patterned using laser micromachining (Universal Laser System VLS 3.5). Paper reservoirs featuring hydrophilic chamber with hydrophobic wax boundaries were made by heat pressing commercially available wax paper (Reynolds CutRite) onto Whatman #1 filter paper. The gold electrodes were prepared by depositing 100 nm gold on PMMA substrates with chrome as the adhesion layer using e-beam evaporation. Copper tape (3M^{TM} copper conductive tape) was attached to the contact pads with silver conductive paint (PELCO® Colloidal Silver). Fig. 2 shows a detailed schematic and photo-image of the fully assembled paper-based MFC array

Inoculum and Catholyte

Six microorganisms were tested; *S. oneidensis*, *P. aeruginosa* wild-type PAO1 and another metabolically more voracious organism with four isogenic *pmpR*, *rpoS*, *lasR rhlR* and *fliC pilA* mutants. *P. aeruginosa* PAO1 mutants were generated using classical allelic replacement techniques with sucrose counter-selection as described by Hoang et al [14]. All cultures were grown in L-broth medium (10.0 g tryptone, 5.0 g yeast extract and 5.0 g NaCl per liter). The catholyte for the six MFC units was 50 mM ferricyanide in a 100 mM phosphate buffer in which pH was adjusted at 7.5 ± 0.2 with 0.1 M NaOH.

Measurement Setup

We measured the potentials between the anodes and the cathodes with a data acquisition system (National instrument, USB-6212), and recorded the readings every 1 min via a customized LabView interface (Fig. 3). An external resistor (1 kΩ) connected between the anode and the cathode closed the circuit. The current through this resistor was calculated using Ohm's law.

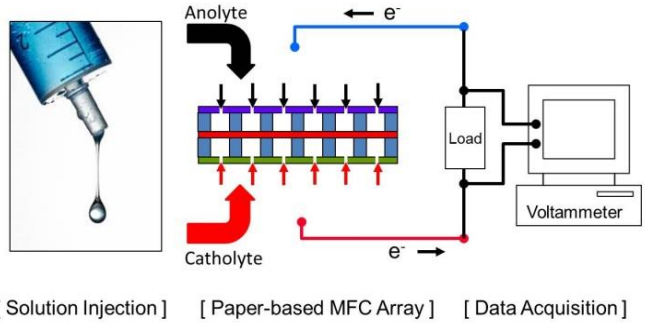

Figure 3. Measurement setup for testing the paper-based MFC array. The array requires only drops of bacterial inoculum and catholyte onto the electrodes for power generation.

RESULTS AND DISCUSSION

Open Circuit Voltages

After the anolyte and the catholyte were injected into the corresponding inlets for each paper reservoir using 100 µL pipettes, the inlets were sealed with tape to prevent solution depletion through evaporation. Before closing the MFC circuits with 1 kΩ resistors, the open circuit voltages were recorded for 3 min. The measured voltages varied between the different MFCs, which clearly indicates performance variations according to the bacterial species injected into each chamber. The open-circuit voltage values ranged from 0.18 to 0.25 V. Given that the open-circuit voltages are the cell's potential differences that indicate the difference between the potential under equilibrium conditions and the thermodynamic losses, *pmpR* mutant's value being substantially lower than the others clearly shows that there is a large energy loss occurring at the anode. The voltage curves with and without load are shown in Fig. 4.

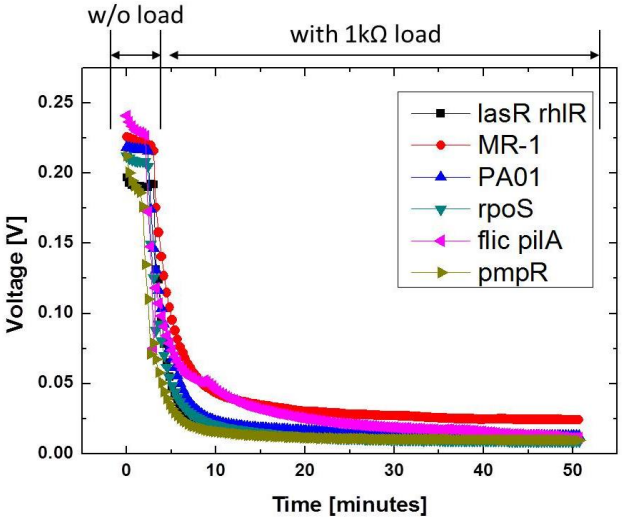

Figure 4. Voltages measured from the device with different bacterial species. The open-circuit voltages were measured for the first three minutes and then all MFC cells were connected to 1 kΩ external loads.

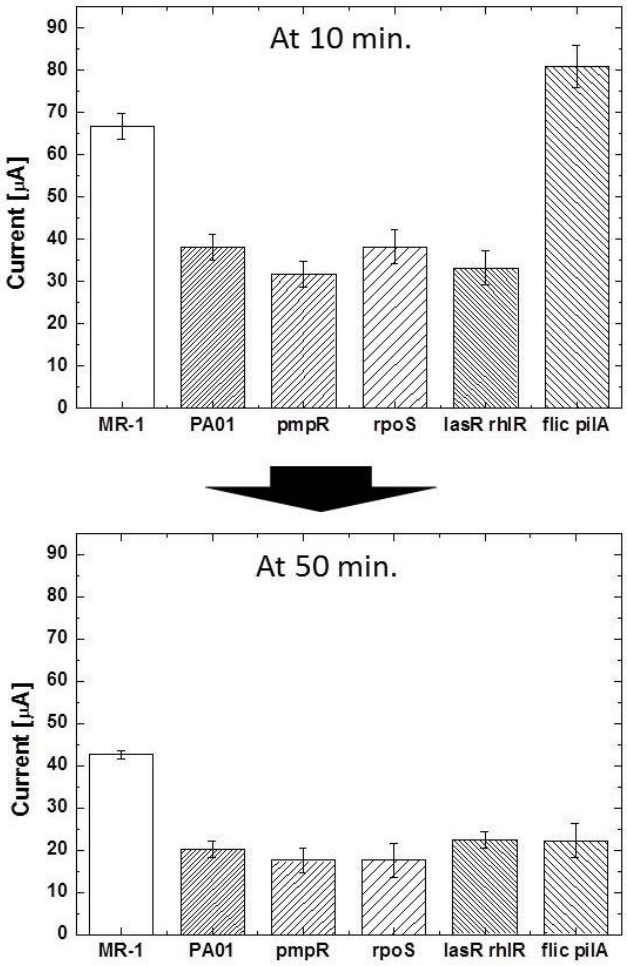

Figure 5. Currents calculated from Fig. 4 in 10 min. and 50 min. At 10 min., the fliC pilA mutant has superior current generation followed by Shewanella sp. (MR-1). At 50 min., however, the fliC pilA performance showed a significant decrease while Shewanella sp. continued to have comparable performances.

Current Measurements

After operating the MFCs under no-load conditions for ~3 minutes, the load resistors were connected to enable current generation and the voltage differences under the load were recorded until their values reached zero due to depletion of the solutions which took ~50 minutes. All experiments were repeated six times and displayed with error bars as depicted in Fig. 5. Current comparison was made two times, the first after 10 min of operation and the second at 50 min.

The operation after 10 min shows significant differences between the various species used in terms of current generation; the array proves useful for bacterial screening and characterization even after this relatively short operation time compared to previous arrays which require longer periods of time. This may be mainly attributed to the ability of the paper reservoirs to rapidly wick the solutions through capillary action and allow for a faster bacterial acclimation and accumulation at the anode surfaces. The current values after 10 min show that the *fliC pilA* mutant has superior current generation followed by *Shewanella sp. (MR-1),* which indicates the ability of these two species to quickly acclimate to the anode electrode and start their metabolic and extracellular electron transfer processes. The lowest current was generated by the *pmpR* mutant, which implies low metabolism capabilities and poor electron transfer capabilities of this particular mutant. The currents calculated after 50 min operation show that the *fliC pilA* performance suffered a considerable decrease, probably because of the substrate depletion in the corresponding MFC which was expedited by its high performance at the beginning of the operation. On the other hand, *Shewanella sp.* showed a relatively lower decrease in the performance and it exhibited the highest current generation among all the tested species. As for the other species, they continued to have comparable performances in the paper-based MFCs but showed a decrease in the current levels as compared with their current levels at 10 min.

In summary, the paper-based array enabled the successful characterization of the electricity-generation capabilities of six different microbial species within only 50 minutes. Moreover, clear differences in the different bacterial species were easily detected. In addition, this paper-based platform required minimal equipment as well as inoculum and catholyte supplies for operation.

CONCLUSION

In this work, we developed a six-well paper-based microbial fuel cell array that allows for the rapid characterization of microbial electricity-generating capabilities. The array was successfully fabricated using paper reservoirs for the anode and the cathode chamber which eliminates the need for expensive substrates such as PDMs and the need for conventional lithography and photolithography fabrication. The use of paper decreased the operating time considerably, and within 50 minutes, the current generation abilities of two known bacterial electrogens and four more isogenic mutants were successfully determined. This array is expected to have wide-spread applications in the screening and characterization of electrogens by virtue of its rapid response, and reduced cost due to the operation with no expensive pumps and only small amounts of inoculum and catholyte required.

ACKNOLOWDGMENT

We would like to thank the Nano-fabrication Lab at SUNY-Binghamton for providing the fabrication facilities and the Binghamton University Research Foundation for funding this work.

REFERENCES

[1] Y. Yang, G. Sun, and M. Xu, "Microbial Fuel Cells Come of Age", J. Chem. Technol. Biotechnol., 86, 625 (2011).

[2] B.E. Logan, and J. M. Regan, "Electricity-Producing Bacterial Communities in Microbial Fuel Cells", Trends Microbiol., 14, 512 (2006).

[3] H. Hou, X. Chen, A.W. Thomas, C. Catania, N.D. Kirchoffer, L.E. Garner, A. Han, and G.C. Bazan, "Conjugated Oligoelectrolytes Increase Power Generation in E. Coli Microbial Fuel Cells", Adv. Mater., 25, 1593 (2013).

[4] J. Biffinger, M. Ribbens, B. Ringeisen, J. Pietron, S. Finkel, and K. Nealson, "Characterization of Electrochemically Active Bacteria Utilizing a High-Throughput Voltage-Based Screening Assay", Biotechnol. Bioeng., 102, 436 (2009).

[5] H. Hou, L. Li, Y. Cho, P. de Figueiredo, and A. Han, "Microfabricated Microbial Fuel Cell Arrays Reveal Electrochemically Active Microbes", PLoS ONE, 4, e6570 (2009).

[6] H. Hou, L. Li, Y. Cho, P. de Figueiredo, and A. Han, " Air Cathode Microbial Fuel Cell Array: A Device for Identifying and Characterizing Electrochemically Active Microbes", Biosens. Bioelectron., 26, 2680 (2011).

[7] H. Hou, C.U. Ceylan, L. Li, Y. Cho, P. de Figueiredo, and A. Han, "A Microfabricated Fuel Cell Array for Electrochemically-Active Microbe Screening and Analysis", Proceedings of 14th International Conference on Miniaturized Systems for Chemistry and Life Sciences (μ-TAS), 10/3-7/2010, Groningen, The Netherlands (2010), pp. 677-679.

[8] H. Hou, L. Li, C.U. Ceylan, A. Haynes, J. Cope, H.H. Wilkinson, C. Erbay, P. de Figueiredo, and A. Han, "A Microfluidic Microbial Fuel Cell Array that Supports Long-Term Multiplexed Analyses of Electricigens", Lab Chip, 12, 4151 (2012).

[9] S. Choi, S. Mukherjee, S. Su, W. Panmanee, R.T. Irvin, and D.J. Hassett, "A 1.5 uL Microbial Fuel Cell array for rapid screening of exoelectrogenic bacteria," Technical Digest of Solid-State Sensor and Actuators Workshop 2012, June 3-7th, 2012, Hilton Head Island, SC, USA, pp. 169 – 172.

[10] S. Mukherjee, S. Su, W. Panmanee, R.T. Irvin, D.J. Hassett, and S. Choi, " A Microliter-Scale Microbial Fuel Cell Array for Bacterial Electrogenic Screening", Sens. Actuat. A, 201, 532 (2013).

[11] S. Chen, C. Dai, A. Fraiwan, and S. Choi, "A Miniaturized Parallel Analyses Platform for Rapid Electrochemical Discoveries of Microbial Activities", Proceedings of the 9th International Conference on NANO/MICRO Engineered and Molecular Systems, Hawaii, USA, 2014, in-print.

[12] A.K. Yetisen, M.S. Akram, and C.R. Lowe, "Paper-Based Microfluidic Point-of-Care Diagnostic Devices", Lab Chip, 13, 2210 (2013).

[13] A. Fraiwan, S. Mukherjee, S. Sundermier, H. Lee, and S. Choi, "A Paper-Based Microbial Fuel Cell: Instant Battery for Disposable Diagnostic Devices", Biosens. Biolectron., 49, 410 (2013).

[14] T.T. Hoang, A.J. Kutchma, A. Becher, H.P. Schweizer, "Integration-Proficient Plasmids for *Pseudomonas Aeruginosa*: Site-Specific Integration and Use for Engineering of Reporter and Expression Strains", Plasmid, 43, 59 (2000).

CONTACT

*S. Choi, tel: +1-607-777-5913; sechoi@binghamton.edu

A JANUS-PAPER PDMS PLATFORM FOR LAB-ON-A-CHIP APPLICATIONS

Rahim Rahimi[1], Manuel Ochoa[1], Tejasvi Parupudi[1], Amy Donaldson[3]
Mehmet R.Dokmeci[2], Ali Khademhosseini[2], Amir Ghaemmaghami[3] and Babak Ziaie[2]
[1]Purdue University, West Lafayette, Indiana, USA
[2]Harvard-MIT Health Sciences and Technology, Cambridge, MA, USA
[3]The University of Nottingham, Nottingham NG7 2UH, UK

ABSTRACT

A commercially available Janus paper with one hydrophobic (polyethylene-coated) face and a hygroscopic/hydrophilic one is irreversibly bonded to a PDMS substrate incorporating microfluidic channels via corona discharge surface treatment. The bond strength between the polymer coated side and PDMS is characterized as a function of corona treatment time and annealing temperature/time. A maximum strength of 392 kPa is obtained with a 2 min corona treatment followed by 60 min of annealing at 120 ºC. The water contact angle of the corona-treated polymer side decreases with increased discharge duration from 98º to 22º. The hygroscopic/hydrophilic side is coated with hydrogel to show its potential for nutrient and chemical delivery in cell culture applications.

INTRODUCTION

There is a plethora of structural materials at the disposal of the microfluidic and lab-on-a-chip community, with PDMS and glass being the most popular and widely used ones. More recently, paper [1], [2] has garnered significant attention as a low-cost disposable platform for chemical [3]-[6] and biological assays. [5], [7] Paper-based devices are often fabricated either by using a hydrophilic paper that is patterned and impregnated with wax to create hydrophobic regions [8], [9] or alternatively by laser-treating a hydrophobic paper to create hydrophilic regions [10], [11]. In both cases, the hydrophilic/hygroscopic pattern is then used to perform colorimetric or electrochemical analyses on aqueous samples. In this manuscript, we introduce a unique and commercially available paper (Janus paper) with one hydrophobic (polyethylene-coated) face and a hygroscopic/hydrophilic one as a substrate for microfluidic and lab-on-a-chip applications. Such Janus papers can open doors to the development of microsystems with enhanced functionality and improved biomaterial integration capabilities. This is particularly true if it can be easily coupled with traditional microfluidics materials and systems.[12]–[14]

A paper exhibiting a Janus property is the freezer paper used to store frozen food. It is composed of a cellulose fiber mesh coated with polyethylene on only one side, thus being hydrophobic on the polymer side and hydrophilic/hygroscopic on the other side. At its hydrophobic face, such Janus paper bonds irreversibly to a polydimethylsiloxane (PDMS) microfluidic networks, enabling the fabrication of PDMS-paper platforms with dual surface energy; meanwhile, the hydrophilic/hygroscopic side is capable of supporting materials compatible with many paper processing techniques (e.g., chemical impregnation, gel coating, cell seeding).

Our experiments show that the polymer coating on freezer paper becomes hydrophilic upon exposure to a corona discharge/plasma. As a result, bonding to freezer paper can be accomplished without the need for additional adhesives, but rather via plasma-induced surface activation followed by thermal annealing (a technique typically used for bonding PDMS to PDMS or PDMS to glass [15]), thus enabling convenient integration of the Janus-paper platform with traditional microfluidic systems.

We implemented various standard microfluidic designs as a proof-of-concept demonstration. Traditionally, these systems are fabricated via a lithography/replica molding [12], [16] technique that requires (expensive) clean room facilities and multiple processing steps. We opted for a less expensive and more straightforward approach by defining channels on a PDMS substrate via a single-step laser ablation method and subsequently bonding them to the Janus paper.

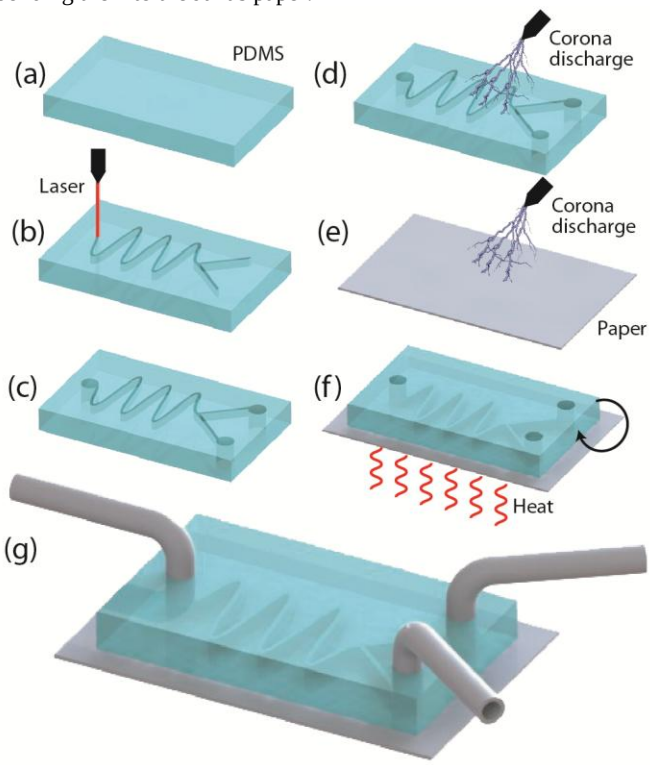

Figure 1: Conceptual illustration of the fabrication process. (a) Cast, crosslink, and release a PDMS substrate. (b) Laser-define the microfluidic network. (c) Punch inlet and outlet ports. (d) Treat the surface of PDMS and (e) the freezer paper with corona discharge or plasma. (f) Flip the PDMS and bring it into contact with the treated paper; press and anneal to bond. (g) Attach tubing to microfluidic ports.

DESIGN AND CHARACTERIZATION

Figure 1 illustrates the fabrication technique for creating PDMS/Janus-paper devices. First, a CO_2 laser engraver system (Universal Laser Systems Inc., Scottsdale, AZ) is used to directly write microchannel patterns on a substrate of crosslinked PDMS (Dow Corning Sylgard® 184, 10:1 ratio, cured at 60 ºC for 5 h) by surface ablation (power 15 W, speed 4 mm/ms). The resulting

9781940470016/HH2014/$25©2014TRF
DOI 10.31438/trf.hh2014.34

channels have a Gaussian cross-section (200 µm wide, 100 µm deep); the shape can be further modified (e.g., rounder or deeper) by using an unfocused laser beam [17], [18] or multiple passes of the beam. After defining the channels on the PDMS, two 800µm-diameter holes are punched out to create inlet and outlet ports. Next, the PDMS and Janus paper (Freezer Paper, Reynolds Consumer Products, Inc.) are exposed to corona discharge using a hand held corona discharge unit (BD-10A High Frequency Generator, Electro-Technic Products, Inc.), and the two surfaces are subsequently brought into contact to create a permanent bond. The device is then annealed on a hotplate. Finally, 800 µm-diameter pieces of Tygon® tubing are attached to the inlet and outlet ports.

Three major parameters that are known to affect the bond quality of PDMS to PDMS or PDMS to glass are the duration of corona treatment, the annealing temperature, and the annealing time. If the bonding process for PDMS-Janus-paper mimics that of the aforementioned ones, then similar trends can be expected for this structure. In particular, the surface energy of the polymer coating on the Janus paper is expected to decrease with increasing corona discharge exposure time, in turn increasing the affinity of one surface to the other. Higher annealing temperatures and extended annealing times can also increase the bond strength by relaxing the polymer on the paper and a allowing more intimate contact between the two bonding surfaces. To create strongly bonded PDMS-Janus-paper devices, we investigated the effect of these parameters on the overall bond strength.

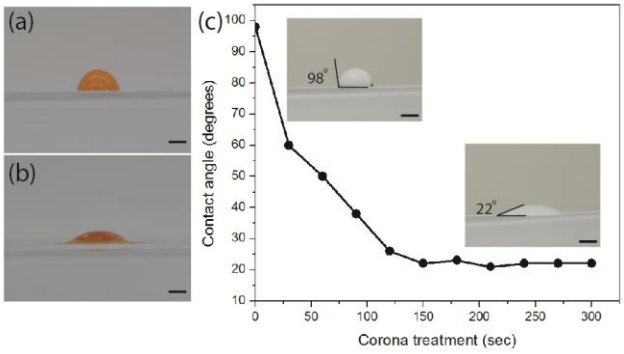

Figure 2: Surface properties of Janus freezer paper. Dyed agarose gel on (a) the hydrophobic (polymer-coated) and (b) the hydrophilic side of the paper. (c) Contact angle of a water droplet on the hydrophobic surface of freezer paper as a function of corona treatment duration. All droplet have a 4 µL volume. All scale bars: 1 mm.

A goniometry test setup was used to characterize the effect of corona discharge on the surface energy of the Janus paper (polymer-coated side only). The paper was exposed to corona discharge for various durations (0−300 s) and the water contact angle was subsequently measured using a 4µL droplet. The contact angle is plotted in Figure 2 as a function of exposure time. As is the case with PDMS, the corona treatment causes a significant reduction in angle (from 98º to 22º).

This decrease can be attributed to the generation of oxygen polar groups on the polyethylene surface by plasma exposure [19], [20]. We observed that hydrophilicity of the polymer surface of the paper increases with plasma exposure time but saturates after 2 minute; therefore, this exposure time was used for all the PDMS-paper structures discussed in this manuscript.

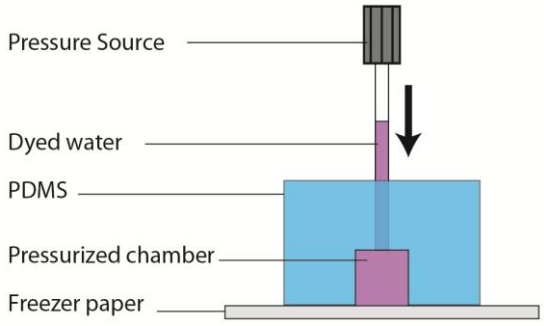

Figure 3: Test setup for measuring bond strength between freezer paper and PDMS. A gas source with a pressure gauge provided the pressure.

To characterize the maximum strength of the PDMS/Janus-paper bond as a function of the annealing time and temperature, we fabricated multiple test devices with the design illustrated in Figure 3. The structure consisted of a cylindrical chamber in a block of PDMS bonded to a Janus paper substrate. The PDMS block (15mm × 15 mm × 5 mm) was formed from a master mold consisting of a laser-cut acrylic cylinder (5 mm diameter × 2 mm height) adhered onto a petri dish with UV-curable adhesive (Loctite® 3105). Next a 800µm-diameter inlet port was cored out of the center of the PDMS block to create an inlet for the pressuring gas during the bonding test. A sheet of freezer paper was cut to match the dimensions of the PDMS mold. The PDMS and paper were then bonded together via corona discharge as previously described.

The ideal combination of annealing time and temperature required for a strong bond was determined by measuring the bond strength of the PDMS-paper structure created with various annealing temperatures (40−140ºC) and durations (0−180 min). To assess the quality of the bonding between the paper and the PDMS, a 800µm-diameter syringe needle was inserted into the inlet port of the PDMS block and its perimeter was sealed with a polyurethane-based adhesive (Gorilla GlueTM, Gorilla Glue Inc.). The needle was connected to a syringe that was filled with dyed water to reveal potential leakages or device failure during the high pressure measurements. The open end of the syringe was connected to a pressure gauge and a flow-regulated nitrogen source in order to control the pressure in the PDMS/paper chamber. The pressure was gradually increased at a rate of 250 Pa/s until the first sign of fluid leakage. Bonding failure was determined either by delamination of the two layers or by paper failure (tearing at the interface).

The pressure test data are plotted in Figure 4. The measurements show that low temperatures and short annealing times result in weaker bonds; in such cases, device failure occurs at the paper/PDMS interface. By increasing the annealing temperature and time the bond strength also improves up to 392 kPa. This is comparable to bond strengths achieved via traditional oxygen plasma bonding and adhesive tape-PDMS techniques [21], [22]. The bond becomes strong enough that device failure occurs as a tear in the surface of the paper (rather than at the bonding interface), due to limitations in the paper mechanical strength of the paper. The data reveal an optimal annealing temperature and time of 120 ºC and 60 minutes for creating a strong irreversible bond between the paper and the PDMS.

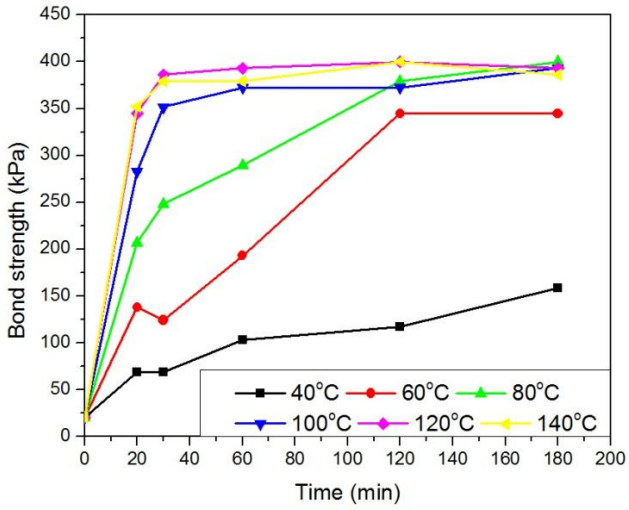

Figure 4: Bond strength as a function of annealing temperature and annealing. Note that at temperatures above 100ºC annealing times beyond 20 minutes do not increase the bond strength significantly. Maximum strength occurs within 60 min at T>80ºC (for T>100ºC 20 min annealing time is adequate).

The optimal fabrication parameters obtained from the characterization experiments were implemented in the fabrication of PDMS-paper prototypes. Figure 5(a-d) shows two fabricated channel designs with a channel depth of 100 µm and a width of 200 µm fabricated using a single pass of the laser. The performance of each device was tested by injecting dyed water into the inlet ports at a flowrate of 20 µL min^{-1} and observing the flow behavior. Figure 5a shows an empty Y-junction with a 15 mm long microchannel. Figure 5b shows two liquids being pumped into the channel; the insets highlight the laminar flow that is maintained throughout the channel length. Figure 5c presents a hybrid PDMS/paper microfluidic mixer. Figure 5d depicts red and green liquids entering the serpentine microchannel with a laminar flow, each at a flow rate of 10 µL min^{-1} and mixing together in the serpentine channel; the inset shows the resulting mixed solution at the end of the channel.

The double-sided nature of the Janus paper can be used to integrate materials compatible with many paper processing techniques on the hygroscopic/hydrophilic side. Figure 5(e-f) shows an application in which the hydrophilic side is coated with a hydrogel layer (a popular material for tissue engineering applications in which the hydrogel is seeded with live cells kept alive by providing nutrients and disposing the waste). Here, a modified device with laser-defined holes on the paper is used to deliver liquid to the hydrogel-coated hygroscopic side. The gel used for this experiment is a yellow-dyed 1% (w/v) agarose gel, which adheres to the surface without any additional treatment. When two liquids are pumped into the PDMS-paper serpentine channel, they mix together and subsequently diffuse into the gel through small laser defined openings on the paper (denoted in the inset of Figure 5f). The direct control and delivery of liquids on such a low-cost platform can be adapted for use in cell culturing and tissue engineering procedures, making PDMS-Janus paper structure an inexpensive but practical microfluidic platform.

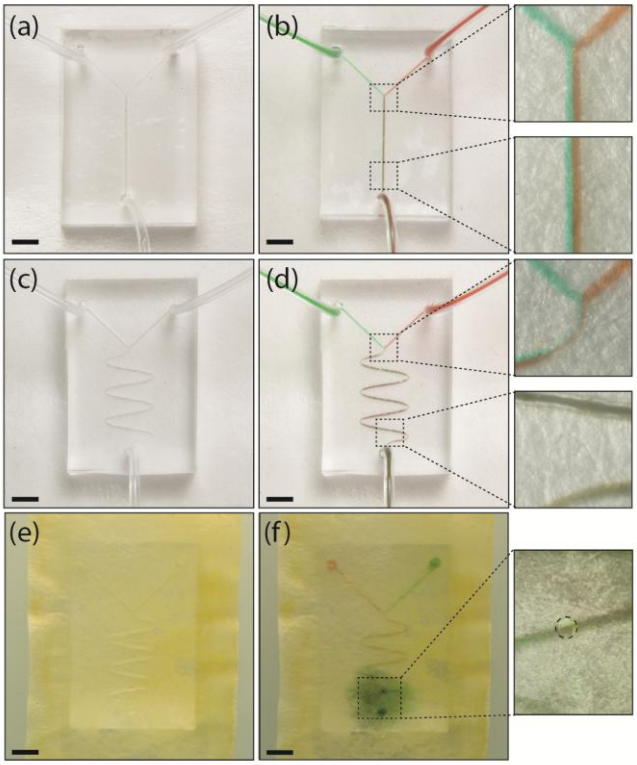

Figure 5: Various microfluidic devices fabricated using PDMS and freezer paper. All channels have a Gaussian cross-section (200 µm width and 100 µm depth). (a) An empty Y-junction connected to a straight channel imaged from the PDMS side and (b) with liquid flowing; the insets show a 10X magnified view of the laminar flow. (c) An empty serpentine channel imaged from the PDMS side and (d) with two dyes flowing and mixing together; the insets (10X magnification) highlight the mixing. (e) A serpentine channel imaged from the paper side, with a yellow-colored gel coating the hydroscopic face of the paper. (f) Two dyes mixing in the serpentine channel exiting the channel though a 250 µm-diameter hole in the paper (shown in the inset) and diffusing into the gel. All scale bars: 2 mm.

CONCLUSIONS

We successfully implemented several microfluidic devices on a commercially available Janus paper (freezer paper) with one hydrophobic face and a hygroscopic one. By corona treating the hydrophobic side and the PDMS, the two were bonded irreversibly. We optimized the corona discharge duration, annealing time, and annealing temperature to achieve a strong bond. Furthermore, the hygroscopic side of the paper offers a surface morphology ideal for depositing hydrogel layers, thus enabling its use for cell culture and tissue engineering applications.

ACKNOWLEDGEMENTS

Funding for this work was provided by the National Science Foundation under grant EFRI-BioFlex #1240443.

REFERENCES

.

[1] A. Lee, “The third decade of microfluidics.,” *Lab Chip*, vol. 13, no. 9, pp. 1660–1, May 2013.

[2] X. Li, D. R. Ballerini, and W. Shen, “A perspective on paper-

based microfluidics: Current status and future trends.," *Biomicrofluidics*, vol. 6, no. 1, pp. 11301–1130113, Mar. 2012.
[3] D. D. Liana, B. Raguse, J. J. Gooding, and E. Chow, "Recent advances in paper-based sensors.," *Sensors (Basel).*, vol. 12, no. 9, pp. 11505–26, Jan. 2012.
[4] F. Yue, T. S. Ngin, and G. Hailin, "A novel paper pH sensor based on polypyrrole," *Sensors Actuators B Chem.*, vol. 32, no. 1, pp. 33–39, Apr. 1996.
[5] R. Rahimi, G. Chitnis, P. Mostafalu, M. Ochoa, S. Sonkusale, and B. Ziaie, "A low-cost oxygen sensor on paper for monitoring wound oxygenation," in *The 7th International Conference on Microtechnologies in Medicine and Biology*, 2013.
[6] H. Liu and R. M. Crooks, "Paper-based electrochemical sensing platform with integral battery and electrochromic read-out.," *Anal. Chem.*, vol. 84, no. 5, pp. 2528–32, Mar. 2012.
[7] A. W. Martinez, S. T. Phillips, M. J. Butte, and G. M. Whitesides, "Patterned paper as a platform for inexpensive, low-volume, portable bioassays.," *Angew. Chem. Int. Ed. Engl.*, vol. 46, no. 8, pp. 1318–1320, Jan. 2007.
[8] M. Reches, K. a Mirica, R. Dasgupta, M. D. Dickey, M. J. Butte, and G. M. Whitesides, "Thread as a matrix for biomedical assays.," *ACS Appl. Mater. Interfaces*, vol. 2, no. 6, pp. 1722–8, Jun. 2010.
[9] W. Dungchai, O. Chailapakul, and C. S. Henry, "A low-cost, simple, and rapid fabrication method for paper-based microfluidics using wax screen-printing.," *Analyst*, vol. 136, no. 1, pp. 77–82, Jan. 2011.
[10] G. Chitnis, Z. Ding, C.-L. Chang, C. a Savran, and B. Ziaie, "Laser-treated hydrophobic paper: an inexpensive microfluidic platform.," *Lab Chip*, vol. 11, no. 6, pp. 1161–5, Mar. 2011.
[11] G. Chitnis, T. Tan, and B. Ziaie, "Laser-assisted fabrication of batteries on wax paper," *J. Micromechanics Microengineering*, vol. 23, no. 11, p. 114016(5pp), Nov. 2013.
[12] B. Ziaie, A. Baldi, M. Lei, Y. Gu, and R. A. Siegel, "Hard and soft micromachining for BioMEMS: review of techniques and examples of applications in microfluidics and drug delivery," *Adv. Drug Deliv. Rev.*, vol. 56, no. 2, pp. 145–172, Feb. 2004.
[13] A. Folch, *Introduction to BioMEMS*, 1st ed. Boca Raton, FL: CRC Press, 2012.
[14] A. C. R. Grayson, R. S. Shawgo, A. M. Johnson, N. T. Flynn, Y. Li, M. J. Cima, and R. Langer, "A BioMEMS Review: MEMS Technology for Physiologically Integrated Devices," *Proc. IEEE*, vol. 92, no. 1, pp. 6–21, Jan. 2004.
[15] J. Zhou, A. V. Ellis, and N. H. Voelcker, "Recent developments in PDMS surface modification for microfluidic devices.," *Electrophoresis*, vol. 31, no. 1, pp. 2–16, Jan. 2010.
[16] Y. Xia and G. M. Whitesides, "Soft Lithography," *Angew. Chemie Int. Ed.*, vol. 37, no. 5, pp. 550–575, Mar. 1998.
[17] L.-M. Fu, W.-J. Ju, R.-J. Yang, and Y.-N. Wang, "Rapid prototyping of glass-based microfluidic chips utilizing two-pass defocused CO2 laser beam method," *Microfluid. Nanofluidics*, vol. 14, no. 3–4, pp. 479–487, Oct. 2012.
[18] P.-A. Vidi, T. Maleki, M. Ochoa, L. Wang, S. M. Clark, J. F. Leary, and S. A. Lelièvre, "Disease-on-a-Chip: Mimicry of Tumor Growth in Mammary Ducts," *Lab Chip*, 2013.
[19] M. Lehocký, H. Drnovská, B. Lapčíková, a. . Barros-Timmons, T. Trindade, M. Zembala, and L. Lapčík, "Plasma surface modification of polyethylene," *Colloids Surfaces A Physicochem. Eng. Asp.*, vol. 222, no. 1–3, pp. 125–131, Jul. 2003.
[20] P. Slepička, a. Vasina, Z. Kolská, T. Luxbacher, P. Malinský, a. Macková, and V. Švorčík, "Argon plasma irradiation of polypropylene," *Nucl. Instruments Methods Phys. Res. Sect. B Beam Interact. with Mater. Atoms*, vol. 268, no. 11–12, pp. 2111–2114, Jun. 2010.
[21] J. Kim, R. Surapaneni, and B. K. Gale, "Rapid prototyping of microfluidic systems using a PDMS/polymer tape composite.," *Lab Chip*, vol. 9, no. 9, pp. 1290–3, May 2009.
[22] C. S. Thompson and A. R. Abate, "Adhesive-based bonding technique for PDMS microfluidic devices.," *Lab Chip*, vol. 13, no. 4, pp. 632–5, Feb. 2013.

CONTACT

*B.Ziaie, tel:+1-765-404-0726; bziaie@purdue.edu

BI-DIRECTIONAL SWITCHING OF MICRODROPLET ADHESION ON DOPED POLYPYRROLE MICROSTRUCTURES

W. Xu, X. Li, A. Palumbo, C.-H. Choi, and E.-H. Yang
Stevens Institute of Technology, Hoboken, New Jersey, USA

ABSTRACT

This paper presents a study of bi-directional switchable adhesion of an organic microdroplet on dodecylbenzenesulfonate doped polypyrrole (PPy(DBS)) microstructures at ultra-low voltages (0.9 V) in an aqueous environment. The PPy(DBS) switched between an oxidized and a reduced state upon application of low voltages. The PPy(DBS) microstructure oxidized at 0.6 V behaved like a super sticky surface in regard to an organic droplet; in contrast, the PPy(DBS) microstructure reduced at -0.9 V was super slippery. Utilizing the tunable adhesion property of PPy(DBS) microstructures, we demonstrated a capture/release manipulation of an oil-based dichloromethane (DCM) microdroplet at a voltage of 0.9 V.

INTRODUCTION

The manipulation of microdroplets has broad applications in microfluidics, biochemistry, and lab-on-chip devices [1-3]. Surfaces with tunable adhesion have been studied for the manipulation of microdroplets through external stimuli, such as light, magnetic field, mechanical force, or electrical field [4-8]. Recently, conjugated polymers have attracted a lot of interest due to their tunable wetting properties, which can be induced by a low voltage [9-11]. For example, dodecylbenzenesulfonate doped polypyrrole (PPy(DBS)) exhibits tunable surface wetting property upon application of the ultra-low reduction and oxidation voltages (~0.9 V). During the redox process, the change of surface wetting property of PPy(DBS) from hydrophobic to hydrophilic is caused by the reorientation of the surfactant dopant molecules (i.e., DBS) in PPy(DBS) (Figure 1) [12].

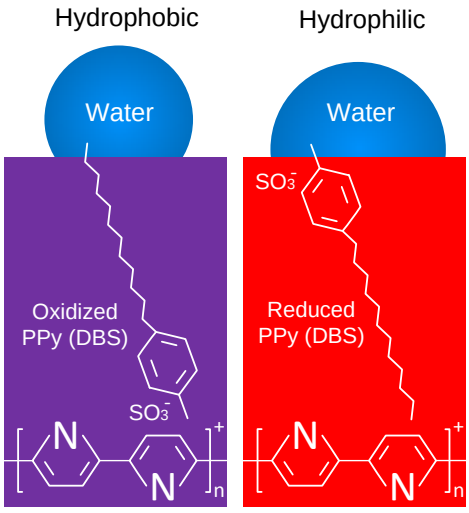

Figure 1: The surface state of PPy(DBS) switched between hydrophilic and hydrophobic during the redox processes initiated by low voltage application. Due to the reorientation of the surfactant dopant molecules in PPy(DBS), oxidized PPy(DBS) is hydrophobic and reduced PPy(DBS) is hydrophilic. The surface adhesion of PPy(DBS) also changes between an oxidized and a reduced state with the change of surface wetting property.

The surface adhesion of conjugated polymers also changes between an oxidized and a reduced state with the change of surface wetting property. Ding *et al*. have utilized polyaniline nanowire films with potential-modulated tunable adhesion for the transport of an oil droplet by a capture/release process [13]. However, the release of a microdroplet from the surface is still an issue to overcome without the contact of microdroplet with another more adhesive surface. In this work, we demonstrate a reversible switch of surface adhesion, from super sticky to super slippery, by using micropillar patterned PPy(DBS) surfaces, which enables an independent capture and release of microdroplets.

EXPERIMENTAL METHODS

Micropillar patterned PPy(DBS) samples were fabricated by electropolymerization on Au/Cr coated microstructured silicon substrates. The silicon substrates were micropatterned through a photolithography process followed by a deep reactive ion etching (DRIE). The micropatterned silicon substrates were then coated with Cr (100 nm) and Au (100 nm) by using e-beam evaporation (PVD 75, Kurt Lesker). During the electropolymerization of PPy(DBS), the Cr/Au coated silicon substrates acted as working electrodes and were submerged in an aqueous pyrrole solution consisting of 0.1 M pyrrole (Aldrich) and 0.1 M sodium dodecylbenzenesulfonate (NaDBS) (Aldrich). A saturated calomel electrode (SCE) (Fisher Scientific Inc.) and an Au coated silicon wafer were also submerged in the solution as reference and counter electrodes. The deposition of PPy(DBS) on the Au surface was performed at 0.8 V versus SCE by using a potentiostat (263A, Princeton Applied Research, Oak Ridge, TN) [11]. The coating thickness was controlled with coating time.

After the microstructured PPy(DBS) samples were prepared, we first studied the change in the surface adhesion of microstructured PPy(DBS) surfaces upon application of reductive and oxidative potentials in a two-electrode system. The PPy(DBS) coated substrate was used as a working electrode and copper tape was connected as the counter electrode. A potential was applied to the PPy(DBS) substrate for the reduction (-0.9 V) and oxidation (+0.6 V) reactions. After either reduction or oxidation, the change in the surface adhesion of the PPy(DBS) microstructured surface was analyzed according to the sliding angle of a dichloromethane (DCM) microdroplet in an aqueous environment (0.1 M $NaNO_3$) by using a goniometer system (Model 500, Ram é-hart instrument co., Netcong, NJ, USA).

We then investigated the capture/transport/release process of a micro-liter DCM droplet on the micropatterned PPy(DBS) surface in an aqueous electrolyte environment (0.1 M $NaNO_3$). A droplet of DCM was placed on a glass substrate in a 0.1 M $NaNO_3$ solution. The PPy(DBS) microstructure was submerged in the solution and oxidized first by applying a positive potential (e.g., 0.6 V). Then, the PPy(DBS) microstructure was placed in contact with the DCM microdroplet in order to capture it. Once transported to the desired location, a potential of -0.9 V was then applied to the PPy(DBS) microstructure in order to release the captured microdroplet. The entire capture, transport, and release process was monitored with the goniometer system.

9781940470016/HH2014/$25©2014TRF
DOI 10.31438/trf.hh2014.35

Solid-State Sensors, Actuators and Microsystems Workshop
Hilton Head Island, South Carolina, June 8-12, 2014

RESULTS AND DISCUSSION

Figure 2 shows the fabricated micropillar patterned PPy(DBS). Figure 2a is the Au/Cr coated silicon substrate with micropillar patterns before PPy(DBS) coating. The diameter and height of the Au/Cr coated micropillars are approximately 6 μm and 5 μm, respectively. The Au and Cr layers are each 100 nm thick. Figure 2b shows the micropatterned substrate coated with PPy(DBS) through electropolymerization. As shown, the PPy(DBS) is uniformly coated on the micropillar structures. The thickness of the PPy(DBS) layer is approximately 1 μm, and the diameter of the PPy(DBS) coated micropillars is approximately 8 μm.

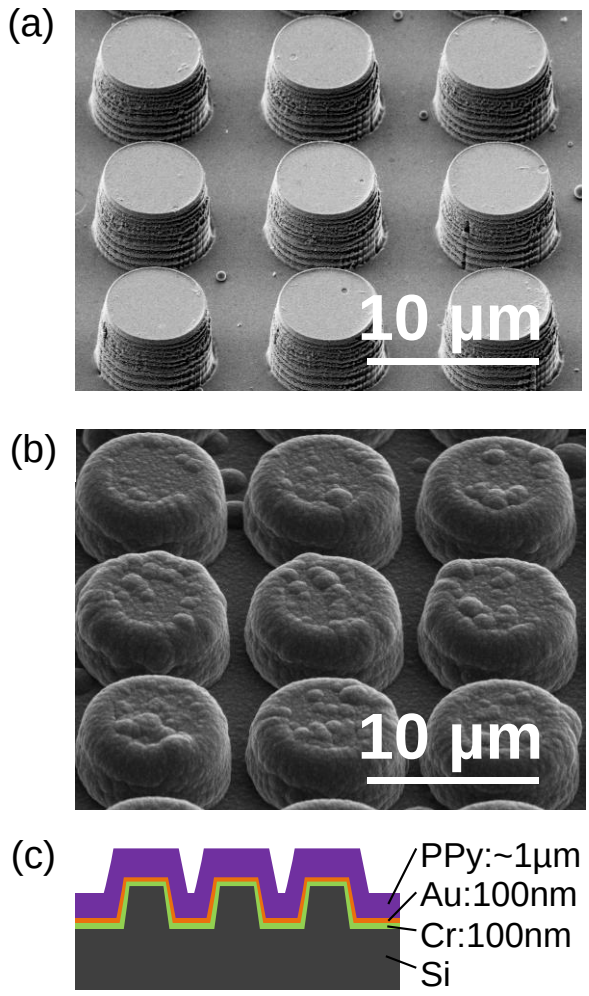

Figure 2: (a) The Au/Cr coated micropatterned silicon substrate used for the electrodeposition of PPy(DBS). (b) The PPy(DBS) microstructures fabricated by using the substrate shown in (a). (c) The Au and Cr layers are each 100 nm thick, and the thickness of the PPy(DBS) coating is approximately 1 μm.

Figure 3 shows the tunable adhesion property of oil-based dichloromethane (DCM) microdroplets on the PPy(DBS) microstructure in either the oxidized or reduced state. The PPy(DBS) microstructure oxidized at +0.6 V behaved like a super sticky surface in regard to the DCM droplet even when the substrate was tilted 90 degrees in an aqueous environment (0.1 M $NaNO_3$ solution). Upon reduction at -0.9 V, the DCM droplet easily slid off the substrate even with a tilting angle as small as 0.5 degree. These results indicate that the reduced PPy(DBS) microstructures provide a strongly amplified switchable adhesion between super sticky and super slippery.

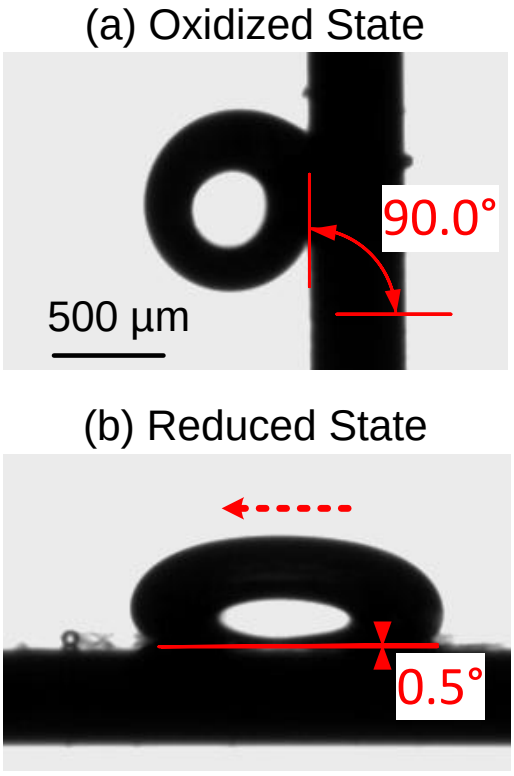

Figure 3: Sliding angles of DCM microdroplets on PPy(DBS) microstructures. (a) When the PPy(DBS) microstructure was oxidized at +0.6 V, the DCM microdroplet was pinned even when the substrate was tilted to 90 degrees. (b) When PPy(DBS) microstructure was reduced at -0.9 V, the microdroplet easily slipped off the surface.

Utilizing this switchable adhesion property, we demonstrated a capture/transport/release process of an organic microdroplet at ultra-low voltages in an aqueous environment. The droplet manipulation mechanism is shown in Figure 4. The PPy(DBS) microstructure is first oxidized at a positive potential (e.g., 0.6 V) to capture the organic microdroplet since the oxidized PPy(DBS) behaves a super sticky surface. The PPy(DBS) substrate containing the captured microdroplet is then transported to the desired location (Figure 4b). At this location, a negative potential (e.g, -0.9 V) is then applied to the PPy(DBS) microstructure (Figure 4c). Since the reduced PPy(DBS) microstructure behaves like a super slippery surface in regard to the organic droplet, the captured microdroplet is released from the substrate by gravity.

Figure 5 shows a demonstration of droplet capture, transport, and release using the PPy(DBS) microstructure. The PPy(DBS) microstructure was first oxidized at +0.6 V before being placed in contact with a DCM microdroplet (Figure 5a). Once in contact, the droplet was immediately attached to the oxidized PPy(DBS) microstructure due to a strong adhesion force (Figure 5b) and lifted up from the glass substrate (Figure 5c). After the transportation (Figure 5d), the DCM microdroplet was released from the PPy(DBS) microstructure upon application of the reductive potential of -0.9 V (Figure 5e) and placed at the desired location (Figure 5f). There was no necessity for the microdroplet to contact

another more adhesive surface to release from the PPy(DBS) microstructure. During this whole process, the DCM microdroplet remained fully intact and there was no residual droplet left on the PPy(DBS) microstructure.

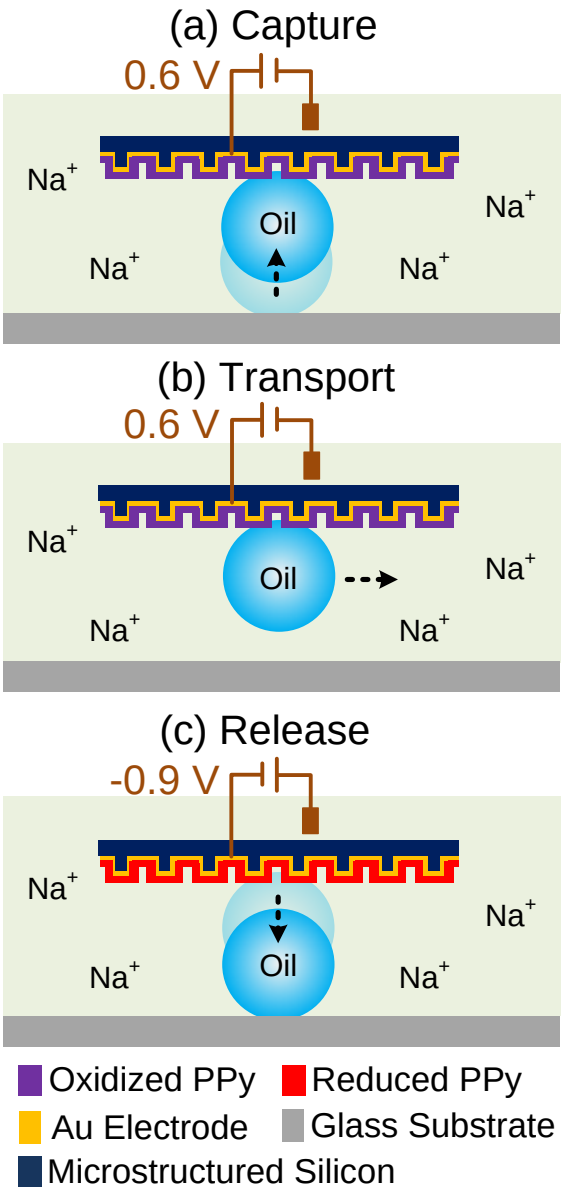

Figure 4: Scheme for the capture and release of an organic droplet in an aqueous electrolyte environment (e.g. $NaNO_3$ solution) utilizing the tunable adhesion of a PPy(DBS) microstructure. (a) The PPy(DBS) microstructure oxidized at 0.6 V has a strong adhesion with the organic droplet and is used to capture the microdroplet. (b) Transportation. (c) The reduced PPy(DBS) microstructure, which behaves as a super slippery surface, releases the captured microdroplet after the transportation.

CONCLUSIONS

In summary, we have demonstrated an ultra-low-voltage controlled capture/release process of organic microdroplets utilizing the tunable adhesion on PPy(DBS) microstructures. This technique has promising applications in microfluidics, antifouling, and oil-water separation.

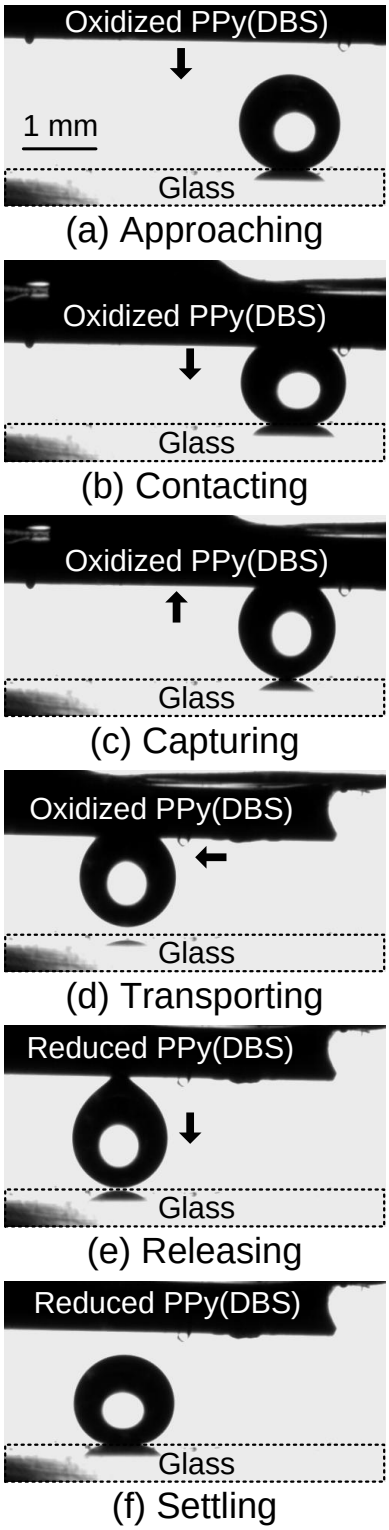

Figure 5: The process of capturing, transporting and releasing a DCM microdroplet by changing the oxidization state of a micropatterned PPy(DBS) substrate. The DCM microdroplet was captured and transported by the micropatterned PPy(DBS) substrate in an oxidized state and released by reducing the micropatterned PPy substrate. No loss of DCM droplet has been observed during the whole process.

ACKNOWLEDGEMENTS

This work has been supported in part by National Science Foundation (EECS-1040007, ECCS-1104870, ECCS-1202269 and EEC-1138244) and Air Force Office for Scientific Research (FA9550-11-1-0272, FA9550-12-1-0326).

REFERENCES

[1] J.R. Dorvee, A.M. Derfus, S.N. Bhatia, and M.J. Sailor, "Manipulation of Liquid Droplets using Amphiphilic, Magnetic One-Dimensional Photonic Crystal Chaperones", Nature Materials, 3, 896 (2004).

[2] O.D. Velev, B.G. Prevo, and K.H. Bhatt, "On-Chip Manipulation of Free Droplets", Nature, 426, 515 (2003).

[3] V. Srinivasan, V.K. Pamula, and R.B. Fair, "Droplet-Based Microfluidic Lab-on-a-chip for Glucose Detection", Analytica Chimica Acta, 507, 145 (2004).

[4] P.-Y. Chiou, Z.H. Chang, and M.C. Wu, "Droplet Manipulation with Light on Optoelectrowetting Device", Journal of Microelectromechanical Systems , 17, 133 (2008).

[5] D. Wu, S.-Z. Wu, Q.-D. Chen, Y.-L. Zhang, J. Yao, X. Yao, L.-G. Niu, J.-N. Wang, L. Jiang, and H.-B. Sun, "Curvature-Driven Reversible In Situ Switching Between Pinned and Roll-Down Superhydrophobic States for Water Droplet Transportation", Advanced Materials, 23, 545 (2011).

[6] X. Yao, J. Gao, Y. Song, and L. Jiang, "Superoleophobic Surfaces with Controllable Oil Adhesion and Their Application in Oil Transportation", Advanced Functional Materials, 21, 4270 (2011).

[7] X. Zhao, H. Fan, J. Luo, J. Ding, X. Liu, B. Zou, and Y. Feng, "Electrically Adjustable, Super Adhesive Force of a Superhydrophobic Aligned MnO_2 Nanotube Membrane", Advanced Functional Materials, 21, 184 (2011).

[8] X. Hong, X. Gao, and L. Jiang, "Application of Superhydrophobic Surface with High Adhesive Force in No Lost Transport of Superparamagnetic Microdroplet", Journal of the American Chemical Society, 129, 1478 (2007).

[9] E. Smela, "Microfabrication of PPy Microactuators and Other Conjugated Polymer Devices", Journal of Micromechanics and Microengineering, 9, 1 (1999).

[10] Y.-T. Tsai, C.-H. Choi, and E.-H. Yang, "Low-Voltage Manipulation of an Aqueous Droplet in a Microchannel via Tunable Wetting on PPy(DBS)", Lab on a Chip, 13, 302 (2013).

[11] Y.-T. Tsai, C.-H. Choi, N. Gao, and E.-H. Yang, "Tunable Wetting Mechanism of Polypyrrole Surfaces and Low-Voltage Droplet Manipulation via Redox", Langmuir, 27, 4249 (2011).

[12] K.S. Teh, Y. Takahashi, Z. Yao, and Y.-W. Lu, "Influence of Redox-Induced Restructuring of Polypyrrole on its Surface Morphology and Wettability", Sensors and Actuators A: Physical, 155, 113 (2009).

[13] C. Ding, Y. Zhu, M. Liu, L. Feng, M. Wan, and L. Jiang, "PANI Nanowire Film with Underwater Superoleophobicity and Potential-Modulated Tunable Adhesion for No Loss Oil Droplet Transport", Soft Matter, 8, 9064 (2012).

CONTACT

* E.-H. Yang, tel: +1-201-216-5574; eyang@stevens.edu

COMPACT, SCALABLE, HIGH-RESOLUTION, MEMS-ENABLED TACTILE DISPLAYS

X. Xie[1], Y. Zaitsev[1], L.F. Velásquez-García[2], S. Teller[2], and C. Livermore[1]*
[1]Northeastern University, Boston, Massachusetts, USA
[2]Massachusetts Institute of Technology, Cambridge, Massachusetts, USA

ABSTRACT

The design, fabrication, and test of a new type of tactile display for the blind is reported. An array of piezoelectric extensional actuators vibrates in plane, and microfabricated scissor mechanisms convert the in-plane actuations into robust, higher-amplitude, out-of-plane vibrations. Information can be conveyed by varying the vibration patterns in space and time. Analytical and FEM models were used to design individual tactile elements, which were implemented with PZT actuators and both SU-8 and 3D-printed scissor amplifiers. The measured displacements of 3 mm x 10 mm tactile elements exceed 10 µm, in agreement with models, with measured forces exceeding 45 mN. The creation of a 28-element prototype is also reported.

INTRODUCTION

Providing information to those who are blind or have low vision is critical for enhancing mobility, situational awareness, education, and more. Tactile information delivery can be effective, rapid, and private. Examples include Braille [1,2] and the Optacon [3], both of which convey text to the user through the motion of several-centimeter-long piezoelectric bending beam actuators. Graphical information that cannot be expressed as text is most commonly embossed on paper. Although refreshable 2D graphical interfaces are preferred, it is challenging to create actuators that are compact enough to be arrayed into an unlimited number of rows and columns while still being robust, easy to sense, and rapidly switchable. Electroactive polymer actuators are small enough to be arrayed with a few millimeter pitch and provide quasistatic millimeter-scale actuations, but they typically have actuation times on the order of seconds (see [4] and references therein). An alternative integrates piezoelectric bending beam actuators perpendicular to the tactile sensing plane, enabling large bending beam actuators to be tightly packed for fully 2D displays [5,6]. MEMS technology is also increasingly being leveraged to create tactile displays, as in [7-9]. Important challenges nonetheless remain, including spatial resolution, refresh rate, and cost.

Ideally, the display's resolution should leverage the approximately one receptor per mm^2 spacing of mechanoreceptors in human finger pads and be extendable to full 2D. It should be refreshable in real time, allowing the contents of the display to keep up with rapidly changing inputs. The display should also code information in a way that is easily detected and interpreted. Since humans are much more sensitive to motions and changing stimuli than they are to static patterns [10], the display should code information not only as static patterns, but also as simulated motion against the user's finger pads. Finally, its power consumption should be compatible with portable use, and it should be manufacturable by efficiently scalable means to ensure that its cost is compatible with the resources of its target user base. Although existing displays have met various subsets of these requirements, no existing display has been able to meet all of these requirements simultaneously.

This paper presents the concept, design and modeling, fabrication, and characterization of a new type of tactile actuator created to target these requirements. This new actuator concept comprises a single-layer, 2D array of in-plane, extensional piezoelectric actuators, each of which is capped with a scissor amplifier and blunt "pin" that the user feels with his or her fingers (Figure 1). When the extensional actuators expand and contract, the tops of the scissors fall and rise. The ratio of scissor amplitude to actuator amplitude depends on the scissor angle. In the final display, each actuator is driven with an oscillating voltage to create patterns of vibration on the display surface.

This display concept is dictated by the requirements above. To minimize cost, the design avoids the large, multi-layer actuators of refreshable Braille. The tactile elements (tactels) comprise a single layer of actuators to enable scalable integration to 2D. The technology is compatible with down-scaling tactels to the 1-2 mm^2 scale, but actuators with such a small footprint can be expected to create smaller vibrations than larger actuators can. The actuators are therefore designed to operate between tens and hundreds of Hz, where humans sense small actuations most readily [11]. This high frequency design is also consistent with rapid refreshability and the creation of moving patterns. The use of high frequency actuations eliminates polymer actuators and supports the use of piezoelectric, magnetic, or shape memory alloy actuators. Among these, the need to minimize power favors piezoelectrics. Finally, the actuator plus scissor amplifier architecture maximizes the vibrational amplitudes that the system can create from a small extensional actuator.

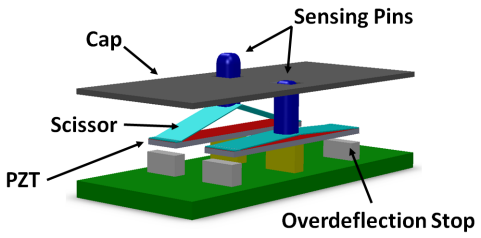

Figure 1: Schematic diagram of piezoelectric extension actuators (red) topped by scissor amplifiers (light blue) and cap plate.

DESIGN

Device Specifications

The initial specification for vibrational amplitude was set to >10 µm to accommodate the wide range of human finger sensitivities at tens to hundreds of Hz. This threshold has been validated through laboratory testing of the devices presented below. Although many individuals can detect vibrations at or below the few micron scale, the ability to use amplitudes of >10 µm remains useful. In practice, the frequency can be varied between 10 Hz and 400 Hz to create different user experiences.

Actuator force can also matter for sensing; if the tactile element has insufficient stiffness, the force that it applies to the user's fingers may be too small for robust detection. A design specification of > 10 mN of oscillatory force for most users is chosen by correlating measured forces with the user experience.

Ideal Tactel Performance

The piezoelectric extensional actuators comprise y-poled lead zirconate titanate (PZT) bilayer beams that are actuated by

9781940470016/HH2014/$25©2014TRF
DOI 10.31438/trf.hh2014.36

applying a voltage between electrodes on their top and bottom surfaces. The scissor converts the resulting lengthwise extension or contraction into vertical displacement. For a scissor with ideal pinned hinges, the scissor's vertical displacement Δy is related to the PZT's lengthwise extension Δx by $\Delta y = \Delta x \cot(\theta)$, where θ is the angle between scissor and actuator (Figure 2). The ratio of vertical displacement to horizontal displacement (the amplification factor) can be large when the scissor angle θ is small. For example, an angle of 1.25º corresponds to an amplification factor of > 45.

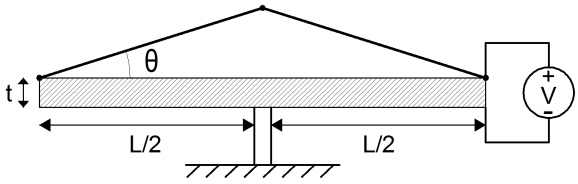

Figure 2: Geometrical parameters for tactel with ideal scissor.

User-applied loads during sensing can impart forces to the PZT beams and scissor amplifiers, affecting the system's performance. For an ideal scissor with rigid arms and pinned hinges, the vertical force F applied at the scissor's peak produces larger axial forces of F/(2sin(θ)) in the scissor arms. The axial forces in turn apply vertical forces of F/2 and horizontal forces of Fcot(θ)/2 at the ends of the PZT beam. The vertical forces tend to bend the PZT and must be limited to prevent breakage. The horizontal forces tend to stretch the PZT and will oppose its contraction. The relationship among the horizontal force from the user, the blocking force, and the target displacement drive the design. A smaller scissor angle offers larger amplification, but a larger scissor angle reduces deflection limits due to the blocking force. Figure 3 illustrates the amplification/blocking force tradeoff by plotting predicted vibrational amplitude vs. scissor angle for tactels using both a MEMS scale actuator (2500 μm x 400 μm x 250 μm) with an applied voltage of 150 V and a milliscale actuator (10 mm x 3 mm x 0.38 mm) with an applied voltage of 100 V. The user-applied force per tactel is taken to be 0.1 N. The maximum deflections are calculated as 15.5 μm at an angle of 1.1° and 55.1 μm at 0.25° for MEMS and milliscale tactels, respectively. The optimal scissor angle for this applied force is therefore in the range of about 1° or less, depending on the size scale.

Supporting the actuator at the center frees its ends to move in extension and contraction, but the suspended ends can bend or break under applied loads. The maximum stress in the PZT under an applied load of 0.1 N was calculated at 40 MPa and 26 MPa for the MEMS-scale and milliscale devices, respectively, less than the predicted failure stress of 90 MPa. Deflection-limiters are included for additional safety. First, the ends of the actuator beams rest on underlying support surfaces. Second, the tactile display is capped by a perforated plate. The user can sense the pins' vibration where they protrude through the holes, but the cap prevents overdeflection of the tactile elements under load. The cap also provides electrical isolation and prevents tactile distraction.

The key advantage of this architecture as compared with the bending beam actuators of refreshable Braille is that it enables both robustness and large amplitude actuations. The thick, short extensional actuator creates large actuation forces while providing excellent robustness against bending under user-applied load, and the scissor amplifier converts the resulting small, in-plane deflections into large vibrations. In contrast, a piezoelectric bending beam of comparable length would have to be thinner than the actuators used here to achieve sufficient vibrational amplitude, and its thinness would sacrifice robustness against applied forces.

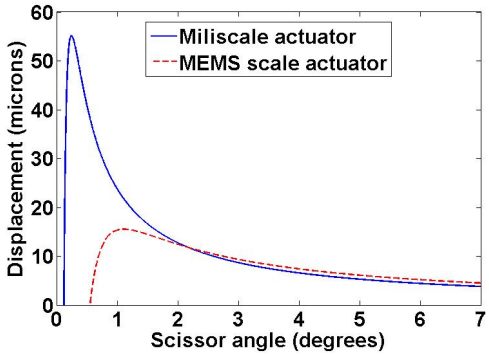

Figure 3: Plot of predicted deflection amplitude as a function of scissor angle for actuators at the MEMS and milli scales.

Scissor Design

For ease of fabrication, the present scissors use bending flexures in place of pinned hinges. Figure 4a shows a diagram of the flexural scissor along with its integrated sensing pin. The dimensions of the nominally rigid elements and the flexural hinges are chosen to ensure that the actuator force is sufficient to make the peak of the scissor vibrate and that the scissor does not deform excessively or experience excessive stress under applied loads. Finite element analysis (FEA) was used to predict the performance of the scissors under actuation and user-applied loads. To avoid fatigue, the maximum acceptable stress was set to 100 MPa, about 20 times less than the failure stress of SU-8 and the 3D printed material. Based on these results, the hinges are designed with thickness t_h of 300 μm for the SU-8 hinges and 400 μm for the 3D printed hinges; the hinge widths w_h are designed as 1.5 mm and 2.8 mm for the SU-8 and 3D-printed scissors, respectively. The hinge length l_h for both scissor types is 800μm out of a total 9.6 mm length. Each scissor includes a 6 mm tall sensing pin. The FEA results of Figure 4b show that the predicted peak displacement of an SU-8 scissor with the final, as-fabricated dimensions under an anchor displacement corresponding to an applied voltage of 95 V is 2 μm (corresponding to a peak-to-peak amplitude of 4 μm). The maximum stress in this case is 34 MPa.

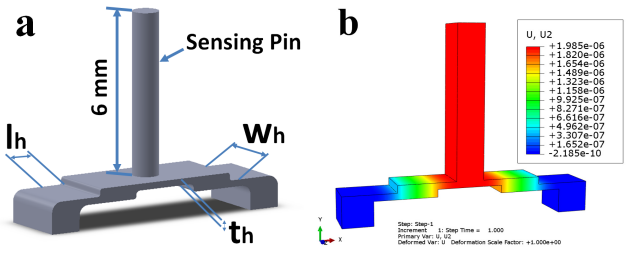

Figure 4: (a) Diagram of scissor with flexural hinges and (b) deformation (μm) of SU-8 scissor under 95 V predicted using FEA.

FABRICATION

The individual tactels include a combination of micro and milliscale features. Custom y-poled PZT actuators (Piezo Systems, Inc.), laser cut to 10 mm x 3 mm x 380 μm, comprise the in-plane actuators. The scissor actuators were manufactured by two

methods, photolithographic definition in 1.5 mm thick SU-8 and 3D printing. To pattern the SU-8 scissors, 40 nm of OmniCoat (MicroChem) was spun onto a silicon substrate in three layers. A 1.5 mm thick double layer of SU-8 2150 (MicroChem) was spun over the OmniCoat and patterned photolithographically. The Omnicoat was dissolved to lift the SU-8 scissors off the substrate. The 3D-printed scissors were defined from Veroblack Fullcure 870 UV-curable resin in an Objet Eden 333 3D printer. The as-fabricated hinge dimensions are 800 μm long x 1470 μm wide x 270 μm thick and 800 μm long x 2900 μm wide x 390 μm thick for the SU-8 and 3D-printed scissors, respectively. The difference in hinge thickness primarily reflects the use of two different designs. The difference in scissor width reflects SU-8 process constraints.

Although larger arrays of tactels would ultimately be soldered to a base plate (e.g. a printed circuit board), the devices for single tactel tests and small array tests were connected by soldering wires to nickel electrodes on the upper and lower actuator surfaces. The scissors were adhered to the actuators with a cyanoacrylate adhesive. For single tactel testing, the alignment of the scissor to the actuator did not affect performance, and no provisions were made for alignment. The final tactels are shown in Figure 5.

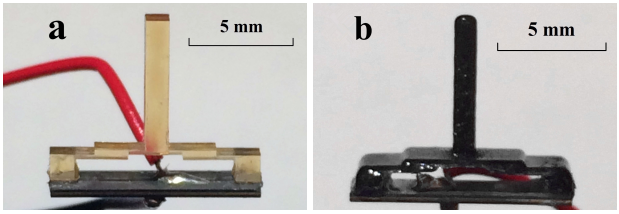

Figure 5: Photographs of fabricated tactels with (a) SU-8 and (b) 3D printed scissors.

For array fabrication, alignment is critical because the sensing pins must align with the holes in the cap plate. The scissors were mechanically aligned to the actuators using a reference surface. Twenty-eight actuators and scissors were then aligned by electrically insulating mechanical stops in a passive alignment plate. The tactels form an offset array to minimize pitch. A thin foam interlayer placed between the actuators and the alignment plate prevents parasitic vibrations on neighboring pins but also somewhat reduces the vibrational signal at the pin. The electrical wires pass through vias in the alignment plate and are soldered to an underlying printed circuit board. The alignment plate provides mechanical support to prevent deflection of the actuator under load. A mechanical spacer controls the height of the cap plate to ensure that the pins protrude by approximately 300 μm, and all plates are aligned relative to each other by a set of alignment pins. The package and its alignment features are shown in Figure 6.

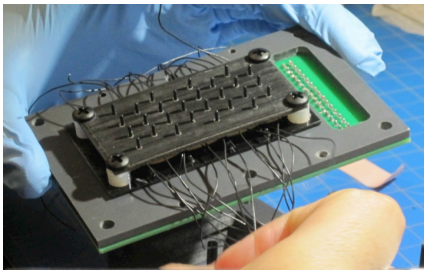

Figure 6: Photograph of 28-element tactile array during assembly.

EXPERIMENT

The individual tactels were mounted on a testing stage under an optical stereomicroscope so that deformations of the scissor were visible in the microscope's viewing plane, and displacement was measured under actuation. Square wave voltages with a frequency of 0.5 Hz were output by a function generator and amplified to achieve peak voltage amplitudes of up to 170 V. The voltage was increased in 10 V steps from a starting value of 40 V to the maximum value of 170 V. Two or three images of the tactel in each of its maximum and minimum positions for each voltage were captured using a microscope camera. The scissor displacement was measured from the captured images by counting pixels; the 1.16 μm pixelization dominates the measurement error.

The measured peak-to-peak displacement is plotted in Figure 7. The markers represent data points, and the error bars reflect a +/- one pixel measurement error. The solid lines are the displacement predicted analytically for a tactel with an ideal, pinned-hinge scissor. For the purposes of this calculation, the flexural hinges are approximated as pinned hinges located on the neutral plane of the flexural hinge directly adjacent to the anchor support and the central pin. For the device with an SU-8 scissor, the displacement ranges from a minimum of of 3.8 μm measured at 40 V to a maximum of 10.7 μm measured at 170 V. For the device with a 3D printed scissor, the displacement ranges from 2.7 μm to 8.9 μm over that voltage range. In all cases, the increase in displacement with applied voltage is similar to the linear trend that is predicted using the ideal pinned hinge model. The FEA model slightly under-predicts the measured displacement at 95 V (2 μm peak predicted as compared with ~3 μm peak determined from the measured ~6 μm peak-to-peak displacement). The larger displacement of the SU-8 scissor for the same voltage reflects the SU-8 scissor's thinner hinge and narrower width, both of which reduce its mechanical stiffness under horizontal actuation.

To measure the amplitude of the force that the tactels apply when they vibrate in contact with a rigid surface, the individual tactels were mounted on a second testing stage that is mounted to the grips of a mechanical tester (Instron 5943). The tensile tester was preloaded to apply a force of 40 mN to the sensing pin when zero voltage was applied. A square wave voltage with a frequency of 10 Hz was applied to the tactel, and its peak amplitude was increased from 40 V to 170 V in increments of 10 V. The resulting forces were measured by the mechanical tester's load cell. The raw data were post-processed in MATLAB to eliminate signals at frequencies other than 10 Hz (noise and drift).

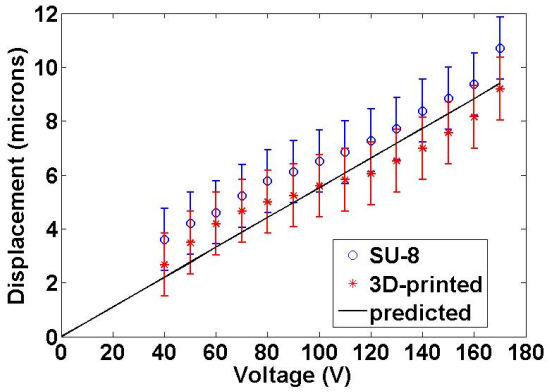

Figure 7: Plot of tactel displacement vs. applied voltage measured with SU-8 and 3D-printed scissors and predicted for ideal scissors.

Figure 8 plots the measured peak-to-peak amplitude of the tactel's oscillating force. The markers represent the measured forces, and the connecting lines are included as guides to the eye. Each force measurement is repeated over 15 to 20 voltage cycles, resulting in 15 to 20 nominally identical force measurements. The error bars represent the maximum variation that was observed between nominally identical repeated measurements. Whereas the measured displacements were similar for the SU-8 and 3-D printed devices and matched the models well in all cases, the measured forces differ widely between the designs. The forces from the tactel with the 3D printed scissor have larger values, increasing from 6.9 mN at 40 V to 48.7 mN at 170 V. The forces from the tactel with the SU-8 scissor are smaller, ranging from 2.3 mN to 14.7 mN. The lower forces from the tactel with the SU-8 scissor primarily reflect the SU-8 scissor's lower stiffness due to differences in geometry (hinge thickness and width); their Young's modulus values are similar.

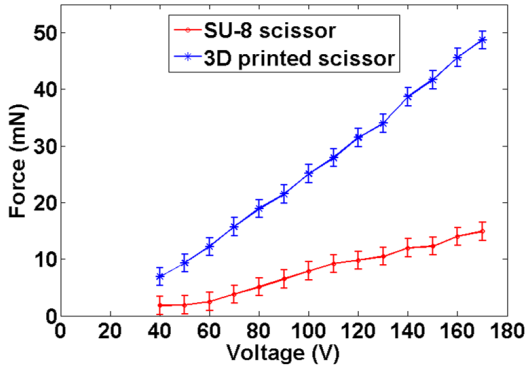

Figure 8: Measured tactel force vs. peak amplitude of the applied voltage. Markers represent data; lines are guides to the eye.

Individual tactels with SU-8 and 3D-printed scissors were tested by sighted volunteers to determine the minimum voltages at which vibration can be sensed and is comfortable. Each measurement was repeated at 20 Hz, 100 Hz, and 250 Hz. Although the small number of testers to date precludes a statistically significant analysis, several initial trends emerge. At all three frequencies, the level of comfortable vibration is typically ~2-4 μm. For 3D-printed scissors, the comfortable level of force is typically around ~8-10 mN, whereas SU-8 scissors enable comfortable detection at the ~2 mN scale. The difference in necessary force for SU-8 and 3D printed scissors indicates either that sensing is dominated by displacement rather than by scissor deformability in this design range, or that the details of the pin's shape (e.g. SU-8's square corners as compared with the 3D printed pin's rounded top) are critical determinants of the force required for sensing. The minimum detectable levels are lower than the values for comfortable usage. Since the minimum detectable voltages (typically ~10-30 V) lie below 40 V, the corresponding forces and displacements cannot be determined from Figures 7 and 8. Higher frequencies typically permit sensing of smaller forces and displacements, in agreement with the literature [11].

Sensing of the tactile arrays was less robust and required higher voltages. The difficulty of sensing vibrations in the arrays is attributed to the thin foam interlayer included in the array package. Although this layer successfully minimizes parasitic vibrations to neighboring pins, it has a detrimental effect on the sensed vibrational amplitude on the target pin. Future work will focus in part on minimizing vibrational damping at the target pin.

CONCLUSION

Tactile elements based on the actuator plus amplifier design are shown to be effective at the milliscale. Their measured performance agrees with the models, with maximum deflections of greater than 10 μm and maximum forces above 45 mN that place the devices well above the sensing threshold. An analytical model based on ideal pinned hinges is shown to be useful for predicting the behavior of tactels with flexural hinges, especially when coupled with FEA to predict hinge failure. The analytical model validation provides support for further downscaling of the tactile elements to the 1-2 mm^2 scale, since the models also predict successful functioning at this scale. At the MEMS scale, the display's resolution would correspond to up to 100 tactels/cm^2. The measured performance confirms sensing thresholds of less than 4 μm and 2 mN for the most effective tactile devices.

ACKNOWLEDGMENTS

The authors thank Patrick Murphy and Constantinos Mavroidis for assistance with the 3D printing, which was done in Northeastern's Biomedical Mechatronics Laboratory. The research was funded by the Andrea Bocelli Foundation. Travel support has been generously provided by the Transducer Research Foundation.

REFERENCES

[1] M. Nakajima, K. Suzuki, H.R. Su, Y. Tani, and A. Morita, "Braille Cell", U.S. Patent 5226817, 1991.

[2] Y. Tani, Y. Shiraishi, H.R. Su, A. Morita, and K. Suzuki, "Tactile reading device", US Patent 5449292, 1993.

[3] J.C. Bliss, M.N. Katcher, C.H. Rogers, and R.P. Shepard, "Optical-to-tactile image conversion for the blind", IEEE Transactions of Man-Machine Systems, 11, 1, pp. 58 - 65, (1970).

[4] Y. Bar-Cohen, "Refreshable Braille displays using EAP actuators" SPIE 7642 Electroactive Polymer Actuators and Devices, International Society for Optics and Photonics, San Diego, CA, (2010), pp. 764206 - 76420.

[5] J. Pasquero and V. Hayward, "STReSS: A Practical Tactile Display System with One Millimeter Spatial Resolution and 700 Hz Refresh Rate", Proc. of Eurohaptics 2003, Dublin, Ireland (2003), pp. 94 - 110.

[6] Metec AG, http://web.metec-ag.de/cell%20d2.html

[7] N. Kitamura, J. Chim, N. Miki, "Micro-needle electrode array for electro tactile display", Technical Digest of the 2013 Transducers, Barcelona, Spain, Transducer Research Foundation, (2013), pp. 106 - 107.

[8] N. Torras et al., "Nematic opto-mechanical actuators for the fabrication of refreshable tactile systems", Technical Digest of the 2013 Transducers, Barcelona, Spain, Transducer Research Foundation, (2013), pp. 1691 - 1694.

[9] Ninomiya, T., Y. Okayama, Y. Matsumoto, X. Arouette, K. Osawa, and N. Miki. "MEMS-based hydraulic displacement amplification mechanism with completely encapsulated liquid." Sensors and Actuators A: Physical, 166, 2: pp. 277 - 282. (2001).

[10] J. Downar, A.P. Crawley, D.J. Mikulis, and K.D. Davis, "A multimodal cortical network for the detection of changes in the sensory environment", Nature Neuroscience, 3, pp. 277 - 283, (2000).

[11] E. Kandel, J. Schwartz and T. Jessell's, "Principles of Neural Science (Fourth Edition)," McGraw-Hill, New York, 2000.

CONTACT

*X.Xie, tel: +1-617-373-2048; x.xie@neu.edu

HIGH FREQUENCY AND HIGH FILL FACTOR PIEZOELECTRIC MICROMACHINED ULTRASONIC TRANSDUCERS BASED ON CAVITY SOI WAFERS

Yipeng Lu, Stefon Shelton and David A. Horsley
University of California, Davis, USA

ABSTRACT

This paper presents a high frequency and high fill factor piezoelectric micromachined ultrasonic transducer (PMUT) array, which is fabricated with a simple and CMOS compatible process based on commercially available cavity SOI wafers. This 2-mask process eliminates the need for through-wafer etching and enables 10× higher fill factor and thereby higher acoustic performance. PMUTs based on both lead zirconium titanate (PZT) and aluminum nitride (AlN) piezoelectric layers are designed, fabricated and characterized. For the same 50 µm diameter, PZT PMUTs show large dynamic displacement sensitivity of 316 nm/V at 11 MHz in air, which is ~20× higher than that of AlN PMUTs. Electrical impedance measurements of PZT PMUTs show high electromechanical coupling $k_t^2 = 12.5\%$, and 50 Ω electrical impedance that is well-matched to circuits. The resonant frequency and static displacement of PMUTs with different diameters are measured and agree well with FEM results. The acoustic pressure generated by an unfocused 9×9 array of 40 µm diameter PZT PMUTs was measured with a needle hydrophone, showing a pressure sensitivity of 2 kPa/V.

INTRODUCTION

Ultrasonic transducers have been used in many applications, such as nondestructive testing (NDT), ranging and velocity sensing, industrial automation, object recognition, collision avoidance, and particularly medical imaging [1-2]. Conventional ultrasonic transducers are largely based on bulk piezoelectric ceramic that has poor acoustic coupling to air or water, and is also expensive to machine into two-dimensional (2D) transducer arrays needed for 3D imaging [3]. In contrast, micromachined ultrasonic transducers (MUTs) have a compliant membrane structure with low acoustic impedance for good coupling to air and liquids. Furthermore, MUTs have several other advantages over conventional ultrasonic transducers, including small element size, low power consumption, improved bandwidth, low cost, easy fabrication of large arrays with compact designs, and easy integration with supporting electronics [4-5].

MUTs can be divided into two types based on the actuation mechanism: capacitive MUT (CMUT) and piezoelectric MUT (PMUT). To achieve the same sensitivity as that of a PMUT, a CMUT needs either a very small gap, increasing fabrication complexity and cost, or a high DC bias [6]. Previous PMUTs were fabricated by a through-wafer etching approach to produce 400 µm diameter PMUT operating in air [7-8]. However, MHz-range PMUTs are an order of magnitude smaller, and through-wafer etching results in a low fill-factor, small element count, and therefore poor acoustic efficiency [9]. Front side etching can also be used to make a high fill factor array, but it results in a more complicated fabrication process and requires an additional layer to seal the etching holes, which reduces fluid-immersed PMUT performance [6]. Here, we present a PMUT array with a simple process based on cavity SOI wafers. This 2-mask process eliminates the need for through-wafer etching [9] and enables 10× higher fill factor, which is important for minimizing grating lobes of the acoustic beam and obtaining a high array gain and coupling ratio.

DESIGN

A 3D schematic diagram of a PMUT array based on cavity SOI wafers and the cross section of a single PMUT are shown in Figure 1. In the 72×9 array, the top electrodes of the 9 PMUTs in each column are connected together to minimize the number of electrical connections to the die. Each PMUT functions as both a transmitter and receiver. As a transmitter, the electric field between the top electrode (TE) and the bottom electrode (BE) creates a transverse stress in the piezoelectric layer due to the inverse piezoelectric effect. The generated stress causes a bending moment which forces the membrane to deflect out of plane, launching an acoustic pressure wave into the environment. As a receiver, an incident pressure wave deflecting the plate creates transverse stress which results in a charge between the electrodes due to direct piezoelectric effect.

The PMUTs demonstrated here are fabricated using cavity SOI wafers with a 2.5 µm device Si layer over 2 µm deep vacuum-sealed cavities of various diameters. Devices were fabricated using both lead zirconium titanate (PZT) and aluminum nitride (AlN) piezoelectric layers to allow the performance of these two types of PMUTs to be compared. Both analytical methods and finite element method (FEM) simulations were used to determine the best piezo/silicon layer stack to optimize receiving performance. The optimal designs for PZT and AlN PMUTs are 1.1 µm PZT/ 2.5 µm Si and 0.8 µm AlN/ 2.5 µm Si, respectively. These layers are sufficiently thin that they allow the PMUT diameter to be smaller than half the acoustic wavelength (λ/2), which minimizes grating lobes and enables efficient beam forming. In addition, the top electrode area is optimized at half the membrane area to maximize electromechanical coupling.

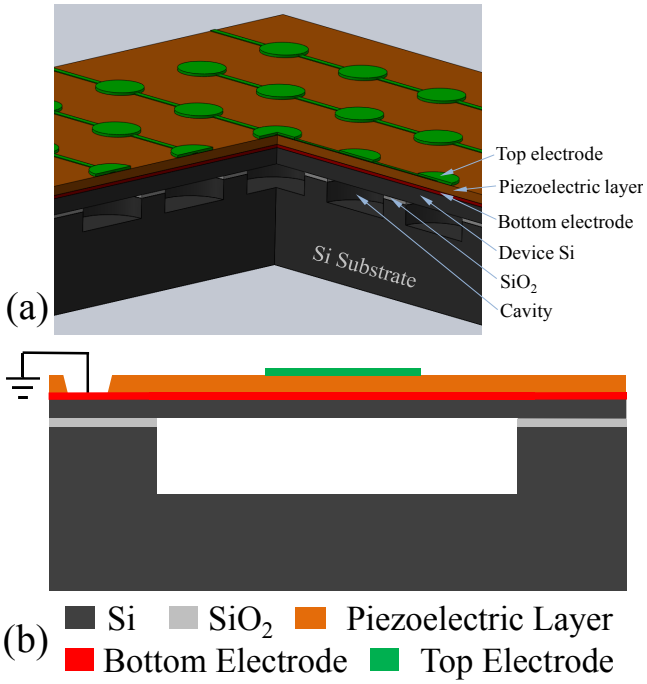

Figure 1: (a) 3D schematic diagram of a PMUT array based on cavity SOI wafers; (b) cross section of a single PMUT.

9781940470016/HH2014/$25©2014TRF
DOI 10.31438/trf.hh2014.37

Solid-State Sensors, Actuators and Microsystems Workshop
Hilton Head Island, South Carolina, June 8-12, 2014

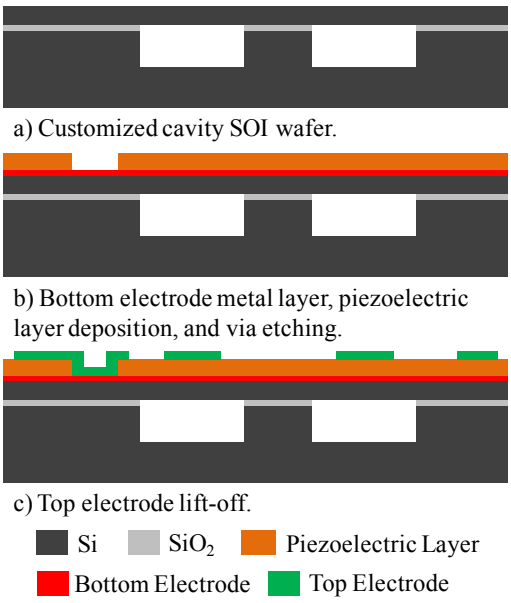

Figure 2: Fabrication process flow of PMUT array.

FABRICATION

PMUT arrays were fabricated via a simple 2-mask process. A cross-section of the fabrication process flow is shown in Figure 2. The process is based on custom-fabricated cavity SOI wafers (IceMos Technology, Belfast, Ireland), as shown in step (a). The cavity SOI wafers are prepared by wafer bonding in vacuum, resulting in a vacuum-sealed cavity beneath the PMUT and eliminating the possibility of squeeze-film damping beneath the PMUT membrane. The bottom electrode metal and piezoelectric layer are then deposited via sputtering. In AlN PMUTs, sputtering is conducted at <400 °C and begins with a 25 nm AlN seed layer, followed by a 100 nm Mo layer and the 800 nm AlN layer. The PZT sputtering process is conducted at 600 °C and a 20 nm conductive oxide layer $SrRuO_3$ (SRO) is sputtered between the PZT layer and the 100 nm Pt bottom electrode to improve the lifetime by reducing oxygen defects accumulating at the Pt/PZT interface when the polarization is switched. After sputtering, the first mask is used to define vias to the bottom electrode through wet etching, step (b), with HNO_3/BHF/H_2O in a volumetric ratio of 4.5/4.55/90.95 at room temperature used to etch PZT [10], and TMAH-based developer (MF-319) at 60 °C used to etch AlN. In the final step, step (c), the second mask is used to define the top electrode through lift-off of 150 nm of Al deposited by sputtering. Devices were fabricated with diameters range from 25 µm to 50 µm, corresponding to theoretical fundamental mode frequency range from 13 MHz to 55 MHz. The minimum pitch used was 45 µm, which is composed of 25 µm PMUT diameter and 20 µm space between adjacent PMUTs. Figure 3 shows a top view optical image

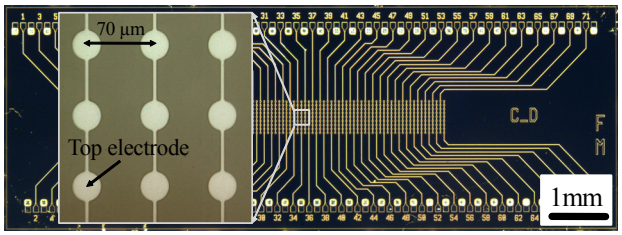

Figure 3: Optical image of 72×9 PMUT array.

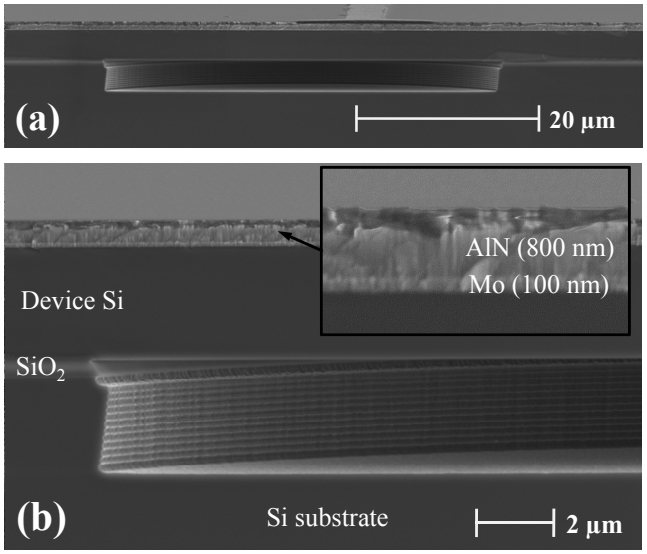

Figure 4: SEM cross section images of a 50 µm AlN PMUT showing the vacuum cavity beneath the device layer Si.

of a 72×9 PMUT array with 70 µm pitch and 50 µm PMUT diameter, which has a fill-factor 40%. Scanning electron microscope (SEM) images of the cross section of a single PMUT are shown in Figure 4.

CHARACTERIZATION

Frequency responses of displacement sensitivities for PZT and AlN PMUTs measured via laser doppler vibrometry (LDV) in air are shown in Figure 5. The PZT PMUT shows a large dynamic displacement sensitivity 316 nm/V, ~20× higher than that of AlN PMUTs for the same 50 µm diameter. Because the quality factor (Q) is limited by anchor loss, measurements conducted in air and in vacuum show the same Q. While Q diminishes with diameter, as expected, no significant difference was observed between the Q of AlN and PZT devices, confirming that material dissipation losses are negligible in comparison to the anchor loss.

FEM and measured results of the center frequencies in air for both PZT and AlN PMUTs with various diameters are shown in Figure 6 (a). The measurement results agree well with FEM results, indicating the FEM model can be used to efficiently guide PMUT design. The theoretical frequency of the PMUT's fundamental

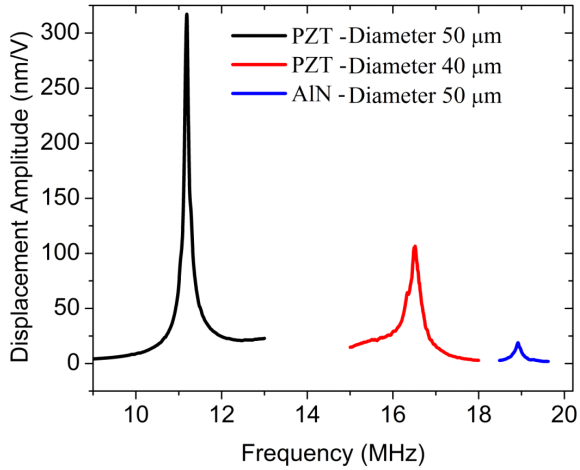

Figure 5: Frequency response of displacement sensitivity in air: PZT PMUTs (1.1 µm PZT/ 2.5 µm Si) vs. AlN PMUTs (0.8 µm AlN/ 2.5 µm Si).

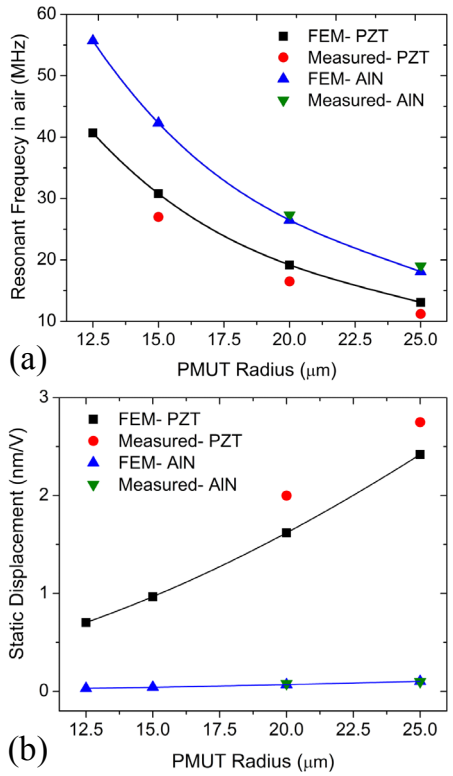

Figure 6: Measured and FEM (a) resonant frequency and (b) static displacement of PZT and AlN PMUTs in air versus radius.

vibration mode in air can be obtained from:

$$f_n = \sqrt{(3.2/a)^4 \frac{D}{\rho}} \Big/ 2\pi \qquad (1)$$

where a is the radius, ρ is area mass density and D is the flexural rigidity of the plate. D can be obtained by integrating from the bottom surface of the Si device layer to the top electrode:

$$D = \int_{Bottom}^{Top} \frac{E(z)z^2}{1-\nu(z)^2} dz \qquad (2)$$

where $E(z)$ is Young's Modulus and $\nu(z)$ is Poisson's ratio of the material at a distance z from the neutral axis. Referring to (1), because PZT has a smaller Young's modulus (E_{PZT} = 76 GPa, E_{AlN} = 330 GPa) and larger density (ρ_{PZT} = 7.7 g/cm^3, ρ_{AlN} = 3.2 g/cm^3) than that of AlN, PZT PMUTs show a ~40% lower resonant frequency than that of AlN PMUTs of the same diameter.

Figure 6 (b) shows FEM simulation and measured results of static displacement in air for both PZT and AlN PMUTs with various diameters. The displacement sensitivity (nm/V) scales approximately as f_n^{-2}. The static displacement per unit volt is an important metric to characterize PMUTs, and can predict the pressure per volt when the PMUT is immersed in fluid, because the large damping in the fluid results in low Q (≈ 1). The PMUT static displacement sensitivity, d_s, can be expressed as:

$$d_s \propto \frac{e_{31} Z_n}{D} \qquad (3)$$

where e_{31} is the piezoelectric coefficient, and Z_n is the distance from the middle of the piezoelectric layer to the neutral axis. For the same diameter, 50 μm, the PZT PMUT shows a ~28× higher static displacement than that of the AlN PMUT, which indicates a higher transmitting efficiency and pressure sensitivity when immersed in fluid. Referring to (3), the difference in d_s is due to the lower rigidity D, the greater distance from the piezo layer to the neutral axis Z_n, and the 16× higher piezoelectric coefficient (e_{31} = -8 pC/m^2 for PZT vs. -0.5 pC/m^2 for AlN) of the PZT PMUT.

Impedance measurements of single PZT and AlN PMUTs with 50 μm diameter are shown in Figure 7 (a) and (b), respectively. The resonant frequencies extracted from the impedance measurement agree well with the values extracted from LDV measurements. The electromechanical coupling coefficient, k_t^2, can be extracted from these impedance measurements using:

$$k_t^2 = \frac{f_a^2 - f_r^2}{f_a^2} = \frac{C_{MEMS}}{C_0 + C_{MEMS}} \qquad (4)$$

where f_a and f_r are the anti-resonant frequency and resonant frequency, respectively, and C_{MEMS} and C_0 are the motional capacitance and the electrical capacitance, respectively. From impedance measurements, the dielectric constants of the PZT and AlN films are extracted to be $\varepsilon_{33,PZT}$ = 528 and $\varepsilon_{33,AlN}$ = 9, respectively. After calibration to remove the parasitic capacitance C_p (74 pF) caused by pad and interconnect, the PZT PMUT shows k_t^2 = 12.5% (C_{MEMS} = 0.6 pF and C_0 = 4.17 pF). In addition, the PZT PMUT has 50 Ω impedance, which is matched to the impedance of conventional remote readout electronics and coaxial cables. However, PZT's high dielectric constant results in large parasitic C_p. C_p can be reduced by removing PZT from beneath the interconnect and bond pads, by adding an additional dielectric layer, or both.

Figure 8 shows acoustic pressure measurements conducted on a 9×9 array of 40 μm PZT PMUTs using a needle hydrophone with 40 μm probe (Precision Acoustics) in fluid. Fluorinert-70 is used for

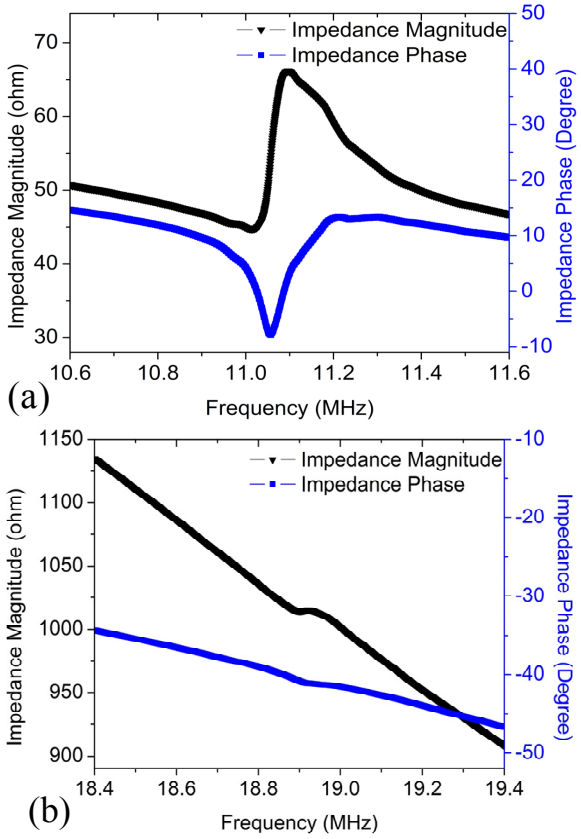

Figure 7: Impedance measurement of a single 50 μm PMUT with (a) PZT and (b) AlN piezoelectric layers.

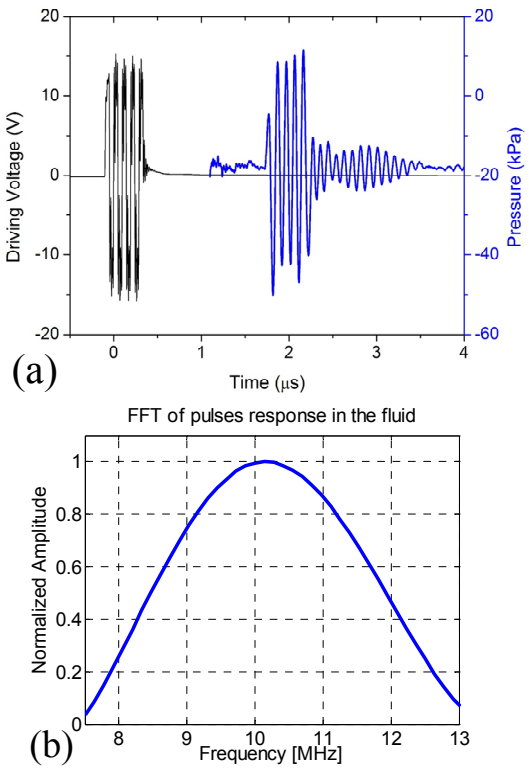

Figure 8: Acoustic pressure output from a 9×9 PMUT array: a) time domain b) FFT of received pulse.

the fluid immersed measurement, because it has acoustic impedance similar to that of human tissue and high electrical resistivity which eliminates the need for epoxy protection of the bondwires. Four cycles of 25 V_{pp} short-duration (0.4 μs) pulses were used to drive the PMUT array. PMUTs are driven individual phase control, resulting in an unfocused acoustic beam. The 1.5 μs time delay between the driving signal and the received pressure signal, shown in Figure 8 (a), is consistent with the 1.25 mm distance between the needle hydrophone and the PMUT array. In addition, the measurements show a high pressure response, 2 kPa/V, from the unfocused array. As shown in Figure 8 (b), the fast Fourier transform (FFT) of the received pressure signal shows a 3.4 MHz bandwidth at 10.4 MHz center frequency, sufficient for medical imaging. The measured pressure is in good agreement with the measured displacement, and can be further increased using beam forming to focus the acoustic beam.

CONCLUSION

This paper presents high frequency (10 - 55 MHz), fine pitch (45 - 70 μm) PMUT arrays, which are fabricated with a simple 2-mask process based on commercially available cavity SOI wafers. This process eliminates the need for through-wafer etching and enables 10× higher fill factor and thereby higher acoustic performance. PMUTs based on both PZT and AlN piezoelectric layers are designed with 1.1 μm PZT/ 2.5 μm Si and 0.8 μm AlN/ 2.5 μm Si layer stacks. Measurement results for PZT PMUTs with 50 μm diameter show a large dynamic displacement sensitivity of 316 nm/V at 11 MHz, a high electromechanical coupling coefficient k_t^2 = 12.5%, and 50 Ω electrical impedance that is well-matched to circuits. 50 μm diameter PZT PMUTs have 2.75 nm/V static displacement sensitivity, ~28× higher than that of AlN PMUTs of the same diameter, because PZT has a larger piezoelectric coefficient e_{31}, smaller Young's modulus E and higher density ρ than that of AlN. Acoustic pressure generated by an unfocused 9×9 array of 40 μm diameter PZT PMUTs was measured with a needle hydrophone. The measurement results show pressure sensitivity of 2 kPa/V at 1.25 mm away from the array, and a 3.4 MHz bandwidth at 10.4 MHz center frequency, sufficient for medical imaging.

ACKNOWLEDGEMENT

The authors thank Robin Wilson at IceMos Technologies for cavity SOI wafer fabrication, Kansho Yamamoto at Murata Manufacturing for assistance with PZT sputtering, the UC Berkeley Marvell Nanofabrication Laboratory for device fabrication, and Berkeley Sensor and Actuator Center (BSAC) Industrial Members for financial support.

REFERENCES

[1] B. A. Griffin, M. D. Williams, C. S. Coffman, and M. Sheplak, "Aluminum Nitride Ultrasonic Air-Coupled Actuator," Journal of Microelectromechanical Systems, vol. 20, pp. 476-486, Apr 2011.

[2] P. Muralt and J. Baborowski, "Micromachined ultrasonic transducers and acoustic sensors based on piezoelectric thin films," Journal of Electroceramics, vol. 12, pp. 101-108, Jan-Mar 2004.

[3] I. Ladabaum, X. C. Jin, H. T. Soh, A. Atalar, and B. T. Khuri-Yakub, "Surface micromachined capacitive ultrasonic transducers," IEEE Transactions on Ultrasonics Ferroelectrics and Frequency Control, vol. 45, pp. 678-690, May 1998.

[4] F. Akasheh, J. D. Fraser, S. Bose, and A. Bandyopadhyay, "Piezoelectric micromachined ultrasonic transducers: Modeling the influence of structural parameters on device performance," IEEE Transactions on Ultrasonics Ferroelectrics and Frequency Control, vol. 52, pp. 455-468, Mar 2005.

[5] Z. H. Wang, W. G. Zhu, O. K. Tan, C. Chao, H. Zhu, and J. M. Miao, "Ultrasound radiating performances of piezoelectric micromachined ultrasonic transmitter," Applied Physics Letters, vol. 86, Jan 17 2005.

[6] Y. Lu, A. Heidari, S. Shelton, A. Guedes and D.A. Horsley, "High frequency piezoelectric micromachined ultrasonic transducer array for intravascular ultrasound imaging," Proc. IEEE MEMS, pp. 745-748 (2014).

[7] S. Shelton, A. Guedes, R. Przybyla, R. Krigel, B. Boser, D. Horsley, "Aluminum Nitride Piezoelectric Micromachined Ultrasound Transducer Arrays", 2012 Solid-State Sensors, Actuators and Microsystems Workshop, Hilton Head, SC, Jun 2012, pp. 291-294.

[8] R. Przybyla, S. Shelton, A. Guedes, R. Krigel, D. Horsley, B. Boser, "In-Air Ultrasonic Rangefinding and Angle Estimation Using an Array of AlN micromachined Transducers", 2012 Solid-State Sensors, Actuators and Microsystems Workshop, Hilton Head, SC, Jun 2012, pp. 50-53.

[9] W. Liao, W. Liu, J. E. Rogers, F. Usmani, Y. Tang, B. Wang, H. Jiang and H. Xie, "Piezoelectric micromachined ultrasound tranducer array for photoacoustic imaging," Proc. Transducers, pp. 1831-1834 (2013).

[10] L. Che, E. Halvorsen and X. Chen, An optimized one-step wet etching process of $Pb(Zr_{0.52}Ti_{0.48})O_3$ thin films for microelectromechanical system applications, Vol. 21 (10), 105008 (6pp), J. Micromech. Microeng. (2011)

CONTACT

*Yipeng Lu, tel: +1-530-752-4158; yplu@ucdavis.edu

LOW VOLTAGE PIEZOELECTRIC NEMS RELAYS FOR ULTRALOW POWER DIGITAL CIRCUITS

Usama Zaghloul[1, 2] and Gianluca Piazza[1]**

[1]Electrical and Computer Engineering Department, Carnegie Mellon University, Pittsburgh, Pennsylvania, USA

[2]Microelectronics Department, Electronics Research Institute, Cairo, Egypt

ABSTRACT

The paper presents the design, synthesis, and characterization of the first piezoelectric nanoelectromechanical relays with sub-1-Volt actuation (850 mV). The relays are normally closed and exhibit high mechanical restoring forces at relatively low voltage. This is enabled by (i) employing ultrathin piezoelectric aluminum nitride film (10 nm) with high *c*-axis orientation and controlled residual stress, (ii) demonstrating a relay design with a stress-compensating geometry, and (iii) optimizing the thicknesses of the layers forming a four-layer unimorph actuator. The relays exhibit a very low energy dissipation per switching cycle (46 aJ), an extremely small subthreshold slope (0.015 mV/dec), and a low contact resistance (16 kΩ).

INTRODUCTION

NEMS relays have been proposed as very promising successors or hybrid complements to metal-oxide-semiconductor field-effect transistors (MOSFETs) [1]. The fundamental physics of MOSFETs limit their further scaling due to the sharp increase in static power consumption and the inability to lower the supply voltage below few 100s of milliVolts [2]. NEMS relays, however, have been demonstrated to implement digital logic [3, 4] and memory [5-6] elements with low leakage and extremely steep subthreshold slope. They are also more suitable for harsh environments compared to MOSFETs [7]. Despite these merits, the high voltage presently used to drive NEMS relays (2.5-22 V) stands against their use in ultralow-power applications. Although electrostatic NEMS relays were recently demonstrated to operate at 0.4 V [8], piezoelectric relays with sub-1-Volt actuation have never been reported. Two main challenges stand against achieving low actuation voltage in miniaturized piezoelectric relays: (i) synthesizing ultrathin piezoelectric films with high quality, and (ii) controlling the stress-induced deflection in the multi-layer stack of piezoelectric actuators to maintain few nanometers height switching gaps. An actuation voltage smaller than 1 V could not be achieved even for aggressively scaled piezoelectric NEMS relays which use ultrathin (25 nm) AlN films and ~28 nm switching gaps [9].

This work reports the design and fabrication of normally closed (NC) piezoelectric NEMS relays which exhibit an actuation voltage smaller than 1 V. The relays are formed by the thinnest to date piezoelectric AlN films (10 nm) and use a stress-compensating geometry and an optimized unimorph actuator to maximize the restoring mechanical forces.

RELAY DESIGN AND OPERATION

The NC relay has four terminals: source, drain, gate, and body (see Fig. 1), and is based on piezoelectric unimorph actuators. The relay makes use of a stress-compensating geometry, and consists of three suspended beams placed next to each other (Fig. 1a and b). The center beam carries the piezoelectric actuator and the metal tip (the conductive channel) in the longitudinal direction of the beams while the two outer symmetric beams carry the source and drain bottom contacting metals in the transverse direction. The outer beams are connected together by an insulating layer of AlN, hence forming a folded beam structure surrounding the center actuator (see Fig. 1c). We refer to this arrangement as a triple-beam structure. From a stress perspective, the triple beam geometry resembles a differential topology. The residual stress and stress gradient of the center beam are an average of the stresses of the outer beams, independently of whether the stresses of the outer beams are equal or different. Consequently, the stress-induced deflection of the center beam is an average of the deflections of the outer beams. This compensates the differences in stresses between the three beams and maintains the nanometer height switching gaps. Note that the relay geometry makes use of curved beams which average the in-plane stresses in *x* and *y* directions simultaneously between the center and outer beams across the whole beams' length. This in turn reduces further the displacement difference due to any stress asymmetry in the three beams. Rectangular beams, however, would compensate only the stress in either *x* or *y* directions. FEA simulations were performed for the proposed triple beam structure under different residual stresses using COMSOL. Fig. 1b shows an example of these results where the left, center and right beams with respective residual stresses of 230, 140 and 35 MPa exhibit comparable deflections.

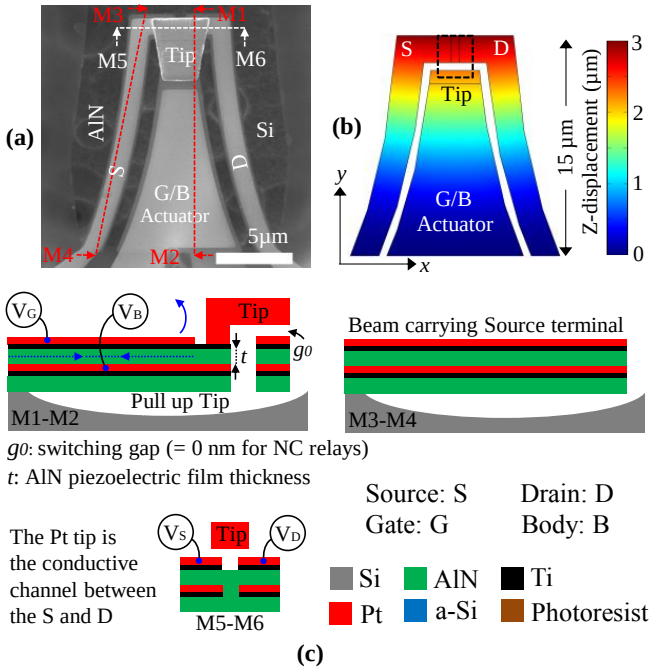

Figure 1: NC NEMS relays based on the triple-beam geometry: (a) SEM images of as fabricated piezoelectric NC relay using 10 nm thick AlN films; (b) FEA simulation showing the stress-induced deflections for the three suspended beams; (c) cross sections describing the layer stack of the beams and the relay structure.

In NC relays, the tip contacts the source and drain upon releasing the device without any applied voltage (*i.e.* the relay is normally *on* as shown in Fig. 2). In order to achieve that, the residual stresses in the layers forming the beams were reduced, yet kept large enough to yield a higher divergence in the stress levels

9781940470016/HH2014/$25©2014TRF
DOI 10.31438/trf.hh2014.38

of the three beams than the stress margin that can be compensated by the triple beam geometry. This margin depends also on the initial switching gap determined by the thickness of the sacrificial layer. For the switches realized in this work, the residual stresses of the AlN and Pt films were -250 and ±75 MPa, respectively and the sacrificial layer thickness was 60 nm. To turn off the relay, a small restoring force is required to overcome only the stress asymmetry in the three beams (in addition to surface adhesion), hence a low actuation voltage is expected.

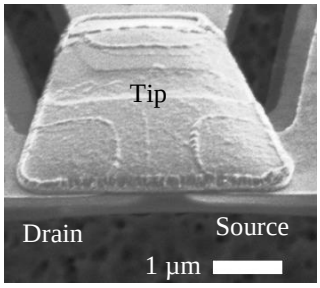

Figure 2: Magnified SEM image of the contact area for as fabricated NC relay. The tip contacts the source and drain upon releasing the device due to asymmetric in-plane stresses.

We performed a FEA simulation to determine the stress-induced z-deflections for the three beams forming the relay shown in Fig. 1a. The analysis made use of the measured residual stress values for AlN and Pt (mentioned above), and assumed a 20% variance in the stress levels between the three beams. An initial gap of 60 nm (the sacrificial layer thickness) was included between the metal tip and the source and drain contacting metals. Also, no contact pair was defined between the tip and the source and drain in order to determine the deflection of the center beam at the contact area. The simulation shows that the z-deflections at the contact area for the left, center and right beams are 2.079, 1.986 and 2.035 µm, respectively (see Fig. 3). In other words, the z-position of the metal tip is 93 and 49 nm below the source (left beam) and drain (right beam), respectively, hence forming a NC relay. The simulation highlights also that if the residual stress of AlN and Pt is reduced to -50 MPa, and the stress variation between the three beams is decreased to 5%, a normally open (NO) relay with 8 nm switching gap can be obtained.

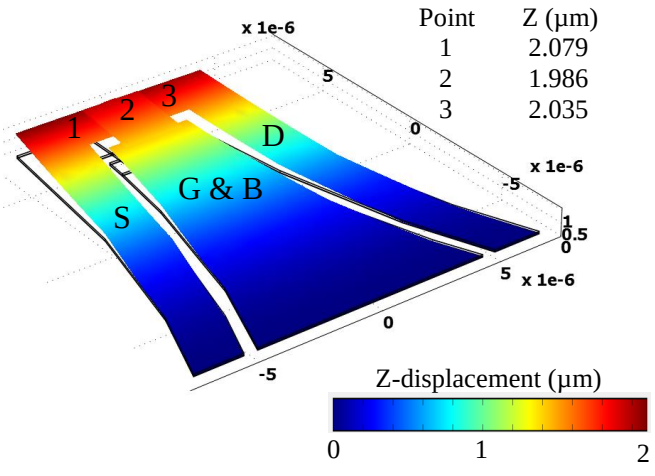

Figure 3: FEA simulation for the residual stress-induced deflections in the synthesized NC relays. The measured residual stresses for the sputtered AlN and Pt films were used in simulation.

The NC relay demonstrated in this study uses a four-layer piezoelectric unimorph actuator (see Fig. 4a). The actuator consists of a piezoelectric film (AlN) sandwiched between two metal electrodes (the gate and body), and bonded to an elastic layer (AlN). Applying an electric field between the body and gate terminals generates a lateral strain in the piezoelectric film. Due to the constraint imposed by the elastic layer, the lateral strain is translated to a transverse moment around the neutral axis of the actuator's stack causing a bending motion. The direction of the electric field across the piezoelectric film determines the bending direction of the actuator. In the synthesized NC relay, the actuator bends in the upward direction upon applying the actuation voltage, which pulls the tip (the conductive channel) far from the source and drain, hence turning the relay off (Fig. 4a). Removing the applied voltage causes the actuator to return to its original position, shortening the source and drain. Thus, the gate-body potential difference is used to create or remove a conducting channel between the source and drain via a metal tip.

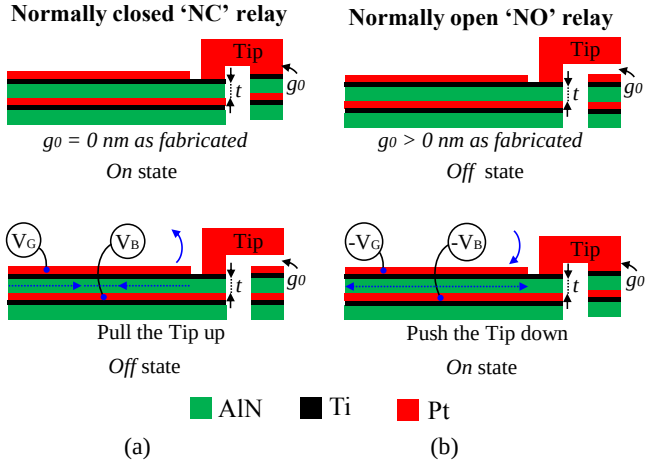

Figure 4: Cartoon schematic describing the operating principle of piezoelectric (a) NC and (b) NO relays.

The thicknesses of the elastic layer (the bottom AlN) and the Ti/Pt electrodes forming the piezoelectric unimorph actuator were optimized to maximize the electromechanical coupling. As a result, the synthesized NC relay exhibits high mechanical restoring force at relatively small voltage. Therefore, a low actuation voltage can be achieved. This analysis was performed using FEA simulation and a complex analytical model that considers all layers in the actuator stack [10]. Here it is worth mentioning that the optimization goal of the unimorph actuators used to realize NC and NO relays is different. In NC relays, the initial switching gap, g_0, is 0 nm (*i.e.* the relay is in the *on* state as fabricated as highlighted in Fig. 4a). The thicknesses of the layers forming the actuator are optimized to result in a maximum restoring force in order to break the contact during the opening of the relay at small voltages. In a NO operation (Fig. 4b), the initial g_0 is larger than 0 nm, and the actuator has to close this gap to turn the relay on. In this case, the thicknesses of the actuator's layers are selected as a compromise between generating maximum displacement and maximum contact force. This is required to assure that the relay can be turned on using a small voltage while exhibiting a low contact resistance.

FABRICATION PROCESS FLOW

The relays were fabricated using a seven masks process as described in Fig. 5. The most critical and new step in the process with respect to what was reported in [9] was the reactive sputtering of highly *c*-axis oriented 10 nm thick AlN films with controlled

residual stress over ultrathin Pt layers (5 nm). A two-step deposition recipe was developed to sputter AlN using a dual cathode S-Gun magnetron source. Each step exhibited a different process work point on the hysteresis curve of the magnetron discharge via changing the N_2 and Ar partial pressures to provide better conditions for AlN nucleation on the ultrathin Pt surface. The in-plane stress of the AlN films was controlled via modifying the Ar flow gradually during the reactive sputtering process.

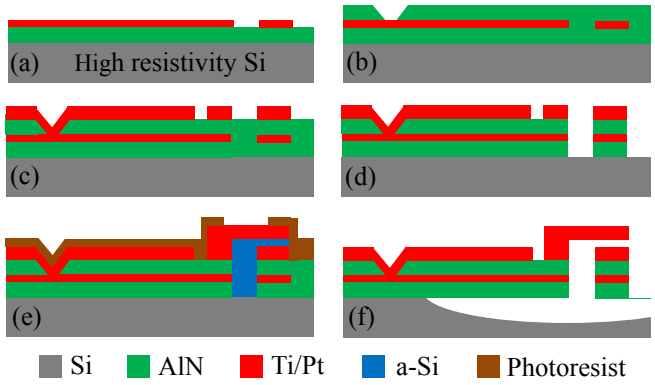

Figure 5: The fabrication process described at the cross section M1-M2 shown in Fig 1a: (a) Sputter 10 nm AlN seed layer on (100) Si substrate, sputter and pattern Ti/Pt (2/5 nm) layers using lift-off to define the actuator's bottom electrode; (b) deposit 10 nm piezoelectric AlN film using reactive sputtering, open vias (not shown) in the AlN using the AZ400K developer to access the bottom electrode; (c) deposit and pattern Ti/Pt layers to define the actuator's top electrode and the source and drain; (d) define the lateral dimensions of the relay by AlN etching using $Cl_2/BCl_3/Ar$ chemistry; (e) sputter and pattern a sacrificial layer of amorphous Si (60 nm) by lift-off, deposit and pattern a Pt layer via lift-off to define the tip and contact pads, define release openings using a photoresist mask; (f) etch the sacrificial layer and the Si substrate using XeF_2 to release the relay and remove the photoresist by plasma ashing.

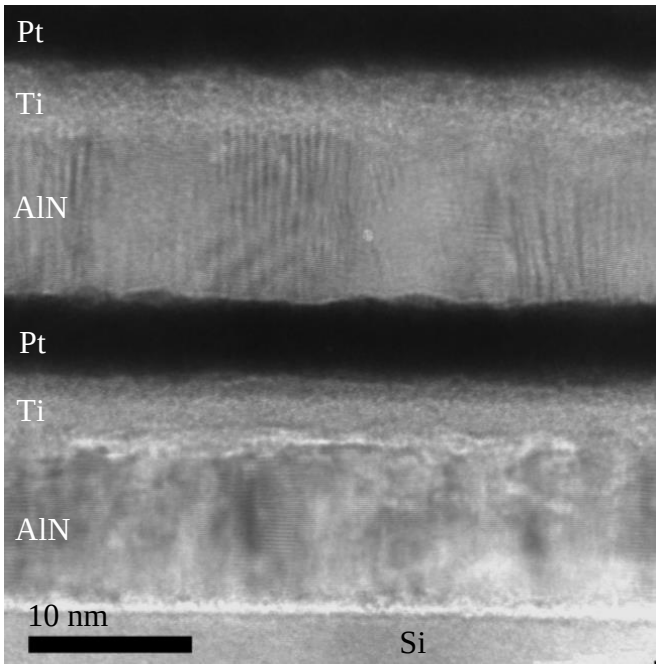

Figure 6: HRTEM image showing the layer stack of the piezoelectric unimorph actuator used to realize the NC relays.

Cross-sectional high-resolution transmission electron microscopy (HRTEM) image of the four-layer piezoelectric actuator used to realize the NC relays is shown in Fig. 6. The image highlights the high *c*-axis orientation and the fine columnar grain structure of the synthesized 10 nm AlN films. This can be observed for the piezoelectric film (top AlN) as well as the elastic layer (bottom AlN). Moreover, the arrangement of the lattice planes in the grown ultrathin AlN film can be seen, and emphasize the continuous lattice microstructure within a single grain from the AlN/Pt interface up to the film surface. The full width at half maximum (FWHM) of x-ray diffraction rocking curve measurements around the diffraction peak of AlN (0002) for the sputtered 10 nm films is 4.7°. Also, the deflection profiles of the synthesized four-layer unimorph actuators were measured under different applied voltages using an optical profilometer. These measurements were fitted to the computed deflections from the analytical model in [10] in order to calculate the d_{31} piezoelectric coefficients for the sputtered piezoelectric films. The extracted d_{31} coefficient for the synthesized 10 nm AlN films is -1.75 pC/N, which is 91% of the reported d_{31} value for 1 µm thick and highly oriented AlN films. This clearly highlights the significance of the developed two-step recipe for the reactive sputtering process.

EXPERIMENTAL RESULTS AND DISCUSSION

Figure 7a presents typical I-V measurements for the synthesized NC relays based on 10 nm thick piezoelectric AlN films. The measurements were done in ambient air using the body-biased actuation method [11]. The shown turn-off voltage sweeps were recorded while the body terminal was biased using different voltages. The role of the bias applied to the body, V_B, is to increase the mechanical restoring force of the actuator (see Fig. 1 and 4a) so that a small complementary voltage applied to the gate terminal (V_G) can break the contact and turn the relay off. The gate voltage at which the relay is turned off is called the threshold voltage, V_{th}. As shown in the figure, V_{th} can be precisely tuned and reduced to few millivolts via adjusting V_B. The relay exhibits an actuation voltage ($V_{act} = V_{th} - V_B$) of 850 mV and a source-drain resistance of 16 kΩ (Pt-to-Pt contact).

The average V_{th} measured under different V_B for the demonstrated NC relays is plotted in Fig. 7b. The linear dependence of V_{th} on V_B is obvious. For comparison, the measurements of a NO relay which uses 25 nm thick piezoelectric AlN film and 28 nm switching gap is also plotted in the figure [9]. Thanks to the scaling of the AlN film thickness to 10 nm and the proposed NC design demonstrated in this work, the relays exhibit an actuation voltage smaller than 1 V compared to 1.6 V for the NO relays. A comparison between the synthesized NC relays in this study and prior work on NO AlN relays is summarized in Table 1. The sub-1-Volt actuation of the NC switch designated as S1 comes with more than 3X reduction in the relay active area compared to S2, the NO relay that used 25 nm AlN films. The NC relays exhibit also a very high I_{on}/I_{off} ratio (10^8) and an extremely small subthreshold slope (0.015 mV/dec), three orders of magnitude smaller than what is achieved by state-of-the-art MOSFETs.

The extremely small data dispersion in the measured V_{th} at a given V_B for the demonstrated NC relays (Fig. 7b) indicates the weak influence of the contact's surface adhesion on the switching process (*i.e.* negligible hysteresis). Moreover, the precise control of V_{th} in the range of few millivolts highlights the possibility of performing the switching function with just few millivolts. The NC piezoelectric relays demonstrated here have superior performance compared to the reported sub-1-Volt electrostatic relays [8] which exhibit unstable I-V characteristics and a high subthreshold slope

of 10 mV/dec. The NC relays have a relatively small actuator's footprint and an extremely small V_{th}, which lead to a greatly reduced switching energy. For example, when V_G = 10 mV (more than one order of magnitude larger than the minimum V_{th} shown in Fig. 7a), the computed energy consumed per switching event is 46 aJ. This calculation assumes charging and discharging of an equal size gate. However, the active area of the NC relays is much larger than the active area of MOSFETs. A scaling analysis of AlN relays shows that the footprint of these devices could be reduced to 0.16 μm^2 if 1 nm thick piezoelectric AlN films were to be used. In this case, the actuation voltage could be scaled to 41 mV.

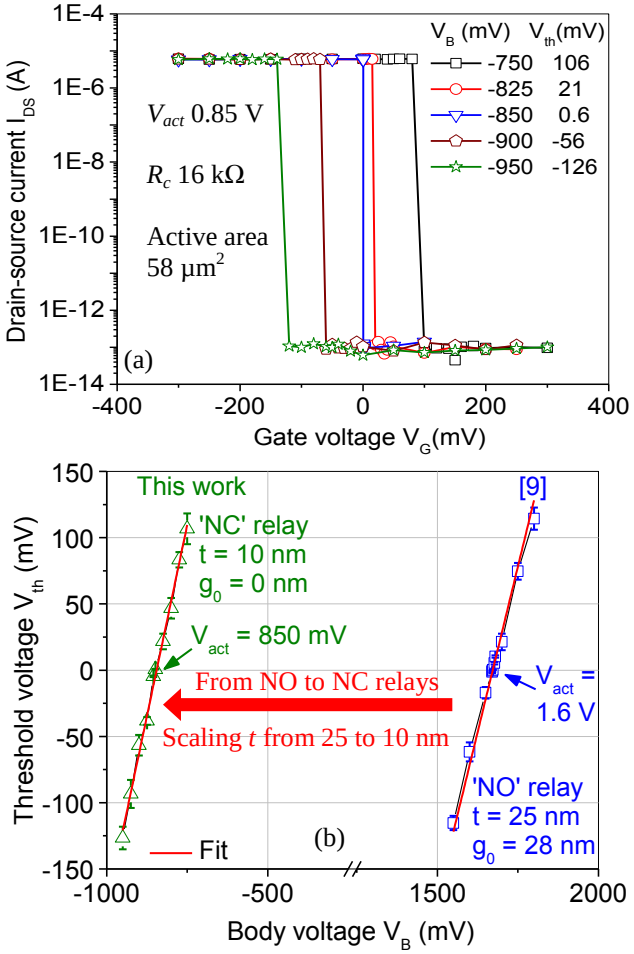

Figure 7: (a) The turn-off voltage sweeps of piezoelectric NC relays measured in ambient air using the body-biased method. The source-drain potential difference, V_{DS}, was 100 mV, and the minimum used V_G step was 0.1 mV. (b) The average measured V_{th} at different V_B for the demonstrated NC relays. The results of prior work on NO relays which use 25 nm AlN piezoelectric films is also plotted for comparison.

CONCLUSION

We demonstrated normally closed NEMS relays which use a stress compensating structure and 10 nm thick piezoelectric AlN films. The relays are the first to exhibit an actuation voltage smaller than 1 V, and are capable of performing reliable switching with just few millivolts thanks to their extremely small subthreshold slope. The active area and actuation voltage of the demonstrated NC relays are respectively three and one orders of magnitude smaller compared to the normally open relays formed by 250 nm thick piezoelectric AlN films. These results clearly highlight the significant potential of scaling the AlN film thickness as well as employing the NC relay geometry. We believe this work has paved the way toward building ultralow-power microprocessors and low voltage memories.

Table 1: Summary of the measured data for the demonstrated NC relays and a comparison to prior work on AlN relays. The switches are referenced as S1, S2 and S3. Note that S is the subthreshold slope and Rc is the source-drain resistance. The contact area of S1 is 2.4 μm^2.

Switch (NC or NO)	S1 (NC) This work	S2 (NO) [9]	S3 (NO) [11]
t/g_0 (nm)	10/0	25/28	250/400
V_{act} (V)	**0.85**	**1.63**	**8.45**
Active area (μm^2)	**58**	**187**	**40000**
I_{on}/I_{off}	10^8	10^7	10^7
S (mV/dec)	**0.015**	0.033	0.065
R_c (kΩ)	16	5.14	0.02

REFERENCES

[1] O. Y. Loh and D. E. Horacio, "Nanoelectromechanical contact switches," *Nature Nanotech.*, vol. 7, pp. 283-295, 2012.

[2] S. G. Narendra and A. Chandrakasan, "Leakage in Nanometer CMOS Technologies," Springer, New York, 2006.

[3] J. Jeon, V. Pott, H. Kam, R. Nathanael, E. Alon, and T. J. K. Liu, "Perfectly complementary relay design for digital logic applications," *IEEE Electron. Dev. Lett.*, vol. 31, pp. 371-373, 2010.

[4] R. Proie, R. Polcawich, J. Pulskamp, T. Ivanov, and M. Zaghloul, "Development of a PZT MEMS switch architecture for low-power digital applications," *J. of Microelectromech. Sys.*, vol. 20, pp. 1032-1042, 2011.

[5] K. Akarvardar and H. S. Wong, "Ultralow voltage crossbar nonvolatile memory based on energy-reversible NEM switches," *IEEE Electron. Dev. Lett.*, vol. 30, pp. 626-628, 2009.

[6] W. Xiang and C. Lee, "Nanoelectromechanical torsion switch of low operation voltage for nonvolatile memory application," *Appl. Phys. Lett.*, vol. 96, Art. # 193113, 2010.

[7] T. Lee, S. Bhunia, and M. Mehregany, "Electromechanical computing at 500°C with silicon carbide," *Science*, vol. 329, pp. 1316-1318, 2010.

[8] J. O. Lee, Y. H. Song, M. W. Kim, M. H. Kang, J. S. Oh, H. H. Yang, and J. B. Yoon, "A sub-1-volt nanoelectromechanical switching device," *Nature Nanotech.*, vol. 8, pp. 36-40, 2013.

[9] U. Zaghloul and G. Piazza, "10–25 nm piezoelectric nano-actuators and NEMS switches for millivolt computational logic," *in Digest Tech. Papers MEMS'13 Conference*, 2013, pp. 233-236.

[10] D. L. DeVoe and A. P. Pisano, "Modeling and optimal design of piezoelectric cantilever microactuators," *J. Microelectromech. Syst.*, vol. 6, pp. 266-270, 1997.

[11] N. Sinha, T. Jones, Z. Guo, and G. Piazza, "Body-biased complementary logic implemented using AlN piezoelectric MEMS switches," *J. of Microelectromech. Sys.*, vol. 21, pp. 484–496, 2012.

CONTACT

*G. Piazza: piazza@ece.cmu.edu
*U. Zaghloul: uzheiba@andrew.cmu.edu

MINIATURIZING THE MECHANICAL RELAY FOR SIGNAL AND POWER CONTROL

Chris Keimel, Marco Aimi, Oliver Boomhower, Alex Corwin and Andrew Detor
GE Global Research, Niskayuna, New York USA

ABSTRACT

Traditionally, most Micro ElectroMechanical Systems (MEMS) have been made using silicon as the mechanical material; we have developed a metal based MEMS device technology that miniaturizes the basic DC, AC and RF relay. Advances in MEMS switches have primarily focused on RF switches [1], with power levels typically in the 10s to 100W [2] and contact related failure mechanisms [3,4]. We have developed an electrostatically actuated MEMS relays, has been developed (Fig. 1) and is capable of switching in ~3usec, sustaining more than 400V across its open contacts and controlling loads of 100s of watts to a few kilowatts.

Figure 1: A Ni-alloy relay containing 400 switches capable of switching kilowatts of power.

INTRODUCTION

Mechanical relays used to switch electrical current or signals are not a new technology, being first invented by Joseph Henry in the 1830s to improve the electric telegraph. Mechanical relays have seen significant improvements in their materials, design, and performance in the following century. Mechanical relays provide a highly conductive Ohmic pathway when closed and the isolation of an air gap when open. The invention of the transistor in 1947 provided the foundation for the solid state relay that was a smaller, faster, and lower power consumption device than the mechanical relay. However, solid state devices lacked the isolation of an air gap and the low on state losses of an Ohmic contact. With the development of MEMS in the 1970s came the opportunity to miniaturize the mechanical relay while also giving it the speed and low power operation of solid state devices. In recent decades MEMS relay technology has, and is continuing to be, developed for high performance RF switching applications.

Newly engineered micromechanical structural materials are required to go beyond the signal transmission and sensing capabilities of present silicon based MEMS sensors. To manipulate significant power at the micro scale requires materials with the mechanical properties near that of silicon along with the conductivity of metals. We have developed and characterized a nanostructured Ni-alloy electroplating process that has the conductivity of nickel, a tensile strength >1GPa and demonstrated the alloy's process integration capability by

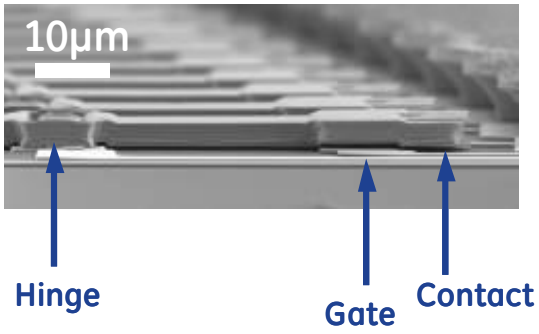

Figure 2: A cross sectional SEM view showing the beam, gate and contact of an individual MEMS relay in a switch array.

fabricating arrays of switches (figure 2) capable of transmitting and switching more than 1 kilowatts of power. The minimal strain rate of the nanostructured Ni-alloy makes possible cantilever switches with decades of operation at elevated temperatures. We have characterized the time-dependent mechanical behavior of the nickel alloy in comparison to other materials and through micro-tensile measurements extracted validated materials parameters, such as activation energy and activation volume, and used those parameters in a lifing model to predict operational life of the actuator.

In addition, hundreds of volts can be sustained across micro scale contacts separated by just a 1 micron gap. This sustained voltage of more than 300V is possible due to the gap being smaller than the mean free path of the gas molecules and thus minimizing the effect of avalanche breakdown by minimizing the ionization potential [5]. At gaps smaller than the Paschen minimum of 327V in air, field emission becomes significant. The contacts and their roughness have been designed and fabricated to minimize field emission effects at small gaps and have enabled sustained voltages >300V across a 1um gap, a value that exceeds the perceived limits of the modified Paschen curve.

RESULTS

Silicon's mechanical properties have established MEMS as a technology for sensors and actuators and the numerous devices on the market today are a testament to its success. To move beyond sensors and actuators requires a micro fabrication compatible material set that provides added functionality by combining the mechanical properties of silicon with the electrical properties of a conductor. Enabling actuators to efficiently conduct allows them to now transmit, without significant joule heating, substantially more power than if they were composed of silicon. Actuators that can transmit and control signals and power have the capability to enable a new class of micro scale devices that move beyond sensing energy to now being able to manage and manipulate electrical signals and energy.

9781940470016/HH2014/$25©2014TRF
DOI 10.31438/trf.hh2014.39

The inherent material challenge in enabling an Ohmic MEMS switch is that pure metals are great conductors, however their low yield stress (10s to 100s MPa) limits the actuator design space and their grain structure instability under temperature limits device reproducibility and reliability. Resistance to permanent creep deformation during operation is a requirement for any cantilever style MEMS switch. If the cantilever beam material cannot withstand operating stresses during switching cycles, the contact gap in the 'off' state can decrease to such an extent that the switch itself no longer functions (i.e. it remains 'on' even without an applied gate voltage). Figure 3 demonstrates how contact gap in the 'off' state can change over time at several different temperatures during operation of a pure gold cantilever beam MEMS device. It is important to note that the time in figure 3 refers to total 'on' time of the switch where the beam experiences higher stresses that drive creep deformation. Gold cantilever switches, operated at ~100MPa stress, cycled at a 50% duty cycle between 40C and 100C showed a downward deflection (of the open state) in the beams.

A Ni-alloy based electroplating conditions and MEMS based process integration were developed to produce cantilevered micro actuators that have the combined mechanical properties near that of silicon with the conductivity of a metal. The electroplated Ni-alloy has a yield strength >1 GPa and a resistivity around 7 x 10^{-6} Ohm-cm. The alloy's nanocrystalline grain structure (<10 nm) has been extensively characterized through TEM analysis and its composition engineered to maintain both grain stability and a minimal strain rate, for typical MEMS loads, up to 500 °C under a variable load as shown in figure 4. To evaluate the creep behavior of MEMS cantilever beam materials in the microtensile tester displacement is fixed and load is measured over time. In one test it is possible to back out strain rate over a range of stresses. Another advantage of the stress relaxation test is that accurate strain measurement in the gage section of the specimen is not needed.

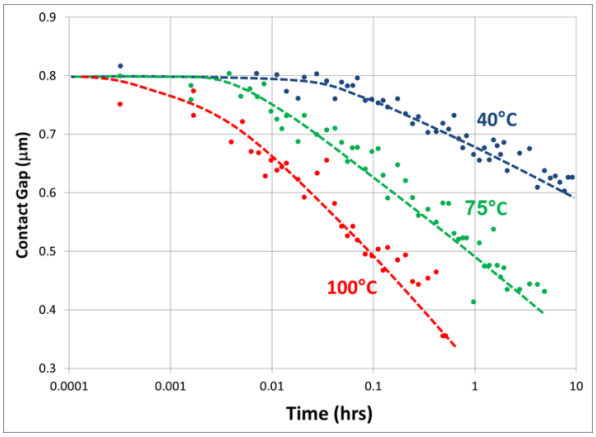

Figure 3: MEMS switch contact gap in the 'off' state as a function of 'on' time, demonstrating how the gap can decrease over time due to creep of a pure gold cantilever beam material. Increasing temperature promotes more rapid creep deformation.

With small specimen geometry and using resistance heating, the stress relaxation test only requires a constant fixed displacement, which the machine is capable of, and accurate load measurement from the load cell. Displacement is rapidly increased to a prescribed starting load, and then held fixed. Load drop is then measured as a function of time and temperature. The results of the stress relaxation tests determine a strain rate profile and enable the determination of the material specific parameters used to model time-dependent deformation of a suspended microstructure under load.

The plot in figure 5 depicts the modeled and expected deformation of three different materials, gold, a gold alloy and a nanocrystalline nickel alloy, under a typical peak stress of 120 MPa at the anchored hinge point when the system is isothermal at 85 °C. The displacement model shows that the pure Au cantilever deflects 20% of its original 1 µm gap in only 4 days while it takes more than 2 decades for the nanocrystalline Ni-alloy cantilevers to deflect 20% under the identical load conditions.

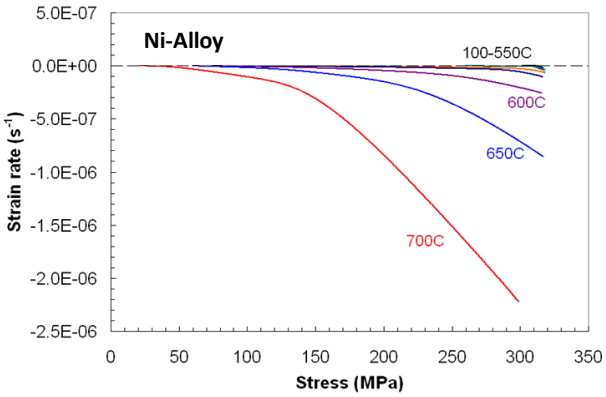

Figure 4: Strain rate as a function of applied stress derived from the raw load-time data. The data in this plot are directly used to calibrate a creep model for the material as explained in the text.

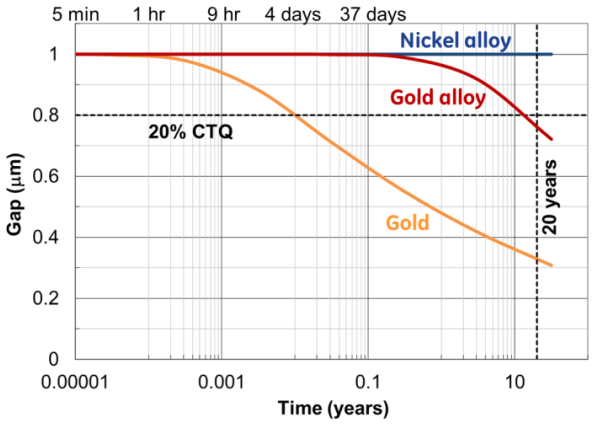

Figure 5: Predicted gap change as a function of time for three different beam materials. This prediction uses the model outlined in using the material parameters from microtensile testing described in previous plot.

Grain size and uniformity were controlled during the electroplating process to eliminate cantilever warp and allow multiple microns of deposition with a very smooth surface finish. Unlike polysilicon, the deposition is done near room temperature which allows the formation of the structural elements to take place at any point during a device process flow, even after metal deposition. Released cantilevers and other thin film electroplated test structures were used in accelerated life tests to experimentally validate decade long projections. Both experimental and model results indicate that the nanocrystalline material sets exhibit reduced stress induced deformation that limits device performance.

In addition to a structurally stable metal beam, the ability to withstand hundreds of volts across micro and sub-micro gaps is required for relays to switch and control power. The standoff voltage is the maximum voltage that can appear between the substrate contact and the beam before electrical breakdown occurs across the air gap. This failure mode can be observed through two mechanisms. The first is the traditional electrical breakdown / arcing between two conductors across a gap, while the second is based on self-actuation of the MEMS switch. Similar to how a voltage between the gate and beam provides an electrostatic force to moves the beam, a voltage between the contact and the beam will also generate an electrostatic force. As the voltage between the beam and contact increases the beam begins to deflect towards the contact. As this voltage increases further, the beam goes beyond the instability point and snaps into the contact causing a self-actuation failure. This failure mode can be mitigated by altering the stiffness of the beam, beam to contact gap, and the nominal area of the contact and bump. Of these variables, only the areas of the bump and contact can be changed without affecting other aspects of the operation of the switch, such as gate voltage. Both simulation and experiments were run to determine the impact of changing these feature sizes. The results (Figure 6) show that as the contact electrode overlap area is decreased, the standoff voltage increases, up to a point where the electrical breakdown occurs at approximately 350 V as shown in blue. The pink data points are simulated breakdown voltages due to self-actuation limit of the switch. There is good agreement between the experiment and simulation below 350 V, but experiments showed an upper limit to the max voltage despite reduced contact size. The observed experimental limit coincided with the minimum of the Paschen curve [6].

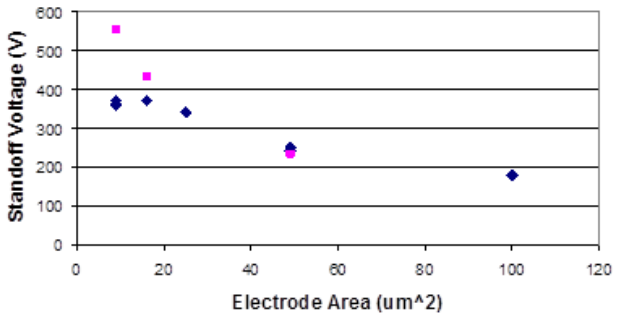

Figure 6: Single switch stand-off voltage vs. contact area, with simulated data shown as pink squares and experimental data in blue diamonds, showing good agreement until breakdown around 350V.

At first approximation, a contact with a gap in this range should have a standoff voltage of <100 V. In the literature [7], experiments have been run to better understand the modified Paschen curve where a curved surface (pin) is place in proximity with a flat plane. This configuration shows a low withstand voltage capability and has since been used as an upper limit to the typical MEMS switch design space. Experimental results of 300-350 V for <1 µm gaps determined that the configuration used for the modified Paschen curve did not apply to micro scale relays. This sustained voltage across the contacts is likely due to the gap being smaller than the mean free path of the gas molecules and thus minimizing the effect of avalanche breakdown by minimizing the ionization potential. At gaps smaller than the Paschen minimum of 327 V in air, field emission becomes significant. The contacts and their roughness have been designed and fabricated to minimize field emission effects at small gaps and have enabled sustained voltages >300V across a 1 µm gap, a value that exceeds the limits of the modified Paschen curve

Switch designs capable of taking advantage of both the nickel alloy's structural robustness and conductivity as well as the small contact gap geometries that sustain a few hundred volts were fabricated into various device design configurations capable of handling kilowatts of power to efficiently transmitting RF signals in the GHz range. These designed leveraged the development of the nickel based alloy that serves as the electrically conductive spring element in the MEMS based (<100um) cantilever switch unit cell. The alloy's mechanical properties greatly expand the design space and enable high withstand voltage (>250V) designs, a significant reduction in switch size (~5X) compared to pure metals and improved lifetime and reliability of the device.

The process flow utilizes surface micromachining and uses the substrate as a carrier for the fabrication processing. Because the switch is surface micromachined with a maximum processing temperature of 300 ° this process is transferable to different substrate materials. High power devices (>1 kW) are fabricated on silicon substrates for improved thermal conduction, while RF devices are fabricated on quartz or fused silica substrates for best in class RF isolation of better than -35 dB @ 6 GHz by minimizing RF capacitive coupling through the substrate. The processing techniques used include lithography, physical vapor deposition (PVD) methods (electron beam evaporation and DC Magnetron sputtering), plasma enhanced chemical vapor deposition (PECVD), reactive ion etching (RIE), wet chemical etching, electroplating and other cleanroom based fabrication techniques.

The basic unit cell switch element is a free standing ~50 µm wide cantilever beam that is anchored on one end, and that extends ~50 µm *towards* and 1 µm *above* its separated contact on its opposite end. The basic switching element is fabricated using the Ni-alloy and each switching unit is copied multiple times on a die and arrayed in parallel to enhance a die's ability to carry current as needed. The array of beams simultaneously deflects approximately 1 µm after it has been electrostatically actuated to make Ohmic contact between an upper and lower contact. When the switches are closed, they have a resistance of about 1 Ω per unit cell switch element and a parallel array of hundreds of switches on a small die is capable of carrying 5 A of continuous current with very low on-state losses. Arc free mechanical switching is critical for switching power and has been achieved through a combination of fast switching speed and the ability to open the contacts at a forced and momentary artificially induced zero voltage. An example of the how the

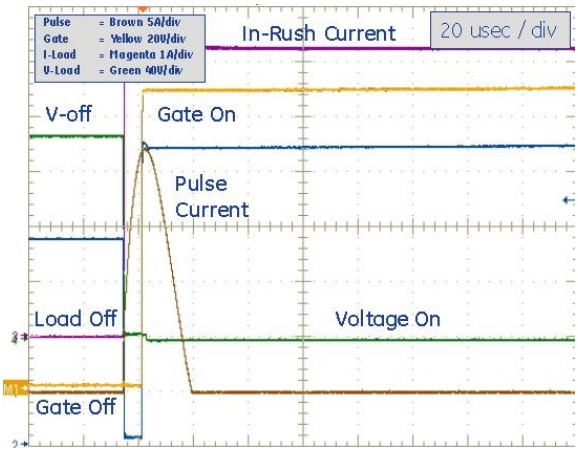

Figure 7: An oscilloscope trace capturing the switch turn on event (Gate Off to Gate On), at the microsecond scale, where the initial load current (Load Off to In-Rush Current) raises to 5 amperes on the resistive load.

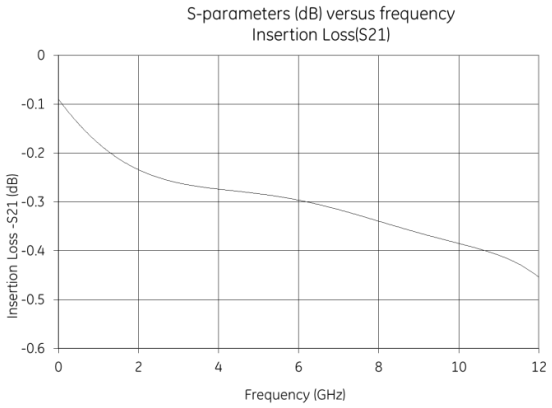

Figure 8: Insertion loss measurement of a 50-ohm impedance matched single unit cell RF MEMS switch showing better than 0.3dB of loss at frequencies below 6GHz.

switch and its circuitry closes into and turns on a 500W load is captured in the scope trace of figure 7.

In addition to low frequency (DC and AC) device and array configurations for the unit cell switch, 50-ohm impedance matched single unit cell RF MEMS relays were designed and fabricated on fused silica substrates. The fused silica enabled better than 35dB of isolation and minimal on state insertion losses better than 0.3dB on a given channel as measured in figure 8. Radio frequency tests are typically performed by a Vector Network Analyzer (VNA) that is capable of sweeping the frequency of interest. Electrical connections of MEMS switches are made with 50-Ω GSG probes for VNA ports.

CONCLUSIONS

Newly engineered micromechanical structural materials will be required to enable a novel class of MEMS devices that go beyond the signal transmission and sensing capabilities of present commercial sensors and initiate a new class of MEMS based devices capable of manipulating kilowatts of power. This new class of devices requires nanostructured materials with the mechanical properties near that of silicon along with the conductivity of noble metals. We have developed an electroplated nanostructured Ni-alloy that has the conductivity of Nickel and a yield strength >1GPa and demonstrated its device practicality by fabricating both die capable of transmitting and switching more than 1 kilowatts of power and die capable of low loss (<0.3dB) and high isolation (>35dB) RF MEMS relays.. The minimal strain rate of the nanostructured Ni-alloy makes possible the material resistance to stress induced deformation and enables a device to repeatedly operate for years at temperature. The combination of fast switching speed and broadband (DC to RF) signal operation along with the ability to control amperes of current and sustain hundreds of volts across micron sized air gaps has enabled the miniaturization of the mechanical relay to the chip scale for wide ranging applications in industrial sectors for power control to consumer communication driven applications requiring RF relays.

ACKNOWLEDGEMENTS

The authors would like to acknowledge the many people at GE Global Research who have had a hand in enabling all aspects of this technology from materials development through fabrication and into device test and integration; specifically Glenn Claydon for years of help and expertise in device layout and electrical test, Don Lipkin for his expertise and guidance in materials development, Sairam Sundaram and Sia Sarva for the work on lifing analysis and Steven Go, Robert Butler, Yongjae Lee and Joseph Iannotti for their guidance and help with RF design and characterization.

REFERENCES

[1] Rebeiz, Gabriel M., “RF MEMS Theory, Design, and Technology”, Wiley, Hoboken, NJ 2003

[2] J. Wong, J. Lang, M. Schmidt, “An electrostatically-actuated MEMS switch for power applications”, Proceedings of the IEEE MEMS 2000 Conference, Miyazaki, 2000, pp. 633

[3] Majumder, S.; McGruer, N.E.; Adams, G.G.; , "Adhesion and contact resistance in an electrostatic MEMS micro switch," Micro Electro Mechanical Systems, 18th IEEE International Conference, 215- 218, 2005

[4] Hyman, D. and Mehregany, M., "Contact physics of gold microcontacts for MEMS", in Electrical Contacts, 1998.Proceedings of the Forty-Fourth IEEE Holm Conference. 133-140, 1998

[5] Townsend, J.S., “The Theory of Ionization of Gases by Collision”, London: Constable & Co. Ltd.1910

[6] Paschen, F., "Ueber die xum Funkenubergang in Luft, Wasserstoff und Kohlensaure bei verschiedenen Druckenerforderliche Potentialdifferenz", Annalen der Physik, .37, 69-96, 1889

[7] Slade, P., Taylor, E., “Electrical Breakdown in atmospheric air between closely spaced (0.2um-40um) electrical contacts”, IEEE Transactions on Componenents and Packaging Technologies, vol. 25, pp 390-396, 2001

CONTACT

C. Keimel, tel: +1-518-387-7893; keimel@research.ge.com

THIN-FILM PZT BASED MONOLITHIC TRANSLATIONAL/TILT MICRO-SCANNER FOR VERTICAL CROSS-SECTIONAL IMAGING WITH DUAL AXES CONFOCAL ENDOMICROSCOPE

Zhen Qiu[*], *Choong-Ho Rhee, Jongsoo Choi, Thomas D. Wang, and Kenn R. Oldham*
University of Michigan, Ann Arbor, MI, USA

ABSTRACT

A multi-axis micro-scanning mechanism actuated by thin-film PZT is presented for optical cross-sectional imaging in dual axes confocal microscopy. The actuator achieves large translational vertical displacement (200 µm at 18 V_{dc}) by active piezoelectric forcing and large rotational horizontal scanning (±6° mechanical angle at >3 kHz) by resonance of passive oxide cantilevers. Devices are produced from SOI wafers using vertical silicon dioxide barrier trenches for robust encapsulation of structural silicon during XeF_2 release of PZT bending beams. The resulting monolithic micro-scanner is compatible with endomicroscopic systems for acquiring vertical cross-sectional images from tissue.

INTRODUCTION

Compared to other endomicroscope systems, dual axes confocal microscopy has been shown to perform superior rejection of out-of-focus and scattered light [1], while its high dynamic range allows for deep imaging in tissue with high contrast [2-4]. To take full advantage of the excellent z-axis performance of dual axes confocal microscopy in a miniature 5 mm outer diameter (OD) dual axes architecture, vertical cross-sectional imaging with a MEMS scanner has been proposed in [5]. This requires translating a micro-mirror with large displacement (~500 µm) in the into-tissue direction, while also providing rotational, in-plane scanning in at least one axis.

Only a limited number of prior microactuators feature the necessary combination of degrees of freedom desirable for real-time cross-sectional imaging. The majority of existing optical scanning mechanisms provide lateral rotational scanning in one or more axes. Large displacement vertical actuators are less common, though existing large displacement vertical actuators have been demonstrated based on electrothermal, piezoelectric, and electromagnetic transduction, among others. Combined vertical and rotational scanning has previously been achieved in a few instances, including by electrothermal tip-tilt actuators [6] and three-axis electrostatic scanning mirrors (z-θ_x-θ_y) [7]. However, electrostatic axial stroke distance is limited, while electrothermal actuators are restricted in speed by thermal time constants. Lateral/translational piezoelectric actuation has also been implemented [8], but designs to date are limited in z-axis displacement and/or rotational axis scanning speed.

This paper presents a novel, monolithic scanning actuator combining large stroke vertical piezoelectric actuation with high frequency resonant rotational scanning using lead-zirconate-titanate (PZT) thin-films. Thin-film PZT actuators are known to generate fast axial and translational responses [9] and have large force capacity with modest voltage requirements [10]. The actuator in this work produces large static or dynamic z-axis displacement with a serpentine two-beam thin-film PZT vertical actuation structure. At the same time, high-frequency rotational motion can be excited from an inner scanning mirror supported by resonating passive silicon dioxide springs. A sample actuator is shown in Fig. 1 and a schematic view of the actuator structure in Fig. 2. The combined mechanism provides increased displacement range from previous works and higher-frequency rotation about the in-plane axis, thus directly supporting real-time cross-sectional imaging from dual axes or similar microscopes.

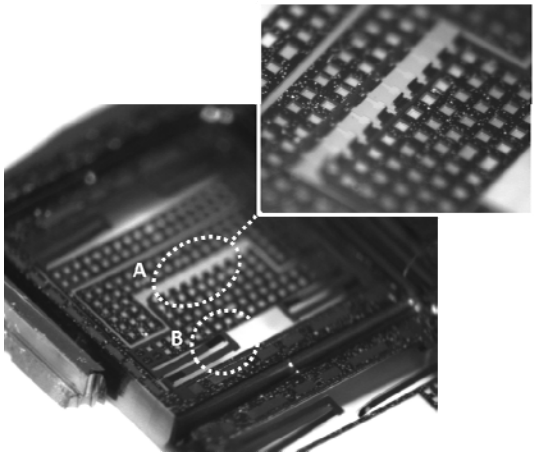

Figure 1: Optical microscope image of translational/tilt micro-scanner with inner resonant spring structure for angular scanning (A), in detail, and symmetric piezoelectric beam bending actuators for vertical translation (B).

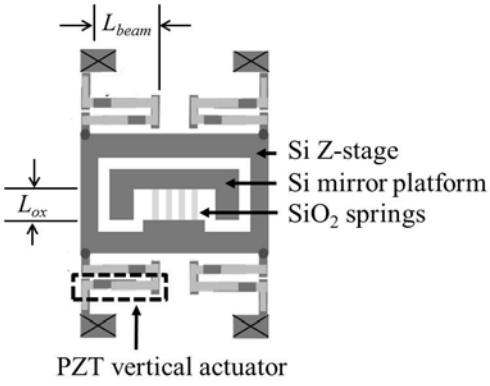

Figure 2: Schematic of the translational/tilt micro-scanner showing key components, including mirror platform and PZT actuator locations.

MICRO-SCANNER DESIGN

The translational-tilt micro-scanner is designed to feature vertical and rotational motions through compliant deformation of active and passive thin-film beams at two locations. Vertical motion is generated actively by bending of thin-film PZT unimorphs, arranged in a bend-up/bend-down configuration as in a previous purely vertical bending actuator in [9]. Rotational motion of a central mirror-platform is permitted by passive resonance of inner silicon dioxide beam elements, fabricated from the buried oxide layer of the SOI wafer, and driven by high frequency excitation of that active outer vertical legs.

9781940470016/HH2014/$25©2014TRF
DOI 10.31438/trf.hh2014.40

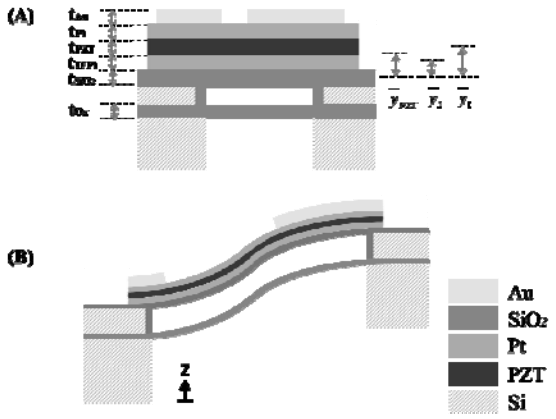

Figure 3: (a) Material layers in typical thin-film piezoelectric (lead-zirconate-titanate) and electrode stack; (b) Bend-up/bend-down translational vertical motion produced by bending axis manipulation with an additional gold layer.

For use in cross-sectional imaging in endoscopic microscopy, critical attributes of a translational-tilt scanner are range-of-motion and frequency of scanning. Fast-axis motion, in this case from the passive resonant angular vibration, should occur at frequencies of several kilohertz, with scan angles on the order of 5 to 10^0, while slow-axis motion should occur at DC to 100 Hz, with at least 5 Hz bandwidth required to avoid motion artifacts. Between 200 and 500 μm of displacement are required to fully support dual axes confocal penetration depth, depending on the setting.

Vertical (slow-axis) displacement and scanning speed can be estimated from the vertical stiffness of the piezoelectric leg structures. Each of these leg structures consists of a thin-film composite consisting of thin-film PZT, metal electrodes, and a base silicon dioxide layer, as shown in Fig. 3(a). The natural bending direction of the PZT beams is upward, due to the presence of the underlying silicon dioxide layer, but a thick gold film is added to portions of each beam to provide translation rather than rotation at the tip of the beam, as shown in Fig. 3(b). Net vertical stiffness in the first (vertical) axis, k_1, can be estimated as:

$$k_1 = \frac{4k_{v,F}}{N_{beam}} \tag{1}$$

where

$$k_{v,F} = \left(\frac{{L_{Au}}^3}{3(EI)_1 + 3(EI)_{ox}} + \frac{(L_{beam} - L_{Au})^3}{3(EI)_2 + 3(EI)_{ox}} \right)^{-1} \tag{2}$$

with N_{beam} the number of folded piezoelectric beams in each of the four legs supporting the stage, L_{Au} the length of the portion of the beam covered with gold (bend-down) and L_{beam} is the total beam length. Three bending moduli are relevant, the composite moduli with and without the gold layer, $(EI)_1$ and $(EI)_2$, and that of the buried oxide layer under the beams, $(EI)_{ox}$, left behind by the fabrication process. The effect of the buried oxide as a parallel spring is simplified into the denominators of (2). Note also that $k_{v,F}$ in (2) represents the equivalent stiffness of the single vertical actuator, marked by the dash-line box in figure 2, obtained from a displacement-force relation.

The natural frequency of the system for vertical translation may then be estimated according to

$$f_n = \frac{\omega_n}{2\pi} = \frac{1}{2\pi}\sqrt{\frac{4k_{v,F}}{m_{total} N_{Beam}}} \tag{3}$$

where m_{total} is the total mass of the inner stage and scanning mirror.

Static displacement of the translational stage may be estimated from the internal moments generated by the bend-up and bend-down actuator sections,

$$z = N_{beam}\left(\frac{(M_1 + M_L)L_{au}^2}{2(EI)_1 + 2(EI)_{ox}} + \frac{(M_2 - M_L)(L_{beam} - L_{au})^2}{2(EI)_2 + 2(EI)_{ox}} \right) \tag{4}$$

where M_L is a reaction moment maintaining angular compatibility between bend-up and bend-down segments of the leg,

$$M_L = \frac{M_{act,1}L_{Au}((EI)_2 + (EI)_{ox}) - M_{act,2}(L_{beam} - L_{Au})((EI)_1 + (EI)_{ox})}{L_{Au}((EI)_2 + (EI)_{ox}) + (L_{beam} - L_{Au})((EI)_1 + (EI)_{ox})} \tag{5}$$

Fast-axis rotation in the current scanner design is generated from resonance of a central mirror platform supported by passive silicon dioxide cantilever beams. A low-voltage, high-frequency AC signal is added to the low-frequency voltage controlling vertical translation. This excites resonance of the inner mirror platform, leading to substantial rotational scan angles. However, it would likewise be possible to use thin-film PZT bending beams for active rotational scanning, and comparative performance is estimated in this section.

One advantage of a passive rotational scanner is simplified multi-axis scanner design. The use of a single voltage input to generate both vertical and rotational motions simplifies wiring in compact imaging instruments, and eliminates the need for additional interconnects from the fixed exterior frame of the device to the moving vertical stage, which would reduce vertical scanning range. This is the primary driver behind passive resonant design in the current micro-scanner for dual axes endomicroscopy. Nonetheless, it is useful to compare performance of the passive versus active rotational scanning. To model passive resonant behavior, first the resonant frequency of the inner mirror platform, f_{inner}, can be estimated from the cantilever beams modeled as an additional mass-spring damper system,

$$f_{inner} \approx \frac{1}{2\pi}\sqrt{N_{ox}\frac{3(EI)_{inner}}{{L_{ox}}^3 m_{inner}}} = \frac{1}{2\pi}\sqrt{\frac{k_2}{m_{nner}}} \tag{6}$$

where N_{ox} is the number of parallel inner silicon dioxide cantilevers, $(EI)_{inner}$ is the composite modulus and area moment of inertia of those cantilevers, L_{ox} is the cantilever length, m_{inner} is the mass of the central mirror platform, and k_2 is the net effective inner beam array stiffness.

FABRICATION

The fabrication process used to produce prototype thin-film PZT micro-scanner in this paper has been presented in detail in [11], with key features highlighted in this section. The process provides two key features for the two-axis micro-scanner: a robust encapsulation strategy that protects silicon structures supported by thin-film PZT actuator, and process compatibility with backside patterning and thus multi-level fabrication of a full-wafer-thickness

fixed frame and silicon features from a silicon-on-insulator (SOI) device layer integrated with the PZT thin film.

The process begins with a silicon-on-insulator (SOI) wafer with a 30 µm thick device layer, 2 µm thick buried oxide layer, and 500 µm thick handle layer. 3 µm wide trenches are etched to the buried silicon dioxide layer along the sidewalls of bulk-micro machined silicon structures, such as silicon connectors between two PZT unimorphs in a serpentine vertical actuator pair. Pre-furnace-cleaned trenches are then filled with silicon dioxide by low pressure chemical vapor deposition (LPCVD). Since keyholes are formed in the oxide-filled trenches, the top oxide is removed by either chemical mechanical polishing (CMP) or reactive ion-etching (RIE), and the upper part of the trench is etched by short RIE to open the keyholes. The LPCVD process is repeated to fill in the opened trenches. Several iterations of LPCVD and polishing may diminish the size of keyholes but it is difficult to eliminate them entirely. Eventually, planarization of the surface of refilled oxide trenches is followed by additional silicon dioxide deposition by plasma-enhanced chemical vapor deposition (PECVD) to reach a minimum target base oxide thickness of 2000 Å.

After SOI wafers have been processed with the silicon dioxide trenches, PZT and electrode layers were deposited and patterned at the U.S. Army Research Laboratory (Adelphi, MD) and Radiant Technologies, Inc. (Albuquerque, NM). The resulting metal stack consists of a platinum bottom electrode, PZT film, and platinum top electrode. Two argon milling steps for the top electrode and PZT layers, and a wet etch for contact vias to the bottom electrode are next performed. Then a 1 µm-thick Ti/Au layer is deposited on top of the PZT actuator surface where desired by a lift-off process. Next, the silicon microstructure in the top device layer is patterned and micro-machined by deep reactive ion-etching (DRIE).

To begin device release, oven-baked photoresist is used to protect the microstructure of the top device layer, and the backside of the SOI wafer is patterned to open the area underneath the central mirror-stage. Backside patterning and etching also provide the open area for XeF_2 to etch the underneath silicon layer of the actuator. During the XeF_2 under-etching process of thin-film PZT actuator and silicon microstructure layer, a uniform undercut length of the PZT/Au unimorph actuator structure is obtained thanks to the oxide barrier trenches. Figure 4 shows a scanning electron microscopic image of a sample vertical actuator at the connection of the two beams, including the encapsulated silicon connector between the beams and buried oxide as it extends from underneath the beam structure.

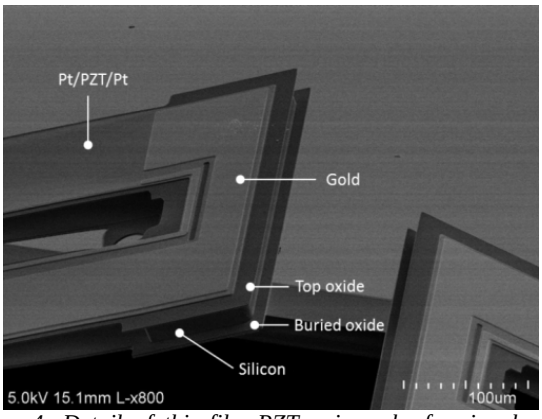

Figure 4: Detail of thin-film PZT unimorphs forming legs of a translational-tilt micro-scanner, showing clearly defined silicon rigid structures between thin-film composite beams produced through the silicon encapsulation process.

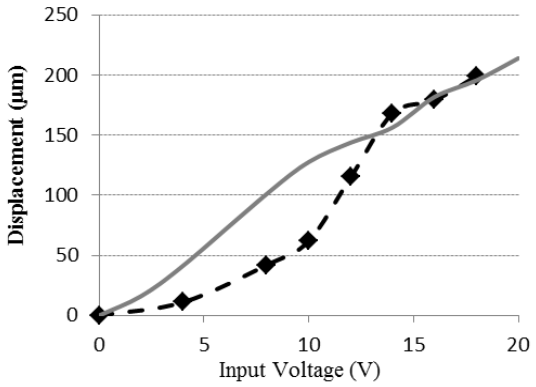

Figure 5: Translational displacement of the central stage platform under various static voltages (solid:model; dash:experiment) .

RESULTS

Micro-scanner translational and angular displacements were measured experimentally using a Keyence laser displacement sensor and Polytec Laser Doppler Vibrometer (LDV). Static displacement of the central platform of the actuator at various applied voltages is shown in Fig. 4. As can be seen, actuator displacement exceeds 200 µm at less than 20 V. Once the effective electroactive piezoelectric coefficient of the thin-film PZT is known from independent experiments [11], the model presented in *(1)-(5)* predicts large displacement frequency reasonably well, but shows much greater nonlinearity at low voltages, possibly due to non-ideal asymmetry of individual legs, especially at heights where stage position is nearly equal to the height of the surrounding frame. Dynamic testing of stage displacement shows the resonant frequency of the stage for vertical translation to be approximately 150 Hz, although a tilting mode of the outer portion of the platform at lower frequencies limits low-frequency scanning bandwidth in practical usage to between 0 and

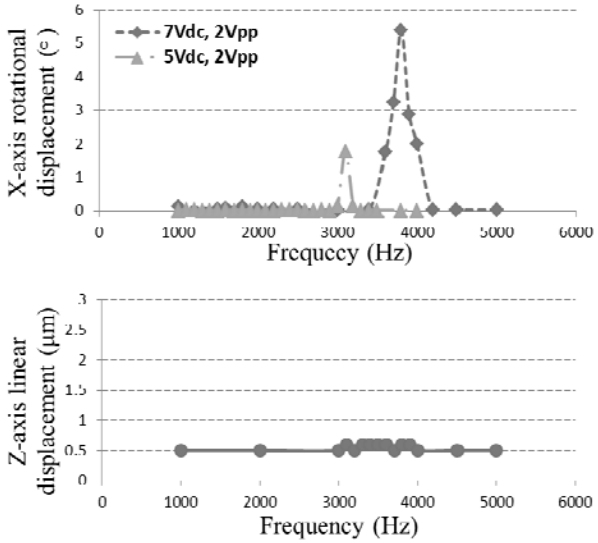

Figure 6: Experimentally measured resonant peaks of inner-axis rotational motion at 5 V and 7 V dc bias, with 2 Vpp ac excitation show large scanning angles at certain stage positions, but substantial variability in behavior depending on stage height. Disturbance of outer frame vertical height is negligible.

80 Hz. In either event, vertical actuation rate is more than adequate to avoid motion artifacts during endoscopic imaging.

Measurement of inner mirror platform tilt angle indicates large angular displacement, to as much as 5.5^0 mechanical scanning angle, at as little as 2 Vpp AC excitation of the outer PZT leg structures, as shown in Fig. 6. This angular rotation of the inner mirror platform is accompanied by almost negligible (<0.1 μm) displacement of the outer, vertical translating frame due to large frequency separation between the vertical slow axis and inner fast axis resonances. However, there is substantial nonlinear behavior in the inner axis resonance, as the inner resonant frequency was observed to vary between 3 and 3.8 kHz, depending on the DC offset to the piezoelectric actuators (i.e., the height of the mirror platform).

CONCLUSION

Combining active and passive flexural beam structures for vertical and rotational translation of a central mirror platform is shown to provide suitable scanning actuation for cross-sectional imaging in dual axes confocal endomicroscopy. Both large translational vertical displacements and high-frequency resonant tilting actuation are achieved. Limitations of the device include nonlinear behavior of the inner resonance for tilt scanning at different vertical displacements.

REFERENCES

[1] T.D. Wong, M.J. Mandella, C.H. Contag, and G.S. Kino, "Dual-axis Confocal Imaging for High-Resolution *in vivo* Imaging," Optical Letters, 28, 6 (2003).

[2] J.T.C. Liu, M.J. Mandella, J.M. Crawford, S. Friedland, R. Soetino, C.H. Contag, G.S. Kino, and T.D. Wang, "A Dual Axes Confocal Reflectance Microscope for Distinguishing Colonic Neoplasia," Journal of Biomedical Optics, 10 (2006).

[3] Z. Qiu, Z. Liu, X. Duan, S. Khondee, B. Joshi, M.J. Mandella, K.R.Oldham, K. Kurabayashi, and T.D. Wang, "Targeted Vertical Cross-sectional Imaging with Handheld Near-infrared Dual Axes Confocal Fluorescence Endomicroscope," Biomedical Optics Express, 4 (2013).

[4] Z. Qiu, S. Khondee, X. Duan, H. Li, M.J. Mandella, B.P. Joshi, Q. Zhou, S.R. Owens, K. Kurabayashi, K.R. Oldham, and T.D. Wang, "Vertical Cross-Sectional Imaging of Colonic Dysplasia *in vivo* with Multi-spectral Dual Axes Confocal Endomicroscopy," Gastroenterology, 146, 3 (2014).

[5] W. Piyawattanametha and T.D. Wang, "Miniature Dual Axes Confocal Microscope for Real Time *in vivo* Imaging," Advances in Solid State Circuit Technologies (2010).

[6] L. Wu and H. Xie, "A Large Vertical Displacement Electrothermal Bimorph Microactuator with Very Small Lateral Shift," Sensors and Actuators A (2010).

[7] D. Lee, K. Krisnamoorthy, K. Yu, and O. Solgaard, "Single-Crystalline Silicon Micromirrors Actuated by Self-aligned Vertical Electrostatic Comb Drives with Piston-motion and Rotational Capabilities," Sensors and Actuators A: Physical, 114, 2-3 (2004).

[8] Y. Zhu, W. Liu, W. Liao, H. Xie, "A piezoelectric unimorph actuator based tip-tilt-piston micromirror with high fill factor and small tilt and lateral shift," Sensors and Actuators A: Physical, 167, 6 (2011).

[9] Z. Qiu, J.S. Pulskamp, X. Lin, C.H. Rhee, T.D. Wang, R.G. Polcawich and K.R. Oldham, "Large Displacement Vertical Translational Actuator based on Piezoelectric Thin Films," Journal of Microelectromechanical Systems, 20, 7 (2010).

[10] P. Muralt, R.G. Polcawich, and S. Trolier-McKinstry, "Piezoelectric Thin Films for Sensors," MRS Bulletin, 34 (2009).

[11] C.H. Rhee, J.S. Pulskamp, R.G. Polcawich, and K.R. Oldham, "Multi-degree-of-freedom Thin-film PZT-actuted Microrobotic Leg," Journal of Microelectromechanical Systems, 21, 6 (2012).

CONTACT

*Z Qiu, tel: +1-734-615-4834; zqiu@umich.edu.

A MICRODEVICE FOR EXAMINING CARDIAC GAP JUNCTION

X. Zhang, and Y. Zhao[*]
The Ohio State University, Columbus, Ohio, USA

ABSTRACT

This paper reports a microengineered device capable of applying electrical stimulation to the selected cell, and examining intercellular electro-mechanical propagation through the gap junction of the stimulated and the un-stimulated cell in a longitudinally connected doublet of adult cardiac myocytes. Since the contractile performance of the un-stimulated cells due to direct electrical stimulation is eliminated, this work provides a quantitative tool for studying intercellular electro-mechanical transduction at the gap junction and is expected to develop a comprehensive understanding of the role of intercellular communication in various heart diseases.

INTRODUCTION

Intercellular electro-mechanical transduction in adult cardiac myocytes plays an important role in regulating heart function. Within heart muscle, the intercellular communication is mainly orchestrated by a thin structure located at the longitudinal end of the cardiac myocytes, named the intercalated disc. The intercalated discs connect individual cardiac myocytes into an electrochemical syncytium and are primarily responsible for electro-mechanical transmission during heart contraction [1]. Until recently, the properties of the intercalated discs have been primarily studied within the intact animal heart or using perfused tissue blocks [2, 3]. However, the intrinsic heterogeneity and complexity of the native cardiac environment, which contains multiple types of interconnected cells that are morphologically and functionally distinct, have hampered the quantitative study of cardiac intercellular communication. Cell-based studies, on the other hand, mainly use cultured embryonic and neonatal myocytes [4-6], where the changes in expression of ion channels, contractile protein isoform and contractile performance during development may make it problematic to apply the results to the fully differentiated adult myocardium[7]. In this perspective, an *ex vivo* cell-based model using adult cardiac myocytes is preferred, because it is immune to the complications arising from heterogeneity in electrical excitation and contraction in the native cardiac environment [8, 9], while the adult cardiac myocytes isolated from the hearts largely preserve the characteristics of native myocardium.

The predominant methods for investigating cardiac myocyte intercellular communications include examination of the expressions of characteristic connexin proteins at the intercalated discs using molecular biological assays [10]. To investigate the role of specific connexin proteins, transfected cells can be used to control the connexins by an artificial promoter. Transgeneic animals in which one or more connexins have been totally deleted are also used (*e.g.* Cx43 knockout mice)[11]. Fluorescence tags can be applied to junctional proteins to allow *in-situ* evaluation of temporal and spatial arrangements of these proteins. Besides, commonly used biophysical approaches for assaying gap junctional intercellular communication, including dye transfer [12], $[Ca^{2+}]_i$ propagation [13] and dual patch clamp [14], have also been applied to study the intercellular communication of cardiac myocytes. Although these methods can provide quantitative measurements to a certain extent, the most critical function of cardiac myocytes, the mechanical contractile performance, has been largely ignored. Indeed, the studies of gap junction proteins are often based on the assumption that the quantities of gap junction proteins are correlated, to a certain extent, to mechanical contractile performance. Similarly, $[Ca^{2+}]_i$ propagation measurement and electrophysiological studies target transport of ions, which is also believed to be correlated with mechanical properties through excitation-contraction coupling. The missing knowledge of such correlations leaves a gap between current technological approaches and investigations of cardiac function.

To address these technical challenges, we developed a microdevice for assessing intercellular cardiac mechanical performance at the gap junction using isolated adult cardiac myocytes. This device applies electrical stimulations to a selected adult cardiac myocyte in a longitudinally connected cell doublet, and quantifies the intercellular electro-mechanical transduction by comparing the contractile performance of stimulated and un-stimulated cells in the same doublet. Since the contractile performance of the un-stimulated cells due to direct electrical stimulation is eliminated, this work provides a quantitative tool for studying intercellular electro-mechanical transduction at the gap junction in adult cardiac myocytes.

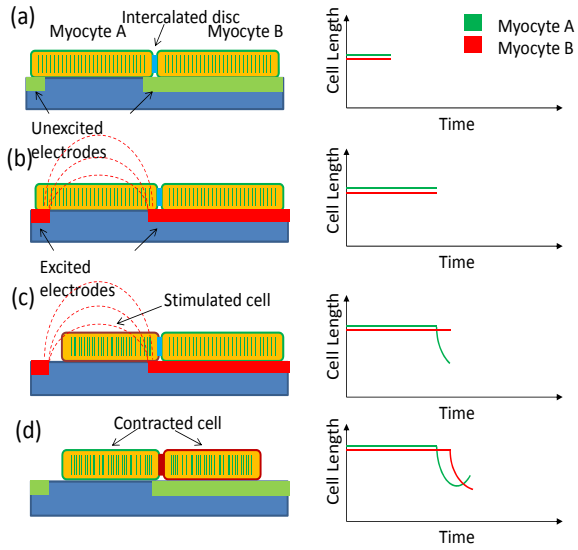

Figure 1: Schematics of the microengineered device for intercellular communication studies. Left: schematics of electrical stimulation and cell contraction; Right: schematic curves showing the changes in cell length.

THEORY

To assess intercellular communication at the gap junction between adjacent cells, the contractile performances caused by external electrical stimulation and from intercellular communication have to be separated. This can be implemented by confining the electric field to one cell while shielding the adjacent cells from electric stimulation. The working principle of the microdevice is illustrated in Figure 1. A longitudinally connected cell doublet is positioned in the electrodes array where one cell resides on top of an electrode finger (myocyte B), and the other one in the same cell doublet resides between two neighboring electrodes (myocyte A). When a pulse voltage is applied to the electrodes pair, the cell sitting between the two electrodes is subjected to a local

9781940470016/HH2014/$25©2014TRF
DOI 10.31438/trf.hh2014.41

electric field and contracts accordingly, while the cell on the electrode finger is not stimulated due to the isopotential electrode surface. The contraction of the un-stimulated cell, if any, is hence solely due to the intercellular communication with the stimulated cell through the intercalated disc. During the whole process, the cell length changes over time in both the stimulated and the un-stimulated cells provide a quantitative measure of the intercellular communication. The localized electric field was examined using finite element simulation (Figure 2). The result showed that when a voltage bias (1 V) was applied to two neighboring electrodes (200μm in width and 70μm in spacing), the electric field induced in the dielectric region between the two electrodes (~1.5×10^4 V/m) was an order of magnitude larger than that on the electrode surface (<10^3 V/m).

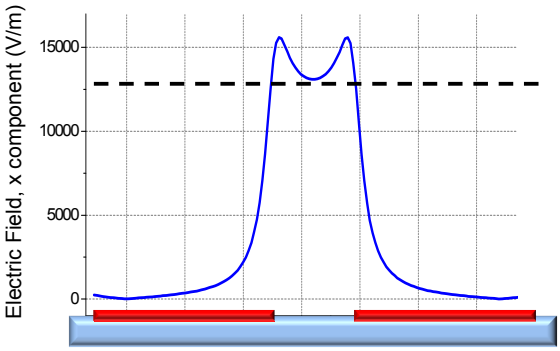

Figure 2: Finite element analysis of the localized electric field in the close vicinity of the excited electrodes (red). The dotted line denotes the approximate electric field threshold for inducing cell contraction.

EXPERIMENTAL

Device design and fabrication

The device was fabricated by patterning an array of interdigitated microelectrodes on a dielectric glass slide using a standard photolithographic process (Figure 3). The typical length of adult cardiac myocytes used in this study is ~80-120μm. Accordingly, the gap between the two electrodes was designed as 70μm to ensure that the maximal voltage can be applied to the cell lying across the two neighbouring electrodes. The width of electrodes was designed as 200μm so that the second cell in the doublet can completely reside within the electrode surface. In addition, all of the electrodes pairs were numbered and corresponded to the electrode leads patterned on the both ends of the glass slide, so that the external voltage can be easily applied to any single pair of these electrodes as needed. An array of spring contact probes was made contact to the numbered electrode leads. Finally, a breadboard socket was used to control the electrical connection between a function generator (Agilent 3220A) and the contact probes for selective stimulation.

Cell isolation

Hearts were removed from anesthetized rats for left ventricular (LV) myocyte isolation during week 8. The heart was mounted on a Langendorff apparatus and was perfused with Tyrode's solution (131mM NaCl, 4mM KCl, 10mM HEPES, 1mM $MgCl_2$, 1mM $CaCl_2$ and 10mM glucose) supplemented with 10mM 2,3-butanedione monoxime (BDM), followed by perfusion buffer and then digestion with trypsin/Liberase-TH. LV myocytes were mechanically dispersed in perfusion buffer containing 12.5μM $CaCl_2$ and 10% FBS, filtered, and resuspended in increasing concentrations of $CaCl_2$ to achieve a final concentration of 1mM $CaCl_2$. Isolated myocytes were incubated on laminin-coated chambers in plating media for 1 hour followed by culture media for 1 hour. This procedure yielded >95% viable cardiac myocytes, of which ~3% to 8% were longitudinally connected doublets.

Electrical cell stimulation

Before the experiment, the device was sterilized and coated with laminin (5μg/ml) overnight at room temperature. The cells were then transferred into the culture well on the device and cultured for 1-2 hours to allow cell attachment on the substrate. Prior to the electrical stimulation, the culture media was replaced by Tyrode's solution in order to facilitate cell contraction. For the blocked gap junction group, 1.08mM 1-Heptanol (Sigma-Aldrich) was added to the culture media and cells were treated for 5 minutes before Tyrode's solution was added. During the experiment, electric voltage pulses with a frequency of 1 Hz and a width of 8 ms were applied between the two neighbouring electrode fingers of a selected electrode pair where the subject myocyte doublet lay. The voltage magnitude ramped slowly from zero to an appropriate value to ensure that the selected cell was appropriately stimulated. To determine the threshold voltage for cell excitation, the cell length change under the applied voltage was monitored. When a threshold of the electric voltage optimal for cell stimulation was identified, the voltage magnitude was maintained as low as possible and kept constant during the whole stimulation process. Changes in cell lengths upon electrical stimulation were recorded at 7 frames per second (fps) with a CCD camera (Olympus DP71) attached to an upright microscope (Olympus BX51). A dual gooseneck illuminator was used as a complementary light source to obtain a high brightness.

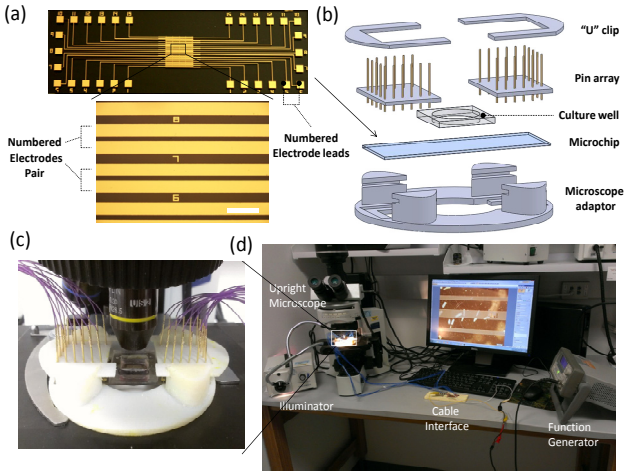

Figure 3: The device and the testing rig for selective electrical stimulation and cell contraction assessment: (a) micropatterned interdigitated electrodes. Scale Bar=500μm; (b) schematics showing the device configuration; (c) the device was mounted on the stage of an upright microscope; and (d) the selective electrical stimulation system.

Quantification and data analysis

The cell length was measured using Image J (NIH), where the cell contractility was derived by dividing the cell length reduction upon contraction by the un-stimulated cell length. Cell contractility was determined from 15-20 cells with three independent experiments, and expressed as mean ± standard deviation from 6 measurements. The differences between groups were analyzed by Student's t-test, with $p<0.05$ set as statistically significant.

RESULTS

Characterization of single cell contractile performance

Contractile performance of single myocytes was experimentally investigated by applying a local electric field to a single adult cardiac myocyte lying perpendicularly across the 70μm wide gap between two neighbouring electrodes (Figure 4a). The cell was stimulated at three different frequencies (0.5 Hz, 1.0 Hz and 2.0 Hz). The cell length change showed that the frequency of the induced cell contraction was fairly consistent with that of the electrical stimulation (Figure 4b&c), namely, 0.5 Hz electrical stimulation resulted in 0.5 Hz cell contraction, *etc*. In contrast, the cell contractility was inversely proportional to the stimulation frequency (Figure 4d), suggesting a negative force-frequency relationship.

Besides the stimulation frequency, effect of stimulation intensity on cell contractile performance was also investigated (Figure 4e). An optimal "window" of electrical voltage was found that can induce cell contraction. Given the electrode configuration and the gap distance between the neighbouring electrodes, most cells contracted under a voltage between 1.0 V and 1.3 V. A lower voltage could not induce cell contraction while a higher voltage led to immediate cell death. Within the voltage "window", there was no significant correlation between the cell contractility and the voltage magnitude (Figure 4f). This result was in good agreement with the "all-or-none" law for electrical stimulation of cardiac myocytes, namely, the cell responds to the best of its ability if the stimulus is above the threshold [15].

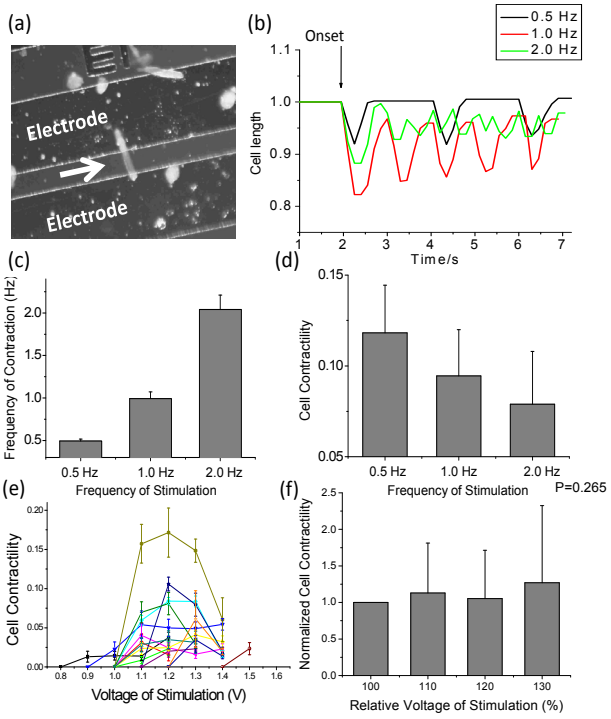

Figure 4: Electrical stimulation of single cardiac myocytes. (a) A cardiac myocyte lying across the gap between the neighboring electrodes. (b) Contractile performance of the cell responding to electrical stimuli at different frequencies. Contraction frequency (c) and cell contractility (d) both depend on the stimulation frequency. (e) Cell contractility as a function of the stimulation intensity. Each curve represents the data recorded from one cell. (f) Statistics showing the effect of stimulation intensity on the cell contractility.

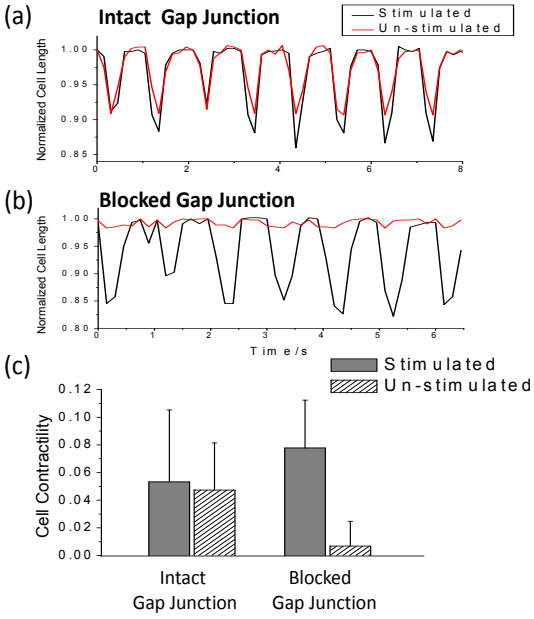

Figure 5: Selective electrical stimulation was validated by comparing the contractile performance of a cell doublet before (a) and after (b) a gap junction blocker was applied. Statistic result was shown in (c).

Assessment of intercellular electro-mechanical transduction

To validate the selective electrical stimulation, cell doublets were positioned in the electrode array where one cell resided on top of an electrode finger, and the other cell resided between two adjacent electrodes. The cell contractions under electric stimulation were measured by tracking the changes in cell length. In a doublet with intact gap junction, synchronized contractions of the two cells were observed (Figure 5a). However, once the intercellular communication through the gap junction was blocked using a gap junction blocker (1-Heptanol), the un-stimulated cell on the electrode surface no longer exhibited periodic contraction, with the length kept approximately constant, while the stimulated cell between the two electrodes was still in active contraction (Figure 5b). This was confirmed by the repeating measurements from a number of cell doublets (Figure 5c). While both cells of the doublets with intact gap junctions contracted at a comparable magnitude (~ 0.053 to ~ 0.047), the contractility of the stimulated cell when the gap junction was blocked (~ 0.078) was an order of magnitude larger than that of the un-stimulated one (~ 0.007). The results suggested that the contraction of the un-stimulated cell was solely attributed to the electro-mechanical transduction from the stimulated cell through the gap junction.

Finally, a proof-of-concept study was conducted to examine the efficacy of the device in assessing the intercellular electro-mechanical transduction within adult cardiac myocytes doublets. The first cell doublet was isolated following the regular protocol, while the second cell doublet was prepared with the reduced calcium concentration in the digestion buffer (14.5μM $CaCl_2$). In the first cell doublet (Figure 6a&b), the two cells contracted at the same frequency and at the same phase, which were in register with the applied electrical stimulation. The result suggested that the gap junction in the first pair was well-preserved and was able to synchronize the contractile functions in the two coupled cells in the doublet. This is similar to that in a healthy heart where all cells are contracting synchronously so that the ventricle can exhibit a maximal pumping performance. In the second cell doublet (Figure 6c&d), the un-stimulated cell exhibited an irregular

contractile performance with a discernible phase delay comparing to the stimulated cell. Meanwhile, there was a greater difference in cell contractility between the stimulated cell and the un-stimulated cell. The unsynchronized contractions indicated an impaired conductance in the gap junction or an altered electro-mechanical coupling mechanism, which may represent the conditions of myocardium in the cardiac fibrillation.

Besides the capability of examining gap junction change due to varying calcium concentration, the reported device is also able to examine alterations in the intercellular performance due to other extrinsic and intrinsic factors that may cause asynchronous contraction and the contractility degradation between the two cells in a longitudinally connected doublet. In this perspective, this work not only develops a quantitative platform for studying the role of intercellular electro-mechanical transduction under various heart diseases, but also provides a powerful tool to assess the possibilities of pharmacological approaches towards efficient clinical therapies.

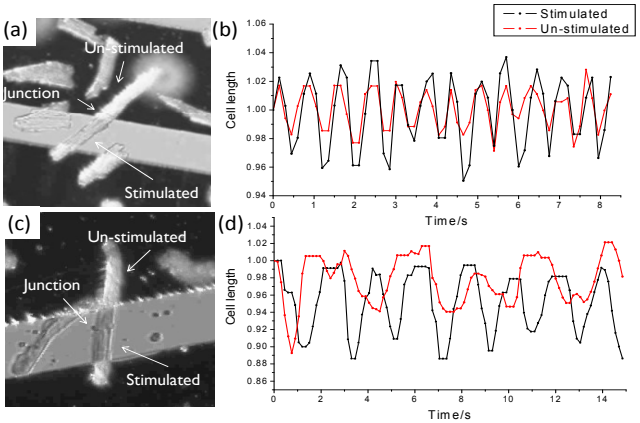

Figure 6: Contractile performance of the cell doublets with regular (a) and impaired (c) gap junctions. (b) The two cells recorded in (a) showing a synchronous contraction; (d) while the two cells recorded in (c) showing an asynchronous contraction accompanied with a reduced contractility in the un-stimulated cell.

CONCLUSIONS

This study presents a microengineered approach to study intercellular communication in cardiac cells by measuring the contractile performance of isolated doublets of adult cardiac myocytes. The work provides a quantitative tool for studying intercellular mechanotransduction at the gap junction and is expected to establish a comprehensive understanding of intercellular communication in various heart diseases.

ACKNOWLEDGMENTS

This work is funded by National Science Foundation under the grant numbers 0954013 and 1138236. Student travel support (XZ) has been generously provided by the Transducer Research Foundation.

REFERENCES

[1] A. R. Akester, "Intercalated discs, nexuses, sarcoplasmic reticulum and transitional cells in the heart of the adult domestic fowl (Gallus gallus domesticus)," J Anat, 133, 161 (1981).

[2] G. L. Aistrup, et al., "Pacing-induced heterogeneities in intracellular Ca2+ signaling, cardiac alternans, and ventricular arrhythmias in intact rat heart," Circ Res, 99, 65 (2006).

[3] M. Cooklin, et al., "Changes in cell-to-cell electrical coupling associated with left ventricular hypertrophy," Circ Res, 80, 765 (1997).

[4] N. Inoue, et al., "Rapid electrical stimulation of contraction modulates gap junction protein in neonatal rat cultured cardiomyocytes: involvement of mitogen-activated protein kinases and effects of angiotensin II-receptor antagonist," J Am Coll Cardiol, 44, 914 (2004).

[5] C. K. Liao, et al., "PKCvarepsilon mediates serine phosphorylation of Connexin43 induced by lysophosphatidylcholine in neonatal rat cardiomyocytes," Toxicology, 314, 11 (2013).

[6] M. F. Taha, et al., "Electron microscopic study of mouse embryonic stem cell-derived cardiomyocytes," Cytotechnology, 64, 197 (2012).

[7] J. S. Mitcheson, et al., "Cultured adult cardiac myocytes: future applications, culture methods, morphological and electrophysiological properties," Cardiovasc Res, 39, 280 (1998).

[8] I. Komuro, et al., "Mechanical loading stimulates cell hypertrophy and specific gene expression in cultured rat cardiac myocytes. Possible role of protein kinase C activation," J Biol Chem, 266, 1265 (1991).

[9] J. L. Balligand, et al., "Control of cardiac muscle cell function by an endogenous nitric oxide signaling system," Proc Natl Acad Sci U S A, 90, 347 (1993).

[10] Y. Xia, et al., "Regulation of gap-junction protein connexin 43 by beta-adrenergic receptor stimulation in rat cardiomyocytes," Acta Pharmacol Sin, 30, 928 (2009).

[11] A. G. Reaume, et al., "Cardiac malformation in neonatal mice lacking connexin43," Science, 267, 1831 (1995).

[12] K. Sai, et al., "Prevention of the down-regulation of gap junctional intercellular communication by green tea in the liver of mice fed pentachlorophenol," Carcinogenesis, 21, 1671 (2000).

[13] M. J. Sanderson, et al., "Mechanical Stimulation and Intercellular Communication Increases Intracellular Ca-2+ in Epithelial-Cells," Cell Regulation, 1, 585 (1990).

[14] J. Durig, et al., "Intercellular communication between bone marrow stromal cells and CD34(+) haematopoietic progenitor cells is mediated by connexin 43-type gap junctions," British Journal of Haematology, 111, 416 (2000).

[15] H. P. Bowditch, "Uber die Eigenthumlichkeiten der reizbarkeit, welche die muskelfasern des herzens zeigen," Ber Sachs Ges Wiss, 23, 652 (1871).

CONTACT

*Y. Zhao, tel: +1-614-247-7424; zhao.178@osu.edu

AN INDUCED-FLOW KIDNEY-BREAST CANCER *IN VITRO* MODEL FOR STUDY OF CANCER SUPPRESSION BY VITAMIN D_3 DERIVATIVES

Seungbeom Noh[1], Po Ki Yuen[2], Vasiliy N. Goral[2] and Hanseup Kim[1]
[1]Electrical and Computer Engineering, University of Utah, Salt Lake City, UT, USA
[2]Science and Technology, Corning Incorporated, Corning, NY, USA

ABSTRACT

This paper reports an *in vitro* platform that demonstrates the suppression of cancer cells by vitamin D_3 derivatives on a single system, by simultaneously enabling (1) co-culture of multiple cells; (2) induced fluidic flows among cells; and (3) cancer suppression by the vitamin D_3 derivatives. This *in vitro* model mainly consists of three wells, each containing kidney cells, breast cancer cells, and final transferred media. The wells are connected by porous membranes that allow fluidic flows by hydrostatic pressure. The developed model successfully (1) co-cultured kidney cells (HKC8) and breast cancer cells (MCF7) to the confluency of >1,800cells/mm^2 under the same media; and (2) showed the suppression of cancer cells by the vitamin D_3 derivatives: 25-hydroxyvitmain D_3 ($25(OH)D_3$) and 1,25-dihydroxyvitamin D_3 ($1,25(OH)_2D_3$); and (3) demonstrated fluidic flow effects on cancer suppression.

INTRODUCTION

Breast cancer has been one of the top five causes for mortality in the US in recent years [1]. In 2007 it was reported that 125 people in every 100,000 women had breast cancer and 23 people died of the breast cancer [1]. To lower the fatalities, numerous efforts have been reported covering from drug-treatment [2] to X-ray based chemotherapy [1], resulting in notable reduction of fatalities in recent years. However, the treatment processes have been often criticized for accompanied harsh side effects of weight loss, abnormal hormone discretion, and even mental instability [3,4,5].

Breast cancer has recently been proven to be suppressed by the vitamin D_3 derivatives, $1,25(OH)_2D_3$ [6]. As illustrated in Fig.1, the vitamin D_3, gained by food intake or by sun exposure [7], produces subsequent derivatives: first, $25(OH)D_3$ in the liver and then, $1,25(OH)_2D_3$ from the $25(OH)D_3$ in the kidney [8]. The $1,25(OH)_2D_3$, when transferred to the breast cancer cells, suppresses cyclin D-dependent kinases activity and delays G1/S phase of cell cycle, ultimately inhibiting further growth of breast cancer cells [6]. Previous literature reported that the growth of breast cancer cells (MCF7) started to slow down after day 2 of introducing 10^{-7}M of $1,25(OH)_2D_3$ in *in-vitro* 96 wells and at day 7, approximately 10× decreased in cell number was observed [6]. However, detailed studies of cancer suppression by vitamin D_3, such as translation of individual derivatives among organs and their cross-effects [9], have been much limited mainly due to the lack of low-cost, high-throughput co-culture model. Conventional *in vivo* models, such as animals, present the issues of cost, throughput, repeatability, controllability as well as ethics, while *in vitro* 96-well models failed to provide co-culture environments and fluidic flows among cell groups, which is critical to study translational effects that have not been studied yet [10].

To resolve such limitations, we report the development of a low-cost, high-throughput, and co-culture model where the suppression of cancer cells by vitamin D_3 derivatives has been demonstrated. Particularly, the fabrication, testing, and measurement results of the developed kidney-breast cancer model are reported.

STRUCTURE AND FABRICATION

Structure

The induced-flow *in vitro* model consists of three wells, each containing kidney cells, breast cancer cells and final transferred media (Fig. 2), which was described in details in a previous publication [11]. The three wells were fluidically connected through cellulose membranes with either 1.2, 5.0 or 8.0μm pore size, and induced fluidic flow from the first well through the second to the third well by fluidic potential difference. The fluidic potential difference was applied by maintaining the media volumes as 320μl, 170μl, and 20μl at the kidney, breast cancer, and drain wells, respectively. The media volume was re-adjusted according to the pore size used. The diameter of each well was 6.5mm and the height was 10.5mm. Cellulose membranes provided the fluidic path among wells. The footprint of the membrane was 1mm×3.5mm, while their thicknesses were between 105 and 140μm.

Fabrication

The fabrication of the platform was previously described [11]. Briefly, each set of three holes of a standard flat bottom 96-well holey (bottomless) microplate (Corning Inc., Corning, NY) are linearly connected using two cellulose membranes (1mm×3.5mm) with either 1.2, 5 or 8μm pore size . A polystyrene film, which was taken from a Corning® HYPERStack™ Cell Culture Vessel (Corning Inc., Corning, NY) was adhered to the bottom of the standard flat bottom 96-well holey microplate using a double-sided

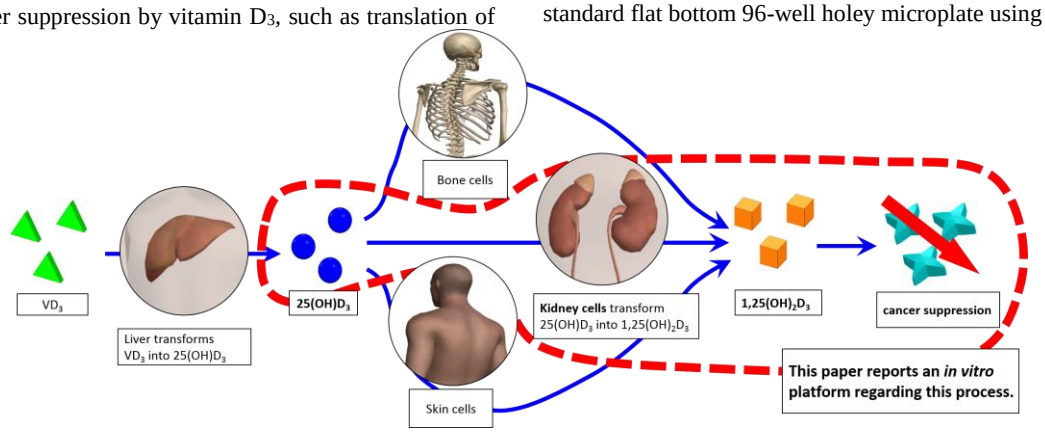

Figure 1. Motivation: Vitamin D_3 is converted into its subsequent derivatives through different organs, ultimately being capable of suppressing breast cancer cells.

9781940470016/HH2014/$25©2014TRF
DOI 10.31438/trf.hh2014.42

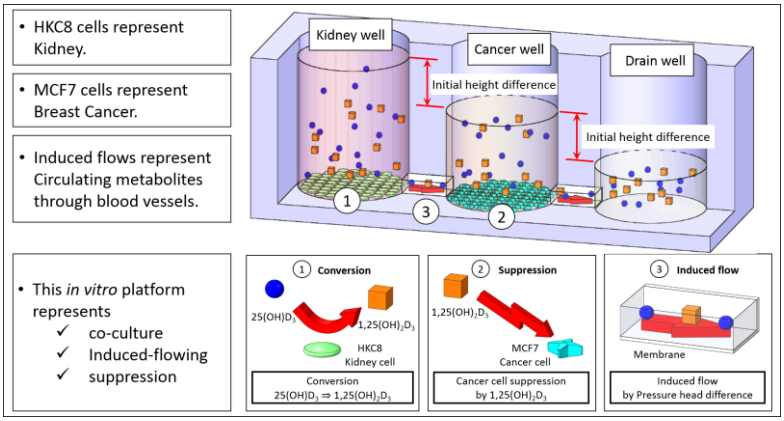

Figure 2. Proposed model that combines multi-cell co-culture, induced-flow, and cancer suppression into a single in vitro platform.

pressure sensitive adhesive sheet (110mm×75mm) where holes and channels are cut out for the wells and the cellulose membranes, respectively (Fig.2) [11].

Cell culture

Both HKC8 (ATCC, Manassas, VA) and MCF7 (ATCC, Manassas, VA) cell lines, each representing the kidney and the breast cancers, were cultured in Dulbecco's modified Eagle's medium: Ham's F12 (Cassison Labs, North Logan, UT) supplemented with 10% fetal bovine serum (Fisher Scientific, Pittsburgh, PA), 1% amphotericin B (Corning Inc., Manassas, VA) and 1% penicillin/streptomycin (Lonza, Walkersville, MD). These cell lines were cultured until they reached 80% confluency in a monolayer in a T75 flask (Corning Inc., Corning, NY). The culture conditions of 37℃ in a humidified atmosphere containing 5% CO_2 were utilized in the incubator (NU-4750, Nuaire, Plymouth, MN). The media was changed every 3~4 days.

Vitamin D_3 derivatives, $1,25(OH)_2D_3$ and $25(OH)D_3$, were diluted in pure ethanol into various ranges of concentrations (10^{-5}~10^{-10} M) and stored in freezer at -20°C. The concentrations of $1,25(OH)_2D_3$ and $25(OH)D_3$ were finally adjusted again in the media right before the use. Note that the concentration of ethanol dilution did not exceed 0.8% to avoid any toxicity effects on cell growth. The utilized chemical compounds were purchased from EMD Millipore (EMD Chemicals Inc., San Diego, CA).

TESTING METHODOLOGY

Cell viability measurement

In order to establish a cell growth reference, the fluorescence intensity of the incubated cells was monitored every 24 hours over 9 days by utilizing a fluorescence spectrometry (Synergy HY, BioTEK Instrument, Winooski, VT). When the HKC8 kidney cells and MCF7 breast cancer cells were cultured to a confluency of 80%, they were harvested by washing twice with PBS and adding 4ml Trypsin EDTA (Corning Inc,. Manassas, VA). These harvested cells were then seeded in triplicate in the standard 96-well microplate (Corning Inc., Corning, NY). The initial cell numbers ranged between 5,000 and 100,000 cells/well. After 1 day, a cell viability reagent, PrestoBlue (Invitrogen, Frederick, MD), was applied to stain the cells for fluorescence measurement. The mixture ratio was 10µl of PrestoBlue and 90µl of media. After incubation for 30 minutes at 37℃ and 5% CO_2, the fluorescence intensity of the incubated cells was measured utilizing the light wavelengths at 530 and 590nm.

Cancer suppression measurement

By $1,25(OH)_2D_3$: To confirm the cancer suppression effect of $1,25(OH)_2D_3$, the proliferation of the MCF7 cancer cells was monitored every 24 hours over 9 days utilizing fluorescence spectrometry under direct supply of $1,25(OH)_2D_3$. MCF7 breast cancer cells were seeded in the standard 96-well microplate in a concentration of approximately 5,000 cells/well in triplicate. They were supplied with different dosing concentrations between 10^{-9} and 10^{-6}M every 24 hours over 7 days. The cell viabilities were measured every 24 hours by the spectrometer. The optical images of the cells were also collected for comparison purposes.

By $25(OH)D_3$: The cancer suppression effect of $25(OH)D_3$ on MCF7 breast cancer cells have been additionally examined by utilizing the identical method described above. In this case, different concentrations of $25(OH)D_3$ between 10^{-5} and 10^{-8}M were applied. Note that to the best of our knowledge, cancer suppression effects of $25(OH)D_3$ on MCF breast cancer cells has not been reported previously. However, the hypothesis that mammary cells express CYP27B1 and locally produce $1\alpha,25(OH)_2D_3$, which acts in an autocrine manner to regulate cell turnover had been studied previously [12]. CYP27B1 is a cytochrome P450-containing hydroxylase expressed in kidney and other tissues that generates $1\alpha,25(OH)_2D_3$. In Bland *et al.*'s study, CYP27B1 mRNA was detected in both MCF7 and HKC8 cells lines, but expression was higher in MCF7 cultures compared with HKC8 cells [12], which were characterized previously as an *in vitro* model of vitamin D metabolism [9]. Thus we suspected that MCF7 cells may also convert $25(OH)D_3$ into $1,25(OH)_2D_3$ by itself.

By indirectly produced $1,25(OH)_2D_3$: In comparison to direct applications of $25(OH)D_3$ and $1,25(OH)_2D_3$ onto the cancer cells (MCF7), the application of $25(OH)D_3$ onto the kidney cells (HKC8) was examined. HKC8 cell has been known to produce $1,25(OH)_2D_3$ from $25(OH)D_3$ [9]. Thus, HKC8 cells were cultured at the upstream well, while MCF7 cells were cultured at the downstream well. In this case, HKC8 and MCF7 cells were separately cultured in the wells of a standard 96-well microplate. Every 24 hours, $25(OH)D_3$ was added to the HKC8 cells and after 5 hours of adding $25(OH)D_3$ to the HKC8 cells, the media in the HKC8 cell well was exchanged with fresh media without $25(OH)D_3$ while the "used" HKC8 media was exchanged with the media in the MCF7 cell well. The proliferation was measured every 24 hours over 9 days utilizing fluorescence spectrometry. The concentrations of the supplied $25(OH)D_3$ ranged between 10^{-5} and 10^{-7}M.

Measurement of flow effects on cancer suppression

In order to measure the flow rate effects on the cancer suppression, the proliferation of the MCF7 cancer cells in the *in vitro* platform were monitored using cellulose membranes with different pore sizes (1.2, 5.0 or 8.0 µm) (Fig. 2). The average flow rates were previously measured as 1.3, 3.3, and 6.7µl/hr for the

membrane pore sizes of 1.2, 5.0, and 8.0μm, respectively [11]. In the first well HKC8 kidney cells were seeded, while MCF7 breast cancer cells were seeded in the second well (Fig.2). The initial cell numbers were approximately 5,000 cells/well. Depending on the induced flow rates (pore sizes of cellulose membranes), the applied media with or without 25(OH)D_3 was adjusted in the first HKC8 cell well and the third drain well every 1, 2 or 3 days, respectively. After 5 days, the cell viabilities were measured by the same protocol as the previous tests.

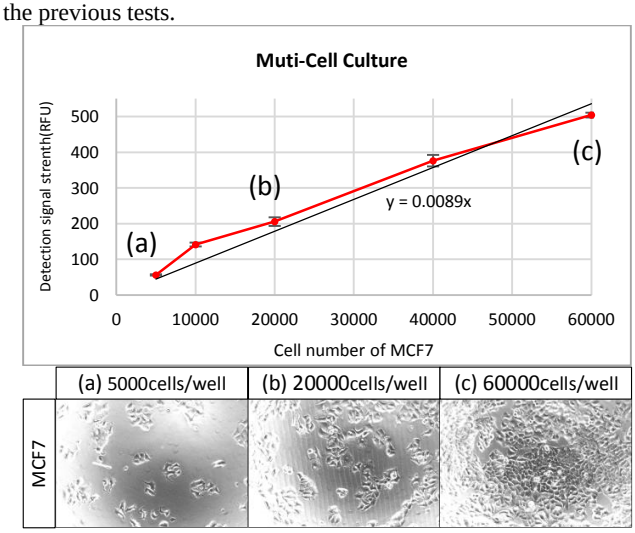

Figure 3: (Top) Measured reference curve from breast cancer (MCF7) cells. PrestoBlue in DMEM media (Reagent:Media=10μl:90μl) was utilized to stain the cells for optical spectrometry for proliferation measurement (Synergy HT - BioTEK with fluorescence 560/590nm). (Bottom) Photos of the cell growth

RESULT

Cell viability: MCF7 breast cancer cells

The fluorescence measurement showed that the relative fluorescence unit (RFU) monotonously increased from 56 to 504 with the increasing number of MCF7 cells from 5,000 to 60,000 cells/well (Fig. 3-(top)). A positive linear correlation was observed with a slope of 0.0089 RFU/cells, indicating the validity of the curve as a cell growth reference. In the case of 5,000 cells/well, the surface of the well was covered with sparsely-distributed cells, while the well with 60,000 cells were nearly fully packed with the cells (Fig. 3-(bottom)).

Breast cancer suppression by 1,25(OH)$_2$D$_3$

The measurement results showed that 1,25(OH)$_2$D$_3$ with concentrations of 10^{-6}M and 10^{-7}M suppressed the proliferation of MCF7 cells by 36% in comparison to lower concentrations (10^{-8}M and 10^{-9}M) and control (0M) on day 7, as shown in Fig.4-(top). The suppression was clearly distinguished from day 4, and the proliferation difference further increased with the time. The suppression differences were measured as 22, 30, 33% at day 4, 5, and 6, respectively. The concentrations of 10^{-8}M and 10^{-9}M did not show any noticeable suppression in comparison to the control (0M). The optical images of 10^{-7}M (suppression) and 10^{-9}M (no suppression) present the clear differences in cancer cell proliferation (Fig.4-(bottom)). After day 7, MCF7 cells in the control and 10^{-8}, 10^{-9}M wells, started peeling off from the wall due to extremely high cell density from cell growth.

Breast cancer suppression by 25(OH)D$_3$

The suppression data indicated that concentrations of 25(OH)D_3 above 10^{-6}M were capable of suppressing the proliferation of MCF7 cells by 54% on day 7, while the lower concentrations (10^{-7}M and 10^{-8}M) showed little suppression, as shown in Fig.5-(top). To the best of our knowledge, this is the first experimental results that showed the cancer cell suppression by 25(OH)D_3. The cancer suppression effects become distinct from day 4, and the proliferation difference further increased with time. The suppression differences were measured as 32, 44, 46% at day 4, 5, and 6, respectively. The optical images of 10^{-5}M (suppression) and 10^{-8}M (little suppression) presented the clear differences in cancer cell proliferation (Fig.5-(bottom)).

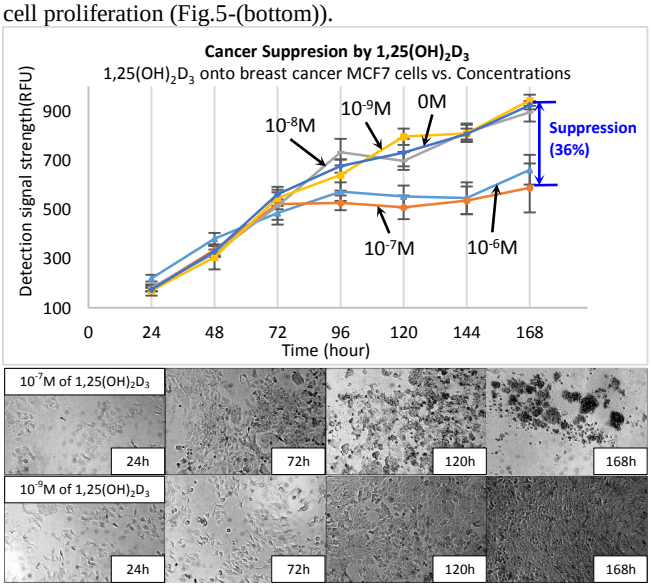

Figure 4: (Top) Measured MCF7 suppression in fluorescence intensities over time under different dosing concentrations by 1,25(OH)$_2$D$_3$, indicating the effects of concentrations. (Bottom) Photos of breast cancer cells showing the suppression effects at higher concentrations of >10^{-7}M.

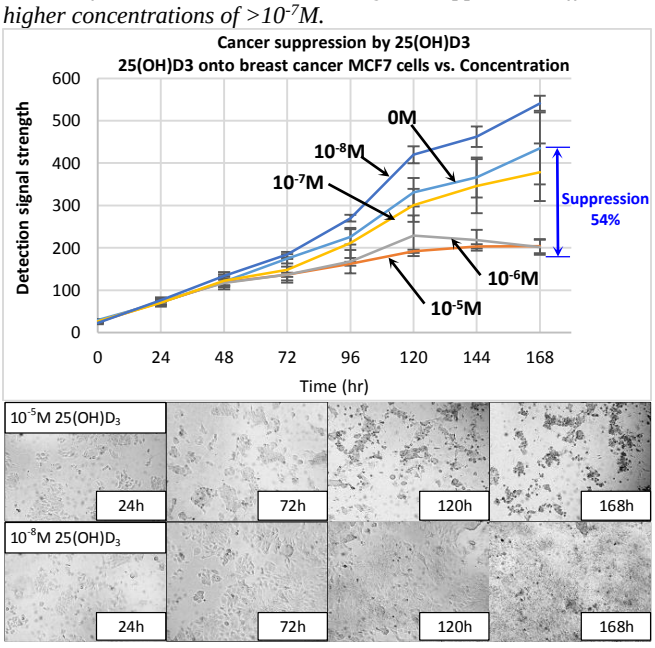

Figure 5: (Top) Measured MCF7 suppression in fluorescence intensities over time under different dosing concentrations by 25(OH)D$_3$. (Bottom) Photos of breast cancer cell suppression over time, demonstrating the effects of dosing concentrations (>10^{-8}M).

Breast cancer suppression by converted 1,25(OH)$_2$D$_3$

The normalized cell proliferation data showed that MCF7

cancer cells, located at the downstream, were suppressed under the application of 25(OH)D_3 onto the HKC8 kidney cells upstream. The suppression was up to 48% in comparison to the control (0M) samples after 7 days (Fig. 6-(top)), which was close to the results from the direct application of 25(OH)D_3 onto the MCF7 breast cancer cells (Fig. 5-(top)). Although this small difference (48% compared with 54%) was within our experimental error, more experiments are needed in order to isolate the path of MCF7 suppression to whether 25(OH)D_3 was indeed converted into 1,25(OH)D_3 by the HKC8 kidney and/or MCF7 cells. Further study is needed to explain the exact causes.

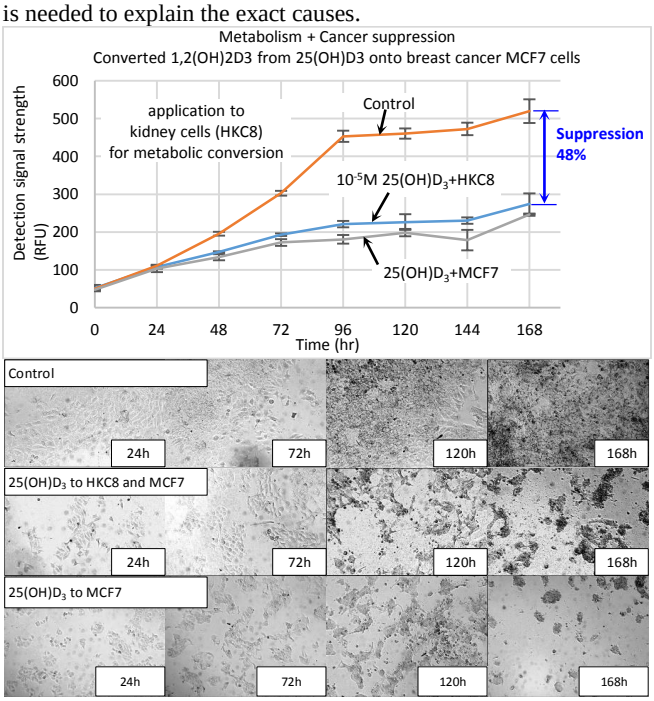

Figure 6: (Top) Measured MCF7 suppression in fluorescence intensities over time under different dosing conditions of 25(OH)D_3: (top) control, (middle) onto HKC8 kidney cells, and (bottom) onto MCF7 cells. (Bottom) Photos of breast cancer cell suppression over time.

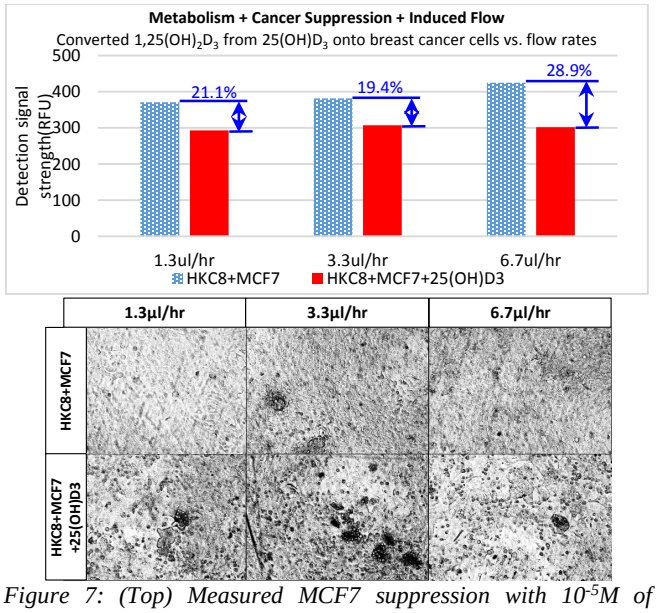

*Figure 7: (Top) Measured MCF7 suppression with 10^{-5}M of 25(OH)D_3 added to the HKC8 cell wells upstream by measuring the fluorescence intensities in the induced flow in vitro model after 5 days culture. (Bottom) Photos of cell suppression under different flow rates of 1.3, 3.3, and 6.7*ul/hr.

Breast cancer suppression at different flow rates

The measurement data demonstrated that different flow rates of 1.3, 3.3 and 6.7ul/hr resulted in different levels of cancer cell suppression of 21.1, 19.4 and 28.9% with 10^{-5}M of 25(OH)D_3 added to the HKC8 cell well, as illustrated in Fig.7-(top). The maximum suppression of 28.9% was observed at the highest flow rate of 6.7ul/hr. We are still trying to understand the relatively lower suppression compared with previous cases (Fig. 4-6-(top)). The optical images also supported the trend: different levels of MCF7 suppression under different flow rates.

DISCUSSIONS AND CONCLUSIONS

This paper presents an *in vitro* platform that simultaneously enables (1) co-culture of multiple cells in one system; (2) induced fluidic flows by different pressure; (3) cancer suppression by the derivatives of vitamin D_3. The cancer suppression distinctly appeared at the concentrations of 1,25(OH)$_2$$D_3$ above 10^{-7}M after 96 and 72 hours for each cases and of 25(OH)D_3 above 10^{-6}M after 96 hours, while the suppression differences, in comparison to control (0M), were measured as 36%, 54% and 48%, respectively. The measurement data also showed that the cancer suppression reaches 28.9, 21.1, 19.4% with 10^{-5}M of 25(OH)D_3 at the flow rates of 6.7, 1.3 and 3.3µl/hr, respectively.

ACKNOWLEDGEMENTS

Fabrication was performed at the state-of-the-art University of Utah Nano Fabrication Facility located in the Sorenson Molecular Biotechnology Building. The authors thank Prof. Hamid Ghandehari's group (University of Utah, Salt Lake City, UT) for the access of HPLC instrument, advice and support. HKC8 human renal proximal tubule cell lines and MCF7 breast cancer cell lines were kindly provided by Dr. Anthony A. Portale (University of California, San Francisco, CA) and by Dr. Alana Welm (University of Utah, Salt Lake City, UT), respectively. The 96-well perfusion microplate was generously provided by Corning Incorporated (Corning, NY).

REFERENCES

[1] National Institutes of Health, Fact Sheet, Oct, 2011.
[2] Bernard Fisher et al., Journal of the National Cancer Institute, 1998, 90, pp.1371–88
[3] Clarke M, et al., the Lancet, 2005, 366, pp.2087-2106
[4] Charles L. Shapiro, et al., The New England Journal of Medicine, 2001, 344, pp.1997-2008
[5] Early Breast Cancer Trialists' Collaborative Group, Lancet, 2005, 365, pp.1687–1717
[6] Simon Skjode Jensen, et al., Molecular Endocrinology, 2001, 15, pp.1370-1380
[7] Axmin Zittermann, British Journal of Nutrition, 2003, 89, pp.552-572
[8] Daniel Zehnder, et al., Journal of Clinical Endocrinology, 2001, 86, pp.888-894
[9] Rosemary Bland, et al., Endocrinology, 1999, 140, pp.2027-2034
[10] Ross Booth, et al., Lab on a Chip, 2012, 12, pp1784-1792
[11] Vasiliy N. Goral, et al., Lab on a Chip, 2013, 13, pp.1039-1043
[12] Carly M. Kemmis, et al., The Journal of Nutrition, 2006, 136, pp.887-892

CONTACT

*Seungbeom Noh, tel: +1-801-585-4766; moses.noh@utah.edu

DOUBLE-SIDED MICROPILLAR ARRAYS FOR CELL CONTRACTION FORCE MAPPING USING OPTICAL MOIRÉ METHOD

F. Zhang[1], S.W. Anderson[2], X. Zheng[3], Y. Qiu[4], R. Liao[4], and X. Zhang[1]*
[1]Boston University, USA
[2]Boston University Medical Center, USA
[3]Lawrence Livermore National Laboratory, USA
[4]Brigham and Women's Hospital, USA

ABSTRACT

The mapping of cellular traction forces is fundamental to deeply understanding a wide range of cellular functions and behaviors. The moiré phenomenon has been leveraged as a visualization tool for cellular force mapping, yielding both a magnification effect as well as the capacity for whole-field force measurements. This paper reports the development of a double-sided micropillar array (DMPA) made of PDMS for use in moiré-based cellular force analyses. Herein, the fabricated DMPAs were validated by mapping neonatal rat ventricular myocyte (NRVM) contraction forces. The advantages of the DMPA-based approach yield an improved moiré contrast and enable efficient moiré pattern generation.

INTRODUCTION

Cellular traction forces and the mechanical interaction of cells with their local microenvironment and extracellular matrix (ECM) have been found to be essential to a variety of cell functions ranging from migration to proliferation and apoptosis, among others [1]. In addition, cellular traction forces are fundamental to a variety of processes in both the maintenance of health as well as the development of disease such as, for example, wound healing and inflammation, in addition to cancer invasion and metastasis [2]. In order to study these processes, microfabricated polymeric pillar arrays have been developed and successfully employed for precisely mapping cellular traction forces [3]. Inherent to the application of fabricated micropillar arrays as tools for studying cellular forces is the need for tracking and monitoring the deflections of each individual micropillar as these pillar deflections are employed to calculate the displacement vectors of the cellular traction forces. Since the deflection of pillars is traditionally measured with conventional optical microscopy using a fixed numerical aperture of the objective lens, small-scale deflections or motions of individual sensing units that are in the sub-micrometer to nanometer range may readily fall below the limits of detection, limiting the range of measurable cell force. In addition, conventional optical microscopy is time-consuming and requires complex algorithms in order to track and interpret individual deflections and motions of the high-density micropillar arrays and therefore cannot meet the demands for automated, real-time monitoring of cellular and sub-cellular behaviors. This lack of efficiency precludes the capacity for high-throughput whole-field cellular force mapping of multiple cells in a large field-of-view.

The moiré phenomenon occurs when two periodic patterns overlap to produce a virtual periodic pattern. This phenomenon has previously been employed for measuring strain and deformation, using the moiré effect produced by the specimen and reference gratings to magnify the surface deformations and create a contour map which is related to surface displacement [4]. We have previously leveraged the moiré phenomenon in order to develop an optomechanical approach to cellular force mapping which yields several distinct advantages when compared to conventional approaches, including its marked sensitivity to micropillar displacements, enabling a dramatic expansion of the range of measurable forces as well as high-throughput, real-time whole-field force mapping [5]. In the optical moiré setup, cells are seeded onto the top surface of the micropillar array in a culture dish, while a reference substrate featuring an identical pattern is located below the culture dish on a translation axis stage. The moiré pattern generated by these two substrates is obtained and the displacements of the pillars are recorded in the moiré pattern and may be readily retrieved using a variety of image analysis algorithms, thereby yielding cellular force maps. The distance between these two parallel patterns plays a critical role in the image quality of the moiré pattern and demands precise alignment in order to generate a single moiré pattern with appropriate contrast. Furthermore, since the reference substrate is exposed to air and PDMS is inherently sticky, dust and particulate residue is often found on the reference substrate and any such discrepancy between two substrates results in a degradation of the image quality, ultimately affecting the accuracy of cellular force mapping. In order to address the aforementioned existing limitations of the two-dimensional moiré-based approach, the method reported in this work utilizes a double-sided micropillar array (DMPA) in order to map the cellular force distribution, as shown in Figure 1.

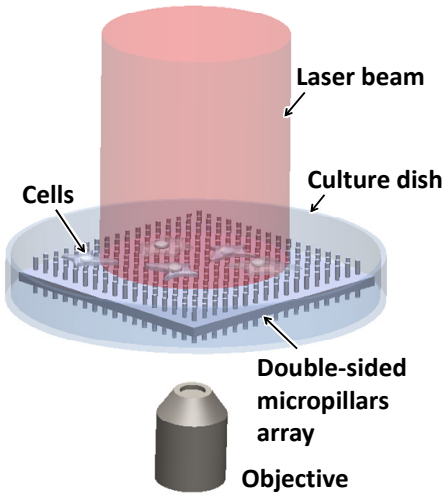

Figure 1: Optical configuration for two-dimensional moiré-based cell force mapping using double-sided micropillar arrays. (Size of the cells and pillars are exaggerated as compared to the light beam.)

RESULTS

The DMPA was fabricated using a two-sided replica molding process involving two molds, as illustrated in Figure 2. In this

9781940470016/HH2014/$25©2014TRF
DOI 10.31438/trf.hh2014.43

work, the micropillar arrays on the cell culture side were fabricated with a micropillar diameter of 2 µm, micropillar height of 6 µm, and a center-to-center distance of 4 µm; the micropillar arrays on the reference side of the DMPA featured an identical diameter and center-to-center distance as the cell culture side but a height of 2 µm. Conventional photolithography techniques were used to

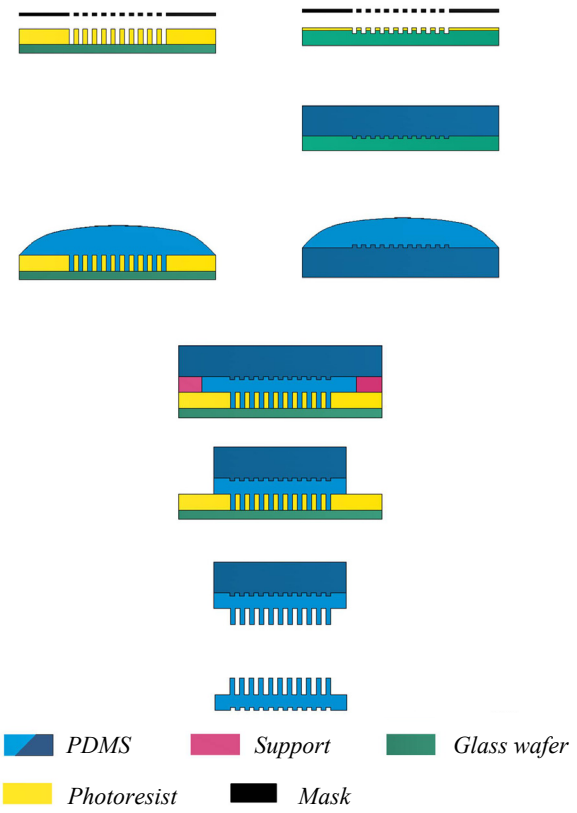

Figure 2: Process flow for PDMS pillar fabrication. The fabrication employs conventional photolithography and a two-step PDMS molding process with a final double casting step which yields double-sided pillar arrays for force mapping.

fabricate the AZ9260 photoresist molds. After replica molding using a glass wafer covered by the patterned photoresist, a PDMS mold with a lower aspect ratio was formed as the mold for the reference pattern side of the DMPA. Both the PDMS mold and the photoresist mold were silanized using (tridecafluoro-1,1,2,2-tetrahydrooctyl)-1-trichlorosilane for 10 h under vacuum in a desiccator to assist with the subsequent release of the two molds and the DMPA. During this process, four pieces of cover glass were used as the supporting structures. After applying 50 µL of uncured PDMS prepolymer on one side of each cover glass, the glass wafers were turned over and attached to the four edges along the periphery of the photoresist mold. The photoresist mold with the cover glass was cured at 65°C for 30 min to fix the cover glass, ensuring that is served as a support structure and spacer during the following molding process. PDMS prepolymer was then poured over the surface of both the photoresist and PDMS molds; after 30 min of degassing, the two molds were carefully brought together and gradually attached from one side to another, in order to avoid any bubble formation. The relative pattern orientation of the two molds was precisely controlled using the alignment of the patterned photoresist and the PDMS mold, while the thickness of the supporting glass determined the distance between two periodic patterns. After curing for 2 h at 65 °C (corresponding to Young's modulus of PDMS of 1 MPa), the DMPA was released from the molds and attached to a glass slide for subsequent surface treatment and cell seeding., as shown in Figure 3.

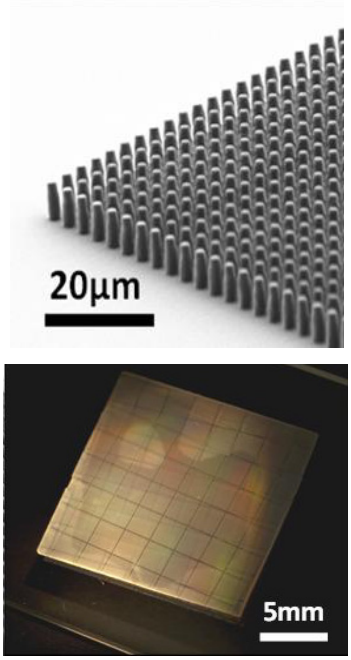

Figure 3: SEM image of pillars at the periphery of an array (top). Double-sided PDMS micropillar array attached to a glass slide (bottom).

Herein, as a validation of the optomechanical DMPA-based cell force mapping approach, we employed neonatal rat ventricular myocytes (NRVM). With a cell size of 10-30 µm in diameter, the NRVMs are capable of spontaneously generating forces in the range of 10-200 nN; compared to adult rat cardiac myocytes, NRVMs are small in size and generate relatively weak contraction forces. With the advantages of an inherent magnification factor and real-time, whole-field monitoring capacity, the moiré cell force mapping method is an ideal tool for the high-throughput study of NRVMs.

Following fabrication, the DMPAs were prepared for cell attachment using a microcontact printing technique. DMPAs were initially treated by O_2 plasma in a Plasma Asher at 300 sccm flow rate and 150 W for 2 min. PDMS stamps were immersed in a laminin solution (50 µg/mL) for 1 h and were subsequently placed in conformal contact with the plasma treated DMPAs, thereby coating the top surfaces of the pillars with laminin in order to ensure that subsequently seeded cells adhered only to the top surface of the micropillar arrays. One hundred thousand NRVMs per mL were seeded onto the cell culture side of the DMPAs and cultured for 2-3 days, allowing the cells to adhere and spread out onto the micropillars. After 2-3 days of culturing, the samples were washed using fresh culture medium to remove the dead cells and the cellular forces analyzed.

RESULTS

The algorithm for mapping cellular force from the deformed

moiré patterns involves decoupling the phase distribution from the distorted moiré fringe patterns. The displacement information of the pillars is encoded within the aforementioned, cell-induced distortion of the moiré pattern, requiring a series of image-processing steps to derive cell force maps. For a moiré pattern, the light intensity may be expressed as:

$$I(x,y) = a(x,y) + b(x,y)[\exp(2\pi j f_0 x + \Phi(x,y))] \quad (1)$$

where $a(x,y)$ is the background intensity, $b(x,y)$ is the amplitude of the moiré pattern, f_0 is the frequency of the moiré pattern and the phase information, and $\Phi(x,y)$ contains the deformation of the moiré pattern. In order to compute the contraction force distribution from the moiré patterns, a Fourier transform was applied to the moiré patterns. After frequency filtering, the frequency carrying the information of the moiré fringes was selected from the original frequency map. Subsequently, a reverse Fourier transform was carried out on the filtered frequency domain image and a matrix of complex numbers was obtained. The phase of each complex element in the matrix is calculated and, subsequently, a phase unwrapping algorithm was applied to the wrapped phase images to eliminate 2π jumps, yielding unwrapped phase images. By comparing the unwrapped phase map with the phase map derived before cell spreading and contracting, the average ascending trend could be subtracted and the deformation field derived. The deformation field is linearly correlated with the force distribution described as:

$$u(x,y) = d\Phi(x,y)/2\pi \quad (2)$$

which allows for the simple derivation of a cellular force map using the following relationship:

$$F(x,y) = k \cdot u(x,y) \quad (3)$$

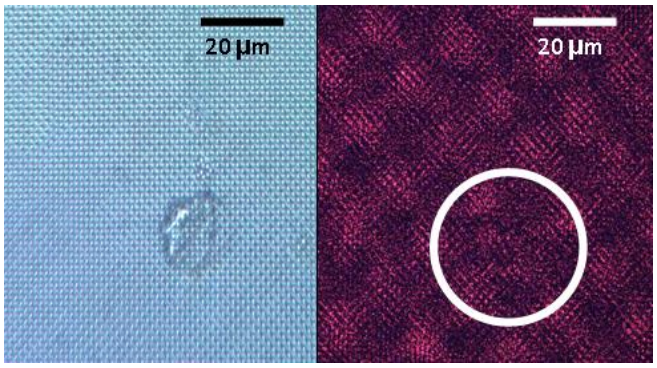

Figure 4: Microscopic image of neonatal rat ventricular myocyte cell cultured on the double-sided pillar arrays (left). Moiré pattern generated by the deformed cell (right). Circle indicates the distorted moiré grid. Note that the pillar deformation is readily visible in the moiré pattern due to the inherent magnification effect of the moiré phenomenon.

Following seeding of the DMPAs with the neonatal rat ventricular myocytes, pillars on the cell culture side of the substrate were deformed by exertion of cellular traction forces (Figure 4). Given the deformation of one of the matched patterns of the DMPAs, distorted moiré patterns were formed, yielding the capacity for cellular force mapping as detailed above (Figure 4). Due to the magnification of moiré effect, though the deformation of the pillars in the microscopic image is unapparent to visual inspection, the magnified deformation of one grid within the moiré pattern (represented by dashed circle) is readily apparent using the 40X objective.

Utilizing the image processing algorithm detailed above, the deformed moire pattern demonstrated in Figure 4 was converted into a cell force map shown in Figure 5. In the case of the moiré force mapping method, the peak value of the NRVM contraction force was found to approximate 120 nN, with the maximal force located at the left side of the cell body. Figure 5 also illustrates the force map generated by calculating each pillar's displacement using the conventional microscopy-based approach which serves as a reference standard. The peak value of the cellular force using this approach was also found to be at the leftward periphery of the cell with a value of approximately 132 nN. Compared to this direct measurement approach using the conventional microscopy image, the cellular force derivation using the moiré mapping method is consistent with this reference standard method in force magnitude, but is significantly less time-consuming as the force map is generated from a larger field of view without observing individual pillars, a direct result of the magnification effect. This capacity to efficiently derive whole-field cellular forces in real-time offers a significant advantage compared to the conventional approach.

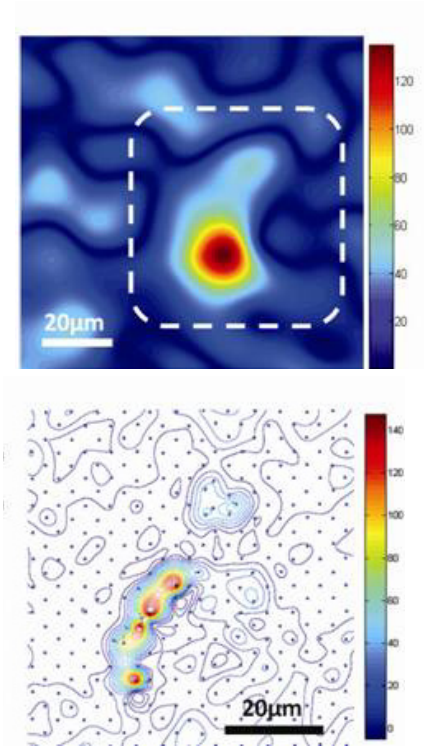

Figure 5: Comparison of force map generated by moiré method (top) and conventional microscopic image analysis (bottom).

CONCLUSION

In summary, this work reports a double sided micropillar array capable of generating moiré patterns that map cellular force distribution without utilizing any additional reference substrate or light source. These unique arrays improve the efficiency of moiré pattern generation as well as optimize the moiré contrast. NRVM

were employed to validate the DMPA-enabled optomechanical approach, demonstrating the capacity for efficiently generating accurate cellular force maps. The double-sided structure reported in this work has the potential for enabling the facile integration of moiré-based cell force mapping with microfabricated cell culture environments or lab-on-a-chip devices.

ACKNOWLEDGEMENT

The authors would like to express thanks and gratitude for the contributions from the staff of the Photonics Center of Boston University. We also thank Xiaoguang Zhao, Erin Roberts, Paul Lou, and other members at the Laboratory for Microsystems Technology (LMST), Boston University, for thoughtful discussions and help with the experiments.

REFERENCES

[1] V. Vogel and M. Sheetz, "Local Force and Geometry Sensing Regulate Cell Functions", Nature Reviews. Molecular Cell Biology, 7, 265 (2006).

[2] Z. Li, J. Song, G. Mantini, M. Lu, H. Fang, C. Falconi, L. Chen, and Z. Wang, "Quantifying the Traction Force of a Single Cell by Aligned Silicon Nanowire Array", Nano Letters, 9, 3575 (2009).

[3] M. T. Yang, J. Fu, Y. K. Wang, R. A. Desai, and C. S. Chen, "Assaying Stem Cell Mechanobiology on Microfabricated Elastomeric Substrates with Geometrically Modulated Rigidity", Nature Protocols, 6, 187 (2011).

[4] B. Han, D. Post, and P. Ifju, "Moiré Interferometry for Engineering Mechanics: Current Practices and Future Developments", The Journal of Strain Analysis for Engineering Design, 36, 101 (2001).

[5] X. Zheng and X. Zhang, "An Optical Moiré Technique for Cell Traction Force Mapping", Journal of Micromechanics and Microengineering, 18, 125006 (2008).

CONTACT

* X. Zhang, tel: + 1.617.358.2702; xinz@bu.edu

A MAGNETIC FLOW CYTOMETER WITH INTEGRATED MICROFLUIDICS

Pramod Murali[1], Igor Izyumin[1], Sandeep Prabhu[1,2], Daniel Cohen[1,3], Bernhard Boser[1]
[1]University of California, Berkeley, USA
[2]Currently at University of California, Los Angeles, USA
[3]Currently at Stanford University, Palo Alto, USA

ABSTRACT

A chip scale flow cytometer realized in a standard CMOS process uses magnetic beads as labels. The material dependent complex susceptibility is used to differentiate between label classes for multi-target flow cytometry. The chip is embedded in a microfluidic cartridge and operation verified with an embryonic fibroblast assay.

INTRODUCTION

Flow cytometers are used to quantify cells or other particles in a biological sample such as blood and are indispensable tools in hematology, medical diagnostics, and food safety. Current optical flow cytometers use wavelength specific fluorescent molecules as tags. Although this approach achieves high throughput, the equipment is quite costly, too large for fieldwork, and suffers from background noise that requires calibration and extensive sample preparation. Replacing the fluorescent labels with superparamagnetic nanoparticles alleviates these problems, thereby enabling point of care flow cytometry [1].

In this paper, we present a flow cytometer that uses magnetic labels and a custom CMOS integrated circuit for self-contained detection. Details of the electronic circuit design are presented in [2]. This paper describes the theory of operation and microfluidic integration. The first section describes how susceptibility can be used to differentiate multiple magnetic label classes analogous to the wavelength division multiplexing commonly employed with fluorophores. This is followed by a description of the self-contained magnetic sensor amenable for integration in a standard IC technology, embedding in a microfluidic cartridge and experimental verification.

COMPLEX SUSCEPTIBILITY OF MAGNETIC NANOPARTICLES

Many applications of flow cytometry require establishing the relative counts of several distinct species such as CDs and CD4 cells. Optical approaches meet this requirement with labels that fluoresce at different wavelengths. Magnetic labels instead rely on differences of the magnetic material properties.

The labels used in these experiments consist of superparamagnetic single-domain nanoparticles with 8nm-15nm diameter encapsulated in a polymer or silica matrix. The complex susceptibility [3]

$$\chi(\omega) = \chi'(\omega) - i\chi''(\omega)$$

of such an assembly of nanoparticles can be described in terms of its parallel and perpendicular components [4],

$$\chi(\omega) = -\left(\chi_{\parallel}(\omega) + \chi_{\perp}(\omega)\right)$$

where, owing to their characteristics, $\chi_{\parallel}(\omega)$ and $\chi_{\perp}(\omega)$ are also referred to as the relaxation and resonant components of susceptibility.

Relaxation is an exponential function of nano-particle volume V, while resonance is primarily affected by the effective magnetic anisotropy constant K of the nanoparticle, a material property [4].

Either effect can, in principle, be used to distinguish between different labels, fabricated in the first case from nanoparticles of different size and different materials in the second case.

Figure 1 shows the simulated phase angle of the susceptibility as a function of frequency for 6nm and 8nm diameter nanoparticles, respectively made of the same material (magnetite, $\overline{K}=12\times10^3$J/m^3). The dotted lines apply to mono-disperse nanoparticles and demonstrate a phase difference of up to 28 degrees at 475 kHz that can be easily detected.

In practice, it is difficult to manufacture mono-disperse nanoparticles. The solid line represents the frequency response of an assembly of particles with a more realistic log-normal volume distribution with standard deviation σ_V=0.3 and log-normal K distribution with standard deviation σ_K=0.58. In this case the maximum phase difference between labels shrinks to 8.3 degrees, a value that is easily exceeded by particle-to-particle variations and is thus not suitable for differentiation.

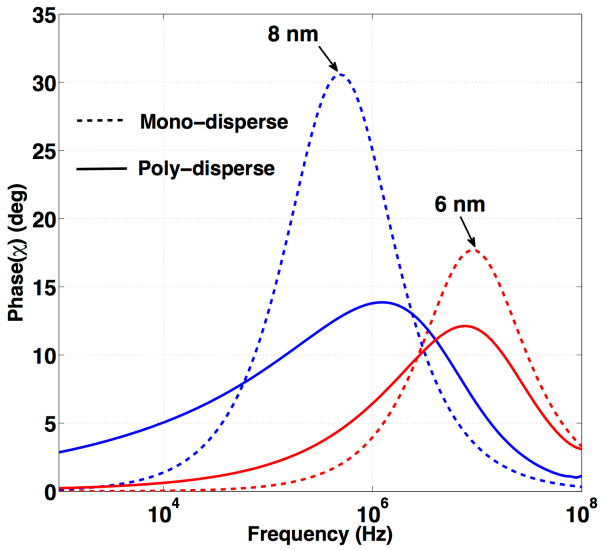

Figure 1. Phase vs. frequency of relaxation component of complex susceptibility for mono-disperse (dotted) and particles with log-normal size and K distribution.

Unlike relaxation, magnetic resonance is only weakly sensitive to nanoparticle volume and is instead dominated by material properties. Figure 2 shows the frequency response of magnetic labels consisting of two different materials with magnetic anisotropy constant $\overline{K}=12\times10^3$J/m^3 (magnetite) with log-normal distribution (σ_K=0.58) and $\overline{K}=70\times10^3$J/m^3 (cobalt) with log-normal distribution (σ_K=0.1) respectively for identical particle volume distributions as before. At 1.2GHz, the phase difference is

9781940470016/HH2014/$25©2014TRF
DOI 10.31438/trf.hh2014.44

greater than 70° thus enabling reliable classification.

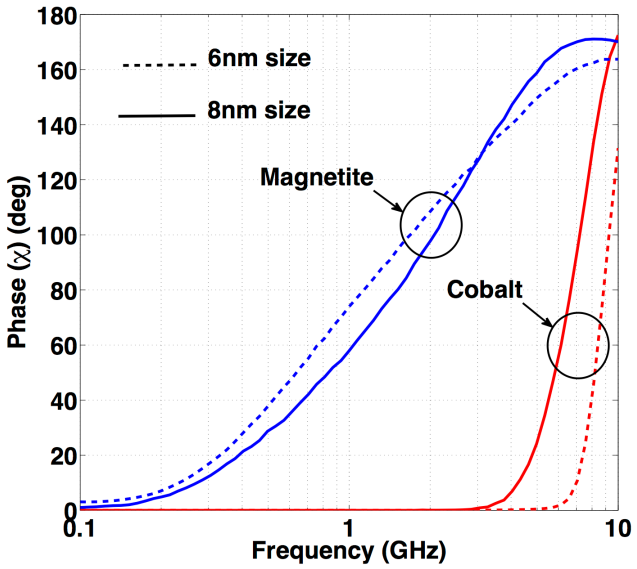

Figure 2: *Phase vs. frequency of resonant component of complex susceptibility for poly-disperse particles of mean diameter 6nm and 8nm with log-normal distribution for two different materials.*

SENSOR DESIGN

Identification of different label classes based on magnetic resonance requires a sensor capable of magnetizing at frequencies in excess of 1GHz to measure not only the magnitude, but also the phase of the response. On-chip coils fabricated in standard CMOS processes are ideally suited for this task. The sensor consists of a polarization coil driven by an AC waveform at the detection frequency to generate a field that is uniform in the detection area.

A pair of secondary coils is used to detect the presence and phase response of a magnetic particle as shown in Figure 3. Without a particle present, magnetic field in both coils is identical and produces equal responses. Series connection with opposite winding directions results in a net zero response.

The presence of a bead modifies the coupling of the polarization field. By choosing the size of the pick-up coils larger than the particles (approximately 10µm for typical cells), the change is localized to one of the two coils and the resulting imbalance produces a voltage at the sensor output. In the actual design slightly larger coils with dimension 30µm by 30µm are chosen as a compromise between detection area and sensitivity.

A cell decorated with magnetic particles and passing over the two detection coils results in a bipolar response. For clarity, the GHz modulation is omitted from the graph. Demodulation occurs on-chip with a synchronous quadrature receiver [2].

INTEGRATION OF CMOS CHIP WITH MICROFLUIDCS

Figure 5 shows the microfluidic setup. The surface of the chip is exposed to a 50µm tall and 200µm wide channel that guides labeled cells over the detection area. Although the magnetic labels do not require optical access, a transparent setup has been chosen to aid debugging. The setup can be easily disassembled for cleaning. In the actual application, a disposable cartridge is preferred.

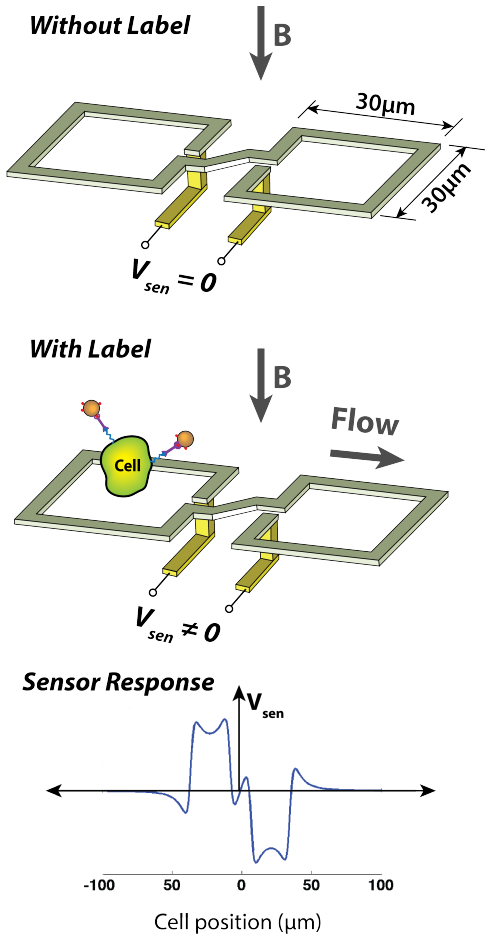

Figure 3: Schematic showing the secondary pick-up coil for detecting the change in magnetic flux due to the presence of a cell decorated with magnetic labels.

Figure 4 shows the fabrication process starting with a standard printed circuit board (PCB) used for mechanical support and electrical interconnects. An adhesive tape temporarily holds the 2.5×2.5mm^2 CMOS chip in place inside a cavity in the PCB and avoids steps in the final microfluidic channel that would result in unwanted turbulence. In the next step, the cavity is filled with epoxy and allowed to cure for 1 hour. The tape is then removed from the PCB surface. The chip is then wire-bonded to the PCB, and the wirebonds are protected with Crystalbond (Structure Probe, Inc.).

The PDMS micro-channel is fabricated with an SU8 mold (Stanford Microfluidics Foundry). PDMS (Sylgard 184) was mixed with the polymerizing agent in the ratio 10:1, degassed for half an hour and poured on the mold and allowed to cure at 60°C for 3 hours. The PDMS is cut to appropriate dimensions.

The PDMS micro-channel is placed on the chip and aligned visually to the detection coil on the chip using a microscope. A cavity is made in the PDMS micro-channel to accommodate the wirebonds. A glass slide applies uniform pressure and compression seals the channel against the PCB using acrylic supports. Figure 5 schematically shows the device after complete integration.

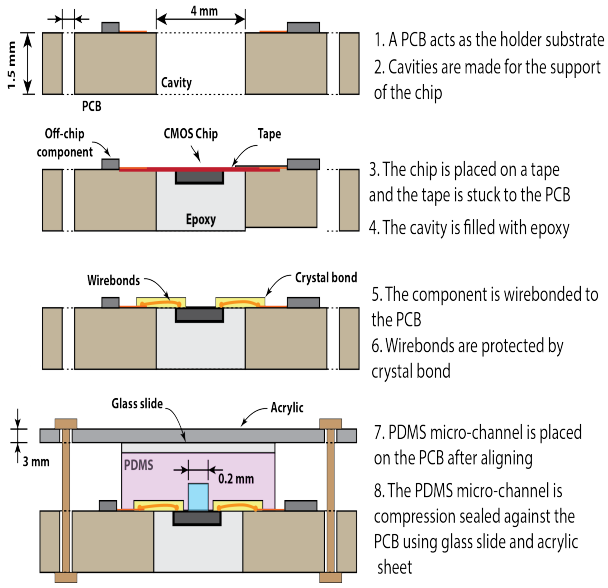

Figure 4: Steps to integrate the CMOS chip with PDMS micro-channel.

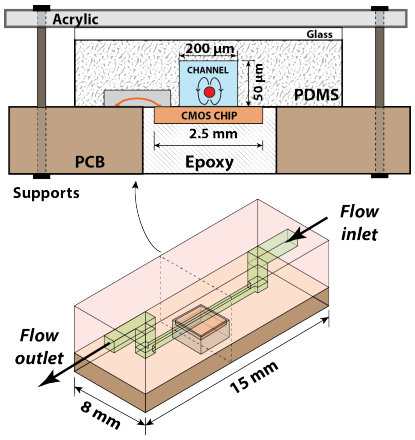

Figure 5. Schematic showing the cross-section of the integrated flow cytometer.

MAGNETIC LABELING OF CELLS

Device operation is demonstrated with mouse embryonic fibroblasts (mEFs) conjugated to magnetic labels as shown in Figure 6. The mEFs are obtained from the Tissue Culture Facility at UC Berkeley. The cells are grown in standard DMEM (Dulbecco's Modified Eagle Medium) with added penicillin-streptomycin and 10% FBS (fetal bovine serum). Cells are maintained at 37°C and 5% CO_2 in air. An antibody buffer consisting of 1X PBS, 0.5 % BSA, and 2 mM EDTA was prepared fresh before the experiment.

Once cells achieve 75-80 % confluence, the cells are labeled with biotinylated mouse CD-29 primary antibody [Biolegend] at a concentration of 0.25µg (from a stock solution of 0.5 mg/ml) per 10^6 cells. Following a 15 minute incubation at 37°C, the cells are washed twice with buffer. Then, 2µl of streptavidin coated Dynabeads [5] (from a stock solution of $4x10^8$ beads/ml) per 10^6 cells is diluted in buffer, added to the cells as a secondary label for the CD-29, and incubated at 37°C for another 15 minutes. Following incubation, the excess beads are washed off with buffer three times with rigorous mixing. It is imperative that cells be visualized under a microscope to ensure that excess beads are removed as they may overwhelm the cell detection by the chip. The cells are then treated with 0.25% trypsin for 5 minutes at 37°C. The trypsin was neutralized with calcium-free PBS; necessary because calcium would allow cells to aggregate. These cells are harvested and run through the cytometer within 2 hours of harvesting.

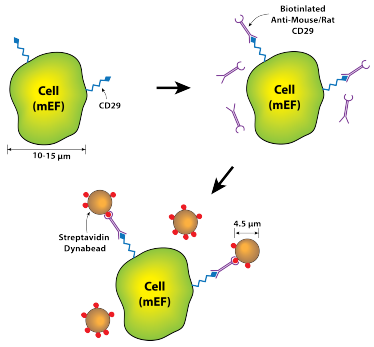

Figure 6. Magnetic labeling of mouse stem cells (mEFs).

EXPERIMENTAL SETUP

The setup for carrying out the experiment is shown in Figure 7. The micro-channel is initially flushed with DI water to remove any contaminants and air bubbles. The sample containing the labeled cells is connected to the inlet port of the micro-channel. A syringe pump controlled by custom software is connected at the output port of the micro-channel and applies suction to carry the cells through the micro-channel. The flow rate for measurements is about 1mm/s. In a final design this function can be integrated (e.g. using a micro-pump or degas-driven flow [6]).

The circuits on PCB provide the supply and biasing required for the CMOS chip. The output of the chip is buffered and amplified and then digitized with an NI PXIe-5122 data acquisition system. Custom software implemented in NI LabView digitally processes the signals. A microscope is used to help visualize the flow of labeled cells over the sensor coil.

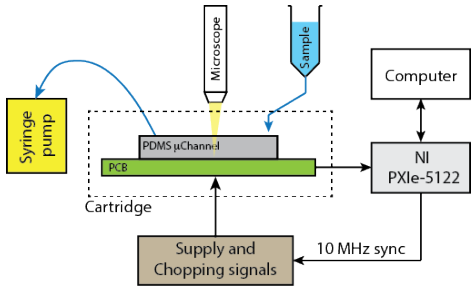

Figure 7: Experimental setup for flow measurements.

MEASUREMENT RESULTS

Figure 8 shows the completed flow cytometer. The inset shows the microfluidic channel on the surface of the CMOS chip with a

magnetically labeled cell flowing over the sensor. The measured bipolar response of the chip to Dynabeads is shown in Figure 9. The measured response to labeled cells is presented in [2]. The throughput of the system is 50 beads/s or 20 labeled cells/s, which is comparable to the point-of-care flow cytometer described in [1]. The labeled cells are detected with an SNR of 16dB. Figure 10 shows the results of a phase measurement of iron oxide and cobalt beads (Ocean Nanotech). The measured phase angle is $<\varnothing_{Dynabead}>$=91° (σ=9°) and $<\varnothing_{Cobalt}>$= 56° (σ=6°) and is independent of magnitude. This is expected since Dynabeads made of iron oxide has smaller $\overline{K}$ compared to cobalt.

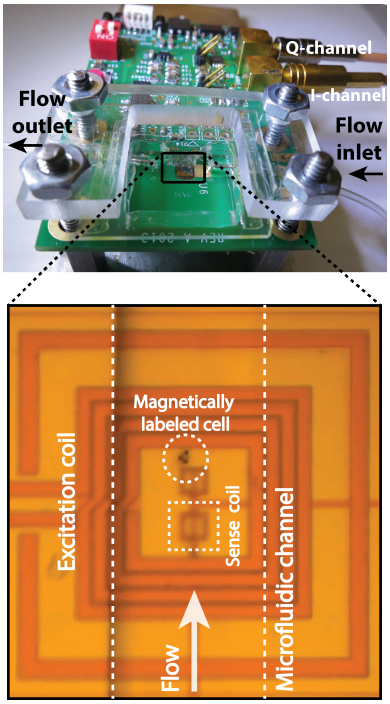

Figure 8: Fabricated flow cytometer cartridge (top) and sensor chip (bottom).

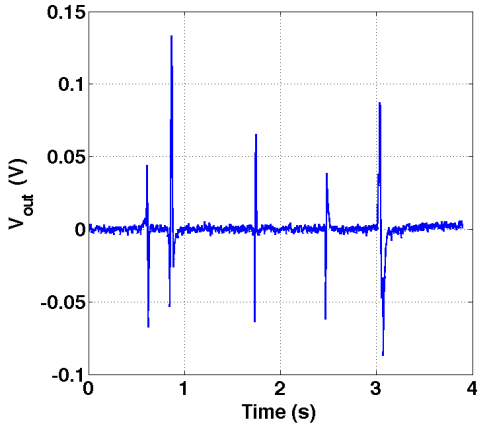

Figure 9. Measured time domain response of the flow cytometer for Dynabeads.

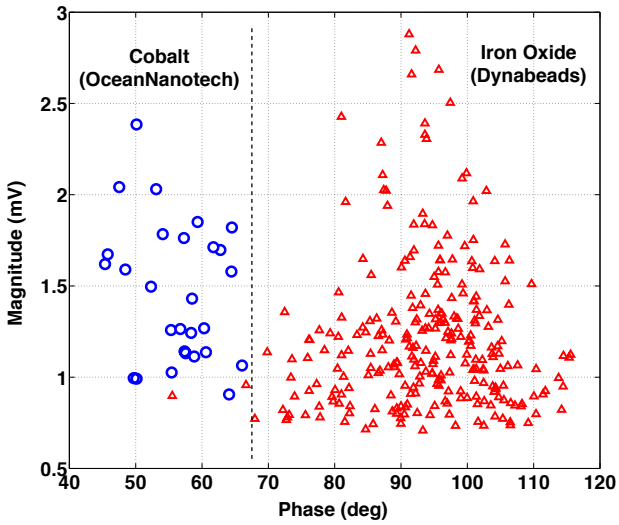

Figure 10: Phase measurement of iron oxide and cobalt beads. A clear differentiation of the two label classes can be seen.

CONCLUSIONS

Magnetic labels allow the entire detection process of a flow cytometer to be realized on a millimeter-sized electronic circuit fabricated in a CMOS process, allowing for a compact and economical implementation that is particularly attractive for point-of-care applications. By measuring not only the magnitude, but also the phase of the induced magnetic field, the chip is capable of differentiating between magnetic labels fabricated from different materials.

REFERENCES

[1] "Time-of-Flight Magnetic Flow Cytometry in Whole Blood with Integrated Sample Preparation." Helou, Michael, et al. Lab on a Chip 13.6 (2013): 1035-1038.

[2] "A CMOS Micro-Flow Cytometer for Magnetic Label Detection and Classification.", P. Murali, et al. 18, ISSCC (2014).

[3] "Wideband Measurement and Analysis Techniques for the Determination of the Frequency-Dependent, Complex Susceptibility of Magnetic Fluids.", P. C. Fannin, Advances in Chemical Physics, Volume 104 (1998), 181-292.

[4] "Experimental and Theoretical Profiles of the Frequency-Dependent Complex Susceptibility of Systems Containing Nanometer-Sized Magnetic Particles.", P. C. Fannin, et al., Physical Review B, vol. 55, no. 21, pp. 14423-14428, 1997.

[5] "Characterization of Dynabeads® by magnetization measurements and Mössbauer Spectroscopy." Fonnum, Geir, et al. Journal of Magnetism and Magnetic Materials 293.1 (2005): 41-47.

[6] "Systematic Characterization of Degas-Driven Flow for Poly (dimethylsiloxane) Microfluidic Devices." Liang, David Y., et al. Biomicrofluidics 5 (2011): 024108.

CONTACT

*Pramod Murali, tel: +1-510-355-4643;
pramodm@eecs.berkeley.edu

A REAL-TIME BACTERIAL BIOFILM CHARACTERIZATION PLATFORM USING A MICROFLUIDIC SYSTEM

S. Subramanian, Y.W. Kim, M.T. Meyer, H.O. Sintim, W.E. Bentley and R. Ghodssi *
University of Maryland, College Park, Maryland, USA

ABSTRACT

We present a real-time multi-experiment biofilm analysis platform using a valve-actuated microfluidic system, designed to reduce growth variance of *in-vitro* biofilms. After 24 hours of biofilm growth in the microfluidic device the biofilms exhibited only a 9% variation in biomass, showing significantly reduced deviation in comparison to the biomass variation seen in our previous work conducted in separate microfluidic channels. A linear array charge-coupled device enabled real-time tracking of both average biomass and localized morphology by monitoring the change in optical density. We demonstrate the multi-experiment capability of the microfluidic device and the spatiotemporal monitoring capacity of the system by tracking the growth of biofilms when subjected to different treatments.

INTRODUCTION

Bacterial biofilms are the primary cause of infections in medical implants and catheters [1]. They are composed of complex communities of bacteria that are enveloped in an extracellular matrix (ECM) [1]. The presence of the ECM restricts the molecular diffusion of typical treatments like antibiotics, thereby requiring higher doses of antibiotics (500-5000x in comparison to planktonic bacteria) for treatment [1, 2]. The widespread use of such high doses of antibiotics for treatment is leading to the emergence of antibiotic-resistant strains. Additionally, increased ingestion of antibiotics also increases the risk of harmful side effects. Therefore, there is an urgent need for the development of new methods for the effective treatment of biofilms. However, the experimental evaluation of biofilm treatment is strongly hindered by the stochastic nature of biofilm growth [3]. Hence, it is required to develop a system that can not only facilitate multi-experiment studies for new treatment evaluation, but also enable the growth of uniform biofilms that can be used as reliable controls.

Previously, we developed microfluidic platforms that utilized simple single channel devices integrated with optical measurement methods for biofilm characterization [3, 4]. However, non-uniform biofilm growth was a key challenge in these microfluidic systems. The biomass variation observed between the single channel devices was about 25%. In this work, we have developed a microfluidic platform that reduces biofilm growth variation to less than 10%. This was achieved by integrating hydraulic valve actuators that were used for sectioning of biofilms grown in a horizontal channel by maintaining a single source of bacterial suspension. The detection of biofilm growth was achieved using a linear array charge-coupled device (CCD) that was used to measure the change in optical density (OD) of the biofilms. This was previously demonstrated as a reliable method for measuring the biomass of bacterial biofilms [3, 4]. The spatial resolution of the CCDs enabled real-time monitoring of both the average biomass variation and the localized biofilm morphology.

We evaluate the performance of the platform by monitoring the growth of *Escherichia coli* (*E. coli*) W3110 biofilms. The biofilm is grown in the center horizontal channel of the microfluidic reactor for 24 hours, following which the center horizontal channel is sectioned into four and each section is then subjected to different treatments for an additional 24 hours. By utilizing one of the biofilm sections as a reference, we ensure that the results of the various experiments performed on the same device are compared to a common control. The three treatments used include a traditional antibiotic (gentamicin), a small molecule inhibitor (autoinducer-2 (AI-2) analog) and a detergent (sodium dodecyl sulfate (SDS)). While antibiotics and detergents are established treatments for bacterial infections, AI-2 analogs have recently been shown to inhibit biofilms by preventing bacterial communication or quorum sensing (QS) that is critical to biofilm formation [5].

Thus, the multi-experiment capability of the microfluidic device enabled the evaluation of multiple treatments on the same biofilm while providing an integrated control. Additionally, the integration of the valved microfluidic reactor with a real-time OD monitoring system enabled high-throughput analyses on uniform biofilms and demonstrated significant reduction of biofilm growth in an analog environment. Furthermore, the unique capabilities of this microsystem can be useful in various biological studies, including new drug discovery.

METHODS

Microfluidic Biofilm-Sectioning Device

The microfluidic biofilm-sectioning device consists of a single horizontal channel that can be sectioned into multiple parts using hydraulically actuated push-down valves. The push-down valves can be operated in open or close mode through the application of pressure through the valve actuation channel. In the push-down valve configuration, a membrane between the channels is pushed down using pneumatic or hydraulic pressure, thus sealing

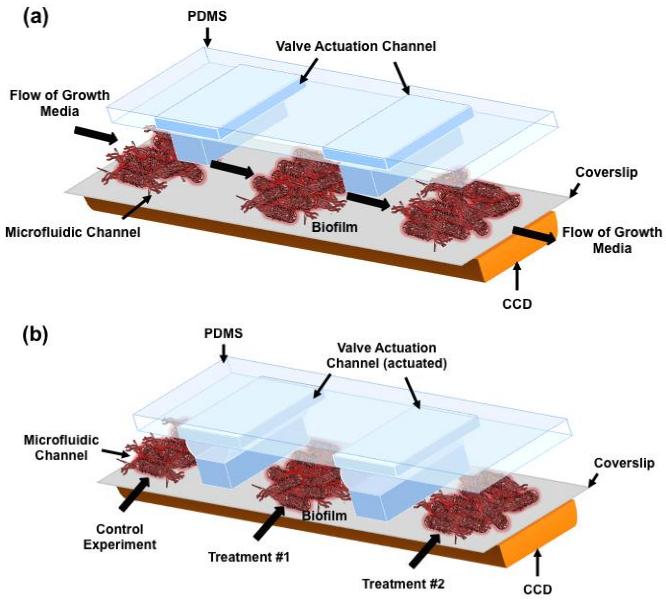

Figure 1: Schematic of platform operation. (a) Biofilm growth in the open channel, (b) Sectioning of the grown biofilms (actuated valves). The CCD monitors the biofilm growth across the length of the microfluidic channel in real-time.

9781940470016/HH2014/$25©2014TRF
DOI 10.31438/trf.hh2014.45

the lower microfluidic channel that contains the fluid of interest [6].

The valved microfluidic biofilm reactor is a Polydimethylsiloxane (PDMS) based two-level device. On the top is the valve actuation channel layer and on the bottom is the microfluidic channel layer. A schematic of the valve-actuated microfluidic system and the continuous OD monitoring system is shown in Figure 1. A single uniform biofilm is grown in the center horizontal channel by actuating only one set of valves known as the side valves. The biofilm is then divided into multiple sections by hydraulically actuating a second set of valves called the sectioning valves, thereby enabling multi-experiment studies on the same biofilm.

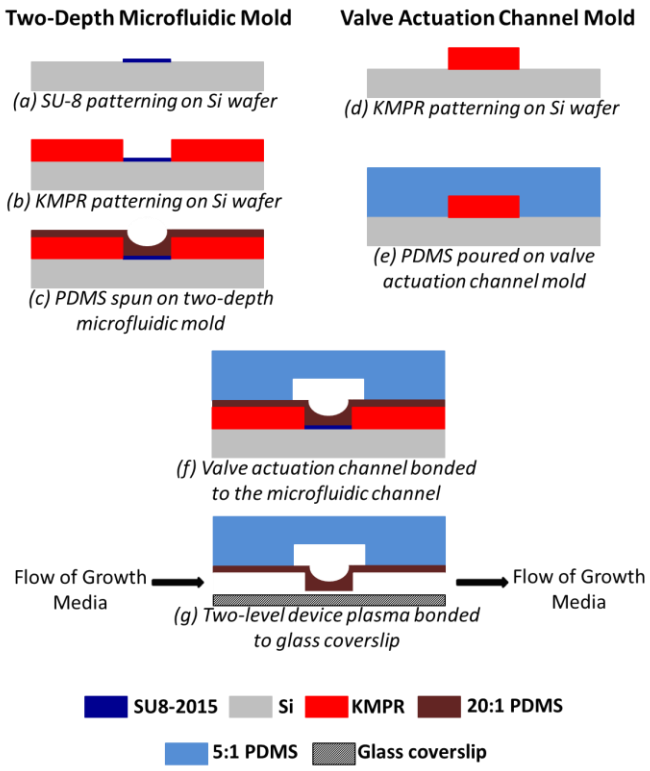

Figure 2: Fabrication process flow for the two-level valved microfluidic device. The direction of the fluid flow is along the page, from the left to the right of the microfluidic channel just above the coverslip, as indicated by the arrows. The valve actuation channel is perpendicular to the fluidic channel.

We fabricate the two-level microfluidic device using traditional multilayer soft lithography techniques. The process flow for the fabrication of the device molds and the microfluidic device are shown in Figure 2. The two-step photolithography using negative photoresists, a 20 µm thick valve region using SU8-2015 allows for easy sealing of the valves and a 100 µm tall microfluidic channel region using KMPR-1050, provides the necessary growth area for biofilms. This process allows for the patterning of a multi-depth microfluidic mold without the need for additional passivation of the first resist layer, thereby demonstrating a simplified and reliable fabrication process flow (Figure 2 (a)-(b)). The valve actuation channel mold is fabricated by patterning a single 100 µm tall KMPR-1050 layer (Figure 2 (d)). Both molds can be reused to produce multiple devices. PDMS (Sylgard 184, Dow Corning, USA) in the ratio of 20:1 silicone elastomer to curing agent is spun over the two-depth microfluidic mold (Figure 2 (c)), and a ratio of 5:1 silicone elastomer to curing agent is poured over the valve actuation channel (Figure 2 (e)) and both molds are cured at 60 ºC for 15 minutes. The valve actuation channel layer is peeled off the mold and the inlet ports are punched using a 2 mm dermatological punch. The two PDMS layers are then aligned and baked at 80 ºC for 3 hours to promote bonding between them. The final two-level device is peeled off the microfluidic channel mold and irreversibly plasma bonded to a glass coverslip. Ports for interfacing the inlets and outlets of the microfluidic channel are finally punched using the 2 mm dermatological hole punch. Tygon tubing is connected to the inlets and outlets of the device using a tubing coupler, and the other end of the tubing is connected to a syringe pump (KDS-230, KD Scientific). The valve actuation channel is primed with water mixed with standard food coloring at a rate of 20 µl/hr, to enable hydraulic actuation.

Optical Density Monitoring Platform

The optical density monitoring of biofilms has been previously demonstrated using the CCD devices [4]. In this work, the CCDs (TSL1402R, Texas Advanced Optoelectronic Solutions) feature 258 x 1 linear pixel arrays with individual photodiodes measuring 120 µm (H) by 70 µm (W) spaced 55 µm apart, thereby spanning an overall array length of 1.6 cm. An external diffusive edge-lit LED light panel (Luminous Film USA) was used to illuminate the platform uniformly. The wavelength of the light source was tuned to be at 630 nm in order to match the sensitivity of the CCDs. The PDMS microchannels that were bonded to a transparent coverslip substrate allow for light transmission to the CCD photopixels. The CCD devices were actuated by an external power supply and function generators (Agilent E3631A) and were used to control the data sampling and provide power to the electronics. The signal readout from the device was achieved using a data acquisition card (NI USB-6221, National Instruments) that was programed to record data using a Labview program.

Experimental Procedure

The CCD platform was used to continuously monitor the growth of *E. coli* W3110 biofilms from time t=0 hrs to t=48 hrs, in all the sections of the microfluidic device. An overnight culture of *E. coli* W3110 suspension was diluted in Luria Broth (LB) media, to a final OD_{600} of 0.3 AU. Biofilm growth is achieved by initially seeding the center horizontal microfluidic channel (side valves actuated) with the diluted bacterial suspension for 2 hours at 37 ºC with no flow to allow for microbial attachment to the substrate. Fresh LB media is then flowed through the center horizontal channel at a rate of 10 µl/hr using a syringe pump for 24 hours (Figure 1a and 3a). This provides the bacteria with the necessary nutrients and environment that promotes biofilm growth. We note that the increased shear in the valve region prevents biofilm growth locally. Following the growth, the center channel was sectioned into four by actuating the sectioning valves (Figure 1b and 3b). Different treatment: control (LB media, section 1), antibiotic (gentamicin, 10 µg/mL, section 2), a small molecule biofilm growth inhibitor, (autoinducer-2 analog (AI-2 analog), 100 µM, section 3), and a detergent (sodium dodecyl sulfate (SDS), 0.2%, section 4), were introduced into the four sections of the device for an additional 24 hours at the rate of 10 µl/hr. The control biofilm section was provided with LB media at the same flow rate as the other sections in order to provide a reference, thereby ensuring that the results of the treatments are compared to an integrated control.

OD measurements were recorded every 8 minutes, across the length of the microfluidic channel, for each section of the device.

These measurements enabled the monitoring of the spatio-temporal development of the bacterial biofilms in each section of the microfluidic device, both during the biofilm growth and treatment.

RESULTS AND DISCUSSION

Microfluidic Valve and Device Operation

The valves of the microfluidic device belong to one of the following two sets: 1) the side valves, and 2) the sectioning valves. Either set of valves can be actuated by application of 10 psi of pressurized nitrogen. By actuating the side valves of the device as shown in Figure 3 (a), the fluid can be directed from the inlet to the outlet of the center horizontal channel of the device, whereas actuating the sectioning valves as shown in Figure 3 (b) results in the center horizontal channel being sectioned into four sections of equal length. Thus, both sets of valves were successfully demonstrated. Therefore, using this platform, a uniform biofilm grown in the horizontal channel of the device (Figure 3a), is sectioned into four using the hydraulically actuated valves following which each section is individually treated using different methods (Figure 3b).

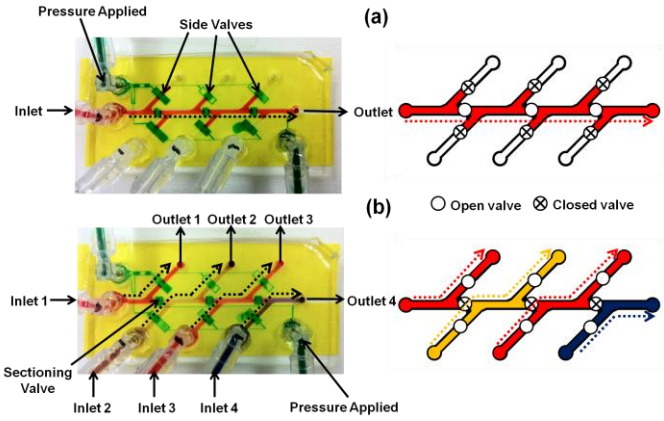

Figure 3: Device in different modes of operation. (a) Side valves actuated to allow for biofilm growth in the center channel, (b) Sectioning valves actuated to allow introduction of four different treatments in four sections of the device. The four sections are shown in different colors (from left to right): section 1 (red), section 2 (yellow), section 3 (red), and section 4 (blue). The dotted arrows show the direction of fluid flow.

Optical Density Monitoring

It has been previously demonstrated that the total biomass of the biofilm can be indirectly measured by monitoring the change in OD [3, 4]. Figure 4 shows the measured average change in OD during biofilm growth in each of the four sections of the device with respect to the baseline OD measured at time t=0 hrs. The error bars represent the spatial variation of the biofilm across the length of the microfluidic section. After 24 hours of growth, the change in OD in each section is observed to converge to a single point. Statistical correlation was demonstrated between the OD measurements obtained for the four sections at the end of 24 hours (ANOVA, P > 0.05), thereby validating the growth of a uniform biofilm across the center channel. After 24 hours of growth, the variation in biomass between the four sections was calculated to be only 9%, as compared to the 20-25% biomass variation seen in our previous work conducted in separate microfluidic channels [3]. Although a sharp increase in OD, corresponding to an increase in biomass is observed around t=18 hrs during the biofilm growth, the OD then rapidly decreases and converges to a single point. We hypothesize that this reduction in biomass and therefore the convergence of the OD of the four sections of the device to a single point at t=24 hrs is possibly a result of a self-leveling effect due to the increased shear experienced by the thick biofilms in the constricted microfluidic channels.

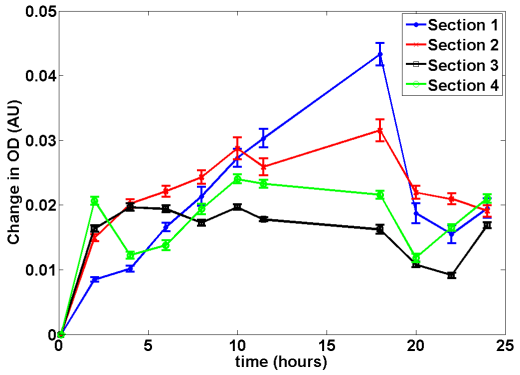

Figure 4: Measured average change in OD across the length of each section (n=162) at representative time points during biofilm growth. The error bars represent the spatial variance of the biofilm in each section of the channel. The variation in OD across the four sections was observed to reduce to 9% (P>0.05) after 24 hours of growth. It is hypothesized the reduction in biomass variation between sections is possibly a result of a self-leveling effect due to increased shear in constricted channels.

Figure 5 plots the change in OD during the 24-hour biofilm treatment. The three treatments, the antibiotic (gentamicin, 10 µg/mL), the small molecule biofilm growth inhibitor, (AI-2 analog, 100 µM), and the detergent (sodium dodecyl sulfate (SDS), 0.2%) applied to sections 2, 3, and 4 respectively, showed a reduction in biofilm growth compared to the control section (pure LB media, section 1). As seen from Figure 5, the section 3 treated with the AI-2 analog treatment resulted in the slowest growth. This correlates with previously obtained results which demonstrate the efficacy of analogs to interrupt the bacterial communication in

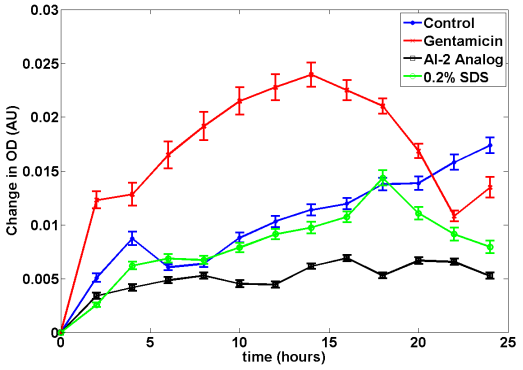

Figure 5: Measured average change in OD across the length of each biofilm section (n=162) at representative time points, during biofilm treatment in the four sections. The section treated with AI-2 analog shows the least increase in biomass. The error bars represent the spatial variation of the biofilm in each section of the microfluidic channel.

biofilms, also known as quorum sensing (QS) that is required for biofilm growth, thereby reducing increase of total biomass [5, 7].

The percentage relative change in average biomass was also calculated for each section of the device after the 24-hour treatment. It is calculated as the ratio of the increase in biomass after treatment to the total biomass formed at the end of the initial 24-hour biofilm growth. The equation used to calculate the percentage relative change in average biomass and the calculated values for each section are plotted in Figure 6a. As expected, the control shows the most increase in biomass, with a 166% relative increase in average biomass. Treatment with gentamicin resulted in a small decrease in biomass in comparison to the control and showed a 114% increase in average biomass. The AI-2 analog and the detergent (SDS) resulted in the similar reduction in biomass growth with relative change in average biomass of 68% and 66%

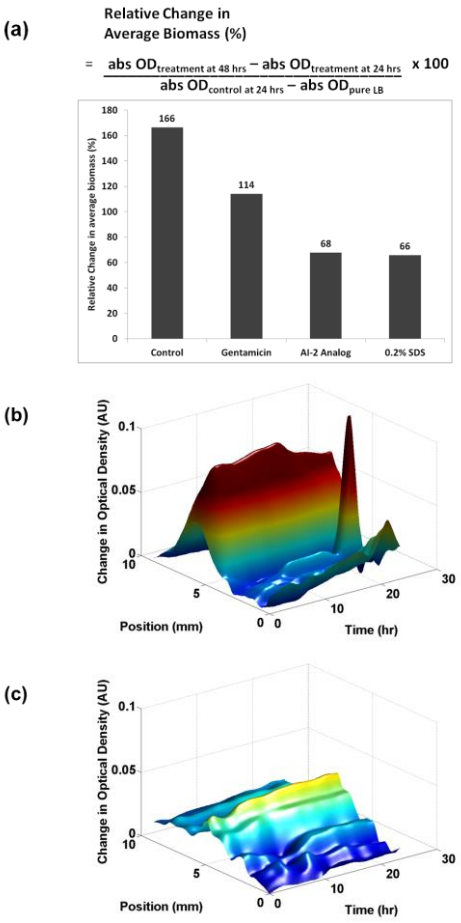

Figure 6: (a) Relative percentage change in average biomass calculated using the OD measured after the biofilm treatment in each of the four sections of the microfluidic optical platform. 3D spatiotemporal plot of biofilm during treatment in (b) section 1 (control) showing a significant change in OD (~ 0.1 AU) indicative of a large increase in biomass, and (c) section 3 (AI-2 analog treatment) showing a smaller change in OD (~ 0.03 AU) indicative of a less significant increase in biomass.

respectively. Specifically, the analog reduced the average biomass 88% more than the antibiotic. Additionally, Figures 6 (b) and 6 (c) demonstrates the capability of this OD based real-time monitoring system to track the localized change in biofilm morphology thereby alleviating the need for additional imaging equipment. As shown in the plots, the control (Figure 6 (b)) shows a significant change in OD (~ 0.1 AU) indicative of a large increase in biomass, whereas the section treated with AI-2 analog (Figure 6 (c)) shows a much smaller change in OD (~ 0.03 AU). These spatiotemporal plots provide a 3-dimensional representation of the reduction in biofilm growth due to analog treatment, as compared to non-treated biofilms.

CONCLUSIONS

The growth of uniform biofilms using valve-actuated microfluidics for multi-experiment analyses is demonstrated in this work. The biomass variance of the biofilms grown in the microfluidic reactor was significantly lower than the biomass variation of biofilms grown in separate microfluidic channels. Using this platform, three different biofilm treatments were evaluated and compared to the integrated control. Treatment of the biofilm with AI-2 analog resulted in the slowest growth and reduced the average biomass 88% more than the antibiotic. Thus, the unique capability of this valved microfluidic biofilm reactor to section uniform biofilms combined with the real-time OD monitoring platform can facilitate high-throughput biofilm studies, including new drug discovery.

ACKNOWLEDGEMENT

The authors would like to acknowledge the Robert W. Deutsch Foundation for financial support. The authors would also like to thank the Maryland Nanocenter and its Fablab for facility support. Travel support has been generously provided by the Transducer Research Foundation.

REFERENCES

[1] J.W. Costerton, P.S. Stewart, and E.P. Greenberg, “Bacterial Biofilms: A Common Cause of Persistent Infections,” Science, 21, 284 (1999).

[2] H. Anwar, M.K. Dasgupta, and J.W. Costerton, “Testing the susceptibility of bacteria in biofilms to antibacterial agents”, Antimicrobial Agents and Chemotherapy, 34, 2043 (1990).

[3] M.T. Meyer, V. Roy, W.E. Bentley, and R. Ghodssi, “Development and validation of a microfluidic reactor for biofilm monitoring via optical methods,” Journal of Micromechanics and. Microengineering, 21, 054023 (2011).

[4] Y.W. Kim, M.P. Mosteller, M.T. Meyer, H. Ben-Yoav, W.E. Bentley, and R. Ghodssi, “Microfluidic biofilm observation, analysis and treatment (Micro-BOAT) platform”, Technical Digest of the 2012 Solid-State Sensor and Actuator Workshop, Hilton Head Isl., SC, 6/3-6/7, Transducer Research Foundation, Cleveland (2012), pp. 233-236.

[5] V. Roy, M.T. Meyer, A.I. Smith, S. Gamby, H.O. Sintim, R. Ghodssi, and W.E. Bentley, “AI-2 analogs and antibiotics: a synergistic approach to reduce bacterial biofilms”, Applied Microbiology and Biotechnology, 97, 2627 (2013).

[6] V. Studer, G. Hang, A. Pandolfi, M. Ortiz, W.F. Anderson, and S.R. Quake, "Scaling properties of a low-actuation pressure microfluidic valve", Journal of Applied Physics, 95, 393 (2004).

[7] V. Roy, J.A.I. Smith, J. Wang, J.E. Stewart, W.E. Bentley, and H.O. Sintim, “Synthetic analogs tailor native AI-2 signaling across bacterial species”, Journal of American Chemical Society, 132, 11141 (2010).

CONTACT

*R. Ghodssi, tel: +1-301-405-8158; ghodssi@umd.edu

A WHOLE BLOOD SAMPLE-TO-ANSWER LAB-ON-A-CHIP WITH ASYMMETRIC CAPILLARY FORCE BASED BLOOD PLASMA SEPARATOR

Kang Kug Lee and Chong H. Ahn*
Microsystems and BioMEMS Laboratory
Department of Electrical Engineering and Computing Systems,
University of Cincinnati, Cincinnati, Ohio, USA

ABSTRACT

An innovative 'smart' sample-to-answer (S-to-A) polymer lab-on-a-chip (LOC) with asymmetric capillary force based blood/plasma separator has been proposed, developed, and fully characterized for point-of-care clinical testing (POCT) applications. A spray layer-by-layer (LbL) nanoassembly method has been developed and applied for the superhydrophilic surface coated on a cyclic olefin copolymer (COC). Then, the developed superhydrophilic surfaces were designed and optimized for three device applications such as lateral transportation of whole blood in the device by capillary pumping, on-chip whole blood/plasma separation with an asymmetric capillary force, and detection using a capillary-driven lateral flow colorimetric assay. With the integration of the developed three devices, the S-to-A polymer LOC platform has been successfully developed for the colorimetric assay of bovine serum albumin (BSA) from undiluted human whole blood without an external power source.

INTRODUCTION

A blood test is the most common medical diagnostic tool to monitor the health condition of patients who have chronic diseases (such as diabetes) and is of great importance in global health applications. This is because faster or more efficient treatment can be delivered due to the rapid and precise diagnosis of diseases with the human whole blood that contains a massive amount of critical information concerning the function of the body [1]. The blood test is also the best clinical diagnostic for urgent care patients in regions with constrained resources, in the field, or in combat zones. Typical blood tests are performed in a central laboratory which is equipped with bulky and expensive analyzers, and usually require a considerable volume of blood sample, trained personnel, and need relatively long analysis time [2]. Furthermore, the separation of blood plasma from the whole blood is a critical step for most clinical blood analysis based on fluorescence immunoassays to minimize the noise from blood cells interfered with excitation optics. These limitations can be removed with the development of more practical on-chip blood analytical systems.

The microfluidic LOC platform has been developed for the various fields in chemistry, biology, engineering, and biomedical and pharmaceutical research over the past decades [3–6]. With the recent development of microfluidic LOC technology, the miniaturization of laboratory instruments and assays has been realized, leading to lower costs per measurement, reduced sample analysis times, reduced sample volume, and better reproducibility in several applications. Compared with the 96-well based microtiter plate which needs a sample volume of ~100 μL, the LOC requires a sample of less than ~1 μL. More importantly, the assay time can also be reduced from several hours to several minutes. The reduction of assay time is mainly due to the short diffusion length that the molecules must travel to immobilize on the solid phase surface because the cross-sectional dimension of a microchannel is around 10 μm to 100 μm [7]. However, most of the previously reported LOC platforms have limitations in their use because of the need for an external power source in fluid handling such as high-voltage power supplies for the electrokinetic flow, pressure sources such as syringe pumps for the pressure-driven flow, and a mechanical rotator for the centrifugation induced flow [8, 9]. These instruments are often bulky and expensive, and restrict the use of microchips as an integrated on-chip platform for POCT. Furthermore, at a central laboratory equipped with these instruments, the total turnaround time (TAT) from sample-to-result is extended by the time required for the transportation of sample to the central laboratory. Due to these restrictions, it is very desirable to design and develop a further practical POCT platform for the patients who need an urgent or emergence care.

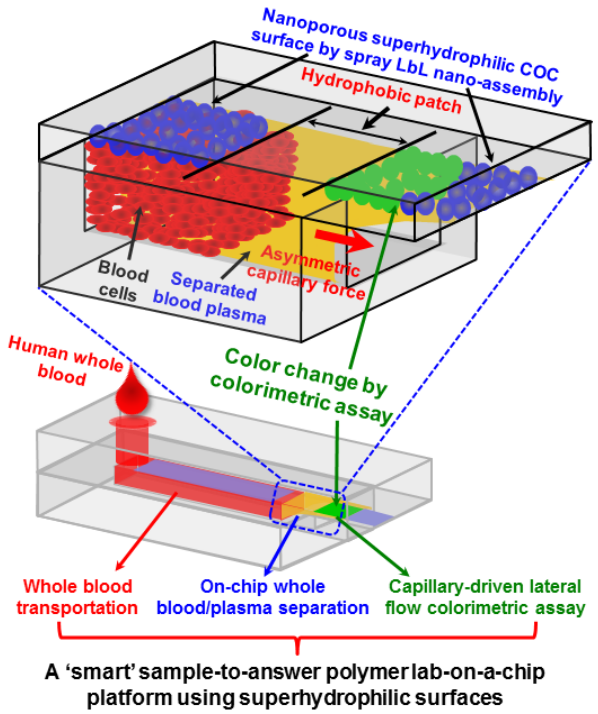

Figure 1: Conceptual diagram for a 'smart' S-to-A polymer LOC platform that simply integrates an on-chip blood/plasma separator with a detection bioassay component without an external power source targeted to POCT applications.

In this work, a new 'smart' whole blood S-to-A polymer LOC platform has been proposed and developed. This platform simply integrates an on-chip blood/plasma separator with a capillary-driven lateral flow colorimetric assay component without an external power source as shown in Figure 1. The developed superhydrophilic surface by a spray LbL nanoassembly method was developed and applied to three specific devices for the lateral transportation of whole blood in the device by capillary pumping, on-chip whole blood/plasma separation with an asymmetric capillary force, and detection using a capillary-driven lateral flow

9781940470016/HH2014/$25©2014TRF
DOI 10.31438/trf.hh2014.46

colorimetric assay. The developed S-to-A polymer LOC can be a practical platform for POCT applications.

DESIGN AND FABRICATION

Microfabrication of S-to-A Polymer LOC Platform

Figure 2 summarizes the fabrication process of the S-to-A polymer LOC platform integrated with an on-chip blood/plasma separator. A CNC milling machine was used for fabricating a master mold. The CNC milling machine manufactures various sizes of structures in the range of μm to mm in scale. The microchannel was designed to transport the introduced whole blood, measure the separated volume of plasma from whole blood, and to characterize the asymmetric capillary movement of blood plasma for colorimetric assay. The volume of the inlet reservoir was approximately 3 μL, which is comparable to the volume of whole blood taken from a finger prick using a commercial device.

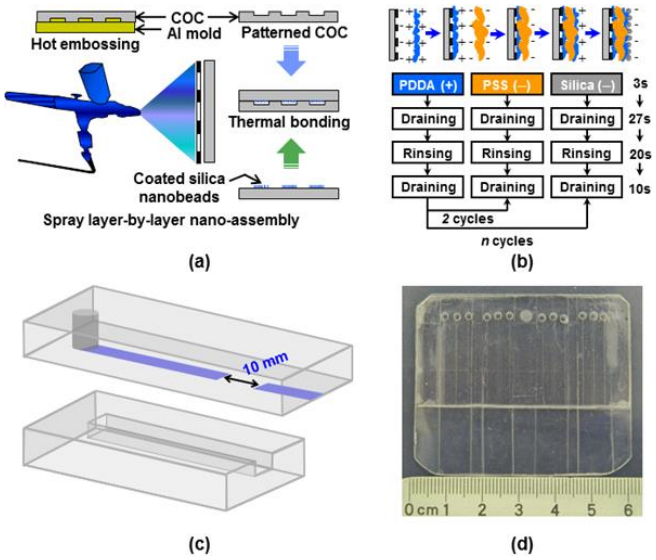

Figure 2: Summary of fabrication process of the S-to-A polymer LOC device.

Then, COC substrates were patterned with microfluidic channels using a hot embossing technique for the spray LbL coating process. After this, the spray LbL nanoassembly process with silica nanoparticles [10] was performed for the asymmetric superhydrophilic surface with a 10 mm hydrophobic patch over the COC microchannel. Finally, the COC substrate with microchannels was bonded with the spray functionalized COC substrate by a thermoplastic fusion bonding technique using an embossing machine [11]. The designed microchannel with 400 μm × 100 μm × 50 mm (W × D × L) and the 10 mm hydrophobic patch are shown in Figure 2(c). The fabricated S-to-A polymer LOC device is shown in Figure 2(d).

Preparation of Colorimetric Assay for Protein Quantification

The 0.3 μL of 500 mM citrate buffer solution (pH 2.5, Fisher Scientific, IL) was placed onto the superhydrophilic COC surfaces, followed by the layered 0.3 μL of 3.3 mM of tetrabromophenol blue (TBPB, Sigma-Aldrich, St. Louis, MO) in 95% ethanol (Fisher Scientific, IL) shown in Figure 3(b). The reagents on the superhydrophilic surface were allowed to dry at 25 ºC for 10 min.

Introducing the spiked whole blood with BSA into the S-to-A polymer LOC device, the blood plasma successfully separated from the whole blood was transferred to the detection zone for colorimetric assay described in Figure 3(d). This colorimetric protein assay uses the nonspecific binding of TBPB to proteins. The reaction is through a combination of electrostatic (sulfonate) and hydrophobic (biaryl quinone methide) interactions [12]. When reacted, the phenol in TBPB deprotonates and the color of the dye shifts from yellow to blue, which indicates the presence of proteins in separated blood plasma [12, 13]. This colorimetric protein assay was calibrated and characterized with spiked concentrations ranging from ranging from 0 – 5 mg/mL (0 μM to 75 μM) of BSA, which is clinically relevant range [14].

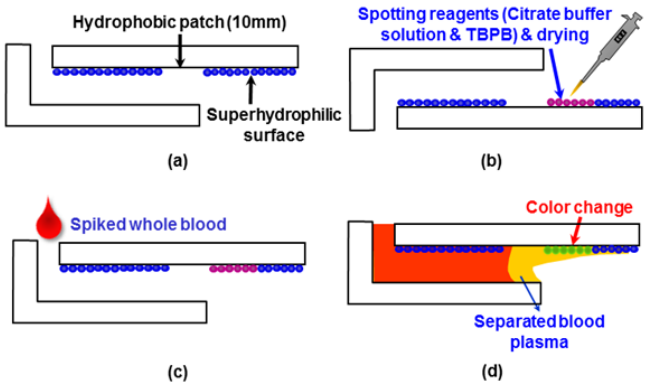

Figure 3: Preparation of colorimetric assay for protein quantification in a S-to-A polymer LOC platform.

EXPERIMENTAL RESULTS

Capillary-driven Lateral Flow Colorimetric Assay

Figure 4 shows a 'smart' S-to-A polymer LOC platform that integrates an on-chip blood/plasma separator with capillary-driven lateral flow colorimetric assay. The reagents for colorimetric assay were placed onto the patterned superhydrophilic surfaces, which were modified by the spray LbL nanoassembly depicted in Figure 4(a). The BSA concentration for spiking in whole blood was measured first using an analyzer in laboratory and then used as a background reference before spiking. Single droplet of 3.0 μL human whole blood, a suitable amount for disposable single-use platform for POCT, spiked with different concentrations of BSA solution were injected into the inlets of the S-to-A LOC device shown in Figure 4(b). When the mixture of whole blood and BSA solution was injected into the inlet of the device, the top superhydrophilic surface generated capillary flow of whole blood through the microchannel. When the mixture encountered the 10 mm hydrophobic patch region, the flow of the whole blood was effectively retarded for a short period of time (< 1 min). This retarding effect caused a continuous selective accumulation of blood cells within the hydrophobic patch region. The movement of the blood cells were effectively reduced, allowing the blood plasma to move forward due to the differences in flow velocity between the cellular component and the blood plasma over the patch region. Thus, the blood plasma was successfully separated from the whole blood throughout this accumulated column of blood cells, a so-called 'self-built-in blood cell microfilter' [15]. The color changes from yellow to blue were obtained in Figure 4(b). The intensity of the blue color was increased depending on the concentrations of BSA spiked in whole blood. Figure 4(c)

shows a magnified image of moving separated blood plasma. This picture demonstrates the filtering efficiency by asymmetric capillary force and the patterned hydrophobic patch.

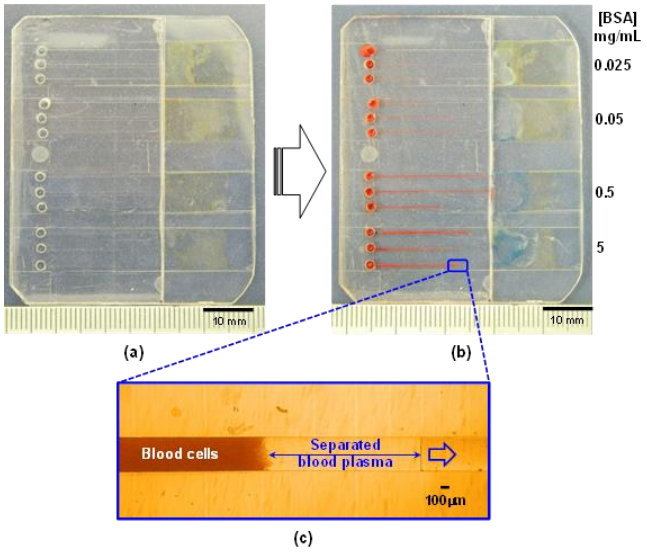

Figure 4: Capillary-driven lateral flow colorimetric assay in a S-to-A polymer LOC device.

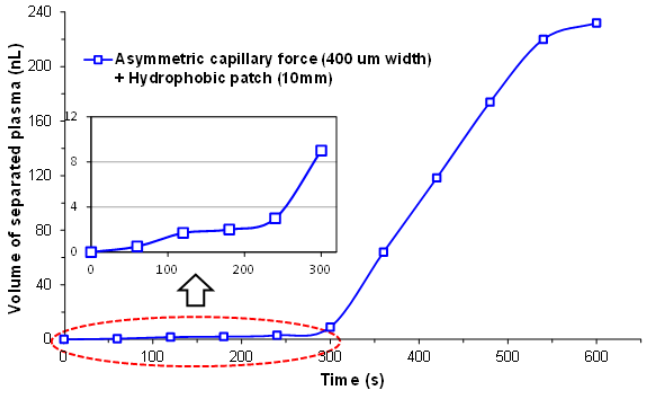

Figure 5: Volume of the separated plasma (nL) over time in the S-to-A polymer LOC platform; 400 µm width microchannel with a 10 mm hydrophobic patch.

The movement of the separated plasma was monitored with an optical microscope by using reference marks along the microchannel. The volume of separated plasma was obtained by measuring the length of the leading edges between separated blood plasma and blood cells over time. The blood plasma shown in Figure 4(c) was successfully separated through a 5.8 mm long microchannel, where its cross-sectional area was 400 µm × 100 µm (W × D). A volume of 232 nL of separated plasma from a single droplet (3.0 µL) of whole blood was finally obtained in a microchannel as shown in Figure 5. The summated total volume of the separated plasma from three microchannels in the device was used for blood analysis using capillary-driven lateral flow colorimetric assay. The summated volume of the separated plasma was large enough for on-chip POCT with undiluted human whole blood. The volume of the separated plasma below 300 seconds in Figure 5 was slightly increased over time due to the accumulation of blood cells over the hydrophobic patch during the separation. The volume of the separated plasma was dramatically increased after 300 seconds due to strong asymmetric capillary force throughout the 'self-built-in blood cell microfilter' developed in a 10 mm hydrophobic patch.

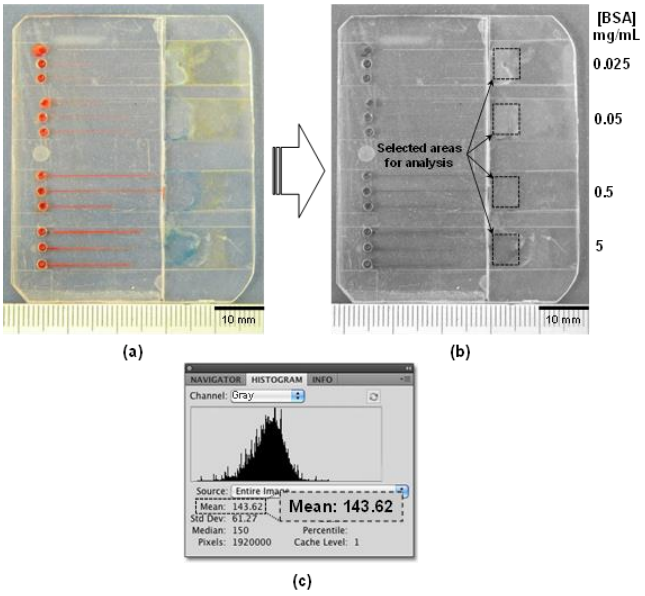

Figure 6: Procedure for quantifying protein levels in separated blood plasma through a S-to-A polymer LOC device using Adobe Photoshop software.

Calibration Curve for Colorimetric Assay with Spiked Proteins

In clinical point of view, the quantification of proteins in human whole blood is significant in the diagnostics of various diseases. The variations in protein level in blood plasma or serum separated from whole blood is attributed from a variety of diseases such as blood disorders, digestive disorders, kidney disorders, and cancers [16]. In this assay, the concentration of BSA spiked in whole blood was successfully quantified by the S-to-A LOC device using capillary-driven lateral flow colorimetric assay. TBPB ionizes and binds with proteins to cause a color change. A positive result is indicated by a color change from yellow to blue. The intensity of the blue color is proportional to the amount of the proteins spiked in blood plasma or whole blood. To generate the calibration curve from the colorimetric assay in the device, the same method used in paper-based colorimetric assay was accomplished [17]. The images of the color changes were captured using a digital camera and the intensity was obtained with Adobe Photoshop in a gray scale mode (Figure 6). The mean values of the selected area through Adobe Photoshop software correlate with the concentration of the spiked proteins in Figure 6(c).

The intensity of color change was quantified by a calibration curve in terms of the protein concentrations in Figure 7. The regression equation is $Intensity = 8.1348ln(x) + 54.405$ ($R^2 = 0.8958$), where x is the concentration of protein (in mg/mL). The colorimetric assay was calibrated with blood plasma samples

separated from three microchannels with known protein concentrations ranging for 0 – 5 mg/mL (0 μM to 75 μM) of BSA. The limit of detection was 25μg/mL, which is better than that from paper-based microfluidic device or conventional method [17–19]. For improving of the detection limit, the assay need to be further optimized or the exploration of new assay methods is desirable. Both blood plasma separation and quantitative analysis in whole blood was simultaneously demonstrated in a S-to-A polymer LOC platform that integrates an on-chip blood/plasma separator with capillary-driven colorimetric assay.

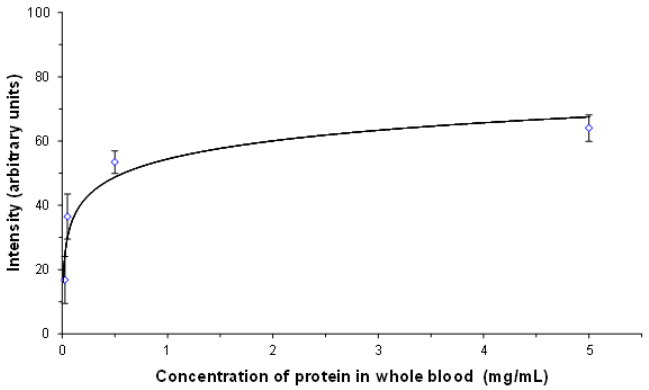

Figure 7: Quantification of protein concentration in human whole blood samples using a S-to-A polymer LOC device with integrated on-chip blood/plasma separator. The limit of detection was 25μg/mL.

CONCLUSION

In conclusion, the newly developed superhydrophilic surfaces were applied for the realization of a capillary-driven lateral flow colorimetric assay platform targeted to a 'smart' S-to-A polymer LOC device. Both high-quality blood plasma separated from whole blood and its quantitative analysis were simultaneously demonstrated in the S-to-A polymer LOC platform. The limit of detection (LoD) in the S-to-A polymer LOC platform for BSA was comparable to or better than that of the paper-based colorimetric assay. The developed S-to-A polymer LOC device is a new platform for the POCT. There is still a plenty of room for the improvement of the LoD by the optimization of the assay or adoption of other assay methods. The developed S-to-A polymer LOC can be a practical platform for POCT applications.

REFERENCES

[1] M. Toner and D. Irimia, "Blood-on-a-chip," Annu. Rev. Biomed. Eng., 7, 77 (2005).

[2] D. Mabey, R. W. Peeling, A. Ustianowski, and M. D. Perkins, "Diagnostics for the developing world," Nat. Rev. Microbiol., 2, 231 (2004).

[3] P. A. Auroux, D. Iossifidis, D.R. Reyes, and A. Manz, "Micro total analysis systems: Analytical standard operations and applications," Anal. Chem., 74, 2637 (2004).

[4] S. K. Sia, V. Linder, B. A. Parviz, A. Siegel, and G. M. Whitesides, "An integrated approach to a portable and low cost immunoassay for resource-poor settings," Angew. Chem., Int. Ed., 43, 498 (2004).

[5] H. Craighead, "Future lab-on-a-chip technologies for interrogating individual molecules," Nature, 442, 387 (2006).

[6] J. El-Ali, P. K. Sorger, and K. F. Jensen, "Cells on chips," Nature, 442, 403 (2006).

[7] S. Cesaro-Tadic, G. Dernick, D. Juncker, G. Buurman, H. Kropshofer, B. Michel, C. Fattinger, and E. Delamarche, "High-sensitivity miniaturized immunoassays for tumor necrosis factor a using microfluidic systems," Lab Chip, 4, 563 (2004).

[8] P. Mitchell, "A perspective on protein microarrays," Nat. Biotechnol., 20, 225 (2002).

[9] A. Ulman, "Formation and structure of self-assembled monolayers," Chem. Rev., 96, 1533 (1996).

[10] K. K. Lee and C. H. Ahn, "Superhydrophilic Multilayer Silica Nanoparticle Networks on a Polymer Microchannel Using a Spray Layer-by-Layer Nanoassembly Method," ACS Applied Material & Interfaces, 5(17), 8523 (2013).

[11] C. H. Ahn, J. W. Choi, G. Beaucage, J. H. Nevin, J. B. Lee, A. Puntambekar, and J. Y. Lee, "Disposable smart lab on a chip for point-of-care clinical diagnostics," Proceedings of the IEEE, 92, 154 (2004).

[12] W. Cao, Q. Jiao, Y. Fu, L. Chen, and Q. Liu, "Mechanism of the interaction between bromophenol blue and bovine serum albumin," Spectrosc. Lett., 36, 197 (2006).

[13] J. D. Jr. Peele, R. H. Gadsden, and R. Crews, "Semi-automated vs. visual reading of urinalysis dipsticks," Clin. Chem., 23, 2242 (1997).

[14] A. W. Martinez, S. T. Phillips, M. J. Butte, and G. M. Whitesides, "Patterned paper as a platform for inexpensive, low-volume, portable bioassays," Angew. Chem., Int. Ed., 46, 1318 (2007).

[15] K. K. Lee and C. H. Ahn, "A new on-chip whole blood/plasma separator driven by asymmetric capillary forces," Lab Chip, 13, 3261 (2013).

[16] A. J. Ninfa, D. P. Ballou, and M. Benore, *Chapter 4: Quantification of Protein Concentration*, Fundamental Laboratory Approaches for Biochemistry and Biotechnology, 2nd Ed., Wiley, 2009.

[17] A. K. Yetisen, M. S. Akram, and C. R. lowe, "Paper-based microfluidic point-of-care diagnostic devices," Lab Chip, 13, 2210 (2013).

[18] W. Wang, W.-Y. Wu, and J.-J. Zhu, "Tree-shaped paper strip for semiquantitative colorimetric detection of protein with self-calibration," J. Chromatogr. A, 1217(24), 3896 (2010).

[19] W. Dungchai, O. Chailapakul, and C. S. Henry, "Use of multiple colorimetric indicators for paper-based microfluidic devices," Anal. Chim. Acta, 674, 227 (2010).

CONTACT

*Kang Kug Lee, tel: +1-513-535-9030; Leek8@mail.uc.edu

A NANOSTRUCTURED IMPEDANCE MICROSENSOR FOR THE REAL-TIME MONITORING OF MACROMOLECULAR ASSEMBLY AND ELISA-ON-A-CHIP

F. Zang, X.Z. Fan, K. Gerasopoulos, L. Naves, J. Culver, and R. Ghodssi[*]
University of Maryland, College Park, Maryland, USA

ABSTRACT

This paper presents an impedimetric microsensor that monitors nano sensing probe functionalization in real-time to optimize on-chip enzyme-linked immunosorbent assays (ELISA). The self-assembly dynamics of *Tobacco mosaic virus*-like particle (VLP) bioreceptors were studied using continuous measurement of the electrical impedance between the interdigitated microelectrodes, which contributed to an optimized and reduced VLP assembly time from 18 hours to 3 hours. The impedance sensor with optimized VLP assembly effectively sensed antibody binding in on-chip ELISA which showed a 64% higher impedance change compared to the control experiment. These results combined highlight the significant potential of genetically modified VLPs as selective nanostructured probes for rapid immunoassays.

INTRODUCTION

Pathogenic microorganisms, including viruses, bacteria, fungi, parasites, etc., are major sources of diseases that threaten public health and food safety [1]. The rapid mutations of pathogens have degraded the efficacy of traditional therapies. A selective and sensitive diagnosis of pathogens is a crucial step in identifying the source of disease and form the right strategy for treatment. Immunoassays such as sandwiched enzyme-linked immunosorbent assays (ELISA) are among the most effective and widely used methods to sense specific types of pathogens. The sensing efficacy of immunoassays is largely determined by the density and binding affinity of the immobilized sensing probes. Currently, one major problem associated with the most commonly used antibody sensing probes in immunoassays is their low capture efficiency on the immobilized surface [2]. Because of this, surface functionalization is not maximized and the sensitivity of the immunoassay is not optimized. Besides, most surface functionalization procedures for immunoassays require several steps of chemical treatments on the surface. This prolongs the immunoassay, making it a time consuming and complex process. For these reasons, there is a need for development of sensing probes that are capable of functionalizing sensor surfaces rapidly and densely.

Tobacco mosaic virus (TMV) and its derivative virus-like particle (VLP) are emerging biomaterials that can serve as viable candidates for biosensing probes. TMV, a nanorod-structured plant virus with thousands of identical coat proteins on its outer surface, can be genetically modified to express functional residues. These include cysteines that facilitate self-assembly onto various substrates and peptides with high affinity to target molecules. Recent developments have led to the use of TMV as a biological nano-scaffold for surface decoration in energy applications or as a high affinity bioreceptor for selectivity enhanced sensing of chemical and biological molecules, respectively [3]. Owing to its high aspect ratio characteristic, the vertically self-assembled TMV is able to exhibit thousands of binding sites on its nanorod surface while maintaining a small footprint on a sensor surface. The latest research has successfully produced the genetically modified TMV coat proteins separately in bacteria cells. These coat proteins self-assembled into nanorod structured virus-like particles (VLPs) similar to TMVs in the absence of RNA strain with a much higher yield. VLPs are capable of creating dense functional surfaces in sensors for selective sensing of the biological binding events.

Previously, VLPs were used both as free floating particles in solution to capture explosives and immobilized receptors on transducers for antibody sensing [4, 5]. In the latter case, loss of VLPs due to repeated wetting and drying, combined with the long assembly time required to fully functionalize the surface, limited the device stability and throughput. Consequently, improving the procedure to perform immunoassays on-chip rapidly in liquid environments is required. Electrical impedance sensors provide suitable platforms for sensing macromolecular binding in liquid based on the changes in surface capacitance and resistance at low frequency due to the presence of particles between electrodes[6].

In this work, we leverage the benefits of impedance sensors such as good compatibility with liquid environments and high sensitivity to the surface capacitance/resistance change to monitor the nanoscale sensing probe functionalization in real-time and optimize on-chip ELISA. VLPs modified with cysteine groups and FLAG-tag peptides (VLP-FLAG) were used as sensing probes to anti-FLAG antibody to study the antigen-antibody interaction. The electrical impedance between the interdigitated microelectrodes is continuously monitored in the process of VLP-FLAG self-assembly in order to understand the dynamics of the VLP surface functionalization. The sensing efficacy of the VLP-FLAG functionalized impedance sensors with varying self-assembly time is studied by impedance shifts during the subsequent process of the on-chip ELISA. VLPs without binding peptides (VLP-1cys) are used in control experiments in the ELISA. The sensing efficacy and selectivity of VLP-FLAG and VLP-1cys are compared using independent impedimetric and colorimetric sensing methods.

METHODS

Impedance sensor designs and microfabrications

Impedance sensors with minimum feature size of 1μm were microfabricated and used for continuous monitoring of the VLP assembly dynamics and on-chip ELISA process.

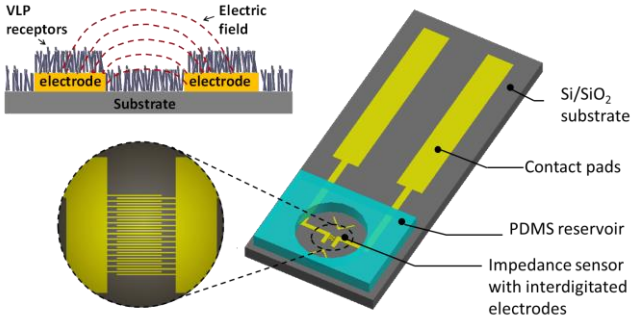

Figure 1: Schematic of the impedance sensor

Figure 1 shows a schematic of the impedance sensor which comprises gold interdigitated electrodes, contact pads and a PDMS reaction chamber. In the fabrication process, Cr/Au (200Å/1500Å) layers were first deposited on a SiO_2/Si substrate using e-beam evaporation. The contact pads were defined by patterning Shipley 1813 positive photoresist via photolithography and etching the

9781940470016/HH2014/$25©2014TRF
DOI 10.31438/trf.hh2014.47

Solid-State Sensors, Actuators and Microsystems Workshop
Hilton Head Island, South Carolina, June 8-12, 2014

exposed Cr/Au layer on the substrate. A 1.1µm thick 495 polymethyl methacrylate (PMMA) A10 layer was spin-coated and patterned via e-beam lithography. The subsequently deposited Cr/Au (200Å/1500Å) layer was lifted off to create interdigitated electrodes with 1µm finger width and spacing. The geometries of the interdigitated fingers were designed to be comparable to VLP dimensions in order to obtain a high sensitivity for monitoring the VLP sensing probe assembly dynamics and antibody binding events [6]. The effective sensing area of the interdigitated electrodes is 250µm×500µm. A 3 mm thick Polydimethylsiloxane (PDMS) reaction chamber with a volume of 50µl was fabricated separately and bound onto the sensor substrate. During the experiments, an additional layer of PDMS is temporarily bound with the PDMS reaction chamber to seal the cavity, therefore, preventing the 50µl sample from evaporation and maintaining a constant analyte concentration. The reaction chamber and cover layer was used throughout the VLP self-assembly on the impedance sensor as well as the on-chip ELISA experiments.

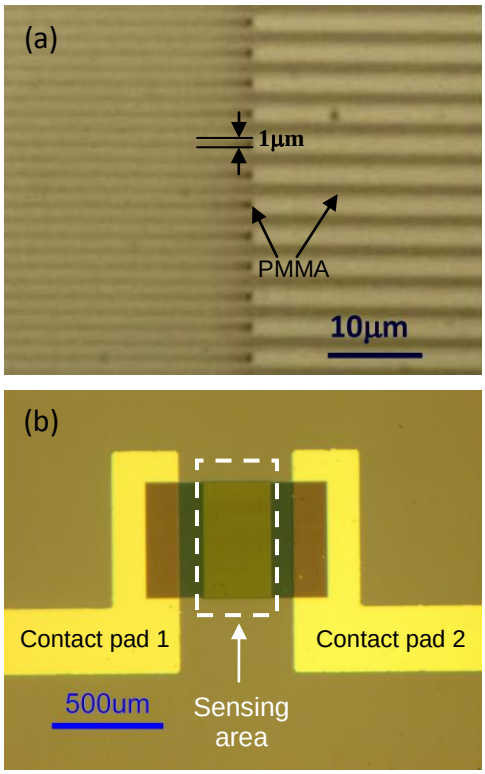

Figure 2: Optical images of (a) electrode features after e-beam lithography with PMMA e-beam resist and (b) the impedance sensor after fabrication

Figure 2a shows optical images of the 495 PMMA A10 resist after the e-beam lithography and the O_2 plasma cleaning process. The plasma cleaning helps to remove PMMA residues from e-beam lithography and development, which contributes to clean interdigitated features. The patterned interdigitated electrodes after e-beam deposition of Cr/Au and lift-off are shown in Figure 2b.

VLP genetic modifications and surface functionalization

The VLP sensing probes (VLP-FLAG) are synthetized by the helical arrangement of thousands of genetically modified and identical TMV coat proteins inside *Escherichia coli* bacterial cells.

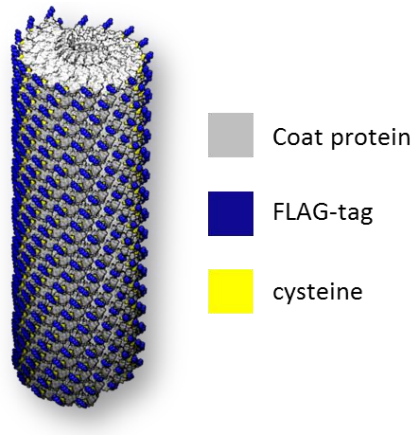

Figure 3: Schematic of a 3 dimensional segment of VLP with helical arrangement of genetically modified cysteine residues and FLAG-tag sequences on coat proteins

Each coat protein produced expresses a cysteine residue (marked in yellow in Figure 3) that promotes surface attachment and a FLAG-tag sequence (DYKDDDDK, marked in blue in Figure 3) that enables selective binding with the target anti-FLAG antibody. The genetic modification, culture and purification procedures were reported in detail previously [7]. The purified VLPs were diluted and suspended in deionized (DI) water at a previously characterized concentration of 0.2mg/ml. This VLP stock solution was used in the surface functionalization of the impedance sensors.

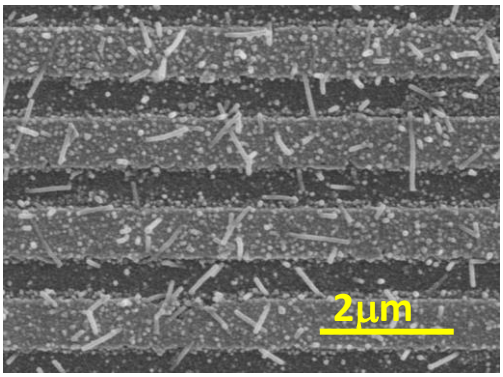

Figure 4: SEM images of interdigitated electrodes after VLP-FLAG assembly in deionized water

The VLP-FLAG sensing probes suspended in the stock solution were added in the PDMS reaction chamber to functionalize the impedance sensor. The cysteine residue exposed at the terminals of the VLP-FLAG nanorods contributed to vertical self-assembly of VLPs on the electrode area. The time of self-assembly was varied from 0 to 18 hours in the study. The VLP assembly for 18 hours was previously used as a standard assembly process to get a uniform VLP functional coating. The surface morphology of the VLP functional layer in the interdigitated electrode sensing area after 18 hours of assembly was studied by scanning electron microscopy (SEM). An electroless plating of nickel was performed before SEM imaging to promote the conductivity of the surface. The SEM image in Figure 4 shows the distribution of the VLP sensing probes on the sensing area of the impedance sensor after 18 hours of self-assembly. The

self-assembled VLPs were observed both on the gold electrode and silicon oxide substrate.

The impedance between the interdigitated electrodes is monitored at a 15-minute interval using a potentiostat (VSP-300, Bio-Logic) to study the dynamics of the VLP assembly process. The real-time impedance monitoring is aimed at minimizing the VLP self-assembly time, shortening the duration of functionalization and ensuring the efficacy of antibody binding.

Sandwiched ELISA on-chip with VLPs as sensing probes

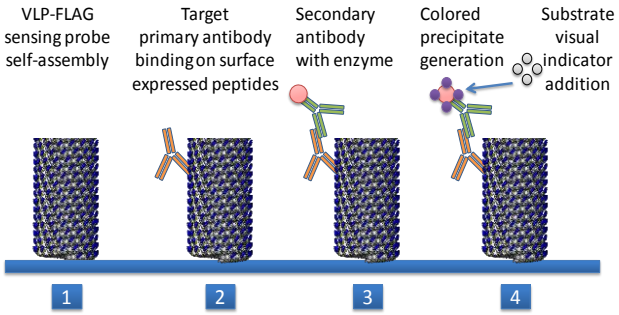

Figure 5: Sandwiched on-chip ELISA using VLP-FLAG

Sandwiched ELISA (Figure 5) was used as a model system to investigate the sensing efficacy of assembled VLP-FLAG sensing probes to anti-FLAG antibody targets. In the process, VLP-FLAG sensing probes were introduced in the reaction chamber and self-assembled on the impedance sensor surface. After washing with DI water, 5% milk in 1X Tris-buffered saline (TBS) buffer solution was introduced for 30 minutes to saturate the nonspecific bindings. After milk blocking and 3 times of 1X TBS washing, a 1:1000 dilution of primary anti-FLAG antibody produced in rabbit (Sigma-Aldrich) was introduced to bind with VLP sensing probes due to antigen-antibody interaction. A 1:5000 dilution of enzyme-linked anti-rabbit secondary antibodies (Sigma-Aldrich) were introduced in the reaction chamber subsequently after TBS and TBS/Tween washing steps. In the final step, the nitro-blue tetrazolium chloride and 5-bromo-4-chloro-3'-indolyphosphate p-toluidine salt (NBT/BCIP) substrates (Fischer Scientific) were added into the chamber and interacted with the enzyme on the secondary antibody, which produced dark-purple insoluble precipitates on the surface. The impedance of the sensor was continuously monitored during the ELISA experiments.

RESULTS AND DISCUSSIONS

The electrical impedance between the interdigitated electrodes is continuously monitored using the potentiostat while the frequency is swept from 7MHz to 1Hz with a peak-to-peak potential of 50mV. The electrical impedance is analyzed at the frequency of 100Hz where the interfacial capacitance on the electrodes and the serial connected solution resistance are dominant in the electrical model [6].

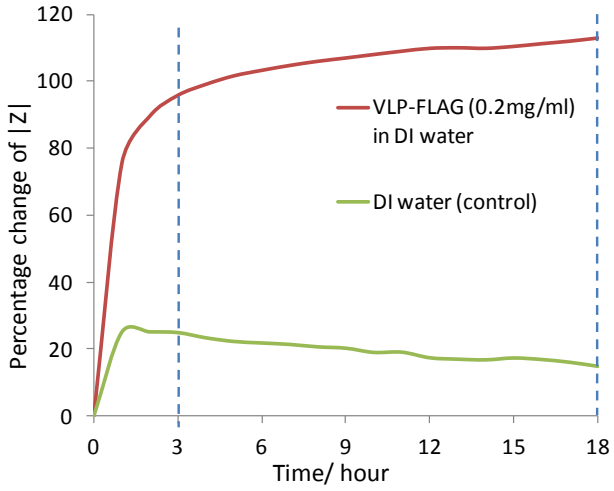

Figure 6: Percentage changes of impedance in the presence or absence of VLP-FLAG

VLP-FLAG sensing probes suspended in DI water (0.2mg/ml) was added into the reaction chamber, and the impedance between interdigitated electrodes was monitored in real-time over the 18-hour period to study the VLP assembly dynamics. DI water, which acts as the solvent for VLP, was used in the parallel control experiment to generate a baseline impedance response. The percentage changes in the amplitude of impedance at the frequency of 100Hz in the presence and absence of VLP probes are plotted in Figure 6. In the control experiment with DI water, the normalized impedance amplitude shows an increase of 25.1% in the first 1.5 hours and is stabilized at approximately 14.8% over the 18-hour period. The normalized impedance of the sensor in the presence of VLP-FLAG increases dramatically in the first 3 hours by 95.7% after which it starts to saturate, gradually reaching up to 112.8% after 18 hours of assembly. The increase in the impedance amplitude can be a composite effect of the increase in the thickness of interface and the solution resistance between the electrodes due to the nonconductive VLP coating. These experimental results indicate the self-assembly of VLP-FLAGs on the impedance sensor saturates the surface within the first 3 hours. Therefore, the self-assembly procedure of VLP sensing probes can potentially be accelerated by shortening the assembly time while still maintaining a dense surface coverage. In the later experiments, the sensing efficacy of the impedance sensor with a 3-hour or 18-hour of VLP assembly is compared using on-chip ELISA.

The impedance sensors functionalized by 3-hour and 18-hour VLP-FLAG self-assembly or 18-hour of VLP-1cys self-assembly was used to study the sensing efficacy of VLP probes. VLP-1cys, expressing only cysteine residues without antibody binding peptide sequences, was used as a control probe. The impedance after each process during the ELISA (blocking, primary and secondary antibody binding and substrate introduction) was measured in 1X TBS buffer to normalize the background.

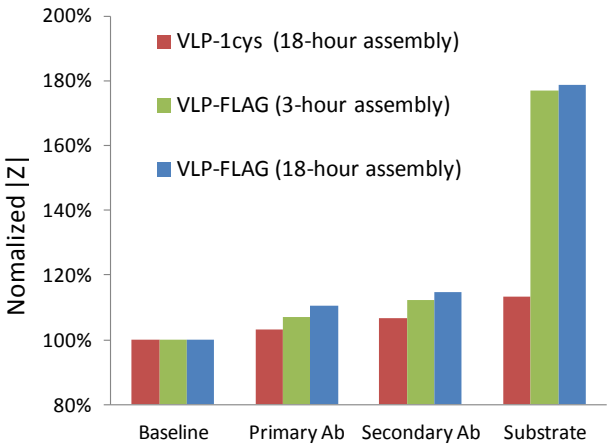

Figure 7: Normalized impedance of VLP-FLAG or unmodified VLP functionalized sensors during ELISA

Figure 7 shows the normalized impedance amplitude during ELISA experiments. The baseline for each experiment was acquired based on the measured impedance after 30 minutes of 5% milk nonspecific blocking. The total normalized impedance for sensors functionalized for 3 hours and 18 hours using VLP-FLAG increased by 77.1% and 77.8%, respectively, indicating a similar biosensing efficacy in immunoassay. The significant change in impedance is due to the formation of insoluble precipitates that cover the sensing area and alter the surface morphology. This change prevents the ion transfer to the electrode, and creates thicker interface capacitance; thus, both the real and imaginary parts of impedance between electrodes show significant increase. In comparison, when VLP-1cys control probes are used, the impedance change is only 13.3%, which is attributed to non-specific binding. The distinguishing difference of impedance after ELISA between the VLP-FLAG and VLP-1cys assembled sensors verified the selectivity of the genetically modified VLPs to the target antibodies.

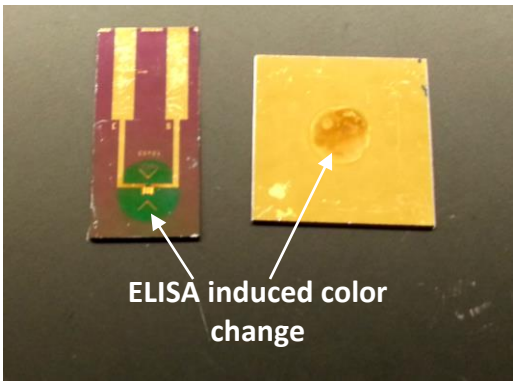

Figure 8: Optical image of (left) the impedance sensor and (right) bare gold chips with identical 3 hours of VLP-FLAG self-assembly after ELISA

The functionality of the VLP-FLAG as sensing probes in ELISA was independently validated by colorimetric experiments conducted in parallel with the impedimetric sensing experiments. Dark-purple colored precipitates due to the interaction between substrate and enzymes on the secondary antibodies were observed on impedance sensors and gold chips which were decorated with VLP-FLAG through self-assembly (Figure 8).

SUMMARY

Impedance sensors were developed to study the dynamics of biological sensing probe assembly on sensor surfaces and the impedimetric responses during immunoassays. The continuous impedance monitoring over 18 hours of VLP-FLAG assembly showed an optimized assembly time of 3 hours which saturated the impedance sensor surface. ELISA experiments validated the selectivity and sensing efficacy of the sensor surface functionalized by the VLP-FLAG sensing probes with 3 hours of self-assembly.

This work provided important self-assembly parameters of VLP sensing probes to reduce the functionalization time of transducer surfaces and accelerate immunoassays. It will contribute to the future development of programmable VLP-based biosensors for rapid macromolecule sensing.

ACKNOWLEDGEMENTS

The work was supported by the Army Research Office Biochemistry Program (Grant No. W911NF1110138) and National Science Foundation Nanomanufacturing Program (Grant No. NSF-CMMI 0927693). The authors would like to acknowledge the staff in Maryland Nanocenter for the support in fabrication process.

REFERENCES

[1] L. Yang and R. Bashir, "Electrical/electrochemical impedance for rapid detection of foodborne pathogenic bacteria," Biotechnology Advances, 26, 135-150, (2008).

[2] M. Varshney, Y.B. Li, B. Srinivasan, and S. Tung, "A label-free, microfluidics and interdigitated array microelectrode-based impedance biosensor in combination with nanoparticles immunoseparation for detection of Escherichia coli O157 : H7 in food samples," Sensors and Actuators B-Chemical, 128, 99-107, (2007).

[3] X.Z. Fan, E. Pomerantseva, M. Gnerlich, A. Brown, K. Gerasopoulos, M. McCarthy, J. Culver, and R. Ghodssi, "Tobacco mosaic virus: A biological building block for micro/nano/bio systems," Journal of Vacuum Science & Technology A, 31, (2013).

[4] F. Zang, X.Z. Fan, K.D. Gerasopoulos, H. Ben-Yoav, A.D. Brown, J.N. Culver, and R. Ghodssi, "Scale-down effects: Towards miniaturization of an electrochemical sensor using biomolecules," in IEEE Sensors 2013, Baltimore, USA, 2013, pp. 1-4.

[5] X.Z. Fan, L. Naves, N. P. Siwak, A.D. Brown, J. N. Culver, and R. Ghodssi, "A Novel Virus-like-particle (VLP) Bioreceptor Coated Optical Disk Resonator for Biosensing,," presented at the 2013 MRS Spring Meeting, San Francisco, CA, USA, (2013).

[6] P. Van Gerwen, W. Laureyn, W. Laureys, G. Huyberechts, M.O. De Beeck, K. Baert, J. Suls, W. Sansen, P. Jacobs, L. Hermans, and R. Mertens, "Nanoscaled interdigitated electrode arrays for biochemical sensors," Sensors and Actuators B-Chemical, 49, 73-80, (1998).

[7] A.D. Brown, L. Naves, X. Wang, R. Ghodssi, and J.N. Culver, "Carboxylate-Directed In Vivo Assembly of Virus-like Nanorods and Tubes for the Display of Functional Peptides and Residues," Biomacromolecules, 14, 3123-3129, (2013).

CONTACT

*R. Ghodssi, tel: +1-301-405-8158; ghodssi@umd.edu

A FLEXIBLE PH SENSOR ARRAY ON PAPER USING LASER PATTERN DEFINITION AND SELF-ALIGNED LAMINATED ENCAPSULATION

Rahim Rahimi[1], Manuel Ochoa[1], Tejasvi Parupudi[1], Xin Zhao[2], Mehmet R. Dokmeci[2], Ali Khademhosseini[2], and Babak Ziaie[1]
[1]Purdue University, West Lafayette, Indiana, USA
[2]Harvard-MIT Health Sciences and Technology, Cambridge, MA, USA

ABSTRACT

Chronic wound pH is a key indicative parameter for assessing the healing progress. Due to their size and inability to sample multiple wound regions independently, commercial pH meters are not well-suited for spatial maping of wound pH. To address this issue, we present an inexpensive, flexible array of pH sensors on a paper platform. Each sensor consists of two electrodes screen-printed (using a laser-defined mask) on an acrylic-coated paper (i.e. palette paper), a Ag/AgCl reference electrode, and a carbon electrode coated with a conductive proton-selective polymer, (polyaniline, PANI). Laser-machining is further used to create a self-aligned passivation layer that is bonded over the sensors by lamination technology. Characterization of the pH sensors reveal a linear (r^2 = 0.9734) relationship between output potential and pH for values in the pH range of 4−10, with an average sensitivity of −49.5 mV/pH. The sensors feature a response time of 4 min and very limited hysteresis over four pH cycles (pH 4 to 10 to 4).

INTRODUCTION

The pH level in the wound bed is a key indicative parameter for assessing the healing progress of chronic wounds. Unlike healthy skin or healing acute wounds that have a slightly acidic pH (5.5−6.5), chronic wounds often exhibit pH values higher than 7.4 due to alkaline byproducts of bacterial colony proliferation [1]–[3]. Thus, pH monitoring offers a method for promptly identifying such infections in order to effectively treat them in a timely manner.

Commercial pH meters can be used in acute or uniformly-healing wounds, but their practical efficacy in chronic wounds is limited by their inability to sample multiple wound regions independently and efficiently. In many cases, the irregular vascular structure of chronic wounds causes a heterogeneous distribution of infection in the wound bed, resulting in drastic pH variations throughout the affected area [4]. The design of most commercial pH meters makes their use impractical for assessing such wounds. Traditionally, these sensors consist of a doped glass membrane (e.g., thin amorphous silicon dioxide with alkali metals). The electric potential across the glass membrane is sensitive to changes in the concentration of H^+ ions in the solution. The potential difference is measured with respect to a reference electrode that is immersed into the same solution (usually combined with the working electrode into one device) [5]. Although many improvements over the decades have achieved a small device footprint, many drawbacks still remain, including a limitation to single-point measurements, a hard structure that may cause tissue insults, and a lack of mechanical flexibility that prevents it from conforming to the wound bed. A more practical alternative to wound pH monitoring would be a flexible array of pH sensors that can cover the wound site and generate a map of pH levels throughout the wound site, thus revealing the location and concentration of bacterial infections.

To improve compatibility of pH sensors with soft materials, recent research has produced several sensor designs that further minimize size and increase mechanical flexibility. A common approach the use of ion sensitive field effect transistors (ISFETs) [6]–[8], which feature a small size and fast response and are suitable for in vivo applications. Their main drawback, however, is the fabrication process which requires time consuming and costly cleanroom processing. An alternate approach is the use of metal oxides (e.g. IrO_x, RuO_2, SnO_2) formed on various substrates by processes such as sputtering, electro-deposition, and sol-gel [9]–[12]. These sensors feature a near-Nernstian performance, potential and thermal stability, and a sensitivity as high as −77 mV/pH [13]; however, they usually exhibit significant drift [14].

More recently, researchers have developed polymer-based pH sensors, including chemo-mechanical sensors based on pH-responsive hydrogels [15]–[17] as well as electrodes coated with a proton-selective polymer film (e.g., polyaniline, polypyrrole) [18], [19]. While the former type boasts unmatched mechanical compliance, its slow response time and requirement for special storage (hydrated) conditions limit its practical utility. The latter type, in contrast, offers a satisfactory degree of flexibility along with a straightforward and inexpensive fabrication process. For these reasons, such conductive polymer-based pH sensors have shown great promise for biomedical applications.

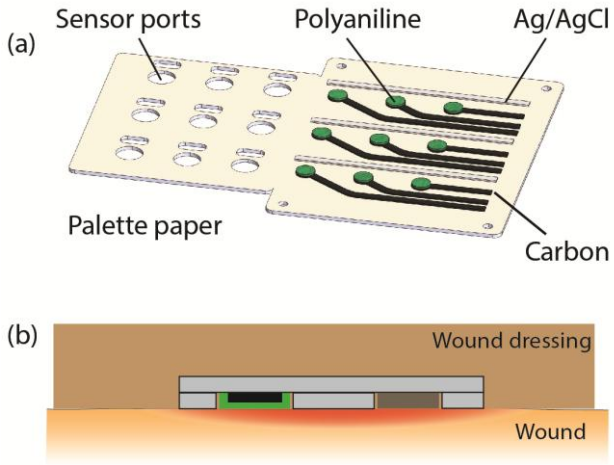

Figure 1: (a) A 3D exploded view of the 3 × 3 pH sensor array on paper with self-aligned encapsulation. (b) Illustration of its implementation as a component of wound dressings for advanced wound monitoring.

In this work, we followed a similar conductive polymer approach and employed PANI to develop an inexpensive and flexible array of pH sensors on a paper substrate. The sensor array features fabrication using commercial technologies for rapid prototyping. Figure 1 shows a schematic of a 3 × 3 array of sensors on a paper substrate. Each individual sensor consists of two electrodes, one being a Ag/AgCl reference electrode and the other a carbon electrode coated with a conductive proton-selective polymer, polyaniline (PANI). The sensors are screen-printed on an acrylic-coated paper (i.e., palette paper) using a laser-patterned tape as a mask. This method features a simple technique for

9781940470016/HH2014/$25©2014TRF
DOI 10.31438/trf.hh2014.48

directly patterning the mask on the paper substrate. Laser machining is further used to create a self-aligned passivation layer that is bonded over the sensors by using a commercial laminating machine.

SENSOR DESIGN AND MEASUREMENT

Theory of operation

The operation of the pH sensors is based on the protonation and de-protonation of nitrogen atoms in the polymer chains of PANI [20]. In acidic solutions the polymer is doped with H^+ ions to create the emeraldine salt (ES) form of PANI, which is known for its high electrical conductivity. This resulting surface charge increases the electrical potential of the electrode relative to the reference. When the polymer is subsequently immersed in an alkaline solution, the captured H^+ ions are neutralized, resulting in decreased surface charge (and hence potential) on the polymer. The deprotonated or neutralized form of PANI is referred to as its emeraldine base (EB) form and is not electrically conductive. This pH-dependent electrochemical equilibrium between the ES and EB moieties of PANI results in an inverse relationship between the electrochemical potential of the sensing electrode and the pH of its environment.

Sensor fabrication

Figure 2 shows the fabrication process of the pH sensor array. First, a single layer of tape (3M® MagicTape™) is attached to a piece of palette paper substrate to act as a mask (Figure 2b). The electrode mask pattern is then defined on the tape by directly writing on the tape with a laser engraver (Universal Laser Systems, Inc., Scottsdale, AZ). This process ablates the cellulose acetate backing of the tape, leaving behind only the adhesive layer (Figure 2c). To eliminate the need for alignment, the insulating layer is fabricated on the same substrate with the tape mask by laser machining openings on the side of the paper without traces. Next, the carbon and silver patterns are screen-printed onto the palette paper (Figure 2d). The inks are allowed to cure at 100 °C for 30 min. After curing, the tape mask is peeled off, revealing 9 carbon and 3 silver electrodes on the palette paper.

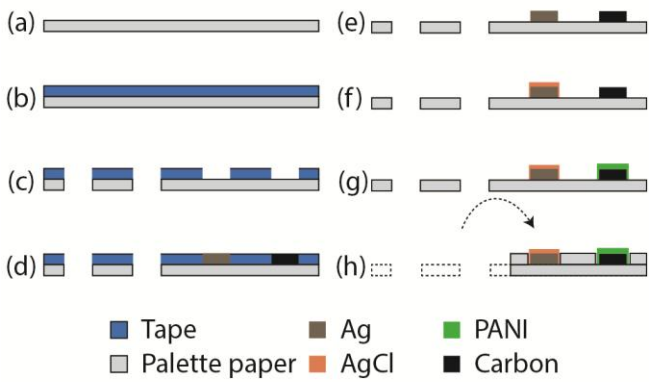

Figure 2: Fabrication process of the sensor: (a-c) laser-pattern tape to act as a direct mask; (d) screen print silver and carbon electrodes; (e) remove tape mask; (f) chloridate silver electrodes as the reference electrodes; (g) drop-cast PANI on carbon electrode with HCl doping; (h) fold the isolation layer over the electrodes, and bond by lamination.

Following that, the silver chloride electrode is prepared by selectively electroplating a layer of silver chloride on the silver electrodes using a current of 1 mA for 2 min in a 1.0 M NaCl solution. After the electrolysis process, the surface of the electrodes is rinsed with de-ionized water and allowed to dry at 70 °C for at least 3 hours.

Meanwhile, a polyaniline solution is prepared by dissolving 25 mg of polyaniline emeraldine base in 25 mL dimethyl sulfoxide (DMSO). The base form is used since it is very soluble in organic solvents such as DMSO and ensures uniform coating of the polyaniline on carbon. The polyaniline emeraldine solution is stirred with a magnetic rod for 5 hours before use.

After the electrodes on the paper have dried, a 4 µL volume of polyaniline solution (ion selective membrane) is drop-casted on the carbon electrode and allowed to dry on the carbon traces for 24 hours at room temperature. Following that, the PANI is doped with HCl in a vacuum chamber for 5 hours. The HCl fumes in the vacuum chamber introduce H^+ ions into the polyaniline emeraldine base film to produce the polyaniline emeraldine salt [20]. During the doping process the polyaniline base film is protonated changes color from dark blue to dark green, which has a higher conductivity compared to emeraldine base.

The electrodes are then rinsed with de-ionized water and desiccated by heating in an oven at 70 °C for 3 hours. Finally, the palette paper substrate is folded in half to create a structure with 9 pH sensor interconnections sandwiched between the two layers of palette paper. Bonding between the two layers of paper is accomplished using a hot roll laminator (Apache AL13P Professional) at 143 °C.

Measurement setup and procedure

To evaluate the performance of the pH sensor array, potentiometric measurements were conducted in different pH buffer solutions from pH 4 to pH 10. For pH values of 4, 7, and 10, commercial buffer solutions were purchased (Pinnacle pH Buffers, Nova Analytics) and used directly. To achieve a complete range of pH 4 to pH 10, additional pH buffer solutions (pH 5, 6, 8, and 9) were prepared by mixing different ratios of the commercial solutions. The pH for all buffer solutions was verified with a commercial pH meter (Model IQ125, IQ Scientific Instruments, USA) prior to all experiments.

The potentiometric measurements were conducted at room temperature using an Agilent 34401A digital multimeter. The multimeter was set to high impedance mode in order to reduce the current driven from the sensors. A computer was connected to the multimeter via a GPIB interface, and continuous data acquisition was implemented using Agilent's IntuiLink software in combination with Microsoft Excel. The measurements were carried out by immersing the working and reference electrodes of each sensor in different buffer solutions and measuring the potential across the electrodes.

To assess the sensor in terms of stability and repeatability the sensors were tested in titrated cycles from pH 4 to pH 10 and back to pH 4. The sensors were sequentially placed in different levels of pH solution (without rinsing the sensors in between solutions). Meanwhile, the potential between the working and reference electrodes was recorded as a function of time at a sampling frequency of 1 Hz.

The conductive traces of individual sensors on the array must remain electrically isolated from each other in a moist wound environment in order to minimize noise in the output of the sensors. To evaluate the reliability of the packaging used here, we investigated current leakage in a modified array of metallic traces on various substrates. The experimental setup for these tests is illustrated in Figure 3. Each test sample consisted of two conductive traces patterned on palette paper and sealed with a thermally laminated layer of various insulating materials (75 µm-thick Kapton® tape, Scotch® MagicTape™, and palette paper). The

samples were placed in a phosphate-buffered saline (PBS) solution, to mimic wound fluid. A 1 volt bias was then applied to the two ends of the electrodes using a Hewlett-Packard E3630A DC power supply. Meanwhile, the leakage current between the two electrodes was monitored over a period of 24 hours using a multimeter with the data acquisition setup described above. As control samples, two conductive traces without insulating layer were also tested under the same conditions. In all cases, the solution was stirred constantly during the experiments using a magnetic stirrer.

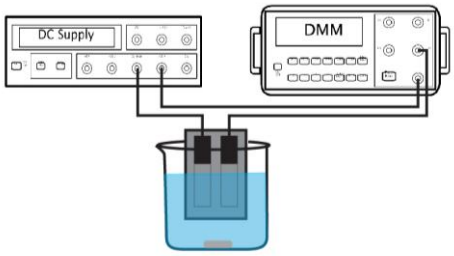

Figure 3: Scheme of the test setup for testing leakage current.

RESULTS AND DISCUSSION

Figures 4(a-b) show photographs of the sensor array in its final fabrication steps (folding and lamination); the final device is shown in Figure 4c. The resulting array is flexible and comfortably wearable. The working areas of the pH-sensitive electrodes have a 2 mm diameter. The number and density of sensors can be further adjusted during the design to accommodate specific wound sizes and geometries. Such sensor platform offers versatile adaptability for either low-production patient-customized fabrication or high-volume roll-to-roll manufacturing. The next two subsections discuss the performance of the sensor array.

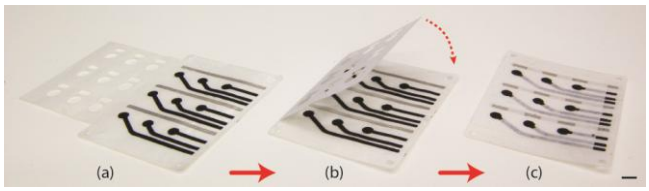

Figure 4: Photograph of the fabricated pH sensor array, (a) fabricated electrodes on paper; (b) folding the encapsulation layer over the electrodes; (c) the final array of pH sensors after lamination. Scale bar: 5 mm.

Sensor performance

Figure 5 shows the potentiometric response of each sensor as a function of pH. The data reveal a linear (r^2 = 0.9734) relationship for 7 different pH conditions (in the range pH 4−10), with average sensitivity of −49.5 mV/pH. This response is characteristic of Nernstian theory for pH sensors.

Figure 6 shows the results of the stability and reliability experiments. The sensors exhibit satisfactory stability and produce a distinct response for each pH condition between pH 4 and pH 10, with very limited hysteresis. Additionally, the average response time of the sensors (to 90 % of the steady-state output potential) is 4 min. The slow response time is attributed to thickness variations of the drop-cast PANI membrane. Although previous reports of PANI-based pH sensitive electrodes have featured a faster response time (i.e., seconds), their fabrication process employed electro-deposition of PANI [5]. Such techniques are difficult to adapt for arrays of sensors on flexible materials. Drop-casting, in contrast, offers a more favorable approach at the expense of a slower response time. For wound healing applications, however, this tradeoff is justified since the pH of the wound is not expected to vary drastically over time [1]. Hence, the sensitivity and response time of our sensor render it suitable for integration with in low-cost wound monitoring dressings and microsystems.

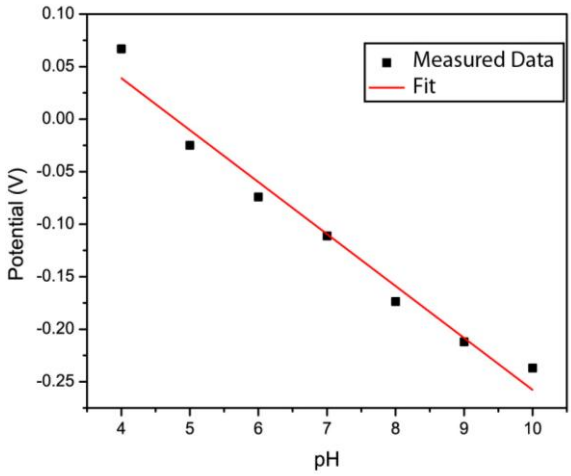

Figure 5: The measured sensor response to various pH conditions between pH 4 and pH 10. The data show a linear response (r^2 = 0.9734) with average sensitivity of −49.5 mV/pH.

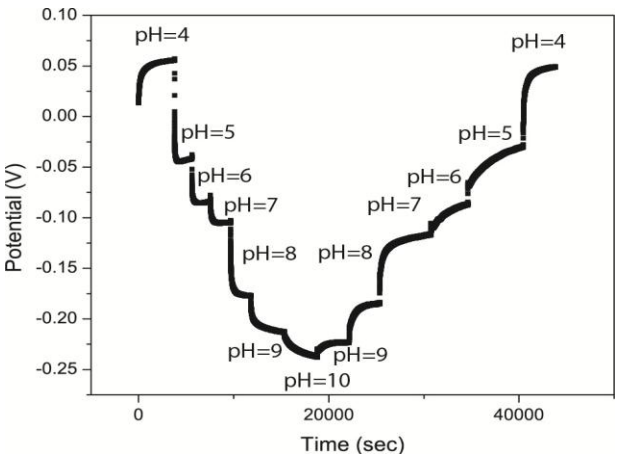

Figure 6: Stability and repeatability of the pH sensor from pH 4 to 10 and back to 4. The test was repeated for four cycles. The data show a distinct response for each pH value, very little drift, and negligible hysteresis.

Leakage current characterization

The results of the packaging investigations are depicted in Figure 7. The data show that the samples laminated with Kapton® tape and Scotch® tape both exhibited a leakage current after a few hours in PBS (45min for samples with Scotch tape; 13.5 hours for samples with Kapton® tape). Upon inspection of the samples, the cause of the leakage was determined to be delamination of the tapes from the electrodes. In contrast, the samples packaged by laminated pallette paper revealed no signs of current leakage. The results imply that the latter method produces a satisfactory mositure barrier and can be reliably used for packaging sensors to be used in wet environments such as wounds.

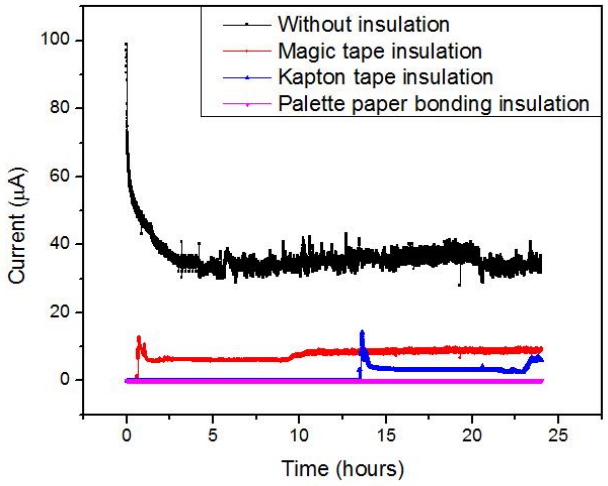

Figure 7: Electrical isolation properties of the palette paper bonding compared to Scotch® MagicTape™ and Kapton® tapes. The current was measured across two electrodes with different isolations materials in a PBS solution with an applied voltage bias (1 V). The data reveal the superior performance of thermally-laminated palette paper.

CONCLUSION

An inexpensive, flexible array of pH sensors was fabricated on a paper substrate for use in wound monitoring. The developed fabrication process takes advantage of low-cost materials, laser machining, and self-aligned passivation with lamination technology. The sensor performance in different buffer solutions of pH 4 to pH 10 showed a linear potential (r^2=0.9734) with and a sensitivity of -49.5 mV/pH. The obtained sensors features good flexibility, sensitivity and repeatability making it appropriate for integration with low-cost wound monitoring dressings.

ACKNOWLEDGEMENTS

The authors thank the staff of the Birck Nanotechnology Center for their assistance in this work. This work was funded by the National Science Foundation under the EFRI Program, grant #1240443.

REFERENCES

[1] L. A. Schneider, A. Korber, S. Grabbe, and J. Dissemond, "Influence of pH on wound-healing: a new perspective for wound-therapy?," *Arch. Dermatol. Res.*, vol. 298, no. 9, pp. 413–20, Feb. 2007.

[2] S. Schreml, R. J. Meier, O. S. Wolfbeis, M. Landthaler, R.-M. Szeimies, and P. Babilas, "2D luminescence imaging of pH in vivo.," *Proc. Natl. Acad. Sci. U. S. A.*, vol. 108, no. 6, pp. 2432–7, Feb. 2011.

[3] J. R. Sharpe, S. Booth, K. Jubin, N. R. Jordan, D. J. Lawrence-Watt, and B. S. Dheansa, "Progression of wound pH during the course of healing in burns.," *J. Burn Care Res.*, vol. 34, no. 3, pp. e201–8, 2012.

[4] G. Urban, G. Jobst, F. Keplinger, E. Aschauer, O. Tilado, R. Fasching, and F. Kohl, "Miniaturized multi-enzyme biosensors integrated with pH sensors on flexible polymer carriers for in vivo applications," *Biosens. Bioelectron.*, vol. 7, no. 10, pp. 733–739, Jan. 1992.

[5] O. Korostynska, K. Arshak, E. Gill, and A. Arshak, "Review on State-of-the-art in Polymer Based pH Sensors," no. 1, pp. 3027–3042, 2007.

[6] D. Lee and T. Cui, "Low-cost, transparent, and flexible single-walled carbon nanotube nanocomposite based ion-sensitive field-effect transistors for pH/glucose sensing.," *Biosens. Bioelectron.*, vol. 25, no. 10, pp. 2259–64, Jun. 2010.

[7] V. Pachauri, K. Kern, and K. Balasubramanian, "sensitive metal-semiconductor field-effect transistor Field-effect-based chemical sensing using nanowire-nanoparticle hybrids : The ion-sensitive metal-semiconductor field-effect transistor," vol. 023501, 2013.

[8] C.-S. Lee, S. K. Kim, and M. Kim, "Ion-sensitive field-effect transistor for biological sensing.," *Sensors (Basel).*, vol. 9, no. 9, pp. 7111–31, Jan. 2009.

[9] W.-D. Huang, H. Cao, S. Deb, M. Chiao, and J. C. Chiao, "A flexible pH sensor based on the iridium oxide sensing film," *Sensors Actuators A Phys.*, vol. 169, no. 1, pp. 1–11, Sep. 2011.

[10] M. Yuqing, C. Jianrong, and F. Keming, "New technology for the detection of pH.," *J. Biochem. Biophys. Methods*, vol. 63, no. 1, pp. 1–9, Apr. 2005.

[11] P. J. Kinlen, J. E. Heider, and D. E. Hubbard, "A solid-state pH sensor based on a Nafion-coated iridium oxide indicator electrode and a polymer-based silver chloride reference electrode," *Sensors Actuators B Chem.*, vol. 22, no. 1, pp. 13–25, Oct. 1994.

[12] S. Kakooei, M. C. Ismail, and B. Ari-wahjoedi, "Review Article An overview of pH Sensors Based on Iridium Oxide : Fabrication and Application," vol. 1, no. 1, pp. 62–72, 2013.

[13] O. Korostynska, K. Arshak, E. Gill, and A. Arshak, "Review Paper : Materials and Techniques for In Vivo pH Monitoring," vol. 8, no. 1, pp. 20–28, 2008.

[14] P. Kurzweil, *Metal Oxides and Ion-Exchanging Surfaces as pH Sensors in Liquids: State-of-the-Art and Outlook.*, vol. 9, no. 6. 2009, pp. 4955–85.

[15] A. Richter, G. Paschew, S. Klatt, J. Lienig, K. Arndt, and H. P. Adler, "Review on Hydrogel-based pH Sensors and Microsensors," vol. c, pp. 561–581, 2008.

[16] V. Sridhar and K. Takahata, "A hydrogel-based passive wireless sensor using a flex-circuit inductive transducer," *Sensors Actuators A Phys.*, vol. 155, no. 1, pp. 58–65, Oct. 2009.

[17] A. Nocke, A. Schröter, C. Cherif, and G. Gerlach, "Miniaturized textile-based multi-layer ph-sensor for wound monitoring applications," *Autex Res. J.*, vol. 12, no. 1, pp. 20–22, Jan. 2012.

[18] P. Malkaj, E. Dalas, E. Vitoratos, and S. Sakkopoulos, "pH electrodes constructed from polyaniline/zeolite and polypyrrole/zeolite conductive blends," *J. Appl. Polym. Sci.*, vol. 101, no. 3, pp. 1853–1856, Aug. 2006.

[19] B. Lakard, O. Segut, S. Lakard, G. Herlem, and T. Gharbi, "Potentiometric miniaturized pH sensors based on polypyrrole films," *Sensors Actuators B Chem.*, vol. 122, no. 1, pp. 101–108, Mar. 2007.

[20] K. Hamdani and K. L. Cheng, "Polyaniline pH Electrodes," *Microchem. J.*, vol. 61, no. 3, pp. 198–217, Mar. 1999.

CONTACT

*B.Ziaie, tel:+1-765-404-0726; bziaie@purdue.edu

A SEWING-ENABLED STITCH-AND-TRANSFER METHOD FOR ROBUST, ULTRA-STRETCHABLE, CONDUCTIVE INTERCONNECTS

Rahim Rahimi, Manuel Ochoa, Wuyang Yu, and Babak Ziaie
Purdue University, West Lafayette, Indiana, USA

ABSTRACT

Fabricating highly stretchable and robust electrical interconnects at low-cost remains an unmet challenge in stretchable electronics. Previously reported stretchable interconnects require complicated fabrication processes that result in devices with limited stretchability, poor reliability, and large gauge factors. Here, we demonstrate a novel sew-and-transfer method for rapid fabrication of low-cost, highly-stretchable interconnects. A zigzag pattern of thin metal wires is sewn into a polymeric film using a commercial sewing machine and a double-thread stitch, where one of the threads is water-soluble polyvinyl alcohol (PVA). The pattern is subsequently transferred onto a stretchable elastomeric substrate by dissolving the PVA in warm water. The resulting structures exhibit extreme stretchability exceeding 500 % strain for a zigzag angle of 18°. They are also highly robust, capable of withstanding thousands of repeated stretch-and-release cycles (18,000 at 110 % strain, 50,000 at 55 % strain, and >120,000 at 30 % strain) without any noticeable change in resistance even at maximum strain levels. Using this technique, we demonstrate a stretchable inductive strain sensor for monitoring balloon expansion in a Foley urinary catheter. The sensor is capable of detecting changes in balloon diameter from 9 mm to 38 mm, with an average sensitivity of 4 nH/mm.

INTRODUCTION

The concept of stretchable electronics has garnered significant interest over the past decade with its promise of providing an adaptable platform for wearable electronics, implantable microsystems, and soft robotics [1–5]. Stretchable interconnects are a key component in such systems, with recent publications reporting various approaches using patterned meander/wavy metallic thin films [6–9] or liquid metal-filled microchannels integrated onto elastomeric substrates [10,11]. Designs such as these offer acceptable operation under limited strain values. Their fabrication, however, requires cleanroom facilities (deposition and lithography) and the resulting interconnects suffer from various functional limitations including structural weakness, limited stretchability, liquid metal leakage, and a large impedance change with applied tensile strain (although of limited value for electrical interconnects, this effect has been used to fabricate strain sensors, [12–15]).

As an alternative to expensive cleanroom fabrication techniques, we present a sewing machine-enabled stitch-and-transfer method for the fabrication of extremely-robust and highly-stretchable electrical interconnects embedded in elastomeric substrates. Sewing machines provide extraordinary and sophisticated capabilities for precise manipulation of threads to form complex patterns on fabric and polymeric substrates. Although they are currently limited to the textile industry, the economical nature of sewing machines may soon place them among a growing toolset of rapid-prototyping technologies that have been featured in recent publications, including cutter plotters, [16] laser engravers, [17,18] inkjet printers, [19,20] and 3D printers [21–25]. Using this technology, we were able to create intricate arrays of metallic wires sewn onto a poly(ethylene terephthalate) (PET) sheet, transfer them to a stretchable substrate (Ecoflex®), and release them from the PET by dissolving one of the threads in water (due to its strechability and stickiness, direct sewing onto elastomers is not feasible/practical). By adjusting the tension, geometry, and length of the patterns, a variety of interconnects were fabricated showing stretchabilities of up to 500 %. In addition, since solid wires were used in their construction, the resistance remained constant throughout the strain cycle, an important criterion for proper function of electronic circuits. This technique extends the applicability of sewing machines from commercial textiles to the fabrication of smart electro-opto-fluidic microsystems on stretchable substrates.

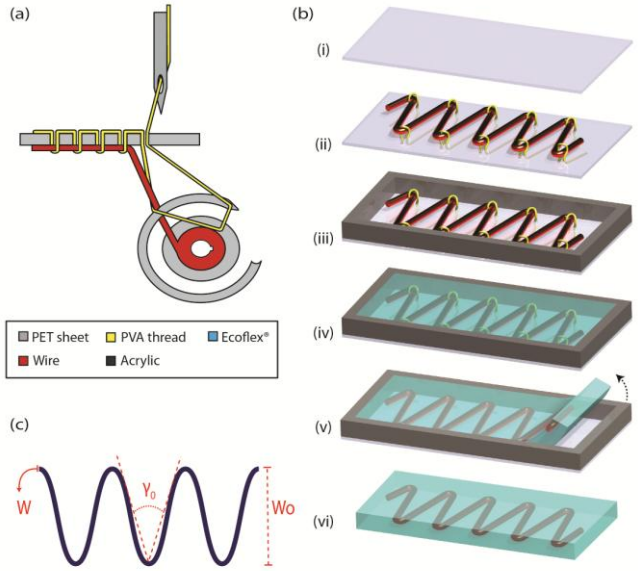

Figure 1: (a) A schematic of the primary sewing machine components illustrates the process of creating zigzag wires using a metallic wire and a water-soluble PVA thread. (b) An overview ofthe stitch-and-transfer process for fabricating stretchable interconnections. (c) A sketch of a sewn zigzag pattern, identifying the design parameters of the pattern (W_o is the un-stretched width and γ_o is the pitch angle).

FABRICATION PROCESS

Figure 1a illustrates the main operational components of a sewing machine, comprising a needle threaded with the primary thread, a substrate for processing, and a second thread source (bobbin). During operation, the threaded needle penetrates the substrate, and its thread is interlaced with that of the bobbin to create a secure sewn pattern with a different thread on each side of the substrate. Most modern sewing machines can additionally control the lateral motion of the needle during sewing, allowing for the creation of various sewing patterns (e.g., zigzags). The patterns are selected by the operator by using dedicated knobs or levers on the machine, and they can be fine-tuned by adjusting the tension of the primary thread. This capability of generating various patterns, along with the ability to accommodate two types of threads (e.g., a

9781940470016/HH2014/$25©2014TRF
DOI 10.31438/trf.hh2014.49

dissolvable polymer as the primary thread and a thin wire as the secondary one) are key features for fabricating robust stretchable interconnects.

The complete fabrication process is illustrated in Figure 1b. The zigzag patterns are fabricated using a conventional sewing machine (Singer® 2277 Tradition). First, a dissolvable PVA thread (80 µm-diameter, purchased from Superior Threads) is positioned on the spooling pin, and a thin (90 µm) magnet wire (TEMCo® Industrial Power Supply, Fremont, CA) is loaded into the bobbin of the machine. The PVA is threaded thought the needle, and its tension is adjusted such that the conductive wire remains on one side of the substrate throughout the sewing process. Next, an appropriate stitch setting is selected (i.e. zigzag with desired track width and angle). The trace pattern is then transferred onto a 100 µm-thick PET sheet (3M® PP2500) by a standard sewing technique (Figure 1b-i,ii). Subsequently, the wire side of the PET sheet is covered with an elastomer pre-polymer (Ecoflex®, Smooth-on, Inc.); an acrylic frame is used as a spacer to control the thickness of the elastomer. The Ecoflex® is allowed to crosslink at room temperature for 5 hours. This step transfers the sewn metallic pattern onto an elastic substrate. Finally, the stretchable embedded wires in Ecoflex® are released from the PET by soaking the structure in water at 40 ºC for 15 min. By submerging the structure in warm water the PVA thread dissolves, allowing the stretchable connections to be easily peeled off the PET sheet, (Figure 1b-iii,iv). Finally, the PET substrate is peeled off releasing the stretchable substrate with the embedded patterned wire (Figure 1b-v,vi).

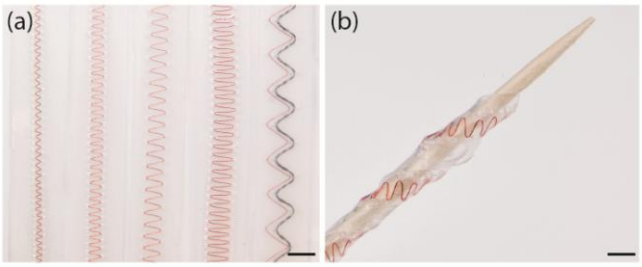

Figure 2. (a) Photograph of stretchable interconnects with different un-strained pitch angles (γ_o); the right-most pattern features a wire/conductive thread hybrid implementation. (b) Fabricated stretchable interconnect wound around a toothpick. All scale bars: 3 mm.

Figure 1c illustrates a typical pattern. The stitching parameters can be easily adjusted to create various zigzag patterns with controllable un-strained width (W_o) and pitch angle (γ_o). For a zigzag pattern, stretchability is primarily determined by the pitch angle, which is inversely proportional to the maximum elongation of the structure. Theoretically, the angle can be made arbitrarily small; in practice, however, γ_o has a lower limit, below which the concentrated stress at the sharp concave trace corners results in plastic deformation and eventual failure of the wire. In addition, a very small pitch angle limits the amount of elastomeric material between adjacent legs, resulting in a weaker bond between the wire and the elastomer. To avoid these issues, our devices were fabricated with a minimum un-strained pitch angle of 18°, which was experimentally determined to be the best for the wire diameters. Various zigzag patterns were fabricated using the method just described; Figure 2a shows several implemented patterns embedded in Ecoflex®. Upon qualitative inspection, the structures were found to be highly elastic, soft, and partially adhesive, all qualities that enable uniform contact between the wires and any adjacent surface even at high curvatures (> 0.52 mm^{-1}), Figure 2b.

MECHANICAL AND ELECTRICAL CHARACTERIZATIONS

The stretchable interconnects were quantitatively evaluated in terms of their impedance stability in response to strain and their robustness under repeated stretch/release cycles. As mentioned above, stretchable conductive patterns that are fabricated via thin metal layer deposition on elastomeric substrates or rely on liquid-alloy-filled microchannels show a significant increase in their impedance as the structures are subjected to strain. In contrast, our structures use zigzag solid microwires, which exhibit very low impedance change even at strain levels as high as 500 %. The resistance of interconnects with different un-strained pitch angles γ_o was measured under variable tensile strain. Each interconnect sample was clamped by its two ends and connected to a multi-meter to continuously record the resistance change in the tracks. The tensile strain was continuously increased until the wires were completely straightened ($\gamma = 180°$).

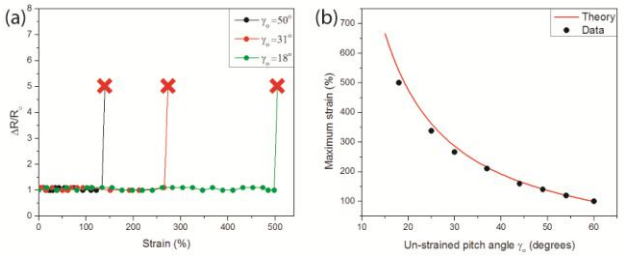

Figure 3. (a) Normalized resistance change for stretchable interconnects under various strains for 50º, 31º and 18º un-strained pitch angles. (b) Maximum stretchability of zigzag interconnections as a function of un-strained pitch angle γ_o.

Figure 3a shows percentage resistance change ($\Delta R/R_o$) vs. strain for patterns with different un-strained pitch angles of 18º, 31º, and 50º (R_o is the initial resistance, < 1 Ω, and R is the strained resistance). The red X marks show the strain levels at which interconnect fails (open circuit). As can be seen, the impedance values are stable up to the breaking point, with 18º pitch angles being able to withstand 500 % strain. Furthermore, as long as the stretchable interconnects were not subjected to strains beyond elastic limit, no hysteresis was observed. We also investigated the maximum strain for stretchable interconnects having different values of un-strained design parameters (γ_o and W_0), Figure 3b. As expected, the maximum attainable mechanical tensile strain of various samples shows an inverse relationship with the un-strained pitch angle γ_o (no dependence with W_0 was observed).

Figure 4a shows the normalized resistance change of different stretchable interconnects with different un-strained pitch angle γ_o in response to various degrees of bending. In order to evaluate the reliability of interconnects; the patterns were subjected to repeated stretch-and-release cycles at various strain levels (30−110 %). Each test sample was clamped at one end and attached to a magnetically-controlled diaphragm at the other end. The diaphragm displacement stretched the sample at a rate of 60 % per second for 120,000 cycles. The electrical resistance of the sample was measured continuously during the stretching and releasing

cycles. The test was repeated for five samples having different γ_o values. Figure 4b shows the results in which the samples exhibited no failure or resistance increase for more than 15,000 cycles at both strain levels. For 30 % strain, satisfactory device performance was maintained for more than 120,000 cycles. For larger strains (110 %), however, the devices showed degraded performance and failure at a lower number of cycles. Interconnect failure was primarily due to wire breakage at the corners of the zigzag pattern caused by metal fatigue.

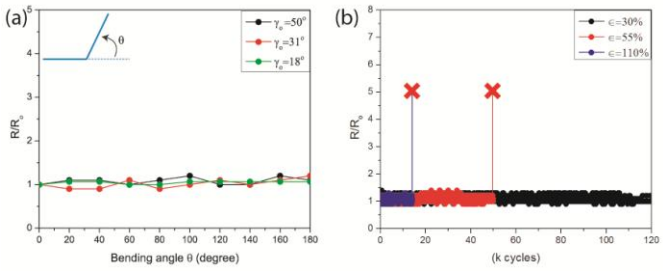

Figure 4. (a) Normalized resistance change for stretchable interconnections under various bending angles for 50º, 31º and 18º un-strained pitch angles γ_o. (b) Normalized resistance change during 120,000 stretch/release cycles at 30 %, 55 % and 110 % strain levels.

STRETCHABLE INDUCTIVE STRAIN SENSOR

To demonstrate a practical application, we fabricated an inductive strain sensor that was subsequently mounted onto the balloon of Bardex® Foley urinary catheter for monitoring the inflation of the catheter balloon inside bladder. The device consisted of a stretchable single loop coil created on Ecoflex® via the sew-and-transfer method and bonded around the balloon region of a 20F Foley catheter using uncrosslinked Ecoflex®. The coil was made of a single loop of wire (100 µm thick) patterned into a curved zigzag with 400 µm spacing between each zigzag. Figure 5a shows a photograph of a Bardex® Foley catheter with the sensor attached. By inflating the balloon, the spacing between the zigzag angle and coil diameter increases significantly, Figure 5b. Since the inductance of a coil is directly proportional to its diameter (L ~ d), inflating the balloon leads to an increase in the coil inductance. The inductance was continuously monitored at 200 kHz with an LCR meter (GW Instek LCR-819), Figure 6a.

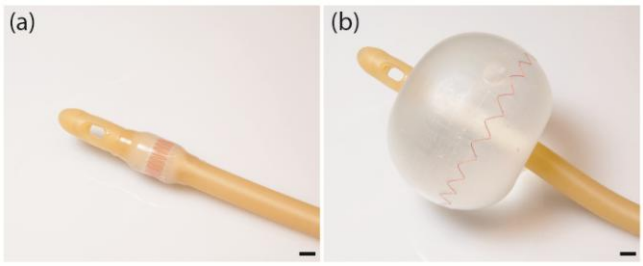

Figure 5. Stretchable inductive strain sensor attached to the balloon of a Foley urinary catheter (a) before inflating the balloon of the catheter and (b) after inflating it and stretching the coil. All scale bars: 3 mm.

The sensor was tested by gradually inflating the balloon with water and subsequently deflating it. The measured inductance vs. balloon diameter (between 9 mm and 38 mm) is plotted in Figure 6b, showing a positive trend between the inductance and the diameter with an average sensitivity of 4 nH/mm and very little hysteresis (a maximum of 3.1%).

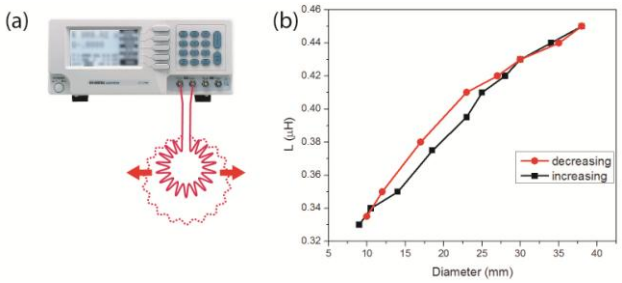

Figure 6. (a) Schematic of the experimental setup. (b) Sensor inductance change versus diameter of the coil.

CONCLUSIONS

We successfully developed a method of fabricating extremely robust and highly stretchable electrical interconnections via a sew-and-transfer technique. The stretchable pattern is formed using a combination of a water soluble thread and a thin metallic wire sewn onto a polymeric substrate and subsequently transferred to an elastomeric substrate. The structures can stretch up to 500 % without significant loss of conductivity. The devices tolerate repeated stretch-release cycles (> 120,000 for 30 % strain, up to 18,000 for 50 % strain) with failure at high strain levels mainly due to the metal fatigue at the sharp concave corners. As a proof of concept, we fabricated a stretchable inductive strain sensor that can be attached to a commercial Foley urinary catheter to measure inflation of the balloon tip in the bladder.

ACKNOWLEDGEMENTS

Funding for this work was provided by the National Science Foundation under grant EFRI-BioFlex #1240443.

REFERENCES

[1] D.-H. Kim and J. a. Rogers, "Stretchable Electronics: Materials Strategies and Devices," *Adv. Mater.*, vol. 20, no. 24, pp. 4887–4892, Dec. 2008.

[2] S. P. Lacour, S. Benmerah, E. Tarte, J. FitzGerald, J. Serra, S. McMahon, J. Fawcett, O. Graudejus, Z. Yu, and B. Morrison, "Flexible and stretchable micro-electrodes for in vitro and in vivo neural interfaces.," *Med. Biol. Eng. Comput.*, vol. 48, no. 10, pp. 945–54, Oct. 2010.

[3] J. A. Rogers, T. Someya, and Y. Huang, "Materials and mechanics for stretchable electronics.," *Science*, vol. 327, no. 5973, pp. 1603–7, Mar. 2010.

[4] N. Lu and D.-H. Kim, "Flexible and Stretchable Electronics Paving the Way for Soft Robotics," *Soft Robot.*, vol. 1, no. P, pp. 53–62, Jul. 2013.

[5] J.-H. Ahn and J. H. Je, "Stretchable electronics: materials, architectures and integrations," *J. Phys. D. Appl. Phys.*, vol. 45, no. 10, p. 103001, Mar. 2012.

[6] J. Jones, S. P. Lacour, S. Wagner, and Z. Suo, "Stretchable wavy metal interconnects," *J. Vac. Sci. Technol. A Vacuum, Surfaces, Film.*, vol. 22, no. 4, p. 1723, 2004.

[7] P. Görrn, W. Cao, and S. Wagner, "Isotropically stretchable gold conductors on elastomeric substrates," *Soft Matter*, vol. 7, no. 16, p. 7177, 2011.

[8] W. M. Choi, J. Song, D.-Y. Khang, H. Jiang, Y. Y. Huang, and J. A. Rogers, "Biaxially stretchable 'wavy' silicon

nanomembranes.," *Nano Lett.*, vol. 7, no. 6, pp. 1655–63, Jun. 2007.

[9] D.-H. Kim, S. Wang, H. Keum, R. Ghaffari, Y.-S. Kim, H. Tao, B. Panilaitis, M. Li, Z. Kang, F. Omenetto, Y. Huang, and J. a Rogers, "Thin, Flexible Sensors and Actuators as 'Instrumented' Surgical Sutures for Targeted Wound Monitoring and Therapy.," *Small*, pp. 1–6, Aug. 2012.

[10] H.-J. Kim, C. Son, and B. Ziaie, "A multiaxial stretchable interconnect using liquid-alloy-filled elastomeric microchannels," *Appl. Phys. Lett.*, vol. 92, no. 1, p. 011904, 2008.

[11] H.-J. Kim and B. Ziaie, "A Biaxial Stretchable Interconnect With Liquid-Alloy-Covered Joints on Elastomeric Substrate," *J. Microelectromechanical Syst.*, vol. 18, no. 1, pp. 138–146, Feb. 2009.

[12] C. Lucarotti, C. M. Oddo, N. Vitiello, and M. C. Carrozza, "Synthetic and bio-artificial tactile sensing: a review.," *Sensors (Basel).*, vol. 13, no. 2, pp. 1435–66, Jan. 2013.

[13] P. Dario, "Tactile sensing: Technology and applications," *Sensors Actuators A Phys.*, vol. 27, pp. 251–256, 1991.

[14] H. Yousef, M. Boukallel, and K. Althoefer, "Tactile sensing for dexterous in-hand manipulation in robotics—A review," *Sensors Actuators A Phys.*, vol. 167, no. 2, pp. 171–187, Jun. 2011.

[15] M. I. Tiwana, S. J. Redmond, and N. H. Lovell, "A review of tactile sensing technologies with applications in biomedical engineering," *Sensors Actuators A Phys.*, vol. 179, pp. 17–31, Jun. 2012.

[16] P. K. Yuen and V. N. Goral, "Low-cost rapid prototyping of flexible microfluidic devices using a desktop digital craft cutter.," *Lab Chip*, vol. 10, no. 3, pp. 384–7, Feb. 2010.

[17] A. Toossi, M. Daneshmand, and D. Sameoto, "A low-cost rapid prototyping method for metal electrode fabrication using a CO2 laser cutter," *J. Micromechanics Microengineering*, vol. 23, no. 4, p. 047001, Apr. 2013.

[18] G. Chitnis, Z. Ding, C.-L. Chang, C. A. Savran, and B. Ziaie, "Laser-treated hydrophobic paper: an inexpensive microfluidic platform.," *Lab Chip*, vol. 11, no. 6, pp. 1161–5, Mar. 2011.

[19] E. Beckert, R. Eberhardt, O. Pabst, F. Kemper, Z. Shu, A. Tünnermann, J. Perelaer, U. Schubert, and H. Becker, "Inkjet printed structures for smart lab-on-chip systems," in *Proc. of SPIE*, 2013, vol. 8615, pp. 86150E–1–10.

[20] O. Pabst, E. Beckert, J. Perelaer, U. S. Schubert, R. Eberhardt, and A. Tünnermann, "All inkjet-printed electroactive polymer actuators for microfluidic lab-on-chip systems," in *Proc. SPIE*, 2013, vol. 8687, pp. 86872H–1–6.

[21] M. D. Symes, P. J. Kitson, J. Yan, C. J. Richmond, G. J. T. Cooper, R. W. Bowman, T. Vilbrandt, and L. Cronin, "Integrated 3D-printed reactionware for chemical synthesis and analysis.," *Nat. Chem.*, vol. 4, no. 5, pp. 349–54, May 2012.

[22] M. S. Mannoor, Z. Jiang, T. James, Y. L. Kong, K. a Malatesta, W. O. Soboyejo, N. Verma, D. H. Gracias, and M. C. McAlpine, "3D printed bionic ears.," *Nano Lett.*, vol. 13, no. 6, pp. 2634–9, Jun. 2013.

[23] J. S. Miller, K. R. Stevens, M. T. Yang, B. M. Baker, D.-H. T. Nguyen, D. M. Cohen, E. Toro, A. A. Chen, P. A. Galie, X. Yu, R. Chaturvedi, S. N. Bhatia, and C. S. Chen, "Rapid casting of patterned vascular networks for perfusable engineered three-dimensional tissues.," *Nat. Mater.*, vol. 11, no. 9, pp. 768–74, Sep. 2012.

[24] I. D. Ursan, L. Chiu, and A. Pierce, "Three-dimensional drug printing: a structured review.," *J. Am. Pharm. Assoc. (2003).*, vol. 53, no. 2, pp. 136–44, 2013.

[25] T. Billiet, M. Vandenhaute, J. Schelfhout, S. Van Vlierberghe, and P. Dubruel, "A review of trends and limitations in hydrogel-rapid prototyping for tissue engineering.," *Biomaterials*, vol. 33, no. 26, pp. 6020–41, Sep. 2012.

CONTACT

*B.Ziaie, tel:+1-765-404-0726; bziaie@purdue.edu

BIOLOGICALLY ENABLED MICRO- AND NANOSTENCIL LITHOGRAPHY USING DIATOMS

J. Cai[1, 2], S.W. Anderson[3], X. Wang[1], and X. Zhang[1]*
[1]Boston University, Boston, Massachusetts, USA
[2]Beihang University, Beijing, China
[3]Boston University Medical Center, Boston, Massachusetts, USA

ABSTRACT

Diatoms are incredibly diverse, photosynthetic microalgae, which are widely distributed in aquatic environments. The wide array and intricate morphology of the micro- and nanostructured silica exoskeletons encasing the single-celled diatoms offer a tremendous opportunity for biologically-assisted fabrication approaches. Herein, *Coscinodiscus sp.* diatom frustules were aligned on a silicon substrate and subsequently employed as shadow masks during the electron beam deposition of gold. This diatom frustule enabled stencil lithography approach yielded the capacity to precisely pattern gold structures on the silicon substrate with a large range of feature sizes, ranging down to the nanoscale.

INTRODUCTION

Diatoms are microscopic, unicellular photosynthetic algae, which are ubiquitous in aquatic environments, with approximately 100,000 different species ranging from 1 μm to 4 mm in size [1]. The silica exoskeletons of diatoms, termed frustules, feature thousands of distinct morphologies and possess an incredibly wide range of intricate micro- and nanoscale patterns. The unique morphologies of these biologically evolved exoskeletons have been evolutionarily optimized for a variety of functions including photosynthesis, gas and nutrient exchange, as well as offering mechanical protection. Given their highly organized morphology, diatoms represent promising candidates for developing biologically-assisted fabrication approaches [2]. To date, using various molding and templating approaches, the capacity to replicate the intricate morphologies of the diatom frustule has been reported, thus demonstrating the potential of these biological templates to serve as the foundation for next generation, biologically enabled micro- and nanofabrication strategies. For example, the nanoporous morphology of the diatom frustules has been employed to yield nanotextured substrates composed of metal as well as polydimethylsiloxane (PDMS) [3]. Beyond the capacity to generate nanotextured surfaces, however, the use diatoms to create micro- and nanoscale patterns of various materials, such as metals or polymers, on a variety of underlying substrates has not been demonstrated. This capacity to create patterns of materials, which mirror the intricate morphology of the diatom frustule has the potential to facilitate a variety of practical applications and will be specifically addressed in this work. An outstanding limitation of the majority of the prior efforts which employed diatoms in biologically enabled fabrication strategies is the fact that they have focused on either collections of randomly distributed diatoms or single diatoms. However, with the exception of a previously reported method using inkjet printing of diatom frustules, there has been little progress in the development of fabrication strategies which employ uniformly arrayed diatom frustules, a critical step towards the realization of scalable diatom-based micro-/nanomanufacturing and another important focus of this work [4]. In this work, we report the development of a versatile, diatom-enabled fabrication approach with the capacity to generate precisely patterned gold micro- and nanostructures, which mirror the highly-organized, porous frustule morphology on underlying silicon substrates. Specifically, *Coscinodiscus sp.* diatom frustules were uniformly aligned on silicon substrates and employed as shadow masks in a stencil lithography approach during the electron beam deposition of gold (Au). This novel, biologically-enabled stencil lithography approach yielded the capacity to precisely pattern gold structures on the silicon substrate over large areas with a range of feature sizes, ranging down to the nanoscale.

METHODS

Initial steps in the development of the diatom frustule-based approach included the purification and separation of the frustules. To this end, the diatom *Coscinodiscus sp.* (CCMP 1583) was purchased from the National Center for Marine Algae and Microbiota (NCMA) at the Bigelow Laboratory for Ocean Sciences. Initially, the *Coscinodiscus sp.* diatoms were harvested from 2L of culture media using a sieve, a process which yielded an approximately 10 mL solution of highly concentrated diatoms. This concentrated diatom solution was subsequently gradually poured into a beaker containing 100 mL of concentrated sulfuric acid (98% H_2SO_4)-based solution. Next, this pickling solution was heated in a water bath at 65 ºC for 40 min, thereby ensuring the complete removal of the entirety of the organic contents of diatoms. After cooling this solution, the diatom exoskeletons were filtered with a 40 μm mesh size cell strainer and subsequently continuously flushed for five minutes with deionized (DI) water.

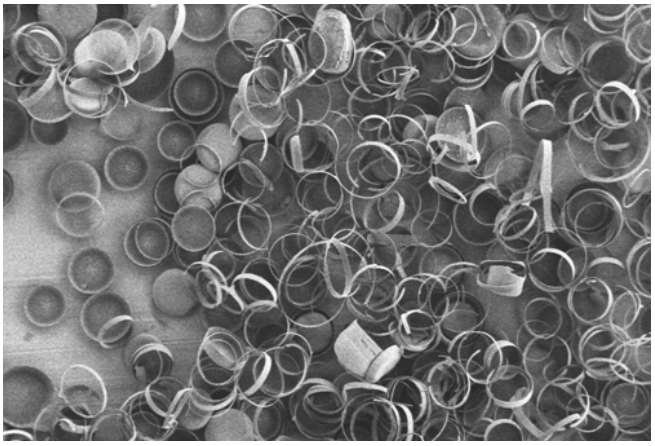

Figure 1: SEM image demonstrates diatom valves and girdle bands following purification steps and prior to separation of the two components using a combination of filtering/settling.

In order to further separate the diatom frustule components (Figure 1), the thus cleaned frustule valves and girdle bands were again dispersed in DI water and filtered with another 70 μm mesh size cell strainer. Next, leveraging the difference in settling rates of the two components of the diatom frustules (diatom valves and girdle bands), a series of settling processes in DI water were used to separate the diatom valves from the girdle bands [5]. In some

9781940470016/HH2014/$25©2014TRF
DOI 10.31438/trf.hh2014.50

Solid-State Sensors, Actuators and Microsystems Workshop
Hilton Head Island, South Carolina, June 8-12, 2014

cases, in order to eliminate nanopore layer along the outer surface of the diatom valves, the diatom frustules were further treated with 0.1% HF solution for 1 min, followed by filtering with a 40 µm mesh size cell strainer and flushed thoroughly with DI water.

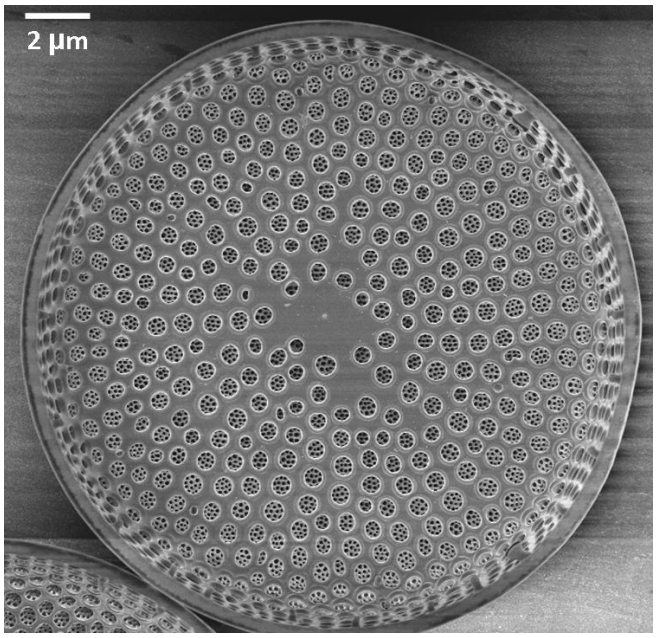

Figure 2: SEM image demonstrates a single Coscinodiscus sp. diatom valve in the 'concave-up' orientation and reveals an intricate, multi-layered pore structure.

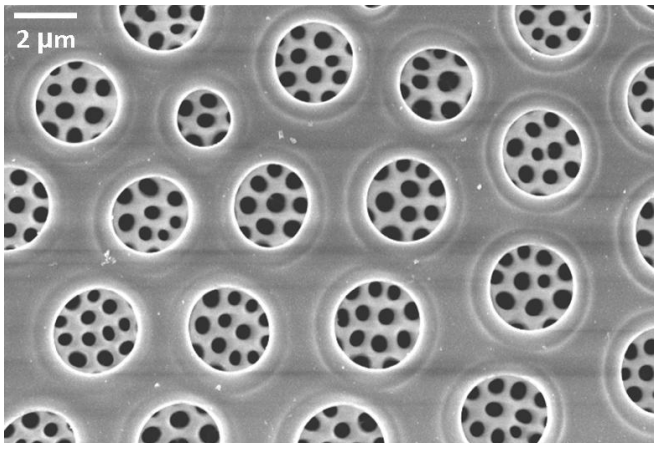

Figure 3: Magnification of Figure 2 demonstrates the sub-micron and nanopore structure of the Coscinodiscus sp. diatom valve.

Following the cleaning and separation of the diatom frustule components, the assembly of a diatom frustule monolayer was undertaken. Firstly, a 20 mm x 20 mm silicon wafer was immersed in 10% HF solution for 10 min to eliminate the native oxide layer, after which it was flushed for one minute with DI water. Next, approximately 500 µl of the condensed diatom frustule solution, containing ~2000 frustules/ml, was pipetted onto the as-prepared silicon wafer, after which the wafer was placed on a heating plate at 130˚C to accelerate the water evaporation. In this case, the diatom-containing solution was heated to the water boiling point in approximately 1 min, yielding the continuous generation of bubbles along the substrate surface and compact monolayers of diatom frustules on the underlying silicon substrate upon evaporation of the water. Next, thin gold films (10 nm to 20nm in thickness) were deposited at a rate of 0.5 Å/s on the diatom monolayers in an electron beam evaporator (Solution, CHA Industries, CA). Following the gold deposition, the diatom frustules were completely removed from the underlying silicon substrate by etching for five minutes using a 1% HF solution. After HF etching and flushing the substrate with DI water, only the patterned gold array persisted on the silicon substrate.

Finally, in order to characterize the deposited gold patterns, a thin gold-platinum layer (approximately 5 nm in thickness) was deposited on dried frustules, after which SEM (Supra 55VP FESEM from Carl Zeiss Microscopy, NY, USA) was employed to image the morphology of diatom frustules.

RESULTS

Of fundamental importance to the approach developed herein were the initial diatom sorting steps, which yield highly monodisperse diatom valves for subsequent alignment upon an underlying substrate. Herein, this was accomplished with a combination of double-filtering to yield highly monodisperse diatom components followed by a series of settling processes to efficiently separate the diatom valves from the girdle bands. The detailed morphology of the unique multi-layered porous structure of the diatom valves is illustrated in Figures 2 and 3.

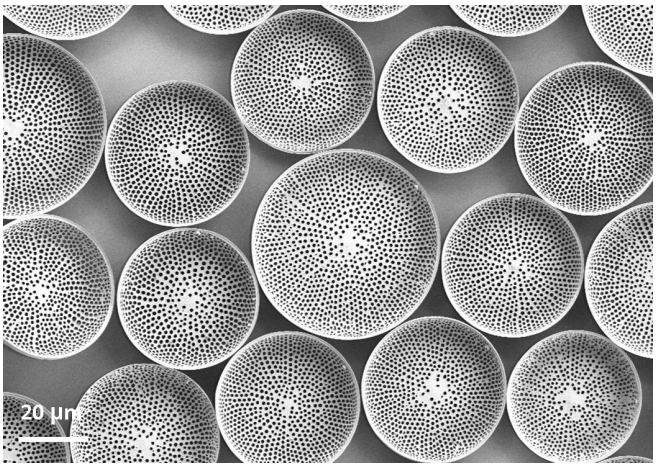

Figure 4: SEM image demonstrates assembled diatom valve monolayer. Note preferred 'concave-up' orientation of the assembled valves.

Following the isolation of high-purity, cleaned diatom valves, the abovementioned assembly process was employed to yield large-area, close-packed diatom monolayers, illustrated in Figure 4. As noted above, the diatom containing solution was quickly heated to evaporate the DI water, yielding the presence of bubbles along the silicon substrate surface. It is hypothesized that these bubbles yielded an efficient assembly of the diatom frustules in the optimal 'concave-up' orientation due to the perturbation of the frustules, causing them to orient in this more stable 'concave-up' orientation along the underlying silicon substrate. This hypothesis is supported by the fact that condensed diatom frustule solutions

pipetted onto silicon and allowed to dry at room temperature resulted in assemblies in which the 'concave-up' and 'concave-down' orientations were represented in relatively equal proportions. In addition to resulting in an optimal 'concave-up' orientation, the rapid evaporation of the frustule-containing water droplets was found to drive the diatom frustules to form a compact monolayer on the silicon substrates. Using the approach herein, we achieved monolayers of diatoms of up to approximately 4 mm^2.

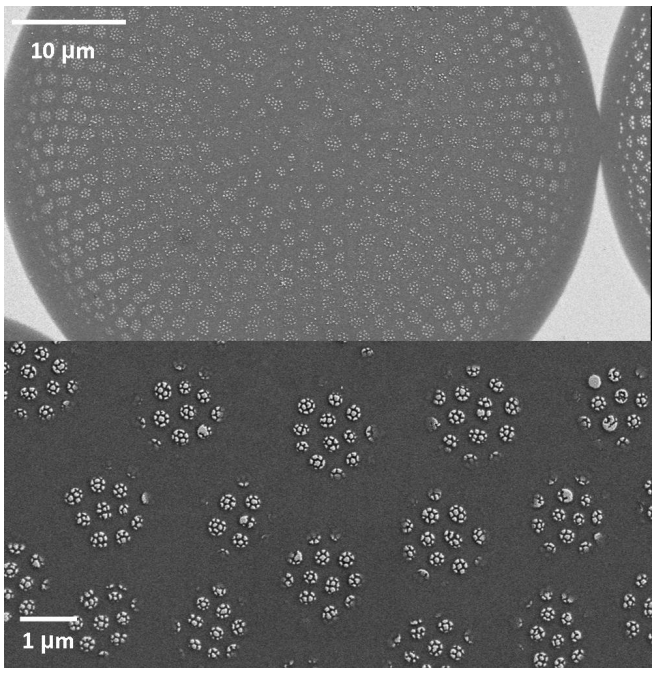

Figure 5: SEM images demonstrate gold nanopatterns following dissolution of the diatom frustules reflecting the nanohole pattern of the diatom valves.

The diatom monolayers overlying the silicon substrates were subsequently employed as shadow masks in a stencil lithography process during which gold thin films were deposited using electron beam evaporation. Figure 5 illustrates the appearance of the silicon substrate following diatom dissolution. In this case, the gold nanopatterns demonstrate feature sizes on the order of 20-40 nm, mirroring both the size and pattern of the nanopores of the diatom frustule valves. Of note, using thin gold films on the order of 10-20 nm, as were employed herein, the distinct nanoscale features reflecting the sizes of the nanopores were readily reproduced. In addition to the gold nanopatterns, the diatom valves, which were modified by removal of the nanopore layer prior to assembly, were employed to yield gold patterns with larger, sub-micron feature sizes. In this case, following valve assembly and gold deposition, patterns with feature sizes on the order of 200 nm were achieved, illustrated in Figure 6, reflecting both the size and periodicity of the second layer of the diatom valve holes.

DISCUSSION

The diatom-enabled approach reported herein, which was specifically employed to fabricate precisely patterned gold structures reflecting the micro- and nanoscale features of the diatom frustule, may find utility in a range of photonics applications. For example, the reported diatom-enabled stencil lithography approach, given its capacity to pattern a landscape of rationally designed gold micro- and nanostructured features, has the potential to be uniquely suited towards the scalable fabrication of SERS substrates. Beyond photonics applications, the capability to fabricate a precisely patterned landscape of micro- and nanoscale features of various materials using a diatom enabled stencil lithography technique potentially enables a wide array of applications, from photovoltaic devices to a host of biomedical technologies.

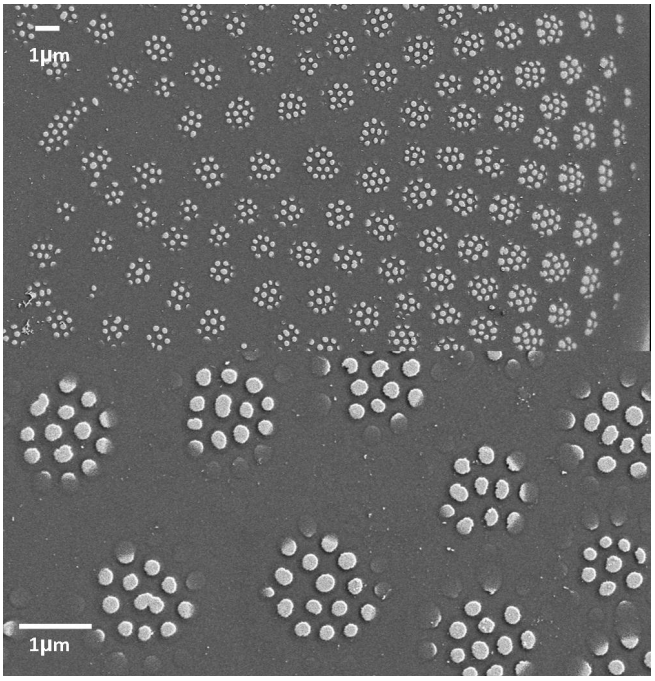

Figure 6: SEM images demonstrate sub-micron scale gold patterns reflecting the sub-micron pore layer of the diatom valve following initial dissolution of the nanopore layer prior to gold deposition.

Finally, it is instructive to consider the potential advantages of the biologically enabled approach reported in this work in comparison to alternative approaches to large area nanopatterning. While enabling the requisite precision to create nanopatterned surfaces, conventional nanolithography techniques such as electron-beam lithography or focused ion beam approaches are fundamentally serial in nature and lack the scalability required for many practical applications. Beyond conventional nanolithography approaches, a host of nanoimprint lithography-based techniques have been developed for diverse applications. However, while imprint lithography approaches yield the requisite precision and their parallel, scalable nature achieves the capacity for increasingly large-area nanopatterning, there remains an inherent need for master molds, which are typically fabricated using costly, serial nanolithographic approaches such as electron-beam lithography. As an alternative, a host of 'bottom-up', self-assembly-based methods have been developed. These 'bottom-up' methods offer a highly scalable approach to nanomanufacturing but lack a similar degree of control over and variety of the patterned nanoscale features when compared to the aforementioned 'top-down' approaches. In comparison to the diverse array of alternative approaches noted above, the diatom enabled stencil lithography approach reported herein mitigates several existing limitations of

these techniques. The proposed diatom-based approach is envisioned to be yield the requisite scalability to enable a diverse array of applications given the capacity to assemble these naturally occurring templates into large-area arrays. In addition to the scalability of diatom enabled lithography given its biological templates, leveraging the staggering variety of nanoscale features, which exist in these naturally occurring organisms yields a large degree of freedom in the achievable nanopatterns.

In summary, this paper reports a novel micro- and nanostencil lithography approach using diatom frustules. Beyond the materials employed herein, this biologically enabled approach may be readily tailored to pattern a variety of materials on various substrates and has the potential to represent a next generation micro- and nanomanufacturing technology which may be optimized towards a diverse array of applications.

REFERENCES

[1] J. Parkinson and R. Gordon, "Beyond micromachining: the potential of diatoms", Trends in Biotechnology, 17, 190 (1999).

[2] R. Gordon, D. Losic, M.A. Tiffany, S.S. Nagy, and F.A. Sterrenburg, "The Glass Menagerie: diatoms for novel applications in nanotechnology", Trends in Biotechnology, 27, 116 (2009).

[3] D. Losic, J. G. Mitchell, R. Lal, and N.H. Voelcker, "Rapid fabrication of micro- and nanoscale patterns by replica molding from diatom biosilica", Advanced Functional Materials, 17, 2439 (2007).

[4] W. Wang, T. Gutu, D.K. Gale, J. Jiao, G.L. Rorrer, and C.H. Chang, "Self-assembly of nanostructured diatom microshells into patterned arrays assisted by polyelectrolyte multilayer deposition and inkjet printing", Journal of the American Chemical Society, 131, 4178 (2009).

[5] D. Zhang, Y. Wang, J. Pan, J. Cai, "Separation of diatom valves and girdle bands from Coscinodiscus diatomite by settling method", Journal of Materials Science, 45, 5736 (2010).

CONTACT

*X. Zhang, tel: + 1.617.358.2702; xinz@bu.edu

MODELING OF A MICROMAGNETIC IMPRINTING PROCESS

O. D. Oniku, A. Garraud, E. E. Shorman, W. C. Patterson, and D. P. Arnold
Interdisciplinary Microsystems Group, University of Florida, Gainesville, FL, USA

ABSTRACT

In this article, we present the magnetic modeling of a batch-fabrication process to imprint microscale pole patterns in hard-magnetic thick films. The imprinting process enables the creation of complex magnetic field patterns from permanent magnetic layers. The selective magnetic imprinting and the resultant stray fields are modeled in a two-step process using COMSOL Multiphysics in conjunction with measured magnetic hysteresis behavior. The models are used to evaluate the process design space and to predict the resulting stray magnetic field distribution in a patterned, 10-µm-thick Co-Pt magnetic film.

INTRODUCTION

In the past decade, there has been substantial advancement in the synthesis of high-performance, thick-film magnetic materials intended for MEMS applications [1, 2]. This advancement has spawned growing interest in the integration of microfabricated magnetic materials into functional microsystems devices. However, the ongoing evolution of magnetic MEMS demands development of processes to microfabricate more complex, multi-pole magnetic structures to create spatially varying microscale magnetic field-patterns for microactuators, vibrational energy harvesters, lab-on-a-chip, and other applications [2].

Permanent magnetic materials require poling to induce a magnetization in a specific direction. This poling process is typically achieved by applying a large, external pulsed magnetic field. For wafer-scale fabrication, this standard approach restricts the magnetization of all magnetic materials on a wafer to only one single direction. Various approaches to realize fine-pitch (<1 mm wide) multi-pole magnetic patterns have been investigated. These methods include: using patterned electrical conductors [3] or soft magnetizing heads [4,5] to create shaped magnetic fields or, using materials with differing coercivities [6] or thermally reduced coercivities [7]. Micro-assembly has also been investigated [8].

Differing from these previous approaches ([3-8]), a key advantage of the imprinting process developed in this work is the ability to create diverse, complex pole geometries at the wafer scale with microscale pole widths. The process uses a microfabricated [9] or a laser-machined [10] soft-magnetic material as a "magnetic mask" (or a flux concentrator) to locally amplify the amplitude of an externally applied, pulsed magnetizing field. This shaped field is used to selectively reverse prescribed regions of a pre-magnetized hard magnetic layer.

We have utilized this process to imprint sub-100 µm features in 10-µm-thick Co-rich CoPt magnetic layer [10]. However, the experimentally measured stray field patterns (12 mT peak-peak) did not match the ~40 mT peak-peak flux density or shape of the expected north/south pole pattern. In this article, we present magnetic modeling of the imprinting process (1) to help improve our understanding of the process; (2) to create a tool for optimization of the process; and (3) for predicting the final stray fields of imprinted magnetic layers.

PROCESS DESCRIPTION

A schematic representation describing the imprinting process is shown in Fig. 1. First a magnetically hard magnetic layer (film) is fabricated on a substrate (10-µm-thick $Co_{80}Pt_{20}$ [11]) and pre-magnetized "up" using a conventional pulsed magnetic field from a magnetizing fixture. A magnetically soft magnetic mask is then placed in contact with the pre-magnetized magnetic layer, and a second pulsed magnetic field (reversal field) is applied in the "down" direction. The magnetic masks used here are 125-µm-thick Fe foils that were laser-machined with slits to create lines and spaces for creating stripe-like magnetization patterns.

Owing to the field concentrating effect of the soft magnetic mask, different field intensities are "felt" by various regions in the magnetic layer. Figure 2 shows a COMSOL simulation that illustrates the field concentrating effect of a soft magnetic mask (in this case, Fe). The field distribution along the mid-plane of the 10-µm-thick Co-Pt layer is plotted in Fig. 2b. For a 0.5 T applied reversal field, a ~0.65 T field amplitude is obtained in the Fe region, whereas a 0.35 T field amplitude is obtained in the air region.

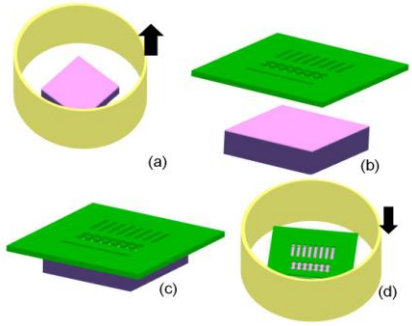

Figure 1: Magnetic patterning process: (a) initially magnetize a hard magnetic layer, (b) prepare magnetic mask by micro-machining desired patterns on a soft magnetic foil, (c) bring mask in contact with magnetic layer, (d) apply a pulse reverse field.

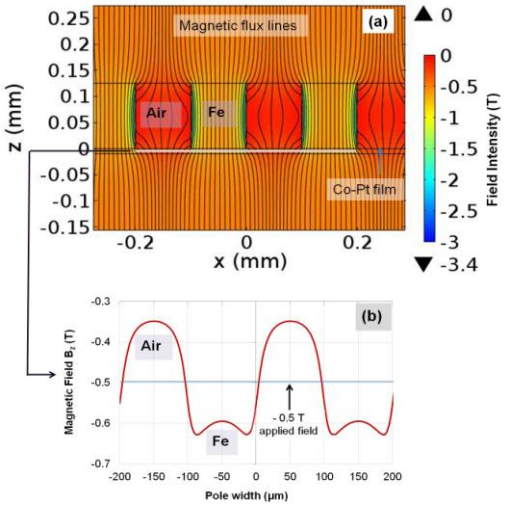

Figure 2: COMSOL simulation of the flux-concentrating effect of an Fe magnetic mask for a 0.5 T amplitude field applied in the downward direction: (a) cross-section distribution of magnetic flux density, (b) magnetic flux density along the mid-plane of the Co-Pt magnetic layer.

MAGNETIC PROPERTIES

For later use in finite-element models, the magnetic properties of both the soft Fe magnetic mask and the hard Co-Pt magnetic layer are measured using a vibrating sample magnetometer (VSM)

9781940470016/HH2014/$25©2014TRF
DOI 10.31438/trf.hh2014.51

(ADE Model EV9). Figure 3 presents the magnetic properties of the magnetic mask ($\mu_0 M_{sat}$ = 2.1 T; μ_r = 800), with the inset showing its optical image. Figure 4 presents the full hysteresis loop along with recoil curves for the 10-µm-thick Co-Pt magnetic layer ($\mu_0 H_{ci}$ = 0.41 T) used in this work. The recoil curves are measured at various fields, corresponding to the applied reversal field amplitudes and will be useful for later modeling of the patterned magnetic structure. The inset is a plot showing the recoil remanence for various reverse fields.

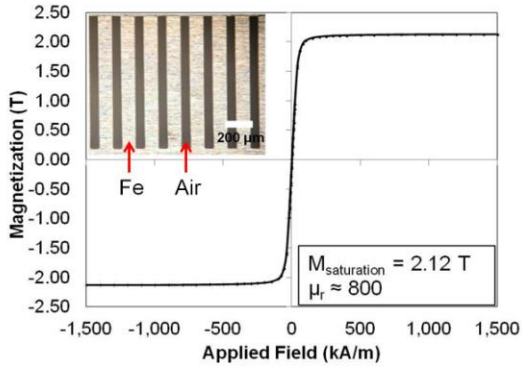

Figure 3: Magnetic properties of laser-micromachined soft-magnetic Fe foil mask. Inset shows an optical image of the mask with a feature size of 100 µm.

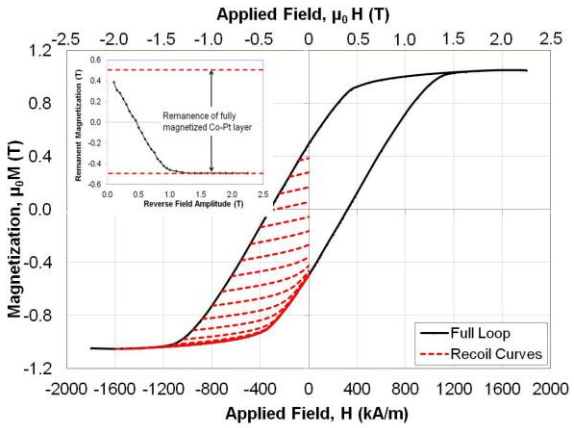

Figure 4: Magnetic properties of electroplated Co-Pt film showing recoil curves at various reversal fields. The inset shows the remanent magnetization of the Co-Pt layer as a function of the reversal field amplitude.

MODELING

The imprinting process is modeled in two stages using 2D magnetostatic finite-element simulations in COMSOL Multiphysics. The first stage simulates the shaped magnetic fields during the peak of the pulsed reversal field. The second stage simulates the final patterned magnetic layer after the imprinting process, making use of information from the first stage simulation. All simulations model the nonlinear magnetic properties using the measured magnetic hysteresis curves presented in Figs. 3 and 4.

Stage 1: Simulation of Pulse Reversal Field

First, the field-concentrating effects of the 125-µm-thick Fe magnetic mask and a 10-µm-thick Co-Pt magnetic layer are simulated for various reversal field amplitudes. Figure 5 shows how the field amplitudes at the mid-plane of the Co-Pt layer (i.e. 5 µm below the mask) evolve with the reversal field. The data points and connecting lines represent the field at the mid-point (center) underneath the Fe and air, respectively. The error bars represent the peak fields of the "bunny ear" features that arise due to edge-effects under the Fe regions (refer to Fig. 2b).

For good pattern transfer, the intrinsic coercivity (H_{ci}) of the hard magnetic layer must lie in between the field amplitudes in the air and that in the Fe regions, i.e. $|B_{air}| < |H_{ci}| < |B_{Fe}|$. This ensures that the field in the Fe region is sufficient to flip the magnetization, whereas the field in the air region is not strong enough. Another consideration is the field-contrast

$$\gamma = \frac{B_{Fe} - B_{air}}{B_{Fe} + B_{air}} \qquad (1)$$

which quantifies the difference between the B-field intensities in the Fe and air regions, and should be maximized for good pattern transfer. As shown in Fig. 6, the field contrast appears to be fairly constant for all applied reverse field amplitudes until reaching the saturation level of the magnetic mask (2.1 T in this case).

These simulations suggest a reversal field amplitude of ~0.5 T, which correlates well with the reversal field amplitude found previously to yield good pattern transfer [10]. Example magnetic patterns are shown in Fig. 7.

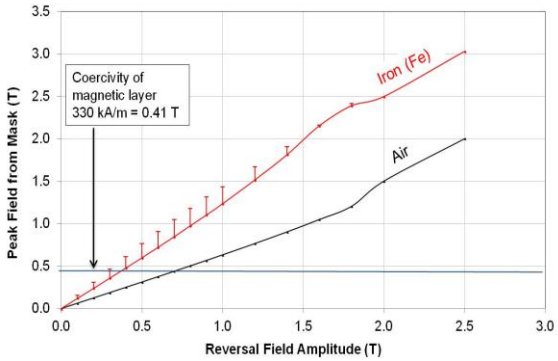

Figure 5: COMSOL simulation of field amplitudes in the Fe and air regions at the mid-plane of the 10-µm-thick Co-Pt magnetic layer for a 125-µm-thick Fe magnetic mask for various applied pulse reverse fields.

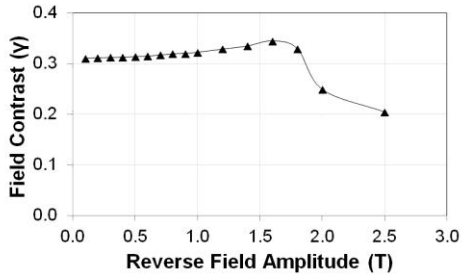

Figure 6: Field contrast for the data shown in Figure 5 as a function of applied reverse field.

Figure 7: Optical images of magnetic masks and resulting patterned magnetic layers (magneto-optical images) showing good pattern transfer using a 0.5-T reversal field: (a) simple stripe-like pattern with 100-µm feature size, (b) text/graphic pole pattern.

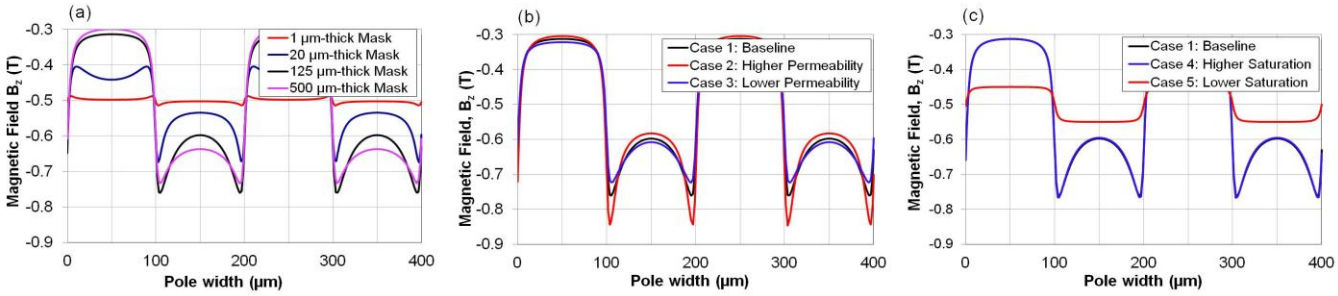

Figure 8: Study of the effects of mask properties and geometry for a 0.5 T reversal field: (a) effect of mask thickness. (b) effect of saturation magnetization, and (c) effect of relative permeability. All simulations are for a 10-µm thick Co-Pt magnetic layer.

To further study the field concentrating effects of the magnetic mask, additional simulations are performed with parametric variations of the mask geometry and mask magnetic properties. Table 1 summarizes the different magnetic properties considered in this study. Figure 8 shows different parametric variations of the magnetic mask, assuming a 0.5 T pulse reversal field and a 10-µm-thick Co-Pt magnetic layer.

Table 1: Magnetic properties of the magnetic mask considered in the parametric simulations.

Case	**1 (Baseline)**	**2**	**3**	**4**	**5**
M_{sat} (T)	2.1	2.1	2.1	3.0	0.2
μ_r	800	10000	50	800	800

Figure 8a indicates that in order to obtain a good pattern transfer, the thickness of the magnetic mask should be significantly greater than the thickness of the hard magnetic film. If the mask is too thin (e.g. the 1 µm case), there is little field contrast in the underlying magnetic layer. In the case considered here, the mask thickness (125 µm) is 12x greater than the thickness of the magnetic film (10 µm), which yields about 80% of the maximum field contrast.

Figure 8b shows that while the relative permeability of the magnetic mask does not significantly affect the field contrast, a higher permeability will produce more pronounced edge effects that increase the non-uniform field distribution ("bunny ears") in the Fe region. (In this case the mask is not saturated)

Figure 8c shows that the saturation magnetization of the magnetic mask appears to be a significant factor in the field contrast—a high saturation material yields a larger field contrast and vice versa. Figure 9 studies this effect with more detail, showing the predicted shaped fields for various mask saturation values. It is observed that when the saturation magnetization of the mask is at below the pulse reversal field (0.5 T)—meaning the mask is saturated—the field distribution in the Fe and air regions is fairly smooth and symmetric, with a peak-peak variation approximately equal to half the saturation magnetization of the mask. When the mask has a higher saturation—and is not saturated—the field pattern becomes more non-uniform, i.e. the "bunny ears" get larger and larger.

Stage 2: Simulation of Imprinted Magnetic Layer

To further explore the modeling of the selective imprinting process, a second model is developed to predict the resultant stray fields from the selectively magnetized layer. For this model, the magnetic layer is sub-divided into discrete sectors that describe the spatial field distribution from the mask in a piecewise fashion.

Figure 10 shows an example of the piecewise representation. The magnetic properties of each sector are defined by a specific recoil-magnetization curve (shown in Fig. 4), which depends on

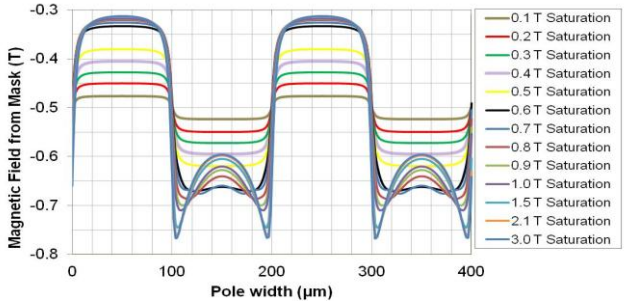

Figure 9: Magnetic field distribution from masks with various saturation magnetizations (M_{sat}) using a 0.5-T reversal field. Result indicates the disappearance of the "bunny-ear" shape effect for materials with M_{sat} close to or lower than the applied reversal field. (All results are evaluated at 5 µm distance from the mask).

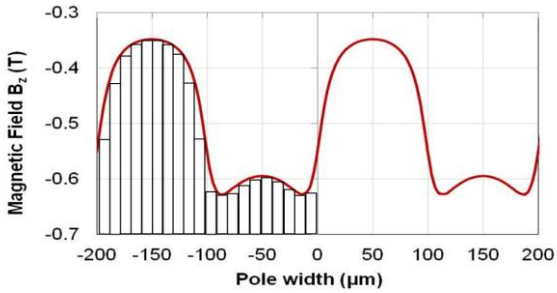

Figure 10: Piecewise representation of the mask field distribution where each discrete sector represents the amplitude and position of the field felt during the selective magnetization process. Ten sectors (each 10-µm wide) are used to represent the field distribution in each of the Fe and air regions.

the amplitude and position of the field experienced during the reversal process. By simulating the ensemble of these sectors, the net magnetic field from the multi-pole patterned layer can then be evaluated at various heights.

Using this method, Fig. 11 shows the simulated stray magnetic flux densities at various heights above the surface for a 10-µm-thick Co-Pt film patterned using the 125-µm-thick Fe magnetic mask with a 0.5 T pulse reversal field. Nearer to the surface of the magnetic layer, there is evidence of the non-uniform magnetization in the Fe regions (the "bunny ears"). As the evaluation height is farther away from the surface of the patterned magnetic layer, the field distribution becomes more uniform and sinusoidal. As indicated earlier, this non-uniformity arises from the fact that the saturation magnetization of the Fe magnetic mask (2.1 T) is significantly higher than the applied reversal field (0.5 T).

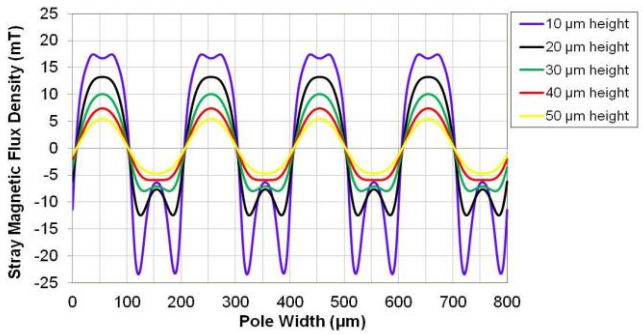

Figure 11: COMSOL simulation of stray magnetic flux density from patterned magnetic film using the modeling approach described in the article.

Furthermore, a comparison is made between the COMSOL simulations and experimental field measurements obtained from a quantitative magneto-optical indicator film (MOIF) [12]. Figure 12 shows the measured fields in comparison to the fields predicted by our process model and the expected fields for an "ideal" magnetization (where each pole is uniformly magnetized to its remanent value). The simulated data matches quite well in both amplitude and shape to the measured field pattern. In contrast, the fields predicted for the ideal magnetization significantly overpredict the amplitude and do not capture the shape of the real field pattern. The difference between the ideal results and the actual results are due to the imperfect magnetization, as described earlier. The complex shape of the measured and simulated stray field is attributed to the field shaping of the mask.

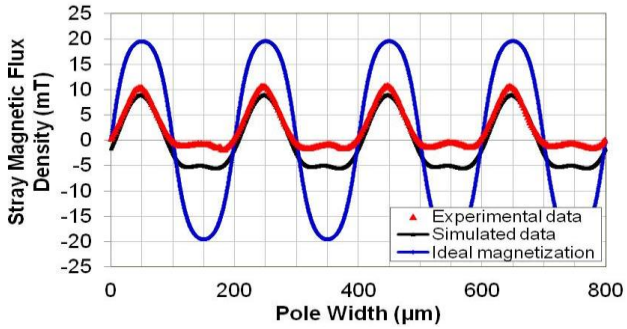

Figure 12: Comparison of measured stray magnetic flux density with simulated results at ~35 µm above the surface of a patterned Co-Pt magnetic layer.

CONCLUSION

We have introduced a modeling approach for a microscale magnetic imprinting process. This model provides a tool for the prediction of the stray magnetic field and the optimization of the magnetic pattern transfer. The pulsed field amplitude required for the process is determined by the magnetic properties of the magnetic layer to be patterned. However, simulations show that the thickness and saturation magnetization of the magnetic mask are important factors to be considered to obtain a good field concentrating contrast and consequently a desirable pattern transfer. We show that the magnetic mask thickness should be at least 10x greater than the thickness of the magnetic layer, and the saturation magnetization should be approximately equal to the required reversal field amplitude. The relative permeability of the magnetic mask is not so important, so long as it is significantly greater than that of air.

The modeling process is experimentally evaluated by patterning simple stripe patterns in 10-µm-thick Co-Pt film using a 125-µm-thick Fe foil magnetic mask. A stray magnetic flux density of 12 mT peak-peak is measured above the patterned film, showing reasonable agreement in both amplitude and shape with the model simulations.

ACKNOWLEDGEMENT

This work was supported in part by US Army Research Office (Grant #W911NF-09-1-0511) and DARPA (Grant #N6601-11-1-4198).

REFERENCES

[1] D. P. Arnold, and N. Wang, "Permanent Magnets for MEMS," *J. Microelectromechanical Systems*, vol. 18, no. 6, pp. 1255-1266, 2009.

[2] N. M. Dempsey, "Hard Magnetic Materials for MEMS Applications," *Nanoscale Magnetic Materials and Applications*, J. P. Liu, E. Fullerton, O. Gutfleisch *et al.*, eds., pp. 661-680: Springer, 2009.

[3] J. Töpfer, B. Pawlowski, H. Beer *et al.*, "Multi-pole magnetization of NdFeB magnets for magnetic micro-actuators and its characterization with a magnetic field mapping device," *J. Magnetism and Magnetic Mat.*, vol. 270, no. 1–2, pp. 124-129, 2004.

[4] I. Zana, F. Herrault, D. P. Arnold, and M. Allen, "Magnetic patterning of permanent-magnet rotors for microscale motor/generators," *PowerMEMS 2005*, Tokyo, Japan, 2005, pp. 116-119.

[5] O. D. Oniku, R. Regojo, Z. A. Kaufman, W. C. Patterson and D. P. Arnold, "Batch magnetic patterning of hard magnetic films using pulsed magnetic fields and soft magnetizing heads," *IEEE Trans. Magnetics*, vol. 49, no. 7, pp. 4116-4119, *2013*.

[6] F. M. F. Rhen, E. Backen, and J. M. D. Coey, "Thick-film permanent magnets by membrane electrodeposition," *J. Appl. Phys.*, vol. 97, no. 11, pp. 113908-4, 2005.

[7] F. Dumas-Bouchiat, L. F. Zanini, M. Kustov *et al.*, "Thermomagnetically patterned micromagnets," *Appl. Phys. Lett.*, vol. 96, no. 10, pp. 102511-3, 2010.

[8] B. A. Peterson, W. C. Patterson, F. Herrault, D. P. Arnold and M. G. Allen ., "Laser-micromachined Permanent Magnet Arrays with Spatially Alternating Magnetic Field Distribution, *PowerMEMS 2012*, Atlanta, GA, pp 319-322.

[9] A. Garraud, O. D. Oniku, W. C. Patterson, E. Shorman, D. LeRoy, N. Dempsey, and D. P. Arnold, "Microscale Magnetic Patterning of Hard Magnetic Films Using Microfabricated Magnetizing Masks," *MEMS 2014*, San Francisco, CA, 2014.

[10] O. D. Oniku, P. V. Ryiz, A. Garraud, and D. P. Arnold, "Imprinting of fine-scale magnetic patterns in electroplated hard magnetic films using magnetic foil masks," *J. Appl. Phys.*, vol. 115, 2014.

[11] O. D. Oniku, and D. P. Arnold, "Microfabrication of High-Performance Thick Co80Pt20 Permanent Magnets for Microsystems Applications," *ECS Trans.*, vol. 50, no. 10, pp. 167-174, 2013.

[12] W. C, Patterson, E. E. Shorman, N. Garraud, and D. P. Arnold, "A Magnetic Microscope for Quantitative Mapping of the Stray Fields from Magnetic Microstructures" *Hilton Head 2014*, Parallel publication,

CONTACT

*O. D. Oniku, tel: +1-352-514-5820; ololadeoniku@ufl.edu

DIRECT PRINTING OF SILVER NANO-PARTICLES BASED INK ON POLYDIMETHYLSILOXANE (PDMS) FOR MEMS DEVICES

Yoontae Kim[*]*, Xiang Ren, and Hongseok (Moses) Noh*
Drexel University, Philadelphia, Pennsylvania, USA

ABSTRACT

We introduce the use of inkjet printing techniques for rapid fabrication of conductive silver microelectrodes on polydimethylsiloxane (PDMS). An extensive experimental characterization study on the effect of printing parameters on the electrode quality is presented here. We also demonstrate the utility of the microelectrode-printing technique by making quadruple electrodes and using for dielectrophoretic (DEP) manipulation of polystyrene microbeads.

INTRODUCTION

Microfabricated PDMS devices are widely used for a variety of applications such as microfluidic components, lab-on-a-chip systems, chemical and biological sensors. These devices often requires integrated micropatterned electrode for electrokinetic manipulation of liquids and particles, and electrical/ electrochemical sensing. Conventional methods to create micropatterned electrodes are based on photolithography and thin-film deposition techniques[1-3]. Such fabrication process is time consuming, cost-ineffective, and often involves harmful chemicals. Alternative methods have been reported including microcontact printing using patterned PDMS stamp[4], direct injection and solidification of the conductive solution into PDMS channels[5]. However, even these methods necessitate photolithography for master mold fabrication.

In recent years, direct inkjet printing of the conductive solution has attracted research community and industries because of its low-cost and mask-free deposition of materials on various substrates, like terephthalate (PET) or polycarbonate (PC)[6-7]. Silver is a good electrode material because of its high electrical conductivity. A number of researchers have studied on direct printing of ink containing silver nanoparticles using an inkjet printing system. However, most of previous studies focused on making drops and continuous tracks on the polymeric substrates with the exception of PDMS. There has been one study on printing conductive silver line on PDMS with UV ozone treatment as a surface modification[8], but the dimension of the printed line was in millimeter scale and no experimental characterization of the process was reported.

In this paper, we report an extensive experimental characterization study on the effect of printing parameters on the electrode quality for silver ink printing on PDMS substrates. PDMS surface was treated with air plasma prior to printing and various conductive silver lines have been printed on the PDMS substrates. The width and thickness of the printed line and their electrical resistance were carefully measured as varying printing parameters, such as drop spacing (DS), platen temperature, nozzle temperatures, sintering temperatures and time durations. We also printed quadruple electrodes and used them for dielectrophoretic (DEP) manipulation of polystyrene microbeads in order to demonstrate the utility of the printed silver electrodes.

EXPERIMENTS

Silver Ink

A wide variety of inks are commercially available for the DMP-2800 printing system used in this study. Viscosity, surface tension, and particle size were taken into account for the selection of the ink for the present application. We chose silver ink (DGP 40LT-15C, ANP, Korea) that contains 30 wt% of silver nanoparticles dispersed in Triethylene Glycol Monoethyl Ether (TGME). The physical properties of the ink at 20 ℃ were: viscosity 15.4 cps, surface tension 40.2 mN m^{-1}, and average particle size 50 nm.

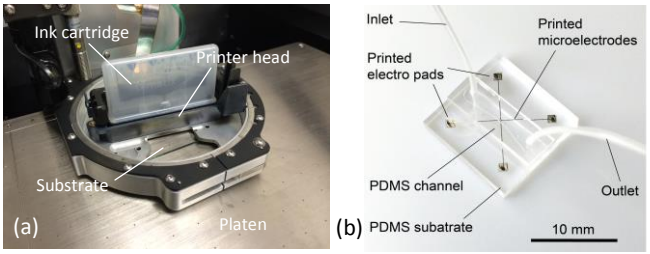

Figure 1: (a) Picture of the inkjet printing system, and (b) printed device used for DEP manipulation of polystyrene microbeads.

Printer Head

The printer head has 16 nozzles and the nozzle diameter is related to the generated drop size through that nozzle. In this study, we used 1 pL cartridge (DMC-11601, Fujifilm, Japan) which has 9 μm diameter nozzle. One single nozzle was used at a time. Although the piezoelectric print-head can operate at acoustic frequencies in the range of 1-15kHz, it was fixed at 1 kHz for simplicity and thus its influence in drop volume and velocity is ignored[9].

Inkjet Printer and Printing Conditions

The piezoelectric inkjet printer (Dimatix Material Printer DMP-2800, Fujifilm, Japan) is a software controlled inkjet printer system that allows the user to deposit colloidal fluid on various substrates. This inkjet printing system consists of a printer head, ink cartridges, a platen (substrates holder), two cameras, and Dimatix Drop Manager (DDM) software. Most of printing parameters can be controlled by the user via DDM software.

The printability of fluid highly depends on the fluid characteristics including viscosity and surface tension at jetting temperature. The printer head has a built-in heater, and the fluid is heated up to target jetting temperature. The platen is connected to a vacuum pump to hold thin flexible substrates and this part also has a built-in heater enabling to control substrate temperature, which in turn directly affects evaporation rate of the solvent. There are two cameras on this printing system. The fiducial camera is used to monitor the printed pattern and to measure the pattern sizes. The drop-watcher camera is used to inspect drop formation at the nozzle-air interface. We observed the shape of drops when they are ejected from the nozzles. Moreover, the velocity of ejected drops was monitored by the drop-watcher camera. The nozzle cleanliness also influenced the quality of printed patterns. There are three software-driven methods of cleaning for the nozzle such as purge, blot and spit. These cleaning methods run individually before starting of printing. More printing parameters and detailed printing conditions that we used in this study are presented in Table 1.

9781940470016/HH2014/$25©2014TRF
DOI 10.31438/trf.hh2014.52

Solid-State Sensors, Actuators and Microsystems Workshop
Hilton Head Island, South Carolina, June 8-12, 2014

Table 1.Printing process parameters and used printing conditions during the experiments.

Printing Process Parameters	Predetermined Values
Nozzle temperature (℃)	29
Jetting frequency (kHz)	1 kHz
Jetting velocity (m/s)	7-8
Drop spacing (µm)	5, 6, 8, 10, 15, 20, 25, and 30
Nozzle height (mm)	1
Platen temperature (℃) (Measured substrate temperature)	30 (29.2), 40 (38.4), 50 (47.9), and 60 (57.2)
Sintering temperature (℃)	90, 120, 150, and 180
Sintering time duration (min)	15, 30, 45, and 60

PDMS Substrate

Non-uniform substrate thickness can affect printing quality because the distance between nozzle and substrate will change accordingly. In order to minimize the variation in the PDMS substrate thickness, spin coating technique was used. Dow Corning® (Sylgard 184) PDMS are supplied as two-part liquids, a base resin and a curing agent. The base resin and the curing agent were mixed with 10:1 mass ratio, and degassed in a vacuum desiccator for 30 minutes. The mixture was then spin-coated on a soda-lime glass (2"× 2") at 500 rpm for 30 seconds. The PDMS coated soda-lime glass was cured at 80 ℃ temperature for 2 hours.

Measurement

The printed silver lines sintered by a conventional oven under different sintering temperatures and times. After sintering process, the resistance was measured by the 4-wire resistance measurement using a digital multi-meter (2400 SourceMeter®, Keithley, USA). The images of printed silver lines were taken by an optical microscope equipped with a CCD camera, so the printed lines had different color map compared to the printing substrate. Matlab can capture each pixel of the images and tell the boundary of the printed lines by a pre-set threshold data. Using this method, we could obtain the average width of the printed lines. In order to get the width of antinodes and nodes, we compared one position's width to its neighbor's width, by setting a confidence interval. The cross-sectional profiles of printed silver lines were obtained using the optical profilometry (NewView 6200, Zygo, USA) before and after sintering.

Quadruple Silver Electrodes Device

The quadruple silver microelectrodes were printed on PDMS, and then sintered at 180℃ for 15 minutes. The sintered PDMS part was then attached to a PDMS microchannel (H:100 µm × W:1 mm × L:10 mm) that was fabricated using replica molding technique with negative photoresist patterns (SU-8 2035, Microchem, USA). The inlet and outlet holes were punched into the channel and silicone tubes were connected to them. Polystyrene microspheres (Polysciences, Inc., USA) with a diameter of 2 µm were mixed with deionized water to make a low conductive colloidal mixture for the dielectrophoretic experiments. The measured electrical conductivity of the mixture was 5.68×10^{-5} S m^{-1}.

RESUTLS AND DISCUSSION

Substrate and Surface Treatment

Direct printing of silver ink on PDMS is challenging because of its elastomeric and hydrophobic nature. There are various techniques to modify the surface properties of PDMS. In this work, PDMS surfaces were modified by an air plasma system (COVANCE-MP, FEMTO science, Korea). The LF plasma power was 120 W of 50 Hz frequency, and the plasma treatment time was 1 min.

Figure 2 shows the dramatic effect of air plasma treatment on printing. The ejected drops evenly spread on plasma-treated PDMS resulting in uniform and continuous silver patterns. In contrast, the ink did not spread, and formed separated on the plasma-untreated PDMS under exactly same printing conditions due to the hydrophobicity of PDMS. The thin silver line created on plasma-treated surface dried quickly while the drops on untreated surface remained as liquid for a long time.

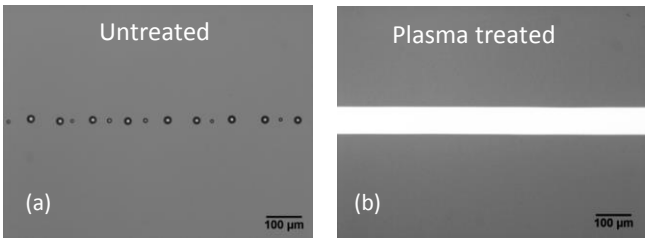

Figure 2: Effect of air plasma treatment on printing (a) Untreated, (b)Plasma treated.

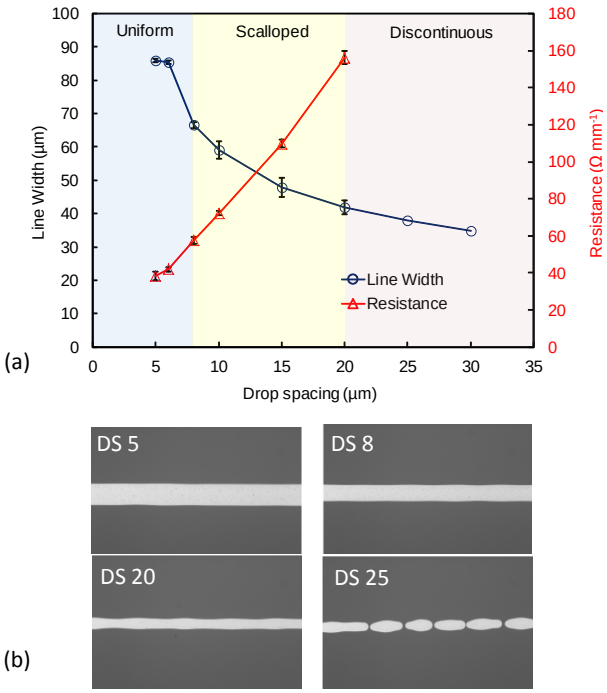

Figure 3: (a) Effect of DS on line width and electrical resistance uniformity, and resistance as function of drop spacing (b) images of printed line with different DS.

Drop Spacing

The meaning of drop spacing (DS) is the center distance between two drops. Figure 3(a) presented that the printed line width highly depends on the DS due to the drop density (drops per inch: dpi) is decided by DS. In this work, we used several different DS, as shown in the table 1. The maximum drop density was achieved using DS 5 µm, its resolution was 5080 dpi. A pattern printing with DS 30 µm, the resolution was decreased to 847 dpi. Therefore, the printed line width decreases as DS is increased. In addition, the

electrical resistance of the conductive lines increases. We also observed that relatively straight lines can be produced when DS is below 10 µm. If DS is higher than 20 µm, the printed lines were disconnected and the images are shown in figure 3(b).

Substrate Temperature

We investigated an influence of substrate temperatures on printed silver lines. The platen temperature was changed from 30 ℃ to 60℃ in 10℃ increments. Generally, the surface temperatures of PDMS were slightly lower than platen temperature due to the low thermal conductivities of PDMS and soda-lime glasses. The measured surface temperatures of PDMS were presented in table 1. The heated substrate promotes the evaporation of ink solvent and prevents line broadening[10]. Figure 4(a) and figure 5 show the effect of substrate temperature. We observed that printed line width decreased with the increase of platen temperature. In contrast, the printed line height gradually increased after increasing platen temperature. As a result, the electrical resistance decreased with line width decrease due to substrate temperature increase because the cross-sectional area actually increased. It means that more silver ink was deposited at higher substrate temperature. It might be due to heat transfer between the substrate and nozzle. If heat was transferred from the platen to the printer head, viscosity and surface tension of silver ink would be decreased while printing. Those physical properties are related to the drop tear off at the nozzle outlet. The ability to withdraw liquid back into the nozzle would be reduced due to decreased surface tension. Therefore, slightly bigger drops can be ejected on PDMS. In practice, the nozzle temperature was slightly increased from 29 ℃ to 30.7 ℃ while two-line printing. Each line was 13 mm in length and the platen temperature was 60 ℃.

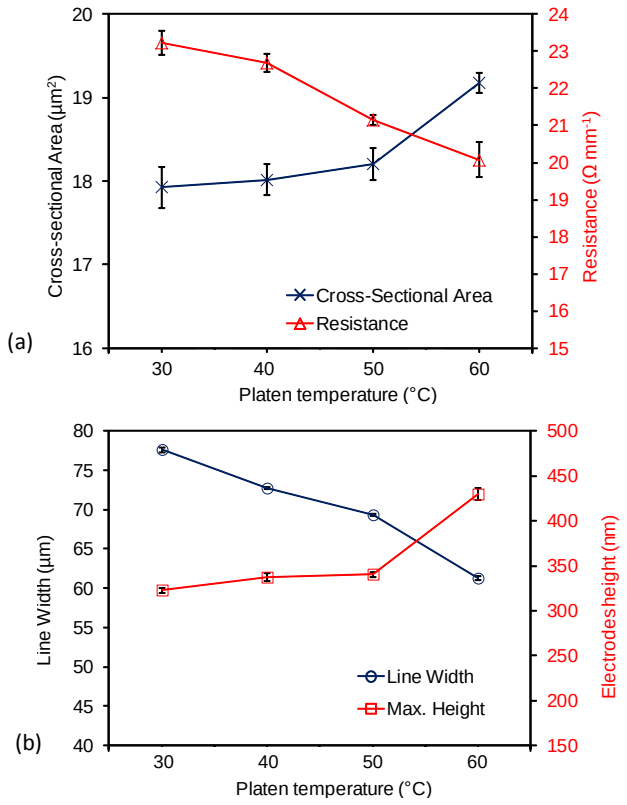

Figure 4: Effect of substrate temperature on (a) line width and height, (b) cross-sectional area and resistance.

We observed the Marangoni effect from the printed silver lines, especially, at side peaks in figure 5(a) and (b). The printed silver lines on PDMS have longer drying time than other materials which have higher thermal conductivities. During the longer period of drying time, the nanoparticles in printed lines can move at the side peaks due to the Marangoni flow[11].

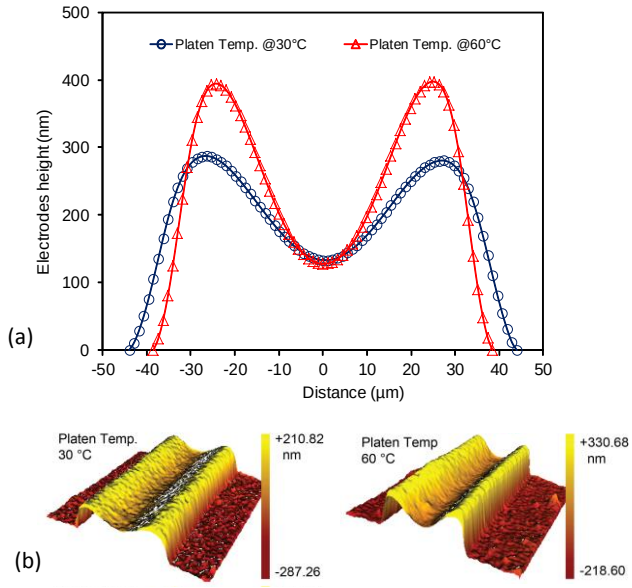

Figure 5: (a) and (b) The cross-sectional profiles of the sintered electrode at the platen temperature of 30 ℃ and 60 ℃ (obtained from optical profilometry).

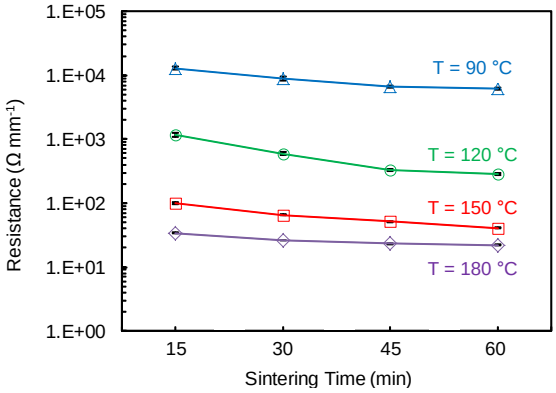

Figure 6: Effect of sintering temperature and time on electrical resistance.

Sintering Temperature

The printed silver ink must be sintered at high temperature for solvent evaporation and densification. Sintering temperatures and duration times have significant effect on the electrical property of the printed silver electrodes[12]. We printed conductive silver lines and applied four different temperatures for different time durations to investigate the sintering conditions and the results were shown in figure 6. The electrical resistance of the printed lines decreased significantly with the increase in sintering temperature. The resistance also decreased slightly with sintering time for all different temperatures. We found that the lowest resistance was obtained at 180℃ for 1 h, and PDMS substrates were not damaged under the

sintering condition. Note that this sintering temperature is higher than other polymeric substrates such as PET, and PC (< 150℃).

Dielectrophoretic Experiments

In order to demonstrate the performance of the printed silver electrodes, we printed quadruple microelectrodes on PDMS and used them for dielectrophoretic manipulation of polystyrene microbeads. The optical microscope with a CCD camera was used to monitor the motions of the particles. A function generator (HP 33120A, HP, USA) was connected to four electrode pads to apply AC electric signals.

Figure 7 (b) and (c) show that particles are collected along the edge of the electrodes. This is indicative of positive DEP at mid frequencies (200~300 kHz, 10 V_{pp}), and the particles move toward area of high electric field strength. At higher frequencies (700 kHz, 10 V_{pp}) particles experience strong negative DEP forces, therefore the particles were pushed away from the edge of the electrodes as shown in figure 7(d).

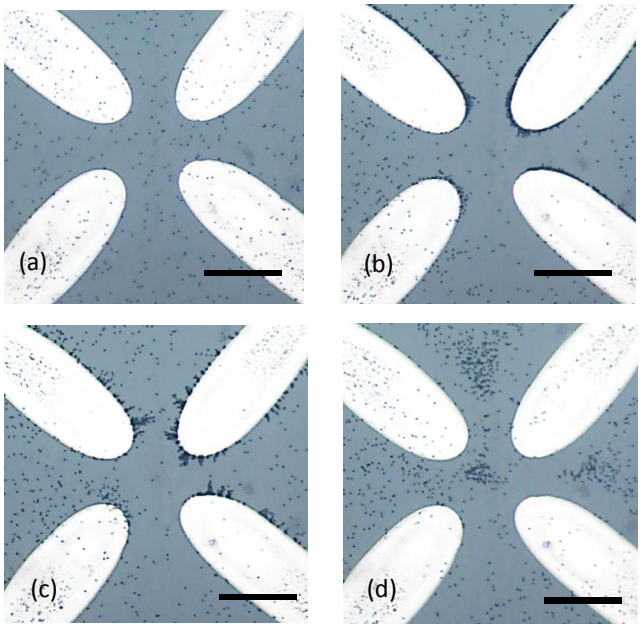

Figure 7: DEP experiment with printed quadruple electrodes: (a) initial random distribution, (b) positive DEP at 200 kHz, 10V_{pp}, (c) positive DEP at 300kHz, 10 V_{pp}, and (d) negative DEP at 600 kHz, 10V_{pp}. (scale bar: 100μm).

CONCLUSIONS

We explored direct inkjet printing of silver nanoparticle-based ink on PDMS substrates. Major printing parameters and sintering conditions were thoroughly investigated to identify optimal conditions for electrode fabrication. The findings from the characterization study were then applied to the fabrication of quadruple electrodes for DEP manipulation of microbeads. The direct printing of silver microelectrode on PDMS overcomes many disadvantages of conventional fabrication methods and thus can find many applications.

ACKNOWLEDGEMENTS

This research was partially supported by the National Science Foundation (Grant No. CBET 0923173, DUE 1022757). Travel support has been generously provided by the Transducer Research Foundation.

REFERENCES

[1] J.Y. Baek, J.H. An, J.M. Choi, K.S. Park, and S.H. Lee, "Flexible polymeric dry electrodes for the long-term monitoring of ECG," Sensors and Actuators A: Physical, 143, 2 (2008).

[2] S. Chung, J. Lee, H. Song, S. Kim, J. Jeong, and Y. Hong, "Inkjet-printed stretchable silver electrode on wave structured elastomeric substrate," Applied Physics Letters, 98, 15 (2011).

[3] C.Y. Chen, C.L. Chang, T.F. Chien, and C.H. Luo, "Flexible PDMS electrode for one-point wearable wireless bio-potential acquisition," Flexible PDMS electrode for one-point wearable wireless bio-potential acquisition, 203, (2013).

[4] H.L. Gou, J.J. Xu, X.H. Xia, and H.Y. Chen, "Air Plasma Assisting Microcontact Deprinting and Printing for Gold Thin Film and PDMS Patterns", ACS Applied Materials & Interfaces, 2, 5 (2010).

[5] A.C. Siegel, D.A. Bruzewicz, D.B. Weibel, and G.M. Whitesides, "Microsolidics: Fabrication of Three-Dimensional Metallic Microstructures in Poly(dimethylsiloxane)", Advanced Materials, 19, 5 (2007).

[6] J. Wu, S.L. Hsu, M. Tsai, and W. Hwang, "Inkjet Printing of Low-Temperature Cured Silver Patterns by Using AgNO3/ 1-Dimethylamino-2-propanol Inks on Polymer Substrates," The Journal of Physical Chemistry C, 115, 22 (2011).

[7] T.F. Guo, S.C. Chang, S. Pyo, and Y. Yang, "Vertically Integrated Electronic Circuits via a Combination of Self-Assembled Polyelectrolytes, Ink-Jet Printing, and Electroless Metal Plating Processes," Langmuir 18, 21 (2004).

[8] S. Chung, J. Lee, H. Song, S. Kim, J. Jeong, and Y. Hong, "Inkjet-Printed Stretchable Silver Electrode on Wave Structured Elastomeric Substrate," Applied Physics Letters, 98, 15 (2011).

[9] N. Reis, C. Ainsley, and B. Derby, "Ink-jet Delivery of Particle Suspensions by Piezoelectric Droplet Ejectors," Journal of Applied Physics, 97, 9 (2005).

[10] T.H. van Osch, J. Perelaer, A.W. de Laat, and U.S. Schubert, "Inkjet Printing of Narrow Conductive Tracks on Untreated Polymeric Substrates," Advanced Materials, 20, 2 (2008).

[11] E.L. Talbot, A. Berson, P.S. Brown, and C.D. Bain, "Evaporation of Picoliter Droplets on Surfaces with a Range of Wettabilities and Thermal Conductivities," Physical Review E, 85, 6 (2012).

[12] J.R. Greer, and R.A. Street, "Thermal Cure Effects on Electrical Performance of Nanoparticle Silver Inks," Acta Materialia, 55, 18 (2007).

CONTACT

*Yoontae Kim, tel: +1-215-895-5820; yk373@drexel.edu

ENGINEERING HIGH-SPEED, ULTRA-SMOOTH REACTIVE PHASE GLASS ETCHING IN AN INDUCTIVELY COUPLED PLASMA

Chenchen Zhang, Gokhan Hatipoglu, and Srinivas Tadigadapa
Department of Electrical Engineering, Pennsylvania State University, USA

ABSTRACT

In this paper we report a modified inductively coupled plasma reactive ion etch (ICP-RIE) tool and using NF_3 and H_2O gases generated plasma species as the primary chemistry for glass etching. Using this technique we have been able to achieve etch rates as high as 0.81 μm/min and a surface smoothness (R_a) of ~ 6 Å for quartz and 0.68 μm/min and a surface smoothness of ~ 4 Å for borosilicate glass. The modified etch chamber described here allows for a systematic study of the glass etching process with capability to tune the physical and chemical (species dissociation) components during the etching process.

INTRODUCTION

Dating back to 1980's, silicon dioxide plasma etching processes were originally developed for realizing features for microelectronics applications such as interconnect vias, waveguides, phase shift masks, etc [1, 2, 3]. The primary focus of this earlier work was improving the selectivity of SiO_2 with respect to silicon [4], reducing gate oxide damage [5], etc. The advent of microelectromechanical systems (MEMS) and microsystems in the last decade, has markedly shifted the research in this field towards the development of silicon dioxide etching processes with high etch rate, smooth etched profiles, high etch selectivity to mask materials, high anisotropy, uniformity within a pattern and across the wafer, etc for applications in microfluidics [6], microsensors [7] and lab-on-a-chip applications.

ICP-RIE process is widely used in microfabrication because it allows to independently control plasma density (controlled by source power) and energy of etchant ions (controlled by substrate power). As a result, it provides stable high density plasma even in a relative low pressure environment (10^{-3} Torr– 10^{-4} Torr). There have been several spurts of research developments in the field leading to reported etch rates of glass in the range of 0.6 – 0.9 μm/min under ICP-RIE [8 - 10].

Conventional ICP-RIE is a physical/chemical mixed etching process. Usually, inert gases such as xenon and argon are used in process to physically bombard silicon dioxide [8], while halogen molecules are used in the process to affect chemical reaction with silicon dioxide. Due to the high inert gas content and long mean free path and high-energy typically used in a conventional ICP-RIE, glass etching is dominated by physical etching processes [8-10]. In this paper, we present a novel modification to the plasma etch chamber with a gas diffuser ring which is able to further tune the physical and chemical components during the etching process.

EXPERIMENT SETUP

Sample Preparation

500 µm thick, double-side polished 4 inch borosilicate and quartz wafers were cleaned in Nanostrip® for 30 mins and then deposited with 15 nm chromium and 150 nm gold seed metal layers using an evaporator. Wafers were patterned by photoresist AZ 1127 and 25% Microposit™ 351 developer to form 3.5µm thick photoresist pattern. 2–3 µm thick nickel was electroplated to form the hard mask with feature widths ranging from 100 µm - 1000 µm.

Modified Etching Chamber

Alcatel AMS 100 ICP-RIE etch tool was modified in this work. Instead of conventionally feeding gases through the ICP source, a stainless steel gas diffuser ring was attached to the metal plate of the mechanical clamping plate of the etcher and is used to locally introduce NF_3 and H_2O vapor gases in the vicinity of the wafer as shown in Figure 2. The substrate bias power drives the high energy ions from the plasma towards the NF_3 and H_2O gas cloud near the glass wafer and breaks down the highly unstable NF_3 gas into NF_x radicals – this is a radical departure from when the NF_3 gas is fed through the ICP chamber where the gas is completely fragmented into N and F radicals and ions and is not as effective in etching glass substrates. An *in-situ* residual gas analyzer (RGA) is connected to the reactor chamber in order to analyze the reaction and product species, stylus profilometer (P-16, Tencor®) and AFM was used to characterize the smoothness of the obtained etch topography and an *ex-situ* X-ray photoelectron spectroscopy (XPS) was used to analyze the atomic and molecular species on the surface of the etched glass regions. Ring diffused NF_3 and H_2O vapor gases are controlled by separate mass flow controllers. Available ranges of power and gas flow rates of individual gases for the modified etch system are listed in Table 1.

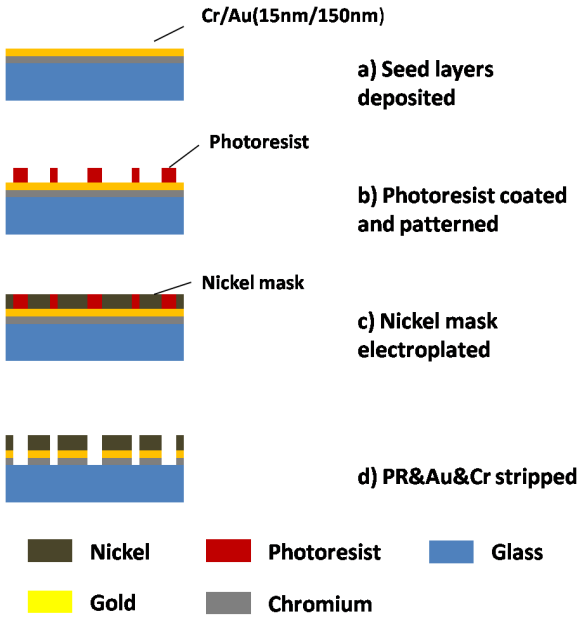

Figure1: Samples process flow

RESULTS AND DISSCUSSIONS

Chamber Modification Analysis using RGA Data

Gas species were detected and characterized using a quadrupole residual gas analyzer (RGA) ExTorr® XT100 connected directly to the modified etch chamber. RGA data was acquired for three different conditions: (i) background gases, (ii)

9781940470016/HH2014/$25©2014TRF
DOI 10.31438/trf.hh2014.53

NF_3 and Ar introduced as the primary plasma source gases from top of the chamber and (iii) $SF_6/NF_3/H_2O$ gases with SF_6 as the primary plasma source gas introduced from top and NF_3/H_2O diffused from ring. Figure 3a) shows that water vapor, nitrogen and oxygen gases are detectable in the initial chamber which is pumped down to 10^{-6} Torr. Clearly no NF_x gas species are generated if NF_3 is used as the plasma source gas as can be seen in Figure 3b). Finally, Figure 3c) shows that NF_x are generated with many other active ions and radicals in diffuser ring system.

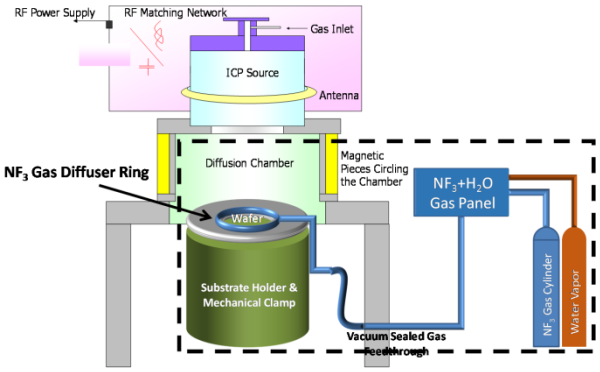

Figure 2: *Schematic illustration of the modified ICP-RIE systems with ring-diffuser system. Inset shows the photos the actual stainless steel showerhead nozzles.*

	Relevant Process Parameters	Range
ICP Source Gases	SF_6	0 – 200 sccm
	Ar	0 – 100 sccm
	O_2	0 – 100 sccm
Ring Diffuser Gases	NF_3	0 – 250 sccm
	H_2O	0 – 300 sccm
	ICP Power	0 – 3000 W
	Substrate Power	0 – 600 W
	Pressure	0 – 0.1 mbar

Table 1. Summary on capability of modified etching system

$SF_6/NF_3/H_2O$ based etching is compared with SF_6-only plasma etching. The results are shown in Table.2. Wafers were processed using 2000 W source power and 400 W substrate power. The substrate temperature was set to 20 ℃ and the source-substrate distance was set to 120 mm. Wafers were etched for 15 minutes. Four different etch-gas compositions are demonstrated for borosilicate glass and quartz etching respectively. Processes #1 and #3 were developed with diffuser ring system while processes #2 and #4 are listed for comparison with conventional SF_6 plasma etching process. To make comparisons between the two entirely different etch approaches we adjusted the flow range of the various gases in experiments #1 and #2, and #3 and #4 to result in identical chamber pressure. Same plasma power and pressure in the two different etches helps easier comparison since the plasma density and ion bombardment rates in the two cases should be comparable and any differences can be discussed in terms of achievable chemical etching between diffuser ring system and conventional etching. Table.2 shows that the etch rate of borosilicate glass and quartz glass in diffuser ring system is higher by 33% and 31% as compared to conventional etching method. Furthermore, we measured the average etched surface roughness (Ra) using precision scans of the region using the profilometer stylus which has a resolution in the Angstrom range and followed the most promising results with Atomic Force Microscope (AFM) scans. For both glass and quartz substrates the achieved surface smoothness of the etched areas from the ring diffuser set-up was an order of magnitude better than conventional etch process.

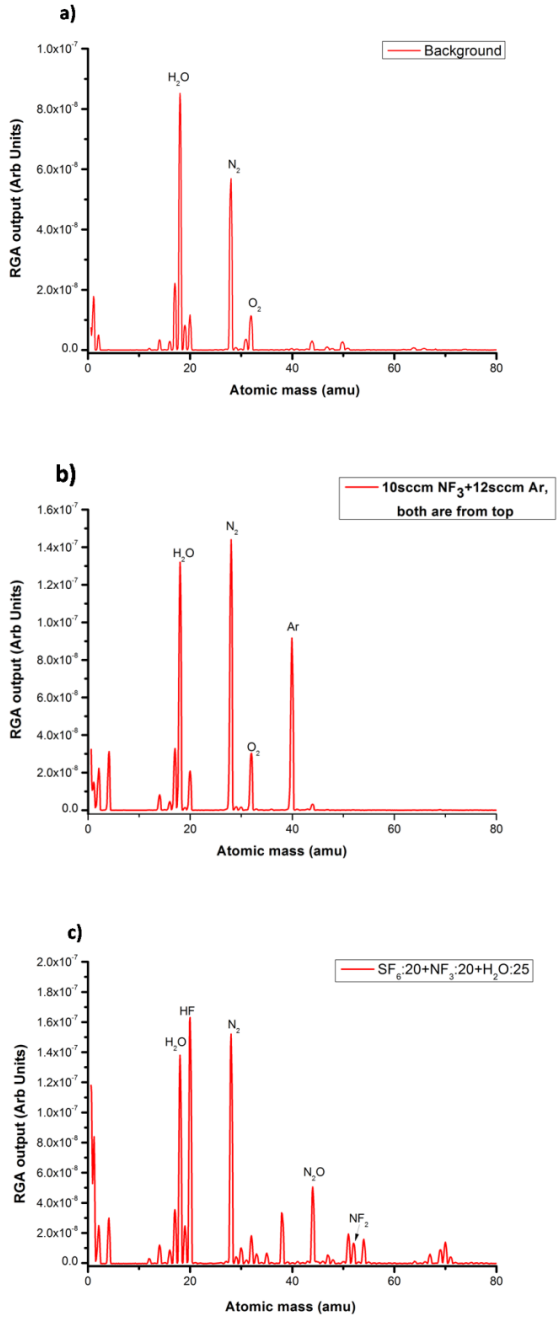

Figure.3: *Residue gases analysis on a)background, b)top 10sccm NF_3+top 12sccm Ar, c)top 20sccm SF_6+ ring 20sccm NF_3+ ring 25sccm H_2O*

In fact the achieved smoothness of the order of few Angstroms has not been reported before. The voltage shown in the table represents the electrical potential between plasma and substrate, which is read out on Alcatel AMS 100 tool automatically.The potential in the SF_6–only plasma is ~5% larger than for the NF_3+H_2O ring diffuser plasma conditions indicating that the energy of the bombarding ions should be higher in the conventional SF_6 based etching. In spite of this situation, both the etch rate and the surface smoothness conditions are improved in the ring diffuser etch. RGA data, from Figure.3(c), suggests the plasma conditions in ring diffused gases are able to produce active radicals and ions such as NF_x, NO and HF etc. The formation of active chemicals at vicinity of the wafer increases the effects of chemical etching and optimizes the etching performances. AFM shows surface roughness (Ra) of #1 and #3 recipe samples are 4 Å and 6 Å. Statistical analysis of AFM scanning on #3 recipe sample is shown in Figure 4(a). The SEM picture at right side of Figure 4 presents the cross section and trench bottom under ring diffused $SF_6/NF_3/H_2O$ based etching.

Borosilicate	SF_6 (sccm)	NF_3 (sccm)	H_2O (sccm)	Pressure (mTorr)	Voltage (V)	Etching rate (μm/min)	Roughness (Å)*
#1	20	20	25	3	73	0.68	0.7
#2	60	0	0	3	78	0.51	9.4

Quartz	SF_6 (sccm)	NF_3 (sccm)	H_2O (sccm)	Pressure (mbar)	Voltage (V)	Etching rate (μm/min)	Roughness (Å)*
#3	60	100	50	9	78	0.81	0.6
#4	200	0	0	9	82	0.62	21.9

*Table 2: Comparison between $SF_6/NF_3/H_2O$ based etching and single SF_6 plasma etching. *Roughness is measured by profilometer*

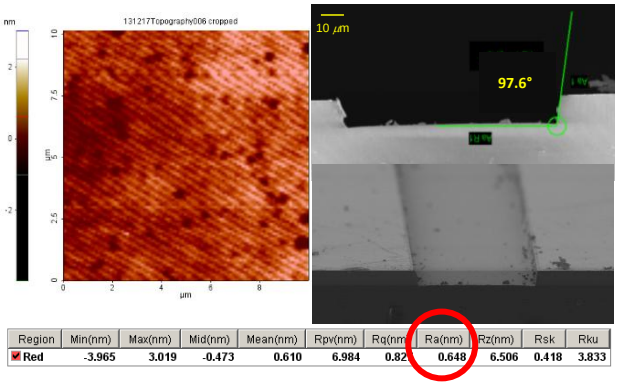

Figure 4: (a) AFM image of the smoothest substrate obtained with ring active etch. (b) The inset shows the SEM picture of the etch region cross section

Etch Rate with Diffuser Ring

Using the ring diffuser system, we were able to achieve 0.81μm/min and 0.68μm/min etch rates for quartz and borosilicate glass respectively. Fig. 5 shows the various process gas flow rates explored and clearly shows that although the two substrates predominantly consist of SiO_2 in composition, the optimal etching conditions for quartz and borosilicate glass are quite different. This is to be expected since they have different structure and material composition. Borosilicate contains 80.6% SiO_2, 12.6% B_2O_3, 4.2% Na_2O, 2.2% Al_2O_3, 0.04% Fe_2O_3, 0.1% CaO, 0.05% MgO, and 0.1% Cl, while quartz is pure silicon oxide.

Borosilicate contains more non-bridging oxygen bond than quartz in $(SiO_4)^{4-}$ tetrahedral network structure. The most important impurity of borosilicate is boron atom. Since this impurity has on less electron to contribute to the covalent bonding than does silicon. The missing electron induced by such impurity in the center of tetrahedron results in the elimination of bridging oxygen ions. In the case of the elimination of a bridging oxygen bond, a non-bridging oxygen is created which tends to weaken the network and thus should improve the etch rate [11]. On the other hand, alumina and alkalis components in borosilicate are hard non-volatile materials, which slows down the etch rate. Table 3 lists the XPS date on borosilicate glass surface composition for different process conditions. The obtained data shows a significantly larger percentage of surface aluminum and sodium content for the wafers etched with 80 sccm NF_3 flow rate than in the case of 20 sccm flow rate and explains the slower etch rate obtained for the former condition.

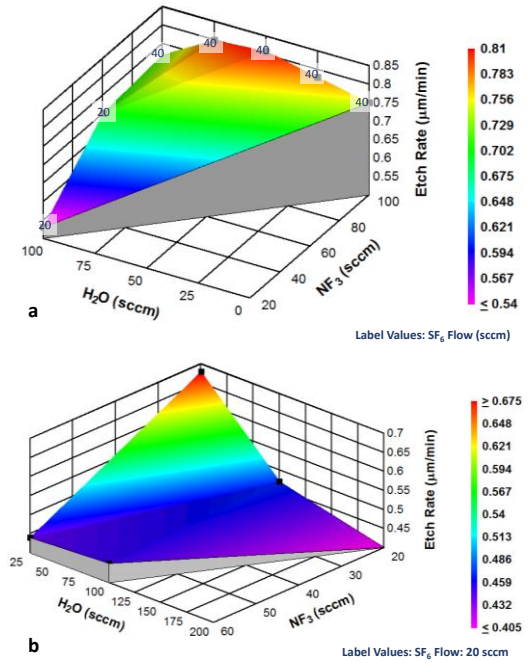

Figure **5:** *Etch rate as a function of SF_6, NF_3, and H_2O flow rates for (a) Fused Quartz and (b) Borofloat® wafers. SF_6 flow rate is 20 sccm for all the points shown in (b).*

	Si 2s	O 1s	F 1s	Na 1s	B 1s	Al 2s	K 2s	Ni 2p
Ring active etch- 20 sccm NF_3	20.7	51.696	15.751	7.526	2.105	2.22	ND*	ND*
Ring active etch- 80 sccm NF_3	4.483	6.487	56.448	20.946	4.144	5.102	1.887	ND*
Unprocessed Borofloat wafer	27.91	66.92	ND*	0.46	4.69	ND*	ND*	ND*

*Table 3: Approximate atomic percent calculations from XPS surveys for 2 different etch cases. All values are in percent. * ND: Not Detectable amount.*

Skin Layer Formation on the Etched Trench Walls

Another interesting observation was the formation of a few 100 nm thick layer on the side walls of the etched trenches. This layer could be readily stripped in nickel TFB etchant (Transene^{TM}) but was inert in nickel Type 1 etchant (Transene^{TM}). The study on skin layer composition and formation is currently being studied but is likely related to the reaction of the nickel masking layer with the etch gases.

CONCLUSION

In this report, a specially modified ICP-RIE etch tool using NF_3 and H_2O gas chemistry for glass etching is presented. Instead of conventionally feeding gases through the ICP source, a stainless steel gas diffuser ring on the metal plate of the mechanical clamping plate of the etcher has been incorporated to supply NF_3 and H_2O vapor gases. 2000W source power and 400W substrate power for novel $SF_6/NF_3/H_2O$ plasma based etching has been explored. An etch rate of 0.81μm/min and 0.68μm/min was obtained for quartz and borosilicate wafers respectively. Comparison between $SF_6/NF_3/H_2O$ etching and conventional single SF_6 etching was undertaken on both borosilicate and quartz glass. Initial results on the etch rate, surface roughness and selectivity of $SF_6/NF_3/H_2O$ based ring diffuser etching suggest that the etching mechanism is clearly shifted from physical etching to chemically dominated etching. AFM scans have shown unprecedented ultra-smooth surface roughness (Ra) as ~6 Å at 0.81 μm/min etching rate for quartz.

ACKNOWLEDGEMENTS

This work was supported in part by the DARPA under U.S. Army Research Office Grant W31P4Q-13-1-002 and Corning Inc. GH acknowledges partial support from Scientific and Technical Research Council of Turkey (TUBITAK) for a 2213-International PhD. Fellowship Program. The use of facilities at the PSU Site of the NSF National Nanotechnology Infrastructure Network (NNIN) under Agreement 0335765 is acknowledged.

CONTACT

S. Tadigadapa: Tel. (814) 865 2730, sat10@psu.edu

REFERENCE

[1] S. Karecki, R. Chatterjee, L. Pruette, R. Reif, T. Sparks, L. Beu, V.Vartanian, K. Novoselov, J. Electrochem. Soc. 148 (2001) 141.

[2] S.S. Choi, D.W. Kim, M.J. Park, J. Korean Phys. Soc. 45 (2004)1500.

[3] C.-H. Yang, C.-M. Dai, in: Proceedings of the SPIE – The International Society for Optical Engineering Optical Microlithogra-phy XI, 25–27 February 1998, 3334, 1998, p. 553.

[4] F.H. Bell, O. Joubert, G.S. Oehrlein, Y. Zhang, D. Vender, J. Vac.Sci. Technol. A (Vac. Surf. Films) 12 (1994) 3095.

[5] G. Adegboyega, I. PerezQuintana, A. Poggi, E. Susi, M. Merli, J.Vac. Sci. Technol. B 15 (1997) 623.

[6] C.H. Lin, G.B. Lee, Y.H. Lin, G.L. Chang, J. Micromech. Microeng. 11 (2001) 726.

[7] X.H. Li, T. Abe, M. Esashi, Sensor Actuat. a – Phys. 87 (2001) 139.

[8] Li, L., T. Abe, and M. Esashi, Smooth surface glass etching by deep reactive ion etching with SF_6 and Xe gases. Journal of Vacuum Science & Technology B (Microelectronics and Nanometer Structures), 2003. **21**(6): p. 2545.

[9] Goyal, A., V. Hood, and S. Tadigadapa, High speed anisotropic etching of Pyrex for microsystems applications. Journal of Non-Crystalline Solids, 2006. **352**(6-7): p. 657.

[10] Queste, S., et al., Manufacture of microfluidic glass chips by deep plasma etching, femtosecond laser ablation, and anodic bonding. Microsystem Technologies, 2010. **16**(8-9): p. 1485-1493.

[11] Wolf, S. and Tauber, R, Silicon processing for the VLSI Era, Volume 1: processing technology, Lattice Press, California

HIGH STRENGTH, LOW VOLTAGE MICROFABRICATED ELECTROADHESIVES ON NON-CONDUCTIVE SURFACES

*Abraham Simpson Chen, Alexi Charalambides, and Sarah Bergbreiter**
Department of Mechanical Engineering, University of Maryland, College Park, USA
The Institute for Systems Research, University of Maryland, College Park, USA

ABSTRACT

This work demonstrated microfabricated all-polymer electroadhesive devices, which obtained a maximum shear strength of 78 kPa at 200 V on a glass slide; these shear strengths are higher than previous work when operated at voltages an order of magnitude lower. A mold was microfabricated in silicon with features across multiple length scales, from centimeters to microns. The mold was refilled using conductive and dielectric polymers to decrease device stiffness over traditional metal electrodes, promoting a more conformal contact between the adhesive layer and substrate. Parylene was deposited to create a thin compliant dielectric between the electrodes and substrate, thereby reducing the voltage required to turn on the adhesives. Results show the effect of compliance on adhesive shear strength as well as the effect of gap spacing and number of electrodes.

INTRODUCTION

Electroadhesives are simple in nature; conductive electrodes coated with a dielectric material induce charge on a surface and adhere using electrostatic forces. Electroadhesion has been widely used for handling flat silicon wafers by means of rigid metal electrodes [1]. Recently, there have been developments to integrate electroadhesion into wall climbing robots [2], [3], where the adhesion can be easily controlled via voltage to turn on or off adhesion. Unlike wafers, these robots need to be able to adhere to relatively rough surfaces.

Previously, electroadhesives for wall climbing purposes have been made with metal deposited on Mylar films [2] or metal electrodes embedded in polymer [2], [3]. However, these methods produce dielectric layers that were typically tens to hundreds of microns thick which hindered shear strength at low voltages [4]. Other works have studied the effect of electrode geometries [3], [5], dielectric thickness [1], and adhesion substrate [2], [3], [6], but have been limited in shear strength, have required kilovolts to operate, or had electrode gaps on the order of millimeters to centimeters (thereby limiting the minimum adhesive sizes). The best shear strength obtained on a nonconductive surface in prior work was 62 kPa at 5 kV on glass [6]. Prior to this, others have only achieved a maximum 4.2 kPa at 4 kV [2].

Other approaches to adhesion have used inspiration from biology to create gecko-like adhesives with maximum shear strengths up to 300 kPa on glass surfaces [7], [8], [9]. Geckos have hierarchical setae hairs on their toes that stick to surfaces by van der Waal forces. This, however, requires complex loading and peeling mechanisms to obtain strong adhesion, while being capable of detaching with minimal force. The Stickybot, which imitates a gecko's adhesive microstructures, employs directional polymer-stalks that adhere primarily by van der Waals forces. When loaded onto a surface, the stalks' directional adhesion allows it to stick when pulled tangentially in one direction but releases when pulled in the opposite direction [10]. However, the adhesives often require cleaning and can not be turned on and off for more complex maneuvers.

Microfabrication provides the ability to create thin dielectric layers that reduce operating voltage while maintaining the ability to turn on and off adhesion. Gecko adhesives and the best

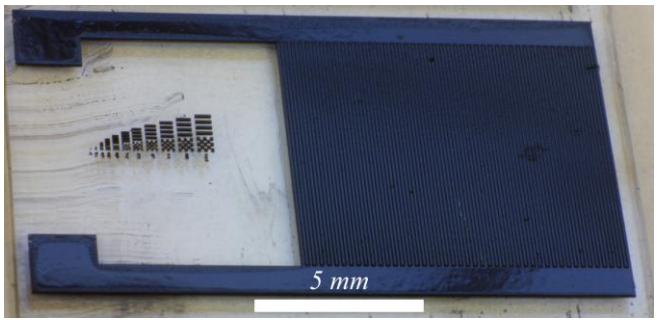

Fig. 1: Fabricated electroadhesive device.

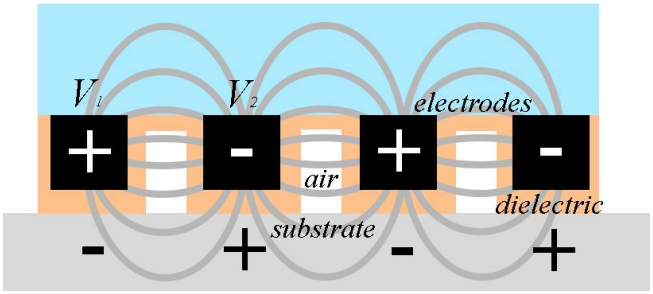

Fig. 2: Operation principle of electroadhesive device.

electroadhesives have demonstrated that compliance is key to the ability to conform and better adhere to rough substrates [6, 7]. Therefore, this work uses patterned conductive elastomer electrodes with a parylene dielectric to both improve adhesion and reduce operating voltage. An electroadhesive device created by this process can be seen in Fig. 1.

ELECTROADHESIVE DESIGN

Electrostatic adhesion utilizes the attraction between two oppositely charged surfaces separated by a dielectric layer. When adhering to nonconductive surfaces, two interdigitated electrodes are used to polarize the substrate, Fig. 2. In this case, Koh et al. developed a simple model based on the electrostatic attraction between the electrodes and surface as well as the fringing fields generated between the electrodes, Eq. 1 [4].

$$F_e = \frac{\epsilon_o \epsilon_r w L V^2}{2d^2} + \frac{0.265 \epsilon_o \epsilon_r w^{0.5} L V^2}{g^{1.5}} \qquad (1)$$

V is the applied voltage, w and L are the width and length of the electrodes, d is the distance between the electrodes and the substrate, g is the gap between the pair of electrodes, ϵ_0 is the permittivity of a vacuum, and ϵ_r is the dielectric constant (assuming that the same dielectric exists between the electrodes and the substrate).

Electric field clearly has a large effect on this electrostatic adhesive force. Previous work generally used dielectric thicknesses

9781940470016/HH2014/$25©2014TRF
DOI 10.31438/trf.hh2014.54

on the order of tens of microns [2-6]. Reducing dielectric thicknesses to the order of microns can proportionally reduce operating voltage requirements. In addition, this model shows that reducing the gap between electrodes can also improve adhesion. Microfabrication can be used to address both of these design goals.

However, electrostatic force is not the only factor that contributes to adhesion. In practice, the distance between electrodes and substrate varies across the interface due to non-flat surfaces. Results from work in gecko adhesives show that rigid materials exacerbate this effect [11], so conductive elastomer electrodes were used to reduce device stiffness in order to promote conformal contact.

In this work, three types of devices were fabricated to investigate electroadhesive shear strength. Non-patterned devices are simply conductive elastomers coated with a parylene dielectric. These devices were used to explore the effect of dielectric thickness and compliance on adhesion. "Type A" devices used patterned electrodes to adhere to non-conductive substrates and varied the gap between electrodes. Each Type A device had only 4 interdigitated electrode pairs. "Type B" devices were also patterned and varied the number of interdigitated electrodes. The gap was maintained at 10 μm. The device surface area was held constant at 1 cm^2 for all three device types.

FABRICATION

Conductive electrodes in all three devices were made from a conductive polymer prepared using carbon black nanopowder (Alfa Aesar), Sylgard 184 polydimethylsiloxane (PDMS), and hexane. The carbon was mixed with PDMS at a ratio of 10 wt% carbon to 90 wt% PDMS, which was qualitatively found to be both conductive and elastic. The PDMS itself was prepared using a base to curing agent ratio of 10:1. Hexane was added to the mixture at a weight ratio of 2.5:1 hexane to PDMS to decrease viscosity, which helped facilitate mixing and mold refilling for the patterned adhesives. This mixture will be referred to as C/PDMS in the following sections.

Non-patterned adhesives

The non-patterned adhesives were prepared by pouring the C/PDMS mixture over a glass plate and applying a blade to set the thickness. The mixtures were cured in a vacuum oven at 90 C for 20 minutes. Samples were then cut to size with a razor blade and coated with parylene C using the Parylene Deposition System Model 2010 from SCS. A small section of the device was covered with tape to later interface with the voltage source.

Type A and B patterned adhesives

The fabrication process for the patterned devices, Fig. 3, was based on previous work for tactile sensors [12]. First, 250 nm of silicon dioxide was deposited on a bare silicon wafer using PECVD, patterned, and used as a mask for a deep reactive ion etch (DRIE). Trenches were etched to a depth of approximately 30 μm. A fluoropolymer solution (DuPont) was used as an anti-stick layer for subsequent polymer processing. It was poured over the mold and vacuumed for 5 min to ensure a conformal coating. Then, it was spun for 60 s at 1000 rpm, and cured for 5 min at 145 C.

The C/PDMS was then poured over the mold and vacuumed for 3 minutes to remove air bubbles, ensure a conformal refill, and evaporate the hexane. Molded structures fabricated on a separate wafer with 100 μm trenches show features down to 10 μm are refilled and features down to 20 μm have high yields, Fig. 4. Next, a conventional razor blade was squeegeed over the wafer surface to planarize the C/PDMS, after which it was cured on a hot plate for 15 minutes at 120 C.

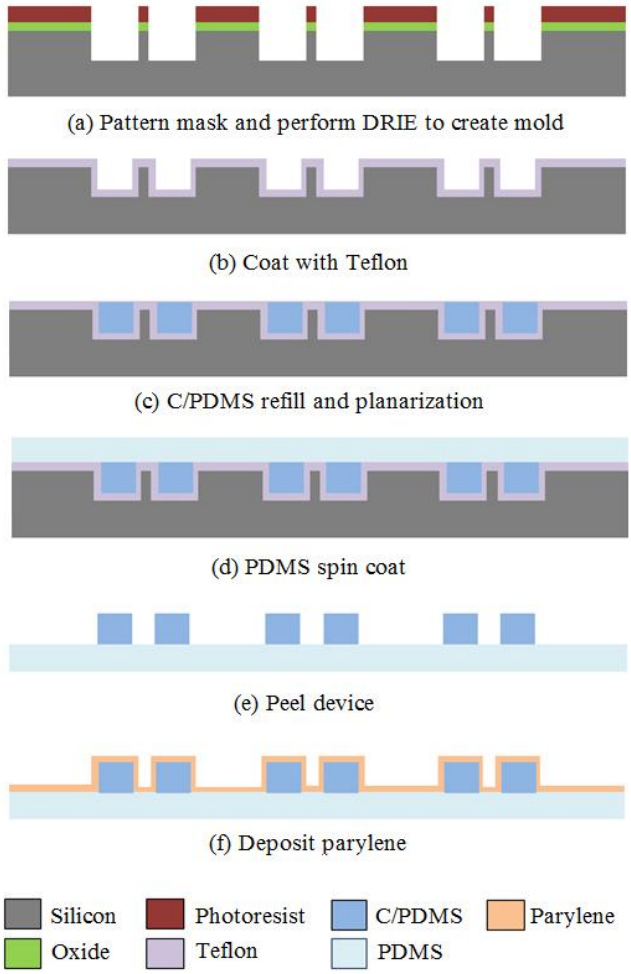

Fig. 3: Microfabrication flow chart.

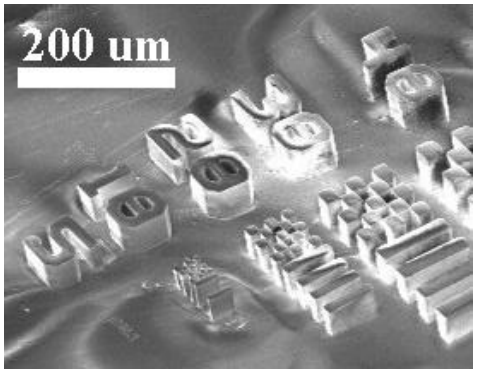

Fig. 4: Scanning electron microscope image of the refilled resolution marks. Aspect ratios of up to 10:1 were achieved.

Next, PDMS was poured over the mold and placed in vacuum for 15 minutes to remove air bubbles and ensure a strong bond between the PDMS and C/PDMS. It was spun for 30 seconds at 250 rpm to attain a thickness of 400-500 μm, after which it was placed on a hot plate for 15 min at 120 C. Note that the PDMS was prepared with 20:1 base to curing agent ratio in order to minimize out-of-plane warping; warping was observed for PDMS ratios of 10:1, and may have been due to residual thermal stresses during

curing or non-uniform dispersion of polymer chains during spinning [13].

Once cured, the PDMS layer was then gently peeled away, bringing with it the adhered conductive polymeric features. This sheet was manually cut into individual die, and finally coated with parylene C to act as a thin film dielectric.

TEST SETUP

Fig. 5 shows the test setup used to measure shear strengths for the fabricated devices. Samples were placed on the substrate and preloaded with a 20 g mass placed on top of the device (i.e. a 2 kPa pre-load force for a 1 cm^2 sample). The substrate was a silicon wafer for the non-patterned adhesives and a glass slide for the patterned adhesives. A voltage was applied between the substrate and the adhesive for the non-patterned samples and between the two electrodes in the patterned adhesives. This voltage was varied for the non-patterned adhesives and fixed at 200 V for both the Type A and B patterned adhesives. This voltage was applied for 2 min to ensure that the surface was fully polarized. The pre-load mass was then removed and the shear force on the sample was slowly increased via a pulley and applied mass. Shear force was increased until failure.

RESULTS & DISCUSSION

In Fig. 6, various C/PDMS thicknesses were used to study the effect of adhesive compliance on adhesion strength. These adhesives were tested at 75 V with a parylene dielectric thickness of 1.1 µm. Each point in Fig. 6 represents the maximum shear strength a single device was able to achieve over 3 trials. Even though these devices were adhered to the smooth surface of a polished silicon wafer, adhesive thickness (and therefore compliance) has a large effect on the shear strength at failure. While absolute shear strengths are large for these devices, it is important to note that these non-patterned adhesives can only adhere to conductive substrates.

Non-patterned adhesives were also used to investigate the effect of varying the parylene dielectric thickness on adhesion strength, Fig. 7. As expected from Eq. 1, shear strength showed a quadratic relationship with voltage. In addition, shear strength decreased for larger parylene thicknesses; doubling dielectric thickness resulted in approximately doubling the voltage required to achieve the same shear pressure. At least three samples were tested three times at voltages that yielded shear strengths lower than 50 kPa and at least three devices were tested one time for voltages that yield shear strengths above 50 kPa. These measurements were taken from devices with an average C/PDMS thickness of 470 µm.

For Type A patterned samples, three parametric devices were tested with different electrode gaps (250 µm, 100 µm, and 50 µm), while the electrode geometry and number of electrodes were held constant, Fig. 8; average shear strengths were 78 kPa, 57 kPa, and 48 kPa, respectively. Maximum shear strength of 78 kPa was obtained with the smallest fabricated electrode gap of 50 µm. The trend seen in Fig. 8 is expected, in part, due to the increased contribution of fringing fields to electrostatic force as the electrode gap decreases [4]. Decreasing the electrode gap from 250 µm to 50 µm showed a 40% improvement in shear strength.

For Type B samples, the number of electrode pairs was varied (83, 45, 20, 10, and 5) while an electrode gap of 10 µm was held constant, Fig. 9. Each point represents the maximum shear strength a single device was able to achieve over 3 trials. It was found that as the number of pairs increased the shear strength decreased. This is because the rate at which shear strength increases as interdigitated electrode pairs increases (fringing field term) is less than the rate at which shear strength decreases as electrode width decreases (direct field term).

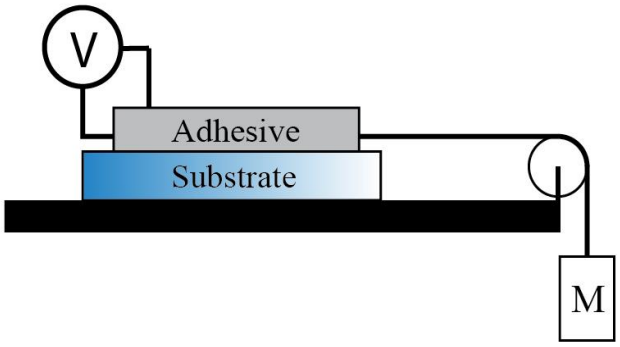

Fig. 5: Electroadhesive test setup.

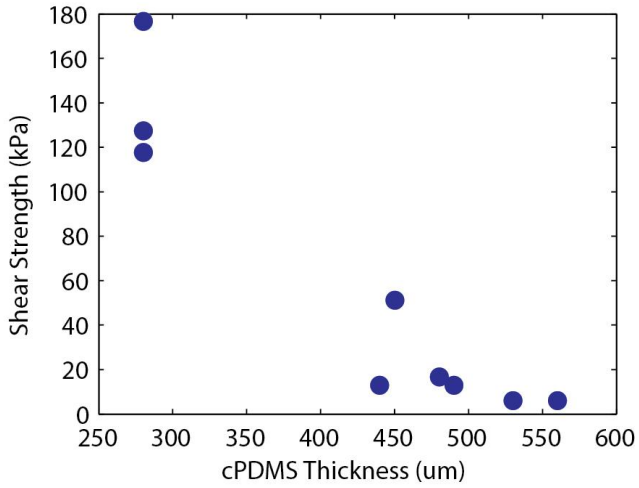

Fig. 6: Shear strength as a function of voltage, for various carbon-PDMS thicknesses.

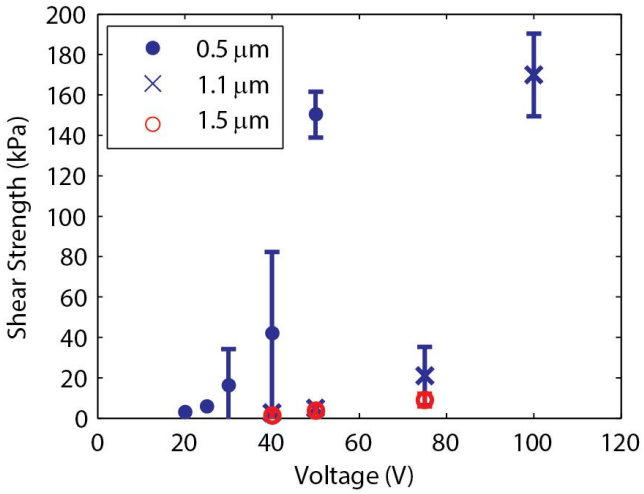

Fig. 7: Shear strength as a function of voltage for non-patterned conductive polymer, for various dielectric thicknesses.

By using parylene C as the dielectric layer and polymers as the bulk material, the dielectric thickness and device conformity were favorable for generating high shear strength at low voltages. This is a great improvement compared to most works that require kilovolts while only obtaining shear strength in the single kPa.

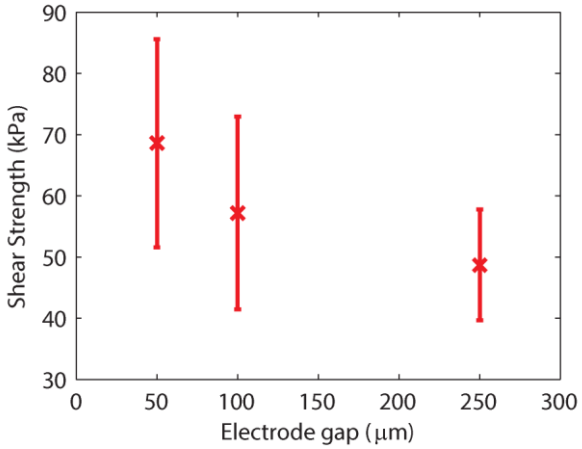

Fig. 8: Shear strength versus electrode gap (250 μm, 100 μm, and 50 μm) of the Type A devices at 200 V. Deviation bars are from 3 tested devices.

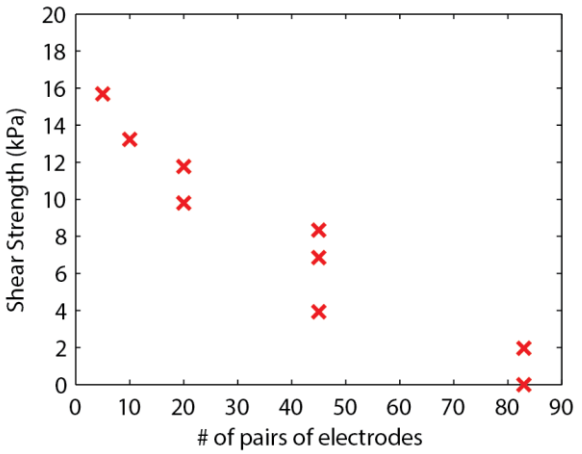

Fig. 9: Shear strength versus number of pairs of interdigitated electrodes of the Type B devices at 200 V.

This fabrication process also supports electroadhesives that have over a hundred interdigitated fingers with electrode gaps as low as 10 μm. This is also because of the mold depth of 30 μm, which effectively reduces attraction between adjacent electrodes. Deeper molds will introduce a tradeoff between added electrode compliance and the possibility of electrode structures pulling in to adjacent electrodes. The dielectric breakdown of 1 μm thick parylene (average for our devices) was measured to be at 300 V, which is significantly higher than at 200 V, the operating voltage of the Type A and B samples.

CONCLUSION

These results demonstrate the potential for microfabricated electroadhesive devices and for the first time, demonstrates electroadhesives that are comparable to the best gecko adhesives with shear strengths of approximately 300 kPa [7]. The demonstrated design is advantageous due to its low voltage requirement, ability to adhere to nonconductive surfaces, and compliant to adhere to rough surfaces. In the future these adhesives can be used on small scale climbing robots and robotic grippers.

ACKNOWLEDGEMENT

This material is based upon work supported by NASA under Award #NNX12AM02G. The authors would also like to thank the staff of the Maryland Nanocenter for their support.

REFERENCES

[1] K. Asano, F. Hatakeyama, and K. Yatsuzuka, “Fundamental study of an electrostatic chuck for silicon wafer handling,” IEEE Transactions on Industry Applications, vol. 38, no. 3, pp. 840–845, 2002.

[2] H. Prahlad, R. Pelrine, S. Stanford, J. Marlow, and R. Kornbluh, “Electroadhesive robotswall climbing robots enabled by a novel, robust, and electrically controllable adhesion technology,” in IEEE International Conference on Robotics and Automation, 2008. ICRA 2008. IEEE, 2008, pp. 3028–3033.

[3] J. P. D. Tellez, J. Krahn, and C. Menon, “Characterization of electroadhesives for robotic applications,” in 2011 IEEE International Conference on Robotics and Biomimetics (ROBIO). IEEE, 2011, pp. 1867–1872.

[4] K. H. Koh, R. Kuppan Chetty, and S. Ponnambalam, “Modeling and simulation of electrostatic adhesion for wall climbing robot,” in 2011 IEEE International Conference on Robotics and Biomimetics (ROBIO). IEEE, 2011, pp. 2031–2036.

[5] D. Ruffatto, J. Shah, and M. Spenko, “Optimization and experimental validation of electrostatic adhesive geometry,” in Aerospace Conference, 2013 IEEE. IEEE, 2013, pp. 1–8.

[6] D. Ruffatto III, J. Shah, and M. Spenko, “Increasing the adhesion force of electrostatic adhesives using optimized electrode geometry and a novel manufacturing process,” Journal of Electrostatics, 2014.

[7] A. G. Gillies and R. S. Fearing, “Shear adhesion strength of thermoplastic gecko-inspired synthetic adhesive exceeds material limits,” Langmuir, vol. 27, no. 18, pp. 11 278–11 281, 2011.

[8] J. Krahn and C. Menon, “Electro-dry-adhesion,” Langmuir, vol. 28, no. 12, pp. 5438–5443, Mar. 2012.

[9] O. Unver, A. Uneri, A. Aydemir, and M. Sitti, “Geckobot: a gecko inspired climbing robot using elastomer adhesives,” in Robotics and Automation, 2006. ICRA 2006. Proceedings 2006 IEEE International Conference on, 2006, pp. 2329–2335.

[10] D. Santos, B. Heyneman, S. Kim, N. Esparza, and M. R. Cutkosky, “Gecko-inspired climbing behaviors on vertical and overhanging surfaces,” in Robotics and Automation, 2008. ICRA 2008. IEEE International Conference on, 2008, pp. 1125–1131.

[11] Geim, A. K., et al. "Microfabricated adhesive mimicking gecko foot-hair." Nature materials 2.7 (2003): 461-463.

[12] A. Charalambides and S. Bergbreiter, “All-elastomer in-plane mems capacitive tactile sensor for normal force detection,” in Sensors, 2013 IEEE. IEEE, 2013, pp. 1–4.

[13] P. Damman, S. Gabriele, S. Copp´ee, S. Desprez, D. Villers, T. Vilmin, E. Rapha¨el, M. Hamieh, S. Al Akhrass, and G. Reiter, “Relaxation of residual stress and reentanglement of polymers in spin-coated films,” Physical review letters, vol. 99, no. 3, p. 036101, 2007.

CONTACT

*sarahb@umd.edu, 301-405-6506

MICRO-/NANO-STRUCTURED ANODES FOR ENHANCED PERFORMANCE OF MICRO-SIZED MICROBIAL FUEL CELLS

*A. Fraiwan[1], S.P. Adusumilli[2], D. Han[3], A.J. Steckl[3], D.F. Call[4], C.R. Westgate[2], and S. Choi[1]**
[1]Bioelectronics & Microsystems Laboratory, State University of New York at Binghamton, New York, USA
[2]Center for Autonomous Solar Power, State University of New York at Binghamton, New York, USA
[3]Nanoelectronics Laboratory, University of Cincinnati, Ohio, USA
[4]Environmental Biotechnology Lab, Syracuse University, New York, USA

ABSTRACT

Microbial fuel cells (MFCs) are gaining acceptance as a future alternative green energy technology and energy-efficient wastewater treatment method. Despite their vast potential, however, our ability to harness the potential of MFC technology lags from its low power density limiting its practical applications. Among a number of factors that can affect the MFC's performance, the anode material has the greatest impact on the performance by determining the actual accessible surface area for bacteria to attach and affecting the interfacial electron transfer resistance. In this work, microbial electricity generations on six micro/nano-structured anodes in micro-sized MFCs (57 μL) have been investigated by probing the behavior and physiology of microbial biofilm and their interaction with each anode at a new level of detail and efficiency. Six anodes are carbon nanotube (CNT), carbon nanofiber (CNF), gold/PCL microfiber (GPM), gold/PCL nanofiber (GPN), planar gold (PG), and conventional carbon paper (CP).

INTRODUCTION

Microbial fuel cell (MFC) technology is considered to be a promising alternative technology for clean energy production that could help alleviate the global energy crisis and environmental pollution [1]. This has caused an increase in the MFC research focusing on the use of MFCs for renewable energy production. The past few years have witnessed significant developments and performance improvements in MFC technology [2]. These advances are reflected in the increasing number of scientific publications and patents [3, 4]. Despite advances, the promise of the MFC technology has not yet been translated into commercial reality, because existing MFCs demonstrate low power density [5].

Aside from all the other factors affecting the MFC performance such as bacterial inoculums, chemical substrates, and reactor configuration [3], the anode materials play a major role in influencing the power generation by determining: (i) the actual accessible area for bacteria to attach; (ii) the extracellular electron transfer efficiencies; and (iii) chemical species diffusion rates [6-8]. Therefore, many of the studies to date have concentrated on improving anode performance by the search of effective anode material and/or modifications to the anode surface [9-11].

Recently, many unconventional three-dimensional micro-/nano-scale and/or micro-fabricated anode materials have been explored to increase surface area, porosity, biocompatibility, conductivity and biofilm formation [7, 9-11]. However, their performances are often more dependent on the specific MFC architecture, electrode spacing, environmental conditions, operating conditions, cathode materials, solution ionic strength and conductivity of the fuel cells. Therefore, power densities produced by a certain anode in one study cannot be directly compared with another anode unless the MFC architecture, bacteria, and chemical solution are the same. In addition, most of these anode studies for improving the MFC anode performances did not provide long-term analyses beyond ten days even though microbial communities and their electron generating capabilities on anode materials will likely be affected by long-term operation. Therefore, the studies on micro-/nano-structured anode materials reported to date would not provide useful information unless the results are compared in the same condition for a long period of time.

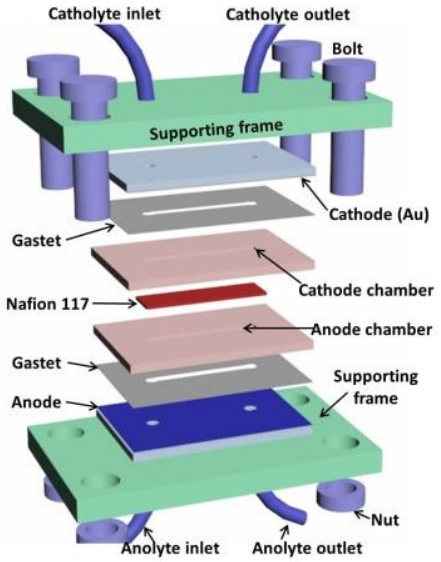

Figure 1: Schematic of the microfabricated MFC. The MFC contains vertically-stacked 57 μL anode and cathode chambers separated by a PEM (Nafion 117). Each layer except for the PEM was micro-patterned using laser micromachining.

In this paper we compare six popular micro- and nano-structured anode materials in 57 μL micro-sized MFCs under the same experimental condition for 1 month. The six anodes are carbon nanotube (CNT), carbon nanofiber (CNF), gold/poly(Ɛ-caprolactone) microfiber (GPM), gold/poly(Ɛ-caprolactone) nanofiber (GPN), planar gold (PG), and conventional carbon paper (CP). The biofilm profiles, activation loss, internal resistances, and mass transfer losses on each anode material are thoroughly analyzed. The reported results will provide an insightful understanding of the relationship between micro-/nano-structured anodes and active microbial biofilm, which will pave the way for future applications of these novel anode materials in MFC technology.

MATERIALS AND EXPERIMENTAL SET-UP

Device Fabrication

Six micro-sized MFCs were prepared with different anode materials; carbon nanotube (CNT), carbon nanofiber (CNF), gold/poly (Ɛ-caprolactone) (PCL) microfiber (GPM), gold/PCL nanofiber (GPN), planar gold (PG), and conventional carbon paper (CP). Each MFC contains vertically-stacked 57 μL anode and cathode chambers separated by a PEM (Nafion 117) (Fig. 1). Each

9781940470016/HH2014/$25©2014TRF
DOI 10.31438/trf.hh2014.55

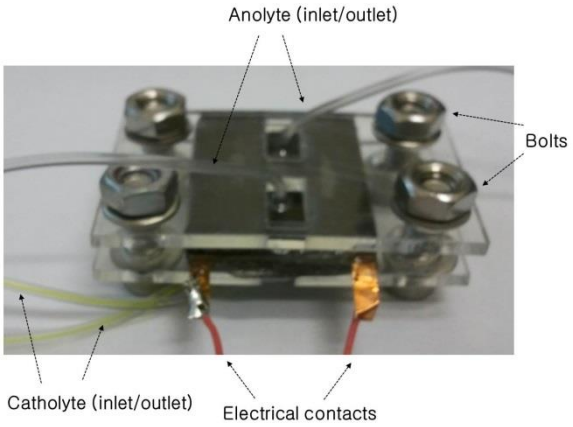

Figure 2: Photography of the fully assembled MFC. All layers were manually stacked in sequence while carefully aligning the tubing holes for the microfluidic channels. 4 tubes were plugged into the holes to form 2 independent routes for anolyte/catholyte access. Copper tape was attached to the contact pads with silver conductive paint.

layer except for the PEM was micro-patterned using laser micromachining (Universal Laser Systems VLS 3.5). Each chamber volume (4 cm x 3 cm) was defined by 0.158 cm-thick patterned PMMA and 100 μm-thick thin plastic gasket. The exposed anode/cathode area was 0.28 cm^{-2}. The Nafion 117 was sandwiched by the two PMMA chambers and thermally bonded at 125ºC for 1 hour. We fabricated 4 cm x 6.2 cm PMMA supporting frames (0.5 inch thick) with the laser and drilled 6 holes for fluidic inlet/outlet and screws. All layers were manually stacked in sequence while carefully aligning the tubing holes for the microfluidic channels. 4 tubes (CODAN, 0.35 mL volume) were plugged into the holes to form 2 independent routes for anolyte/catholyte access. Copper tape (3MTM copper conductive tape) was attached to the contact pads with silver conductive paint (PELCO® Colloidal Silver) (Fig. 2).

CNT and CNF Fabrication

Quartz was used as the substrate. A 60 nm thick aluminum oxide (Al_2O_3) layer was deposited by atomic layer deposition (ALD) and a 5-15 nm thick Fe layer was deposited by thermal evaporation. The substrate was placed inside the quartz tube in atmospheric pressure chemical vapor deposition (AP-CVD) setup and flushed by argon gas for 30 min. Then the furnace was turned on to the desired temperature (600-800 °C). Hydrogen flow of 10 sccm and argon flow of 200 sccm were passed through the tube. When the temperature reached the set temperature, the flow of ethylene was initiated, and after 2 minutes of ethylene flow, the water molecules were released from the bubbler through argon gas in the range of 150-400 sccm. After 60 min of growth time, the furnace, ethylene flow and water flow were turned off and the furnace was cooled to 20 °C in 20 min. For carbon nanofibers (CNFs), the synthesis procedure was the same except that the catalyst used is Ni in the CNF synthesis compared to Fe for CNT synthesis.

GPM and GPN Fabrication

PCL fibers were prepared by electrospinning, we have used poly(Ɛ-caprolactone) (PCL) (Sigma-Aldrich, M.W.=90 KDa) as a fiber material. To fabricate PCL microfiber membranes for the GPM device, the polymer solution dissolving 10wt% of PCL in 2,2,2-Trifluoroethanol (TFE) (Acros Organics, 99.8% purity) solvent was constantly fed at 1.2 mL hr^{-1} by a syringe pump. High voltage ~ 12 kV was applied across a gap of 20 cm between the needle and the collector. To fabricate PCL nanofiber sample for GPN device without any additives, PCL solution was prepared by dissolving 25 wt% of PCL into a highly ionic formic acid (Acros Organics, 88 % purity). This solution was fed at 0.1 mL hr^{-1} and the high voltage of 24 kV was applied across a gap of 25 cm. Because of very vigorous whipping and stretching actions of the ejected liquid jet, solidified fibers were attached to the collector. After electrospinning, the collected fiber mats were dried in a vacuum oven for 12 hr to remove any residual solvent. For gold coating on PCL electrospun fiber mats, sputtered gold was deposited on fibers for 10 min using Desk II mini-sputter system (Denton).

CP and PG Fabrication

Carbon paper (Fuel Cell Store, 0.48 g cc^{-1}, 0.2 mm) was cut into 3 cm x 4 cm pieces and put on the PMMA. The PG was prepared by depositing 100 nm gold on the PMMA substrate with chrome as the adhesion layer using e-beam evaporation.

Measurement Setup

We measured the potential between the anode and the cathode by a data acquisition system (NI, USB-6212) and recorded the results every 1 min via a customized LabVIEW interface. An external resistor was used to close the circuit by connecting the anode and cathode. The current through the load was calculated via Ohm's rule and the output power was calculated via P=V×I. Current and power densities were normalized to the anode area.

Anolyte and Catholyte

We obtained pre-acclimated anode-respiring bacteria from an acetate-fed MFC initially inoculated with primary clarifier influent and operated for several months. We fed the anode chamber with acetate (1g L^{-1} in mineral medium) as the sole electron donor. The catholyte was 100 mM ferricyanide in a 100 mM phosphate buffer in which the pH was adjusted at 7.5 ± 0.2 with 0.1 M NaOH.

Bacterial Fixation and SEM Imaging

The MFCs were disassembled, rinsed, and adherent bacteria on each anode were immediately fixed in 2% glutaraldehyde solution overnight at 4 ℃. Samples were then dehydrated by serial, 5 min transfers through 50, 70, 80, 90, 95, and 100% ethanol. Fixed samples were examined using a FESEM (Supra 55 VP, Zeiss).

RESULTS AND DISCUSSION

To allow for the accumulation and the acclimation of bacteria on the anode, the anolyte and catholyte were slowly introduced into the anode and cathode chambers. The six MFCs were first operated under open-circuit conditions for 10 days (Fig. 3a). The open-circuit voltage profiles show that there are three different trends corresponding to three stages of biofilm formation: (i) initial bacterial attachment; (ii) biofilm formation through exopolysaccharide substance; (iii) saturation releasing bacteria in the planktonic form and continuing the cycle again. The voltage curves show a significant increase over the first day of operation, followed by a slower increase until the MFCs reached constant voltages at day 7 except for the CNT and CNF anodes whose open-circuit voltages kept increasing even after 10 days of operation which may be attributed to the continuing biofilm formation on the larger surface area. After the initial operation under no load conditions, we measured cell polarization curves and power

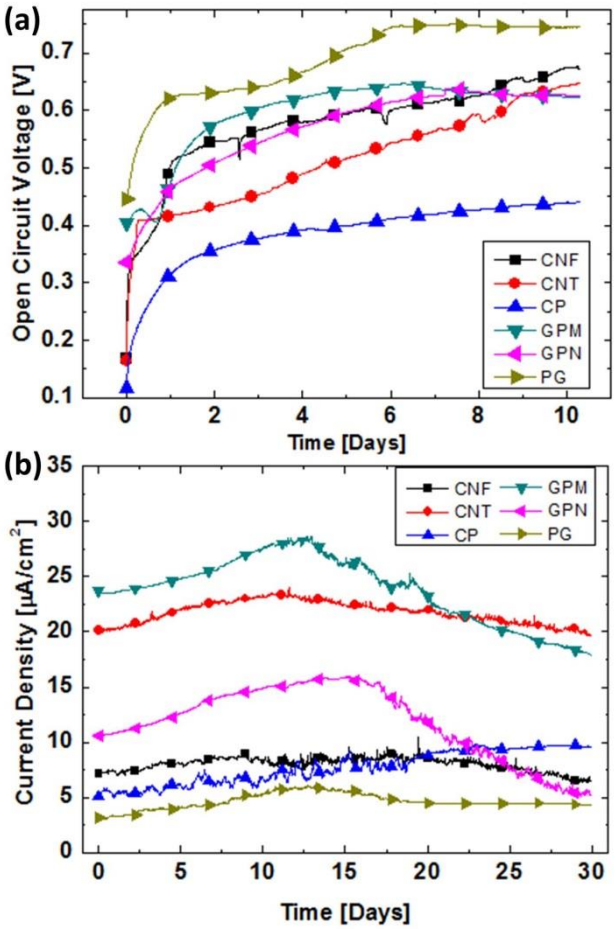

Figure 3: (a) Open circuit voltages and (b) current densities produced form the six MFCs. The maximum open circuit voltages obtained with CNT (680 mV), CNF (660 mV), GPM (620 mV), GPN (610 mV) and PG (720 mV) were greater than the CP (400 mV). Additional current increase under closed circuit operation indicates the viability recovery of biofilms formed under closed circuit.

outputs for the six cells to obtain the optimal load resistor for maximum power generation for each of the MFCs (Fig. 4). The optimal resistors were used to run the individual MFCs under closed-circuit operation: CNF-22kΩ, CNT-10kΩ, CP-4kΩ, GPM-10kΩ, GPN-47kΩ, and PG-100kΩ. The measured current generations under these resistors are shown in Fig. 3b.

The open-circuit voltage curves show that CP generated the lowest voltage which clearly indicates the substantial energy loss at this anode. Under closed circuit operation, the current density curves showed an additional increase to the values measured in the polarization curves under the same resistor, which is a clear indication of the viability recovery of the biofilms under closed-circuit operation. The biofilm formed in open circuit operation includes an unviable domain in the inner layer of the biofilm because of the inefficient nutrient/oxygen/proton transfer. Switching into closed circuit operation could provide favorable electron acceptor and sufficient energy to support cell growth and metabolisms inside the biofilms, recovering those unviable domains with increases in current. Larger current increases indicate that more unviable regions were recovered. For the long-term operation, CNT and CNF anodes reached maximum current densities within approximately 10 days, followed by a slight

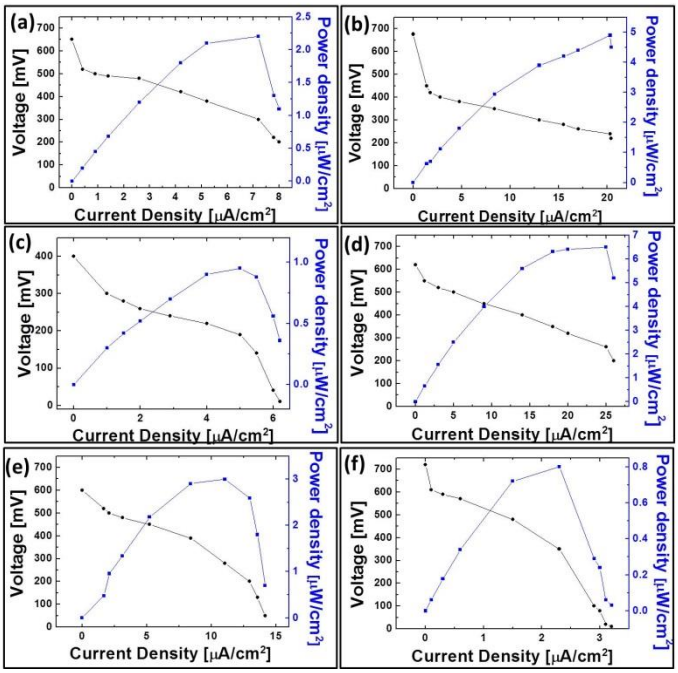

Figure 4: Polarization curve (black circle) and power output (blue square) of the MFCs with six different anode materials, measured as a function of current; (a) CNF, (b) CNT, (c) CP, (d) GPM, (e) GPN, and (f) PG. The values are derived and calculated based on the maximum current value at a given external resistance (680k, 470k, 330k, 220k, 150k, 100k, 47k, 22k, 10k, and 1kΩ). The individual losses are divided into three zones according to their occurrence at different polarization levels; activation loss, ohmic loss, and mass transfer loss.

Table 1: Overview of the resistivity, OCV, major electrochemical losses, and current densities during closed circuit operations of the MFCs with different anode materials

	OCV (mV)	Activation loss (mV)	Internal resistance (kΩ)	Mass transfer loss (mV)	Maximum current density at optimal external resistance (μA/cm²)
Carbon fiber (CNF)	660	~ 130	22	~100	8.3
Carbon nanotube (CNT)	680	~ 226	12	~50	23.4
Carbon paper (CP)	400	~ 100	30	~200	9.6
Gold/PCL microfiber (GPM)	620	~ 70	10	~60	28.5
Gold/PCL nanofiber (GPN)	610	~ 80	23	~170	15.8
Planar gold (PG)	720	~ 90	112	~350	5.8

decrease over the next 10 to 15 days. This is likely due to the cellular toxicity of carbon –based nanomaterials that could lead to proliferation inhibition and cell death [12]. GPM and GPN anodes also showed similar current profiles to those of the carbon nanomaterials but with significant current drop from a peak value. The PG anode also experienced current decrease after 12 days.

According to the polarization curves (Fig. 4), three types of electrochemical losses in MFCs could be identified; activation loss, ohmic loss, and mass transfer loss. The values of these losses were calculated for the six MFCs and are given in table 1. Also using

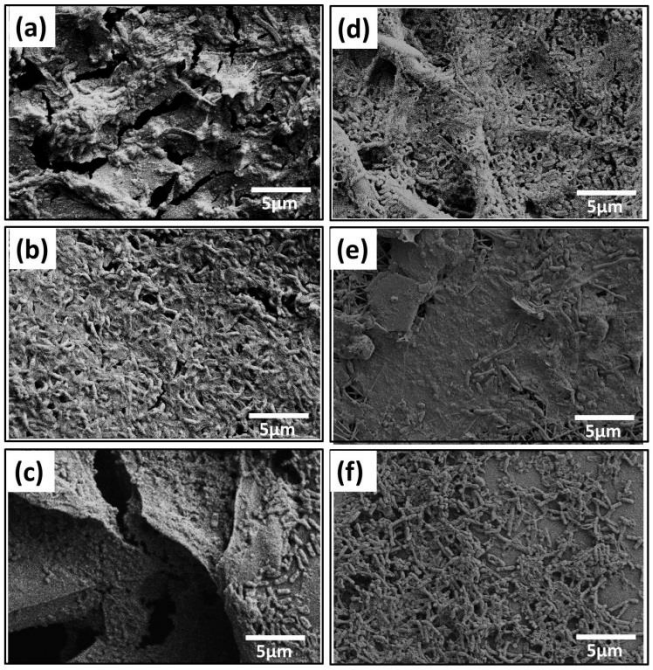

Figure 5: SEM images of all anodes from MFCs after biofilm formation; (a) CNF, (b) CNT, (c) CP, (d) GPM, (e) GPN, and (f) PG (scale bar is shown).

the polarization curve, we estimated the internal resistances from the ohmic loss region by linear fitting of the curve and the resistor values were in good agreement with the external resistor values used for optimal power generation. Carbon-based nanomaterials such as CNT and CNF showed higher activation losses due to the lower conductivity while their mass transfer losses were relatively less than others. The PG-based MFC showed the highest internal resistance (112 kΩ), while other three-dimensional micro-/nano-anodes had lower resistances of 10~30 kΩ, which demonstrates the ability of three dimensional anodes in decreasing the MFC internal resistance. Micro-sized MFCs generally have high internal resistances due to inefficient proton transfer rate [13]. Therefore, three dimensional anodes can allow a more efficient proton flux through the biofilm and a subsequent decrease in the internal resistance.

Finally, SEM images of all anodes from the six MFCs were taken after biofilm formation (Fig. 5) in order to observe the presence of attached biofilms on the different anode materials. In general, the images indicate that biofilms are fully formed on each anode surface, displaying rough uneven topography. On the other hand, the image of the planar gold (PG) surface showed that there is not complete coverage with bacterial cells, which suggests that the biofilm formation on the PG surface was slower than the other materials or that gold is not an optimal surface for bacterial cell attachment. The images also provide good comparative information demonstrating clear differences in the architectures of the biofilm established on the anode surface and the MFC performances.

CONCLCUSION

This work provides a direct comparison of the performance of six high-surface area anode materials under identical experimental conditions. The MFCs using three dimensional anode structures (CNT, CNF, GPM, and GPN) exhibited lower internal resistances than the macroscopic CP and two-dimensional PG anodes. However, those novel anode materials suffered from major issues such as high activation loss and instability for long-term operation, causing an enduring problem in creating widespread commercial MFC applications. The reported work provides an in-depth understanding of the interplay between micro-/nano-structured anodes and active microbial biofilm, suggesting future directions of those novel anode materials for MFC technologies.

ACKNOWLEDGMENT

We thank the Nanofabrication Lab at SUNY-Binghamton for providing the fabrication facilities, and the Binghamton University Research Foundation for funding this work. This work was also supported in part by S^3IP Small Grant Award.

REFERENCES

[1] B. E. Rittmann, "Opportunities for Renewable bioenergy using microrganisms", Biotechnol. Bioeng., 100, 203 (2008).
[2] D. R. Lovley, "Electromicrobiology", Annu. Rev. Microbiol., 66, 391 (2012).
[3] B. E. Logan, and J. M. Regan, "Microbial Fuel Cells-Challenges and Applications", Environ. Sci. Technol., 40, 5172 (2006).
[4] J. C. Biffinger, and B. R. Ringeisen, "Engineering Microbial Fuel Cells: Recent Patents and New Directions", Recent Pat. Biotechnol., 2, 150 (2008).
[5] B. E. Logan, "Scaling Up Microbial Fuel Cells and Other Bioelectrochemical Systems", Appl. Microbiol. Biotechnol., 85, 1665 (2010).
[6] V. Flexer, J. Chen, B. C. Donose, P. Sherrell, G. G. Wallace, and J. Keller, "The Nanostructure of Three-Dimensional Scaffolds Enhances the Current Density of Microbial Bioelectrochemical Systems", Energy Environ., Sci., 6, 1291 (2013).
[7] X. Xie, G. Yu, N. Liu, Z. Bao, C. S. Criddle, and Y. Cui, "Graphene-Sponges as High-Performance Low-Cost Anodes for Microbial Fuel Cells", Energy Environ. Sci., 5, 6862 (2012).
[8] J. E. Mink, and M. M. Hussain, "Sustainable Design of High Performance Micro-sized Microbial Fuel Cell with Carbon Nanotube Anode and Air Cathode", ACS Nano, 7, 6921 (2013).
[9] H. Ren, and J. Chae, "Scaling Effect on MEMS-Based Microbial Fuel Cells: Toward a Carbon-Neutral Miniaturized Power Source", Technical Digest of the 2012 Solid-state Sensors Actuators and Microsystems Workshop, Hilton Head Island, SC, 6/3-7/2012, pp. 501-504.
[10] V. Jayaprakash, R.D. Sochol, R.Warren, A. Kozinda, K. Iwai, and L. Lin, "Stackable Cow Dung Based Microfabricated Microbial Fuel Cells," Proceedings of 26th IEEE Micro Electro Mechanical Systems Conference, Taipei, Taiwan, 1/20-24/2013, pp. 881-884.
[11] A. Fraiwan, S. Sundermier, D. Han, A. Steckl, D.J. Hassett, and S. Choi, "Enhanced Performance of MEMS Microbial Fuel Cells Using Electrospun microfibrous Anode and Optimizing Operation," Fuel Cells, 13, 336 (2013).
[12] M. Ghasemi, W. R. W. Daud, S. H. A. Hassan, S. Oh, M. Ismail, M. Rahimnejad, and J. M. Jahim, J. Alloys Compd., "Nano-Structured Carbon as Electrode Material in Microbial Fuel Cells: A Comprehensive Review", 580, 245 (2013).
[13] R .S. Renslow, J. T. Babauta, P. D. Majors, and H. Beyenal, "Diffusion in Biofilms Respiring on Electrodes", Energy Environ. Sci., 6, 595 (2013).

CONTACT

*S. Choi, tel: +1-607-777-5913; sechoi@binghamton.edu

LOW-VOLTAGE THIN-FILM PIEZOELECTRIC SENSE-ACTUATE FAN PAIR FOR CHIP-SCALE GAS-SENSOR

V. Gund[*1], *L. Sanchez*[2], *R.G. Polcawich*[2], *and A. Lal*[1]
[1]*Sonic*MEMS Laboratory, Cornell University, USA
[2]Army Research Laboratory, USA

ABSTRACT

Chip-scale gas sensing devices based on ion-mobility measurements of analytes offer the potential for fast and reliable detection of toxic compounds and chemical warfare agents, which maybe odorless or colorless. The ability to produce required ion-flow rates using low-power architectures is critical in order to maximize sampled air volume for fast detection. In this paper, we present a novel thin-film piezoelectric sense and actuate pair of fans as a component for controlled ion flow in ion-mobility-based gas detectors. The drive-fan achieves low-power operation (13.5 mW/sccm), low voltage (10.8V/sccm) with sufficiently small form-factor (0.1mm^3/sccm) along with feedback flow signal from the sense-fan to measure the flow and detect the onset of turbulent flow. This device has the potential for monolithic integration with CMOS devices for chip-scale label-free gas detection.

INTRODUCTION

Micro-scale gas pumping devices are important components of portable gas-sensors and gas chromatographs for emission content monitoring in industry, automation and food packing as well as environmental sensors for maintaining air quality [1]. Gas pumps also find applications in microfluidic devices for laminar flow control and manipulation of gases in microfluidic fuel cells with precise mass transport requirements to the electrodes, to reduce electrode size and improve power density [2]. Furthermore, convective air-flow generation for cooling and thermal management of electronic devices is a growing area of interest in order to optimize overall power requirements without affecting device performance [3].

In ion-mobility gas sensors, high ion-flow rates are often required without any turbulence. To accomplish this, inertial fluid forces must be weaker than viscous damping forces in order to produce laminar flow in micro-channels. Centrifugal pumps using scratch-drive rotary fans have been used for air-flow generation via conversion of rotational kinetic energy to hydrodynamic energy of air [4]. These fans have resonant frequencies in a few-kHz range and require 30V$_{p-p}$ operation but are prone to frictional wearing inherent in their operational mechanism. In order to achieve high flow rates and large pressure differentials on chip for gas-chromatographs and ion-mobility based sensors, micro-valve based multi-stage gas pumps in mm-scale packages have been extensively explored [5]. To minimize device footprint and complexity for integration in miniaturized micro-packages, torsional axial fans based on resonant electrostatic actuation have been used to produce flow rates of up to 25 µL/min using arrays of fans [6]. However, operation voltages required for electrostatically actuated device vary from 100-150 V.

Axial piezo-electric fans provide a low-power and low-voltage solution for chip-scale ion flow generation. Bulk lead zirconate titanate (PZT) plates with mylar or steel plates attached to them have been previously used for cooling of electronic devices by convective removal of heat in confined spaces [3]. Such a fan has low-power consumption and low-noise operation. However, the large size is not suitable for ultra-portable packaged sensors, used in burgeoning handheld smart-phone and tablet markets. This work presents the design, analysis and characterization of a novel thin-film sense-actuate piezo-fan pair for chip-scale gas-sensors.

A schematic of the fan-pair with the gas-sensing system is shown in Figure 1. We have previously demonstrated a laser micro-machined low-voltage ion-mobility spectrometer (IMS) array [7] which uses lateral electric fields for segregation of analytes on individual electrode islands, and high-aspect ratios for ion-flow confinement in the device channel. The sense-actuate fan pair in this work can be integrated at the input of the IMS channel, as shown, along with radioactive electron-emitting ^{63}Ni for ionizing analytes following initial pre-concentration of analytes, if any. At resonance, the actuation fan produces ion flow via acoustic streaming. For large driving voltage on the actuator, the sense-fan becomes unstable due to the larger random-motion from the flow indicating a threshold, and starts to flutter providing a feedback signal for limiting or eliminating the turbulent flow.

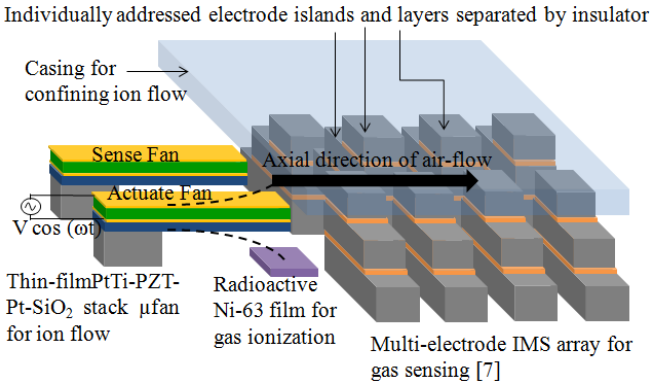

Figure 1:Chip scale ion-mobility gas sensor schematic - IMS array gas sensor, radioactive ^{63}Ni film for gas ionization integrated with piezoelectric sense-actuate microfans for producing ion-flow

PIEZO-FAN MODEL

Flow generation from oscillating beams has been studied by several authors, particularly for larger beams, but not fully understood due to the complicated non-linear flow dynamics. 2-D flow near the tips of flexible plates with large oscillation amplitudes have been investigated [8] and Toda et al. derived the theory for air-flow generation from a vibrating piezoelectric multi-morph under resonant operation [9].

For a piezoelectric film with an applied electric field *E* the strain vector *s* is given by -

$$s = DE$$

Here, *s* is a 6x1 column vector of three axial and shear strains each, *E* is a 3x1 column vector of electric-field and *D* is the 6x3 coupling coefficient matrix. For our device with metal electrodes patterned on the piezoelectric layer and an elastic layer of SiO_2, the d_{31} component is important for operation - vertical E-field in the PZT produces a longitudinal strain causing the multimorph to bend. The modeling equation of motion for our 4-layer piezoelectric multimorph actuate fan is-

$$M\ddot{y} + ky + f_{air} = F\cos(\omega t)$$

9781940470016/HH2014/$25©2014TRF
DOI 10.31438/trf.hh2014.56

Here, M is the effective mass of the oscillating fan concentrated at the center of the inertial force an effective length L away from the hinge, k is the spring constant of this beam, f_{air} is the force for driving the air-motion, F is the driving force for the fan by a sinusoidal AC signal for a flat-plate model as described in [9]. The force f_{air} is usually ignored in resonator analysis as a loss term. However, it is important in our analysis to calculate the streaming flow produced by the fan.

The width of air-region above and below the vibrating fan-edge that is streamed radially at resonance $D \approx 2y_0$ where y_0 is the fan-edge amplitude. A radial torque T is required to accelerate this volume of air. At resonant operation, the air mass directed radially outwards in time dt near the fan edge *is* $2\rho_{air}Wy_0v_{//}dt$. Here, ρ_{air} is the density of air ~ 1.225 kg/m^3, W is the fan width and $v_{//}$ is the air flow velocity. The time derivative of this mass multiplied by the lever arm i.e. fan length and maximum fan edge velocity is the required torque T, and the corresponding $f_{air} = T/L'$ at the center of the inertial force [9] -

$$f_{air} = 1.573\rho_{air}WDv_{\perp}v_{\text{II}}$$

The numerical factor is a normalization for the distance of the inertial force center from the clamping point. The input mechanical power to the air mass is then -

$$P_M = T\frac{d\theta}{dt} = \rho_{air}WDv_{\text{II}}v_{\perp}^{\,2}$$

For ideal coupling, all of this mechanical power is transferred to the air mass and used to produce streaming motion. However, some of this energy is dissipated as heat due to air viscosity [8]. Hence, there is an efficiency η which is the coupling coefficient between the mechanical input power and acoustic streaming power in the air-mass flown out radially. The output air-mass power is then the product of the static pressure p and volume flow-rate near the fan edge and is related to the input power as -

$$P_A = pDWv_{\text{II}} = \eta P_M$$

The air-mass and fan-edge velocities can be estimated and related to each other using the Bernoulli energy equation while including the static pressure energy term produced by the fan. The velocities are related as $v_{\text{II}} = \sqrt{2\eta}\,|v_{\perp}|$ for the case of incompressible flow assuming negligible resistance to air flow in the device channel. For an experimentally determined resonance frequency ω, and fan-edge amplitude y_0, $v_{\perp}=\omega y_0$. Thus, the measured air-velocity directly gives a lower-bound estimate of the power-transfer efficiency η from the fan to the air-mass.

In order to compute the air-mass velocity, f_{air} derived above is substituted in the non-linear equation of motion. The resonance frequency is $\omega = \sqrt{K/M}$ while the amplitude term is solved for using Fourier analysis as in [9]. The forcing function E relates the applied voltage V across the piezoelectric to the fan-edge displacement at resonance which yields the expression for air-velocity [9] as -

$$v_{\text{II}} = C\sqrt{\eta}\left(\frac{d_{31}V}{t_{PZT}\sqrt{\eta}}\right)^{1/3}\frac{y_0^{\,1/2}}{L}$$

Here, C is constant with appropriate dimensions for lumping together numerical coefficients from the Fourier analysis and the densities of the air and beam materials. Finally the total volume flow-rate can be estimated as -

$$Q = 2y_0Wv_{\text{II}}$$

Thus, for thin-film d_{31} coefficient values of the order of those for bulk PZT, the 500nm thickness thin-film devices offer ~ 30x enhancement in E-field for the same applied voltages, compared to 0.5 mm thick bulk PZT, enabling low-voltage operation for comparable flow-rate production.

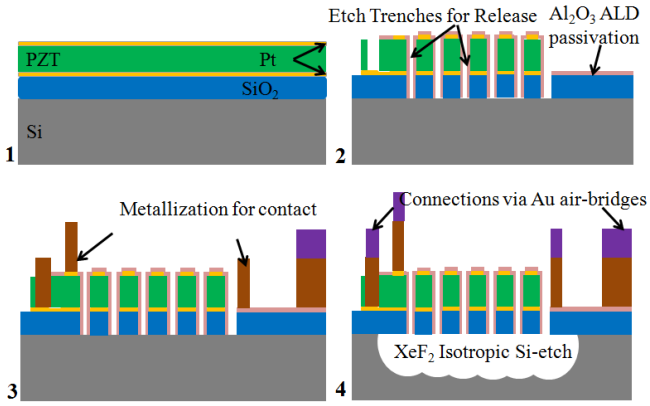

Figure 2: Process flow for fabrication of sense-actuate fan pairs

FABRICATION

The devices were fabricated using the thin-film PZT growth process at ARL[10] shown briefly in Figure 2. A combination of thermal oxidation, CVD, sputtering, and ion-milling were used to deposit and pattern layers while the PZT films were made via sol-gel solution deposition, and adding between 0 and 30% excess lead to account for losses during crystallization. Contact to the top Pt electrode was made with Cr/Pt/Au air-bridges followed by release via etch-trenches using XeF_2 for isotropic Si etch.

Fabricated devices have a SiO_2 elastic layer of 500 nm, bottom electrode of TiO_2/Pt with thickness 36 nm/100 nm, PZT of 500 nm and top electrode of 100 nm with gold air-bridges for contact. Sense-actuate fan pairs of widths 200 um each and lengths 800 um and 1000 um with separations of 300 um show in Figure 3 were tested for this report.

PZT CHARACTERIZATION

The fan edges bend and curve out of the wafer-plane due to residual film stresses after release, a consequence of the long axial dimension. As a result, optical profilometry or laser Doppler vibrometry was not used for direct displacement measurements

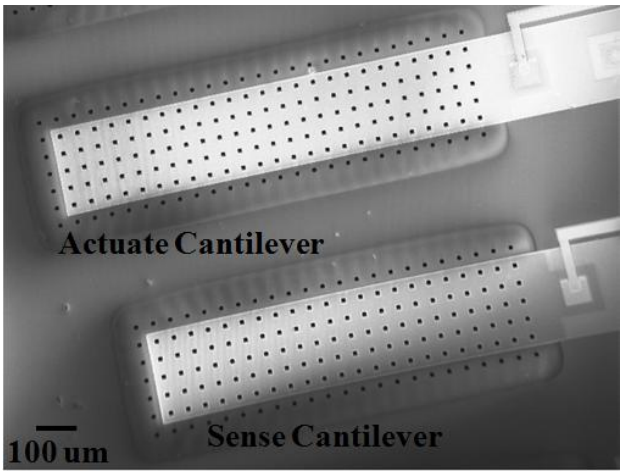

Figure 3: Scanning electron micrograph (SEM) of the unreleased sense-actuate fan-pair

since the laser light used in these systems does not return back to the detector due to angled incidence on the fan surface, the angle for each fan being a parameter which is difficult to control or tune. Hence for PZT characterization, fans were mounted at 90 degrees to the wafer-plane such that the fan bending, along its thickness when actuated, was in the plane of imaging to optically measure displacements accurately. This was used to measure the d_{31} co-efficient of PZT. In this analysis, it was assumed that shear-effects during bending are negligible and residual stress-induced curvature is ignored. DC actuation up to 6V was used to measure fan-edge displacement up to 121 um (for 800 um long fan) and 148 um (for 1000 um long fan) following which, multilayer analysis for arbitrary piezoelectric-elastic layer stacks was used to calculate d_{31} [11]. Typical poling field strengths for PZT are of the order of 300 kV/cm [12], hence, the actuation voltages are not expected to affect PZT performance or depolarize it. For isotropic Poisson's ratio υ_i, the effective Young's moduli Y_i and coupling coefficients $d_{31,i}$ of the i-th layer in the multi-morph stack are modified for this analysis as follows -

$$Y_i \rightarrow Y_i/(1-\nu_i^2)$$

$$d_{31,i} \rightarrow d_{31,i}/(1+\nu_i)$$

By using the fact that axial forces and moments at any cross-section for a DC-actuated beam are in equilibrium and assuming equal radius of curvature for all layers in the multi-morph, the d_{31} for PZT = -85.8±5 pC/N. This value is less than typical d_{31} values of bulk PZT-5H close to -275 pC/N but within reasonable expectation for multi-layer stressed thin-film devices.

FLOW MEASUREMENTS

Resonance frequencies for the 800 um and 1000 um fans were measured to be at 614 Hz and 505 Hz with 2.5 mW power input for charging-discharging the PZT capacitance. A commercial resistance temperature detector (RTD) element was used to measure air-velocity as a function of drive frequency. At each drive frequency, the RTD element stabilizes to a peak measured air-velocity which is plotted in Figure 4. The 800 um long fan has produces a peak air-velocity of 7 cm/sec at resonance. As expected from the piezo-fan model, this peak air-velocity produced by the fans varies inversely as the fan length. Also, the actuation frequency for peak air-velocity corresponds to the resonance frequency of the fans. Based on the measured fan velocities and fan-edge displacement at resonance, the calculated flow-rates and mechanical to air-mass flow power conversion efficiency are summarized in Table 1.

The piezo-fan model in [9] predicts a flow rate independent of length, assuming the Bernoulli equation holds true and no-resistance to air-flow. However, our measurements are done very close to the RTD sensor element which is housed in a metal casing, and is likely to add some resistance for air-flow. Also, the large vibration amplitude ~ 110 um for 800 um fan and 140 um for 1000 um fan, means not all the air-flow is directed radially outwards towards the sensor. Figure 5 plots the voltage dependence of the measured peak air-velocity from the fan. The equation for air-velocity $v_{\|}$ predicts a $V^{5/6}$ voltage dependence - there is a $V^{1/3}$ in the equation derived and a further $V^{1/2}$ due to $y_0^{1/2}$ dependence on edge-displacement since y_0 is directly proportional to V. The data-fit for this dependence are plotted as dotted lines with the expected factor being 1/L for each curve. Table 2 summarizes the performance of our PZT-based fan and compares it to electrostatically actuated micro-fan and valve-based micro-pumps for chip-scale pumping.

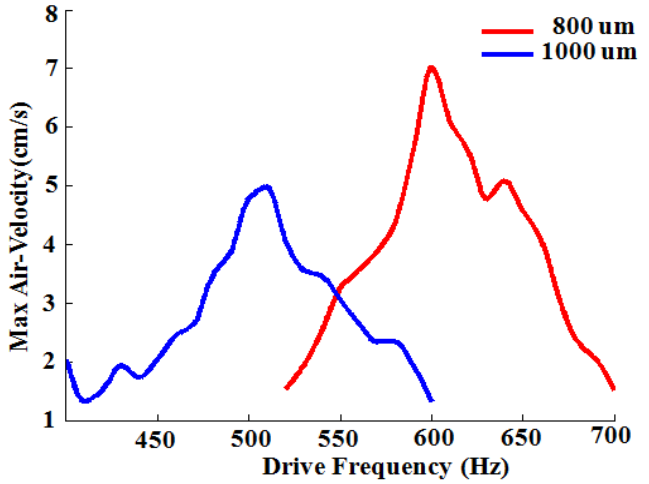

Figure 4: Plot of measured maximum air-velocity with RTD sensor element at the tip of the drive fan as a function of frequency for 800 um and 1000 um long piezofans

Table 1: Summary of flow-velocities, flow rates and mechanical to air-mass flow power transfer efficiencies

Device Length	Flow (cm/sec)	Flow-Rate (µL/min)	Efficiency (η)
800 um	7.01	185.1	1.3%
1000 um	4.97	167	0.7%

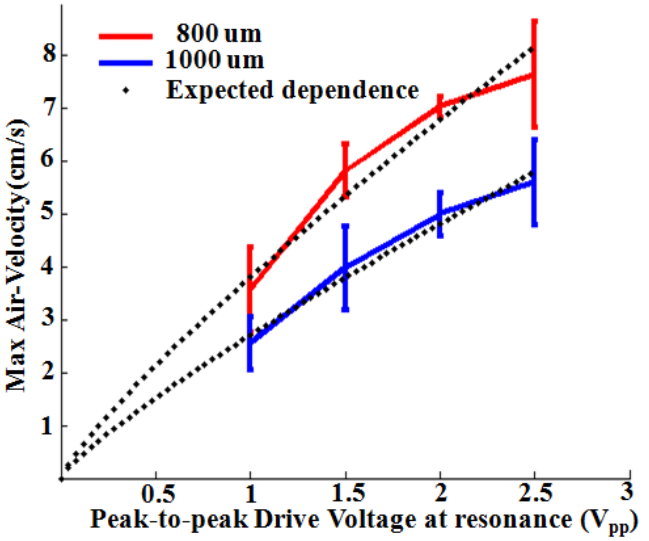

Figure 5: Plot of measured maximum air-velocity with RTD sensor element at the tip of the drive fan and expected $V^{5/6}$ dependence

Table 2: Comparison of this work with previous reports for chip-scale fans and pumps

Work	Max Flow (µL/min)	Nominal Voltage	Power (mW)
Valve-based Micropump [5]	4000	100V	57
Electrostatic Microfan [6]	10	$100V_{p-p}$	-
Piezo fan - This work	185.1	$2V_{p-p}$	2.5

SENSE FAN MEASUREMENTS

The novel sensing scheme introduced in our pumping system is the sense fan which measures potential lateral turbulent air-flow, if any, due to large drive on the actuator. To prevent turbulence in micro-channels, inertial fluid forces must be weaker than viscous forces allowing layers of fluid air to slide. Any kind of lateral convection can be considered a signature of turbulence which is where the sense-fan provides a feedback signal via flutter. Our experiments demonstrate a proof-of-concept for this system, rigorous analysis of the turbulent air-flow is not discussed.

In the sense-actuate fan pair testing, the 1000 um long actuate fan was driven with increasing drive amplitude. Correspondingly, the voltage developed across the sense fan due to a force applied by turbulent lateral air-flow, if any, was sensed via the reverse piezoelectric effect. Figure 6 plots direct time-domain signals obtained from the sense-fan flutter for various drive voltages on actuator at the resonance frequency of the actuator. Since the quality factors for the resonant operation of our fans in air are low (~10), precise frequency matching is not required.

Figure 7 plots the DC and AC voltage-signal levels as a function of drive voltage on the actuator at resonance. Clearly, as the drive is increased both a constant force (indicated by the DC level) and a flutter (indicated by the AC level) are seen on the sense and these increase with the drive. The FFT of the signals shows a peak at 1108 Hz, roughly twice the drive frequency and suppressed signal at the drive, perhaps since the force due to lateral air-pressure is modulated at twice the frequency.

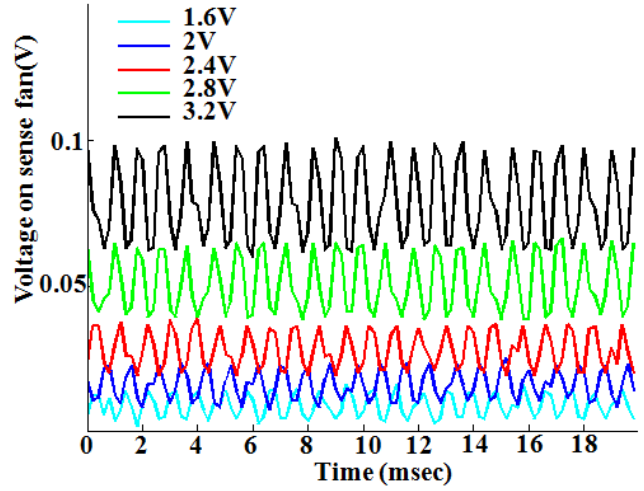

Figure 6: Sense-fan time-domain voltage output for different drive voltages on the actuator at resonance

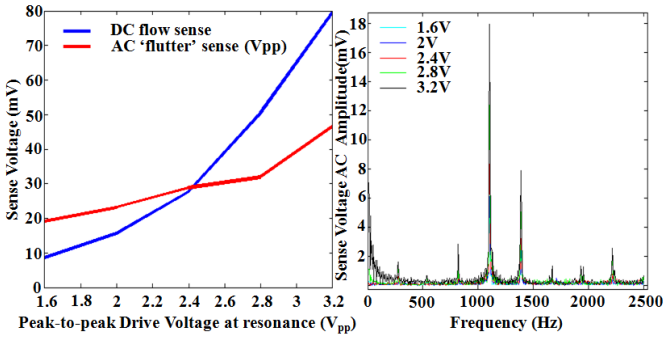

Figure 7: DC flow sense indicating constant lateral air-stream force and AC fluctuation showing increasing flutter/turbulence as actuator drive is increased and FFT of the AC signals with a peak at 1108Hz, which is twice the resonant drive frequency

CONCLUSIONS

In this paper, we have presented a novel low-voltage sense-actuate piezo-fan pair for potential integration in chip scale gas sensing applications. The thin-film PZT process enables scaling to achieve required electric fields with low voltage operation, for CMOS compatible operation. The sense-fan allows for feedback turbulent flow-sensing without complicated circuitry and extensive additional on-chip real-estate. By integrating the fan with ion-mobility-based sensors as in [7] and benign electron-emitting ^{63}Ni for ionization and self-powering as previously demonstrated [13], the system can have self-sustained performance for long periods limited only by the ionizer half-life.

ACKNOWLEDGEMENTS

The authors would like to acknowledge the ARL fabrication facility for assisting in device fabrication and Cornell Nanofabrication Facility (CNF) for post-processing development and testing equipment. Travel support has been generously provided by the Transducers Research Foundation (TRF).

REFERENCES

[1] X. Liu et al., "A Survey on Gas Sensing Technology," *Sensors*, pp. 9635-9665, 2012

[2] R. S. Jayashree et al., "Air-Breathing Laminar Flow-Based Microfluidic Fuel Cell," *J. of American Chemical Society*, pp. 16758-59, 2005

[3] S. M. Wait et al., "Piezoelectric Fans Using Higher Flexural Modes for Electronics Cooling Applications," *IEEE Trans. on Components and Packaging Technologies* pp. 119-128, 2007

[4] R. Linderman et al., "Development of the micro rotary fan," *Sensors and Actuators A: Physical*, Vol. 95 pp. 135-142, 2002

[5] H. Kim et al., ""A Fully Integrated High-Efficiency Peristaltic 18-Stage Gas Micropump with Active Valves," *IEEE MEMS*, pp. 131-134, 2007

[6] R. Linderman et al., "The resonant micro fan gas pump for active breathing microchannels," *IEEE Transducers*, Vol. 2 pp. 1923-1926, 2003

[7] V. Gund et al., "Low-voltage (<5V) ion-mobility spectrometer array for label-free gas detection," *IEEE Transducers*, pp. 2767-2770, 2013

[8] A. Ihara and H. Watanabe , "On the Flow Around Flexible Plates, Oscillating with Large Amplitude," *J. of Fluids and Structures*, Vol. 8, pp. 601-619, 1994

[9] M. Toda, "Theory of air flow generation by a resonant type PVF2 bimporh cantilever vibrator," *Ferroelectrics*, Vol. 2 pp. 911-918, 1978

[10] T.G. Ivanov et al., "Analog RF MEMS Attenuator with PZT Actuators," *Transducers*, pp. 2767-2770, 2013

[11] D. L. DeVoe and A. P. Pisano, "Modeling and Optimal Design of Piezoelectric Cantilever Microactuators," *J. of Microelectromechanical Systems*, Vol. 6 pp. 266-270, 1997

[12] G. Park et al., "Measurement of piezoelectric coefficients of lead zirconate titanate thin films by strain-monitoring pneumatic loading method," *Applied Physics Letters*, Vol. 8, pp. 4606-4608, 2002

[13] R. Duggirala et al., "Radioisotope Thin-Film Fueled Microfabricated Reciprocating Electromechanical Power Generator," *J. of Microelectromechanical Systems*, Vol. 7, pp. 837-849, 2008

CONTACT

*Ved Gund, tel: +1-650-521-1172; vvg3@cornell.edu

SINGLE CHIP MICRO GC WITH INTEGRATED HETEROGENEOUS NANOMATERIAL SENSOR ARRAY FOR MULTIPARAMETER GAS SENSING

S. MacNaughton[1], and S. Sonkusale[1]*
[1]Tufts University, Department of Electrical and Computer Engineering, Medford, MA 02155

ABSTRACT

We present a PDMS micromolded gas chromatography system on chip with integrated gas sample injection, heating elements, as well as a nanomaterial based chemiresistor array for gas detection. This device is the first realization of a micromolded (as opposed to etched) microscale gas chromatography (μGC) system. The PDMS mold serves the dual purpose of creating the column geometry as well as acting as the stationary phase during the gas chromatography analysis. A glass wafer acts not only to seal to column but also as a platform for a micropatterned detector and heating element. A chemiresitor array consisting of carbon nanotubes (CNT), vanadium oxide nanowires (VO_x) and reduced graphene oxide (rGO) provide cross-calibrated detection of gas constituents after chromatographic separation to yield a multiparameter gas analysis.

INTRODUCTION

Conventional gas sensors excel at identifying single gas analyte but are confounded by mixtures of gases. Therefore, gas chromatography is a pillar of gas analysis due to its ability to separate the constituents of a gas phase mixture. However, current available gas chromatography systems are bulky benchtop devices, which necessitate sampling gases and returning the samples for analysis. Because this process consumes time and has the potential to compromise gas analysis, there is a need for portable, low-power gas chromatography devices for use in the field. Much research has been dedicated to the realization of highly effective, miniaturized gas chromatography systems over the past three decades[1, 2]. However, despite their successes, no commercial development of micro-gas chromatography (μGC) devices has been realized. The reasons for this is two-fold: first, the majority of μGC systems developed do not incorporate micro-scale components for all facets of the measurement, so they still rely on bulky components, which undermine their utility versus a conventional benchtop device. Second, the typical fabrication process for these devices (reactive ion etching, anodic bonding and stationary phase coating) is complex, difficult to reproduce, and requires expensive vacuum and plasma systems. The presented device includes all the necessary components for gas chromatography in a low cost, easily fabricated device.

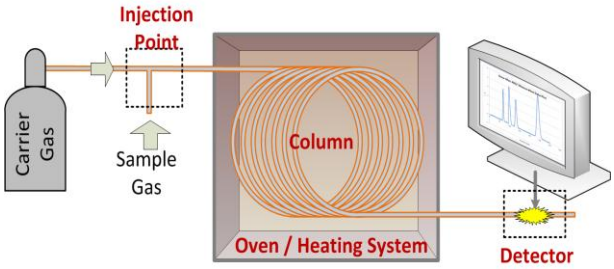

Figure 1 - Schematic representation of conventional gas chromatography device

Gas chromatography separates the constituents of a sample of gas mixture based upon their interactions with the sidewall of a long tube known as the gas column. The column is coated with a special adsorbent material known as the stationary phase which is often a waxy polymer or silicone. As the gas sample is pushed through the column by a carrier gas, analytes with stronger affinity for the stationary phase adsorb and condense making them travel though the column more slowly. A detector at the end of the column registers when each gas species elutes after a specific characteristic time known as the retention time. The miniaturization of columns aids in the separation efficiency of chromatography columns as it increases the surface area per volume of gas analyte.

The general components of a gas chromatography system are shown in Figure 1. These components are the injection system, the heating element, the detector, and, finally, the detector itself. Each of these components presents distinct challenges in their miniaturization and will be detailed in the ensuing sections.

Injection Mechanism

Micromachined gas columns place especially onerous constraints on the gas sample injection strategy due to the especially small volumes of gases that are injected. Generally, volumes on the order of nanoliters or less are required. An effective and common strategy to achieve adequate injection is illustrated in Figure 2. A cross-flow pattern is used to capture a small pocket of the gas sample and direct it through the column [3]. This process is mediated by high-speed valves (Clark Solutions, Model number 2026).

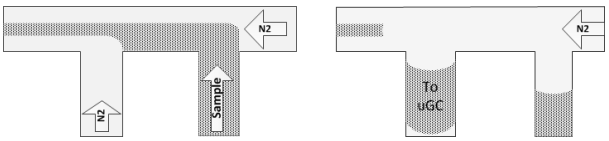

Figure 2 - Illustration of gas injection technique.

Detector

A chemiresistor array was chosen as the detection strategy. Chemiresistors are natural microscale allowing for their facile integration into a microscale column. Furthermore, an array allows for multiparameter analysis of gas constituents based upon the magnitude of the response to the various elements in the heterogeneous array. Nanoscale chemiresistors also possess the necessary response time for time domain analyses as in gas chromatography. Carbon (reduced graphene oxide and carbon nanotubes) and metal oxide nanowires (vanadium oxide) were chosen as chemiresistive elements due to prior experience with the materials [4].

Drawbacks of chemiresistor array include a memory effect and lack of correlation between analyte quantity and magnitude of response. Chemiresistors are known to have their response be a function of not only the current chemical environment, but also their chemical history. Methods have been developed to account for this [5]. The lack of correlation between response magnitude and analyte quantity makes it difficult to determine the relative concentrations of each constituent of the gas mixture. Although all

9781940470016/HH2014/$25©2014TRF
DOI 10.31438/trf.hh2014.57

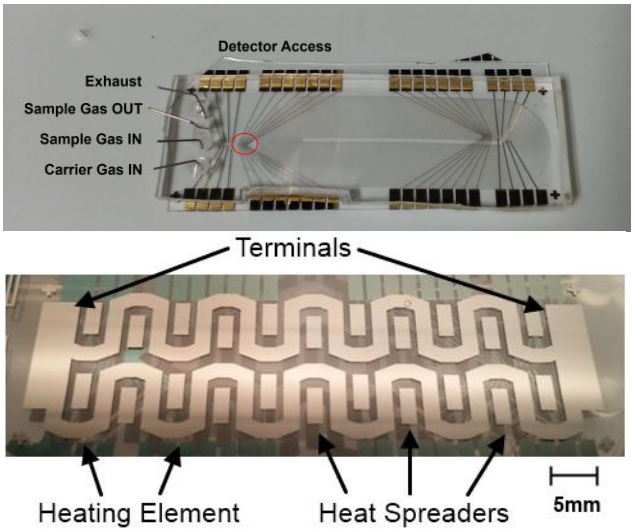

Figure 3 - Image of fabricated device from above (top) and below (bottom). The heating element is removed from the top picture to make the column spiral more visible versus the white background. The device is same size as a common microscope slide (25mm x 75mm). The chemiresistor detector is circled in red.

detectors have to be calibrated by weighting coefficients for any individual analyte, this is much more pronounced in the case of chemiresistors. However, it is this dynamic range of response which allows another parameter upon which to identify gas components.

Heating Element

The interaction between the stationary phase and gas samples is very dependent on temperature. As such it is critical to be able to maintain an accurate and consistent temperature profile throughout the course of the measurement. A nichrome heating element (200nm thick) patterned directly on the device accomplishes this (see Figure 3).

The heating element drives the power consumption of the device, which is of prime importance when designing for use in the field under battery power. The heating element is able to maintain the temperature of the device at 100°C with 1.67watts of power, very much within the capability of batteries. The temperature is monitored with a thermocouple.

Column

Finally, the most important element of the design is the column. Polydimethylsiloxane (PDMS) and similar compounds have long been used as excellent stationary phases for the separation of nonpolar analytes in gas chromatography, and, with the massive volume of interest in PDMS for microfluidics, it would seem that gas chromatography would be a natural application for micromolded PDMS. However, the high permeability of PDMS to many gas compounds presents a significant hurdle in the development of a micromolded gas column. With micromolded columns, there are two parallel paths through the column. The first (preferred) path is through the column as in a conventional capillary column. The second parasitic path is driven by the permeation of gas analytes through the walls of the column between adjacent turns.

There are two strategies to mitigate this in designing the column geometry. First, the column walls can be made very thick. This presents a high resistance to permeation, but limits the amount of turns and therefore column length which can drive down separation efficiency. The second strategy is to increase the cross sectional area of the column, which conversely reduces the resistance of flow propagating through the column, but also limits the interaction between the gas sample and column sidewalls.

A combination of these two strategies was used. An increased wall thickness was used in the first third of the column where the pressure differential and therefore permeation between adjacent turns is greatest. A modest column width and height of nominally 20µm was used for the entirety of the column, which was 10m in length. The length of the column was chosen to be rather long as a conservative measure in case the separation efficiency was lower than expected so that successive peaks could still be resolved.

METHODS

Fabrication

The fabrication of the device is represented in Figure 4. The fabrication proceeds as follows. A PDMS micromold containing the column geometry is created using standard micromolding techniques with SU-8 photolithography. Concurrently, a glass wafer is patterned on two sides by standard photolightography, metallization (sputtering) and liftoff. The first side is patterned with gold electrodes and pads for the chemiresistor array and its monitoring. The obverse side is patterned with the heating element pattern shown in Figure 3.

Dielectrophoresis is used to assemble nanomaterials (reduced graphene oxide flakes, carbon nanotubes and vanadium oxide nanowires). Dielectrophoresis is the motion of a polarizable particle in a dielectric medium as a result of a time-varying electric field, and it can be used to pull nanomaterials out a liquid dispersion to form a resistive assembly between two electrodes. This process is described in detail in previous work [6].

The nanomaterials were procured as follows: the reduced graphene oxide was synthesized in the procedure described in previous work . The carbon nanotubes were procured from Helix Material Solutions, and the VO_x nanowires from Novarials Corporation.

Once the chermiresistor array is created the glass wafer is subjected to a low power (50W) oxygen plasma for 30s at 200Torr. This allows covalent bonding between the PDMS micromold and glass wafer, thus sealing the column.

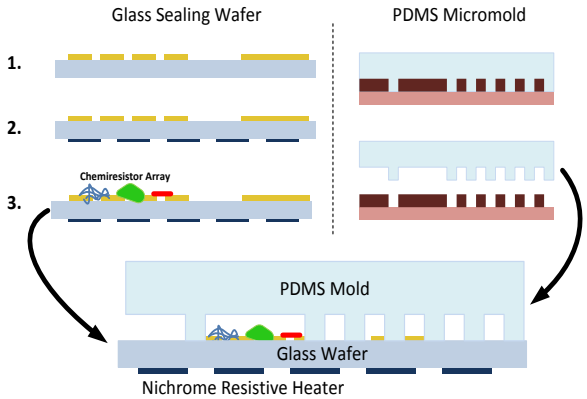

Figure 4 - Fabrication of micromolded gas chromatography device.

It should be noted that the fabrication method is very low cost. Almost every step can be performed with inexpensive benchtop equipment. The exception is the photolithography processes. However, even the photolithography is not especially

technically challenging with critical dimensions greater than 20µm.

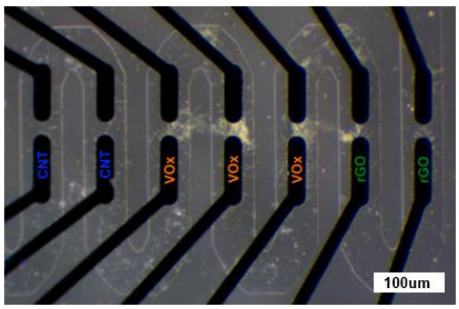

Figure 5 - Micrograph of chemiresistor array

Gas analysis

High purity (>99.999%) nitrogen gas was used as the carrier gas regulated to 40psi. An analytical standard calibration set of aliphatic compounds (Sigma-Aldrich part number 4-8244) was used to verify the function of the device. This set contains unfunctionalized carbon chains ranging in length from 12 to 17 carbon atoms dissolved dichloromethane.

After waiting for the temperature of the device to stabilize (approximately 10 minutes), the gas was injected per the procedure outlined in the introduction. A simple circuit (shown in Figure 5) was developed to monitor the chemiresistor array. The circuit consists of three portions: a variable current source, an analog switch to select a single chemiresistor array element, and a voltage readout buffer. Continuous monitoring of an entire array is made possible by time multiplexing or scanning through the array. The circuit was designed to be compact to allow for future integration onto the gas chromatography device without significant size expansion. The readout circuitry connects to a laptop via a LabView data acquisition board (NI-6009) and software interface.

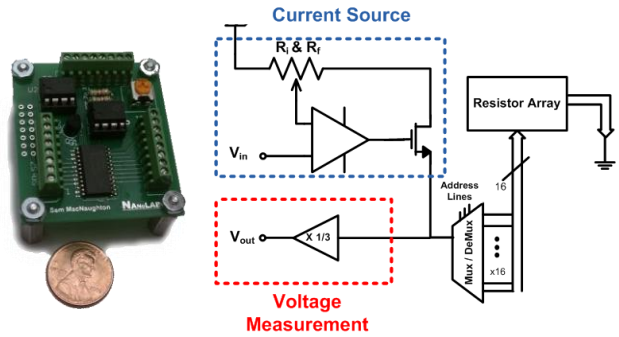

Figure 6 – Image and schematic of monitoring electronics for the chemiresistor array detector.

The resulting chromatograph is shown in Figure 7, and a zoomed in portion of the rGO trace is shown in Figure 8 with the peaks identified. Each of the six peaks resultant from the six components of the analytics standard is clearly resolvable. A trace from a CNT assembly is omitted as they did not respond. It is hypothesized that the oxygen plasma treatment for bonding the glass wafer to the PDMS rendered the CNTs inert to the gas analytes.

As noted in the introduction, some limitations of chemiresistors are clearly evident. The magnitude of the responses decrease over time regardless of the analyte concentration. While this could be attributed to the peaks being widened or sampled at points other than their maximum, it is most likely due to the memory effect of the chemiresistors.

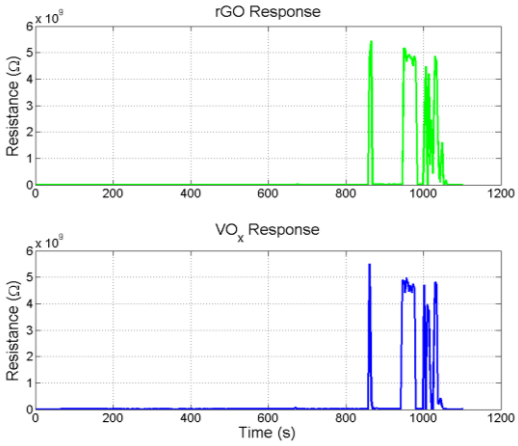

Figure 7 –Chromatograph for aliphatic compound analytical standard. The sample was introduced at 650s, once the temperature and chemiresistor resistance had stabilized.

The typical gauge of the separation efficiency of is the theoretical number of plates. This is given by the following relation:

$$N = 5.54\left(\frac{t_r}{W_{0.5}}\right)^2$$

N is the number of plates, t_r is the retention time, and $W_{0.5}$ is the half-width at full height of the peak. Calculating with respect to dodecane (which would give the worst case number) yields 4650 or 465 plates per meter. This value is comparable to other low power µGC devices found in the literature fabricated with the conventional etching and anodic bonding paradigm [2, 7, 8].

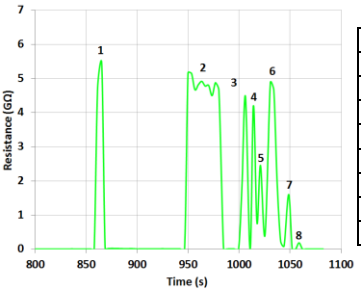

#	Component	Concentration
1	Air Peak	N/A
2	DCM	N/A
3	$C_{12}H_{26}$	497.5 µg/ml
4	$C_{13}H_{28}$	756.1 µg/ml
5	$C_{14}H_{30}$	1251 µg/ml
6	$C_{15}H_{32}$	1526 µg/ml
7	$C_{16}H_{34}$	2041 µg/ml
8	$C_{18}H_{36}$	2064 µg/ml

Figure 8 - Resistance of RGO assembly during gas chromatography run. It should be noted that resistances greater than 5GΩ could not be recorded due to hardware limitations.

DISCUSSION

We present the first micromolded PDMS column. The injection mechanism, heating element and a chemiresistor array detector were all integrated into a single device through a facile, inexpensive fabrication flow. This demonstrates the capability to integrate every necessary component into a small scale, low cost device for measurements in the field. The power consumption of less than three watts is in line with what is necessary for a portable device.

Furthermore, the addition of chemiresistor array as the

detector adds a potential new dimension upon which to identify gas constituents based upon the characteristic response of a gas analyte across the elements of the array.

Further investigation is being pursued on many facets of this design. The integration of the passive valves in the PDMS channel and the electronics onto the device would eliminate all the external components used in the gas measurement. Using air as a carrier gas is also being investigated to eliminate the need for a tank of carrier gas, which is by far most bulky component of a gas chromatography measurement.

REFERENCES

[1] S. C. Terry, J. H. Jerman, and J. B. Angell, "A gas chromatographic air analyzer fabricated on a silicon wafer," *Electron Devices, IEEE Transactions on*, vol. 26, pp. 1880-1886, 1979.

[2] M. Agah, J. A. Potkay, G. Lambertus, R. Sacks, and K. D. Wise, "High-performance temperature-programmed microfabricated gas chromatography columns," *Microelectromechanical Systems, Journal of*, vol. 14, pp. 1039-1050, 2005.

[3] F. G. Bessoth, O. P. Naji, J. C. Eijkel, and A. Manz, "Towards an on-chip gas chromatograph: the development of a gas injector and a dc plasma emission detector," *Journal of Analytical Atomic Spectrometry*, vol. 17, pp. 794-799, 2002.

[4] S. MacNaughton, S. Sonkusale, S. Surwade, S. Ammu, and S. Manohar, "Electronic nose based on graphene, nanotube and nanowire chemiresistor arrays on silicon," in *IEEE Sensors 2011*, Hawaii, 2011, pp. 125-128.

[5] Y. W. Chang, J. S. Oh, S. H. Yoo, H. H. Choi, and K.-H. Yoo, "Electrically refreshable carbon-nanotube-based gas sensors," *Nanotechnology*, vol. 18, p. 435504, 2007.

[6] C.-L. Chen, V. Agarwal, S. Sonkusale, and M. R. Dokmeci, "The heterogeneous integration of single-walled carbon nanotubes onto complementary metal oxide semiconductor circuitry for sensing applications," *Nanotechnology*, vol. 20, p. 225302, 2009.

[7] J. A. Potkay, G. R. Lambertus, R. D. Sacks, and K. D. Wise, "A low-power pressure-and temperature-programmable micro gas chromatography column," *Microelectromechanical Systems, Journal of*, vol. 16, pp. 1071-1079, 2007.

[8] H.-s. Noh, P. J. Hesketh, and G. C. Frye-Mason, "Parylene gas chromatographic column for rapid thermal cycling," *Microelectromechanical Systems, Journal of*, vol. 11, pp. 718-725, 2002.

CONTACT

*S. Sonkusale, tel: +1-617-627-5113; sameer@ece.tufs.edu

CREATING A GAS-LIQUID INTERFACE IN A MICROCHANNEL USING POROUS POLYDIMETHYLSILOXANE (PDMS)

Xiang Ren[1], Miao Yu[1], Hongseok (Moses) Noh[1], and Jack G. Zhou[1]*
[1]Drexel University, Philadelphia, Pennsylvania, USA

ABSTRACT

In order to realize gas-liquid interface in microchannel, porous polydimethylsiloxane (PDMS) was fabricated and assembled with microchannels. Carbon dioxide absorption was used to demonstrate the effect of the gas-liquid interface. The carbon dioxide absorption was determined by pH color indicator and Matlab image processing method. The results demonstrated that the carbon dioxide was able to pass through the porous PDMS and be dissolved into the fluid with little water leakage and evaporation.

INTRODUCTION

There is an increasing need for creating a gas-liquid interface in lab-on-a-chip community. Devices for cell culture [1, 2], recreation of organ models [3], and cell-based sensing [4] often require certain gas compositions in the microfluidic environment (e.g. a lung-on-a-chip device demand an accurate gas-liquid interface to simulate the functional unit of the organs [5]). Another example is an artificial photosynthesis system for energy harvesting that requires constant supply of carbon dioxide (CO_2) [6, 7]; at the same time, an artificial photosynthesis system requires for little water evaporation as a chemical reaction unit without keeping living cells inside. Currently, creating a gas-liquid interface in microfluidic channels remains challenging. This paper reports a novel way of creating a gas-liquid interface using porous PDMS. Porous PDMS provides enough contact between gas and liquid media while effectively preventing water leakage and evaporation due to its hydrophobic property [8]. To study the feasibility of porous PDMS as interface media, carbon dioxide absorption was analyzed. The experimental results indicated that our gas-liquid interface made with porous PDMS could allow CO_2 penetration while preventing water leakage and evaporation.

GAS-LIQUID INTERFACE

Device Structure

To study the performance of porous PDMS as a gas-liquid interface media, we separated the two microchannels by a porous PDMS layer (Figure 1). CO_2, which can be dissolved in water, was selected to test the performance of our gas-liquid interface. The porous PDMS (see below for its fabrication) was "locked" in to solid PDMS layers as shown in Figure 1. Extra solid PDMS surrounding the porous PDMS was necessary for this purpose and it was permanently bonded to the middle layer PDMS after plasma treatment.

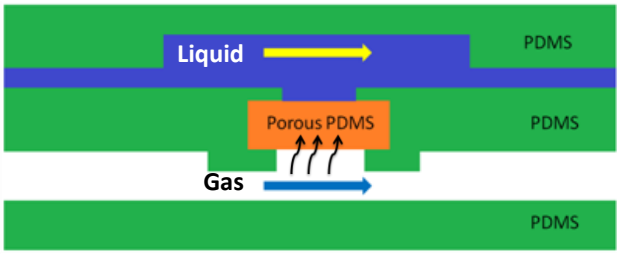

Figure 1: Cross-sectional view of the device constructed to test the gas-liquid interface created by porous PDMS.

CO_2 was introduced into the lower layer of the microchannel. CO_2 molecules penetrated through the porous PDMS layer, and then continuously diffused into the fluid in the upper channel. A pH sensitive pigment was added in the fluid to monitor the color change during the CO_2 absorption process.

Porous PDMS

Porous PDMS was fabricated by sugar leaching technique where sugar cubes were used as sacrificial materials (Figure 1) [9, 10]. The sugar particles in sugar cubes were connected together; therefore, the created porous PDMS had interconnected micro pores after the removal of sugar.

A mixture of PDMS pre-polymer (Sylgard® 184 silicone elastomer, Dow Corning) and curing agent (Sylgard® 184 silicone elastomer curing agent, Dow Corning) were mixed at 10:1 mass ratio and degassed in vacuum. Sugar cubes ($15\times15\times10$ mm^3) were then immersed in the mixture with a depth of 3 mm in a vacuum container for 1 hour allowing the sugar cubes fully filled with PDMS by capillary effect. The PDMS with sugar cube was then cured in an oven at 60°C for 24 hours. The cured PDMS-sugar cubes were cut into a cylindrical disc shape (diameter = 3 mm, height = 2 mm) and washed in 50°C water to remove the sugar followed by air dry. As shown in Figure 2b, the surface of porous PDMS was still hydrophobic.

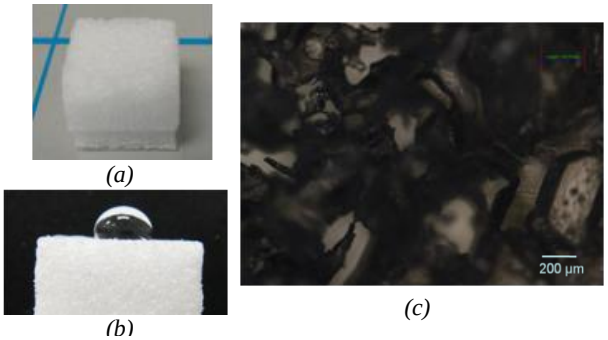

Figure 2: (a) Picture of porous PDMS; (b) Porous PDMS's hydrophobic property; (c) Optical microscope image of porous PDMS.

Two main properties that characterize porous structures are porosity and average pore size. The average pore size could be roughly observed by the optical microscope image of the cross-section of the porous PDMS (Figure 2c), which was around 150~200 µm. The porosity was defined as the empty space volume over the total volume of a material. By measuring the mass of a certain block of porous PDMS, we could calculate the existing PDMS volume (the pure PDMS's density is 0.965×10^3 kg/m^3). The PDMS block's volume was measured by the out profile's dimensions. We measured 20 different porous PDMS samples to reduce the errors. The porosity of the porous PDMS was calculated as 69.8±0.2%.

Microchannel Fabrication

The porous PDMS was then sealed inside PDMS channels

9781940470016/HH2014/$25©2014TRF
DOI 10.31438/trf.hh2014.58

manufactured by stereolithographically defined molds (Figure 3). The PDMS microchannels served as gas channel and liquid channel (Figure 4).

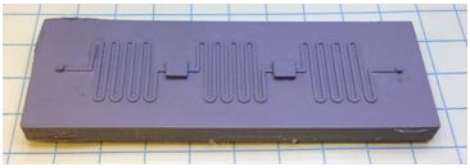

Figure 3: Stereolithography mold for PDMS microchannels.

The mold for PDMS replica was made of a photo-sensitive polymer (Photosilver, EnvisionTec) using stereolithography machine (EnvisionTEC, model Perfactory, Germany; voxel resolution: 35 μm). After the mold was prepared, the standard PDMS replica molding was used to fabricate the microchannels. PDMS pre-polymer and the curing agent were mixed at a weight ratio of 10:1. The mixture was then placed in a vacuum container for 30 min to remove all the air bubbles. The degassed PDMS mixture was poured onto the mold and placed in a 60°C oven for 24 hours for the solidification of PDMS.

After fabricating the top microfluidic channel, bottom gas channel, and middle layer porous PDMS holder (porous PDMS are partially sealed inside), three layers of PDMS were permanently bonded after plasma treatment (Covance, Femto Science, South Korea).

CO_2 Measurement

Bromothymol blue solution (BBS, SigmaAldrich) was used as CO_2 absorption indicator [11]. BBS contains stable pigments that will not have any chemical reactions with either water or CO_2. The color of BBS depends on the solution's pH value: pH > 7.6 (blue); 6.0 < pH < 7.6 (green); pH < 6.0 (yellow). The microchannel inlet was connected to a syringe with BBS. The water's initial color is adjusted to blue by adding pH buffers, in order to reach the largest capacity of CO_2 absorption and the corresponding pH value change.

The color alteration of the BBS was monitored over time at different flow rates (8~30 μL/min) in addition to the static condition. However, if using the color change from blue to green to yellow to identify the pH, the data is not accurate enough to calculate the exact amount of CO_2 absorbed. Therefore, we recorded the video of the color change process, and used Matlab to analyze the pixels of the color changing region. PDMS is clear and optically transparent to any light wavelength of 240~1100 nm, which contained the BBS color change wavelength.

EXPERIMENT

In order to test the gas-liquid interface performance, the liquid with BBS was applied to one channel using a syringe pump, and CO_2 was imported to the other channel using a glass flask filled with dry ice. The flow rate of CO_2 was considered constant during the dry ice sublimation because of the significant smaller gas channel volume compared to the glass flask.

The fluid with BBS was connected to the inlet. Syringe pump (Harvard Apparatus Pump 33, Holliston, MA) was set with a flow rate from 8~30 μL/min with a step of 2 μL/min. The whole color change was recorded by a high-resolution camera for further image processing. Therefore, a white background was placed behind the experimental device, and the lighting conditions as well as the camera were fixed during all the experiment process.

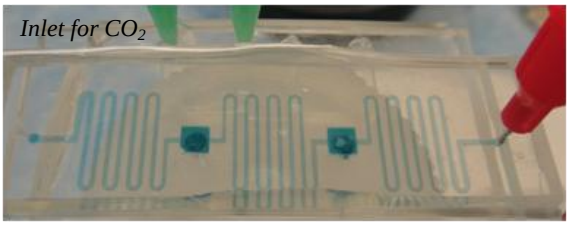

(a) Before CO_2 introduction

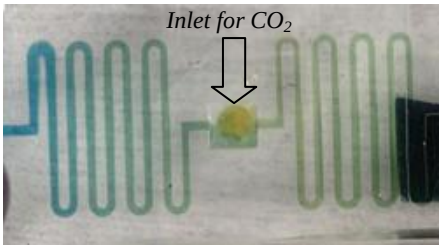

(b) After CO_2 introduction

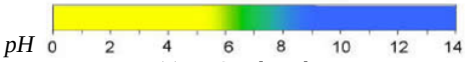

(c) BBS color chart

Figure 4: BBS color alteration before and after introducing CO_2.

However, the flow rate should be moderate; otherwise, the pressure tends to increase with higher flow rate. Once the pressure reached the maximum threshold that the porous PDMS could hold, the fluid would overcome the hydrophobic resistance of the porous PDMS layer and penetrate through the layer.

RESULTS

The color images were imported into Matlab and isolated into red, green, and blue (RGB) color maps (Figure 6). By comparing the data of gray map and RGB map, the fluid's color was represented by relative intensity numbers from 0 to 255. The algorithm we used was demonstrated in Figure 5 by flow chart. The first step was changing the video into image frames. The "mov" file was changed into "avi" file, and then cut into 10 frames per second; in another word, between two images, the time step was 0.1 s. Matlab could change each color image into gray map to roughly tell the difference when the pH color changed.

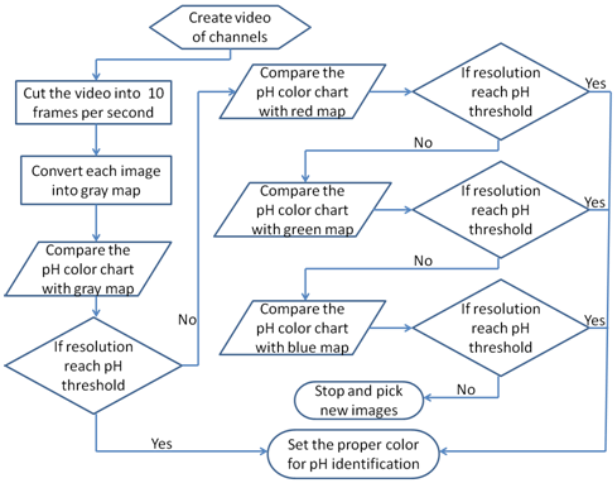

Figure 5: Algorithm of the fluid's pH identification by Matlab.

In order to improve the accuracy of the image matrix's relative intensity numbers representing the pH value, we used four comparisons: gray map, red, green, and blue maps. A pre-set relative intensity threshold was established to identify the best resolution of pH value correlating with the image's relative intensity number. If a single color map could not represent pH value in some part of the pH, we could use other color maps to further divide the color into intensity numbers. For example, when the color was green or blue, the red map's data of each image pixel were almost same by the changing of time, which meant the red map data could not identify the pH value during that small period of time. Therefore, we should continue to use the green and blue map to identify the pH value during that period of time. These data were then analyzed to calculate the fluid's pH value (Figure 7) by comparing the fluid's color with standard BBS color chart (Figure 4c).

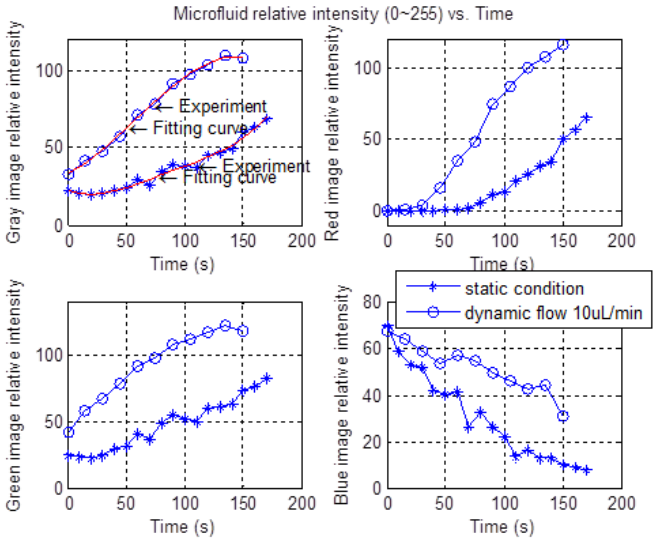

Figure 6: RGB color intensity analysis.

The data of static condition and one of the dynamic conditions (10 μL/min) were shown in this paper for clearer demonstration. The static case data indicated that CO_2 was dissolved and diffused into the liquid channel through porous PDMS; the dynamic flow case showed faster transfer of CO_2.

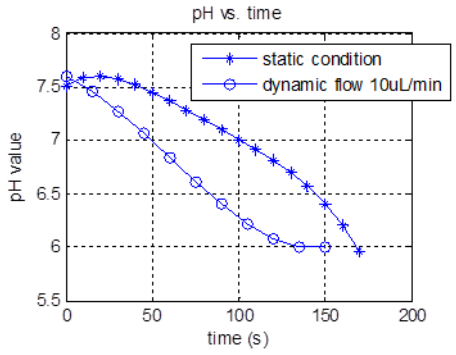

Figure 7: pH value change over time in static and dynamic conditions.

DISCUSSIONS

At room temperature, CO_2 dissolves in water to form carbonic acid (H_2CO_3) that gradually changes pH value of the solution, which contains H^+, CO_2, H_2CO_3, HCO_3^-, and CO_3^{2-}. The pH value is defined by the proton H^+ concentration in the solution; however, measuring the H^+ concentration was difficult in microfluidic environment, so we used the data for other negative ions. The hydration equilibrium constant (K_h) of CO_2 and H_2CO_3 in water (25°C) is:

$$K_h = \frac{[H_2CO_3]}{[CO_2]} = 1.70 \times 10^{-3} \quad (1)$$

where the "[]" represents the compound concentration [12].

The hydrolysis of H_2CO_3 in water follows the dissociation equation below:

$$H_2CO_3 \rightleftharpoons HCO_3^- + H^+ \quad (2)$$

and the dissociation constant (K_{a1}) of this reaction at 25°C are [12]:

$$K_{a1} = 2.5 \times 10^{-4} \text{mol/L}$$

$$pK_{a1} = 3.6$$

However, when $[H_2CO_3] \ll [CO_2]$, the dissociation of H_2CO_3 in water follows:

$$H_2CO_3^* \rightleftharpoons HCO_3^- + H^+ \quad (3)$$

The dissociation constant ($K_{a(app)}$) of this reaction at 25°C is:

$$K_{a(app)} = 4.6 \times 10^{-7} \text{mol/L}$$

$$pK_{a(app)} = 6.3$$

The further hydrolysis of HCO_3^- is:

$$HCO_3^- \rightleftharpoons CO_3^{2-} + H^+ \quad (4)$$

The dissociation constants (K_{a2}) of this reaction at 25°C are [12]:

$$K_{a2} = 4.69 \times 10^{-11} \text{mol/L}$$

$$pK_{a2} = 10.329$$

Finally, the pH value can be related to the concentration of carbon-containing species by Henderson-Hasselbach equation [12],

$$pH = pK_a + \log \frac{[HCO_3^-]}{[H_2CO_3]} \quad (5)$$

This equation was used to calculate the overall concentration of the absorbed carbon in the solution, as shown in Figure 8. The concentration of CO_2 molecule, H_2CO_3, HCO_3^-, and CO_3^{2-} can be calculated individually. According to equation (5), the concentration of H_2CO_3 and HCO_3^- was obtained from the pH value. Based on equation (4), the concentration of CO_3^{2-} was much smaller than any other ions in the water. Because the unhydrolyzed CO_2 keep the molecule status in the water and not affecting the proton's concentration, CO_2 molecule didn't affect the pH value of the fluid. The concentration of CO_2 molecules was calculated by the hydration equilibrium constant K_h in equation (1). For example, we listed some concentrations with different pH values in Table 1.

Table 1: Absorbed CO_2, H_2CO_3, HCO_3^-, and CO_3^{2-} concentration (unit: mol/L) with the change of pH.

pH	$[CO_2]$	$[H_2CO_3]$	$[HCO_3^-]$	$[CO_3^{2-}]$
7.00	3.36×10^{-10}	5.71×10^{-13}	1.42×10^{-9}	7.90×10^{-13}
6.94	3.36×10^{-9}	5.71×10^{-12}	5.90×10^{-9}	1.90×10^{-12}
6.81	3.36×10^{-8}	5.71×10^{-11}	9.16×10^{-8}	3.30×10^{-11}
6.42	3.36×10^{-7}	5.71×10^{-10}	3.78×10^{-7}	4.53×10^{-11}
5.92	3.36×10^{-6}	5.71×10^{-9}	1.19×10^{-6}	5.57×10^{-11}

The overall carbon concentration was the combination of CO_2 molecule, H_2CO_3, HCO_3^-, and CO_3^{2-}. Therefore, the overall carbon

atom that absorbed into the fluid was defined as carbon fixation rate, represented by "[C]" in Figure 8.

As observed in Figure 7 the dynamic fluid condition presented a faster CO_2 transfer compared with the static fluid condition. With the consumption of CO_2, more CO_2 molecules would be hydrolyzed into HCO_3^-, and the equilibrium would continue to shift to create more HCO_3^-, allowing more CO_2 molecules to diffuse into the fluid.

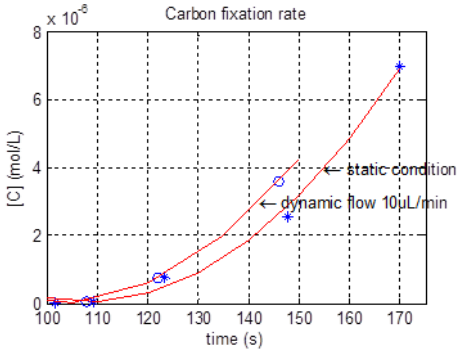

Figure 8: Carbon concentration in the liquid chamber.

Considering the microchannel dimensions, the average CO_2 absorption rates was 13.7 µmol/ (L·min) in static condition and increased to 18.2 µmol/(L·min) under flow rate of 8~10 µL/min. We can further modify the microchannel dimensions and the inlet flow rate to increase the CO_2 absorption rate. Besides, the porosity and average pore size may also affect the CO_2 penetration rate as well as the absorption rate.

CONCLUSIONS

We developed a novel method of creating a gas-liquid interface in microchannel systems using porous PDMS and demonstrated its performance using CO_2 absorption. We believed that this gas-liquid interface method could be applied to many applications in lab-on-a-chip systems, especially in artificial photosynthesis systems, which is our ultimate target system. Such system will simulate the leaf function: absorbing CO_2 with less water evaporation.

ACKNOWLEDGEMENTS

The authors would like to thank Centralized Research Facilities in Drexel University. Travel support has been generously provided by the Transducer Research Foundation. This research project is supported by National Science Foundation CMMI-1141815 and CMMI-1300792.

REFERENCES

[1] J. El-Ali, P.K. Sorger, and K.F. Jensen, "Cells on Chips", Nature, 442, 7101 (2006).

[2] E. Pedraza, A.C. Brady, C.A. Fraker, and C.L. Stabler, "Synthesis of Macroporous Poly(dimethylsiloxane) Scaffolds for Tissue Engineering Applications", Journal of Biomaterials Science, Polymer Edition, 24, 9 (2013).

[3] Y.B.A. Kang, S. Rawat, J. Cirillo, M. Bouchard, and H.M. Noh, "Layered Long-term Co-culture of Hepatocytes and Endothelial Cells on a Transwell Membrane: Toward Engineering the Liver Sinusoid", Biofabrication, 5, 4 (2013).

[4] P.S. Dittrich, and A. Manz, "Lab-on-a-chip: Microfluidics in Drug Discovery", Nature Reviews Drug Discovery, 5, 3 (2006).

[5] D. Huh, Y. Torisawa, G.A. Hamilton, H.J. Kim, and D.E. Ingber, "Microengineered Physiological Biomimicry: Organs-on-chips", Lab on a Chip, 12, 12 (2012).

[6] X. Ren, M. Yu, X. Zhou, Q. Zhang, and J.G. Zhou, "Fabrication of Chitosan Porous Structure and Applications on Artificial Photosynthesis Device", ASME 2013 International Manufacturing Science and Engineering Conference, Madison, WI, 6/10-14/2013, American Society of Mechanical Engineers (2013) pp. V002T03A012.

[7] X. Ren, Y. Kim, and J.G. Zhou, "Design and Fabrication of Chitosan for Applications of Artificial Photosynthesis", Journal of Mechanics Engineering & Automation, 3, 12 (2013).

[8] J. Zhao, G. Luo, J. Wu, and H. Xia, "Preparation of Microporous Silicone Rubber Membrane with Tunable Pore Size via Solvent Evaporation-Included Phase Separation", ACS Applied Materials & Interfaces, 5, 6 (2013).

[9] J. de Jong, M.J. Geerken, R.G. Lammertink, and M. Wessling, "Porous Microfluidic Devices – Fabrication and Appilcaitons", Chemical Engineering & Technology, 30, 3 (2007).

[10] K.J. Cha, and D.S. Kim, "A Portable Pressure Pump for Microfluidic Lab-on-a-chip Systems Using a Porous Polydimethylsiloxane Sponge", Biomedical Microdevices, 13, 5 (2011).

[11] P.K. Yuen, H. Su, V.N. Goral, and K.A. Fink, "Three-dimensional Interconnected Microporous Poly(dimethyl-siloxane) Microfluidic Devices", Lab on a Chip, 11, 8 (2011).

[12] D.L. Nelson, A.L. Lehninger, and M.M. Cox, Lehninger principles of biochemistry, Macmillan Publishers Ltd., London, U.K., 2008.

CONTACT

*Xiang Ren, tel: +1-215-808-7369; xiang.ren@drexel.edu

MICROFLUIDIC DESIGN ENABLES LOW-INFRASTRCUTURE YET LARGE-SCALE SCREENING OF MOLECULAR BINDING REACTIONS

Yuchen Pan[1], T.A. Duncombe[1], C.A. Kellenberger[2], M.C. Hammond[2,3] and A.E. Herr[1]*
[1] UC Berkeley / UC San Francisco Joint Graduate Group in Bioengineering, USA
[2]Department of Chemistry, University of California, Berkeley, California, USA
[3]Department of Molecular & Cell Biology, University of California, Berkeley, California, USA

ABSTRACT

We detail the development and optimization of a low-infrastructure and high-throughput microfluidic electrophoretic mobility shift assays (EMSAs). The platform screens molecular binding in our recently published photopatterned free-standing polyacrylamide gel electrophoresis (*fs*PAGE) system [1]. The new electrophoresis modality supports concurrent 96 separations and is operated with the standard equipment available in any experimental biology lab. We applied computational modeling of *fs*PAGE sample injection to minimize injection-dispersion and subsequent separation. In addition, a thermal model was established to analyze joule heating and gel evaporation, based on which two complimentary approaches (modified geometry and run buffer) were proposed to minimize the moisture loss and elongate the effective electrophoresis time course. Unit-to-unit variations in *fs*PAGE were quantified and used to inform design optimization which eliminates spatial variations across a 96-plex array. Lastly, a cyclic-di-GMP (CDG) riboswitch binding reaction was demonstrated in a 96-plex *fs*PAGE - showing good quantitative capability.

INTRODUCTION

As a crisis in antimicrobial resistance intensifies, novel antibiotics are urgently needed. Consequently, academic labs and federal agencies are ramping up efforts to tackle this health challenge. Molecular binding screening is one of the key tools in our arsenal to identify effective new compounds for the drug targets of interests. However, gold-standard screening tools (i.e., fluorescence polarization (FP) [2] & Fluorescence resonance energy transfer (FRET) [3]) are sample-consuming, slow, and require substantial infrastructure. These functional limitations are exaggerated by scarce compound library resources, which lead to weak statistical validation. Even though droplets microfluidic has been introduced to improve the throughput of FP [4] and FRET [5], the complex technical facilities are way beyond the scope of a standard biology laboratory.

To facilitate the measurements, we propose electrophoretic mobility shift assays (EMSAs) to analyze molecular binding. However, traditional EMSAs rely on slab-gel electrophoresis, a decades-old, slow and high sample-consuming technique, thus inadequate for a large-scale molecular screening. Several studies have detailed the efforts in bringing microfluidic electrophoresis to speed up the analysis, including 384-plex radial microfluidic capillary electrophoresis (Emrich et al., 2002 [6]), multiplexed Gradient Elution Moving Boundary Electrophoresis (Ross et al., 2008 [7]) and microfluidic μMSA (Karns et al., 2013 [8]). Nevertheless, these technologies have their own challenges to adoption, including complex electric interfacing and difficult operation.

To overcome these severe limitations, we introduce a new screening framework for quantitative molecular binding discovery that tests miniscule sample volumes rapidly with substantially reduced infrastructure needs. For the first time, we report a microfluidic 96-plex screening platform to support concurrent electrophoretic mobility shift assays.

*fs*PAG is a mm-sized and um-tall gel structure photopolymerized on a piece of surface-functionlized substrate (GelBond®) [1]. The gel is simply comprised of a customizable sample reservoir and a separation lane. The entire prototyping cycle takes only 30min to complete, including mask design, printing and *fs*PAG fabrication. Our previous results show that 96 concurrent protein separations can be completed in 10min. The multiplexed analysis made the *fs*PAG an ideal platform for massive screening assay. For operation, the platform only requires a commercial electrophoresis power supply. Fig. 1 shows the architecture of a 96-plex *fs*PAG layout.

In this work, we optimize the platform to screen for riboswitches. Riboswitches are structured bacterial mRNA molecules that are considered promising and largely unexplored drug targets [9]. Compound screening aims to identify effective riboswitch binders. Upon ligand binding, riboswitches compact (change size) and result in an electrophoretic mobility shift between bound and unbound forms which is measured by high-performance EMSAs.

Here we discuss the key factors that affect a successful EMSA and detail engineering approaches to optimize *fs*PAGE in the following aspects: 1) low-dispersion injection; 2) minimization of evaporation during electrophoresis - due to the high joule heating; 3) reduced "unit-to-unit" variation across a 96-plex array. The optimized *fs*PAG EMSAs is used to perform 96-plex concurrent EMSAs to evaluate the binding reaction of a CDG riboswitch.

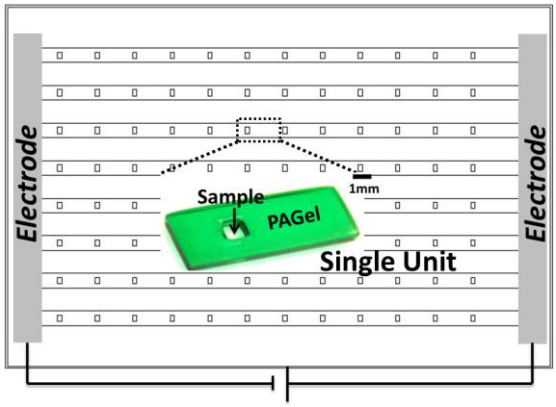

Figure 1: Layout of a 96-plex fsPAG. The spacing of separation units correspond to a 96 well-plate format.

MATERIALS AND METHODS

Materials

Solutions of 30% (w/v) (29 : 1) acrylamide/bis-acrylamide, glycerol, glacial acetic acid and Triton X-100 were purchased from Sigma Aldrich (St. Louis, MO). 10X TBMK buffer was prepared in house by dissolving 890 mM tris base (Fisher Scientific, Hampton, NH), 890 mM boric acid (Fisher Scientific, Hampton, NH), 30 mM magnesium chloride (EMD chemical, Gibbstown, NJ) and 100 mM potassium chloride (Sigma Aldrich, St. Louis, MO) into 1 L water. Photoinitiator 2,2-azobis[2-methyl- N -(2-hydroxyethyl) propionamide] (VA-086) was purchased from Wako Chemical

9781940470016/HH2014/$25©2014TRF
DOI 10.31438/trf.hh2014.59

(Richmond, VA). GelBond® PAG film and Gel Slick® glass plate coating were purchased from Lonza (Base, Switzerland). AlexaFluor 488 (AF488) conjugated Trypsin Inhibitor (TI*, 21kDa), Ovalbumin (OVA*, 45kDa) and Transferrin (TRF*, 80kDa) were purchased from Life Technologies Corporation (Carlsbad, CA). Photo-masks were designed with AutoCad® student edition (Autodesk, San Rafael, CA) and printed on a transparent film (3M, St. Paul, MN). Otherwise stated, all the reagents are prepared with molecular biology grade (DNase-, RNase- and Protease-free) water purchased from Mediatech (Manassas, VA).

Riboswitch RNAs were prepared using standard protocols. DNA templates were generated using primers that appended the T7 promoter sequence directly before the aptamer sequence. RNAs were then *in vitro* transcribed using T7 RNA polymerase following standard protocols. Following oxidation of the 3' ribose with $NaIO_4$, AlexaFluor 488 was conjugated to the RNAs following standard procedures for 3' end labeling.

To prepare the binding reaction solution, riboswitch, 10X TBMK buffer, 1mg/ml yeast tRNA and water are added and mixed in a non-stick surface 0.5ml eppendorf tube at indicated concentrations. The final mixture solution contains 1X TBMK buffer and 100ug/ml yeast tRNA. The mixture is then heated at 70℃ for 3min and cooled at room temperature for 10min to renature the RNA. Subsequently, cyclic-di-GMP at indicated concentration and was added into the solution along with an internal standard (TI*). The sample mixture were placed in dark and equilibrated at room temperature for 1 hour. The reaction was quenched by adding 1.5ul of 50% glycerol into every 10ul reaction.

fsPAG fabrication

*fs*PAG was fabricated with UV photopatterning. The PAG precursor solution contained 20%T acrylamide, 3.3%C bis-acrylamide crosslinker and 0.2% VA-086 photo-initiator (w/v). The precursor solution was then degassed for 2-3min under house vacuum system with a sonicator and then subject to UV exposure. The choice of exposure time and intensity depends on the total acrylamide concentrations. For 20% *fs*PAG, it takes 65seconds under 20mW/cm^2 UV.

***fs*PAG electrophoresis operation**

Before electrophoresis, the fsPAG was soaked in the run buffer for 10min. Next, the fsPAG was taken out from the run buffer solution and placed into a custom designed environmental chamber [1] on top of a borosilicate glass. Electrode wicks (Serva, Heidelber, Germany) soaked in run buffer were aligned on two ends of a separation lane on top of the gel. Excess run buffer on the electrode wicks were removed with Kimwipe. Two graphite electrodes are placed right above in contact with the electrode wicks and were connected to the external power supplier. Sample solution was pipetted into the sample well. Eventually, the environmental chamber was sealed with a borosilicate glass plate. A voltage was applied using a PowerPac HV power supplier (Bio-Rad Laboratories) to initiate the electrophoresis. The power supplier enables real-time current reading. In the current monitoring experiments, the current was recorded manually every 10seconds for up to 6min.

fsPAG height measurement

The height of the fsPAG was measured with MicroXAM-100 Optical Profilometer (ADE Phase Shift, Tucson, AZ).

Imaging and data analysis

Fluorescence imaging was conducted on an inverted epifluorescence microscope (Olympus IX-70) equipped with a 2X objective (PlanApo, N.A. = 0.08, Olympus, Center Valley, PA) and an X-Cite® exacte mercury lamp (Lumen Dynamics, Mississauga, Canada). The light was filtered through a XF100-3 filter (Omega Optical, Battleboro, VT). A Peltier cooled charge-coupled device (CCD) camera (CoolSNAP HQ2, Roper Scientific, Trenton, NJ) attached to the microscope was used to capture image. Large area image acquisition was performed with Metamorph software (Molecular device, Sunnyvale, CA).

Post-processing of the image was conducted in ImageJ (NIH, Bethesda, MD) and subsequence data analysis was performed with OriginPro 8.0 (OriginLab, Northampton, MA). The intensity profiles were plotted over the transverse direction of the fsPAG.

RESULTS AND DISCUSSION

Low dispersion and high resolution separations are the goals for *fs*PAG EMSAs. This is crucial especially for molecular binding pairs that exhibit small mobility shifts upon interaction, such as riboswitch RNA. The previously published open channel 3-D structure of the *fs*PAG renders less consistency in sample loading in terms of the height and potentially can suffer from premature termination of electrophoresis owing to moisture loss. In this work we study the sources of inconsistency and develop an optimized *fs*PAGE with improved reliability.

Sample loading height

Unlike its microfluidic counterpart, where sample injection and subsequent separations are achieved using additional channels, the two are combined in one step for *fs*PAGE. Consequently, the analyte band shape can be distorted due to a non-uniform electric field distribution. Electric field non-uniformity can occur from both a gel-free solution conductivity mismatch and a height mismatch between the *fs*PAG and the loaded sample. As a key aspect of the electrokinetic property of the *fs*PAGE, the electric field distribution determines the migration velocity and therefore the quality of the separation. Fig. 2 shows COMSOL® simulations demonstrating the relationship between analyte band shape and sample height. The simulations show that low sample loading can result in reverse skewing of injected analyte bands as well as streaking behind the main band. Further, low sample loading (<20%) corresponds to a reduction in migration distance – caused by a lower electric field, as most of the voltage drop occurs across the sample well. Altogether, low sample heights lead to worse separation resolution (SR), making small mobility shifts difficult to resolve. SR is described by:

$$SR=D/2(\sigma_1+\sigma_2) \quad (1)$$

Where D is the distance between two bands, σ_1 and σ_2 are the standard deviation of the bands. >50% relative sample loading height is suggested to ensure the quality of the separation.

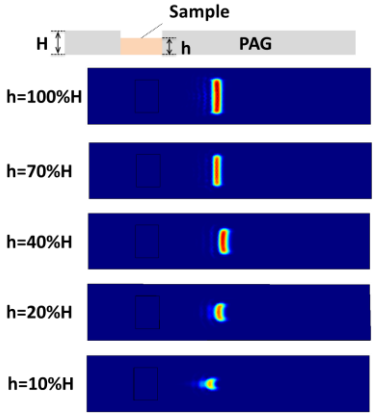

Figure 2: Comsol® simulation results of fsPAG band shape for different sample loading height. Low sample loading (<20%) results in heavily skewed band and low migration distance, reducing the separation resolution.

Thermal control of *fs*PAG

Evaporation is a problem for *fs*PAGE due to its open nature. While microfluidic in-channel electrophoresis is generally operated under high electric field, the "sub-mm size" of the open *fs*PAG places limitation on the highest working voltage due to a worse heat dissipation that accelerates the evaporation and reduces the overall effective electrophoresis time. Theoretical analysis predicts that a lower temperature slows down water loss, and this can be accomplished by altering the surface area-volume ratio of the *fs*PAG structures. In addition, glycerol was added into the run buffer to further slow evaporation. Fig 3A shows the current monitoring during *fs*PAG electrophoresis up to 6min under 60V/cm at different gel heights (run buffer contains 20% glycerol). We clearly observe improved stability in the relative electric current as *fs*PAG height is reduced from 600µm to 100µm, while no remarkable difference is observed between 70µm and 100µm devices. *fs*PAG smaller than 70µm is unreliable in both fabrication and in sample loading (due to sub 200nL volumes). In previously conducted in-chip CDG riboswitch separations (not shown), a 3min electrophoretic separation was required to fully resolve the CDG mobility shift. In Fig. 3B, we plotted the relative current drop at 3min for each of the *fs*PAG heights tested. The 100µm structure was retained 91.3% of its initial current value, highest among all other gel heights.

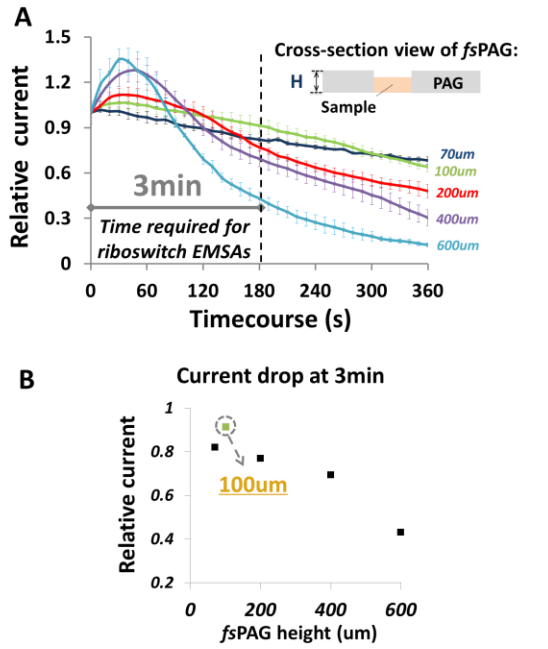

Figure 3: fsPAG height affects gel evaporation. A) Current monitoring of fsPAG electrophoresis for different gel heights up to 6min. The current is normalized by the initial value for comparison. E=60V/cm. B) Current drop at 3min. Theoretical prediction suggests riboswitch binding pairs resolves at this time point.

Glycerol forms tight hydrogen bonds with water molecules and run buffer with glycerol experiences lower vapor pressure which slows down the evaporation process (data not shown here). In addition, glycerol adheres to the matrix of the gel and improves the structural integrity (data not shown here). One drawback of adding glycerol into run buffer is the increasing viscosity and therefore larger hydrodynamic resistance slows down the migration, which decreases the separation resolution. Therefore, a tradeoff between evaporation and migration velocity points to an optimal glycerol concentration that renders the highest separation quality. Experimental study on the relationship between the separation resolution and glycerol concentration indicates the optimal point is reached at 20% glycerol concentration.

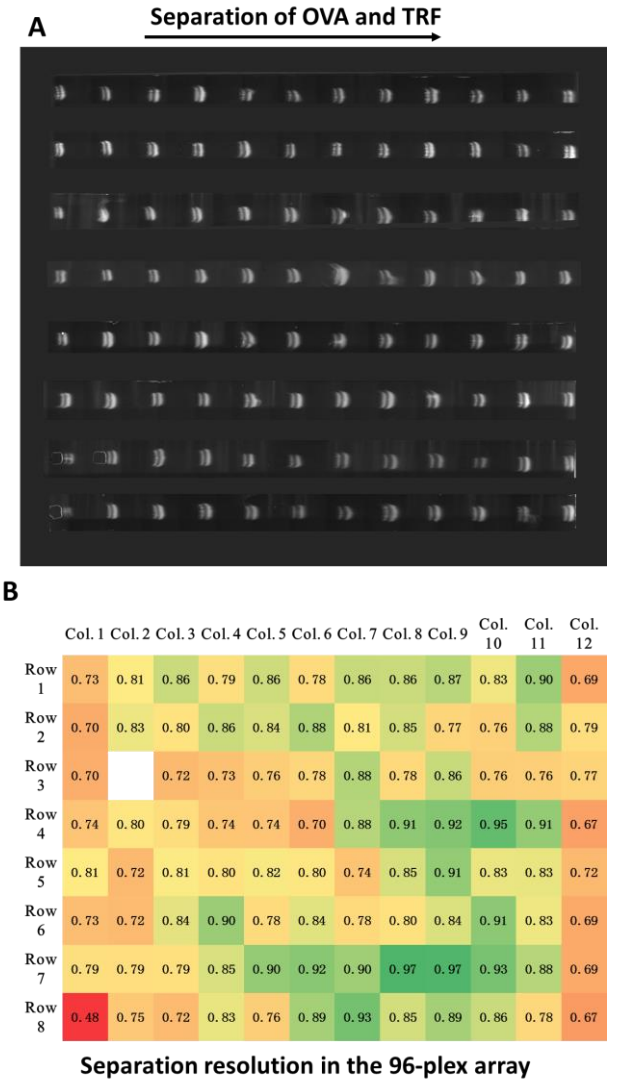

Figure 4: Electrophoresis of OVA and TRF on a 96-plex fsPAG platform. A) Fluorescence imaging of OVA-TRF at 2 min. E=60V/cm. B) Heatmap of the SR in each separation unit. The green cell has larger SR and red cell has smaller. Unit of row 3 and col 2 was not quantified due to a gel defects there

Unit-to-unit variation

Low unit-to-unit variation in analyte concentration, mobility and separation resolution are key aspects to developing a robust *fs*PAG electrophoresis which facilitates parallel comparison between columns/lanes in the 96-plex separation and supports easier data analysis. Factors that can induce variations are: sample loading inconsistency (well shape and loading amount), mobility and electric field non-uniform distribution. Among these factors, loading inconsistency induces random errors and can be minimized with well-trained experimental operation or with automated fluid delivery. The mobility/electric field non-uniformity introduces

systematic error and is studied here. We performed electrophoresis of Ovalbumin (OVA) and Transferrin (TRF) in a 100um tall 20%T fsPAG with 1x TBMK (20% glycerol) for 2min (Fig. 4A). To quantify any non-uniformity, the separation resolutions (indicative of both mobility and band width) for each unit are listed below (Fig. 4B). A heat map was generated based on the values to help analysis. Unit of row 3 and col 2 was not quantified due to a gel defects there. It can be seen from the heat map that the two columns on the sides have lower SR. This observation was further confirmed by ANOVA test (α=0.05). In addition, no row-to-row variation was observed. We believe this variation was a result of electrode side effects. The conjunction of electrodes and electric wicks expand the current conducting areas, which then act to spread out the electric field lines, therefore lowering the electric field strength.

To reduce the side effect, a new *fs*PAG that has electrodes farther from the separation units are designed. For the same experiment, no significant side effects are observed (data not shown).

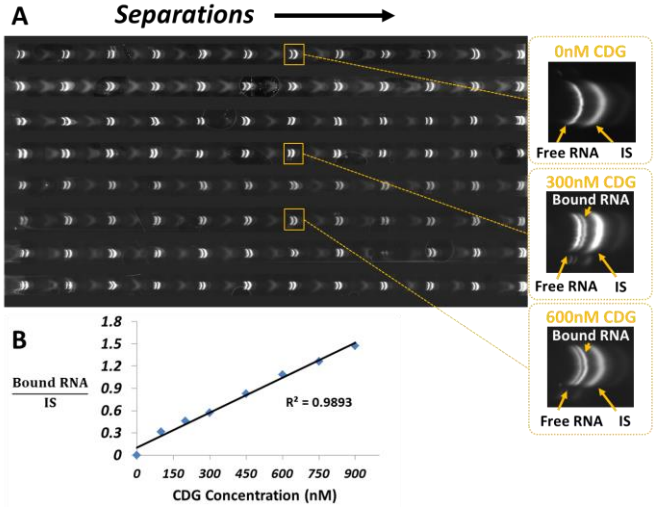

Figure 5: CDG riboswitch EMSAs on a 96-plex fsPAG. A) Fluorescence imaging of the separation at 3 min. Three separation units at 0, 300, 600nM CDG were shown on the right. Increasing fluorescent signals of bound RNA are observed. IS: Internal Standard.

Quantitative 96-plex fsPAG µEMSA of CDG riboswitch

We investigated the binding reaction of CDG riboswitch on the *fs*PAG as a first step towards a successful massive screening platform. Structural data has shown that the CDG riboswitch forms a more compact structure when in complex with its ligand, which indicates that the ligand-bound RNA should encounter less hydrodynamic resistance in the *fs*PAG. The resultant larger electrophoretic mobility causes the ligand-bound RNA to separate from the ligand-free RNA in the gel matrix and the shift can be quantified to reveal the amount of CDG in the sample. The geometrical design for such a 96-plex ensures that the minimal distance in between the adjacent separation units should accommodate a full separation. As such, we devised a 96-plex 20%T fsPAG with 4.5mm horizontal well-to-well spacing and 9mm lane-to-lane distance. Fig. 5 shows the fluorescence imaging of the EMSAs results. The reactions were prepared by incubating 1 uM riboswitch with increasing concentration of CDG (ranging from 0 nM to 900 nM). 500nM trypsin inhibitor is used as internal standard (IS). Zooming in on the electropherogram reveals the separation of the different RNA states at 0, 300 and 600 nM. Clear evidence shows that the fluorescence ratio of the bound RNA over IS increases with higher concentrations of CDG, and quantification shows good linearity. In summary, the 96-plex *fs*PAG is a robust high-throughput platform for EMSA and possesses great quantitative precision.

CONCLUSION

We have successfully integrated *fs*PAG and EMSAs to form a massive and robust molecular binding reaction screening platform. Careful optimization of the platform enabled low-dispersion injections and improved electrophoresis stability with minimized gel evaporation. Concern of non-uniformity of 96-plex separation was addressed by a geometric redesign. 96-plex EMSAs for CDG riboswitch binding reactions were demonstrated with good linearity over a titration.

Overall, the low-infrastructure yet powerful *fs*PAG EMSAs offers a promising platform for rapid and reliable binding reaction analysis.

ACKNOWLEDGEMENT

The authors acknowledge the Herr Lab members for helpful discussion. This work was supported by NSF C AREER Award (CBET-1056035 to A.E.H.). A.E.H. is an Alfred P. Sloan Foundation Research Fellow in chemistry.

REFERENCE

1. T.A. Duncombe, A.E. Herr, "Photopatterned free-standing polyacrylamide gels for microfluidic protein electrophoresis", Lab Chip, 13 (11), 2115-2123 (2013).
2. J.C. Owicki, "Fluorescence polarization and anisotropy in high throughput screening: Perspectives and primer", J Biomol Screen, 5 (5), 297-306 (2000).
3. L. Mere, T. Bennett, P. Coassin, P. England, B. Hamman, T. Rink, S. Zimmerman, P. Negulescu, "Miniaturized FRET assays and microfluidics: key components for ultra-high-throughput screening", Drug Discov Today, 4 (8), 363-369 (1999).
4. J.W. Choi, D.K. Kang, H.Park, A.J. deMello, S.I. Chang, "High-throughput analysis of protein-protein interactions in picoliter-volume droplets using fluorescence polarization", Analytical chemistry, 84 (8), 3849-3854 (2012).
5. M. Srisa-Art, D.K. Kang, J. Hong, H. Park, R.J. Leatherbarrow, J.B. Edel, S.I. Chang, A.J. deMello, "Analysis of Protein-Protein Interactions by Using Droplet-Based Microfluidics", Chembiochem, 10 (10), 1605-1611 (2009).
6. C.A. Emrich, H.J. Tian, I.L. Medintz, R.A. Mathies, "Microfabricated 384-lane capillary array electrophoresis bioanalyzer for ultrahigh-throughput genetic analysis", Analytical chemistry, 74 (19), 5076-5083 (2002).
7. D. Ross, J.G. Kralj, "Simple Device for Multiplexed Electrophoretic Separations Using Gradient Elution Moving Boundary Electrophoresis with Channel Current Detection", Analytical chemistry, 80 (24), 9467-9474 (2008).
8. K. Karns, J.M. Vogan, Q. Qin, S.F. Hickey, S.C. Wilson, M.C. Hammond, A.E. Herr, "Microfluidic Screening of Electrophoretic Mobility Shifts Elucidates Riboswitch Binding Function", Journal of the American Chemical Society, 135 (8), 3136-3143 (2013).
9. K.F. Blount and R.R. Breaker, "Riboswitches as antibacterial drug targets", Nat. Biotechnol., 24, 1558–1564 (2006).

CONTACT

*A.E. Herr, tel: +1-510-666-3396; aeh@berkeley.edu

NANO-PARTICLE SEPARATION USING MARANGONI FLOW IN EVAPORATING DROPLETS

Hwapyeong Jeong[1, 2], Joël van Tiem[1, 3], Yogesh B. Gianchandani[1] and Jaesung Park[1, 2]
[1]Center for Wireless Integrated MicroSensing and System (WIMS[2]), U. Michigan, Ann Arbor, MI 48109, USA
[2]Pohang University of Science and Technology, Republic of Korea
[3]University of Twente, The Netherlands

ABSTRACT

The "coffee ring effect" is known to result from the concentration of particles at the perimeter of a dried droplet. Raising the temperature of the substrate provides a temperature gradient induces "strong" Marangoni circulatory flow inside the droplet. This "strong" Marangoni can reverse the "coffee ring" effect. Here, we describe a method of particle separation based on the size of particles using Marangoni flow and the related "coffee ring" effect. Suspended particles of different sizes ranging from 100nm to 15μm are separated by using a combination of the "strong" Marangoni flow and coffee ring effects. Additionally, the effects of droplet contact angle with the substrates and temperature gradient in droplets are evaluated. Experiments show that, a temperature gradient of 1°C/mm, and contact angle (15°) can separate 100nm-particles from 1μm-particles successfully. The distance between the dried ring patterns is ~ 30 μm. In contrast, the separation between rings of particles without "strong" Marangoni is only 5.4μm. The "strong" Marangoni flow induced by temperature gradient enhances the separation of nano-particles at the contact line of a droplet.

INTRODUCTION

The "coffee ring effect" is a commonly observed upon evaporating liquid droplets containing colloidal particles. A coffee droplet leaves a ring pattern behind from the coffee droplet as it dries in the absence of a temperature gradient. Deegan *et al*.[1] were the first to propose the physical model which showed that the main cause of "coffee ring" effect is the outward capillary flow within evaporating liquid droplet with a pinned contact line. Here, liquid evaporating from the edge is replenished by liquid from the interior. Later, Hua *et al*. showed that a "weak" Marangoni flow is also induced by surface tension gradients associated with the latent heat of evaporation, and reverses "coffee ring" deposition [2].

However, in the case that circulating flow ("weak" Marangoni flow) is induced by capillary effect of the drying contact line, particles inside the evaporating liquid droplets can be easily free from this unclear weak capillary flow due to small buoyance from smaller temperature gradient from latent heat, and cannot contribute to ring formation.

Unlike "weak" Marangoni flow, "strong" Marangoni circulatory flow is developed inside the droplet by raising temperature of the substrate (Fig. 1). In this case, colloidal particles in the droplet move faster in the overall circulatory flow, because larger buoyancy is developed by the applied temperature gradient. Additionally, this larger buoyancy makes more particles move along the circulatory flow. This "strong" Marangoni flow can carry more particles at faster speed.

Recently, methods utilizing evaporating liquid droplets have drawn attention for various applications, such as particle self-assembly, film coating and particle separation and concentration for spot test analysis [3-6]. Most of the studies use evaporating droplets without an applied temperature gradient, and focus on "coffee ring". In our previous work, we reported that "strong" Marangoni flow deposit larger micro-particles at the center of droplets, and small micro-particles at the contact line of the droplet in size-orderly fashion [7].

This paper describes the use of droplet drying as a method for separating 100nm-particles from 500nm-particles that are in aqueous solution. Substrates with different contact angles for the droplets are tested, and the shallowest contact angle, 15° shows separated "coffee ring" pattern. For enhancing the spatial resolution of the pattern, "strong" Marangoni flow is used. The results show that hydrophilic substrates with 15° contact angle can separate 100nm-particles, and "strong" Marangoni flow improves the resolution about 6 times. The proposed conditions can be useful for improving chromatography and disease diagnosis in health care fields.

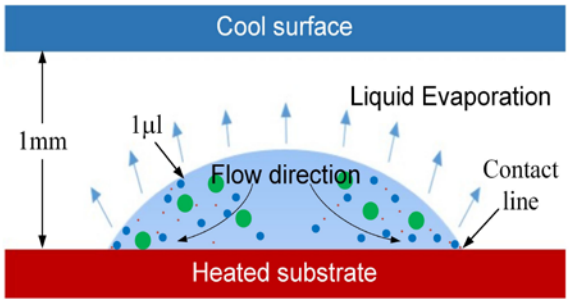

Figure 1: *A scheme of concept of particle separation system with temperature gradient. The liquid in the droplet evaporates on the free surface and causes "weak" Marangoni flow while the temperature gradient imposed by the hot and cold surface causes "strong" Marangoni flow.*

THEORY AND SIMULATION

The presence of a surface-tension gradient on a liquid droplet creates circulatory flow in the droplet. A surface-tension gradient can be induced by either latent heat of evaporation or a temperature gradient forced by boundary conditions (Fig. 1). These gradients create Marangoni flow. In Marangoni flow, the thermo-capillary shear stress is proportional to the temperature gradient [7]:

$$\tau_S = \mu \frac{\partial v_S}{\partial \hat{n}} = -\sigma_T \nabla T_S \qquad (1)$$

where μ is the dynamic viscosity of the liquid, τ_s denotes the surface stress, v_s is the surface velocity, T is the temperature, $\hat{n}$ and $\hat{t}$ are the unit normal and tangential vector to the surface, respectively, and σ_T is the surface tension temperature coefficient. Marangoni flow is generated inside the liquid droplet. (The surface tension increases with a decreasing temperature due to negative value of σ_T for common fluids) As a result of surface tension gradient induced by temperature gradient, flow moves toward to colder regions at the liquid interface. It causes viscous drag, which moves fluid, establishing a convective Marangoni flow. When a temperature gradient is applied to a liquid droplet, usually parasitic effect, buoyancy effect are present at the same time. The relative strengths of the Marangoni effect and buoyancy are estimated by the dimensionless numbers, Marangoni number (Ma) and Rayleigh number (Ra) [8].

9781940470016/HH2014/$25©2014TRF
DOI 10.31438/trf.hh2014.60

Solid-State Sensors, Actuators and Microsystems Workshop
Hilton Head Island, South Carolina, June 8-12, 2014

$$Ma = \frac{\sigma_T \Delta T R}{\mu \kappa} \quad (2)$$

$$Ra = \frac{\alpha \rho g \Delta T R^3}{\mu \kappa} \quad (3)$$

where ΔT is temperature difference, R is the characteristic length (droplet radius), κ is the thermal diffusivity, ρ is the liquid density, α is the liquid thermal expansion coefficient, and g is the gravitational acceleration. The ratio of both numbers provides an indication of the dominance of thermo-capillary force over buoyancy force.

$$\frac{Ma}{Ra} = \frac{\sigma_T}{\alpha \rho g R^2} \quad (4)$$

The Marangoni effect is dominant over buoyancy force when $Ma/Ra >> 1$. In this research, buoyancy force is negligible because the size of droplet, 1μL is small. However, temperature gradient is imposed by a constant temperature boundary condition (Fig. 1). Accordingly, depending on the situation, buoyancy forces may play important roles.

The flow pattern inside liquid droplets is analyzed using finite element analysis (COMSOL™). The temperature difference and the distance between substrates are 1°C and 1mm, respectively. To confirm the impact of contact angle, various geometries are chosen in such a way that the droplets have the same volume. Marangoni flow results in recirculation and transport of the suspended particles inside the droplets (Fig. 2 a-c). Since the profile of the droplet on the hydrophobic substrate is much higher than on the hydrophilic, the liquid surface is closed to the cold substrate. Therefore, the temperature gradient is higher and the magnitude of velocity increases. However, the velocity outward to the contact line of the droplet is faster on the hydrophilic substrate than on the hydrophobic substrate, indicating that particles near the hydrophilic substrate experience more drag force than those on the hydrophobic substrates. According to simulations, trajectories of 5μm- and 50μm-particles are different due to the difference in buoyancy force (Fig 2d). Therefore, the larger particles circulate near the center of the liquid droplet, and the smaller particles move toward to contact line by outward flow along the bottom substrate.

EXPERIMENTS

The fluorescence polystyrene sphere of 15μm, 3μm, 1μm, 500nm, 100nm in diameter were prepared in deionized water with an initial volume fraction of about 0.003%. The density of these particles is 1.05g/cm^3. The temperature of the substrate was maintained by using constant temperature blocks connected to a circulating water bath at 35˚C for cases without an applied temperature gradient. In other cases, the temperatures of the lower hot substrate and upper cool surface were maintained 36˚C and 35˚C, respectively, by using a hot plate and a circulating water bath, respectively. The distance between the heated and cooled surfaces was 1mm. The volume of a droplet was 1 μL.

To confirm the effect of contact angle, samples were placed on various surfaces with different contact angles, such as commercial slide glass, parylene coated glass and polydimethylsiloxane (PDMS). Contact angle of commercial slide glass, PDMS and parylene- coated glass are ~15°, ~ 90° and ~110°, respectively. Then the samples were placed on those substrates and dried with or without temperature gradient. After the droplets on the substrates were dried, "coffee ring" patterns appeared near the contact lines between the droplets and the substrates. The ring patterns were observed by using fluorescence microscope. The experiment environment was maintained under 40% humidity of ambient air to minimize the effect of evaporation time.

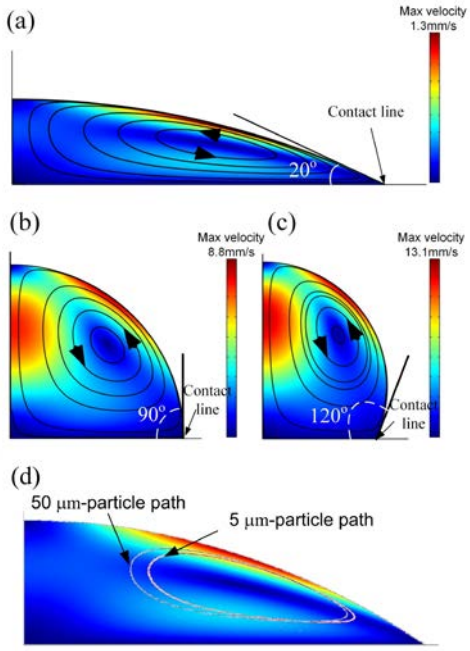

Figure 2. *Modeling results in 1μL droplet. (a) flow velocities on hydrophilic substrate with shallow contact angle (20˚). (b) flow velocities on hydrophobic substrate (90°). (c) flow velocities on hydrophobic substrate (120˚). (d) trajectories of 5μm and 50μm particles.*

RESULTS

To evaluate the effects of temperature and contact angle, 100nm-particles and 1μm particles were mixed and suspended in aqueous droplets (1μL volume, 0.003 % volume fraction). First, the effect of contact angle was investigated. The glass, PDMS, and parylene-coated glass substrates were compared without temperature gradient. Droplets were deposited on each substrate. On glass (contact angle ~ 15°), the dried ring patterns of 100 nm- and 1 μm-particles became separated by ~ 5.4μm (Fig. 3 a). This separation was estimated visually under a microscope. On PDMS substrates (contact angle ~90˚), the dried ring patterns were partially overlapped and not distinguishable, although the dried particle rings showed a gradual color change from green to blue inward (Fig. 3 c). In case of the hydrophobic parylene-coated substrates (contact angle ~110°), the dried ring patterns were likely to overlap or oppose to the previous cases. The results indicate that the contact angle between the droplet and substrate is critical in separation of particles in the droplets, and nano-particles can be separated from micro-particles using hydrophilic substrate (contact angle ~ 15°).

To investigate the effect of strong Marangoni flow, with temperature gradient of 1˚C/mm, the same experiments were repeated on the same substrates. The measured separation between the dried ring particles (100nm and 1μm) was measured to be 29.4μm on the glass substrate (contact angle ~15˚) (Fig. 3 b). Compared to the case of "weak" Marangoni flow, the distance of patterns was 6 X larger. On the PDMS substrate (contact angle ~ 90˚), the dried ring pattern of 100nm-particles become wider and overlapped with that of 1μm-particles (Fig. 3d). On the hydrophobic parylene-coated glass substrate (contact angle ~110°), the dried ring patterns of 100nm- and 1μm-particles were overlapped, and not distinguishable.

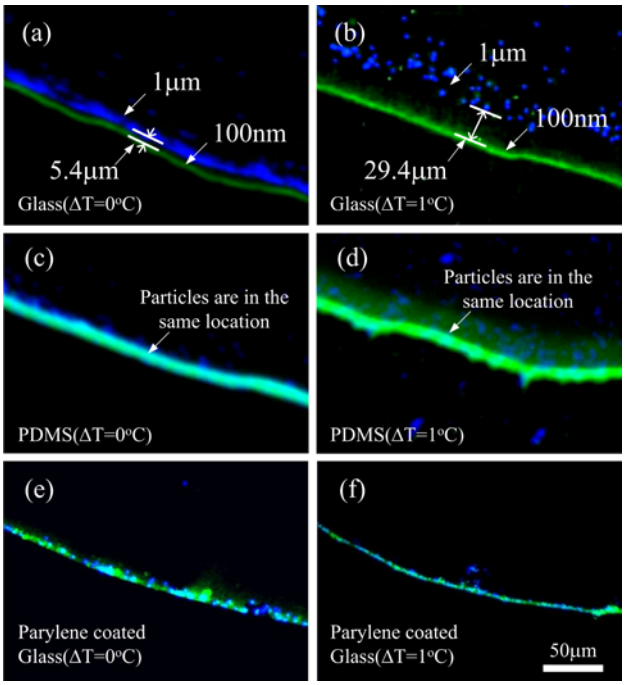

Figure 3. *Fluorescence images of the dried patterns separation of 1μm (blue) and 100nm (green)-particles. (a) on hydrophilic glass substrate without an applied temperature gradient. (b) hydrophilic glass substrate with temperature gradient (ΔT=1°C). (c) hydrophobic PDMS substrate without an applied temperature gradient. (d) hydrophobic PDMS substrate with temperature gradient. (e) hydrophobic parylene-coated glass substrate without an applied temperature gradient. (f) hydrophobic parylene-coated glass substrate with temperature gradient.*

When the substrate is hydrophilic, the contact line is pinned because the aqueous droplet tends to adhere to the substrate (Fig. 4a). During evaporation, "weak" Marangoni flow induced by latent heat pushes the particles toward the contact line, and the suspended particles are kinematically pinched between the free surface line of the droplet and substrate (Fig. 4a). As the droplet evaporates, the contact angle becomes smaller and able to pinch particle larger than the previously pinched ones. These explanation match well with experimental results (Fig. 3). Compared to the case with "weak" Marangoni flow, the case with "strong" Marangoni flow shows better separation distance. The reason may be that the "strong" Marangoni flow pushes harder toward the contact line because "strong" Marangoni flow has higher speed than "weak" Marangoni flow. As a result, the distance between the dried ring patterns increases (Fig. 3b).

The distance between successive ring patterns, Δd, can be simply estimated from the geometry of droplet profile if surface is hydrophilic [9]:

$$\Delta d = \frac{\Delta D}{2\tan(\theta/2)} \qquad (5)$$

where ΔD is difference of diameter of particles, and θ is initial contact angle of droplet below 90°. According to this equation, as the contact angle, θ increases, the separation distance, Δd decreases.

For the 100nm- and 1μm particles, the distance calculated from Equation (5) is 3.14μm while the measured distance for "weak" Marangoni without temperature gradient was 5.4μm and for "strong" Marangoni with temperature gradient, it was 29.4μm (Fig. 3a, b).

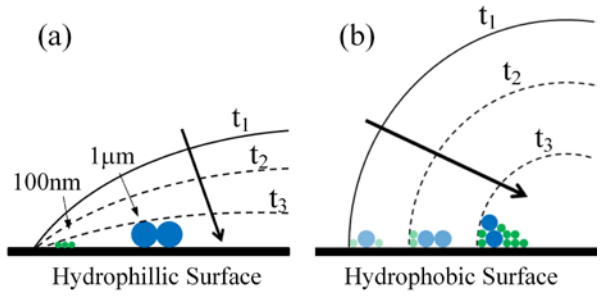

Figure 4*. Scheme for dynamic motion of suspended particle inside the liquid droplet during evaporation. (a) the line on the hydrophilic substrate does not move due to strong adhesion between the droplet and the substrate, whereas the contact angle changes smaller. (b) the contact angle on the hydrophobic substrate does not change due to weak adhesion between the droplet and the substrate, whereas the contact line move inwardly.*

In contrast to the hydrophilic substrate, the contact line on hydrophobic substrate is not pinned because the aqueous droplet does not stick on the substrates as strong as the hydrophilic substrate (Fig. 4b). Unlike the hydrophilic substrate, the contact angle does not change during evaporation. With the large contact angle, particles are not pinched, and are transported away from the contact line by Marangoni flow (Fig 2c). Eventually, the suspended particles do not form distinguishable patterns at the contact line (Fig 3f). As proof of that, the diameters of the dried ring pattern on hydrophobic substrate were smaller than the hydrophilic substrate. (Fig. 4).

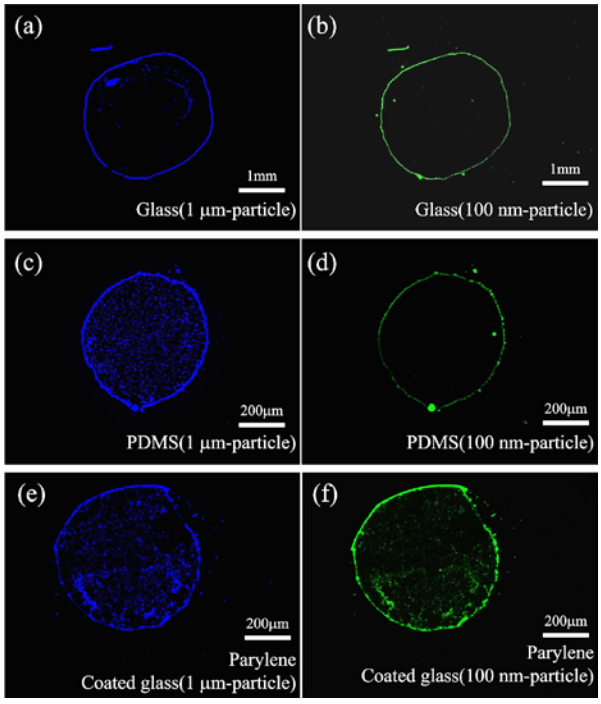

Figure 5*. Scheme for dynamic motion of suspended particle inside the liquid droplet during evaporation. (a) on glass substrate (contact angle ~15°), the diameter of the dried ring pattern did not shrink. (b),(c) on PDMS (contact angle ~90°) and parylene-coated (~ 110°), the diameters of the dried ring patterns shrunk, compared to the initial diameters.*

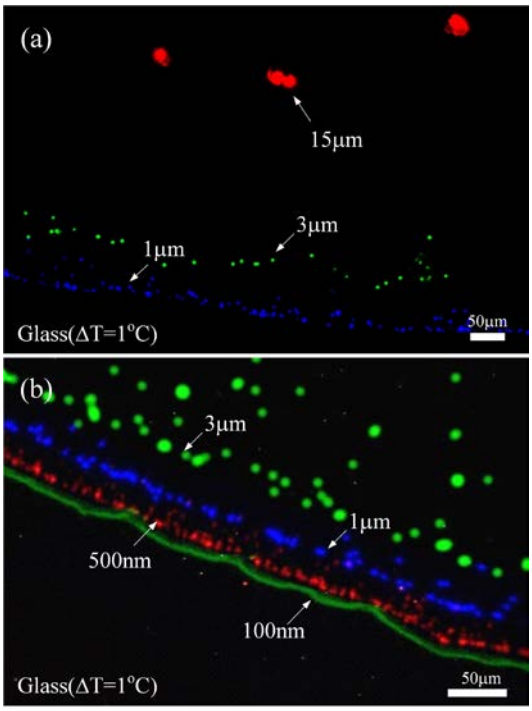

Figure 6. *(a) A fluorescence image of the separation of 1μm (blue), 3μm (green), 15μm (red) particles after evaporation on hydrophilic substrate (glass) with temperature gradient. (b) A fluorescence image of the separation of 100nm (green), 500nm (red), 1μm (blue), 3μm (green)- particles after evaporation on hydrophilic substrate (glass) with temperature gradient.*

Leveraging the findings described above, experiments were also performed to test separation across a wide range of particle sizes. The experiments were repeated with suspended particles in range of 100nm~15μm (1μL droplet volume, 0.003% volume fraction) under the same conditions described previously. For better separation, "strong" Marangoni flow with 1°C/mm was used. First, dried pattern showed that micro-particles, 1μm, 3μm and 15μm, were clearly sorted based on their sizes. Once the smallest particles were deposited at the outermost ring near the contact line, the second and third size patterns were arranged and deposited sequentially by their size, as expected (Fig. 6 a). The 100nm-, 500nm-, 1μm- and 3μm-paricles, were also separated clearly (Fig. 5 b). Separation of 100nm and 500nm was particularly successful. The particles ranging from 100nm to 3μm were separated in orderly fashion, and the ring patterns were clearer than the patterns of micro-particles. One possible reason for this difference is larger size tolerance in micro-particles. This result shows that the separation method using Marangoni flow on evaporating liquid droplet can be used to separate and concentrate various sizes of particles simultaneously.

CONCLUSION

This effort demonstrated nano-particle separation method using Marangoni flow and contact angle. It was found that only hydrophilic substrates can be used to separate suspended particle inside the liquid droplet. On hydrophobic substrates, the suspended particles cannot not be pinned at the contact line and are transported by receding movement during evaporation. The distance between smaller and larger particles is amplified by using "strong" Marangoni flow that is induced by a forced temperature gradient during evaporation. This technique is simple and low-cost, minimizing contamination of samples, and small amount of sample volume. In the future, this method can be extended to diagnostic applications.

ACKNOWLEDGEMENTS

This work was supported in part by the National Research Foundation of Korea (NRF) grant funded by the Korea government (MSIP) (No. 2011-0030075, 2011-0028845) and in part by the University of Michigan.

CONTACT

Jeasung Park, tel: +82-54-279-2188; jpark@postech.ac.kr
Yogesh B. Gianchanani: +1-734-615-6407;yogesh@umich.edu

REFERENCES

[1] R. D. Deegan, O. Bakajin, T. F. Dupont, G. Huber, S. R. Nagel, and T. A. Witten, "Capillary flow as the cause of ring stains from dried liquid drops," *Nature*, vol. 389, pp. 827-829, 1997.
[2] H. Hu and R. G. Larson, "Marangoni effect reverses coffee-ring depositions," *The Journal of Physical Chemistry B*, vol. 110, pp. 7090-7094, 2006.
[3] J. R. Trantum, D. W. Wright, and F. R. Haselton, "Biomarker-mediated disruption of coffee-ring formation as a low resource diagnostic indicator," *Langmuir*, vol. 28, pp. 2187-2193, 2011.
[4] J. R. Trantum, M. L. Baglia, Z. E. Eagleton, R. L. Mernaugh, and F. R. Haselton, "Biosensor design based on Marangoni flow in an evaporating drop," *Lab on a Chip*, vol. 14, pp. 315-324, 2014.
[5] T.-S. Wong, T.-H. Chen, X. Shen, and C.-M. Ho, "Nanochromatography driven by the coffee ring effect," *Analytical chemistry*, vol. 83, pp. 1871-1873, 2011.
[6] V. Vohra, A. Bolognesi, G. Calzaferri, and C. Botta, "Self-assembled nanofibers of fluorescent zeolite L crystals and conjugated polymer," *Langmuir*, vol. 26, pp. 1590-1593, 2010.
[7] E. Hendarto and Y. B. Gianchandani, "Size sorting of floating spheres based on Marangoni forces in evaporating droplets," *Journal of Micromechanics and Microengineering*, vol. 23, p. 075016, 2013.
[8] S. T. Chang and O. D. Velev, "Evaporation-induced particle microseparations inside droplets floating on a chip," *Langmuir*, vol. 22, pp. 1459-1468, 2006.
[9] X. Shen, C.-M. Ho, and T.-S. Wong, "Minimal size of coffee ring structure," *The Journal of Physical Chemistry B*, vol. 114, pp. 5269-5274, 2010.

PORTABLE MICROFLUIDIC OPTOELECTRONIC DEVICE FOR SALIVARY DIAGNOSTICS OF STOMACH CANCER

Yael Zilberman and Sameer R. Sonkusale[*]
Nano Lab, Tufts University, Medford, MA, USA

ABSTRACT

Stomach cancer is the second most common cause of cancer-related deaths in the world and its primary identified cause is infection by a gram-negative bacterium *Helicobacter pylori*. These bacteria survive in a highly acidic stomach environment by converting urea into bicarbonate and ammonia that decreases acidity. We present a microfluidic optoelectronic sensor for detection of ammonia and carbon dioxide in saliva, for early diagnosis of stomach cancer. The sensor is composed of an array of microwells embedded in a microfluidic device. The microwells are filled with polymeric ion-exchange microbeads doped with organic dyes. Instead of monitoring response at a single wavelength, the optoelectronic monitoring of this unique sensor platform is done over broad wavelength spectrum providing excellent sensitivity and specificity to different concentrations of carbon dioxide and ammonia dissolved in saliva with a detection limit in a ppm range. Our ultimate goal is to develop a non-invasive, fast and portable diagnostic platform that can be used for early screening of gastric cancer, as an alternative to currently existing diagnostic procedures.

INTRODUCTION

Gastric cancer is one of the most common causes of death from cancer worldwide. In the United States, the estimated new cases from gastric cancer in 2013 are 21,600, including 10,990 deaths [1]. Because of unspecific clinical symptoms and not well-defined risk factors, the diagnosis is often delayed, leading to low survival rate. In Europe, the 5-year survival is below 25%, and the situation is even worse in the United States. Earlier diagnosis substantially improves the rate of survival: 95% of patients with cancerous growth, which is confined to the inner stomach lining, will survive longer than 5 years [2]. The primary marker for early identification of stomach cancer is infection with gram-negative bacterium *Helicobacter pylori* [3]. It has been shown that when the bacterium is eliminated in treated patients at early stage of gastric cancer, the risk of developing a second gastric cancer decreases by two-thirds [1]. To survive in the harsh, acidic environment of the stomach, *H. pylori* secretes the enzyme urease that converts urea into bicarbonate and ammonia (neutralizing the acidic environment locally).

Gastric cancer diagnosis is normally done by endoscopy with biopsy and histopathological evaluation, which provides a high diagnostic accuracy of 95-99% [4]. However, the invasive and relentless character of this procedure makes it less suitable for fast screening. In addition, the method is relatively expensive and requires highly skilled medical personnel. Moreover, some early gastric cancers provide very little optical contrast with the surrounding tissues and could be missed during endoscopic examination. Endoscopy with biopsy can be also used for the identification of *H. pylori* infection, when combined with a rapid urease test and microbial culture. Urease can be also detected in serum, using enzyme-linked immunosorbent assay (ELISA), but collecting blood is required in this case [5]. Another approach is breath analysis: isotopically-labeled urea is orally ingested by the patient and the breath sample is subsequently analyzed by mass spectrometry, to test for (isotopically labeled) nitrogen and carbon. This approach is noninvasive, but requires expensive equipment.

Recently, saliva has been proposed as a promising diagnostic fluid for early screening of gastric cancer. Salivary diagnostics is much more convenient than biopsy or blood test: sample collection is simple, non-invasive and, therefore, not painful [6-8]. With respect to the gastric cancer screening, saliva is commonly analyzed for the presence of abnormal genetic material, or of specific biomarkers, which are detected by analyte-specific interactions using immunoassay arrays [9]. While these techniques are effective in early detection of gastric cancer, they are rather inappropriate for fast and high throughput screening, particularly outside of medical facilities. In addition, immunoassays are analyte-specific and, therefore, limited to measurement of just a few, among many, biomarkers.

It has been shown recently by means of gas chromatography/mass spectrometry (GC-MS) that, just as in the case of exhaled breath, there are a variety of volatile compounds in saliva [8]. Some volatile compounds found in exhaled breath, such as ammonia and carbon dioxide, are related to gastric cancer [10]. It is expected that volatile compounds exhaled from the oral cavity should be present both in the exhaled breath and in saliva, suggesting that salivary ammonia and carbon dioxide analysis has a potential for non-invasive early screening of gastric cancer. However, GC-MS is time consuming, not portable and requires complex and expensive equipment, which makes it less suitable for fast and portable screening.

An alternative approach is implementation of gas-phase cross-reactive sensor arrays known as ″electronic noses″, using chemiresistors or field-effect transistors that provide an ensemble electrical response [11]. The research in this field is quite advanced and this concept has been already implemented for detection of numerous volatiles related to various types of cancer, including gastric cancer [11]. Another approach is based on the use of optical arrays, composed of various organic dyes which sensitive to a particular group (or groups) of volatiles, providing an ensemble optical response, which is used for analyte classification [12].

So far, cross-reactive sensors have not been implemented for detection of ammonia and carbon dioxide in saliva. There are some important advantages in analyzing liquid samples. First, collected samples can be easily stored, since only tiny volumes are required. Second, salivary materials concentrations are higher than those in breath samples, where the exhaled materials are diluted by air. Finally, it is simpler to prevent contamination from the environment. We have developed a portable optoelectronic device based on a microfluidic platform and the sensing material is composed of three different organic dyes encapsulated in ion exchange resin beads. Conventionally, optical sensors rely on a response at a single wavelength, or a narrow range. Our cross-reactive sensor reads the entire visible spectrum and therefore, could extract unique multi-dimensional signatures based on colorimetric or fluorescent response of various dyes at different wavelengths. Such readouts from the microsensor array will capture multiple physical and chemical interactions between the dissolved gases (ammonia and carbon dioxide) and the composite sensing material and, therefore, are expected to be more sensitive and selective than other conventional techniques. Here, we demonstrate the excellent performance of our miniature optical sensor for analyzing ppm-level concentrations of ammonia and carbon dioxide dissolved in human saliva.

9781940470016/HH2014/$25©2014TRF
DOI 10.31438/trf.hh2014.61

SENSOR FABRICATION

Sensing Material

1. Ion pair preparation: The procedure of ion pair preparation was based on our previously published work [13]. Briefly, the pH-sensitive dyes were either cresol red or pyranine (Aldrich) and tetraoctylammonium hydroxide (TOAOH) was used as an ion-pairing agent. TOAOH was prepared from tetraoctylammonium bromide (TOABr) (Aldrich) and silver oxide (Aldrich). The dye containing solution (S1) was prepared by dissolving either cresol red or pyranine in 0.1 M NaOH. TOABr solution in organic phase (S2) was prepared by dissolving TOABr in toluene. Solutions S1 and S2 were mixed and stirred and the organic phase was removed and washed with 0.1 M NaOH. The resulting organic phase contained the pure ion pair of either [cresol red–/TOA+] or [pyranine–/ TOA+] dissolved in toluene.

2. Ion pair encapsulation: The ion pair consisting of an organic quaternary ammonium cation and a pH indicator dye anion was encapsulated within ion exchange resin beads according to the following procedure: 560mg of anion exchange resin microbeads (Dowex® chloride form, 200-400 mesh, Sigma-Aldrich), 1mL of TOAOH, 1mL of ion pair solution in toluene and 2mL of toluene were mixed and homogenized by stirring for 1h. The resulted suspension was dried in an oven at 50°C overnight in order to evaporate the toluene. The dry powder was dissolved in 5ml ethanol. Eventually, 5mL water was added to the dye-doped microbeads suspension before the microbeads deposition into the wells of microfluidic device.

3. Zn(TPP) encapsulation: The dye solution was prepared by dissolving 22.5mg of 5,10,15,20-Tetraphenyl-21H,23H-porphine zinc (Zn(TPP)) dye (Sigma-Aldrich) in 1 ml of ethanol (> 99.5 %, Sigma-Aldrich), followed by addition of 4 ml of deionized water. Subsequently, 560mg of cation exchange resin microbeads powder (Dowex® 50WX4 hydrogen form, 200-400 mesh, Sigma-Aldrich) and 5 ml of deionized water were added to the dye solution and stirred for 5h at room temperature, in order to create ionic bonding between the Zn(TPP) dye and the beads.

Saliva Collection

A volunteer was instructed to expectorate every 30 s into a 50 mL glass beaker after being asked to stay 30 min without food and liquid. A total of 10 mL of whole saliva was collected. The saliva was diluted ten-fold by adding deionized water under continuous stirring using a Teflon magnetic stirrer bar. The saliva sample was analyzed immediately after the collection.

Microfluidic Device

1. Master fabrication: A mask with desired master features was previously fabricated. 1 ml of SU-8 2100 was spin-coated on the 4″ wafer, followed by soft bake at 65°C for 30 min and subsequently at 95°C for 90 min. The wafer was then placed into the OAI Model 204 mask aligner and exposed to 365nm light with 20mW/cm^2 energy dose for 30sec, followed by post exposure bake at 65°C for 1 min and subsequently at 95°C for 20 min. The wafer was developed in the SU-8 developer for ~25-30 min. After the development, the wafer was rinsed with isopropanol and dried using a nitrogen gun.

2. PDMS mold fabrication: The base/curing agent ratio (of the PDMS pre-polymer components) was 10:1. The prepared PDMS mixtures were first placed in a vacuum desiccator for 30min (for degassing) and subsequently poured on top of the master, followed by vacuum degassing for 30min. The master was then placed inside an oven at 70 °C for 4h to cure the device layer. The PDMS mold was cut around the edge of the master wafer and peeled up. Fluid inlet and outlet holes of the PDMS device were punched using a 16-gauge needle before placing it into the RIE chamber. The March CS-1701F Reactive Ion Etcher was used (50mT). Oxygen was flowed for 30sec at 50Watt RF power. Immediately after removing from the RIE chamber, the PDMS molds were pressed gently, ensuring that a strong bond is formed.

EXPERIMENTAL SETUP

Fig. 1 shows the experimental setup complete with flow system and optical readout. White LED is used as a light source. Light transmitted through the sensor array is guided by a 400µm premium fiber through a collimating lens connected to a portable spectrometer (USB650, Ocean Optics). The spectrometer captures the entire spectrum instead of conventional readout approach using optical filters that measures response at a single wavelength.

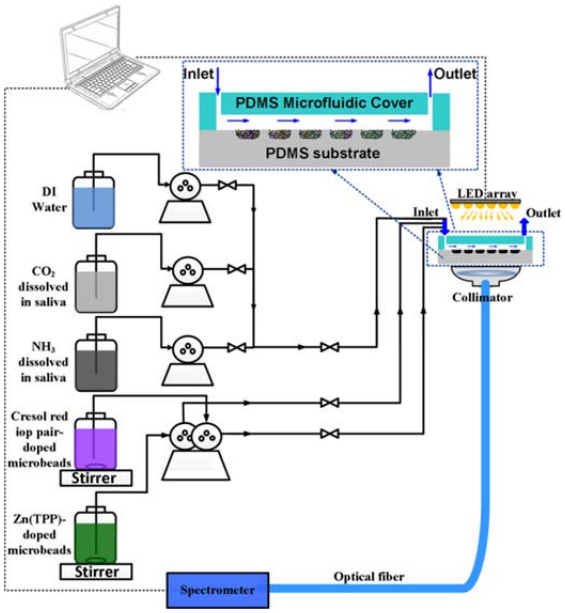

Figure 1: Schematic representation of the microfluidic sensor device, an array of microwells embedded in a microfluidic device. Optoelectronic setup and flow system are also shown.

DYE-DOPED MICROBEADS DEPOSITION

Ion exchange resin microbeads (~40-80µm) doped with organic dye (Zn(TPP) and either cresol red/quaternary ammonium or pyranine/quaternary ammonium cation ion pair) were deposited into the microwells (500µm diameter and depth) of the microfluidic device by circulating the microbeads suspension through the device using a peristaltic pump (Fig. 1 and 2). The device has three inlets and three outlets. Two inlets and outlets are used for deposition (for two different types of resin microbeads doped with dyes) and the ones in the middle are used for the device exposure to analyte solutions. The cation Zn(TPP) dye is encapsulated within cation exchange resin beads, while the anion pH dye ion pair is encapsulated within anion exchange resin beads. The opposite charge of two types of the microbeads makes their simultaneous deposition using a single microfluidic channel challenging, since the microbeads coagulate strongly because of electrostatic interactions. To resolve this issue, the deposition of two types of microbeads was done using separate channels. Figure 2 shows the microfluidic device embedding the array with about a half of microwells filled with microbeads doped with pH dye/quaternary ammonium cation ion pair and another half with microbeads doped with Zn(TPP).

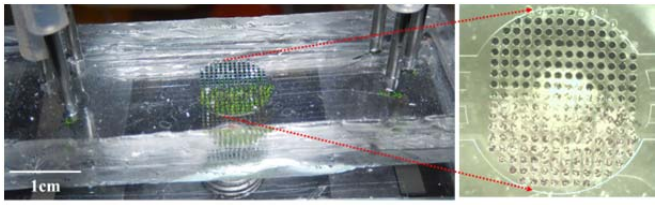

Figure 2: The array (d=10mm, each microwell is 500μm) is embedded in the microfluidic device with inlet and outlet channels. The array microwells are filled with microbeads doped with pyranine or cresol red-based ion pairs and with Zn(TPP).

SENSOR PERFORMANCE

In the following discussion, 100% concentration of dissolved CO_2 and NH_3 refers to 150ppm and 18ppm, respectively. Figure 3 shows transmission spectra recorded under the sensor exposure to the mixture of 90% CO_2 (135ppm) and 10% NH_3 (1.8ppm) dissolved in DI water (Fig. 3a) and human saliva (Fig. 3b). White LED was used as a light source and the irradiation intensity transmitted through the array was measured in the visible spectrum (440-680nm) using a portable spectrometer (schematic representation of the optical setup is shown in Fig. 1). All spectra were first normalized to the maximal transmission intensity and the reference spectrum obtained with deionized water was subsequently subtracted, i.e. $\Delta T = 0$ means no response and higher ΔT (absolute) magnitude indicates higher response.

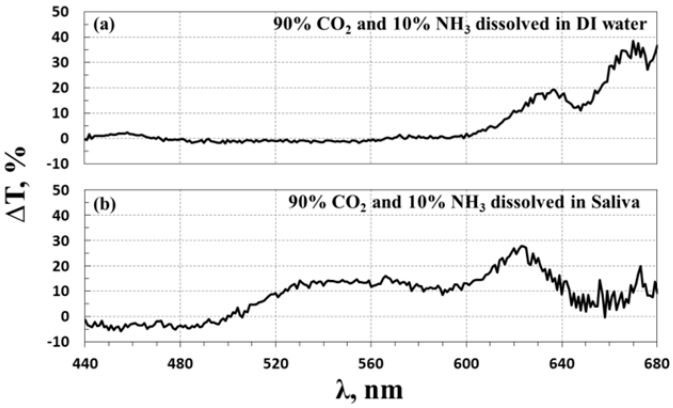

Figure 3: Transmittance spectra recorded under the sensor exposure to mixture of 130ppm CO_2 and 1.8ppm NH_3 dissolved in (a) DI water and (b) diluted saliva.

There are clear changes in transmittance upon the exposure to the mixture of CO_2 and NH_3 dissolved in either DI water (Fig. 3a) or diluted human saliva (Fig. 3b). It can be seen that the response magnitude and the shape of the obtained spectra differ significantly depending on the media (DI water or diluted saliva). There are spectral shifts in different ranges of the spectrum. In the case of DI water the shift was positive for 440-470nm and 600-680nm, while no response was recorded for 470-600nm. In the case of saliva the shift was positive for 500-680nm and negative for 440-500nm. In principle, such ″signatures″ over a broad optical spectrum can be used to distinguish dissolved CO_2 and NH_3 from other analytes that present in human saliva, as well as in other complex environments.

The observed spectral shifts correspond to the change in the dye color. The color of Zn(TPP) changes from green to purple under the exposure to dissolved NH_3. On the other hand, the colors of the pyranine-based ion pair and of the cresol red–based ion pair change under the exposure to dissolved CO_2 from shiny yellow to transparent and from purple to yellow, respectively. All these changes correspond to increase or decrease in the transmission spectrum. This observation emphasizes the advantage of the sensing strategy that employs hyperspectral imaging by analyzing the entire visible spectrum instead of focusing on a specific wavelength or a narrow range, as it is often done with optical sensors.

Figure 4 shows representative examples of the sensor response to mixtures of CO_2 and NH_3 with different concentrations, dissolved in either DI water (Fig. 4a) or diluted human saliva (Fig. 4b), at two wavelengths (640nm and 680nm). The response is shown in terms of the measured intensity (I) normalized to the baseline intensity (I_b, recorded when the device is exposed to distilled water), as a function of concentrations (maximum (100%) concentrations of CO_2 and NH_3 are 150ppm and 18ppm, respectively). The sensor contained an array composed of microbeads doped with a mixture of microbeads doped with Zn(TPP) and pyranine- or cresol red-based ion pair.

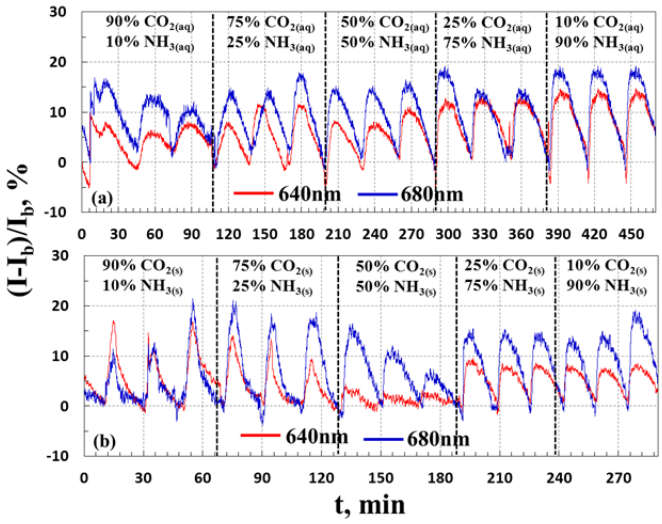

Figure 4: Sensor response to different concentrations of mixture contained CO_2 and NH_3 dissolved in (a) DI water and (b) diluted saliva at 640nm (red colour) and 680nm (blue color).

The response magnitude is quite different for DI water and human saliva, while the response shape is similar for most of concentrations. However, the shape of the responses for the mixture of 90% CO_2 and 10% NH_3 and 75% CO_2 and 25% NH_3 in human saliva is very different. This indicates that the response of ion pairs based on halochromic dyes (cresol red and pyranine) to CO_2 in the presence of NH_3 is more pronounced in human saliva than in DI water. For DI water the sensor response is dominated by the response to NH_3 even at its low concentrations (10% and 25%, which corresponds to 1.8ppm and 4.5ppm).

Figure 5 summarizes the results obtained in the entire (visible) spectrum, in terms of the response magnitude in the two-dimensional plane of wavelength vs. concentration. Evidently, the sensor is sensitive to different concentrations of diluted saliva (Fig. 5a, 100% corresponds to the saliva sample ten-fold diluted by DI

water) and to different mixtures of CO2 and NH3 dissolved in DI water (Fig. 5b) and human saliva (Fig. 5c).

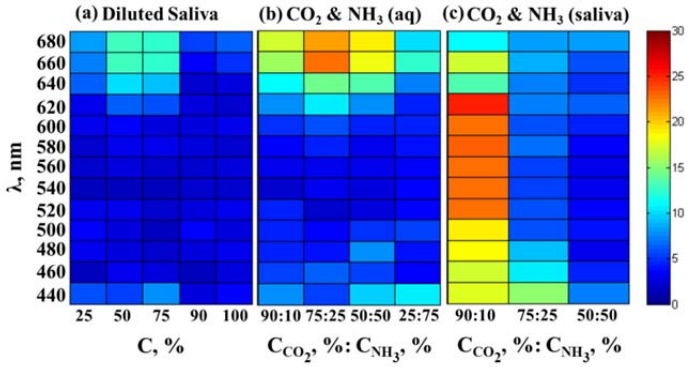

Figure 5: Sensor response magnitude at a range of wavelengths for diluted saliva (a) and for the mixture of CO_2 and NH_3 dissolved in deionized water (b) and diluted human saliva (c).

The saliva of healthy person contains low concentrations of CO_2 (ppm level) and NH_3 (sub-ppm level) [8, 10]. However, in the presence of the *H. pylori* infection in the stomach, concentrations of CO_2 and NH_3 in saliva are significantly higher. The obtained ″fingerprints″ differ sufficiently in order to discriminate between diluted saliva, CO_2 and NH_3 dissolved in DI water, and CO_2 and NH_3 dissolved in human saliva. These results indicate feasibility of this sensor platform for early diagnostics of gastric cancer sensor based on its ability to distinguish between the saliva of a healthy person and the saliva with elevated concentrations of CO_2 and NH_3 (*H. pylori* infection).

CONCLUSIONS

We have developed a novel optoelectronic sensor for cross-reactive detection of CO_2 and NH_3 dissolved in human saliva. The sensor is based on a microfluidic platform and contains a cross-reactive array composed of metalloporphyrin dye and halochromic dye/quaternary ammonium ion pair ionically bonded to ion-exchange polymeric microbeads. The use of the composite sensing material and broad spectrum optical readout offers important advantages for sensitive detection of dissolved CO_2 and NH_3 in complex environments, directly in liquid samples and without the use of any separating membrane. Strong ionic interactions between the ion-exchange microbeads and the dyes prevent the wash out of the sensing material.

The procedure for composite microbeads deposition into the sensing device is simple and robust and allows easy incorporation of virtually any combination of organic dyes, providing a route for cross-reactive sensing. Due to the flexible optical setup, the sensor can be easily modified for a variety of applications, where portable detection of dissolved volatiles in small liquid samples is required. The overall platform is low cost and portable. The sensor is sensitive to ppm levels of dissolved CO_2 and NH_3 in human saliva. This provides a potential for a variety of medical diagnostic applications, for early gastric cancer diagnosis in particular.

High surface-to-volume fraction of the composite microbeads is expected to provide relatively fast response times, but the chemical interaction between the dissolved CO_2 and NH_3 and the organic dyes maybe a limiting step. Residence time inside the microfluidic devices yet to be optimized. A trade-off between fast response times and sensor array stability and durability is yet to be identified. To achieve a truly cross-reactive approach, a large number of various organic dyes should be implemented. Possible interference with other chemical compounds should be also carefully investigated.

ACKNOWLEDGMENTS

The authors would like to acknowledge the partial support from National Science Foundation under grant EFRI: 1240443. The device fabrication was performed at the Tufts Micro and Nanofabrication facility.

REFERENCES

[1] National Cancer Institute, www.cancer.gov.
[2] K. D. Crew and A. I. Neugut, "Epidemiology of Gastric Cancer," World Journal of Gastroenterology, 12, 354 (2006).
[3] N. Uemura, S. Kamoto, S. Amamoto, N. Atsumura, S. Amaguchi, M. Amakido, K. Aniyama, N. Sasaki and R. J. Schlemper," Helicobacter Pylori Infection and the Development of Gastric Cancer", The New England Journal of Medicine, 345, 784 (2001).
[4] C. P. Dooley, A. W. Larson, N. H. Stace, I. G. Renner, J. E. Valenzuela, J. Eliasoph, P. M. Colletti, J. M. Halls and J. M. Weiner, "Double-Contrast Barium Meal and Upper Gastrointestinal Endoscopy: A Comparative Study", Annals of Internal Medicine, 101, 538 (1984)
[5] J. Parsonnet, I. M. Samloff, L. M. Nelson, N. Orentreich, J. H. Vogelman and G. D. Friedman, "Helicobacter Pylori, Pepsinogen, and Risk for Gastric Adenocarcinoma," Cancer Epidemiology, Biomarkers & Prevention, 2, 461 (1993).
[6] C. F. Streckfus and L. R. Bigler, "Saliva as a Diagnostic Fluid," Oral Diseases, 8, 69 (2002).
[7] H. J. Martin, S. Riazanskaia and C. L. Thomas, "Sampling and Characterisation of Volatile Organic Compound Profiles in Human Saliva using a Polydimethylsiloxane Coupon Placed within the Oral Cavity," Analyst, 137, 3627 (2012).
[8] H. A. Soini, I. Klouckova, D. Wiesler, E. Oberzaucher, K. Grammer, S. J. Dixon, Y. Xu, R. G. Brereton, D. J. Penn and M. V. Novotny, "Analysis of Volatile Organic Compounds in Human Saliva by a Static Sorptive Extraction Method and Gas Chromatography-Mass Spectrometry," J Chem Ecol, 36, 1035 (2010).
[9] W. Tan, L. Sabet, Y. Li, T. Yu, P. R. Klokkevold, D. T. Wong, C. M. Ho, "Optical Protein Sensor for Detecting Cancer Markers in Saliva," Biosensors and Bioelectronics, 24, 266 (2008).
[10] B. Timmer, W. Olthuis, A.V.D. Berg, "Ammonia Sensors and their Applications—a Review", Sensors and Actuators B, 107, 666 (2005).
[11] Z. Q. Xu, Y. Y. Broza, R. Ionsecu, U. Tisch, L. Ding, H. Liu, Q. Song, Y. Y. Pan, F. X. Xiong, K. S. Gu, G. P. Sun, Z. D. Chen, M. Leja, H. Haick, "A Nanomaterial-based Breath Test for Distinguishing Gastric Cancer from Benign Gastric Conditions," British Journal of Cancer, 108, 941 (2013).
[12] N. A. Rakow and K. S. Suslick, "A Colorimetric Sensor Array for Odour Visualization," Letters to Nature, 406, 710 (2000).
[13] Y. Zilberman, S. K. Ameri, S. R. Sonkusale, "Microfluidic Optoelectronic Sensor based on a Composite Halochromic material for Dissolved Carbon Dioxide Detection", Sensors and Actuators B, 194, 404, (2014).

CONTACT

* S. R. Sonkusale, tel: +1-617-627-5113; sameer@ece.tufts.edu

A COMPACT INTEGRATED HYPERSPECTRAL IMAGER MADE BY GRAY-TONE LITHOGRAPHY

M. Christophersen[1], A. J. Boudreau[1], M. J. DePrenger[2], and M. K. Yetzbacher[1]*
[1]US Naval Research Laboratory, Washington, District of Columbia, USA
[2]Tekla Research Corporation, Dumfries, Virginia, USA

ABSTRACT

Optical elements of precise thickness profiles are desired for instruments such as coronagraphs [1], wavefront coding systems [2], and compact hyperspectral imagers [3, 4]. Lack of sub-wavelength precision in the fabrication of these optical elements has required additional optical components, reducing the manufacturing yield and degrading performance. Here, we demonstrate a fabrication technique allowing for the control of surface fabrication errors of less than 1 nm and use this technique to fabricate a compact hyperspectral imager with the capability of high yield manufacturing.

INTRODUCTION

Any micro-fabricated optical device is in some way limited by the "fabrication errors". Fabrication errors are deviations of the actual optical surface from the designed surface. These errors arise from imperfections in the fabrication process. Wavefronts produced by imperfect optical surfaces are also imperfect, suffering from aberrations. For optical elements of precise thickness profiles, primary concerns are the deviations in material thickness, homogeneity, and surface smoothness. A "classical optical device" with a defined thickness and a low roughness requirement is the Fabry-Pérot (FP) etalon. A FP etalon is typically made of a transparent plate with two reflecting surfaces. Its transmission spectrum as a function of the incident wavelength exhibits peaks of large transmission corresponding to resonances of the etalon cavity.

Multiple FP etalons can be combined and used as a hyperspectral spectrometer. Our device exploits the fact that the transmission through such a FP etalon exhibits sharp peaks at cavity resonances and is very small between those. Our Hyperspectral imagers divide the light spectrum into finely tuned interferograms by using multiple FP etalons. This enables the imager to capture the "spectral signature" of an object. Applications for hyperspectral imagers range from medical diagnosis to security applications. There are multiple ways to achieve hyperspectral imaging. Conventional spectrometers typically use dispersive elements uncoupled from the photosensitive detector to separate light into its spectral components, requiring space and precise alignment of optics. The requirement of holding imaging optics and dispersive optics in precise alignments adds substantially to the size, weight, and assembly costs of optical systems. The size, weight and cost of spectrometers can be reduced by building an integrated optical device on the image sensor.

Several types of integrated spectrometers have previously been demonstrated by using micro-scale FP etalon array. A micro-fabricated FP etalon is made of a transparent medium bounded by two reflecting surfaces to create an optical cavity. The transmission spectrum of the cavity exhibits peaks of transmission corresponding to resonances of the optical cavity. The micro-fabrication challenge for a FP etalon array is the formation of multiple, flat levels. The FP etalons described in [3, 4] use combinatorial etching. A straightforward implementation of the staircase structure would use successive lithographic patterning and etching steps. This technique requires a large number of processing steps in order to produce a staircase with k steps, with k typically being > 50 or even 100. By using a combinatorial patterning process the number of required steps can be reduced to $\log_2(k)$. Sabatyan et al. have used a single gray-tone patterning step to produce a ramp without discrete levels [6]. Our micro-fabrication process for the FP Etalon array is based on a single gray-tone lithographic step on a bi-layer stack, see microfabrication section for details.

MICROFABRICATION

Our approach allows fabrication with a single lithograph-etch step followed by a chemical etch step. The number of distinct levels achievable is independent from the number of lithograph steps and is independent of the number of resolvable gray-scale lithography levels. This allows for a processing sequence that is much faster and more robust than previously demonstrated.

Our process is based on gray-tone lithography on a bi-layer stack, see Figure (1) for a schematic of the basic process sequence. Standard lithography generates a "black-white" image with a distinct top-down, two-level, profile. Gray-tone lithography on the other hand can generate full three-dimensional (3-D) resist structures like ramps. The variability of photoresist exposure and development in gray-tone lithography can be partially mitigated to create smooth photoresist structures. The 3-D resist structure can be transferred by a RIE (reactive ion etching) step into almost any type of material. We transfer a gray-tone resist ramp into a bi-layer stack a few micrometers thickness. After the RIE step, a roughened surface remains due to variability in material, photoresist homogeneity, and the random nature of the etch process. This has historically limited the resolvable gray-tone levels. In our process, a chemical etch then digitizes the levels. Each bilayer is comprised of two dielectric materials wherein one material acts as a chemical etch stop (i.e. one etches quickly and the other one very slow when exposed to the same etch process). The etch stop of each bilayer defines these individual levels. Our fabrication sequence is based on four basic process steps, as shown in Figure (1).

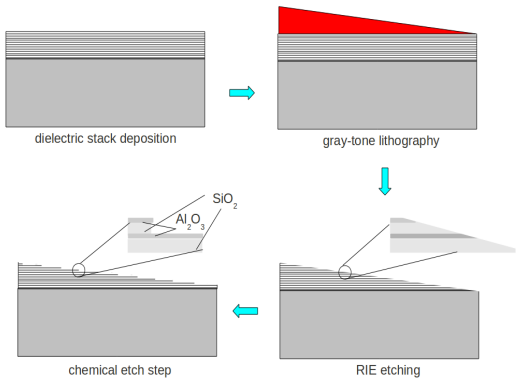

Figure 1: Basic process sequence, (i) bi-layer deposition of bi-layer stack, (ii) gray-tone lithography, (iii) transfer of into stack by RIE, and (iv) chemical etch, formation of individual levels.

9781940470016/HH2014/$25©2014TRF
DOI 10.31438/trf.hh2014.62

Figure (2) shows schematically the finished etalon on a standard image sensor. Our device utilized a commercially available imaging sensor provided by Aptina® (MT9V111), a standard FSI (front side illuminated) CMOS imager. The top mirrors were always thin gold layers (10 nm with 2 nm Ti adhesion layer). Two types of bottom mirrors were used: (i) 2 nm Ti/10 nm Au (like top mirror) or a (ii) dielectric stack of tantalum pentaoxide, Ta_2O_5, and SiO_2. Our silicon test substrates had Au bottom mirrors, and the Aptina imager had the dielectric stack as bottom mirror.

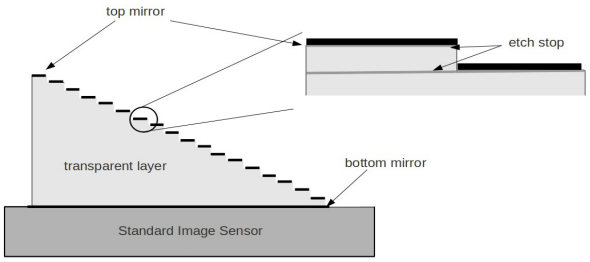

Figure 2: Schematic of the Etalon structure on a standard image sensor. The individual FP levels are defined by etch stops. Top and bottom mirrors form the optical cavity.

The dielectric stack can be deposited by different thin film deposition techniques. Plasma-enhanced chemical vapor deposition (PECVD) and atomic layer deposition (ALD) were chosen for our process. The stack is comprised of two materials (A and B). A is always deposited on top of B; so the stack is comprised of multiple A-B bilayers. The refractive indices of material A and B need to similar in value to avoid unwanted reflections during the numerous interface changes. One material of the stack (e.g. B) will act as an "etch stop" (described below). Silicon dioxide (SiO_2) and alumina (Al_2O_3) were used as components for the bi-layers. The number of etalon levels is determined by the number of bi-layers within the stack and the geometry of the gray-tone photoresist structure.

Gray-tone lithography is ideal for the fabrication of 3-D micro-structures. Gray-tone lithography is a specialized lithography process which results in continuously variable resist profiles. A gray-tone optical mask is used to transmit only a portion of the intensity of incident light, partially exposing sections of a positive photoresist to a certain depth. This exposure renders the top portion of the photoresist layer more soluble in a developer solution, while the bottom portion of the photoresist layer remains unchanged. The number of resolvable levels in gray-tone lithography has been limited by photoresist exposure nonlinearity, variability in development, and material homogeneity to less than 80 levels under common conditions. Continuous structures can be produced by heating the photoresist to smooth out surface non-uniformity.

The developed photoresist structures may be transferred, for example by plasma etching, to reproduce a scaled or unscaled version of the three dimensional structure in a target material. As the etch proceeds the photoresist mask slowly erodes exposing the underlying material, in our case a dielectric stack, to the high etch rate plasma. Gray-scale technology relies on specifically developed RIE chemistries and plasma conditions to control the relative etch rate of the dielectric stack to photoresist called "etch selectivity". This aspect defines the final vertical dimensions of a 3D structure. RIE etching is known to create surface non-uniformities due to the random nature of the etching process and material inhomogeneity, see Figure 3 for an optical micrograph.

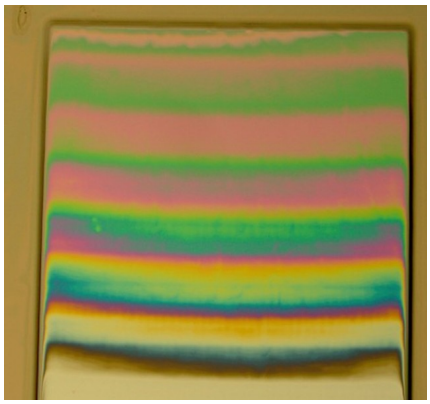

Figure 3: Optical micrograph, top-view: After ICP etching there are no distinct levels.

After transferring the gray-tone resist into the stack a chemical etch step is performed. The chemical selectively only etches one material of the bi-layer (e.g. when A is etched B is not). This selective chemical etch step will transform the ramp into distinct levels. Vapor hydrofluoric acid (HF) was used to etch SiO_2 selectively over the Al_2O_3. This leads to digitally distinct levels at a resolution controlled by the deposition technique of the bilayer stack which in this case is atomic layer precision. Figure (4) shows the stair-step structure on a test substrate. Figure (5) shows an optical profiometer scan from 5 individual steps.

Figure 4: Optical micrograph after vapor HF etching, top view, white light fringe pattern (step width ~ 10 µm, bi-layer height 10 nm: 7 nm SiO_2 + 3 nm Al_2O_3). The different optical levels (~70 distinct levels) are clearly visible. The sharp transitions between steps are due to a finely digitized staircase. This micrograph only shows a section of our ramp. Overall, the Fabry-Pérot etalon array is comprised of 140 distinct levels.

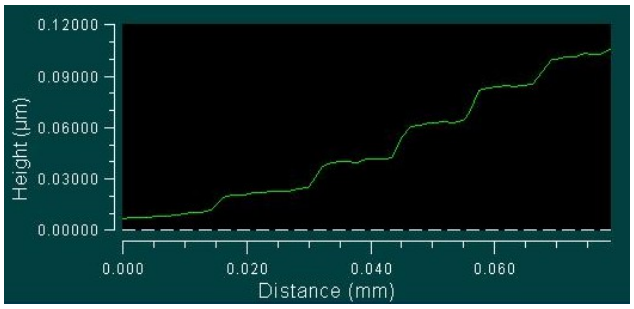

Figure 5: Optical profilometer scan from 5 individual steps. The roughness of each level is ~ 1 nm rms.

METHODS

The gray-tone lithography was done by using a Novolak resist (AZ P4330 Clariant, ~ 3 µm thick). According to standard soft-bake procedure the wafer was heated to 100ºC for 60 s on a hotplate in order to drive solvents out of the resist prior to UV exposure. We used "diffuser-based" gray-tone lithography, see [7] for details, with a 15 second exposure time. According to standard development procedure the resist was developed using the puddle method. 1:4 DI water to 400K AZ developer was used for ~ 40 sec which was followed by a sound DI (de-ionized) water rise. After development the resist was hard-baked at 150ºC for 120 seconds. The hard-bake makes the resist more resistant during the RIE etching step. Figure (4) shows an optical micrograph from a gray-tone resist ramp made by "diffuser gray-tone lithography". The numerous distinct etalon heights or clearly shown.

The gray-tone resist patterns were transferred into the stack via an ICP (induction coupled plasma) RIE etch process step. The ICP etch was performed using an Oxford 100 fluorine etcher (30 sccm CF_4, 20 mTorr, 20 W FW power, 500 W ICP power, 90 min etch time).

We used vapor HF (hydrofluoric acid) for the chemical etch step (Primaxx Etch System). Vapor HF only etches the silicon oxide and leaves the alumina intact. Hydrofluoric acid's reaction with SiO_2 forms water acting as a catalyst which will cause aqueous HF to etch the alumina. Commercial HF vapor etch systems minimize the formation of HF(aqu.) by injecting alcohol into the system.

RESULTS AND DISCUSSION

Our substrate was a standard imaging sensor, MT9V111 from Aptina®. Figure (6) displays the spectral response from the FP Etalons with 0.64, 1.0, and 1.5 µm effective heights on an imager. The light detection was done with the Aptina imager array underneath the etalon structure. The transmission versus frequency for FP Etalons is normally described with an Airy function. Figure (7) shows the calculated (Airy Function) FP etalon level heights derived from measurement of the spectral sensitivity of our device using a sequence of images captured under monochromatic light. The fabricated device achieves 10 nm discrete level resolution, enabling compact, hyperspectral imaging with high-yield device manufacture. Figure (8) shows a photograph from a prototype device.

Figure (9) shows a SEM, scanning electron microscope, cross-sectional micrograph from a thick Etalon. The CMOS chip with top wiring and its passivation is visible. The bottom mirror is comprised of Ta_2O_5, and SiO_2 layers. One cannot distinguish individual SiO_2 and Al_2O_3 bi-layers.

Since the MT9V111 is a FSI CMOS imager, normally microlenses are placed on top of the passivation layer. These

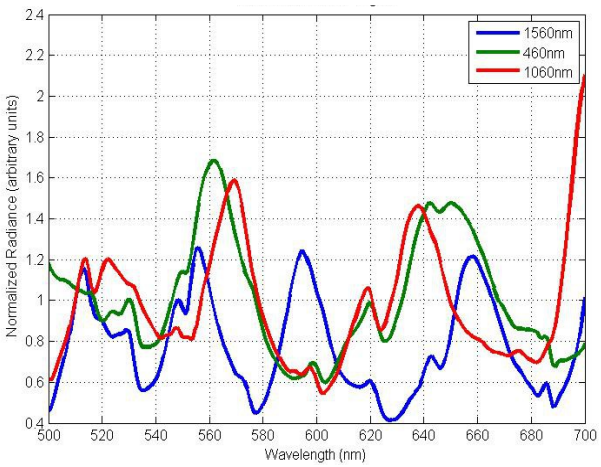

Figure 6: Fringes from Fabry-Pérot Etalons 0.64, 1.0, and 1.5 µm effective heights. The light detection was done with a MT9V111 from Aptina.

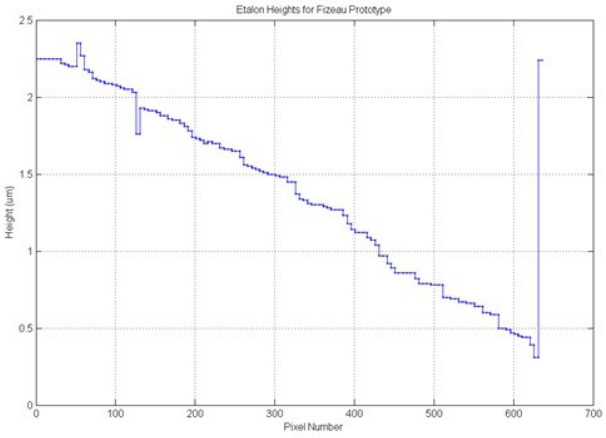

Figure 7: Plot of distinct levels calculated from illumination of an Aptina imager with monochromatic light using a superposition Airy function.

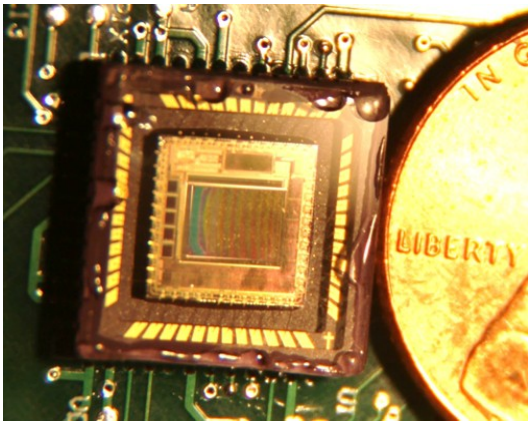

Figure 8: Photograph of the prototype device with a penny for scale. The wedged etalon array on the sensing chip is composed of 140 distinct levels. The striping of the first two layers is clearly visible on this scale. Since the color resolution of our device is much finer than that of the camera used to take this image, groups of etalon levels may appear to be the same color. A moiré pattern of interfering colors is visible over the larger steps. The shortest steps have etalon thicknesses of approximately 150 nm, while the tallest steps have etalon thicknesses of approximately 1.5 microns.

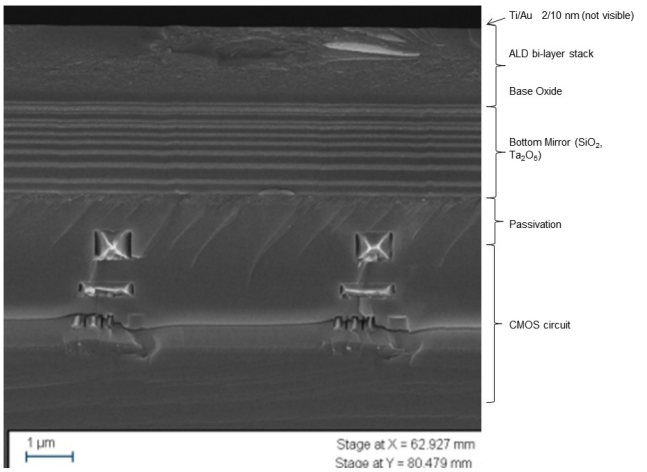

Figure 9: SEM micrograph, cross-section from the final prototype device. This image shows a thick Etalon; most of the bi-layer stack is visible.

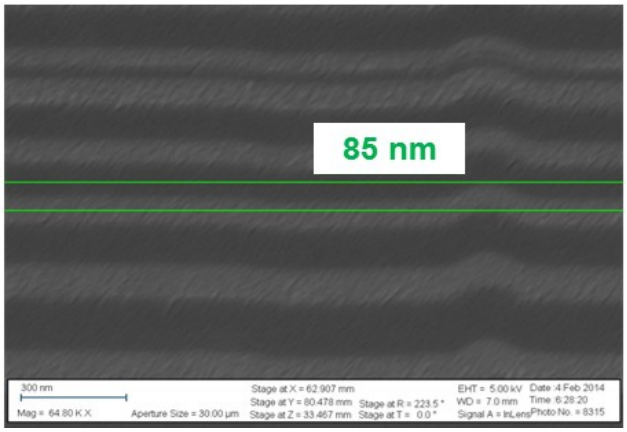

Figure 10: SEM micrograph, cross-section, bottom mirror stack. The interconnect lines introduce surface steps.

lenses are engineered to gather the light and confine it to a narrowed beam as it passes through the stack of interconnect metals and isolation. Our current design does not includes any lenses, so there is light scattering from the stack of interconnect metals, introducing noise and acting as parasitic mirrors. Furthermore, the interconnect lines introduce some small steps on the imager top surface, see Figure (10). Since all of our coating techniques are conformal these steps will remain and introduce noise into the system.

FUTURE WORK

Future work will include improving the finesse of the Etalon. The finesse describes the narrowness of the peaks relative to the spacing between the peaks.

Since the MT9V111 is a FSI CMOS imager, normally microlenses are placed on top of the passivation layer. These lenses are engineered to gather the light and confine it to a narrowed beam as it passes through the stack of interconnect metals and isolation. Our current design does not include any lenses, leading to light scattering and parasitic mirrors. Furthermore, the interconnect lines introduce some small steps on the imager top surface, see Figure (10). Since all of our coating techniques are conformal these steps will remain and introduce noise into the system.

In the future, we will switch to BSI, back side illuminated, CMOS imagers as substrates for our FP Etalons in order to circumvent the problems with respect to the interconnect lines. A pixel built for backside illumination eliminates the need to pass light through the layers of metal interconnections. Hence, no light scattering can occur on interconnects. Since BSI CMOS imagers are made by thinning down and bonding wafers, the top surface is extremely flat. This flatness will lead to better FP Etalons on BSI CMOS imagers. Furthermore, compared to FSI sensor, BSI senor shows much better quantum efficiency and chief ray angle.

SUMMARY

We introduce a new fabrication technique that allows for the creation of an arbitrary number of distinct levels with a single gray-scale lithography technique. Our technique allows the fabrication of distinct levels of 1 nm rms flatness with 10 nm step heights. In this paper, we present the fabrication technique and characteristics of an active imager.

ACKNOWLEDGMENTS

This work was funded by the Office of Naval Research (ONR). We thank Aptina for helpful discussion with respect to the CMOS imager. Furthermore, we would like to thank the Institute for Nanoscience (NSI) at the U.S. Naval Research Laboratory and the NSI staff members – “thanks Dave”.

REFERENCES

[1] J. Mazoyer, P. Baudoz, R. Galicher, M. Mas and G. Rousset, “Estimation and correction of wavefront aberrations using the self-coherent camera: laboratory results”, Astronomy & Astrophysics, 557, A9 (2013).

[2] C.-C. Chang and C.-C. Lee., “Effect of surface manufacturing error of cubic phase mask in wavefront coding system”, Optics Express, 17, 6245 (2009).

[3] N. Tack, A. Lambrechts, P. Soussan, and L. Haspeslagh, “A compact, high-speed, and low-cost hyperspectral imager”, Proceedings of Silicon Photonics VII, San Francisco, CA, 01/21/12-01/26/12, SPIE, Bellingham (2012), pp. 8266-8279.,

[4] S.-W. Wang, C. Xia, X. Chen, W. Lu, M. Li, H. Wang, W. Zheng, and T. Zhang, “Concept of a high-resolution miniature spectrometer using an integrated filter array”, Optics Letters, 32, 632 (2007).

[5] A. Emadi, H. Wu, S. Grabarnik, G. De Graaf, K. Hedsten, P. Enoksson, J.H. Correia, and R.F. Wolffenbuttel, “Fabrication and characterization of IC-Compatible Linear Variable Optical Filters with application in a micro-spectrometer”, Sensor and Acutators A, 162, 400 (2010).

[6] A. Sabatyan and A. Hemmat, “Study of a novel and simple method of generating binary mask for microprism fabrication”, Applied Optics, 51, 525 (2012).

[7] M. Christophersen and P. F. Phlips, “Gray-tone lithography using an optical diffuser and a contact aligner”, Applied Physics Letters, 92, 194102 (2008).

CONTACT

*Marc Christophersen, tel: +1-202-404-2884; marc.christophersen@nrl.navy.mil

A MEMS OPTICAL MOIRÉ SHEAR STRESS SENSOR FOR HARSH ENVIRONMENT APPLICATIONS

D. Mills[1], T.-A. Chen[2], and M. Sheplak[1]*
[1]Interdisciplinary Microsystems Group, University of Florida, Gainesville, Florida, USA
[2]Interdisciplinary Consulting Corp., Gainesville, Florida, USA

ABSTRACT

This paper describes the development of a shear stress sensor for use in harsh environments as well as experimental characterization of the sensor system. The microelectromechanical systems (MEMS) sensor utilizes optical moiré transduction of a floating element structure created using a silicon-on-Pyrex fabrication process. Interrogation of the amplified moiré displacement is achieved via a four-channel fiber optic array. The sensor and array are packaged in a robust housing to enable installation in multiple test facilities. Mean flow characterization of the system demonstrates a sensitivity of 13.4 mrad/Pa, minimum detectable shear stress of 54 mPa at 1 kHz with a 1 Hz bin, and experimentally verified dynamic range of 39.2 dB.

INTRODUCTION

The MEMS community has developed floating element shear stress sensors using several different transduction mechanisms, including capacitive [1,2], piezoresistive [3], and optical techniques [4]. The majority of sensors described in the literature, however, pose significant limitations on the ability to achieve real-time, continuous measurements in harsh environments, such as water tunnels and high-temperature wind tunnels. For these harsh-environment applications, optical sensors provide several advantages over traditional electrical sensing methods including being passive, immune to electromagnetic interference, and nonconductive.

Previous work presented by Horowitz et al. [5] and Chen et al. [6] has attempted to address this technology gap via the development of optical shear stress sensors that utilize a geometric moiré fringe to amplify the mechanical sensor displacement. The sensor presented herein is an extension of these efforts to improve upon sensor performance, packaging simplicity, and robustness. The design, fabrication, and packaging of the sensor are detailed, followed by mean flow characterization and noise floor measurement.

SENSOR DESIGN

Geometric Moiré Fringe Formation

A geometric moiré fringe pattern is an optical phenomenon that occurs when two bar and space gratings are superimposed. Moiré fringe formation for the shear stress sensor is accomplished by aligning two sets of parallel binary gratings with one another. In this method of fringe formation, a translation in the transverse direction of one of the gratings of pitch g_1 relative to a fixed reference grating of pitch g_2 creates an amplified relative motion of the moiré fringe period G in the same direction. From Yokozeki et al. [7], it can be shown that the moiré fringe period for such a pair of gratings under pure translation can be determined using the expression

$$\frac{1}{G} = \frac{1}{g_1} - \frac{\cos\alpha}{g_2}, \qquad (1)$$

where α represents angular misalignment. Furthermore, for a small displacement δ of the movable grating, the amplified relative displacement Δ of the moiré fringe can be expressed as [8]

$$\Delta = \delta \frac{G}{g_1}, \qquad (2)$$

which is illustrated in Figure 1. For the sensor presented in this work, g_1 = 9.9 µm and g_2 = 10.0 µm, resulting in a moiré fringe period G = 990 µm. Thus, the fringe displacement Δ will be amplified by a factor of 100 times the grating displacement.

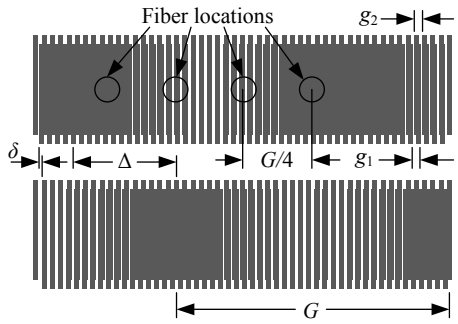

Figure 1: Illustration of the amplified displacement of a moiré fringe and optical fiber locations for quadrature phase shift estimation.

Quadrature Phase Estimation

The optical configuration used for interrogation of the moiré fringe is shown in Figure 2. A single LED source is coupled to four individual 1x2 fiber-optic couplers via a fiber bundle in order to minimize uncertainty due to fluctuations in the source. The four send/receive fibers packaged with the sensor are connected by a multiple-fiber push-on (MPO) connector to the fiber couplers to transmit the reflected light to an array of fiber-pigtailed photodiodes which then convert the incident light to voltage outputs via the use of transimpedance amplifier circuits.

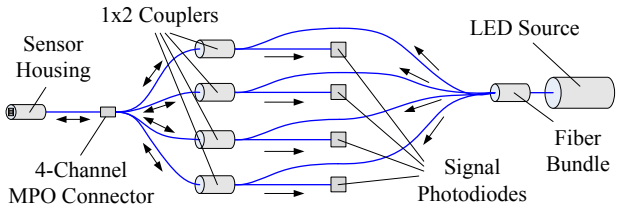

Figure 2: Fiber-optic configuration for interrogation of the moiré shear stress sensor.

Determination of the moiré fringe displacement requires the use of a phase shift estimation technique. Previous efforts have used various methods to determine the amplified displacement Δ of the moiré fringe [5,6]; however, these techniques necessitated the use of bulky and/or custom optical components. The new sensor utilizes a simple quadrature technique that requires only four optical fibers spaced such that they are separated by a distance $G/4$ as shown in Figure 1 [9]. The phase ϕ can thus be calculated using the expression

$$\phi = \frac{2\pi\Delta}{G} = \tan^{-1}\left(\frac{V_{03} - V_{01}}{V_{04} - V_{02}}\right), \qquad (3)$$

9781940470016/HH2014/$25©2014TRF
DOI 10.31438/trf.hh2014.63

where V_{0n} represents the output voltage of the n^{th} channel.

The result is a simple expression in which the dc offset in the signal is removed, reducing sensitivity to pressure fluctuations that can alter the reflected intensity. The fewer number of fibers enables smaller floating element sizes to increase sensor bandwidth. In addition, larger fiber spacing reduces cross-talk between channels and makes possible the use of v-groove arrays to locate the optical fibers more accurately than the 16-channel array used by Chen et al. [6].

Sensor Structure

The mechanical structure of the shear stress sensor is shown in Figure 3. The silicon (Si) floating element is suspended over a cavity by four tethers that are anchored to a fixed Pyrex substrate. Fluid flow across the surface of the floating element exerts an integrated shear force which causes a lateral displacement, and the tethers act as restoring springs to return the floating element to its central position under zero load. Similar to the design of previous optical moiré shear stress sensors [5,6], optical gratings patterned on both the floating element and the fixed substrate create a moiré fringe which amplifies the floating element displacement as previously discussed; however, the use of only four fibers facilitates leaving out sections of the gratings, creating four discrete moiré fringe segments to minimize cross-talk between channels, thereby improving device sensitivity.

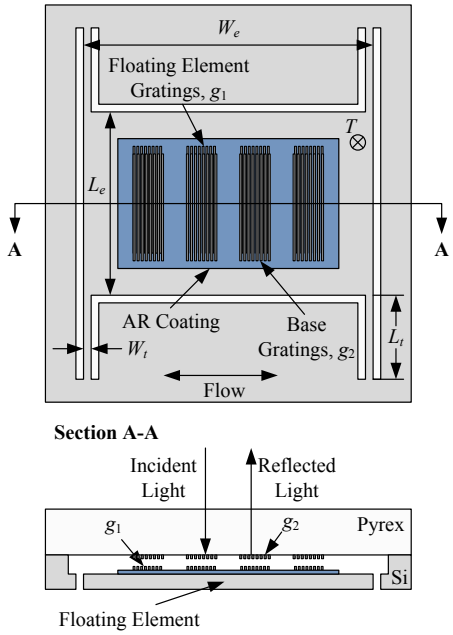

Figure 3: Top and cross-sectional views of the shear stress sensor structure.

Because of the relatively high reflectance (≥30%) of silicon over the visible and near-infrared range [10], an anti-reflective (AR) coating is used to improve the fringe contrast and increase the sensitivity of the sensor. The minimum reflectance is achieved when using a quarter-wavelength film thickness and the material's index of refraction n_1 is the geometric mean of the refractive indices of the surrounding medium n_0 and the substrate n_s, i.e., $n_1 = \sqrt{n_0 n_s}$. Using an 850 nm LED as the light source and silicon nitride (Si_3N_4) as the AR coating, the minimum reflectance is $R = 1.65 \times 10^{-3}$, resulting in a nearly 200x improvement in the contrast between the aluminum gratings and the bare Si surface.

The model used to determine the static and dynamic response of the mechanical structure is available in [5]. The physical dimensions, mechanical sensitivity, resonant frequency, and maximum shear stress for the chosen design are listed in Table 1.

Table 1: Sensor geometry and mechanical performance specifications.

W_e (μm)	L_e (μm)	W_t (μm)	L_t (μm)	T (μm)	f_{res} (kHz)	δ/τ (nm/Pa)	τ_{max} (Pa)
1100	1000	22.5	1430	45.0	5.0	9.8	480

FABRICATION

The sensor is fabricated using a six-mask silicon-on-insulator (SOI) micromachining process to create the floating element structure supported by an anodic-bonded Corning 7740 Pyrex base as shown in Figure 4. The process is similar to that used by Horowitz et al. [5], with the addition of the AR coating and a vent etch to prevent rupture of the sensors during the final floating element release step.

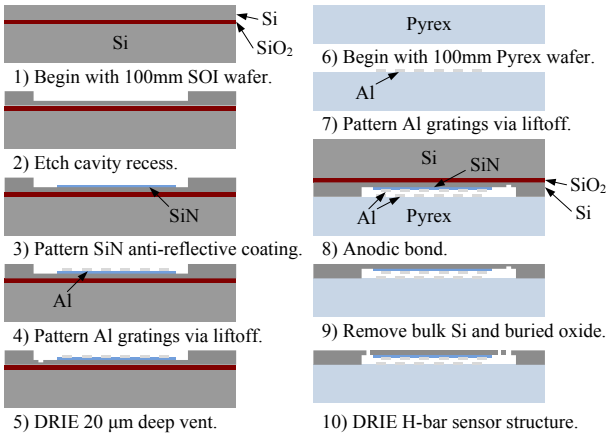

Figure 4: Illustration of the silicon-on-Pyrex process used for device fabrication.

The process begins by etching a 5 μm recess into a 100 mm diameter SOI wafer with a 50 μm device layer using a deep reactive-ion etch (DRIE) process to create a gap between the floating-element structure and the fixed gratings. The Si_3N_4 AR coating is then deposited using plasma-enhanced chemical vapor deposition and patterned using buffered oxide etch (BOE). Liftoff photolithography is used to pattern evaporated aluminum on the SOI wafer and a 300 μm thick Pyrex wafer to create the floating and fixed gratings, respectively. Vent holes are then etched partially through the SOI device layer prior to anodic bonding of the wafers.

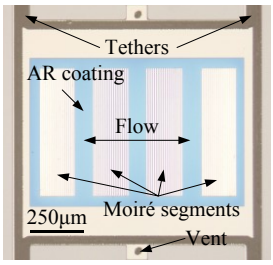

Figure 5: Back-side microscope image of the completed shear stress sensor highlighting the moiré fringe segments.

After the wafers are bonded, removal of the bulk silicon and buried oxide layers is performed using DRIE and BOE, respectively. The remaining device layer is patterned and etched using a DRIE process to define the floating-element structure. Finally, the devices are diced into 5 mm x 5 mm die using heat release tape to protect the released floating elements during dicing. After removal of the heat release tape the sensor die are ready for packaging. Figure 5 shows a microscope image of the back side of the completed sensor after dicing.

PACKAGING

Sensor Packaging

The desire to make meaningful fluid dynamics measurements in harsh environments necessitates that the sensor package be hydraulically smooth [11], robust, and small. The lack of interface electronics near the sensor enables a simple package comprised of three components: the sensor itself, a four channel fiber-optic v-groove array, and an aluminum housing as shown in Figure 6. The compact form factor of the package allows the sensor to be mounted in a variety of different characterization facilities.

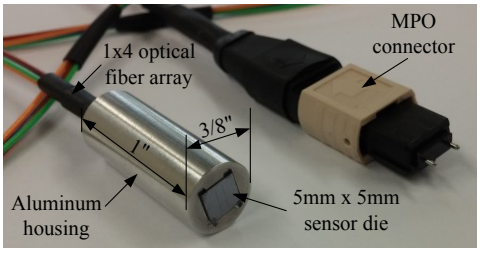

Figure 6: The assembled package showing the aluminum housing, flush-mounted sensor die, and 1x4 optical fiber array with MPO connector.

The 0.375 in diameter housing features a recess to flush mount the sensor as well as a through hole to accommodate the fiber-optic array. The array used for optical interrogation of the four moiré fringe segments was fabricated by Senko Advanced Components and features 250 μm spacing of 62.5 μm core diameter graded-index fibers. The array is aligned with the moiré fringe segments and bonded using a special fixture mounted to a Semiconductor Equipment Corp. Model 850 Flip Chip Placement System.

Transimpedance Circuit

A transimpedance circuit is used to convert the currents I_{sn} generated by the Thorlabs FDSP625 photodiodes to output voltages V_{0n} to be sampled by the data acquisition (DAQ) system. A schematic for a single channel of the four-channel array is shown in Figure 7 with a simplified model of the photodiode. The transfer function of the transimpedance circuit is [12]

$$V_{0n} = I_{sn} \frac{R_f}{1 + s\left(R_f C_f + \frac{1}{\omega_c}\right) + s^2 \frac{R_f\left(C_f + C_i\right)}{\omega_c}} \qquad (4)$$

where R_f and C_f are the feedback resistance and capacitance, respectively, C_i is the parallel combination of the junction and parasitic capacitance of the photodiode and the common-mode and differential capacitances of the OPA129 Ultra-Low Bias Current amplifier, R_i is the parallel combination of the photodiode shunt resistance and the common-mode and differential resistances of the amplifier, and ω_c is the unity gain frequency of the amplifier. Equation (4) shows that the dc gain of the amplifier circuit is determined by the 1.5 MΩ feedback resistance. The value of the feedback resistance is selected to provide sufficient gain while maintaining a large usable bandwidth. A 1.5-5.0 pF variable feedback capacitor is used to tune the circuit to improve stability at high frequencies and maximize the bandwidth.

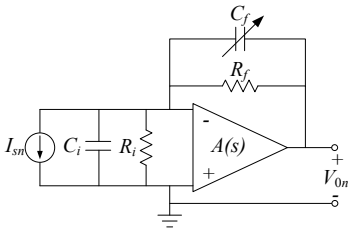

Figure 7: Schematic of the transimpedance amplifier circuit with a simplified electrical model of a photodiode.

EXPERIMENTAL SETUP AND RESULTS

Mean Flow Characterization

To assess the performance of the packaged sensor, static characterization is performed within a known shear stress field to determine the sensitivity of the device. The sensor is mounted in a laminar flow cell constructed of two aluminum plates separated by a metal shim to form a thin flow channel 330 mm long by 100 mm wide. If steady, incompressible, 2D Poiseuille flow through the channel is assumed, the wall shear stress may be expressed as [13]

$$\tau_w = \frac{h}{2}\frac{dP}{dx}, \qquad (5)$$

where h is the channel height and dP/dx is the pressure gradient at the sensor location. The pressure gradient is approximated by the differential pressure between two pressure taps P_1 and P_2 separated by a known distance Δx as shown in Figure 8. The mass flow rate is adjusted by an Aalborg GFC47 mass flow controller (MFC) connected to a Keithley 2401 source meter and the pressure drop is recorded through a serial connection to a Heise ST-2H pressure indicator with a 0-10" H_2O HQS-1 differential module. The four output voltages from the photodiode array are simultaneously sampled at each shear stress level by using two National Instruments (NI) PXI-5122 cards in an NI PXI-1045 chassis connected to a PC via an NI PXI-ExpressCard8360.

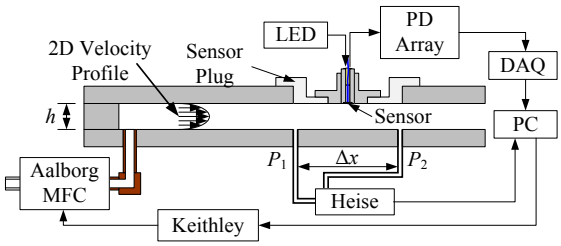

Figure 8: Schematic of the laminar flow cell used for static characterization of the shear stress sensor.

To determine the static sensitivity of the sensor, a shim height of 547 μm is used, and the input voltage to the MFC is increased from 1.0-5.0 V in 0.5 V steps, providing nine flow conditions with shear stress values ranging from 1.1 to 4.9 Pa. The four output voltages are sampled at 2 kHz for a block length of 10000 samples. Serial communication with the pressure indicator limits the data acquisition speed, and thus only 31 samples are recorded for the pressure drop at each flow rate. Figure 9 shows the resulting plot including 95% confidence intervals for the mean shear stress and phase. Linear regression analysis yields a static sensitivity of 13.4 mrad/Pa with a normalized residual (R^2) value of 0.998.

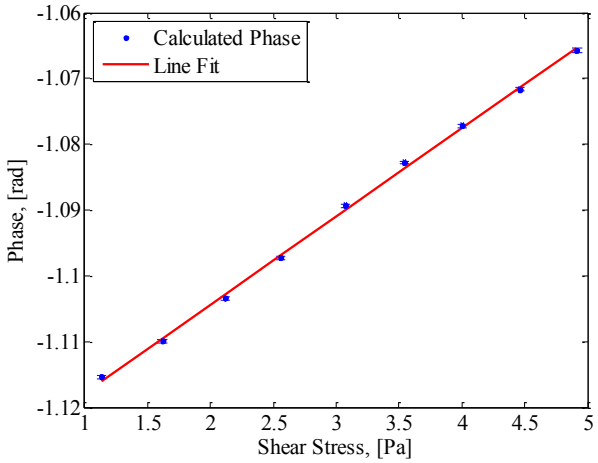

Figure 9: Plot of phase versus mean shear stress used to determine the static sensitivity of the sensor.

Noise Floor Measurement

The noise floor of the packaged sensor is determined by using a Stanford Research Systems SR785 spectrum analyzer with the packaged sensor and battery-powered optoelectronics placed inside a Faraday cage for shielding. A user-defined function is implemented to determine the phase noise power spectral density (PSD) shown in Figure 10. At 1 kHz for a 1 Hz bin the noise floor is 0.72 mrad. The minimum detectable shear stress (MDSS) is determined by dividing the voltage noise by the flat band sensitivity, which is equivalent to the static sensitivity assuming the sensor structure is a second-order mechanical system. Using the sensitivity determined during mean shear stress characterization, the MDSS of the sensor is 54 mPa.

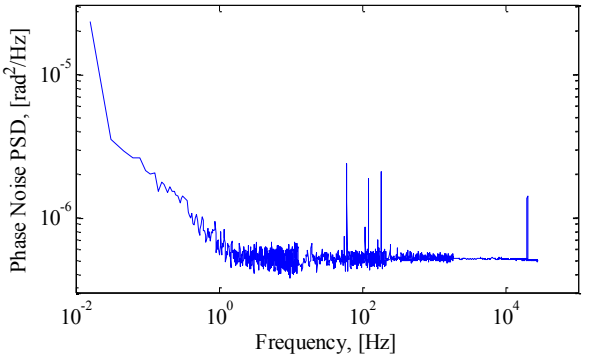

Figure 10: Differential noise measurement of the packaged shear stress sensor.

CONCLUSIONS

The design, fabrication, packaging, and static characterization of a moiré optical shear stress sensor were described in this paper. Characterization of a packaged device yielded a static sensitivity of 13.4 mrad/Pa and a noise floor of 0.72 mrad at 1 kHz with a 1 Hz bin, resulting in an MDSS of 54 mPa. Combining the MDSS with the maximum tested shear stress of 4.9 Pa gives an experimentally verified dynamic range of 39.2 dB, with the potential to extend the range to 79.0 dB based on a theoretical maximum shear stress of 480 Pa. These performance characteristics are on par with other sensors in the literature, demonstrating the potential for the sensor developed in this work to provide a direct measurement tool for estimating mean shear stress values in multiple harsh-environment flow facilities.

ACKNOWLEDGMENTS

The authors would like to thank Phil Carlson for his expertise in phased gratings and the Nanoscale Research Facility for assistance with fabrication. Travel support has been provided by the Transducer Research Foundation.

REFERENCES

[1] J. Meloy, J. Sells, V. Chandrasekharan, J. Griffin, L. Cattafesta, D.P. Arnold, et al., "Experimental Verification of a Capacitive Shear Stress Sensor for Low-Speed Wind Tunnel Applications", Technical Digest of the 2012 Solid-State Sensor and Actuator Workshop, Hilton Head Isl., SC, 6/4-7/12, Transducer Research Foundation, Cleveland (2012), pp. 303-306.

[2] M.A. Schmidt, R.T. Howe, S.D. Senturia, and J.H. Haritonidis, "Design and Calibration of a Microfabricated Floating-Element Shear-Stress Sensor", IEEE Transactions on Electron Devices, 750-757, 35 (1988).

[3] H. Goldberg, K. Breuer, and M. Schmidt, "A Silicon Wafer-Bonding Technology for Microfabricated Shear-Stress Sensors with Backside Contacts", Technical Digest of the 1994 Solid-State Sensor and Actuator Workshop, Hilton Head Isl., SC, 6/13-16/94, Transducer Research Foundation, Cleveland (1994), pp. 111-115.

[4] A. Padmanabhan, H. Goldberg, K.D. Breuer, and M.A. Schmidt, "A Wafer-Bonded Floating-Element Shear Stress Microsensor with Optical Position Sensing by Photodiodes", Journal of Microelectromechanical Systems, 307-315, 5 (1996).

[5] S. Horowitz, T.-A. Chen, V. Chandrasekaran, K. Tedjojuwono, T. Nishida, L. Cattafesta, et al., "A Wafer-Bonded, Floating Element Shear-Stress Sensor", Technical Digest of the 2004 Solid-State Sensor and Actuator Workshop, Hilton Head Isl., SC, 6/13-16/94, Transducer Research Foundation, Cleveland (2004), pp. 13-18.

[6] T.-A. Chen, D. Mills, V. Chandrasekharan, H. Zmuda, and M. Sheplak, "Optical Miniaturization of a MEMS-Based Floating Element Shear Stress Sensor with Moiré Amplification", 48th AIAA Aerospace Sciences Meeting, Orlando, FL, 1/4-7/10, AIAA Paper 2010-0498 (2010), pp. 1–13.

[7] S. Yokozeki, Y. Kusaka, and K. Patorski, "Geometric Parameters of Moiré Fringes", Applied Optics, 2223–2227, 15 (1976).

[8] D. Post, B. Han, and P. Ifju, *High Sensitivity Moire: Experimental Analysis for Mechanics and Materials*, Springer, New York, 1994.

[9] J.T.M. Stevenson, and J.R. Jordan, "Metrological Gratings and Moiré Fringe Detection Methods for Displacement Transducers", Physical Science, Measurement and Instrumentation, Management and Education, IEE Proceedings A, 243–253, 136 (1989).

[10] E.D. Palik, *Handbook of Optical Constants of Solids*, Academic Press, San Diego, 1985.

[11] J.W. Naughton, and M. Sheplak, "Modern Developments in Shear-Stress Measurement", Progress in Aerospace Sciences, 515–570, 38 (2002).

[12] J. Graeme, *Photodiode Amplifiers*, McGraw-Hill, New York, 1996.

[13] R.W. Fox, and A.T. McDonald, *Introduction to Fluid Mechanics*, Fifth Edition, John Wiley & Sons, Inc., New York, 1998.

CONTACT

*M. Sheplak, tel: +1-352-392-3983; sheplak@ufl.edu

A SINGLE-MEMBRANE PERMEATION-BASED SENSOR CONCEPT FOR THE MEASUREMENT OF MULTIPLE GASES

S. Schwebke[1,2], V. Bazargan[1], and B. Stoeber[1]*
[1]The University of British Columbia, Vancouver, B.C., Canada
[2]Ilmenau University of Technology, Ilmenau, Germany

ABSTRACT

A new concept for a gas sensor for measuring the partial pressures of multiple gases is demonstrated. The system is based on the pressure changes in two chambers, caused by the selective permeation of gases through a connecting membrane. A mathematical model based on permeation flow is developed to formulate measurement equations. Based on this model, a system for the measurement of specific gases that are typically dissolved in water is designed. A microfluidic multilayer polydimethylsiloxane (PDMS) device is fabricated for a proof of concept study. In experiments with air and nitrogen gas mixtures, pressures are recorded as a function of time, and this data is analyzed to calibrate the system and to determine the concentration of gases in a mixture.

INTRODUCTION

One important parameter in the assessment of water quality is the total amount of dissolved gas in water. Gas extraction probes that use a membrane to extract gases from water and measure their total pressure are already commercially available, and they are commonly used to assess the water quality of lakes and ponds. For more advanced water quality management there is a need for a device that can measure the concentration of individual gases dissolved in water, in particular oxygen, nitrogen, and carbon dioxide, which typically occur at the highest partial pressures.

Lazik and Geistlinger [1] proposed a permeation-based method with m membranes to measure the partial pressures of n ($\leq m$) different gases by observing approximately linear pressure changes across these membranes and solving a system of linear equations. In contrast, our method allows for the measurement of the partial pressures of several gases in a mixture using a single membrane and at least one pressure sensor. It uses the solution of a system of permeation equations or parameter fitting to find the initial gas fractions. Both methods rely on a difference in membrane permeability for different gases.

We establish a mathematical model for our system based on the underlying physics, and we use this model to design a proof of concept device. The device is fabricated with processes commonly used in microfluidics. Permeation experiments with different mixtures of air and nitrogen are conducted to validate the model and demonstrate the measurement principle.

SENSOR FUNCTION AND MODEL

Sensor Structure and Measurement Procedure

Figure 1 shows our sensor concept, which includes two chambers of volumes V_s and V_r separated by a membrane of thickness d, area A and permeability $\mathcal{P}$, one pressure sensor for each chamber measuring $p_s(t)$ and $p_r(t)$ and inlets and outlets that can be opened and closed by valves.

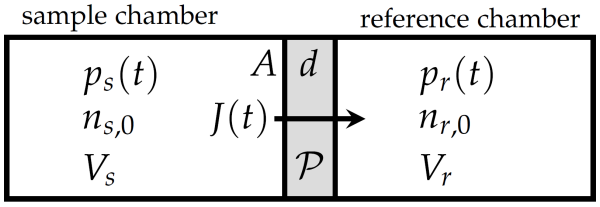

Figure 1: Two-chamber system with membrane.

The measurement procedure follows the sequence:

1. The reference chamber (V_r) is flushed with a reference gas or a gas mixture of known composition (e. g. air), and it is then closed off.
2. The sample chamber (V_s) is flushed with the gas mixture of interest and closed off.
3. The chamber pressures are measured over a certain amount of time (depending on time constants of the permeation processes).
4. Our algorithm is applied to the pressure signals to determine the initial gas volume fractions in the inflow chamber.
5. The system can be re-initialized by purging both chambers.

Mathematical Model

The mathematical model of the permeation process is based on a single-gas molar permeation flux driven by the pressure difference, proportional to permeability $\mathcal{P}$ and membrane surface A and inversely proportional to membrane thickness d:

$$J = \mathcal{P} A \frac{p_s(t) - p_r(t)}{d} \qquad (1)$$

For a system of given initial conditions as shown in Figure 1, we can use (1) and the law of ideal gases, $pV = nRT$, to describe the reference chamber pressure

$$p_r(t) = \frac{RT}{V_r}\left(n_{r,0} + \int_{t_0}^{t} J(\tau)\,\mathrm{d}\tau\right) \qquad (2)$$

Here, the molar amount $n_r(t)$ is made up by the initial molar amount $n_{r,0}$ plus the permeation flux over time into the chamber. Differentiating (2) with respect to time yields a differential equation governing the pressure changes over time; its solution is

$$p_r(t) = (p_{r,0} - p_{r,e})\mathrm{e}^{-kt} + p_{r,e} \qquad (3)$$

with

$$k = RT\mathcal{P}A\frac{V_r + V_s}{V_r V_s d}, \quad p_{r,e} = \frac{p_{r,0}V_r + p_{s,0}V_s}{V_r + V_s},$$

where $p_{r,0}$ and $p_{s,0}$ are the initial pressures for the chambers and $p_{r,e}$ is the final equilibrium pressure (identical for both chambers).

This model is extended to multiple-gas systems using Dalton's law of partial pressures,

9781940470016/HH2014/$25©2014TRF
DOI 10.31438/trf.hh2014.64

$$p = \sum_{k=1}^{n} p_k, \tag{4}$$

which is valid for gases of limited solubility in the membrane (Lacey and Loeb [2]). This allows us to describe the total reference chamber pressure $p_r(t)$ as the sum of the individual pressures $p_{r,a}(t)$, $p_{r,b}(t)$ etc.; the individual partial pressures change in a different way due to the different gas permeabilities $\mathcal{P}_k$ of the membrane and the different initial partial pressures in the two chambers.

Figure 2 shows predicted pressure signals $p_r(t)$ over time for a system of three gases with different initial gas fractions, based on our model.

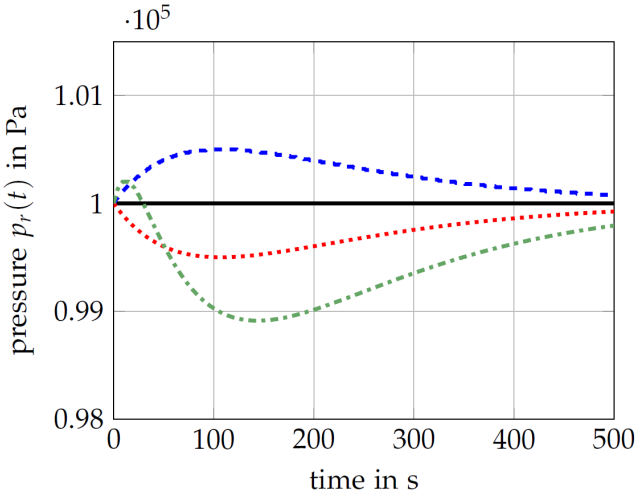

Figure 2: Reference chamber pressure over time for different fractions of up to three sample gases in the sample chamber. Reference chamber: 78% N_2, 22% O_2. Black, solid: equal gas mixture and initial pressure in both chambers; blue, dashed: 74% N_2, 26% O_2; red, dotted: 82% N_2, 18% O_2; green, dash-dotted: 89% N_2, 8% O_2, 3% CO_2.

From (3) we can see that in general, a permeation function for a single gas *a* can be written in the form

$$p_{r,a} = p_{r,a,0} \cdot a_1(t) + p_{s,a,0} \cdot a_2(t), \tag{5}$$

where

$$a_1(t) = \mathrm{e}^{-k_a t} \cdot \left(1 - \frac{V_r}{V_r + V_s}\right) + \frac{V_r}{V_r + V_s}, \quad a_2(t) = \frac{V_s}{V_r + V_s}\left(1 - \mathrm{e}^{-k_a t}\right).$$

In our measurement process, the sum of the partial pressures of *n* gases form the total pressure p_r, and this problem has *n* unknown variables ($p_{s,a,0}$, $p_{s,b,0}$, *etc.*). If we assume *n* pressure measurements $p_r(t_i)$ at time points t_i, we can establish a system of *n* equations to solve for these unknowns. If we write (5) in the form

$$p_{r,a} - p_{r,a,0} \cdot a_1(t) = a_2(t) \cdot p_{s,a,0},$$

the system of equations for *n* gases and *n* time points can be written in the corresponding matrix form:

$$\boldsymbol{p_r} - \boldsymbol{A_1} \cdot \boldsymbol{p_{r,0}} = \boldsymbol{A_2} \cdot \boldsymbol{p_{s,0}}, \tag{6}$$

where $\boldsymbol{p_r}$ is the vector of the total pressure measurements $p_r(t_i)$ for the reference chamber, $\boldsymbol{p_{r,0}}$ is the vector of the known initial reference chamber partial pressures, $\boldsymbol{A_1}$ and $\boldsymbol{A_2}$ are permeation matrices of the time dependent coefficients $a_1(t_i)$ and $a_2(t_i)$, and $\boldsymbol{p_{s,0}}$ is the vector of the initial sample chamber partial pressures, which are the desired measurement result. If all permeabilities $\mathcal{P}_k$ for the different gases are different from one another, $\boldsymbol{A_2}$ can be inverted in order to yield the measurement equation

$$\boldsymbol{p_{s,0}} = \boldsymbol{A_2^{-1}} \cdot \left(\boldsymbol{p_r} - \boldsymbol{A_1} \cdot \boldsymbol{p_{r,0}}\right). \tag{7}$$

That means that, as expected, gases of identical permeability cannot be discerned. For practical purposes, the sensor concept can be used to measure the sum of the partial pressures of such gases.

In an experimental investigation, either the measurement equation (7) or a curve fit to our permeation model can be used to evaluate the data and find all inflow gas fractions.

DESIGN, FABRICATION AND EXPERIMENTS

Design of a Proof of Concept Device

A material that offers sufficient selectivity (higher permeability of one gas over another) between nitrogen, oxygen and carbon dioxide is polydimethylsiloxane (PDMS). Compared to other polymers it also has a high gas permeability (Merkel et al. [3]), which makes it a desirable membrane material for our concept.

PDMS is often used for the fabrication of microfluidic devices, and thin layers can be achieved with commonly used fabrication processes.

A membrane thickness of d = 40 µm is chosen in order to achieve permeation time constants in the range of a few minutes. Since the expected pressure differences during the measurement process can reach up to 2000 Pa as shown in Figure 2, the thin membrane has to be supported. For this purpose, a narrow grid of rectangular support pillars on either side of the membrane is designed for this two-layer PDMS device.

To open and close the inlet and outlet channels, microfluidic valves are included, as described by Unger et al. [4]. These valves are made from crossing channels in the two device layers – when a pressure is applied to one of the channels (control channel), the thin membrane separating the channels deflects and blocks the other channel.

Assuming that the pressure measurements as well as the membrane properties possess an uncertainty, the combined uncertainty for the measured gas fractions was calculated from Equation (7). This study was used to optimize the sensor geometry for a minimum measurement error.

The parameters of the final system are shown in Table 1. The expected time constants are based on typical permeability values from literature [3].

Table 1: System design parameters

d (µm)	A (cm²)	$V_s = V_r$ (cm³)	τ_{N2} (min)	τ_{O2} (min)
40	0.2	0.125	6.5	3.2

Device Fabrication

The two layers that make up the system are shown in Figure 3; the lower layer includes the membrane and its bottom support pillars (not shown). The mask design in Figure 4 shows the inlet and an outlet of the sample gas chamber that allows the sample gas to be flushed in quickly.

Attached to both chambers are wide sensor connector areas to

allow connecting the external pressure sensors.

The fabrication steps follow the standard procedure for fabricating multi-layer soft lithography devices described in [5] and consist of spin-coating a 10 µm thick photoresist layer on one silicon wafer for each of the two layers, structuring them via lithography, spin-coating the bottom layer with 50 µm PDMS and pouring a thick PDMS layer (ca. 1 cm) on the other wafer. The layers are cured at a temperature of 80°C for 45 minutes, and then the thick top layer is cut into individual chips which are bonded to the bottom layer after surface activation in air plasma. The bonded system is cured again, and then it is cut and peeled off the silicon wafer. All holes for in-/outlets are punched using a biopsy punch and the systems are finally bonded to glass substrates after a final air-plasma activation.

A finished device can be seen in Figure 5. Pressure sensors and gas supply for inlets and control channels are externally connected via Tygon tubing.

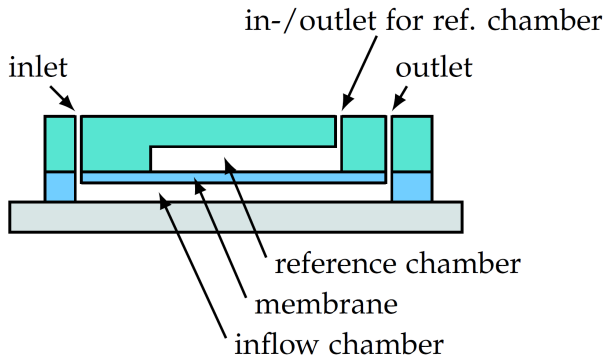

Figure 3: Schematic of the microfluidic PDMS device layers.

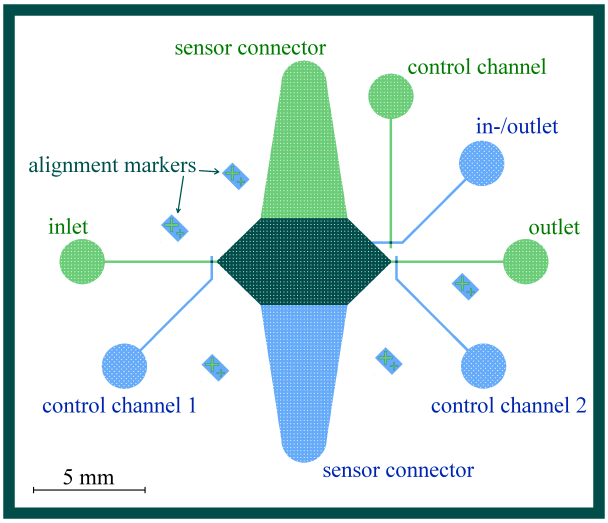

Figure 4: Mask design for the two-layer device. Colored segments are open channels/volumes within the system. The central hexagon is the 40 µm thick membrane.

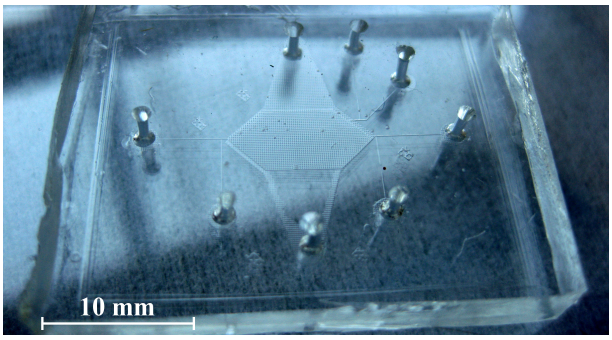

Figure 5: A device fabricated in multi-layer soft lithography using the masks in Figure 4.

Permeation Experiments

Each chamber was connected to a differential pressure sensor; in addition, the absolute pressure was also monitored during an experiment. The sample gas was connected to the inlet and controlled by the internal microfluidic valves of the device, which were actuated by a multi-channel pressure control system with control pressures up to 10^5 Pa.

For the permeation measurements, the reference chamber was filled with air at ambient pressure as the reference gas. The sample chamber was filled with the sample gas mixture, and then closed off using the valves. The permeation process between the sample chamber at an initial pressure slightly above the ambient pressure and the reference chamber at ambient pressure was then observed via the absolute chamber pressures. Air (ca. 78 % N_2, 21 % O_2) and nitrogen were used as sample gases.

For the air permeation test, the reference chamber was filled with air at ambient pressure and was left open, whereas the sample chamber was filled with air at a pressure of about 1500 Pa above the ambient pressure. We used our two-gas permeation model:

$$p_s(t) = (p_{s,O_2,0} - p_{s,O_2,e})\,e^{-k_{O_2}t} + (p_{s,N_2,0} - p_{s,N_2,e})\,e^{-k_{N_2}t} \qquad (8)$$

based on Equation (3) to fit the measured pressure over time using the oxygen permeability, the nitrogen permeability and the reference chamber volume as curve fit parameters. It was found that the permeation time constants were affected by the diffusion path between the internal sensor volume and the membrane; for this reason the connector tubing between the two was kept as short as possible (ca. 2 cm).

The air permeation result is shown in Figure 6. The fit result gives a chamber volume of $V_s = 0.17$ cm³, which is dominated by the pressure sensor's internal volume (0.11 cm³ according to the manufacturer) and the volume of the tubing.

We found the following permeability estimates: $\mathcal{P}_{N_2} \approx 730$ Barrer, $P_{O_2} \approx 1480$ Barrer (1 Barrer = 3.30×10^{-16} mol mm^{-2} s^{-1} Pa^{-1}). The corresponding time constants are $\tau_{N2} = 7.7$ min and $\tau_{O2} = 3.8$ min. The selectivity ratio $P_{O2}/P_{N2} \approx 2$ is similar to literature values [3], but the absolute permeabilities are larger than most values from literature. The membrane thickness was not measured separately, so it is likely that the permeabilities just appear larger due to the membrane being thinner than assumed for the calculation. In effect this can be neglected since the ratio P_k/d governs the exponential permeation term.

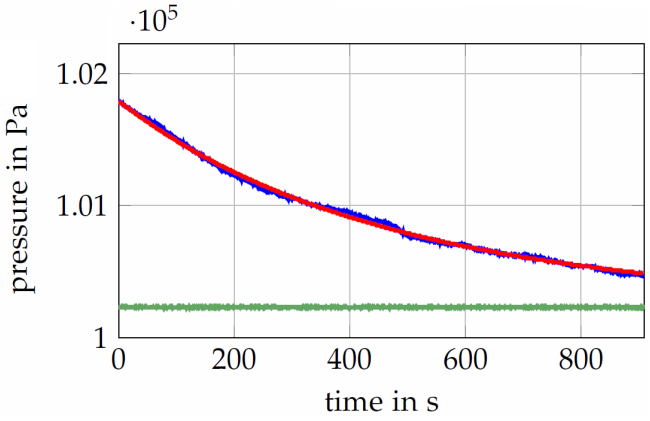

Figure 6: Results from the air permeation test with the microfluidic device. Green: pressure in the reference chamber. Blue: pressure in the sample chamber. Red: curve fit to the analytical model.

In another experiment, nitrogen was added into the inflow chamber. We used the previously identified permeabilities and chamber volumes to fit the measured pressure over time to our model with the initial gas fractions in the sample chamber as parameters. As expected, an elevated nitrogen level was identified. A good fit was achieved with 81.8 % N_2 and 18.2 % O_2. A plot of the result is shown in Figure 7.

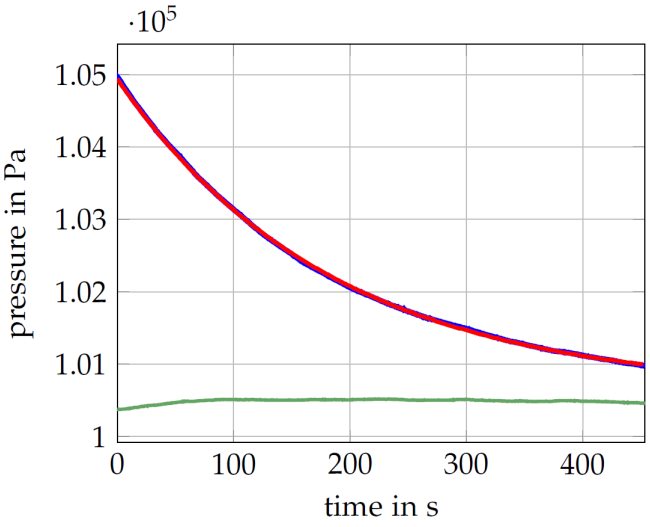

Figure 7: Nitrogen permeation test. Green: pressure in the reference chamber. Blue: pressure in the sample chamber. Red: a curve fit of the sample chamber pressure to the analytical model identifies the initial conditions: 81.8 % N_2, 18.2 % O_2. Note: The inflow chamber was initially pressurized with respect to the reference chamber, unlike in the simulation in Fig. 2 with identical initial pressures.

CONCLUSIONS

Based on literature and existing models of the permeation of gases through thin membranes, we derived a model for the permeation of multiple gases. The inversion of the permeation matrix leads to measurement equations that show the viability of a single-membrane sensor for multiple gases.

A microfluidic device with a PDMS membrane between two chambers was fabricated. The pressure changes during the permeation of different two-gas mixtures were measured.

The measurement data was used to find curve fits; a good agreement between model and experiment was found. After using one permeation experiment to identify the permeabilities of the membrane for oxygen and nitrogen and the chamber volume, these parameters were used in a permeation process with unknown initial partial pressures to find an estimate for the unknown gas fractions.

It was found that the connecting tubing to the external pressure sensors dominated the system volume and therefore the time constants of the permeation process between the chambers. This delay could be reduced greatly by bringing the sensors closer to the chambers, e. g. by integrating them on the substrate in future designs.

While a PDMS membrane offers the potential to measure partial pressures of nitrogen and oxygen (as well as carbon dioxide fractions in the order of magnitude of at least 1%), materials with different gas selectivities could be chosen for a sensor system for the measurement of other gases.

REFERENCES

[1] D. Lazik, H. Geistlinger, “A new method for membrane-based gas measurements,” Sensors and Actuators A: Physical, 117, pp. 241–251 (2005).

[2] R. E. Lacey, S. Loeb, “Industrial Processing with Membranes,” John Wiley & Sons, p. 299 (1972).

[3] T. C. Merkel et al., “Gas Sorption, Diffusion, and Permeation in Poly(dimethylsiloxane),” Journal of Polymer Science Part B: Polymer Physics, 38, no. 3, pp. 415–434 (2000).

[4] M. A. Unger et al., “Monolithic Microfabricated Valves and Pumps by Multilayer Soft Lithography,” Science, 288, no. 5463, pp. 113–116 (2000).

[5] V. Bazargan, “Micro Flow Control Using Thermally Responsive Polymer Solutions,” Master Thesis, University of British Columbia, October 2008.

CONTACT

* s.schwebke@gmail.com

DESIGN, SIMULATION AND FABRICATION OF THERMAL ANGULAR ACCELEROMETERS

Hommood Alrowais[1], Oliver Brand[1], and Pamela T. Bhatti[1,2]*
[1] School of Electrical and Computer Engineering, Georgia Institute of Technology, Atlanta, GA, USA
[2] School of Medicine, Emory University, Atlanta, GA, USA

ABSTRACT

This paper introduces a bio-inspired sensor design for detecting angular acceleration in a single plane using thermal convection as a potential sensor platform for a vestibular prosthesis. The working principal of the device is based on probing temperature profile changes along a micro-torus caused by angular acceleration. By properly choosing the locations of the heaters as well as the temperature sensors, the output signal will correlate to in-plane angular acceleration of the microstructure, while canceling out linear acceleration within the plane. Measured devices show a sensitivity of 16.1 μV/rad/s^2, and a frequency response of DC to 80 Hz, while consuming a non-optimized 1.1 mW of power.

INTRODUCTION

In mammals, the vestibular system plays an important role in keeping vision focused and balancing posture. Falls are the leading cause of both fatal and non-fatal injuries for people above the age of 65. Many of these falls are the result of bilateral vestibular loss, which can cause vertigo and imbalance [1]. Although physical rehabilitation is an option for unilateral loss, it is not an option for bilateral vestibular dysfunction. One proposed remedy is a vestibular prosthesis [2,3]. Vestibular prostheses replace balance sensing by electrically stimulating vestibular nerve fibers with electrical currents as resulted by head motion and tilt found in nature. A key element of such vestibular prostheses is the sensing element, which senses angular acceleration. In the present work, we investigate a bio-inspired, thermal angular acceleration sensor for this purpose.

Capacitive and piezoresistive linear accelerometers and gyroscopes are widely used in navigation, consumer electronics, manufacturing and automotive applications [4,5]. The first microfabricated capacitive angular accelerometer was presented by Brosnihan *et al* [6], with a similar device investigated by O'Brien *et al* [7]. Both devices operate on the parallel-plate principle using a suspended disk as proof mass. Piezoresistive angular accelerometers were initially developed in [8] using a suspended cantilever to measure angular acceleration. Elkund *et al* [9] introduced a design that uses the output of four linear accelerometers to discern linear accelerations from rotational ones. Finally, Amarasinghe *et al* [10] presented a 6-degree of freedom, piezoresistive inertial sensor that detects all three axes of both linear and angular accelerations. By using a proof mass suspended by four tethers, the researchers were able to strategically place piezoresistors to differentiate the motions.

An alternative approach is to use the semi-circular canals (SCCs) of the human vestibular system as inspiration. Arms *et al* [11] proposed a bio-inspired approach using a pressure sensor to sense the flow in the channel. Ploechinger [12] proposed to use thermal convection to measure the fluid velocity and correlating it to the angular acceleration, but no device was implemented. This method follows principles similar to those explored in thermal linear accelerometers and gyroscopes, first developed in [13].

The device proposed in this work is based on detecting the change in temperature profile along a micro-torus, mimicking a SCC, caused by angular acceleration, similar to [14]. By properly choosing the locations of the heaters as well as the temperature sensors, the output signal will correlate to in-plane angular acceleration of the microstructure. This approach provides a promising sensing platform without any moving parts for medical applications. The basic microstructure follows principles similar to those explored in thermal, linear accelerometers [13], but extends them to angular accelerations.

Consistent with human detection capabilities, the optimal angular accelerometer for a vestibular prosthesis targets a resolution of 1 rad/s^2 and a maximum angular acceleration of 175 rad/s^2 (10,000 deg/s^2). The device should consume less than 10 mW and cover a frequency range from 0-20 Hz. The present paper discusses design, fabrication and preliminary characterization of the angular acceleration sensor, and provides design guidelines for optimizing the detection of angular acceleration.

DESIGN AND SIMULATION

Design

The proposed design comprises four or more linear thermal accelerometers that are placed along the circumference of a micromachined torus to detect the tangential acceleration along the torus (Figure 1a). The tangential acceleration relates to the angular acceleration though α = a/R, where α, a, and R are the angular acceleration, tangential acceleration, and major radius of the torus, respectively. Each of the four linear accelerometers consists of a central heating resistor and two symmetrically arranged resistive temperature probes that monitor the temperature profile generated by the heater.

(a)

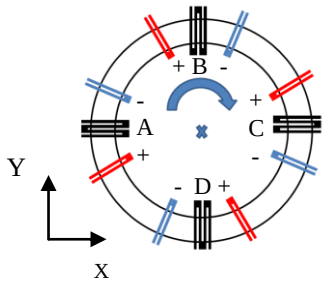

(b)

Acc.	A		B		C		D	
	+	-	+	-	+	-	+	-
α	↑	↓	↑	↓	↑	↓	↑	↓
+X	Ø	Ø	↑	↓	Ø	Ø	↓	↑
+Y	↑	↓	Ø	Ø	↓	↑	Ø	Ø

Figure 1: (a) Basic schematic and operating principle of thermal angular acceleration sensor with four linear thermal accelerometers; (b) Table summarizing the temperature changes of the individual temperature probes as a function of applied acceleration (↑: temperature increase; ↓: temperature decrease, Ø: no temperature change).

9781940470016/HH2014/$25©2014TRF
DOI 10.31438/trf.hh2014.65

Solid-State Sensors, Actuators and Microsystems Workshop
Hilton Head Island, South Carolina, June 8-12, 2014

A clockwise angular acceleration applied to the structure increases the temperature of the four red probes, while the four blue probes experience a temperature decrease. Thus, the resulting temperature difference is a measure of the applied (tangential) acceleration. An angular acceleration yields the same output for all four sensors, while linear accelerations can be distinguished by their characteristic response patterns (Figure 1b). In addition, a closed torus structure (similar to the human SCC) is intrinsically insensitive to linear accelerations.

Aluminum is the material chosen for the resistors for its relatively high thermal coefficient of resistance of 3900 ppm/K. The fluid chosen in this work was air at standard conditions. The main property of the fluid that affects the device's performance is the gas diffusivity [15], affecting both the frequency response and the sensitivity of the device. More diffusive fluids such as helium will have a higher bandwidth but a lower sensitivity. Less diffusive fluids such as CO_2 or liquids will have higher sensitivity, but a reduced bandwidth.

Finite Element Analysis

COMSOL 4.3b was used to simulate the device using the conjugate heat transfer physics module. Initial device simulations were performed on a 3D linear structure: to this end, the torus was unwrapped and turned into a linear pipe, with periodic boundary conditions for fluid flow and heat transport being applied to the ends of the device, as shown in Figure 2. Subsequently, a comprehensive 3D torus model was simulated.

As an example, Fig. 3 shows the temperature distribution in the center of the pipe around the heating element for the cases of zero applied angular acceleration and α = 1000 deg/s^2. From the difference of both temperature profiles, the optimal distance between heater and T-probe can be deduced (Figure 3).

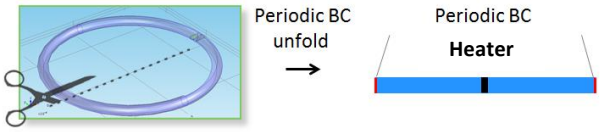

Figure 2: Simplifying the 3D torus structure into a linear pipe with periodic boundary conditions for computational purposes.

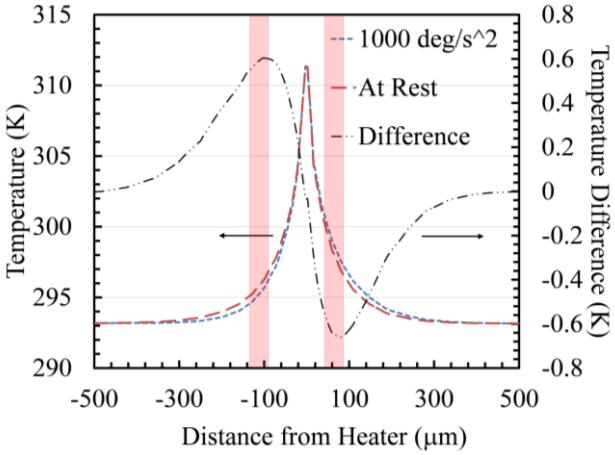

Figure 3: Simulated temperature profile along torus (left and right of a heater) for α=0 and 1000 deg/s^2 as well as temperature difference between both profiles, showing the optimal location of the temperature sensors highlighted in red.

FABRICATION

The two-mask fabrication process is schematically highlighted in Figure 4. First, 3400 Å of low-stress PECVD SiO_2 is deposited on a silicon wafer (a). Using a lift-off process, a 1200 Å layer of aluminum is sputtered and patterned, forming the resistors and the bonding pads (b). A second mask is used to pattern and etch the oxide film using Deep Reactive Ion Etching (DRIE) (c). Finally, the torus is etched and the SiO_2 bridges containing the aluminum resistors are released by isotropic XeF_2 etching of silicon (d).

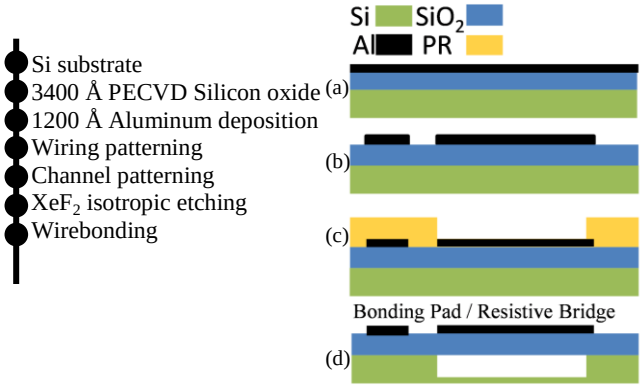

Figure 4: Summary of fabrication process.

Figure 5 shows an optical image of a fabricated angular accelerometer design with R = 2.85 mm. The inset reveals a different design with R = 1 mm, having two resistive heaters, and four resistive temperature sensors, each bridging across an etched channel. Different designs were used to study the effect of geometry on sensor performance. Each heater bridge has a length and width of 750 µm and 390 µm, respectively, while the temperatures sensor bridges are 750 µm long and 45 µm wide. These dimensions were chosen to maximize the temperature elevation in the sensing resistors, thus maximizing device sensitivity.

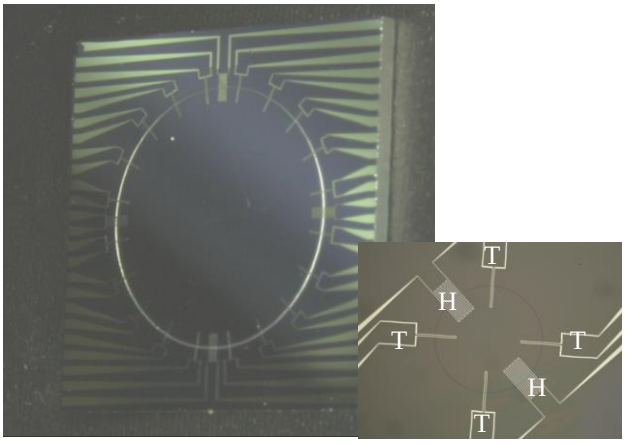

Figure 5: Optical image of fabricated device with R=2.85mm, featuring 4 heaters and 20 temperature probes. The inset shows a second design with R=1mm, having two heaters (H) and four temperature sensors (T). Each heater bridge has a length and width of 750 µm and 390 µm, respectively, while the temperatures sensor bridges are 750 µm long and 45 µm wide.

TESTING

The angular accelerometers were tested using an Ideal Aerosmith rate table as well as a rotational setup similar to the one described in [14]. The frequency range tested was from DC to 4Hz, because of setup limitations. A constant 1mA current was applied to the heating resistor, while a differential current was applied to the temperature resistors such that a zero differential output voltage across both resistors results at rest. A Stanford Research Systems 830 lock-in amplifier was used to detect the differential output voltage. The time constant was set to 3 s and the roll-off to 24 dB. The measured voltage from the lock-in amplifier was collected using a Keithley 2636A Sourcemeter. The angular acceleration magnitude was monitored using an Invensense IXZ-500 gyroscope.

RESULTS

The temperature distribution around the heating resistor was experimentally analyzed using a QFI InfraScope II infrared camera (Figure 6). The base plate with the sample was raised to 60˚C and used as a reference. A 10 mA current was supplied to the 550 Ω heating resistor, resulting in a 22.3˚C temperature elevation in the center of the suspended bridge. The device was at rest during the IR imaging.

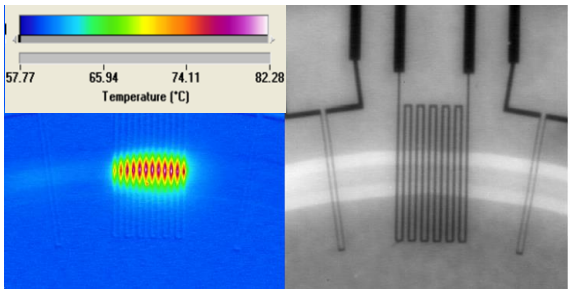

Figure 6: (left) IR image of heater structure with 10mA applied current; (right) Optical image of same heating element with neighboring temperature probes.

Figure 7 shows the response of an example sensor to applied angular acceleration; the particular design tested had an etched channel depth of 350 µm and a main radius R = 2.5 mm. A rate table was used to apply different angular accelerations with a frequency of 2Hz. The measured device sensitivity was 16.1 µV/rad/s^2. The device consumed 1.1 mW of power.

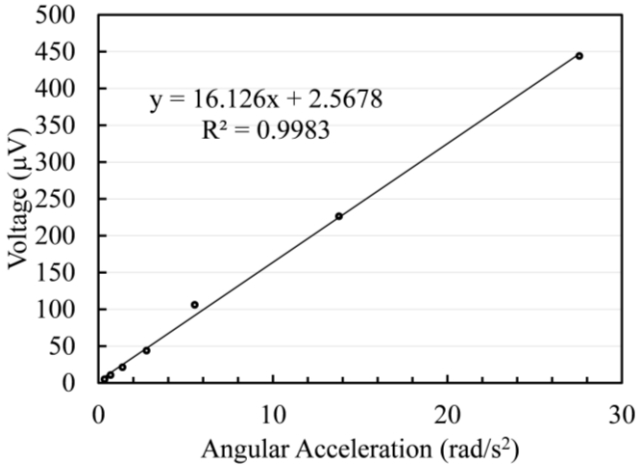

Figure 7: RMS output voltage change across temperature sensor biased with 1mA as a function of the angular acceleration applied (f = 2 Hz). The sensitivity is 16.1 µV/rad/s^2.

Due to frequency limitations of the rate table, the frequency response of the device could not be directly measured. Instead of applying a time varying angular acceleration, we applied an ac current directly to the heater and analyzed the frequency dependence of the resulting differential voltage drop across the temperature probes (Figure 8). While this method clearly does not probe the mechanical behavior of the air column inside the torus, but only the frequency dependence of the thermal transport, the resulting frequency characteristic is very similar to FEM results where a tangential acceleration is applied to the gas inside the torus structure. The measured (thermal) cut-off frequency was approx. 80 Hz for the tested device. The (mechanical) cut-off frequency is proportional to ~χ/r^2, where χ is the gas diffusivity, and r is the minor radius of the channel [15].

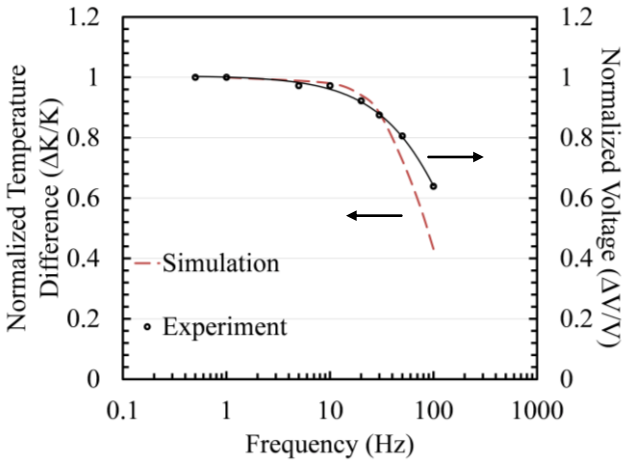

Figure 8: Simulated mechanical and measured thermal frequency transfer characteristic of a thermal angular accelerometer with a major radius of 1.425 mm and a minor radius of 65µm. A peak angular acceleration of 1000 deg/s^2 was applied in case of the FEM simulation.

In order to test the ability of the angular acceleration sensors to distinguish between linear and angular accelerations as described in Figure 1b, a sensor with a major radius of 1 mm and a minor radius of 250 µm was tested first in the center of the rate table and then at the edge of the rate table (approx. 20 cm from the center). While the angular acceleration is the same in both cases, a much larger linear acceleration is superimposed in case of the sensor being mounted off-center (keeping in mind that the rate table undergoes periodic small-angle rotations).

When mounted at the perimeter of the rate table, there is a clear difference between the measured signals of the tangential sensors (1 and 4) as compared to the perpendicular sensors (2 and 3), as seen in Figure 9. The difference in sensor output largely stems from the superimposed linear acceleration, which causes a larger signal in the tangentially aligned sensors . If mounted in the center of the rate table, there is a no significant difference between the measured signals of the four sensors, as shown in Figure 10. Thus, it is believed that by proper analysis of the signals coming from the different sensors, linear and angular accelerations can be distinguished. However, the recorded initial measurement data showed unexpected offsets that did not allow for a detailed analysis of the individual signal components. More detailed sensor

characterization is needed in the future.

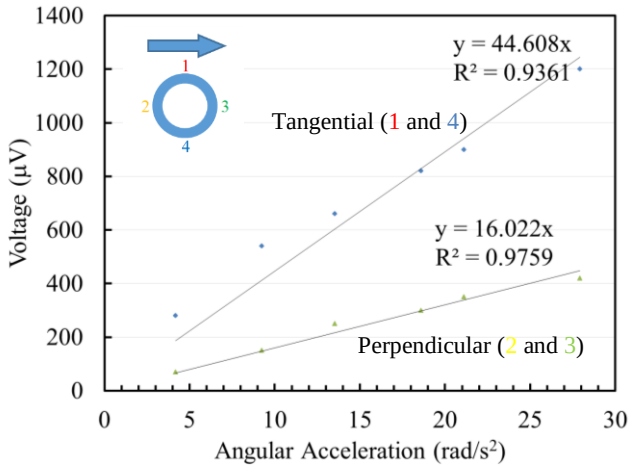

Figure 9: Differential output voltage changes (rms values) across different temperature sensor pairs on the same device as a function of the applied angular acceleration with the sensor being mounted on the edge of the rate table.

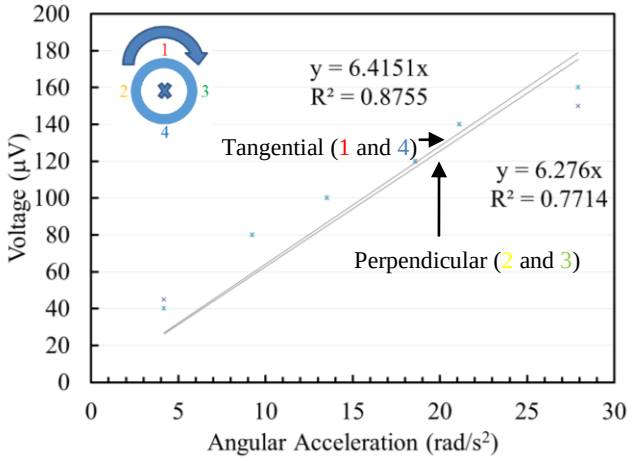

Figure 10: Differential output voltage changes (rms values) across different temperature sensor pairs on the same device as a function of the applied angular acceleration with the sensor being mounted in the center of the rate table.

CONCLUSION

A thermally sensed, bio-inspired angular accelerometer was designed, simulated, fabricated and tested. Its thermal response was linear to the angular acceleration input within the measured range with a sensitivity of 16.1 μV/rad/s^2. The device consumes a non-optimized 1.1 mW of power.

ACKNOWLEDGMENTS

This work was supported in part by an NSF CAREER award ECCS-1055801, the National Center for Advancing Translational Sciences of the National Institutes of Health under Award Number UL1TR000454, KL TR000455, and the Saudi Arabian Ministry of Higher Education. Travel support has been generously provided by the Transducers Research Foundation. The authors would like to thank the Georgia Tech IEN cleanroom staff for fabrication assistance, as well as Prof. F. Ayazi, Prof. L. Degertekin, and Prof. I. Papapolymerou for providing access to their lab facilities.

REFERENCES

[1] J.M. Goldberg, V.J. Wilson, K.E. Cullen, D.E. Angelaki, D. M. Broussard, J. Buttner-Ennever, K. Fukushima, and L.B. Minor, *The Vestibular System, A Sixth Sense*, Oxford University Press, New York, 2012.

[2] G. Fridman, and C.D. Santina, "Progress Toward Development of a Multichannel Vestibular Prosthesis for Treatment of Bilateral Vestibular Deficiency," The Anatomical Record, vol. 295, (2012) pp. 2010-2029.

[3] D.M. Merfeld, and R.F. Lewis, "Replacing Semicircular Canal Function with a Vestibular Implant", Current Opinion in Otolaryngology & Head and Neck Surgery, vol. 20, (2012), pp. 386-392.

[4] N. Yazdi, F. Ayazi, and K. Najafi, "Micromachined Inertial Sensors," Proceedings of the IEEE, vol. 86, (1998), pp. 1640–1659.

[5] B.Chiang, G.Y. Fridman, C.Dai, M.A. Rahman, and C.C. Della Santina, "Design and Performance of a Multichannel Vestibular Prosthesis that Restores Semicircular Canal Sensation in Rhesus Monkey," IEEE Transactions on Neural System Rehabilitation Engingeering, vol. 19, (2011), pp. 588–598.

[6] T.J. Brosnihan, A. Pisano, and R. Howe. "Surface Micromachined Angular Accelerometer with Force Feedback." Digest ASME International Conference (1995), pp. 941-947.

[7] G.J. O'Brien, D.J. Monk, and K. Najafi. "Angular Accelerometer with Dual Anchor Support." TRANSDUCERS, International Conference on Solid-State Sensors, Actuators and Microsystems, (2003), pp. 1371-1374.

[8] Furukawa, Naoyuki, and K. Ohnishi. "A Structure of Angular Acceleration Sensor Using Silicon Cantilevered Beam with Piezoresistors." Industrial Electronics, Control, Instrumentation, and Automation, (1992), pp. 1524-1529.

[9] E.J. Eklund, and A.M. Shkel, "Single-mask Fabrication of High-G Piezoresistive Accelerometers with Extended Temperature Range," Journal of Micromechanics and Microengineering, (2007), pp. 730.

[10] R. Amarasinghe, D.V. Dao, T. Toriyama, and S. Sugiyama, "Design and Fabrication of Miniaturized Six-Degree of Freedom Piezoresistive Accelerometer," in IEEE International Conference on Micro Electro Mechanical Systems (2005), pp. 351–354.

[11] S.W. Arms, and C.P. Townsend, "MEMS-based Angular Accelerometer," Patent, (2003), US 0047002.

[12] H. Ploechinger, "Sensor for Detecting a Rotational Movement or an Angular Acceleration," Patent, (2004), US 6722199.

[13] A.M. Leung, J. Jones, E. Czyzewska, J. Chen, and B. Woods, "Micromachined Accelerometer based on Convection Heat Transfer," in IEEE International Conference on Micro Electro Mechanical Systems, (1998), pp. 627–630.

[14] J. Groenesteijn, H. Droogendijk, M.J. de Boer, R.G.P. Sanders, R.J. Wiegerink, and G.J.M. Krijnen, "An Angular Acceleration Sensor Inspired by the Vestibular System with a Fully Circular Fluid-channel and Thermal Read-out," in IEEE International Conference on Micro Electro Mechanical Systems, (2014), pp.696-699.

[15] J. Courteaud, N. Crespy, P. Combette, B. Sorli, and A. Giani, "Studies and Optimization of the Frequency Response of a Micromachined Thermal Accelerometer," Sensors and Actuators A: Physical, vol. 147, no. 1 (2008), pp. 75–82.

CONTACT

*Hommood Alrowais, Georgia Institute of Technology, 777 Atlantic Drive NW, Atlanta, Georgia 30332, USA; Tel: +1-404-809-5463; E-mail: hommood.alrowais@gatech.edu

GOBLIT: A GIANT OPTO-MECHANICAL BULK-MACHINED LIGHT TRANSDUCER

Ajay K. Bhat, Laura C. Fegely and Sunil A. Bhave
OxideMEMS Lab, Cornell University, Ithaca, NY, USA

ABSTRACT

We report guided-light opto-mechanical sensing of the mechanical vibrations of a toroidal-lipped SiO_2 GOBLiT. An optical quality factor of $1.7x10^5$ allowed us to measure mechanical vibrations of the GOBLiT with mechanical quality factor 206 in air for the n=2 degenerate wineglass mode. Light was coupled into the resonator via a tapered optical fiber and used to sense mechanical motion of the GOBLiT. This result shows the viability of the toroidal-lipped GOBLiT for applications such as opto-mechanical gyroscopes.

INTRODUCTION

In recent years there has been much interest in opto-mechanical systems as displacement sensors, mass sensors, inertial sensors and oscillators. Shot noise limited displacement sensitivity of 10^{-19} m.Hz$^{-1/2}$ has been shown in microresonators [1]. Usually these devices have been two-dimensional disk type structures anchored at the center. Their mechanical quality factor is limited by anchor loss due to direct coupling of the anchor to the resonance modes. They also have various parasitic out-of-plane mechanical modes that populate the frequency spectrum. One solution proposed to solve these problems is to use a three dimensional wineglass structure where the anchor is decoupled from the mechanical modes of interest and the structure does not have any parasitic modes [2]. Many sensor applications require highly isotropic stiffness and damping properties [3], as well as high mechanical quality factors, ruling out conventional electrostatically transduced materials [4][5].

The performance of an optomechanical device is strongly dependent on optical quality factor. Optical losses depend on material properties, surface roughness and the curvature of the optical cavity. 2D optical disk structures such as [1] have used a CO_2 laser to selectively heat the oxide and reflow the rim of the disk to form a toroid. This improves the optical quality factor by orders of magnitude. The GOBLiT presented in this paper seeks to combine the toroidal optical cavity with the 3D mechanical resonator to achieve high quality device performance.

FABRICATION

The GOBLiT fabrication process flow is shown in Fig. 1. The resonator consists of an oxide hemispherical shell with an extended lip melted into a toroid at the outermost circumference, supported at the base by a silicon pedestal as shown in the SEM in Fig. 1g). The mechanical quality factor and frequency split of degenerate modes of the n=2 wineglass mode will be heavily dependent on the isotropy and smoothness of the bowl. In order to achieve better mode-matching which is necessary for gyroscopes, we start with a <111> silicon wafer to form the mold, as shown in [6][7]. After alignment marks are patterned, a masking layer of stoichiometric nitride is deposited using LPCVD. Once patterned, an HNA etch is used to create hemispherical molds within the bulk of the silicon wafer. Hot phosphoric acid is used to remove the nitride mask, thermal oxide is grown to a thickness of 1.1µm, and the lip of the GOBLiT is patterned. The device is then partially undercut using XeF_2 and heated with a CO_2 laser to reflow the oxide at the edge of the lip. The XeF_2 partial undercut is crucial in controlling the uniformity of the reflow. Any difference in thermal path length

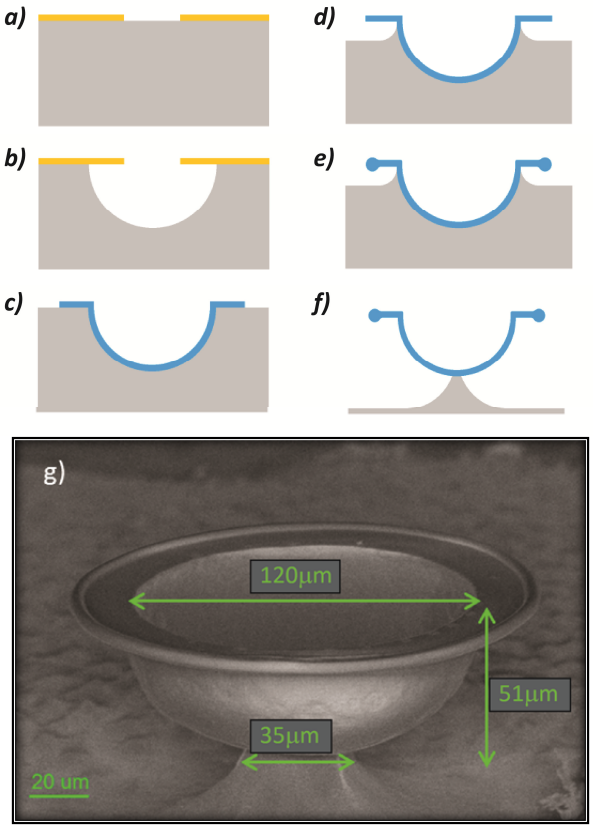

Figure 1: a) LPCVD silicon nitride mask is patterned with the etch hole. b) Silicon is isotropically etched in HNA. c) Thermal silicon dioxide is grown and the lip patterned. d) Partial undercut etch of silicon in XeF_2. e) Oxide is reflown using a CO_2 laser to form the toroidal optical cavity. f) Device is timed-etched in XeF_2 to define the anchor. g) SEM of a final device.

will cause inconsistent reflow, so the GOBLiT is only undercut up to the edge of the bowl. Undercutting any further will greatly exaggerate any path length differences between the rim and bowl due to the 3D shape of the device. Once the toroidal lip has been formed, XeF_2 etching is continued to release the device for measurements.

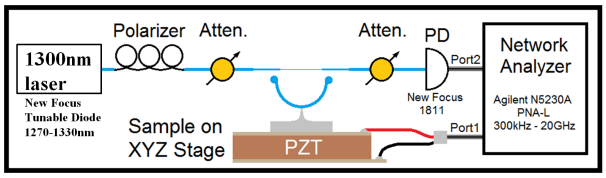

Figure 2: Schematic of the measurement setup for optically detecting the mechanical motion of the GOBLiT. Port 1 of the network analyzer is used to drive the PZT stage which in turn drives the mechanical modes of the GOBLiT. The mechanical motion intensity modulates the light in the tapered fiber which is detected by the photodetector and subsequently measured using port 2 of the network analyzer.

9781940470016/HH2014/$25©2014TRF
DOI 10.31438/trf.hh2014.66

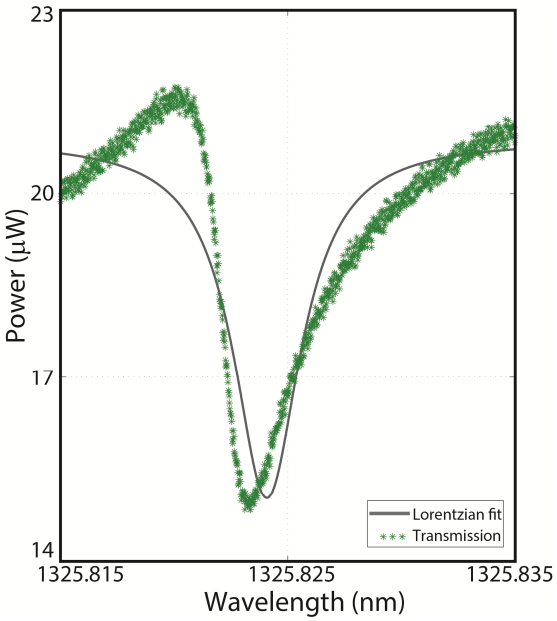

*Figure 3: Optical transmission measurement showing the dip at optical resonance (1325.823nm) of the cavity with an optical quality factor 1.7*10^5.*

EXPERIMENT

The toroidal lip forms the optical cavity of the GOBLiT. We use a tapered fiber to couple light into the GOBLiT, and interrogate it. Fig.2 shows a schematic of this measurement scheme. To obtain the tapered fiber we start with a 125μm diameter single mode (1550nm wavelength) optical fiber. We then use a hydrogen flame to heat a portion of the fiber and simultaneously pull from the two ends to draw out the fiber. The transmission of the 1300nm laser through the fiber is continuously monitored during this process and the heating and pulling is stopped when the fiber is single mode. At this point the diameter of the fiber is ~1.3μm with a glass "core" and an air "cladding". A part of the optical mode now sits outside the fiber with the amplitude falling off exponentially in the radial direction. This evanescent portion of the optical mode can now be used to couple light into the optical cavity when the GOBLiT is in the near-field of the taper.

The governing equations of motion of the optical field and the mechanical mode are [8],

$$\dot{a} = i(\Delta + Gx)a - \frac{\kappa}{2}a + \sqrt{\kappa_{ex}}s \qquad (1)$$

$$\ddot{x} + \Gamma_m \dot{x} + \omega_m^2 x = \frac{F_{drive}}{m} \qquad (2)$$

where, a is the normalized electric field amplitude of the optical field inside the cavity, Δ is the detuning of the laser from the optical cavity resonance (ω_L-ω_C), G (defined as $-\delta\omega_c/\delta\ell$ where $\delta\ell$ is the change in cavity length) is the optomechanical coupling factor, κ is the total optical loss rate, κ_{ex} is the coupling rate of the optical cavity to the external environment, i.e. the tapered fiber, and s is the normalized electric field amplitude of the input laser drive. The transmitted field amplitude is given by

$$a_{out} = s - \sqrt{\kappa_{ex}}a \qquad (3)$$

is monitored with a photodetector. When the laser drive scans across a resonance mode of the optical cavity, we measure a transmission dip as shown in Fig. 3. The mechanical mode is modeled as a driven simple harmonic oscillator in equation *(2)*. In our setup, the driving force comes from the piezoelectric stage of the sample. From the equations it is clear that the mechanical motion modulates the optical field amplitude and this is picked up as an intensity modulation of the detected transmission at the photodetector. This measurement is performed using a network analyzer in an S_{21} configuration with port 1 being the piezo drive and port 2 being the photodetector signal (Fig. 2).

Fig. 4 shows the spectrum of the mechanical signal measured using this scheme. The majority of the peaks shown are lip flapping, radial and rocking modes of the GOBLiT. The modes of interest (labeled 1 and 2) are the n=2 and n=3 wineglass modes of the GOBLiT. This measurement was carried out in air, with the quality factor of the n=2 wineglass mode calculated to be 206. The wineglass modes were identified with a spectral scan of the resonance frequencies of the GOBLiT using a Laser Doppler Vibrometer (LDV) setup followed by 2D surface scan by raster scanning the LDV laser over the entire device to map out each mode. This is used to confirm the actual mode shape and enables the characterization of the spectrum for mode identification. Fig. 5 shows the spectral scan of the LDV with 2D maps of the modes of interest as insets.

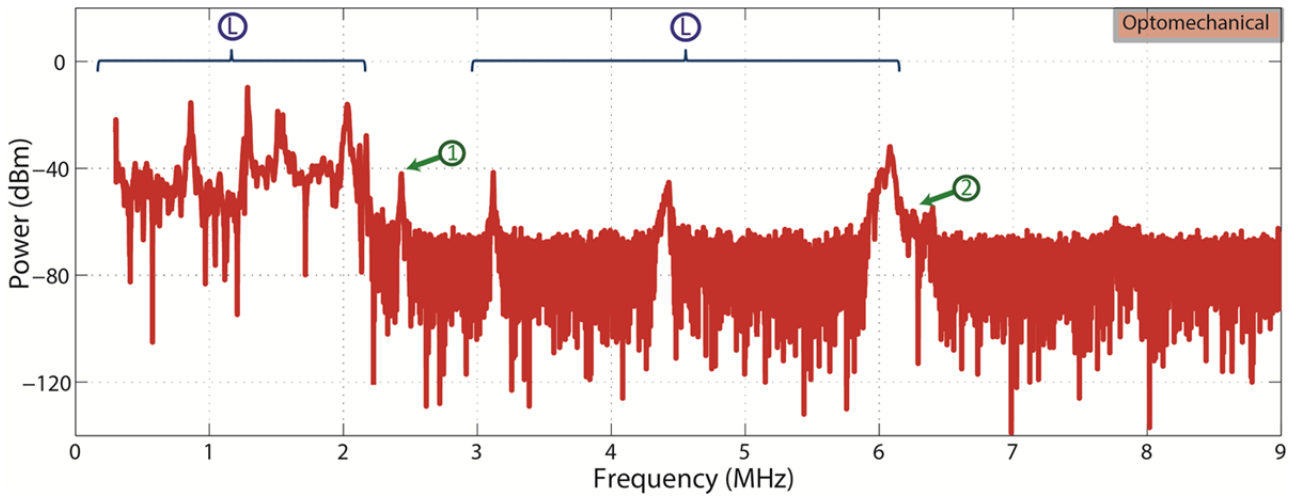

Figure 4: Mechanical frequency response measured using a fiber taper. Modes of interest are labeled 1 and 2 for the n=2 and n=3 wineglass resonance modes, respectively. Resonance modes marked with L refer to modes attributed to the lip or bowl extensional/tilting modes.

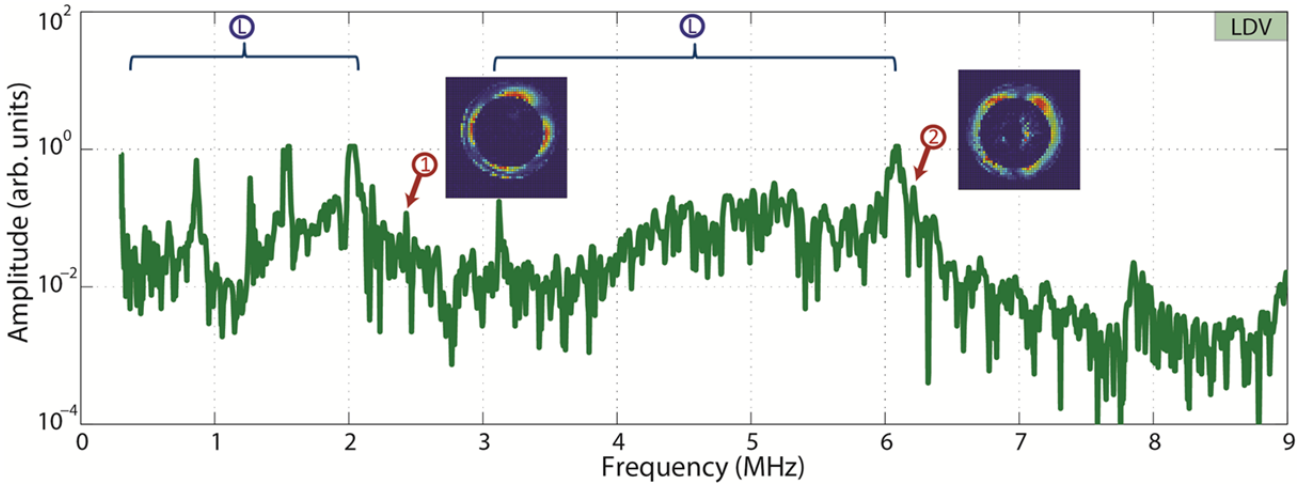

Figure 5: Mechanical response of GOBLiT measured using the LDV sweep. Modes labeled 1 and 2 are the n=2 and n=3 wineglass modes of the GOBLiT and the insets are the corresponding 2D scan of the mode profile carried out using the LDV.

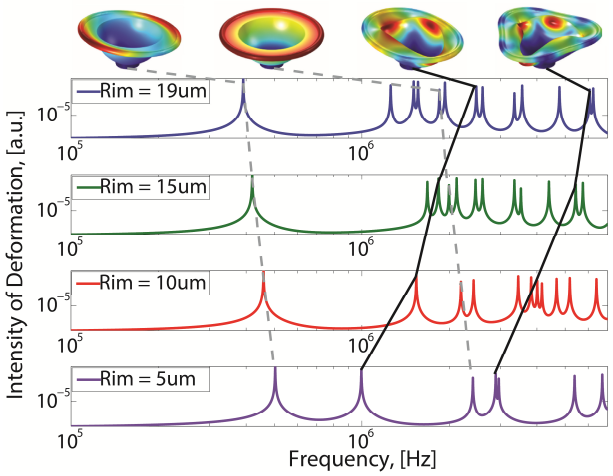

Figure 6: COMSOL simulation of mechanical modes of the GOBLiT with decreasing lip width. Solid lines track the resonance frequency of the n=2 and n=3 wineglass modes and it can be seen that they decrease as the lip width decreases. At the same time, the resonance frequencies of all the lip flapping modes increase, leaving behind the mode of interest. The device simulated matches the dimensions of the structure from Fig.1g with a radius of 60μm and oxide thickness of 1.1μm.

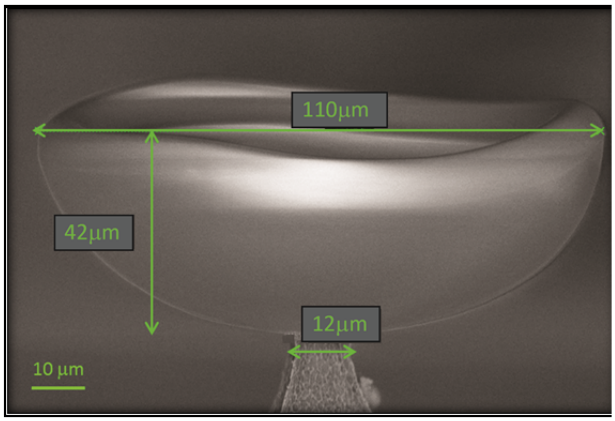

Figure 7: SEM of a GOBLiT with fully reflowed lip.

To understand the dependence of all the modes on the various dimensions of the device, we carried out simulations in COMSOL. As expected, the majority of modes are primarily dependent on the width of the lip, as shown in Fig. 6. As the width of the rim is reduced, the resonance frequencies of the parasitic modes increase and are separated from the n=2 wineglass mode.

To obtain smaller lip width of the GOBLiT, we modified the fabrication process. At the step of partial release in Fig. 1(d), we continue the XeF_2 etch until the edge of the rim meets the bowl.

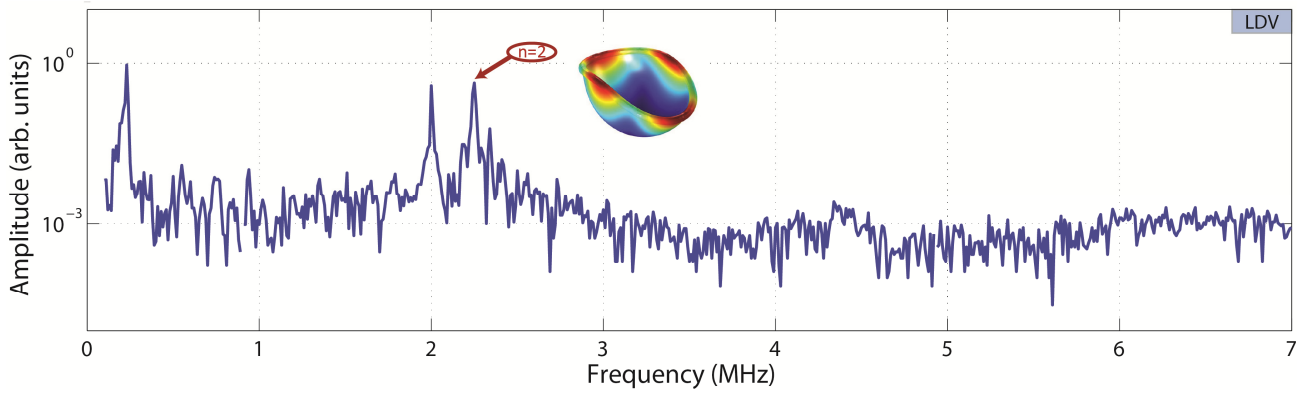

Figure 8: Mechanical response of a GOBLiT without an overhanging lip measured using LDV.

This allows us to reflow the oxide further in towards the rim, moving the lip flapping modes to higher frequencies, or completely eliminating them. Fig. 7 shows an SEM image of such a GOBLiT showing the fully reflowed lip. Fig.8 presents the measured LDV frequency response of the device showing a cleaner spectrum in the absence of lip flapping modes. However, we were not able to perform the analogous optomechanics measurement due to uneven reflow of the rim as seen in Fig. 7. This highlights the importance of the need for a symmetric undercut etch as the subsequent reflow step is critically dependent on the undercut.

CONCLUSION

We have demonstrated the first guided light measurement of the mechanical modes of a GOBLiT structure. By modifying the fabrication process we were able to incorporate a toroidal optical cavity on the GOBLiT for higher optical quality factor, as well as reduced parasitic mechanical modes of vibration in the region of our modes of interest. The effect of the width of the lip was simulated and experimentally measured using LDV. Continued improvement of the fabrication process will allow pure optical drive and sense of the mechanical modes, and make viable the use of this structure as a fully optomechanical sensor.

ACKNOWLEDGEMENT

The authors would like to thank DARPA MRIG program for sponsoring this research. The devices were fabricated in the Cornell Nanoscale Science and Technology Facility (CNF). Travel support has been generously provided by the Transducer Research Foundation.

REFERENCES

[1] A Schliesser, G Anetsberger, R Rivière, O Arcizet and T J Kippenberg, “High-sensitivity monitoring of micromechanical vibration using optical whispering gallery mode resonators”, New J. Phys. 10 095015 (2008).

[2] D. M. Rozelle "The hemispherical resonator gyro: From wineglass to the planets (AAS 09-176)", Proc. 19th AAS/AIAA Space Flight Mechanics Meeting, pp.1157 -1178 2009.

[3] L. Sorenson, P. Shao, and F. Ayazi, "Effect of thickness anisotropy on degenerate modes in oxide micro-hemispherical shell resonators" IEEE International Conference on Micro Electro Mechanical Systems (MEMS 2013), Taibei, Taiwan, Jan. 2013, pp. 169-172.

[4] M.L. Chan ,J. Xie, P. Fonda, H. Najar, K. Yamazaki, L. Lin and D.A. Horsley, “Micromachined Polycrystalline Diamond Hemispherical Shell Resonators” Hilton Head 2012 Solid-State Sensors, Actuators & Microsystems Workshop, Hilton Head Island, SC, Jun. 3-7, 2012.

[5] Doruk Senkal, Christopher R. Raum, Alexander A. Trusov, Andrei M. Shkel, “Titania Silicate / Fused Quartz Glassblowing for 3-D Fabrication of Low Internal Loss Wineglass Micro-structures”, Solid-State Sensors, Actuators, and Microsystems Workshop 2012, Hilton Head Island, South Carolina, USA, June 3-7, 2012.

[6] L. C. Fegely, D. N. Hutchison, S. A. Bhave, "Isotropic Etching of 111 SCS for Wafer Scale Manufacturing of Perfectly Hemispherical Silicon Molds”, Transducers ‘11, pp. 2295-2298, Beijing, China, 2011.

[7] A. Heidari, M.-L. Chan, H.-A. Yang, G. Jaramillo, P. Taheri-Tehrani, P. Fonda, H. Najar, K. Yamazaki, L. Lin, D.A. Horsley, “Micromachined Polycrystalline Diamond Hemispherical Shell Resonators”, Transducers ‘13, pp. 2415-2418, Barcelona, Spain, 2013.

[8] T.J. Kippenberg and K.J. Vahala, "Cavity Opto-Mechanics", Optics Express 15, 17172 (2007).

CONTACT

*Ajay K. Bhat, tel: +1-607-220-7146; akb96@cornell.edu

MICROSYSTEM FOR PARTICLE COUNTING AND SIZING WITH TUNABLE SENSITIVITY AND THROUGHPUT

T.E. Winkler[1], H. Ben-Yoav[1], D.L. Kelly[2], and R. Ghodssi[1]*
[1]University of Maryland, College Park, Maryland, USA
[2]University of Maryland, Baltimore, Maryland, USA

ABSTRACT

We present the first comprehensive study of integrating hydrodynamic focusing to provide tunable sensitivity and throughput in impedance cytometry. This interplay has never been investigated with respect to particle counting and sizing performance. Our microfluidic lab-on-a-chip (LOC) differs from previous designs in the added tunability while featuring simpler fabrication. Here, we demonstrate a 2.7-fold increase in sensitivity with hydrodynamic focusing. Systematic studies of the coupling between integrated LOC components enable optimal utilization of microsystem capabilities.

INTRODUCTION

Characterization of large quantities of individual particles is highly relevant to multiple fields, particularly blood analysis [1]. A simple cell count is useful, e.g. to diagnose anemia, but the utility of such measurements increases significantly with the ability to also determine size, surface markers, and interior composition. Applications range from CD4 T-cell monitoring in cases of HIV to stem cell characterization in research. The current gold standard for such measurements is bulky benchtop flow cytometers. These rely on a focused stream of blood cells being subjected to multiple analysis methods, involving fluorescent labels for population-specific surface antigens (e.g. CD4, CD8, ...), laser light scattering, and absorbance, or impedance measurements. Flow cytometers allow for highly accurate analysis, but rely on labels and complex optics. These factors are major barriers in bringing this technology to the point of care (POC), where it would benefit patients as well as physicians by providing immediate results and increasing accessibility, especially in remote locations [2].

The impedance measurement aspect, however, is ideally suited for integration into small, portable lab-on-a-chip (LOC)-type devices, with electronics having a long history of miniaturization. The approach in its most basic form applies the Coulter principle [1]. As a particle (or cell) of diameter d_p passes through an aperture of diameter D_A between two chambers, it causes a change in impedance ΔZ measured between two electrodes on either side of the aperture. A first-order approximation for this change is $\Delta Z = \frac{4\rho_m d_p^3}{\pi D_A^4}$, where ρ_m is the resistivity of the electrolyte. Consequently, this signal can be used to differentiate particles based on their size. By extension into the alternating current domain, this allows for probing more generalized changes in dielectric properties caused by particles within the interaction volume [3].

Multi-frequency impedance cytometry was presented as an attractive method for multi-dimensional single-cell analysis in LOC systems [4], [5]. However, current implementations still suffer from limited resolution, and employ multi-layer fabrication processes. Here, we propose an LOC combining impedance cytometry with hydrodynamic focusing for adjustable throughput (sample volume/time) and improved performance. This relies on constricting the sample flow through a virtual aperture (*VA*) of a non-conductive fluid. In contrast to physical channel confinement, this is inherently more versatile and limits the danger of channel clogging. While flow focusing has been utilized to enhance the performance of coulter counter-type devices, to date no systematic study has been conducted on the interplay between flow ratios, particle sizing sensitivity, and throughput [6]. It is only through such studies, both in models and experiments, that optimal utilization of microsystem capabilities becomes possible.

MATERIALS AND METHODS

Design

We propose a simple design, shown in Figure 1, comprising two physical layers. The first layer incorporates four pairs of microelectrodes for impedance measurements (25 µm wide, 25 µm gap). The microfluidic channels constitute the second layer, with a cross-section of 75×20 µm² (width × height).

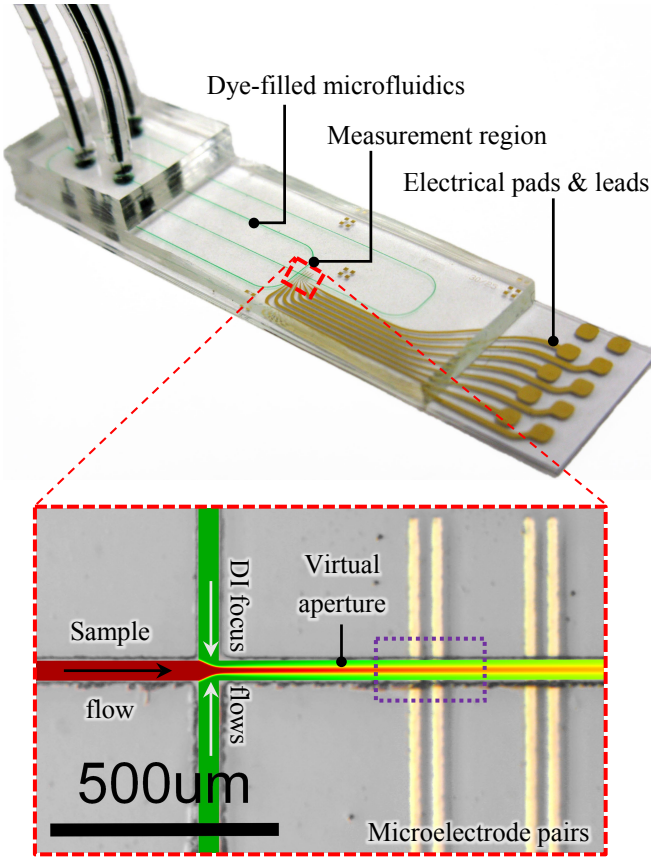

Figure 1: Top: Photograph of our impedance cytometry LOC. The microfluidic channels were filled with dye to enhance visualization. Bottom: Micrograph of the measurement region highlighted by the red dashed box in the photograph. Hydrodynamic focusing is schematically illustrated by overlaid FEM simulation for a ratio of sample (particles in electrolyte; red) to DI-H_2O focus (green) flows of FR = 1:1. The virtual aperture effect is conserved downstream, where impedance is measured across the gold microelectrode pairs. The purple dotted box indicates the region simulated by electrodynamic FEM (Figure 2).

9781940470016/HH2014/$25©2014TRF
DOI 10.31438/trf.hh2014.67

Solid-State Sensors, Actuators and Microsystems Workshop
Hilton Head Island, South Carolina, June 8-12, 2014

We made extensive use of finite element modeling (FEM), in combination with equivalent circuit modeling, to guide the design process, as described below. Critical parameters such as channel cross-section and electrode gap were chosen based on model optimization.

Fabrication

Gold (200 nm; on 20 nm chrome adhesion layer) was deposited on a pyrex wafer by sputtering. We transferred the electrode pattern through contact photolithography in Shipley 1813 positive photoresist, followed by wet etching. The wafer was diced, and the chips were cleaned by immersion piranha solution (sulfuric acid and hydrogen peroxide, 3:1 ratio) to remove any organic contaminants.

For the microfluidic layer, a mold was created using SU-8 2015 negative photoresist patterned on silicon using contact photolithography. Using this master, we cast channels from poly(dimethylsiloxane) (PDMS). After thermal curing at 60 °C, the PDMS was diced and 2 mm diameter fluidic connections were punched.

We utilized contact profilometry and optical microscopy to confirm that all dimensions were within 10% of the design parameters. A combination of oxygen plasma and 80 °C thermal treatment was applied to irreversibly bond both layers for individual devices.

Modeling

Finite element modeling (FEM) was performed in COMSOL Multiphysics (COMSOL, Inc.; Palo Alto, CA), using the MEMS and Microfluidics packages.

The 2D hydrodynamic model considered a slow-diffusing species (particles) and a fast-diffusing species (ions) introduced through a center sample channel, focused symmetrically by deionized water (DI-H_2O) flows. A representative simulation is overlaid on the micrograph in Figure 1 (inset). The main model outputs of interest are the cross-sectional concentration profiles 125 µm downstream from the flow focusing inlets – the respective full width at half maximum (*FWHM*) for the ions can be considered equivalent to the *VA* width.

The 3D electrodynamic model simulates a particle of radius r, conductivity σ, and permittivity ε, suspended in a section of microfluidic channel between two coplanar electrodes. To approximate the impact of hydrodynamic focusing, we incorporate two distinct environments (apart from the particle) within the channel segment – electrolyte in the center at a certain width corresponding to *VA*, DI-H_2O towards the sides. A sample model geometry is displayed in Figure 2. The model output is the change in impedance $|\Delta Z|$ measured across electrodes between particle and no-particle conditions.

Experiments

The fabricated LOCs were connected to syringes using Tygon tubing (Cole-Parmer; Vernon Hills, IL). Constant flow was provided through syringe pumps (KDS230 (KD Scientific, Inc.; Holliston, MA), Genie Plus (Kent Scientific Corporation; Torrington, CT), NE-300 (New Era Pump Systems, Inc.; Farmingdale, NY)). Admittance measurements for model verification were done using a VSP-300 potentiostat (Bio-Logic; Claix, France). Impedance cytometry data was recorded via LabView utilizing an E4980A Precision LCR Meter (Agilent; Santa Clara, CA). The background signal was determined through MATLAB (MathWorks, Inc.; Natick, MA) robust local regression smoothing of the raw data, the signal peaks using a peak finding algorithm. Population averages were calculated using histogram peak fits in OriginPro (OriginLab Corporation; Northampton, MA).

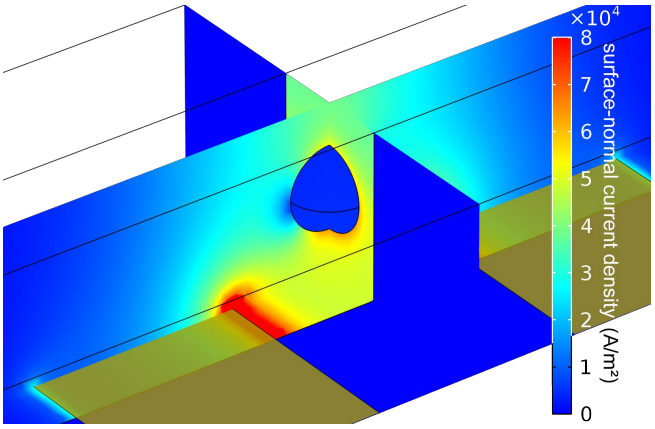

Figure 2: Exemplary electrodynamic COMSOL simulation result with particle (center; blue sphere) suspended in channel between two electrodes (bottom; gold rectangles). This matches the region highlighted by the purple dotted box in the inset to Figure 1. The colors correspond to the surface-normal current density from blue (low) to red (high), clearly illustrating the particle (no conduction), the focused electrolyte in the center of the channel (green, good conduction), and the virtual aperture of pure water on either side (blue, no conduction).

Prior to use, the LOCs were rinsed with Fetal Bovine Serum (FBS; Life Technologies; Carlsbad, CA) to reduce PDMS hydrophobicity. Polystyrene particles (r = 3 µm and 5 µm; sulfate-type) were purchased from Life Technologies (Carlsbad, CA) and suspended in phosphate-buffered saline (PBS; 1x from tablet; Sigma-Aldrich; St. Louis, MO). To reduce settling velocity through density matching, sucrose (Sigma-Aldrich; St. Louis, MO) was added to 14% w/v. All solutions were based on DI-H_2O (ρ = 18 Ωcm).

RESULTS AND DISCUSSION

Hydrodynamic Model and Validation

The flow rates are the main external parameters to control the *VA* width, the critical parameter for impedance cytometry performance. To elucidate their correlation, we utilize hydrodynamic FEM to determine the ionic *FWHM* for a range of flow ratios (*FR*) of PBS-based sample to DI-H_2O focus. The

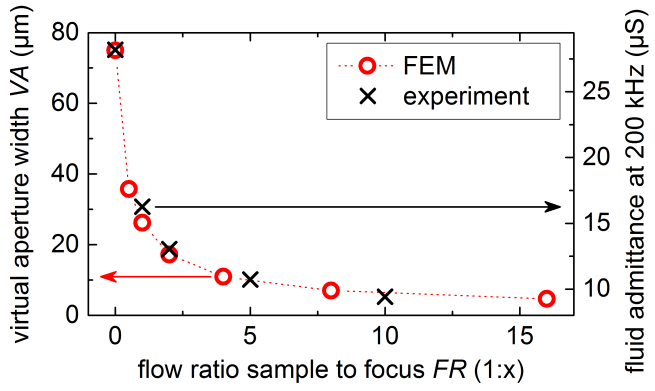

Figure 3: FEM simulation showing the dependence of VA width on FR (red circles). Experimental verification through fluid admittance measurements in the LOC (black crosses).

results, plotted in Figure 3, are in qualitative agreement with theory [7]. As expected intuitively, the virtual aperture width decreases drastically as flow focusing is introduced, with the effect saturating at high flow ratios. The behavior is independent of flow rate, at least in the laminar flow regime.

To verify these results in our LOC, we introduced a pure PBS sample flow (10, 20, 50, 100 µl/h) and DI-H2O focus flows (100 µl/h combined). To achieve FR = 0, PBS was substituted for the DI-H2O. We measured the admittance of the fluid across electrodes, which at 200 kHz is dominated by ionic conduction. Thus, this parameter is expected to linearly correlate with the ionic FWHM. Indeed, the overlaid experimental data in Figure 3 aligns well with model results. The fact that the measured trend is toward a non-zero value at high FR can be attributed to parasitic currents in the real-world instrument-LOC circuit.

Electrodynamic Model

To illustrate the advantages of hydrodynamic focusing in impedance cytometry, we initially rely on electrodynamic FEM. In Figure 4, we display the relative $|\Delta Z|$ (*i.e.*, as a percentage of the empty-channel Z) induced by an $r = 5$ µm particle for a range of VA widths. We found a frequency of $f = 200$ kHz to be most sensitive to resistive properties, and thus r, and this was used throughout this work. The plot shows data for channel widths of 25 µm and 50 µm, revealing the signal is independent of the actual channel width (memory constraints prevented simulations for 75 µm width). Therefore, at the chosen f, the VA is expected to function identical to a physical constriction. As expected, the relative $|\Delta Z|$ induced by an $r = 5$ µm particle increases significantly with decreasing VA. Specifically, reducing the aperture from 50 µm to 5 µm enhances the signal 10-fold from $|\Delta Z| = 1.8\%$ to $|\Delta Z| = 18\%$. At very low $VA \leq r$, the signal saturates, which can be attributed to the fact that in this regime, only part of the particle is in electrolyte and thus contributing to the signal. We expect that in reality, a boundary layer of PBS would surround the particle, which would alter the results. However, considering the underlying approximation of a well-defined boundary between PBS and DI-H_2O in this model, the additional error introduced by the omitted particle boundary layer is likely negligible.

Integrated Lab-on-a-Chip

In Figure 5, we illustrate the impedance-based particle counting principle using our LOC with a mixture of both $r = 3$ µm and 5 µm bead populations at a sample flow of 45 µl/h, $FR = 1{:}0$.

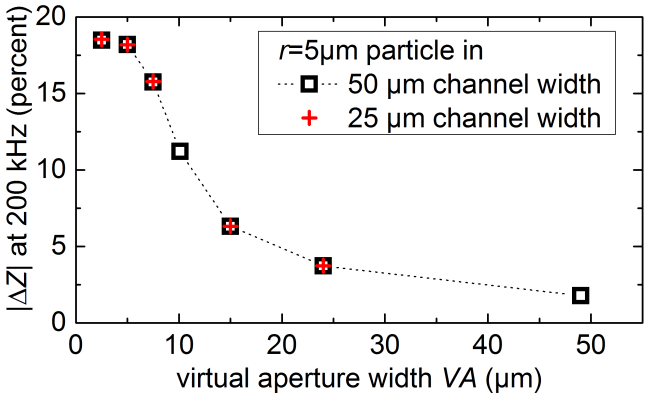

Figure 4: FEM simulations predict flow focusing can significantly enhance impedance-based particle measurements. The effect is independent of actual channel width (black squares, red plusses).

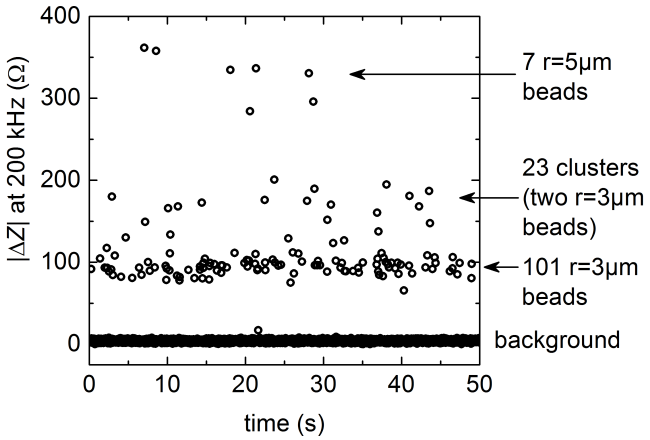

Figure 5: Exemplary experimental $|\Delta Z|$ data recorded using LOC with mixture of $r = 3$ µm and 5 µm beads at $FR = 1{:}0$.

The MATLAB-processed data shows distinct peaks in $|\Delta Z|$ corresponding to particles passing between the electrodes. Furthermore, three distinct populations become apparent, corresponding in order of increasing signal to 3 µm beads ($|\Delta Z| = 94 \pm 9$ Ω), clusters of two 3 µm beads ($|\Delta Z| = 162 \pm 23$ Ω), and 5 µm beads ($|\Delta Z| = 329 \pm 29$ Ω). While clusters of three or four 3 µm beads are statistically unlikely, their mis-identification as a 5 µm bead cannot be ruled out in this data due to their similar volume. Although the 3 µm bead population signal is well-defined, we note a larger spread in the cluster signals, which is in line with their non-spherical shape – based on orientation relative to the electrodes, the signal magnitude is expected to vary, as the electric field is not isotropic. In future work with particle mixtures, this may enable more definitive differentiation between clusters of small particles and larger single particles through analysis of the transient signal during passage between the electrodes.

To determine the impact of hydrodynamic focusing on sensitivity of our device, we utilized single-population samples of beads, and varied FR while keeping the total flow rate (sample + focus) constant at 45 µl/h. From histograms based on data

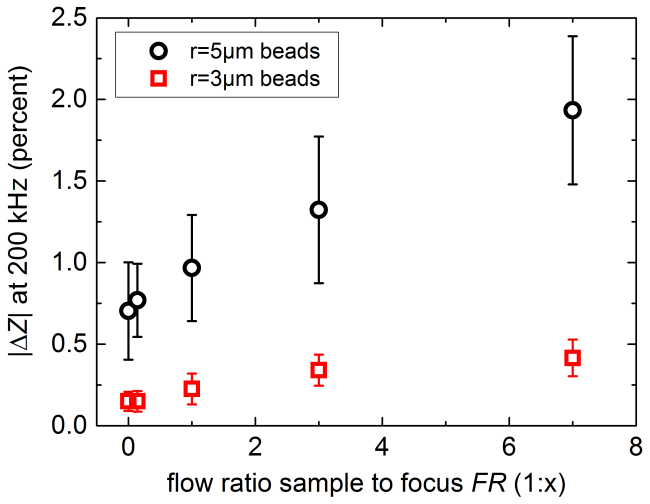

Figure 6: Experimental $|\Delta Z|$ recorded using LOC for both $r = 3$ µm and 5 µm beads increases significantly with increased FR, as does the relative separation between those populations.

analogous to that shown in Figure 5, we produce Figure 6, plotting the average $|\Delta Z|$ for separate bead populations as a function of *FR*. The graph indicates up to 276% enhanced size-based differentiation, from $\Delta|\Delta Z| = 0.55\%$ to $\Delta|\Delta Z| = 1.52$. Underlying this are overall increases in $|\Delta Z|$ by 277% and 275% for 3 µm and 5 µm beads, respectively. These numbers highlight the tunable sensitivity enabled through our approach.

While the trend agrees with modeling (Figure 4), the magnitudes are lower than predicted. Specifically, at *FR* = 1:7, modeling predicts $VA \approx 8$ µm (Figure 3), and in consequence $|\Delta Z| \approx 15\%$ for $r = 5$ µm beads (Figure 4). This almost order-of-magnitude difference compared to experimental results warrants further investigation. One potential explanation is the aforementioned model assumption of well-defined boundaries between PBS and DI-H_2O in the electrodynamic FEM. However, this is unlikely to be solely responsible for the discrepancy. Experimental causes such as parasitic capacitances, which become more dominant at high absolute *Z* (correlating with higher *FR*), will need to be explored.

Overall, separation efficiency increases with *FR*; at the same time, the sample throughput (equaling sample input flow rate) in our experiments decreases (as total flow is kept constant). However, the sample flow rate is inherently independent from *FR*. In the laminar flow regime, sensitivity and throughput are thus decoupled in our LOC, enabling tailoring of these parameters to the specific experimental needs.

CONCLUSIONS

In conclusion, our LOC provides a simple yet efficient platform for impedance cytometry. We utilize it to systematically study the integration of hydrodynamic focusing. Thereby, we demonstrate a 2.7-fold improvement in signal amplitude, as well as a size-based population separation enhancement of similar magnitude. Compared to physical channel constriction, this approach offers a distinctly lower risk of clogging, and provides tunable, rather than static, sensitivity and throughput. Extensive modeling provides the underpinning for our design and corroborates experimental results such as the relationship between flow ratios and virtual apertures. It also provides guidance for future investigations, as simulations predict even higher performance increases due to flow focusing.

Our design allows for straightforward expansion to multi-frequency signal recording. This will provide high-resolution multi-dimensional particle characterization towards an integrated microsystem capable of full differential blood cell counting. Furthermore, our approach illustrates the benefits of model-guided design as well as in-depth study of systems interplay in LOC devices. With many examples of exciting LOC technologies – sensors, blood handling components, microfluidic components – published in the literature, we believe it is only through such studies that they can be optimally realized in integrated POC microsystems.

ACKNOWLEDGEMENTS

The authors would like to thank the Robert W. Deutsch Foundation and the Maryland Innovation Initiative for financial support. The authors likewise appreciate the support of the Maryland NanoCenter and its FabLab. Travel support has been generously provided by the Transducer Research Foundation.

REFERENCES

[1] K. Kottke-Marchant and B. Davis, *Laboratory Hematology Practice*, John Wiley & Sons, Ltd, Chichester, 2012.

[2] H. Craighead, "Future lab-on-a-chip technologies for interrogating individual molecules", Nature, 442, 387–393 (2006).

[3] T. Sun and H. Morgan, "Single-cell microfluidic impedance cytometry: a review", Microfluidics and Nanofluidics, 8, 423–443 (2010).

[4] D. Holmes, D. Pettigrew, C.H. Reccius, J.D. Gwyer, C. van Berkel, J. Holloway, D.E. Davies, and H. Morgan, "Leukocyte analysis and differentiation using high speed microfluidic single cell impedance cytometry", Lab on a Chip, 9, 2881 (2009).

[5] X. Han, C. van Berkel, J. Gwyer, L. Capretto, and H. Morgan, "Microfluidic Lysis of Human Blood for Leukocyte Analysis Using Single Cell Impedance Cytometry", Analytical Chemistry, 84, 1070–1075 (2012).

[6] X. Xuan, J. Zhu, and C. Church, "Particle focusing in microfluidic devices", Microfluidics and Nanofluidics, 9, 1–16 (2010).

[7] G.-B. Lee, C.-C. Chang, S.-B. Huang, and R.-J. Yang, "The hydrodynamic focusing effect inside rectangular microchannels", Journal of Micromechanics and Microengineering, 16, 1024 (2006).

CONTACT

*R. Ghodssi, tel: +1-301-405-8158; ghodssi@umd.edu

OPTOMECHANICAL VISCOMETER

K. Han[*]*, K. Zhu, and G. Bahl*
Mechanical Science and Engineering, University of Illinois at Urbana Champaign, IL, USA

ABSTRACT

Recently, the first microfluidic optomechanical device driven by radiation pressure – and capable of operating with non-solid states of matter (viscous fluids, bioanalytes) – was demonstrated. Here we show that the vibrational noise spectrum of the device mechanical modes enables quantification of the viscosity of fluids inside the device. A linear relation between the spectral linewidth and square root of viscosity is predicted and experimentally measured in the low viscosity regime. For the first time, an all-optical sensor of liquid viscosity using a microfluidic optomechanical resonator is demonstrated. Our result is a step towards performing high-frequency studies of fluids and boundary layer viscosities, and performing high-throughput viscoelastic measurements on flowing cells.

INTRODUCTION

The optical and mechanical modes of high-Q resonant systems can be parametrically coupled through optical radiation-pressure induced mechanical instabilities [1-3]. Ultra-sensitive optomechanical sensors based on this concept have been demonstrated for measuring acceleration [4,5], mass [6,7], and atto-Newton forces [8,9], but are all solid-state techniques. Recently, opto-mechano-fluidic resonators (OMFRs) were demonstrated [10] that enable optomechanical sensing with liquids [11] and gases [12]. In OMFRs, a liquid is confined inside the resonator, rather than outside it, preventing acoustic energy from being lost [13]. The optically actuated mechanical vibrational modes of OMFRs are able to penetrate into the fluid within [10,11] and permit an opto-mechanical interface to the fluid. Furthermore, OMFRs vibrational modes extend to the GHz regime, which is important to study the viscoelastic nature of the fluid, since such nature becomes prominent when the frequency is high. OMFRs can thus provide a novel path towards high-resolution analysis of the viscoelastic properties of fluids and bioanalytes. In this work we demonstrate an experimental system for optomechanically measuring the dynamic viscosity, μ, of various test fluids.

METHODS

The fabrication of OMFRs (Fig. 1a) has been reported in [10]. Briefly, fused-silica capillary preforms are heated and softened by means of high-power CO_2 lasers and then drawn linearly into microcapillaries. Modulation of the laser power varies the capillary diameter creating "bottle"-shaped OMFRs. We test two devices in this work - "Device 1" with 238 μm widest diameter and 21 μm wall thickness, and "Device 2" with 150 μm widest diameter and 13 μm wall thickness. One end of the device is left open while the other is connected to a syringe by which analytes can be infused (Fig. 1d). The sensing volume needed in Fig 1d is about 20 nl, and can be brought lower by reducing the capillary diameter and modifying fabrication parameters.

Continuous-wave 1550 nm laser light is coupled into the optical whispering-gallery modes (Q-factor ~ 10^7, Fig. 1b) of the OMFR through a tapered optical fiber. The radiation pressure of light actuates eigenmechanical oscillations (Q-factor ~ 10^3-10^4, Fig. 1c) through the optomechanical parametric instability [11], allowing the measurement of density of infused fluids [10,11]. Mechanical modulation of the device geometry generates optical sidebands of the input light (Fig. 1d). We electronically measure the noise spectrum (Lorentzian lineshape) of the mechanical mode using low input optical power, by observing the beating between input and scattered light on a photodetector (Fig. 1d). Here, $\Omega_{mech} = 8$ MHz and $\Omega_{mech} = 13$ MHz vibrational modes are selected for Device 1 and Device 2, respectively, corresponding to high-order wineglass modes (Fig 1c). The mechanical losses in these hybrid shell-fluid modes are obtained through optical measurement of their stochastic thermal fluctuations (Fig. 2b,c). To calibrate the optomechanical viscometers we use four viscosity standard oils (Cannon Instrument Company – Table 1) whose densities are closely matched so as to minimize frequency variations through effective mass change.

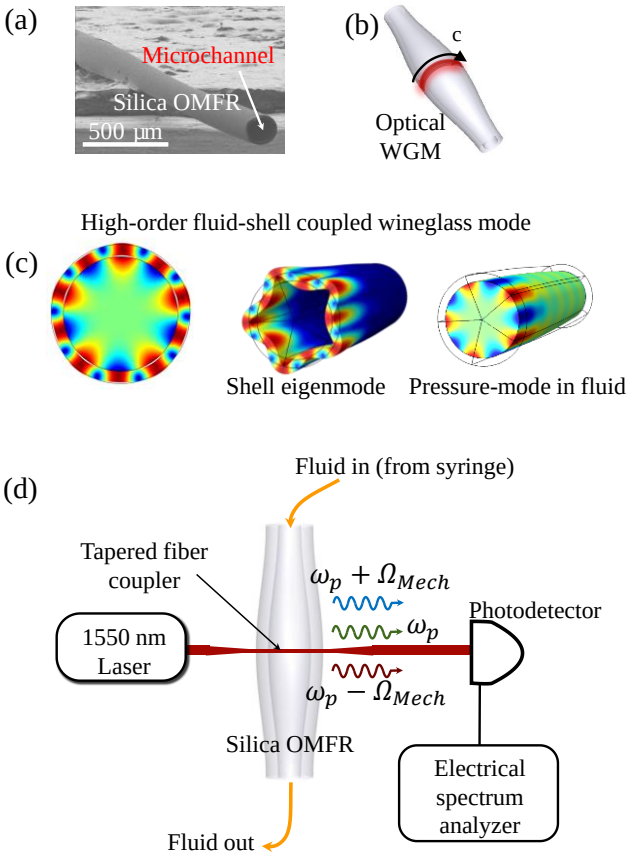

Figure 1: (a) SEM of a fused-silica opto-mechano-fluidic resonator (OMFR) based viscometer. (b) Ultra-high-Q circumferential optical whispering gallery mode (WGM) of the OMFR. (c) Multiphysical simulation of solid OMFR shell and coupled pressure waves in fluid, for a high-order wineglass mode (8 MHz - Device 1 and 13 MHz - Device 2); (d) Light is coupled to ultra-high-Q optical WGMs through a tapered fiber, enabling extremely sensitive measurement of the vibrational noise spectrum. Fluid viscosity affects damping of the shared fluid-shell mechanical modes.

9781940470016/HH2014/$25©2014TRF
DOI 10.31438/trf.hh2014.68

Solid-State Sensors, Actuators and Microsystems Workshop
Hilton Head Island, South Carolina, June 8-12, 2014

RESULTS AND DISCUSSION

Because of liquid entrainment, viscous damping occurs at the solid-fluid interface [14] caused by both shear and normal motion of the fluid relative to a vibrating plate (as in the case of the OMFR shell). For thin shells or plates, the damping is primarily caused by the shear motion of the fluid relative to the resonator wall. The attenuation coefficient due to viscous damping, α, is proportional to $\sqrt{\mu}$ at low values of viscosity [14,15]. The attenuation coefficient saturates due to the viscoelastic nature of the fluid at high viscosity. Using Maxwell's model [14], a critical viscosity value, μ_c, which separates low and high viscosity regimes, can be determined by:

$$\mu_c = \tau G_\infty \tag{1}$$

$$2\pi\Omega_{mech}\tau = 1 \tag{2}$$

where τ is the viscoelastic relaxation time in the liquid and G_∞ is the high-frequency elastic rigidity modulus. Given a typical G_∞ value of 1 GPa [14], the μ_c for a 10 MHz device is 1.6×10^9 cP (centipoise), indicating that our experiment is well within the linear regime. And the relationship between attenuation coefficient, α, and Q_{visc} is given by:

$$Q_{visc} = \pi\Omega_{mech}/(v\alpha) \tag{3}$$

where v is the speed of sound in the fluid. Since the intrinsic Q-factor of the shell mechanical modes is very high, the acoustic energy loss mostly occurs from viscous damping associated with the fluid, and partially from the tapered fiber that is contact with the device. Q_{visc} can thus be measured.

$$\frac{1}{Q_{measured}} = \frac{1}{Q_{visc}} + \frac{1}{Q_{taper}} + \frac{1}{Q_{other\ sources}} \tag{4}$$

We know that the linewidth of the vibrational spectrum is inversely proportional to Q by:

$$Q_{measured} = \Omega_{mech} \,/\, Linewidth \tag{5}$$

We plot the experimentally measured mechanical mode linewidth vs root-viscosity $\sqrt{\mu}$ in Fig. 2a for both devices. The attenuation increases linearly at first and saturates in the end. Since the viscosity values tested here fall well in the low viscosity regime, we suspect this saturation is caused by the taper contact. Each device has multiple vibrational modes that can be used in their linear regions as a viscometer.

Table 1. Experimentally measured mechanical frequencies of the acoustic resonant modes, and properties of the calibration viscosity oils.

Test oil sample	Density (g/cc)	Dynamic viscosity (cP)	Device 1 frequency (MHz)	Device 2 frequency (MHz)
N2	0.76	2.17	8.29	12.9
N4	0.79	5.25	8.37	13.4
S6	0.87	9.57	8.64	13.8
N44	0.82	90.2	8.42	13.1

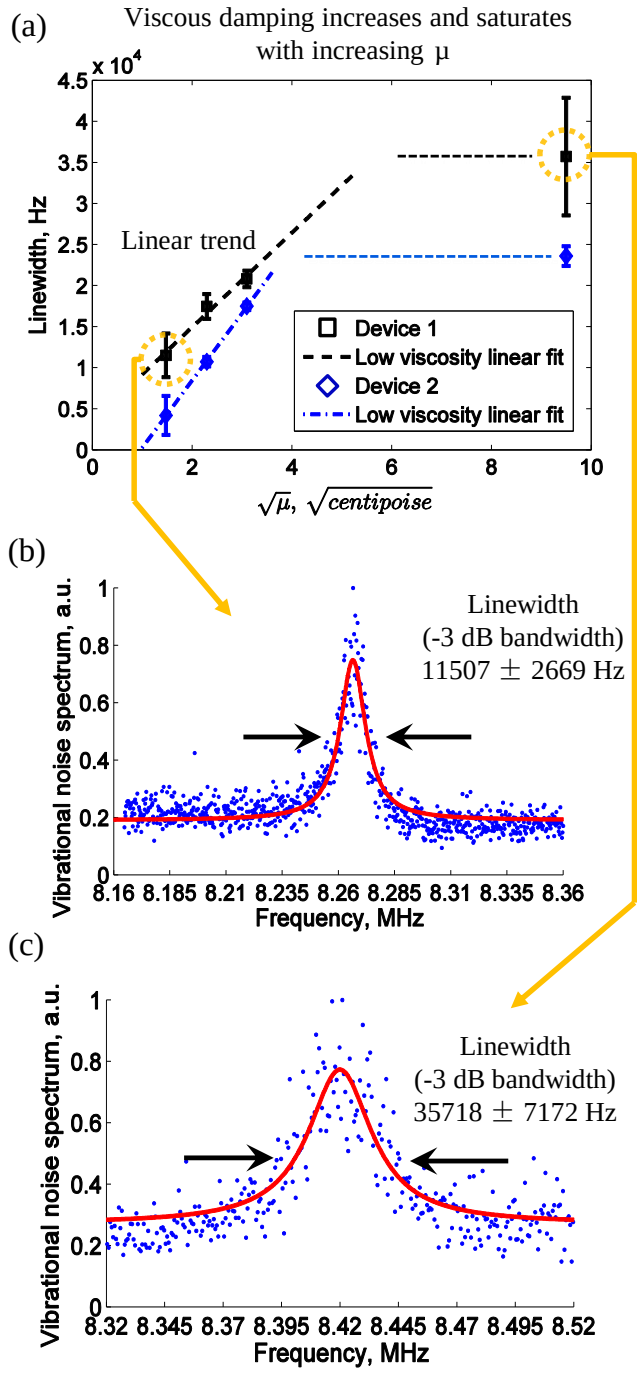

Figure 2: Calibration and sensing with optomechanical viscometers. (a) Measured linewidth of selected mechancial modes on Device 1 and Device 2 operating with viscosity standard oils. (b) Vibrational noise spectrum of 8 MHz mode on Device 1 with N44 viscosity oil, and (c) N2 viscosity oil.

Viscometer sensitivity and dynamic range are both influenced by the OMFR shell thickness. As discussed in [14], the attenuation rate is inversely proportional to the plate thickenss because a thicker plate can transmit more wave energy compared with the amount lost in viscous dissipation. Thus a thicker plate should be used for the obtaining wider sensing range, while a thinner plate should be used

for better sensitivity. However, as revealed by [16], the usage of thick shell can prevent the acoustic modes from penetrating into the liquid. On the other hand, a thin shell is more sensitive to undesired pressure effects when pumping liquids [12]. A suitable shell thickness must be sought.

CONCLUSION

Many different optical techniques – such as refractive index measurement [17], fluorescence [18], and surface enhanced Raman spectroscopy [19] – have been used together with microfluidics, enabling several unique biochemical sensor technologies. The introduction of OMFRs provides a new mechanical degree of freedom to perform such bio-analyses. Here we have demonstrated, for the first time, an all-optical sensor of liquid viscosity based on a simple microfluidic optomechanical resonator. Our result supplements the established microrheological techniques [20,21] since it neither contaminates the fluid with dispersed particles, nor does it require fluid transparency. As the device is made entirely of fused silica it is capable of operating in high temperature and harsh environments and is also biocompatible. The electronics-free fiber-optic interface further enables remote operation of this viscometer.

ACKNOWLEDGMENTS

Funding for this research was provided through a University of Illinois Startup Grant. Travel support has been generously provided by the Transducer Research Foundation. We would like to acknowledge stimulating discussions and guidance from Prof. Rashid Bashir, Prof. Randy Ewoldt, Prof. Taher Saif, and Prof. David Saintillan.

REFERENCES

[1] H. Rokhsari, T. Kippenberg, T. Carmon, and K. J. Vahala, "Radiation-pressure-driven micro-mechanical oscillator," Opt. Express, 13, 14, pp. 5293–5301, (2005).

[2] T. Carmon, H. Rokhsari, L. Yang, T. J. Kippenberg, and K. J. Vahala, "Temporal behavior of radiation-pressure-induced vibrations of an optical microcavity phonon mode," Phys. Rev. Lett., 94, 22, p. 223902, (2005).

[3] T. J. Kippenberg, H. Rokhsari, T. Carmon, A. Scherer, and K. J. Vahala, "Analysis of Radiation-Pressure Induced Mechanical Oscillation of an Optical Microcavity," Phys. Rev. Lett., 95, 3, p. 033901, (2005).

[4] A. G. Krause, M. Winger, T. D. Blasius, Q. Lin, and O. Painter, "A high-resolution microchip optomechanical accelerometer," Nat. Photonics, 6, 11, pp. 768–772, (2012).

[5] D. N. Hutchison and S. A. Bhave, "Z-axis optomechanical accelerometer," in 25th IEEE 25th Conference on MEMS, (2012), pp. 615–619.

[6] F. Liu and M. Hossein-Zadeh, "Mass Sensing With Optomechanical Oscillation," Sensors Journal, IEEE, 13, 1, pp. 146–147, (2013).

[7] F. Liu and M. Hossein-Zadeh, "On the spectrum of radiation pressure driven optomechanical oscillator and its application in sensing," Opt. Commun., 294, pp. 338–343, (2013).

[8] E. Gavartin, P. Verlot, and T. J. Kippenberg, "A hybrid on-chip optomechanical transducer for ultrasensitive force measurements.," Nat. Nanotechnol., 7, 8, pp. 509–14, (2012).

[9] Y. Liu, H. Miao, V. Aksyuk, and K. Srinivasan, "Wide cantilever stiffness range cavity optomechanical sensors for atomic force microscopy," Opt. Express, 20, 16. p. 18268, (2012).

[10] G. Bahl, K. H. Kim, W. Lee, J. Liu, X. Fan, and T. Carmon, "Brillouin cavity optomechanics with microfluidic devices.," Nat. Commun., 4, p. 1994, (2013).

[11] K. Hyun Kim, G. Bahl, W. Lee, J. Liu, M. Tomes, X. Fan, and T. Carmon, "Cavity optomechanics on a microfluidic resonator with water and viscous liquids," Light Sci. Appl., 2, 11, p. e110, (2013).

[12] K. Han, J. H. Kim, and G. Bahl, "Aerostatically tunable optomechanical oscillators," Opt. Express, 22, 2, p. 1267, (2014).

[13] T. P. Burg, M. Godin, S. M. Knudsen, W. Shen, G. Carlson, J. S. Foster, K. Babcock, and S. R. Manalis, "Weighing of biomolecules, single cells and single nanoparticles in fluid.," Nature, 446, 7139, pp. 1066–9, (2007).

[14] B. A. Martin, S. W. Wenzel, and R. M. White, "Viscosity and density sensing with ultrasonic plate waves," Sensors Actuators A Phys., 22, 1–3, pp. 704–708, (1989).

[15] D. H. Johnston, "The attenuation of seismic waves in dry and saturated rocks." Massachusetts Institute of Technology, (1978).

[16] G. Bahl, X. Fan, and T. Carmon, "Acoustic whispering-gallery modes in optomechanical shells," New J. Phys., 14, 11, p. 115026, (2012).

[17] I. M. White, H. Oveys, and X. Fan, "Liquid-core optical ring-resonator sensors," Opt. Lett., 31, 9, p. 1319, (2006).

[18] N. Ganesh, W. Zhang, P. C. Mathias, E. Chow, J. A. N. T. Soares, V. Malyarchuk, A. D. Smith, and B. T. Cunningham, "Enhanced fluorescence emission from quantum dots on a photonic crystal surface," Nat. Nanotechnol., 2, 8, pp. 515–520, (2007).

[19] S. Nie, "Probing Single Molecules and Single Nanoparticles by Surface-Enhanced Raman Scattering," Science, 275, 5303, pp. 1102–1106, (1997).

[20] T. Mason and D. Weitz, "Optical Measurements of Frequency-Dependent Linear Viscoelastic Moduli of Complex Fluids," Phys. Rev. Lett., 74, 7, pp. 1250–1253, (1995).

[21] T. A. Waigh, "Microrheology of complex fluids," Reports Prog. Phys., 68, 3, pp. 685–742, (2005).

CONTACT

*khan56@illinois.edu, 1206 W. Green St., Urbana, IL 61801

A MICROFABRICATED BIO-SOLAR CELL FOR SELF-SUSTAINABLE FIELD APPLICATIONS

*H. Lee and S. Choi**

Bioelectronics and Microsystems Laboratory, Department of Electrical and Computer Engineering, State University of New York at Binghamton, New York, USA

ABSTRACT

We report an entirely self-sustainable microfabricated bio-solar cell from which the power is generated through microbial photosynthetic and respiratory activities. The self-sustained bio-solar cell can continuously generate electricity from solar energy without the need for external input of organic matter (anolyte) and electron acceptor (catholyte). To enhance the bacterial attachment/electron coupling and solar energy capture, screen-printed carbon ink based anode was used instead of conventional transparent indium tin oxide and the anode structure was designed to face the sun while the produced protons traveled toward the cathode through perforations at the periphery of the anode. We generated a maximum power density of 90 nW/cm^2 through photosynthetic reactions of cyanobacteria, *Synechocystis sp.* PCC 6803.

INTRODUCTION

With increasing concerns about the energy crisis and global warming, solar energy is gaining more attention since it is extremely abundant and is a carbon-free, renewable energy source. However, the techniques for harnessing solar energy are limited primarily due to the semiconductor-based photovoltaic devices which have many enduring issues, including sustainability, high costs of materials and fabrication, and limited operational lifetimes. A new approach to convert solar energy into electricity has evolved with advances in microbial fuel cell technologies [1, 2].

Bio-solar cells are microbial fuel cells that utilize natural photosynthetic microorganisms such as cyanobacteria or algae. During photosynthesis, the microorganisms harvest solar energy to convert carbon dioxide and water into oxygen and carbohydrates, which will subsequently be used for their respiratory reaction, re-generating carbon dioxide and water [3]. During these reactions, electrons are released through extracellular electron transfer pathways and flow to the cathode through the external electrical circuit (Fig. 1). Simultaneously, the released protons diffuse from the anodic chamber to the cathode, where they re-combine with electrons and O_2 to re-form H_2O.

As a result, the bio-solar cell can continuously generate electricity from solar energy without additional organic matter since light energy absorbed by the photosynthetic reaction splits water and generates oxygen, protons, and electrons [4]. Only requiring sunlight, water and carbon dioxide to operate, bio-solar cells will offer advantages over current microbial fuel cells, chemical fuel cells, or photovoltaic cells, in that the catalytic microorganisms used in the devices are self-sustainable, relatively inexpensive, and capable of power production during the day and night. This system resembles the Earth's natural ecosystem, where living organisms work in conjunction with the nonliving components of their environment to offer self-sustainable and self-maintainable features as a system. To date, successive efforts have focused on demonstrating the photosynthetic electrogenic activities of various cyanobacteria or algae [1-5]. However, the metabolic pathways involved are only partially understood, and their significantly low power density and low energy efficiency makes them unsuitable for practical applications.

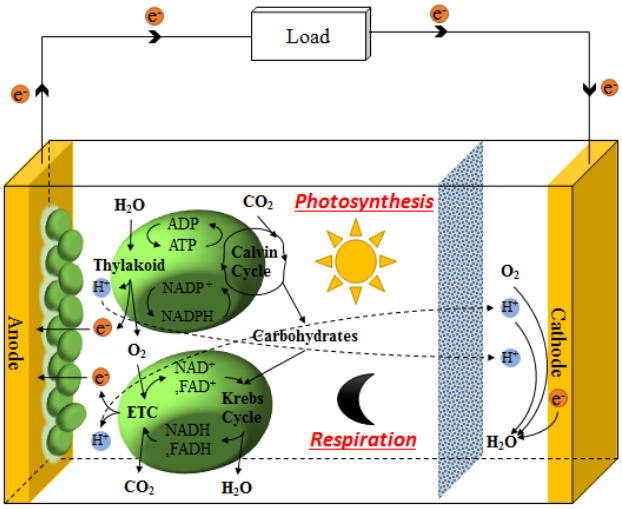

Figure 1: Principle of operation in a bio-solar cell. Schematic representation of the photosynthetic and respiratory electron transport pathways in cyanobacteria

Recently, we reported a micro-sized bio-solar cell (57 μL) that can produce sustainable energy through the photosynthetic reactions of cyanobacteria, *Synechocystis sp.* PCC 6803, in the anode [6]. We significantly increased the power density of micro-sized bio-solar cells by increasing surface area-to-volume ratio, obtaining a maximum power density of 7.09 nW/cm^2. This is 170 times more power than ever previously reported for MEMS bio-solar cells, however, the bio-solar cell performance is still insufficient for applied use and complete self-sustainable power generation is not yet possible. One of the major issues with our previous bio-solar cells is that the anode material and the device architecture were inappropriate for adequate solar energy capture/bacterial attachment and light penetration into the first layer of any biofilm growing on the surface. This resulted in a decrease in power/current generation, mainly because the bio-solar cell had a conventional dual-chamber device configuration with a face-to-face arrangement of electrodes. In addition, the thin gold anode showed poor interaction between the bacteria and anode. Another concern about our previous bio-solar cell system was the need to continuously introduce potassium ferricyanide as an electron acceptor (catholyte). Although this chemical has the advantages of fast cathodic reaction and low overpotential, these liquid-state electron acceptors may be impractical and unsustainable for applied use due to their requirement to regenerate chemicals.

In this paper, we developed a novel single-chambered device structure that is different from the conventional, dual-chambered

9781940470016/HH2014/$25©2014TRF
DOI 10.31438/trf.hh2014.69

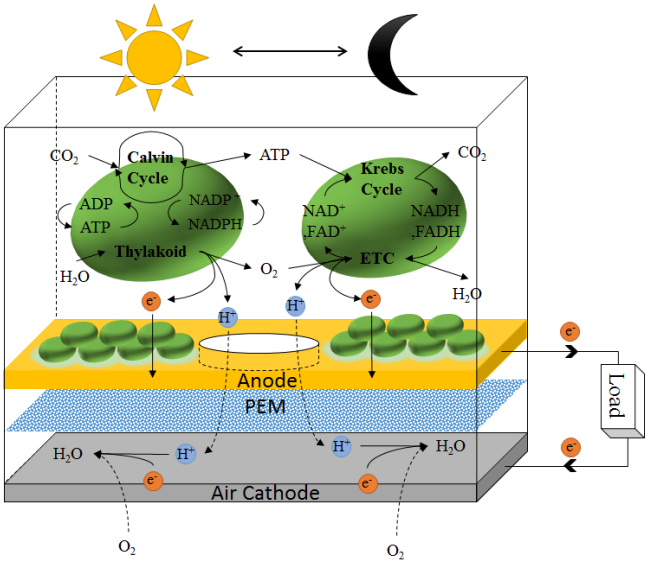

Figure 2: Principles of operation of our new bio-solar cell. The anode structure was designed to face the sun while produced protons travel toward the cathode through holes at the periphery of the anode.

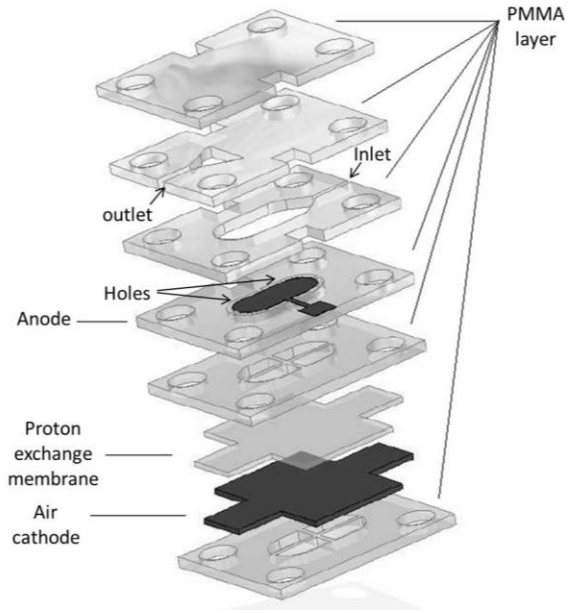

Figure 3: Schematic of the individual layers in the microfabricated bio-solar cell. There are holes at the periphery of the anode layer.

microbial fuel cells with a face-to-face electrode arrangement. Both the anode and cathode were configured upright (face-up) to ensure that (i) the capture of solar energy can be maximized and (ii) the carbon-based materials can be utilized as an anode material instead of an inefficient, transparent indium tin oxide or thin gold for bacterial attachment/electron coupling (Fig. 2). Produced protons travel toward the cathode through perforations on the anode instead of through aqueous cathode systems.

Based on this innovative device structure, we significantly increased the power density of the MEMS bio-solar cell up to one order of magnitude larger than that of our previous device [6].

MATERIALS AND EXPERIMENTAL SET-UP

Device Fabrication and operation

Fig. 3 and Fig. 4 show the schematic of the bio-solar cell and of the fully assembled micro-fabricated bio-solar cell, respectively. The device consisted of five functional layers: anode chamber layers, an anode layer, a proton exchange membrane, an air-cathode layer, and supporting layers. A thin rubber layer (~100 μm) was sandwiched between each layer and the entire device was assembled by the two supporting frames with bolts and nuts. The bio-solar cell had a ~300-μL single chamber defined by laser-machined PMMA substrates. Carbon anodes were deposited on the poly(methyl methacrylate) (PMMA) substrate using screen/stencil printing methods. Previously reported air-cathode techniques were applied for this small-scale bio-solar cell system; the catalyst layer directly faced the liquid, and the opposite side faced air, with diffusion layers to avoid water leakage and limit oxygen diffusion into the anode chamber [7]. The air-cathode bio-solar cell allowed the use of freely-available oxygen in the air as the electron acceptor, considerably improving the process's sustainability and decreasing the cell's operational costs. The bio-solar cell generated power/current output without the need to add organic fuel (anolyte) or electron acceptor (catholyte), making it entirely self-sustainable.

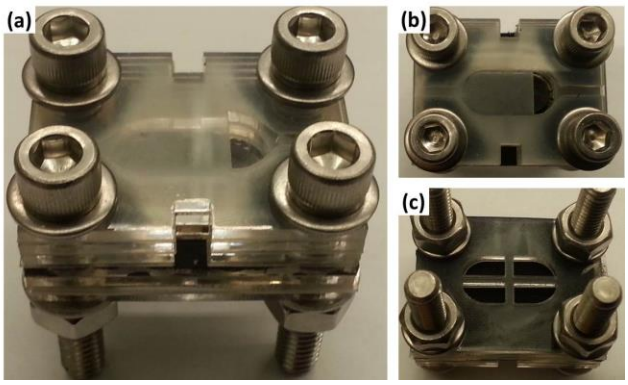

Figure 4: (a) A photo-image of the fully assembled MEMS bio-solar cell, (b) its top-view, and (c) its bottom-view. The cell has a ~300-μL single chamber defined by PMMA and rubber layers.

Inoculum

Cultures of *Synechocystis sp.* PCC 6803 were grown at 30 °C in BG-11 medium under continuous aeration and illumination provided by a fluorescent lamp. BG-11 medium contains 1.5 g $NaNO_3$, 40 mg K_2HPO_4, 75 mg $MgSO_4$, 36 mg $CaCl_2$, 1 mg of EDTA, and 6 mg of citric acid and of ferric ammonium citrate per 1 L distilled water. The anolyte with bacteria was injected continuously at a rate of 1 μL/min until the anode chamber was completely filled. Once the chamber was fully filled, the supply of the anolyte stopped and the microfluidic tubings were sealed with clamps.

Measurement Setup

We measured the potential between the anode and the cathode by a data acquisition system (NI, USB-6212) and recorded the results every 1 min via a customized LabVIEW interface. An

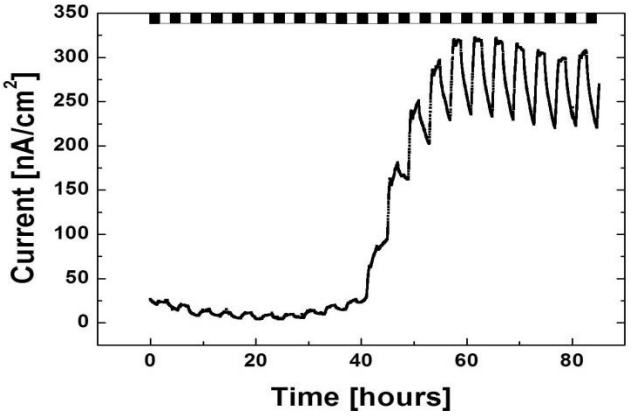

Figure 5: Positive light response of the bio-solar cell under 100 kΩ resistor. The device was examined under 2 hour light/dark intervals. The white bars indicate the illuminated period and the shadow indicates the dark period.

external resistor was used to close the circuit by connecting the anode and cathode. The current through the load was calculated via Ohm's rule and the output power was calculated via P=V×I. Current and power densities were normalized to the anode area.

RESULTS AND DISCUSSION

Biofilm formation

Cultivation of photosynthetic bacterial biofilms directly onto anode surfaces appears to be critical for high performance bio-solar cells. Microorganisms in the device can be planktonic cells (suspension) and/or biofilms [8]. Many bio-solar cells use planktonic cells and exploit an exogenously-supplied redox mediator to transfer electron from the cell surface to the anode [4, 9]. Therefore, power outputs from the planktonic cells are very low and the use of exogenous mediators is undesirable for sustainable field applications. More recently, the use of exogenous mediators has been avoided by growing photosynthetic bacterial biofilms directly onto anode surfaces to exploit the endogenous exoelectrogenic properties associated with biofilm development [4, 10]. Moreover, microorganisms in biofilms play a more important role in increasing bioelectricity. Davila et al. showed that the contribution of suspended bacteria was only about 20% of the total power generation in the microbial fuel cell [11]. In this work, noticeable biofilm growth was also observed over time. Along with the biofilm formation, the gradual increase in current density was monitored as shown in Fig. 5. It should be noted that *Synechocystis sp.* PCC 6803 can grow and form biofilm without the need of additional nutrition.

Current and power generation

Fig. 5 shows a current profile of the bio-solar cell under a 100 kΩ resistor. The current showed a decreasing trend immediately after the supply of the anolyte stopped and the microfluidic tubings were sealed with clamps. However, the current generation gradually increased over time. During operation at 2h/2h light/dark cycles, the device showed positive light response: the current increased under illumination and decreased in dark. After 40 h of operation, significant increase in current density was observed with a noticeable green biofilm formation on the anode. The difference of the current generation between the light/dark periods became distinct at 40h. This is mainly due to the biofilm formation. During dark, the current output was not zero due to the cellular

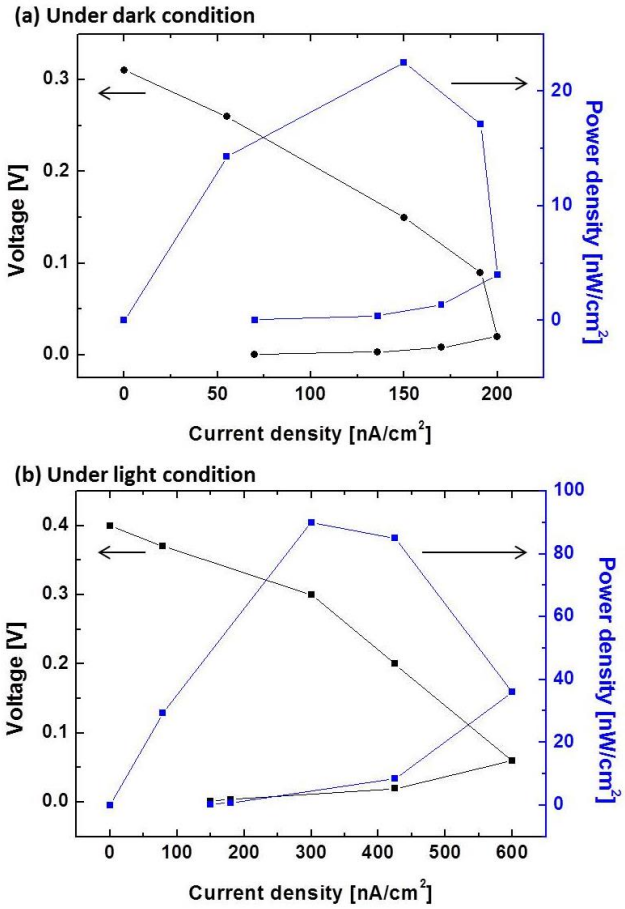

Figure 6: Polarization curve and output power measured as a function of current (a) under dark and (b) light conditions

respiration creating energy from the carbohydrates produced during the day. Temperature remained constant at 30 ± 2 ℃ throughout the experiment and changes in current output did not correlate to the minor fluctuations in temperature observed. This indicates that the current/power responses monitored were mainly light dependent.

Fig. 6 shows polarization curves and power outputs of the bio-solar cell under light and dark conditions. The values were derived and calculated based on the maximum current value at a given external resistance (4.7 M, 1M, 470k, 100k, 47k, 22k, & 10kΩ). We obtained a maximum power density of 90nW/cm^2 under four fluorescent lamps, which is the highest power density among all miniaturized bio-solar cells [6, 12, 13]. However, this power density is still in several orders of magnitude lower than that of even the smallest power microbial fuel cells [14]. The current limit in the performance of the bio-solar cell is primarily due to the high internal resistance, resulting in reduced power densities. Using the polarization curve in Fig. 6, we estimated their internal resistance in that the increased current is accompanied with a maximum power output when the external resistance approaches the internal resistance [15]. The internal resistance of the bio-solar cell yielded about 470 kΩ both during light and at night, which are several orders magnitude higher internal resistance than that of other biofuel cells (several Ω) [16]. The high internal resistance observed in our experiments might be due to the poor electron transfer from cyanobacteria to the anode surface and from the

inefficient interactions between the biological material and anode. However, a proper understanding of their metabolic pathways involved in extracellular electron transfer is still lacking. The evolution of this technology requires comprehensive understanding of (i) the behavior and physiology of those photosynthetic bacteria and (ii) their interaction with the electrode at a new level of detail and efficiency. In that sense, microsized bio-solar cells can facilitate studies of those microbial behaviors in a smaller group of cells with excellent control over the microenvironment.

CONCLCUSION

We developed a micro-sized bio-solar cell for self-sustainable field applications. A carbon-based single-chambered device with a face-to-face electrode arrangement was designed so that capture of solar energy can be maximized and bacterial cell attachment/electron coupling can be enhanced. The maximum power density of 90 nW/cm^2 at a current density of 300 nA/cm^2 was generated through photosynthetic reactions of cyanobacteria, *Synechocystis sp.* PCC 6803, which is the highest power density among all miniaturized bio-solar cells. This sustainable micropower source will be essential for a large array of military mobile and wireless applications, including perimeter defense networks, environmental protection sensors and micro vehicle applications. Furthermore, this work will (i) contribute to an in-depth understanding of the interplay between miniature device architectures and photosynthetic microorganisms and reveal fundamental problems in electron transfer at the microbial/anode interface, and (ii) result in a barrier-transcending advancement in bio-solar cells, attaining higher power density and energy efficiency that can release bio-solar cell technology from its restriction to conceptual research, advancing its translational potential toward practical, real-world applications.

ACKNOWLEDGMENT

We thank Prof. Gretchen Mahler for providing bacteria. We also would like to thank the Nanofabrication Lab at SUNY-Binghamton for providing the fabrication facilities, and the Binghamton University Research Foundation for funding this work. This work was also supported in part by S^{3}IP Small Grant Award.

REFERENCES

[1] M. Rosenbaum, Z. He, and L.T. Angenent, “Light energy to bioelectricity: Photosynthetic microbial fuel cells,” Curr. Opin. Biotechnol., 21, 259 (2010).

[2] D. Strik, R.A. Timmers, M. Helder, K. Steinbusch, H. Hamelers, and C.J.N. Buisman, "Microbial solar cells: applying photosynthetic and electrochemically active organisms", Trends in Biotechnology, 29, 41 (2011).

[3] R. W. Bradley, P.Bombelli, S.J.L. Rowden, and C. J. Howe, “Biological photovoltaics: intra- and extra-cellular electron transport by cyanobacteria”, Biochem. Syst. Trans., 40, 1302 (2012)

[4] A.J. McCormick, P. Bombelli, A.M. Scott, A.J. Philips, A.G. Smith, A.C. Fisher, and C. J. Howe, “Photosynthetic biofilms in pure culture harness solar energy in a mediatorless bio-photovoltaic cell system”, Energy & Environmental Science, 4, 4699 (2011).

[5] Z. He, J. Kan, F. Mansfeld, L.T. Angenent, and K.H. Nealson, “Self-Sustained Phototrophic microbial fuel cells based on the synergistic cooperation between photosynthetic microorganisms and heterotrophic bacteria”, Environ. Sci. Technol., 43, 1648 (2009).

[6] S. Yoon, H. Lee, A. Fraiwan, C. Dai, and S. Choi, “A Micro-sized Microbial Solar Cell”, Proceedings of the 9th IEEE International Conference on Nano/Micro Engineered and Molecular Systems, Apr. 13 - 16, 2014, Hawaii, USA, in-print.

[7] H. Liu and B.E. Logan, “Electricity generation using an air-cathode single chamber microbial fuel cell in the presence and absence of a proton exchange membrane”, Environ. Sci. Technol., 38, 4040 (2004).

[8] A.P. Borole, G. Reguera, B. Ringeisen, Z. Wang, Y. Feng, and B.H. Kim, “Electroactive biofilms: Current status and future research needs”, Energy & Environmental Science, 4, 4813 (2011)

[9] V.M. Luimstra, S. Kennedy, J. Guttler, S.A. Wood, D.E. Williams, and M.A. Packer, “A cost-effective microbial fuel cell to detect and select for photosynthetic electrogenic activity in algae and cyanobacteria”, J. Appl. Phycol., 26, 15, (2014).

[10] P. Bombelli, M. Zarrouati, R.J. Thorne, K. Schneider, S.J.L. Rowden, A. Alik, K. Yunus, P.J. Cameron, A.C. Fisher, D.I. Wilson, C. J. Howe, and A.J. McCormick, “Surface morphology and surface energy of anode materials influence power outputs in a multi-channel mediatorless bio-photovoltaic system”, Phys. Chem. Chem. Phys., 14, 12221 (2012).

[11] D. Davila, J. P. Esquivel, N. Sabate, & J. Mas, “Silicon-based microfabricated microbial fuel cell toxicity sensor”, Biosens. Bioelectron., 26, 2426 (2011).

[12] M. Chiao, K.B. Lam, and L. Lin, “Micromachined microbial and photosynthetic fuel cell”, Journal of Micromechanics and Microengineering, 16, 2547 (2006).

[13] K.B. Lam, E.A. Johnson, M. Chiao, and L. Lin, “A MEMS photosynthetic electrochemical cell powered by subcellular plant photosystems”, Journal of Microelectromechanical Systems, 15, 1243 (2006).

[14] A. Fraiwan, S. Sundermier, D. Han, A. Steckl, D.J. Hassett, and S. Choi, “Enhanced Performance of MEMS Microbial Fuel Cells using Electrospun microfibrous anode and optimizing operation”, Fuel Cells, 13, 336 (2013).

[15] Y. Fan, E. Sharbrough, and H. Liu, “Quantification of the internal resistance distribution of microbial fuel cells”, Environ. Sci. Technol., 42, 8101 (2008).

[16] S. Choi, H.-S. Lee, Y. Yang, P. Parameswaran, C.I. Torres, B.E. Rittmann and J. Chae, “A μL-scale Micromachined Microbial Fuel Cell Having High Power Density”, Lab on a Chip, 11, 1110 (2011).

CONTACT

*S. Choi, tel: +1-607-777-5913; sechoi@binghamton.edu

MICROFABRICATED BULK PZT PIEZOELECTRIC DISK TRANSFORMERS

Mona Mirzaeimoghri, Prakruthi Hareesh, Isaac Misri and Don L. DeVoe
Dept. of Mechanical Engineering, University of Maryland, College Park, USA

ABSTRACT

A new class of miniature monolithic piezoelectric transformer that leverages a simple two-mask bulk piezoelectric microfabrication process is presented. A millimeter-scale transformer design based on a disk-shaped resonator topology with annular electrodes is fabricated to produce step-up voltages in a compact form factor. The radial vibration characteristics and voltage gain of the bulk transformers under varying impedance loads have been analyzed experimentally, and compared against an electromechanical model of transformer performance. A maximum voltage gain of 7.3 was obtained.

INTRODUCTION

Piezoelectric transformers are resonant electromechanical devices which enable efficient AC voltage conversion. Compared to conventional electromagnetic transformers, piezoelectric transformers offer many advantages including low weight, high efficiency, and high input and output impedances to minimize loading effects. In addition, favorable scaling of piezoelectric transduction allows device dimensions to be significantly reduced while retaining acceptable performance[1].

Piezoelectric transformers have been widely studied[2,3,4]. At the macro scale, multilayer Rosen type bar transformers are commonly used in many applications, such as cold cathode fluorescent lamps, inverters for liquid crystal displays, and AC-DC converters for power supplies [1,2,5]. However, the fabrication of multilayer Rosen transformers is not well suited to miniaturization, prohibiting their use in a range of small scale systems such as interfaces for micro power harvesting platforms that demand efficient and high gain voltage conversion. An alternate transformer topology based on a disk-shaped resonator with annular electrodes can avoid this limitation, but fabrication by traditional machining or solution casting methods have limited the size of these devices to the range of several centimeters or more[6,7,8].

In this paper, disk-type step-up transformers with diameters ranging from 1-10 mm are studied. The step-up transformers are fabricated by a micro powder blasting technique that provides photolithographic control over transformer geometry, using high quality bulk lead zirconate titanate (PZT) as the piezoelectric substrate material. While microfabricated thin film piezoelectric transformers employing high-Q silicon substrates have been reported, a significant advantage of the bulk PZT transformers described in this work is their high power handling capabilities. While heat removal presents an upper limit to power handling in macro scale piezoelectric transformers, the small Biot numbers associated with the millimeter scale devices reported here ensure that power handling is limited by energy density rather than thermal performance. As a result, power handling scales linearly with piezoelectric layer thickness, enabling the microfabricated bulk transformers to support power levels of 3.4-9.2 W/cm^3.

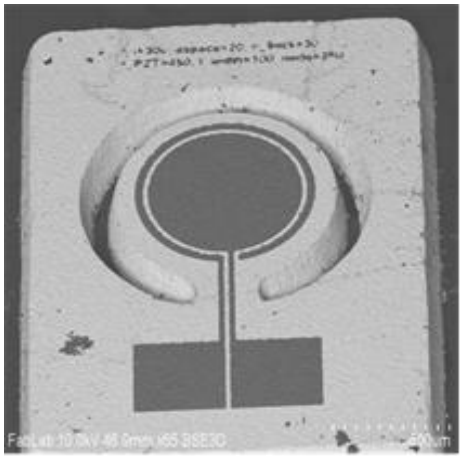

Figure1: Fabricated 500 µm radius bulk PZT transformer.

A micrograph of a fabricated 1 mm diameter PZT transformer is shown in Figure 1. The transformer is operated in its fundamental radial vibration mode. An electric field (E) is applied across the thickness of the bulk PZT through an input electrode. A radial strain is thereby generated within the PZT through the transverse d_{31} coupling coefficient, and converted to a voltage at the output electrode [9]. Using the developed microfabrication methods[9], millimeter-scale piezoelectric transformers were successfully fabricated and characterized. The radial vibration characteristics and voltage gain of the bulk transformers under varying impedance loads were analyzed experimentally, and compared against an electro-mechanical model of transformer performance.

THEORETICAL BACKGROUND

Figure 2 shows the schematic diagram of a disk-type transformer, with R represents total radius and h defines the thickness of the transformer. The planar vibration analysis of a thin (h << R) circular disk is[10,11,12]:

$$\frac{d^2U}{dr^2} + \frac{1}{r}\frac{dU}{dr} - \frac{U}{r^2} - \rho\omega^2 S_{11}^E\left(1 - v_p^2\right)U = 0 \quad (1)$$

$$U(r) = C\,J_1(\beta r) \quad (2)$$

$$\beta^2 = \rho\omega^2 S_{11}^E(1 - v_p^2) \quad (3)$$

$$f = \frac{\beta}{2\pi\sqrt{\rho S_{11}^E(1 - v_p^2)}} \quad (4)$$

where $U, \rho, S_{11}^E, v_p, \beta$ represent the displacement of the vibration, density, elastic compliance coefficient, Poisson's ratio, and Bessel function coefficient of the piezoelectric transformer respectively.

The equivalent circuit of the piezoelectric transformer is shown in Fig. 3. Turn ratio, effective mass, stiffness and damping factor can be calculated as follow:

$$F(s) = (j\omega)U(s)(L_m S + R_m + \frac{1}{C_m S}) \quad (5)$$

$$L_m = m_{eff} = \frac{2\pi\rho\int_0^R rJ^2(\beta r)\,dr}{J^2(\beta R)} \quad (6)$$

$$C_m = \frac{1}{\omega o^2 . L_m} \quad (7)$$

$$R_m = \frac{\omega o^2 . \mathrm{L_m}}{\mathrm{Q}} \quad (8)$$

$$n_1 = \frac{2\pi\,(RJ_1(\beta R) - R_i J_1(\beta R_i))d_{31}}{S_{11}^E(1-\sigma)J_1(\beta R)} \quad (9)$$

$$n_2 = \frac{I_{out}'}{U'(\beta R)} = \frac{2\pi\,(R_o J_1(\beta R_o)d_{31}}{S_{11}^E(1-\sigma)J_1(\beta R)} \quad (10)$$

9781940470016/HH2014/$25©2014TRF
DOI 10.31438/trf.hh2014.70

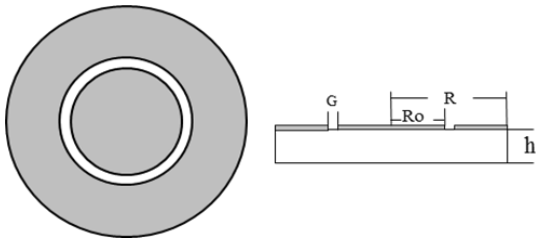

Figure 2: Schematic diagram of a transformer showing electrode geometry.

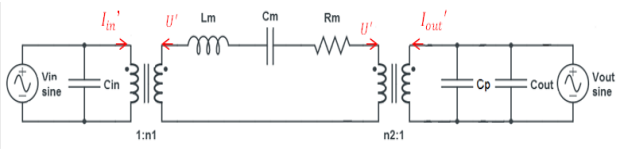

Figure 3: Equivalent circuit of a piezoelectric transformer.

Based on the equivalent circuit, the theoretical model and PZT characteristics the optimum designs for the maximum gains for different range of PT have been obtained.

Experimental Studies

Aluminum (Al) wet etch for electrode patterning and micropowder blasting for selective PZT etching were combined in a two-photomask process to fabricate bulk piezoelectric transformers from a 7.24 cm square and 127 µm-thick type-5A PZT sheet (PSI5A4E sheets, Piezo Systems, Inc.). In order to provide a robust substrate the PZT was temporarily bonded to a 10 cm diameter silicon wafer using a sacrificial layer of an adhesive wax (Crystalbond 509). Bonding was performed by mounting the PZT sheet manually on melted wax at 130 °C. The PZT has nickel metal layer on both sides. The nickel was removed using a 5 min wet etch in a nickel etchant. The transformer's input and output electrodes were patterned by 500 nm Al deposition by electron beam evaporation followed by spin coating a 1.5 µm thick layer of positive imaging resist. UV exposed resist was developed using CD-30 developer for 1 min and Al was wet etched in Aluminum etchant for 5 min at 55 °C to create the electrode patterns on the PZT surface. Micropowder blasting of the PZT was performed by laminating a 50 µm thick dry film photoresist as an etch mask for micropowder blasting of the PZT in a commercial laminator followed by UV exposure.

A benchtop microabrasive blasting workstation was applied for micropowder blasting using 25 µm alumina particles. The abrasive nozzle pressure was 55.16 N/cm^2 and its distance from the PZT substrate was 7 cm.

RESULTS AND DISCUSSION

Using the developed microfabrication methods, PZT transformers were fabricated and characterized. The radial vibration and voltage gain of the bulk transformers under varying impedance loads was analyzed experimentally, and compared against an electro-mechanical model of transformer performance. AC voltage generated by a function generator was applied to the transformer and the output voltage of the input and output electrodes were measured by an oscilloscope. An LM6172IN operational amplifier and a 100 kΩ resistor were used to make a unity gain buffer to eliminate the loading effect of the function generator in the input and the oscilloscope at the output of the transformer. Based on the manufacturer's data, the PZT sheet exhibits a typical mechanical quality factor of 80. An experimental quality factor of approximately 40 was measured in our tests, presumably due to air damping since all measurements were conducted at atmospheric pressure, Theoretical gains, calculated using the measured quality factor of 40, are presented in Table 1 together with the resonance frequency for three selected resonator designs.

Table 1. Resonance frequency and maximum gain for three general dimensions

Device radius (mm)	R_o range (mm)	G (mm)	Resonant freq. (kHz)	Max. gain (Theory)	Max. gain (Experiment)
2.5	0.2-0.6	0.5	440	5.78	5.08
3.5	0.4-1	0.5	320	6.5	6.34
5	0.75-2.5	0.5	220	7.43	7.3

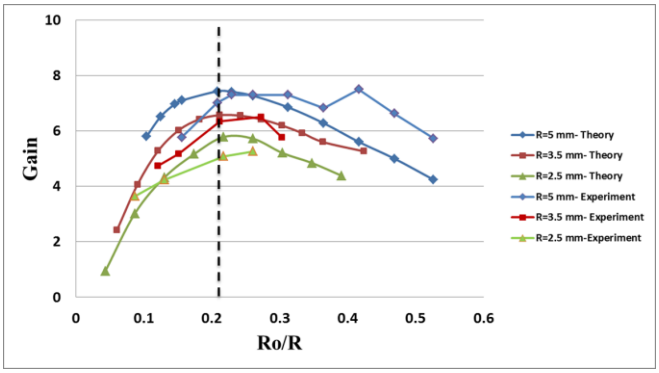

Figure 4: Experimental and theoretical gain versus R_o/R for devices of outer radius R=5 mm, 3.5 mm and 2.5 mm. The optimal ratio of 0.2 predicted by the analytical model is denoted by a dashed line. There is good overall agreement between the experimental and analytical data.

The correlation between theoretical and experimental device gain and output electrode radius ratio is shown in Figure 4. In the symmetric vibration of the PZT disk the radial displacement and radial stress are function of position along the radial direction of the disk. In order to operate in the third radial vibration mode, the transformer should be designed such that the annular gap is located at the position where the stress is minimum. For all devices, a maximum gain was found to occur when the output diameter was approximately 20% of the total diameter, in agreement with the analytical model predictions.

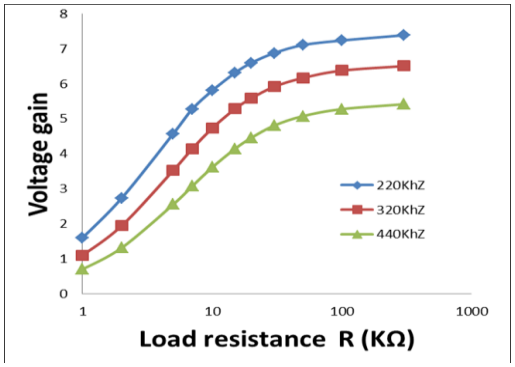

Figure 5. Voltage gain vs. load resistance for different resonance frequency

Figure 5 illustrates the voltage gain of bulk transformers under varying impedance loads. Voltage gain increases rapidly with increasing load resistance and saturates at higher load

resistance. This can be explained by the equivalent circuit of piezoelectric transformers. The load resistance R_L can affect the gain when is not much larger that the output capacitor $1/(\omega_o C_o)$ and the output voltage increases with the load resistance. The load can be considered as open when R_L is much larger than the output capacitor.

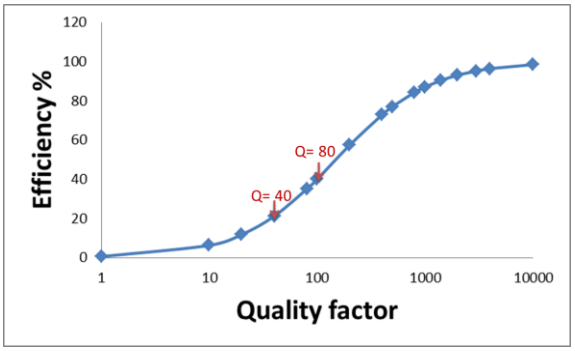

Figure 6. Efficiency vs. quality factor in theory. Efficiency of the transformer at the quality factor of 80 is equal to 40.

The maximum efficiency of a piezoelectric transformer can be obtained when the load resistance equals matching load, $1/(\omega_o C_o)$. The quality factor of the bulk PZT under vacuum is 80. According to the theoretical model the efficiency at this quality factor should be 40%. The vibration of the transformers has been measured in the air where the measured quality factor was 40. The experimental efficiency at this quality factor was 27% which showed a good agreement with the theoretical model. Since this transformer has high voltage gain and average efficiency, it is suitable for high voltage applications. The theoretical efficiency for different PZT quality factors are shown in Figure 6. The maximum gain measured at the maximum efficiency was 4.

Maximum output voltage of 58 V with respect to 20 V input voltage was measured for a 7 mm diameter device when different load resistances were used. The power density at the matching load of 5 kΩ was measured to be 9.2 W/cm^3. However the transformer behaved stable, when the input voltage was greater than 10 V the temperature increased in the input opamp and limited the applied input voltage. The output gain for input voltage <10 at the matching load was 4 and it decreased to 2.9 for input values >10. Power densities of 7.1 W/cm^3 and 3.4 W/cm^3 were also measured for output load resistances of 1 kΩ and 100 Ω, respectively.

Figure 7 illustrates the linear relationship between gain and transformer radius. Gains of 3-7 were readily achieved by varying the radius from 1.5 mm to 5.5 mm while the gap was held constant at 500μm. As shown in equations 5-10, the turn ratios and the vibrational behavior of the transformers are a function of the total radius and their value increases with the greater device radius.

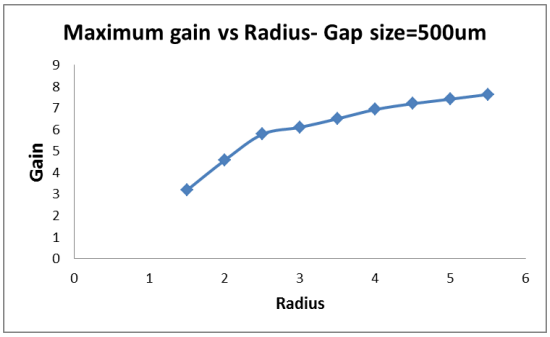

Figure 7. Gain vs transformer radius

CONCLUSION

The characteristics of a disk-shaped piezoelectric transformer have been studied theoretically and experimentally. A maximum gain of 7.3 at ideal load and maximum gain of 4 at the maximum efficiency were obtained, the highest reported gains for piezoelectric transformers of this size. For examples, these results compare favorably to the smallest disk transformer previously reported, which provided a maximum gain of 1.9 for a 1.3 cm diameter device [6].

REFERENCES

[1] K. Insung, J. Hyeonkyu, J. Soonjong, K. Minsoo, S. Jaesung, and V. T. Vo, "Output Power of a Ring-type Stacked Piezoelectric Transformer with Pure Ag Electrodes," J. Korean Phys. Soc., vol. 58, no. 31, p. 627, Mar. 2011.

[2] M. Guo, D. M. Lin, K. H. Lam, S. Wang, H. L. W. Chan, and X. Z. Zhao, "A lead-free piezoelectric transformer in radial vibration modes.," Rev. Sci. Instrum., vol. 78, p. 035102, 2007.

[3] S. Priya, H. Kim, S. Ural, and K. Uchino, "High power universal piezoelectric transformer.," IEEE Trans. Ultrason. Ferroelectr. Freq. Control, vol. 53, pp. 810–816, 2006.

[4] K. Insung, J. Hyeonkyu, S. Jaesung, J. Soonjong, and K. Minsoo, "Ring-dot-shaped Multilayer Piezoelectric Step-down Transformers Using PZT-based Ceramics," J. Korean Phys. Soc., vol. 57, no. 41, p. 963, Oct. 2010.

[5] J. Y. J. Yang, "Piezoelectric transformer structural modeling - a review," IEEE Trans. Ultrason. Ferroelectr. Freq. Control, vol. 54, pp. 1154–1170, 2007.

[6] J. H. Hu, H. L. Li, H. L. W. Chan, and C. L. Choy, "A ring-shaped piezoelectric transformer operating in the third symmetric extensional vibration mode," Sensors Actuators A Phys., vol. 88, no. 1, pp. 79–86, Jan. 2001.

[7] K.-T. Chang and C.-W. Lee, "Fabrication and characteristics of thin disc piezoelectric transformers based on piezoelectric buzzers with gap circles.," Ultrasonics, vol. 48, pp. 91–97, 2008.

[8] P. Půlpán and J. Erhart, "Transformation ratio of 'ring-dot' planar piezoelectric transformer," Sensors Actuators A Phys., vol. 140, pp. 215–224, 2007.

[9] P. Hareesh, I. Misri, S. Yang, and D. L. DeVoe, "Transverse Interdigitated Electrode Actuation of Homogeneous Bulk PZT," J. Microelectromechanical Syst., vol. 21, no. 6, pp. 1513–1518, Dec. 2012.

[10] S.-T. H. S.-T. Ho, "Modeling of a disk-type piezoelectric transformer.," IEEE Trans. Ultrason. Ferroelectr. Freq. Control, vol. 54, pp. 2110–2119, 2007.

[11] T. Hemsel and S. Priya, "Model based analysis of piezoelectric transformers.," Ultrasonics, vol. 44 Suppl 1, pp. e741–e745, 2006.

[12] H. L. Li, J. H. Hu, and H. L. W. Chan, "Finite element analysis on piezoelectric ring transformer.," IEEE Trans. Ultrason. Ferroelectr. Freq. Control, vol. 51, no. 10, pp. 1247–54, Oct. 2004.

MICROFABRICATED WORKBENCH DESIGNED TO INVESTIGATE THERMOELECTRIC PROPERTIES OF LOW-DIMENSIONAL MATERIALS

DukSoo Kim[1], James Kally[2], Nitin Samarth[3,4], and Srinivas Tadigadapa[1,4]
[1]Department of Electrical Engineering, The Pennsylvania State University, University Park, USA
[2]Department of Materials Science and Engineering, The Pennsylvania State University, University Park, USA
[3]Department of Physics, The Pennsylvania State University, University Park, USA
[4]Materials Research Institute, The Pennsylvania State University, University Park, USA

ABSTRACT

Microfabricated workbench has been developed to investigate thermoelectric properties of low-dimensional materials. The central area of the chip has high density of test sites for improving the probability of landing single nanowire or nanotube at desired position on the workbench when it is drop cast from solution. This obviates the extensive effort of nanomaterial manipulation required for measurement and provides a reliable platform to measure the thermal, thermoelectric, and electrical characterization across various nanomaterials. To demonstrate the efficacy of the device, the three thermal and electrical transport properties and thermoelectric figure of merit ZT of GaAs/MnAs core/shell nanowire were successfully measured using the workbench at temperatures ranging from 150 K to 300 K.

INTRODUCTION

Low-dimensional materials (LDMs), such as nanoribbons, nanowires, and nanotubes, have attracted great attention as thermoelectric materials due to their potential for having improved thermoelectric efficiency [1, 2]. However, the lack of a thermal equivalent of an "ammeter" makes the measurement of thermal and thermoelectric properties (thermal conductivity and Seebeck coefficient) in LDMs challenging. Although thermal workbenches have been reported earlier, these devices require considerable effort in terms of placement and alignment of the LDMs on the workbench or are dedicated for measurement of a single material and cannot be used for a variety of LDMs [3, 4]. In this work, we have designed and fabricated micro-workbenches with high surface density of test-sites in the central area of the chip to enhance the probability of landing a single LDM at the desired positions without any physical manipulation when drop casting from a solution containing the LDMs.

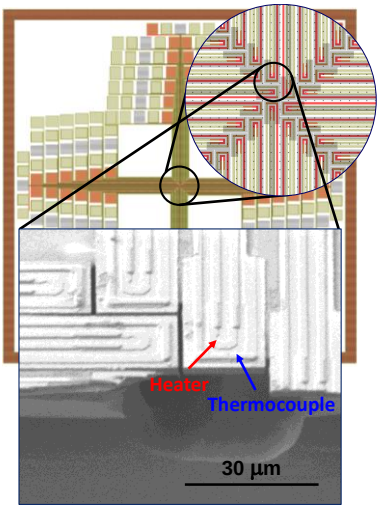

Figure 1: Mask overview of the overall workbench chip. Insets show the zoom-in of the workbenches and an oblique view SEM of the fabricated workbench showing the undercut tip areas.

The workbench consists of several closely placed thermally isolated platforms (Figure 1). Each platform has an integrated heater, thermocouple temperature sensor and platinum contact pad. The heater and thermocouple junction are placed at tip of the thermally isolated and freestanding part of the platform. The platinum pad is on top of platform and provides electrical connection to the LDM and is electrically isolated from the thermocouple and heater. 60 platform tips are located in 250 µm × 250 µm central area of the workbench for improving the probability of landing a single LDM bridging two neighboring platform tips when solution containing materials is drop cast. Neighboring platform tips are 1 µm apart from each other (inset, Figure 1). Polysilicon-gold thermocouple is used for high-sensitivity temperature measurements.

FABRICATION PROCESS

The fabrication process is shown in Figure 2. First, silicon nitride (0.3 µm)/silicon oxide (1.4 µm)/silicon nitride (0.3 µm) is deposited on silicon wafer as a stress-compensated stack using low pressure chemical vapor deposition (LPCVD) and deposition of polysilicon (LPCVD, 0.4 µm, boron-doped, 10^{19} cm^{-3}) is followed. The polysilicon layer is patterned to define heater and one leg of thermocouple using photolithography and reactive ion etching (RIE). And titanium (20 nm)/gold (400 nm) layer is deposited and patterned using lift-off process to complete the thermocouple structure (Figure 2(a)). Afterward, aluminium oxide (20 nm)/hafnium oxide (30 nm) is deposited using atomic layer deposition (ALD), which electrically insulates heater and thermocouple from the following titanium (30 nm)/platinum (100 nm)/nickel (150 nm) layer patterned using lift-off process (Figure 2(b)). RIE and deep reactive ion etching (DRIE) then are performed to etch the ALD layer, stress-compensated stack and silicon substrate using nickel layer and photoresist as a mask. Lastly, the silicon substrate is etched in an isotropic manner by xenon

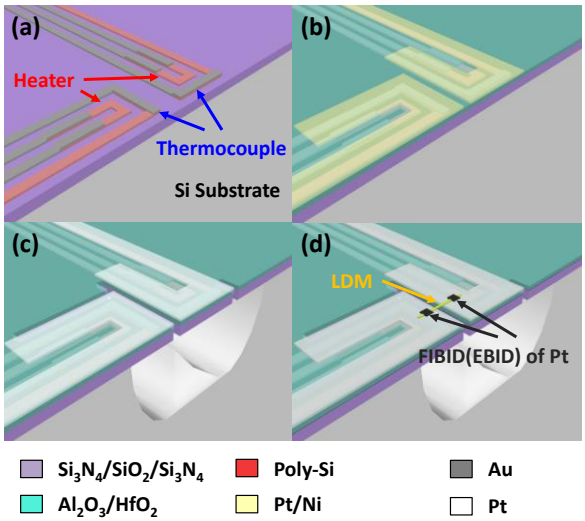

Figure 2: Schematic diagram of fabrication process.

9781940470016/HH2014/$25©2014TRF
DOI 10.31438/trf.hh2014.71

difluoride etching and wet etching of nickel is followed (Figure 1(c)). Placement of the LDM on workbench is achieved by drop casting from solution. And focused ion beam (FIBID) or electron beam induced deposition (EBID) of platinum is used to provide mechanical anchors and good electrical and thermal contact between the material and platinum pads of workbench (Figure 1(d)).

CALIBRATION OF THERMOCOUPLE

Polysilicon-gold thermocouple was made for measuring the temperature of platform tips. However, a calibration is necessary for extracting temperature rise from the thermocouple voltage. For such calibration, the workbench has a special structure where two platform tips connected to each other through a 2 µm-wide bridge consisting of stress-compensated stack/ALD/titanium/platinum layers (insect, Figure 3(a)) and was used as follows.

Seebeck coefficient at 300 K was obtained using heater, on same platform with thermocouple, as a thermistor. Initially, resistance of heater was measured with small current (±20 µA) using Keithley 2400 at a temperature of 310 K. Thereafter, resistance of heater and thermocouple voltage were simultaeously measured, at an ambient temperature of 300 K, while sweeping current through the heater from 20 µA to 600 µA. Keithley 2182A nanovoltmeter was used to measure the thermocouple voltage. Figure 3(a) shows resistance of heater and thermocouple voltage as a function of heating power. By matching the resistance of the heater corresponding to that obtained at 310 K, the thermocouple voltage at 310 K was obtained. The Seebeck coefficient of thermocouple would be calculated by dividing the extracted thermocouple voltage with temperature rise of thermocouple junction. COMSOL finite element model (FEM) simulation was performed to check the temperature difference between heater and thermocouple junction. It was determined that the temperature rise

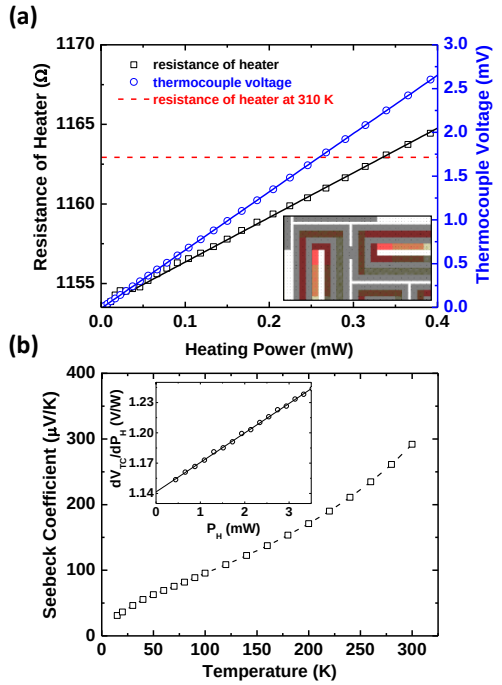

Figure 3: (a) Resistance of heater and thermocouple voltage as a function of heating power at 300 K (b) Seebeck coefficient of polysilicon-gold thermocouple as a function of temperature. Inset shows derivative of thermocouple voltage with respect to heating power as a function of heating power at 280 K (V_{TC}: thermocouple voltage, P_H: heating power).

of the thermocouple junction is 24.1 % smaller than that of heater which allowed accurate calibration of the thermocouple junction from that of heater.

The Seebeck coefficient at lower temperatures was obtained using the value at 300 K. If it is supposed that Seebeck coefficient changes linearly with respect to temperature and temperature of thermocouple junction changes linearly according to heating power, thermocouple voltage can be expressed as

$$S(T+\Delta T) = S(T) + a\Delta T \tag{1}$$

$$V_{TC} = \int_0^{\Delta T} S(T+\Delta T')d\Delta T' = S(T)\Delta T + \frac{a}{2}\Delta T^2 = S(T)bP_H + \frac{ab^2}{2}P_H^{\,2} \tag{2}$$

where S is Seebeck coefficient, T is the temperature of cryostat, ΔT is temperature rise of thermocouple junction, P_H is heating power, a is the rate of change of Seebeck coefficient with respect to temperature, and b is a ratio of temperature rise of thermocouple junction to heating power. Differentiating equation (2) gives

$$\frac{\partial V_{TC}}{\partial P_H} = S(T)b + ab^2P_H \tag{3}$$

Inset of Figure 3(b) shows the derivative of thermocouple voltage with respect to heating power as a function of heating power at the cryostat temperature of 280 K. In this case we used the heater of neighboring platform that is thermally connected, through a bridge, to the platform with thermocouple. We found that using heater and thermocouple of the same platform resulted in a noisy derivative of thermocouple voltage. Equation (1) and (3) allow us to calculate $S(280)$ using the intercept and the slope of inset of Figure 3(b) and known value of $S(300)$. The Seebeck coefficient of thermocouple was obtained using this method at temperatures ranging from 300 K down to 15 K (Figure 3(b))

MEASURING THERMOELECTRIC PROPERTIES OF LOW-DIMENSIONAL MATERIALS

The workbench on which LDM was anchored as explained previously is placed in a vacuum cryostat with pressure below 5×10^{-6} Torr to minimize the effect of parasitic heat transport through ambient air. And a sinusoidal voltage with angular frequency ω is applied to polysilicon heater of one platform using Keithley 3390 function generator and it in turn produces 2ω temperature fluctuation. Temperature rise of heated or neighboring platform tip is obtained by measuring 2ω voltage of polysilicon-gold thermocouple using SR 830 lock-in amplifier. And 2ω voltage between two platinum pads is also measured using lock-in amplifier, which represents thermoelectric voltage induced in LDM-platinum thermoelectric circuit. The amount of heat dissipated in the heater (heating power) is calculated by measuring applied voltage and current to the heater using Keithley 2001 and Keithley 2000 multimeters.

Thermal Conductivity

Initially, the thermal conductivity of LDM at 300 K is extracted by matching FEM simulation to measured heating power and temperature rise of both thermocouple junctions. For FEM simulations, bulk values of thermal conductivity of gold and silicon were used and the thermal conductivity of platinum was extracted using Wiedemann-Franz law from measured electrical conductivity. The thermal conductivity of rest of the materials was obtained from reference papers [5-9]. However, FEM cannot be used at low temperatures since the temperature dependence of thermal conductivity of all materials constituting workbench is not available. For this reason, thermal conductivity of LDM at lower temperatures

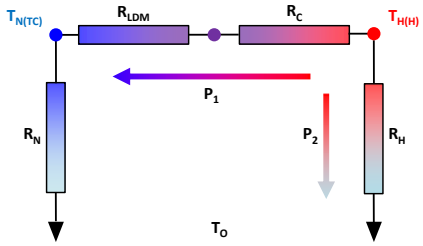

Figure 4: Equivalent thermal circuit of two platforms connected to each other through LDM.

is obtained using an equivalent thermal circuit (Figure 4).

The equivalent thermal circuit was built based on the fact that the heat generated in heater will transfer to the substrate (heat sink) through two paths. One is direct path to bottom of substrate. Another is path through LDM. Considering it, one obtains

$$P_H = P_1 + P_2 \tag{4}$$

where P_H, P_1, and P_2 are heating power, the amount of heat flowing through LDM, and the amount of heat sinking directly to the bottom of the substrate. Temperature rise of heater of heated platform and thermocouple junction of neighboring platform can be expressed as

$$\Delta T_{H(H)} = P_1(R_{LDM} + R_N + R_C) = P_2 R_H \tag{5}$$

$$\Delta T_{N(TC)} = P_1 R_N \tag{6}$$

where $\Delta T_{H(H)}$, $\Delta T_{N(TC)}$, R_{LDM}, R_N, R_H are the temperature rise of heater of heated platform, temperature rise of thermocouple junction of neighboring platform, thermal resistance of LDM, thermal resistance from thermocouple junction of neighboring platform to bottom of substrate, thermal resistance from heater of heated platform to bottom of substrate, respectively. R_C represents sum of thermal resistance from heater to LDM and from LDM to thermocouple junction. Using equation (4) and (6), equation (5) can be reorganized to

$$R_{LDM} = \frac{P_H}{\Delta T_{N(TC)}} R_H R_N - R_H - R_N - R_C \tag{7}$$

R_H, R_N, and R_C at 300 K are extracted by FEM. However, we still need to know how these change with temperature for calculating R_{LDM} at various temperatures. In addition, temperature rise of thermocouple junction of neighboring platform produced by heat flow through substrate from heated platform needs to be subtracted from measured $\Delta T_{N(TC)}$ for accurate measurement. These could be investigated using platforms on which LDM is not anchored. The voltage was applied to heater and heating power and temperature rise of thermocouple junctions of heated and neighboring platforms was measured at various temperatures. We could then acquire temperature dependence of thermal resistance from platform tip to heat sink by dividing temperature rise of thermocouple junction by heating power. R_H and R_N should have same tendency with it even if there might be a small variation in magnitude caused by distance between heater and thermocouple junction. Considering that thermal resistance from platform tip to heat sink mainly originates from thermal resistance of suspended part of platform, it is also reasonable to assume that R_C also has same temperature dependence. And, from this measurement, we also obtained the ratio of temperature rise of thermocouple junction of neighboring platform to that of heated platform, which is used to subtract the temperature rise produced by heat transfer through substrate from measured $\Delta T_{N(TC)}$. We found that the amount of heat transferred through substrate is equivalent to that through LDM having thermal conductance of ~1×10^{-8} W/K. Therefore, if the thermal conductance of LDM is comparable to or smaller than this value, the parasitic heat flow will reduce the accuracy of the measurement of the thermal conductivity of LDM.

Seebeck Coefficient

Seebeck coefficient of LDM can be calculated by

$$S_{LDM} - S_{Pt} = \frac{V_{TE}}{\Delta T_{H(TC)} - \Delta T_{N(TC)}} \tag{8}$$

where S_{LDM}, S_{Pt}, V_{TE}, and $\Delta T_{H(TC)}$ are Seebeck coefficient of LDM, Seebeck coefficient of platinum, and measured thermoelectric voltage, and temperature rise of thermocouple junction of heated platform, respectively. In most cases, S_{Pt} is negligibly small compared to S_{LDM} because we are interested in material which has high Seebeck coefficient. However, in case that S_{LDM} is small, S_{Pt} needs to be added to the measured Seebeck coefficient. Also, there might be a temperature difference between thermocouple junction and end of LDM if they are positioned far from each other or thermal conductance of LDM is large. Then, instead of $\Delta T_{H(TC)}$-$\Delta T_{N(TC)}$, we can use temperature difference between two ends of LDM calculated as

$$\Delta T = P_1 R_{LDM} = \Delta T_{N(TC)} \frac{R_{LDM}}{R_N} \tag{9}$$

Electrical Conductivity

Electrical conductivity is measured using two platinum layers connected to each other through LDM. However, resistance of platinum layer should be subtracted from measured resistance. One method is to calculate resistance of platinum layer by using the resistivity measured with calibration structure (inset, Figure 3(a)). Another method is to electrically connect platform tip with one right next to it using FIBID and measure the resistance of the platinum structures. In addition, two probe measurements can also have errors arising from contact resistance but in the case of highly conductive LDMs this is not such a major source of inaccuracy.

Thermoelectric Properties of GaAs/MnAs Core/shell Naowires

We investigated thermoelectric properties of Gallium Arsenide (GaAs)/Manganese Arsenide (MnAs) core/shell nanowire using the workbench. GaAs/MnAs core/shell nanowire is a suitable material for investigating magneto-thermoelectric effects, such as magneto-caloric, magneto-Seebeck, and spin-Seebeck effects, of quasi-one-dimensional system because MnAs is a ferromagnetic material whose Curie temperature is near room temperature. As a preliminary experiment for magneto-thermoelectric effects, we measured thermoelectric properties as a function of temperature. The nanowire was grown by molecular beam epitaxy and, according to TEM analysis, cross-section of nanowire is a hexagon and the longest diagonal of GaAs core and the thickness of MnAs shell are estimated to be 200 nm and 15 nm, respectively. IPA solution containing nanowires was drop cast on workbench and FIBID of

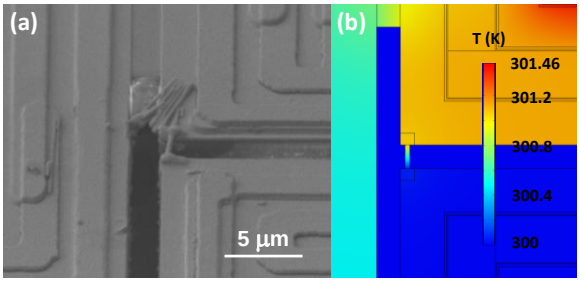

Figure 5: (a) SEM images of workbench on which GaAs/MnAs core/shell nanowire is anchored (b) Color plot of temperature distribution at 300 K (COMSOL finite element model simulation).

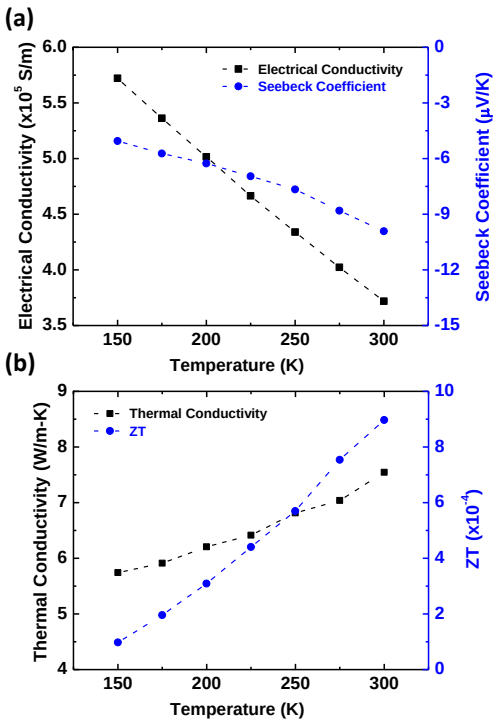

Figure 6: (a) Electrical conductivity of MnAs shell, Seebeck coefficient of nanowire-platinum thermoelectric circuit (b) Thermal conductivity and ZT of nanowire as a function of temperature.

platinum was used to make mechanical contact and improve electrical and thermal contact between nanowire and platinum pad. Figure 5(a) is SEM image of workbench on which single GaAs/MnAs core/shell nanowire is anchored and Figure 5(b) shows temperature distribution of the sample that is FEM simulation result.

Figure 6(a) shows temperature dependence of electrical conductivity of MnAs shell and Seebeck coefficient of nanowire-platinum thermoelectric circuit. The electrical transport (electrical conductivity and Seebeck coefficient) of nanowire are dominated by MnAs shell because GaAs core is intrinsic. Considering Seebeck coefficient of platinum is -5 μV/K [10], absolute Seebeck coefficient of MnAs shell is -16.9 μV/K at 300 K which is larger than previously reported Seebeck coefficient of bulk MnAs (-13 μV/K) [11]. It might be explained by quantum size effect on Seebeck coefficient.

Figure 6(b) shows the temperature dependence of thermal conductivity and thermoelectric figure of merit ZT of the nanowire. In contrast with electrical transport, most part of thermal transport occurs through the GaAs core because of its large cross-sectional area and dominant lattice thermal conductivity. The thermal conductivity of nanowire is 7.5 W/m-K at 300 K. It is smaller than theoretical value (20 W/m-K) of 200 nm-diameter GaAs nanowire which is recently reported [12]. It decreases with decreasing temperature whereas theoretical value has a maximum value near 100 K. These are thought to be because GaAs core has stacking faults perpendicular to the wire axis. In some regions, the nanowires undergo a transformation in crystal structure from zinc blende with a [111] growth direction to wurtzite with a [0001] growth direction [13]. It would increase phonon-boundary scattering and lead to smaller thermal conductivity than the theoretical value. Furthermore, it would make phonon-boundary scattering more dominant than Umklapp phonon-phonon scattering that results in the increasing thermal conductivity with decreasing temperature. For calculating ZT, the Seebeck coefficient of platinum [12] was added to the measured Seebeck coefficient of nanowire-platinum thermoelectric circuit. Also, the electrical conductivity was recalculated with dimension of core and shell instead of only shell because we need electrical conductivity of core/shell nanowire instead of that of shell for obtaining ZT.

ACKNOWLEDGEMENT

This work was supported by the NSF under MRSEC Grant DMR-0820404. The authors acknowledge use of facilities at the PSU site of NSF NNIN. Travel support has been generously provided by the Transducer Research Foundation.

REFERENCES

[1] M. Dresselhaus, G. Dresselhaus, X. Sun, Z. Zhang, S. Cronin, and T. Koga, "Low-dimensional thermoelectric materials," *Physics of the Solid State*, vol. 41, pp. 679-682, 1999.

[2] A. I. Hochbaum, R. Chen, R. D. Delgado, W. Liang, E. C. Garnett, M. Najarian, A. Majumdar, and P. Yang, "Enhanced thermoelectric performance of rough silicon nanowires," *Nature*, vol. 451, pp. 163-167, 2008.

[3] L. Shi, D. LI, C. Yu, W. Jang, D. Kim, Z. Yao, P. Kim, and A. Majumdar, "Measuring thermal and thermoelectric properties of one-dimensional nanostructures using a microfabricated device," *Journal of heat transfer*, vol. 125, pp. 881-888, 2003.

[4] A. I. Boukai, Y. Bunimovich, J. Tahir-Kheli, J. K. Yu, W. A. Goddard Iii, and J. R. Heath, "Silicon nanowires as efficient thermoelectric materials," *Nature*, vol. 451, pp. 168-171, 2008.

[5] M. A. Panzer, M. Shandalov, J. A. Rowlette, Y. Oshima, Y. W. Chen, P. C. McIntyre, and K. E. Goodson, "Thermal properties of ultrathin hafnium oxide gate dielectric films," *Electron Device Letters, IEEE*, vol. 30, pp. 1269-1271, 2009.

[6] Y. Sungtaek Ju, X. REN, W. XIAO, N. Smith, R. Fontana, W. Lee, K. Carey, M. Ho, D. Hsiao, and B. Gurney, "A combined experimental and numerical study of temperature rise in GMR sensors due to self-heating," *IEEE transactions on magnetics*, vol. 37, pp. 1701-1703, 2001.

[7] C. H. Mastrangelo, Y.-C. Tai, and R. S. Muller, "Thermophysical properties of low-residual stress, silicon-rich, LPCVD silicon nitride films," *Sensors and Actuators A: Physical*, vol. 23, pp. 856-860, 1990.

[8] M. B. Kleiner, S. A. Kuhn, and W. Weber, "Thermal conductivity measurements of thin silicon dioxide films in integrated circuits," *Electron Devices, IEEE Transactions on*, vol. 43, pp. 1602-1609, 1996.

[9] A. D. McConnell, S. Uma, and K. E. Goodson, "Thermal conductivity of doped polysilicon layers," *Microelectromechanical Systems, Journal of*, vol. 10, pp. 360-369, 2001.

[10] R. Huebener, "Size effect on phonon drag in platinum," *Physical Review*, vol. 140, p. A1834, 1965.

[11] U. Neitzel and K. Barner, "The thermoelectric power of MnAs1-xPx compounds," *Journal of Physics C: Solid State Physics*, vol. 11, p. 4975, 1978.

[12] P. N. Martin, Z. Aksamija, E. Pop, and U. Ravaioli, "Reduced thermal conductivity in nanoengineered rough ge and gaas nanowires," *Nano letters*, vol. 10, pp. 1120-1124, 2010.

[13] N. Dellas, J. Liang, B. Cooley, N. Samarth, and S. Mohney, "Electron microscopy of GaAs/MnAs core/shell nanowires," *Applied Physics Letters*, vol. 97, p. 072505, 2010.

CONTACT

*Srinivas Tadigadapa, sat10@psu.edu

1 GHZ GAN RESONANT BODY TRANSISTORS WITH ENHANCED OFF-RESONANCE REJECTION

Laura C. Popa and Dana Weinstein
Massachusetts Institute of Technology, Cambridge, Massachusetts, USA

ABSTRACT

We present 1 GHz Gallium Nitride (GaN) Resonant Body Transistors (RBTs) with >100× improvement in signal-to-noise ratio relative to previously reported devices. This is realized by strong mechanical coupling of a 1-port resonator with a second resonator in which a High Electron Mobility Transistor is used for sensing. As the first demonstration of GaN RBTs in gold-free technology, this work enables *Q*s up to 3077 at 1 GHz, with $f \cdot Q$ product of 3.1×10^{12}. We also demonstrate an acoustic transconductance (g_{em}) of 72 µS, >2× higher than previously demonstrated GaN RBTs. With such high *Q* and g_{em}, as well as reduced feed-through, these GaN RBTs can enable high performance, low phase-noise oscillators monolithically integrated with high power electronics for clocking.

INTRODUCTION

As third and fourth generation (3G, 4G) wireless communications have emerged over the past few years the demand for higher bandwidth wireless data transfer has increased. This has placed great importance on the performance of radio base stations, requiring low phase-noise frequency sources that exhibit immunity to nearby interferers and excellent power handling [1]. With quality factors in the thousands at GHz frequencies, small footprints, and the ability to achieve multiple frequencies on the same chip, MEMS resonators can provide building blocks for low phase-noise oscillators operating over a wide frequency range.

Single-stage frequency sources are typically preferred for reduced cost, size, weight and power. As a wide bandgap semiconductor, GaN provides high electron velocities, charge densities (1×10^{13} cm^{-2} in AlGaN/GaN), and critical electric fields, ideal for high power (>10W/mm), high frequency (>300 GHz) integrated circuits. As a result, GaN High Electron Mobility Transistors (HEMTs) have been increasingly used for microwave monolithically integrated circuits (MMICs) and high power electronics. The ability to amplify and deliver higher power densities than gallium arsenide makes GaN a great candidate for use in single-stage oscillators without the need for additional amplifiers.

GaN also exhibits excellent electromechanical properties, such as high piezoelectric coefficients (electromechanical coupling k_T^2 up to 2% in FBARs [2]), high acoustic velocities and low acoustic losses. Hence, this technology offers a platform for seamless integration of high performance RF MEMS resonators with high power, high frequency electronics. Monolithic integration of MEMS resonators with ICs would lead to reduced matching constraints and parasitics, which ultimately translate into lower phase-noise and reduced jitter clocks, especially at high frequency.

For successful implementation in low phase-noise oscillators, these resonators must satisfy two requirements [1]: (1) High net signal-to-noise ratio and (2) small half-power bandwidth, i.e., high *Q*. For broadband operation, resonators must be scaled to multi-GHz frequencies. At such high frequencies, passive resonators suffer from capacitive feed-through between drive and sense transducers which overwhelms the mechanical peak and lowers the signal-to-noise ratio (SNR). Active Field Effect Transistor (FET) sensing has been shown to overcome this challenge by providing internal electromechanical amplification of the resonant signal. In

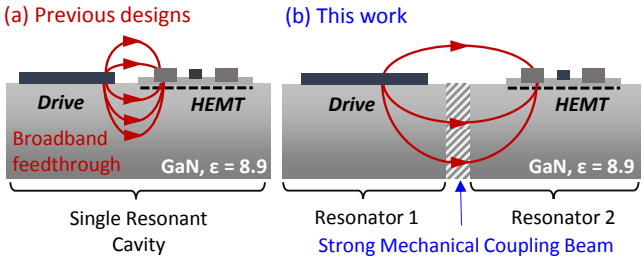

Figure 1: Schematic of GaN Resonant Body Transistor. (a) Placement of drive transducer and sense transistor in the same acoustic cavity leads to broadband feed-through. (b) Electrical isolation between drive transducer and sense transistor is done by mechanically coupling two resonators.

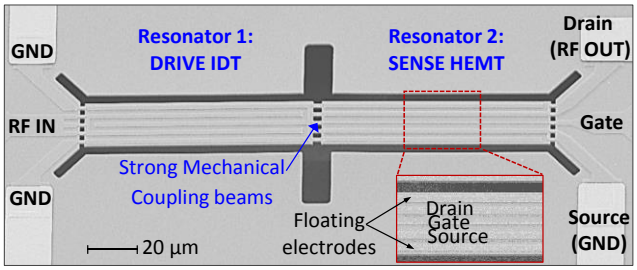

Figure 2: SEM of mechanically coupled drive and sense resonators. Source and drain electrodes, and two additional floating electrodes are patterned to match the drive transducer. A 5-tether approach is implemented to allow for a larger heat sink due to the HEMT current, as well as for improved power handling and spurious mode reduction [7]. Trenches are patterned through GaN to provide stress relief and better isolation between drive/sense.

Silicon, FET sensing has enabled resonators over 37 GHz [3]. In GaN, multi-GHz HEMT-sensed resonators have been demonstrated in contour mode [4] and thickness mode resonators [5]. These previously demonstrated RBTs implement a single resonant cavity containing both drive transducer and sense transistor, resulting in direct electrical coupling between the RF input and transistor terminals (Fig. 1(a)), which increases the broadband floor of the device. Instead, we propose an RBT in which drive transducer and sense transistor are embedded in two electrically isolated, mechanically coupled resonators (Fig. 1(b)). While mechanical coupling of two or more passive MEMS resonators has been previously used to achieve tunable, low insertion-loss filters [6], this is the first implementation that takes advantage of active transistor sensing.

PRINCIPLE OF OPERATION

Fig. 2 shows the SEM of a mechanically coupled GaN RBT. Acoustic waves are launched piezoelectrically with an interdigitated transducer (IDT) in resonator 1. This first resonator is mechanically coupled to resonator 2, via an array of beams of length equal to half wavelength of the beam vibration at the desired resonant frequency. This guarantees that the two bars will resonate in phase [6]. A HEMT is embedded in resonator 2 for sensing. At resonance, standing waves are induced in both drive and sense resona-

9781940470016/HH2014/$25©2014TRF
DOI 10.31438/trf.hh2014.72

tors, leading to strain fields that modulate the carrier concentration of the 2D electron gas (2DEG) in the channel of the HEMT. Then these strains induce a polarization field through the direct piezoelectric effect:

$$\overrightarrow{\boldsymbol{P_{PE}}} = e_{51}\epsilon_{zx}\hat{\boldsymbol{x}} + e_{51}\epsilon_{yz}\hat{\boldsymbol{y}} + \\ +\left(e_{31}\epsilon_z + e_{31}\epsilon_y + e_{33}\epsilon_z\right)\hat{z}, \quad (1)$$

where ϵ_x, ϵ_y, and ϵ_z are the strains along the x, y and z-axis respectively and ϵ_{yz} and ϵ_{zx} are shear strains. Here, e_{31}, e_{33} and e_{51} are the piezoelectric coefficients corresponding to the Wurtzite crystal structure. This piezoelectric polarization induces strain-dependent bound charge throughout the AlGaN/GaN heterostructure as discussed in [4, 8]. As a result, free carriers flow from the Ohmic contacts to compensate for this piezoelectrically modulated charge which results in an AC modulation of the drain current.

The AC current modulation is represented in the equivalent small signal model in Fig. 3. In the electrical domain, this device can be decomposed into two branches. The RLC branch corresponds to the mechanical resonance induced in the two coupled bars, and is equivalent to a 1-port passive device. The second branch is a modified HEMT equivalent circuit, where the normal transistor transconductance is now replaced by an electromechanical transconductance, g_α [9]. The parasitic feed-through between the input and output of the RBT includes a capacitance, C_{ft} and a substrate resistance, r_{ft}. This parasitic feed-through is what the mechanically coupled RBT design addresses, with an order of magnitude improvement from previously demonstrated RBTs that contain both drive and sense in the same resonant cavity.

While mechanically coupled RBTs can be implemented in various bulk or flexural modes, in this work we focus on the zero order symmetric Lamb mode, S_0. The authors have previously optimized and investigated the transduction capability of these modes in standard MMIC technology, achieving Qs as high as 5500 and effective electromechanical coupling (k_{eff}^2) of 0.39% for resonators between 1-2 GHz [10]. Fig. 4(a) shows a 3D simulation of 2 mechanically coupled Lamb mode resonators. The 2D cross-section of the strain under the HEMT, with maximum modulation

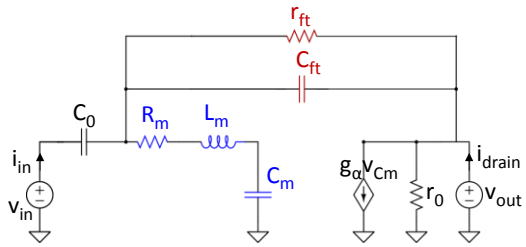

Figure 3: Equivalent circuit model of the mechanically coupled RBT. Blue elements represent the equivalent mechanical RLC branch, according to a Butterworth Van Dyke model while the right side captures the electromechanical transconductance.

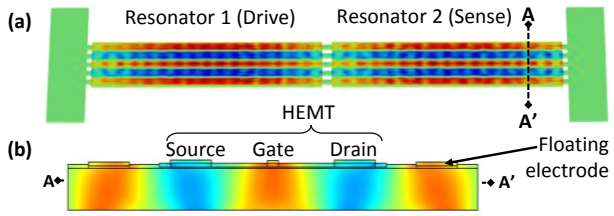

Figure 4: (a) 3D mode shape of strongly coupled resonators. (b) Gate of sense HEMT is placed at maximum strain. Source, drain and floating electrodes are patterned to match drive IDT.

under the gate for optimal drain current modulation, is presented in Fig. 4(b). The gate of the embedded HEMT is designed at 500 nm. Two floating electrodes are patterned in gate metal on either side of the HEMT in order to maintain mass loading symmetric to the drive IDT.

FABRICATION

Devices were fabricated at MIT using Raytheon's standard MMIC GaN-on-Si heterostructure, comprised of Molecular Beam Epitaxy (MBE) AlGaN(25nm)/GaN(1.7µm) on (111)-Si using a thin AlN nucleation layer (Fig. 5(a)).

This is the first implementation of GaN MEMS resonators in a Au-free HEMT process flow. While typical HEMT MMIC processes use Au electrodes to make Ohmic contact to the 2DEG channel and for low-resistance transistor gates, many efforts have been made to realize Au-free metallization schemes in order to allow for the integration of GaN MMICs in CMOS foundries [11]. Au-based Ohmic contacts involve a final anneal step at very high temperatures (850-950˚C) that allows the metal to diffuse and contact the 2DEG. As a result, the electrodes that undergo this step suffer from rough morphology and poor line acuity, which leads to yield and performance limitations in MEMS resonators, especially when scaling to higher frequencies. In the case of the RBT, where the HEMT is embedded in the resonant cavity, these rough Ohmic contacts can degrade mechanical performance. In this work we make use of Au-free Ohmic contacts that undergo a lower temperature anneal (600˚C). Eliminating Au-electrodes from the resonators also allows for higher resonator quality factors, since Au is known to cause additional dissipation through mass loading, phonon-electron scattering and interfacial losses.

We fabricate mechanically coupled RBTs in a standard GaN HEMT flow with only two additional steps. Processing starts with a shallow AlGaN etch in a BCl_3/Cl_2 chemistry which removes the 2D electron gas (2DEG) between the AlGaN/GaN layers in areas where IDTs will be patterned. This allows for transduction through the entire volume of the GaN film. The 2DEG is only kept in the areas where HEMTs will be fabricated. Next, the Ohmic metal (5 nm Ta/100 nm Al/20 nm Ta) is deposited, and a 10 minute anneal at 600˚C is used to drive the metal in to contact the 2DEG. The gate metal of the transistor (100 nm Ni) is then patterned. This step is also used to define piezoelectric IDTs (Fig. 5(b)). A PECVD Si_3N_4 layer (180 nm) is then deposited to passivate the surface and protect the 2DEG channel. One modification to the standard MMIC process involves a deep Cl_2 GaN etch in an inductively coupled plasma (Fig. 5(c)) which defines the acoustic cavities. Metal pads (50 nm Ti/300 nm Au) are then connected to the gate and Ohmic electrodes through vias in the passivation layer, for easy device probing. Finally, a XeF_2 silicon etch releases the resonators (Fig. 5(d)).

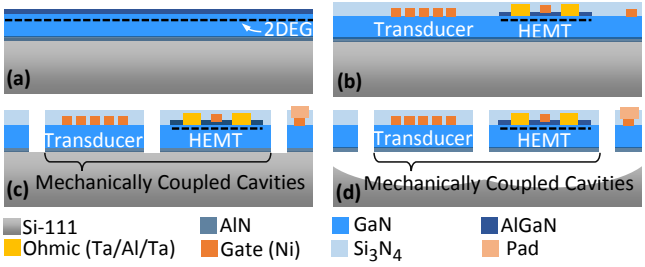

Figure 5: Mechanically coupled RBTs are fabricated in Au-free standard HEMT process with two additional steps for defining the acoustic cavity and for the final release.

EXPERIMENTAL RESULTS

Mechanically coupled RBTs were measured in vacuum on a Cascade RF probe station using a standard 2-port measurement on an Agilent 5225A Network Analyzer, and de-embedded using an on-chip Open structure. For each of these devices, the electromechanical transconductance is defined as:

$$g_{em} = Y_{21} - Y_{12} \quad (2)$$

Low-velocity coupling

Fig. 6 plots the measured electromechanical transconductance, g_{em}, of the device shown in Fig. 2. The 1.012 GHz resonance exhibits Q of 3077, with $f{\cdot}Q$ product of $3.1{\times}10^{12}$. The off-resonance floor in this device is below 0.8 µS, which is >10× lower than previously reported RBTs [4, 5]. This corresponds to an SNR of 20.4. As discussed before, this broadband suppression is critical for the realization of low phase-noise oscillators, especially when scaling to GHz frequencies. The effect of reduced broadband floor can be seen in the inset of Fig. 6, which shows a clear 180˚ shift at the mechanical resonance.

The DC behavior of the embedded HEMT used for electromechanical sensing is shown in Fig. 7(a). The transistor drives a maximum current of 12 mA in saturation, and has a threshold voltage of -4 V. The current degradation at drain bias (V_{DS}) > 2 V can be attributed to self-heating, as the HEMT is released from the substrate so the heat can only dissipate through the 5 anchoring tethers. In Fig. 7(b), the dependence of g_{em} on drain bias in the linear regime is shown, exhibiting a linear increase in electromechanical transconductance at resonance. It is important to note that the broadband floor remains constant independent of drain voltage. This behavior yields an increase in SNR from 7.6 for V_{DS}=0.9 V to 13.6 for V_{DS}=1.1 V. In Fig. 7(c), the effect of gate bias (V_{GS}) on the electromechanical transconductance is shown for a fixed drain voltage. Optimal performance is obtained when V_{GS} is set to -2V.

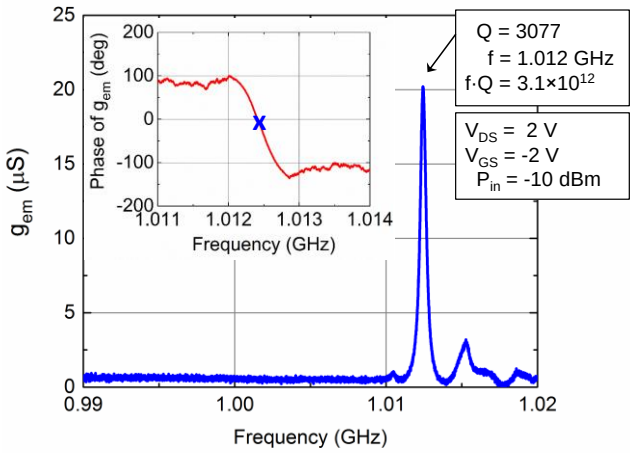

Figure 6: Measured g_{em}=Y_{21}-Y_{12} of mechanically coupled RBT in Fig. 2 shows >10× reduction in broadband floor compared to previously reported results. Inset shows 180˚ phase shift corresponding to mechanical resonance.

High-velocity coupled RBTS

Fig. 8 presents an SEM of an RBT where the mechanical coupling between the drive and sense resonators is realized at the point of maximum velocity. This design opens up additional tethers on the sense resonator to enable routing for multi-finger HEMTs, necessary to achieve higher electromechanical transconductance, g_{em}. To optimize performance, both gates of the multi-finger HEMT are placed at points of maximum strain. The 2-gate transistor reaches a saturation current of 30 mA. The measured g_{em}

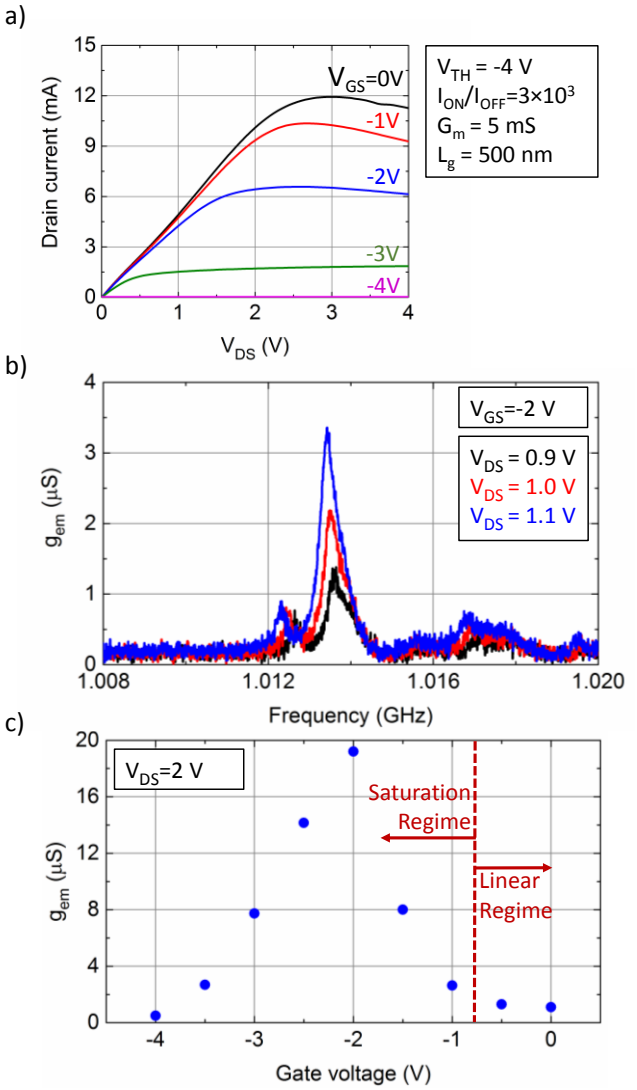

Figure 7: (a) DC behavior of embedded HEMT. (b) Dependence of g_{em} on drain voltage in the linear regime shows linear increase in acoustic transconductance, while floor remains mainly unchanged. (c) Dependence of g_{em} on gate voltage in the saturation regime shows optimal performance when the gate is set to -2 V.

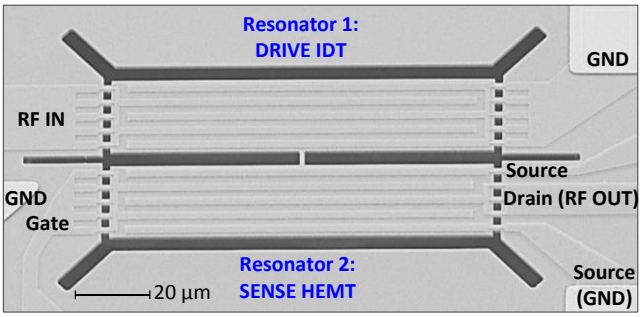

Figure 8: SEM of mechanically coupled RBT, with coupling beam at maximum velocity point. The embedded HEMT has two fingers, with gate length of 3.7 µm. Similar to the low-velocity case, trenches etched in GaN are used for stress relief and better isolation between drive/sense. An extra ground electrode is placed between the RF input and gate for better shielding.

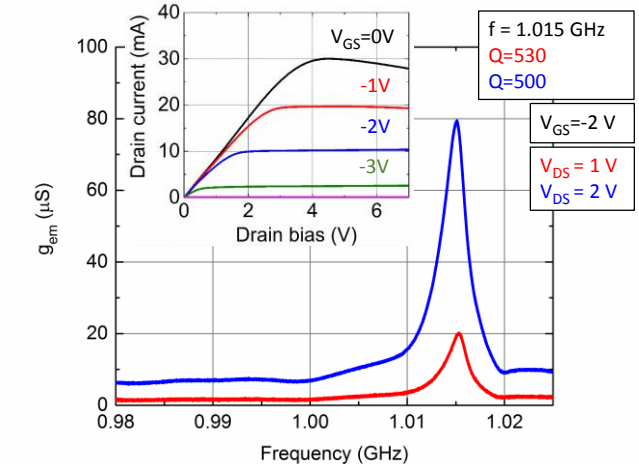

Figure 9: Measured g_{em} for double-gate RBT shows an acoustic transconductance of 72 µS, >2× higher than previously reported GaN RBTs, with SNR > 50.

for two drain bias points is shown in Fig. 9. While there is a small change in the broadband floor with biasing conditions, the floor at V_{DS}=2 V is still smaller than previously demonstrated devices, while the g_{em} of 72 uS is the largest achieved in GaN RBTs to date. Possible reasons why this device provides less isolation than the low-velocity coupling case include spatial proximity of electrode routing outside the resonant structure, larger overlap area between the drive and sense cavity, and a higher overall transistor transconductance. However, the SNR for this device is higher than in the low-coupling case.

Table 1 summarizes the results for 3 devices described in this work, including 2 low-velocity coupled RBTs (one with L_{gate}=3.7 µm and the other shown in Fig. 1) and one high velocity coupled RBT (Fig 8). These resonators are compared with HEMT-sensed GaN resonators published in literature, and demonstrate order-of-magnitude improvement in SNR.

Table 1: Summary of mechanical performance of state-of-the art GaN RBTs shows 100× improvement in SNR in this work.

	f (GHz)	Q	G_M (mS)	I_{max} (mA)	g_{em} (µS)	floor (µS)	SNR
[4]	2.67	650	2.5	7.5	6	14	0.4
[5]	4.23	250	3	8	25	50	0.5
Low vel. 1	1.013	3068	4.3	11	9	0.8	11.3
Low vel. 2	1.013	3077	5	12	19	0.9	20.4
High vel.	1.015	530	10	30	72	1.4	51.4

Frequency Tuning

One consequence of HEMT sensing in the GaN RBT is self-heating of the suspended structure, which is thermally grounded only through small suspension beams. This self-heating leads to a change in the elastic constants of the resonant cavity, resulting in a frequency shift. A previous study by the authors found the temperature-coefficient of frequency of these 1GHz Lamb modes [10] to be -24.2 ppm/°C. Here, we investigate the frequency shift as a function of applied drain current, as shown in Fig. 10, with over 0.2% frequency shift at 6.6mA bias current. The device provides a built-in microheater enabling tuning capabilities for frequency drift compensation due to temperature, packaging stresses, or other time-dependent parameters.

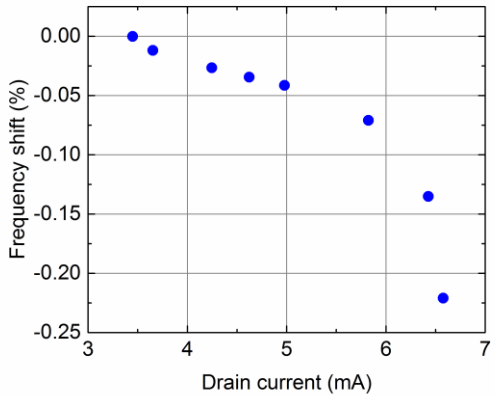

Figure 10: Measured resonant frequency shift with drain current for low-velocity coupling device shows 0.2 % tuning capability.

CONCLUSION

We have demonstrated a method for suppressing off-resonance feed-through in GaN RBTs, enabling >100× improvement in SNR. These devices were fabricated in a Au-free process which has yielded the highest *f·Q* products in GaN RBTs to date. At the same time, the RBTs presented here achieved >2× higher acoustic transconductance than previous GaN devices. Realized in standard MMIC technology, these devices can leverage strong piezoelectric coupling, large breakdown fields, and high speed HEMTs for monolithically integrated, low phase-noise clocks.

ACKNOWLEDGEMENTS

We thank William Hoke, Brian Schultz and Thomas Kazior (Raytheon) for GaN growth. Fabrication took place at MIT's MTL under DARPA DAHI Foundry N66001-13-1-4022 and NSF Career ECCS-1150493 funding.

REFERENCES

[1] R. J. van de Plassche, J.H. Huijsing, W.M.C. Sansen, *Analog Circuit Design*, Kluwer Academic Publishers, Boston, 1997.

[2] A. Muller, D. Neculoiu, G. Konstantinidis, et. al., "6.3 GHz Film Bulk Acoustic Resonator structures based on Gallium Nitride/Silicon Thin Membrane", Elec. Dev. Lett., 30, 8 (2009).

[3] D. Weinstein, S.A. Bhave, "Acoustic Resonance in an independent-gate FinFET," Hilton Head 2010, pp.459-462.

[4] L.C. Popa, D. Weinstein, "Switchable Piezoelectric Transduction in AlGaN/GaN MEMS Resonators," Transducers 2013, pp.2461-64.

[5] A. Ansari, M. Rais-Zadeh, "A Thickness-Mode AlGaN/GaN Resonant Body High Electron Mobility Transistor", Trans. Elec. Dev, 61, 4 (2014).

[6] F.D. Bannon, J.R. Clark, and C.T.-C. Nguyen, "High-*Q* HF Microelectromechanical Filters", IEEE Journ. Sol. St. Circ, 35, 4 (2000).

[7] M. Shahmohammadi, B. Harrington, R. Abdolvand, "Concurrent Enhancement of Q and Power-handling in Multi-Tether High-Order Extensional Resonators", MTT, pp.1452-1455 (2010).

[8] M. Faucher, et al, "Amplified piezoelectric transduction of nanoscale motion in gallium nitride electromechanical resonators," Appl. Phys. Lett., 94, 233506 (2009).

[9] R. Marathe, B. Bahr, W. Wang et. al., "Resonant Body Transistors in IBM's 32 nm SOI Technology," J. MEMS, no. 99 (2013).

[10] L.C. Popa, and D. Weinstein, "L-band Lamb mode resonators in Gallium Nitride MMIC technology", to be presented at IFCS 2014.

[11] H.-S. Lee, D.S. Lee, T Palacios, "AlGaN/GaN High Electron-Mobility Transistors Fabricated Through a Au-free Technology", Elec. Dev. Lett., vol. 32, no. 5, 2011.

CONTACT

*L.C. Popa, lpopa@mit.edu

DIAMOND HEMISPHERICAL RESONATOR FABRICATION BY ISOTROPIC GLASS ETCH

Jonathan Bernstein, Mirela Bancu, Eugene Cook, Thayne Henry, Peter Kwok, Tenzin Nyinjee, Gayatri Perlin, Bill Teynor, and Marc Weinberg*
Draper Laboratory, Cambridge, Massachusetts, USA

ABSTRACT

We have fabricated polycrystalline diamond hemispheres by Hot-Filament CVD (HFCVD) in spherical cavities wet-etched into a novel high temperature glass substrate. These resonators are 1.4 mm in diameter and have a Q of up to 143,000 in the fundamental wineglass mode, for a ringdown time of 2.4 seconds. As-fabricated resonators have the two degenerate modes frequency matched to as close as 7 Hz, or 0.04% of the resonant frequency (~16 kHz). We have demonstrated laser trimming on a segmented lip resulting in mode matching to better than 0.3 Hz. These resonators show great promise for use as Hemispherical Resonant Gyroscopes (HRGs) on a chip.

INTRODUCTION

There have been many types of gyroscopes successfully miniaturized by MEMS technology. The HRG is a robust, high accuracy vibratory gyroscope which can be operated either in rate or whole-angle mode [1,2]. The HRG requires closely matched frequencies of paired degenerate vibratory modes to operate properly, which in turn requires the resonator to be extremely symmetric (round). Previous axisymmetric ring gyros have been essentially two-dimensional, including the planar ring gyro [3], the disc resonator gyroscope [4], and the BAE-Sumitomo gyro [5].

HRGs have a vibrational node at the bottom where attachment can be made with low anchor losses. Previous approaches to forming round, 3D resonators include blowing glass bubbles [6, 7] and etching cavity molds into silicon [8]. A hemispherical diamond resonator fabricated on silicon substrates by combined rotary electron discharge machining and wet etching was reported in [9]. Our approach to etching a round cavity is to wet etch a hole into an isotropic (glass) substrate. In contrast, it is difficult to etch perfectly round holes in Si which has preferred crystal orientations.

Diamond was selected as the structural material because of its very high strength, low coefficient of thermal expansion (CTE) and high thermal conductivity. This combination of properties gives diamond low thermo-elastic damping (TED), making it an excellent material for high Q resonators. Recently diamond resonators have set records for f –Q product [10]. Although single crystal diamond yields the highest Q ($>10^6$ at room temperature [11, 12]) due to a lack of grain boundaries, it would be difficult to create a single crystal diamond hemisphere. Microcrystalline, nanocrystalline and ultra-nanocrystalline diamond (UNCD) can be deposited by varying the deposition conditions in hot filament or plasma chemical vapor deposition (CVD) reactors. UNCD has very low thermal conductivity [13] and the high density of grain boundaries introduce bulk damping losses. Larger grain size and lower boron doping were found to give higher Q in a wide range of cantilevers and double-ended tuning fork structures [14]. Undoped single crystal diamond was also found to have higher Q than doped diamond [10].

To match the average CTE of diamond and polysilicon (the sacrificial layer) from room temperature to the deposition temperature (~715°C) we require a high temperature glass with a CTE of 3 to 3.5 ppm/°C [15]. Attempts to deposit on fused silica were unsuccessful due to CTE mismatch stress. We used wafers of Corning 1715 glass obtained from the Corning Research group for this purpose [16]. Corning 1715 has a CTE of 3.6 ppm/°C (average from 0 to 800°C), and has an anneal point of 866 °C, which is 305 °C higher than Schott Borofloat.

Testing of the resonators was carried out using a Polytec MSA-400 Laser Doppler Vibrometer with a custom vacuum chamber. Resonators were actuated either electrostatically (using the integrated electrodes) or by shaking the whole chip with a piezoelectric stack. A custom trim station was constructed with a femtosecond laser used to ablate small Au pads from a segmented lip on the hemispheres. Mode frequencies and positions were recorded on the Polytec; this information was used to set up a trim recipe to bring the two degenerate modes to the same frequency.

FABRICATION

Figure 1 shows cross-sections at key steps in the process. A bi-layer of 2 µm UNCD (Ultra Nano-Crystalline Diamond [17]) on top of 2 µm of polysilicon was used to mask the wet etch. Some wafers used 1µm of CVD SiC [19] instead of diamond. The diamond layer was coated with a 1.3 µm layer of PECVD SiO_2 which was used as an etch mask for the diamond. The diamond film was plasma etched in pure O_2 in an ULVAC model NE-550 etcher. Because the glass contains significant concentrations of Al and Ca, a mixture of 50% HCl, 46% H_2O and 4% HF was used at 40 °C to etch the glass. The high ratio of HCl to HF prevents Ca and Al fluorides from precipitating and interfering with the etch. Following the glass etch, the diamond and polysilicon films were stripped in an O_2 plasma and XeF_2 respectively.

Electrode layer: to electrically contact the diamond layer at the anchor, a metal compatible with high temperature diamond deposition is needed [18]. We have used Zr and Nb for this layer. Nb was etched in an SF_6/Ar plasma, Zr was etched using a BCl_3/Ar etch. Some wafers were fabricated without these metal layers.

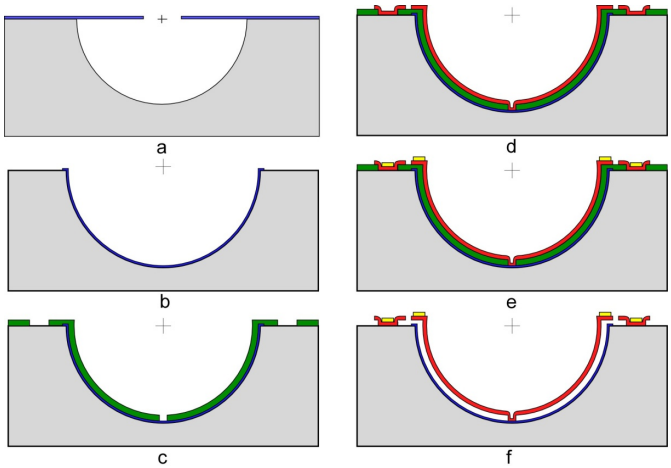

Figure 1: Fabrication cross-sectional drawings: a. isotropic glass etch using UNCD diamond or SiC mask. b. metal sputtering and patterning c. PECVD oxide and polysilicon sacrificial layer deposition and patterning d. HFCVD of micro-crystalline diamond film and patterning e. Liftoff of Cr/Au metal pads f. XeF_2 release (more details in the text).

9781940470016/HH2014/$25©2014TRF
DOI 10.31438/trf.hh2014.73

Solid-State Sensors, Actuators and Microsystems Workshop
Hilton Head Island, South Carolina, June 8-12, 2014

Cavity Formation: An etched cavity is shown in Figure 2 before stripping the etch mask. Automated image-based measurements are made of cavity size, roundness and centricity with respect to the diamond mask hole. 90 diameters are drawn through the center of the hole and a histogram is made (Fig. 3). Due to the isotropic nature of glass, very round holes are possible.

Corning 1715 glass is a high temperature glass made in small batches at the Corning Research facility, and the quality of samples received so far is highly variable. Some wafers yield cavities with diameter, shape and centricity of 80%, some wafers yield near zero. We believe this is due to variations in the concentration of Ca and Al, which cause fluoride precipitates and smaller, off-center or misshapen holes. Commercialization of these resonators will require a supply of high quality, striation-free glass substrates.

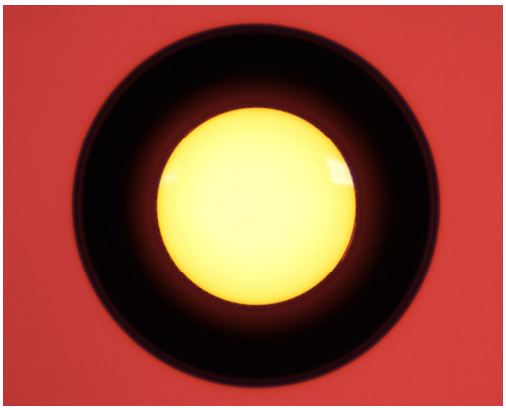

Figure 2. Etched cavity before stripping diamond/polysilicon mask viewed in transmitted light. Central circle is the edge of the diamond mask, black circle is the extent of wet etch (1.38mm).

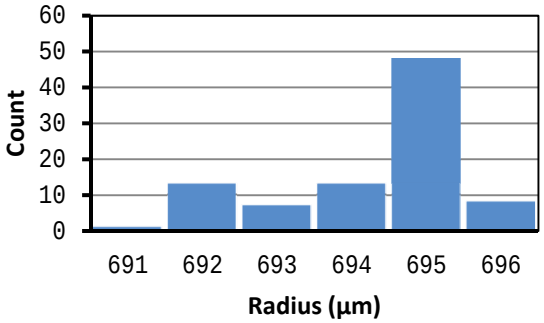

Figure 3. Histogram of hole radii (spaced every 4 degrees) for hole shown in figure 2. Radius variation is +/- 1 µm, close to measurement error.

The electrode metal (Zr or Nb) needs to be protected from the sacrificial Si layer, which would react with the metal and form a silicide. We used a combination of 100 nm of Atomic Layer Deposited (ALD) ZrO_2 or Al_2O_3, followed by 400 nm of PECVD SiO_2 as a barrier between the metal layer and the sacrificial poly-Si. A 5 µm thick layer of polysilicon was then deposited at 650 °C, and patterned in an SF_6 plasma etch. Figure 4 shows a device after polysilicon deposition on top of patterned Nb electrodes.

Lithography: Once the deep cavities are etched into the wafer, subsequent resist must be applied by spraying a mixture of AZP-4620 photoresist, MEK and PGMEA solvents. Most exposures were carried out using a Suss MA6 contact aligner, however, neither contact lithography nor a stepper is capable of forming an image at the bottom of a 0.7 mm deep cavity. Lithography in the cavities was accomplished using a JPSA IX-1000 excimer laser system at 248 nm to ablate 50 µm diameter anchor regions into the photoresist. Once the polysilicon is patterned, the oxide and ALD layers are plasma etched to allow ohmic contact from diamond to metal.

The wafers were then sent out for Hot-Filament CVD (HFCVD) at SP3 diamond technologies. Microcrystalline diamond was deposited at 715 °C in 1.5 % CH_4 in H_2 and 444 ppm tri-methyl boron for doping. The diamond film is coated with 1.5 µm of PECVD oxide, which is used to pattern the diamond in pure O_2 plasma. After stripping the mask SiO_2, Cr/Au is deposited and lifted off to leave bond pads for electrical contacts and trim-pads on diamond tabs at the edge of the hemispheres. The wafer is then diced and a final release is carried out in XeF_2 to remove the polysilicon layer. This release can be carried out before or after packaging.

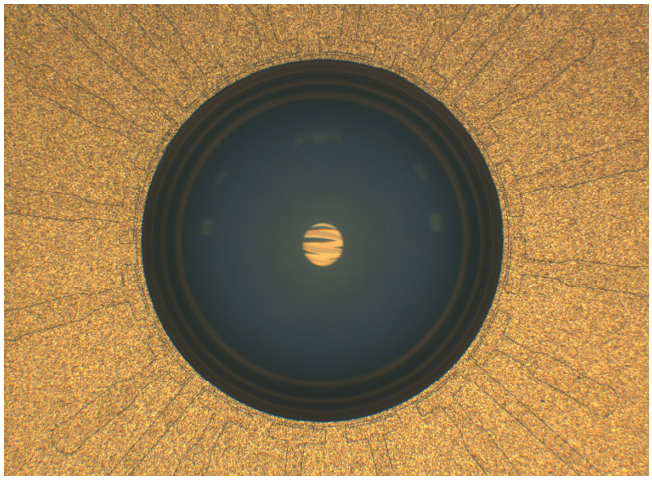

Figure 4. Nb metal pattern around etched cavity, covered with 1 um of SiO2 and 5 um of polysilicon. Central bright spot is an image of the tungsten filament from the microscope illuminator.

Figure 5 shows a diamond hemisphere pulled from its cavity with tape for SEM inspection. The small hole at the top was the anchor.

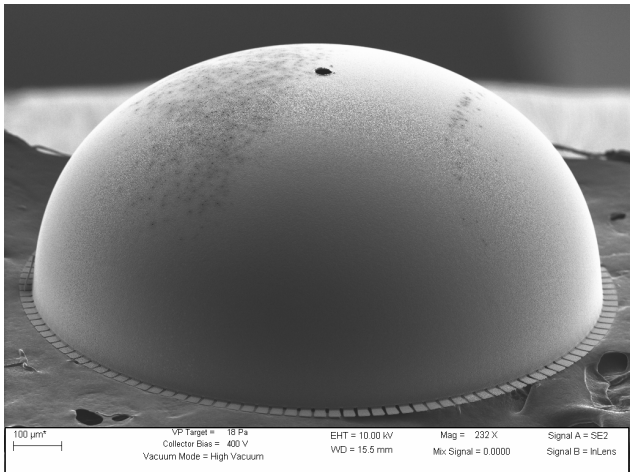

Figure 5. A diamond hemisphere pulled out with tape for examination.

Figure 6 shows a completed device with 16 radial diamond electrodes after dicing. These electrodes were used to drive and sense the resonant motion by edge capacitance.

FREQUENCY TRIMMING

To perform as an HRG, the two degenerate modes used for the gyroscope must be extremely well matched in frequency. Minor imperfections in fabrication cause some mode splitting, which is corrected by laser trimming. Diamond tabs at the lip of the resonator are coated with Cr/Au (Figure 7), which is laser ablated. Mass is removed at the four amplitude peaks of the lower frequency mode, corresponding to the nodes of the upper mode (Figure 8), raising the lower mode with little affect on the upper.

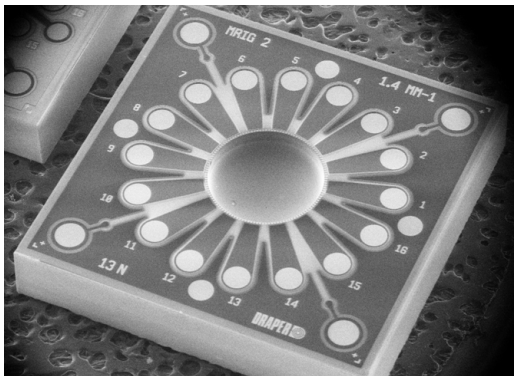

Figure 6. Completed device with 16 radial diamond electrodes.

The laser used for ablation was a Spectra Physics Ti: Sapphire Hurricane producing 100 fs pulses with 1 mJ/pulse power. Apertures were used to reduce the power to avoid damaging the diamond tabs under the Au layer (Figure 8).

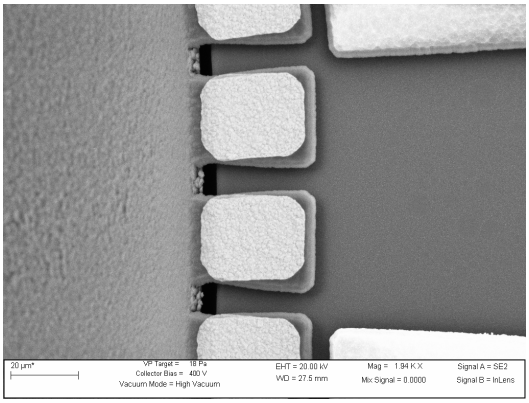

Figure 7. Trim tabs at edge of hemisphere are coated with Cr/Au.

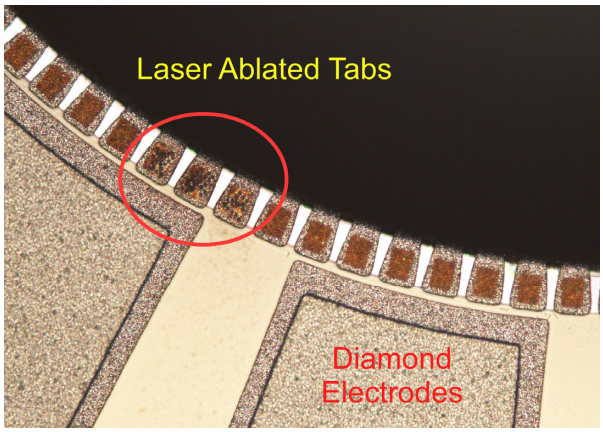

Figure 8. Laser trim tabs after low power laser ablation of the Au layer. Diamond electrodes in proximity to the tabs are used to drive and sense device motion.

TEST RESULTS

A vacuum chamber with electrical feedthroughs and a glass window was constructed for use with a Polytec MSA- 400 scanning laser vibrometer system. Inside the vacuum chamber a pair of Physik Instrument piezoelectric stacks were attached for in-plane and out-of-plane actuation. Chips were mounted temporarily on the piezo stacks using a low melting point wax and a heat lamp. Devices with integrated on-chip actuation electrodes were actuated electrostatically after wirebonding in ceramic chip carriers. Drive signals from the Polytec were used to drive the piezo stacks or the device electrodes, while the resonant modes were measured using a ring of laser spots on the rim of the hemispherical resonators. Drive signals used were 5V of pseudo-random noise offset by 5VDC, with opposite sign applied to an opposing pair of electrodes. The laser vibrometer computes mode shapes which can be viewed as static images or animations. Mode shape and frequency are compared with FEA predictions.

Figure 9 shows data for as-built frequency separation of the n=2 modes of 7 Hz. From the Polytec mode image, the peaks of the lower mode (nodes of the higher node) are noted for laser trim. Figure 10 shows mode data of a chip with as-built separation of 35.5 Hz which was laser trimmed to 0.35 Hz.

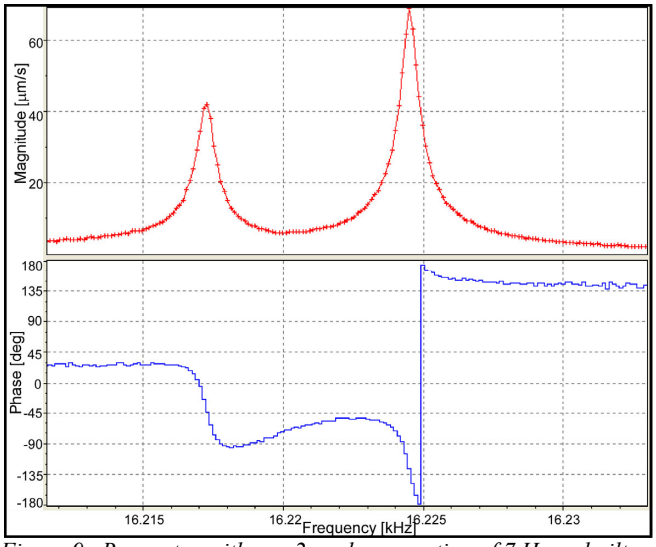

Figure 9. Resonator with n = 2 mode separation of 7 Hz as-built.

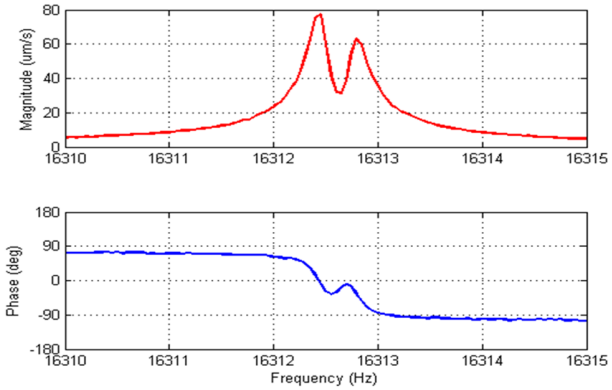

Laser trimmed Δf of 0.35 Hz

Figure 10. Two n = 2 wineglass modes laser-trimmed from 35.5 Hz (as built) to 0.35 Hz final mode separation.

Q and Ringdown: Q was measured using the laser vibrometer either in the frequency domain ($Q = f_0 / \Delta f_{-3dB}$) or time domain by the ringdown method. The ringdown time constant τ is related to the quality factor by $\tau = Q/(\pi f_0)$. Time series data was exported to Matlab for curve fitting to extract τ. Typical Q for these hemispherical resonators ranged from 60,000 to 150,000. A ringdown time of 2.4 seconds is shown in figure 11.

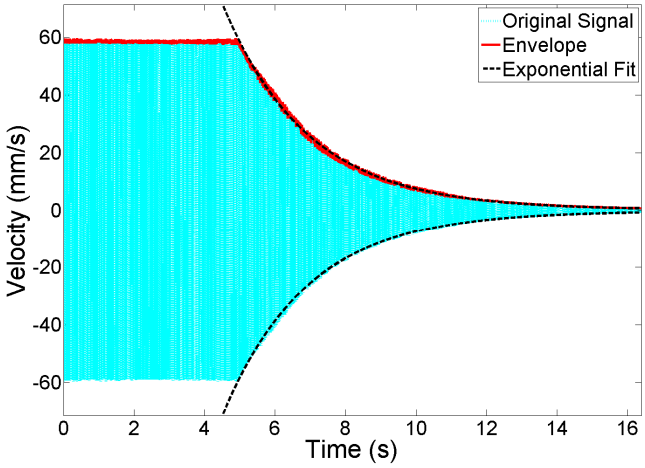

Figure 11. Ringdown measurement for n = 2 mode at 18.399 kHz. Data collected with laser vibrometer. Q = 143,000. τ = 2.4 s at P < 10^{-5} Torr.

CONCLUSIONS

A process for fabrication of high-Q diamond hemispherical resonators has been developed based on isotropic wet etching of a novel high-temperature glass. Diamond-compatible metals (Nb and Zr) survive the high temperature diamond deposition with protective ALD and PECVD oxide layers.

Trimming the n = 2 modes to 0.35 Hz Δf was accomplished by laser ablation of Cr/Au pads on diamond trim-tabs around the periphery of the resonator.

Diamond is a high Q resonator material of extreme strength and chemical resistance. Q as high as 143,000 was observed. Energy loss mechanisms are currently being studied to extend the Q even higher. These hemispherical resonators should form the foundation technology for a new generation of small, accurate MEMS hemispherical resonant gyroscopes.

ACKNOWLEDGEMENTS

The authors gratefully acknowledge the DARPA MRIG program (contract # HR0011-11-C-0045), and Corning Inc. for supplying C-1715 glass. The views expressed are those of the authors and do not reflect the official policy or position of the Department of Defense or the U.S. Government.

REFERENCES

[1] Bryan, G. H., *On the Beats in the Vibrations of a Revolving Cylinder or Bell,* Cambridge Phil. Soc., vol. VII, pt. III, p. 101, Nov. 24, (1890).

[2] Loper, E.J.; Lynch, D.D.; Stevenson, K.M. "Projected Performance of Smaller Hemispherical Resonator Gyros", *Proceedings of Position Location and Navigation Symposium Plans 86*, Las Vegas, NV, USA, Nov. 4-7, pp. 61-64, (1986).

[3] Putty, M. W., and Najafi, K. 1994 ''A micromachined vibrating ring gyroscope.'' *Technical Digest, Solid-State Sensor and Actuator Workshop*, Hilton Head Island, S.C., Transducers Research Foundation, Cleveland, June 13–16, (1994) pp. 213–220.

[4] H.H. Ge and A.D. Challoner, "Environmentally Robust Disc Resonator Gyro", US Patent # 8,393,212 Mar. 12, 2013.

[5] I. Hopkin, "Performance and Design of a Silicon Micromachined Gyro", Symposium Gyro Technology 1997, pp. 1.0-1.11, Stuttgart, Germany, 16-17 September 1997.

[6] D. Senkal, M.J. Ahamed, A.A. Trusov, and A.M. Shkel, "Achieving Sub-Hz Frequency Symmetry in Micro-Glassblown Wineglass Resonators", JMEMS Vol. 23, No. 1, pp. 30-38 (2014).

[7] J.Y. Cho, J.-K. Woo, J. Yan, R.L. Peterson, and K. Najafi, "Fused-Silica Micro Birdbath Resonator Gyroscope (μ-BRG), JMEMS Vol. 23, No. 1, pp. 66-77 (2014).

[8] C.-H. Han and E.S. Kim, "Fabrication of Dome-Shaped Diaphragm with Circular Clamped Boundary on Silicon Substrate," IEEE International Micro Electro Mechanical Systems Conference, Orlando, FL, January 17-21, pp. 505-510 (1999).

[9] M.L. Chan, J. Xie, P. Fonda, H. Najar, K. Yamazaki, L. Lin and D.A. Horsley, "Micromachined Polycrystalline Diamond Hemispherical Shell Resonators", Solid State Sensors, Actuators and Micro-Systems Workshop, Hilton Head Island SC, 6/3-6/12, Transducers Research Foundation, Cleveland (2012), pp. 355-358.

[10] T.L. Naing, T. Beyazoglu, L. Wu, M. Akgul, Z. Ren, T. O. Rocheleau, and C. T.-C. Nguyen, "2.97-GHz CVD Diamond Ring Resonator With Q >40,000," *Proceedings*, 2012 IEEE Int. Frequency Control Symposium, Baltimore, Maryland, May 22-24, pp. 570-575 (2012).

[11] Y. Tao, J.M. Boss, B.A. Moores, and C.L. Degen, "Single-Crystal Diamond Nanomechanical Resonators with Quality Factors > 1 Million", arXiv:1212.1347v1 [cond-mat.mes-hall] 6 Dec 2012.

[12] P. Ovartchaiyapong, L. M. A. Pascal, B. A. Myers, P. Lauria, and A. C. Bleszynski Jayich "High quality factor single-crystal diamond mechanical resonators" Appl. Phys. Lett. 101, 163505 (2012).

[13] P.W. May, W.J. Ludlow, M. Hannaway, P.J. Heard, J.A. Smith, K.N. Rosser, "Raman and conductivity studies of boron-doped microcrystalline diamond, facetted nanocrystalline diamond and cauliflower diamond films", Diamond & Related Materials 17, pp. 105–117 (2008).

[14] H. Najar, M.L. Chan, J. Xie, L. Lin, and D. A. Horsley, "Impact of Doping and Microstructure on Quality Factor of CVD Diamond Micromechanical Resonators", IEEE International Frequency Control Symposium, pp. 82-86, 21-24 May 2012.

[15] D.J. Pickrell et al., "Thermal Expansion of Polycrystalline diamond produced by chemical vapor deposition", Appl. Phys. Lett. 64 (18), p. 2353-2355, 2 May (1994).

[16] J. Bernstein, M. Bancu, E. Cook, M. Chaparala, W. Teynor and M. Weinberg, "A MEMS diamond hemispherical resonator", J. Micromech. Microeng. 23 (2013) 125007.

[17] Advanced Diamond Technologies, www.thindiamond.com, Romeoville, IL.

[18] B. Lux & R. Haubner, "Diamond substrate interactions and the adhesion of diamond coatings", Pure & Appl. Chem., Vol. 68, No. 9, pp. 1783-1788, (1994).

[19] Bill Flounders, bill@eecs.berkeley.edu Marvell Nanofabrication Laboratory University of California, Berkeley, CA 94720-1754.

EXPERIMENTAL VALIDATION OF 3D INTUITIVE MODELING APPROACH FOR ANCHOR LOSS IN MEMS RESONATORS

J. Lake[1], Y.-H. Hwang [1] E. Ng[2], C.-H. Ahn[2], V. Hong[2], Y. Yang[2], Y. Dai[1], and R. Candler[1,3]*
[1]Department of Electrical Engineering, University of California, Los Angeles, CA, USA
[2]Department of Mechanical Engineering, Stanford University, CA, USA
[3]California NanoSystems Institute, University of California, Los Angeles, CA, USA

ABSTRACT

This work introduces a modified anchor loss model that is experimentally validated over an unprecedented range of low frequency (200 kHz – 13 MHz) devices. All measured designs, covering nearly two orders of magnitude in frequency, fell within 12% of the model's prediction. This experimentally validated model provides a framework for designers to modify designs (e.g., stem length, anchor area) in order to reduce anchor loss for arbitrary 3D geometries and identifies key process parameters (e.g., stress) for control of anchor losses.

INTRODUCTION

Silicon micro-electro-mechanical (MEMS) resonators have been developed for a variety of applications including mass sensing [1], energy harvesting [2], position navigating [3] and CPU clock timing [4-7]. In all of these applications, device performance is dependent on Quality factor (*Q)*, which is determined by various energy dissipation mechanisms, such as air damping [8], Akhieser effect [9], Landau-Rumer effect [10], Thermoelastic dissipation (TED) [11], clamping loss [12-14], and surface loss [15]. While air damping, Akhieser, Landau-Rumer, and TED can be accurately modeled, clamping loss and surface loss models require further development. Energy dissipation can only be minimized with better understanding of fundamental energy dissipation mechanisms.

Accurate anchor loss models have been developed for a variety of 2D geometries and a select geometries in 3D, however, a general 3D model that is accurate for low to mid-range frequencies (Hz-kHz) has not been validated previously. One example geometry where analytical anchor loss models have been developed are in-plane flexural vibrations [12]. The technique of perfectly matched layers (PML) has been successful in predicting anchor loss behavior of high frequency resonators [13]. Our modeling approach captures the power loss through the anchor by directly calculating the stress and velocity fields at the anchor point. This approach has been successful previously [14] and this work applies this model to 3D wineglass mode resonators commonly utilized for MEMS gyroscopes.

Over the past two decades, high performance MEMS gyroscopes have been developed and successfully deployed in many military and commercial applications, including aeronautics and ballistics. While these MEMS gyroscopes have been very successful, the performance of these gyroscopes is still significantly inferior to the larger macroscopic gyroscopes. Many of these MEMs gyroscopes are operated at low frequencies and there is strong experimental evidence that suggests clamping loss is causing this performance degradation. Unfortunately, accurate clamping loss models applicable to these resonators have not been successfully utilized and research in this area to date has relied primarily on a trial-and-error approach.

This work outlines the development of a modeling approach that can accurately predict clamping loss in arbitrary 3D MEMS structures. This model also identifies key design characteristics that affect clamping loss and has the potential to lead the way in developing high performance MEMS gyroscopes.

The physical concept describing clamping loss is relatively simple. Clamping loss is caused by acoustic waves propagating in the substrate that carry energy away from the resonator. These waves are generated by the forces at the region of clamping, caused by the resonator's harmonic motion. Despite the relatively simple concept, clamping loss models in low frequency devices to date lacks sufficient experimental verification. Fabrication inconsistencies and fabrication induced stresses are likely causing the current conflicting experimental results. Our modified anchor loss model identifies intrinsic stress as a critical variable that provides a previously missing link enabling the accuracy of this approach.

METHOD

In order to model clamping loss, an intuitive modeling approach is adopted that involves calculating the stress and velocity fields at the anchor point and calculating the power loss per cycle. From the ratio of this power loss to the stored energy in the resonator, the quality factor can be calculated using the following equations:

$$Q_{Anchor} = \frac{\omega U}{\Pi} \qquad \Pi = \iint_S \frac{1}{2}\mathrm{Re}\left(-\sigma_{ij} v_j^{\,*}\right)$$

$$U = \frac{1}{2}\iiint_V \{\sigma\}^T \{\varepsilon\}$$

Where Q_{Anchor} is the anchor limited quality factor, U is strain energy stored in the resonator, Π is the average power lost to the substrate, σ is stress, ε is strain and v is the velocity field at the anchor attachment point.

This approach is general and is directly related to a power calculation based on the force and velocity at the anchor point. The resonator dynamics are modeled utilizing a frequency response function, which is forced by a harmonic boundary load representing the actuation force (Figure 1). The high mesh density and accurate material parameters are crucial to obtaining accurate results with this approach. Intrinsic stress is included in the model as the calculated clamping loss and the resulting quality factor is highly dependent on this value. Q_{Anchor} can vary by orders of magnitude with changes in intrinsic stress, so knowledge of this parameter is critical to calculate accurate results.

For our resonators, a value of 0.3 MPa compressive stress was estimated from knowledge of the fabrication process. In order for the solution to converge, a damping term is included. The damping term is based on TED, the only other relevant damping mechanism in the experimental devices used in this work. TED is also modeled using the Comsol multiphysics package.

In order to experimentally validate this model, ring resonators were fabricated using the Stanford vacuum Episeal process. The anchor structure design parallels the anchor structures of experimental gyroscopes, which often utilize a wine glass resonator mode attached to the substrate with a center post. Rings were scaled with various diameters in order to validate our modeling approach

9781940470016/HH2014/$25©2014TRF
DOI 10.31438/trf.hh2014.74

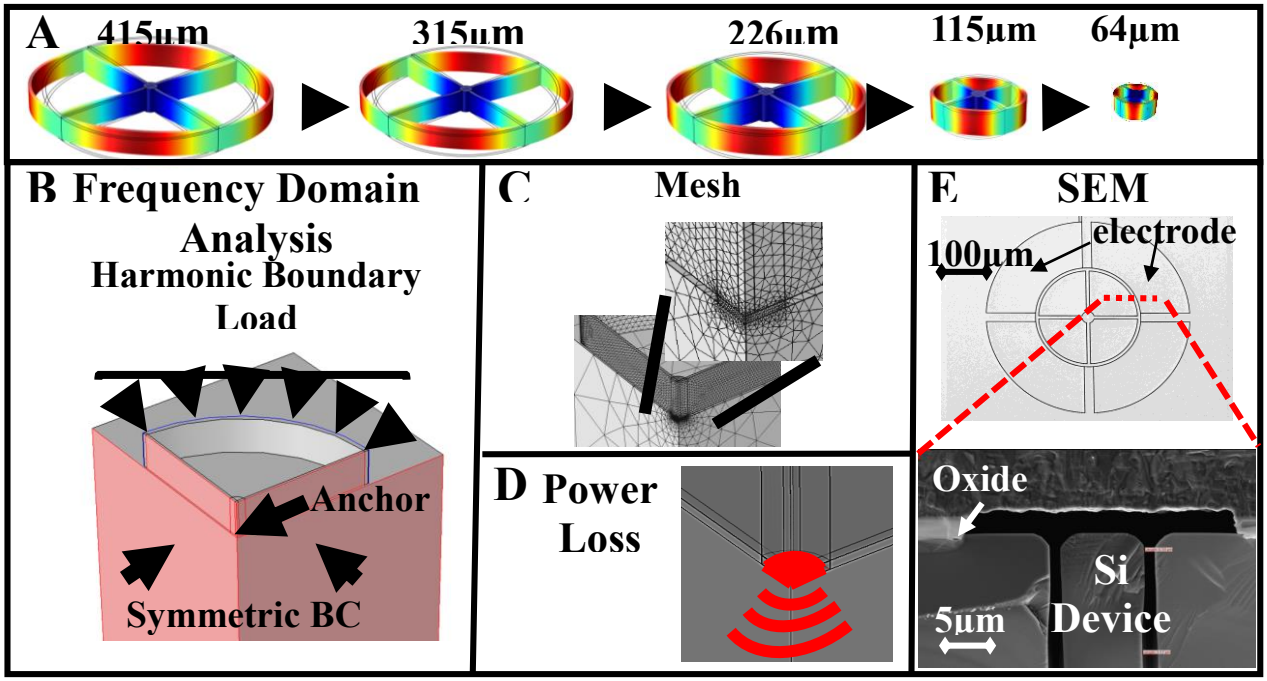

Figure 1: A) Scaled wineglass ring resonators. B) Frequency response model utilizing a boundary load and quarter symmetry C) Mesh distribution. High density mesh required at anchor point. D) Power loss is modeled by calculating the stress and velocity distribution at the anchor point. E) SEM pictures of the top of a 226 µm ring and a cross-section of the same device.

across a wide frequency range (200 kHz – 13 MHz).

The stable manufacturing process provided by the Stanford *epi-seal* encapsulation [16] allows for thorough investigation of the various dissipation mechanisms since it provides consistency across hundreds of devices in a stable vacuum-sealed package. The *epi-seal* encapsulation process was proposed by researchers at the Robert Bosch Research and Technology Center in Palo Alto and then demonstrated in a close collaboration with Stanford University. This collaboration is continuing to develop improvements and extensions to this process for many applications, while the baseline process has been brought into commercial production by SiTime Inc.

RESULTS

Devices were tested using the HP 4920A Network analyzer and probed using a SUSS PM5probe station, as seen in Figure 2. Several device designs, with radii 64 µm, 115 µm, 215 µm 315 µm and 415 µm, were characterized and compared with simulated values.

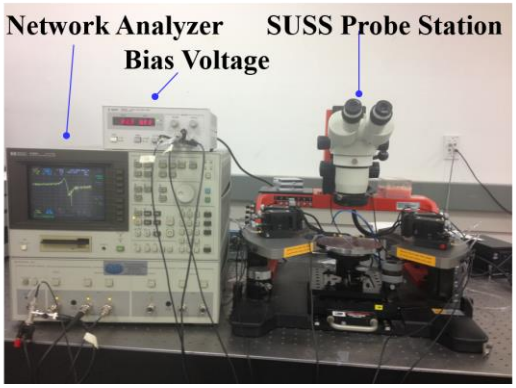

Figure 2: Measurement setup for resonator characterization.

In order to compare experimental results to modeling, it is first necessary to identify the exact dissipation mechanisms for these ring resonators. Air damping was avoided with the vacuum encapsulation of the Stanford *epi-seal* process. Additionally, surface losses were likely negligible since the device dimensions provide a relatively low surface area to volume ratio compared to the nanoscale resonators where surface dissipation has been reported [17]. Also, at these lower frequency ranges, (200 kHz - 13 MHz) Akhieser, and Landau-Rumer are negligible. Therefore, TED and clamping loss were the only two relevant dissipation mechanisms for these resonators.

As can be seen in Figure 3 and Table 1, the measured *Q* was within 12% (approximately the experimental error) for each of the five different resonator designs spanning nearly two orders of magnitude in frequency. Our model combines the two relevant dissipation mechanisms, TED and clamping loss. These results represent unprecedented matching of experiment and anchor loss simulations for a broad range of low frequency resonators.

In order to compare experimental results to modeling, it is first necessary to identify the exact dissipation mechanisms for these ring resonators. Air damping was avoided with the vacuum encapsulation of the Stanford *epi-seal* process. The *epi-seal* encapsulation process was proposed by researchers at the Robert Bosch Research and Technology Center in Palo Alto and then demonstrated in a close collaboration with Stanford University. This collaboration is continuing to develop improvements and extensions to this process for many applications, while the baseline process has been brought into commercial production by SiTime Inc. Additionally, surface losses were likely negligible since the device dimensions provide a relatively low surface area to volume ratio compared to the nanoscale resonators where surface dissipation has been reported [17]. Also, at these lower frequency ranges, (200 kHz-13 MHz) Akhieser, and Landau-Rumer are negligible. Therefore, TED and clamping loss

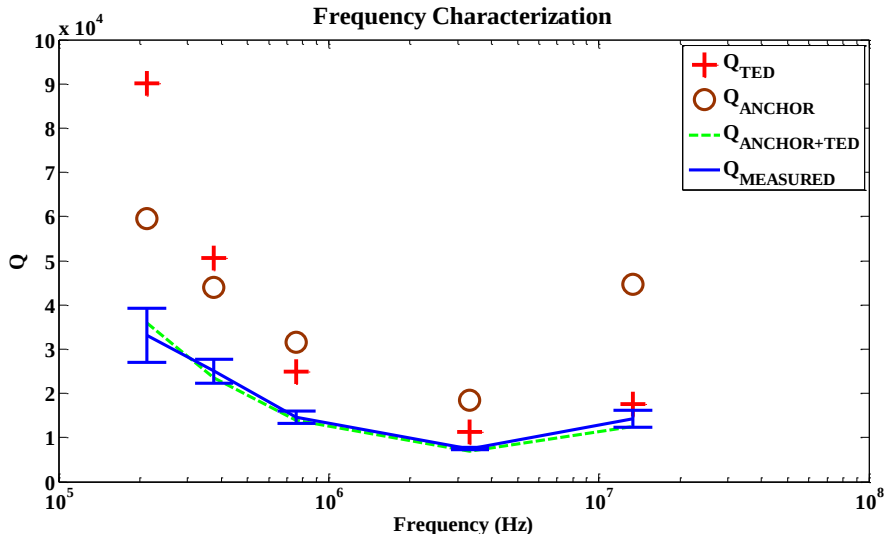

Figure 3: Plot of measured and simulated values of different dissipation mechanisms. Each data point represents 5 devices. Q_{TED} was solved using COMSOL thermal mechanical multiphysics package. The simulated Q is within 12% of the measured Q for all resonators.

were the only relevant dissipation mechanisms for these resonators.

As can be seen in Figure 3 and Table 1, the measured *Q* was within 12% (approximately the experimental error) for each of the five different resonator designs spanning nearly two orders of magnitude in frequency. Our model combines the two relevant dissipation mechanisms, TED and clamping loss. These results represent unprecedented matching of experiment and anchor loss simulations for a broad range of low frequency resonators.

Table 1: Measurement and simulation data

Frequency (Hz)	$Q_{MEASURED}$	$Q_{ANCHOR+TED}$ SIMULATED	Stress (MPa)
212,221	33148	39653	0.3
376,115	25070	25163	0.3
759,482	14659	12658	0.3
3,328,706	7517	8598	0.3
13,381,370	14246	13947	0.3

CONCLUSIONS

This work provides experimental validation of anchor loss models for an extensive range of low frequency (200 kHz – 13 MHz) devices. All measured designs, covering nearly two orders of magnitude in frequency, fell within 12% of the model's prediction. This experimentally validated model provides a framework for designers to modify designs (e.g., stem length anchor design) in order to reduce anchor loss for arbitrary 3D geometries and identifies key process parameters (e.g., stress) for control of anchor losses. Continued improvement in the understanding of energy dissipation will greatly improve the design of high quality factor resonators for the design of high performance MEMS gyroscopes.

ACKNOWLEDGMENTS

The authors would like to acknowledge support from DARPA contract # N66001-13-1-4032. This work was also supported by DARPA grant N66001-12-1- 4260, "Precision Navigation and Timing program (PNT)," managed by Dr. Andrei Shkel and Dr. Robert Lutwak,. The fabrication work was performed at the Stanford Nanofabrication Facility (SNF) which is supported by National Science Foundation through the NNIN under Grant ECS-9731293.

REFERENCES

[1] Y. T. Yang, C. Callegari, X. L. Feng, K. L. Ekinci and M. L. Roukes, "Zeptogram-scale nanomechanical mass sensing," Nano Letters 6, 4, (2006).

[2] S. P. Beeby, M. J. Tudor and N. M. White, "Energy harvesting vibration sources for Microsystems applications," Measurement Science and Technology, 17, 12, (2006).

[3] E. P. Quévy and R. T. Howe, "Redundant MEMS Resonators for Precise Reference Oscillators," Technical Digest of the 2005 Radio Frequency Integrated Circuits (RFIC) Symposium., IEEE, Long Beach , CA 6/12-14/05,(2005), pp. 113-116.

[4] R. Melamud, S. A. Chandorkar, S. F. Lord and T. W. Kenny, "Real-Time Temperature Compensation of MEMS Oscillators Using an Integrated Micro-Oven and a Phase-Locked Loop," Journal of Microelectromechanical Systems, 19, 1, (2010).

[5] C. T.-C. Nguyen, "MEMS technology for timing and frequency control," IEEE Transactions on Ultrasonics, Ferroelectrics and Frequency Control, 54, 2, (2007).

[6] K. Sundaresan, G. Ho, S. Pourkamali and F. Ayazi, "Electronically Temperature Compensated Silicon Bulk Acoustic Resonator Reference Osillators," IEEE Journal of Solid-State Circuits, 42, 6, (2007).

[7] D. Weinstein and S. Bhave, "The Resonant Body Transistor," Nano letters, 10, 4, (2010).

[8] M. Bao and H. Yang, "Squeeze film air damping in MEMS," Sensors and Actuators, 136, 1, (2007).

[9] S. Chandorkar, M. Agarwal, R. Melamud, R Candler, K. Goodson, and T. Kenny, "Limits of Quality Factor in Bulk-Mode Micromechanical Resonators,"

International Conference on Micro Electro Mechanical Systems (MEMS), Tucson, AZ, 1/13-17/08, IEEE, 2008, pp. 13-17.

[10] J. Hasson and A. Many, "Observation of Akhiezer and Landau-Rumer Regimes in the Frequency Dependence of Shear-Wave Lattice attenuation in CdS," Physical Review Letters, 35, 12, (1975).

[11] C. Zener, "Internal friction in solids: I. Theory of internal friction in reeds," Physical Review, 52, (1937).

[12] Z. Hao, A. Erbil, and F. Ayazi," An analytical model for support loss in micromechanical beam resonators with in-plane flexural vibrations" Sensors and Actuators A: Physical,109, 1-2,(2003).

[13] D. Bindel, E. Quévy, T. Koyama, S. Govindjee, J. W. Demmel, and R. T. Howe, "Elastic PMLs for resonator anchor loss simulation," International Journal Numerical Methods in Engineering, 64, 6, (2005).

[14] J. Judge D. M. Photiadis, J. F. Vignola, B. H. Houston, and J. Jarzynski, "Attachment loss of micromechanical and nanomechanical resonators in the limits of thick and thin support structures,"Journal of Applied Physics, 101, (2007).

[15] Y. Wang, J. A. Henry, A. T. Zehender, and M. A. Hines, "Surface Chemical Control of Mechanical Energy Losses in Micromachined Silicon Structures," Journal of Physical Chemistry B, 107,(2003).

[16] R.N. Candler , et al. "Long-Term and Accelerated Life Testing of a Novel Single-Wafer Vacuum Encapsulation for MEMS Resonators." Journal of Microelectromechanical Systems, 15, 6, (2000).

[17] J. A. Henry, Y. Wang, D. Sengupta and M. A. Hines. "Understanding the Effects of Surface Chemistry on Q: Mechanical Energy Dissipation in Alkyl-Terminated (C_1-C_{18}) Micromechanical Silicon Resonators," Journal of Physical Chemistry B, 111, (2007).

LAMB WAVE MICROMECHANICAL RESONATORS FORMED IN THIN PLATES OF LITHIUM NIOBATE

R.H. Olsson III[*], *K. Hattar, M.S. Baker, M. Wiwi, J. Nguyen, C. Padilla, S.J. Homeijer, J. R. Wendt and T.A. Friedmann*

Sandia National Laboratories, Albuquerque, New Mexico, USA

ABSTRACT

We study and compare high coupling symmetric and shear mode Lamb wave resonators realized in thin plates of X-cut lithium niobate. Fundamental mode bar resonators with a plate width of 20 µm, a plate thickness of 1.5 µm, apertures of 50, 90 and 130 µm and acoustic wave propagation rotated 30° (symmetric) and 170° (shear) to the +y-axis were realized on a single die for direct comparison. As expected, the symmetric Lamb wave resonators exhibited a higher sound velocity of ~6400 m/s when compared to the shear velocity of ~3900 m/s. The shear mode resonators, however, were found to have a significantly higher effective piezoelectric coupling coefficient of 16.3%, compared to a maximum of 9.1% for the symmetric Lamb wave resonators. In addition, the shear mode resonators were found to be less sensitive to the device aperture and to have fewer spurious responses. Based on these results, the shear mode resonators were selected for scaling to higher operating frequencies. A shear mode lithium niobate Lamb wave resonator operating at 350 MHz has been demonstrated with an effective piezoelectric coupling of 16%, a quality factor in air of 2200 and a device figure-of-merit of 420, among the highest reported for Lamb wave resonators [1-3].

INTRODUCTION

Microresonator filter arrays have been studied as a smaller, more highly integrated replacement for the numerous filters dies that currently reside in the RF front-end of a multi-band cellular handset. In particular, microresonators realized in thin films of lithium niobate ($LiNbO_3$) [1-3] have demonstrated the high piezoelectric coupling needed to realize band select filters with percent bandwidths of 2-5%, while simultaneously exhibiting the high quality factors required for duplexers with narrow frequency gaps between the transmit and receive bands.

In this paper we study and compare the properties of Lamb wave resonators vibrating in the fundamental symmetric (S0) and shear (SH0) modes. These modes were chosen because they are predicted [4] to have both low dispersion and high coupling coefficient over a wide range of thickness-to-wavelength ratios (h/λ). Both of these properties are important for realizing multi-frequency band select filters in a single $LiNbO_3$ layer.

Fundamental mode resonators with a plate width of 20 µm, a plate thickness of 1.5 µm, varying apertures and acoustic wave propagation rotated 30° (S0) and 170° (SH0) to the +y-axis to maximize piezoelectric coupling [4] were realized on a single die for direct comparison. The h/λ of 0.04 is very close to the optimum value to maximize piezoelectric coupling of 0.05 found for both the S0 and SH0 modes in [4]. We find that while the S0 Lamb wave has a 1.6 times higher sound velocity than the SH0 mode, the SH0 mode is predicted to and consistently exhibits a 1.6-1.8 times higher effective piezoelectric coupling coefficient, k_{eff}^2. The SH0 mode also exhibits higher quality factor (Q), higher figure-of-merit (M) and fewer spurious responses.

Finally, a fundamental SH0 mode Lamb wave resonator realized in a 4.4 µm wide plate is demonstrated with an operating frequency of 350 MHz, a $k_{eff}^2 = 16\%$, a $Q = 2200$ in air and a $M = 420$, among the highest reported for Lamb wave resonators.

DEVICE FABRICATION

The resonators are fabricated using the process flow shown in Fig. 1 [3], where selective ion irradiation of a $LiNbO_3$ wafer creates a damaged release layer that selectively etches in a HF chemistry, allowing suspended membranes to be formed. The advantages of this fabrication process when compared to prior art [1,2] are: 1) the ability to lithographically define the undercut of the device, 2) no wafer bonding, polishing or fracturing and 3) the ability to realize custom and potentially multiple $LiNbO_3$ thicknesses on a single substrate.

The process begins with an X-cut $LiNbO_3$ wafer upon which a 100 nm layer of Cr is deposited and patterned to form alignment marks. Next, a SiO_2 layer is deposited and patterned to determine where the release layer will be formed via ion irradiation. The sample is then implanted with a He dose of 1×10^{16} atoms/cm^3 at an energy of 0.9 MeV to create an ion damaged release layer of $LiNbO_3$ approximately 2 µm below the wafer surface. This energy was found to give a final plate thickness after release of approximately 1.5 µm. The implants are performed in a 3 MV NEC Pelletron using a current of < 7 µA. A low sample temperature is maintained via liquid nitrogen cooling using a Cu braid during implantation. The ion implant is intentionally performed through the Cr electrode layer to promote adhesion. After ion implantation, the SiO_2 implant masking layer is stripped and the $LiNbO_3$ is patterned using an oxide hard mask and Cl dry etching to define the final plate dimensions. Next, the Cr electrodes are patterned and a layer of Au is deposited and patterned via lift off to protect the –z face of the $LiNbO_3$ device, which can have a significant etch rate in HF during the release. During our research we found that the structural rigidity of this Au protection layer also led to significantly improved device yield through the release process. Finally the devices are released in a HF based chemistry and the Au protect layer is stripped in KI-I_2.

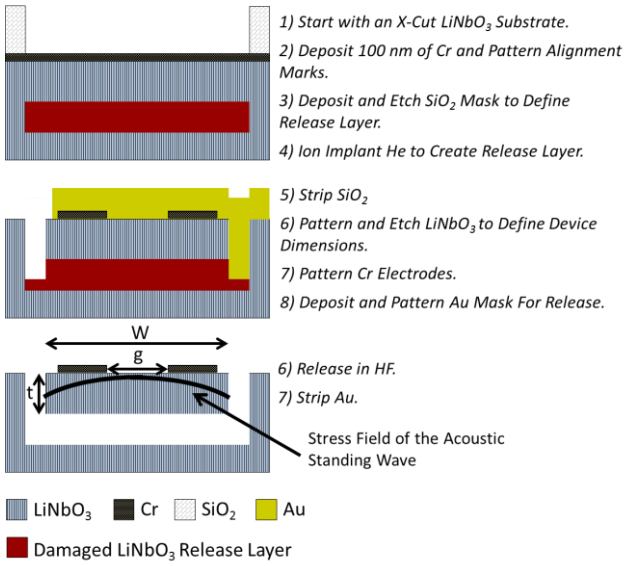

Figure 1: $LiNbO_3$ microresonator fabrication process.

9781940470016/HH2014/$25©2014TRF
DOI 10.31438/trf.hh2014.75

DEVICE STRUCTURE AND DIMENSIONS

A final cross-section schematic of the resonator is shown in the bottom of Fig. 1 and a scanning electron microscope (SEM) image of one of the resonators studied in this work is shown in Fig. 2. The resonator consists of a 1.5 µm thick suspended membrane of $LiNbO_3$ with a width, $W = 20\ \mu m$. The device was designed to resonate in the fundamental S0 or SH0 mode, see Fig. 3, with a resonant frequency, $f_s = c/2W$, where c is the sound velocity of the Lamb wave. The thickness-to-wavelength ratio, $t/\lambda = 0.04$, is closer to the optimum value to maximize k_{eff}^2 of 0.05 [4] than previous work [3]. The space between the electrodes and device substrate anchor, s, was 45 µm for all devices. While it was found in [2,3] that to maximize k_{eff}^2 the electrodes should be placed at the edges of the resonator, 5 µm wide electrodes with a gap, $g = 5\mu m$, were designed slightly offset from the resonator edge for ease of fabrication. Electrode apertures, a, which define the resonator static capacitance, of 50, 90 and 130 µm were modeled, fabricated and characterized.

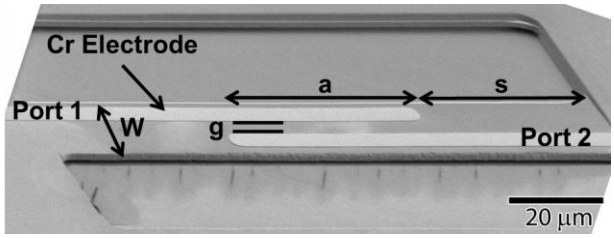

Figure 2: $LiNbO_3$ microresonator SEM image.

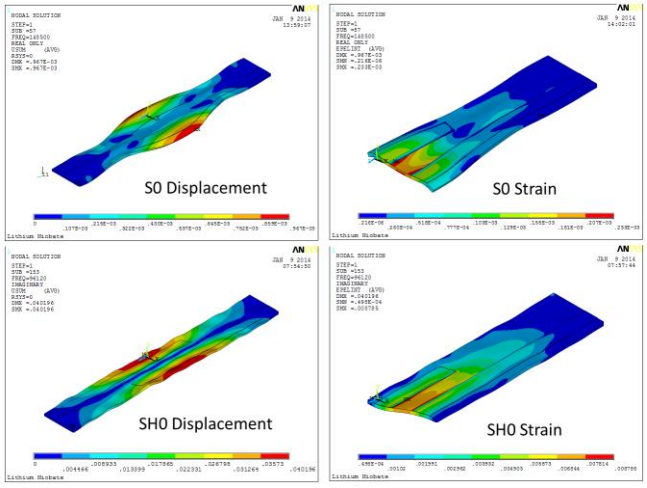

Figure 3: Displacement (Full) and strain (Half) profiles of the S0 and SH0 resonator modes with an aperture of 50 µm.

FINITE ELEMENT MODELING RESULTS

The six devices with three different apertures and two different rotations to the +y-axis described above were studied using finite element modeling (FEM) and experimentally. The FEM was a full 3D representation of the device including the anchors and electrodes. Figure 3 shows the displacement and strain profiles from ANSYS FEM for the S0 Lamb wave resonator rotated 30° to the +y-axis and for the SH0 Lamb wave resonator rotated 170° (SH0) to the +y-axis, both with apertures of 50 µm. The maximum strain is seen to appear between the Cr electrodes and is thus efficiently transduced by the electric field applied across these same electrodes. The strain between the electrodes at the edges of the aperture for the S0 Lamb wave resonator is seen to dramatically decrease, indicating that the S0 Lamb wave k_{eff}^2 will be significantly impacted by the device aperture. The k_{eff}^2 for each device was studied using harmonic analysis in ANSYS. The piezoelectric coupling, K^2, was calculated from the simulated resonator admittance using eq. 1,

$$K^2 = \frac{1}{2\pi f_s Q R_X C_S}\ , \qquad (1)$$

where f_s is the frequency of minimum resonator admittance, R_X is the resonator motional impedance, C_s, is the resonator static capacitance and Q is the resonator quality factor which is an input to the FEM. The effective piezoelectric coupling was then calculated using eq. 2,

$$k_{eff}{}^2 = \frac{K^2}{1+K^2}\ . \qquad (2)$$

In our previous work [3] k_{eff}^2 was calculated from the simulated resonator admittance using eq. 3,

$$k_{eff}{}^2 = \frac{f_p{}^2 - f_s{}^2}{f_p{}^2}\ , \qquad (3)$$

where f_p is the frequency of maximum resonator admittance. The results of equations 2 and 3 are equal when no spurious resonances are seen near f_s or f_p. In this work, however, we find in both FEM and in experiments that spurious modes cause a significant increase in f_p and overestimation of k_{eff}^2 if equation 3 is used. We note here that the piezoelectric coupling coefficient, k_t^2, reported in [1] is equal to,

$$k_t{}^2 = \frac{\pi^2}{8}\frac{C_X}{C_S} = \frac{\pi^2}{8}K^2 = \frac{\pi^2}{8}\frac{k_{eff}{}^2}{1-k_{eff}{}^2}\ . \qquad (4)$$

The simulated k_{eff}^2 vs. aperture is shown in Fig. 4 and summarized in Table 1 for both the S0 and SH0 Lamb wave resonators. The S0 Lamb wave resonator is predicted to have a significantly lower k_{eff}^2 that is much more sensitive to the aperture than the SH0 Lamb wave resonator.

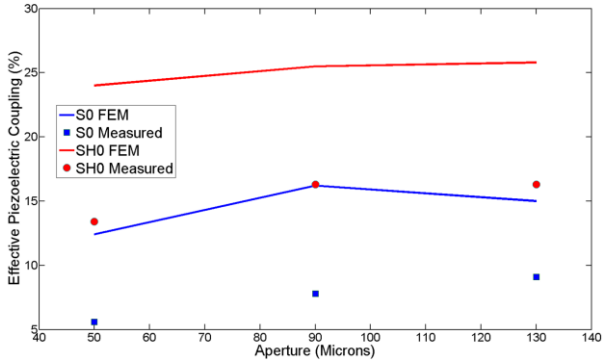

Figure 4: FEM and experimental k_{eff}^2 vs. aperture.

EXPERIMENTAL RESULTS

The admittance of the six different resonators realized on the same die was measured in air using a network analyzer. The responses for the S0 and SH0 mode resonators with an aperture of 90 µm are shown in Fig. 5 (S0) and in Fig. 6 (SH0). Also shown in Fig. 5 and Fig. 6 are the results of the FEM for each device simulated with the measured quality factors. Each resonator measurement was fit to the modified Butterworth Van Dyke (MBVD) equivalent circuit model shown in Fig. 7 using eq. 5-7,

Table 1. Experimental and FEM results for the S0 and SH0 Lamb wave micromechanical resonators.

Mode	Orientation to +Y axis	Aperture (μm)	Freq. (MHz)	R_S (Ω)	R_X (Ω)	C_S (fF)	FEM Model k_{eff}^2 (%)	Measured k_{eff}^2 [2,3] (%)	Measured k_t^2 [1] (%)	Q_{Total}	Q_A	FOM $k_{eff}^2 Q_A/(1-k_{eff}^2)$
S0	30°	50	158.9	194	3516	9	12.4	5.6	7.4	500	528	31
S0	30°	90	160.6	233	1386	12	16.2	7.8	10.5	600	701	59
S0	30°	130	161.5	272	944	18	15.0	9.1	12.3	450	580	58
SH0	170°	50	98.4	194	922	8.5	24.0	13.4	19.1	1100	1331	206
SH0	170°	90	96.9	233	702	12	25.5	16.3	24.1	750	999	195
SH0	170°	130	94.8	272	783	17	25.8	16.3	24.1	480	647	126

$$R_X = \frac{1}{2\pi f_S C_S K^2 Q_A}, \quad (5)$$

$$C_X = \frac{C_S}{K^2}, \quad (6)$$

$$L_X = \frac{R_X Q_A}{2\pi f_S} = \frac{(R_X + R_S) Q_{Total}}{2\pi f_S}, \quad (7)$$

where C_X and L_X are the motional capacitance and inductance, R_S is the series electrical resistance, Q_A is the acoustic quality factor and Q_{Total} is the measured 3 dB bandwidth of the acoustic admittance divided by f_s, which includes the losses from both R_X and R_S. R_S was measured directly on a separate test structure allowing it to be extracted from R_X. The simulated response of the MBVD electrical equivalent circuit model for the S0 and SH0 mode micromechanical resonators with an aperture of 90 μm are shown in Fig. 5 and Fig. 6 along with the equivalent circuit parameters.

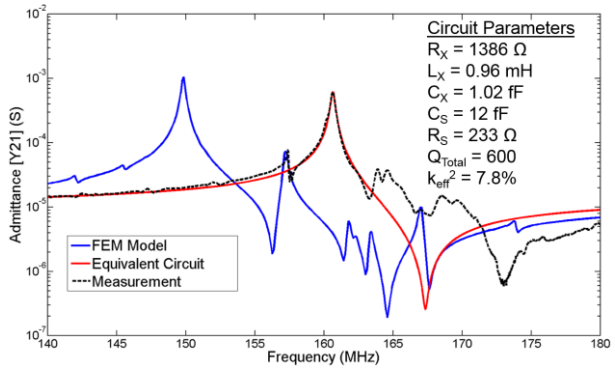

Figure 5: FEM and experimental results for the S0 Lamb wave resonator with an aperture of 90 μm.

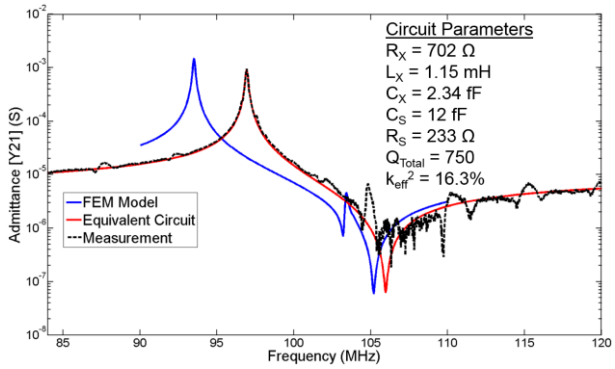

Figure 6: FEM and experimental results for the SH0 Lamb wave resonator with an aperture of 90 μm.

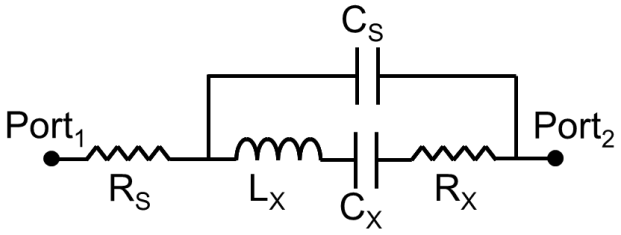

Figure 7: Modified BVD resonator equivalent circuit model.

The simulated MBVD results and experimental measurements are in good agreement far from resonance and close to the series resonance. The experimental k_{eff}^2 for each resonator was calculated from the MBVD equivalent circuit model using either equation 2 or 3 which yield identical results since no spurious responses are modeled using the circuit in Fig. 7. From Fig. 5 it is apparent that using the measured frequency of maximum admittance in equation 3 dramatically overestimates the k_{eff}^2 due to the spurious modes between f_s and f_p. The measured f_s, R_S, R_X, C_S, k_{eff}^2, k_t^2, Q_{Total}, Q_A and acoustic figure-of-merit are summarized for all the resonators in Table 1, while the measured k_{eff}^2 vs. aperture is shown in Fig. 4. The SH0 resonators are found to have significantly higher effective piezoelectric coupling coefficient and figure-of-merit.

SCALING TO HIGHER FREQUENCIES

From Table 1, the resistance of the Cr electrodes is seen to significantly degrade the total resonator quality factor. Higher frequency operation can only result in further degradation in Q_{Total} as the electrode cross sectional area will decrease, causing R_S to increase and R_X to decrease (see eq. 5). For this reason, when scaling to higher operating frequencies, the Cr electrodes in Fig. 1 were replaced with 100 nm of Au (lower resistivity compared to Cr) and the Au –z face protection mask step was omitted from the fabrication process.

The measured admittance of a SH0 Lamb wave resonator rotated 170° to the +y-axis with a plate width, $W = 4.4$ μm, an aperture, $a = 60$ μm, an electrode width of 1 μm and a gap between the electrodes, $g = 2$ μm, is shown in Fig. 8 and Fig. 9. Also shown in both figures is the simulated response of the MBVD equivalent circuit. The narrowing of the plate width to 4.4 μm has increased the series resonant frequency to 350 MHz. The inclusion of the Au electrodes has reduced the series electrical resistance to the point where it need not be modeled, $R_S = 0\ \Omega$ and $Q_A = Q_{Total}$. The increase in the effective electrode aperture to nearly 7 wavelengths has enabled a corresponding increase in the device quality factor to 2200. The ultra-high frequency (UHF) band resonator maintains a high effective coupling coefficient, $k_{eff}^2 = 16\%$ and a device figure-of-merit, $M = 420$. The performance of the UHF, fundamental SH0 mode $LiNbO_3$ micromechanical resonator is summarized in Table 2.

Table 2. Experimental results for a SH0 Lamb wave resonator operating in the ultra-high frequency (UHF) band.

Mode	Orientation to +Y axis	Plate Width (μm)	Aperture (μm)	Freq. (MHz)	R_X (Ω)	C_S (fF)	Measured k_{eff}^2 [2,3] (%)	Measured k_t^2 [1] (%)	Q	FOM $k_{eff}^2Q/(1-k_{eff}^2)$
SH0	170°	4.4	64	350	68	16	16	23.6	2200	420

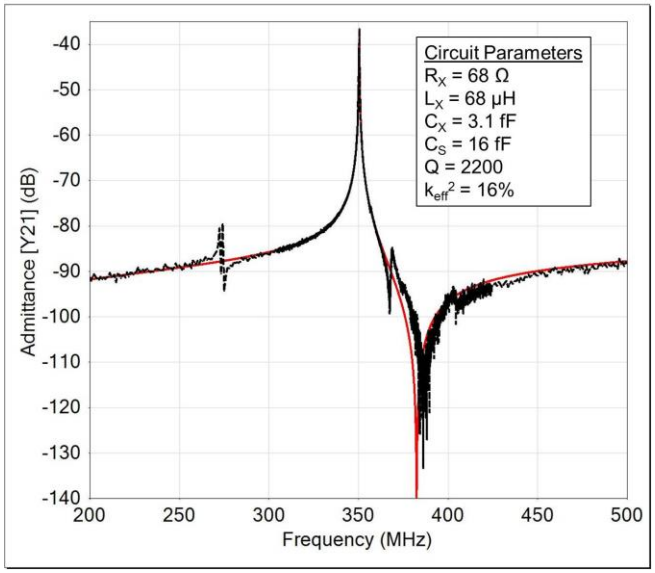

Figure 8: Experimental (black) and equivalent circuit model (red) admittance for a SH0 Lamb wave resonator with a plate width of 4.4 μm.

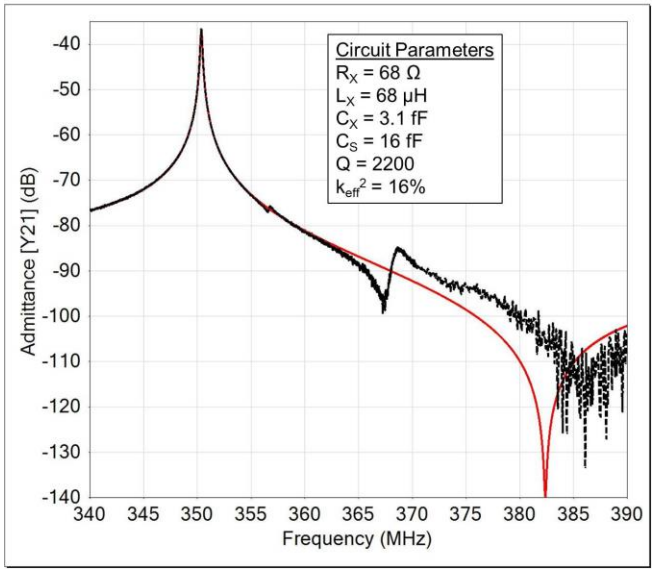

Figure 9: Experimental (black) and equivalent circuit model (red) admittance for a SH0 Lamb wave resonator with a plate width of 4.4 μm.

CONCLUSIONS

We have studied, theoretically and experimentally, fundamental mode S0 and SH0 Lamb wave resonators realized in thin plates of $LiNbO_3$. The devices are fabricated using a newly developed process that allows the formation of a damaged $LiNbO_3$ sacrificial layer using Helium ion implantation. This damaged $LiNbO_3$ is subsequently etched in a HF acid based wet release. The plate width, which determines the resonant frequency, is 20 μm wide for both the S0 and SH0 mode resonators and the thickness-to-wavelength ratio for both types of resonators is 0.04, near the optimum value to maximize piezoelectric coupling found in [4]. The acoustic wave propagation is rotated 30° (S0) and 170° (SH0) to the +y-axis for the resonators, also an optimum condition to maximize piezoelectric coupling reported in [4]. We find that the SH0 mode microresonators consistently exhibit higher effective piezoelectric coupling, quality factor and figure-of-merit when compared to identically designed S0 mode structures. The properties of the SH0 mode resonators are less sensitive to the device aperture and the SH0 mode resonators exhibit fewer spurious responses. While the initial study was performed on $LiNbO_3$ microresonators operating at 97 (SH0) and 160 (S0) MHz, a SH0 mode microresonator in a 4.4 μm wide $LiNbO_3$ plate has been demonstrated at 350 MHz. The $k_{eff}^2 = 16\%$, $Q = 2200$ and $M = 420$ for the 350 MHz microresonator are among the highest demonstrated for this new class of resonant micro-devices.

ACKNOWLEDGEMENTS

This project was partially supported by the Laboratory Directed Research and Development (LDRD) Program at Sandia National Laboratories. Sandia National Laboratories is a multi-program laboratory managed and operated by Sandia Corporation, a wholly owned subsidiary of Lockheed Martin Corporation, for the U.S. Department of Energy's National Nuclear Security Administration under contract DE-AC04-94AL85000.

REFERENCES

[1] S. Gong and G. Piazza, "Design and analysis of lithium-niobate-based high electromechanical coupling RF-MEMS resonators for wideband filtering", IEEE Trans. on Microwave Theory and Tech., 61, 1 (2013).

[2] R.R. Wang, S.A. Bhave, and K. Bhattacharjee, "Thin-film high k_t^2Q, multi-frequency lithium niobate resonators", Technical Digest of the IEEE International Conference on Micro Electro Mechanical Systems, (2013), pp. 165-168.

[3] R.H. Olsson III et al., "A high electromechanical coupling coefficient SH0 Lamb wave lithium niobate micromechanical resonator and a method for fabrication", Sensors and Actuators A 209 (2014) 183–190.

[4] I.E. Kuznetsova et al., "Investigation of acoustic waves in thin plates of lithium niobate and lithium tantalite", IEEE Trans. on Ultrasonics, Ferroelectrics and Frequency Cntrl., 48, 1 (2001).

CONTACT

*R.H. Olsson III, tel: +1-505-284-6375; rholsso@sandia.gov

MEASUREMENT OF THE NONLINEAR ELASTICITY OF DOPED BULK-MODE MEMS RESONATORS

Yushi Yang[1], Eldwin J. Ng[1], Vu A. Hong[1], Chae Hyuck Ahn[1], Yunhan Chen[1], Elia Ahadi[1], Mark Dykman[2], and Thomas W. Kenny[1]
[1]Stanford University, California, USA
[2]Michigan State University, East Lansing, Michigan, USA

ABSTRACT
In this paper, we present measurements of the nonlinear amplitude-frequency (A-f) coefficients for three types of bulk-mode silicon MEMS resonators with different doping type and concentration. Our experimental results clearly show a strong dependence of the nonlinearity character on the orientation, doping level, and vibrational mode shape. These results indicate that the doping can have a significant impact on the character and strength of the elastic nonlinearities in MEMS devices.

INTRODUCTION
High performance MEMS oscillators have gained much attention as an alternative for quartz since they offer potential benefits such as volume and cost reduction, low power consumption, and IC compatibility [1, 2]. The use of MEMS oscillators in wireless communication requires device performance characteristics such as high stability, high quality factor (Q), and large power handing capability. These will provide a larger signal-to-noise ratio and reduced phase noise [3]. However, because the power handling capability of MEMS oscillators is inversely related to the resonator size, oftentimes the device has to be driven into nonlinear regime to obtain suitable signal-to-noise ratio and performance [4].

Another aspect that has gained wide attention is frequency-temperature compensation. Recent research has demonstrated the use of heavily doped p- or n-type silicon for passive frequency-temperature compensation [5, 6], thus making it attractive for this study. Adding dopants to the silicon lattice will not only introduce free charge carriers, but will also cause a strain in the lattice due to a size dissimilarity between the silicon and the dopant atoms. These effects shift the semiconductor energy bands and result in a change in the material elastic constants, since any change in the total electronic energy content of the crystal will also contributes to the total elastic energy [7]. Nonlinearities in lightly doped silicon resonators have been studied [8], and the effect has also been noted in heavily doped silicon [9]. This examines the nonlinear effects for a variety of doping types/levels and devices, showing that substantial changes in the strength and character of the nonlinearity should be expected in doped silicon resonators

One common way of characterizing the nonlinear behavior of a resonator is to analyze the amplitude-frequency effect (A-f effect). For nonlinear analysis, correction terms are added to the equation of motion (EOM) of the resonator, which yields:

$$m\ddot{x} + 2\lambda\dot{x} + k_0 x + k_1 x^2 + k_2 x^3 = F\cos(2\pi f t) \qquad (1)$$

where k_1 and k_2 are the 2nd and 3rd order nonlinear forcing terms respectively. The linear natural frequency is defined as $f_0 = \frac{1}{2\pi}\sqrt{k_0/m}$. Analytically it has been shown that the peak frequency is a function of the peak amplitude in the presence of the nonlinear terms [10]:

$$f_0' = f_0 + \kappa X_0^2 \qquad (2)$$

where X_0 is the resonator peak amplitude, f_0' is the shifted frequency at large displacement, and κ is the A-f coefficient, which is calculated as:

$$\kappa = \left(\frac{3k_2}{8k_0} - \frac{5k_1^2}{12k_0^2}\right) f_0 \qquad (3)$$

In this paper, we present the modeling and experimental observation of how doping affects the devices' nonlinear behavior.

DESIGN AND FABRICATION
Three types of bulk-mode resonators are designed and fabricated (See Table.1 for resonator dimensions): length extensional mode resonator (***LE***), Lamé mode resonator (***Lamé***), and dual breathe mode ring resonator (***Ring***). Nonlinearities in capacitive resonators are usually classified into electrostatic and mechanical (geometric and material). Compared with flexural-mode resonators, bulk-mode resonators are usually dominated by material nonlinearity effects, thus making them suitable candidates for studying the effect of doping [8].

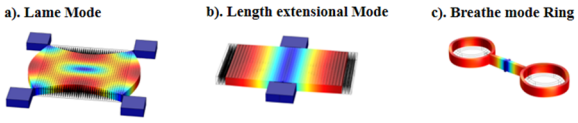

Figure 1: Mode shape of the three types of bulk-mode resonators

Four different types of doping levels are investigated, with the measured device layer resistivity listed as follows: Phosphorus (***NP***) 1.78mΩ-cm, Arsenic (***NA***) 3.1mΩ-cm, Antimony (***NS***) 17.1mΩ-cm, and Boron (***PB***) 15.8mΩ-cm. These doping densities are representative of the characteristics of commercially-available silicon-on-insulator (SOI) wafers

The devices are fabricated using a wafer-level encapsulation process (*epi-seal*). The process starts off with (100) SOI wafer with a 40μm single-crystal device layer doped as described above, and a 2μm buried oxide layer. First, deep reactive ion etching is used to etch the device structural outline. A 2μm sacrificial oxide layer is then deposited and electrical contacts to the device layer are etched. Afterwards, the first epitaxial polysilicon cap layer is deposited. Vent holes are then etched and the resonant structures are released using vapor phase HF. Immediately after the release, the second polysilicon cap layer, which acts as the final encapsulation layer is deposited. Residual hydrogen is then diffused out to create a low pressure cavity (< 1Pa). Finally, electrical contacts are etched and aluminum is deposited and patterned. This process provides a clean and low pressure environment, which allows the devices to achieve long-term stability [11].

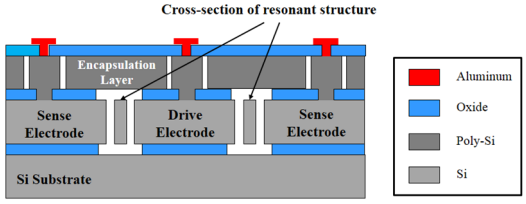

Figure 2: Final cross section view of the epi-seal process

9781940470016/HH2014/$25©2014TRF
DOI 10.31438/trf.hh2014.76

RESONATOR MODELING

In this section, we present lumped mass models following the method given in [8] to analyze the nonlinear dynamics of these continuum systems. To begin, the resonators are transformed into single degree-of-freedom systems with the lumped EOM given as:

$$m_{eff}\ddot{X} + c\dot{X} + k(X)X = F_{tot} \qquad (4)$$

where X is the maximum resonator displacement, m_{eff} is the effective mass, c is the linear damping coefficient, $k(X)$ represents the spring constants, and F_{tot} is the total electrostatic driving force. The effective mass of the resonators are simulated using COMSOL as:

$$m_{eff} = \iiint_V \rho\left(\frac{u}{X}\right)^2 dV \qquad (5)$$

Here the resonator's displacement field u is first normalized with respect to the resonator's maximum displacement, followed by an integration across the entire resonator volume. Accounting for a lateral blowout of 0.1µm during the definition etch, the simulated results are listed in Table.1.

Table 1: Resonator dimensions and other design parameters

LE	<100>	<110>
L (µm)	600	
W (µm)	300	
h (µm)	40	
d (µm)	0.7	
f_0 (MHz)	6	7
Q	200k	220k
m_{eff} (e-9kg)	7.1345	7.4202

Lame	<100>	<110>
L (µm)	400	
h (µm)	40	
d (µm)	0.7	
f_0 (MHz)	8	10
Q	120k	80k
m_{eff} (e-9kg)	7.0630	7.1677

Ring	<110>
R_{in} (µm)	59
R_{out} (µm)	69
h (µm)	40
d (µm)	1
f_0 (MHz)	19.7
Q	240k
m_{eff} (e-9kg)	0.4596

* L: Resonator length
* d: Designed gap size
* W: Resonator width
* R_{in}: Ring inner radius
* h: Resonator height
* R_{out}: Ring outer radius

To account for the nonlinear effects, higher order correction terms are incorporated into the spring constant model:

$$k(X) = (k_{0m} + k_{0e}) + (k_{1m} + k_{1e})X + (k_{2m} + k_{2e})X^2 \qquad (6)$$

For electrostatically driven resonators, the spring constants include both mechanical and electrical terms due to the electrostatic softening effect [10].

The electrical contribution to the spring constants can be found via studying the electrostatic driving force:

$$F = \frac{\partial U}{\partial X} = \frac{\Delta V^2}{2}\frac{\partial C_{tot}}{\partial X} \qquad (7)$$

where ΔV is the potential difference across the electrodes and C_{tot} is the total capacitance. Based on the electrode placement and the corresponding driving/sensing method (i.e, fully differential), the electrical spring constants for the three types of resonators can be estimated, assuming that the ac drive voltage (V_{ac}) is significantly less than the bias voltage (V_{bias}), and electrodes remain as parallel plates.

To account for the mechanical nonlinearities, a nonlinear strain-dependent modulus is needed to solve for the EOM. For the LE and Ring resonators, a nonlinear Young's modulus is taken into account:

$$E = E_0 + E_1\gamma + E_2\gamma^2 \qquad (8)$$

where γ is the engineering strain. Substituting the nonlinear Young's modulus into the wave equation and integrating over the mode shape, the nonlinear spring constants can be obtained.

- LE: $k_{0m} = \frac{\pi^2 E_0 A_0}{2L}$, $k_{1m} = \frac{4\pi^2 E_1 A_0}{3L^2}$, $k_{2m} = \frac{3\pi^4 E_2 A_0}{8L^3}$ (9)

The Lamé mode resonator on the other hand, can be considered as a pure shear structure, therefore to simplify the calculation, a nonlinear shear modulus should be introduced.

$$G = G_0 + G_1\gamma + G_2\gamma^2 \qquad (10)$$

The calculated mechanical spring constants incorporating the nonlinear material effects can be found:

- Lame: $k_{0m} = \pi^2 G_0 h$, $k_{1m} = 0$, $k_{2m} = \frac{9\pi^4 G_2 h}{4L^2}$ (11)

EXPERIMENT CHARACTERIZATION

For all experiments, the resonators were tested in an oven at a temperature of 40 ± 0.2°C to eliminate temperature drift effects. To operate the devices, a dc polarization voltage was applied to the resonant structure and an ac drive voltage was applied to the drive electrodes. The output current generated by the motion of the resonator is transformed into a voltage signal and amplified by an off-chip trans-impedance amplifier.

Two types of experiments were performed to characterize the nonlinear behavior of these devices: open-loop frequency sweeps with bias voltage variations and closed-loop experiments for operation beyond the critical bifurcation limit.

Open-loop Electrostatic Frequency Tuning

For electrostatic resonators, knowing the gap size is crucial before any analysis can take place. However, due to fabrication uncertainties, the actual gap size may vary from the layout design. This will introduce errors if one uses the design gap size (Table 1) in the data analysis. In order to have a better estimation of the effective gap size, the electrostatic softening effect can be utilized. Due to the electrostatic softening effect, the resonant frequency will decrease as V_{bias} increases (Fig. 3).

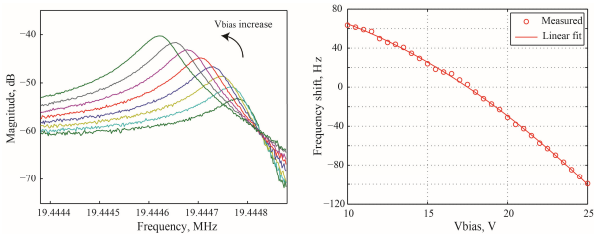

Figure 3: Example of the frequency tuning effect for ring resonator. The frequency decreases as V_{bias} increases.

Neglecting the higher order electrostatic and mechanical softening/stiffening effects, the first order relation between V_{bias} and resonant frequency f_0 can be calculated as:

Table 2: Fitted linear mechanical spring constant and gap size

Dopant type	LE<100>		LE <110>		Lame <100>		Lame <110>		Ring	
	k_{0m} (N/m)	d (µm)	k_{0m} (N/m)	d (µm)	k_{0m} (N/m)	d (µm)	k_{0m} (N/m)	d (µm)	k_{0m} (N/m)	d (µm)
NP	9.9174e+06	0.941	1.3997e+07	0.904	1.7338e+07	1.059	2.7920e+07	0.805	6.9559e+06	1.407
NA	1.0074e+07	0.991	1.4083e+07	0.912	1.7661e+07	1.088	2.7955e+07	0.955	6.8603e+06	1.332
NS	1.0338e+07	0.882	1.4233e+07	0.841	1.8223e+07	0.860	2.8341e+07	0.828	7.0838e+06	1.360
PB	1.0320e+07	0.841	1.4189e+07	0.809	1.8232e+07	0.848	2.8300e+07	0.796	7.0779e+06	1.260

$$f_0 = \frac{1}{2\pi}\sqrt{\frac{k_{0m}-k_{0e}}{m_{eff}}} = \frac{1}{2\pi}\sqrt{\frac{k_{0m}-V_{bias}^2\epsilon_0 A_{tot}/d^3}{m_{eff}}} \qquad (12)$$

where A_{tot} is the total electrode area for the resonators. By substituting the simulated effective mass given in Table 1, and fitting the experimental data with Eqn.12, the fitted linear mechanical spring constant and gap size can be found (Table.2). It should be noted that the gap size obtained from the fitting is the effective gap size due to parallel plate assumption.

Closed-loop Measurement

The driving condition and stability criteria differs between the closed-loop and the open-loop measurement. In the open-loop experiment, the resonator is driven at a particular frequency, therefore instability can occur when the resonator is driven beyond the nonlinear bifurcation point. In the closed-loop setup, the feedback circuit sets a phase between the input and output of a resonator, allowing stable operation under any frequency and amplitude condition [4]. To create a variable-phase closed-loop feedback system, a Zurich HF2LI lock-in amplifier is used to track the resonant peak and fix the operating phase (Fig. 4). For each type of resonator, the DC bias voltage was held constant and the AC drive voltage was gradually increased until the resonant peak begins to show nonlinear behavior.

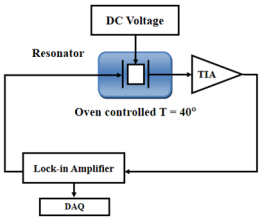

Figure 4: Close-loop experimental setup

The closed-loop frequency response plots for the different resonators are shown in Fig. 5. From Fig. 5, a few points can be observed:

1. For any particular type of resonator oriented along the same crystalline direction, the nonlinear behavior varies dramatically as doping changes. For example, the ring resonator shows a hardening effect for NP and NA doping, whereas for NS and PB doping, the resonator shows a softening effect.
2. For any particular type of resonator under the same doping condition, the nonlinearity is affected by device orientation. For example, the Lamé mode resonators oriented in the <100> direction have a completely opposite nonlinear behavior than those oriented in the <110> direction.
3. The nonlinearity also has strong correlations to the resonator's vibrational mode shape.

DISCUSSION

Following (2), the A-f coefficients have been extracted based on the above experimental results to further study the A-f effect.

$$\kappa = \frac{f_0' - f_0}{X_0^2} \qquad (13)$$

The resonator displacement can be back calculated from the measured voltage output following:

$$X \cong \frac{V_{out}\, d^2}{2\pi f_0' G V_{bias} \epsilon_0 W h} \qquad (14)$$

where G is the gain of the trans-impedance amplifier. Fig.6 plots the extracted frequency shift versus displacement square for the resonators, with the fitted κ listed in Table. 3.

From the extracted results, the general trend is that the higher the n-type doping, the larger the absolute value of κ for all the resonators tested, and a trend of $|\kappa_{NP}| > |\kappa_{NA}| > |\kappa_{NS}| > |\kappa_{PB}|$ can also be observed.

It should be note that the values reported in Table. 3 represents approximations to the A-f coefficient for four reasons:

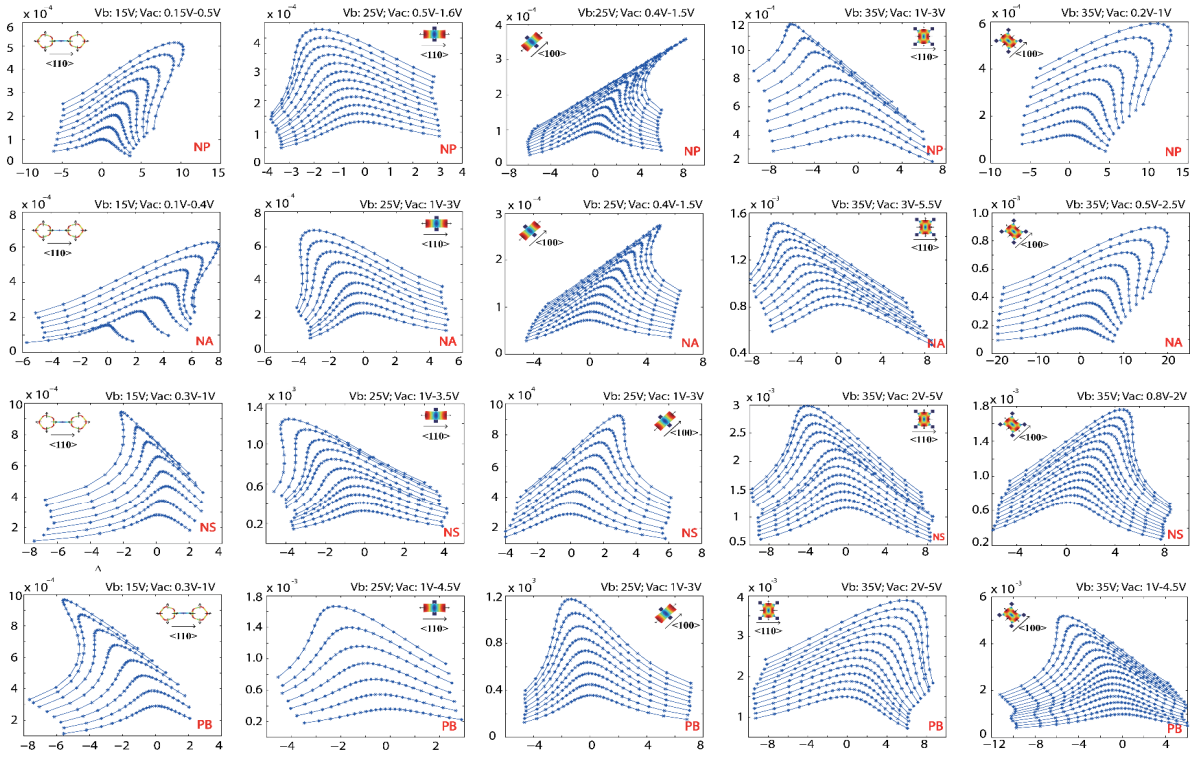

Figure 5: Measured close-loop amplitude frequency response curve for the three type of devices oriented in the <100> and <110> crystalline directions under different doping. For each plot, the x axis is labeled $\Delta f/f_0$ in ppm, and the y axis is the measured output voltage in Vrms.

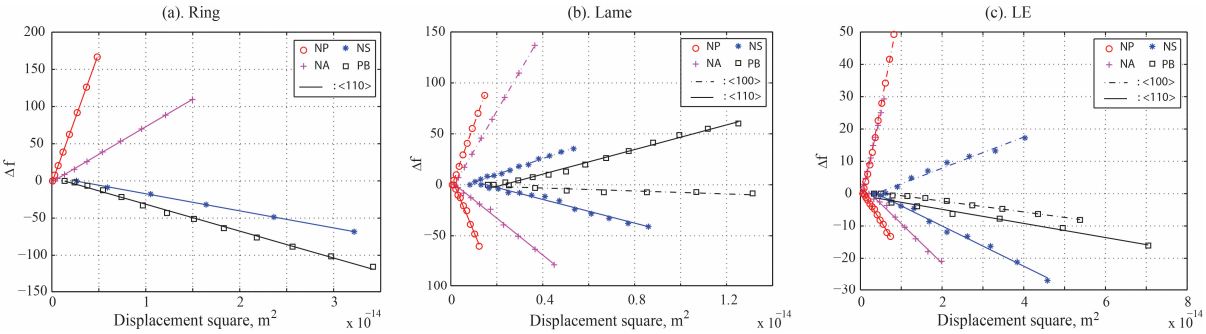

Figure 4: Plotted frequency shift vs. displacement square for different kind of resonators under various doping and orientation. Here the A-f coefficient κ is represented by the slope of each line.

1. The parallel plate assumption neglects the displacement distribution effect due to the resonator mode shape and anchor location, which will contribute errors in terms of data extraction (i.e. Lamé mode resonator).
2. In order to release large areas in the epi-seal process, release holes must be added to the resonator body. This in turn may introduce certain errors when estimating certain parameters for the resonators (e.g. spring constants).
3. The resonator mode shape may not be correctly estimated. For example, the mode shape of the Ring resonator has strong dependence by the anisotropy of the silicon material, as well as the coupling beam length that connects the two rings. A mismatch between the coupling beam length and the ideal beam length may lead to distortion in the mode shape.
4. Electrostatic softening effects may come into play at higher bias voltages. If taking the PB-doped Lame<100> resonator as example, the fitted κ is -1.1475e15 Hz/m^2, from this value the 3rd order mechanical spring constant can be back calculated as $k_{3m} \cong -7.1e15\ N/m^3$, while the 3rd order electrical spring constant is found to be $k_{3e} \cong -1.5e15\ N/m^3$.

Table 3: Fitted A-f coefficients

κ (Hz/m^2)	V_{bias} = 25V		V_{bias} = 35V		V_{bias} = 20V
	LE<100>	LE<110>	Lame<100>	Lame<110>	Ring<110>
NP	6.4621e+15	-2.0376e+15	6.2551e+16	-5.4349e+16	3.4988e+16
NA	5.3959e+15	-1.2247e+15	3.9018e+16	-1.9866e+16	7.4221e+15
NS	4.8171e+14	-6.2194e+14	7.7634e+15	-5.8247e+15	-2.2885e+15
PB	-1.6825e+14	-2.1780e+14	-1.1475e+15	6.0437e+15	-3.6134e+15

CONCLUSION

In this paper, we have investigated the effect of doping on the nonlinear behavior of three types of bulk-mode silicon MEMS resonators. By utilizing the electrostatic frequency tuning effect, the effective electrode gap size can be obtained. Based on the closed-loop amplitude frequency response measurement, the A-f coefficient can then be extracted. It can be seen that for a certain family of resonators, the device with the highest doping gives the largest absolute value of κ. A trend of the resonator's nonlinear performance can also be seen as the doping level varies. Our measurements clearly demonstrate that the resonators' nonlinear characteristics are strongly dependent on the crystal orientation, doping level, and operating mode shape. Future work will focus on utilizing these parameters to study the nonlinear elasticity for doped silicon.

REFERENCES

[1] C. Nguyen, "MEMS Technology for Timing and Frequency Control", *IEEE Trans. Ultrasonics, Ferroelectrics and Frequency Control,* vol. 54, no. 2, pp. 251-270, Feb. 2007.

[2] J.T.M van Beek, et al, "A review of MEMS oscillators for frequency reference and timing applications", *J. Micromech. Microeng,* vol.22, no.1, 013001.

[3] M. Pardo, et al. "Phase Noise Shaping via Forced Nonlinearity in Piezoelectrically Actuated Silicon Micromechanical Resonators", *MEMS 2011*, Cancun, MEXICO.

[4] H.K. Lee, et al, "Stable operation of MEMS oscillators far above the critical vibration amplitude in the nonlinear regime", *JMEMS*, vol.20, no.6, 2010.

[5] A. K. Samarao, et al. "Temperature Compensation of Silicon Micromechanical Resonators via Degenerate Doping", *IEDM 2009*, pp. 789-792.

[6] E.J. Ng, et al. "Localized, degenerately doped epitaxial silicon for temperature compensation of resonant MEMS systems", *Transducers 2013*, pp. 2419-2422.

[7] J. J. Hall, "Electronic Effects in the Elastic Constants of n-Type Silicon", *Physical Review*, vol. 161, no. 3, 1967, pp. 756-761.

[8] V. Kaajakari, et al, "Nonlinear Limits for Single-crystal Silicon Microresonators", *JMEMS*, vol.13, no.5, 2004.

[9] M. Shahmohammadi, et al, "Nonlinearity reduction in silicon resonators by doping and re-orientation", *MEMS 2013,* Taipei, Taiwan.

[10] L. D. Landau, et al. "Resonance in non-linear oscillations", Mechanics, vol. 1, *Course of Theoretical Physics, 3 ed.*, MA USA: Butterworth-Heinemann, pp. 87-92, 1982.

[11] B. Kim, et al, "Frequency stability of wafer-scale film encapsulated silicon based MEMS resonator", *Sensors and Actuators A (Physical)*, vol. 136, no.1, pp.125-131, 2007.

[12] M. Agarwal, et al, "A study of electrostatic force nonlinearities in resonant structures", *APL*, 92, 104106, 2008.

ACKNOWLEDGEMENTS

This work was supported by DARPA grant FA8650-13-1-7301, "Mesodynamic Architectures (MESO)," managed by Dr. Jeff Rogers. The fabrication work was performed at the Stanford Nanofabrication Facility (SNF) which is supported by National Science Foundation through the NNIN under Grant ECS-9731293. The authors would like to thank the staffs at SNF for their help during the fabrication process.

CONTACT

*Yushi Yang, tel: +1-765-404-0884; ysyang88@stanford.edu

MICRO-SCALE DIAMOND HEMISPHERICAL RESONATOR GYROSCOPE

P. Taheri-Tehrani[1], T.-H. Su[1], A. Heidari[1], G. Jaramillo[1], C. Yang[2], S. Akhbari[2], H. Najar[1], S. Nitzan[1], D. Saito[2], L. Lin[2], and D. A. Horsley[1]*

[1]University of California Davis, USA

[2]University of California Berkeley, USA

ABSTRACT

This paper concerns a micro-scale gyroscope based on a 1 mm diameter diamond hemispherical resonator with embedded polysilicon electrodes. Frequency mismatch and quality factor of the wineglass vibration modes are studied. The device has embedded electrodes used for electrostatic transduction of resonator vibration and for electrostatic mode-matching. The air gap between the resonator and electrodes is small to increase the frequency tuning range for a given supply voltage. The 2θ-mode resonant frequency mismatch can be minimized from 2.4% to 0.1% by applying a low 2.5V tuning voltage.

KEYWORDS

Gyroscope, Diamond, Hemispherical Resonator, Electrostatic Tuning, Quadrature.

INTRODUCTION

The principle of the vibratory gyroscope is Coriolis acceleration coupling between two degenerate resonant modes of a vibratory structure. Mechanical structures such as rings, disks, and hemispheres have pairs of degenerate wineglass modes (i.e. 2θ, 3θ, 4θ, … modes) which exhibit Coriolis coupling. The Coriolis acceleration amplitude for a given rotation rate, referred to as angular gain, depends on the geometry and mode-shape of the resonator. The main advantage of these structures is that they have a highly symmetric structure, enabling the device to have a low split between the resonant frequencies ($\Delta f/f < 1/Q$). Appropriately designed electrodes can be used to null the residual frequency and quadrature error through electrostatic tuning.

Here, we present a rate gyroscope based on a 1 mm hemispherical resonator made of thin-film microcrystalline diamond (MCD). Resonator vibration is excited and sensed using electrostatic transduction using electrodes that also provide electrostatic tuning. First, an overview of the fabrication is presented, then design of the device is discussed. Information on the characteristics of the devices is provided. The devices are tested as gyroscopes and their performance is reported.

DESIGN AND FABRICATION

The device, shown in Figure 1, is a 1 mm diameter, 250 µm deep hemispherical resonator formed from 1 µm thick MCD. The device diameter is four and six times smaller than gyro designs reported in [1-2], respectively. Eight boron doped polysilicon electrodes are embedded in the silicon cavity surrounding the hemispherical resonator with a 1 µm capacitive gap. The polysilicon electrodes are isolated with a 1 µm silicon nitride (Si_3N_4) layer from the <111> silicon substrate. The resonator is anchored to the substrate, enabling dc voltage to be applied through the silicon substrate. A similar structure is presented in [3-4], but no gyroscope performance is reported.

A novel self-aligned process is employed in the fabrication. First, hemispherical molds are formed via a silicon isotropic etch using HNA (HF/nitric/acetic acids) with a 1.2 µm LPCVD Si_3N_4 hard mask. Then, a 1.2 µm thick LPCVD Si_3N_4 layer and a 500 nm boron doped polysilicon layer are conformally deposited inside the silicon molds. The self-aligned electrodes are formed by patterning

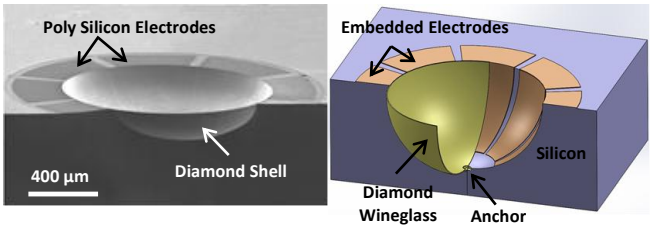

Figure 1: SEM and schematic images of hemispherical resonator gyroscope with embedded electrodes.

the polysilicon layer within the cavities using spray-coating (EVG 101 Spray Coater), lithography and plasma etching. A 1 µm SiO_2 layer is deposited as sacrificial layer on the top of the polySi electrodes. Then, the 60 µm diameter anchor is patterned, followed by CVD of 1 µm boron doped diamond. The diamond on the wafer surface is removed using CMP and O_2 plasma etching, after which the resonator is released in HF. The fabrication process flow is illustrated in Figure 2.

The scale factor (S_Ω) from input rate to output displacement on the sensing axis is:

$$S_\Omega = 2AG\frac{m_A Q_B}{k_B} M(\Delta f) 2\pi f_A q_A \qquad (1)$$

where Q_B, m_B, and k_B are the quality factor, modal mass, and spring constant of the sense-axis, q_A is the displacement of the drive axis, f_A is the drive oscillation frequency, AG is the Coriolis coupling (or angular gain), Δf is the frequency mismatch between the drive and sense modes and $M(\Delta f)$ represents the normalized magnitude of the sense-axis transfer function evaluated at $f_A = f_B - \Delta f$,

$$M(\Delta f) = \{Q_B^2[1-(1-\Delta f/f_B)^2]^2 + (1-\Delta f/f_B)^2\}^{-\frac{1}{2}}. \qquad (2)$$

In a mode-matched gyro, $\Delta f = 0$ and $M(\Delta f) = 1$.

Frequency mismatch and quadrature error arise from imperfections in the resonator that cause the resonator's stiffness matrix to be non-diagonal and to have unequal diagonal entries. These can be corrected using electrostatic tuning [5]. In the current gyro, the tuning electrodes only allow the on-diagonal stiffness components to be adjusted,

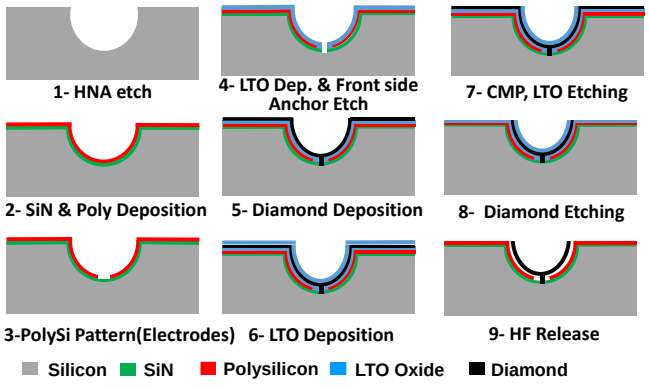

Figure 2 : Fabrication process of the hemispherical resonator.

9781940470016/HH2014/$25©2014TRF
DOI 10.31438/trf.hh2014.77

$$\begin{bmatrix} k_A & k_{AB} \\ k_{AB} & k_B \end{bmatrix} = \begin{bmatrix} k_{A0} & k_{AB} \\ k_{AB} & k_{B0} \end{bmatrix} - \begin{bmatrix} k_{TA} & 0 \\ 0 & k_{TB} \end{bmatrix} \quad (3)$$

where k_{A0} and k_{B0} denote the initial spring constants of the A and B axes, k_{TA}, k_{TB} denote the electrostatic spring constants, and k_{AB} represents the cross-axis coupling. Cross-axis coupling results in quadrature error; the tuning electrodes used here have an angular extent of 45° and are therefore unable to change these off-diagonal components to null the quadrature error.

Angular gain (AG) is a measure of Coriolis coupling between the degenerate resonant modes in a gyroscope ($0 < AG < 1$). The scale factor is proportional to AG, which is solely dependent on the geometry and mode-shape of the resonator. AG can be estimated using the displacement field of the two resonant modes of interest using a FEM model of the structure [6],

$$\vec{m}_c = \sum \vec{X}_i \times \vec{Y}_i \cdot m_i \quad (4)$$

$$\overrightarrow{AG} = \frac{\vec{m}_c}{m_{eff}} \quad (5)$$

where the index *i* refers to each mesh element in the FEM model and m_i corresponds to the mass of each element. $\vec{X}_i$ and $\vec{Y}_i$ correspond to the normalized displacement vectors of the two degenerate modes. $\vec{m}_c$ is a three component vector and the absolute value of each component divided by the modal mass of drive resonant mode gives the AG value for each axis. The three components of $\overrightarrow{AG}$ correspond to the angular gain for rotation rate in each axis ($\Omega_x, \Omega_y, \Omega_z$).

FEM simulations were conducted to study the effect of the depth-to-radius ratio of the hemispherical resonator on the angular gain. The simulation results, shown in Figure 3, demonstrate the increase in angular gain and reduction in normalized 2θ-mode resonant frequency of the hemispherical resonator as the depth-to-radius ratio increases. However, the depth of devices reported here are limited to 250 µm due to the HNA etch used to form the resonator molds.

A numerical calculation was performed based on the analytical mode-shape of the hemispherical resonator [7] to calculate the electrode parameters. The electrode capacitance (C) and displacement sensitivity dC/dx are estimated to be 1.3 pF and 0.6 µF/m, respectively. Modal stiffness and modal mass of the 2θ-mode estimated from FEM simulation are 25 N/m and $8 \cdot 10^{-10}$ kg, respectively. High capacitance and low stiffness result in a wide tuning range: only 1 V tuning voltage will cause ~1 N/m electrostatic softening, corresponding to a 2% reduction in natural frequency.

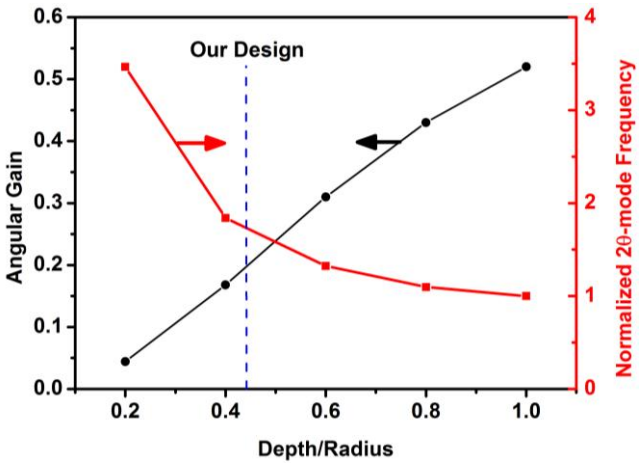

Figure 3 : Angular gain and normalized 2θ-mode natural frequency versus depth-to-radius ratio.

RESONATOR CHARACTERIZATION

The vibration frequency response of several hemispherical resonators was characterized using a Laser Doppler Vibrometer (LDV, Polytec Inc.) both in air and in vacuum. They were mounted vertically onto a shear mode piezoelectric actuator (Noliac A/S) with a bandwidth of 1.7 MHz to excite vibration. The single point LDV laser spot was focused through a 10x microscope objective onto the rim of the shell to measure the radial displacement of the vibrating shell. Measurements of the frequency and Q-factor of the 2θ, 3θ and 4θ vibration modes are shown in Figure 4. As can be seen in this figure, higher-order modes have higher Q-factor. The 2θ-mode Q-factor of 24,000 was obtained at a pressure <1 mTorr.

The diamond resonator was also mounted in a vacuum probe station (MMR Technologies Inc.) to allow measurement using capacitive excitation and readout via the embedded electrodes. The frequency response of a hemispherical shell in vacuum at 30 µTorr is shown in Figure 5. The observed resonances at 26.68 kHz and 26.75 kHz correspond to the two 2θ elliptical vibration modes. The frequency mismatch between these two degenerate resonant modes is 75 Hz, which corresponds to $\Delta f/f$ of 0.28%. The observed Q-factors are approximately 12,100 and 14,800. The lower Q in observed in this experiment may be due to increased gas damping or from electrical loading from the testing setup.

GYROSCOPE PERFORMANCE

The hemispherical resonator is surrounded by eight electrodes. Two vibration axes are required for gyroscope operation, one for the drive axis (in this paper, axis A, which corresponds to the mode A resonant frequency) and the other for the sense axis (in this paper, axis B, which corresponds to the mode B resonant frequency). For each axis, two electrodes are used for differential sensing to decrease the feedthrough, one electrode is used for single-ended drive, and one electrode for direct tuning. For rate-sensing experiments, resonator dice were mounted in 28-pin packages using conductive epoxy and wire-bonded to the pads. As shown in Figure 6, the package was mounted on a PCB with differential sense circuitry. A digital lock-in amplifier (Zurich Instruments HF2LI) was used to provide dc tuning voltages, closed-loop amplitude control of the drive axis, and demodulate the sense axis vibration.

The resonators have direct tuning electrodes that can be used to compensate for Δf. However, without quadrature nulling electrodes, devices exhibiting high quadrature cannot be perfectly

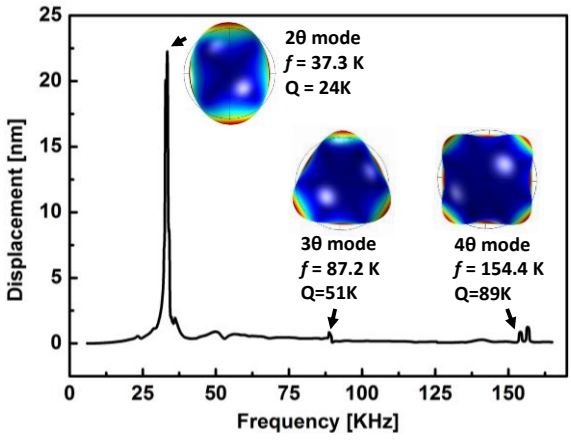

Figure 4: Frequency spectrum showing 2θ, 3θ and 4θ modes of the wineglass resonator.

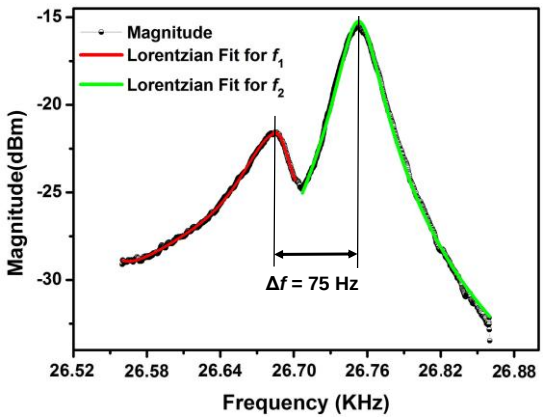

Figure 5: Measured frequency response showing the 2θ elliptical modes (f_B =26.68 kHz, f_A =26.75 kHz, Δf=75 Hz, Q_A=12.1 K, Q_B=14.8 K, ΔQ=2700, Vacuum: 30μTorr).

mode-matched ($\Delta f = 0$). The tuning plots from two devices, one with low quadrature (device 1), and the other with high quadrature (device 2) are presented in Figure 7 and 8. Figure 7(a) shows the frequency change for the both 2θ-modes for device 1 versus the tuning voltage applied to axis A. As shown in the Figure 7(b), the two frequencies can be tuned to a minimum Δf = 28 Hz. The 2θ-mode resonant frequency split ratio ($\Delta f/f$) is minimized from 2.4% to 0.1% by applying a low 2.5 V tuning voltage in device 1. Figure 8(a) presents the tuning curves for device 2. With an initial Δf of 550 Hz (Figure 8(b)), the minimum Δf achieved is 290 Hz, as shown in Figure 8(c). The 2θ-mode resonant frequency split ratio ($\Delta f/f$) is minimized from 2.2% to 1.1% by applying a 1.8 V tuning voltage in device 2. High quadrature error in this device makes mode-matching impossible.

In the hemispherical resonators studied here, the dominant quadrature error term results from the cross-axis stiffness component k_{AB} (see Eqn. (3)). In other words, the resonator's primary axis of stiffness is not aligned with the sense electrodes. In addition, because the electrodes have a 45° arc length, some A-axis vibration is always detected by the B-axis sensing electrodes (and vice-versa). A measure of this effect is the ratio of the capacitance change in the A and B axes resulting from A-axis vibration, $(dC_A/dq_A)/(dC_B/dq_A)$. In an ideal gyro, this ratio would be infinite, since A-axis vibration q_A would have no effect on the B-axis sense

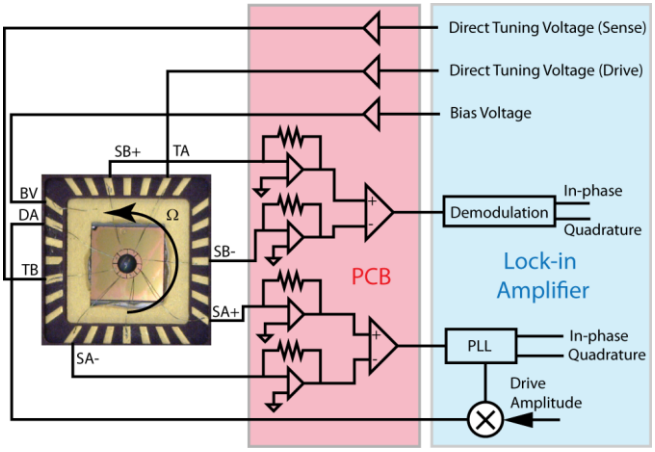

Figure 6: Testing platform used for gyroscope experiments. Key: tuning voltages (TA, TB), drive voltages (DA, DB), sensing voltages (SA, SB), resonator bias voltage (BV).

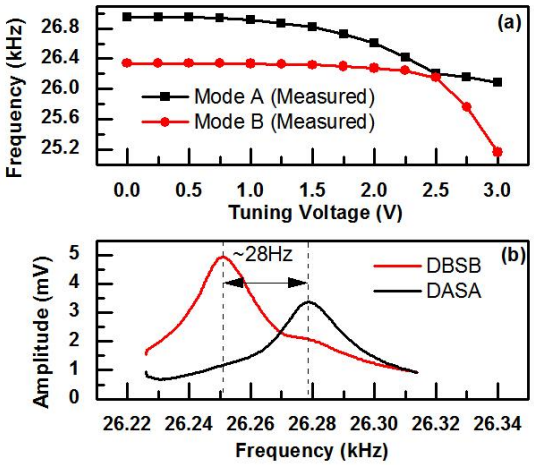

Figure 8: Device 1 results showing: (a) Mode A and mode B frequencies versus axis A tuning voltage; (b) Frequency responses from drive A to sense A (DASA) and drive B to sense B (DBSB) in the 2.5V mode-matched condition.

capacitance C_B. In a real gyro, this ratio diminishes as the electrode's arc length is increased from 0° to 45°, as shown in Figure 9. The plot also shows that the ratio depends on the angle θ of the primary axis of stiffness relative to the electrode axes. When θ = 22.5°, the primary axis of stiffness is exactly midway between the A and B axis electrodes, corresponding to the worst case for quadrature error. The plot demonstrates that while large electrodes achieve high sense capacitance, they result in larger quadrature error.

Gyroscope experiments were conducted using a rate table (Aerosmith 1291BR). Rate table testing was conducted with a poor vacuum and as a result the observed *Q* factors were over an order of magnitude lower than the values measured in vacuum probe station experiments. The sensitivity plots for two devices are shown in Figure 10. Device 1 with lower $\Delta f/f$ of 0.1% and higher Q-factor of 1000, shows an order of magnitude greater scale factor than device 2 with higher $\Delta f/f$ of 1.2% and lower Q-factor of 600. Device 1 achieved a scale factor of 140 μV/deg/s while device 2 achieved a scale factor of 13 μV/deg/s. The difference in scale factor is due to the difference in Q and because device 2 was operated relatively far from the mode-matched condition.

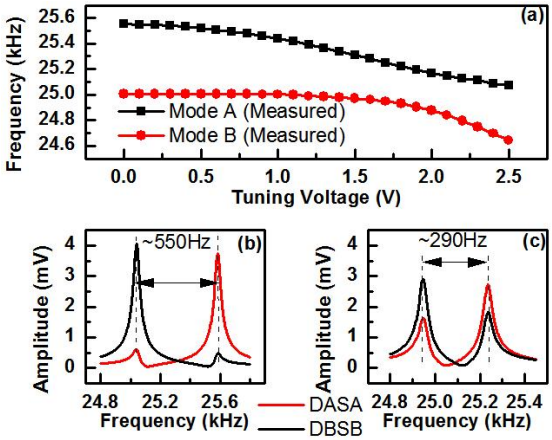

Figure 7: Device 2 results showing: (a) Mode A and mode B frequencies versus axis A tuning voltage; (b) As-fabricated frequency responses before mode-matching; (c) Frequency responses with the minimum achievable Δf = 290 Hz at 1.8V tuning voltage.

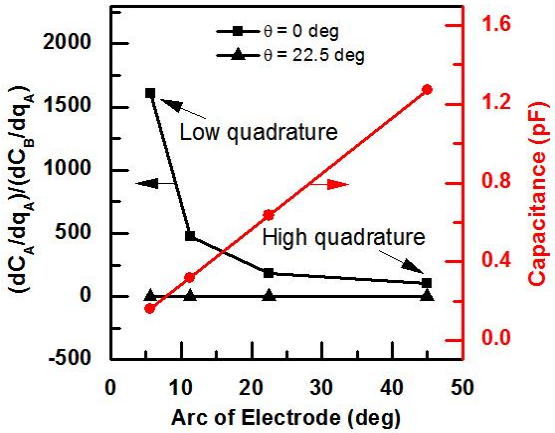

Figure 9: The ratio of the capacitance sensitivity to mode A motion (dC_A/dq_A)/(dC_B/dq_A) illustrates that mode A vibration, q_A couples into the mode B sense capacitor, C_B resulting in quadrature error. With quadrature nulling electrodes, the rotation of the primary axis of stiffness (θ) can be reduced from a maximum value of 22.5° to 0°. In either case, large electrodes (>15°) result in high quadrature error.

The zero-rate output spectrum from both devices shows that the output noise is shaped by the gyro's mechanical frequency response, which has a 3 dB bandwidth of 27 Hz and 43 Hz for the two devices, respectively (Figure 11). Dividing the output noise at 0 Hz (1.6 μV/√Hz and 1.1 μV/√Hz) by the scale factor results in calculated angle random walk (ARW) of 11 mdeg/s/√Hz and 85 mdeg/s/√Hz, for devices 1 and 2, respectively. The calculated ARW is approximately twice the theoretical Brownian noise (700 nV/√Hz) limit calculated due to electronic forcing noise contributed by the sense/drive electrodes. The electronic noise floor is 300 nV/√Hz for both devices.

CONCLUSION

In conclusion, we have reported the first micro-scale diamond hemispherical rate gyroscope. The gyroscope operates on the 2θ wineglass resonant mode using embedded electrodes with 1 μm gap. The 8 electrode design is shown to allow mode-matching within 0.1% at 2.5V tuning voltage in a device that has low initial quadrature error resulting in 140μV/deg/s scale factor and 11 mdeg/s/√Hz ARW.

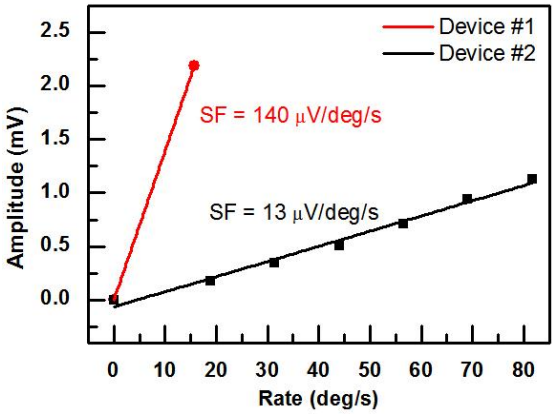

Figure 10: Rate table test results showing the output voltage versus input rate and the resulting scale factor (SF).

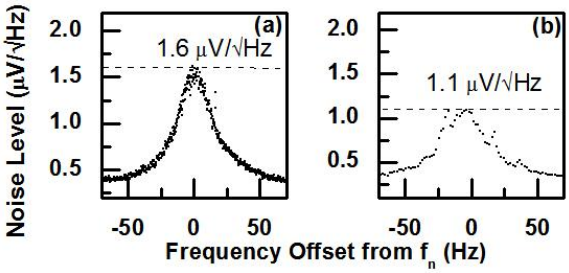

Figure 11: Zero rate output spectra for (a) device 1, (b) device 2.

ACKNOWLEDEGMENT

This work is supported by DARPA under grant W31P4Q-11-1-0003. The authors would like to thank the support of the staff in UC Davis Northern California Nanotechnology Center and UC Berkeley Marvell Nanolab.

REFERENCES

[1] D. Senkal, M. J. Ahamed, A. A. Trusov, and A. M. Shkel, "Demonstration of Sub-1 Hz Structural Symmetry in Micro-Glassblown Wineglass Resonators with Integrated Electrodes", Transducers 2013, pp. 1380-3.

[2] J. Cho, J. -K. Woo, J. Yan, R. L. Peterson, and K. Najafi, "A High-Q Birdbath Resonator Gyroscope (BRG)", Transducers 2013, pp. 1847-50.

[3] L. D. Sorenson, X. Gao, and F. Ayazi, "3-D Micromachined Hemispherical Shell Resonators with Integrated Capacitive Transducers", MEMS 2012, pp. 168-71.

[4] A. Heidari, M.-L. Chan, H.-A. Yang, G. Jaramillo, P. Taheri-Tehrani, P. Fonda, H. Najar, K. Yamazaki, L. Lin, D. A. Horsley, "Hemispherical wineglass resonators fabricated from the microcrystalline diamond", J. of Micromechanics and Microengineering, Vol. 23, No. 12, December 2013 , pp. 125016-23(8).

[5] B. J. Gallacher, J. Hedley, J. S. Burdess, A. J. Harris, A. Rickard, and D. O. King, "Electrostatic Correction of Structural Imperfections Present in a Microring Gyroscope", Journal of Microelectromechanical Systems, Vol. 14, No. 2, April 2005, pp. 221-34.

[6] J. Cho "High Performance Micromachined Vibratory Rate- and Rate-Integrating Gyroscopes" PhD dissertation, Electrical Engineering Department, The University of Michigan, 2012.

[7] S. Gao, J. Wu, "Theory and Finite Element Analysis of HRG", International Conference on Mechatronics and Automation, August 5-8, 2007, pp. 2768-72.

CONTACT

*Parsa Taheri-Tehrani; Tel: +1-530-341-3080;
ptaheri@ucdavis.edu

A PASSIVE MICROMECHANICAL FREQUENCY DIVIDER

B.S. Strachan[1,2], K.R. Qalandar [3], B. Gibson[3], M. Sharma[3], P. Polunin[1,4], S.W. Shaw[1], and K.L. Turner [3]
[1] Department of Mechanical Engineering, Michigan State University, East Lansing, MI USA 48824
[2] Department of Electrical Engineering, Michigan State University, East Lansing, MI USA 48824
[3] Department of Mechanical Engineering, University of California, Santa Barbara, CA, USA 93106
[4] Department of Physics and Astronomy, Michigan State University, East Lansing, MI USA 48824

ABSTRACT

We report on the design and experimental characterization of a passive MEMS frequency divider that is based on a cascade of parametrically coupled nonlinear resonator vibration modes. The device is designed to have 1:2 frequency ratios between adjacent modes with an orientation that promotes the necessary nonlinear modal coupling. We characterize the fabricated device and map the normalized parametric instability parameter regions for the first two modes. We successfully activate the cascade by parametrically driving the second mode and, by operating in the intersection of the instability regions, the energy cascades to the first mode, resulting in an input-to-output frequency ratio of four.

INTRODUCTION

Passive frequency conversion is an essential component for sensor networks and is ideal for critical applications requiring low power and good phase noise characteristics, such as in frequency synthesizers[1]. Currently, passive frequency dividers for RF applications are limited to electronic topologies which are large compared to MEMS resonators[2]. The divider device presented here is based on a cascade of subharmonic resonances in a set of N vibration modes tuned with relative $1:2$ frequency ratios [3]. It takes an input signal of 423.6 kHz and passively divides it through two modal stages, producing signals at 211.8 kHz and 105.9 kHz. We specify the operating region for this system in the drive frequency and drive amplitude parameter space. This novel divider design has simple design rules and can be extended to a large number of modal stages, ultimately dividing by 2^N.

FREQUENCY DIVIDER

Figure 1 shows an SEM image of the fabricated device along with a diagram of the conceptual scheme on which it is based [3]. It consists of a set of flexible beams that are orthogonally coupled, providing parametric driving from the shorter beam to the adjacent longer beam. The released structure is fabricated in single-crystal silicon. The microbeam elements are uniformly $10\mu m$ in depth and $1.85\mu m$ wide, and the beam lengths increase by approximately $\sqrt{2}$ to tune adjacent modal frequencies to the required $1:2$ ratios. The device is driven capacitively, providing a force proportional to the DC and AC applied voltages. The velocity of the in-plane motion of each beam is detected using a Polytec UHF-120 Laser Doppler Vibrometer. To direct the laser beam perpendicular to the motion, 45° angled mirrors are etched using focused ion beam (FIB) milling. Measurements are performed at a driving voltage of $100\ V_{DC}$ and $0-50\ V_{AC}$ at a pressure of ~ 400mTorr.

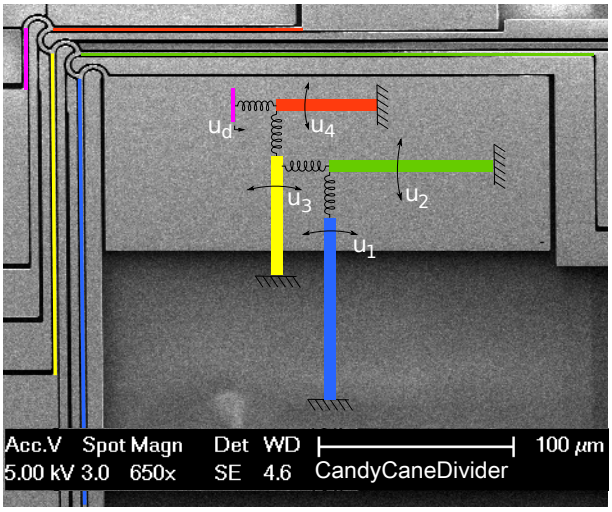

Figure 1: An SEM image of the fabricated device; inset shows the conceptual model that inspired the design [3].

For this device, each mode is spatially localized in a given beam in order to promote the required nonlinear intermode coupling. The high frequency mode (beam) is driven parametrically at twice its natural frequency. This beam, in the desired operating regime, will parametrically drive the next beam, and so on down the cascade, due to the $1:2$ frequency ratios, their relative orientation, and nonlinear modal coupling. The device of Figure 1 has four beams; we were able to activate only the first and second modes, resulting in division by four, due to modal frequency mistuning. Figure 2 shows the first two vibration modes for a COMSOL model of the device, with the required $1:2$ frequency ratio. Simulations of this COMSOL model in fact show division by 16, and this should be achievable in devices with more precise modal tuning.

RESULTS

Figure 3 shows the regions of drive amplitude and frequency for which modes 1 and 2 are individually excited into parametric resonance. The overlap region is where the cascade is expected to become activated. Figure 4 shows the measured response amplitudes from modes 1 and 2, and theoretical response curves from [3], over the frequency range of interest. Note that the mode 2 amplitude drops when mode 1 becomes active. The presence of a mode 1 response represents passive frequency division by a factor of 4.

9781940470016/HH2014/$25©2014TRF
DOI 10.31438/trf.hh2014.78

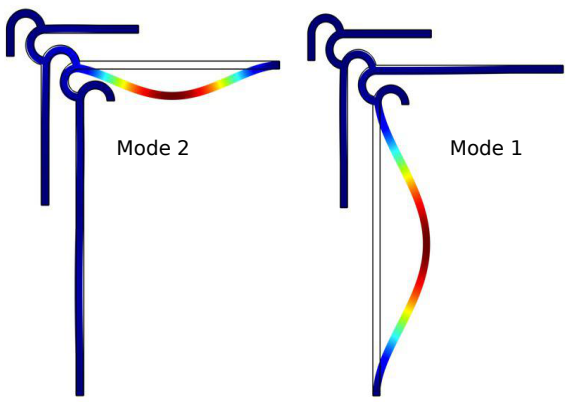

Figure 2: First two vibration modes from a COMSOL model. Mode frequencies are 105.95 *kHz (mode* 1*) and* 211.7 *kHz (mode* 2*).*

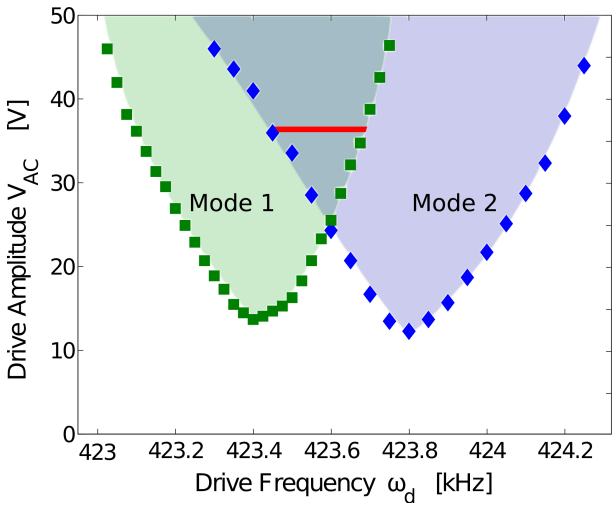

Figure 3: Parametric resonance zones for the first two modes of the device. The shaded overlap region is where the divide-by-four operation is achieved. The red segment indicates the operating voltage and frequency range of interest.

CONCLUSION

The results demonstrate passive frequency division in MEMS using a cascade of parametric resonances. Division by 2^N requires mutual overlap of N regions such as those shown in Fig. 3, which can be achieved for larger N by improved tuning of device frequencies, a topic of current investigation. Also of interest are methods for designing devices with desired levels of nonlinear modal coupling, which will promote activation of the cascade, and the phase noise performance of these devices.

ACKNOWLEDGMENTS

We thank Alice Ma for her preliminary work on the divider design. This work was supported by an NSF collaborative project under grants 1234067 and 1234645.

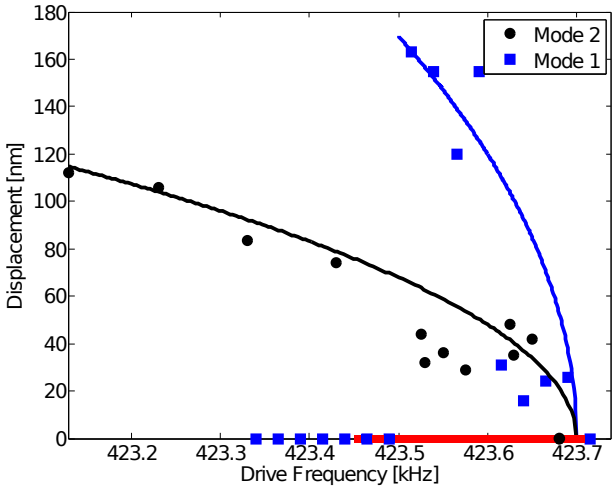

Figure 4: Measured mode 1 *and* 2 *amplitudes, extracted from the spectrum at* $1/2$ *and* $1/4$ *of the drive frequency from the response measured at the center of the respective mode localized beam, versus drive frequency, along with curve fits based on the analytical model [3], over the frequency range of interest. The AC driving amplitude is* 36 *V. The frequency range marked with red corresponds to that of Figure 3, where the cascade is predicted to occur. Note that these data were taken on separate sweeps, since simultaneous measurement of both modes was not possible, and that the mode* 1 *response data was slightly frequency shifted to account for drift between the runs.*

REFERENCES

[1] M.M. Driscoll, "Phase Noise Performance of Analog Frequency Dividers", IEEE Transactions on Ultrasonics, Ferroelectrics and Frequency Control, 37, 4 (1990).

[2] J. Lee, B. Razavi,"A 40-Ghz Frequency Divider in 0.18-mm CMOS Technology", IEEE Journal of Solid State Circuits, 39, 4 (2004).

[3] B.S. Strachan, S.W. Shaw, and O. Kogan, "Subharmonic Resonance Cascades in a Class of Coupled Resonators", Journal of Computational and Nonlinear Dynamics, 8, 4 (2013).

AN 8.7 GHZ GAN MICROMECHNAICAL RESONATOR WITH AN INTEGRATED ALGAN/GAN HEMT

Azadeh Ansari and Mina Rais-Zadeh
University of Michigan, Ann Arbor, MI, USA

ABSTRACT

A thickness-mode GaN resonator is presented in this work, showing fourth-order thickness-mode resonance at 8.7 GHz with an extracted quality factor (*Q*) of 330, exhibiting the highest resonance frequency measured to date on GaN micromechanical resonators with a high *frequency* × *Q* value of 2.87×10^{12}. With the goal of implementing an all-GaN multi-GHz oscillator, the resonator is monolithically integrated with an AlGaN/GaN high electron mobility transistor (HEMT). The results reported in this paper mark critical steps in development of high-frequency, high-power GaN microsystems.

INTRODUCTION

Gallium nitride (GaN), with a wide band gap of 3.4 eV, and excellent electronic properties, is a prime candidate for high-temperature, high-power, and high-frequency applications. GaN material systems can also benefit from a two-dimensional electron gas (2DEG) induced at AlGaN/GaN hetero-interface. High electron mobility transistors (HEMTs) with 2DEG conducting channel are widely used in power amplifiers in base stations. GaN also shows strong piezoelectric properties and chemical stability, making it a perfect electro-mechanical material. GaN material system allows for incorporation of diverse functionalities on the same substrate. GaN micromechanical resonators and filters, AlGaN/GaN HEMTs, optoelectronic components, and high-*Q* passives can all be integrated on the same substrate to build GaN-based integrated circuits such as timing references or harsh environments sensors.

Our group has previously reported on bulk-mode GaN micromechanical resonators with frequencies ranging from 10s of MHz to 3 GHz [1, 2]. Higher frequency resonators are sought for use as local oscillators (LOs) in high-power mm-wave GaN transceivers. Higher frequency resonances have been achieved using resonant body HEMTs [3-5], which offer intrinsic filtering and signal amplification. However, the acoustic gain of reported resonant body HEMTs proved to be too small for implementing an LO without the need of external amplifiers. In this work, we demonstrate a piezoelectrically transduced GaN resonator at 8.7 GHz connected to an on-chip AlGaN/GaN HEMT. The resonator is 40×60 μm^2 (Fig. 1) and exhibits the highest resonance frequency measured for GaN resonators to date. It shows good linearity with third-order input intercept point (IIP_3) of 29.2 dBm. The response of the resonator cascaded with the HEMT is tuned by ~7 dB. Further optimization of the resonator and HEMT allows for realization of multi-GHz all-integrated GaN LOs.

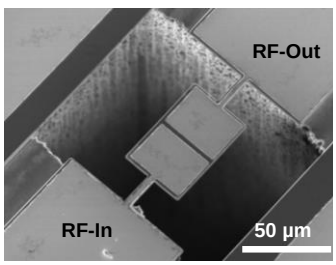

Figure 1. SEM image of a fabricated 40 μm × 60 μm GaN BAW resonator, with tethers of 20 μm in length and 5 μm in width.

GAN MICROMECHANICAL OSCILLATORS

The main goal of this work is to design a GaN MEMS-based oscillator. Two approaches are taken to realize a GaN oscillator in GaN/AlGaN MMIC (Fig. 2): (1) Resonant body HEMTs, shown in [3-5], which are readily scalable to higher frequencies, but suffer from low acoustic gain insufficient for self-oscillation, and (2) cascade of a resonator and a HEMT (focus of this work). Capacitive feed-through, which becomes a critical issue at higher frequencies, can be removed from the resonator response using a dummy, unreleased resonator in a differential amplifier configuration [6], hence allowing to scale the resonant frequencies deep into the GHz regime where GaN ICs usually operate at.

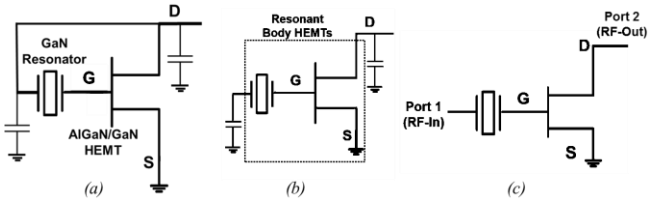

Figure 2. (a) A simple pierce oscillator configuration. (b) A resonator and a transistor can be combined forming a single resonant body HEMT. (c) A cascade of a resonator and a HEMT that is implemented in this work, as the main building block of an oscillator.

DISCUSSION

The GaN resonator of this work consists of a 1.8-μm-thick GaN layer epitaxially grown on a Si substrate by metal-organic chemical vapor deposition (MOCVD) technique. The fabrication process of the resonator and HEMT is reported in [7]. The measured response of the resonator in the frequency range of 1-10 GHz is shown in Fig. 3, along with the corresponding mode shape for each harmonic of the thickness-mode resonance. The fundamental thickness-mode resonance at 2.22 GHz shows an acoustic velocity of ~7920 m/s.

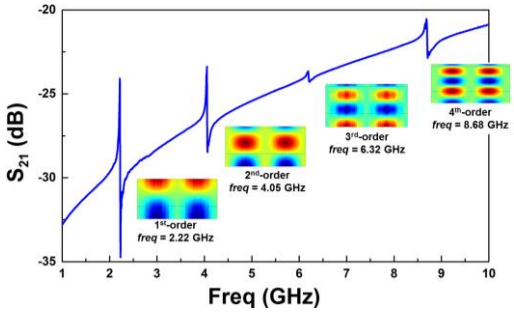

Figure 3. Wide-band frequency response of the 40 μm × 60 μm GaN resonator. The effect of capacitive feed-through is not de-embedded from the response. The mode shape for each thickness-mode resonance is also shown.

The fourth-order thickness-mode harmonic of the resonator shown in Fig. 1, exhibits a *Q* of 330 at 8.7 GHz, resulting in a high *frequency* × *Q* (or $f \times Q$) value of 2.87×10^{12} (Fig. 4). Operation at the fourth-order thickness-mode resonance as compared to lower harmonics, primarily benefits from reduction of three loss mechanisms, (1) visco-elastic damping, (2) thermo-elastic damping

9781940470016/HH2014/$25©2014TRF
DOI 10.31438/trf.hh2014.79

(TED), and most importantly (3) phonon-phonon scattering, as the intrinsic material loss is limited by the Landau–Rumer regime at such high frequencies [8], hence larger $f\times Q$ values are expected. With the current tether design, the anchor loss is not the dominant Q limiting factor. Whereas, metal loading from both the top and bottom electrode is a source of Q degradation, which can be alleviated by using 2DEG as the conductive top/bottom electrode.

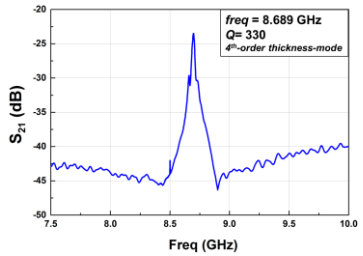

Figure 4. De-embedded frequency response of the 40 µm × 60 µm GaN resonator with a resonant frequency of 8.7 GHz, and an extracted Q of 330 at room temperature and ambient pressure. Capacitive feed-through is de-embedded from the resonator response using an unreleased but otherwise identical resonator.

Owing to its wide band gap and large breakdown electric field, GaN can handle high-power RF signals. GaN HEMTs can deliver 10 times as much output power as their GaAs counterparts. Similarly, GaN MEMS resonators show high power handling capability. The power handling of the resonator is characterized in Fig. 5. The fundamental mode and the third-order intermodulation product are extrapolated, showing an IIP_3 of 29.2 dBm. Furthermore the device shows 1-dB compression at input power level of ~16 dBm, most likely limited by the anchor design.

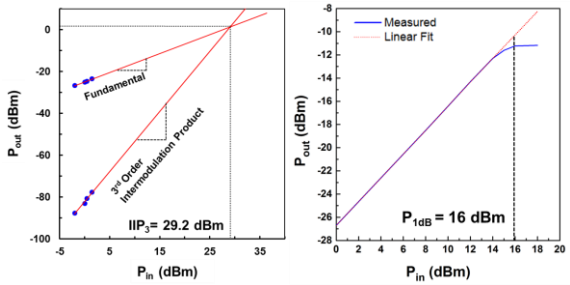

(a) *(b)*

Figure 5. (a) Two-tone power measurement of the fourth-order thickness mode resonance at 8.7 GHz. The extracted IIP_3 value is 29.2 dBm. (b) 1-dB gain compression occurs at input power level of 16 dBm at 8.7 GHz.

An integrated HEMT is used to amplify the response of the GaN resonator. Using this configuration, the signal is amplified by more than 7 dB when the HEMT is switched ON as shown in Fig. 5(b). The $f\times Q$ value reported in this work is compared to previous work, including GaN-on-Si resonators [2], resonant HEMTs [3, 5] (Fig. 7).

CONCLUSION

High-Q and high power handling capability of multi-GHz GaN resonators presented in this work suggest that GaN is a strong candidate for low phase-noise, multi-GHz power oscillators. Future work includes co-integration of high-Q capacitors and matching networks for implementing an on-chip oscillator using similar GaN-based micromechanical resonators.

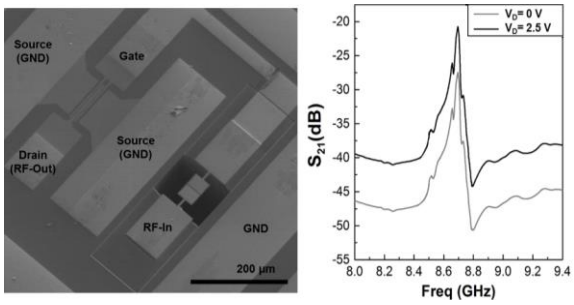

(a) *(b)*

Figure 6. (a) An SEM image and (b) the frequency response of a cascade of a resonator and a HEMT. The output of the resonator is fed to the gate of the HEMT, and the output signal is picked up from the drain. The gate DC bias is kept at 0 V. The drain voltage is varied to tune the transistor gain. The insertion loss is improved by ~7 dB when the drain voltage is at 2.5 V.

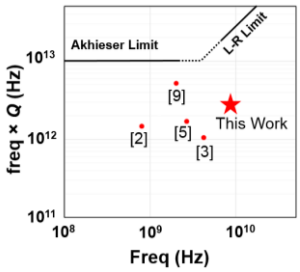

Figure 7. Comparison of f×Q value of GaN-based resonators with the phonon-phonon loss limits.

REFERENCES

[1] V. J. Gokhale, J. Roberts, and M. Rais-Zadeh, "High performance bulk mode gallium nitride resonators and filters," *International Solid-State Sensors, Actuators and Microsystems Conference (Transducers)*, Beijing, 2011, pp. 926-929.

[2] A. Ansari, V. J. Gokhale, V. A. Thakar, J. Roberts, and M. Rais-Zadeh, "Gallium nitride-on-silicon micromechanical overtone resonators and filters," *IEEE Electron Device Meeting (IEDM)*, Washington, DC, 2011, pp. 20.3.1- 20.3.4.

[3] A. Ansari and M. Rais-Zadeh, "A thickness-mode AlGaN/GaN resonant body high electron mobility transistor," *IEEE Transactions on Electron Devices*, Feb. 2014.

[4] A. Ansari and M. Rais-Zadeh, "HEMT-Based readout of a thickness-mode AlGaN/GaN resonator," *IEDM 2013*, Washington, DC, pp. 18.3.1- 18.3.4.

[5] L. C. Popa and D. Weinstein, "Switchable piezoelectric transduction in AlGaN/GaN MEMS resonators," *Transducers* 2013, pp. 2461-2464.

[6] K. E. Wojciechowski, "Single-chip precision oscillators based on multi-frequency, high-Q aluminum nitride MEMS resonators," *Transducers* 2009, Denver, CO, pp. 2126 – 2130.

[7] A. Ansari, V. J. Gokhale, J. Roberts, M. Rais-Zadeh, "Monolithic integration of GaN-based micromechanical resonators and HEMTs for timing applications," *IEDM* 2012, San Francisco, CA, pp. 15.5.1-15.5.4.

[8] R. Tabrizian, M. Rais-Zadeh, and F. Ayazi, "Effect of phonon interactions on limiting the f.Q product of micromechanical resonators," *Transducers* 2009, pp. 2131-2134.

[9] L. Popa, D. Weinstein, "L-Band Lamb Mode Resonators in Gallium Nitride MMIC Technology," *IFCS*, May 2014.

CONTACT

*A. Ansari, Tel. +1-734-757-3188; azadans@umich.edu

JUMPING-DROPLET ENERGY HARVESTING WITH NANOENGINEERED SURFACES

*N. Miljkovic, D.J. Preston, E.N. Wang**
Massachusetts Institute of Technology, Cambridge, Massachusetts, USA

ABSTRACT

We experimentally demonstrate jumping-droplet-based energy harvesting with nanoengineered surface designs. With recent advancements in micro/nanofabrication techniques, non-wetting engineered surfaces have enabled condensing coalesced droplets to spontaneously jump and simultaneously obtain electrostatic charge. In this work, we take advantage of these droplet characteristics to demonstrate energy harvesting for the first time. The charged droplets jump between superhydrophobic copper oxide (CuO) and hydrophilic copper (Cu) surfaces to create an electrical potential and generate electrical power during formation of atmospheric dew. We demonstrated power densities of ~0.06 nW/cm^2, which can be improved near term to ~100 μW/cm^2.

INTRODUCTION

Controlling micro/nano-scale wetting phenomena has been an active research area for over two decades, promising improvements in power generation, thermal management, and desalination [1]. With the significant advancements in micro/nanofabrication techniques, engineered surfaces have enabled improved non-wetting characteristics, and in certain cases, allow condensing coalesced droplets to spontaneously jump *via* the conversion of surface energy into kinetic energy [2]. Furthermore, we recently discovered that these jumping droplets are electrostatically charged and can be manipulated with electric fields [3, 4]. In this work, we take advantage of these unique droplet characteristics with nanoengineered surface designs to demonstrate energy harvesting for the first time.

EXPERIMENTAL APPROACH

To create these nanoengineered surfaces (Fig. 1) for energy harvesting, commercially purchased Cu was chemically oxidized to form CuO nanostructures [3]. These structures were then coated with a ≈30 nm conformal fluoropolymer coating (Fig. 1b) [3].

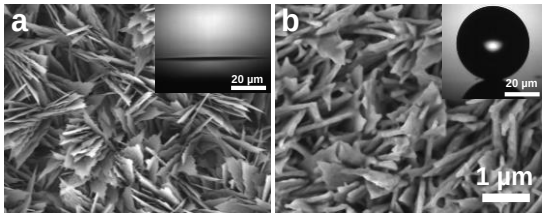

Figure 1: Field emission scanning electron micrographs (FESEM) of (a) a 10 min oxidized CuO surface (Inset: water droplet contact angle on the clean nanostructured CuO surface, $\theta_a \approx 0°$) and (b) a CuO surface coated with a ≈30 nm thick layer of P2i fluoropolymer (Inset: Water droplet advancing contact angle on the superhydrophobic nanostructured surface, $\theta_a = 171°\pm3°$). The sharp, knife-like CuO structures have characteristic heights $h \approx 1$ μm, a solid fraction $\varphi \approx 0.023$, and a roughness factor $r \approx 10$.

To first demonstrate jumping-droplet charging and field control, we used an external electrode biased to manipulate the positively charged droplets. Figures 2a and b show the concept, where a copper electrode placed beneath the tube was voltage biased with -300 and +300 V, respectively, to form an electric field. Due to electric-double-layer charge separation at the liquid-hydrophobic coating interface, the jumping droplets depart the surface with a droplet radius dependent electrostatic charge (≈10-100 fC) [3] and are easily manipulated by the external electric field.

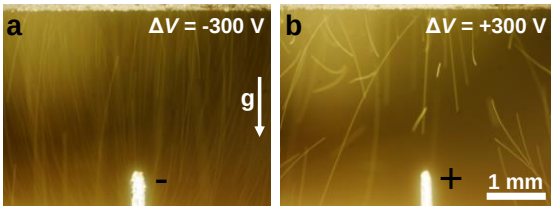

Figure 2: Droplet interactions with an electric field. A copper wire electrode was placed ≈5 mm beneath the superhydrophobic nanostructured surface and voltage biased relative to the sample (ΔV). The voltage potential difference created an electrostatic field allowing for charged droplet interactions with the field. The results indicate that the droplets are positively charged (chamber water vapor pressure P_v = 2,700±68 Pa, and supersaturation $S = P_v/P_{sat}(T_c) = 1.04$).

Analogous to the electric field control of droplet motion, jumping-droplet energy harvesting was achieved where charged droplets jump between a superhydrophobic and hydrophilic surface to create an electrical potential and generate electrical power. To investigate the jumping-droplet energy harvesting mechanism, we interdigitated nanostructured superhydrophobic CuO and hydrophilic Cu combs (Fig. 3a).

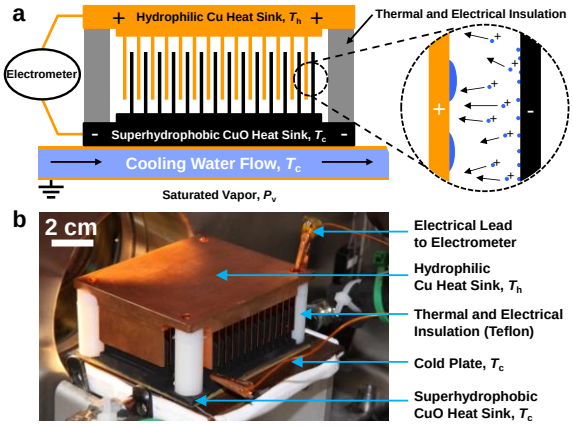

Figure 3: (a) Schematic of the jumping-droplet power generator showing the two combs in an interdigitated arrangement. The combs were electrically and thermally isolated from each other. Images of the jumping-droplet power generator showing (b) an isometric view of the two combs integrated in the test chamber for experimentation. Commercially purchased Cu combs were used (478 copper) with dimensions 26 x 89 x 75 mm (height x width x depth) (E1U-NPFSS-30, Cooler Master). To observe droplet jumping, the interdigitated device was tested in a controlled condensation chamber.

9781940470016/HH2014/$25©2014TRF
DOI 10.31438/trf.hh2014.80

The temperature of the CuO comb (T_c) was reduced *via* a cooling water flow until jumping-droplet-condensation commenced. The jumping-droplets travelled from the CuO comb fins to the conducting Cu hydrophilic fins (Figure 3a inset), resulting in an electrical potential buildup, which was measured using an electrometer (6517B Electrometer, Keithley).

EXPERIMENTAL RESULTS AND DISCUSSION

To replicate atmospheric dew conditions, the energy harvesting potential was studied at $T_c \approx 8°C$ and $P_v \approx 1800$ Pa. Figures 4a and b show the experimentally measured open circuit voltage (V_{OC}) and short circuit current (I_{SC}) of the device, respectively. Prior to condensation, V_{OC} and I_{SC} were ≈0 (Fig 4, no condensation region). After condensation began, charge separation resulted in the buildup of positive charge on the hydrophilic comb and V_{OC} and I_{SC} reached +15 V and +1.15 nA, respectively. The maximum energy harvesting rate in these experiments was ≈0.06 nW/cm^2. The relatively low energy density of our device was mainly due to: i) the low cooling rates (<0.01 W/cm^2), and ii) the non-optimum fin arrangement, resulting in the coldest temperature being at the base of the superhydrophobic fins and the inability to maximize the use of the whole comb area for droplet jumping.

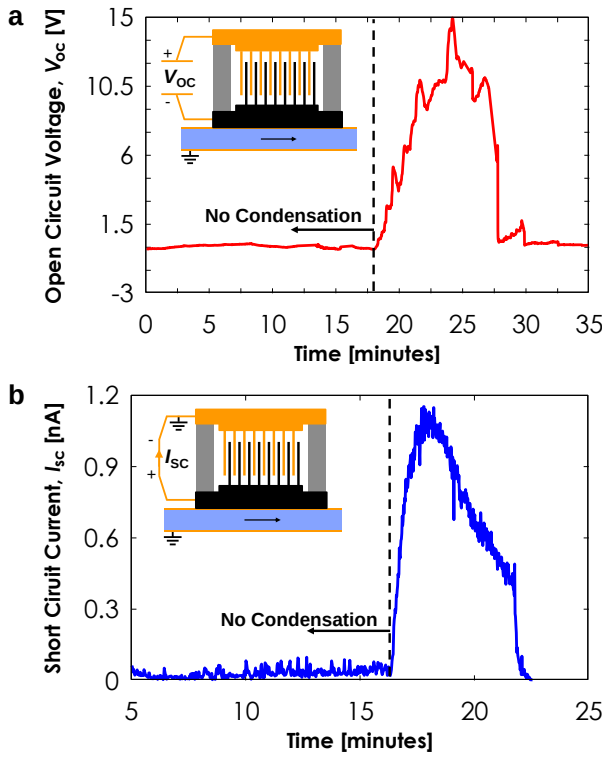

Figure 4: Experimentally measured (a) open circuit voltage (V_{OC}) and (b) short circuit current (I_{SC}) of the interdigitated device. The maximum energy harvesting rate in these experiments ($P = V_{OC}I_{SC}$) was ≈17.3 nW or ≈0.06 nW/cm^2 (based on the prototype active jumping area of 278 cm^2). The experiments were conducted by filling the controlled chamber with saturated water vapor and closing off the vapor inlet valve. Once pressure and temperature equilibrium was reached, the cooling water temperature (T_c) was gradually decreased and the water vapor began to condense. Due to the finite volume of water vapor in the chamber, the saturation pressure decreased as well, resulting in a corresponding decrease in droplet-jumping frequency, V_{OC}, and I_{SC}.

Future devices with higher condensation rates (>0.1 W/cm^2) and high-surface-area designs have the potential to achieve energy harvesting rates in the 10-100 μW/cm^2 range (Fig. 5), making them more attractive to power small electronic devices (>1 μW, *i.e.*, chemical batteries, thermoelectrics, and piezoelectrics).

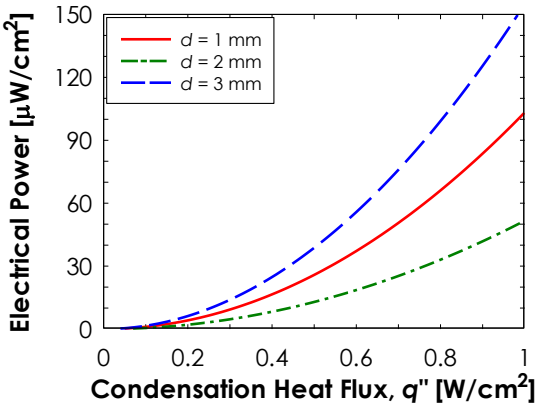

Figure 5: Theoretically calculated electrical energy harvesting rate from jumping-droplet condensation. By dividing the heat flux (q") with the latent heat of phase change (mh_{fg}) per droplet, a jumping-droplet frequency per unit area (f) was determined. Assuming departing droplets with radii ≈5 μm [1], individual droplet charge ≈8 fC [3], and an active area ≈1 cm^2, I_{SC} and V_{OC} were calculated and multiplied to obtain the harvesting power.

This work demonstrates a novel surface engineered platform for atmospheric energy harvesting and electric power generation.

ACKNOWLEDGEMENTS

We gratefully acknowledge funding support from the MIT S3TEC Center, an Energy Frontier Research Center funded by the Department of Energy, Office of Science, Basic Energy Sciences, under Award DE-FG02-09ER46577, and the Office of Naval Research (ONR) with Dr. Mark Spector as program manager. We acknowledge support from P2i for the hydrophobic layer depositions. D.J.P. acknowledges funding received by the National Science Foundation Graduate Research Fellowship under Grant no. 1122374. Any opinion, findings and conclusions or recommendations expressed in this material are those of the authors(s) and do not necessarily reflect the views of the National Science Foundation.

REFERENCES

[1] N. Miljkovic, and E. N. Wang, "Condensation heat transfer on superhydrophobic surfaces", MRS Bulletin, 38, 5, p. 397-406, (2013).

[2] J. B. Boreyko and C. H. Chen, "Self-Propelled Dropwise Condensate on Superhydrophobic Surfaces", Physical Review Letters, 103, 18, 184501, (2009).

[3] N. Miljkovic, D. J. Preston, R. Enright, E. N. Wang, "Electrostatic charging of jumping droplets", Nature Communications, 4, 2517, (2013).

[4] N. Miljkovic, D. J. Preston, R. Enright, E. N. Wang, "Electric-Field-Enhanced Condensation on Superhydrophobic Nanostructured Surfaces", ACS Nano, 7, 12, p. 11043–11054, (2013).

CONTACT

*E.N. Wang, tel: +1-617-324-3311; enwang@mit.edu

CHARACTERIZATION OF THE ROTATIONAL DYNAMICS OF MAGNETIC MICRODISCS IN SUSPENSION

N. Garraud[*] *and D.P. Arnold*
Interdisciplinary Microsystems Group, University of Florida, Gainesville, Florida, USA

ABSTRACT

We present the fabrication and dynamic characterization of magnetic microdiscs suspended in liquid. The free-floating discs function like synchronized micro-shutters when actuated by an external magnetic field. Their motion is monitored via light transmission in response to a rotating magnetic field. We demonstrate that their dynamic rotation depends on the amplitude and the rotation frequency of the applied magnetic field. Consequently, the discs can function as local microsensors of their environment to optically study fluid viscosity change or particles/biological environment interactions.

INTRODUCTION

As depicted in Fig. 1, low-aspect-ratio (~micron in diameter, tens of nanometer thick) soft ferromagnetic discs exhibit a unique magnetic ground state, known as a "spin vortex" [1]. A key advantage of this closed magnetic spin arrangement is that the discs exhibit near-zero magnetic remanence and hence do not agglomerate with each other when in free suspension. With particle volumes 10,000× larger than superparamagnetic nanoparticles and the ability to impart large torques, these microdiscs are of extreme interest for tagging, trapping, actuating, or interrogating biological samples [2][3]. However, their dynamic response in a fluidic/biological environment is largely unknown, hence motivating this work.

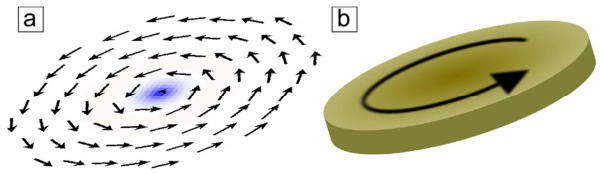

Figure 1: Magnetic spin vortex discs present no net remanence because of their closed magnetization configuration. (a) Magnetization ground state simulated by finite difference with OOMMF [4] (each arrow represents a magnetic moment). (b) Representation of the internal closed magnetization.

When subjected to an external magnetic field $\overrightarrow{B_{ext}}$, a magnetic structure will tend to rotate to align its easy-axis with the field. For soft magnetic discs with a small thickness t compared to their diameter $\emptyset$, the easy-axis is in-plane. Hence, an ensemble of discs in suspension will operate synchronously and can function as an optical light shutter. In a quasi-static mode, when the magnetic field is aligned with the light path, the transmitted light is maximal (Fig. 2a). However, when the magnetic field is transverse, the discs act as a shutter and lower the transmitted light intensity (Fig. 2b).

This general optical shutter behavior has been previously demonstrated by Vitol, et al. [5]. They explored two different ways to enact rotation of the discs in suspension: a single-axis and a 2-axis coil system supplied with square wave currents. The 2-axis system was shown to better control the discs orientation over a larger frequency range. In this article we use a similar 2-axis coil setup, but excited by sinusoidal current waveforms rather than square waves. The resulting B-field is a well-controlled rotating field, with constant amplitude and rotational velocity.

This approach gives us the opportunity to monitor both the light modulation amplitude and its phase shift. Unlike the amplitude, the phase is independent of the overall light intensity and the disc density/concentration. This overcomes many practical experimental challenges in quantifying the dynamics of the discs. As will be shown, at steady state, and for a given magnetic field amplitude, the phase shift can be derived from the balance between the magnetic torque and the hydrodynamic torque (Fig. 3a), each of which depends on the disc and fluid parameters, like the disc dimensions and the fluid viscosity. Hence monitoring of the phase shift can provide a valuable method for interrogation of one or more of these properties.

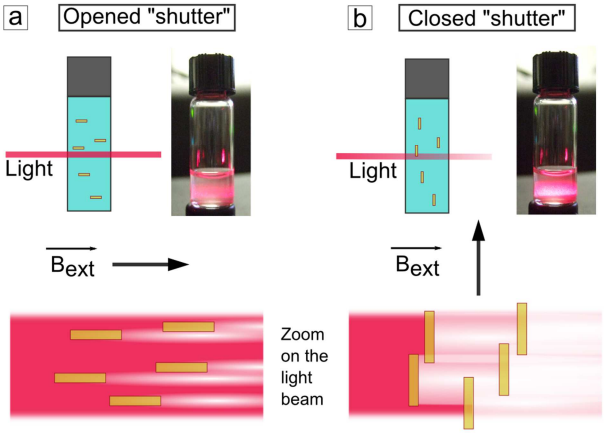

Figure 2: Light transmission modulation principle: the free-floating magnetic microdiscs in suspension rotate together and act as a shutter. The transmitted light is (a) maximal when the B-field is aligned to the beam axis and (b) minimal when the B-field is perpendicular to the beam axis.

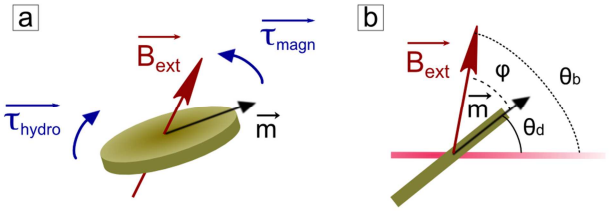

Figure 3: (a) The microdisc in a magnetic field, subjected to the magnetic torque and the hydrodynamic torque. (b) Definition of parameters used in the dynamic model.

THEORY ON THE DISC MAGNETIC ACTUATION

The external magnetic field $\overrightarrow{B_{ext}}$ modulated at $\omega = 2\pi f$ makes an angle $\theta_b = \omega t$ with the light path, whereas a disc makes an angle θ_d with respect to the light path (Fig. 3b). The angle difference between the disc plane and the magnetic field is the phase shift φ. Due to their small size dispersion, all the discs are assumed to have the same magnetic and mechanical behavior. Therefore, the recorded light intensity I_{meas} depends on $\theta_d = \omega t - \varphi$:

$$I_{meas} = I_0 - I_{block} = I_0(1 - \Delta I) = I_0(1 - \delta|\sin\theta_d|) \qquad (1)$$

I_0 is the measured light without any discs in the solution, which

9781940470016/HH2014/$25©2014TRF
DOI 10.31438/trf.hh2014.81

depends on the optical system. ΔI is the percentage of light blocked by the discs in suspension and depends on the projection of the disc area in a plane perpendicular to the light path, the disc density in the solution, and the length of the light path. For one mechanical revolution of the discs, there are two variations in intensity (mathematically represented by the rectified sine term), and hence the light is modulated at a double frequency $2f$.

The results are analyzed by studying the in-phase $\Delta I'$ and the out-of-phase $\Delta I''$ components of the signal variation ΔI, defined by:

$$\begin{cases} \Delta I' = \delta \cos\varphi \\ \Delta I'' = \delta \sin\varphi \end{cases} \quad (2)$$

Phase shift dependency

By neglecting the angular inertia torque (which is assumed to be small), the equation of motion of a magnetic disc in a uniform magnetic field is given by the equilibrium of the magnetic and the hydrodynamic torques:

$$\overrightarrow{\tau_{magn}} + \overrightarrow{\tau_{hydro}} = \vec{0} \quad (3)$$

The magnetic field is chosen low enough to operate in the linear domain described by the initial susceptibility χ_0. Moreover, as shown in [6], the magnetic moment $\vec{m}$ of a flat vortex disc remains mainly in-plane, due to its high shape anisotropy, even when $\overrightarrow{B_{ext}}$ presents an out-of-plane component.

The magnetic moment is given by

$$|\vec{m}| = Vol\ \chi_0 \left|\overrightarrow{H_{ext}}\right|_{in-plane} = \frac{\pi \emptyset^2 t}{4\mu_0} \chi_0 \left|\overrightarrow{B_{ext}}\right| \cos\varphi \quad (4)$$

The magnetic torque is thus calculated as

$$\overrightarrow{\tau_{magn}} = \vec{m} \times \overrightarrow{B_{ext}} = \pi\, t\, \emptyset^2\, \chi_0\, |\overrightarrow{B_{ext}}|^2 sin(2\varphi)/8\mu_0 \quad (5)$$

Due to its dependency on 2φ, the torque is null when the B-field is in-plane and out-of-plane with respect to the disc ($\varphi = 0$ or $\varphi = \pi/2$), and reaches a maximum for $\varphi = \pi/4$.

The hydrodynamic torque is given by:

$$\left|\overrightarrow{\tau_{hydro}}\right| = -\eta\, K_r \dot{\theta_d} \quad (6)$$

with η the fluid viscosity and K_r the rotational resistance depending on the disc dimensions and aspect ratio [7].

By solving (3), the rotational dynamics of the discs in suspension are governed by a critical frequency limit

$$\omega_{lim} = \left|\overrightarrow{B_{ext}}\right|^2 \frac{\pi\, \emptyset^2\, t\, \chi_0}{8\, \mu_0\, \eta\, K_r} \quad (7)$$

This limit defines two distinct frequency ranges:

i. $\omega < \omega_{lim}$: The discs rotate synchronously with $\overrightarrow{B_{ext}}$. A stable steady-state solution is found for $0 < \varphi < \pi/4$:

$$\varphi = \frac{1}{2} arcsin\left(\frac{\omega}{\omega_{lim}}\right) \quad (8)$$

ii. $\omega > \omega_{lim}$: The discs rotate asynchronously with $\overrightarrow{B_{ext}}$ and $\pi/4 < \varphi < \pi/2$.

It is noted from (8) that the phase shift depends mainly on the magnetic field parameters (ω and $|\overrightarrow{B_{ext}}|$) and the magnetic suspension characteristics (the fluid viscosity and the disc sizes and magnetic properties), which can be identified. It is also noted from (7) that the amplitude of the magnetic field can be adjusted to change ω_{lim}.

Later experimental studies focus on the influence of the magnetic field frequency and magnitude on the phase shift and the light amplitude change.

EXPERIMENTAL SETUP

Microdisc fabrication and characterization

The microdiscs are microfabricated on a silicon substrate using a metal lift-off procedure (Fig. 4). Three layers are spin coated: a 200-nm thick PMMA sacrificial layer (A4 MicroChem), a 300-nm thick LOR 3A lift-off layer (MicroChem), and an 800-nm thick S1813 photosensitive layer (Shipley, Microposit). The resist layers are patterned with a dense array of dots by direct-write UV laser at 405 nm (DWL 66fs Heidelberg) and developed to obtain the photoresist mask. A 70-nm-thick permalloy ($Ni_{80}Fe_{20}$) layer is then deposited through the mask by magnetron sputtering followed by metal lift-off in AZ400K (AZ Electronic Materials).

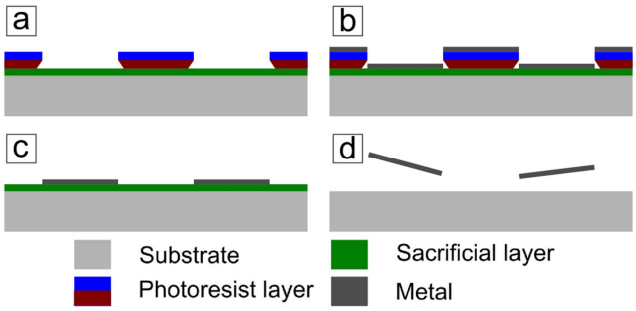

Figure 4: Microfabrication process: (a) Photoresist mask fabrication on a sacrificial layer. (b) 70-nm thick permalloy ($Ni_{80}Fe_{20}$) sputtering. (c) Metal lift-off. (d) Discs releasing in water.

A dense array of 2.5-µm-diameter, 70-nm-thick magnetic microdiscs is obtained on the sacrificial layer (Fig. 5a). Figure 6 shows the dramatic change of the magnetic behavior between a separately fabricated blanket permalloy layer (in blue) and the patterned array of microdiscs (in orange): the relative remanence drops from 20 % to 0 %. By dissolving the sacrificial PMMA layer in acetone and by rinsing it in deionized water, 30 million discs are released into 1 mL of water (Fig. 5b).

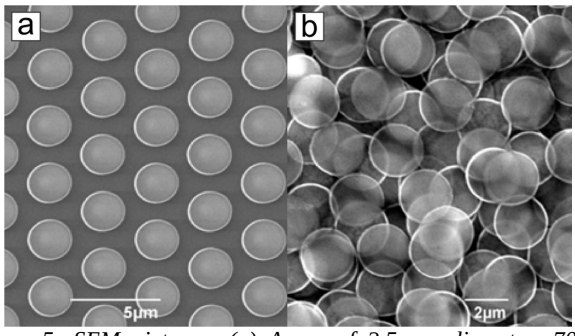

Figure 5: SEM pictures: (a) Array of 2.5-µm diameter, 70-nm thick magnetic microdiscs on the sacrificial layer. (b) Released discs on a substrate after the sacrificial layer dissolution.

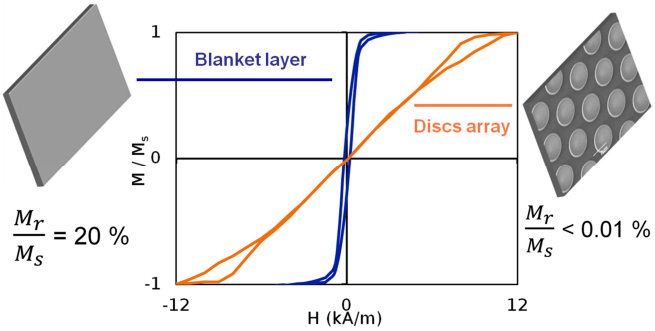

Figure 6: Magnetic characterization: in blue, the hysteresis loop of a 70-nm thick permalloy blanket layer; in orange, the behavior of spin vortex discs, showing no remanence.

Optical interrogation stage

Inspired by [5], the experimental stage combines magnetic actuation with optical detection via a laser and photodiode (Fig. 7). A rotating magnetic field is created by a Helmholtz coil pair and an orthogonally oriented solenoidal coil, on top of which sits a glass vial with the disc suspension (Fig. 8). The Helmholtz pair and solenoid are supplied by two sinusoidal current waveforms in quadrature (frequency *f*), where the amplitude of each waveform is adjusted so as to supply equal field intensity on the sample. The volume of the disc suspension interacting with the light beam ($2\times5\times10$ mm^3) is small enough that the discs are subjected to a spatially uniform rotating magnetic field up to 4 mT. Together the discs, rotating coherently, act as an optical shutter modulating the transmission path of a 650-nm, 5-mW laser. The transmitted light is measured by a photodiode, and the output signal is characterized by the DC component I_0, the relative AC amplitude ΔI and the phase shift φ, measured on an oscilloscope.

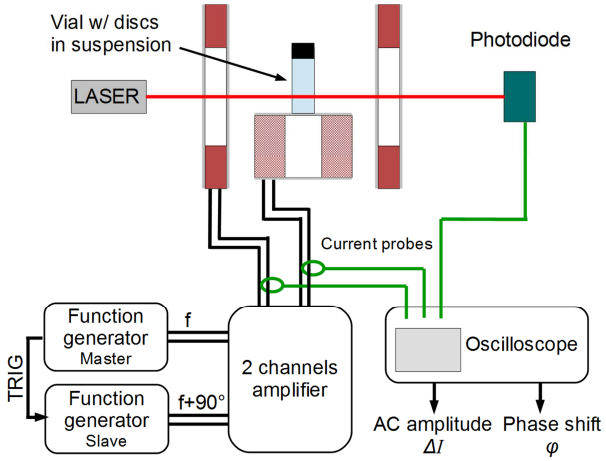

Figure 7: The experimental setup combines two orthogonal coils, a laser, and a photodiode. The coils are supplied with two sinusoidal current waveforms in quadrature, and all signals are monitored by an oscilloscope.

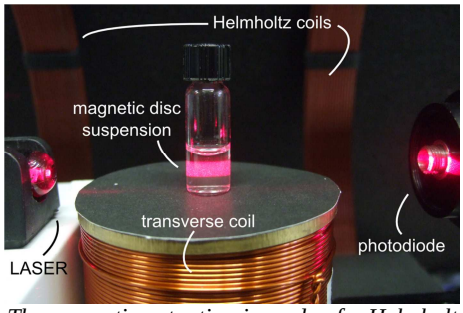

Figure 8: The magnetic actuation is made of a Helmholtz coil pair (parallel to the light path) and a transverse coil, which working together create a homogeneous rotating field in the vial space.

Figure 9 shows an example time-waveform of the light intensity modulation for $f = 10\ Hz$ in water. While varying the frequency, the electrical impedances of the coils are changing. As a consequence, the amplitudes of the two current waveforms in quadrature (Fig. 9a) are always controlled by changing the input currents, so the amplitude of the magnetic field is constant (Fig. 9b). The measured light is, as expected, a rectified sine modulated at $2f = 20\ Hz$ and phase-shifted by φ (Fig. 9c).

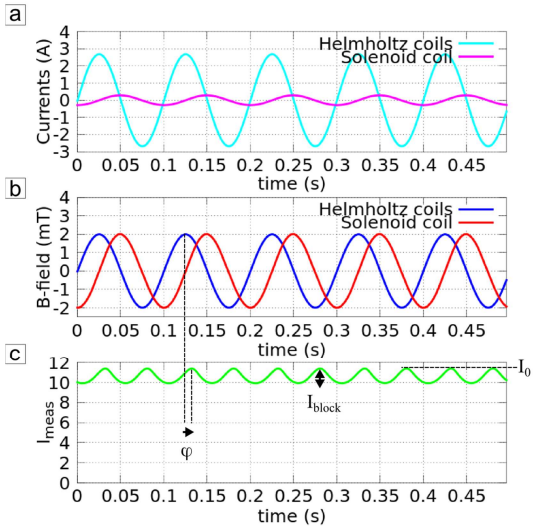

Figure 9: Example experimental results: (a) Recorded coil currents in quadrature at f = 10 Hz. (b) Resulting rotating magnetic field. (c) Light intensity modulation at $2f$ = 20 Hz.

Before dynamic experiments, the disc solution is sonicated for 5 min to disperse the discs into suspension. To investigate the overall stability of the experimental approach and the longevity of the discs in suspension, the light modulation parameters are measured for one hour (Fig. 10). Without any surfactant, the discs remain well suspended for at least one hour, allowing plenty of time for dynamic experiments.

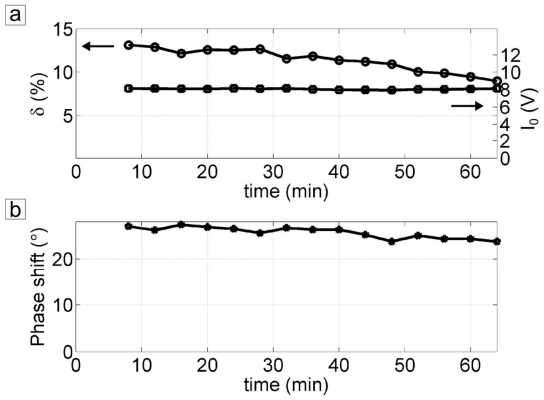

Figure 10: Suspension stability studied for 1 hour at f = 10 Hz under 1 mT. (a) Light modulation amplitude vs. time. (b) Phase shift vs. time.

RESULTS

Effect of the modulation frequency

Figure 11 shows the typical overall frequency response of the discs in suspension in water subjected to a 1 mT rotating magnetic field. The amplitude and phase of ΔI are presented in Fig. 11a. The real $\Delta I'$ and imaginary $\Delta I''$ components are reported in Fig. 11b. Three frequency ranges are observed in Fig. 11 a. Below 10 Hz, the phase shift is smaller than $\pi/4$, and the relative variation of the light intensity decreases rapidly. At medium frequencies, between 10 Hz and 30 Hz, the disc rotation is still synchronous with the external magnetic field. In this range, the intensity modulation amplitude ΔI is constant, and the phase continues to increase. Above the critical frequency $f_{lim} = 40\ Hz$,

the viscous effects from the hydrodynamic torque lead to a decrease in amplitude and an increase in phase shift above $\varphi_{lim} = \pi/4$. Fig. 11b shows another key feature—a maximum in the imaginary part at $f_0 = 30\ Hz$. This peak position, depending on the disc interactions with their environment, is a relevant parameter to extract to follow any change in the disc suspension (such as the viscosity).

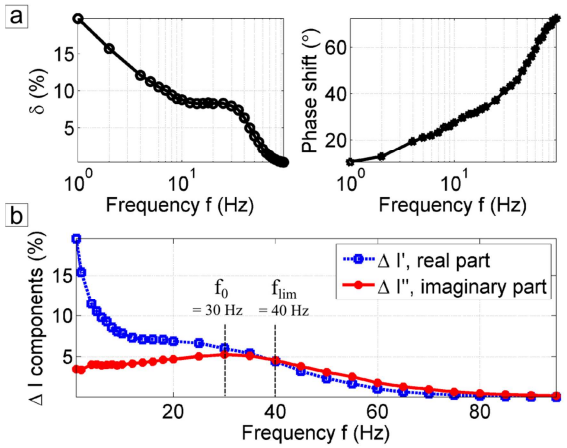

Figure 11: Frequency dependence of discs in suspension in water. (a) AC light amplitude and phase shift vs. magnetic field frequency. (b) Real and imaginary components projection. The imaginary peak is related to the discs environment properties.

The simple model developed in the theoretical section explains the observed behaviors as the synchronous (10 Hz – 40 Hz) and the asynchronous modes (>40 Hz) delimited by ω_{lim}. However, further investigations are needed to model the disc suspension behavior at lower frequencies (<10 Hz in this case).

Effect of the magnetic field magnitude

Figure 12 shows the dynamics response by changing the magnetic field magnitude over a range from 0.5 to 4 mT at several different fixed frequencies.

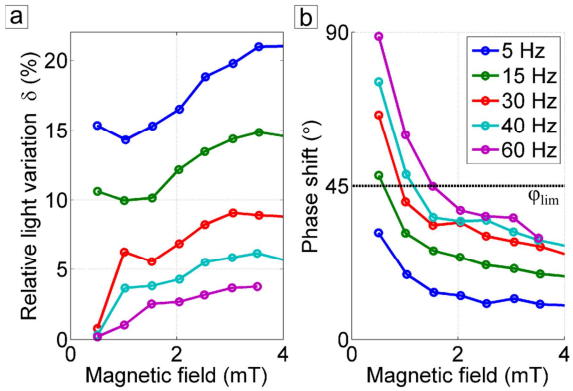

Figure 12: Magnetic field magnitude dependence of discs in suspension in water at several frequencies. (a) AC light amplitude and (b) phase shift vs. magnetic field magnitude.

The largest changes in δ and φ occur for frequencies around f_0 and f_{lim}. At low frequencies (such as 5 Hz), δ and φ changes are smaller than for higher frequencies, since the phase shift never reaches the critical phase of $\pi/4$. Therefore, changes in the rotational dynamics of the suspension due to the change of one environmental parameter can be studied by monitoring δ and φ while doing an amplitude magnetic field sweep at frequencies around f_{lim}. Also, experimentally, changing the field amplitude presents the advantage to be much faster and easier than sweeping the frequency.

CONCLUSION

We present an optical interrogation methodology for studying the rotational dynamics of suspended magnetic microdiscs in response to a constant-amplitude rotating magnetic field. The system enables measurement of the phase shift as a function of the frequency and amplitude of the magnetic field. The phase shift measurement is particularly interesting because it is independent of experimental variables such as the disc density in solution and uncontrolled variations in intensity. The system functionality is demonstrated using 2.5-µm-diameter permalloy microdiscs. The dynamics of the discs above 10 Hz are explained by a simple model. However further modelling is needed to understand the dynamic behavior at lower frequencies.

In future work, measurements obtained with this setup will be coupled with parameter identification procedures and dynamic computational simulations (as done on magnetic ellipsoids [7]) to explore more complex models. Potential future applications include optical determination of viscosity or detection of specific molecule adsorption on the discs, which may alter the hydrodynamic diameter and hence dynamic properties.

ACKNOWLEDGEMENT

This work was supported in part by the UF Office of Sponsored Research. The authors acknowledge Dr. Carlos Rinaldi for his valuable technical discussion on the rotational dynamics of magnetic particles in suspension.

REFERENCES

[1] R.P. Cowburn, D.K. Koltsov, A.O. Adeyeye, M.E. Welland, and D.M. Tricker, "Single-domain circular nanomagnets", Physical Review Letters, **83**, 1042 (1999).

[2] D-H. Kim, E.A. Rozhkova, I.V. Ulasov, S.D. Bader, T. Rajh, M.S. Lesniak, and V. Novosad, "Biofunctionalized magnetic-vortex microdiscs for targeted cancer-cell destruction", Nat. Mater., **9**, 165 (2010).

[3] S. Leulmi, H. Joisten, T. Dietsch, C. Iss, M. Morcrette, S. Auffret, P. Sabon, and B. Dieny, "Comparison of dispersion and actuation properties of vortex and synthetic antiferromagnetic particles for biotechnological applications", Appl. Physics Letters, **103**, 132412 (2013).

[4] M.J. Donahue, and D.G. Porter, "OOMMF User's Guide, Version 1.0", Interagency Report NISTIR 6376, National Institute of Standards and Technology (1999).

[5] E.A. Vitol, V.G. Yefremenko, S. Jain, J. Pearson, E.A. Rozhkova, S.D. Bader, and V. Novosad, "Optical transmission modulation by disk-shaped ferromagnetic particles", J. of Applied Physics, **111**, 07A945-1 (2012).

[6] N. Garraud, and D.P. Arnold, "Experimental investigation of magnetic anisotropy in spin vortex discs", J. Applied Physics, **115**, 17D128 (2014).

[7] J.H. Sánchez, and C. Rinaldi, "Rotational Brownian dynamics simulations of non-interacting magnetized ellipsoidal particles in d.c. and a.c. magnetic fields", J. of Magnetism and Magnetic Material, **321**, 2985 (2009).

CONTACT

*N. Garraud, tel: +1-352-328-8556; ngarraud@ufl.edu

DIELECTRIC-TO-DIELECTRIC CHARGING CHARACTERISTIC IN MEMS SWITCHES WITH CONTINUOUS AND DISCONTINUOUS CONTACT

D. Molinero[1], S. Cunningham[1], D. DeReus[1] and A. Morris[2]*
[1]Wispry, Inc, Irvine, California, USA

ABSTRACT

A dielectric charging characterization is presented based on simple MEMS structures with continuous and discontinuous insulator-insulator contact. The amount of surface charging generated by triboelectric effects when both insulators are in contactis strongly dependent of the area of contact and electric field. Electrostatic simulation and hold-down measurements were done to characterize the surface charging on continuous and discontinuous teststructures that minimizes the contact area and electric field. The results have shown a considerable decrease of surface charge generation on discontinuous contact.

INTRODUCTION

The increase of mobile communication has driven the already busy and complex radio signal spectrum to a new level. The massive transfer of voice and data makes almost mandatory the use of tunable filters to maintain optimal signal strength values[1]. As the complexity and saturated spectrum increase, the demand of new tunable designs with extremely linear characteristic is needed. It is in this particular case where RF Micro-ElectroMechanical Systems (RF MEMS) can provide the necessary performance compared to conventional semiconductor devices. The high RF MEMS performance in linearity and quality factor are well-known [2]. Recently, integration of reliable RF MEMS with CMOS has propelled the devices into high volume mobile handsets [3]. The most significant characteristics of Wispry's RF MEMS-CMOS integrated tunable capacitor are its high linearity (IIP3 > 80dBm), high quality factor (>100 at 1 GHz), and long lifetime (2.5B cycles at 65 ºC), enabling use in a wide range of mobile handset applications [4]. Data communication increases over a wide range of bands in the radio spectrum are leading to increasing number of tuning events over the life of the handsets, which will require extended and improved tunable lifetime.

One of the main reliability issues of RF MEMS switches is dielectric charging [5]. The high electrostatic field needed to close the switch generates charge inside the dielectric layers causing undesired drift of the switch characteristic, hence deteriorating the tuning performance and leading, on the extreme case, to an irrecoverable stiction. The origin of dielectric charging varies depending on the location, type of contact and mechanism involved. Charging can occur in the dielectric bulk through injection from the electrodes into the dielectric with relatively quick charge/discharge dynamics. In the other hand, surface charging depends on the type of contact used. Metal–dielectric contact produces surface charge by injection when the switch is actuated while triboelectric effects will be the main mechanism when two dielectrics are in contact, where charge exchange can occur between dielectrics without injection from the metal due to both dielectric thicknesses [6]. In both cases, charging is a fast mechanism when the switch is actuated under high voltage, but discharge is comparatively slow when the voltage is removed. Once the surface charge is created and the contact is broken after removing the applied voltage, the only way for the charge to dissipate is through diffusion across the thickness of the dielectric, which is difficult because bulk diffusivity is low in high-quality dielectric. Therefore, surface charging is particularly detrimental because, once the charge is generated on the surface, it cannot be removed, and cumulative deterioration will take place.

Previous work has shown how bulk charging is minimal in our test structures; however, surface charging by triboelectric effects has an important role, being the key factor limiting the switch lifetime [6]. Although triboelectric effects have been studied for centuries, and while the physical mechanism involved on the charge exchange is not always, it is understood that ion or electron transfer at contact leads to charge generation in MEMS switches. Many parameters can contribute to surface dielectric charging, such as the dielectric materials used, the fabrication process and the ambient operating conditions [7], which can be difficult to control. Whether electrons or ions are present in the charge exchange, reducing the electric field and area of contact will mitigate the amount of charge accumulation. It is well-known that the triboelectric effect is strongly proportional to the area of contact, and the energy associated to transfer ions or electrons to the electric field [7]. Therefore, by reducing both parameters will assure a reduction of the rate of charging and the total amount of charge generated, with the consequential lifetime increase.

In this paper, we show how to reduce the amount of charging by the inclusion of spatially distributed bumpers associated with a patterned metal that reduces the electric field in the area of contact. Representative simulations and measurements are provided for comparison over a range of voltages and temperatures for various designs.

SIMULATIONS

The inclusion of insulating bumpers reduces the contact area and minimizes the surface charge generation. However, the benefit of such bumpers alone may not be sufficient for newer reliability requirements, particularly at high temperature. In this particular analysis, electrostatic simulations were performed to study the impact of a patterned top metal hole over the bumper area to reduce the electrostatic field.

Simulations were done with Matlab © PDE toolbox [8], where a single bumper was characterized. The lateral dimensions were chosen as the same as the bumper pitch to enable use of periodic boundary conditions. Fig. 1(a) shows the simulated cross-section used to simulate the electrostatic field. A permanent gap of 4 nm was intentionally left between the bumper zone and the lower dielectric to emulate the effect of surface roughness when in contact. It is theorized that the electric field in this residual gap is the key driver for the charge transfer. Fig. 1(b) and 1(c) show the solution on a particular case of a 1400 nm patterned metal hole. It can be seen that the maximum electric field both under the bumper and in the parallel plate area away from the bumper have values around 3 MV/cm. However, surface charge is only generated under the bumper where intimate contact occurs.

Fig. 2(a) shows the surface electrostatic field near the bumper for different hole dimensions, where the inclusion of a bumper with no metal pattern reduces the electrostatic field from 10.5 to 8

9781940470016/HH2014/$25©2014TRF
DOI 10.31438/trf.hh2014.82

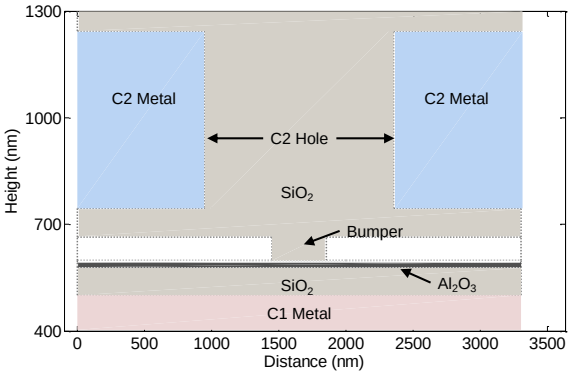

(a)

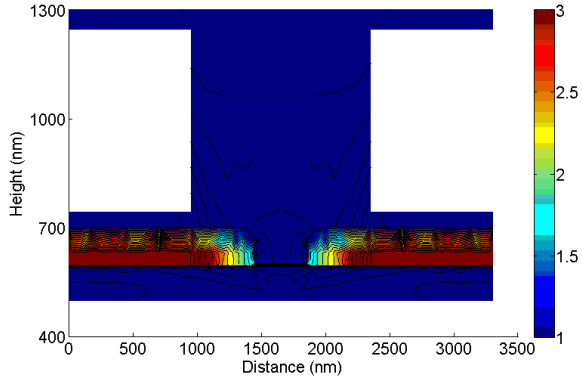

(b)

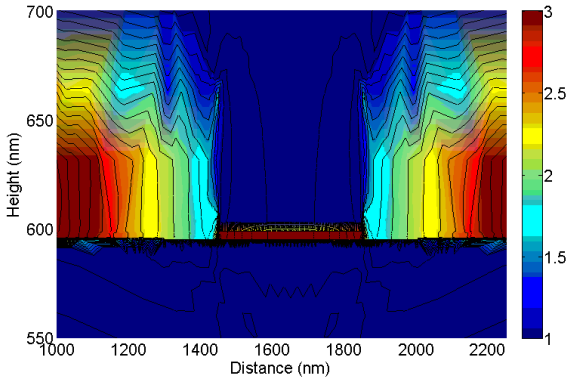

(c)

Figure 1: (a) Cross-section of the simulated test structure defined in the Matlab© PDE Toolbox and (b) the electrostatic result for a given bumper/C2 Hole parameter. (c) Close up view of the electrostatic field surrounding the bumper zone.

MV/cm. As the metal hole diameter increases, the electrostatic field is reduced. Fig. 2(b) shows the electrostatic variation as function of the metal hole diameter under different voltages. Simulations have shown two clear sections depending on the metal hole dimensions: a fast transition from high to low field when the hole and the bumper dimensions are comparable, and a semi steady state condition when the lateral dimensions of the hole are larger than the bump. Based on these simulation results, the optimal metal pattern diameter should be at least 3x times larger than the bumper dimension. Even larger dimensions will not provide significant change when balanced against the increase in actuation voltages when the hole area becomes comparable to the initial gap

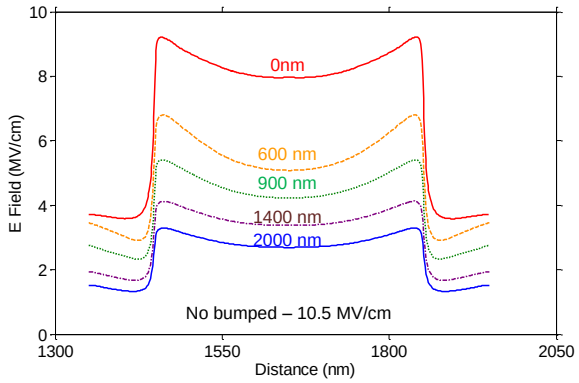

(a)

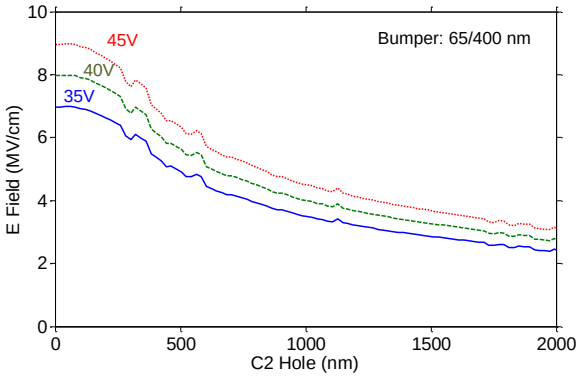

(b)

Figure 2: (a) Surface Electrostatic field under the bumper are for different top metal hole diameter, and (b) its center value as function of different top metal hole diameter and voltage.

(2 µm) [9]. For the experimental study, a 1400 nm metal diameter was chosen.

FABRICATION AND EXPERIMENTAL

Two test structures were designed to intentionally monitor dielectric charging while being fabricated alongside MEMS capacitive switch array products on the same hermetically sealed wafer using a 0.18-µm, 5 V CMOS/50 V LDMOS process [10]. Electrostatic cantilever-type MEMS capacitors were used for the test structures, which were formed with the final three AlCu metal levels in chemical vapor deposited SiO_2 dielectric to form a metal-oxide-metal composite structure. The MEMS cavities were formed using a planar sacrificial silicon process that is processed at less than 400 ºC. The cantilever consists of a SiO_2 sandwiched by thin AlCu above and below. The capacitor electrodes are formed between the lower AlCu of the cantilever and the AlCu at the bottom of the lower cavity, where the lower metal is covered by thin layers of SiO_2 and Al_2O_3 and the upper metal is covered only by SiO_2(Fig. 3(a)). Bumpers are made of the same SiO_2 that is under the dielectric top electrode. In this particular case, bumpers were 65 nm tall, 400 nm wide and spaced by 3300 nm from each other.

Both test structures have active area of approximately 40x40 μm^2 with similar pull-in and release voltages of approximately 20V and 10V, respectively. The capacitance ratio is drastically reduced on the discontinuous test structure due to the bumpers. Fig. 3(b) shows the capacitance – voltage (C-V) of both structures.

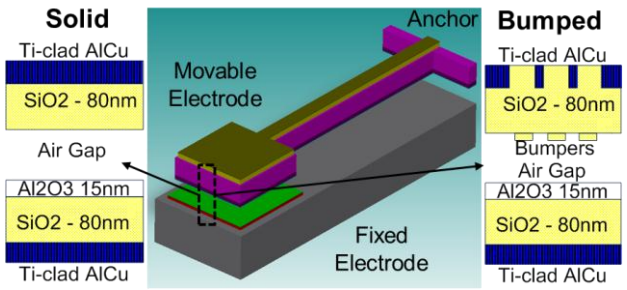

(a)

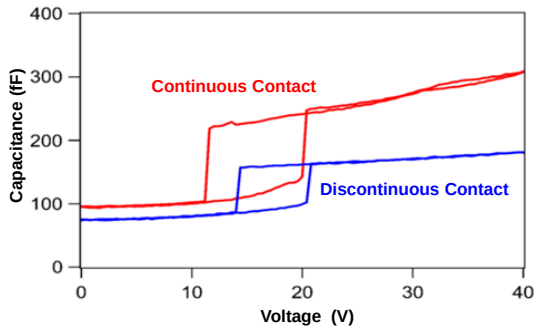

(b)

Figure 3: (a) Schematic cross-section of Wispry's dielectric charging continuous and discontinuous test structure. The cantilever consists of SiO_2 sandwiched by thin AlCu above and below. The capacitor electrodes are formed between the lower AlCu of the cantilever and the AlCu at the bottom of the lower cavity, both of which are coated with thin layers of SiO_2 and Al_2O_3. (b) Capacitance-Voltage (C-V) sweeps of both test structures.

The characterization was performed on wafer with an Agilent E4980A LCR meter that was used to monitor the capacitance values at the specific voltage provided by the Keithley 2400 source. An appropriate bias tee was used to isolate the DC signal from the LCR meter. The measured capacitance was calibrated at the probe tips. The setup and measurement extraction were controlled by an external PC and Labview program. The charging characterization consisted of applying a constant DC hold-down voltage for 100 min. A triangular sweep was used on logarithmic intervals during the hold-down stress to measure the C-V characteristics and extract the pull-in and release voltages.

RESULTS

Fig. 4 shows the measurements results of both test structures topologies under different hold-down voltages and temperature. The actuation voltage shifts in both devices increase at any hold-down voltage and remains unaltered once the applied voltage is removed, providing a clear indication of surface charging and minimal or non-existent bulk charging. The transient characteristic shows a clear impact of the discontinuous contact versus the continuous contact test structure, where the amount of surface charge generated has decreased notably. Both test structures show a different transient performance, while the continuous contact has a fast early build up followed by a more gentle charging behavior, the discontinuous contact shows a more linear increase of the surface charge. The actuation voltage shift transients also present a different behavior at elevated temperatures. The continuous contact presents less variation of the actuation voltage shift as the temperature increase, but a faster transition. On the other hand, the discontinuous contact shows a slight increase in both the final state and transition. This behavior can be attributed to two situations:

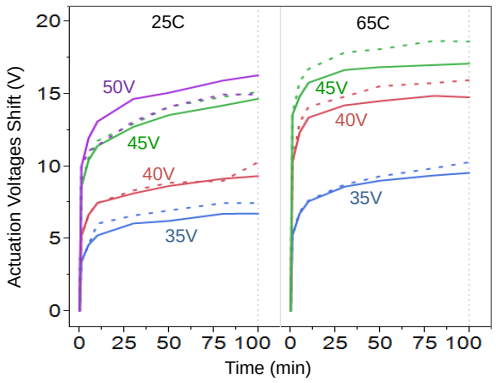

(a)

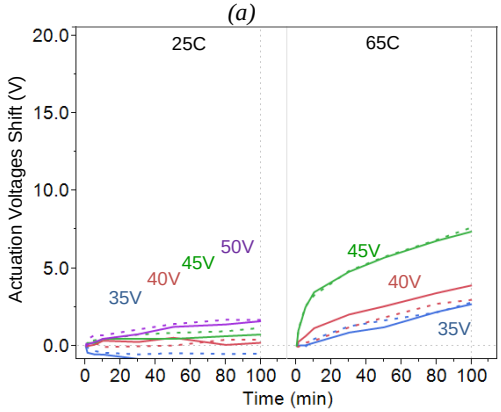

(b)

Figure 4: Pull-in an (solid) and release (dash) voltage shift for continuous (a) and discontinuous (b) contact at different voltages and temperatures. Bumpers and top metal holes reduced the surface charging considerably and hence improved switch lifetime.

first, the reduced electric field and contact delays the charging characteristic seen in the continuous devices, and second, the resulting charge distribution will modify in a different manner the actuation voltage shift [911].

The final actuation voltage shift presents a better evaluation of the improvement due to the bumped contact and patterned top metal. Fig. 5 shows the actuation voltage shift results at 100 min under a wide range hold-down voltages and temperature. The results show a clear reduction of the amount of surface charging between the two test structures. A linear characteristic is extracted with different slopes over voltage, enhanced by elevated temperature. It should be pointed out that the results of the continuous contact are similar in any given point of the hold-down stress but with less voltage shift, indicating a unique mechanism behind the surface charge generation. In the discontinuous contact, the same approach can be taken but for longer times. At short times, the slope at room temperature is difficult to acquire, however, at elevated temperature shows a decrease of the voltage dependence. The measured data is not enough to indicate that two different mechanisms are involved on the surface charge generation, and we attribute this effect to the charge distribution being created from the bumper inclusion. This explanation can also be attributed to the differences in the linear response over voltage of the actuation voltages shift. The charge generation mechanism in both devices are the same and attributed to triboelectric effects, moreover, both test structure were fabricated on the same wafer, and hence having similar fabrication process and impurities associated with it. The charge generation mechanisms are the same but have reduced impact in the discontinuous contact due to the

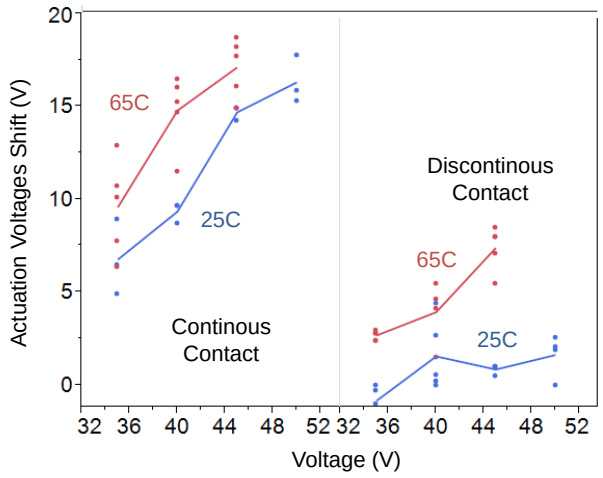

Figure 5: Actuation voltage shift after 100 min hold down test for continuous and discontinuous contact. Both results show a linear characteristic with significantly lower value and slope for the discontinuous contact.

inclusion of bumpers and the reduced electrostatic field. Note that the resulting charge generation also has a lateral distribution corresponding to the bumper pattern, which leads to non-uniform charge and charge evolution across the surface which affects the actuation voltage shift characteristic [911].

Based on the test structure design and considering a homogenous surface charge, the maximum charge density can be calculated as follow

$$q\ (\mathrm{C/m^2}) = \Delta V_{P,R} \cdot \epsilon_0 / \left(\frac{t_S}{\epsilon_S} + \frac{t_A}{\epsilon_A}\right) \quad (1)$$

Where ε_0 is the air relative permittivity, ε_S and ε_A are the silicon oxide and alumina relative permittivity, t_S and t_A are the dielectric thickness. Considering a normal operation at 40V at elevated temperature, the total amount of charge density extracted after the 100 min hold down test for the continuous and discontinuous contact is about 6 and 1.6 mC/m^2 respectively. While the discontinuous contact and patterned metal reduce the charge significantly, work continues to reduce even more the amount of charge for future applications.

CONCLUSION

In conclusion, a full study based on simulations and experimental data is shown for capacitive MEMS test structures with continuous and discontinuous contact. It has been shown how the inclusion of bumpers considerably reduces the amount of charge created by triboelectric effects. However, bumpers alone are not sufficient to achieve certain reliability criteria. For this purpose, electrostatic simulations were performed to study the effects of a metal pattern on one of the electrodes to reduce the electrostatic field in the contact area. The results showed that the inclusion of a bumper only reduces the electrostatic field from 10 to 8 MV/cm, but adding a top metal pattern reduces this much further to around 4MV/cm. The results have shown a top metal pattern of about 3x larger than the bumper size is an effective compromise between charging reduction and actuation area. In this experiment, a 1400nm metal pattern was chosen, with minimal change on the actuation voltage as the value is smaller than the initial gap.

Experimental data comparing both test structures with continuous and discontinuous contacts were performed. The results show that the discontinuous contact decreases notably the amount of charge generated. A change in the transient characteristic is clearly appreciated, but mostly due to the reduction of the amount of charge and its distribution over the surface due to the bumpers contact. Both test structures follow a linear relationship with voltage; however, the slope is different due to the electrostatic field reduction from the top metal pattern. Overall, adding the metal pattern significantly improves the reliability capability of RF MEMS capacitors in terms of dielectric charging.

REFERENCES

[1] J.L. Hilbert, "RF-MEMS for Wireless Communications," Communications Magazine, IEEE, vol.46, no.8, pp.68-74, August 2008.

[2] G. M. Rebeiz, RF MEMS Theory Design Technology. Hoboken: Wiley, 2003.

[3] A. S. Morris, S. P. Natarajan, Q. Gu, and V. Steel, "Impedance tuners for handsets utilizing high-volume RF-MEMS," in Proc. European Microwave Conf., Oct.-Nov. 2012, pp. 193-196.

[4] www.wispry.com

[5] W. M. van Spengen, "Capacitive RF MEMS switch dielectric charging and reliability: a critical review with recommendations". J. Micromechanics & Microengineering, vol. 22, no. 7, pp. 1-23, June 2012.

[6] D. Molinero et al.,"Dielectric charging in MEMS with dielectric-dielectric contacts", Transducers & Eurosensors XXVII: The 17th Int. Conf. on Solid State Sensors, Actuators and Microsystems, pp.1400 -1403, 16-20 June 2013.

[7] D. J. Lacks and R. M. Sankaran, "Contact electrification of insulating materials", J. Phys. D: Appl. Phys. 44, 453001 (2011).

[8] http://www.mathworks.com/products/pde/

[9] G. M. Rebeiz, RF MEMS, Theory, Design. And Technology, John Wiley and Sons Publications, 2003.

[10] A.K. Stamper et al., "Planar MEMS RF capacitor integration" Transducers 2011, 16th International,pp.1803-1806, 5-9 June 2011.

[11] X. Rottenberg et al.,"Distributed dielectric charging and its impact on RF MEMS devices", in Proc. European Microwave Conf., Oct., 2004, pp. 77-80.

CONTACT

*D. Molinero, tel: +1-949-334-8825; david.molinero@wispry.com

MULTIFUNCTIONAL ATOMIC FORCE MICROSCOPE CANTILEVER WITH LORENTZ FORCE ACTUATION AND SELF-HEATING FOR NANOMECHANICAL MEASUREMENTS IN AIR AND WATER

S. Somnath[1], J. O. Liu[1], M. Bakir[1], C. B. Prater[2], and W. P. King[1]*
[1]University of Illinois, Urbana-Champaign, Illinois, USA
[2]Anasys Instruments, Santa Barbara, California, USA

ABSTRACT

This paper reports a multifunctional cantilever capable of self-heating and Lorentz force actuation for nanomechanical measurements over a large temperature range. The novel electrical design of the cantilever allows for high current to flow through the cantilever, resulting in high Lorentz force. The cantilever can self-heat beyond 800 °C, and the heating is mostly independent of actuation force. When operated at its resonance frequency of 102 kHz, the cantilever generates more than 5.3 µN of Lorentz force while self-heating only to 44 °C. This cantilever can generate about 7X larger Lorentz force than other heated cantilevers. The cantilever can be operated in air or water.

INTRODUCTION

The atomic force microscope (AFM) is a widely used tool for nanometer-scale measurements [1, 2]. Some characterization techniques oscillate the cantilever at resonance to acquire additional spectroscopic information and to maximize the signal-to-noise. Cantilevers with integrated heater-thermometers can measure the temperature-dependence of material properties, and are widely used for materials characterization, especially for pharmaceuticals and composites [3]. However, heated cantilevers have not been designed for nanomechanical measurements and are limited in their ability to control and measure tip-sample forces due to parasitic resonances in piezoelectric cantilever actuation [2, 4, 5].

Several strategies have been used to actuate AFM cantilevers, including photothermal excitation [6], integrated themomechanical elements [7], as well as piezoelectric [8] and electrostatic [9] actuation. However, these actuators are not suitable for actuating heated cantilevers due to the preexisting temperature distribution in the heated cantilever, and modifications necessary in the AFM hardware, and cantilever design. Electromagnetic actuation via Lorentz force [10] can actuate heated cantilevers with high signal-to-noise without any modifications to the cantilever design or AFM hardware [4]. Most heated cantilevers have been developed for thermal topography sensing or data storage applications and are typically operated in contact mode [11-13]. Furthermore, heated cantilevers developed for tapping-mode were too small to generate sufficient Lorentz force or for operation in many commercial AFMs [5]. Thus, there is a need and an opportunity to design heated cantilevers optimized for Lorentz force actuation.

This paper reports the development of a Lorentz-thermal cantilever for nanomechanical measurements. We show how the novel cantilever design significantly increases the Lorentz force and allows independent control of heating and actuation compared to the state-of-art.

CANTILEVER DESIGN

Figure 1 shows the principle of the multifunctional Lorentz-thermal cantilever. Alternating current passing through a U-shaped cantilever in the presence of a perpendicular magnetic field generates a Lorentz force at the cantilever free-end [4]. The magnitude of the Lorentz force is proportional to the strength of the magnetic field, the current, and the distance over which the current travels perpendicular to the magnetic field. Most of the heat generated in the cantilever heater flows into the substrate through the air, and this cantilever heat flow varies inversely with the distance between the cantilever and the substrate. The substrate topography is measured by tracking changes in the cantilever temperature [14]. Typically, heated cantilevers have a high resistance heater at the cantilever free-end [11]. The Lorentz-thermal cantilever has low resistance Lorentz path in parallel with the high resistance heater to minimize the cantilever resistance.

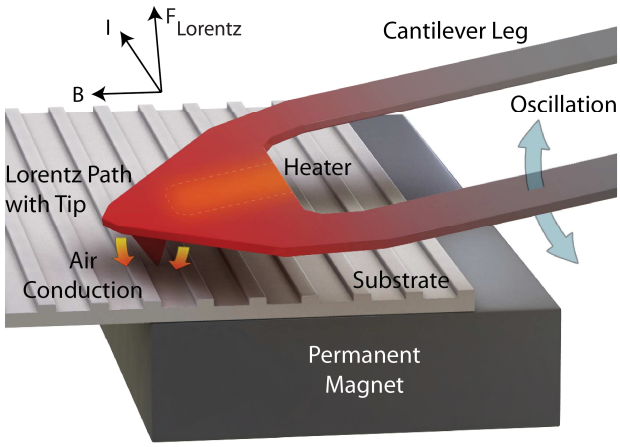

Figure 1: Working principles of Lorentz force cantilever actuation and thermal topography sensing. Alternating current flowing through the cantilever in the presence of a magnetic field generates a Lorentz force at the cantilever free-end that oscillates the cantilever. Heat flow from the cantilever varies with the cantilever-substrate distance. The substrate topography is measured by the cantilever temperature.

The Lorentz-thermal cantilever was designed to meet five main requirements. First, the cantilever must have a resonance frequency of at least 90 kHz for tapping mode operation. Second, the cantilever must be capable of generating at least 2 µN of Lorentz force. Third, it must be possible to operate the cantilever in a commercial AFM. Fourth, it must be possible to fabricate the cantilever using existing batch fabrication techniques [11]. Fifth, the cantilever should have thermal topography sensitivity that is comparable to that of the state-of-art Legacy cantilever (0.3 mV/nm at 300 °C) [15].

Figure 2 illustrates how the Lorentz-thermal cantilever was designed to meet the performance goals. We developed finite-element models using commercial software, COMSOL, to study how each design parameter affects the cantilever mechanical, electrical, and thermal characteristics. The cantilever length was shortened to achieve the desired resonance frequency, but this increased the cantilever stiffness. The cantilever stiffness was lowered by reducing the width of the cantilever legs, but a minimum leg width was maintained to ensure sufficient area for

9781940470016/HH2014/$25©2014TRF
DOI 10.31438/trf.hh2014.83

the AFM laser to reflect off the cantilever legs. Enlarging the distance between the cantilever legs increased the Lorentz force at the cost of the resonance frequency. We used a U-shaped cantilever geometry to localize the Lorentz force to the cantilever free-end. Since the cantilever was designed to have a 1 µm tall tip, the cantilever free-end was tapered to ensure that the substrate contacted the tip instead of the cantilever body. The cantilever current was limited by the resistance of the cantilever legs, whose geometry was constrained by the mechanical performance goals of the cantilever. The cantilever current was maximized by enlarging the width of the Lorentz-path and shrinking the heater size. In contrast, the thermal topography sensitivity is maximized by increasing the heater size, which increases the heater resistance. Finally, the cantilever design was altered to account for the error and resolution of our photolithography system.

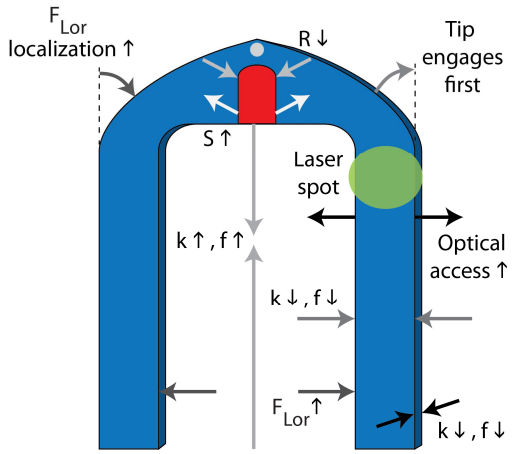

Figure 2: Illustration of how the cantilever geometry was varied to meet performance goals for the Lorentz-thermal cantilever. Our goal was to design a cantilever with resonance frequency (f) at least 90 kHz, stiffness (k) no more than 1.5 N/m, peak Lorentz force (F_{Lor}) at least 2 µN, electrical resistance (R) no more than 0.2 kΩ, and thermal topography sensitivity (S) of 0.3 mV/nm at 300 °C.

CANTILEVER CHARACTERIZATION

Figure 3 shows a schematic and a scanning electron microscope (SEM) image of the fabricated Lorentz-thermal cantilever. The cantilever legs are short for tapping mode operation and 50 µm apart to maximize Lorentz force. The cantilever has a 1 µm tall tip with 10 nm apex radius at the cantilever free-end. The cantilever has a stiffness of 1.7 N/m, resonance frequency of 102 kHz, and electrical resistance of 0.17 kΩ. The Lorentz-thermal cantilever was batch fabricated using the same procedure used for fabricating Legacy cantilevers. Table 1 compares the geometry and the characteristics of the Lorentz-thermal and Legacy cantilevers.

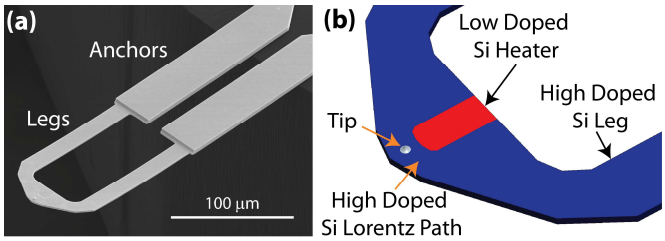

Figure 3: (a) Scanning Electron Microscope image and (b) schematic of the Lorentz-thermal cantilever. The cantilever free-end consists of two parallel current paths – a high resistance path through the heater and a low resistance Lorentz path around the heater.

Table 1: Comparison of cantilever geometry, characteristics and performance for Lorentz-thermal and Legacy cantilevers.

	Legacy	Lorentz
Geometry:		
Cantilever Length (µm)	167	130
Leg width (µm)	20	15
Thickness (µm)	1	1.5
Distance between legs (µm)	20	50
Heater area (µm^2)	137	102
Characteristics:		
Electrical resistance (kΩ)	2.2	0.17
Resonance Frequency (kHz)	64	108
Stiffness (N/m)	0.53	1.71
Mechanical performance:		
Peak amplitude (µm)	1.373	> 2.779
Peak force (µN)	0.725	> 5.309
Amplitude improvement over Legacy	1	> 2.03
Force improvement over Legacy	1	> 7.32
Mean temperature rise per force rise (°C/µN)	1429.8	5.64

Electrical and thermal characterization show that larger currents can flow through the Lorentz-thermal cantilever compared to the Legacy cantilever. The cantilevers were operated in series with a 1 kΩ current-limiting sense resistor. A Renishaw inVia Raman spectroscope measured the heater temperature as a function of DC heating voltage. Figure 4 shows the electrical and thermal properties of the two cantilevers. The cantilever current, resistance, and power vary non-linearly with the DC heating voltage in both cantilevers since the thermal conductivity and electrical resistivity of doped silicon vary with temperature [11]. Both cantilevers are capable of self-heating beyond 550 °C. The Lorentz-thermal cantilever has electrical resistance which is almost an order of magnitude smaller than that of the Legacy cantilever. Consequently, the Lorentz-thermal cantilever allows more than 10 mA to pass through the cantilever which is higher than that of the Legacy cantilever (1.2 mA). The experimentally measured values are close to those from the simulation and the error is attributed to variations in the cantilever geometry and material properties due to limitations in the fabrication process.

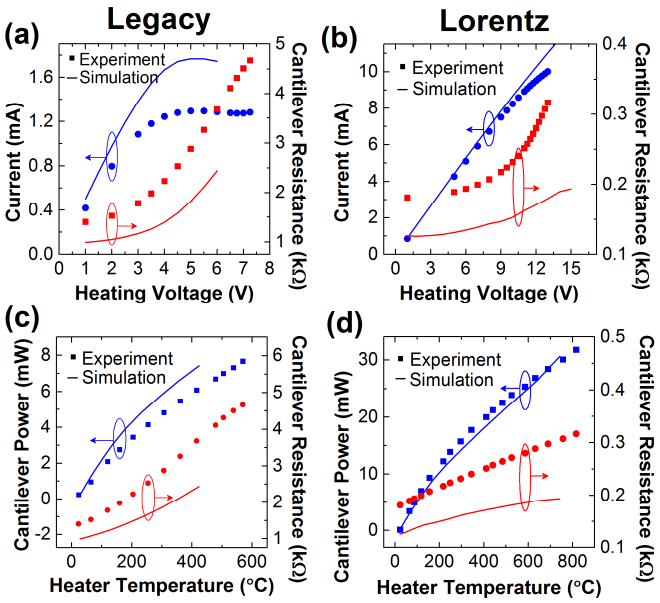

Figure 4: Electro-thermal characterization of Legacy and Lorentz-thermal cantilevers. (a-b) Cantilever current and resistance as functions of DC heating voltage. (c-d) Cantilever power and resistance as functions of heater temperature.

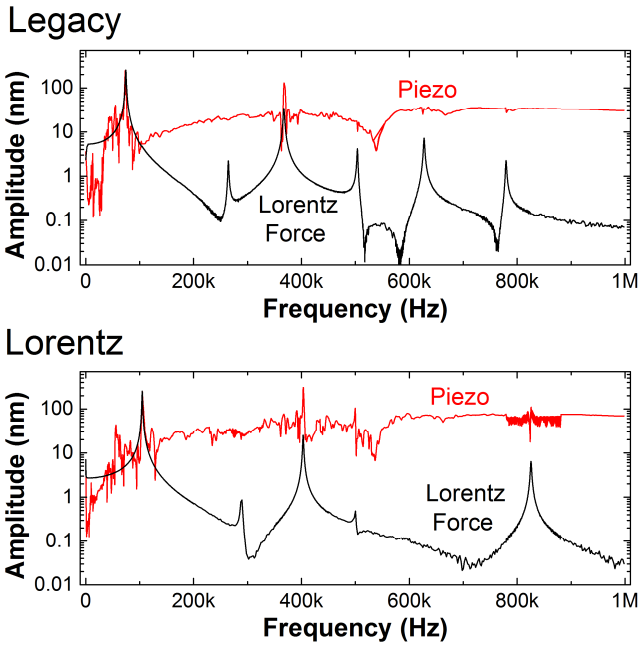

Figure 5: Cantilever oscillation amplitudes as functions of excitation frequency for piezoelectric and Lorentz force actuation. Piezoelectric actuation shows several parasitic peaks. Lorentz force actuation only shows amplitude peaks at the fundamental frequencies of the cantilever.

The characteristics of cantilever actuation via Lorentz force and the piezoelectric actuator, used in typical AFMs, were compared. We mounted the cantilevers in an Asylum Research MFP 3D SA AFM. The cantilevers were positioned at the edge of a NdFeB cube magnet where the magnetic field is strongest [4]. A function generator supplied sinusoidal voltage to the piezoelectric actuator or the cantilever heating circuit for Lorentz force actuation. The cantilevers were operated in series with a 47 kΩ sense resistor to ensure a nearly pure sinusoidal current through the circuit [4]. The excitation frequency was increased from 100 Hz to 1 MHz and the AFM optics recorded the cantilever oscillation amplitude. Figure 5 compares the cantilever response to piezoelectric and Lorentz force actuation schemes. The piezoelectric actuation shows numerous spurious peaks arising from resonances in the intermediate components between the actuator and the cantilever like the cantilever chip and cantilever holder. In contrast, Lorentz force actuation shows minimal noise and sharp peaks only at the cantilever harmonics since the force is applied directly at the cantilever free-end.

The mechanical and thermal performance of the Lorentz-thermal cantilever was compared with that of the Legacy cantilever. [4]. A function generator increased the sinusoidal voltage to the cantilevers at the cantilever resonance frequency. Figure 6 shows the cantilever mechanical and thermal response to periodic current. The Lorentz force, oscillation amplitude and mean heater temperature increased with increasing periodic current. The lower resistance of the Lorentz-thermal cantilever enables larger current and Lorentz force (5.3 µN) compared to the Legacy cantilever (0.7 µN). With periodic current input, both cantilevers are capable of self-heating beyond 500 °C and the majority of the temperature rise occurs over a small range in cantilever current. The Lorentz thermal cantilever oscillated with larger amplitude (2.8 µm) than the Legacy cantilever (1.4 µm) despite having higher stiffness (1.71 N/m) than the Legacy cantilever (0.53 N/m). Due to the novel cantilever design the Lorentz-thermal cantilever self-heats only to 44 °C while

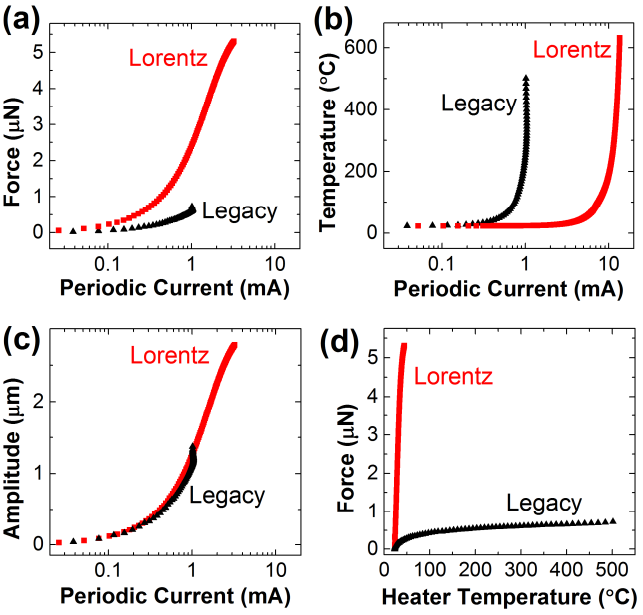

Figure 6: Cantilever response to periodic current for the Legacy and Lorentz-thermal cantilevers. (a) Generated Lorentz force, (b) time-averaged heater temperature, and (c) cantilever amplitude as functions of the periodic current amplitude. (d) Lorentz-force as a function of heater temperature.

generating 5.3 µN of force whereas the Legacy cantilever self-heats beyond 500 °C when generating 0.7 µN Lorentz force. Thus, the Lorentz-thermal cantilever enables precise and independent control of Lorentz force and heater temperature via combinations of AC and DC excitation voltages. This capability is critical for

accurate nanomechanical measurements over a large temperature range. Table 1 summarizes the performance of both cantilevers.

The Lorentz-thermal cantilever imaged a 100 nm tall silicon grating substrate in water to demonstrate the high signal-to-noise ratio of Lorentz force actuation and the ability to exert large actuation forces. The cantilever was submerged in a droplet of deionized water which was on the substrate. Lorentz force actuation clearly showed peaks at all the cantilever harmonics while it was impossible to actuate the cantilever using piezoelectric actuation. The cantilever scanned the grating in tapping mode via Lorentz force actuation at 1 µm/sec. The cantilever was heated below 100 °C to prevent bubble formation. Figure 7 shows a topography image of the grating obtained from the cantilever thermal signal. The thermal signal had a noise-limited vertical resolution of 14 nm. To our knowledge, this is the first demonstration of tapping mode operation via Lorentz force actuation and thermal topography sensing in a liquid medium.

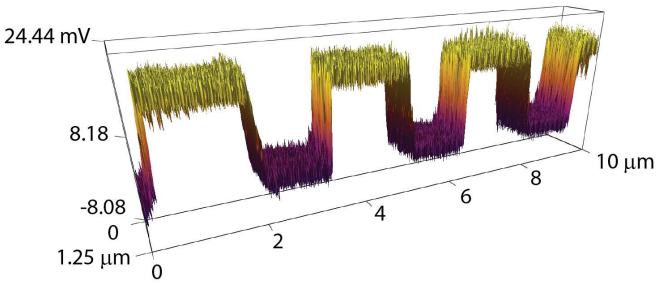

Figure 7: Topography image of a silicon grating acquired from the thermal signal of the Lorentz-thermal cantilever. The cantilever scanned the grating in tapping mode using Lorentz force actuation while being submerged in water.

CONCLUSION

This paper reports the design, characterization, and application of a multifunctional cantilever capable of Lorentz-force actuation and self-heating. The Lorentz-thermal cantilever uses a conductive path around the resistive heater that lowers the cantilever resistance to increase the cantilever current, and the Lorentz force. Lorentz force actuates the cantilever without introducing parasitic peaks since the force is applied directly at the cantilever free-end. The novel design of the Lorentz-thermal cantilever allows precise and independent control of Lorentz force (up to 5.3 µN) and self-heating (beyond 800 °C). Overall this cantilever can generate about 7X larger Lorentz force compared to the state-of-art Legacy cantilever. This cantilever can be used for nanomechanical measurements using techniques such as contact resonance. Similar cantilever technology can be also be used to improve the sensitivity of microcantilever hotplates for thermogravimetry applications.

ACKNOWLEDGEMENTS

This work was supported by the NSF Center for Chemical-Electrical-Mechanical Manufacturing Systems, NSF CMMI 10-68723, and DARPA TBN.

REFERENCES

[1] G. Binnig, C. Quate, and C. Gerber, "Atomic force microscope," Physical review letters, 56, 930-933, (1986).

[2] P. A. Yuya, D. C. Hurley, and J. A. Turner, "Contact-resonance atomic force microscopy for viscoelasticity," Journal of Applied Physics, 104, 7, (2008).

[3] W. P. King, B. Bhatia, J. R. Felts, H. J. Kim, B. Kwon, B. Lee, *et al.*, "Heated Atomic Force Microscope Cantilevers and their Applications," Annual Review of Heat Transfer, 16, 287-326, (2013).

[4] B. Lee, C. B. Prater, and W. P. King, "Lorentz force actuation of a heated atomic force microscope cantilever," Nanotechnology, 23, 055709, (2012).

[5] B. Lee, S. Somnath, and W. P. King, "Fast nanotopography imaging using a high speed cantilever with integrated heater–thermometer," Nanotechnology, 24, 135501, (2013).

[6] G. C. Ratcliff, D. A. Erie, and R. Superfine, "Photothermal modulation for oscillating mode atomic force microscopy in solution," Applied Physics Letters, 72, 1911-1913, (1998).

[7] J. Lee and W. P. King, "Microcantilever actuation via periodic internal heating," Review of Scientific Instruments, 78, -, (2007).

[8] T. Sulchek, R. Hsieh, J. D. Adams, S. C. Minne, C. F. Quate, and D. M. Adderton, "High-speed atomic force microscopy in liquid," Review of Scientific Instruments, 71, 2097-2099, (2000).

[9] H. Pozidis, W. Haberle, D. Wiesmann, U. Drechsler, M. Despont, T. R. Albrecht, *et al.*, "Demonstration of thermomechanical recording at 641 Gbit/in(2)," IEEE Transactions on Magnetics, 40, 2531-2536, (2004).

[10] A. Buguin, O. Du Roure, and P. Silberzan, "Active atomic force microscopy cantilevers for imaging in liquids," Applied Physics Letters, 78, 2982-2984, (2001).

[11] J. Lee, T. Beechem, T. Wright, B. Nelson, S. Graham, and W. King, "Electrical, thermal, and mechanical characterization of silicon microcantilever heaters," Journal of Microelectromechanical Systems, 15, 1644-1655, (2006).

[12] B. W. Chui, T. D. Stowe, T. W. Kenny, H. J. Mamin, B. D. Terris, and D. Rugar, "Low-stiffness silicon cantilevers for thermal writing and piezoresistive readback with the atomic force microscope," Applied Physics Letters, 69, 2767-2769, (1996).

[13] H. Rothuizen, M. Despont, U. Drechsler, C. Hagleitner, A. Sebastian, and D. Wiesmann, "Design of power-optimized thermal cantilevers for scanning probe topography sensing," in *IEEE MEMS 2009 Conference*, Sorrento, Italy, 2009, pp. 603-606.

[14] K. Kim, K. Park, J. Lee, Z. Zhang, and W. King, "Nanotopographical imaging using a heated atomic force microscope cantilever probe," Sensors and Actuators A: Physical, 136, 95-103, (2007).

[15] S. Somnath, E. A. Corbin, and W. P. King, "Improved Nanotopography Sensing via Temperature Control of a Heated Atomic Force Microscope Cantilever," Sensors Journal, IEEE, 11, 2664-2670, (2011).

CONTACT

*W.P. King, tel: +1-217-244-3864; wpk@illinois.edu

PRINTED MEMS MEMBRANE ELECTROSTATIC MICROSPEAKERS

Apoorva Murarka, Annie Wang, Joel Jean, Jeffrey H. Lang, and Vladimir Bulovic
Massachusetts Institute of Technology, Cambridge, Massachusetts, USA

ABSTRACT

We report the fabrication and operation of *electrostatic* microspeakers formed by contact-transfer of 125-nm-thick gold membranes over cavities patterned in a micron-thick silicon dioxide (SiO_2) layer on a conducting substrate. Upon electrostatic actuation, the membranes deflect and produce sound. Additionally, membrane deflection upon pneumatic actuation can be used to monitor pressure. Our microspeaker fabrication process enables fabrication of MEMS diaphragms without wet or deep reactive-ion etching, thus obviating the need for etch-stops and wafer-bonding. It enables monolithic fabrication of multiple completely-enclosed drum-like structures with non-perforated membranes to displace air efficiently, in both individual-transducer and phased-array geometries. The microspeaker consumes 262 μW of real electric power under broadband actuation in free field, and outputs 34 dB(SPL/Volt) of acoustic pressure at 10 kHz drive. The microspeaker sound pressure level increases with frequency at 40 dB/decade. The total thickness of the microspeakers is dominated by the silicon wafer substrate (~500 μm thick), with the active device thickness of less than 2 μm. These thin microspeakers have potential applications in hearing aids, headphones, and large-area phased arrays for directional sound sources.

INTRODUCTION

Electrostatically actuated capacitive speakers can have high power efficiency. Electrostatic 30-nm-thick graphene speakers in a single transducer configuration were demonstrated by Zhou *et al*. [1]. There, a single graphene diaphragm was formed on nickel foil using high temperature (1000 °C) chemical vapor deposition, and released from the nickel foil via an iron(III) chloride chemical etch. In contrast, we reported room-temperature, etch-free, contact-transfer printing processes for electrostatically actuated, suspended metal membranes on viscoelastic and flexible substrates [2], and on SiO_2 substrates [3]. However, in these early demonstrations, the acetone-assisted contact-transfer method reported in [3] had low device yield for gold membranes larger than 0.8 mm^2 in area, while the stiction of those membranes to cavity bottoms prevented audible sound production by further decreasing the membrane area available for air displacement. These challenges have been overcome in the present study which reports the modified acetone-assisted contact-transfer method that increases the area of transferred gold membranes to 12.5 mm^2 (covering ~16000 25-μm-diameter cavities), and enables the release of membrane areas stuck to cavity bottoms. This increases the total deflectable area of the membranes, enabling demonstration of audible sound production by *electrostatic actuation*. Alternatively, this microcavity array can be used to sense pressure. We note that the additive fabrication of these contact-transferred membranes removes the need for holes typically found in MEMS diaphragms for etching the underlying sacrificial layer.

DEVICE DESIGN

Our variable-capacitance microspeaker comprises an array of 25-μm-diameter circular cavities in a SiO_2 dielectric layer deposited on a conductive silicon substrate. The cavities are bridged by a 125-nm-thick gold membrane which forms a deflectable top electrode. Deflection of this membrane in response to an applied voltage or an applied pressure can be used to produce sounds or sense pressure. The gold membrane, 12.5 mm^2 in area, covers about 16000 of the 25-μm-diameter circular cavities which are biased simultaneously to respond in parallel, hence enabling the production of a detectable sound pressure level under actuation. The circular cavities are hexagonally-close-packed (as shown in Figure 2) to minimize the non-active capacitance from the underlying SiO_2 supports. The gold electrode is in the shape of a parallelogram (see Figure 2).

FABRICATION

Pick-up Stamp Substrates

The pick-up stamp comprises the cavity-patterned substrate onto which the gold membranes are additively fabricated via lift-off from a transfer pad. A silicon wafer which forms the back electrode of the microspeaker is cleaned in Piranha solution. A 1.1 micron thick SiO_2 layer is deposited on the wafer using plasma-enhanced chemical vapor deposition (PECVD). Hexamethyldi-silazane is then applied to the oxide layer. Photoresist is spun on the oxide layer and pre-baked at 95°C for 30 minutes. The photoresist is then exposed in a mask aligner and exposure unit, using a chrome mask. Following exposure, the photoresist is developed and then baked at 120 °C for 30 minutes. The resulting resist layer has circular patterns, with the underlying SiO_2 exposed; see Figure 1. The exposed SiO_2 is dry etched in tetrafluoromethane/hydrogen (CF_4/H_2) to form ~25-μm-diameter circular cavities. The resist is ashed away in O_2. A thin (60-100 nm thick) insulating layer of SiO_2 is then deposited via PECVD to prevent shorting between the gold membrane and the bottom electrode in case of membrane collapse during electrical actuation. The wafer is diced, cleaned, and exposed to O_2 plasma for 5 minutes. The diced chips are then placed in a 1:5 (by volume) solution of 3-mercaptopropyltrimethoxysilane (Sigma-Aldrich) and 2-Propanol at 80 °C to 100 °C to silanize the SiO_2 surface such that thiol groups stick out of the oxide surface, enhancing the adhesion of gold to the oxide. Upon silanization, these pick-up stamp slides are rinsed with 2-Propanol, and then blown dry using nitrogen, immediately prior to the transfer of the gold membrane.

Transfer Pad with Raised Mesas for Gold Membrane Transfer

The reusable master mold that defines the transfer pad geometry is fabricated using SU-8 photoresist (SU-8 3010 MicroChem) spun onto a silicon wafer and pre-baked at 95 °C for 5 minutes. The wafer is then cooled for 2 minutes before the resist is exposed in a UV exposure unit with a transparency mask. After a post-exposure bake at 95 °C for 2 minutes, the photoresist is developed by immersing and agitating the wafer in propylene glycol monomethyl ether acetate (PGMEA) for 4 minutes. Next, the residual SU-8 and PGMEA are rinsed off by spraying the wafer with PGMEA and 2-Propanol in sequence, for 10 seconds each. The wafer is blown dry with nitrogen and hard-baked for >3 hours at 150-175 °C. Following the hard bake, the master mold is silanized with trichloro(1H,1H,2H,2H-perfluorooctyl)silane (Sigma-Aldrich) to ensure easy removal of PDMS that is next cured on top of it [6].

The PDMS transfer pad is molded by pouring a degassed mixture of PDMS (Sylgard 184, Dow Corning Co., 10:1 base-to-

9781940470016/HH2014/$25©2014TRF
DOI 10.31438/trf.hh2014.84

curing-agent ratio by weight) onto the silanized SU-8 master mold, and curing it in an oven at 60-105 °C for ~37 hours. The cured PDMS pad is peeled from the SU-8 master. This pad has parallelogram-shaped mesa structures that rise above the plane of the PDMS substrate and aid the patterning and transfer of the metal electrodes since thermal evaporation is a line-of-sight process [6]; see Figure 1. After curing, a ~20 nm thick layer of aluminum is thermally evaporated on the PDMS transfer pad to prevent any cracks in the underlying PDMS substrate from adversely affecting the topography of the gold films to be deposited, and to slow down the diffusion of TPD into the PDMS substrate. The transfer pad is then exposed to O_2 plasma for 7 seconds, after which a 90 nm thick organic release layer of *N*,*N*'-diphenyl-*N*,*N*'-bis(3-methylphenyl)-(1,1'-biphenyl)-4,4'-diamine (TPD, Luminescence Technology Co.), and a 125 nm thick layer of gold are deposited in sequence via thermal evaporation onto the transfer pad [2]. The vacuum-evaporated gold film above the mesas is much thinner than the height of the mesas. Thus, the gold film breaks along the edges of the mesas and defines a film in the shape of the mesa plateaus with sub-micron edge roughness.

Contact Lift-Off Transfer

Following thermal evaporation, the TPD layer underneath the parallelogram-shaped gold membranes is dissolved by applying 60-100 µL of acetone to a ~1 cm^2 area on the transfer pad. Gold membrane transfer is then initiated by placing the pick-up stamp in contact with the gold membranes, which are still resting on the mesas of the transfer pad. The gold membranes adhere to the MPTMS-treated pick-up stamp upon conformal contact, and are lifted-off. The transferred gold membranes cover the circular air-cavities in the stamp, forming the top electrode of the microspeaker, as shown in Figure 2. The device can then be heated on a hot plate from 100 °C to 260 °C over 30 minutes to release the areas of the transferred gold membrane that have sunk into the underlying cavities.

TEST RESULTS

The yield of the aforementioned MEMS fabrication process can be quantified by the fraction of the area of the transferred gold membrane (of a device) that has not sunk into the cavities in the underlying substrate since that is the active area of the membrane responsible for displacing air during the electrostatically-actuated production of sound. Excessive pressure applied during the contact-lift-off transfer process likely results in the gold membrane coming into contact with the bottom of some cavities. Possible reasons for the membrane then sticking to the bottom are the presence of MPTMS in the cavity wells or acetone-enabled stiction [3]. Increasing the thickness of the silicon dioxide spacer layer decreases the sunk-in area of the transferred membranes, but increases the voltage required to achieve sufficient sound production. Heating the device after membrane transfer, as described above, releases a significant fraction of the sunk-in membrane areas. However, some areas of the transferred membrane remain sunk-in even after the heat treatment, and do not contribute to the production of sound.

The mechanical deflection of the gold membrane is first characterized using optical interferometry. Electrical contact to the gold membrane is made using gold-wire probe tips. A 1 kHz sinusoidally-varying voltage with a 60 V peak-to-peak amplitude and a 30 V DC bias is applied between the gold membrane and the silicon substrate. The resulting deflection of the membrane over the underlying cavities is measured at different phases of the applied signal using an optical interferometer (Wyko NT9100, Bruker Nano Inc.). As the phase of the applied signal increases

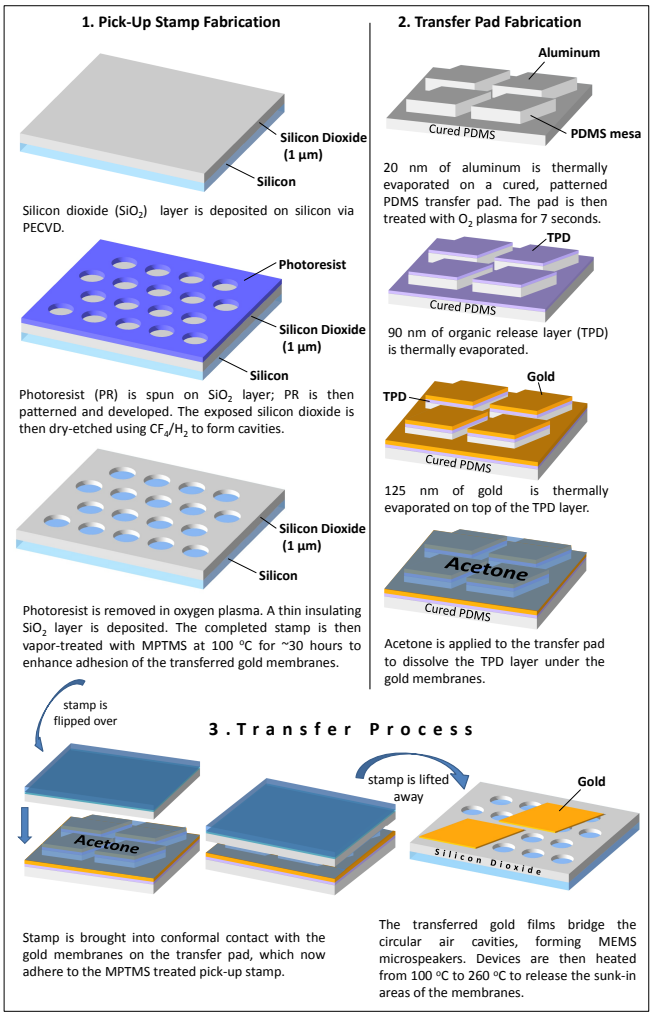

Figure 1: The process flow for the acetone-assisted, contact-transfer MEMS printing process on silicon-based substrates. The drawings above are not to scale.

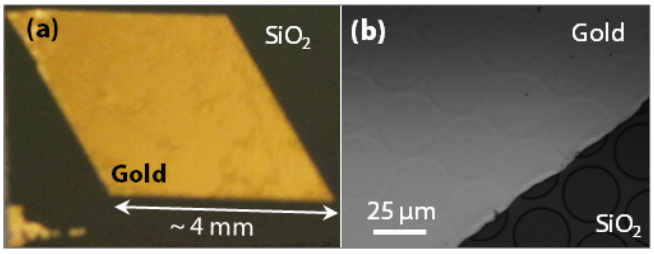

Figure 2: Photographs of large area gold membranes contact-transfer printed on SiO_2 dielectric layers patterned with ~25-µm-diameter cavities to form MEMS microspeakers. (a) A single 12.5-mm^2-area gold membrane covering ~16000 circular cavities, in an individual-transducer configuration. (b) An optical microscopy image of a similar MEMS device, showing a gold membrane bridging several 25-µm-diameter cavities in SiO_2.

from 270° to 90° (450° mod 360°), the voltage between the gold membrane and the underlying substrate increases. As a result, the electrostatic force of attraction between the membrane and the underlying electrode increases, resulting in an increasing downward deflection at the center of the suspended membrane, as shown in Figure 3a (blue triangles); both the applied voltage and deflection are shown. Analysis of the deflection of a gold

membrane over 83 different cavities reveals a repeatable maximum deflection of 121±13 nm across gaps of ~25 microns at 60 V. Figure 3b shows the same data with time as a parameter. However, squared voltage (which is proportional to force) is displayed instead of voltage. Since the membrane deflections are believed to be elastic and recoverable, a linear relation between the applied electrostatic force and the maximum membrane deflection should be observed. The electrostatic force scales with the square of the applied voltage assuming that maximum membrane deflection is small compared to the initial distance between the membrane and the underlying silicon electrode. As a result, one can expect the maximum membrane deflection to scale approximately with the square of the applied voltage, and this is observed in the linear relationship in Figure 3b. However, that graph also shows that the energy conversion cycle encloses net area, which indicates that net electrical energy is converted to mechanical energy. This may result from radiated sound or irrecoverable deformations in the membrane.

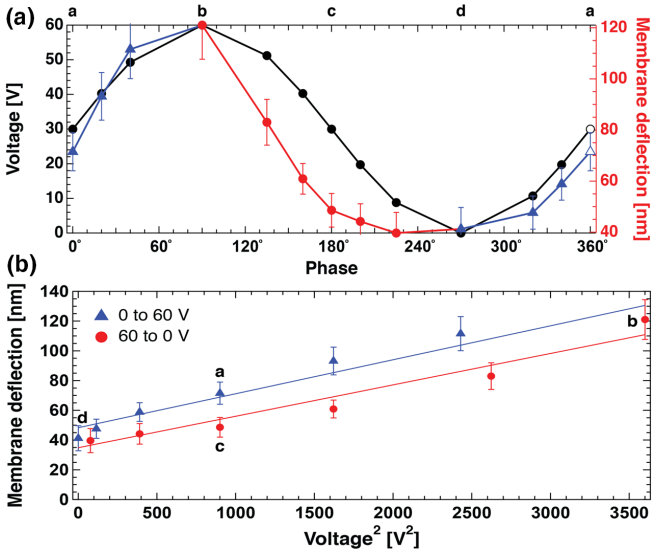

Figure 3: Deflection profiles of a gold membrane suspended over cavities, obtained via optical interferometry during 1 kHz AC actuation. The peak (center) deflections of this membrane over 83 cavities as functions of time were extracted from the profiles and then averaged to yield a single deflection time function. That time function and the corresponding applied voltage are shown here. (a) The applied voltage (black) and the averaged peak membrane deflection (red and blue) are shown as functions of time. (b) The membrane deflections are plotted against the square of the applied voltage with time as a parameter. The points labeled a-b-c-d-a in (b) indicate the position of corresponding points on the periodic deflection and voltage waveforms in (a).

The acoustic performance of the microspeakers is characterized in the free-field using different types of actuation signals such as normally distributed pseudorandom noise signals and chirp signals in the human auditory range. The setup for these tests is shown in Figure 4.

Bandlimited and broadband noise signals are applied as voltages to the microspeaker, at Bose Corporation, under computer control via an audio interface (RME Fireface 800) and a high voltage amplifier. The sound produced in the free field is measured and recorded using a Brüel & Kjær (B&K) 4135 microphone at an on-axis distance of ~4 mm from the devices. The B&K 4135 is a reference microphone with a flat frequency response from 10 Hz to

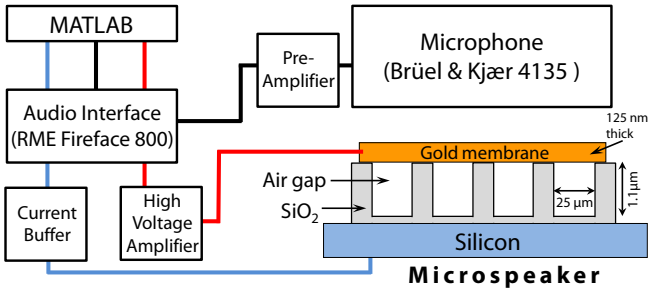

Figure 4: Schematic of the setup used for acoustic characterization of the microspeaker. Signals generated by MATLAB are amplified and applied to the microspeaker to actuate it electrostatically. The resulting generated pressure is sensed using the microphone, and fed back to MATLAB for subsequent processing and analysis.

20 kHz. The current through the microspeaker is simultaneously measured via a current buffer.

Two types of normally distributed pseudorandom noise signals are applied to a device with 12.5-mm^2-area gold membrane. The first input signal is broadband noise from 100 Hz to 22 kHz, biased at 35V, with a standard deviation of ~8 V and a peak deviation of ~35 V (as shown in Figure 5 inset). The second input signal is bandlimited using a third-order Butterworth bandpass filter between 2 kHz and 7 kHz, with a roll-off to ~22 kHz, biased at 35 V. The transfer function, T_{pv}, from the driving voltage, v, to the sound output, p, measured by the microphone is computed as the ratio S_{pv}/S_{vv}, where S_{pv} is the cross-spectral density between p and v, and S_{vv} is the autospectral density of v. The transfer function magnitudes obtained from these measurements

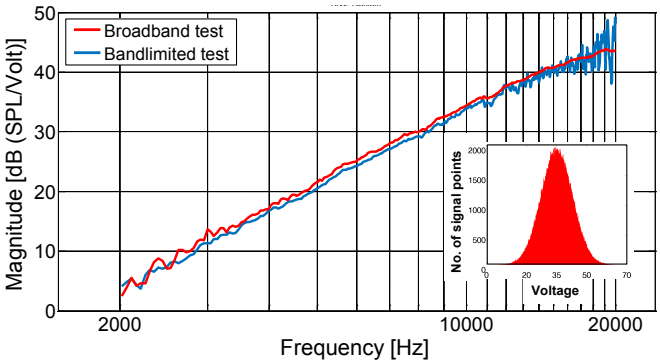

Figure 5: Acoustic frequency response, from 2 kHz to 20 kHz, of a gold membrane microspeaker, 12.5 mm^2 in area. The magnitude of the transfer function, $|T_{pv}|$, from the driving voltage amplitude to the sound output measured by the microphone is converted to decibels using 20 µPa as the reference pressure, i.e., the magnitude plotted is $20\log_{10}(|T_{pv}|/20\mu\text{Pa})$. Inset: Histogram of the normally distributed broadband driving signal amplitudes.

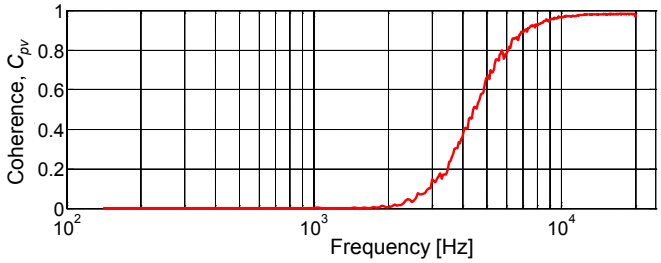

Figure 6: Spectral coherence, C_{pv}, between the sound output measured by the microphone and the driving voltage, for the broadband driving signal.

are shown in Figure 5 for frequencies from 2 kHz to 20 kHz because the microphone output is dominated by incoherent noise below 2 kHz for both measurements. The ~40 dB/decade rise of the frequency response in the range shown in Figure 5 indicates that the sound pressure output of the microspeaker is proportional to the acceleration of the microspeaker diaphragm, as expected in the spring-controlled regime for free field radiation. The frequency response to the bandlimited driving signal is noisier near 20 kHz because the energy in the bandlimited signal is much lower near 20 kHz as compared to that in the broadband driving signal. A reference pressure of 20 µPa is used to calculate the sound pressure level (SPL) per Volt in decibels.

The spectral coherence, C_{pv}, between the sound output and the broadband driving voltage signal is shown in Figure 6, from 100 Hz to 20 kHz. C_{pv} is nearly zero for frequencies less than 2 kHz. Over this range, the recorded sound signal is likely dominated by background noise because the microspeaker signal is weak at low frequencies. Note that the microspeaker pressure output in the free field is proportional to the diaphragm acceleration which is lower at lower frequencies in the spring-controlled regime in which the microspeaker is actuated. The microspeaker response is linear above 10 kHz (C_{pv} > 0.97) for the normally distributed broadband driving signal.

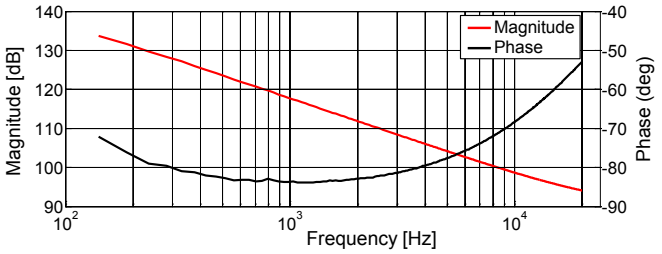

Figure 7: Magnitude and phase of the microspeaker electrical impedance obtained from the broadband test. The ~18 dB/decade decrease in magnitude indicates the primarily capacitive nature of the microspeaker (~200 pF). The reference impedance is 1 Ohm.

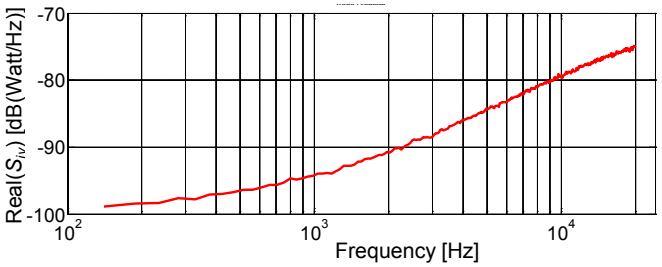

Figure 8: Real part of the cross spectral density, S_{iv}, between the microspeaker current and the driving voltage, for the broadband driving signal. The magnitude plotted is $10log_{10}(\text{Real}(S_{iv}))$. *The reference power spectral density is 1 Watt/Hz.*

The electrical impedance of the microspeaker is shown for the broadband measurement in Figure 7. The ~18 dB/decade decrease of the impedance magnitude indicates that the microspeaker device is primarily capacitive near 200 pF during the broadband operation. Additionally, the impedance phase increase from -84 degrees at 1 kHz to -53 degrees at 20 kHz indicates the presence of a 30 kΩ series resistance. This resistance is too high to be explained by the resistivity of the membrane and the substrate.

The magnitude of the real part of the cross-spectral density, S_{iv}, between the driving voltage, v, and the current, i, through the microspeaker for the broadband driving signal is shown from 100 Hz to 20 kHz in Figure 8. Integrating this curve from 100 Hz to 20 kHz yields 262 µW as the real electric power input to the microspeaker during broadband excitation.

The frequency response of the microspeakers can potentially be improved, especially at the lower frequencies, by combining cavities of larger diameters in parallel, under a single gold diaphragm. The SPL output of the microspeakers can also be increased by using membranes of larger area that displace a larger volume of air, or by actuating multiple smaller membranes simultaneously on the same die. The actuation voltage can be reduced by using a thinner dielectric spacer layer between the gold membrane and the bottom electrode, but this could adversely affect the yield. Additionally, the efficacy of these devices in portable audio applications such as hearing aids and earphones can be better gauged by measuring the acoustic characteristics in a pressure field using a coupling cavity (of 2 cm^3 volume) between the microspeaker and the microphone.

CONCLUSION

A contact-printed electrostatic MEMS microspeaker is demonstrated. It comprises a 125-nm-thick deflectable gold membrane suspended over an array of ~16000 circular cavities patterned in a 1.1-micron-thick dielectric layer. Each cavity is 25 µm in diameter. Its electromechanical performance under AC actuation is characterized via optical interferometry to show a repeatable maximum deflection of 121±13 nm. The microspeaker acoustic response in free field is characterized using normally distributed pseudorandom broadband and bandlimited signals, suggesting potential applications of these microspeakers in hearing aids, earphones, and large-area phased arrays for directional sound sources.

ACKNOWLEDGEMENTS

The authors gratefully acknowledge and thank Ole Nielsen of Bose Corporation for his assistance with the acoustic characterization tests and for the invaluable discussions. This work is supported by the National Science Foundation (NSF) Center for Energy Efficient Electronics Science (E3S) Award ECCS-0939514. The authors also thank Patrick Brown and Andrea Maurano for assistance rendered. The devices described here were fabricated in the MIT Microsystems Technology Laboratories and the MIT Organic and Nanostructured Electronics Laboratory.

REFERENCES

[1] Q. Zhou and A. Zettl, "Electrostatic graphene loudspeaker," Applied Physics Letters, 102 (2013).

[2] A. Murarka, C. Packard, F. Yaul, J. Lang, V. Bulovic, "Micro-contact printed MEMS," Technical Digest of the IEEE MEMS 2011 Conference, Cancun, January 23-27, 2011, pp. 292-295.

[3] A. Murarka, S. Paydavosi, T. Andrew, A. Wang, J. Lang, V. Bulovic, "Printed MEMS membranes on silicon," Technical Digest of the IEEE MEMS 2012 Conference, Paris, January 29-February 2, pp. 309-312.

CONTACT

*A. Murarka, tel: +1-617-4525403; apoorva@mit.edu

ACTIVE SURFACE POTENTIAL CONTROL FOR ARTIFICAL ION PUMPS

M. Pinti[1], H.A. Zambrano[1,2], K.K. Rangharajan[1], B. Wang[1], A.T. Conlisk[1], S. Prakash[1]*
[1]The Ohio State University, Columbus, Ohio, USA
[2]Universidad de Concepción, Concepción, Biobío, Chile

ABSTRACT

Embedded electrodes in 16 nm deep, 30 μm wide, and 0.5 cm long nanochannels were used to pump aqueous electrolyte solutions. Variations in the surface potential due to actively controlled electrodes led to flow gating and flow reversal in nanofluidic channels demonstrated through current-voltage experimental data. Active control of surface potential for pumping aqueous electrolyte solutions provides a key advance towards development of an artificial ion pump.

INTRODUCTION

Ion channels and ion-pumps form the basis of nearly all cellular communication and electrolyte transport for maintaining essential cell functions [1]. Numerous efforts have been made to develop 'smart' nanostructures to understand and implement operational principles of artificial ion channels and ion pumps for applications in bio- and chemical sensing [2], drug delivery [1], and energy conversion systems [3]. There are three main requirements for ion channels and ion pumps to be implemented: (i) sensing of species for (ii) flow gating of the ionic species (e.g., K^+, Na^+, or Ca^{2+}), and (iii) selectively pumping the species of interest in a preferential direction. Significant progress has been made in requirements (i) and (ii) leading to potential development of artificial ion channels, with almost all previous reports using solid-state nanopores in polymers with chemically functionalized surfaces [2]. Some previous reports also show using flow-FETs featuring surface electrodes in nanochannels to modulate nanoflows [4, 5]. Here, experimental current-voltage (I-V) data shows use of asymmetrically distributed surface potential through actively controlled embedded electrodes for pumping aqueous electrolytes where flow gating and flow reversal was achieved – key advances towards developing an artificial ion pump.

METHODOLOGY

Nanofluidic channel networks were fabricated with aspect ratios as low as 0.0005 to enable nanoscale effects similar to biological systems; while providing high throughput and benefits of 1-D theoretical analysis. The devices were fabricated in borosilicate glass substrates using standard UV lithography and wet etching, with unique advances previously reported by our team [6]. The nanochannels were sealed using a thin (< 1 μm) PDMS (poly dimethylsiloxane) adhesion layer supported on a glass cover with patterned Au electrodes (~ 30 μm wide, 15 nm thick, and distributed asymmetrically i.e. with non-uniform spacing along length of nanochannel). Two microfluidic channels with 10 μm depth and either 50 or 100 μm width serve as fluidic reservoirs to the bank of these ultra-low aspect ratio nanochannels with a critical dimensions of 16 nm (Fig. 1). Electrolyte solutions with KCl, NaCl, or $CaCl_2$ in DI water at concentrations varied between 0.1 mM to 100 mM were used as working fluids.

RESULTS

With no surface electrode potential, nanochannel conductance, given by the ratio of current to applied axial potential (I/V), remains constant at low electrolyte concentrations as measured by comparable currents for 0.1 mM and 1 mM KCl (Fig. 2A). However, as the concentration increases to 10 mM,

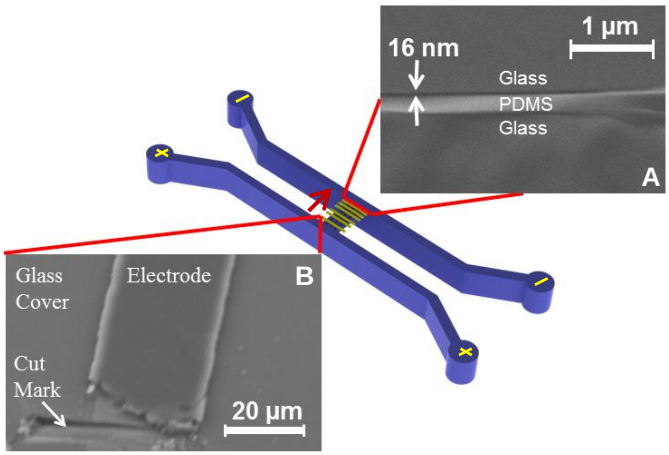

*Figure 1: Schematic for the geometric layout of the active ion pumping device, in a hybrid micro/nanofluidic configuration. Two microchannels connect a bank (3-6) of 16 nm deep x 30 μm wide x 0.5 cm long nanofluidic channels. An array of non-uniformly spaced Au electrodes are patterned on a glass cover and isolated from the liquid by PDMS, which is then used as an adhesion layer to bond and seal the nanochannels. The "+" and "-" signs indicate the anode and cathode used to apply the axial potential respectively. The red arrow indicates the direction of net flow. [**A**] SEM image showing a partial cross section of a 16 nm deep channel to confirm that channels are bonded and open for flow. The 3-layers show the glass substrate, PDMS adhesion layer, and glass cover. Note, the aspect ratio of the nanochannel makes it impossible to view the entire cross-section in one frame. [**B**] SEM image of a gold electrode on a glass cover before it is embedded in PDMS and sealed to form the top of the channel. A thicker electrode (50 nm compared to 15 nm in a typical bonded device) is shown here to allow the full width and finite thickness to be observed in one frame. The cover with the electrode was cut for imaging purposes leading to a partial ripping of the Au film.*

increase in current implies conductance values tend towards those expected from the bulk conductivity, matching previous reports for KCl in nanofluidic channels [4, 5, 7]. Figure 2B shows that ion-type can have a significant impact on the I-V data, with the measured current scaling as a function of valence. Current data from 10 mM KCl and 10 mM NaCl shows no significant difference despite approximately 40% difference in ionic mobility of K^+ and Na^+ (values of 7.63 and 5.18 x 10^{-8} $m^2V^{-1}s^{-1}$, respectively [8]). Comparison of the slopes of the linear portion of the I-V data in Figure 2B indicates NaCl and KCl have nearly 5x higher conductance compared to $CaCl_2$ where the ionic mobility of Ca^{2+} is higher than Na^+ (with a value of 6.15 x 10^{-8} $m^2V^{-1}s^{-1}$ for Ca^{2+}).

The total current through a nanofluidic channels is the summation of contributions due to diffusion, conduction, and convection. Neglecting diffusion, the total current through the nanofluidic channel is given by

$$I = \int_0^h Fw \sum_i z_i(-\Omega_i c_i \nabla\phi + c_i \vec{u})dx$$

9781940470016/HH2014/$25©2014TRF
DOI 10.31438/trf.hh2014.85

where F is Farday's constant, c_i is the concentration of the species in the nanochannel, z_i is the valence, and Ω_i is the ionic mobility given by $\Omega_i = z_i F D_i / RT$ [8]. The potential gradient, $\nabla\varphi$, is given by $-V_{axial}/L_{channel}$ in long channels with the bias configuration shown in Fig. 1 [9]. Considering the values for the valence and ionic mobility, the current values shown in Fig. 2B can be explained by variations in c_i and $\vec{u}$, indicating the difference in transport observed for different cations is dominated by electrostatic interactions between the electrolyte and the charged surface.

Microfluidic particle image velicometry measurements show that the presence of trace amounts of calcium reduces the magnitude of the electroosmotic velocity in KCl/$CaCl_2$ mixtures compared to pure KCl. The effect is attributed to reduction of the surface potential due to calcium adsorption to the wall [10], with similar results reported for KCl/$CaCl_2$ mixtures in nanofluidic pores [11]. To our knowledge, this is the first direct comparison of $CaCl_2$ to NaCl and KCl I-V data and further investigation is required to fully explain the observed trends.

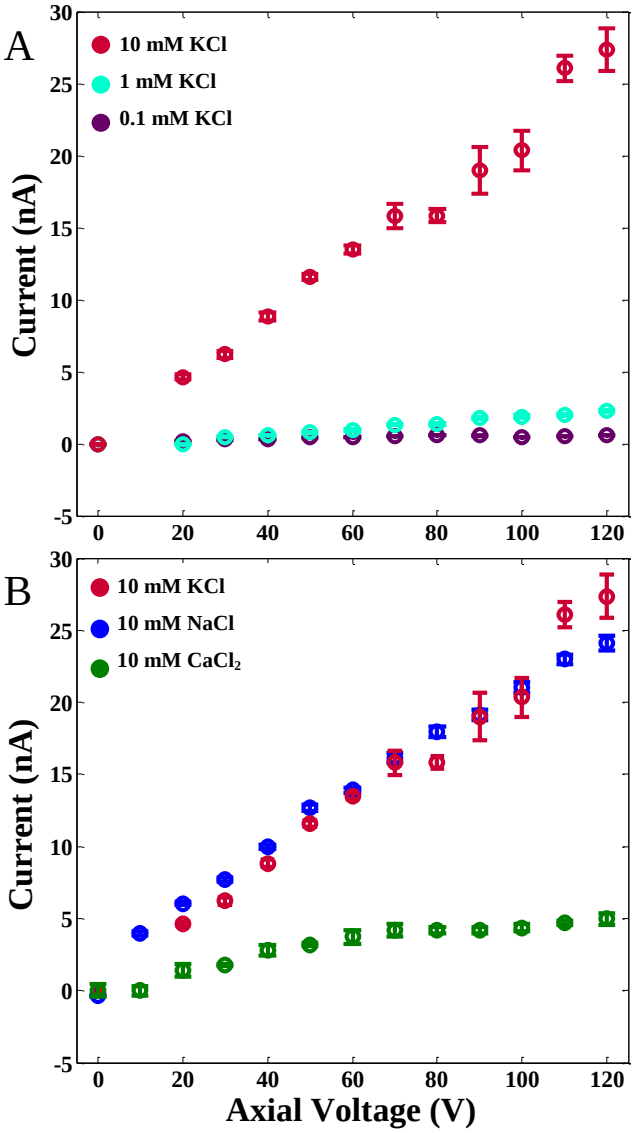

*Figure 2: [**A**] I-V data for KCl confirming operation of a 16 nm deep nanochannel device. Comparable current and, therefore, conductance is observed for 0.1 mM and 1 mM while the 10 mM case shows increased current and, therefore, conductance expected in these types of devices in agreement with previous reports. [**B**] I-V data shows influence of distinct cations on total measured current in absence of a gate potential. At 10mM, KCl and NaCl show comparable values for current. Conductance (slope of I-V curve) of $CaCl_2$ filled channels is nearly 5x lower than NaCl and KCl.*

By controlling the applied electrode potential for a fixed streamwise or axial potential, reversal of net measured current in the nanochannel was observed, demonstrating a reversal in direction of net ionic flow (Fig. 3). In fact, gating to stop flow as indicated by nearly zero measured current, and then reversing polarity of measured current is seen in Fig. 3 for 1 mM NaCl electrolyte solution as a representative case. As the measured current is a total current with contributions from net diffusion, conduction, and convection, the reversal in measured current polarity indicates the reversal of the direction of net ion transport. Leakage current through the PDMS insulation layer was negligible, indicating extraneous current paths do not affect the data shown in Fig. 3.

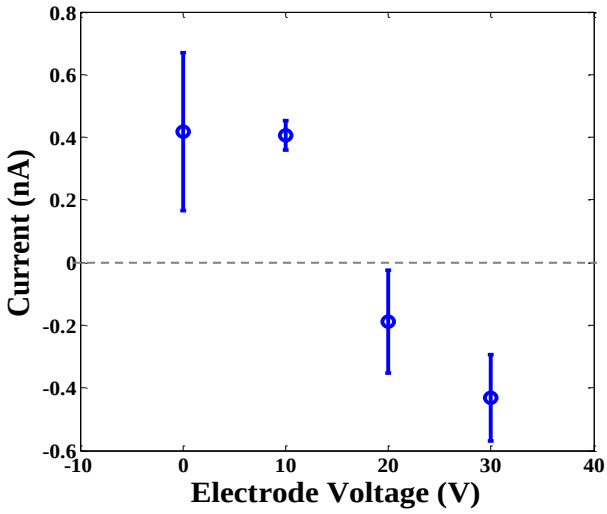

Figure 3: At a fixed axial potential of 15 V using 1 mM NaCl electrolyte, the electrode or gate potential was increased leading to a decrease in current (and therefore conductance) until the channel is effectively "closed" and allows no net flow through the channel. Further increasing the voltage leads to a change in the polarity of the current indicating that the net ion transport within the nanochannel has reversed direction.

Fixing the surface electrode potential to -10 V, pumping of 1 mM $CaCl_2$ was observed with no axial applied potential as indicated by a positive 67 pA current (Fig. 4). Figure 4 shows a representative case where the surface electrode alone was capable of pumping an aqueous electrolyte solution in the nanofluidic channel. An axial potential of 130 V, more than an order of magnitude higher than the surface electrode potential used here, is required to drive a 67 pA current for 1 mM $CaCl_2$ without surface electrodes.

Flow gating and current reversal can also be observed by varying the axial potential. The current reduces in magnitude as the axial potential becomes increasingly negative where full flow gating is observed at –70 V and flow reversal is observed at larger (>-70 V) negative axial potentials. Further investigation is required to determine the origin of the non-linearities observed in the IV data in Figure 4.

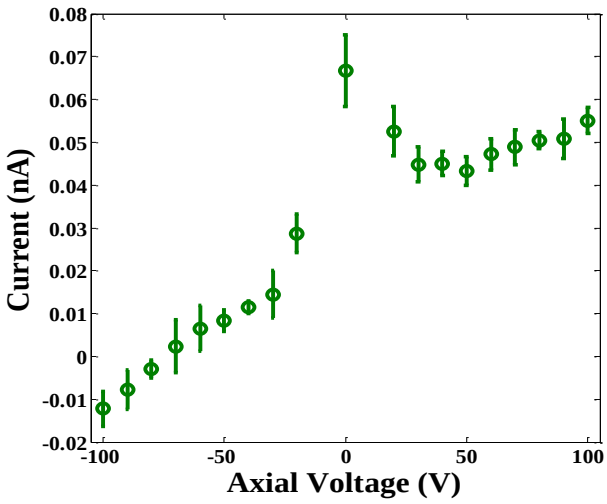

Figure 4: Pumping of 1 mM $CaCl_2$ electrolyte was observed with a potential of -10 V applied to the surface electrode and no axial potential as indicated by a positive 67 pA current. An axial potential of 130 V, more than an order of magnitude higher than the surface electrode potential used here, is required to drive a 67 pA current for 1 mM $CaCl_2$ without surface electrodes. Applying a net negative axial potential led to a decrease in current until the channel is effectively "closed" and allows no net flow through the channel at ~-70 V. Further increasing the magnitude of the negative voltage led to a reversal in net ionic transport as indicated by a negative measured current.

CONCLUSIONS

We have demonstrated for the first time reversal of net ionic transport in a nanofluidic channel through application of a transverse electric field via an embedded surface electrode. The configuration presented here allows for tunable control of the direction of transport in the nanofluidic channel, where gating and flow reversal have been demonstrated. The surface electrode alone pumps the electrolyte solution using an applied potential that is one order of magnitude lower than a streamwise or axial potential to achieve similar electrokinetic pumping, as observed due to measured currents.

ACKNOWLEDGEMENTS

The authors acknowledge the staff at Nanotech West Laboratories for assistance with equipment during fabrication and characterization of devices. We also acknowledge partial financial support from the US Army Research Office (ARO), and the National Science Foundation (NSF). The authors wish to acknowledge computational support from the Ohio Supercomputer Center (OSC).

REFERENCES

[1] R. Duan, F. Xia and L. Jiang, "Constructing Tunable Nanopores and Their Application in Drug Delivery", ACS Nano, 7, 10 (2013) pp. 8344-8349.

[2] X. Huo, W. Guo and L. Jiang, "Biomimetric smart nanopores and nanochannels", Chemical Society Reviews, 40, (2011) pp. 2385-2401.

[3] L. Wen, X. Hou, Y. Tian, F.-Q. Nie, Y. Song, J. Zhai and L. Jiang, "Bioinspired Smart Gating of Nanochannels Toward Photoelectric-Conversion Systems", Advanced Materials, 22, 9 (2010) pp. 1021-1024.

[4] R. Karnik, R. Fan, M. Yue, D. Li, P. Yang and A. Majumdar, "Electrostatic Control of Ions and Molecules in Nanofluidic Transistors", Nano letters, 5, 5 (2005) pp. 943-948.

[5] R. Fan, S. Huh, R. Yan, J. Arnold and P. Yang, "Gated proton transport in aligned mesoporous silica films", Nature Materials, 7, (2008) pp. 303-307.

[6] M. Pinti, T. Kambham, B. Wang and S. Prakash, "Fabrication of Centimeter Long, Ultra-Low Aspect Ratio Nanochannel Networks in Borosilicate Glass Substrates", Journal of Nanotechnology in Engineering and Medicine, 4, 2 (2013) pp. 1-7.

[7] D. Stein, M. Kruithof and C. Dekker, "Surface Charge Governed Ion Transport in Nanofluidic Channels", Physical Review Letters, 93, 3 (2004) pp. 035901 1-4.

[8] A. T. Conlisk, *Essentials of Micro- and Nanofluidics*: Canbridge University Press, 2013.

[9] I. Vlassiouk, S. Smirnov and Z. Siwy, "Ionic Selectivity of Single Nanochannels", Nano letters, 8, 7 (2008) pp. 1978-1985.

[10] S. Datta, A. T. Conlisk, H. F. Li and M. Yoda, "Effect of divalent ions on electroosmotic flow in microchannels", Mechanics Research Communication, 36, (2009) pp. 65-74.

[11] Z. S. Siwy, M. R. Powell, A. Petrov, E. Kalman, C. Trautmann and R. S. Eisenberg, "Calcium-Induced Votlage Gating in Single Conical Nanopores", Nano letters, 6, 8 (2006) pp. 1729-1734.

CONTACT

*S. Prakash, tel: +1-614-688-4045; prakash.31@osu.edu

ELECTRICAL ACTUATION AT NANOSCALE: CONTROLLED ORIENTATION OF PROTEINS DURING IMMOBILIZATION

Sam Emaminejad[1,2,3], Mehdi Javanmard[1,2,3*], Shuai Chang[1], Chaitanya Gupta[1], Ronald W. Davis[2,3], and Roger T. Howe[1]*

[1] Electrical Engineering Department, Stanford University, CA, USA

[2] School of Medicine, Stanford University, CA, USA

[3] Stanford Genome Technology Center, Stanford University, Palo Alto, CA, USA

* Equal Contribution

ABSTRACT

Here, we demonstrate the ability to control protein orientation using electrical field. We used atomic force microscopy (AFM) to verify that the application of electric field results in modulation of the orientation of antibodies (IgG molecules) and also enhancement of immobilization. We also demonstrate the applicability of this technique to improve the performance of fluorescent affinity biosensors.

INTRODUCTION

We previously [1] demonstrated a three stage microfluidic sample preparation platform for filtering cells and highly abundant proteins (using enhanced dielectrophoresis force [2,3]) and presented preliminary results for orienting target proteins for probe-free biosensing platforms. Here, we show significant improvement in the ability to control protein orientation using electrical field. We used atomic force microscopy (AFM) to verify that the application of electric field results in modulation of the orientation of antibodies (IgG molecules) and also enhancement of immobilization. We also demonstrate the applicability of this technique to improve the performance of fluorescent affinity biosensors. Previously Talasaz et al. [4] developed a simulation procedure predicting protein orientation related to its immobilization affected by the electric field at a solid-state support. Here, we exploit the dipole property of IgG and its ability to be oriented with field (Figure 1A,B).

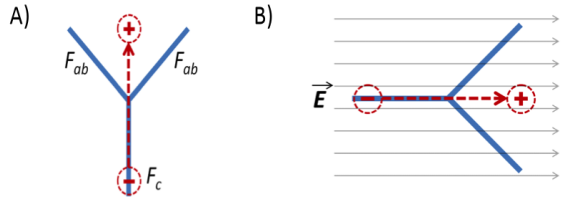

*Figure 1: **A)** Antibodies (IgG) have an Fc region and an Fab region where the isoelectric point of the Fab region is higher compared to the Fab resulting in dipole behavior. **B)** The antibody reorients itself in the field direction.*

METHODS

We study the orientation of antibodies in rectangular microchannels in order to ensure uniform electric field across the channel (fabricated in PDMS 200 µm wide, 50 µm high, and 1 cm long). We apply electric field across the channel while physically adsorbing antibodies (0.02 mg/ml) to the base of the channel (Figure 2). We inserted Ag-AgCl electrodes at the inlet and outlet ports of the microchannel. We excited the electrodes with DC voltages up to 8 V. We independently optically verified that the voltages were not high enough to induce either electroosmotic flow or electrophoretic flow. We then removed the channel and scanned the surface with AFM.

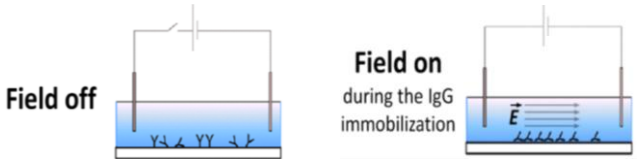

Figure 2: Schematic of AFM assay setup. Antibodies oriented with field during the immobilization step, then imaged with AFM.

RESULTS AND DISCUSSION

Our AFM images illustrated that application of electric field results in uniform orientation and lining up of the antibodies during the immobilization step (Figure 3), compared to the case where electric field is off and molecules become randomly oriented on the surface.

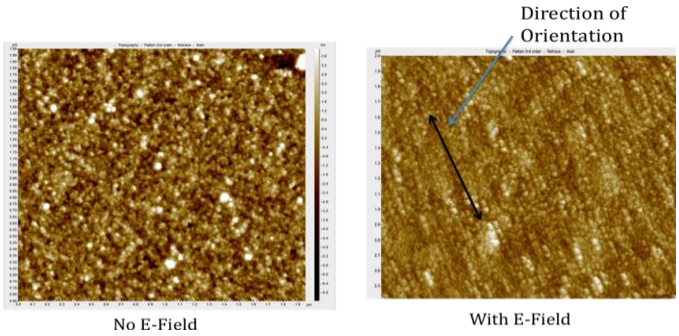

*Figure 3: Comparison of antibody coated surface when field is off during immobilization to when field is on. **A)** Two dimensional AFM image for when field is off. **B)** Two dimensional AFM image for when field is on. Results indicated that field results in antibodies orienting in a uniform direction.*

We diluted the IgG sample even further (1000X) in order to be able to image single antibodies. Results clearly showed that IgG molecules were uniformly oriented in a single direction (Figure 4) as predicted by our hypothesis (Figures 1 and 2).

We also apply this novel method in controlling the orientation of proteins to improve biosensor sensitivity. In the case of affinity-based sensors, the probe protein has specific sites or epitopes where binding occurs. Probe antibody orientation during immobilization onto the surface affects efficiency of target analyte capture. As an example, we studied the interaction of fluorescently tagged (FITC) anti-IgG with surface immobilized IgG (0.02 mg/ml), where only the immobilization process is controlled by electric field (Figure 5).

9781940470016/HH2014/$25©2014TRF
DOI 10.31438/trf.hh2014.86

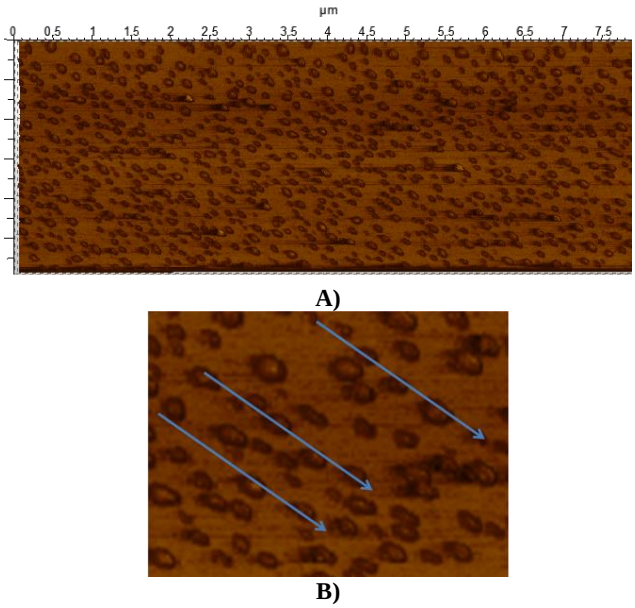

Figure 4: ***A)*** *IgG concentration diluted by 1000X so that single antibodies can be visualized with AFM. Antibodies are all oriented in the same direction.* ***B)*** *A zoomed in view of the original AFM image shown in part A with the arrows showing the orientation of molecules.*

All positive and negative control experiments were performed in parallel. Our negative control was the case where no electrodes were inserted in the channel during IgG immobilization. The representative captured snapshots from our experiments illustrate enhancement in the binding of anti-IgG and IgG as a result of applying lateral electric field during IgG immobilization (Figure 6A). The collective results for the fluorescence assay are presented in Figure 6B, which shows the improvement in signal intensity as we increased applied voltage. Our study demonstrates that the use of electric field can result in up to 40X enhancement in signal to noise ratio compared to normal physical adsorption. The improvement in sensitivity results both from favorable orientation of the antibody and also increase in the density of antibodies immobilized on the surface.

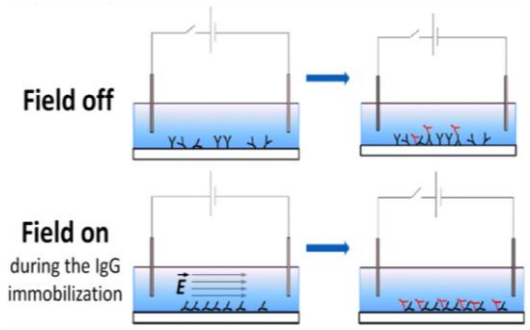

Figure 5: Fluorescent assay experimental setup. Field is modulated during the IgG immobilization. For the case where electric field is off IgG molecules are randomly oriented. For the case where field is on, IgG molecules are oriented on their sides so that the F_c region is exposed allowing an increase in binding of anti-goat IgG molecules.

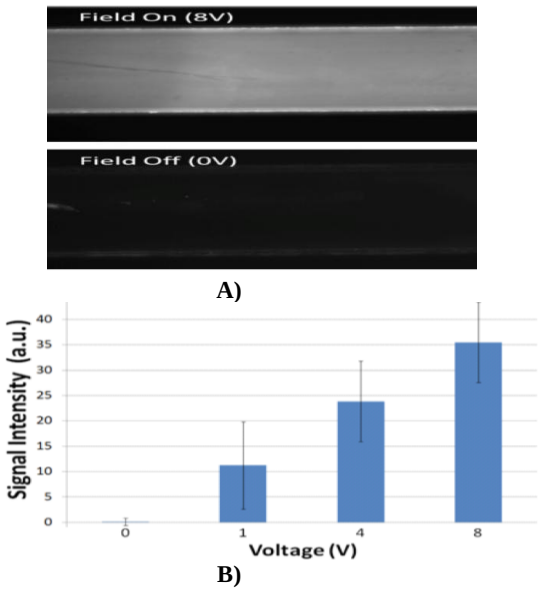

Figure 6: ***A)*** *The representative snapshots from our experiments illustrating enhancement in the binding of anti-IgG and IgG as a result of applying lateral electric field during IgG immobilization.* ***B)*** *Corresponding relationship of the fluorescent intensity verses the voltage applied, demonstrating the improvement in signal intensity as we increased applied voltage*

ACKNOWLEDGEMENTS

This work was supported by the Defense Advanced Research Projects Agency grant DARPA BAA-11-07. Fabrication of the devices was performed in the Stanford Nanofabrication Facility.

REFERENCES

[1] M. Javanmmard, S. Emaminejad, C. Gupta, J. Provine, R.W. Davis, and R.T. Howe, "Depletion of Cells and Abundant Proteins from Biological Samples by Enhanced Dielectrophoresis", Sensors and Actuators B: Chemical, vol. 193, pp. 918-924 (2013).

[2] S. Emaminejad, M. Javanmmard, R.W. Dutton, and R.W. Davis, "Use of Negative Dielectrophoresis for Selective Elution of Protein-Bound Particles", Analytical Chemistry, 84 (3), pp 1432–1438 (2012).

[3] S. Emaminejad, M. Javanmmard, R.W. Dutton, and R.W. Davis, "Smart Surface for Elution of Protein–Protein Bound Particles: Nanonewton Dielectrophoretic Forces Using Atomic Layer Deposited Oxides", Analytical Chemistry, 84 (24), pp 10793–10801 (2012).

[4] A. H. Talasaz, M. Nemat-Gorgani, Y. Liu, P. Stahl, R. W. Dutton, M. Ronaghi, and R. W. Davis , "Prediction of protein orientation upon immobilization on biological and nonbiological surfaces", Proc. Natl. Acad. Sci. (103) 14773 (2006).

CONTACT

*S. Emaminejad, same@stanford.edu

HIGH THROUGHPUT, MULTI-CHANNEL, NANO-MECHANICAL MEASUREMENTS OF SINGLE PLATELET CONTRACTION AS A DIAGNOSTIC MICRODEVICE FOR CLOTTING AND BLEEDING DISORDERS

David R. Myers[1,2], Yongzhi Qiu[1,2], Ashley Carson Brown[2], Yumiko Sakurai[1,2], Reginald Tran[1,2], Byungwook Ahn[1,2], Robert Mannino[1,2], Meredith Fay[1], Hunter Strauss[2], Todd Sulchek[2], Andrew Lyon[2], Thomas Barker[2], Wilbur A. Lam[1,2]

[1] Emory University School of Medicine, Atlanta, Georgia, USA

[2] Georgia Institute of Technology, Atlanta, Georgia, USA

ABSTRACT

Platelet contraction, which occurs during blood clot formation, is highly variable and dependent on the local mechanical and biochemical environment. We present a novel device capable of measuring individual platelet contraction in a high throughput manner. Platelets adhere and contract on micron-sized protein stamps patterned on polyacrylamide strips, which have tunable stiffness. Four polyacrylamide strips are placed in a device and each is encased in a separate microfluidic, enabling precise control of the biochemical and flow conditions around each platelet. Using this device, we demonstrate how forces applied by platelets change with differing biochemical agonists and substrate stiffness.

INTRODUCTION

Clot mechanics and disease

Blood clots are composed of fibrin, platelets, other blood cells, and proteins which interact to prevent hemorrhage (Figure 1). During clot formation, platelets apply tensile forces to the fibrin mesh, reducing its overall size and increasing the stiffness of the clot. Previous studies on clot formation have shown that the mechanical properties of clots are related to thrombotic or hemostatic diseases [1]. For example, clots are 50% stiffer and more resistant to dissolution in young patients with post-myocardial infarction [2] than clots from healthy controls. In addition, mechanical properties of clots formed from peripheral blood are altered in patients who develop idiopathic thromboemboli or acute ischemic strokes compared to those from healthy controls [3, 4]. As such, understanding clot mechanics is of vital importance to fundamentally understanding thrombosis and thromboembolism in cardiovascular disease and stroke.

However, there is currently no diagnostic test to assess platelet contraction force, especially at the single cell level and in the context of different mechanical environments, which has previously been demonstrated to significantly affect the platelet contraction force [5]. Furthermore, platelets have a wide variance in applied forces for a given mechanical and biochemical condition. As such, statistically significant results will require large numbers of measured platelets.

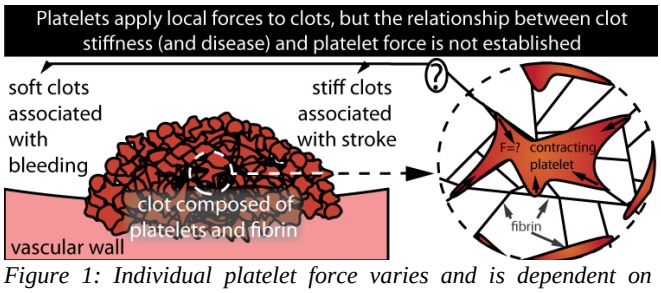

Figure 1: Individual platelet force varies and is dependent on environmental factors. To understand how platelet force correlates to clot stiffness, and thus pathological conditions, population data on platelet contraction in a variety of biophysical and biochemical conditions is needed.

Previous work on platelet contraction

Several methods have been used to measure platelet contraction at the single cell level using atomic force microscopy [5] or traction force microscopy [6]. Other groups have measured small aggregates of platelets using PDMS microposts [7]. The AFM experiments specifically varied the mechanical stiffness of the cantilever and also created an infinite stiffness condition, finding that platelets apply increasing force with increasing mechanical stiffness.

Alternatively, microposts have been used to measure small aggregates of platelets and have been proposed for measuring single platelet contraction. In this scheme, microposts are coated with a protein and platelets adhere to and move the top of the posts. Our calculations estimate the need for sub-micron microposts to measure single platelet contraction, which would be extremely difficult to fabricate and measure with precision. Another concern is that studies examining how platelets are affected by different stiffness conditions are difficult since changing the post stiffness requires changing the surface area exposed to the platelet. Since the proteins which the platelet adheres to during contraction also activate the platelet, any results derived using microposts are confounded by this effect.

A diagnostic capable of measuring the nano-mechanics of single platelet contraction in a high throughput manner can meet this clinical need and potentially revolutionize how we assess platelet function, and ultimately enable clinicians to better predict heart attacks and stroke.

DESIGN CONSIDERATIONS

One recent technique greatly reduced the computational and experimental constraints by creating arrays of fluorescently tagged protein dots on the surface of a polyacrylamide gel using lithographic techniques [8]. Cells adhere to a collection of dots and may move each dot independently. The cell may apply an independent traction force, $\boldsymbol{T}$, to each calculated as:

$$\boldsymbol{T} = \frac{2\pi G a \boldsymbol{u}}{2-\nu} \qquad (1)$$

where G is the shear modulus, a is the dot radius, ν is Poisson's ratio, and $\mathbf{u}$ is the displacement vector. Hence, a simple measurement of the displacement of the dot provides the force applied to the dot by the cell or platelet of interest. The mechanical properties of polyacrylamide are well characterized and can be tuned by simply changing the ratios of precursor materials [9].

Building on this concept, we have created a nanomechanical device which is able to measure the individual contraction of large numbers of platelets in a number of different biophysical and biochemical conditions (Figure 2). Platelets land, attach to, and contract pairs of protein dots which are patterned on a deformable poly-acrylamide (PAA) gel which is well characterized mechanically. The dot movement is linearly proportional to the applied contractile force [8], measured visually and analyzed using

9781940470016/HH2014/$25©2014TRF
DOI 10.31438/trf.hh2014.87

an image processing code written with MATLAB. By miniaturizing the gels into strips and surrounding them with a microfluidic, several different biochemical and biological conditions may be tested simultaneously. Furthermore, the microfluidic reduces the sample size and enables shear flow conditions, but more importantly limits the amount of time platelets spend in solution above the gel surface. All of this is achieved while being optically transparent and bio-compatible.

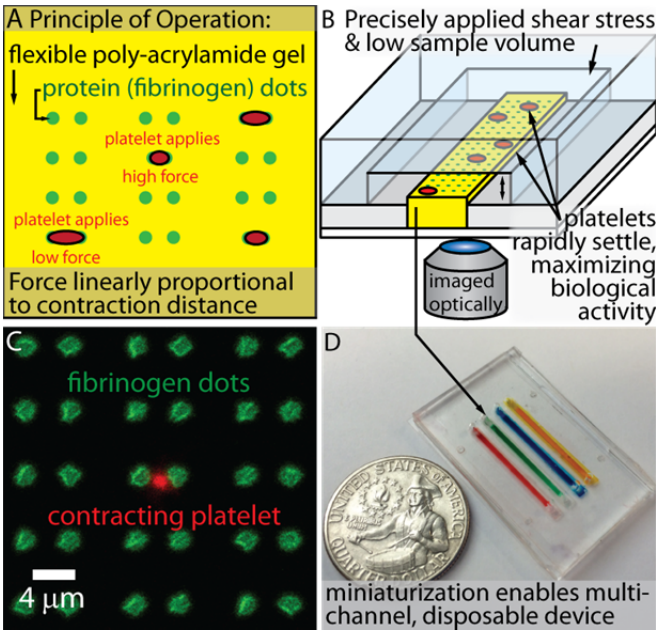

Figure 2: A) Platelets land, adhere, and contract the fibrinogen dots together. The applied force is linearly proportional to the contraction distance. B) Casting the gels in a strip and enclosing in a microfluidic creates the ability to precisely control applied shear stress, minimizes sample volume, and enables platelets to rapidly settle. C) Actual optical image of contracting platelet on fibrinogen dots. D) Actual device with four gel strips, each of different stiffness (and biochemical condition if desired).

In designing this system, it is important to note that platelets circulate through the bloodstream in a discoid, nominally inactive or resting state. When stimulated by certain agonists, such as thrombin or adenosine diphosphate (ADP), platelets experience immediate shape change, adhere to surfaces, and eventually clot. These agonists also upregulate integrins which assist in adhering to the protein dots on the gel (specifically $\alpha_{IIb}\beta_3$). As such, platelets are loaded into the gels with agonist, but since they also begin undergoing shape change, one concern is that the platelet is expending energy which ultimately would be used towards acto-myosin mediated contraction. By capitalizing on the unique ability of microsystems to minimize dimensions, platelets are on the gel surface in a matter of minutes rather than an hour. Once platelets reach the surface of the gel, they attach to a single dot, span to a neighboring dot, and contract. The force applied to the dots by the platelets will move them closer together, and the subsequent applied force can be calculated using equation 1.

The sensitivity of the system is dependent on the optical resolution and the amount of displacement experienced by a protein dot for an applied force. The optical resolution in this system is dependent on how images are acquired. Typically, imaging is done from the bottom of the device. The coverslip is approximately 130 μm thick, and the hydrogels are up to 400 μm thick. As such, imaging was typically performed with a 20x (0.8NA) objective with 488 nm light. In general, it was possible to resolve dot movements of 100nm or greater. As such, it was important to maximize the movements of the dot for a given force. Previous measurements determined average force applied by platelets for a given simulated substrate stiffness [5]. Since the dot size and displacement are inversely proportional for a constant force, as shown in Eq 1, the dot size was minimized to maximize displacement. Since large arrays of dots were needed, the dot diameter was practically limited to 1 μm, which was the photolithographic limit of available tools. This design constraint does assume that the platelet contraction force is independent of the dot area. In extreme cases, this would be of concern since the protein dots themselves contribute to platelet activation and contraction through the $\alpha_{IIb}\beta_3$ integrin.

The optimal dot spacing distance was determined from previous studies which examined the ability of platelets to span protein patterns on glass [10]. Here, it was important to balance the ability of platelets to span the gap between proteins with the range of forces which could be measured. Since the applied force is proportional to the dot distance, smaller gaps preclude the measurement of large forces. Here, a center to center distance of 4 μm was found to enable platelets to span the protein dots but still provide an adequate range to measure all contracting platelets for stiffnesses used in this work.

DEVICE FABRICATION

Laser Cut Gel Mold

To create the microdevice, long rectangular holes (1mm x 25mm) were laser cut into a thin sheet of pre-fabricated PDMS. The PDMS sheet was cleaned with scotch tape and covalently bonded to a 24x40mm No. 1 coverslip after treatment with an O2 plasma for 30s. The initial bonding after bringing the coverslip and PDMS sheet together was weak and reversible, but is improved after heat treating at 60C overnight. The PDMS/coverslip piece was silanized by O2 plasma treating, and subsequently treated with an 10%APTMES/90%Ethanol/0.01%Glacial acetic acid solution for 90 min at 60C. The slides were removed and rinsed with 70%ETOH/30% DI water, then rinsed with DI water. The slides were then placed in DI water for 1 hour at room temperature. This water treatment significantly improved the PDMS flexibility and surface adhesion such that it could create a good seal when pressed against a second coverslip. Next, the slides were then treated with a 2% glutaraldehyde solution at room temperature for 30 minutes. The slides were then rinsed with DI water and dried with nitrogen.

Fibrinogen Stamped Coverslip

Stamped coverslips (No 1.5, 18mm x 18mm) were prepared using an etched silicon mold, previously described [11]. Briefly, AF488 fibrinogen was incubated on 10mm x 10mm x 3mm PDMS squares at 30ug/mL for 1 hour. A silicon mold, composed of an array of etched holes was ultrasonically cleaned in ethanol for 30 min, rinsed with DI water, dried, and treated with an O_2 plasma for 30s. The PDMS squares were rinsed with DI water, air dried, and placed on the silicon mold. After adhering to the mold, the PDMS squares were removed and placed on 25mm coverslips, which had previously been treated with an O_2 plasma for 30s. The silicon mold was preferred over using PDMS pillars to stamp the coverslip since the silicon based technique is capable of creating small fibrinogen features with large empty spaces. Then the PDMS squares were removed, leaving fibrinogen dots the 18mm x 18mm coverslip.

Mold Assembly

The fibrinogen coverslip was then inverted over the PDMS/coverslip piece. The use of the 18mm x 18mm coverslip with the long rectangular holes (25mm), creates a channel with an

enclosed center and open ends. The entire piece was placed in a -30mm Hg vacuum for 30 minutes just prior to placement into the argon glovebox. The vacuum helps remove some of the air from the PDMS, which interferes with gel polymerization. By stamping a large square of fibrinogen dots (15mm x 15mm), and using much smaller channels, some fibrinogen dots were always over the top of the polyacrylamide gel, easing alignment concerns.

Polyacrylamide Gel Preparation and Casting

A polyacrylamide solution with a ratio of acrylamide to bis-acrylamide was created for each desired stiffness [9], with PBS. To assemble, a polyacrylamide solution, TMED, and APS, and NHS-ester were mixed in the glovebox directly prior to use. We specifically optimized this recipe to work in an argon glove box to reduce the amount of unpolymerized gel both along the edges of the coverslip and especially in the microdevice. To do so, the amount of TMED and APS typically used were reduced by 10, and the working time was optimized to several minutes to ensure that the gels could be created in a rapid fashion.

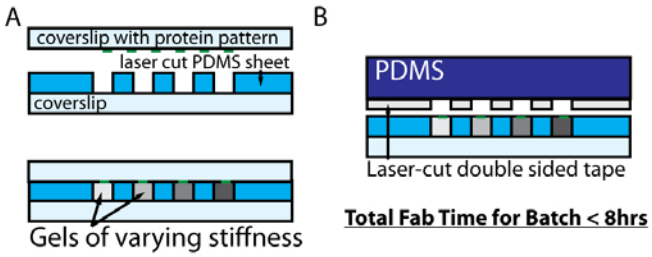

Figure 3: Key fabrication steps: A) Protein is transferred from a stamped coverslip onto gels after the casting process. B) A microfluidic is adhered with a laser-cut double sided tape, leaving the protein intact

The components were kept separate until needed, since the gels will polymerize and since NHS-ester degrades in water. The liquid gel solution was then cast into the channels created by the coverslip and laser machined PDMS using a 20 µL pipette. After polymerization (3 hrs) the gels were removed from the glovebox, and the top coverslip was discarded. Gels were then placed in PBS overnight.

Microfluidic Top

To cover the hydrogels, a separate SU-8 mold was fabricated, enabling the creation of PDMS microfluidic channels which are slightly larger than the hydrogel strips. Similarly, a piece of double sided tape was laser cut with rectangular holes matching that of the PDMS microchannel cover. After an overnight soak, the hydrogel chip was dried, with care taken to keep from displacing the hydrogels. Since PDMS sheet surrounding the hydrogels is hydrophobic, water tends to bead on the surface, facilitating removal with an aspirator. The double sided tape was then placed around the hydrogels, and the PDMS microchannels were then pressed onto the double sided tape. PBS was then flown into the enclosed channel until the device was ready for use. The double sided tape approach is unique in that it provides rapid attachment of a microfluidic without affecting the patterned proteins.

Experiment

Blood was drawn by median cubital venipuncture into acid-citrate-dextose (ACD) solution 2. Blood was spun at 150 G for 15 minutes, platelet rich plasma was subsequently removed and further spun at 900 G. The resulting platelet pellet was resuspended in Tyrode's buffer with 0.1% bovine serum albumin. Platelets, 5mM of $CaCl_2$, 5mM of $MgCl_2$, and agonist were added to the device and allowed to incubate for 2 hours. Platelets were then imaged using a Zeiss LSM 700-405 confocal microscope.

Platelet Analysis

Platelets were analyzed using a MATLAB script which measured the fibrinogen dot areas, and calculated the center to center distance of the fibrinogen dots. High pattern fidelity was achieved in creating the gels, but dots without platelets were also measured for comparison. Only platelets which spread over two dots and were free of significant filiopodia extending to other dots (in the case of thrombin related measurements) were counted. The platelet density was optimized to minimize platelet aggregates, and occasional platelet aggregates were not counted.

RESULTS & DISCUSSION

This device has enabled the measurement of hundreds of platelets to date and has quantitatively measured the contraction force in a number of different biomechanical and biochemical conditions. The data is similar to the measurements taken by AFM, but with a much higher sample size. This specific distribution is not a normal distribution by Shapiro-Wilk at $\alpha = 0.05$ (Figure 4).

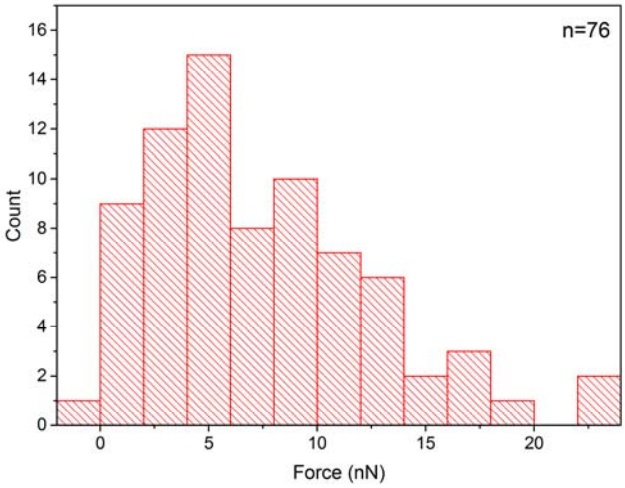

Figure 4. Distribution of platelet forces on a 25 kPa gel with 1U/mL of thrombin. The data agrees with previous measurements, albeit with a much higher sample number.

The casting process for any hydrogel stiffness between 0.5 and 100 kPa is identical, enabling measurements of platelet response to the mechanical microenvironment with a single sample, removing uncertainty with day to day variations. This data shows that platelets are able to modulate the amount of force applied simply by changing the local microenvironment stiffness (Figure 5). Surprisingly, platelet contraction distances remain fairly constant among the different stiffness conditions, and are typically between 0.1 to 0.5 µm. This data also closely matches the previous AFM measurements [5], indicating that platelet contraction forces are generated independent of the exact surface used for measurement. The atomic force microscope experiments specifically used fibrinogen coated silicon nitride cantilevers, and the current experiments are using fibrinogen coated hydrogels.

These current experiments have also begun to quantify the exact differences in platelet contraction depending on the agonist used. Blood clots have been shown to be composed distinct regions, specifically a core of platelets activated by thrombin and a shell, activated by ADP [12]. The shell is composed of loosely attached platelets, permeable to 70kD dextran and eventually reduces in size. Here, it is shown that the contractile forces of platelets activated by ADP are significantly lower than that of

thrombin, adding additional insight into how platelets can modulate their response depending on the local microenvironment.

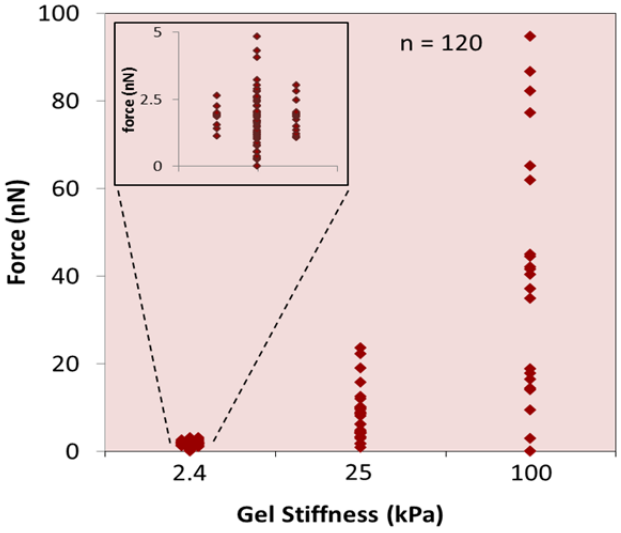

Figure 5: Platelets modulate the applied force based on the substrate stiffness. This data represents some of the most extensive gathered to date. The exerted forces are comparable to a muscle cell when corrected for size.

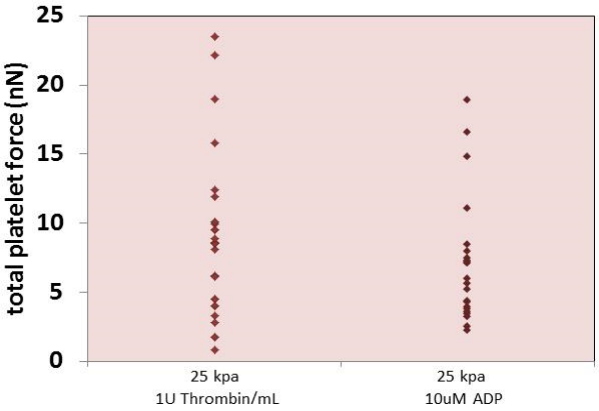

Figure 6: Different biochemicals alter the applied platelet force. Current hemostatic research indicates that a developing clot has two layers, a tightly bound inner layer, activated by thrombin, and an outer layer activated by ADP, which eventually peels off. Here we show that the different platelet activators also modulate the applied platelet force.

More importantly, this work establishes key metrics to identify healthy platelet contraction. By comparing clinical samples of patients with known bleeding disorders, it will now be possible to test the hypothesis that clot mechanics is directly affected by impaired or overactive platelet contraction.

CONCLUSION

Hydrogel casting integrates soft protein patterned surfaces with existing microtechnology, enabling a new class of precision device which more closely resembles the biological microenvironment. This is the first device to ever successfully measure large populations of platelets, with the data presented being the largest accumulated to date on individual platelet contraction. The device combines common microfabrication strategies with poly-acrylamide gel techniques (Figure 3) creating a rapid, disposable diagnostic device which measures real time platelet contraction. We have already characterized the contractile forces of hundreds of platelets, showing that the forces are normally distributed (Figure 4) and change under differing biophysical (Figure 5) and biochemical conditions (Figure 6) found in the body. This data will provide much needed information to inform clot contraction models as well as provide baseline data to characterize abnormal platelet function. This will lead to new diagnostics indicating increased risk for stroke or excessive bleeding, enabling proactive measures and potentially saving lives. Measurements of clinical samples are already underway.

REFERENCES

[1] J. W. Weisel, "Enigmas of Blood Clot Elasticity," *Science,* vol. 320, pp. 456-457, April 25, 2008 2008.

[2] J. P. Collet, Y. Allali, C. Lesty, M. L. Tanguy, J. Silvain, A. Ankri, *et al.*, "Altered Fibrin Architecture Is Associated With Hypofibrinolysis and Premature Coronary Atherothrombosis," *Arterioscler Thromb Vasc Biol,* vol. 26, pp. 2567-2573, November 1, 2006 2006.

[3] A. Undas, A. Slowik, P. Wolkow, A. Szczudlik, and W. Tracz, "Fibrin clot properties in acute ischemic stroke: relation to neurological deficit," *Thromb Res,* vol. 125, pp. 357-61, 2010.

[4] A. Undas, K. Zawilska, M. Ciesla-Dul, A. Lehmann-Kopydlowska, A. Skubiszak, K. Ciepluch, *et al.*, "Altered fibrin clot structure/function in patients with idiopathic venous thromboembolism and in their relatives," *Blood,* vol. 114, pp. 4272-8. Epub 2009 Aug 18., Nov 5 2009.

[5] W. A. Lam, O. Chaudhuri, A. Crow, K. D. Webster, T.-D. Li, A. Kita, *et al.*, "Mechanics and contraction dynamics of single platelets and implications for clot stiffening," *Nat Mater,* vol. 10, pp. 61-66, 2011.

[6] S. S. Henriques, R. Sandmann, A. Strate, and S. Köster, "Force field evolution during human blood platelet activation," *Journal of cell science,* 2012.

[7] X. M. Liang, S. J. Han, J.-A. Reems, D. Gao, and N. J. Sniadecki, "Platelet retraction force measurements using flexible post force sensors," *Lab on a Chip,* vol. 10, pp. 991-998, 2010.

[8] S. Polio, K. Rothenberg, D. Stamenović, and M. Smith, "A micropatterning and image processing approach to simplify measurement of cellular traction forces," *Acta biomaterialia,* vol. 8, pp. 82-88, 2012.

[9] R. T. Justin and J. E. Adam, "Preparation of hydrogel substrates with tunable mechanical properties," *Current protocols in cell biology,* 2010.

[10] A. Kita, Y. Sakurai, D. R. Myers, R. Rounsevell, J. N. Huang, T. J. Seok, *et al.*, "Microenvironmental Geometry Guides Platelet Adhesion and Spreading: A Quantitative Analysis at the Single Cell Level," *PLoS ONE,* vol. 6, p. e26437, 2011.

[11] A. C. von Philipsborn, S. Lang, A. Bernard, J. Loeschinger, C. David, D. Lehnert, *et al.*, "Microcontact printing of axon guidance molecules for generation of graded patterns," *Nature protocols,* vol. 1, pp. 1322-1328, 2005.

[12] T. J. Stalker, E. A. Traxler, J. Wu, K. M. Wannemacher, S. L. Cermignano, R. Voronov, *et al.*, "Hierarchical organization in the hemostatic response and its relationship to the platelet-signaling network," *Blood,* vol. 121, pp. 1875-1885, 2013.

CONTACT

*W.A. Lam, tel: +1-404-727-7473; wilbur.lam@emory.edu

MICROARRAY ELECTRODES FOR IMPEDANCE IMAGING AND ELECTRICAL CHARACTERIZATION OF *EX-VIVO* HUMAN LIVER METASTASES FROM COLORECTAL CANCER

Michael Karnes[1], *Ryan Snodgrass*[1], *Emily Sequin*[1], *Charles Hitchcock*[2], *Edward Martin, Jr*[3], *Shawnn D. Nichols*[3], *Carl Schmidt*[3], *Sherif Abdel-Misih*[3], *Mark Bloomston*[3], *Vish Subramaniam*[1*], *Shaurya Prakash*[1*]

[1] Department of Mechanical and Aerospace Engineering, The Ohio State University, Columbus, Ohio, USA
[2] Department of Pathology, The Ohio State University, Columbus, Ohio, USA
[3] Department of Surgical Oncology, The Ohio State University, Columbus, Ohio, USA

ABSTRACT

An image of morphologically distinct regions in resected human liver tissue containing metastatic colorectal cancer was generated using micro-electrical impedance spectroscopy (μ-EIS), providing quantitative information on tissue properties and structure, reflecting local gradients in electrical conductivity and permittivity. These impedance measurements were able to differentiate between regions of tumor and non-tumor tissue, allowing for the direct inferences of tissue microstructure and disease state. This work consequently provides major advancements toward a microscale instrument for the real time quantitative differentiation of tumor and non-tumor tissues in the surgical field, aiding the surgeon in selecting proper margins, which have proven to be critical in the long term survival of cancer patients.

INTRODUCTION

The mechanisms by which normal cells in the colon mutate to become cancerous are still being elucidated. As the solid tumor grows, cells will migrate from the primary cancer site to distant organs in the body as metastatic disease. In colorectal cancer, the liver is a common site for metastatic spread and surgical resection is the gold standard in managing such patients. A successful surgery is defined as the complete resection of the tumor with a finite rim of healthy or normal surrounding tissue, referred to as the surgical margin. It is within this rim that the transition from tumor to normal tissue occurs, and is termed the tumor interface. In colorectal liver metastases, surgeries with margins of < 1 mm pose a significant risk to patients, with a 5-year post-treatment survival rate of only 17%, compared to 68% for surgeries with a margin of > 1 mm [1]. Current surgical techniques rely on the surgeon's visual and tactile evaluation of the liver, augmented with ultrasound assessment, to identify the target tumors, estimate the margin, and plan the resection. Margins are then confirmed via optical microscopy and pathology post-surgery.

It has been demonstrated that tumors have distinct electrical impedances as compared to surrounding normal tissue [2]. For biological samples, the electrical impedance is often referred to as bioimpedance, and describes the complex electrical resistance of a tissue to a voltage or current signal, comprised of charge flow and charge storage within the sample. Commonly these properties are reported as an admittance, $Y = K\sigma + K\varepsilon_0\varepsilon_r$; where, σ is the electrical conductivity, and ε_r is the relative permittivity of the sample. K is a lumped geometric probe parameter, describing the current path in the sample and probe-sample interactions. The lumped geometric probe parameter is found by calibrating the probe in a range of solutions with known conductivities likely matching the tissue properties [3].

In general, the response of tissues to AC electric fields is determined by tissue architecture and composition. However, certain tissue characteristics become dominant for charge transport, i.e. current flow in specific frequency ranges. It is generally believed that in the α dispersion range, 1 Hz – 100 kHz, counter-ion polarization along the cell membrane dominates the measured impedance. From 100 kHz – 1 MHz, the β dispersion range, the extra cellular fluid is believed to be the major contribution to the measured impedance [4, 5].

Previously, electrical or electrochemical impedance spectroscopy (EIS) measurements have been successfully used for imaging breast and prostate cancers, distinguishing tumor from normal tissue [5]. The purpose of this paper is to demonstrate the use of two μ-EIS measurement probes, one in a single 4-wire configuration used in a physical translation set-up and the second in a microarray configuration to quantify the differences between tissue types. Based on the quantification, an image contour was generated that provides a quick visual guide to tissue morphology and structure as mediated by gradients in electrical properties.

METHODOLOGY

Measurements were conducted on excised human liver tissue containing colorectal metastases as part of a study (protocol #2013C0009) approved by the Institutional Review Board (IRB) at The Ohio State University. After surgical resection, the tissue was immediately transported in a sealed container to the Department of Pathology for sectioning relevant tissue for clinical requirements. Residual remnant tissue was obtained for inclusion into this study, and EIS measurements were collected with all measurements being initiated within 2 hours of tissue removal from the patient.

The physical dimensions and initial weight of the tissue were measured along with ambient temperature. Digital photographs were taken and the tissue marked with India ink as a reference for registration of subsequent measurement locations. The tissue was then placed on a computer controlled stage, where the single 4-wire μ-EIS probe was moved to the origin mark and the coordinates zeroed. From here, the probe was moved to the desired measurement locations, and measurement coordinates were recorded. The probe, as shown in Figure 1, penetrated the tissue to a depth of 4 mm.

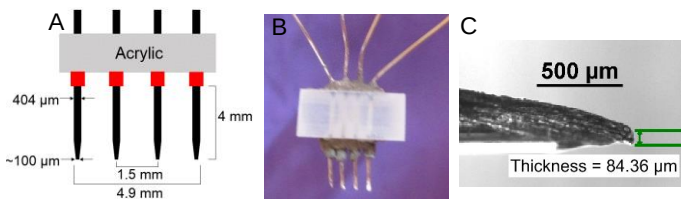

Figure 1: A. Probe schematic with dimensions. B. Digital image showing unit-cell for a 4-wire probe used for μ-EIS. C. Optical microscope image at 4x magnification to show the mechanically sharpened tip which allows easy penetration of tissue.

9781940470016/HH2014/$25©2014TRF
DOI 10.31438/trf.hh2014.88

The 4-wire probe was made using 99.9% pure (Alfa Aesar, MA, USA) Platinum (Pt) wires. In this setup, a 30 μA RMS current was injected by the outer two electrodes, while voltage is measured by the inner two. The entire probe is ~ 4.9 mm in length, and has a pin pitch of 1.5 mm. Once all measurements had been completed, the tissue weight was recorded again to determine the weight lost, most likely due to tissue desiccation.

The recorded impedance data was post-processed using MATLAB. As a representative analysis example, using the marked origin, and location coordinates, the probe footprints were plotted onto the photograph, shown in Figure 2. Each point was then classified as normal, tumor, or interface by measuring the number of pixels between the center of the measurement location to the closest tumor edge, as shown in Figure 2. Points within a half probe length radius (~ 2.45 mm) of a tumor edge were labeled interface. Points within the tumor and greater than a half probe length away from the edge were labeled tumor; while those more than half probe length away from the visible tumor edge on the normal tissue side were classified as normal tissue. The classification of normal and tumor tissue for quantification of liver tissue has also been reported previously [2, 3].

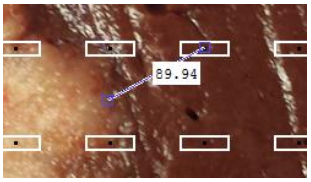

Figure 2: Photograph of specimen liver tissue with probe footprint plotted. The figure also shows the pixel distance measuring tool illustrating classification scheme for determining normal, tumor, or interface region in ex vivo human liver tissue.

The second probe, a microarray probe comprised of a two row arrangement of 16 electrodes each with a 1.3 mm pin pitch and 460 μm electrode or pin diameter as shown in Figure 2. The microarray probe eliminates the need to translate the 4-wire probe and allows for multiple measurements within an area defined by the probe footprint. A microcontroller (Arduino Mega 2560) controls four 32 pin multiplexers enabling the switching of active electrodes (4 per measurement) for sequential measurement of 26 locations without probe translation within a total probe footprint of ~ 2 cm length and ~ 3 mm width. Measurements with the microarray probe were conducted on porcine muscle tissue phantoms as opposed to human liver tissue due to the need to develop proof-of-concept and reliable probe operation before IRB-based protocol implementation on human liver tissue.

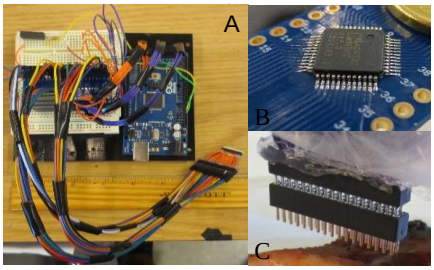

Figure 3: A. Complete electrode array, with probe, microcontroller, and multiplexer, in total taking up a 15 cm square (black supporting tray). B. A zoomed-in image of the 32 pin multiplexer. C. 32-electrode array with wires covered by plastic bag to prevent tissue contact and thereby contamination from likely tissue infections, for use with human tissue.

For all measured values, impedance data was recorded using a commercially available potentiostat (Interface 1000 from Gamry Instruments, PA, USA). A constant current injection of 30 μA RMS amplitude over a frequency range of 100 Hz - 1 MHz was used. Frequencies below 100 Hz are known to induce electrode polarization, and therefore were not included [3,6].

Random error from repeated measurements was estimated to be ~ 4% of the measured value with instrument error being at most ~ 1% of the measured value. The data is presented as an arithmetic mean for the specific tissue type (normal or tumor). The errors bars represent the standard deviation of the mean. The measured phase and the results of a single tail Student t-test for a 95% confidence interval are also presented.

RESULTS AND DISCUSSION

Figure 4 shows conductivity, σ of the data collected compared to previously published values. Note that the mean normal tissue electrical conductivity is lower by nearly an order of magnitude compared to that of the tumor; however, the variation in the tumor tissue is 60% greater than that of the normal as indicated by the error bars denoting the standard deviation. This is not surprising since it is known that tumors are not homogeneous, but consists of tissues at various disease states.

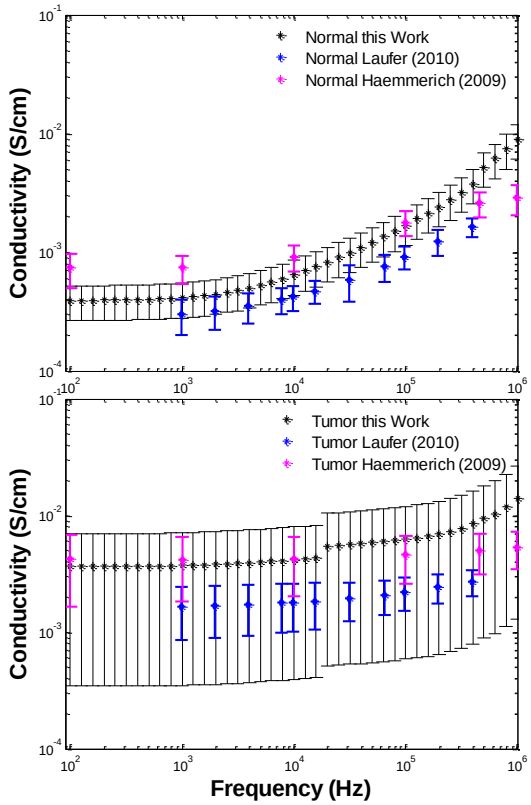

Figure 4: A. Normal tissue conductivity (mean ± SD) vs. frequency for normal tissue determined by methods previously reported. The plot also shows conductivity values reported by Laufer (2010) and by Haemmerich (2009). B. Tumor tissue conductivity (mean ± SD) vs. frequency for normal tissue determined by methods previously reported, and conductivity values reported by Laufer (2010) and by Haemmerich (2009). It should be noted that the two studies cited here are the only two peer-reviewed papers available on electrical properties of human liver tissue with metastatic disease from colorectal cancer.

Figure 5 shows the phase plots for the measured impedance with data reported as the arithmetic mean and standard deviation of the data points. Both normal and tumor tissue have a negative phase angle across the entire measured frequency range, implying that the tissue shows behavior analogous to a capacitive response. The tumor tissue produced a smaller phase shift, having a maximum magnitude of 10°, with the normal tissue at a 37° phase shift with statistical significance verified for a 95% confidence interval by the student t-test.

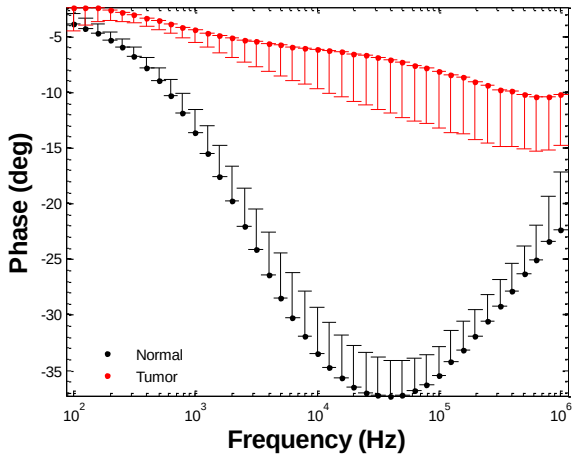

Figure 5: The phase arithmetic mean and standard deviation. Note that the tumor shows a smaller phase shift in the impedance data compared to normal tissue, with the negative phase angle implying a behavior analogous to a capacitive response.

Figure 6 demonstrates the ability of the μ-EIS method to distinguish tissue structural features by generating an equivalent impedance image of the tissue. Figure 6A shows a digital photograph of the specimen liver with measurement locations. The contour plot, in Figure 6B shows the phase shift at each measurement location at ~ 25 kHz, as a representative example. The contour image shows a discernible difference between the tumor and normal tissue with a gradient at the interface region. Furthermore, visual, qualitative comparison between Figures 6A and 6B also shows locations where blood vessels or other structures may have been present *in vivo* but do not exist (appear as holes or dark spots in digital images) in the *ex vivo* specimen.

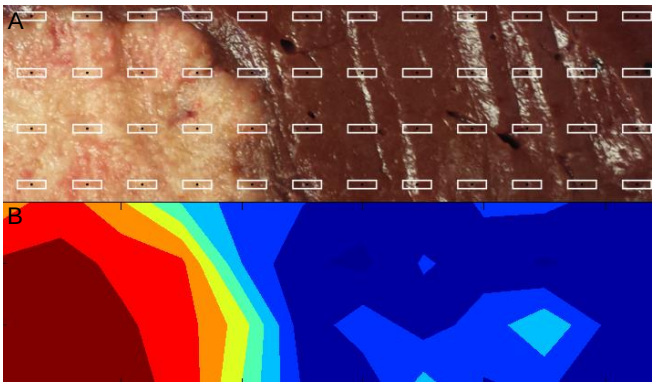

Figure 6: A. Digital image of liver sample. B. Contour plot of the specimen phase shift at ~ 25 kHz, with a visual representation of tissue structure and disease state. The scale goes from red at the highest magnitude of phase to blue at the lowest.

For the multiplexed probe, a representative data set for the porcine muscle tissue phantom is shown in Figure 7. With this probe, each placement yields measurements at 26 unique points within the probe footprint. The fat (as annotated on the digital image) has distinctly higher impedance than the muscle tissue. The point of transition is not clear likely due to the probe being in both parts of tissue during the same measurement, and requires further investigation.

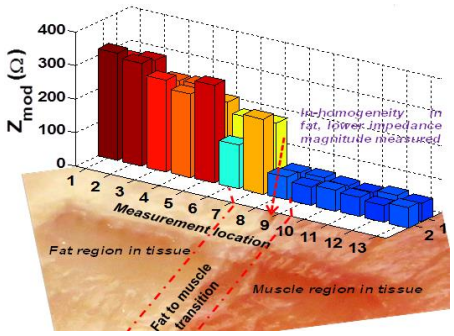

Figure 7: A bar graph plot showing magnitude of impedance and comparing the measurement locations to a visual representation of the tissue phantom.

CONCLUSION

Two μ-EIS probes were demonstrated for use in quantifying tissue types based on electrical impedance data. The phase shift in the impedance data was organized into an image contour to enable impedance imaging of the tissue to depict tumor from normal tissue. With the ability to reach finer spatial resolution underway in other experiments, the method shows promise for accurate tissue microstructure delineation.

ACKNOWLEDGEMENTS

The Authors acknowledge support from Karen Bellman and Benjamin Shurtz in data collection. Partial financial support from Samsung, Inc. is also recognized.

REFERENCES

[1] T.M. Pawlik, C.R. Scoggins, D. Zorzi, E.K. Abdalla, A. Andres, C. Eng, S.A. Curley, E.M. Loyer, A. Muratore, G. Mentha, L. Capussotti, and J.N. Vauthey, "Effect of surgical margin status on survival and site of recurrence after hepatic resection for colorectal metastases", Annals of Surgery, 241, 5 (2005).

[2] D. Haemmerich, D.J. Schutt, A.S. Wright, J.G. Webster, and D.M. Mahvi, "Electrical conductivity measurement of excised human metastatic liver tumours before and after thermal ablation", Physiol. Meas., 24, 251, (2009).

[3] S. Laufer, A. Ivorra, V.E. Reuter, B. Rubinsky, S.B. Solomon, "Electrical impedance characterization of normal and cancerous human hepatic tissue", Physiol. Meas., 31, 995 (2010).

[4] Miklavčič, D., N. Pavšelj and F. X. Hart (2006). Electric Properties of Tissues. Wiley Encyclopedia of Biomedical Engineering, John Wiley & Sons, Inc.

[5] K.R. Foster, H.P. Schwan, "Dielectric properties of tissues and biological material: a critical review", Crit. Rev. Biomed. Eng., 17, 25 (1989).

[6] Schwan, H. P. (1968), "Electrode Polarization Impedance and Measurements in Biological Materials", Annals of the New York Academy of Sciences, 148: 191-209.

CONTACT

*S. Prakash, tel: +1-614-688-4045; prakash.31@osu.edu
*V. Subramaniam, tel: +1-614-292-6096; subramaniam.1@osu.edu

OPTOFLUIDIC DEVICE FOR HIGH RESOLUTION AND MULTIPARAMETRIC MEASUREMENT OF SINGLE BIOLOGICAL CELLS

Antoine Leblanc-Hotte[1], Jean-Sébastien Delisle[2], Sylvie Lesage[2] and Yves-Alain Peter[1]
[1]Department of Engineering Physics, École Polytechnique de Montréal, Canada
[2]Hospital Maisonneuve-Rosemont Research Center, Canada

ABSTRACT

This paper reports a novel optofluidic device providing cellular sub-populations discrimination. We designed an optofluidic device based on an interferometric measurement able to discern cell types without fluorescent tags. The device yields a high sensitivity on the volume refractive index allowing for very small variations between cell populations to be detected. The optical sensing method for a single cell, at a fixed wavelength while the resonance peaks shifts, have proven to report various parameters linked to cellular intrinsic properties. Measurements collected with the device showed a significant difference between two analyzed cell types. To our knowledge, this is the only device that employs optical multiparametric and high-resolution measurements without fluorescent tags or dependency on shape or orientation on flowing cells.

INTRODUCTION

Flow cytometers are state-of-the-art equipments used mainly to classify cells within a given population. They evaluate granularity and size of hundreds of cells per second as well as identify key membrane proteins by fluorescence. However, they aren't able to differentiate some cellular sub-populations and have to use fluorescent tags to improve the specificity. Tagging manipulations are costly and laborious besides it only offers specificity over the presence of a specific protein, associated to a function, which doesn't always reflects a distinct population. Addressing these difficulties consist of the actual challenge for the advancement of research in this field.

Following this direction, we designed an optofluidic device based on an interferometric measurement able to discern cell types without fluorescent tags. The device yields a high sensitivity on the volume refractive index allowing for very small variations between cell populations to be detected. This lab-on-chip device has the potential to act as a tool for health specialists offering a supplementary specificity on diagnostic. To our knowledge, this is the only device that employs optical multiparametric and high-resolution measurements without fluorescent tags or dependency on shape or orientation on flowing cells.

This device is the continuity of a previously reported microsystem [1] which measured refractive indices of homogenous liquids with a resolution as high as 1.7 x10^{-5} RIU (Refractive Index Unit). The latest reported work at uTAS 2012 on this particular device presented results on glass beads measurements [2]. We detailed the working principle, the fabrication process and the classification of glass beads with different sizes. Other publications on similar biosensors either use scattering measurement [3] or resonant transmission spectra of an immobilized cell in an out-of-plane cavity [4]. This paper reports the latest developments on cellular classification based on high resolution and multiparametric measurement of single biological cells.

THEORY

Optical operation

Figure 1 shows the sketched 3D view of the designed optofluidic device.

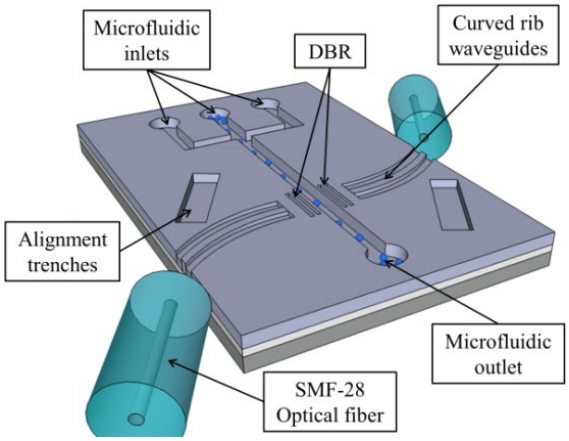

Figure 1: Sketched 3D view of the optofluidic device

Infrared light is coupled from a SMF-28 optical fiber into the integrated on-chip curved rib waveguides. These curved waveguides are used to discard the stray light from being collected in the output optical fiber. Consequently, the alignment trenches seen in the above figure are used for adjusting the angle of the optical fiber to match Snell-Descartes refraction at the interface of the curved waveguide. Also, the waveguides ends are in the shape of triangles (as shown in Figure 2) to prevent a parasitic resonant cavity between the first mirror trench and the end of the waveguide. The buried oxide layer of the SOI acts as an optical confinement structure in the z-axis because of its lower refractive index. Moreover, these rib waveguides were designed to minimize coupling loss due to mismatch of the fundamental modes shapes propagating in the optical fiber and the waveguide.

Propagating light enters a Fabry-Perot cavity consisting of two distributed Bragg mirrors separated by the width of the microfluidic channel. These distributed Bragg mirrors were designed to achieve high reflectivity as well as being easily integrated in the first etching step. Such a configuration exhibits resonance properties on the wavelength due to the optical path restriction. Resonating wavelengths will repeat at a Free Spectral Range (FSR) and their Full Width at Half Maximum (FWHM) is a function of the quality factor of the cavity, related in part to the roughness of the mirrors. To efficiently characterize this Fabry-Perot cavity one must use the finesse defined as:

$$F = \frac{FSR}{FWHM} = \frac{\pi\sqrt{R}}{(1-R)} \quad (2)$$

Were R is the mirror reflectivity.

9781940470016/HH2014/$25©2014TRF
DOI 10.31438/trf.hh2014.89

Solid-State Sensors, Actuators and Microsystems Workshop
Hilton Head Island, South Carolina, June 8-12, 2014

Microfluidic operation

Figure 2 shows a schematic view of the working principle as well as the principal defined structures from microfabrication.

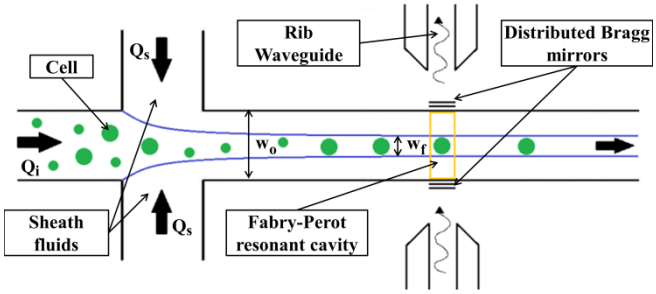

Figure 2: Schematic view of the working principle

The particular disposition of microfluidic channels enables the use of simple in-plane hydrodynamic focusing. The main governing relation is described in Equation 1, showing that only the ratio of sheath flow over inlet flow is enough to control the width of the focused flow, assuming a fixed width of the output channel.

$$\frac{Q_s}{Q_i} = \frac{1}{2\gamma}\left(\frac{w_o}{w_f}\right) - \frac{1}{2} \qquad (1)$$

Where Q_s is the flow rate of sheath fluid, Q_i is the flow rate of the inlet, w_0 is the width of the outlet channel, w_f is the width of the focused flow and γ is a form factor varying between 1 and 1,5.

Microfabrication process

The fabrication of this device uses a 4 inches Silicon On Insulator (SOI) wafer with an 11 µm thick silicon device top layer, a 2 µm thick Buried Oxide layer (BOX) and a 500 µm thick silicon handle layer. The complete microfabrication is achieved through a two-step process for which both steps include photolithography and Deep Reactive Ion Etching (DRIE).

Indeed, the first photolithography defines the microfluidic channels, 50 µm wide in the case of the output channel, and Distributed Bragg Mirrors (DBR). These structures are then etched through the whole thickness of the top device layer. A small percentage of oxygen is used in the DRIE process to reduce the scalloping generated by the alternating plasma deposition and plasma etching of the Bosch process. The second photolithography defines the waveguides which are then etched less deeply to create the targeted rib structure. A dicing saw was employed to polish while cutting the waveguides coupling side of the chips. The specially engineered blade, a resin matrix containing diamond with a low grit size, yields a roughness on the edge of the coupling area around 25 nm. Finally, a perforated Pyrex layer was anodically bonded on the top of the device sealing it for microfluidic operation. This top layer has ultrasonic etched holes aligned with microfluidic inlets and outlet of the device for subsequent tubes insertion and fixation with UV cured glue.

Figure 3 shows the profile of the rib waveguide and its fundamental optical mode as calculated by beam propagation method.

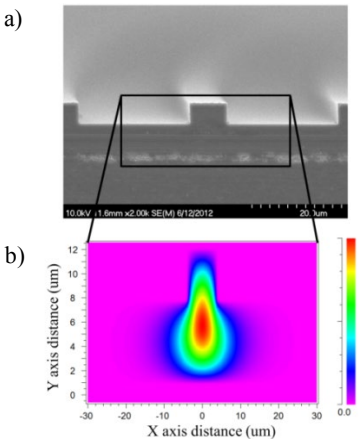

Figure 3 : a) SEM of the microfabricated rib waveguide and b) fundamental optical mode

Measurement principle

Figure 4 shows the image of a cell at the center of the cavity.

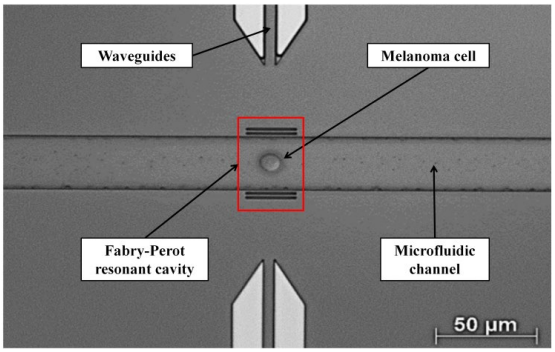

Figure 4: Cell flowing through the resonant cavity

When a cell flows through the cavity it modifies the resonance properties due to the variation of the volume refractive index. The increased optical path caused by a cell shifts the optical resonance positions towards longer wavelength as shown in Figure 5. Thus, a measurement at a fixed wavelength on the right slope of the resonance will record intensity variations. A tunable laser is used to adjust the working wavelength and an InGaAs photodetector is connected to an oscilloscope for fast acquisition of data.

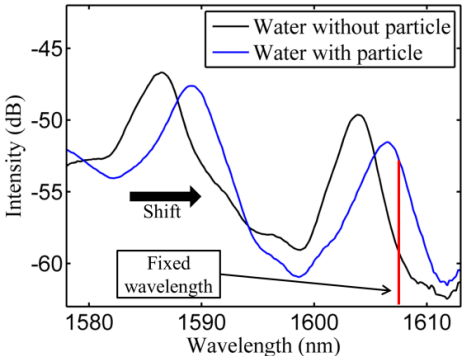

Figure 5: Position of Fabry-Perot resonance with and without a particle

Data collected on the oscilloscope was recorded for each cell flowing in the sensing area. A trigger was set to a value slightly higher than the background noise to avoid capturing a false cellular event. This type of measurement doesn't only report the volume refractive index of the cell flowing through but also various other parameters such as maximum value, rising time, full width at half maximum (FWHM), area under the wavelength resonance, etc. as shown in Figure 6, hence the term multiparametric. These parameters are correlated to intrinsic properties of the cell, such as size, granularity, nucleus size and density, cytoplasmic volume and composition, etc. Although the exact relation between measured parameters and intrinsic properties of the cell hasn't been determined yet, discrimination of cell sub-populations can still be achieved with only two independent parameters or combination of parameters.

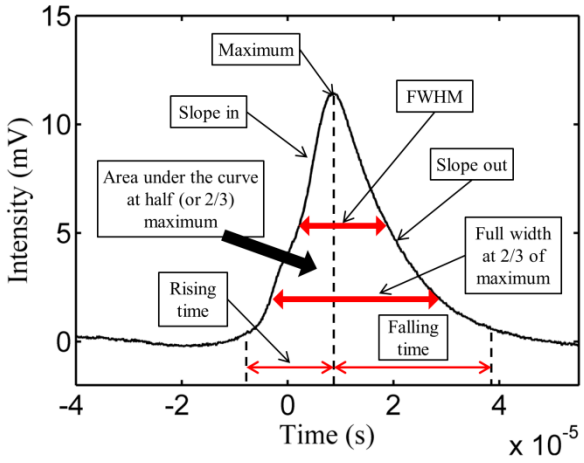

Figure 6: Parameters of a cell measurement at a fixed wavelength

RESULTS

Microfluidics

Hydrodynamic focusing was experimentally verified for different focused width. Varying the ratio of sheath flow over sample flow, as expressed in equation 1, gave a wide tunable range and control over the hydrodynamic focusing behavior.

Figure 7 shows in the upper image a low flow ratio of sheath over sample and the lower image shows a high ratio. In both cases the focused flow profile was very stable and well defined. The sample fluid was stained with trepan blue to gain optical contrast in the microscope.

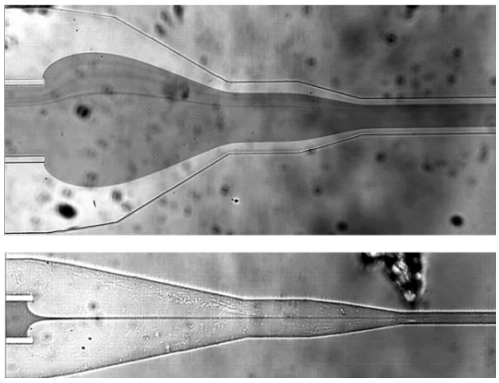

Figure 7: Hydrodynamic focusing under different conditions

Optics

Figure 8 shows the spectrum obtained from the integrated on-chip Fabry-Perot.

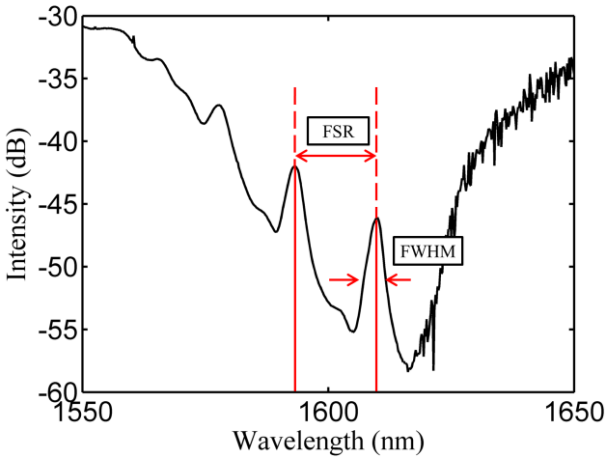

Figure 8: Typical optical spectrum from the on-chip Fabry-Perot

From the above spectrum, this device measurement revealed a FSR around 17 nm and a FWHM around 3.1 nm, thus yielding a finesse around 5.5 corresponding to a reflectivity (R) of 57%. Even if the finesse value is low, it is sufficient for the application described here. Indeed, assuming a sensitivity of 500 nm/RIU and an experimental setup detection limit of 0.01 nm the average resolution is expected to be of $2x10^{-5}$ RIU [1]. The calculated volume refractive index variation caused by a single cell (n_{cell}=1.36, d=10um) inside the resonant cavity filled with water (n_{water}=1.33, w=50um) is around $4x10^{-3}$ RIU. This refractive index variation is theoretically enough to be measured with our device since it corresponds to a shift around 2 nm of the resonance.

Single cell measurements

B16 cells and EL4 cells were cultivated following standard operating protocol and collected for analysis. B16 cells are adherent melanoma cells originating from mouse skin cancer and EL4 cells are suspended lymphoma cells originating from mouse T lymphocytes. These two immortal cell lines were chosen for a proof of concept because of their resemblance in size and granularity but still being distinguishable in a flow cytometer without fluorescent dye. Even with their resemblance, these cells have a totally different origin and role, thus a different composition and potential parameters measurable by our device.

Three different solutions were prepared for this experiment: two control solutions containing only one type of cells and a mixture in a ratio of 1:1. Collected measurements were statistically analyzed using a simple graphical gating program. The chosen parameters for cell classification were in this case FWHM and area under the curve at half maximum as shown in Figure 9. A comparative test was made with a Becton Dickinson FACSCalibur Flow Cytometry System without any fluorescent tags as shown in Figure 10. In both cases, each cell type was first tested alone to determine its specific region and delimitations.

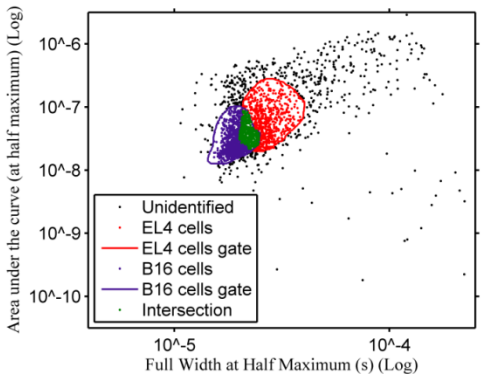

Figure 9: Typical cellular classification of the optofluidic device

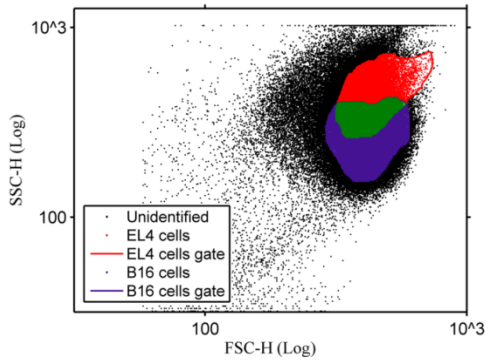

Figure 10 : Typical cellular classification of the flow cytometer

Graphically, it can be seen that for both the optofluidic device and the FACSCalibur Flow Cytometry System a similar and significant difference lies between the two cell types. Although both cell types are well identified, they still overlap each other. The magnitude of overlapping cells can be tuned by reducing the gates size of each cell type. Large gates include more cells but also render a higher overlap whereas small gates include fewer cells but a smaller overlap. The percentage of identified cells in each group is interpreted in term of sensitivity whereas the percentage of overlapping cell is interpreted as specificity. The goal is to identify the levels of sensitivity and specificity required by the experiment. Both the optofluidic device and the flow cytometer results were statistically analyzed when using large gates and small gates. Table 1 reports these statistics for the optofluidic device and Table 2 reports the statistics for the flow cytometer.

Table 1 : Identification statistics for the optofluidic device

	Large gates		**Small gates**	
	# of cells (% total cells)	**% on identified cells**	**# of cells (% total cells)**	**% on identified cells**
Total cells	3731	-----	3731	-----
Identified cells	2683 (72%)	100%	1312 (35%)	100%
EL4 cells	1667 (45%)	62%	601 (16%)	46%
B16 cells	1640 (44%)	61%	711 (19%)	54%
Intersection cells	624 (17%)	23%	0	0%

Table 2 : Identification statistics for the flow cytometer

	Large gates		**Small gates**	
	# of cells (% total cells)	% identified cells	# of cells (% total cells)	% identified cells
Total cells	126 195	-----	126 195	-----
Identified cells	95 923 (76%)	100%	53 236 (42%)	100%
EL4 cells	56 498 (45%)	59%	22 599 (18%)	42%
B16 cells	71 222 (56%)	74%	33 730 (27%)	63%
Intersection cells	31 797 (25%)	33%	3093 (2%)	6%

For the optofluidic device, these values show that large gates identified 72% of total cells for which 23% of cells were overlapping thus couldn't be associated to a group. For small gates, only 35% of total cells are identified but there is no overlap in this case. On the other hand, the flow cytometer statistics with large gates show that 76% of total cells are identified for which 33% are overlapping. For small gates, only 42% of total cells are identified but the intersection cells percentage is at a lower value of 2%. Moreover, the optofluidic device reports a cell type ratio close to 1:1 for the two gates whereas the flow cytometer reports a ratio a little further from this theoretical value.

CONCLUSIONS

In conclusion we have reported a microfabricated optofluidic device based on a Fabry-Perot resonant cavity able to discriminate cell populations. Cells are flowing through an optical sensing cavity by hydrodynamic focusing. Melanoma and lymphoma cells were analyzed with the optofluidic device and a significant difference between the two groups was found. Compared to a commercial flow cytometer, the optofluidic device gave similar results thus validating the proof of concept of our device.

ACKNOWLEDGEMENTS

This work is supported by the NSERC-CREATE ISS Training Program and travel support has been generously provided by the Transducer Research Foundation.

REFERENCES

[1] R. St-Gelais, J. Masson and Y.-A. Peter, "All-Silicon Integrated Fabry-Pérot Cavity for Volume Refractive Index Measurement in Microfluidic Systems", Applied physics letters, 94, 24 (2009).

[2] A. Leblanc-Hotte, R. St-Gelais and Y.-A. Peter , "Optofluidic Device for High Resolution Volume Refractive Index Measurement of Single Cell", International Conference on Miniaturized Systems for Chemistry and Life Sciences, Okinawa, Japan (2012), pp. 1330-1332.

[3] M. Rosenauer, W. Buchegger, I. Finoulst, P. Verhaert and M. Vellekoop, "Minituarized Flow Cytometer with 3D Hydrodynamic Particle Focusing and Integrated Optical Elements Applying Silicon Photodiodes", Microfluidics and Nanofluidics, 10 (2011), pp. 761-771.

[4] W. Wang, D.W. Kisker, D.H. Thamm, H. Shao and K. Lear, "Optofluidic Intracavity Spectroscopy of Canine Hemangiosarcoma", IEEE Transactions on Biomedical Engineering, 58, 4 (2011), pp. 853-860.

CONTACT

*Y.-A. Peter, yves-alain.peter@polymtl.ca

FABRICATION OF MAGNETIC MICROSTRUCTURES BY IN SITU CROSSLINKING OF MAGNETICALLY ASSEMBLED NANOPARTICLES

Camilo Velez [1], Isaac Torres-Díaz [2], Lorena Maldonado-Camargo [3], Carlos Rinaldi [2,3] and David P. Arnold [1]*
[1] Department of Electrical & Computer Engineering, University of Florida, USA
[2] J. Crayton Pruitt Family Department of Biomedical Engineering, University of Florida, USA
[3] Department of Chemical Engineering, University of Florida, USA

ABSTRACT

We present a photolithography-free fabrication technique to create magnetic microstructures using magnetically self-assembled iron oxide (Fe_3O_4) nanoparticles, which are subsequently crosslinked to each other via surface polymerization. This effort is a step toward low-cost roll-to-roll fabrication of free-floating micromagnetic actuators such as microswimmers, micro-stirrers, micro-tweezers, etc. Four main accomplishments are reported: (1) optimization of the particle deposition (self-assembly) conditions to achieve feature sizes down to 5 µm, (2) development of the polymerization process to crosslink the nanoparticles, (3) release of the microstructures from the substrate via a sacrificial layer, and (4) demonstration of the magnetic actuation of prototype structures.

INTRODUCTION

Magnetic microstructures are of growing interest for fluidic, biomedical, and even optical applications. A conventional "MEMS fabrication" approach for achieving such structures involves lithography, thin-film magnetic material deposition, and liftoff or etching [1], but such processes require complex, expensive fabrication tools. An alternative way to create magnetically responsive microstructures is by embedding magnetic particles in photoactive polymers [2]. However, the particle loading fraction is typically low to maintain photolithographic patternability. We introduce here a new method that uses magnetically directed self-assembly (rather than photolithography) to form microstructures of various sizes and shapes. Another group has used this concept to pattern magnetic nanoparticles on hard disk drive substrates to create optical gratings [3]. However, we extend this idea by crosslinking the nanoparticles using polymers and then releasing them from the substrate, with the aim of forming functional magnetic micro-components. Some groups have worked on crosslinking of magnetic nanoparticles for applications such as construction of biological scaffold materials for tissue engineering [4], fabrication of bio hydrogels for controlled drug delivery [5],[6], modification of optical properties in the creation of diffraction gratings [7], and separation of food dyes from water [8]. However, in all these cases the particles are crosslinked in to spheres or loose aggregates and do not possess more complex structure. Our approach facilitates flexible fabrication of complex microstructures that are mostly magnetic, rather than polymer, for maximum magnetic responsiveness.

EXPERIMENTAL METHODS

The overall process is shown in Fig. 1. First, superparamagnetic iron oxide (Fe_3O_4) nanoparticles (in this case, 17 nm diameter) are synthesized by thermal decomposition of an iron oleate precursor. The resulting oleic acid coating is oxidized to form carboxylic acid, which confers colloidal stability and permits subsequent crosslinking using polyamines. The nanoparticles are suspended in aqueous solution and then magnetically self-assembled onto a substrate, wherein regions of high field-gradient define the assembly pattern (e.g. line, circle, etc.). The field-gradient regions are created by spatially magnetized patterns in a magnetic tape, previously coated with a sacrificial layer. After the particles are assembled, they are crosslinked using branched polyethylenimine (PEI). The microstructures formed by this process are then released from the substrate by dissolving the sacrificial layer. More details on each of these steps are provided in subsequent sections.

Magnetic Nanoparticles

Iron oxide nanoparticles were synthesized by thermal decomposition of an iron oleate precursor using procedures described in [9]. This method yields magnetic particles coated with a monolayer of oleic acid, making them soluble only in organic solvents. However, the crosslinking method used in our experiments must be done in a water solution. Hence, the particles were converted to an aqueous solution by using a strong oxidizing agent to cleave the double bond present in the oleic acid chain obtaining carboxylic acid terminal groups [10], as shown in Fig. 2(a). We obtained negatively charged and electrostatic stabilized particles for crosslinking to polyamines.

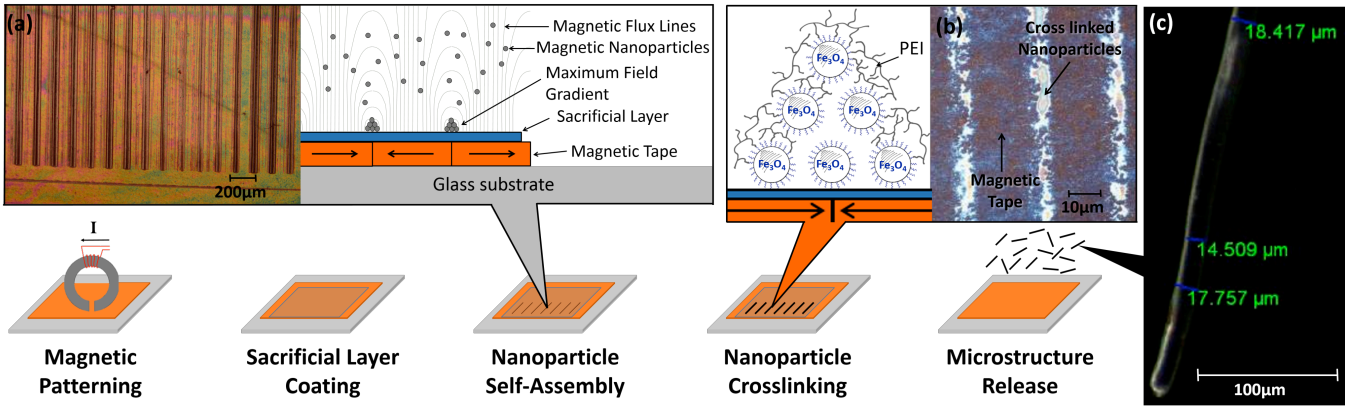

Figure 1: Fabrication method: (a) Nanoparticles self-assembled onto magnetically patterned substrate (audio cassette tape). (b) Nanoparticle surface modification and cross-linking with PEI using EDC and NHS. (c) Sacrificial layer dissolved, releasing magnetic structures.

9781940470016/HH2014/$25©2014TRF
DOI 10.31438/trf.hh2014.90

Solid-State Sensors, Actuators and Microsystems Workshop
Hilton Head Island, South Carolina, June 8-12, 2014

The particles were characterized using dynamic light scattering (DLS) to measure the hydrodynamic diameter (28.0 ± 1.18 nm). The physical diameter (17.0 ± 0.1 nm) was characterized by transmission electron microscopy (TEM) as shown in Fig. 2(c). Magnetic properties of the particles were also measured using a superconducting quantum interference device (SQUID) magnetometer. The data was fit to the Langevin equation using the procedure suggested by Chantrell [11] to estimate the magnetic particle size distribution of the sample, shown in Fig. 2(b). From this, the magnetic volume fraction φ was 0.062 %v/v, and the magnetic core diameter D_p = 9 nm and ln(σ) = 0.44. These results confirm monodispersity of the nanoparticles used during the experiments.

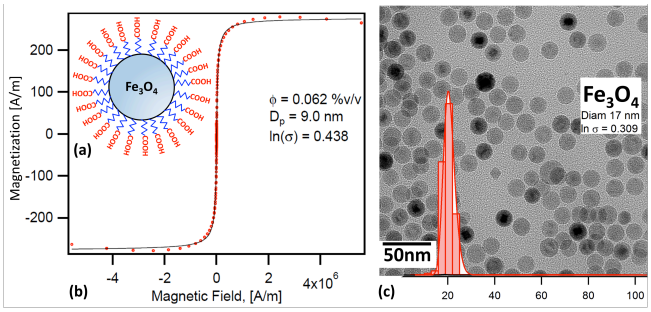

Figure 2: Fe_3O_4 magnetic nanoparticles. (a) Nanoparticle schematic showing the COOH group, (b) Magnetic hysteresis curve measured using SQUID. Red dots represent measured data, while black line represents the fitting of Langevin equation to the curve, (c) Background: TEM image of the nanoparticles. Foreground: size distribution of the particles via TEM image.

Magnetic Patterning of Cassette Tape Substrates

An audiocassette tape was used as a magnetic substrate to magnetically assemble the particles into pre-defined patterns, inspired by [12]. In initial experiments, the tape was recorded with a sinusoidal wave of 500 Hz at 20 kHz sampling rate to generate samples with simple line patterns with a fixed period of 25 µm. These lines were used to characterize the process and to generate a better understanding of the variables involved in assembly. In later experiments, samples of tape were selectively magnetized to generate arbitrary patterns using procedures reported in [13],[14]. Several example patterns are shown in Fig. 3.

Figure 3: Magnetic nanoparticles assembled in arbitrary patterns. Deposition time: 20 hours.

Before self-assembly of the particles, the magnetically patterned tape was coated with a sacrificial layer. Two different sacrificial layers were evaluated: (1) 350 nm of LOR 3B (polydimethylglutarimide based resist) and (2) 85 nm of PMMA-A2 (polymethyl methacrylate). The sacrificial layer has an important role in the particle deposition and must be chosen carefully. The conditions of the nanoparticles and the sacrificial polymer can generate high hydrophobicity, thereby inhibiting deposition or weakening dramatically the adhesion of the nanoparticles to the magnetized substrate. Another important aspect of the sacrificial layer is the thickness. Thick sacrificial layers can enhance the contrast between areas with particles and those without particles, but if the layer is too thick the particles may not assemble at all.

Self-Assembly of Magnetic Particles

The magnetic particle self-assembly was made by immersing the magnetized tape in the nanoparticle suspension. Particles deposited in regions of high field-gradient on the magnetized tape generating defined assembly patterns (e.g. line, circle, letters, etc.), as shown in Fig. 3. A gentle rinse, using 0.5 mL of water with pH 11 (same pH of the nanoparticles suspension) and surface inclination was necessary to eliminate excess particles surplus from the sample and to finalize the deposition.

The experiments were conducted by parametrically varying various self-assembly parameters (time, particle concentration, thickness of sacrificial layer, orientation of the magnetic tape during the deposition, and washing conditions) to determine their influence on the line width of the deposited structures.

The most significant parameter was found to be the nanoparticle concentration, which showed positive correlation with the line width. Figure 4 shows how the line width of the assembled particles could be controlled from 14 µm down to ~5 µm by controlling the particle concentration from 0.36% to 0.0021% by volume for a 5-min deposition time.

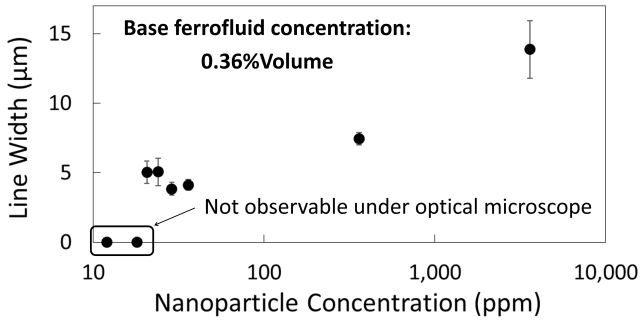

Figure 4: Relationship between concentrations of nanoparticles in suspension and the linewidth of the magnetic structure for 5 minutes of deposition.

Another critical parameter was found to be the deposition time. When the particle concentration is constant, there was a positive correlation of the line width with deposition time. Figure 5 shows results from a qualitative analysis of the effect of deposition time using values varying logarithmically from 6 seconds to 600,000 seconds. For this experiment, the particle concentration was low (0.062%v/v), requiring very long deposition times in order to obtain well-defined patterns.

Particle Crosslinking and Microstructure Release

After particle assembly, a 25% weight solution of the branched poly-cation polyethylenimine (PEI) with molecular weight of 2 kDa was used to crosslink the carboxylic acid groups present on the nanoparticle surfaces with the primary amines in the polymer chain. This reaction was carried out for 1 hour and promoted by 1-ethyl-3-[3-dimethylaminopropyl] carbodiimide hydrochloride (EDC) and N-hydroxysuccinimide (NHS) chemistry [15–18]. A final rinse with deionized water and acetic acid was used to remove free polymer.

To illustrate the results of successful crosslinking, Fig. 6 presents SEM images of the simple line patterns from the audiocassette recording. The light colored regions indicate the

presence of polymer (electrically insulated), meanwhile dark regions represent the magnetic tape (electrically conductive). Figure 6(b) shows an enlarged image of the end of one of the lines to show the agglomeration of crosslinked nanoparticles.

Figure 7 shows images of a more complex, patterned grid microstructure. Figure 7(a) shows the magnetization mask used for the selective magnetization process, and Fig. 7(b) shows the self-assembled and crosslinked patterns before release. Figure 7(c) shows a corresponding SEM image of the patterned grid microstructure after crosslinking.

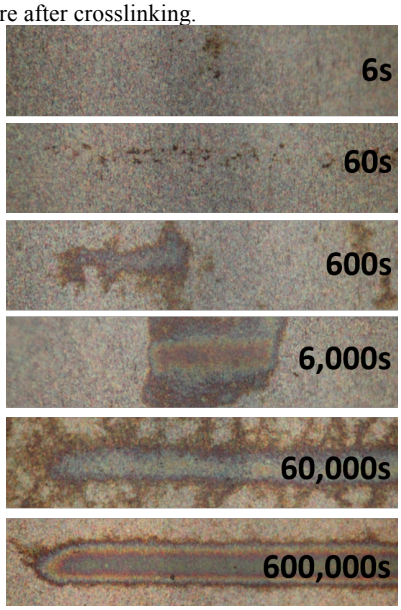

Figure 5: Time deposition qualitative analysis. Particle volume fraction in suspension φ=0.062 %v/v.

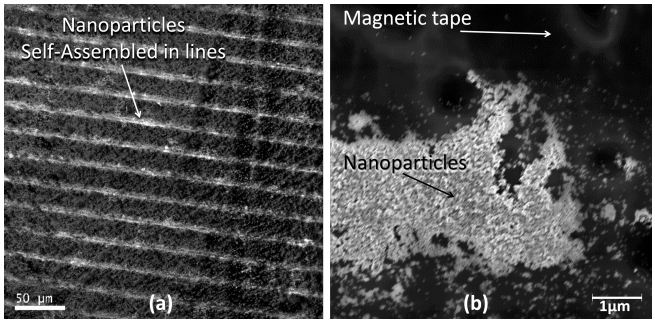

Figure 6: SEM top view pictures of (a) self-assembled nanoparticles on magnetic tape, (b) bonded particle microstructure after crosslinking.

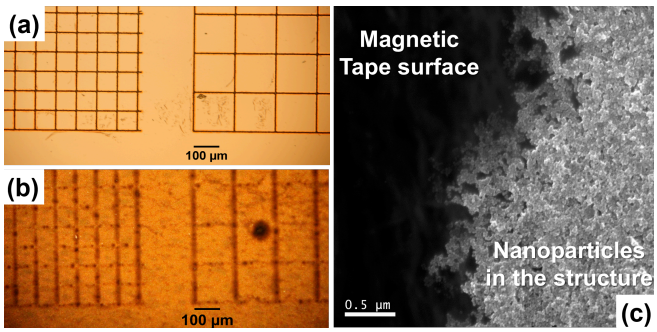

Figure 7: Grid microstructure: (a) Magnetization mask used to create the pattern, (b) crosslinked self-assembled nanoparticles and (c) SEM top view picture of the structure boundary.

Lastly, the underlying sacrificial layer (350 nm of LOR 3B) was dissolved in AZ300 MIF developer (tetra-methyl ammonium hydroxide), releasing the structures into solution. Figure 8 shows an optical image of the released grid structure and distortion of the grid pattern when subjected to a magnetic field. These results prove the successful crosslinking of the magnetic nanoparticles into the patterned microstructures and the magnetic response of said complex structure.

After releasing the sacrificial layer smaller microstructures will float in the releasing solvent, and these free-floating microstructures were shown to be highly responsive to external magnetic fields. Experiments with random variations of surrounding magnetic field applied to free-floating structures resulted in the ability to rotate the structures about different axes, as in Fig. 9. Figure 10 shows flexing of a structure that was partially attached to the substrate. When the changing magnetic field was applied part of the structure bent towards the magnetic field source. When a field was inverted the bending was in the opposite direction. These experiments illustrate the potential application of this fabrication technique to obtain structures that can be actuated magnetically.

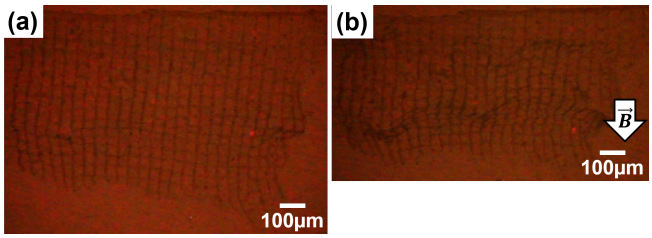

Figure 8: Released grid microstructure: (a) released structures in suspension (b) released structures responding to the presence of a magnetic field, showing distortion of the grid.

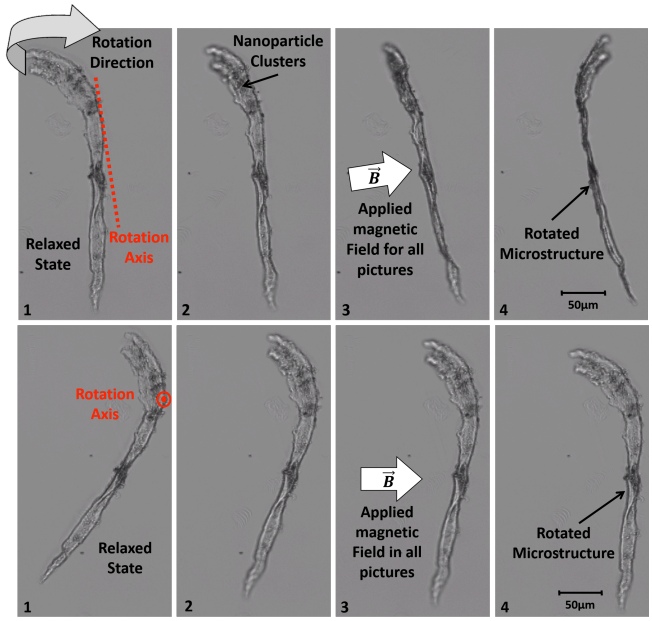

Figure 9: Rotation experiments on microstructure changing the orientation of the magnetic field.

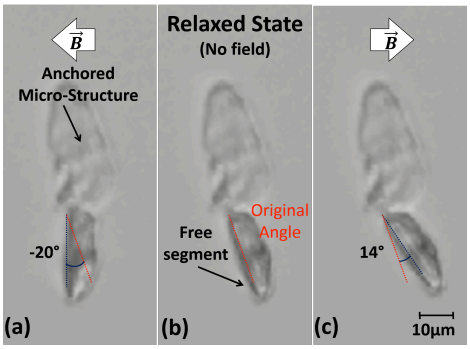

Figure 10: Response of microstructure to the presence of external magnetic field. Panel (b) shows the relaxed state of the structure, whereas panels (a) and (c) represent position after excitation to the left and right, respectively.

CONCLUSIONS

A technique for fabrication of magnetic microstructures by in situ crosslinking of magnetically assembled nanoparticles was demonstrated. Two strategies to create magnetic field gradients to pattern the nanoparticles were evaluated: Recording media data (producing rectangles with linewidth around 10 µm and length of 1 mm) and a selective magnetization technique (to produce arbitrary patterns). Both strategies were successful and generated microstructures that were successfully released in solution. SEM pictures demonstrate the high density of particles inside the structures, and actuation by external magnetic fields validates their magnetic responsiveness.

The most critical parameters for the process are: nanoparticle concentration, deposition time, magnetic field during the selective magnetization, sacrificial layer chemistry and thickness and microstructure release. Further experimentation must be done in order to optimize these parameters for specific structure shapes. The releasing process is a critical step that must be optimized in the future for better conservation of the free microstructures. These results prove the concept of the process for creating more complex shapes, patterns, and functional devices in the future.

ACKNOWLEDGEMENT

This work is funded in part by the UF Office of Research. The authors thank Ololade Oniku and Dr. Alexandra Garraud for their contribution as well as the staff of the UF Nanoscale Research Facility and the UF Major Analytical Instrumentation Center for their assistance in the microfabrication and material characterization.

REFERENCES

[1] B. Dieny, H. Joisten, and P. Sabon, "Magnetic microparticle and method for making such a microparticle," International Patent WO201103308025-Mar-2011.

[2] J. Kim, S. E. Chung, S.-E. Choi, H. Lee, J. Kim, and S. Kwon, "Programming magnetic anisotropy in polymeric microactuators.," *Nat. Mater.*, vol. 10, no. 10, pp. 747–52, Oct. 2011.

[3] J. Henderson, S. Shi, S. Cakmaktepe, and T. M. Crawford, "Pattern transfer nanomanufacturing using magnetic recording for programmed nanoparticle assembly.," *Nanotechnology*, vol. 23, no. 18, p. 185304, May 2012.

[4] E. Alsberg, E. Feinstein, M. P. Joy, M. Prentiss, and D. E. Ingber, "Magnetically-Guided Self-Assembly of Fibrin Matrices with," *Tissue Eng.*, vol. 12, no. 11, pp. 3247–3256, 2006.

[5] R. Barbucci, G. Giani, S. Fedi, S. Bottari, and M. Casolaro, "Biohydrogels with magnetic nanoparticles as crosslinker: characteristics and potential use for controlled antitumor drug-delivery.," *Acta Biomater.*, vol. 8, no. 12, pp. 4244–52, Dec. 2012.

[6] S. Sun, S. Anders, H. F. Hamann, J.-U. Thiele, J. E. E. Baglin, T. Thomson, E. E. Fullerton, C. B. Murray, and B. D. Terris, "Polymer mediated self-assembly of magnetic nanoparticles.," *J. Am. Chem. Soc.*, vol. 124, no. 12, pp. 2884–5, Mar. 2002.

[7] L. Ye, B. Terry, O. T. Mefford, C. Rinaldi, and T. M. Crawford, "All-nanoparticle concave diffraction grating fabricated by self-assembly onto magnetically-recorded templates.," *Opt. Express*, vol. 21, no. 1, pp. 1066–75, Jan. 2013.

[8] Z. Zhou, S. Lin, T. Yue, and T.-C. Lee, "Adsorption of food dyes from aqueous solution by glutaraldehyde cross-linked magnetic chitosan nanoparticles," *J. Food Eng.*, vol. 126, pp. 133–141, Apr. 2014.

[9] J. Park, K. An, Y. Hwang, J.-G. Park, H.-J. Noh, J.-Y. Kim, J.-H. Park, N.-M. Hwang, and T. Hyeon, "Ultra-large-scale syntheses of monodisperse nanocrystals.," *Nat. Mater.*, vol. 3, no. 12, pp. 891–5, Dec. 2004.

[10] M. Wang, M.-L. Peng, W. Cheng, Y.-L. Cui, and C. Chen, "A novel approach for transfering oleic acid capped Iron Oxide Nanoparticles to water phase," *J. Nanosci. Nanotechnol.*, vol. 11, no. 4, pp. 3688–3691, 2011.

[11] R. Chantrell, J. Popplewell, and S. Charles, "Measurements of particle size distribution parameters in ferrofluids," *IEEE Trans. Magn.*, vol. 14, no. 5, pp. 975–977, Sep. 1978.

[12] A. J. Moreno, E. Gonzalez, M. Godoy, J. Pettinari, P. S. Antonel, G. Jorge, and V. Bekeris, "Spatial Resolution in Micrometric Periodic Assemblies of Magnetotactic Bacteria and Magnetic Nanoparticles," *IEEE Trans. Magn.*, vol. 49, no. 8, pp. 4572–4575, Aug. 2013.

[13] A. Garraud, O. D. Oniku, W. C. Patterson, E. Shorman, D. Le Roy, N. M. Dempsey, and D. P. Arnold, "Microscale magnetic patterning of hard magnetic films using microfabricated magnetizing masks," in *MEMS 2014*, 2014, pp. 520–523.

[14] O. D. Oniku, P. V. Ryiz, A. Garraud, and D. P. Arnold, "Imprinting of fine-scale magnetic patterns in electroplated hard magnetic films using magnetic foil masks," *J. Appl. Phys.*, vol. 115, no. 17, p. 17A718, May 2014.

[15] A. López-Cruz, C. Barrera, V. L. Calero-DdelC, and C. Rinaldi, "Water dispersible iron oxide nanoparticles coated with covalently linked chitosan," *J. Mater. Chem.*, vol. 19, no. 37, p. 6870, 2009.

[16] X. Wang, L. Zhou, Y. Ma, X. Li, and H. Gu, "Control of aggregate size of polyethyleneimine-coated magnetic nanoparticles for magnetofection," *Nano Res.*, vol. 2, no. 5, pp. 365–372, Mar. 2010.

[17] H. H. P. Yiu, S. C. McBain, Z. a D. Lethbridge, M. R. Lees, and J. Dobson, "Preparation and characterization of polyethylenimine-coated Fe3O4-MCM-48 nanocomposite particles as a novel agent for magnet-assisted transfection.," *J. Biomed. Mater. Res. A*, vol. 92, no. 1, pp. 386–92, Jan. 2010.

[18] S. A. Madison and J. O. Carnali, "pH Optimization of Amidation via Carbodiimides," *Ind. Eng. Chem. Res.*, vol. 52, no. 38, pp. 13547–13555, Sep. 2013.

CONTACT

*Camilo Velez, tel: +1-352-575-7581; camilovelez@ufl.edu

LOW OHMIC LOSS CYLINDRICAL RADIAL SUPERLATTICE CONDUCTORS USING ALTERNATINGLY ELECTROPLATED MAGNETIC/NONMAGNETIC THIN FILMS FOR MICROWAVE APPLICATIONS

Arian Rahimi[*], and Yong-Kyu 'YK' Yoon
University of Florida, Gainesville, Florida, USA

ABSTRACT

In this work, the first experimental demonstration of the Cylindrical Radial Superlattice (CRS) conductors made of alternating magnetic/nonmagnetic layers grown on a radial conductor operating in the microwave range is reported. The CRS structure has been employed to force the high frequency current to flow through the volume of the conductor by suppressing the generated eddy currents inside the conductor which will lead to reduction of the conductor loss. Also, the implementation of the highest Q-factor microwave inductor made of the CRS conductor with a Q-factor of 45 at 18 GHz, which is attributed to low conductor and dielectric losses, has been demonstrated.

INTRODUCTION

Copper is widely used as a known low loss conductor in standard microfabrication processes in IC and MEMS industries mainly due to its high conductivity, ease of deposition and relatively low cost. However, in higher frequencies, its high conductivity is not as effective and beneficial as it is in the low frequency because of the skin effect, where most current is confined in the outermost surface of the conductor thus reducing the effective cross-section of the conductor and increasing the ohmic resistance. Therefore, the conductor loss together with the dielectric loss will give rise to the total loss of the systems operating in microwave range. The dielectric loss could be suppressed in some devices by carefully removing the dielectric material and let the electromagnetic waves propagating through air ([1-2]). However, there is not much work done to decrease the conductor loss which is a major part of the RF losses.

A planar superlattice structure where alternating metal/ferromagnetic thin films are deposited vertically on each other was proposed in [3] where the stack layers are utilized to suppress the skin effect and lower the conductor loss. Because of the negative permeability of the ferromagnetic metal layers in frequencies above the magnetic resonance (f_{MR}), it would be possible to make the effective permeability of the multilayer consisting of the negative/positive permeability of the ferromagnetic/non-ferromagnetic metals close to zero and increase the skin depth. Therefore, the current will be forced to flow through the volume of the conductor where the effective area is increased leading to a considerably lower conductor loss. Although the planar superlattice conductors have proved to decrease the ohmic loss of the conductors in high frequency region, the electromagnetic discontinuity at the edge of the conductor and therefore large fringing effects, limit the eddy current suppression of the planar superlattice conductors in practice and leave room to further reduce the loss.

We have previously presented the Cylindrical Radial Superlattice (CRS) structure in [4] where theoretical and numerical analyses with circular and conformal boundary conditions have been demonstrated for the suppression of skin effects and therefore that of the RF conductor loss. In this work, we are reporting on (1) the first experimental demonstration of the CRS conductors consisting of alternating magnetic/nonmagnetic nanolayers working in the microwave range and (2) the implementation of the highest Q-factor microwave inductor made of the CRS conductor with a Q-factor of 45 at 18 GHz, which is attributed to low conductor and dielectric losses.

THEORY AND ANALYSIS

At higher frequencies, the ohmic loss of the conductors are totally governed by the conductivity (σ) and the skin depth (δ),

$$\delta = \sqrt{\frac{2}{\omega\mu\sigma}} \qquad (1)$$

Therefore, due to the fact that the skin depth is getting smaller once the frequency increases, the ohmic loss unavoidably keeps rising in a regular conductor. The schematic of the cylindrical radial superlattice (CRS) conductor's cross-section view to suppress the ohmic loss is given in Figure 1. The proposed design is employing the fact that although the permeability of the nonferromagnetic layers is constant with respect to frequency (μ_N=1 at all frequencies), that of the ferromagnetic metal layers is a function of the frequency and is negative between the ferromagnetic resonance frequency, f_{MR} and the anti-resonance frequency, f_{AR}.

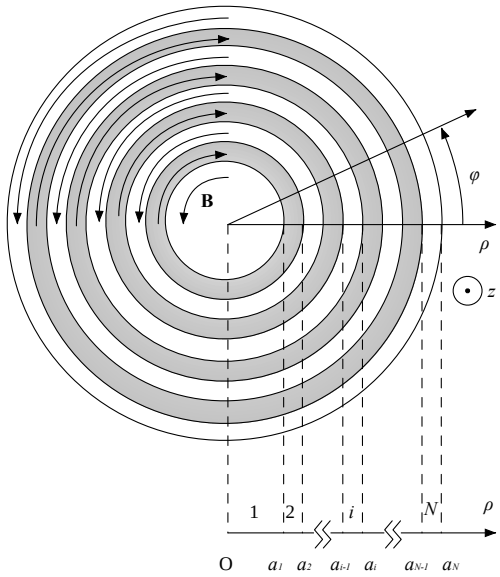

Figure 1: A cylindrical radial superlattice (CRS) conductor composed of metal (white region) and ferromagnetic thin film (grey region) with N layers and total radius a_N in the cylindrical coordinate system. The arrows show the direction of the induced eddy currents where opposing each other in the design frequency region due to negative permeability of the ferromagnetic thin film.

By assuming the non-ferromagnetic/ferromagnetic layers as the conductor carrying the high frequency signal, the effective permeability of the stack layers will be given by,

$$\mu_{eff} = \frac{\mu_N t_N + \mu_F t_F}{t_N + t_F} \qquad (2)$$

where μ_N, μ_F, t_N and t_F are the magnetic permeability of the non-ferromagnetic layer, the magnetic permeability of the ferromagnetic layer, the thickness of the non-ferromagnetic layer, and the

9781940470016/HH2014/$25©2014TRF
DOI 10.31438/trf.hh2014.91

thickness of the ferromagnetic layer, respectively.

The dynamic response of magnetic thin films has been investigated theoretically [5] and experimentally [6]. Permalloy ($Ni_{80}Fe_{20}$) thin films are ones of the most commonly studied soft magnetic materials. Figure 2 shows the calculated permeability of the $Ni_{80}Fe_{20}$ using the Landau-Lifshitz-Gilbert (LLG) equation where the magnetic saturation of M_s = 1T has been assumed for the permalloy. The resonance frequency of the permalloy thin film is $f_{MR} \approx 900$ MHz and the anti-resonance frequency $f_{AR} \approx 28$ GHz.

The device is operating between the ferromagnetic resonance frequency (f_{MR}) and the anti-resonance frequency (f_{AR}) where the real part of the permeability, μ', is negative (Figure 2). The $r = t_N/t_F$ which is the ratio of the thickness of the non-ferromagnetic metal layer (usually copper or aluminum) and the ferromagnetic metal layer is an important design parameter which determines the operation frequency.

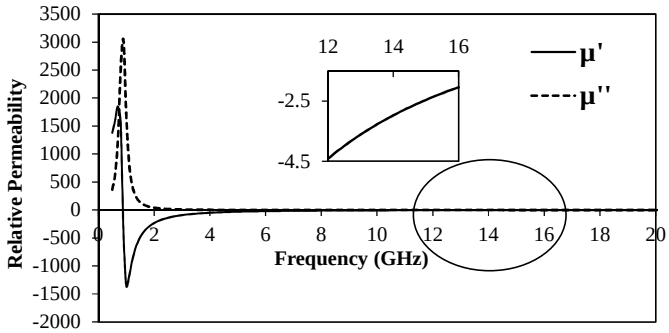

Figure 2: The calculated permeability of the permalloy assuming no external magnetic field. The inset shows the real part μ' for the frequency between 12 to 16 GHz.

SYSTEM DESIGN AND SIMULATIONS

In order to verify the performance of the proposed CRS conductors, a CRS superlattice structure has been analyzed and fabricated on a radial conductor. The single turn air-lifted inductors are fabricated on the radial-shape gold wire with a diameter of 28 μm. Figure 3 shows the schematic of the CRS inductor where the radial gold wire has been implemented using a commercial wire bonder and one-port coplanar waveguide (CPW) input.

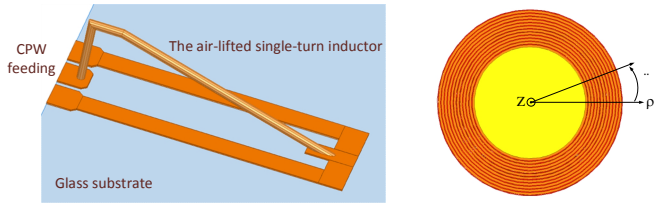

(a) (b)

Figure 3: (a) The schematic of the single-turn air-lifted inductor using 1-port coplanar waveguide (CPW) feeding, (b) the cross section of the wire including the 28 μm-diameter gold wire (yellow) as the core and 21 layers of Cu, NiFe (orange, red) stack to realize the cylindrical radial superlattice (CRS) structure.

The CRS conductors have been analyzed by performing the full-wave simulations using the high frequency structure simulator (HFSS, ANSYS Inc.) that proves the effectiveness of the proposed method for conductor loss reduction. A 10 μm-length unit cell of the CRS conductor consists of a solid core conductor covered by laminated superlattice structures (Figure 1) where a ground plane is used underneath the structure, to allow propagation of transverse electromagnetic (TEM) waves. The lumped element equivalent circuit model, will be used to extract the conduction resistance of the conductor. Figure 4 shows the resistance of the conductor unit cell where $r = t_{Cu}/t_{NiFe} = 2.5$. The minimum resistance spectra occurs when $\mu_{eff} = 0$ which will be satisfied when $\mu_{NiFe} = -2.5$ as expected in Figure 2. The simulation results reveal an ohmic loss reduction of about 3 times compared to the solid-core conductor at the target frequency of 15 GHz. For frequencies above 10 GHz, the resistivity of the superlattice structure falls below that of the solid-core conductor which leads to a relatively wide bandwidth where eddy current cancelling is effective.

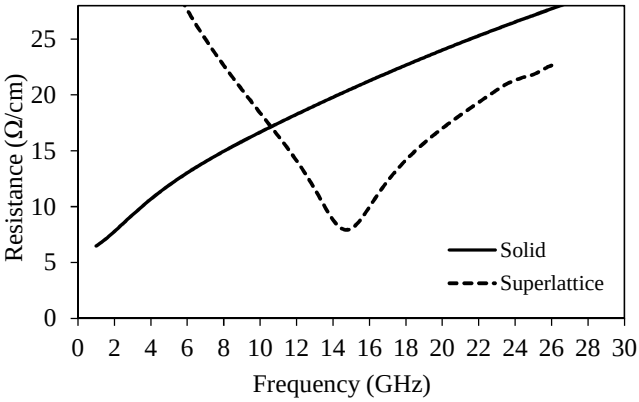

Figure 4: The full-wave simulation results of the Cu/NiFe CRS structures with N=21 and t_{Cu}/t_{NiFe}=400 nm/160 nm.

Figure 5 depicts the simulation results at 15 GHz where the current distribution throughout the CRS conductor is showed (a) and compared with that of the regular conductor made of copper only (b) where a solid gold core with a diameter of 28 μm has been used. Due to the more uniform current distribution at the operation frequency, the ohmic loss has been significantly reduced.

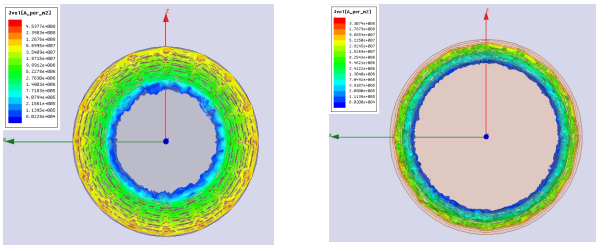

(a) (b)

Figure 5: Current distribution of (a) the CRS conductor using a gold core of 28 μm diameter, (b) the solid core conductor using single layer copper.

FABRICATION AND EXPERIMENTAL RESULTS

Thin film permalloy and copper are used as the magnetic and nonmagnetic metals, respectively, to create the CRS structure where both are electroplated using our in-house solution baths. The fabrication starts with a glass substrate; after the deposition of the seed layers (Ti/Cu/Ti), the pads are patterned on the glass substrate followed by 10μm electroplating of Cu. Then, the low-temperature gold wire bonding has been immediately performed in order to avoid oxidation of the copper and requirement of another metal layer on top of copper for the sake of wire bonding. Electroplating has been selected as the low cost, manufacturing method for the deposition of magnetic/nonmagnetic nanoscopic thin films on radial-shape gold core conductors to ensure conformal coating where most other processes including DC sputtering [7] would be more expensive and

might not work best for the radial-shape devices. After performing the multiple-step electroplating of Cu/NiFe, the devices are released by etching the seed layers. Table 1 shows the utilized solution bath for the deposition of permalloy ($Ni_{80}Fe_{20}$) thin films.

Table 1: The composition of permalloy ($Ni_{80}Fe_{20}$) electrolyte

Compound (g/L)	Concentration
Nickel Sulfate	200
Iron Sulfate	8
Nickel Chloride	5
Boric Acid	25
Saccharin	3
pH	4
Temperature	24° C

Figure 6 shows the pictures of the fabricated single-turn air-lifted CRS inductors. The inductors with the same pad size but different lengths are fabricated on the same substrate.

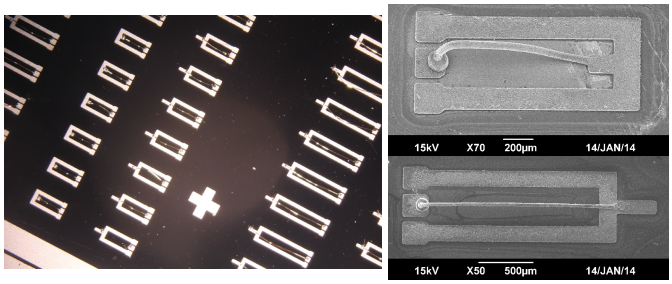

Figure 6: (a) the glass substrate holding the array of CRS inductors, and (b) the CRS inductors of 1 and 2 mm length after electroplating. The backbone wire has been implemented using a gold wire bonder.

The solid core inductors are also fabricated using a single layer of copper with the same thickness as the superlattice multilayers. Figures 7 to 9 show the measurement results of the implemented CRS inductors where regular wire (solid core) inductors are also measured as control devices for comparison.

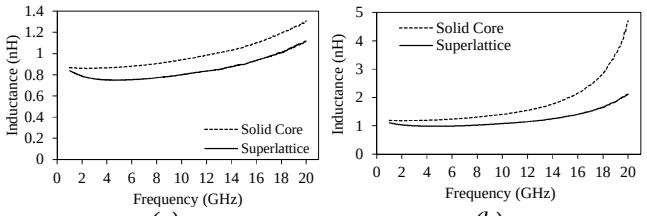

Figure 7: The measured inductance of superlattice and solid core inductors with the distance between the probe and the ground of (a) 1 mm and (b) 2 mm.

The measurement results of two sets of inductors with different lengths but a conformal deposition of 21 layers of NiFe/Cu (160 nm/400 nm) layers are presented in this work. Multiple Ni and Cu targets facing the substrate inside the electroplating bath have been used for a uniform deposition of both NiFe and Cu around the radial-shape inductors. The inductance and resistance of the devices are extracted after analyzing the one-port Y-parameters. The measured inductance values of the CRS and solid-core inductors are depicted in Figure 7. The inductance values of both of them are in the same range while the solid-core inductors show a slightly higher inductance values compared to CRS ones.

Figure 8 shows the measured quality factor (Q-factor) of the implemented inductors. As predicted in Figure 4, the ohmic resistance of the single layer copper constantly increases with the frequency due to the skin effect. The ohmic resistance of the CRS inductors is higher than that of the solid-wire inductors (Figure 4) in frequencies below 10 GHz; however, it starts to fall below the resistance of solid-wire inductors for frequencies above 10GHz. Therefore, the Q-factor of the CRS inductors are higher compared to that of the solid-wire inductors in the operation frequency range of 10 GHz < f < 20 GHz. Therefore, the proposed structure is a solution to the problem of high resistivity/low Q-factor of RF passive devices originating from the skin effect. By changing the $r = t_{Cu}/t_{NiFe}$ ratio, the minimum resistance spectra point will be tuned, and that makes it possible to overpass the skin effect problem and design low loss passive devices operating in an intended operation frequency range.

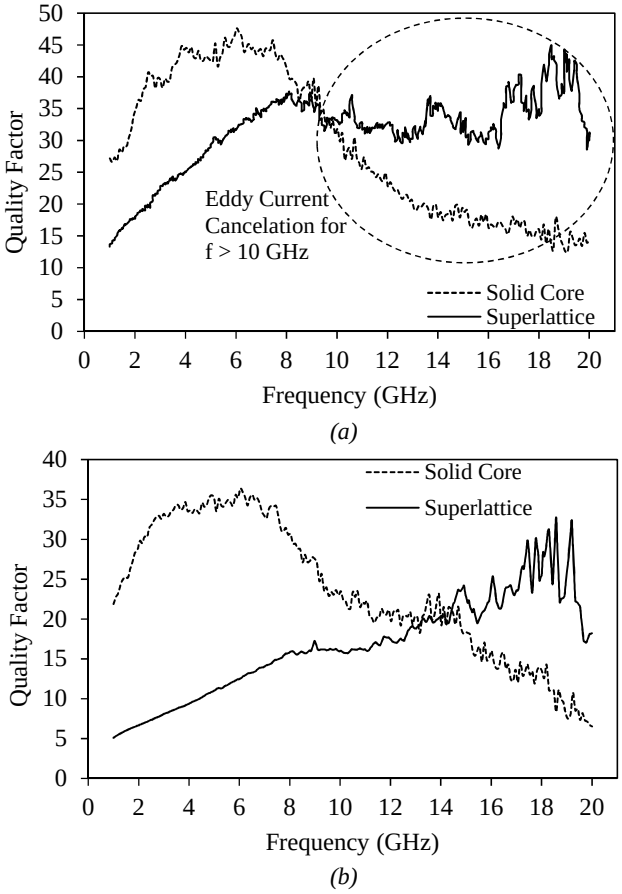

Figure 8: The measured Q-factors of the solid-wire and superlattice-wire inductors of (a) the 1-mm long inductor and (b) the 2-mm long inductor. As predicted in Figure 4, the resistance of the CRS device is lower than that of the solid-wire one in the range of 10-24 GHz. A higher Q-factor is achieved for 10-20 GHz measurement for (a) and 14-20 GHz for (b) proving the effectiveness of eddy current cancellation for the CRS devices. Using single-layer solid-wire devices, the Q-factor continuously decreases for the frequencies above 10 GHz.

Figure 9 shows a comparison of the measured resistance of the conductors of 1-mm and 2-mm length. The CRS conductors have higher resistance in low frequency range due to the high permeability of NiFe thin films in that frequency range which makes the skin depth smaller (equation (1)) and increases the ohmic loss.

However, as the frequency increases, the total CRS resistance is kept below that of solid wire devices and a wide-band of operation is achieved.

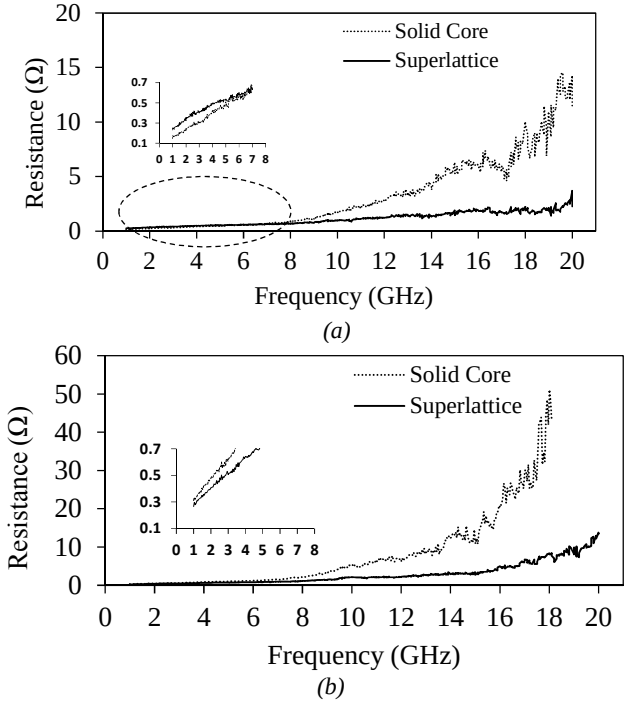

Figure 9: The measured resistance of the superlattice inductor and the solid wire inductor. The resistance is obtained based on the equivalent circuit model of the inductor.

CONCLUSIONS

In this paper, the experimental implementation of the CRS conductors and one of their potential applications as a high Q-factor inductor has been demonstrated. The proposed inductors benefit from the cylindrical radial shape of the conductors which inherently has a closed boundary condition in a radial direction with no fringing effects and therefore is considered more appropriate for eddy current suppression. The simulation and measurement results on the reduction of the conductor loss have been verified. The highest Q-factor Ku band inductor shows a Q-factor of 45 at 18GHz, where the high Q-factor is attributed to the low dielectric loss from the air-lifted architecture and the low conductor loss from the CRS conductor. Besides high Q-factor inductors shown in this work, the technology could be further extended to fabricate low loss passive devices including coaxial transmission lines and antennas. The fabrication method is fully compatible with the standard MEMS and CMOS processes and therefore can be integrated with the current manufacturing processes for reducing the RF loss. In this work, NiFe with f_{AR}=28GHz has been used which limits the maximum frequency of operation to be smaller than f_{AR}; however, other ferromagnetic materials with higher f_{AR} could be used to design low loss passive devices in higher frequency ranges [8-9].

ACKNOWLEDGMENTS

This work is supported in part by NSF ECCS (1132413). Microfabrication and magnetic characterization have been performed in Nanoscale Research Facilities (NRF) cleanroom and Interdisciplinary Microsystems Group (IMG), at the University of Florida.

REFERENCES

[1] B. Pan, Y. Li, M. M. Tentzeris, and J. Papapolymerou, "A novel low-loss integrated 60 GHz cavity filter with source-load coupling using surface micromachining technology," Microwave Symposium Digest, IEEE MTT-S International, pp.639-642, Jun. 2008.

[2] Y.K. Yoon, J.W. Park, and M. G. Allen, "Polymer-core conductor approaches for RF MEMS," IEEE Journal of Microelectromechanical Systems, vol. 14, no. 5, pp. 886-894, Oct. 2005.

[3] B. Rejaei and M. Vroubel, "Suppression of skin effect in metal/ferromagnet superlattice conductors," Journal of Applied physics, vol. 96, no.11, pp. 6863-6868, 2004.

[4] J. Wu and Y.K. Yoon, "A Low Ohmic Loss Radial Superlattice Conductor at 15 GHz using Eddy Current Canceling Effect," IEEE Antenna and Propagation Society International Symp. (APS/URSI), pp. 1552 – 1553, Jul. 2013.

[5] J. B. Youssef, N. Vukadinovic, D. Billet, and M. Labrune "Thickness-dependent magnetic excitations in permalloy films with nonuniform magnetization," *Physical Review B* 69.17, 2004.

[6] Y. Liu, L. Chen, C. Y. Tan, H. J. Liu, and C. K. Ong, "Broadband complex permeability characterization of magnetic thin films using shorted microstrip transmission-line perturbation," *Review of Scientific Instruments*, 76.6, 063911, 2005.

[7] I. Iramnaaz, H. Schellevis , B. Rejaei , R. Fitch , and Y. Zhuang, "Self-Biased Low Loss Conductor Featured With Skin Effect Suppression for High Quality RF Passives," IEEE Transactions on Magnetics, vol. 48, no.11, pp. 4139-4142, Nov. 2012.

[8] Y. Liu, C. Y. Tan, Z. W. Liu, and C. K. Ong "FeCoSiN film with ordered FeCo nanoparticles embedded in a Si-rich matrix," Applied physics letters, 90, 112506, 2007.

[9] A. Rahimi and Y.K. Yoon, "Low Loss Conductors for CMOS and Through Glass/Silicon Via (TGV/TSV) Structures Using Eddy Current Cancelling Superlattice Structure," proceedings of *IEEE Electronic Components and Technology Conference (ECTC)*, Jun. 2014.

CONTACT

*A. Rahimi: arahimi@ufl.edu
YK Yoon: ykyoon@ece.ufl.edu

MICROPATTERNED HIGH DENSITY NANOWIRES ON PAPER SUBSTRATES

*P. Mostafalu, S. Sonkusale**
NanoLab, Department of Electrical and Computer Engineering, Tufts University
Medford, MA, USA

ABSTRACT

In his study we present a novel approach for fabrication of high-density nanowires on paper substrates for improved paper-based electrodes, sensors and electronic devices. Different types of nanowires including platinum, nickel and copper are fabricated and patterned on paper. Nanowires are characterized with scanning electron microscopy and energy dispersive spectroscopy. Nanowires on paper were utilized as a dry electrode with excellent electrode-tissue impedance suitable for the recording of electrocardiogram signals.

INTRODUCTION

Development of low cost reliable environmentally sustainable medical diagnostic devices is receiving increased attention. [1, 2] Accordingly, paper has been suggested as a suitable substrate material for such devices. Paper is a flexible, lightweight and biocompatible platform which has been endorsed for sensing and electronics applications, e.g. capacitive touch pads, glucose sensors and bioassays.[3, 4] Moreover, fabrication of paper-based devices is straightforward and requires low cost, room temperature processing steps depending on the type of the paper used.[3-5]

Nanowires and nanoparticles, with their unique properties such as high surface area and outstanding electrical transport behavior, are emerging materials for implementation of electrodes for sensors, batteries and supercapacitors.[6, 7] Biomedical devices have also benefited from the use of nanomaterials with applications ranging from the recording of neural activity, to the detection of biological targets such as DNA and dopamine using nanowires, nanopores and nanoneedles.[8, 9]

Introducing nanowires and nanopowders on paper substrates will synergistically bring together the low cost paradigm of paper-based substrates with the outstanding physical, electrical and chemical performances of nanomaterials, providing a key enabler to realize ideal electrodes for many applications. Generally, numerous techniques have been reported for the growth of nanowires. Vapor-Liquid-Solid (VLS) and Chemical-Vapor-Deposition (CVD) are two standard methods for nanowires growth but these methods require high temperatures (more than 300^{o}C) which are not feasible owing to low ignition temperature of paper.[10, 11] Consequently, the template-assisted mechanism offers a solution to this problem, which stimulates nanowire growth with a low temperature process that is compatible with paper-based devices. In the template-assisted method, a porous membrane is employed to electrodeposit nanowires through its pores. For the choice of membranes, two kinds have been already proposed: Anodized Aluminum Oxide (AAO) and Poly Carbonate Membrane (PCM). AAO process is simpler and more straightforward, and is used in this study. To make a template, first, a ~ 50 μm thick ultra-pure layer of aluminum film is required. But, difficulty in deposition of such a thick layer and its anodization make direct growth of nanowire on paper unworkable. So we have developed an approach, which involves making an AAO template separately, and then transferring the template on paper for subsequent growth of nanomaterials through them.

In this study we also present a low cost approach not just for the fabrication of metal nanowires on paper substrates but also on their patterning and alignment. The fabrication process is simple and straightforward; screen printing method is used for patterning of electrodes, and double-sided tape engaged for initial attachment. The method is simple and requires no microfabrication facilities, and as such could be applied on other unconventional substrates other than papers.

To demonstrate a viable application for such a nanowire on paper-based electrodes, we utilize them as dry flexible electrode for the recording of electrocardiogram (ECG) signals. Typically, wet gel adhesives are needed for ECG recording, which make them inconvenient for long term monitoring. However, the high surface area and low impedance of the proposed paper based electrodes facilitates ease of recording even with a dry attachment to the skin. While biopotential recording is the only example explored in this study, such nanowire electrodes on paper will find use as electrodes for stimulation and recording from electrogenic cells, electrochemical and biological sensors, supercapacitors, and batteries.

MATERIALS AND METHODS

Chemical and materials

In this study Whatman chromatography paper grade 1 (Sigma-Aldrich) Reynolds parchment paper and photo paper was used as a substrate. Whatman AAO membranes with different pore sizes (20 nm and 200 nm) were used as templates. Thin, solvent resistant double-sided tape (Mcmaster, MA) was utilized for attachment of AAO membrane to the paper. Silver ink (Ag 510, Conductive Compound, MA) was used as a material for screen printing of the electrodes. Copper, nickel and platinum electroplating solutions (Technic Inc, USA) were purchased and used without further modification.

Fabrication process

First, the double-sided tape was patterned as a mask by laser engraving using a laser cutter (Versa VLS2.40) (power 40%, speed 20%) and it was attached to the paper (photo or parchment) which served as a substrate. Then silver ink was spin coated (5000 rpm for 60s) on the top and was cured (15 minute in 121^{o}C) and left in the desiccator (30 minutes) to remove all remaining residues. At the end of this step, interconnects and electrode pads on the paper were prepared. For electrodeposition of nanowire through pores of the AAO membrane, a conductive seed layer is required on top of the AAO. Therefore small circular electrodes (200 nm diameter) were patterned on the top-side of AAO template. To create these circular electrodes, the Mylar shadow mask is prepared by laser cutter and attached to the AAO template using Aerosol spray which is easy to remove adhesive; then either 200 nm of the silver was sputtered (NSC 3000 DC Magnetron Sputter tool) or gallium indium eutectic (Sigma Aldrich USA) was painted. In the next step, patterned interconnects on the paper were covered with a tape and a conductive epoxy (Norland NCA130) was screen printed on the patterned paper-based electrodes. Cover of the double-sided tape was peeled off and the AAO template with patterned electrodes was then attached on the paper; the epoxy was cured using UV light and heat (2 hours, 80^{o}C) to completely cure and provide a good electrical connection. The size of patterned electrodes on the paper is larger than size of electrodes on the AAO to provide simple alignment.

The electrodeposition was performed by chronopotentiometry method with the current density of 1mA/cm^2 using Potentiostat (PGSTATN12, Autolab, Mterohm) for several hours with exact

9781940470016/HH2014/$25©2014TRF
DOI 10.31438/trf.hh2014.92

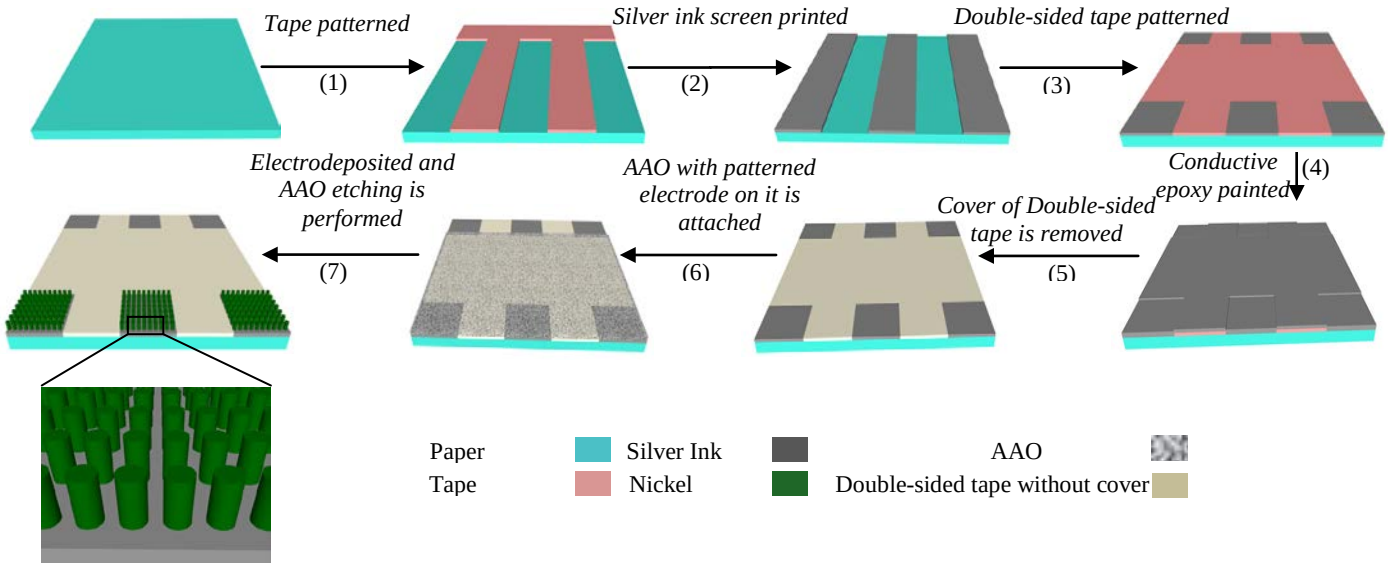

Figure 1: Fabrication process of nanowire on paper.

time depending on the desired length of nanowires. After electrodeposition, the AAO template was etched in sodium hydroxide (2M) for 1 hour. For the electrodeposition and etching the hand-made electrochemical cell has been used. Figure 2 shows patterned nanowires electrodes on the paper.

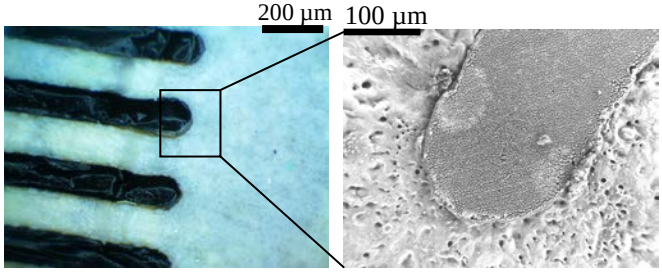

Figure 2: Patterned electrode on the paper after growth of nanowire.

RESULT AND DISCUSSION

The growth of nanowires with the desired length and diameter is one of the important design parameters. In general, the length of nanowires in the template-assisted approach is controlled by varying the time of deposition, current density, thickness of the AAO template, nature and type of the electrodeposited materials and the concentration of elctrodeposition bath. Current density affects the quality of deposition; it always should be kept as low as possible (less than 5mA/cm^2) to get a uniform electrodeposition. Here we have used a current density of 1 mA/cm^2, which gives a deposition rate of 20 nm/minute. The thickness of Whatman AAO templates are 60 µm so the maximum length of nanowire is limited to 60 µm. Electrodeposition time is the most effective parameter in the length of nanowires; the longer time would cause longer nanowires. For example we have performed copper electrodeposition for 1 hour, 2 hours and 5 hours, and nanowires with lengths of 2, 5, 10 µm were achieved respectively. Moreover, another parameter that controls the length and morphology of the nanowires is the type of material itself. Voltage during deposition of the copper is kept very small around 0.2 V; for nickel it is around 0.6V and for platinum it is high around 1.5 V. These numbers were arrived at empirically and the differences could be because of the different resistivity of the plating solutions with copper solution being the least resistive.

The second parameter in growth of nanowires is diameter which is limited to the pore size of AAO template. In this study, we used a commercial Whatman AAO template with pore size of 20 nm and 200 nm. The SEM images in Figure 3a and Figure3b show nickel nanowire with these two different diameters.

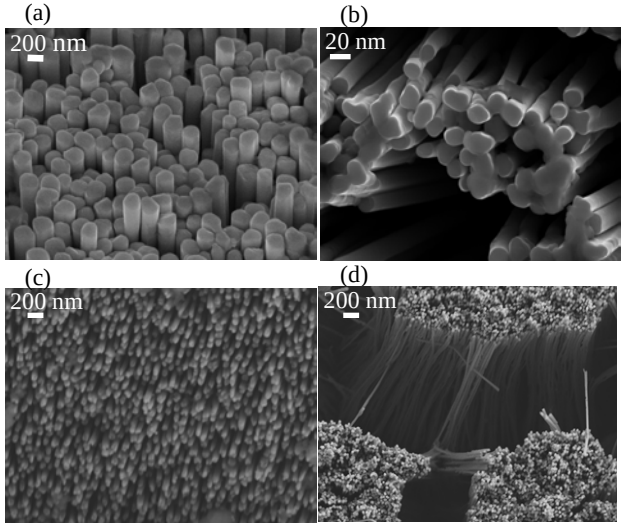

Figure 3: SEM images of paper-based nanowires aand 20nm (a) Nickel nanowires with diameter of 200 nm (b) Nickel nanowires with diameter of 20 nm (c) Platinum nanowires with diameter of 20 nm (d) Copper nanowires with diameter of 200nm.

However, electrodeposition of nanowires on the paper-based electrode has some other issues which should also be considered. Since papers are flexible materials, during electrodeposition different parts of electrodes might be a different distance from the

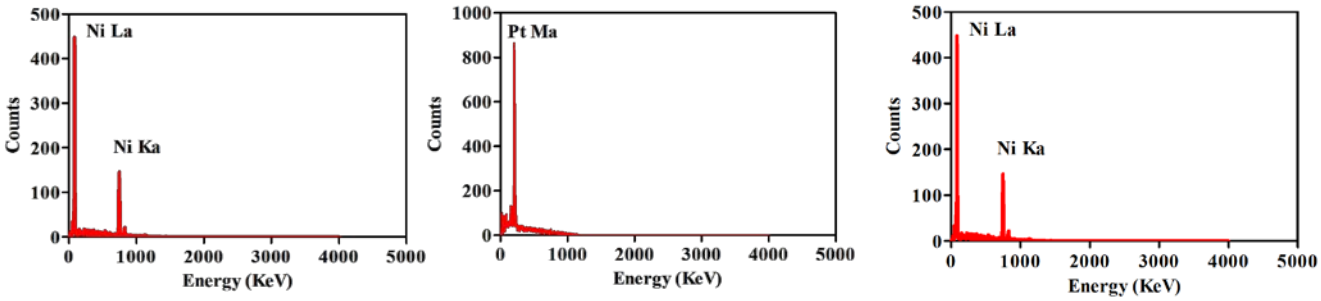

Figure 4: EDS analysis of different types of nanowire on paper (a) Copper nanowire (b) Platinum nanowire (c) Nickel nanowire.

anode and there could be non-uniformity in the length distribution. Utilizing double-sided tape and applied force with a clamp in the handmade cell made it more stable during deposition in our experiments. In this case, double-sided tape should be smooth and clamp tight enough to not let solution go through the pores of AAO template in the unpatterned areas. Leaching of the solution in the unpatterned area reduces the electrodeposition rate but will not stop the nanowire growth.

Another issue which may also be problematic is the unwanted soaking of the paper from the solution even in areas where there are no electrodes. Using hydrophobic paper like a parchment paper, wax paper or photography paper could solve this problem. Another solution is to using wax printing to form hydrophobic channel around the electrodes, which also limits the flow of the solution only in the hydrophillic areas.

Electrode characterization

For the physical characterization of nanowires, scanning electron microscopy (SEM) and Energy-dispersive X-ray spectroscopy (EDS) has been used. SEM images of nanowire electrodes were acquired using FESEM ultra55 (12 KV) to determine the structural features of the fabricated nanowires on paper substrate. Samples were mounted on the aluminum stubs using conductive carbon paint. As shown in Figure 2, we successfully grew nickel nanowires (Figure 3a) platinum nanowires (Figure 3c) and copper nanowires (Figure 3d). Figure 3a shows nickel nanowires with diameters of 200 nm and 20 nm. Copper nanowires with length of more than 10 µm are achieved (Figure 3d). We used Energy Dispersive Spectroscopy (EDS) for investigation of nanowires composition. The electron beam from SEM tools excited the sample and an X-ray spectrum emitted by the sample was obtained using the X-ray detector. Results of EDS analysis for nickel, copper and platinum high density nanowires are shown in Figure 4.

Electrocardiography

Cardiovascular diseases is the leading cause of the death. One could manage chronic heart conditions by continuous monitoring of electrocardiogram (ECG) activity. Development of an electrode and device for long term ECG monitoring is therefore essential to monitor heart activity in at-risk patients.

The electrodes that interface with the skin are very important part of the device to monitor heart's electrical activity. However current ECG electrodes that are typically used for this applications are made from Ag/AgCl with a gel electrolyte interface. It dries over time when used for long time monitoring and also degrades considerably due to sweat and motion; this consequently affects the quality of the signal received from the heart.[12] Moreover wet electrodes are uncomfortable for the patients since direct skin contact is necessary at all times. Recently dry ECG electrodes have been reported as a promising approach for replacement of wet ECG electrodes because they can facilitate long term monitoring with little inconvenience to the patient. However dry electrodes are very sensitive to motion artifacts and poor contact with skin and limited biocompatibility restrict their utility. In this study we have proposed wearable and flexible paper-based nanowire electrode as a viable dry ECG electrode for long term ECG monitoring.

Circular ECG electrodes with a diameter of 10 mm were fabricated according to the fabrication process mentioned in Section 2.1. For the evaluation of the ECG electrode, we have used a 3 electrodes setup; two nanowire-based electrodes and one regular screen printed silver electrode on the paper were connected to left arm, right arm and left leg as it is shown in figure 5b. Since the electrical signal is very small, its amplification and filtration is required. The electrical circuit composed of mentioned components, is implemented on a printed circuit board (PCB) using the circuit topology discussed here. [13]

Flexibility and easy attachment of nanowire on paper electrode using a double sided-tape makes for a very easy to interface electrode system for these measurements.

As mentioned earlier, a critical aspect to receive a high fidelity ECG signal is a good contact between electrodes and skin. The electrode-skin contact impedance has been measured to characterize the proposed ECG electrode. For the measurement of the impedance interface, the configuration which is shown in Figure 5a was used; based on the approach proposed in previous studies.[14] In this set up, 3 electrodes A, B and C were attached to the skin. The electrode B is the main electrode which is addressable for the measuring of its contact impedance with skin; the current in the range of 1-20 µA (using function generator and R_{ext}) is applied to the electrode A while B and C are in open load. The voltage measured between electrodes B and C (V_{out}) will depend only on the drop across the tissue-electrode impedance for electrode B ($R_{e2} = V_{out}/I_{in}$). As figure 6b shows impedance magnitude was changing for 100 KΩ to 1 KΩ when frequency varied from 5 Hz to 1.5 KHz.

CONCLUSION

In this study we have presented micropatterened nanowire electrode on paper substrates. Different types of metal nanowires have been grown and electrodes are characterized using SEM. Using this approach, we were able to fabricate nanowires with different lengths and diameters on flexible paper substrate. Element composition of materials was analyzed using EDS measurements. Finally electrodes were used as a viable dry alternative to wet gel electrodes for recording of the electrocardiogram signal. Impedance between skin and an electrode was measured; it varied from 100 KΩ to 100 Ω when

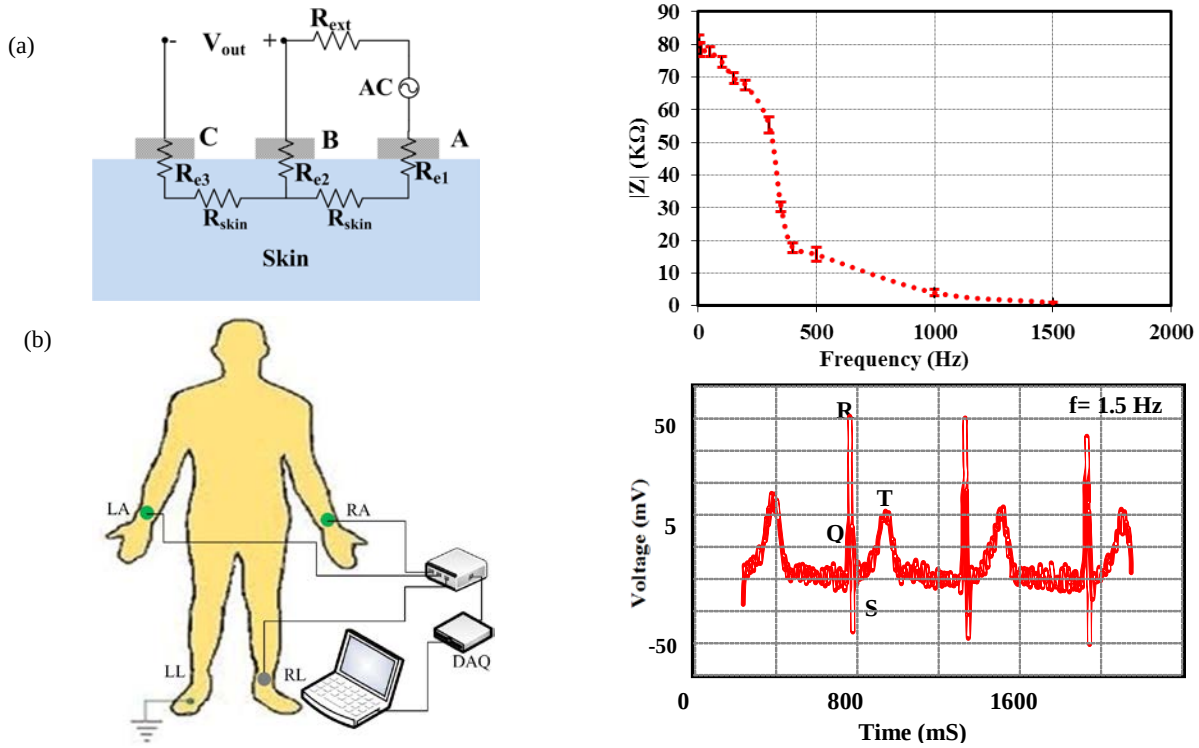

Figure 5: ECG analysis using PNE (a) Electrode-skin contact impedance measurement (b) methodology and recorded ECG signal.

frequency tuned from 5 Hz to 100 KHz and is found to be comparable to the literature.

ACKNOWLEDGMENT

Device was fabricated in Tufts Micro and Nanofabrication Facility. Project was founded by National Science Foundation ECCS-0955024 and EFRI-1240443. Travel support has been generously provided by the Transducer Research Foundation.

REFERENCES

[1] Z. Nie, C. A. Nijhuis, J. Gong, X. Chen, A. Kumachev, A. W. Martinez, *et al.*, "Electrochemical sensing in paper-based microfluidic devices," *Lab on a Chip*, vol. 10, pp. 477-483, 2010.

[2] J. R. Windmiller and J. Wang, "Wearable Electrochemical Sensors and Biosensors: A Review," *Electroanalysis*, vol. 25, pp. 29-46, 2013.

[3] E. J. Maxwell, A. D. Mazzeo, and G. M. Whitesides, "Paper-based electroanalytical devices for accessible diagnostic testing," *MRS Bulletin*, vol. 38, pp. 309-314, 2013.

[4] A. D. Mazzeo, W. B. Kalb, L. Chan, M. G. Killian, J.-F. Bloch, B. A. Mazzeo, *et al.*, "Paper-Based, Capacitive Touch Pads," *Advanced Materials*, vol. 24, pp. 2850-2856, 2012.

[5] G. Chitnis, Z. Ding, C.-L. Chang, C. A. Savran, and B. Ziaie, "Laser-treated hydrophobic paper: an inexpensive microfluidic platform," *Lab on a Chip*, vol. 11, pp. 1161-1165, 2011.

[6] P. Mostafalu and S. Sonkusale, "Paper-based super-capacitor using micro and nano particle deposition for paper-based diagnostics," in *Sensors, 2013 IEEE*, 2013, pp. 1-4.

[7] A. Vlad, A. L. M. Reddy, A. Ajayan, N. Singh, J.-F. Gohy, S. Melinte, *et al.*, "Roll up nanowire battery from silicon chips," *Proceedings of the National Academy of Sciences*, vol. 109, pp. 15168-15173, September 18, 2012 2012.

[8] P. Xie, Q. Xiong, Y. Fang, Q. Qing, and C. M. Lieber, "Local electrical potential detection of DNA by nanowire-nanopore sensors," *Nature Nanotech*, vol. 7, 2012.

[9] R. Esfandyarpour, H. Esfandyarpour, J. S. Harris, and R. W. Davis, "Simulation and fabrication of a new novel 3D injectable biosensor for high throughput genomics and proteomics in a lab-on-a-chip device," *Nanotechnology*, vol. 24, pp. 465301-465311, 2013.

[10] R. S. Wagner and W. C. Ellis, "Vapor-Liquid-Ssolid mechanism of single crystal growth," *Applied Physics Letters*, vol. 4, pp. 89-90, 1964.

[11] D. Wang and H. Dai, "Low-Temperature Synthesis of Single-Crystal Germanium Nanowires by Chemical Vapor Deposition," *Angewandte Chemie*, vol. 114, pp. 4977-4980, 2002.

[12] J. Ha-Chul, M. Jin-Hee, B. Dong-Hyun, L. Jae-Hee, C. Yoon-Young, H. Joung-Sook, *et al.*, "CNT/PDMS Composite Flexible Dry Electrodesfor Long-Term ECG Monitoring," *IEEE Transactions on Biomedical Engineering*,, vol. 59, pp. 1472-1479, 2012.

[13] T. Instruments, "Precision, Low Power Instrumetation Amplifier," vol. INA118 datasheet, Dec. 2011.

[14] M. S. SPACH, R. C. BARR, J. W. HAVSTAD, and E. C. LONG, "Skin-Electrode Impedance and Its Effect on Recording Cardiac Potentials," *Circulation*, vol. 34, pp. 649-656, 1966.

CONTACT

* S. Sonkusale, tel: +1-617-627-5113; sameer@ece.tufts.edu

NOVEL AMORPHOUS METAL THIN FILMS FOR MEMS APPLICATIONS

James E. Abbott[1], John McGlone[2], Kristopher Olsen[2], Greg S. Long[1], Rob Pugliese[1], Arun Agarwal[1], John F. Wager[2], Douglas A. Keszler[2], Jeff Wooden[1], Brian Bolf[1], Paul Krause[1], Todd Berdahl[1], William F. Stickle[1], Mark D. Johnson[1], and Peter Eschbach[2]*

[1]Printing and Technology Development – Hewlett-Packard Company, Corvallis, Oregon, USA

[2]Oregon State University, Corvallis, Oregon, USA

ABSTRACT

Thin film materials development has been critical to modern advances in electronics and Micro Electro Mechanical Systems (MEMS). This present work focuses on the development of advanced amorphous metal thin films for applications in Thermal Ink Jet (TIJ) devices; one of the earliest developed and most commercially successful MEMS devices to date. Collaboration between the printing division of Hewlett-Packard (HP) and Oregon State University (OSU) to develop amorphous metal thin films for thermal ink jet devices has resulted in remarkable progress toward development of thin film amorphous metals capable of handling extreme thermal and chemical shock. These results have been achieved by utilizing typical vacuum deposition processes known to be scalable into a manufacturing environment.

INTRODUCTION

Amorphous metal materials have been in bulk commercial production for years, incorporated into golf clubs, tennis rackets, and more recently rumored to be under investigation for incorporation into Apple products through collaboration with Liquidmetal Technologies [1]. In MEMS, amorphous $TiAl_3$ in Texas Instruments DLP technology stands at the forefront of commercialization of thin film amorphous metal materials [2]. Work on this class of materials continues as a research area for MEMS and electronic devices due to the advantageous atomically smooth surface, mechanical stability, and chemical resistance imparted to them by their amorphous, grain boundary free structure [3, 4].

A TIJ firing event creates one of harshest thermal, mechanical, and chemical environments in the world at the heater surface. By instantly flashing a thin layer of water into steam to eject a drop of aqueous based ink, extreme thermal stress is introduced as well as thermally initiated corrosion. One of the most damaging events occurs when the steam bubble collapses creating a micro jet cavitation event as depicted in Figure 1.

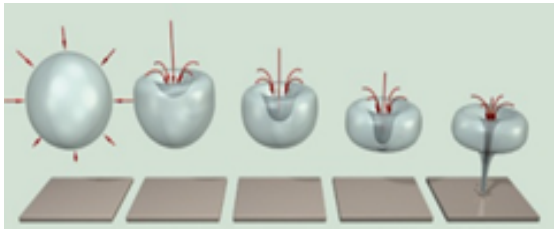

Figure 1: Diagram of Mechanical Damage Due to Microjet Cavitation [5]

Huge engineering efforts have been conducted by HP over more than two decades to protect the central heater element from failure as millions of ink drops are fired over the lifetime of a printhead. This engineering effort has recently enabled HP to release the world's fastest desk top printer: Figure 2 – the Office Jet Pro X. This printer contains more than 42,000 micron scale nozzles across ten MEMS die. Each nozzle has a rated lifetime of several million actuations and must reliably perform over the lifetime of the printer.

Figure 2: Image of HP Pro X Page Wide Printer and Printbar Containing 10 TIJ MEMS Die.[6]

Materials work completed several years ago by HP resulted in the formation of an as deposited amorphous metal based on Cobalt and Chromium alloyed with other materials. Figure 3 demonstrates that we were able to create a high quality, dense thin film with excellent adhesion to the substrate layers. However, Figure 3 also demonstrates that the system did not survive initial thermal shock testing; testing resulted in crack propagation into the substrate and device failure.

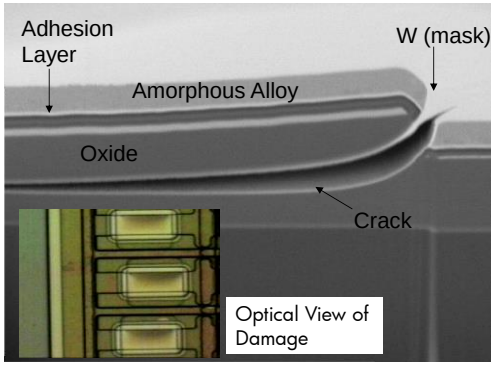

Figure 3: SEM Micrograph and Optical Image of Early HP Attempt at Using a Mechanically Tough Amorphous Alloy – Failure in Thermal Shock Testing

The collaboration with OSU builds upon this foundation and greatly expands the technical depth of the materials design. The current material of focus is based on sputtered TaWSi with additional dopants.

RESULTS AND DISCUSSION

Experimental Approach

At the launch of the project Oregon State University completed an exhaustive search of the scientific literature looking for information on the thin film amorphous metals and leveraging extensive literature for bulk metallic glasses.

9781940470016/HH2014/$25©2014TRF
DOI 10.31438/trf.hh2014.93

From the literature OSU formulated the following materials design guidelines for creation of a thermally stable amorphous metal:

- The material should ***be composed of three or more different elements with refractory metals*** accounting for ~70% of the total composition.
- The components should have a ***wide distribution of atomic radii***, with at least a 12% difference in size between any two components.
- There should be a ***large negative heat of mixing*** among each of the components.
- At least one of the component components should be a ***metalloid*** such as Si.

Starting with these guidelines a number of materials compositions were selected for testing. Ta was used as a central material in the majority of the compositions investigated because it is known to perform well in a thermal ink jet device.

The compositions were created using sputter deposition from two inch and three inch targets at an approximately four inch target to substrate spacing. The targets were fabricated using standard pressed powder techniques by various vendors. Both RF and DC power delivery were investigated for the appropriate deposition conditions with DC power delivery being generally more desirable to increase deposition rate of the thin film. Various power conditions were utilized up to about 150 Watts DC on a three inch target. Process pressures were investigated from 1mT to 20mT on three different sputter deposition platforms.

Thin Film Characterization:

To determine if the materials are suitable for the harsh environment of a thermal ink jet ejection event we devised a series of materials characterization experiments to understand the capability of the different materials. We focused primarily on thermal stability and resistance to chemical reaction as the initial variables of interest.

Thermal Stability

The thin film materials stack directly in contact with ink must heat to more than 250ºC on a time scale of micro seconds to achieve proper steam drive bubble for precise ejection of ink. This places an enormous stress on the thin films during firing. This thermally induced stress can be greatly exacerbated when elements of the thin film stack change morphology through grain growth or other structural conversions commonly activated in a high temperature environment. Ta has performed well for many years in thermal ink jet devices with reasonable stability enabled by the refractory nature of the material. Even though Ta is fairly thermally stable it is still susceptible to structural changes through tens of millions of firing events demanded for baseline reliability by modern TIJ printers. Of the several amorphous metal materials investigated we found a blend of TaWSi provides the most promising thermal stability.

Most vacuum deposited metal thin films are formed in a crystalline phase. Figure 4 provides an example of an as deposited crystalline Ta thin film commonly used in a TIJ device. The columnar structure of the crystalline Ta grains can be clearly observed in Figure 4. The boundaries between the grains provide increased surface area for chemical attack and a dislocation point increasing the probability of mechanical degradation of the Ta thin film during operation of a TIJ device.

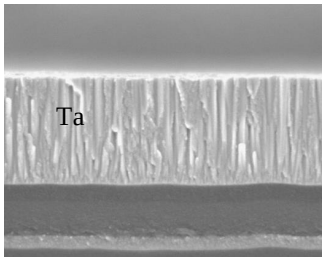

Figure 4: SEM of Cleaved Ta Cross Section

Figure 5 provides a Transmission Electron Microscopy (TEM) micrograph and electron diffraction image of TaWSi from OSU's imaging facility demonstrating that the TaWSi was amorphous as deposited. The TEM image indicates that the TaWSi is a high quality, dense thin film with good adhesion to the underlying thermally grown Silicon Oxide substrate. The diffuse rings in the electron diffraction image indicate that the materials are amorphous as deposited.

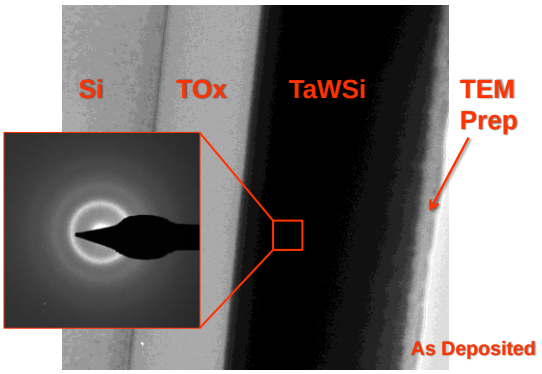

Figure 5: TEM Cross Section with Electron Diffraction of a TaWSi Amorphous Metal Thin Film: as Deposited

The TEM analysis results of a sample heated at 300ºC in air for one hour are provided in Figure 6. The annealed TaWSi sample exhibited evidence of minimal surface oxidation, but the bulk of the film remained as an amorphous metal.

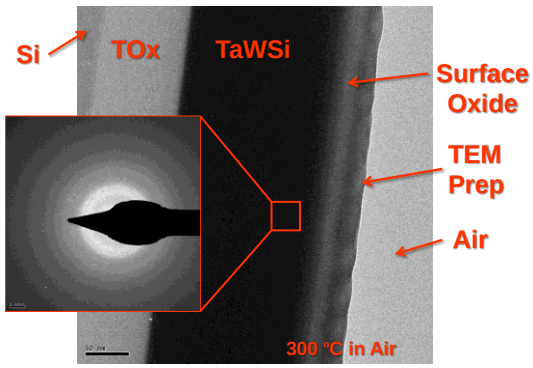

Figure 6: TEM Cross Section with Electron Diffraction of a TaWSi Amorphous Metal Thin Film Heated in Air at 300ºC

An investigation using TEM Energy Dispersive X-Ray Spectroscopy (EDS) was performed on the sample to verify that the oxidation was restricted to the surface of the thin film. Figure 7 provides an example of the EDS data collected. Careful review

of the EDS data confirms that the bulk of the film is a homogeneous mixture of TaWSi with oxygen restricted to the surface of the thin film. This is consistent with the film being high density and free of grain boundaries, additionally confirming the possible benefits for this material set in a prolonged high temperature oxidizing environment.

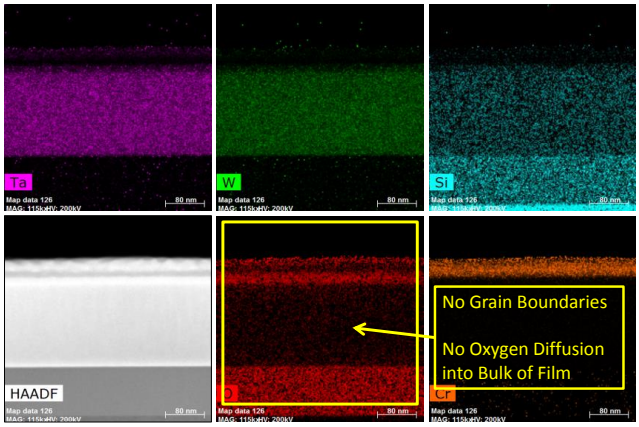

Figure 7: TEM – EDS imaging of TaWSi Thin Film Annealed in Air for One Hour.

Chemical Resistance

The volume of water flashed to steam is so small in TIJ devices that even human cells have been reliably jetted with this technology.[7] However rapid heating of a small volume of an aqueous solution to several hundred degrees Celsius can cause chemical reactions to be initiated that do not occur under more standard conditions. When firing a device millions of times low probability chemical reactions can have a significant impact on the materials used for the heater – ink interface. For initial materials screening HP performs reliability testing in inks under more standard conditions; if any material degradation is observed under these conditions the material is not considered suitable for integration into a TIJ device. In this case careful analysis of oxidation behavior was also conducted to verify stability of the film stack at high temperature.

Chemical resistance was investigated by oxidizing the TaWSi in air and exposing it to relevant HP ink chemistries. The TaWSi materials demonstrated excellent resistance to oxidation and chemical attack in HP ink. Figure 8 provides a comparison of Ta and TaWSi thin films heated under the same experimental conditions to 600ºC in air. Based on the previously discussed Ta cross section and the TEM imaging of TaWSi we believe the completed failure of Ta heated to 600ºC is related to oxidation of the thin film at the grain boundaries. Oxidation at the grain boundaries leads to in plane volume expansion of the thin film, significant in plane stress build up, and eventual failure of the Ta thin film. The TaWSi did demonstrate buildup of a surface oxide, but failure of this film was not observed until heated in air to temperatures in excess of 850ºC. Additional investigation of surface oxide formation at 300ºC by ellipsometry revealed that the surface oxide of Ta and TaWSi both terminated between 5nm and 10nm, further supporting the hypothesis that grain boundary oxidation plays a significant role in failure of the Ta film heated in air.

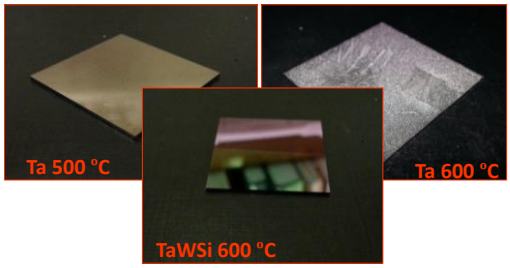

Figure 8: Optical Images Showing Complete Failure of Ta and Stable TaWSi Amorphous Metal Thin Films Heated to 600ºC in Air.

Bench top testing with ink using standard reliability testing conditions revealed no significant difference between Ta and TaWSi. The resistance to chemical attack in ink, thermal stability, and oxidation resistance provided the technical support required to justify construction of a TIJ device using the TaWSi thin film in contact with ink during firing.

Materials Stability During TIJ Firing Event

The TaWSi passed initial blanket film test, but questions regarding stability through a harsh TIJ firing event still remained. A test chip was created to evaluate the thin film materials for adhesion, stability under thermal stress, chemical resistance, and resistance to cavitation. The parts were fired with a pool of ink or water on their surface. This is commonly referred to as a pond test and is designed to deliver the maximum cavitation damage possible. Figure 9A is a tilted view SEM micrograph of a TIJ firing element after more than 100,000 actuations in water. From this image we see that the thin film stack is mechanically stable through the firing events as no delamination of the thin films is present. Some cavitation damage was observed, Figure 9B, after exposure to the extreme cavitation environment.

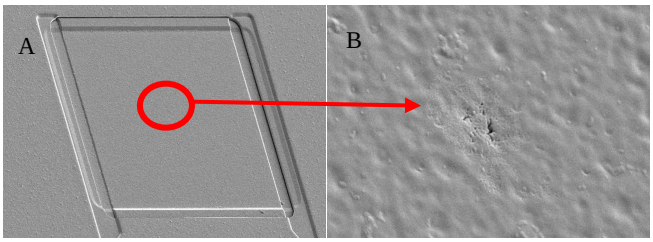

Figure 9: SEM Micrograph of Fired Resistor – A. Circle Identifies location of Cross Section in Figure 9 - Damage Not Visible at This Magnification. B. Magnification of region shown in image A.

Figure 10 provides SEM cross sections comparing the thin film performance in a TIJ firing event for Ta and TaWSi. Both materials demonstrate good adhesion to the substrate and general film integrity through the TIJ firing events. The pitted regions towards the center of each image of Figure 9 were created through cavitation events. From this cavitation information we can conclude that both demonstrate similar cavitation damage under the given harsh cavitation test conditions.

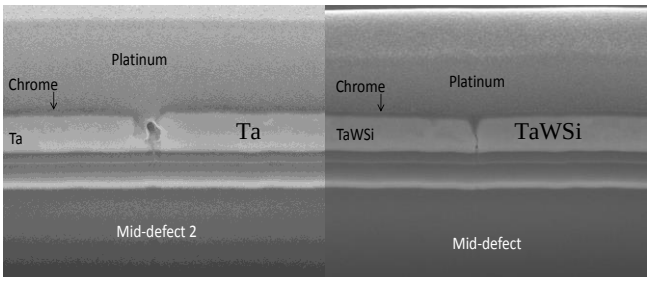

Figure 10. SEM Cross Section of Ta vs. TaWSi Fired Resistors Showing Stable Thin Films and Cavitation Damage

Additional testing was completed using ink to determine resistance to chemical attack through repeated TIJ firing events. No strong differentiation was observed between Ta and the TaWSi thin films of comparable thickness.

All of the testing indicates that TaWSi is likely to perform well in a long lifetime TIJ device. However, at the time of writing this paper, additional work will be required to understand if the amorphous TaWSi is capable of providing a true disruptive advantage in a production TIJ printer environment.

CONCLUSIONS

Research into the design and creation of novel amorphous metal thin films has been completed. We have successfully demonstrated amorphous metal thin films capable of withstanding extreme thermal shock and chemically aggressive environments.

The following conclusions can be made for the TaWSi materials set.

- An amorphous, grain boundary free TaWSi was successfully sputter deposited. The thin film remained amorphous even at high temperatures for extended time in an oxidizing environment.
- The TaWSi materials set demonstrated significantly improved thermal stability relative to Ta when heated to high temperatures in an oxidizing environment. The amorphous metal film did not fail until a much higher temperature than Ta. It also demonstrated the ability to act as an intrinsic barrier to bulk oxidation of the thin film.
- The TaWSi passed all early stage ink based reliability testing with relevant HP inks.
- Testing in a harsh TIJ cavitation environment revealed that the thin film adhesion and cavitation resistance of the TaWSi are at least as good as that observed for a default Ta thin film.

Amorphous TaWSi performed very well in short lifetime TIJ device testing. Successful long life testing more relevant to product will be required if the materials are to be moved into manufacturing for HP printers.

REFERENCES

[1] "Apple Locks in Liquidmetal for Two More Years," Nigam Arora, Forbes, June 6, 2012, Link to Article

[2] "Engineering Materials Achievement Award – Amorphous Titanium Aluminide Hinge," John H. Tregilgas, Advanced Materials & Processes, October (2004).

[3] "Nano-fabrication with metallic glass – an exotic material for nano-electromechanical systems," Sharma, P.; Kaushik, N.; Kimura, H.; Saotome, Y.; and Inoe, A.; Nanotechnology, **18**, 035302 (2007)

[4] "Advancing MIM Electronics: Amorphous Metal Electrodes," Cowell, E.W.; Alimardani, N.; Knutson, C.C.; Conley, J.F.; Keszler, D.A.; Gibbons, B.J.; and Wager, J.F.; Advanced Materials, **23**, 74-78 (2011)

[5] Cartoon of Cavitation; Link to Image

[6] HP Page Wide Technology; Link to White Paper

[7] "At the Printer, Living Tissue," Henry Fountain; The New York Times, August 18, 2013; Link to Online Article

ACKNOWLEDGEMENTS

The team would like to acknowledge the following people and teams for helping to move this project forward:

- Chris Tasker and the OSU Clean Room Team
- John Donovan and Julie Barkman at the University of Oregon CAMCOR facility for assistance with thin film analysis
- The HP Corvallis Analytical Development Labs with special note of Jean A. Burgess, and Gary DeHaan for materials imaging.

CONTACT

*James E. Abbott, tel: +1-541-715-9114; james.abbott@hp.com

POROUS SILICON CARBIDE: A NEW THERMAL INSULATION MATERIAL FOR HARSH ENVIRONMENT MEMS

P.J. Newby[1,2,3], M. Aslaki[1,2], V. Aimez[1,2], and L.G. Fréchette[1,2]*

[1]Institut Interdisciplinaire d'Innovation Technologique (3IT), Université de Sherbrooke, 3000 Boulevard Université, Sherbrooke, J1K OA5, Québec, Canada

[2]Laboratoire Nanotechnologies Nanosystèmes (LN2)- CNRS UMI-3463, Université de Sherbrooke, 3000 Boulevard Université, Sherbrooke, J1K OA5, Québec, Canada

[3]Institut des Nanotechnologies de Lyon, Université de Lyon, CNRS, INSA de Lyon, Villeurbanne, France

ABSTRACT

In this work we demonstrate that porous SiC can be used as a thermal insulation material in MEMS. We have optimised the fabrication process of porous silicon carbide (PSiC), in order to fabricate thick uniform layers. The thermal conductivity of PSiC was measured using the "3 omega" method, showing that it is two orders of magnitude lower than that of bulk SiC. We also carried out chemical etching tests which demonstrate that PSiC has excellent chemical resistance to common cleanroom solvents and etchants. We also studied its high temperature behaviour, in O_2 and N_2, and our results indicate that PSiC is stable up to at least 1000°C. These two properties mean PSiC is compatible with most microfabrication processes, suggesting its applicability as a thermal insulation material, especially for harsh environment MEMS.

INTRODUCTION

Thermal insulation is essential in several types of MEMS (bolometers, PCR devices, or gas sensors for example). Depending on the device, effective thermal insulation can improve sensitivity, reduce power consumption, or decrease response time. Silicon is the substrate material of choice for most MEMS, but due to its high thermal conductivity (156 $W.m^{-1}.K^{-1}$ [1]), other materials or structures must be integrated to provide thermal insulation.

The most common solution is to place the element requiring insulation on a suspended membrane, but such structures are fragile, and impose limits on the design of the device [2]. An interesting approach, well known with silicon, is to locally reduce the thermal conductivity of the single-crystal substrate by selectively nanostructuring it into porous silicon through electrochemical etching [3]. The nanostructures which form porous Si have a characteristic size of approximately 10 nm, which is smaller than the mean free path of phonons in silicon. This causes phonon scattering, and due to this, the thermal conductivity of porous Si is 2-3 orders of magnitude lower than bulk Si [4]. However, porous Si is highly susceptible to chemical etching by many common microfabrication chemicals [5] (photoresist developer for example [6]) and cannot be used above 400°C, as its structure undergoes considerable reorganisation [7]. This is a major obstacle to its integration in a MEMS process flow. To avoid these problems, we propose to nanostructure a semiconductor with vastly superior physical properties: silicon carbide. Several groups have demonstrated that SiC can be nanostructured by making it porous [8]–[12], so in principle, the thermal conductivity of porous SiC (PSiC) should be significantly lower than that of bulk SiC, if the nanostructures are small enough. In order to be used for thermal insulation, porous SiC must not only have a low thermal conductivity, but must also be able to withstand standard microfabrication processes. This implies good chemical resistance and high temperature stability.

Although the fabrication of porous SiC has been demonstrated, these PSiC layers are generally non-uniform and not thick enough for thermal insulation applications. Furthermore, the current literature does not provide enough detail on the effect of fabrication parameters on the morphology of PSiC. The thermal conductivity of PSiC has never been measured to our knowledge, nor has its chemical resistance been characterised. A couple of groups have studied the high temperature behaviour of PSiC, but their results differ, and seem to be morphology dependent [13], [14]. As a consequence, this property must be characterised for our own samples.

We have carried out a systematic study of the fabrication process of PSiC. This study has led to a set of optimized parameters which enable the formation of thick uniform layers. We measured the thermal conductivity of PSiC, using the "3 omega" method, and showed that it is significantly lower than that of bulk SiC. We also carried out chemical etching tests which demonstrate that PSiC has excellent chemical resistance. Finally we studied its high temperature behaviour, in O_2 and N_2, and our results indicate that PSiC is stable up to at least 1000°C.

FABRICATION OF THICK UNIFORM POROUS SIC LAYERS

Porous SiC is made by electrochemical etching in a hydrofluoric acid (HF) based solution. This process is well known and has been described extensively in the case of porous *silicon* [15], [16], and is essentially the same for SiC. The electrolyte we used was a $(1:4:5)_{vol}$ solution of 48% HF, water, and absolute ethanol. The substrates used were n-type 4H or 6H wafers supplied by SiCrystal or Tankeblue. The current density can be varied to control porosity. The main difference with the fabrication of porous Si is that UV lamps can be used to create electron-hole pairs to facilitate etching. There is, however, some debate as to whether illumination is necessary [11], [12]. The last two parameters are variable, and details are specified below for each set of samples.

We carried out a systematic study of the effect of the fabrication parameters on the morphology of the porous SiC layers. These tests led to a set of parameters optimised for the fabrication of thick uniform PSiC layers. Figure 1 shows SEM pictures of a 108 µm thick and uniform layer. This sample was fabricated using a 6H substrate at a current density of 220 mA/cm^2. We also found that fabricating the samples in the dark, without UV illumination, favoured the uniformity of the PSiC layers. From the work on porous *silicon*, it is known that the use of rest times at zero-current during etching can improve the uniformity of the samples. This is also true for PSiC, and we found that the optimal parameter was a cycle of 1s etching followed by an 8s rest. These samples are thicker and more uniform than those published to date.

THERMAL CONDUCTIVITY MEASUREMENTS BY THE 3 OMEGA METHOD

The thermal conductivity of porous SiC was measured using the "3 omega" (3ω) method, initially developed by Cahill [17]. The method has since been used by many groups, and is well suited to thin films with low thermal conductivities [17]–[21]. To carry out the 3ω measurements, a metal line is deposited on the film to be

9781940470016/HH2014/$25©2014TRF
DOI 10.31438/trf.hh2014.94

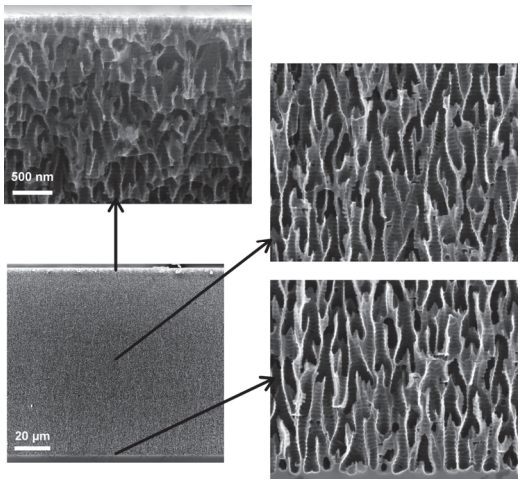

Figure 1: Porous SiC layer fabricated with optimised parameters. The layer is uniform and 108 µm thick. The scale is the same in all three zoomed-in images.

characterised. An alternating sine-wave current, of angular frequency ω, is applied to the line which, due to Joule heating, induces temperature oscillations, ΔT, at double the frequency (2ω). If the line is assumed to be infinitely long, the film thickness semi-infinite, and the frequency low, then the temperature oscillations can be approximated by:

$$\Delta T = \frac{P}{\pi k l}\left(-\frac{1}{2}\ln\omega - \frac{1}{2}\ln\frac{j2b^2}{D} + 0.922\right) \qquad (1)$$

where P is the electrical power, l the length of the line, k the thermal conductivity of the material on which the line is deposited, j the imaginary unit, $2b$ the line width, and D the thermal diffusivity of the material. This equation shows that ΔT varies linearly with ln ω, and its slope is inversely proportional to the thermal conductivity. The metal line has a resistance which varies with its temperature, and at the same frequency as ΔT (2ω). By applying Ohm's law to the metal line, we can show that the voltage of the line contains a third harmonic $V_{3\omega}$:

$$\Delta T = \frac{2V_{3\omega}}{\alpha V_0} \qquad (2)$$

where α is the temperature coefficient of resistance (TCR) of the metal line, and V_0 is the line's potential at the fundamental frequency ω. By combining eqs (1) and (2), the thermal conductivity of the material can be expressed as a function of experimentally measurable quantities:

$$k = -\frac{dR}{dT}\frac{V_{0\,RMS}I_{0\,RMS}^2}{4\pi l}\frac{\ln f_2 - \ln f_1}{V_{3w\,RMS_2} - V_{3w\,RMS_1}} \qquad (3)$$

where R is the resistance of the metal line, V_0 and I_0 the voltage and current amplitudes, and f its frequency.

In practice, $V_{3\omega}$ is measured as a function of the frequency of the sine current applied to the line, using a lock-in amplifier. When the frequency is low enough, $V_{3\omega}$ varies linearly with the logarithm of the frequency. The thermal conductivity of the material can be calculated from the slope of this linear section using equation (3).

The metal line is fabricated on the porous SiC layer by first depositing a thin SiO_2 layer by sputtering to prevent photoresist entering the pores in the subsequent photolithography [6]. The metal line is then made by evaporating 10 nm of chrome and 200 nm of gold and patterning it by lift-off photolithography. The line was 2.9 mm long, and either 4 or 20 µm wide, depending on the sample. The samples used in this case were thick layers (>100 µm), fabricated with the optimised parameters presented in the previous section.

Figure 2 shows an example of a curve obtained during the 3ω measurements. The depth at which thermal conductivity is measured by the 3ω method actually depends on the frequency of the sine current applied to the metal line. At lower frequencies, it is the bulk SiC substrate which is being measured, and at a higher frequency, the depth is shallower, and the thermal conductivity of the porous SiC is measured. This explains why there are two linear zones visible on the graph.

Based on our measurements, averaged over four different samples, we have measured a thermal conductivity of 5.8 $W.m^{-1}.K^{-1}$ ± 2.3 $W.m^{-1}.K^{-1}$. The samples all had a morphology like the sample presented in Fig. 1, and the porous layers had a thickness of ~100 µm. This represents a reduction of almost 2 orders of magnitude compared to bulk SiC. The presence of pores alone cannot account for such a strong reduction. As mentioned earlier, an additional reduction of thermal conductivity is caused by tortuosity and phonon scattering effects [4]. Indeed, the phonon mean free path in bulk SiC is 400 nm [22], and the size of the porous SiC nanostructures of our samples is on the order of 10 nm. Porosification of SiC has therefore been demonstrated to effectively reduce its thermal conductivity.

HIGH TEMPERATURE STABILITY

The aim of this test was to find the maximum temperature at which porous SiC could be used without modifications to its structure. The high temperature behaviour of PSiC was studied by annealing samples of different porosities at different temperatures and under O_2 and N_2.

Samples were made with three different porosity levels. The low, medium, and high porosity samples were made using the Si-face of, respectively 4H, 6H, and 4H substrates at current densities of respectively, 57, 220, and 360 mA/cm^2. All samples were made using UV illumination, and had a thickness of 10-20 µm. Annealing temperatures of 1000, 1200, and 1400°C were used. The furnace was heated at a speed of 20°C/minute, and once the target

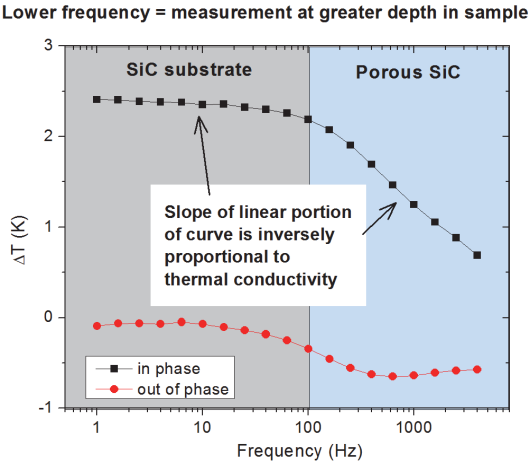

Figure 2: Example of a curve obtained during the 3ω measurements on PSiC.

temperature was reached, it was held for two hours. The samples were characterised by SEM imaging before and after annealing, in order to observe any structural modifications.

Figure 3 shows the results of N_2 annealing, for three porosity levels and different temperatures. Under N_2, the lowest porosity sample shows no sign of structural change, even after annealing at the highest temperature, 1400°C. At medium porosity, the porous structure is unchanged after annealing at 1200°C, but has changed significantly after annealing at 1400°C. This reorganisation was accompanied by a slight reduction of the thickness of the PSiC layer, of ~1 µm, for an initial thickness of 10 µm. The structure of the high porosity sample shows slight signs of reorganisation after the 1200°C anneal.

Figure 4 shows the results of O_2 annealing. After annealing, the nanostructures of the low porosity sample have swelled. At medium porosity, there is no visible change after annealing at 1000°C, but significant swelling has occurred after annealing at 1200°C. The thickness of the low and medium porosity layers did not vary following annealing at 1000 or 1200°C. The structure of the high porosity samples has swelled slightly after annealing at 1000°C. At 1200°C, the structure significantly reorganised and the thickness of the sample was half its initial value.

Swelling of the PSiC nanostructures after annealing under O_2 is inevitable, as SiC is oxidised by oxygen. However, only the structure of the high porosity sample was reorganised after annealing at 1200°C, as evidenced by the reduction of sample thickness, which was not observed for the other samples annealed in oxygen. For both oxygen and nitrogen annealing, our results show that the lowest porosity samples are stable up to higher temperatures, remaining stable up to 1400°C under N_2 and 1200°C under O_2. In all cases, the PSiC samples are stable up to at least 1000°C, suggesting compatibility with a broad range of thermal processes and high temperature SiC MEMS operation. There were probably changes in the surface chemistry of the samples at lower temperatures, but it was not the aim of this study to characterise these effects.

CHEMICAL RESISTANCE

Chemical resistance was tested in a selection of aggressive chemicals commonly used in microfabrication. These products are listed in Table 1 and cover the main operations where chemical solutions are used, *i.e.* cleaning, photolithography and wet etching. The samples were made from 4H substrates on the Si-face. To test

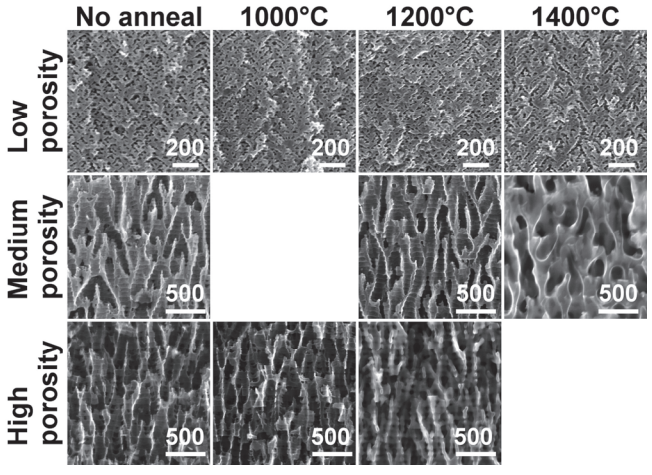

Figure 3: SEM cross-section images of porous SiC samples, before and after annealing under N_2.

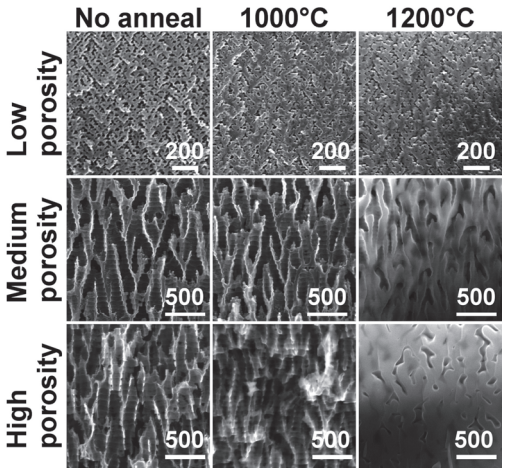

Figure 4: SEM cross-section images of porous SiC samples, before and after annealing under O_2.

the effect of porosity, the samples used were bi-layers formed of a high porosity layer (~19 µm thick) above a low porosity layer (~14 µm thick). The former was made at a current density of 360 mA/cm^2, and the latter at 47 mA/cm^2, and were fabricated under UV illumination. As long as the samples showed no signs of chemical etching, they were reused for other tests, but were dipped in HF first to remove any oxides grown on the surface. In order to detect any chemical etching, the samples were weighed before and after each etch, and SEM imaging was used before the first etch and after the last.

Table 1 shows the chemical solutions to which the porous SiC samples were exposed, the exposure time, and the measured mass variation. The mass variation is expressed in porosity points (for example, a change in porosity of 79% to 80% porosity corresponds to a 1 pp variation). None of the products tested showed any signs of chemical etching, except for RCA-SC1, which caused a slight variation of -2 pp after an exposure of 1h30. SEM imaging of the samples before and after exposure showed no visible signs of chemical etching, for all samples and products. No other signs of etching (*e.g.* bubbles, change of colour) were observed, for all the products tested. The variation of -2 pp observed for RCA-SC1 is only slightly above the measurement resolution. Furthermore, this occurred after an exposure of 1h30, whereas a typical RCA clean would last 10-15 min. Therefore, for all practical applications, porous SiC can be considered inert in RCA-SC1.

The exposure time was variable and was partly dictated by security considerations. In all cases, it was at least equal to a typical exposure time, and often greater. Given the thickness of the samples and the resolution of the balance used, the smallest measurable variation of porosity was 1.4 pp.

In conclusion, porous SiC is practically inert in all the products tested, which cover a wide variety of common microfabrication processes. Combined to its stability up to at least 1000°C, this means that PSiC is compatible with the majority of typical microfabrication processes, and can therefore be integrated into existing MEMS fabrication process flows without having to modify them. Furthermore, this means that porous SiC should be suitable for a variety of applications in harsh environments.

CONCLUSION

We have optimised the fabrication of porous SiC in order to fabricate uniform and very thick layers (up to 108 µm). For the first time, we have demonstrated that porous SiC is chemically inert in

Table 1: Mass variation of PSiC after exposure to common microfabrication chemicals, expressed in porosity points.

	Solution	Exposure time	Mass variation
Cleaning	Piranha	15 min	0
	HF 49%	1 h 13 min	0
	RCA-SC1 75°C	1 h 30 min	-2 pp
	RCA-SC2 75°C	1 h 05 min	0
Photolitho-graphy	MF-319	5 h 28 min	0
	AZ400K - H_2O $(1:4)_{vol}$	17 h 28 min	0
	SU-8 developer	24 h 33 min	0
Wet etching	KOH – H_20 $(1:4)_{vol}$ 70°C	24 h 09 min	0
	HF-HNO_3 $(9:4)_{vol}$ 52°C	1 h	0
	HF-HNO_3-CH_3COOH $(4.5:7.5:8)_{vol}$	1h 10 min	0
	Aqua regia	2 h 05 min	0

common microfabrication solutions, and measured its thermal conductivity. We have also demonstrated that its structure is stable up to at least 1000°C. Therefore porous SiC is a material which is highly suitable for thermal insulation in MEMS, as it is compatible with microfabrication processes, and is ready to be integrated into existing processes and devices, especially harsh environment MEMS.

ACKNOWLEDGEMENTS

The authors would like to thank the Rhône-Alpes region (France), NSERC, FQRNT, the Canada Research Chair program, and NanoQuébec for funding.

REFERENCES

[1] C. J. Glassbrenner and G. A. Slack, "Thermal conductivity of silicon and germanium from 3 K to the melting point," Physical Review, 134, A1058 (1964).

[2] R. M. Tiggelaar, P. van Male, J. W. Berenschot, J. G. E. Gardeniers, R. E. Oosterbroek, M. H. J. M. de Croon, J. C. Schouten, A. van den Berg, and M. C. Elwenspoek, "Fabrication of a high-temperature microreactor with integrated heater and sensor patterns on an ultrathin silicon membrane," Sensors and Actuators A: Physical, 119, 196 (2005).

[3] V. Lysenko, S. Perichon, B. Remaki, and D. Barbier, "Thermal isolation in microsystems with porous silicon," Sensors and Actuators A: Physical, 99, 13 (2002).

[4] G. Gesele, J. Linsmeier, V. Drach, J. Fricke, and R. Arens-Fischer, "Temperature-dependent thermal conductivity of porous silicon," Journal of Physics D: Applied Physics, 30, 2911 (1997).

[5] D. Hamm, T. Sakka, and Y. H. Ogata, "Etching of porous silicon in basic solution," Physica Status Solidi (a), 197, 175 (2003).

[6] M. Lai, G. Parish, Y. Liu, J. M. Dell, and A. J. Keating, "Development of an Alkaline-Compatible Porous-Silicon Photolithographic Process," Journal of Microelectromechanical Systems, 20, 418 (2011).

[7] R. Herino, A. Perio, K. Barla, and G. Bomchil, "Microstructure of porous silicon and its evolution with temperature," Materials Letters, 2, 519 (1984).

[8] J. S. Shor and A. D. Kurtz, "Photoelectrochemical Etching of 6H-SiC," Journal of the Electrochemical Society, 141, 778 (1994).

[9] M. Mynbaeva, "Porous SiC - Prospective Applications (Invited)," in MRS Proceedings, 742, K6.6 (2002).

[10] S. Zangooie, P. O. A. Persson, J. N. Hilfiker, L. Hultman, and H. Arwin, "Microstructural and infrared optical properties of electrochemically etched highly doped 4H-SiC," Journal of Applied Physics, 87, 8497 (2000).

[11] P. Newby, J.-M. Bluet, V. Aimez, L. G. Fréchette, and V. Lysenko, "Structural properties of porous 6H silicon carbide," Physica Status Solidi (c), 8, 1950 (2011).

[12] G. Gautier, J. Biscarrat, D. Valente, T. Defforge, A. Gary, and F. Cayrel, "Systematic Study of Anodic Etching of Highly Doped N-type 4H-SiC in Various HF Based Electrolytes," Journal of the Electrochemical Society, 160, D372 (2013).

[13] M. Mynbaeva, A. Lavrent'ev, I. Kotousova, A. Volkova, K. Mynbaev, and A. Lebedev, "On Current Limitations in Porous SiC Applications," Materials Science Forum, 483-485, 269 (2005).

[14] J. Bai, G. Dhanaraj, P. Gouma, M. Dudley, and M. Mynbaeva, "Porous SiC for HT Chemical Sensing Devices: an Assessment of its Thermal Stability," Materials Science Forum, 457-460, 1479 (2004).

[15] M. J. Sailor, "Porous Silicon in Practice." Weinheim: Wiley-VCH (2012).

[16] V. Lehmann, "Electrochemistry of silicon: instrumentation, science, materials and applications." Weinheim, Allemagne: Wiley-VCH (2002).

[17] D. G. Cahill, "Thermal conductivity measurement from 30 to 750 K: the 3ω method," Review of Scientific Instruments, 61, 802 (1990).

[18] N. O. Birge, "Specific-heat spectroscopy of glycerol and propylene glycol near the glass transition," Physical Review B, 34, 1631 (1986).

[19] N. O. Birge and S. R. Nagel, "Wide-frequency specific heat spectrometer," Review of Scientific Instruments, 58, 1464 (1987).

[20] D. G. Cahill, "Erratum: ``Thermal conductivity measurement from 30 to 750 K: The 3ω method'' [Rev. Sci. Instrum. 61, 802 (1990)]," Review of Scientific Instruments, 73, 3701 (2002).

[21] I. K. Moon, Y. H. Jeong, and S. I. Kwun, "The 3ω technique for measuring dynamic specific heat and thermal conductivity of a liquid or solid," Review of Scientific Instruments, 67, 29 (1996).

[22] E. Ziambaras and P. Hyldgaard, "Phonon Knudsen flow in nanostructured semiconductor systems," Journal of Applied Physics, 99, 054303 (2006).

CONTACT

*P.J. Newby, Pascal.Newby@USherbrooke.ca

A MICRODROPLET-BASED CAPACITIVE SENSING MATRIX FOR TACTILE APPLICATIONS

B. Nie[1], R. Li[1], J.D. Brandt[2], and T. Pan[1]*
[1]Department of Biomedical Engineering, University of California, Davis, USA
[2]Department of Ophthalmology, University of California, Davis, Health System, USA

ABSTRACT

In this paper, we present a highly sensitive microdroplet-based interfacial capacitive sensor matrix device, achieving ultrahigh sensitivity of 0.4nF/kPa and minimal detectable pressure of 33Pa at a 3×3×0.2mm³ packaging. The microdroplet-based sensor is comprised of an array of nanoliter ionic droplets sandwiched between two flexible substrates with patterned transparent electrodes. The sensing principle primarily relies on high elasticity of the sensing droplet and large capacitance presented at the electrode-electrolyte interface. Theoretical analyses and experimental investigations on several design parameters are thoroughly conducted to characterize. Finally, the microdroplet-based pressure sensor is successfully utilized for tactile sensing applications, such as Braille characters scanning and non-invasive cardiovascular pressure recording.

INTRODUCTION

Artificial tactile sensing devices have been extensively researched for their potential utilities in medicines and robotics, in which a wide spectrum of sensing mechanisms have been introduced and investigated, including resistive, piezoelectric and capacitive sensing [1-4]. Among those, elastomeric resistive materials have been frequently employed in building such arrays for their low cost and easy manufacturability [1]. Alternatively, piezoelectric nanomaterial has been incorporated into a pressure sensitive matrix with a sub-millimeter resolution for tactile imaging [2]. Capacitive sensing leads another trend in the development of artificial skins. Conventional capacitive tactile array, using a parallel plate configuration, has been devised for both pressure and force mapping [3]. In more recent effort, a flexible capacitive pressure sensor has been implemented with a microstructured elastomer layer as the sensing element for rapid mechanical responses (in the range of milliseconds) [4].

Latest development on iontronic materials (e.g., ionic liquids) renews long interest in utilizing ionic solutions to regulate the electronic transport at the electrolyte-electrode interface. Upon the solid-liquid contact, an electric double layer (EDL) immediately establishes with an ultrahigh unit-area capacitance on the order of 10μF/cm² at the atomic interface, which is more than thousand times greater than that of the solid-state counterpart (up to 2nF/cm²) [5,6]. It has been shown that the iontronic device can be utilized in transistor or sensors, where the EDL exhibits ultrahigh-density charge accumulation while avoiding reactions by its electrochemical inertness within the potential windows [7-9].

This report present a novel microdroplet-based iontronic sensor array (MISA), utilizing the ultrahigh EDL capacitance at the solid-liquid interface, for tactile sensing applications. Figure 1 illustrates the transparent MISA device of 12×12 elements with the spatial resolution of 1mm. Benefiting from the ultrahigh unit-area capacitance of the EDL, we can achieve a device sensitivity of 0.4nF/kPa and minimal detectable pressure of 33Pa at a 3×3×0.2mm³ packaging, which to our best knowledge is the most sensitive capacitive pressure sensor at its dimension. As the demonstrations of utilities of the iontronic devices, the MISA has successfully resolved the surface topology and detected the dynamic wrist pulses throughout cardiovascular cycles.

Fig. 1: Photography of the sensor array of 12×12 elements with the spatial resolution of 1mm.

THEORY

The MISA device consists of two flexible films with micropatterned transparent electrodes and one spacing layer hosting an array of nanoliter ionic droplets. Figure 2 exhibits the interfacial capacitive sensing principle. The direct ionic droplet-electrode contact immediately establishes the EDL, which possesses a remarkable interfacial capacitance (on the order of 10μF/cm²). Under external loads, the flexible surfaces experience mechanical deformation, resulting in circumferential expansion of the droplet-electrode contact. The corresponding capacitive change over the increased contact area can be detected electronically. Device sensitivity can be modeled both mechanically and electrically. The measured EDL capacitance can be directly related to the area of the droplet-electrode contact, as the invariant unit-area capacitance can be experimentally determined. On the other hand, the mechanical deformation of the membrane can be well defined in the classic mechanic theory [10]. It is worth noting that the interfacial capacitive sensing principle offers an ultrahigh capacitive sensitivity, which is more than thousand times greater than that of the solid-state counterpart, contributed mainly from the nanoscopic charge separation in EDL. The relationship between the measurable capacitive change (ΔC) and the contact pressure applied (ΔP) can be derived from the capacitive sensing principle:

$$\Delta C \approx C_0 \times \left[\frac{\Delta P}{\alpha \times H \times T^3 / L^4} + \left(\frac{\Delta P}{\alpha \times H \times T^3 / L^4} \right)^2 \right]$$

where C_0 and H indicate the initial capacitance and height of the sensing cell, respectively, and the constant $\alpha = 5 \times E \times (1-\upsilon^2)^{-1}$ represents the mechanical deformation of the sensing membrane, influenced by the Young's modulus E and Poisson ratio υ. As can be seen, the relationship between the capacitive change (ΔC) and the contact pressure (ΔP) is highly dependent on the spatial resolution L and the membrane thickness T. In addition, the gravitational effect has been neglected in our consideration, as the microdroplet dimensions are considerably less than that of the capillary length (of ~1.8mm).

9781940470016/HH2014/$25©2014TRF
DOI 10.31438/trf.hh2014.95

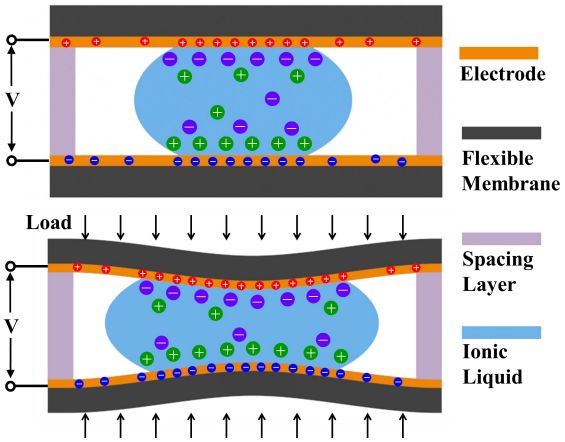

Fig. 2 The interfacial capacitive sensing principle. The EDL capacitance is established at the ionic droplet-electrode contact (top). The contact area expands circumferentially, which is caused by the membrane deformation under external loads and results in an increase in the EDL capacitance (bottom).

METHODS

Device fabrication

The fabrication process starts with micropatterning of conductive ITO electrodes on the flexible PET films using standard photolithography followed by wet etching. In the subsequent step, dry-film photoresist is laminated and photopatterned into a micropillar array on the electrode surface, serving as the supporting structure. To accurately position the microdroplets, surface wettability patterning is applied. A hydrophobic oligomer layer of PDMS is transfer-printed onto both electrode surfaces. Subsequently, using a microfluidic impact printing technique, nanoliter droplets of ionic liquid will be sequentially deposited into a grid matched to the hydrophilic spots formed by the wettability patterning. Prior to the final assembly, two electrode films are aligned face-to-face with the conductive patterns positioned orthogonally to each other, forming a grid of capacitances at the crossover points where the ionic droplet array sits in. The top and bottom layers are then bonded together through the plasma activated hydroxyl groups of the PDMS oligomer layers.

Electrical and mechanical characterization

Experimental investigations of the device sensitivity have been conducted on individual sensing units of the iontronic microdroplet array. The measurement stage is comprised of a force gauge with 1 mN resolution (DFS, Chatillon) amounted on a computer-controlled step motor (VT-80, PImicos) with a spatial resolution of 400nm, from which mechanical loads and displacements can be controlled and monitored simultaneously. The corresponding capacitive changes are directly recorded through an LCR meter (4284A, Agilent). In the characterization of the responsive time, an electromagentically driven pin actuator (Panasonic KX-P1150), powered by a pulsed voltage signal, has been used to apply the periodic contact pressure to the sensor surface. The output signals are measured by a custom circuitry.

RESULTS

Sensing Fluid

As a vital part of the interfacial sensing device, physical properties of the sensing droplet have to satisfy following criteria: high ionic concentration (ensuring high electrical conductance and interfacial capacitance), polarized molecular structure (reversible elasticity on the hydrophobic surfaces) and low fluidic viscosity (allowing rapid mechanical response). Three types of ionic fluids have been considered, such as aqueous electrolytes (e.g., NaCl electrolyte solution), organic solvent solutions (e.g. $KClO_4$/PEO), and ionic liquids, which are commonly investigated in electrochemical processes [11]. Aqueous and solvent-based electrolytes are typically highly evaporative under room conditions and it becomes extremely challenging to maintain the constant electrical performance as both the volume and the physical properties change over time. As an emerging alternative, ionic liquids, consisting of an organic anion or cation, exhibit high electrical conductivity, low volatility, and tunable viscosity [12]. In the report, IL of 1-ethyl-3-methylimidazolium tricyanomethanide has been selected as the sensing fluid for the MISA.

Mechanical-to-capacitive sensitivity

As aforementioned, the overall mechanical-to-electrical sensitivity ($\Delta C/\Delta P$) can be determined by the geometrical confinements (the spatial resolution L and height H of each sensing unit), and the material properties of the membrane, e.g. the thickness T, Young's modulus E and Poisson ratio v. Among those, the spatial resolution of the sensing unit play the most important role, followed by the thickness of the sensing membrane. Experimental investigations have been conducted to verify the above theoretical predications.

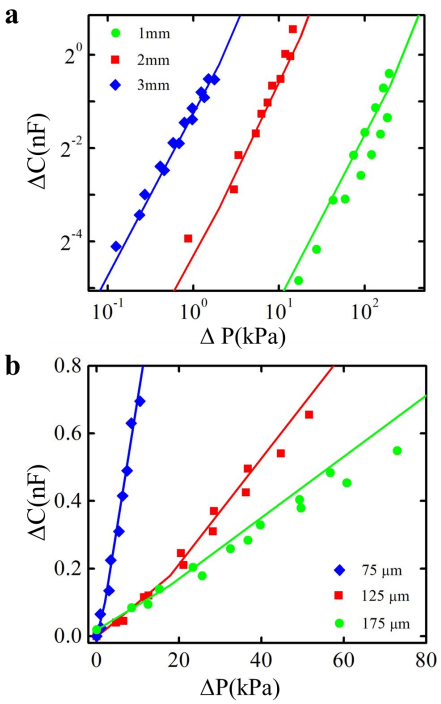

*Fig. 3 Influences of spatial resolution **a** and membrane thickness **b** on the device sensitivity.*

Figure 3 shows the experimental measurements on the device sensitivity with various geometrical designs of spatial resolutions and membrane thicknesses, in which the measurement results (dots) are plotted against the theoretical predications from Equation 1 (curves). As shown in Fig. 3a, the sensitivity exhibits a strong dependence (minor 4th power) on the spatial resolution. By varying the spatial resolution from 1mm to 3mm with a constant membrane thickness of 75μm, the sensitivity can be improved from 3.9pF/kPa to 433.7pF/kPa (more than 100-fold increase), and the device achieves the highest sensitivity with the largest initial capacitance (of 2.3nF) among all the capacitive sensors at the same dimension. In addition, the minimal detectable pressure of 33 Pa is

characterized on the sensor with the highest sensitivity.

Moreover, the membrane thickness plays another notable role in the device performance, as the sensitivity is inversely related to the 3rd power of the thickness. As plotted in Fig. 3b, by adjusting the membrane thickness from 75μm to 175μm, with a fixed spatial resolution of 2mm, the thinner membrane (of 75μm-thick) shows a higher sensitivity of 77.7pF/kPa, while the thicker devices (of 175μm-thick) membranes exhibit a lower sensitivity of 7.8pF/kPa. Furthermore, the targeted dynamic range can be tuned by the geometrical constrains. For instance, in the most sensitive design (3mm in resolution and 75μm in thickness), the maximal pressure is around 7kPa, while the design of 2mm in resolution and 175μm in thickness can extend the measurement range up to 450kPa. Overall, the spatial resolution and the membrane thickness of the MISA could be the determinant factors in the sensor performance (i.e., device sensitivity and dynamic range), allowing highly customizable sensors for a wide range of specifications and applications.

Response Time

Experiments have been conducted to characterize the response time of the MISA devices. A pulsed contact pressure (of ~1.4 kPa) in the frequency ranging from 10Hz to 100Hz has been applied to the device surface through an electromagnetically driven pin actuator. Both the driving voltages to the actuator and the capacitive changes are recorded. As shown in Fig. 4, the capacitive changes of the sensor repeats in the same frequency to the corresponding voltages applied to the pin actuator, suggesting that the sensor can response to the pressure in the frequency up to 100Hz. It is worth noting that the distortion of the recorded pressure signals likely attributes to the open-loop operation of the load applied by the actuator (i.e., the rapid rise edge and slow recovery phase of the capacitive readings).

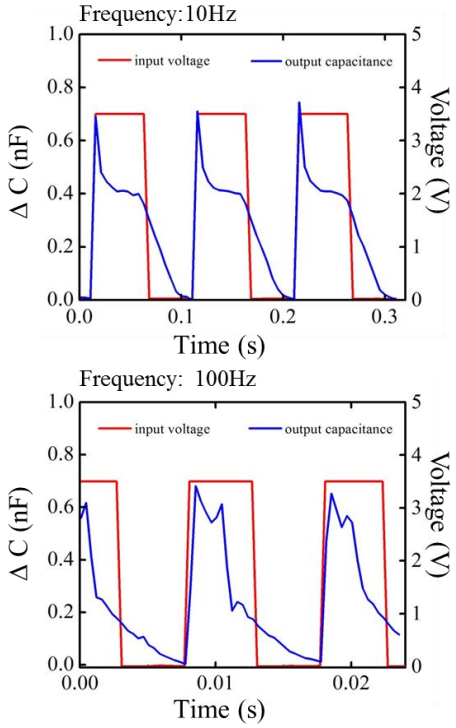

Fig. 4 The time-resolved sensor response measurements under repetitive mechanical loads in the frequency of 10Hz and 100Hz (red curves indicate the input voltage to drive actuator, and the blue curves are the output capacitance measured from a single sensing unit of the MISA device).

Surface Topology Mapping

To demonstrate the flexibility and adaptability of the MISA devices to artificial tactile applications, we have configured a sensor array to detect fine surface topology, such as Braille letters. As can be seen in Fig. 5, the custom MISA consists of 2×3 pixels with the spatial resolution of 2.3mm (to match with the standard Braille letters), and can be worn in a fingertip set up. For the fingertip reading of Braille texts, a gentle contact pressure has been applied to the text surface by the finger. The raised dotted impressions of each Braille character cause the membrane deformation in the corresponding droplet sensing units, which can be subsequently detected by the change of the interfacial capacitance. As shown in bottom panel of Fig. 5, using the finger-amounted MISA device, the letter of "BRAILLE" has been successfully resolved, in which each pressure reading is converted to a digital colorimetric scale. Digital recording of the tactile sensing can be further processed and transmitted into audible readings, and thus, it can be of potential use for Braille education for visually impaired patients.

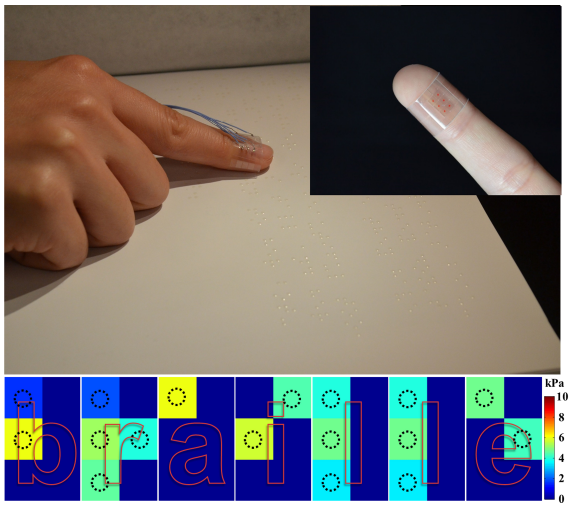

Fig. 5 2×3 MISA device, amounted onto a fingertip, is configured to resolve raised dots of the "BRAILLE" characters in a Braille textbook.

Wrist Pulse Recording

Furthermore, we have utilized the ultrahigh device sensitivity and rapid response time of the iontronic droplet sensors to non-invasive cardiovascular pressure recording. An MISA device of 5×5 array with the spatial resolution of 3mm has been positioned in contact with the skin above the radial artery and fixed by a plastic wristband (Fig. 6a). Real-time pulse recording has been performed by scanning all the sensing elements covering the skin area of 15×15mm² at the sampling frequency of 1kHz in each unit. The MISA device enables two important functions in the pulse recording. First of all, the sensor spatially maps the pulse on the skin surface, from which the sites of the maximal pressure variations can be located. Comparing the pressure mapping results (Fig. 6b) with the sensor position (Fig. 6a), the pressure sensing units right above the radial artery provide the highest capacitive recordings (marked as I, II, III) as expected, and thus, closely reflects the cardiovascular pressure readings using the tonometry principle. In the following step, the pressure wave forms are continuously tracked from these optimal sensing positions. Fig. 6c shows the continuous pulse recordings from the three pixels, respectively. As can be seen, the

maximal pulse variation is around 1.2kPa recorded by Sensor II. Fig. 6d provides a close-up analysis of a single cardiac cycle, which has been characterized into three peaks (P_1, P_2 and P_3). These maxima are caused by traveling waves of the systolic phase and diastolic phase of the blood pressure conducted in the elastic cardiovascular vessels [13]. Clinically significant parameters, such as the radial augmentation index, e.g. AI (=P_2/P_1), can be directly extracted and computed from the maximal pulse recordings, which can be potentially used to screen the arterial compliance [14]. Moreover, the radial pulse waveforms recorded at the optimal sites can be further processed to estimate the central aortic pressure and cardiac output, which reflects the important cardiovascular events and the health states. Though a similar measurement has been conducted recently through a single-channel capacitive sensor, the IMA offers the combined advantage of simultaneous pressure mapping of the optimal recording area and continuous tracking of the blood pressure waveform, in addition to its flexible transparent packaging [4]. In this fashion, the MISA can serve as a flexible sensing device that is highly attractive for the emerging wearable health monitoring applications, in comparison with the conventional invasive cardiovascular monitoring.

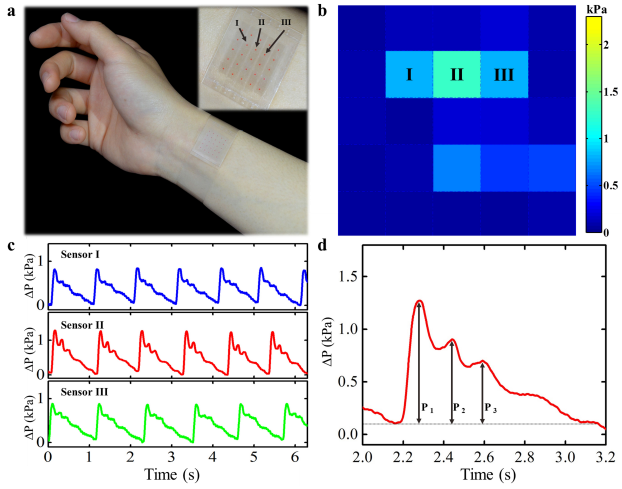

*Fig. 6 Real-time wrist pulse measurements. **a**, illustration of a transparent MISA device of 5×5 array with each pixel size of 3×3mm² embedded in a wrist band for pressure wave recording. **b**, the spatial distributions of the pulse intensities mapped by the MISA. The highest pressure variation readings, marked as I, II and III, are located above the radial artery, in corresponding to the positions of the three units in **a**. **c**, time-resolved strongest pulses recorded by the marked sensing units in **a** and **b**, respectively. **d**, a close-up view of one pulse signal recorded by sensor II in **c**, in which P_1, P_2 and P_3 represent the three consecutive peaks of the pressure wave in each cardiovascular cycle.*

CONCLUSIONS

In this paper, we have presented a novel microdroplet-based iontronic sensor array (MISA) with a very simple architecture and tunable sensitivities. The interfacial sensing principle utilizes the presence of large unit-area EDL capacitance at the elastic droplet-electrode contact. A theoretical model has been proposed to analyze the influences of the geometrical parameters (e.g. spatial resolution and membrane thickness) on the device sensitivity. Taking advantage of ultrahigh sensitivity, fast mechanical response, simple fabrication, mechanical flexibility and optical transparency, the iontronic microdroplet sensors are expected to be employed in a wide range of applications, including robotics, medical prosthetics, surgical instruments, video gaming and wearable computing

ACKNOWLEDGEMENTS

This work is in part supported by the NSF CAREER Award (ECCS-0846502) to TP. BN and RL acknowledge the fellowship support from China Scholarship Council (CSC). Authors would also like to acknowledge the travel support generously provided by the Transducer Research Foundation.

REFERENCES

[1] K. Takei, T. Takahashi, J. C. Ho, H. Ko, A. G. Gillies, P. W. Leu, R. S. Fearing and A. Javey,," Nanowire active-matrix circuitry for low-voltage macroscale artificial skin", Nature Materials, 9, 10 (2010).

[2] W. Wu, X. Wen and Z. L. Wang, "Taxel-Addressable Matrix of Vertical-Nanowire Piezotronic Transistors for Active and Adaptive Tactile Imaging", Science, 340 (2013).

[3] D. J. Lipomi, M. Vosgueritchian, B. C. Tee, S. L. Hellstrom, J. A. Lee, C. H. Fox and Z. Bao, , "Skin-like pressure and strain sensors based on transparent elastic films of carbon nanotubes", Nature Nanotechnology, 6 (2011).

[4] G. Schwartz, B. C.-K. Tee, J. Mei, L. Appleton, D. H. Kim, H. Wang and Z. Bao, "Flexible polymer transistors with high pressure sensitivity for application in electronic skin and health monitoring", Nature Communications, (2013).

[5] H. Yuan, H. Shimotani, A. Tsukazaki, A. Ohtomo, M. Kawasaki, and Y. Iwasa, "High-Density Carrier Accumulation in ZnO Field-Effect Transistors Gated by Electric Double Layers of Ionic Liquids", Advanced Functional Materials, 19, 7 (2009).

[6] M. J. Madou, "Fundamentals of Microfabrication: The Science of Miniaturization", Second Edition, (2002).

[7] J. T. Ye, S. Inoue, K. Kobayashi, Y. Kasahara, H. T. Yuan, H. Shimotani and Y. Iwasa, "Liquid-gated interface superconductivity on an atomically flat film", Nature Materials, 9 (2010).

[8] M. Armand, F. Endres, D. R. MacFarlane, H. Ohno and B. Scrosati, "Ionic-liquid materials for the electrochemical challenges of the future", Nature Materials, 8 (2009).

[9] B. Li, S. Dalgleish, Y. Miyoshi, H. Yoshikawa, M. M. Matsushita and K. Awaga, "Electric double layers allow for opaque electrodes in high performance organic optoelectronic devices", Apply Physics Letters, 101(2012).

[10] S. P. Timoshenko and S. Woinowsky-Krieger, "Theory of Plates and Shells", 1959.

[11] A. Lewandowski, A. Olejniczak, M. Galinski and I. Stepniak, "Performance of carbon-carbon supercapacitors based on organic, aqueous and ionic liquid electrolytes", Journal of Power Sources, 195 (2010).

[12] M. Galinski, A. Lewandowski and I. Stepniak, "Ionic liquids as electrolytes", Electrochimica Acta, 51(2006).

[13] I. B. Wilkinson, N. H. Mohammad, S. Tyrrell, I. R. Hall, D. J. Webb, V. E. Paul, T. Levy and J. R. Cockcroft, "Heart rate dependency of pulse pressure amplification and arterial stiffness", American Journal of Hypertension, 15(2002).

[14] S. Motohiro and K. Kazuomi, "Review: Role of the augmentation index in hypertension", Therapeutic Advances in Cardiovascular Disease, 2(2008).

CONTACT

*T.Pan, tel: +1-530-754-9508; tingrui@ucdavis.com

AN IMPLANTABLE HYDROGEL CHECK VALVE FOR HYDROCEPHALUS TREATMENT—DEVELOPMENT AND IN VITRO MEASUREMENTS

H.N. Schwerdt[1], R.E. Bristol[2], and J. Chae[1]*
[1]Arizona State University, Tempe, AZ
[2]Phoenix Children's Hospital, Phoenix, AZ

ABSTRACT

Permanently stable cerebrospinal fluid (CSF) draining devices are needed for treating hydrocephalus, a debilitating brain disorder. Currently implemented shunts are unreliable as long term implants primarily due to their largely protracted form. The proposed hydrogel valve attempts to generate greater permanency as a chronic implant by forming a direct CSF channel across the physiologically blocked natural valve formations, the arachnoid granulations (AG), and restoring near-natural CSF draining operations. In this way, all CSF draining operations are confined within the cranium. The valve relies on innate hydrogel swelling phenomenon to strengthen reverse flow sealing at idle and negative pressures. *In vitro* measurements in emulated CSF solutions display operation spanning targeted range of normal healthy draining (cracking pressure, $P_T \sim 1 - 110$ mmH_2O and outflow hydraulic resistance, $R_h \sim 24 - 152$ mmH_2O/mL/min), with negligible reverse flow leakage. Overtime tests demonstrate the valve's operational reproducibility and *in situ* feasibility, substantiating its potential for use as a permanent implant.

INTRODUCTION

Hydrocephalus is a chronic brain disorder caused by the inability to drain cerebrospinal fluid (CSF) sufficiently, causing CSF to excessively accumulate within brain ventricles, and leading to fatal increases in intracranial pressures (ICP) [1]-[3]. The disorder may cause abnormal enlargement of the head, convulsions, mental disabilities, and even death. Arachnoid granulations (AGs) serve as a one-way conduit for draining CSF from the interior subarachnoid space (SAS) of the brain to the sinus, immediately exterior (Figure 1), and are in many cases, blocked, in hydrocephalus. Standard treatments to safely lower and maintain ICP in hydrocephalus involve implantation of a large valve (shunt) into the brain to transport CSF through an intracranial tube (catheter) to outside of the skull and to a distal organ. However, more than half of these shunts fail within the first two years requiring additional invasive surgeries [1]. Failure mechanisms are frequently attributed to the shunts' physically obtrusive and lengthy form making them vulnerable to external forces and/or siphoning effects (overdrainage caused by negative pressures created by tube height) [1]. Further, the intracranial catheter element may predispose the brain to risk of infection.

The valve of this work intends to rebuild a CSF channel by directly bypassing the blocked physiological CSF valves or AGs (Figure 1) and utilizes innate hydrogel swelling phenomena to strengthen sealing against leakage. By physically confining drainage channels within the skull, complications caused by the physical bulk of currently implemented shunts – infections, externally induced obstructions, siphoning, trauma, etc. – may be alleviated. This artificial CSF draining valve is intended to be embedded through the meninges and in place of blocked AGs to channel CSF from the SAS to the sinus to restore draining operations of normal healthy AGs. The valve must not only replicate fluid flow behavior of actual ventricular CSF draining without reverse flow leakage, but also be permanently stable in operation over the lifetime of the patient.

To restore CSF draining, the valve must essentially function as a check valve, that is, a one-way channel. In addition, when the valve is open, its hydrodynamic behavior should emulate healthy physiological draining. That is, the cracking pressure (P_T), flow rate (Q_O), and fluidic resistance (R_h) should be in range of normal CSF draining. In summary, the check valves target 3 basic features: 1) infinite diodicity or only flow in the positive direction ($Q_O \geq 0$), 2) zero flow when the pressure difference across the valve, ΔP, is less than the cracking pressure, P_T, ($Q_O = 0$ when $\Delta P < P_T$), 3) a designated non-zero or zero P_T. Such valves have been miniaturized by means of microelectromechanical system (MEMS) technology and are commonly in the form of a cantilever, membrane, duckbill flap, and/or spring-loaded ball [4]-[6]. Despite their enormous progress and development, most MEMS-based valves fall short in one or more of the abovementioned basic operational elements and especially so in avoiding finite leakage ($Q_O < 0$) that occurs due to inadequate sealing mechanisms at idle ($\Delta P \sim 0$) and/or negative pressures ($\Delta P < 0$). In addition, fabrication of MEMS valves usually requires a high degree of complexity to cope with leakage issues.

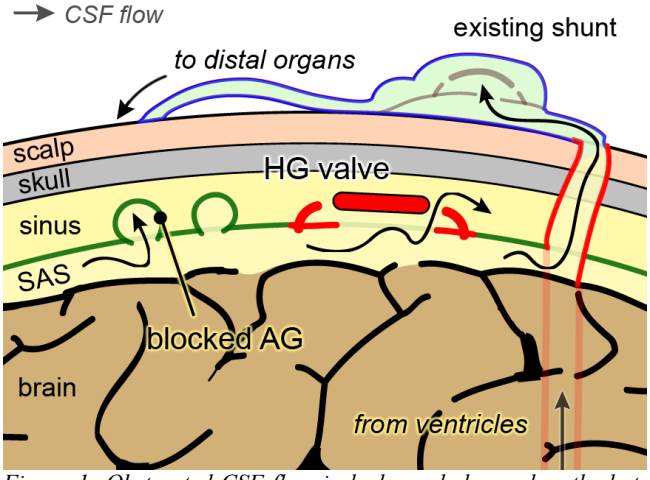

Figure 1: Obstructed CSF flow in hydrocephalus and methods to introduce alternative CSF draining channels (existing shunt treatment approach and hydrogel, HG, valve of this work).

The valve presented here is simple in design (only 3 materials: the silicon valve seat, a parylene coating, and the moveable hydrogel membrane) and fabrication (3 basic steps and no release-related processes and no photoresist). Early work demonstrated the feasibility of the hydrogel valve and its capacity in restoring CSF draining operations [7]. On the other hand, these initial studies addressed little on the following issues: weak operational-reproducibility and long-term durability—aspects critical for permanent medical implants. The use of photoresist in fabrication of the valve was found to compromise its operational stability and functionality. Additionally, the hydrogel membrane experienced large stress causing unpredictable buckling upon hydration. The valve demonstrated here resolves these challenges by eliminating the sacrificial photoresist along with all release-related procedures, and by implementing a stress-relief spiral flexure. Basic benchtop hydrodynamic experiments in emulated

9781940470016/HH2014/$25©2014TRF
DOI 10.31438/trf.hh2014.96

CSF solutions demonstrate targeted behavior in range of normal CSF draining. *In situ* feasibility and practical applicability is further substantiated by measurements of its overtime performance in semi-accelerated conditions emulating amplified pulsatile CSF drainage behavior.

MATERIALS AND METHODS

Basic Operation

The valve entails deflection of a simple circular hydrogel diaphragm anchored by spiral flexures to a silicon substrate (Figure 2). In the closed state, when $\Delta P < P_T$, the hydrogel diaphragm closes the inlet orifice to prevent flow ($Q_O = 0$). The liquid induced swelling behavior of the hydrogel provides a pre-induced sealing force between the hydrogel diaphragm and silicon seat and orifice, effectively establishing a threshold for valve opening (ie. P_T). In the open state, when $\Delta P \geq P_T$, the spiral flexures bend upwards, allowing fluid to flow out through the silicon inlet via. When open, steady state Q_O is primarily governed by the size of the inlet orifice, which acts as a fixed linear hydraulic resistance. The spiral flexure design relieves in-plane stresses caused by the lateral expansion of the hydrated hydrogel and maximizes out-of-plane axial swelling to strengthen sealing.

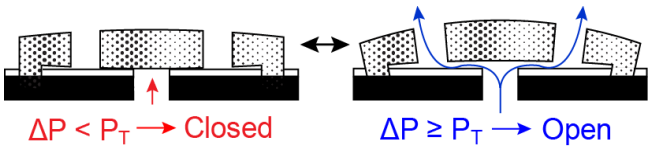

Figure 2: Basic operation of hydrogel membrane valve.

Design

The valve consists of a center circular hydrogel diaphragm hinged to three spiral flexure supports anchored to the silicon substrate and is designed to provide linear flow operation as well as minimal reverse flow leakage. During positive pressure differentials, venous drainage is linear as may be denoted by its outflow resistance, R_h, which ranges from 81.5 – 136 mmH_2O/mL/min as observed in healthy individuals [3]. Design parameters of the valve are listed in Table 1. Membrane deflection is not linearly related to pressure, yet the linear operation may be conceived by rendering flow dependency on the fixed geometries of the valve (ie. the inlet orifice), rather than the pressure-varying displacement of the diaphragm.

Flow rate (Q_O) through the valve may be modeled by a linear expression, $Q_O = \Delta P/R_h$, where R_h is hydraulic resistance. For a deformable membrane valve, R_h may be modeled as a summation of series resistors: the fixed inlet orifice resistance (R_{inlet}), the variable displacement resistance formed by membrane deflection (R_w), and the resistance of the channels formed by the exposed area between flexures (perforations). The latter perforation area is much larger than the area of the former two and may be disregarded in these approximations. The resistance of the circular inlet is [8],

$$R_i = \frac{8\mu L_i}{\pi r_i^4} \qquad (1)$$

where μ is dynamic viscosity of the fluid (μ(water) ≈ 1.002 mPa·s at 20°C and ≈ 0.68 mPa·s at 38 °C, and μ(CSF) ~ 0.72 mPa·s at 38 °C), r_i is the radius of the silicon inlet orifice, and L_i is the length of the orifice or substrate thickness (500 µm). The variable displacement resistance may be approximated to a rectangular orifice,

$$R_w(h_o) \approx \frac{12\mu L_o}{w_o h_o^3 (1 - 0.630\, h_o/w_o)} \qquad (2)$$

where L_o is the channel length formed by the outer edge of the hydrogel center diaphragm and the outer edge of the silicon inlet orifice along the longitudinal axis of the substrate ($L_o = r_o - r_i$), w_o is the channel width or cylindrical circumference formed by the silicon orifice ($w_o = 2\pi r_i$), and h_o is channel height formed by the deflection of the membrane ($h_o \approx w$). Upon increasing ΔP, and hence w, outflow resistance will further become determined by the fixed size and resistance of the inlet orifice (R_i), rather than by the variable membrane gap, and the valve will obtain the desired linear drainage characteristics.

The maximum deflection of the spiral flexures as a function of ΔP may be estimated by [9],

$$w = \frac{3\Delta P \pi r_i^2 L_f^3}{E W_f t^3} \qquad (3)$$

where L_f and W_f are the length and width of the flexure beam, respectively, and E is Young's modulus (~ 10 – 150 kPa for liquid infused HEMA-based hydrogels). By ensuring that $R_i > R_w$, drainage will be further dictated by static R_i, rather than the nonlinear $R_w(h_0)$, and thereby foster targeted linear flow behavior. To ensure that the majority of draining operations are within the linear range, it is informative to estimate the ΔP at which Q_O responds nearly linearly. This minimum ΔP_{min} may be estimated by first equating $R_i = R_w(h_0)$ to find minimum deflection w_{min},

$$w_{\min} \approx \left(\frac{3 L_o r_i^3}{4 L_i} \right)^{1/3} \qquad (4)$$

The w_{min} expression may be substituted into (3) to find ΔP_{min}, which based on design criteria (Table 1), is in the range of $\Delta P_{min} \approx$ 4 – 25 mmH_2O, which is considerably smaller than actual ventricular ΔP that may reach up to 500 mmH_2O, as well as standard designated shunt cracking pressures of $P_T \approx$ 10 – 230 mmH_2O. As ΔP_{min} represents the lower range of ΔP during which outflow behavior is determined by diaphragm deflection rather than static geometries, the low estimated ΔP_{min} indicates that nonlinear behavior only occurs for a small window of operation.

Table 1: Design parameters for valve

Design Variable	Symbol	Value
Hydrogel diaphragm flexure		
Young's modulus	E	10 – 150 kPa
thickness	t	200 – 500 µm
flexure length	L_f	1400 – 2000 µm
flexure width	W_f	100 – 200 µm
center diaphragm radius	r_o	500 – 600 µm
Silicon inlet orifice		
radius	r_i	200 – 400 µm
length	L_i	500 – 750 µm

In the valve's closed state, when the differential pressure between SAS and draining region is less than the cracking pressure ($\Delta P < P_T$), the strength of the reverse leakage seal and the cracking pressure are related to valve geometry and hydrogel material properties. Hydrogel volumetric swelling ratio is given by [10],

$$\left(\frac{V}{V_0} \right)^{-2/3} \approx \frac{k}{\zeta Z} \qquad (5)$$

where V and V_0 are swollen and dry gel volumes, respectively, k is gel elasticity, ζ is degree of gel ionization, and Z is potential ions per dry gel volume. P_T may be estimated by rearranging (3) to solve for pressure (P) as a function of hydrogel expansion.

However, such a crude approximation negates radial expansion that will decrease P_T. Instead, the diaphragm is made sufficiently thick relative its diameter in an attempt to offset vertical displacements caused by lateral swelling-induced stresses concentrated at the anchors.

Fabrication

Hydrogel valve fabrication entails standard micromachining and photolithography processes on a Si <100> wafer and involves three basic steps. The fabrication process is shown in Figure 3. First, 150 nm SiO_2 is PECVD coated on the Si substrate. This oxide layer serves to strengthen adhesion to subsequent hydrogel. A conformal 100 nm film of parylene-C is deposited atop this oxide layer and then patterned using O_2 plasma at 150 – 200 W to create a negative pattern for the hydrogel anchors. The parylene layer provides low surface binding energy to moveable parts of the hydrogel diaphragm. Second, hydrogel is deposited and patterned following substrate adhesion promotion and demarcating hydrogel thickness by fixing 200 – 500 µm thick rubber spacers at wafer perimeters. The hydrogel is synthesized using a chemical composition of the monomer, 2-hydroxyethyl methacrylate (HEMA), crosslinker, ethylene glycol dimethacrylate (EGDA), and photoinitiator, 2,2-dimethoxy-2-phenylacetophenone (DMPA), at a volumetric ratio of 1.0/0.04/0.l. Hydrogel curing and patterning is performed by UV exposure through a mask and developed in isopropyl alcohol and water. Finally, the third step is to form the inlet orifice by deep reactive ion etching (DRIE) the backside of the Si substrate. Residing topside exposed oxide and parylene films are etched using buffered hydrofluoric acid and O_2 plasma, respectively. Fabricated valves are shown in Figure 4.

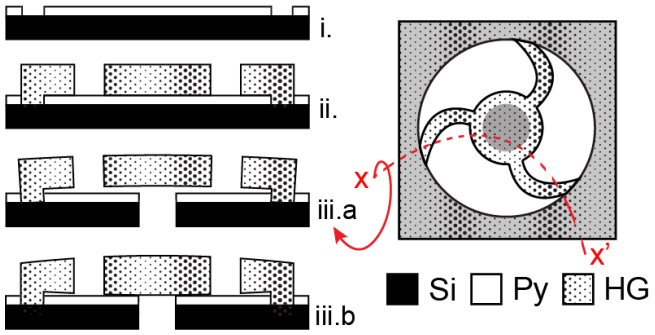

Figure 3. Cross-sectional fabrication process (left) and topside view (right). (i) 0.5–2.0 µm parylene (Py) negative-anchor films deposited on Si and patterned by RIE. (ii) Hydrogel (HG) solution is poured and patterned by UV. (iii.a) Backside inlet formed by DRIE of Si and RIE of Py and (iii.b) then hydrated to swell HG.

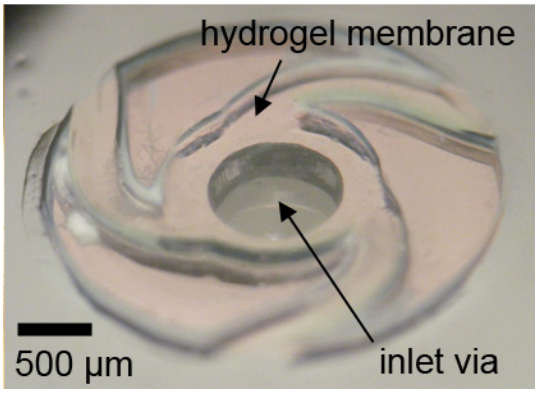

Figure 4. Photograph of fabricated valve.

RESULTS

Experimental Setup

Benchtop testing of the hydrogel valve were performed in a simulated CSF solution (phosphate buffered saline, PBS, or artificial CSF, aCSF) replicating the ionic consistency (pH ~ 7.4) and viscosity of its physiological counterpart, containing 10% blood to exemplify situations of infarction of blood-containing particles. Temperature was maintained at ~ 38 – 40 °C by a constant temperature water bath, to replicate the warmer implant brain environment. The inlet pressure, P_i, outlet pressure, P_o, and ΔP across the valve was measured by amplifying and converting voltage output from a differential pressure transducer (PX26-001DV, Omega) with 1% accuracy, and linearity from -700 < P < 700 mmH_2O with ~ 1 mmH_2O resolution. Q_O was measured by recording the differential pressure across a fixed fluidic resistance: a 35 cm long rigid pipe having an inner diameter of 0.5 mm. The resistor was calibrated directly using a syringe pump input and displayed linearity from -700 < Q_O < 700 µL/min with ~ 2 µL/min resolution. All amplified voltage data were fed to a data acquisition card (DAQ) for computer monitoring. The complete setup encompassing the three sets of measurements is shown in Figure 5.

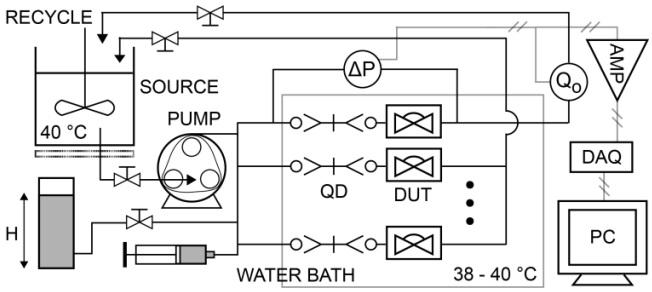

Figure 5. Experimental setup for valve characterization and concurrent parallel testing of multiple valves in hydrodynamic environment for overtime testing.

Basic Hydrodynamic Measurements

Basic hydrodynamic measurements to obtain pressure-flow curves involved inputting flow or pressure and measuring the resulting pressure or flow, respectively. The flow source input was provided by a syringe pump and the pressure source input by a high volume water column. It was found that the type of source did not affect results considerably (Figure 6), and therefore the syringe pump was used for the majority of testing. Figure 6(a) shows multiple measurement sets of pressure-flow data for a valve with t ~ 300 µm, L_f = 1.45 mm, W_f = 200 µm, r_o = 550 µm, and r_i = 250 µm. Measurements were initially performed in water and in a 10% aqueous microparticle (diameter ~ 20 – 53 µm) suspension at ~ 23 °C. Measurements of the valve introduced in the emulated CSF with 10% blood at ~ 38 – 40 °C shifts operation to a lower R_h as expected based on the lower viscosity of the heated *in vitro* fluid. Figure 6(b) displays evaluated range of R_h and P_t for a larger valve with t ~ 250 µm, L_f = 2 mm, W_f = 200 µm, r_o = 600 µm, and r_i = 250 µm in water at ~ 23 °C, in a 10% microparticle aqueous suspension at ~ 23 °C, and in emulated CSF with 10% blood at ~ 38 – 40 °C.

Table 2: Measured specifications for hydrogel valves

	Targeted	Measured
ΔP	-200 – 600 mmH_2O	-800 – 300 mmH_2O
Q_O	0.1 – 3.0 mL/min	0.01 – 1.0 mL/min
P_T	10 – 230 mmH_2O	1 – 110 mmH_2O
R_h	81.5 – 136 mmH_2O/mL/min	24 – 152 mmH_2O/mL/min

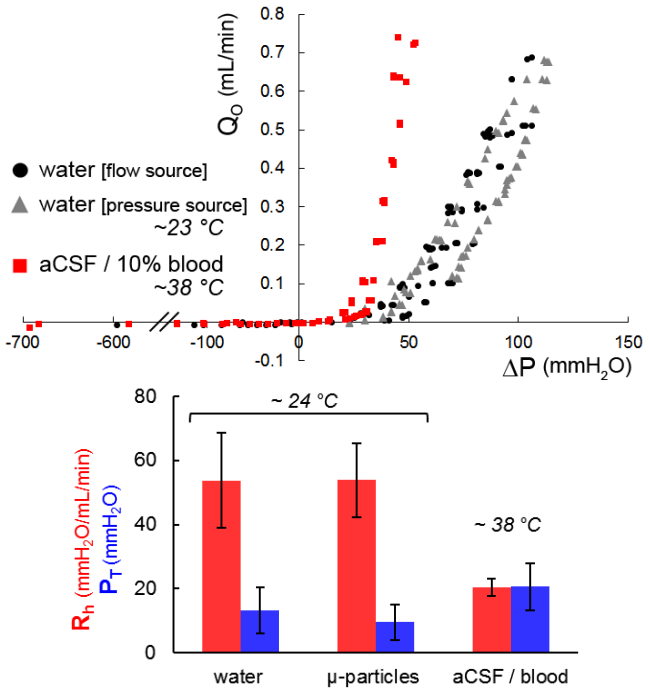

Figure 6: Basic hydrodynamic measurements. (a) Plot of Q_O vs. ΔP for the hydrogel valve with $t \sim 300$ μm and $L_f = 1.45$ mm in water at ~ 23 °C and in emulated CSF with 10% blood at ~ 38 – 40 °C. Measurements in water are shown for both pressure and flow source inputs. (b) Evaluated range of R_h and P_t for another hydrogel valve with $t \sim 250$ μm and $L_f = 2$ mm, in water at ~ 23 °C, 10% microparticle aqueous suspension at ~ 23 °C, and in emulated CSF with 10% blood at ~ 38 – 40 °C.

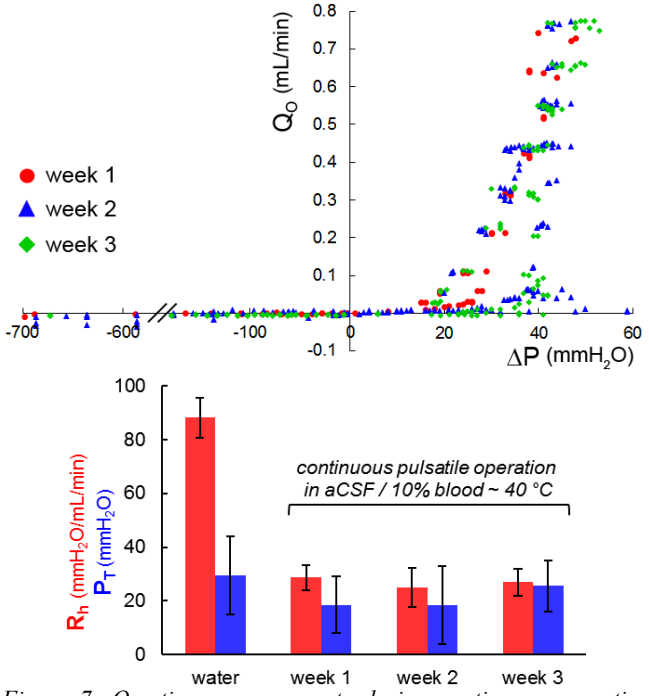

Figure 7: Overtime measurements during continuous operation under semi-accelerated conditions in emulated CSF (10% blood) at ~ 38 – 40 °C: (a) Q_O vs. ΔP for the valve with $t \sim 300$ μm and $L_f = 1.45$ mm. (b) R_h and P_t for the valve during overtime operation and in the initial water environment at ~ 23 °C.

Overtime Measurements

The overtime study involved parallel concurrent operation of multiple hydrogel valve devices subjected to pulsatile flow over several weeks in the emulated CSF solution consisting of 10% blood and at ~ 38 – 40 °C. A peristaltic pump was used to crudely emulate largely amplified and accelerated forms of physiological pressure waves possessing $\Delta P \sim 300 – 800$ mmH$_2$O and frequency of 1 – 4 Hz. Weekly pressure-flow response measurements for the valve with $t \sim 300$ μm and $L_f = 1.45$ are shown in Figure 7(a). The collected data was also analyzed to determine R_h and Pt to quantify relative variation in overtime performance (Figure 7(b)). The deviations seen in R_h and P_t overtime are negligible relative to the variation observed for operation in water prior to prolonged operation under semi-accelerated conditions.

CONCLUSION

The miniature hydrogel valve presented here has been shown to operate with targeted hydrodynamic specifications ($R_h \sim 24 –$ 152 mmH$_2$O/mL/min) in range of actual physiological CSF draining and the desired self-sealing properties to possess negligible leakage. Overtime measurements in amplified pulsatile conditions demonstrate the valve's ability to sustain operationally reproducible draining operations and the potential implant-relevant longevity qualities. The valve is simple in both design and fabrication, and only comprises two or three materials, silicon, hydrogel, and parylene (removable), all of which are biocompatible. These results serve to strengthen the valve's useful application in treating hydrocephalus in a safer and more robust manner than current shunts. Future work to evaluate its ability to drain CSF in real brains will entail *in vivo* testing in animals.

REFERENCES

[1] J.M. Drake, J.R.W. Kestle, and S. Tuli, "CSF shunts 50 years on-past, present, & future," Childs Nerv. Syst., 16, 10 (2000).

[2] M. Czosnyka, Z. Czosnyka, H. Whitehouse, and J.D. Pickard, "Hydrodynamic properties of hydrocephalus shunts: United Kingdom shunt evaluation laboratory," J. Neurol. Neurosurg. Psychiatry, 62(1), 43 (1997).

[3] Z.H. Czosnyka, K. Cieslicki, M. Czosnyka, and J.D. Pickard, "Hydrocephalus shunts and waves of intracranial pressure," Med. Bio. Eng. Comp., 43(1), 71 (2005).

[4] J. Oh, G. Kim, F. Kralick, and H. Noh, "Design and fabrication of a PDMS/parylene microvalve for the treatment of hydrocephalus," IEEE/ASME J. Microelectromech. Syst., 20(18), 811 (2011).

[5] K. Oh and C. Ahn, "A review of microvalves," J. Micromech. Microeng., 16(5), R13 (2006).

[6] P.J. Chen, D. Rodger, E. Meng, M. Humayun, and Y. Tai, "Surface-micromachined parylene dual valves for on-chip unpowered microflow regulation," IEEE/ASME J. Microelectromech. Syst., 16(2), 223 (2007).

[7] H.N. Schwerdt, R.E Bristol, and J. Chae, "Miniaturized Passive Hydrogel Check Valve for Hydrocephalus Treatment," IEEE Trans. Biomed. Eng., 61(3), 814 (2014).

[8] H. Bruus, Theoretical Microfluidics. Oxford University Press, New York, 2007.

[9] S. Timoschenko, Theory of Plates and Shells. McGraw-Hill, New York, 1940.

[10] S.H. Gehrke, G.P. Andrews, and E.L. Cussler, "Chemical aspects of gel extraction," Chemical Engineering Science, 41(8), 2153 (1986).

CONTACT

*H.N. Schwerdt; hschwerd@asu.edu

A MAGNETO-OPTICAL MICROSCOPE FOR QUANTITATIVE MAPPING OF THE STRAY FIELDS FROM MAGNETIC MICROSTRUCTURES

W.C. Patterson, E.E. Shorman, N. Garraud, and D.P. Arnold
Interdisciplinary Microsystems Group, University of Florida, Gainesville, FL, USA

ABSTRACT

A method is presented to quantitatively map the stray fields of microscale magnetic structures, with field resolution down to approximately 50 μT and spatial resolution down to 4 μm. This is accomplished using a magneto-optical indicator film (MOIF), which yields an optical image of the magnetic field when observed with an upright reflective polarizing light microscope. The integrated system including the equipment, image analysis software, and experimental methods are described to extract quantitative magnetic values from optical microscopy images. MOIFs with three different magnetic field ranges have been calibrated, and the entire system is validated by measurement of the field patterns from known samples.

INTRODUCTION

Magnetic fields exist at an extremely broad range of scale, ranging in strength from pico-Tesla to 100's of Tesla. Furthermore, practical engineering systems have spatial field variations ranging in size from nanometers to 10's of meters. Due to the large ranges in both field intensity and spatial resolution, many different methods exist for measuring and mapping magnetic fields. For example, methods such as superconducting quantum interference device (SQUID) are capable of measuring extremely small fields in the pico-Tesla range, while Hall effect sensors can measure fields up to the 100's of Tesla.

Our interests lie in magnetic microsystems, e.g. microscale electromagnets or permanent micromagnets integrated on chip, where the magnet dimensions may range from 1 μm to 100's of μm. To map the stray fields from such structures, we desire a field measurement tool capable of measuring fields ranging from μT to T, while mapping over distances of millimeters with a spatial resolution of ≤1 μm. Table 1 outlines three forms of field mapping [1 – 3] that fit the desired range for magnetic MEMS work, each with their own pros and cons. The first two, magnetic force microscopy (MFM) and scanning Hall probe microscopy (SHPM), are raster methods of field mapping. Due to this rastering, the scans of MEMS scale structures take an immense amount of time, and the required equipment is fickle and often quite expensive. In contrast, magneto-optical imaging (MOI) is an imaging technique that affords the benefit of speed, along with low cost and ease of operation, which outweigh its shortcomings in sensitivity and spatial resolution.

Table 1: Magnetic measurement technique comparison. Red = Bad, Yellow = OK, Green = Good

	MFM	SHPM	MOI
Measurement	Force	B_z	$\beta \propto B_z$
Sensitivity	1 μm/N	0.1-10 μT	> 50 μT
Spatial res.	20 nm	0.5 μm	> 1 μm
Scan size	300 μm	10's mm	100's mm
Field range	Broad	± 16 T	± 500 mT
Scan speed	<100 points/s	< 10 points/s	<30 frame/s

This paper presents a tool called a "magneto-optical microscope" for quantitative imaging and measurement of stray magnetic fields produced from micromagnetic structures. The capability for large-area, high-spatial-resolution measurement of milli-Tesla to Tesla-level magnetic fields fills a critical metrology gap for magnetic microsystems, not served by MFM or SHPM [1]. Benefits of our system are: high magnetic resolution (ranging ±50 μT to ±1 mT), fast characterization (few seconds) over a large spatial area (~cm^2), high spatial resolution (ranging 4.2–20.1 μm), non-destructive, non-invasive, non-contact, and relatively inexpensive total hardware cost (~$50k). The system was designed to require very little custom hardware and to be fairly flexible to varying measurement requirements, as commonly found in a research lab. Herein we report the system design, operation, calibration, and validation.

SYSTEM OPERATION & DESIGN

Magneto-Optical Imaging Film

At the heart of the system functionality is the MOIF, which leverages the Faraday Effect for visualization and measurement of magnetic fields. As illustrated in Figure 1, the Faraday Effect is an interaction between light and a magnetic field in a medium, which causes a rotation of the plane of polarization in proportion to the magnetic field [4].

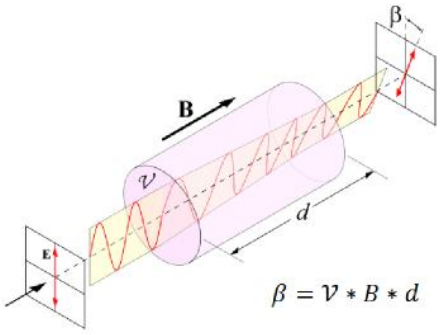

Figure 1: Diagram illustration of the Faraday effect. Diagram represents an example of light transmission completely through a material. On our MOIF one side is reflective, so polarization rotation is further exaggerated as light reflects back through the material again. ("Faraday-effect" by Bob Mellish / CC BY).

As shown in Figure 2 the MOIF is a multi layer sensor that consists of: an optically transparent substrate layer that provides mechanical support and the correct crystal structure for film growth, a magneto-optically active layer (MOL) that has a high Verdet constant υ resulting in a strong Faraday Effect [5], a mirror coating to reflect the light back through the MOL again, and a protective layer made of a high hardness material to protect the mirror and MOL.

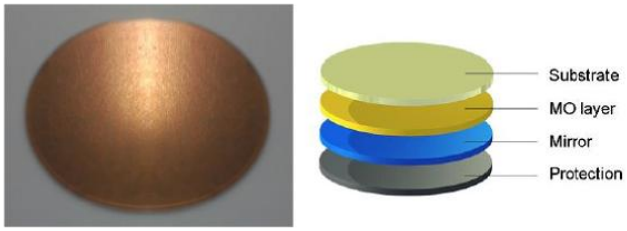

Figure 2: (Left) Commercial MOIF from Matesy, GMBH. (Right) Exploded view of MOIF layers.

9781940470016/HH2014/$25©2014TRF
DOI 10.31438/trf.hh2014.97

The MOL material used in this system is a bismuth substituted yttrium iron garnet (Bi-YIG) grown on a gadolinium gallium garnet (GGG) substrate. The reflective coating is aluminum with a sapphire protective layer deposited on top. The films are purchased from Matesy GMBH, and different saturation/sensitivity films are available. The current system has three MOIFs available with 5, 40, and 250 mT saturation ranges.

Magneto-Optical Microscope System

A block diagram of the magneto-optical microscope is shown in Figure 3. The system is designed around an upright metallurgical microscope for the sake of cost and ease of use. In operation, the MOIF is positioned in close proximity to the magnetic sample to be measured. White light from the standard microscope bulb is linearly polarized and then passed down through the microscope objective. The light then passes through the transparent substrate, translucent magneto-optic layer, and reflects off the mirror coating on the bottom side of the MOIF (see Figure 2). During this transit, the polarization is rotated in proportion to the perpendicular (out-of-plane) magnetic field strength. The rotated light passes back up through the objective and is filtered by the analyzer, which is a second linear polarizer. After the analyzer, the light has an intensity distribution that is proportional to the magnitude of the magnetic field sensed by the MOIF. This intensity image is then captured by the grayscale camera and creates a visual representation of the stray magnetic fields.

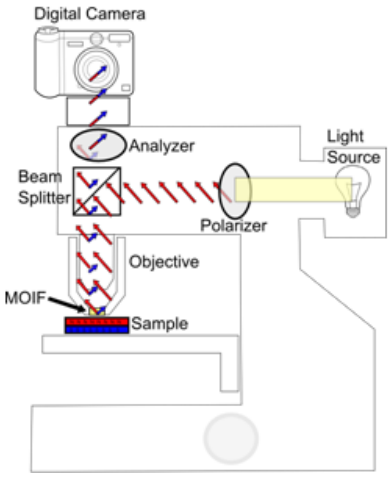

Figure 3: Block diagram of quantitative MOI system.

Magneto-optical Microscope Components

The magneto-optical microscope is shown in Figure 4 and consists of four main components: a reflective polarizing light microscope (Olympus BX51), a grayscale digital camera (Thorlabs DCC1545M), a milled objective sleeve holding the MOIF, and custom digital image processing software.

A grayscale digital camera was chosen due to the difficulties that were encountered in preliminary experiments using a color camera. Under white light illumination, the MOIF exhibits a shift in color in response to a magnetic field. This color shift and the nonlinearities in the pixel color filters used in a color camera, made it difficult to obtain pixel intensity values without saturating some colored pixels, or leaving others without signal completely. The grayscale camera that is used in the system has a fairly low-quality CMOS imaging sensor. Low-noise data can still be obtained by averaging multiple images. For higher resolution images, a larger, scientific quality, grayscale CCD camera could be acquired.

Figure 4: (Left) BX51, upright reflective polarizing light microscope, with MOIF sleeve slid on to objective. (Right) Thorlabs DCC1545M grayscale digital camera.

Previously, MOI processing required that the MOIF be placed directly onto the sample, and then the microscope be focused onto the MOIF to obtain the image. We've found the following drawbacks with this approach:

- It requires that the MOIF be placed carefully on the samples area of interest. Often the desired sample does not have any visible markers apparent to the naked eye making the placement challenging.
- There is a limited measurement area before the MOIF needs to be repositioned.
- Every image is taken on a different area on the MOIF. The MOIF is not necessarily uniform so the calibration becomes difficult.
- The light path can be affected by outside sources, such as the rooms' ambient lighting.
- The MOIF is limited to only measuring at the samples surface.
- The focus is done manually per sample and may cause variability in measurements.

To solve these problems, a sleeve was machined to mount the MOIF onto the microscope objective, as shown in Figure 5. The MOIF is positioned at the focal plane via the adjustable nose piece on the sleeve. The benefits of the sleeve are that: it allows the MOIF to remain at the focal point of the microscope as samples are changed or moved; it prevents the MOIF from rotating or translating; it eliminates all outside light sources; and the spring loaded nose piece can assure repeatable sample contact pressure.

Figure 5: (Left) Custom optic sleeve installed on objective. (Middle) Assembled optic sleeve. (Right) Exploded view of sleeve.

Image Analysis Software

To achieve quantitative data from the images, a reliable correlation must be made between the grayscale intensity values from the camera and the B-field values acting on the MOIF. Unfortunately, making this correlation is hindered by variations in total light intensity, camera exposure time, light path depolarization, and optical non-linearities in the optical path, and electronic non-linearities associated with the camera [5].

All of the previously mentioned signal corruptions could be considered "common mode" noise and could be rejected by differential imaging. Indeed, there is an absolute correlation

between the *differences* of two identical grayscale images with inverse analyzer crossings (e.g. ±15°). With this in mind, a novel method is introduced using three images with symmetric analyzer settings to create a quantitative image. The three images are taken with different analyzer settings, -15º, 0º, and +15º. Then the individual pixels of the grayscale intensity image are entered into the following equation:

$$\Delta = \frac{I_{-15^\circ} - I_{+15^\circ}}{I_{-15^\circ} + I_{+15^\circ} - 2I_{0^\circ}} \quad (1)$$

The resulting delta values create a "normalized image." This normalized image represents only the rotation of the polarization plane, rejecting all the "common mode" error signals described above. Figure 6 shows an example calibration curve/matrix for the MOIF at known magnetic fields supplied by a calibrated electromagnet. When making measurements, the pixel intensities are mapped to their corresponding B-field values to form the magnetic image.

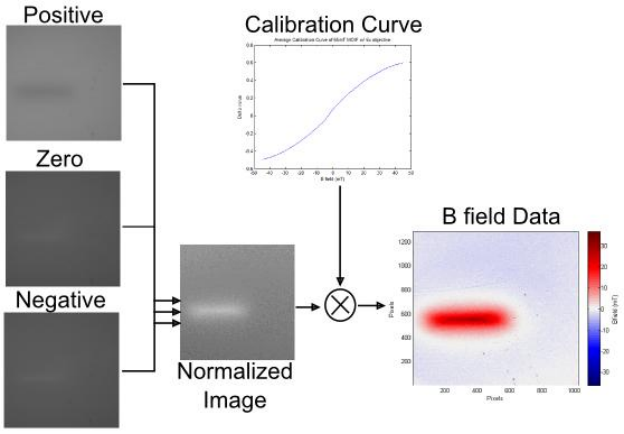

Figure 6: Steps in the quantitative MOI process.

PROCEDURE

Calibration Procedure

The calibration process creates a curve relating the delta value to B-field for every pixel in the image. A representative calibration curve for the entire MOIF is created by averaging all of the pixels calibration curves. An example can be seen in Figure 7.

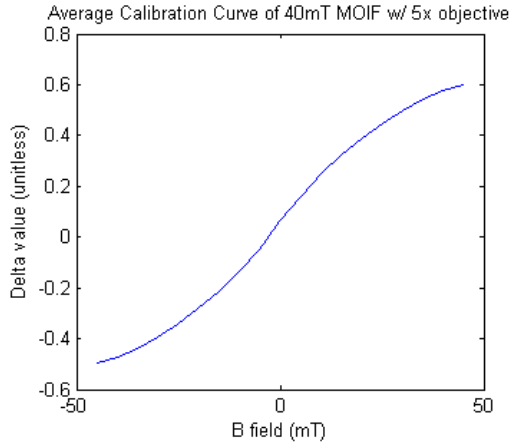

Figure 7: Calibration curve of 40 mT MOIF with 5× objective. B-field is swept from -40 to +40 mT, resulting in a normalized value proportional to polarization rotation.

To create a calibration curve/matrix, the MOIF is subjected to a known uniform field, a delta image is obtained, the field is increased, and the process is repeated across the desired field range until the entire calibration curve/matrix is obtained. To achieve a uniform field, an air core solenoid was designed and wound to fit on the microscope stage around the MOIF sleeve. The field strength and spatial uniformity of the solenoid was then calibrated using a DC current supply and an instrument grade gauss meter (Lakeshore 475 DSP Gaussmeter).

Quantitative Imaging Procedure

To measure unknown samples, three images are taken of the MOIF at three different polarizer settings: -15º, 0º, and +15º. These pixel intensity values of these images are calculated via (1) in order to create a delta image. This image is then interpolated against the calibration data. The result is a quantitative map of the stray magnetic fields of the user's sample.

RESULTS

Calibration

The three different ranged MOIF's were re-calibrated five times over a two-week period to test the repeatability of the MOIF and setup procedure. A representative repeatability test is shown in Figure 8. The overall shape and peak-to-peak amplitude remain consistent. However, there is a small DC offset from calibration to calibration. It was found that the offset is caused by miniscule (< 1º) changes in the absolute position of the analyzer setting. To prove this, three calibrations were performed with the analyzer settings at approximately (-14º, 1º, 16º), (-15º, 0º, 15º), and (-16º, -1º, 14º). This caused the curve to be offset on the y-axis with no change in curve shape or amplitude.

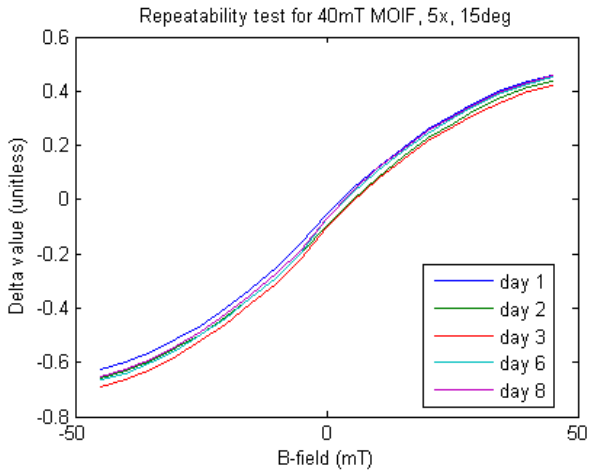

Figure 8: Example calibration repeatability curves for the 40 mT MOIF over an 8 day period.

Validation/Example Measurements

As a proof of operation, a known sample is measured using the magneto-optical microscope. The sample chosen for this test was a commercially purchased NdFeB cylindrical magnet with a 1.0 mm height and 1.0 mm radius. The magnetic properties were first measured using a vibrating sample magnetometer (VSM), and from this information the stray magnetic fields were simulated using finite element analysis software (COMSOL Multiphysics). The stray fields were then experimentally measured using the 250 mT MOIF. Multiple measurements were taken at different heights above the sample.

Figure 9 is a comparison plot between the experimental results and the simulations. Only three heights are shown for clarity. The experimental results match the simulations fairly well. Discrepancies could be caused by slight inaccuracies in the simulation due to magnet size tolerance and a thin protective nickel coating on the outside of the magnet being unaccounted for. On the experimental side, there is some uncertainty in the height above the sample; this error would create a larger effect in measurements closer to the sample surface.

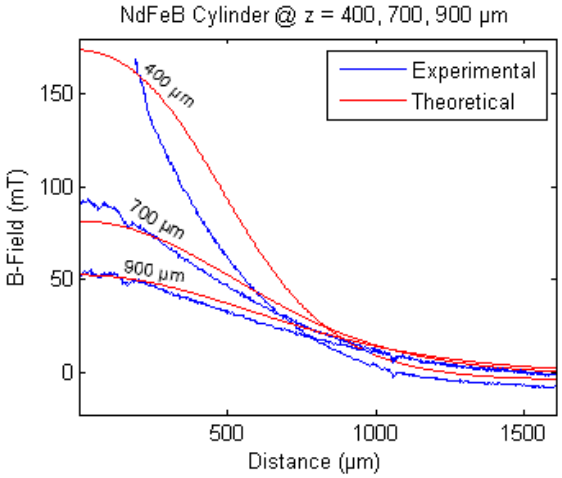

Figure 9: Experimental versus theoretical cross section measurements of a 1 mm NdFeB cylinder magnet at 400,700,and 900 µm above the surface.

An example of a more complex field is seen in Figure 10. This is a two dimensional map of the field intensity at the surface of an interdigitated magnetic micro-undulator [6]. In this sample each finger is magnetized in the opposing direction. The black strips at the center of the fingers are points where the field exceeds the maximum measurable field of the MOIF; at these points the field is not defined (saturated points are plotted black).

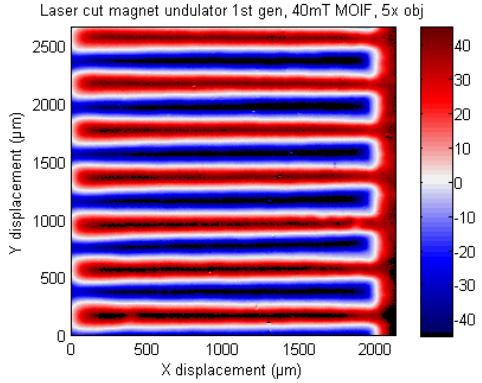

Figure 10: Quantitative image of the alternating field pattern from an interdigitated magnetic micro-undulator.

System Specifications

The measurement specifications of the system are summarized in Table 2. Magnetic resolution is calculated by taking the saturation range for a particular MOIF, and dividing it by the eight bit camera resolution. Spatial resolution is calculated as the total MOL, reflective layer, and protective layer thickness [4]. Actual spatial resolution may vary depending on flatness of the sample, and precision of testing techniques used by the operator. This is because any sample to MOIF gap will be added to the spatial resolution calculation.

Table 2: Minimum specifications for calibrated MOIFs.

MOIF Type	Magnetic Range	Magnetic Resolution	Spatial Resolution
5 mT	±5 mT	±50 µT	4.2 µm
40 mT	±40 mT	±0.5 mT	6.2 µm
250 mT	±230 mT	±1 mT	20.1 µm

CONCLUSIONS

We have developed a system and unique image processing system to quantitatively map the stray fields of microscale magnetic structures. This MOIF-based optical measurement technique allows large areas to be measure nearly instantaneously while still maintaining a useful measurement range (±5 mT to ±230 mT) and resolution (±50 µT to ±1 mT). The system is built using common lab equipment and materials. By using a novel differential imaging method, common mode signal errors can be easily removed. The technique was validated by comparing the data obtained from the magnetic microscope of a known sample against its theoretical model. This system provides a valuable measurement capability to aid in the ongoing development of miniaturized electromagnets, magnetic materials, and other related microsystems.

ACKNOWLEDGMENTS

This work was supported in part by Army Research Office (W911NF-09-1-0511), DARPA (N6601-11-1-4198), and Allegro Microsystems LLC.

REFERENCES

[1] S. J. Bending, "Local Magnetic Probes of Superconductors," *Advances in Physics*, 1999.

[2] J. H. Kindt, "Survey, Screening, Dynamics: A No-Compromise Approach to High-Speed Atomic Force Microscopy," Bruker Nano Surfaces, Santa Barbara, CA, USA, 2011.

[3] F. Laviano, et al., "An improved method for quantitative magneto-optical analysis of superconductors," *Supercond. Sci. Technol.*, vol. 16, p. 71–79, 2003.

[4] R. W. M. Koblischkat, "Magneto-optical investigations of superconductors," *Supercond. Sci. Technol.*, vol. 8, 1995.

[5] B. Azzerboni, et al., "Magnetic Imaging Films," in *Magnetic Nanostructures in Modern Technology*, Springer, 2008, p. 195–224.

[6] B.A. Peterson, et al., "Laser Micro-Micromachined Permanent Magnets With Highly Spatial Alternating Magnetic Field Distribution," in *PowerMEMS*, Dec. 2012.

CONTACT

*William C. Patterson; wmcpatterson@ufl.edu

CANTILEVER-BASED RESONANT MICROSENSOR WITH INTEGRATED TEMPERATURE MODULATION

C. Carron[1], P. Getz[1], J.-J. Su[1], L.A. Beardslee[1,2], S.M. Heinrich[3], F. Josse[4], and O. Brand[1]*
[1]School of Electrical and Computer Engineering, Georgia Institute of Technology, Atlanta, GA, USA
[2]College of Nanoscale Science and Engineering, State University of New York, Albany, NY, USA
[3]Department of Civil, Construction and Environmental Engineering, Marquette University, Milwaukee, WI, USA
[4]Department of Electrical and Computer Engineering, Marquette University, Milwaukee, WI, USA

ABSTRACT

This paper introduces a resonant cantilever platform with integrated temperature modulation for chemical sensing. The embedded heating elements enable rapid thermal cycling of individual resonant microstructures and, thus, allow for analysis of signal transients, which contain information about the sorption kinetics of analytes into the sensing film on the resonator surface. The signal transients are generated without the need for a microfluidic setup to switch between analyte and reference gas streams. Compared to traditional mass-sensitive microsensors operating in steady state, the on-chip generation of signal transients provides additional information for analyte discrimination and quantification.

INTRODUCTION

We live in an information-rich era that has come to expect ubiquitous on-demand data delivered at low cost to mobile platforms. This hunger for ever-increasing amounts and types of data has expanded to include chemical and biological information, with the hope that such data hold keys to improving our life. For example, MEMS-based chemical and biological sensors enable more convenient and advanced forms of Point of Care Testing (POCT), which can provide patient data in real-time at the patient's bedside [1]. MEMS-based chemical sensors, integrated with mobile platforms, further offer the possibility of distributed real-time environmental monitoring in remote or hazardous locations, where conventional techniques would be impractical or even impossible [2,3]. By adding additional value in terms of automation and real-time data collection, MEMS-based sensor technologies are even being developed to displace traditional analysis methods for addressing routine pollution concerns (e.g., municipal water supplies and indoor air quality) [2].

Currently, many standard testing systems for chemical analysis consist of bulky desktop equipment (e.g., gas chromatography, mass spectrometry), requiring costly and complex external support systems to process and treat samples with additional reagents and control fluids [2,4]. Such systems are often expensive and difficult to transport, requiring them to be located at a fixed position in a centrally located facility. Thus, many such standard tests require samples to be transported off-site to a designated testing facility for processing and analysis, which introduces significant time delays and can even lead to inaccuracies in the results due to sample degradation [2]. In instances where the sample analysis leads to a time-sensitive decision (e.g., clinical decision, quarantine of a contaminated location), such delays severely limit the efficacy of the information being gathered. In these cases, the real-time nature of data provided by low-cost MEMS-based sensors can prove more valuable than the superior accuracy of traditional techniques, leading to applications where 'good enough,' in terms of measurement resolution, can be a preferable alternative.

With the goal of developing such real-time mobile sensing platforms, this work demonstrates a resonant cantilever platform with integrated temperature modulation for chemical sensing. The embedded heating elements enable rapid thermal cycling of individual resonant microstructures and, thus, allow for analysis of signal transients, which contain information about the real-time sorption kinetics of analytes into the sensing film on the resonator surface [5,6].

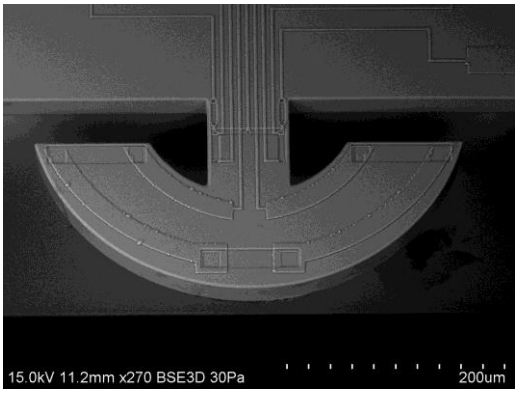

Figure 1: SEM micrograph of resonant microstructure with semicircular head with 200 µm outer radius supported by 75 µm wide and 100 µm long cantilever. Resistors for thermal excitation and piezoresistive detection of in-plane vibrations are located at the cantilever base. Three heating resistors, for rapid thermal modulation, connected in series are clearly visible on the semicircular head.

By generating the signal transients through temperature modulation with integrated heating units, this mode of operation potentially eliminates the need for an external microfluidic setup to switch between analyte and reference gas streams. Additionally, the rapid temperature modulation enables intrinsic drift compensation without the need for a reference resonator and generates measurement data in real-time. Combining these two advantages – no need for external flow system or reference resonator – can dramatically reduce the complexity and cost of the total system, leading to increased deployability in the field as part of low-power mobile platforms. Finally, when compared to traditional mass-sensitive microsensors operating in steady state, the on-chip generation of signal transients provides additional information for analyte discrimination and quantification, which can lead to improved sensing performance in the presence of interfering compounds [5,6,7,8].

DESIGN & FABRICATION

Figure 1 shows an SEM micrograph of a fabricated micro-resonator consisting of a semicircular head region with inner and outer diameters of 100 µm and 200 µm, respectively, supported by a 75 µm wide and 100 µm long cantilever beam. Three integrated heating resistors, connected in series, are defined around the perimeter of the semicircular head region and were formed via high-temperature boron diffusion through an oxide mask. As the thermal

9781940470016/HH2014/$25©2014TRF
DOI 10.31438/trf.hh2014.98

excitation resistors as well as the piezoresistive sensing resistors connected in a Wheatstone bridge are formed in like manner, the integration of the embedded heating resistors does not require any additional process steps. The total series resistance of the embedded heating unit was designed to have a value of approximately 1 kΩ, allowing for significant temperature elevation with modest applied heating current in the low milliamp range. The overall resonator structure was further designed to allow for rapid and uniform heating of the head area with a minimal thermal time constant.

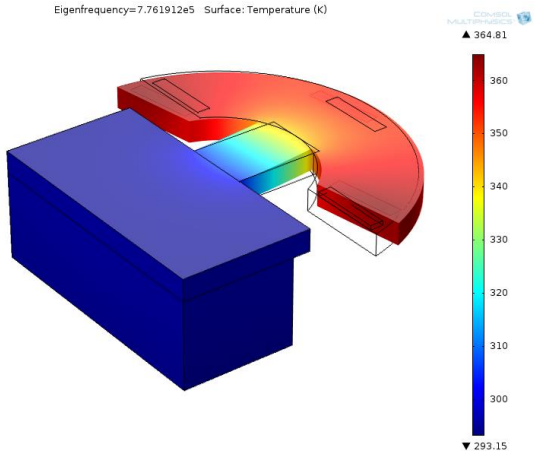

Figure 2: Thermal-modal analysis of resonant microstructure using COMSOL. The applied heating power of 100 mW causes a 71˚C temperature elevation of the head structure (see color coding). The simulated in-plane resonant frequency of the heated structure is 776.19 kHz, representing a shift of -610Hz compared to the unheated structure.

The fabrication approach for this device represents a slight departure from our previous work [9,10,11], in that the sensing platform is formed on silicon-on-insulator (SOI) substrates and does not utilize KOH etching to release the finished devices. Instead, a high-aspect-ratio deep reactive ion etching (DRIE) process is implemented on the reverse-side of the wafer, with the buried oxide (BOX) layer serving as the etch stop. The micromachining used to pattern the top-side of the wafer is similar to our previous designs, with the exception that the DRIE used to pattern the resonator geometry from the top side does not accomplish a final release of the devices but, as with the reverse-side DRIE, stops at the BOX layer. Final release is performed by removing the exposed BOX layer regions with a standard plasma etch for SiO_2. While this process arrangement introduces additional complexity into the fabrication of the resonant devices when compared to our previous work, it also offers the ability to define high-aspect-ratio features onto the reverse-side of the die, making possible novel future designs.

Device operation remains similar to our previous work [9,10,11]. The resonator is driven at its fundamental in-plane resonance mode using the aforementioned diffused silicon excitation resistors at the base of the cantilever beam. Four piezoresistors arranged in a U-shaped Wheatstone bridge configuration generate a sensing signal at the desired in-plane mode and enable closed-loop operation of the resonator at its in-plane resonance frequency of approximately 780 kHz. Typical Q-factors for these devices are approximately 2000 in air.

SIMULATION & CHARACTERIZATION

Prior to fabrication, the device performance was simulated and the device geometry was optimized *via* Finite Element Analysis (FEA). For a 25 µm thick resonator, finite element simulations indicate a maximum temperature elevation of 71˚C at 100 mW of applied heating power and a uniform temperature profile across the heated head area of the cantilever (Figure 2). This simulated result compares well with experiment: for an applied heating power of 100 mW, the observed temperature increase of the device was ~85˚C in air. This result was obtained by placing the device in a temperature-controlled chamber while continuously monitoring the change in resistance of the three series-connected heating resistors as a function of the chamber temperature, and subsequently comparing these data to the change in resistance as a function of applied heating power due to self-heating of the embedded heaters. The discrepancy between the simulated and observed temperature elevations is approximately 15%, and can be explained by taking into account differences between the simulated model and the physical device (e.g., thickness variations). Figure 3 shows the open-loop amplitude transfer characteristic of the fundamental in-plane mode as a function of the applied heating voltage. The resulting frequency drop is linear with the heating power with a slope of -10.1 Hz/mW, or -13 ppm/mW.

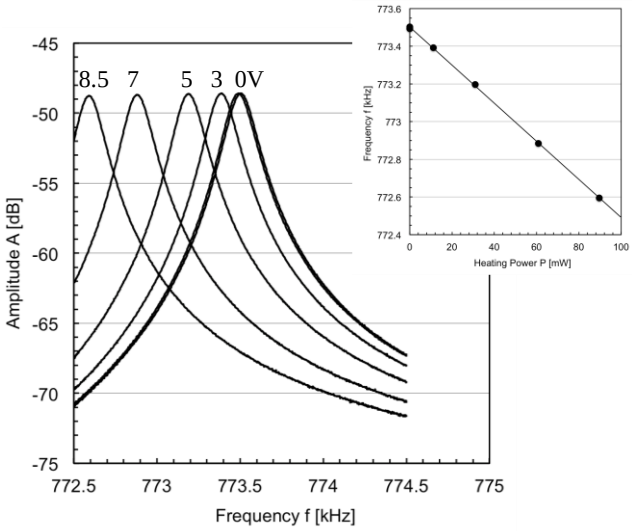

Figure 3: Amplitude transfer characteristic of in-plane resonant mode as a function of the applied heating power. The insert shows the in-plane resonant frequency as a function of the applied heating power with a slope of -10.1Hz/mW or -13ppm/mW.

The thermal time constant of the heated resonator can also be estimated using finite element modeling, and was found to be approximately 1.2 ms for a 25 µm thick resonator. By applying a square-wave heating pulse with a frequency of 100 Hz to the three series-connected heating resistors and measuring the temperature-dependent resistance change of the Wheatstone bridge, a thermal time constant of 1.1 ms was experimentally observed, confirming the simulated results (Figure 4). It is important to note that this thermal time constant is 2-3 orders of magnitude shorter than typical analyte diffusion times into polymeric sensing films with micrometer thicknesses [10]. As a result, the resonators can be quickly heated to desorb the analyte out of the polymer film and then rapidly cooled to monitor the analyte absorption back into the polymer in real time. As a result of the rapid cooling of the device, the resonator quickly returns to its original temperature (i.e. the

baseline temperature of the device, prior to generating the self-heating transient) and analyte absorption into the polymer sorbent film mostly takes place at room temperature. Because the analyte sorption is recorded at the original operating temperature, the unavoidable frequency shift associated with heating the resonator does not affect the measurement.

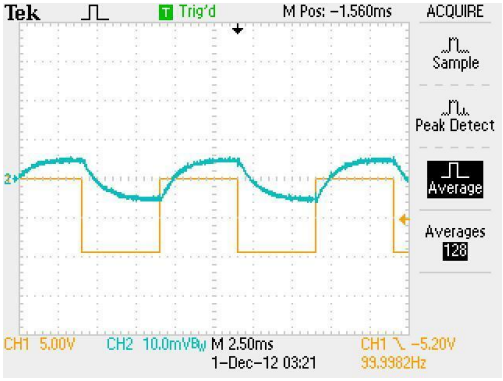

Figure 4: Screen capture of oscilloscope showing the square-wave signal applied to the three series heating resistors on the head region of the resonator, and the voltage across the piezoresistors at a constant current of 1 mA. The extracted thermal time constant is 1.1 ms.

CHEMICAL MEASUREMENTS

Following fabrication, and subsequent electrical and thermal characterization, several micro-resonators were coated with sorbent polymer layers and evaluated for performance as gas-phase chemical sensors. Building on our previous work [11], sorbent polymer layers were applied *via* localized polymer deposition through a shadow mask onto the semicircular head region only. This way, the quality factor is preserved, even in the case of relatively thick sorbent layer films, since the head deformation is negligible; thus, the overall chemical sensitivity can be improved. The coated resonators were then embedded into an amplifying feedback loop and exposed to defined concentrations of volatile organic compounds (VOCs) in a custom gas-flow setup. The gas setup is implemented with high-precision mass flow controllers (MFCs) for flowing precise concentrations of analyte-loaded and reference carrier gas streams over the devices at known flow rates and at known temperatures.

Figure 5a summarizes a typical chemical measurement performed with a 25 µm thick heated resonator coated with a 2 µm thick polyisobutylene (PIB) sorbent polymer layer. After exposing the microstructure to pure carrier gas (N_2), it was subjected to a continuous flow (at 80 ml/min) of toluene at a concentration of 6800 ppm, at a constant temperature of 20˚C. The resulting initial frequency drop of ~1.2 kHz is due to absorption of toluene into the PIB sensing film. While exposing the sensor to a constant toluene concentration, heating pulses of varying power were applied to the three series-connected resistors located on the head region of the resonator, and the resonance frequency of the device was continuously monitored and recorded. As can be seen in Figure 5a, the resonance frequency drops quickly when heating power is initially applied due to a rapid increase in the device temperature, which reduces the stiffness of the cantilever beam (due to the temperature dependence of the Young's modulus). Almost immediately after the heating pulse is applied, the frequency slowly begins to increase as analyte desorbs from the heated polymer film. After the heating power is turned off, the frequency rapidly shifts upward due to the temperature decrease as device and polymer return to their initial state (as demonstrated before, the thermal time constant is approx. 1.1 ms) and then slowly decreases again as analyte is re-absorbed into the polymer layer.

The observed sorption time constant is specific to the particular (or a particular class of) polymer-analyte pair and can be used to improve analyte discrimination, as illustrated in Figure 5b. This plot of normalized frequency change vs. square-root of time compares transients induced by modulation of the integrated heating resistors with a conventional transient induced by rapidly switching between analyte-loaded gas and reference gas streams with a mechanical valve.

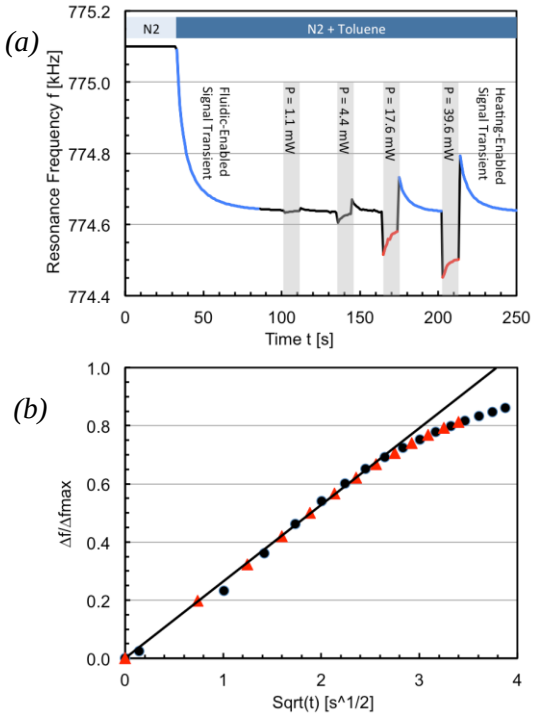

Figure 5: (a) In-plane resonance frequency of 25 µm thick microstructure subject to various levels of applied heating power; the PIB-coated resonator is exposed initially to pure carrier gas (N_2) and then to a constant toluene concentration of 6800 ppm; Blue lines represent analyte absorption phases, red lines analyte desorption phases; (b) Normalized frequency change vs. square-root of time for absorption transients induced by on-chip heating/cooling (P = 40 mW, red symbols) and analyte switching using a gas set-up (black symbols); the slope of the linear portion (solid line) is proportional to √D and yields a diffusion coefficient, $D = 2.4 \times 10^{-9}$ cm²/s [10]. The heating-induced transient agrees very well with the gas-switching-enabled transient.

By plotting the ratio of the frequency change to the maximum frequency change versus the square-root of time, the initial slopes of the transients, which are proportional to the square-root of the diffusion coefficient, *D* [10], are observed to agree within 5%. Thus, signal transients generated *via* modulation of the on-chip heating units are nearly indistinguishable from those generated due to sudden changes in analyte concentration (e.g., switching *via* mechanical valving between analyte and pure carrier gas streams). As such, heater-generated transients carry virtually identical information as the conventional transients and can be used in like manner for chemical sensing of VOCs in the gas-phase. The extracted diffusion coefficient for toluene into PIB is 2.4×10^{-9} cm²/s.

Since the transients are generated in a constant-concentration environment, operation in this mode does not require an external flow system for switching between analyte and reference gas streams, thereby reducing cost and complexity in the total sensing platform.

As another example, Figure 6 represents a series of measurements performed with a resonator coated with an 11 µm thick PIB film exposed to varying concentrations of toluene. The measurements were each performed using the previously-mentioned gas-flow setup, with a constant flow rate of 80 ml/min and at a constant temperature of 20˚C. In each case, 18.8 mW of heating power were applied to the device for a duration of 30 sec once the resonator became saturated with the given toluene concentration. As can be seen from the figure, the slopes of the transients agree very closely and are independent of the analyte concentration for relatively low analyte concentration levels.

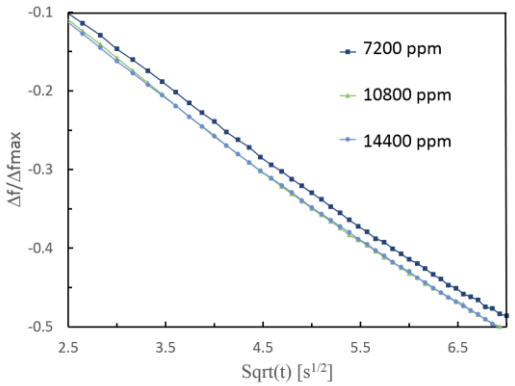

Figure 6: Normalized frequency change vs. square-root of time for the initial portion of the absorption transients induced by on-chip heating/cooling ($P_{applied}$ = 18.8 mW) for resonator coated with an 11 µm thick PIB film exposed to varying concentrations of toluene; the slope of the linear portion is proportional to √D and independent of concentration, for low concentration levels.

Analysis of the measured frequency shifts reveals that the sensors exhibit a linear response with respect to toluene concentration. Another important observation from the data is that the sensor's response is fully reversible and the measurements are made in real-time due to the rapid generation of heating transients. From the baseline frequency data, a short-term frequency stability of 2×10^{-7} was extracted *via* the Allan variance method. Using an experimentally determined chemical sensitivity of 0.18 Hz/ppm for toluene and the Allan variance of 2×10^{-7}, a limit of detection (LOD) of approximately 3 ppm can be expected for this device. However, this LOD value was deduced *via* extrapolation from much higher measured concentrations and must be confirmed by measurements at actual low-ppm level analyte concentrations.

CONCLUSION

The design, fabrication, and characterization of a novel chemical sensor platform with integrated heating units for the on-chip generation of real-time heating transients is demonstrated. The heater-generated transients are shown to carry nearly identical information as compared to conventionally-generated transients (e.g., due to an abrupt change in analyte concentration), enabling a novel mode of sensor operation. This novel operation mode eliminates the need for a reference resonator and external flow system, with a corresponding reduction in total system cost and complexity. Driving down the complexity of chemical sensing systems is essential to improving system deployability in the field and addressing the growing need for real-time information. Furthermore, the thermally-generated signal transients provide additional information for analyte discrimination and quantification. Future work will explore improving the LOD of these devices and the possibility of operating arrays of individually-coated sensors with the goal of reducing the platform's sensitivity to chemical interference.

ACKNOWLEDGEMENTS

This work was performed in part at Georgia Tech's Institute for Electronics and Nanotechnology, a member of the National Nanotechnology Infrastructure Network (NNIN), which is supported by the National Science Foundation. The authors would like to thank the Institute for Electronics and Nanotechnology (IEN) for help and support with process development and fabrication. The authors would also like to thank the National Science Foundation (NSF) for funding this work through awards ECCS-1128554 and ECCS-1128992. Travel support has been generously provided by the Transducer Research Foundation.

REFERENCES

[1] A. Warsinke, "Point-of-care testing of proteins," Analytical and Bioanalytical Chemistry, vol. 393, 2009, pp. 1393-1405.

[2] C. Ho, A. Robinson, D. Miller, and M. Davis, "Overview of sensors and needs for environmental monitoring," Sensors, vol. 5, 2005, pp. 4-37.

[3] J. Gooding, "Biosensor technology for detecting biological warfare agents: Recent progress and future trends," Analytica Chimica Acta, vol. 559, 2006, pp. 137-151.

[4] E. Schleicher, "The clinical chemistry laboratory: Current status, problems and diagnostic prospects," Analytical and Bioanalytical Chemistry, vol. 384, 2006, pp. 124-131.

[5] A. Kummer, T. Burg, and A. Hierlemann, "Transient signal analysis using complementary metal oxide semiconductor capacitive chemical microsensors," Analytical Chemistry, vol. 78, 2006, pp. 279-290

[6] C. Hagleitner, D. Lange, A. Hierlemann, O. Brand, and H. Baltes, "CMOS single-chip gas detection system comprising capacitive, calorimetric and mass-sensitive microsensors," IEEE J. of Solid-State Circuits, vol. 37, 2002, pp. 1867-1878

[7] D. Lange, C. Hagleitner, A. Hierlemann, O. Brand, and H. Baltes, "Complementary metal oxide semiconductor cantilever arrays on a single chip: Mass-sensitive detection of volatile organic compounds," Analytical Chemistry, vol. 74, 2002, pp. 3084-3095.

[8] P. Xu, H. Yu, and X. Li, "Functionalized mesoporous silica for microgravimetric sensing of trace chemical vapors," Analytical Chemistry, vol. 83, 2011, pp. 3448-3454.

[9] L. Beardslee, K. Demirci, Y. Luzinova, B. Mizaikoff, S. Heinrich, F. Josse, and O. Brand, "Liquid-phase chemical sensing using lateral mode resonant cantilevers," Journal of Microelectromech. Systems, vol. 19, 2010, pp. 1015-1017.

[10] J.-J. Su, C. Carron, S. Truax, K. Demirci, L. Beardslee, and O. Brand, "Assessing polymer sorption kinetics using micromachined resonators," Transducers 2011, Technical Digest, 2011, pp. 1420-1423.

[11] C. Carron, P. Getz, J.-J. Su, D. Gottfried, F. Josse, S. Heinrich, and O. Brand, "Cantilever-based resonant gas sensors with integrated recesses for localized sensing layer deposition," IEEE Sensors 2013, Proceedings, 2013, pp. 1-4.

CONTACT

*C. Carron, Tel: +1-404-997-8623; ccarron3@gatech.edu

IN-SITU, REAL-TIME MONITORING OF MECHANICAL AND CHEMICAL STRUCTURE CHANGES IN A V_2O_5 BATTERY ELECTRODE USING A MEMS OPTICAL SENSOR

H. Jung[1], K. Gerasopoulos[1], M. Gnerlich[1], A. Talin[2], and R. Ghodssi[1]*
[1]Department of Electrical and Computer Engineering, University of Maryland, College Park, Maryland, USA
[2]Sandia National Laboratories, Livermore, California, USA

ABSTRACT

This work presents the first demonstration of a MEMS optical sensor for *in-situ*, real-time monitoring of both mechanical and chemical structure evolutions in a V_2O_5 lithium-ion battery (LIB) cathode during battery operation. A reflective membrane forms one side of a Fabry-Perot (FP) interferometer, while the other side is coated with V_2O_5 and exposed to electrolyte in a half-cell LIB. Using one microscope and two laser sources, both the induced membrane deflection and the corresponding Raman intensity changes are observed during lithium cycling. Results are in good agreement with the expected mechanical behavior and disorder change of the V_2O_5 layers, highlighting the significant potential of MEMS as enabling tools for advanced scientific investigations.

INTRODUCTION

Capacity fading due to electrode mechanical and chemical structure changes during electrochemical cycling is a major limiting factor in battery cycle life. Continuous volume change and phase transformations are induced as Li-ions are inserted into and extracted from the electrodes which lead to gradual degradation of the battery performance [1, 2]. However, these mechanical and chemical structure changes are inherently coupled and most analysis techniques such as scanning electron microscopy, transmission electron microscopy and atomic force microscopy typically rely on post-operation inspection of the electrode. The aforementioned methods also can typically evaluate one parameter at a time (mechanical or chemical structure) only using bulky equipment in complex electrochemical apparatuses [3-5]. There is a need for *in-situ* monitoring platforms capable of providing simultaneous information on mechanical and chemical structure evolutions during battery operation in a simple and a reliable fashion.

Recently, several *in-situ* analysis techniques have been used in order to understand the mechanical evolutions in LIB electrodes. Among these, a multi-beam optical sensor (MOS) technique has proven to be an effective method for *in-situ* measurements of the mechanical properties in silicon thin-film electrodes during lithium cycling [6, 7]. In the MOS method, a substrate wafer is coated with a silicon oxide barrier layer, copper current collector and thin-film silicon active battery material. The substrate wafer is assembled into a customized electrochemical cell during electrochemical measurements. An array of parallel laser beams illuminates the substrate wafer surface. Curvature changes of the wafer induced by the stress generated in the silicon film due to lithium insertion/extraction are determined by measuring the relative change in the spacing between the reflected beams. This method provides quantitative information regarding the stress evolutions and bi-axial modulus changes in silicon electrode. However, the method is limited to providing the mechanical changes of the electrode but not the chemical structure changes.

In parallel, significant research has been focused on characterization of structural changes in LIB electrodes during electrochemical cycling. *In-situ* nuclear magnetic resonance (NMR) spectroscopy is used to study (de)alloying reactions of the silicon electrodes [8, 9]. This method provides insight into amorphous and amorphous-to-crystalline transformations that occur during the first and subsequent discharge-charge cycles. *In-situ* SEM/TEM techniques have also been utilized in order to investigate structural evolutions of silicon nanowires and nanoparticles. Direct observation of anisotropic expansion of the silicon nanowires has been reported by Liu et al [10] and sudden crystallization of $Li_{15}S_4$ phase during lithiation has also been observed with electron diffraction [11]. Nevertheless, these methods are restricted to providing only crystalline phase evolution of the electrodes during lithium cycling.

Here, we report a MEMS optical sensor device with important additional metrology functionalities as an *in-situ*, multi-modal sensing platform for monitoring of both mechanical and chemical structure changes of Li-ion battery electrodes in real-time. The V_2O_5 LIB electrode is used as a model system in this work.

DESIGN AND FABRICATION

Design

During battery operation, LIB electrodes experience continuous mechanical and chemical structure changes. The MEMS optical sensor platform is designed for monitoring these mechanical and chemical structure changes using FP interferometry and Raman spectroscopy, respectively. The principle of operation of the platform is shown in Figure 1.

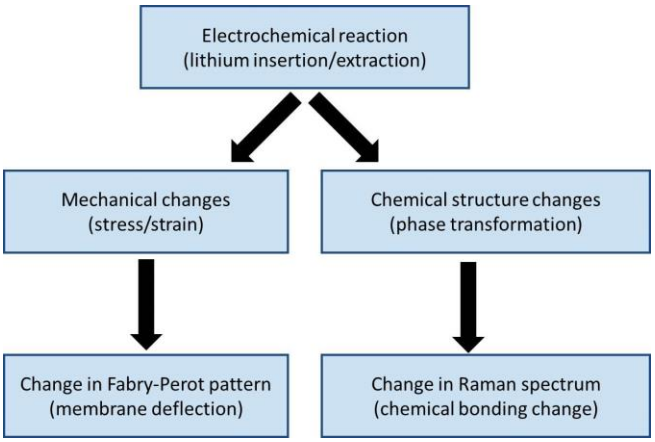

Figure 1: Schematic showing typical evolutions in LIB electrodes during battery operation and the changes recorded by the MEMS optical sensor platform.

The MEMS optical sensor consists of a flexible silicon nitride membrane which separates the device into two cavities (Figure 2(a)). The reflective surface of the membrane forms one side of a FP interferometer, while a bonded Pyrex wafer forms the second interference mirror. The other side of the membrane forms a battery cavity coated with the active battery material (V_2O_5). When the battery cavity is exposed to lithium-conducting electrolyte and metallic Li foil as a counter electrode, it forms a half-cell Li-ion

9781940470016/HH2014/$25©2014TRF
DOI 10.31438/trf.hh2014.99

battery. During electrochemical operation, the V_2O_5 electrode expands and contracts as a result of Li-ion insertion/extraction. These volume changes cause deflection in the silicon nitride membrane. This mechanical change is monitored using FP interferometry. When the light reflects from the membrane and Pyrex glass, it produces an interference pattern. As the membrane deflects, the interference pattern also changes accordingly. These interference pattern changes are recorded and analyzed later for the mechanical change characterization. The chemical structure evolutions are also monitored using Raman spectroscopy, which can simultaneously probe the electrode surface through the partially reflective Pyrex glass and transparent films (Figure 2(b)).

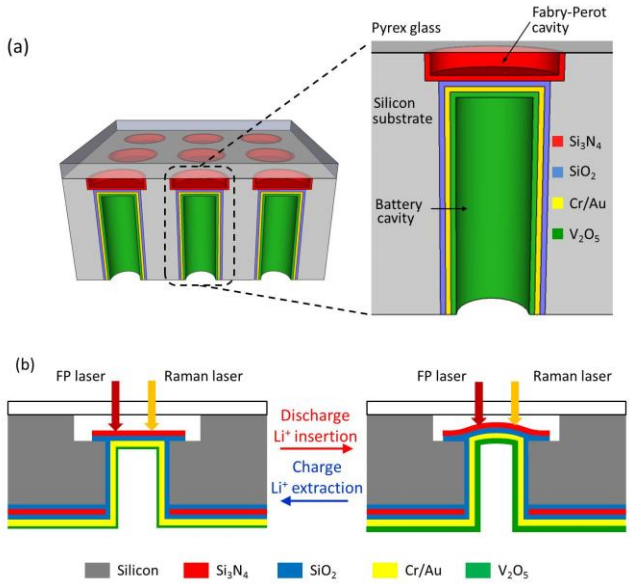

Figure 2: (a) 3D and cross-section diagrams of the MEMS optical sensor, (b) Schematic representation of the mechanical sensing mechanism principle.

Fabrication

The complete fabrication process is described in detail in our previous work [12] but will be briefly described here. A double-side polished silicon wafer is used as the substrate for the MEMS optical sensor fabrication. The FP cavity (12 µm deep) is etched using deep reactive-ion etching (DRIE) (Figure 3(a)). A 300 nm thick layer of SiO_2 is thermally grown followed by the deposition of a 700 nm thick layer of Si_3N_4 on both sides using low pressure chemical vapor deposition (LPCVD). Then, the Si_3N_4 and SiO_2 are masked with photoresist and etched using reactive-ion etching (RIE) from the FP cavity side. The battery cavity (488 µm deep) is formed by DRIE on the wafer backside, aided by a SiO_2 etch-stop layer (Figure 3(b)). The diameter of the battery cavities (150, 200, 250 and 300 µm) determine the diameter of the membranes. A Pyrex cap wafer is anodically bonded to form the optical FP cavity (Figure 3(c)). A SiO_2 passivation layer (50 nm) is deposited using plasma enhanced chemical vapor deposition (PECVD) in order to prevent Li-ion intercalation into the substrate. Subsequently, Cr/Au (5 nm/15 nm) thin films are deposited using sputtering to form the current collector. Finally, the battery cavity is coated with a thin-film V_2O_5 (135 nm) electrode using atomic layer deposition (ALD) (Figure 3(d)). The cross section SEM image of the fabricated MEMS optical sensor is shown in Figure 4. Upon finishing the fabrication process, the MEMS optical sensor device is packaged in a modified coin cell, routinely used in laboratories to test LIB electrodes, which is described in detail in our previous work [12].

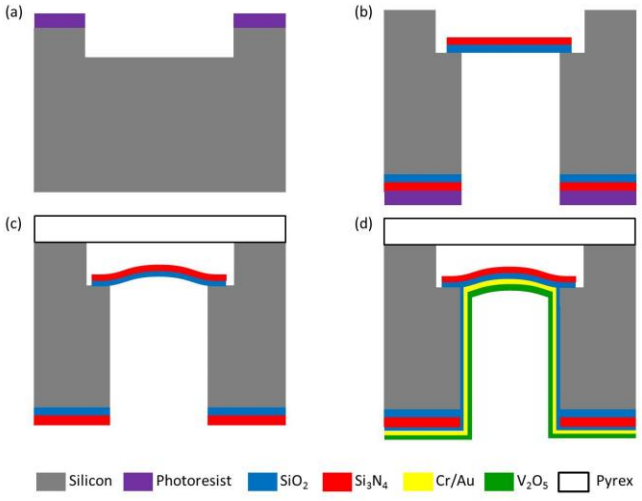

Figure 3: Schematic presentation of the fabrication process of the MEMS optical sensor.

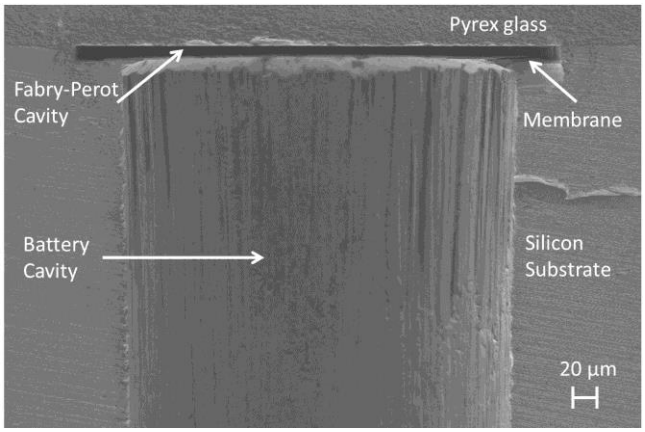

Figure 4: Cross-section SEM image of the MEMS optical sensor with a 300 µm diameter membrane.

EXPERIMENTAL SET-UP

The experimental set-up is a critical component of this work since it impacts the simultaneous monitoring of both mechanical and chemical structure evolutions of the electrode under test. A simplified schematic of the microscope set-up is shown in Figure 5. The white-light illumination source of the Raman microscope has been replaced with a despeckled red laser (638 nm) for measuring the membrane deflection by utilizing FP interferometry [13]. By employing an optical interferometric method, the same microscope used for the Raman spectroscopy analysis (Yvon Jobin LabRam ARAMIS, Horiba, Ltd.) can be modified to collect information on the membrane deflection, thus enabling multi-modal, real-time monitoring in a unified set-up. The red laser (638nm) illuminates

the FP cavity to produce an interference pattern, while the HeNe laser, 633nm is used as the excitation source for Raman spectroscopy measurements. A 10× objective is used to focus the Raman laser onto the electrode surface and the spectra are measured in back-scattering configuration. To avoid local heating of the electrode, the power of the laser beam is adjusted with a neutral density filter (0.9 W). Each spectrum is recorded for 60 seconds with only one accumulation.

The packaged device is connected to a potentiostat (VSP-300, BioLogic) and placed under an experimental set-up as shown in Figure 5. A Galvanostatic lithium cycling is conducted using the potentiostat in the voltage range of 2.8V - 3.5V with a current density of 2 μA/cm^2. All experiments were conducted in air under normal ambient conditions.

The imaging software installed on the computer connected to the Raman microscope supports automation function controlled by user specific operations programmed in JavaScript. This enables automatic switching between the two laser sources repeatedly throughout the experiment and computerized recording of the corresponding data. Two CCD cameras (labeled 1 and 2 in Figure 5) sequentially record the interference pattern (every 40 seconds) and the Raman spectra (every 220 seconds), respectively. The recorded interference pattern and Raman spectra are automatically saved in the computer and later correlated with the time stamped electrochemical data.

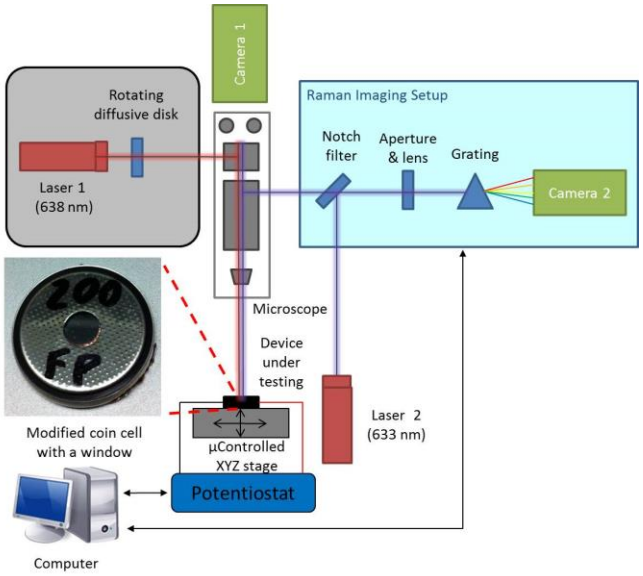

Figure 5: Simplified diagrams of the experimental setup showing the location of the device under test (face up) relative to the microscope.

RESULTS AND DISCUSSION

Changes in the FP interference pattern occur over long time scales since a single battery cycle may take several hours. Measurements in a single cycle can produce hundreds of images taken over hours. To analyze the data, a computerized image processing algorithm is developed using MATLAB. A detailed algorithm description can be found in our previous work [12]. According to the amount of lithium inserted into and extracted from the electrode, the radius of the FP interference pattern (fringe radius) changes due to the membrane deflection. The fringe radius is calculated based upon the comparison between the fringe radius of a pristine electrode and an electrode under electrochemical testing, as show in Figure 6.

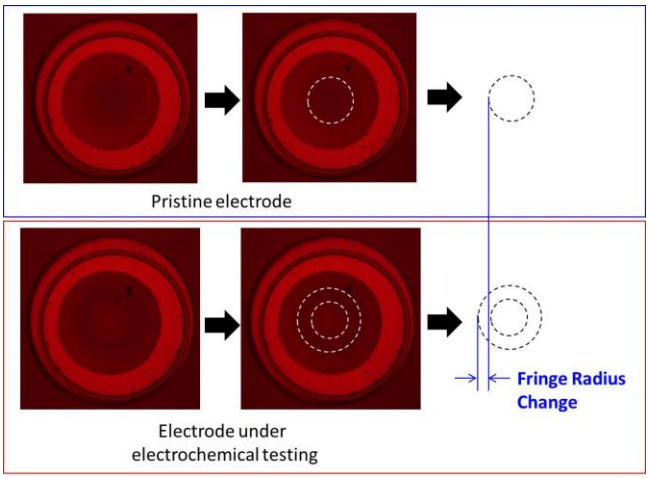

Figure 6: Photographs of the experimentally obtained interference pattern, showing relative fringe radius change.

The correlation between electrochemical data and changes in fringe radius for a membrane with 150 μm diameter during the second electrochemical cycle is shown in Figure 7. Upon lithium insertion (discharge), the V_2O_5 expands and the membrane deflects towards the Pyrex causing an increase in fringe radius. During lithium extraction (charge), the electrode contracts, the membrane deflects away from the Pyrex and the fringe radius returns closely to its original position. This indicates that the V_2O_5 electrode experiences irreversible volume changes during lithium cycling, which corresponds well with the results reported in literature [14]. Rapid increases and decreases in fringe radius are also observed during this process, and are attributed to the phase transition-induced (α, ε, and δ) volume changes in V_2O_5 with varying lithium content.

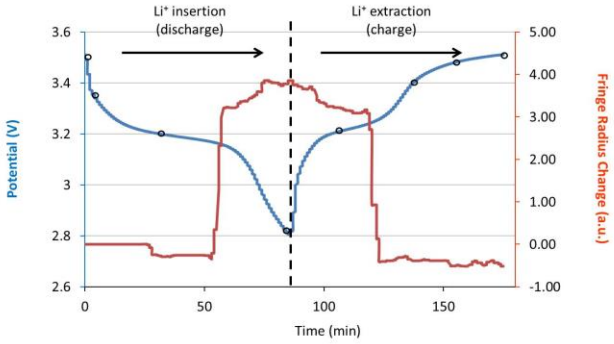

Figure 7: Discharge/charge and fringe radius change vs. time graphs

Simultaneously, the *in-situ* Raman spectra are collected and representative data at various points along the discharge/charge curve (black circles in Figure 7) are plotted in Figure 8. It has been

reported that the Raman intensity change at 145 cm^{-1} indicates the level of disorder between V_2O_5 layers [1]. As the level of disorder increases during lithium insertion, the Raman peak intensity at 145 cm^{-1} vanishes. On the other hand, the Raman peak at 145 cm^{-1} re-appears as lithium ions are extracted indicating which the V_2O_5 lattice is progressively recovered during lithium extraction.

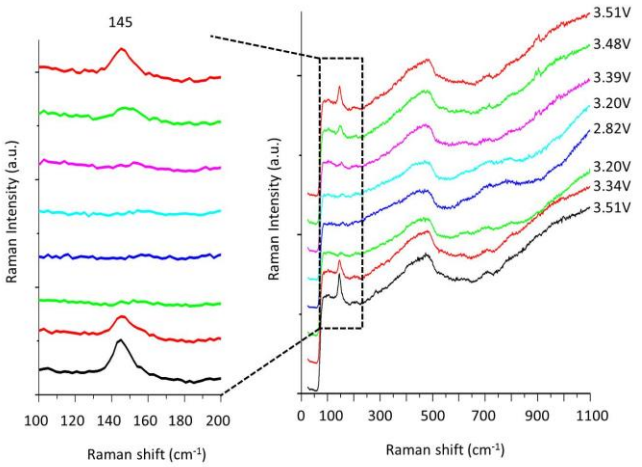

Figure 8: In-situ Raman spectra series at various potentials, highlighting the 145 cm^{-1} peak.

CONCLSION

The work presented here demonstrated the capability of *in-situ*, simultaneous monitoring of mechanical and chemical structure changes occurring in LIB electrodes for the first time.

The membrane deflection is induced by V_2O_5 thin film electrode volume expansion/contraction during electrochemical cycling. The FP interferometry is utilized in order to monitor the deflection of the membrane. At the same time, reversible changes in the level of disorder between the V_2O_5 layers is observed by the Raman spectra intensity change at 145 cm^{-1}. These mechanical and chemical structure changes are monitored simultaneously in a unified set-up using the MEMS optical sensor.

This multi-modal, *in-situ* monitoring technique can be utilized as a discovery platform for a wide variety of thin film LIB electrode materials and combinatorial material libraries of electrodes under test.

ACKNOWLEDGEMENTS

This work was supported by the Nanostructures for Electrical Energy Storage, an Energy Frontier Research Center funded by the U.S. Department of Energy (DOE), Office of Science, Office, Basic Energy Sciences (BES), under award number DESC0001160. The authors acknowledge the staff at Maryland Nanocenter.

REFERENCES

[1] R. Baddour-Hadjean, C. Navone, J.P. Pereira-Ramos, "*In situ* Raman microspectrometry investigation of electrochemical lithium intercalation into sputtered crystalline V_2O_5 thin films", Electrochimica Acta, 54, 6674 (2009).

[2] V.R. Armstrong, C. Lyness, P.M. Panchimatia, M.S. Islam, and P.G. Bruce, "The lithium intercalation process in the low-voltage lithium battery anode $Li_{1+x}V_{1-x}O_2$", Nature Materials, 10, 223 (2011).

[3] X.H. Liu, L. Zhong, S. Huang, S.X. Mao, T. Zhu, and J.Y. Huang, "Size-Dependent Fracture of Silicon Nanoparticles During Lithiation," ACS Nano, 6, 1522 (2012).

[4] L.Y. Beaulieu, V.K. Cumyn, K.W. Eberman, L.J. Krause, and J.R. Dahn, "A system for performing simultaneous *in situ* atomic force microscopy/optical microscopy measurements on electrode materials for lithium-ion batteries", Review of Scientific Instruments, 72, 3313 (2001).

[5] M.J. Chon, V.A. Sethuraman, A. McCormick, V. Srinivasan, and P.R. Guduru, "Real-Time Measurement of Stress and Damage Evolution during Initial Lithiation of Crystalline Silicon", Physical Review Letters, 107, 045503 (2011).

[6] V.A. Sethuraman, M.J. Chon, M. Shimshak, V. Srinivasan, and P.R. Guduru, "*In situ* measurements of stress evolution in silicon thin films during electrochemical lithiation and delithiation", Journal of Power Sources, 195, 5062 (2010).

[7] V.A. Sethuraman, M.J. Chon, M. Shimshak, N. Van Winkle, and P.R. Guduru, "*In situ* measurement of biaxial modulus of Si anode for Li-ion batteries", Electrochemistry Communications, 12, 1614 (2010).

[8] B. Key, R. Bhattacharyya, M. Morcrette,V. Seznec, J. Tarascon, and C.P. Grey, "Real-Time NMR Investigations of Structural Changes in Silicon Electrodes for Lithium-Ion Batteries", Journal of the American Chemical Society, 131, 9239 (2009).

[9] K. Ogata, E. Salager, C.J. Kerr, A.E. Fraser, C. Ducati, A.J. Morris, S. Hofmann, and C.P. Grey, "Revealing lithium–silicide phase transformations in nano-structured silicon-based lithium ion batteries via *in situ* NMR spectroscopy", Nature Communications, 5, 3217 (2014).

[10] X.H. Liu, H. Zheng, L. Zhong, S. Huan, K. Karki, L.Q. Zhang, Y. Liu, A. Kushima, W.T. Liang, J.W. Wang, J.H. Cho, E. Epstein, S.A. Dayeh, S.T. Picraux, T. Zhu, J. Li, J.P. Sullivan, J. Cumings, C.S. Wang, S.X. Mao, Z.Z. Ye, S.L. Zhang, and J.Y. Huang, "Anisotropic Swelling and Fracture of Silicon Nanowires during Lithiation", Nano Letters, 11, 3312 (2011).

[11] M.T. McDowella, S.W. Lee, C. Wang, and Y. Cui, "The effect of metallic coatings and crystallinity on the volume expansion of silicon during electrochemical lithiation/delithiation, Nano Energy, 1, 401 (2012).

[12] E. Pomerantseva, H. Jung, M. Gnerlich, S. Baron, K. Gerasopoulos, and R. Ghodssi, "A MEMS platform for *in situ*, real-time monitoring of electrochemically induced mechanical changes in lithium-ion battery electrodes", Journal of Micromechanics and Microengineering, 23, 114018 (2013).

[13] S.T. Koev, W.E. Bentley, and R. Ghodssi, "Interferometric readout of multiple cantilever sensors in liquid samples", Sensors and Actuators B: Chemical, B146, 245 (2010).

[14] J. Swiatowska-Mrowiecka, V. Maurice, L. Klein, and P. Marcus, "Nanostructural modifications of V_2O_5 thin films during Li intercalation studied in situ by AFM", Electrochemistry Communications, 9, 2448 (2007).

CONTACT

*R. Ghodssi, tel: +1-301-395-8158; ghodssi@umd.edu

LIQUID FLOW SENSOR FOR SMART IMPLANTABLE VP SHUNTS

Eniko T. Enikov[1], Gergo Edes[1], Rein Anton,[2] and Jesse Skoch[2]*
[1] University of Arizona, Advanced Micro- and Nanosystems Laboratory, USA
[2] University of Arizona, Department of Surgery USA

ABSTRACT

This paper describes the development of a novel liquid flow sensor based on the combined use of GMR magnetic sensors and micro-fabricated ferromagnetic sensing elements. A motivating application behind this effort is the development of a "smart" ventriculo-peritoneal (VP) shunt, capable of measuring the amount cerebral-spinal fluid drained from the ventricles of a person suffering from hydrocephalous. Unlike classical liquid flow sensors based on piezo-resistive flaps, the device presented here utilizes electroplated micro-fabricated ferromagnetic flaps (Ni), while the detector is an ultra-sensitive non-contact GMR sensor, separated from the working fluid by the lumen of the shunt.

INTRODUCTION

Motivation

Drainage of cerebral spinal fluid through shunting is a long-term treatment option for hydrocephalus, and is one of the most common neurosurgical procedures with an incidence rate of 5.5 per 100,000 [1]. The shunts are placed through the skull into the ventricle and drain the CSF into the peritoneal cavity as illustrated in Fig. 1a. Implanted cerebrospinal fluid shunts have been in use since 1950s, however approximately 39% of shunts fail within the first year, 53% fail within the first two years, and about 80% fail at some point after implantation [2]–[4]. The diagnosis and repair of failed VP shunts for hydrocephalus is one of the most common neurosurgical procedures, with over 27 000 surgeries performed each year in the United States [5]. Previous efforts to develop smart VP shunts have included integrating pressure sensors for monitoring intra-cranial pressure [6] and development of thermal signature sensors (Shunt Check) to determine presence of flow based on the rate of re-heating of tissue [7]. Unfortunately, none of these methods resulted in a reliable flow sensing. Micro-flow sensors offer a direct method to measure flow and can be miniaturized to fit inside the lumen of a catheter. Existing approaches based on hot-wire anemometry, while small and sensitive, require continuous power in the range of 10-20 mW [8]. Alternatives based on peizo-resistive flap-style flow sensors require stringent encapsulation of the sensing elements to protect them against diffusion of sodium and other interfering ions [9]. The flow sensor presented here alleviates the packaging requirements of the sensor by separating the detector (an ultra-sensitive GMR sensor) from the working fluid interacting with a micro-fabricated ferromagnetic flap as illustrated in Fig. 1b.

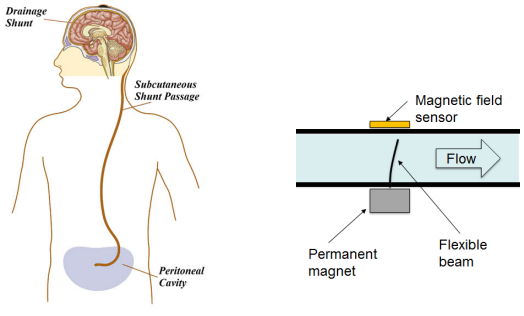

(a) (b)

Figure 1: (a) Placement of VP shunt; (b) Flow detection using flexible ferromagnetic flap.

Sensor Operating Principle

The proposed flow sensing element is a ferromagnetic flap hinged about two attachment points to the substrate. Its magnetization is generated by a permanent magnet as shown in Fig. 2a. Under the action of viscous drag, the flap deflects laterally and alters the distribution of the magnetic field. These small changes are then detected by a GMR sensor placed adjacent to the elastic beam. An order-of-magnitude estimate of the drag force applied on the elastic beam by a slowly moving fluid can be obtained from the solution of Stokes flow past a prolate spheroid with major axis a and minor axis b ($b<a$) using the method of superposition of internal distributions of singularities [10]

$$F_d = 32\pi\mu a v e^3 \left[2e + (3e^2 - 1)\ln\frac{1+e}{1-e} \right]^{-1} \qquad (1)$$

where μ is the dynamic viscosity of CSF, and v is its mean velocity, and $e = \sqrt{1 - a^2/b^2}$ is the eccentricity of the prolate spheroid. In the case of water, with nominal flow rates of 20-30 mL/hr in a channel with cross-section of 1.8 mm × 5 mm, *Eq. (1)* predicts forces in the range of 40-60 μN. Detection of such forces is well within the capabilities of micro-cantilevers.

The following sections describe a more-accurate analysis and experimental validation of the operation of the proposed sensor. Signal-to-noise ratio analysis is provided in the last section of the paper along with suggestions for improvement of the design aimed at demonstrating a functional prototype of the envisioned smart VP shunt.

SENSOR DESIGN

Mechanical Design

Accurate prediction of the response of the transducing element to fluid flow requires fluid-structure interaction analysis. The drag force model represented by *Eq.(1)* neglects the effects of the channel walls and the shape of the transducing element In this work, a channel with a width of 2 mm and depth of 4 mm was chosen in order to meet the constraints of available machining tools while approaching the size restrictions of a future implantable device. The gap between the transducer and the channel wall was chosen to be 0.15 mm, which turned out to be the lowest value allowing semi-manual assembly. The effect of this gap is critical to the sensitivity of the resulting flow sensors. The sensing element is a folded micro-cantilever anchored to the bottom of the channel shown in Fig. 2a.

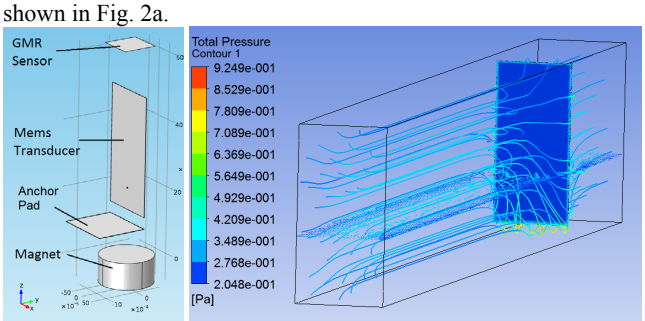

(a) (b)

Figure 2: (a) Geometry for sensing element (left); and (b) The resulting flow pattern around it (right).

9781940470016/HH2014/$25©2014TRF
DOI 10.31438/trf.hh2014.100

A commercial software (CFX, Ansys Inc.) was used to carry out a two-step finite element analysis in order to optimize the size of the flap and the stiffness of the micro-cantilever hinges. The resulting flow and pressure distribution (see Fig 2b) was used to compute the deflection of the plate using a structural finite element model in ANSYS Mechanical (Ansys Inc.). Figure 3a shows the effect of changing the gap between the flap and the channel walls, while Figure 3b shows the effect of changing the hinge length while maintaining a constant total length of the flap. It can be observed that reducing the gap from 150 µm to 50 µm doubles the deflection and hence the sensitivity. Furthermore, optimal hinge length results, since longer hinges lead to softer beam, but also increase the by-pass of the fluid around them. A maximum deflection of around 32 µm microns is observed for a 20 mL/hr flow rate.

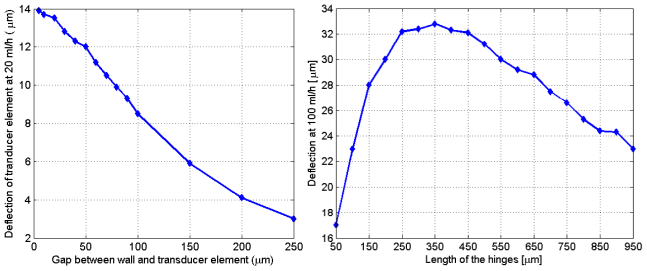

(a) *(b)*

Figure 3: (a) Flap deflection vs. gap; and (b) Flap deflection vs. hinge length for a fixed total length of the transducer. Flow rate is 20 mL/hr.

Magnetic Design

The magnetic field analysis was carried out using commercial finite element code (COMSOL Inc.). The model includes an Alnico magnet (dimensions: ϕ1.6 mm × 0.8 mm) with remnant magnetization of 0.75 T. The transducer material was electroplated Ni with permeability of μ_r= 600, while the GMR sensor was represented by a 1 mm × 1 mm interrogation area above the flap. As anticipated, the simulation shows that the nickel flap is directing the magnetic field lines along its longitudinal axis and thus distorting the magnetic field around the GMR sensor when the transducer is deflected (see Figs. 4a-b). A series of combined electro-mechanical simulations representing flow rates between 5 and 100 mL/hr have been carried out in order to produce a flow rate vs. magnetic field change plot (see Fig. 5). The resulting slope is near constant indicating a sensor sensitivity of 70 nT-hr/mL.

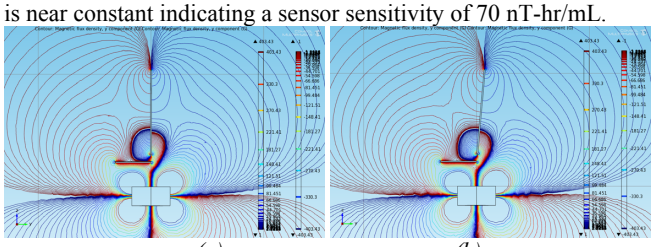

(a) *(b)*

Figure 4: Contours of the magnetic flux density B_y around the transducer element: (a) no deflection; (b) after 5° rotation.

FABRICATION AND TESTING

Fabrication

A Ni flap with lateral dimensions of W = 1.7 mm, L = 350 µm, H = 3.9 mm, and thickness of 10 µm was fabricated via electro-plating into a photoresist mold over a sacrificial Cu seed layer. Release holes with diameter of 30 µm were used to facilitate the release of the flap from the glass substrate. The fabrication sequence is summarized in Fig. 6. Briefly, Cr adhesion layer is evaporated onto a borosilicate glass wafer. A 2-µm-thick Cu layer is then evaporated to serve as a sacrificial release layer. A 10-µm-thick layer of photoresist was spun and patterned to produce a electroplating mold, followed by electro-deposition resulting in a 10-µm-thick layer of nickel. The substrate was diced into individual die, and subsequently, each die was etched individually in Cu and Cr etchants for 17 and 2 minutes, respectively. The release protocol is described earlier [11]. Powerful neodymium magnets were used to erect the transducers out of plane (see Fig. 6 (right)). The raised flaps were then assembled under an inverted U-shaped channel, whereby the glass substrate was used as the bottom wall of the channel (see Fig. 7-8).

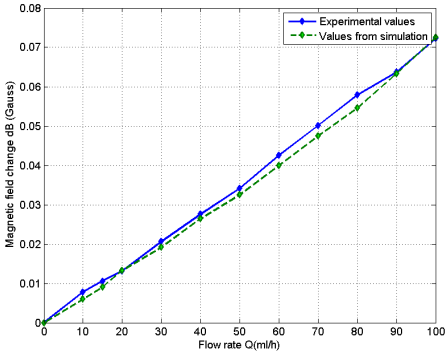

Figure 5: Magnetic field change vs. flow rate.

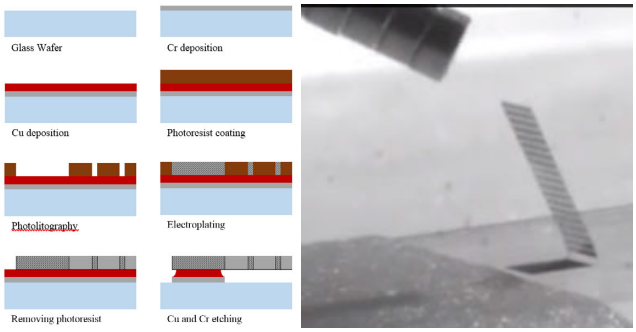

Figure 6: Fabrication sequence (left) and erecting the flap (right) .

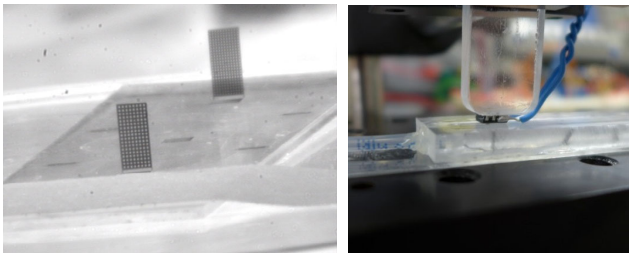

Figure 7: Released sensors prior to insertion in the flow channel (left) and assembled channel-sensor substrate with GMR sensor mounted superiorly (right) .

Experiments

The magnetic field was measured with a Micromagnetics MTJ-240 magneto-resistive sensor placed above the channel was shown in Fig. 7. The manufacturer-supplied sensitivity of the sensor was 1 %/G. The FE analysis described earlier was used to estimate the expected magnetic field change ranging between 0.006 and 0.07 G. This change corresponds to a resistance variation of 0.1 to 1 Ω for a 1340-Ω sensing resistor. A signal

amplification circuit comprised of a Wheatstone bridge, a two-stage amplifier with a total gain of 3300, and a second-order low-pass filter with a cut-off frequency of 6 Hz was used to condition the sensor signal (see Fig. 9).

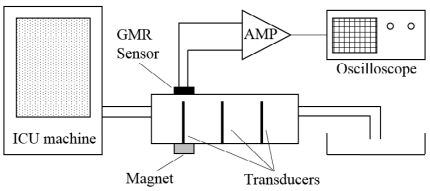

Figure 8: Test setup for flow measurements.

The output from the measurement circuit was connected to a Textronix TDS 3014B oscilloscope, and a Dataq DI-155 13-bit analog to digital converter. The flow rate was controlled by an Alaris PC 815 ICU/8110 syringe pump.

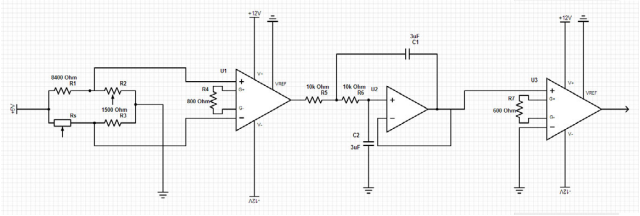

Figure 9: Sensor signal conditioning circuit.

The test procedure consisted of setting the flow rate to values between 10 and 100 mL/hr in increments of 10 mL/hr. At least three interruptions of the flow were made at each flow setting, in order to examine the repeatability of the measurements. A sample data from the measurement taken at 50 mL/hr is shown in Fig. 10.

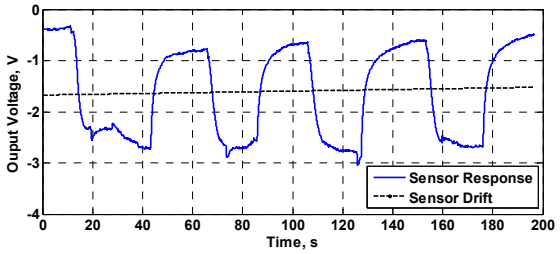

Figure 10: Sensor signal conditioning circuit.

Voltage changes between the on- and off-periods were recorded three times for each flow level to obtain a sensor calibration plot as shown in Fig. 11. Possible sources of the observed errors are the temperature drift of the sensor, environmental EM interference, and bubble formation around the transducer elements.

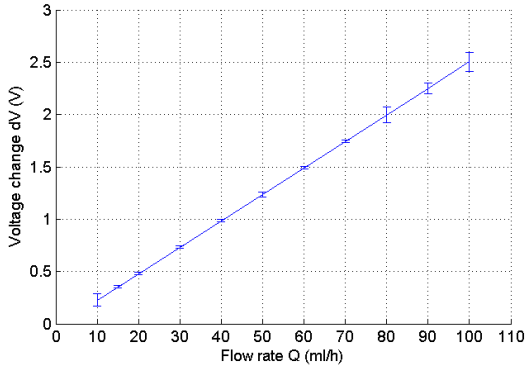

Figure 11: Sensor signal conditioning circuit.

To further analyze the response, the sensor output data were converted to an equivalent magnetic field changes according to

$$\Delta B^{\exp} = \frac{\Delta R^{\exp}}{R_S S}, \qquad (2)$$

where S=1% is the manufacturer-supplied sensitivity of the GMR sensor and R_S=1380 Ω is the sensor resistance at zero magnetic field. The resistance change of the sensor for different flow rates was estimated using

$$\Delta R^{\exp} = \frac{\Delta V^{\exp}(R_S + R_3)^2}{G V_0 R_S}, \qquad (3)$$

where G=3300 is the amplification gain, R_3=1500 Ω is the value of the reference resistors of the Wheatstone bridge, and V_0=5 V is the applied voltage. As demonstrated in Fig. 9, a near-constant sensitivity of 25 mV-hr/mL has been observed over the entire range of interest. A low-frequency drift of 90 mV/min was also observed. The amplified and filtered signal had a noise level of 18 mV-rms and a low-frequency drift of 90 mV over a period of 1 minute.

DISCUSSION AND CONCLUSIONS

Analysis of the sensor output noise level implies a resolution of 1.4 mL/hr and a drift of about 216 mL/hr. The observed low-frequency drift and associated error over a 24-hr period is prohibitively high and needs to be reduced. Possible sources of the drift are fluctuations of the ambient magnetic field, low-frequency noise of the GMR sensor, and thermal noise (drift) due to the exposure of the sensor to the laboratory environment and self-heating. The Earth's ambient magnetic field is 25,000-65,000 nT. Its daily fluctuation however is typically 10-100 nT [12], therefore, the associated drift would be around 1 mL/hr. Vehicular traffic and elevators could cause variations of 10-150 nT, which would imply an error of 2 mL/hr. GMR sensors are known to exhibit 1/*f* low frequency noise [13]. Integrating the noise spectral density published in [13] over a period of one hour results I a noise level of 0.6 mV-rms. Equivalently, the corresponding a drift would be 0.03mL/hr. Given the large difference between this predicted drift and observed one, it is concluded that the most likely source of the experimental drift are thermal fluctuations due to self-heating and thermo-resistive changes. The power dissipated in the sensor was approximately 8.3 mW, which is high compared to the state-of-the art sensor readout schemes.

In summary, the development of a functional VP shunt based on GMR sensors will require cancellation of the Earth's ambient magnetic field, through the use of a second (reference) GMR sensor and reduction of the observed thermal drift. The later could be achieved by reduction of the excitation current and use of thermal compensation circuitry. The former is likely to require an increase in the signal to noise ratio, since the reduction of self-heating by two orders of magnitude would requires a 10-fold reduction in the applied voltage, leading to a 10-fold reduction in the gain of the system. It is therefore likely that an additional 10-fold increase in the signal-to-noise ratio would be required. Such increase can be achieved by reducing the by-pass gap between the flap and the channel walls as demonstrated in Fig. 3a. Further increase in the sensitivity could come from reduction of the distance between the GMR sensor and the transducing flap. Analysis of the magnetic field distribution around the tip of the sensing element showed that for every 400 µm of reduction of the distance between the GMR sensor and the flap, the signal doubles. Finally, the use of a stronger neodymium magnets or micro-magnets, electroplated directly onto the flexible flap, is yet another

approach to achieve the desired increase of signal-to-noise ratio.

ACKNOWLEDGEMENTS

The authors acknowledge the support for this work from the Rosztoczy Foundation through a grant to Gergo Edes and partial support from the National Science Foundation Grant # 1353094

REFERENCES

[1] Y. Wu, N. L. Green, M. R. Wrensch, S. Zhao, and N. Gupta,"Ventriculoperitoneal shunt complications in California: 1990 to 2000," Neurosurgery, vol. 61, no. 3, (2007), pp. 557–563

[2] H.J. Garton, J.R. Kestle, and J.M. Drake, "Predicting shunt failure on the basis of clinical symptoms and signs in children," Journal of neurosurgery, vol. 94, no. 2, (2001) pp. 202–210,

[3] J.M. Drake, J R. Kestle, R. Milner, G. Cinalli, F. Boop, J. Piatt Jr, S. Haines, S. J. Schiff, D. D. Cochrane, P. Steinbok et al., "Randomized trial of cerebrospinal fluid shunt valve design in pediatric hydrocephalus," Neurosurgery, vol. 43, no. 2, (1998) pp. 294–303.

[4] J. Kestle, J. Drake, R. Milner, C. Sainte-Rose, G. Cinalli, F. Boop, J. Piatt, S. Haines, S. Schiff, D. Cochrane et al., "Long-term followup data from the shunt design trial," Pediatric neurosurgery, vol. 33, no. 5, (2001), pp. 230–236.

[5] K. Sheykholeslami and K. Kaga, "The otolithic organ as a receptor of vestibular hearing revealed by vestibular-evoked myogenic potentials in patients with inner ear anomalies," Hearing research, vol. 165, no. 1, (2002), pp. 62–67.

[6] V. Macellari, "Batteryless on-demand-sampling active radiosonde for intracranial pressure measurement," Medical and Biological Engineering and Computing, vol. 19, no. 6,(1981) pp. 686–694.

[7] J.R Madsen, G.S. Abazi, L. Fleming, M. Proctor, R. Grondin, S Magge, P. Casey, and T Anor. "Evaluation of the shuntcheck noninvasive thermal technique for shunt flow detection in hydrocephalic patients." Neurosurgery, v.68(1), (2011), pp.198–205.

[8] A. Glaninger, A. Jachimowicz, F. Kohl, R. Chabicovsky, and G. Urban, "Wide range semiconductor flow sensors," Sensors Actuat. A, 85, (2000), pp.139–146.

[9] J Chen, J Engel, C Liu, "Development of polymer-based artificial haircell using surface micromachining and 3D assembly", TRANSDUCERS, Solid-State Sensors, Actuators and Microsystems, 12th International Conference on, 2. IEEE, (2003).

[10] L.G. Leal, Advanced transport phenomena: fluid mechanics and convective transport processes. Cambridge University Press, vol. 7, 2007

[11] E.T. Enikov and K.V. Lazarov, "PCB-integrated metallic thermal microactuators," Sensors and Actuators A, vol. 105, no. 1, (2003), pp. 76–82.

[12] S. James and P. Spottiswoode, Effect of Ambient Magnetic Field Fluctuations on Performance in a Free Response Anomalous Cognition Task: A Pilot Study, Proceedings of the 36 th Annual Convention of the Parapsychological Association", (1993)

[13] M. Pannetier, C.Fermon, G. Le Goff, J. Simola, E. Kerr, J. Coey, "Noise in small magnetic systems - Applications to very sensitive magnetoresistive sensors", Journal of Magnetism and Magnetic Materials, v. 290-291, (2004), pp 1158-1160.

CONTACT

*ET. Enikov, Public tel: +1-520-621-4506;
enikov@email.arizona.edu

MICROMACHINED BROADSIDE-COUPLED TUNABLE METAMATERIALS

X. Zhao[1], K. Fan[1], J. Zhang[1], G.R. Keiser[1], H.R. Seren[1], R.D. Averitt[1,2], and X. Zhang[1]*
[1]Boston University, Boston, Massachusetts, USA
[2]University of California, San Diego, La Jolla, California, USA

ABSTRACT

This paper reports a micromachined tunable metamaterial based on broadside-coupled split ring resonators (BC-SRRs). The device consists of two layers of SRRs stacked on top of each other with an air gap spacer, forming the BC-SRRs. One of the layers is fixed, while the other can be driven by an electrostatic comb-drive actuator. The lateral displacement between the two layers of SRRs can be changed by the actuator, resulting in the tuning of resonance frequencies of the BC-SRRs and thus the transmission spectrum of the device. The preliminary results show that the resonance frequency can be tuned up to 100GHz corresponding to an 18μm lateral displacement. Our tunable metamaterials have promising applications as THz modulators, filters and sensors.

INTRODUCTION

Metamaterials (MMs) have been considered as a route of engineering the electromagnetic response of micro- and nanostructured materials through resonance excitations [1]. MMs have many remarkable applications, including super lensing [2], negative refractive index [3], cloaking [4] and perfect absorption [5], in security [6, 7], chemical and biology sensing [8], and information processing [9].

In order to enhance the functionalities and practicality of MMs, several approaches have been employed to make the MMs tunable, reconfigurable and dynamic. These include photo-excitation [10], electrical gating [11], thermal tuning [12], adjustment of near-field coupling [13] and structural and mechanical reconfiguration [14]. Among these methods, tuning the near field coupling is of interest because of its high efficiency, stability and ease of controlling [13, 15]. One example of a coupled MM structures is the broadside-coupled split ring resonator (BC-SRR), in which two split ring resonator (SRR) arrays are stacked vertically and rotated 180° relative to each other. Recent study shows that the lateral, in plane displacement between the two SRR layers will tune the MM resonance frequency significantly without altering the amplitude and Q-factor of the resonance [13]. To our knowledge, however, no BC-SRR based real-time tunable MM devices have been reported in the literature.

Micromachined electrostatic actuators provide an intuitive path to realize the functional broadside-coupled tunable devices. Comb drive actuation has been successfully used in single layer MM devices to dynamically alter in-plane coupling between MM inclusions and tune the MM's response [14]. However, thick substrate supporting the fixed elements in the MMs, leads to additional insertion loss. Additionally, the translation range of the movable elements is limited by the single layer design of the structure, limiting tunability.

In this paper, we report a broadside-coupled SRR MM at THz frequencies, tunable via comb drive actuation. The MM is composed of two layered of SRRs, formed BC-SRRs. The first SRR array sits on a thin, moveable silicon layer connected to comb-drive actuators. The second SRR array sits on a fixed silicon nitride film. Notably, the substrate is eliminated in this structure. The MM structure was characterized using the THz Time Domain Spectroscopy at different lateral relative displacement between the SRR layers. The results show that the resonance frequency can be shifted up to 100GHz corresponding to 18μm lateral displacement.

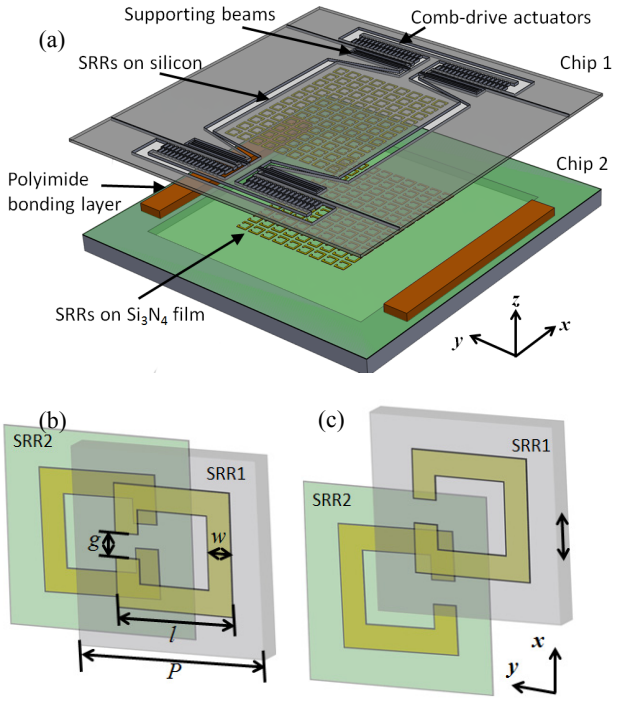

Figure 1: Illustration of the broad-side coupled tunable metamaterials: (a) the exploded diagram of the tunable metamaterials, in which two chips were bonded together with polyimide spacer; (b) and (c) the unit-cell of the MMs with different x-axis shift.

DESIGN AND FABRICATION

The illustration of the designed tunable MMs is shown in Fig.1. The MMs are composed of two layers of SRRs separated by 8μm air gap. One layer is on 10μm thick silicon with electrostatic comb-drive actuators, while the other is fixed on 500nm thick SiN_x thin film. The unit-cell of the MMs with different *x*-axis displacement is shown in Fig.1 (b) and (c). The rings are rotated 180° to each other, forming a broadside-coupled configuration. Since the two layers of MMs are closed to each other, the near-field interaction between them is strong. The relative shift along *x*-axis between the arrays, controlled by the applied voltage, can change the coupling between the SRRs. Thus, it modulates the frequency response of MMs.

The two component SRRs in each unit are not identical because of different substrate materials and designed dimensions as listed in Table 1. Fig.2 shows the simulated transmission responses of individual SRR under the incident THz radiation. The resonance frequency of each resonator is determined by the self-inductance and capacitance since $\omega_0 \sim 1/\sqrt{(LC)}$. When they are forming the broadside-coupled pair, as configured in Fig.1 (b), the near field coupling between the rings result in the dual-band response (black curve in Fig.2). According to [13, 16], the coupling arises from the mutual inductance and capacitance.

9781940470016/HH2014/$25©2014TRF
DOI 10.31438/trf.hh2014.101

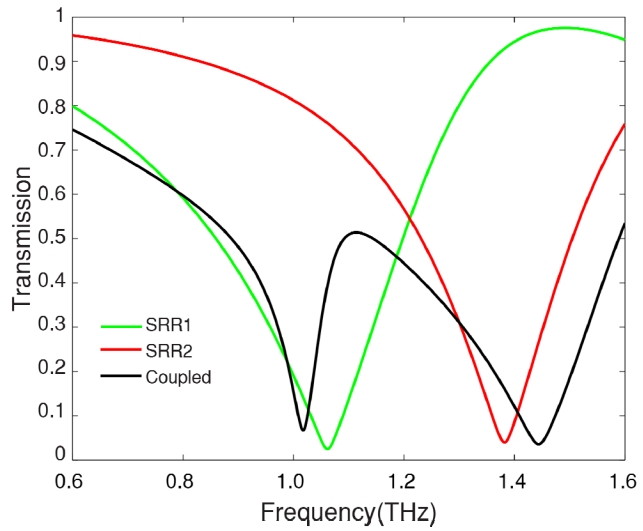

Figure 2: Simulated transmission spectra of the SRRs.

If there is relative lateral displacement between the two layers, the mutual inductance and capacitance will change by reason of the structure reconfiguration. This will in turn alter the transmission spectra.

Fig.3 shows the fabrication process flow that includes two wafers processing and chip integration. One of the wafers is a silicon-on-insulator (SOI) wafer with 10μm thick device layer, 2μm oxide layer and 500μm handle layer. First, both sides of the SOI wafer were coated by 500nm SiN_x film with LPCVD, followed by patterning the top side with RIE. Next, the Al electrodes were patterned by e-beam evaporation and lift-off, followed by rapid thermal annealing at 450°C in H_2/N_2 forming gas for 30min to realize the Ohmic contact. The 150nm thick gold SRRs were also patterned by lift-off process after that. Then, the device layer of SOI wafer was etched to realize the comb finger and beam structure using DRIE. Lastly, the handle layer of silicon was etched through by DRIE and the buried oxide layer was etched by Silox Vapox III etchant (Transene Inc.) to release the structure. The second wafer is a double side polished silicon wafer. It was coated by SiN_x and the SRRs were patterned firstly. Afterward, etching windows were patterned on the backside SiN_x by RIE and the wafer was soaked in KOH solution until a free-standing SiN_x thin film. Both wafers were diced into chips after these processes. Finally, an 8μm thick layer of photo-definable polymer was patterned to bond the two chips with flip chip bonder.

Fig.4 is the microscopic image of a chip with comb-drive actuator. Two identical actuators driven by electrostatic force were placed on both sides of the MMs array. The actuators on each side provide unidirectional in-plane translation along *x*-axis. The movable structure is suspended by four pairs of folded beam. The actuation relationship $\Delta x = AV^2$, where Δx is the displacement, V is the actuation voltage and A is the actuation coefficient. In our structure, the actuation coefficient of the structure is $A = 5\text{nm/V}^2$, which is verified by experiment. This coefficient can be further improved by fabricating smaller gaps between fingers. Fig.5 shows the fabricated device. The two chips were bonded together with polyimide spacer. The chip is wire bonded to a customized PCB for the electric connection. Fig.5 (d) and (e) are showing the SRRs position without displacement and with 18μm displacement.

Table 1: The dimensions of SRRs (unit in μm)

	Periodicity (*P*)	Side-width (*l*)	Linewdith (*w*)	Gap (*g*)
SRR1	58	40	10	14
SRR2	58	40	10	16

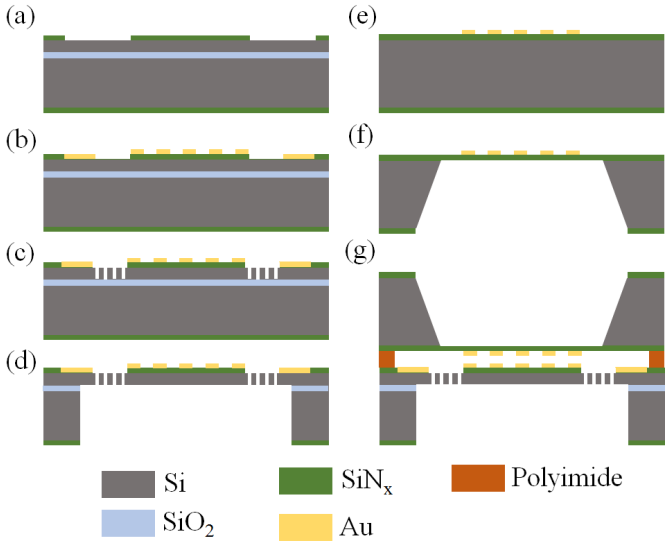

Figure 3: Fabrication process of the tunable metamaterials. (a)-(d) the first (SOI) wafer process, (e)-(f) the second (silicon) wafer process, (g) the flip-chip bonding.

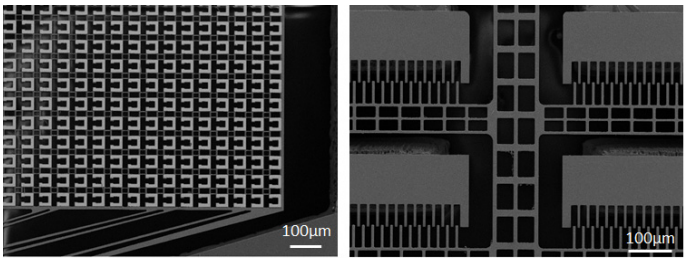

Figure 4: The microscopic image of the chip with comb-drive actuator.

EXPERIMENT AND RESULTS

The fabricated device was characterized by Terahertz Time Domain Spectroscopy (THz-TDS) system [12]. A THz pulse with diameter of 3mm was normally incident on the MM surface with electric component polarized parallel to the sides of SRRs with capacitive gaps. The transmission signal through the tunable MMs was measured at different driving voltage applied to the comb-drive actuator. Another comb-drive structure without SRRs on it was used as reference. The measured transmission spectra are shown in Fig.6. When the lateral shift is 0μm [as shown in Fig.5 (d)], the two SRRs in each unit are not well-aligned in *x*-axis. There are two resonance modes observed at 1.1THz and 1.4 THz. Upon increasing the lateral displacement, the relative position as shown in Fig.5 (e). The coupling between the two SRRs in each unit increases in this configuration. This increase in coupling strength causes a mode splitting redshifting the lower resonance by

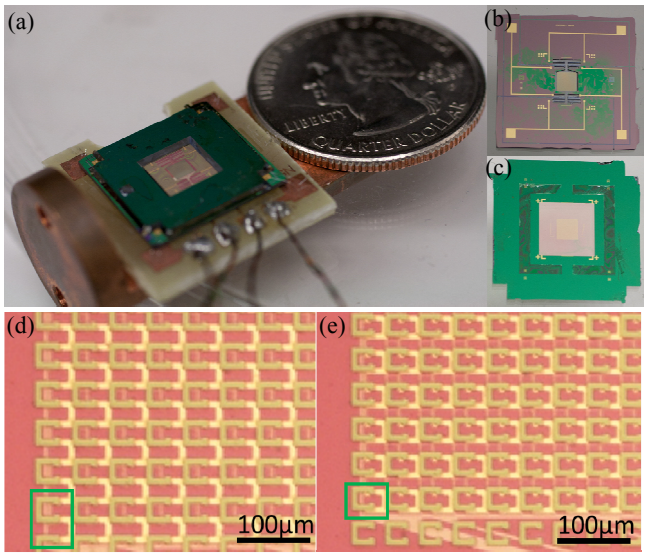

Figure 5: The fabricated deivces. (a) The bonded chip wire bonded on a printed circuit board; (b) the SOI chip (chip 1); (c) the SiN_x chip (chip 2); (d) the SRRs position with 0μm displacement; (e) the SRRs position with 18μm displacement.

50GHz and blueshifting the higher resonance by 100GHz for a lateral displacement of 18μm.

DISCUSSION

Multiple methods exist to model the coupling behavior of broadside-coupled SRRs [17], including coupled mode theory, mode hybridization model and mutual capacitance and inductance model [18]. Herein, we will follow the third method to describe the tuning mechanism in our device.

In order to have better understanding of the coupling mechanism at work in this structure, we performed finite difference analysis on the device with CST Microwave studio. The results are shown in Fig.7. When the lateral shift is 0μm, the current oscillates only in SRR1 at the lower resonance frequency [Fig.7 (b)] and only in SRR2 at higher resonance frequency [Fig.7 (c)]. This suggests that the mutual capacitance and inductance are negligible and the two resonators are resonating independently. For the case of maximum lateral shift, the configuration of the two layers of SRRs in Fig.5 (e), both of the SRRs are excited simultaneously at both resonance modes. At the first mode, the currents in the two SRRs are in phase [Fig.7 (d)] and generate out-of-plane magnetic fields pointing the same direction. Hence, the mutual inductance at this mode is positive, which means it can increase the total inductance of the system. At the second mode, the currents are oscillating out-of-phase [Fig.7 (e)], which will induce magnetic field in the opposite directions. As a result, the mutual inductance is negative and will decrease the total inductance. The mutual capacitance is almost negligible because of the small overlap area between the SRRs. Thus, lateral displacement increases the absolute value of the mutual inductance. Consequently, the total inductance increases and causes a redshift in the first mode but decreases and causes a blueshift in the second mode. The simulated transmission spectra shown in Fig.7 (a) agree well with the experimental results, lending support to this theoretical model.

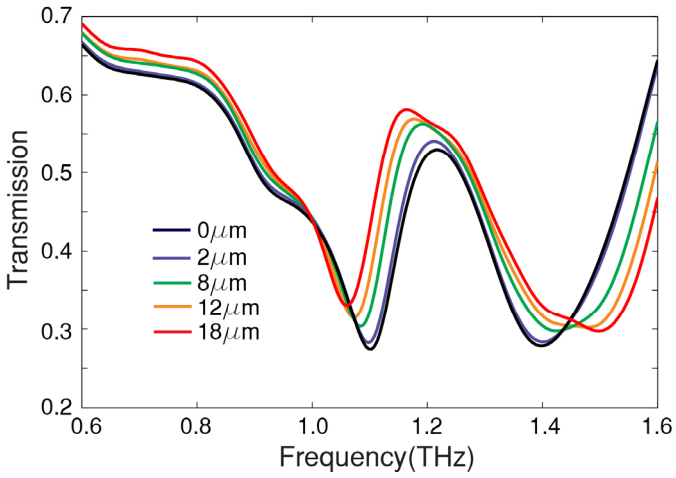

Figure 6: The experimental transmission spectra of the tunable metamaterials at different lateral shift.

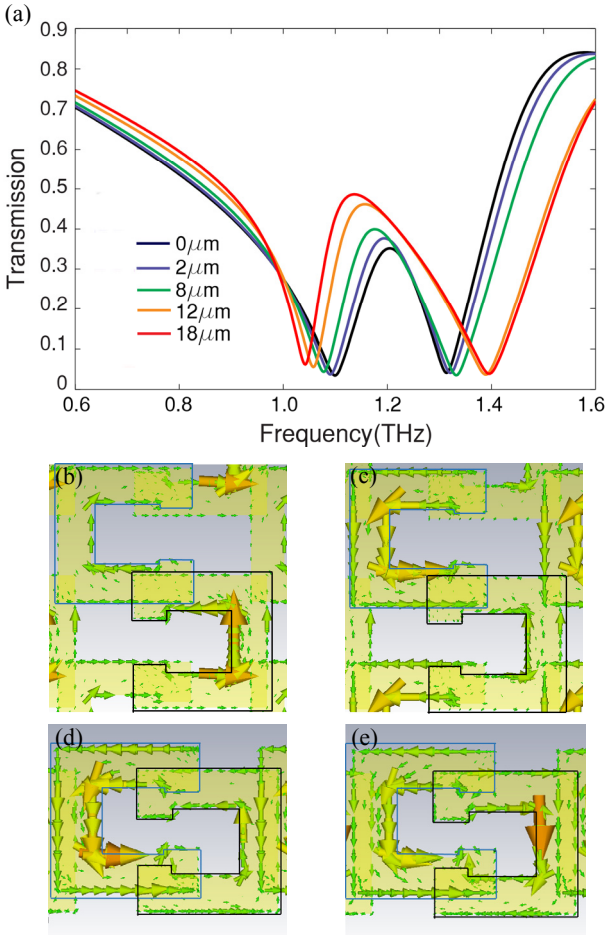

Figure 7: (a) The simulated transmission spectra of the tunable metamaterials at different relative displacement; (b) and (c) the current distribution at 1.10THz and 1.30THz with 0μm displacement; (d) and (e) the current distribution at 1.03THz and 1.40THz with 18μm displacement (The SRR in black frame is SRR1 while the blue SRR2).

CONCLUSIONS

A real-time tunable dual-band MM based on broadside-coupled SRRs with a micromachined actuator was designed, fabricated and characterized. The resonance frequency redshifts 50GHz at the first mode and blueshifts 100GHz at the second mode with 18μm lateral shift. The nature of the frequency shift was studied qualitatively by mutual inductance model. Further optimization of this device will lead to an increased effective frequency scanning range. This MM device has potential applications for spectral sensing of chemicals and dynamic modulation of THz radiation.

ACKNOWLEDGEMENT

This work was supported in part by the National Science Foundation under Contract ECCS 1309835, the Air Force Office of Scientific Research under Contract FA9550-09-1-0708, and DTRA under Contract W911NF-06-2-0040 administered by the Army Research Laboratory. The authors would like to thank Boston University Photonics Center for technical support. Travel support has been provided by Transducer Research Foundation.

REFERENCES

[1] N.I. Zheludev and Y.S. Kivshar, "From Metamaterials to Metadevices", Nature Materials, 11, 917 (2012).

[2] X. Zhang, and Z. Liu, "Superlenses to Overcome the Diffraction Limit", Nature Materials, 7, 435 (2008).

[3] D.R. Smith, J.B. Pendry, and M.C. Wiltshire, "Metamaterials and Negative Refractive Index", Science, 305, 788 (2004).

[4] D. Schurig, J.J. Mock, B.J. Justice, S.A. Cummer, J.B. Pendry, A.F. Starr, and D.R. Smith, "Metamaterial Electromagnetic Cloaking at Microwave Frequencies", Science, 314, 977 (2006).

[5] N.I. Landy, S. Sajuyigbe, J.J. Mock, D.R. Smith, and W.J. Padilla, "Perfect Metamaterial Absorber", Physical Review Letters, 100, 207402 (2006).

[6] L. Feng, Y. Xu, W.S. Fegadolli, M. Lu, J.E. Oliveira, V.R. Almeida, Y. Chen, and A. Scherer, "Experimental Demonstration of a Unidirectional Reflectionless Parity-time Metamaterial at Optical Frequencies", Nature Materials, 12, 108 (2012).

[7] D. Shrekenhamer, C.M. Watts, J. Montoya, S. Krishna, and W.J. Padilla, "Metamaterial-based Imaging for Potential Security Applications", Proceeding of SPIE, 8632, 863321 (2013).

[8] X. Xu, B. Deng, D. Li, J. Zhang, L. Wong, Q. Zhang, S. Wang, and Q. Xiong, "Flexible Visible-Infrared Metamaterials and Their Applications in Highly Sensitive Chemical and Biological Sensing", Nano Letters, 11, 3232 (2011).

[9] N. Engheta, "Circuits with Light at Nanoscales: Optical Nanocircuits Inspired by Metamaterials", Science, 317, 1698 (2007).

[10] K. Fan, X. Zhao, J. Zhang, K. Geng, G.R. Keiser, H.R. Seren, G.D. Metcalfe, M. Wraback, X. Zhang, and R.D. Averitt, "Optically Tunable Terahertz Metamaterials on Highly Flexible Substrates", IEEE Transcation on Terahertz Science and Technology, 3, 702 (2013).

[11] H.-T. Chen, W.J. Padilla, M.J. Cich, A.K. Azad, R.D. Averitt, and A.J. Taylor, "A Metamaterials Solid-State Terahertz Phase Modulator", Nature Photon, 3, 148 (2009).

[12] H. Tao, A.C. Strikwerda, K. Fan, W.J. Padilla, X. Zhang, and R.D. Averitt, "MEMS Based Structurally Tunable Metamaterials at Terahertz Frequencies", Journal of Infrared, Milimeter and Terahertz Waves, 32, 580 (2011).

[13] E. Ekmekci, A.C. Strikwerda, K. Fan, G.R. Keiser, X. Zhang, G. Turhan-Sayan, and R.D. Averitt, "Frequency Tunable Terahertz Metamaterials Using Broadside Coupled Split-ring Resonators", Physical Review B, 83, 193103 (2011).

[14] A.Q. Liu, W.M. Zhu, D.P. Tsai, and N.I. Zheludev, "Micromachined Tunable Metamaterials: A Review", Journal of Optics, 14, 114009 (2011).

[15] A.D. Boardman, V.V. Grimalsky, Y.S. Kivshar, M. Lapine, and N. Litchinister, "Active and Tunable Metamaterials", Laser Photonics Review, 5, 287 (2011).

[16] G.R. Keiser, A.C. Strikwerda, K. Fan, V. Young, X. Zhang, and R.D. Averitt, "Decoupling Crossover in Asymmetric Broadside Coupled Split-Ring Resonators at Terahertz Frequencies", Physical Review B, 88, 023101 (2013).

[17] H. Haus, and W.P. Huang, "Couple-Mode Theory", Proceedings of the IEEE, 79, 10 (1991).

[18] G.R, Keiser, K. Fan, X. Zhang, and R.D. Averitt, "Towards Dynamic, Tunable, and Nonlinear Metamaterials via Near Field Interactions: A Review", Journal of Infrared, Milimeter and Terahertz Waves, 34, 709 (2013).

CONTACT

* X. Zhang, tel: + 1.617.358.2702; xinz@bu.edu

MULTI-CAMERA LAPAROSCOPIC IMAGING WITH TUNABLE FOCUSING CAPABILITY

*A. Kanhere, K. Van Grinsven, C.-C. Huang, Y.-S. Lu, J. Greenberg, C. Heise, Y. Hu and H. Jiang**
University of Wisconsin-Madison, USA

ABSTRACT

This paper presents a comprehensive solution to overcome many of the fundamental challenges faced by current laparoscopic imaging systems. Our design features multiple tunable-focus microcameras integrated with a surgical port to provide panoramic intra-abdominal visualization with enhanced depth perception. Our system can be optically tuned to focus and zoom in on objects within a range of 3 mm to ∞, with a field of view adjustable between 36^0 and 130^0. Our unique approach also eliminates the requirement of an exclusive imaging port and need for navigation of cameras between ports during surgery.

INTRODUCTION

Laparoscopy is a minimally invasive surgical procedure performed through multiple small incisions in the abdomen. These incisions are used to deploy surgical 'trocars' or ports used to introduce cameras and surgical tools inside a surgical cavity. Current laparoscopic imaging technology relies on a single fixed-focus camera through a port, thus facing five fundamental challenges – limited field of view, lack of depth perception, occupation of a dedicated port by the camera, need for extensive maneuvering of the camera during surgery and glare from highly reflective organ surfaces [1].

A panoramic, 3D vision of the surgical field closely resembling the view in a conventional open surgery, is highly desirable in laparoscopy. It helps expedite surgical tasks and enhances the safety of surgical procedures [2]. Research solutions to address these challenges with software techniques for 3-D depth recovery have had limited success [3]. Some commercial systems claim 3D vision by employing a pair of closely spaced cameras. However, the narrow baseline between the cameras and the resulting low disparity limit the accuracy of depth recovery. More importantly, a two-camera pair cannot provide sufficient viewing angles to ensure an unobstructed view of the surgical region despite the presence of surgical instruments.

Current laparoscopes demand one port exclusively for imaging rather than instrumentation. In addition, constant maneuvering of the camera between ports is required to adjust the viewing angle of the surgical field. Several groups have bypassed these requirements by means of imaging tools tethered [4], sutured [5] or magnetically anchored [6] to the abdominal wall. However, these invasive solutions result in additional puncture points or tugging of the abdominal wall, thus diminishing the most appealing benefits of laparoscopy over open surgery.

Existing imaging solutions only address the aforementioned challenges individually and offer partial benefits over the current technology, at best. We previously reported on a reconfigurable fixed-focus, micro-camera array with panoramic vision [7]. Here we present a new comprehensive approach to address the aforementioned challenges in one system.

MECHANISM AND DESIGN

Our proposed design features an integrated trocar-camera assembly (TCA). The TCA is designed so as to be useful in both single-port and multi-port laparoscopic surgeries. Our TCA integrates an array of microcameras with a surgical port so that multiple cameras may be deployed into the abdominal cavity through an incision, without any additional surgical operation. In addition, it is affixed to the distal end of the port to capture images through simple mechanical actuation without the need for manual intervention.

The TCA consists of four microcameras assembled symmetrically around the trocar, connected together by a mechanical structure. The mechanical design of the assembly is similar to an umbrella frame. As shown in Figure 1, the assembly consists of four mechanical arms, each supporting one tunable microcamera. The arms are interconnected via a mechanical assembly that enables opening and closing of the arms, similar to the spokes of an umbrella. The frame is mounted along the periphery of the distal end of a surgical port, thereby keeping the port accessible. This ensures that the imaging system never interferes with the instruments in the port. The design of the actuation frame enables the reconfiguration of the cameras to ensure complete coverage of the surgical scene without the need for constant maneuvering during surgery.

Images acquired from individual cameras in any one frame position will represent distinct yet overlapping viewing perspectives of the same scene. Hence they can be stitched seamlessly for a much wider field of view in the resulting panoramic image. The use of multiple cameras allows for large field-of-view with reduced aberration (e.g. compared with fisheye-lens) while the optical tunability of the microcameras significantly improves the quality and depth perception of the image.

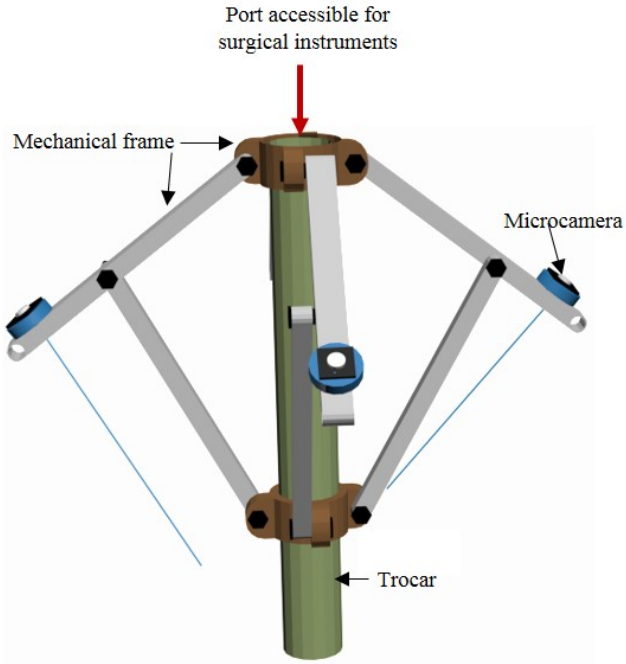

Figure 1: Schematic of the mechanical frame assembly for reconfiguration of camera positions. (Drawing not shown to scale) This design overcomes the problem of dedicated port occupation by imaging tools and keeps all ports accessible for surgical instruments throughout the surgery.

9781940470016/HH2014/$25©2014TRF
DOI 10.31438/trf.hh2014.102

Each camera unit consists of a 1mm × 1mm NanEye commercial CMOS sensor (AWAIBA Lda, Madeira, Portugal) aligned with a thermo-responsive tunable liquid lens, integrated with a microheater at the base and polarizer in front of the lens.

Variable-focus liquid microlenses

Since the microcameras will be affixed to the port, they must possess tunable focus in order to provide focused images of a surgical scene. Given the dimensions of an abdominal cavity and the positioning of the cameras closer to the abdominal wall, the tuning range of the focal length was designed to range from a few mm to ∞.

The tuning of focus was achieved by thermo-responsive hydrogel actuation [8,9]. The principle of operation of the tunable lens is represented in the schematic shown in Figure 2. The design consists of a thermal stimuli-responsive hydrogel ring placed within a microfluidic chamber filled with water. This chamber is sealed with an aperture slip with a circular opening centered over the ring. An oil chamber is then placed on top of the aperture slip. The opening in the aperture slip acts as the lens aperture. The water-oil meniscus is pinned along the lens aperture by surface treating the layers to create a hydrophobic-hydrophilic contact boundary. The initial meniscus, and thus the focal length, is determined by the volume of water filled in the water chamber. When the temperature of the lens structure is increased, the hydrogel ring responds by contracting due to the release of water via the hydrogel network interstitials. This results in a net change in the volume of the water droplet located in the center of the ring. Since the aperture rim of the lens is pinned, this translates to an increase in the radius of curvature and a decrease in the focal length. This process is reversible, which means that a decrease in temperature will cause the focal length to increase.

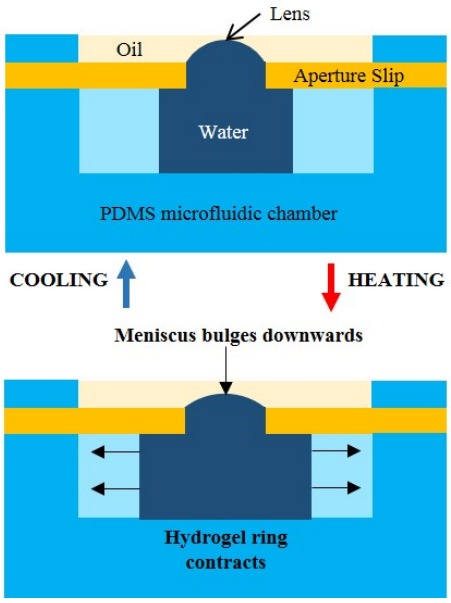

Figure 2 : Schematic representation illustrating the operation of a thermo-responsive tunable liquid lens. As the local temperature increases, the hydrogel releases water and contracts, thereby increasing the radius of curvature and decreasing the focal length of the water-oil lens. This focal length change is reversible.

Microheater for focus tuning

To tune the thermo-responsive hydrogel lens, a microheater was placed at the base of the lens. The temperature range required to tune the microlenses within the desired focal length range of 3mm to ∞ is 25-60 ^{0}C. The factors influencing our choice of the microheater were (1) form factor suitable for easy integration with lenses, (2) uniformity of heat distribution and (3) ease of heat dissipation after operation. We chose a coil type resistive heater design for easy alignment with the hydrogel ring structure. The coil design also minimizes hotspots due to absence of sharp corners [10].

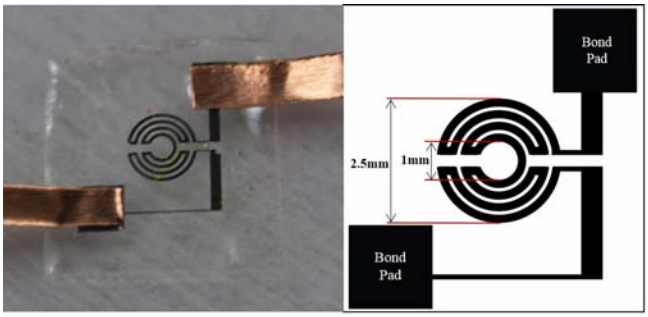

Figure 3 : Image of an aluminum micro heater coil used for tuning the microlenses. Conductive copper tape was used to probe the electrodes.

Polarizer

The presence of bodily fluids in the body makes the internal organ surfaces highly reflective, resulting in a glare while imaging them. Glossy or highly reflecting surfaces often reflect a linearly polarized, component of the incoming light much more strongly than the others. Therefore, our approach to addressing this challenge was to integrate a polarizer in front of our tunable-focus lens. We fabricated a linear polarizer oriented so as to block the reflected linear component. Such selective transmission of incident light based on the plane of polarization enhances the contrast of objects against the background, especially in low light conditions such as a surgical cavity. The effective reduction of glare with the placement of a polarizer in front of our camera can be seen in Figure 4.

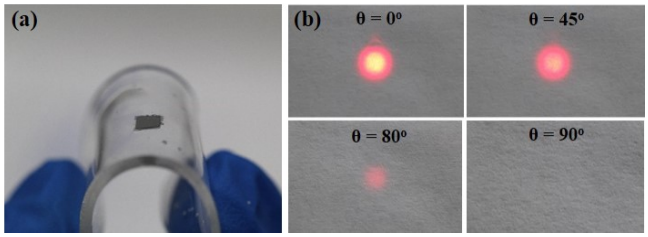

Figure 4 : (a) Image of a thin film Polyvinyl Alcohol (PVA) polarizer patterned on a flexible PDMS substrate. (b) Selective transmission of a linearly polarized He-Ne laser (λ=630nm) when passed through the polarizer.

FABRICATION METHODS

The tunable lenses were fabricated using liquid-phase photopolymerisation (LP^3). A 300-mm-thick cavity was defined on a glass substrate using double-sided adhesive spacers. This cavity was filled with a poly(isobornyl acrylate) (IBA) prepolymer mixture. Poly-IBA posts defining the water container (Ø=2.5 mm) were photopatterned through a photomask aligned on top of the cavity under UV radiance (8.0 mW cm^{-2} for 75 s). The chamber was then rinsed with ethanol to remove the unexposed solution.

Another 200 µm thick chamber was created on top of this structure to define the base of the water container. Then the chamber was filled with pre-cured polydimethylsiloxane (PDMS) and cured at 70 °C for 8 h, before being peeled off the poly-IBA mold. The sidewalls of the PDMS water containers were treated to be hydrophilic by corona discharge plasma. The water containers were filled then with the N-isopropylacrylamide (NIPAAm) hydrogel pre-polymer solution and then were photopatterned under UV radiance (I = 15mW cm^{-2}; t = 18 s) to form hydrogel rings in the containers.

Similar procedures were carried out to form a 250 µm thick PDMS with 1 mm circular openings defining the lens aperture. The side walls of the aperture were surface treated to be hydrophilic so as to form a pinning boundary for the water-oil lens. Then another 250 um thick PDMS layer with a 2.5 mm aperture was bonded on top of the aperture slip to form the oil container. The containers were filled with deionized water and silicon oil consecutively, forming the immiscible water–oil interfaces for the microlenses. The cross section of this fabrication process is shown in Figure 2.

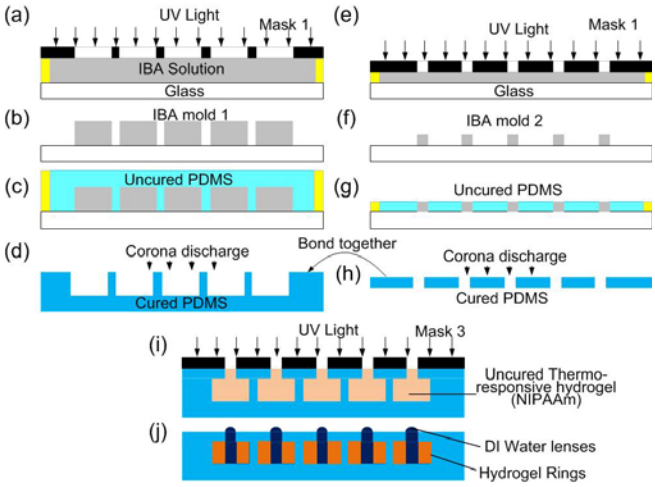

Figure 5 : Fabrication process flow for thermo-responsive hydrogel based tunable liquid lenses.

Thermal actuation and tuning of the lens was achieved with a microheater placed at the base of the lens. To tune the thermo-responsive hydrogel lens, a microheater coil was fabricated using a lift-off process and glued to the base of each lens. As shown in Figure 2(b), a layer of PDMS was first spun onto a photoresist coated glass slide and cured at 70^0C for 4 hours. Subsequently, a 2 um- thick layer of Parylene-C was deposited onto the PDMS layer, to improve the adhesion of metal onto PDMS. A 250 nm thick Aluminium layer was then sputtered onto this layer followed by photolithography and wet etching (H_3PO_4:HNO_3:CH_3COOH:H_2O in ratio 3:3:1:1 at 40^0C for 75 s) to define the microheater coil. The fabrication process for the microheater is demonstrated in Figure 6.

A thin film PVA polarizer was fabricated on a flexible substrate and integrated in front of the camera. First, PDMS elastomer was mixed with a curing agent in 10:1 ratio by weight. The mixture was then placed in the vacuum chamber to extract air bubbles. It was then poured onto a glass slide, cured at 80^0C for 4 hours and then peeled off to form a flexible PDMS substrate. Then, a pre-polymer of doped Polyvinyl Alcohol (PVA) was spin-coated at 1500 rpm for 1 minute onto the PDMS substrate. The surface was heated at 100^0C for 20 minutes to evaporate the solvent and cure the PVA thin film.

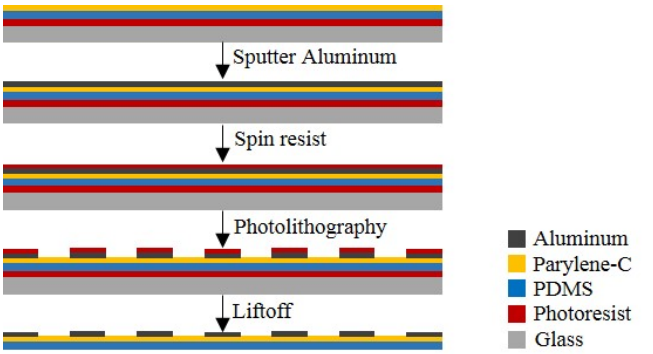

Figure 6 : Fabrication process flow for aluminum micro heater coil patterned on PDMS using lift-off process.

RESULTS AND DISCUSSION

To simulate the surgical environment for our experiments, a test scene was modeled closely on a commonly used scene in laparoscopic training boxes, designed to develop laparoscopic skills in novice surgeons [11]. The test scene was placed in a dark environment with illumination provided solely with a fiber optic light guide to closely resemble a surgical cavity. Since the NanEye image sensors do not have an IR filter, an IR cut was placed at 680nm to filter the incident light for faithful color imaging.

To test the optical zoom and focusing capabilities of our cameras, the position of a single tunable camera was fixed 12 cm away from the test scene. Images of the scene were then captured by the camera while varying the temperature from 25^0C to 45^0C to tune the lens. Figure 7 shows a series of three images captured by a camera while tuning the thermo-responsive lens using a microheater. The scene is first out of focus, then the camera gradually focuses and zooms in on the scene as the lens is tuned.

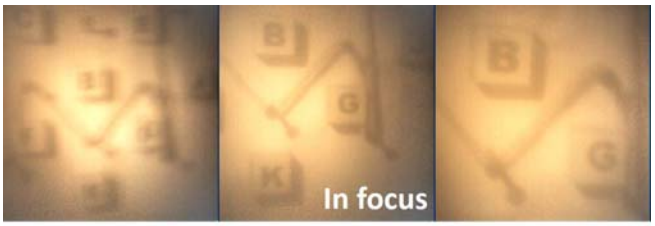

Figure 7 : Images of a test scene as captured by a single camera while the focal length of its tunable liquid lens was being tuned using a microheater.

The effects of integration of a polarizer in front of the camera while imaging reflective surfaces were tested by placing a highly reflective metal nail in the center of the scene being imaged. Figure 8 demonstrates effective glare reduction while imaging with the use of a polarizer.

To test the implementation of our imaging setup in the mock surgical scene, the test scene was sealed within a box with a small opening, similar to an incision in a surgical cavity. The TCA assembly was introduced into the scene along with a fiber optic light guide for illumination. During insertion, the mechanical arms (with the microcameras) were in a closed configuration with the arms parallel to the sidewalls of the port. Once the surgical port was positioned, the arms of the frame were flared out. Initially, the orientation angle of the array was adjusted to provide the desired viewing perspective, depth of field and horizontal field of view. Finer adjustments were then made to ensure distinct but slightly overlapping sub-scenes, as seen by individual cameras. In our

design, the orientation angle of all the microcameras can be simultaneously adjusted within an error margin of 5°.

Figure 8 : Reduction in glare with the use of a polarizer as seen from comparison of an image without using a polarizer in front of a tunable camera (left) and the same image captured with a polarizer in front of the lens (right).

First, the camera lenses were tuned individually to obtain focused images of each of their sub-scenes. This independent optical tuning feature enables our imaging system to handle different object distances without affecting the overall depth perception of the scene. So, sharp images of all the sub scenes are obtained by individual cameras as seen in Figure 9(a-d). These scenes were then stitched together in a commercial software, PTGui to obtain a panoramic image, shown in Figure 9(e). As seen from Figure 9(e), this yields to enhanced depth perception and a significantly large field of view of 128^0, which is greater than that of any of the individual source images.

Image distortion can be observed in the panorama in Figure 9(e) that is not seen in any of the sub-scene source images. This is primarily due to limitations of the commercial software. Most commercial softwares have stringent requirements of significant overlap of adjacent images, constant intensity throughout the scene and between successive frames, and identical exposures throughout the scene. However, our device is designed to operate in a surgical, low-light environment where these requirements cannot be met.

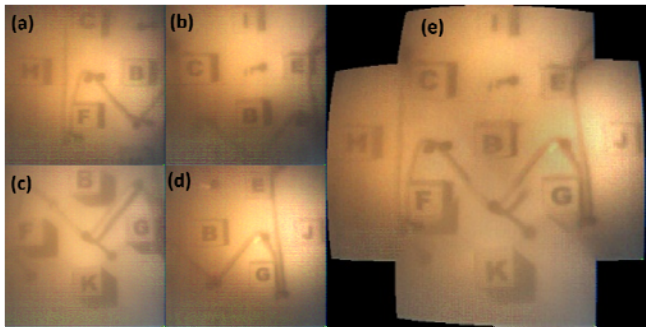

Figure 9 : Images of a mimicked surgical scene as captured by our camera array. (a-d) Sharp images of all the sub scenes were obtained by individual cameras These scenes were then stitched together in a commercial software, PTGui to obtain a very large field of view compared to any single camera alone (e).

CONCLUSION

A multi-camera laparoscopic imaging tool with optical tunability has been demonstrated in this work. Our preliminary results show that our approach offers promising solutions to several challenges including limited field of view and depth perception, need for exclusive imaging ports and extensive maneuvering of the camera during surgery and glare from highly reflective organ surfaces. Our future goals include wireless data transfer, algorithm development for 3D reconstruction, unified user interface design and commercial-grade packaging.

ACKNOWLEDGMENT

This work was supported by the U.S. National Science Foundation through the Emerging Frontiers in Research and Innovation program (EFRI 0937847). The authors would like to thank Dr. Li Zhang for insightful technical discussions and guidance. We would also like to thank the Transducer Research Foundation for their generous travel support.

REFERENCES

[1] H. Xin, J.S. Zelek, and H. Carnahan, “Laparoscopic surgery, perceptual limitations and force: A review”, First Canadian Student Conference on Biomedical Computing, Kingston, Ontario, Canada, 144 (2006).

[2] Y. Naya, K. Nakamura, K. Araki, K. Kawamura, S. Kamijima, T. Imamoto, N. Nihei, H. Suzuki, T. Ichikawa, and T. Igarashi, “Usefulness of panoramic views for novice surgeons doing retroperitoneal laparoscopic nephrectomy”, International Journal of Urology, 16(2008), pp. 177-80.

[3] D. Stoyanov, A. Darzi, and G. Z. Yang, “A Practical Approach towards Accurate Dense 3D Depth Recovery for Robotic Laparoscopic Surgery”, Comput. Aided Surg., 10(2005), pp. 199–208.

[4] C.A. Castro, A. Alqassis, S. Smith, T. Ketterl, S. Yu, S. Ross, A. Rosemurg, P.P. Savage, and R.D. Gitlin, “A Wireless Robot for Networked Laparoscopy”, IEEE Transactions on Biomedical Engineering, 60(2013), pp. 930-936.

[5] H. Tie, P.K. Allen, T. Nadkarni, N.J. Hogle, and D.L. Fowler, “Insertable stereoscopic 3D surgical imaging device with pan and tilt”, IEEE Int. Conf. on Biomedical Robotics and Biomechatronics, Oct 19-22, Scottsdale(2008), pp. 311 – 316.

[6] S.L. Best, and J.A. Cadeddu, “Development of magnetic anchoring and guidance systems for minimally invasive surgery”, Indian journal of urology, 26(2010), pp. 418-22.

[7] A. Kanhere, B. Aldalali, J. A. Greenberg, C. P. Heise, L. Zhang, and H. Jiang, “Reconfigurable Micro-Camera Array with Panoramic Vision for Surgical Imaging”, Journal of Microelectromechanical Systems, 22(2013), pp. 989-991.

[8] L. Dong, A. K. Agarwal, D. J. Beebe and H. Jiang, “Adaptive liquid microlenses activated by stimuli-responsive hydrogels,” Nature, 442(2006), pp. 551-554.

[9] X. Zeng*, C. Li*, D. Zhu, H. Cho, and H. Jiang, "Tunable microlens arrays actuated by various thermo-responsive hydrogel structures," IOP Journal of Micromechanics and Microengineering, 20(2010).

[10] C.F. Chau, and T. Melvin, “Design and fabrication of a quasi-ordered nanoporous silicon membrane suitable for thermally induced drug release”, IOP Journal of Micromechanics and Microengineering, 22(2012).

[11] E. Hiemstra, W. Kolkman, M.A.J. van de Put, and F. W. Jansen, “Retention of basic laparoscopic skills after a structured training program”, Gynecol Surg., 6(2009), pp. 229–235.

CONTACT

*H.Jiang, tel: +1-608-265-9418; hongrui@engr.wisc.edu

NOVEL TOUCH-FREE DRIVE, SENSE, AND TUNING MECHANISM FOR ALL-DIELECTRIC MICRO-SHELL GYROSCOPE

Raviv Perahia, Hung D. Nguyen, Lian X. Huang, Tracy J. Boden, Jonathan J. Lake, Deborah J. Kirby, Richard J. Joyce, Logan D. Sorenson, David T. Chang
HRL Laboratories, USA

ABSTRACT

This paper demonstrates, for the first time, touch-free electrical sensing and frequency tuning of an all-dielectric micro-shell gyroscope without electrically-conductive coatings. Current vibratory gyroscope technologies rely on an electrically-conductive structure or conductive coatings [1-6]. These conductive materials and coatings often compromise the quality factor (Q), thermal stability, and symmetry necessary to achieve navigation grade performance. The novel mechanism presented herein is based on the manipulation of electric fringe fields and their gradients. Several highly-doped Si electrode structures placed adjacent to the micro-shell can drive, sense, and frequency-tune the micro-shell as experimentally demonstrated in this paper. Micro-shell n = 2 wineglass vibration modes with $Q > 10^4$ and frequency splits $\Delta f <$ 50Hz are experimentally demonstrated using the touch-free gradient field transduction mechanism. Tuning of up to 4 Hz is demonstrated for a modest bias of 20V.

INTRODUCTION

The perceived benefit of a micro-scale navigation grade gyroscope is evident by the explosion in interest from commercial, academic, and government entities [7]. To date, MEMS scale vibratory gyroscopes have shown great promise but have yet to achieve navigation grade performance. The difficulty comes from a complex set of tradeoffs and requirements. This paper addresses a tradeoff between optimal structures, materials, and designs in the context of ultra-small devices (< 10 mm^3) that are fabricated only through processes currently available at MEMS foundries.

The use of a high Q, thermally-stable, structurally-isotropic dielectric material often conflicts with the need for electrically-conductive materials or coatings in traditional electrostatic drive/sense mechanisms [1-6]. A technique for transducing a vibrating dielectric micro-shell without placing dissipative conductive coatings directly on the structure will lead to higher performance by maintaining the high native mechanical Q of the dielectric structure [8]. Several experimental groups have recently shown that electric gradient forces can be used to efficiently drive nano-mechanical cantilevers [9-10], control optomechanical cavities [11], and sense acceleration [12]. In previous work, we demonstrated the ability to effectively drive a dielectric-only micro-shell gyroscope structure using electric gradient forces for the first time [13]. This paper reports experimental demonstration of the full drive, sense, and tuning functionality. It is now possible to design a gyroscope that is fundamentally limited by anchor and material loss of SiO_2, which opens up the ability to reach frequency quality factor product greater than 10^9 as experimentally demonstrated for this material [8, 14]. In contrast to our previous work, the transduction mechanism is now fabricated from highly-doped silicon-on-insulator (SOI) wafers in a configuration that is readily amenable to full 3D integration.

The cylindrical shell geometry presented in this paper is beneficial both from manufacturing and performance perspectives. The hemispherical and similar curved shell geometry of structures reported in the literature often use non-standard and complex fabrication processes and materials including glass blowing, specialty glasses for wet etching, specialty epoxies, and topographically-challenging deposition of electrodes pre- and post-hemispherical shell formation [1-6]. In contrast, the cylindrical micro-shell structure proposed here is wafer-scale manufacturable using standard bulk and surface micro-machining processes. The vertical nature of the shell will allow for future 3D wafer-scale integration of the high aspect ratio Si electrodes.

From a performance perspective, a cylindrical shell geometry has the advantage of lowest frequency for a given maximum shell diameter compared with curved/hemispherical shell structures. This is due to the lower effective modal stiffness and larger effective modal mass of cylindrical shells when operated in their wineglass modes. For a gyroscope, this translates into increased sensitivity. While blown glass curved-shell geometries have achieved very high Qs approaching $3x10^5$ [4], this has only been achieved using shell diameters greater than 5 mm and minimum cross-sectional shell thicknesses greater than 13 µm due to the challenge of creating small and thin shells with these non-traditional MEMS processes. In contrast, due to its thin oxide sidewalls, the cylindrical shell developed here can be scaled to smaller total device volume while maintaining a low native wineglass resonance frequency for optimal gyroscope sensitivity.

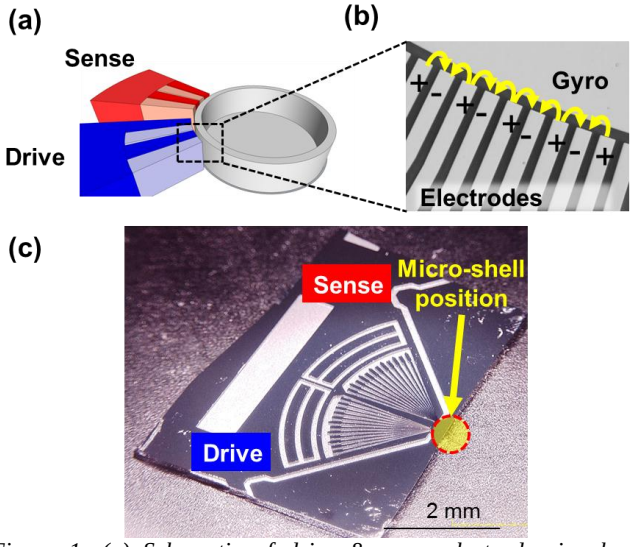

Figure 1: (a) Schematic of drive & sense electrodes in close proximity to a cylindrical shell gyroscope structure. (b) Close up of the electrodes showing alternating potentials and electric field. (b) Fabricated highly-doped Si electrode chip.

DEVICE

The touch-free drive, sense, and tuning mechanism for an all-dielectric micro-shell gyroscope is shown in Fig. 1(a). The gyroscope comprises a cylindrical micro-shell structure and integrated drive and sense electrodes. The electrodes are positioned in close proximity to the micro-shell in order to transduce and detect wineglass vibration modes. Both micro-shell and electrode array include unique design features to mitigate known challenges that limit performance of current vibratory MEMS gyroscopes: film stress, structural asymmetry, anchor loss, and loss

9781940470016/HH2014/$25©2014TRF
DOI 10.31438/trf.hh2014.103

contributions from the electrostatic drive/sense mechanism.

A 1.3 mm diameter, 350 µm tall, 2 µm thick, fabricated cylindrical vibratory micro-shell is shown in Fig. 2 on the left hand side. Compared to a shell with curved sidewalls, vertical sidewalls have fewer design constraints and allow for simpler fabrication using standard wafer-scale MEMS processes, resulting in a structure more compatible with the electrode array. The high aspect ratio of the sidewalls enables lower operating frequencies and increased capacitive area which maximizes drive amplitudes and sensitivity compared to those of curved wineglass structures of comparable diameter and height. Using finite element simulation the angular gain factor of cylindrical micro-shell is calculated to be A_g = 0.26, comparable to a hemispherical shell with the same diameter and thickness (A_g = 0.3) [15-16].

The cylindrical micro-shell is tethered to the anchor by a set of spokes. The spokes are engineered to reduce anchor loss and fabrication stress by isolating the vibrating shell from the substrate. Both the silica spokes and micro-shell are formed monolithically to avoid interfacial defects. The exclusive composition from SiO_2 eliminates anisotropy associated with crystalline materials (i.e. Si) as well as damping and thermal expansion mismatch. Coupled with the touch-free drive and sense mechanisms, the all-dielectric micro-shell gyroscope forgoes the complex manufacturing associated with the deposition of conductive electrodes on dielectric micro-shells (diamond, SiO_2, etc.).

High-aspect-ratio vertical electrodes are fabricated from the heavily doped 100 µm-thick silicon device layer of an SOI wafer. A close-in SEM micrograph of the electrode array is shown in the inset of Fig. 2. Vertical electrodes with 4 µm spacing are achieved using high aspect Si etching (20:1) producing high electrode density along the micro-shell periphery. Fabricating the electrodes from highly doped SOI allows for the electrodes to conform to the periphery of the micro-shell. Furthermore, this electrode geometry presents a clear path towards 3D wafer-scale integration with the micro-shell.

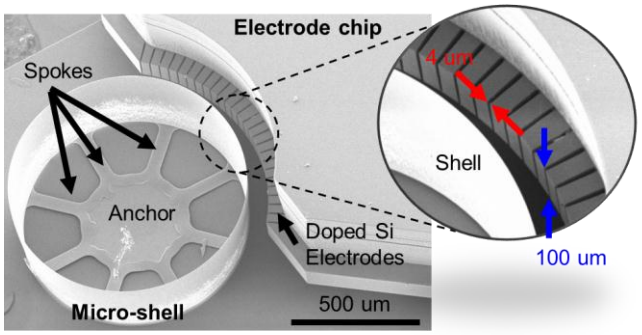

Figure 2: SEM micrograph of fabricated silica micro-shell (D_s = 1.3 mm, height H_s = 350 µm, thickness T_s = 2 µm) with adjacent highly doped silicon electrodes. The micro-shell is suspended from the underlying silicon handle wafer by a 10 µm silica anchor post.

EXPERIMENT AND RESULTS

The electrode dies, comprising of two sets of electrodes spatially-separated by 45 degrees, are mounted on printed circuit boards (PCBs) as shown in Fig. 3(a). The electrode tips overhang the PCB allowing for close proximity placement relative to the micro-shell. The PCBs provide an interface from die level wire bondable bus bars to coaxial lines that facilitate both biasing and current sensing depending on the transduction mode. Within each electrode set, individual electrodes are wire-bonded to the two bus bars in an alternating fashion, forming inter-digitated electrodes with alternating potentials. The PCBs are brought into proximity and aligned to the micro-shell in a vacuum chamber (P = $3x10^{-5}$ Torr) as shown schematically in Fig. 3(b). The top of the electrodes are aligned with the top of the micro-shell. Voltage applied between adjacent electrodes generates fringe fields that interact with the dielectric shell forming the basis for the transduction scheme. In this demonstration, two sets of electrodes are used to drive (E2) and sense (E3) an n = 2 wineglass mode. A Laser Doppler Vibrometer (LDV) focused on the side-wall of the micro-shell provides a reference signal of the vibrational motion for verification of the electrical read out. The focused LDV beam can be seen as a red spot at the periphery of the micro-shell shown in Fig. 3(c).

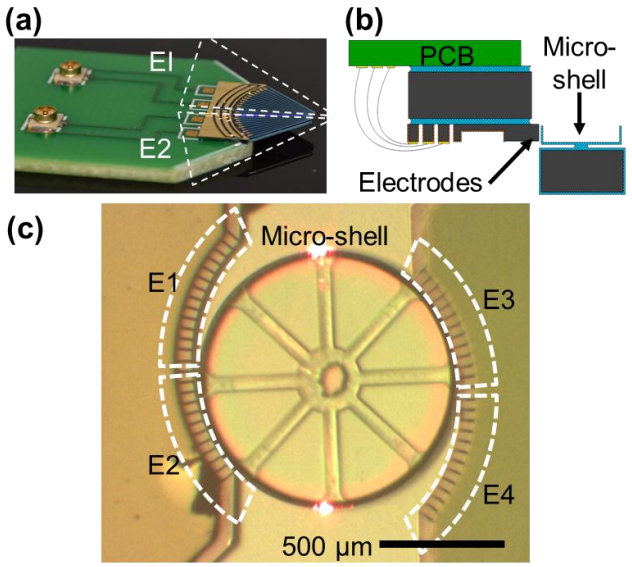

Figure 3: (a) Photograph of PCB-mounted electrode chip. (b) Schematic of micro-shell and PCB-mounted electrodes. (c) Top view of test configuration with two electrode dies (each composed of two electrode sets). The micro-shell (D_s = 927 µm, height H_s = 350 µm, thickness T_s = 2 µm) sits atop a silica anchor (D_a = 100 µm, H_a = 10 µm, spoke width W = 67 µm). Optical beam of the reference LDV, visible in red, is positioned between the electrodes.

Mode spectroscopy is carried out on the micro-shell by applying an electrical pulse (15 V, 10 µs width) across the E2 electrodes and measuring the time response of the motion using the LDV. The Fourier transform (FT) spectrum of the resultant motional response is presented in Fig. 4(a) (dotted red line). Subsequently, the same excitation and measurement scheme is applied to the E3 electrodes (blue line). The electrode dies are aligned at equal but opposite positions from the micro-shell such that the LDV spectra of the vibration generated by electrodes E2 and E3 are approximately the same in amplitude. Several prominent modes are readily apparent in the spectra. Using finite element (FE) simulations, the mode at f = 12.74 kHz is identified as the n = 2 wineglass mode of interest. The simulated wineglass mode pattern, shown in Fig. 4(b), indicates that motion is predominantly confined to the top rim the cylindrical micro-shell, a feature that may aid in the reduction of anchor loss. The observed lower frequency vibration modes are expected to be rocking modes from the FE analysis. The FE result of the simple rocking motion is shown in Fig. 4(c). To determine the quality factor of the n = 2 wineglass mode, a biased sine wave excitation applied across the E2 electrodes ($V_{p\text{-}p}$ = 2 V, V_{offset} = 1 V) is swept in frequency and

the resultant vibration amplitude measured using the LDV. A Lorentzian peak exhibiting a quality factor Q > 10^4 is shown in the inset of Fig. 4(a).

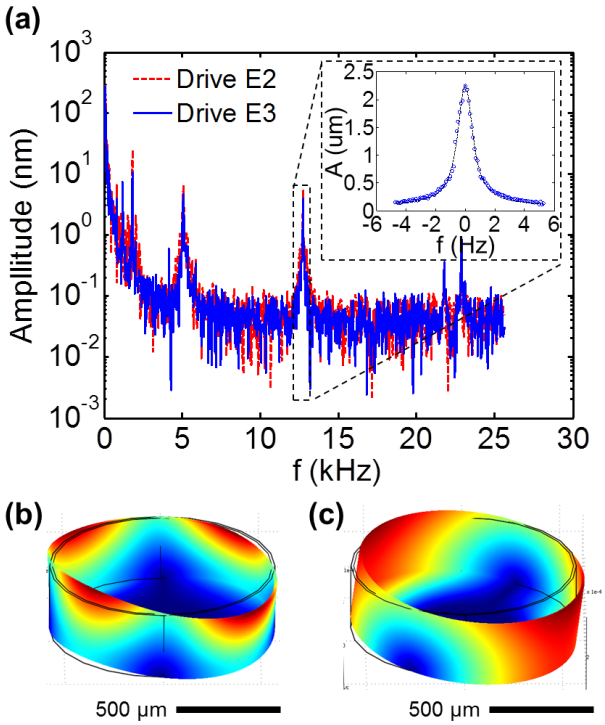

Figure 4: (a) Fourier-transformed impulse response measured by laser vibrometer (LDV). Inset – swept-sine measurement of n = 2 wineglass mode. (b) Finite-element simulation of n = 2 wineglass mode in a cylindrical micro-shell geometry. (c) Finite-element simulation of lower order rocking mode of cylindrical micro-shell geometry.

After both E2 and E3 electrode sets were aligned to the micro-shell and proven capable of driving it to the same vibration amplitude, a full drive and sense measurement was performed. Once again, a swept-sine source is applied to drive electrode E2 ($V_{p\text{-}p}$ = 2 V, V_{offset} = 1 V). One pole of the sense electrode E3 is biased (V_{dc} = 20 V) while the second pole is connected to a trans-impedance amplifier with a gain of nearly 50 MΩ. Matching frequency sweeps (Fig. 5) that capture the two nearly degenerate n = 2 wineglass modes were measured with both the LDV (blue line) and the sense electrodes (dotted red line). Frequency mode splitting of Δf ~ 50 Hz is observed, with the high-frequency mode showing significantly more sensitivity to the E2 drive, indicating favorable vibration pattern alignment with the drive and sense electrodes. The low-frequency mode is nearly un-observable in the electrical response due to spatial orthogonality of the wineglass modes. Interaction between the parasitic feed-through and the motional response results in the characteristic anti-resonance in proximity to the resonance as observed in the electrical response.

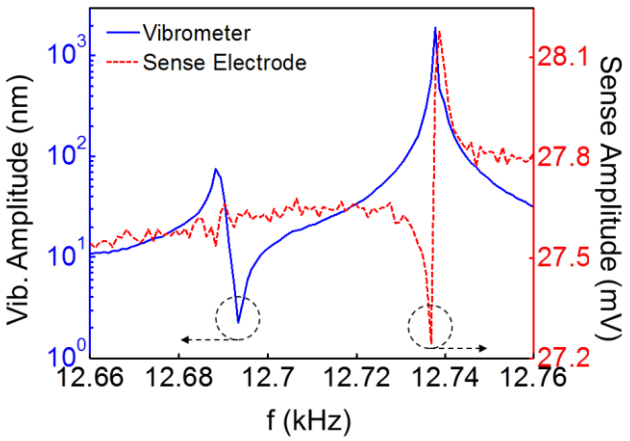

Figure 5: Swept-sine sense electrode measurement driven on E2 and sensed on E3 (g_{TIA}=5×10^7 Ω) and corresponding LDV measurement.

To confirm that the sense signal is indeed a measure of the vibration and coming from the sense electrode, the DC bias applied to the sense electrode, E3, was varied from 0 to 20 V while keeping the drive amplitude constant. The LDV measured peaks (Fig. 6(a)) tune towards lower frequency with increasing voltage. The sense electrode peaks (Fig. 6(b)) perfectly follow the LDV peaks to lower frequency but with increased amplitude.

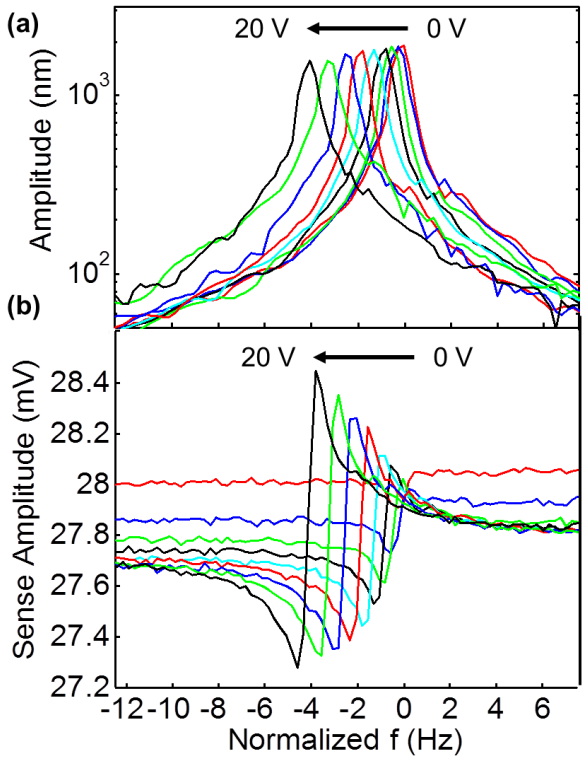

Figure 6: Swept sine measurement of mode amplitude (f=12.74 kHz) with (a) LDV and (b) E3 sense electrode. Modes exhibit red detuning as a function of increased bias voltage on the sense electrode (E3).

A summary of mode frequency and sense signal amplitude is shown in Fig. 7. The sense amplitude increases nearly linearly with increased bias, thus confirming the sense mechanism is an electrostatic effect. As the bias across electrode set E3 is increased, the strength of the fringe field increases and the total charge stored in a capacitor formed by E3 electrodes and the micro-shell must correspondingly increase. Thus, for the same mechanical motion, a larger current is generated. The micro-shell frequency tunes down and is nearly quadratic with bias voltage. This red detuning phenomena is consistent with spring softening in electrostatically-transduced devices. The maximum tuning range at 20 V bias is 4 Hz. This range would allow frequency mode-matching on a gyroscope structure with frequency splits of < 1 Hz. Even for this prototype structure with frequency splits of 50 Hz, due to the quadratic nature of the tuning, only 70 V would be needed for perfect mode matching. To the authors' knowledge, this is the first demonstration of tuning a high Q resonant gyroscope structure via gradient forces.

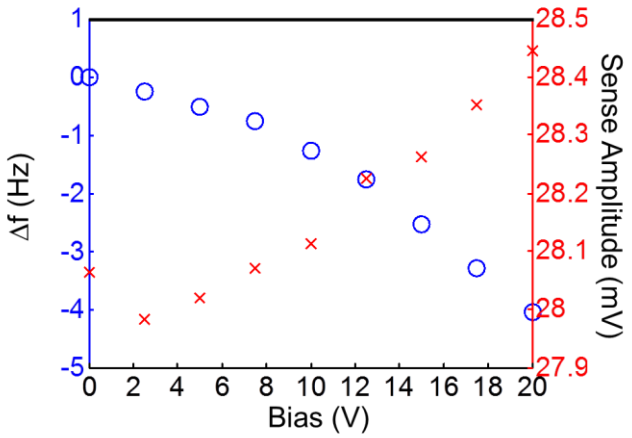

Figure 7: Spring softening frequency shift and sense mode amplitude (including parasitic feed through) vs. sense bias.

CONCLUSION

We reported on a technique for driving, sensing, and tuning a dielectric micro-shell gyroscope without the need for conductive structural materials or conductive coatings on dielectric structures. Shell vibratory motion is transduced and measured using a fully non-contact gradient field transduction mechanism. A unique all SiO_2 cylindrical micro-shell has been fabricated and tested in a gyroscope configuration. Wineglass n = 2 vibration modes with Q > 10^4 and frequency splits Δf < 50 Hz are experimentally demonstrated. Frequency tuning of up to 4 Hz is demonstrated for a modest bias of 20 V.

All aspects of the gyroscope architecture presented herein, including the cylindrical micro-shell and doped Si electrode arrays, are designed to address key limitations that have hindered current MEMS vibratory gyroscope from achieving navigation grade performance. Efficiently transducing the cylindrical micro-shell without electrically conductive coatings paves a path towards achieving material limited gyroscope performance and therefore navigation-grade performance. While the current testing was carried out using separate dies, the geometry is fully amenable to full wafer-scale 3D integration without the introduction of specialty processes.

Future work will focus on achieving material limited gyroscope performance by improving fabrication, spoke design, reducing mechanical stress, and reducing parasitic capacitance of the electrodes.

ACKNOWLEDGMENTS

The authors would like to acknowledge B. Holden, M. Cline, and F. Stratton for the fabrication effort and R. McElwain for assistance in testing.

REFERENCES

[1] N. Yazdi, F. Ayazi, K. Najafi, Proc. IEEE, Vol.86, pp.1640-1659, 1998.
[2] S. A. Zotov, A. A. Trusov, A. M. Shkel, J. MEMS, Vol. 21, No. 3, pp. 509-510, 2012.
[3] L. D. Sorenson, P. Shao, F. Ayazi, Proc. IEEE MEMS 2013, pp. 169-172, 2013.
[4] J. Cho, J.-K. Woo, J. Yan, R. L. Peterson, K. Najafi, IEEE Transducers 2013, pp. 1847-1850, 2013.
[5] A. Heidari, et. al., IEEE Transducers 2013, pp. 2415–2418, 2013.
[6] X. Luo, C. K. Eun, Y. B. Gianchandani, IEEE MEMS 2014, pp. 64-67, 2014.
[7] D. K. Shaeffer, IEEE Comm. Magazine, Vol. 5, pp. 100-109, 2013.
[8] R. Sandberg, K. Mølhave, A. Boisen, W. Svendsen, J. Micromech. Microeng., Vol. 15, pp. 2249–2253, 2005.
[9] Q. P. Unterreithmeier, E. M. Weig, J. P. Kotthaus, Nature, Vol. 458, pp. 1001-1004, 2009.
[10] S. Schmid, C. Hierold, A. Boisen, J. Applied Phys., Vol. 107, p. 54510, 2010.
[11] K. H. Lee, T. G. McRae, G. I. Harris, J. Knittel, W. P. Bowen, PRL, Vol. 104, p. 123604, 2010.
[12] S. Aoyagi, Y. C. Tai, IEEE Transducers 2003, pp. 1382-1386, 2003.
[13] R. Perahia et. al., IEEE MEMS 2014, pp. 721-724, 2014.
[14] W. Zhengzheng et. al, IEEE MEMS 2013, pp. 122-125, 2013.
[15] D. M. Rozelle, 19th AAS/AIAA Space Flight Mechanics Meeting, pp. 1157–1178, 2009.
[16] A. Meyer, D. Rozelle, IEEE/ION PLANS 2012, pp. 24–29, 2012.

CONTACT

*R. Perahia, tel: +1-310-317-5612; RPERAHIA@HRL.com

PICO-WATTS RANGE UNCOOLED INFRARED DETECTOR BASED ON A FREESTANDING PIEZOELECTRIC RESONANT MICROPLATE WITH NANOSCALE METAL ANCHORS

Y. Hui, Z. Qian, G. Hummel, and M. Rinaldi
Northeastern University, Boston, Massachusetts, USA

ABSTRACT

This paper reports on the first demonstration of an ultra-high resolution (*~371 pW/Hz$^{1/2}$*) uncooled infrared (IR) detector based on a high frequency (*136 MHz*) Aluminum Nitride (AlN) piezoelectric resonant micro-plate completely released from the substrate and supported by two nanoscale Platinum (Pt) anchors. For the first time, fully metallic tethers were employed to support the freestanding vibrating body of a piezoelectric resonator and provide electrical connection to it (the device anchors are conventionally defined in the piezoelectric layer). Such innovative design, with minimum anchor cross section, enabled the implementation of an uncooled resonant thermal detector with ultra-high thermal resistance (*~10^5 K/W*) and electromechanical performance (mechanical quality factor, $Q_M \approx 3133$ in air, and electromechanical coupling coefficient, $k_t^2 \approx 1.86\%$). Such unique combination of high sensitivity (*~2.1 Hz/nW*), low noise performance (*~0.78 Hz/Hz$^{1/2}$*) and high resonator figure of merit ($FOM = k_t^2 \cdot Q \approx 58.3$) resulted in the first complete and compelling prototype of a low power (*~11 mW*) and high performance MEMS-CMOS resonant uncooled IR detector with detection limit pushed in *~100s pW/Hz$^{1/2}$* range.

INTRODUCTION

The interest in uncooled IR detectors based on Micro/Nano-Electro-Mechanical Systems (MEMS/NEMS) resonator technologies is steadily growing due to their potentially ultra-high resolution and unique advantages in terms of size and cost, compared to conventional cryogenically cooled semiconductor photon detectors [1-5]. The most important parameters that ought to be considered for the design and optimization of uncooled and miniaturized thermal detectors are the device sensitivity to absorbed radiation, the noise performance and the ease of readout (especially crucial for focal plane array implementations). All these three fundamental challenges are addressed in this work with the experimental demonstration of a novel micromechanical resonant structure that, by taking advantage of advanced material properties and innovative device engineering, is characterized by a unique set of application enabling features, such as: (a) high sensitivity, due to excellent isolation from the heat sink (enabled by the large thermal resistance associated with the nanoscale metal anchors); (b) ultra-low noise performance, due to the intrinsic high *Q* of the resonant device (enabled by the improved confinement of acoustic energy in the resonant body of the device by using nanoscale metal anchors); (c) ease of readout, due to the excellent piezoelectric transduction properties of AlN at micro and nano scale which enables the use of a low power and self-sustained CMOS oscillator as direct frequency readout.

DESIGN AND FABRICATION

A high performance resonant IR detector is composed of a high quality factor, *Q*, MEMS resonator whose resonance frequency is highly sensitive to IR radiation [4]. When IR radiation is absorbed by the resonant structure, the temperature of the device increases (because of the large thermal resistance of the structure) resulting in a shift in resonance frequency due to the temperature coefficient of frequency (TCF) of the piezoelectric resonator [3]. The temperature rise of the resonator due to the incident IR power is given by:

$$\Delta T = \frac{\eta Q_p}{\sqrt{G_{th}^2 + \omega^2 C_{th}^2}} \approx \eta Q_p R_{th} \qquad (1)$$

where η is the absorption coefficient of the resonator, Q_p is the incident IR radiation power, G_{th} is the thermal conductance, C_{th} is the thermal capacity, and ω is the angular frequency of the incident IR radiation. When the incident IR radiation is constant, or slowly changing over time ($\omega \approx 0$), the temperature rise of the resonator is directly proportional to the thermal resistance, R_{th}, between the resonant body and the heat sink. Therefore, the implementation of a resonant structure extremely well isolated from the heat sink is crucial for the achievement of high temperature rise factor, thus high responsivity of the IR detector. The thermal isolation of a resonant thermal detector is mainly determined by the thermal resistance associated with the tethers connecting the freestanding vibrating body of the device to the substrate. In the case of a piezoelectric MEMS resonator, such anchors are conventional composed of a relatively thick piezoelectric layer (directly patterned in the same device layer forming the vibrating body of the resonator) and a relatively thin metal layer employed to route the electrical signal to the electrode placed on top or bottom (depending on the device design) of the freestanding piezoelectric body of the resonator [6]. By completely removing the relatively thick piezoelectric material from the anchors, hence minimizing their thicknesses (ultimately limited by the need of a thin metal layer for electrical routing), maximum thermal isolation of the device resonant body from the heat sink would be readily achieved. Furthermore, the increased acoustic impedance associated with such metal tethers with minimum cross section would act to reduce the energy loss through the device anchors (the acoustic energy would be well confined in the resonant body of the device) which has been identified as a significant source of quality factor, *Q*, degradation in piezoelectric MEMS resonators operating below 1 GHz [7].

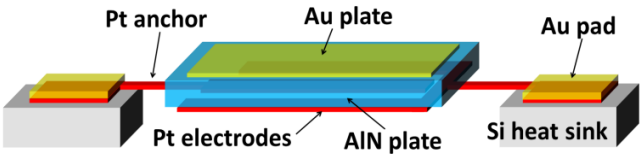

Figure 1: 3-dimensional representation of the AlN micro-plate resonator with nanoscale metallic (Pt) anchors.

According to these considerations, a new device concept, based on the use of fully metallic nanoscale tethers to support the resonant body of a piezoelectric MEMS resonator, is introduced in this work as an innovative design solution to maximize the thermal resistance and the electromechanical performance of piezoelectric MEMS resonant thermal detectors. The core of the proposed piezoelectric resonant uncooled thermal detector is an AlN

9781940470016/HH2014/$25©2014TRF
DOI 10.31438/trf.hh2014.104

piezoelectric resonant micro-plate (working at a higher order contour-extensional mode of vibration employing a lateral field excitation scheme [6]) completely released from the substrate and supported by two nanoscale Platinum (Pt) anchors. Figure 1 shows the 3-dimensional representation of the proposed AlN micro-plate resonator with fully metallic nanoscale anchors: the freestanding vibrating body consists of a *450 nm* thick AlN piezoelectric layer sandwiched between a *100 nm* thick gold (Au) film as top electrically floating electrode and a *100 nm* thick Platinum (Pt) bottom inter-digital transducer (IDT); two nanoscale Pt tethers (*100 nm* thick, *3~6 μm* wide and *22 μm* long) are employed to support the piezoelectric resonant body and provide electrical connection to it.

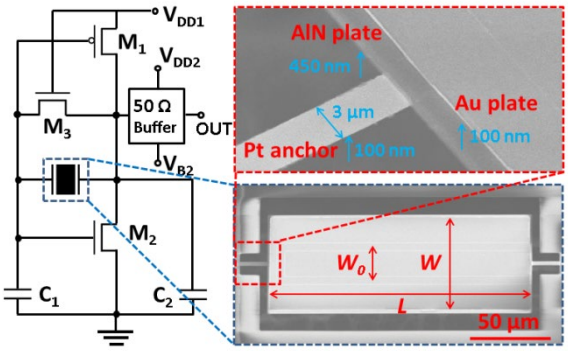

Figure 2: Schematic illustration of the CMOS amplifier and Scanning Electron Microscopy (SEM) images of the fabricated AlN resonator with nanoscle metal anchors: L = 200 μm, W = 75 μm and W_0 = 25 μm.

Such piezoelectric resonant micro-plate with nanoscale metal anchors is directly connected in the feedback loop of a self-sustaining CMOS amplifier as direct frequency readout [8]. The schematic illustration of the CMOS amplifier is shown in Figure 2: the circuit consists of a Pierce oscillator implemented by a CMOS inverting amplifier and a 50 Ω buffer stage. The design of the CMOS circuit is fully described in [9,10]. The AlN resonant uncooled thermal detector was fabricated using a 4-mask post-CMOS compatible microfabrication process [11], while the CMOS circuit was taped out in the ON Semiconductor 0.5 μm CMOS process. The fabricated AlN resonator was directly wire-bonded to the CMOS chip, forming the first complete and compelling prototype of a high performance MEMS-CMOS resonant thermal detector.

EXPERIMENTAL RESULTS

The effectiveness of the proposed design solution was verified with the fabrication and characterization of 17 AlN resonators employing different anchor configurations and operating at two different frequencies as listed in the table in Figure 3. The electrical response of each device was measured by an Agilent E5071C network analyzer after performing an open-short-load calibration on a standard substrate and the mechanical quality factor was extracted by modified Butterworth-Van Dyke (MBVD) model fitting (Figure 3-a). The thermal resistance, R_{th}, of each resonator was estimated by 3-dimensional Finite Element Method (FEM) simulation using CMOSOL Multiphysics (Figure 3-b). The details of the 3D COMSOL simulations are described in [12]. The experimental characterization and the FEM analysis of the 17 fabricated devices indicate that both the mechanical quality factor and the thermal resistance of the AlN resonator were simultaneously improved by a large extent when fully metallic nanoscale Pt anchors were employed: R_{th} was improved by one order of magnitude (from *~10^4* to *~10^5 k/W*) and an average Q_M improvement of *~92%* at *136 MHz* and *~28%* at *222 MHz* was recorded. Such simultaneous improvement in both mechanical quality factor and thermal resistance is crucial for the implementation of ultra-sensitive and low-noise MEMS resonant IR detectors.

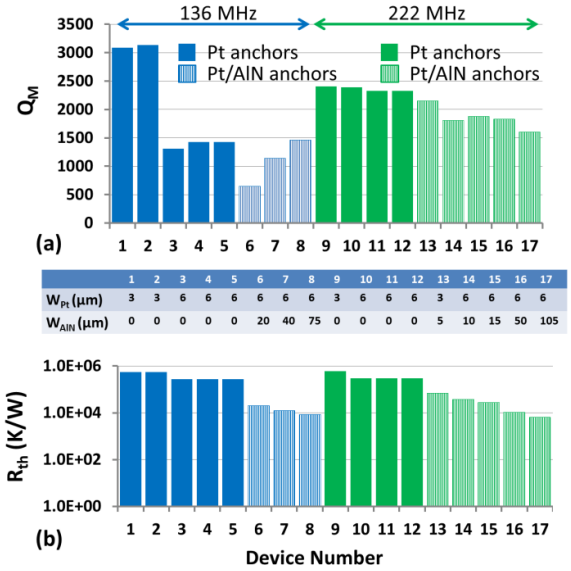

Figure 3: (a) Experimentally extracted mechanical quality factor values of 17 resonators employing different anchor configurations and operating at two different frequencies: solid bars represent the Q_M of devices employing fully metallic Pt anchors while shaded bars represent the Q_M of devices with conventional Pt/AlN anchors. The anchor width for each device is listed in the table (the anchor length and thickness are 22 μm and 100 nm for all the resonators). (b) Finite Element Method (FEM) simulated thermal resistance, R_{th}, of the same 17 resonators.

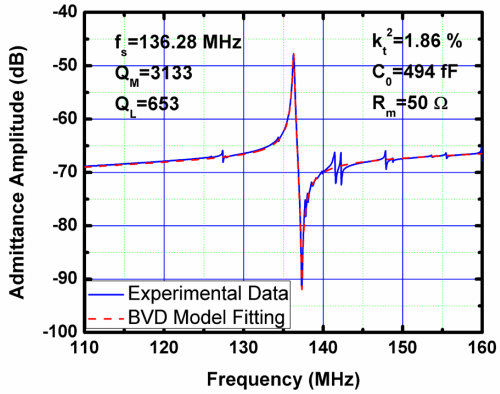

Figure 4: Measured admittance curve versus frequency and modified Butterworth-Van Dyke (MBVD) model fitting of the fabricated AlN resonator with nanoscale metal anchors. The relatively low value of loaded quality factor, Q_L, is due to the large electrical resistivity of the deposited Pt thin-film (~5X the bulk value). Values of Q_L comparable to Q_M could be achieved by optimizing Pt deposition or exploring the use of different metals.

Maximum Q_M and R_{th} were achieved for the *136 MHz* design employing *3 μm* wide Pt anchors. Therefore, this device

configuration was employed for the demonstration of a complete prototype of MEMS-CMOS IR detector. The mechanical quality factor Q_M and electromechanical coupling coefficient k_t^2 were extracted by MBVD fitting and found to be *~3133* and *~1.86%*, respectively (Figure 4). Such high electromechanical performance (Figure of Merit $FOM = k_t^2 \cdot Q_M \approx 58$) enabled the use of a compact and power efficient CMOS oscillator as direct frequency readout. The thermal resistance of the device was estimated by 3D FEM simulation and found to be *~5.5 × 10^5 K/W* (Figure 5-a), which is one order of magnitude higher than what typically achieved with conventional AlN resonator with AlN/Pt anchors [4]. The temperature distribution across the AlN resonant body was also simulated by applying an input power of *500 nW* to the top Au plate of the resonator (simulating IR absorbed power). A maximum temperature rise of *~274.3 mK* at the center of the resonant micro-plate and a maximum temperature difference of *~5.5 mK* across the length of the resonator were recorded, translating into a relative temperature variation of only *~2%* (Figure 5-b). The achievement of such uniform temperature distribution across the AlN resonant body was enabled by the large thermal resistance of the anchors and the relatively low thermal resistance of the AlN micro-plate. The temperature coefficient of frequency (TCF) of the AlN resonator with nanoscale Pt anchors was measured using a temperature controlled RF probe station and a TCF of *-27.8 ppm/K* was recorded. The frequency sensitivity of the AlN resonant device to absorbed radiation was calculated by multiplying the measured frequency sensitivity to temperature (*~ -3788 Hz/K*) by the simulated R_{th} (*~5.5 × 10^5 K/W*), resulting in an absolute responsivity of *~2.1 Hz/nW*, which is one order of magnitude higher than the one achieved with conventional resonators employing AlN/Pt anchors [8].

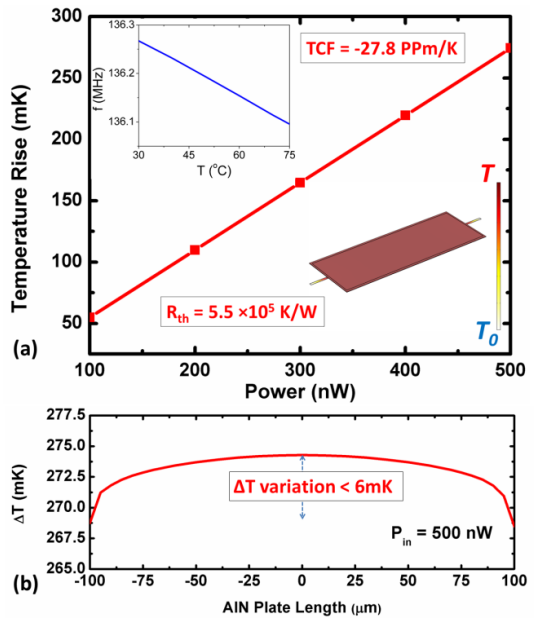

Figure 5: (a) 3-dimensional FEM simulated thermal resistance (R_{th}) of the MEMS resonant IR detector. The inset shows the measured TCF of -27.8 ppm/K. A device responsivity of 2.1 Hz/nW was calculated by multiplying the measured TCF and simulated R_{th}. (b) Simulated temperature distribution across the AlN resonant micro-plate. Extremely uniform heating of the device resonant body was achieved thanks to the large thermal resistance of the anchors and the relatively low thermal resistance of the AlN micro-plate.

The resonator was directly wire-bonded to the CMOS chip, forming a self-sustained piezoelectric MEMS-CMOS oscillator. In order to characterize the limit of detection of the sensor, the short term frequency stability of the oscillator output signal was characterized by measuring its Allan deviation [13]. The frequency measurements were taken with an Agilent 53230A frequency counter (Figure 6). A minimum Allan deviation of *~4.5 Hz* was recorded for a measurement time of *30 ms*, translating into a noise-induced frequency fluctuation of *~33 ppb* and a noise spectral density of *~0.78 Hz/Hz^1/2*. The Noise Equivalent Power (NEP) of the IR detector was extracted by dividing the measured noise spectral density (*0.78 Hz/Hz^1/2*) by the absolute value of the responsivity (*2.1 Hz/nW*), and found to be *~371 pW/Hz^1/2*. Such NEP is one order of magnitude lower than the one achieved with uncooled IR detector based on the same AlN technology but employing conventional AlN/Pt anchors [8], and 2~4X better than commercially available pyroelectric detectors [14].

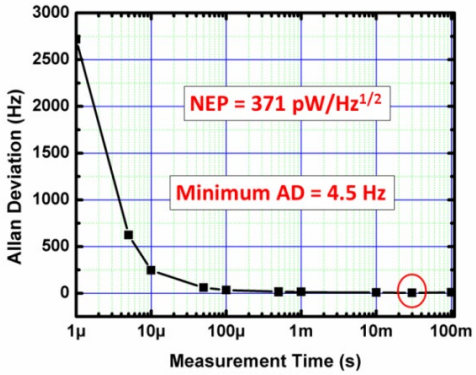

Figure 6: Measured Allan Deviation (AD) of the MEMS-CMOS oscillator: a minimum Allan Deviation of ~4.5 Hz was recorded for a measurement time of 30 ms.

The frequency response of the device prototype to IR radiation was characterized using a Bruker Vertex 70 FTIR and Hyperion microscope, shown in Figure 7. A broadband IR radiation from a Tungsten Halogen lamp (*0.25 μm – 100 μm*) was optically filtered (*0.33 μm – 2.8 μm* transmission) and chopped (*6.25 Hz*) before it was coupled into a Hyperion microscope used to focus the light onto the resonant body of the device. The frequency response of the MEMS-CMOS oscillator was monitored using an Agilent 53230A frequency counter. The measurement was performed in air.

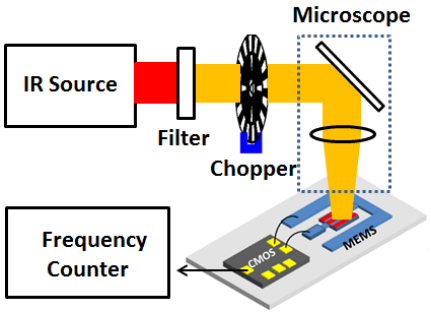

Figure 7: Schematic of the measurement set up used to characterize the response of the IR detector. Note that the measurement was performed without the use of a lock-in amplifier.

The measured output frequency response of the AlN piezoelectric MEMS-CMOS oscillator to near infrared (NIR)

radiation is shown in Figure 8. Despite the fact that no specific IR absorbing element was integrated with the AlN resonator, an absolute frequency shift of ~ *500 Hz* was recorded when the device was exposed to NIR radiation. Such IR radiation induced frequency shift translates into an absorbed NIR power of *~238 nW* (minimal IR absorption due to the intrinsic material loss), considering the device absolute responsivity of *2.1 Hz/nW*. A thermal time constant of *~20 ms* was also experimentally recorded.

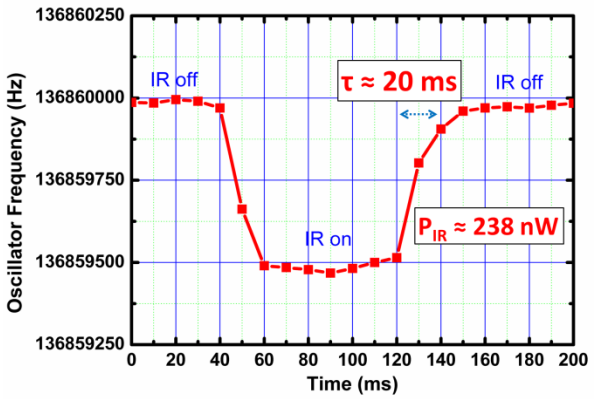

Figure 8: Measured frequency response of the IR detector to NIR radiation. Although no IR absorbing material was integrated on the resonator, an output frequency shift of 500 Hz was recorded; corresponding to an absorbed IR power of 238 nW (due to the intrinsic material losses). A thermal time constant of ~ 20 ms was also recorded.

CONCLUSION

This paper demonstrates a new device concept, based on the use of fully metallic nanoscale tethers to support the resonant body of a piezoelectric MEMS resonator, which enables the implementation of piezoelectric MEMS resonators with maximum thermal resistance and quality factor. Such innovative design, with minimum anchor cross section, enabled the implementation of an uncooled resonant thermal detector with unprecedented performance: (1) the thermal resistance of the device was maximized (R_{th} ~ *5.5* × 10^5 *K/W*, more than *10X* improvement compared to conventional piezoelectric resonators) resulting in a very high frequency sensitivity to absorbed power (*~2.1 Hz/nW*). (2) The acoustic energy was effectively confined in the freestanding resonant body of the device resulting in excellent electromechanical performance (mechanical quality factor Q_M ~ *3133* and electromechanical coupling coefficient k_t^2 ~ *1.86%*) and ultra-low frequency noise (*~0.78 Hz/Hz*$^{1/2}$). Thanks to such unique combination of high sensitivity and low noise performance, an ultra-low detection limit of *~371 pW/Hz*$^{1/2}$ was achieved (*2~4X* better than commercially available pyroelectric detectors). Furthermore, by taking advantage of the high resonator figure of merit ($FOM=k_t^2 \cdot Q \approx 58.3$) a low power (*~11 mW*) self-sustained CMOS oscillator was employed as direct frequency readout resulting in the first complete and compelling prototype of a high performance MEMS-CMOS resonant thermal detector with detection limit pushed in *~100s pW/Hz*$^{1/2}$ range.

ACKNOWLEDGEMENT

The authors wish to thank the staff of the George J. Kostas Nanotechnology and Manufacturing Facility, Northeastern University for their support in device fabrication. This project was supported by DARPA Young Faculty Award N66001-12-1-4221.

REFERENCES

[1] V. J. Gokhale, Y. Sui, and M. Rais-Zadeh, "Novel Uncooled Detector Based on Gallium Nitride Micromechanical Resonators", in proc. SPIE, vol. 8353, pp. 835319, 2012.

[2] M. B. Pisani, K. Ren, P. Kao, and S. Tadigadapa, "Application of Micromachined Y-Cut-Quartz Bulk Acoustic Wave Resonator for Infrared Sensing", Journal of Microelectromechanical Systems, vol. 20, pp. 288-296, 2011.

[3] Y. Hui, and M. Rinaldi, "Fast and High Resolution Thermal Detector based on an Aluminum Nitride Piezoelectric Microelectromechanical Resonator with an Integrated Suspended Heat Absorbing Element", Applied Physics Letters, vol. 102, pp. 093501, 2013.

[4] Y. Hui, and M. Rinaldi, "High Performance NEMS Resonant Infrared Detector Based on an Aluminum Nitride Nano Plate Resonator", in proc. 17th International Conference on Solid-State Sensors, Actuators and Microsystems (Transducers 2013), Barcelona, Spain, June 16-20, pp. 968-971, 2013.

[5] X. C. Zhang, E. B. Myers, J. E. Sader, and M. L. Roukes, "Nanomechanical Torsional Resonators for Frequency-Shift Infrared Thermal Sensing", Nano Letters, vol. 13, pp. 1528-1534, 2013.

[6] M. Rinaldi, and G. Piazza, "Effects of volume and frequency scaling in AlN contour mode NEMS resonators on oscillator phase noise", in proc. IEEE International Frequency Control Symposium, San Francisco, CA, pp. 1-5, 2011.

[7] J. Segovia, M. Cremonesi, C. Cassella, A. Frangi, and G. Piazza, "Experimental Study on the Impact of Anchors Losses on the Quality Factor of Contour Mode AlN Resonators", in proc. 17th International Conference on Solid-State Sensors, Actuators and Microsystems (Transducers 2013), Barcelona, Spain, June 16-20, pp. 2473-2476, 2013.

[8] Y. Hui, and M. Rinaldi, "Aluminum Nitride Nano-Plate Resonant Infrared Sensor with Self-Sustained CMOS Oscillator for Nano-Watts Range Power Detection", in proc. 2013 IEEE International Frequency Control Symposium (IFCS 2013), Prague, Czech Republic, July 21-25, pp. 62-65, 2013.

[9] M. Rinaldi, C. Zuo, J. Van der Spiegel, and G. Piazza, "Reconfigurable CMOS Oscillator based on Multi-Frequency AlN Contour-Mode MEMS Resonators", IEEE Transactions on Electron Devices, vol. 58, pp. 1281-1286, 2011.

[10] M. Rinaldi, C. Zuniga, B. Duick, and G. Piazza, "Use of a Single Multiplexed CMOS Oscillator As Direct Frequency Read-Out for an Array of Eight AlN Contour-Mode NEMS Resonant Sensors", in proc. IEEE Sensors Conference 2010, Waikoloa, Hawaii, November 1-4, pp. 2666-2670, 2010.

[11] M. Rinaldi, C. Zuniga, C. Zuo, and G. Piazza, "Super High Frequency Two-Port AlN Contour-Mode Resonators for RF Applications", IEEE Transactions on Ultrasonics, Ferroelectrics, and Frequency Control, vol. 57, pp. 38-45, 2010.

[12] M. Rinaldi, Y. Hui, C. Zuniga, A. Tazzoli, and G. Piazza, "High Frequency AlN MEMS Resonators with Integrated Nano Hot Plate for Temperature Controlled Operation", in proc. IEEE International Frequency Control Symposium (IFCS 2012), Baltimore, MD, May 21-24, pp. 1-5, 2012.

[13] D. W. Allan, "Statistics of atomic frequency standards", Proceedings of the IEEE, vol. 54, pp. 221-230, 1966.

[14] http://www.fuji-piezo.com/Pyro1.htm

CONTACT

*Y. Hui, tel: +1-617-758-9518; yhui@coe.neu.edu

SUB-DEGREE ANGLE DETECTION USING MICROMACHINED DOME-SHAPED-DIAPHRAGM RESONATOR WITH WINE-GLASS MODE VIBRATION

A. Vafanejad and E.S. Kim
Department of Electrical Engineering, University of Southern California
Los Angeles, CA 90089

ABSTRACT

A sensitive, high quality factor (Q), 3-D piezoelectric microelectromechanical systems (MEMS) gyroscope based on wine-glass mode vibration has been designed and fabricated. Experimental results show the functionality of the device as hemispherical rate integrating gyroscope (HRG). The gyroscope utilizes a 1.5-mm-diameter spherical shell made of a LPCVD silicon nitride diaphragm. When the spherical shell is piezoelectrically actuated to vibrate as a four-node wine-glass mode at 126 kHz through a set of four piezoelectric drive elements, an applied angular rotation causes a change of the mode shape, which is piezoelectrically sensed through a set of four piezoelectric sense elements located at 45° off from the drive elements. A sputter-deposited piezoelectric zinc oxide (ZnO) thin film on the diaphragm is used to actuate and sense vibration at the rim of the fabricated dome. The vibration mode is measured to have a Q of about 10 million, and decays at a time constant of 23 seconds when the piezoelectric actuation is halted. With it, the minimum detectable angle of rotation is measured to be about 0.15°.

INTRODUCTION

Most vibratory gyroscopes measure angular rate in °/sec, and the net angle measurement is obtained by time integration of the measured angular rate. Such rate gyroscopes that have extensive applications in automotive, aerospace and consumer electronics have several drawbacks. Noise and bias in the measured angular rate, when integrated, will cause a diverging error in the measured angle [1]. On the other hand, rate integrating gyroscopes measure the net angle of rotation directly. In this paper we describe a rate integrating gyroscope based on a hemispherical dome. Macroscale hemispherical resonator gyroscope (HRG) has already been used for space application [2], and one of the most successful vibratory gyroscopes is Northrop Grumman's HRG [3], which uses inertial precession of a standing wave in an axisymmetric and isotropic resonator shell. However, the manufacturing technology for macroscale HRG does not provide a path to device miniaturization. Consequently, the need for wafer-level manufacturing of microscale spherical shells (to exploit the advantages offered by a rate integrating gyroscope) motivates the device presented in this paper. One of the reasons why microscale HRG had not been actively pursued is the difficulty of fabricating the needed 3D structure. But recent innovations in microfabrication of dome structures [4, 5] have made microscale HRG become viable.

Our approach to form HRG is to use isotropic etching of silicon in HNA (HF:Nitric:Acetic) to form a spherical etch cavity in silicon for a molding structure, over which low stress silicon nitride film is deposited. When the silicon is etched from the other side of the wafer, the silicon nitride film forms a hemispherical dome or spherical cap with its boundary supported by the same thin silicon nitride. Unlike other approaches in literature, which use a stem to support the dome diaphragm [6], our approach is to support the dome diaphragm with a thin, flexible membrane that provides room for the circular edge of the dome to vibrate in the second circumferential mode without a need to an anchor or stem. The dome-shaped diaphragm is then piezoelectrically actuated to operate in a 4-node wine-glass mode.

FABRICATION AND ASSEMBLY PROCESS

Isotropic etching of silicon is done by a combination of 49% hydrofluoric acid, 70% nitric acid and 99.5% acetic acid (HNA) with a ratio of 20:35:55 at 50ºC [7]. This combination has given the best isotropicity, and we have been able to fabricate large dome diaphragms (up to 1.5 millimeter in diameter) with excellent isotropicity. Figure 1 shows the fabricated transducer. On top of the silicon-nitride dome diaphragm, four piezoelectric sensors and four piezoelectric actuators are formed by depositing ZnO film and electrode layers through shadow masks. The fabrication steps are briefly described in Fig. 2.

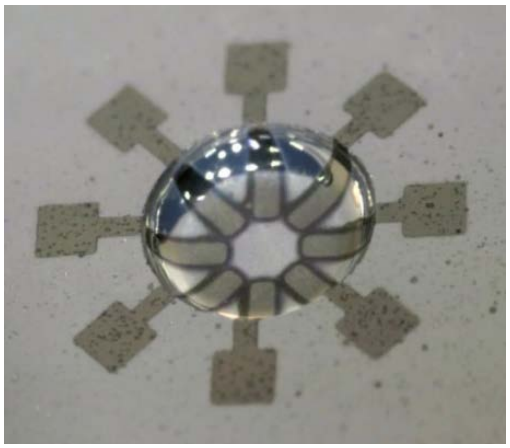

Figure 1: Top-view photo of the fabricated dome-shaped-diaphragm transducer.

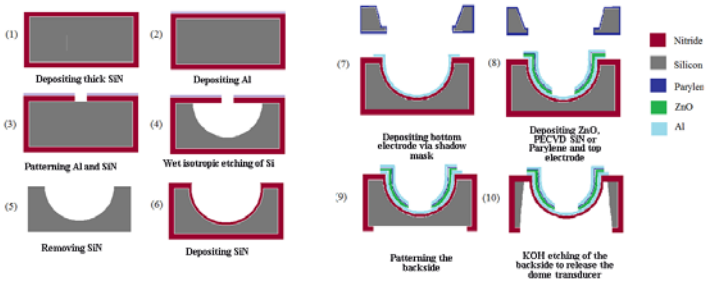

Figure 2: Brief fabrication steps of the dome-shaped-transducer.

SIMULATIONS

We have simulated the dome diaphragm's mode shapes and resonant frequencies with a finite element analysis, using COMSOL Multiphysics package. Finite element modeling (FEM) of the dome diaphragm resonator having 1.5-mm diameter and an average thickness of 4µm shows a 4-node wineglass mode at a frequency of around 126 kHz (Fig. 3) [4, 7].

9781940470016/HH2014/$25©2014TRF
DOI 10.31438/trf.hh2014.105

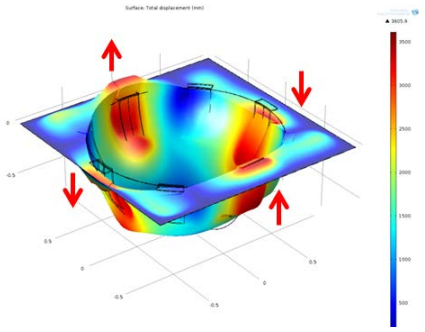

Figure 3: FEM simulation result of the dome-shaped-diaphragm that clearly shows a four-node wine-glass vibration mode.

MEASUREMENTS AND RESULTS

The fabricated dome-shaped-diaphragm piezoelectric resonator was characterized at a vacuum pressure of <50mTorr at room temperature. First, the resonator was mounted on a printed circuit board (PCB), as shown in Fig. 4a and b, which was then placed over a larger PCB that houses the electronic circuits for actuation and sensing.

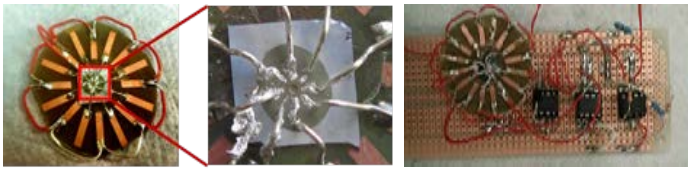

(a) (b) (c)

Figure 4: Photos of the dome diaphragm transducer on a printed circuit board with electrical wires connected to the bonding pads through epoxy: (a) the dome transducer and the whole PCB and (b) a close-up view. (c) Photo of the transducer and electronics for actuation and sensing.

A standing wave in a wine-glass mode is generated by energizing four piezoelectric actuators located on the anti-nodal lines of the wine-glass mode. Two of the four actuators (1 and 5 in Fig. 5) are energized with an identical signal, while the other two (3 and 7 in Fig. 5) are actuated by a signal with 180° phase lag.

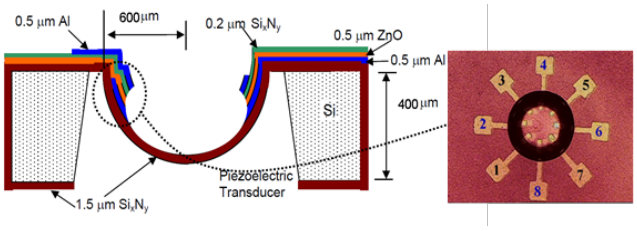

(a) (b)

Figure 5: (a) Cross-sectional diagram, (b) top view photo of the dome-shaped-transducer that is suspended by a thin flexible membrane and actuated by four piezoelectric transducers and sensed by four other ones, placed on the rim of the dome diaphragm.

The vibration of the dome diaphragm is measured by monitoring the electrical signal output of the piezoelectric sensors embedded on the dome diaphragm rim. A schematic of measurement setup is shown in Fig. 6.

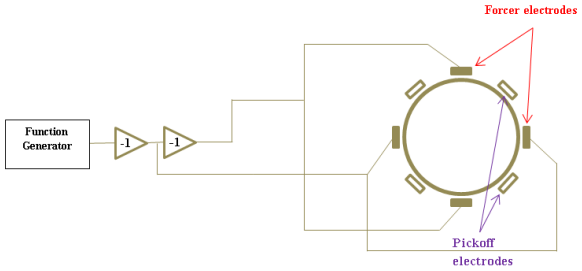

Figure 6: Schematic of the measurement setup.

To confirm the wine-glass mode vibration, we compared the phase difference between the sensor signals and the signals applied to the actuators 1 and 5 in Fig. 5b. Applying electrical signal to a pair of the actuators and picking up the signals from either the Sensor 3 or Sensor 7 (as illustrated in Fig. 8), we observe that the measured signal from the Sensor 3 has 180° phase difference from the signal applied to the Actuator 1, as can be seen in Fig. 7, as expected.

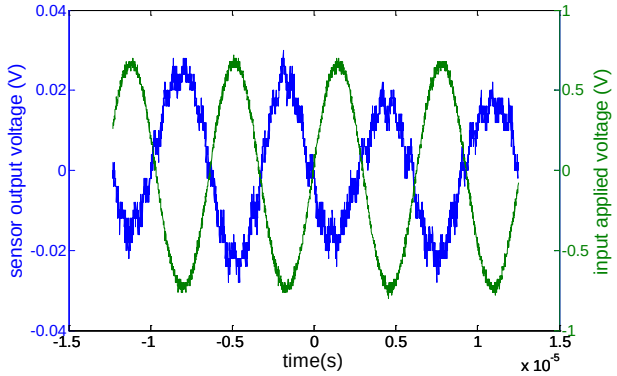

Figure 7: Oscilloscope traces of the applied signal at the Actuator 1 (green curve), measured signal at the Sensor 3 (blue curve). The 180° phase difference between the two curves shows that the vibration mode is indeed a four-node wine-glass mode.

DECAY TIME CONSTANT MEASUREMENTS

One important requirement for rate-integrating gyroscopes in aircraft's inertial navigation system is a large decay time constant through a high Q so that the actuating and sensing elements do not have to work simultaneously and also that the measurable range of the rotation angle may be large [2]. We measure the decay time constant of our fabricated dome-shaped-diaphragm resonators by actuating the resonators at their resonance frequencies, stopping the actuation, recording the decaying amplitudes, and fitting the recorded amplitudes with an exponential function, $A_o exp(-t/\tau)$. As can be seen in Fig. 9, it took 23 seconds for the amplitude of the sensed signal to drop by 63% after the signal to the actuators was turned off. Such a large decay time corresponds to a Q of 8.7×10^6.

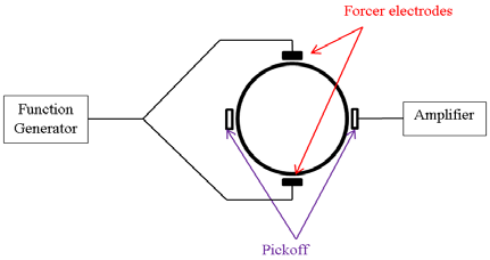

Figure 8: Schematic to illustrate the relative locations for actuation and sensing used to measure the decay time.

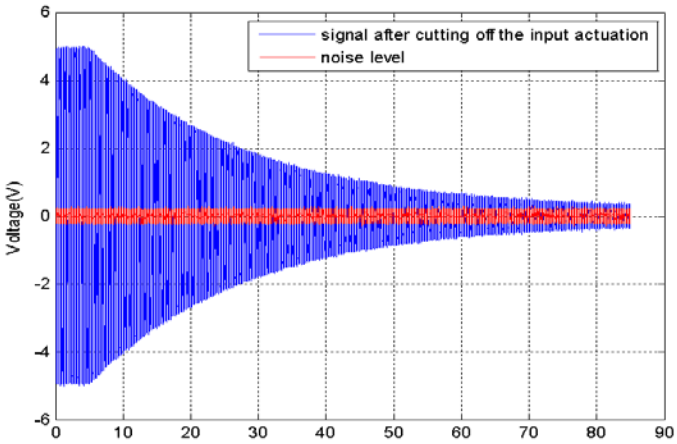

Figure 9: Ring down measurement of the device that shows a large decay time of 23 seconds.

ROTATION MEASUREMENTS

With our fabricated resonator in a vacuum chamber supported on a rotation table, we measured the resonator's response to rotation through monitoring the output signal at one of the nodal points. As the resonator was rotated at a rate of 1°/s, the piezoelectrically sensed signal was recorded in a computer after amplification. As can be seen in Fig. 10, the output voltage of nodal point linearly increases as the net angle of rotation is increased (with the angular rate kept constant at about 1°/s). This result shows the functionality of our resonator as a "rate integrating gyroscope".

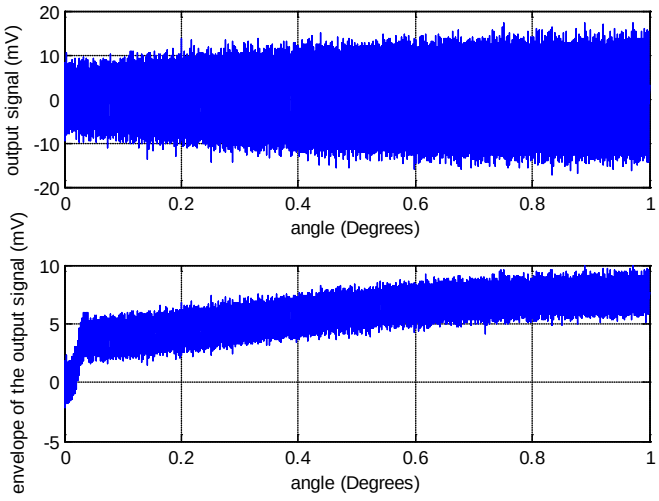

Figure 10: (Top) Measured output signal from a nodal point as a function of the total angle of rotation. (Bottom) Envelope of the measured signal as a function of the total angle of rotation. The large noise level at zero degree is mostly due to electromagnetic interference, and can be reduced substantially through a better packaging technique.

Close-up view on the measured data in Fig. 10 near zero net rotation angle is shown in Fig. 11, from which we see that the minimum detectable angle (or the point where the sensed signal surpasses the noise) is about 0.15°. The sub-degree detectability is highly encouraging for a microfabricated device.

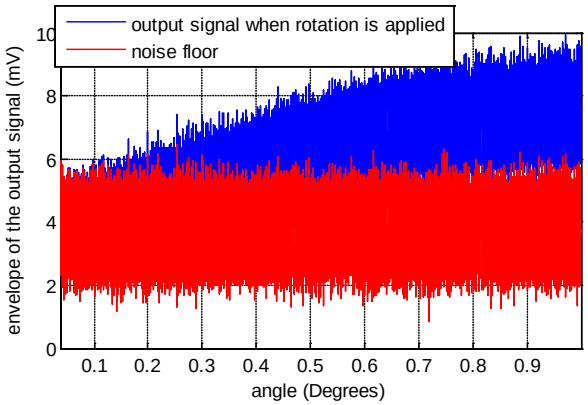

Figure 11: Measured output signal of the transducer when a rotation rate of 1°/s is applied. The noise floor limits the minimum detectable angle to be about 0.15°.

RESPONSE TO FORWARD/BACKWARD ROTATIONS

We have measured how our resonator responds, when we rotate the device in one direction for a time and then reverse the direction of rotation. As depicted in Fig. 12, when the device is rotated for 3 second in one direction and then the direction of rotation is reversed (with a faster rate of change), output voltage of nodal point is also decreasing as the rotation angle is reversed.

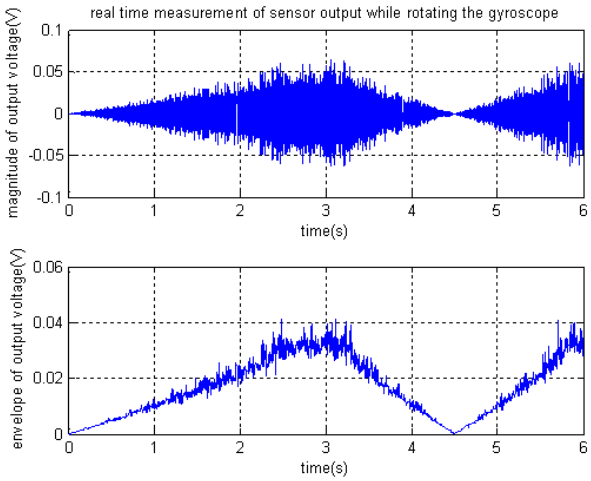

Figure 12: (Top) Measured signal from the sensor when we rotate the device in one direction for a time and then reverse the direction of rotation and (Bottom) the envelope of the measured signal.

By linear fitting of the envelope of the signal and comparing it with the angular rate and absolute angle, we find that the unamplified sensitivity is 4.84 mv/°/s. This sensitivity can be compared with those of published rate-integrating gyroscopes [9, 10]. However, comparison of sensitivities for piezoelectric and capacitive sensing is not straightforward, as the sensitivity of capacitive sensing depends on the polarization voltage (or how the capacitance change is detected), while with piezoelectric sensing unamplified sensitivity can easily be defined due to its capability of producing a voltage difference without any help from a polarization voltage or circuitry.

MINIMUM DETECTABLE RATE OF ROTATION

We also characterized our device to see what its minimum detectable angular rate in °/s is. As can be seen in Fig. 13, our device can detect down to 0.1°/s. At this point, the minimum detectable angular rate and minimum detectable angle are limited by the relatively large noise level that is mostly due to

electromagnetic interferences (EMI) that come from the fact that our device has not yet been packaged with an EMI shielding box. It will be relatively straightforward to reduce the EMI by an order of magnitude.

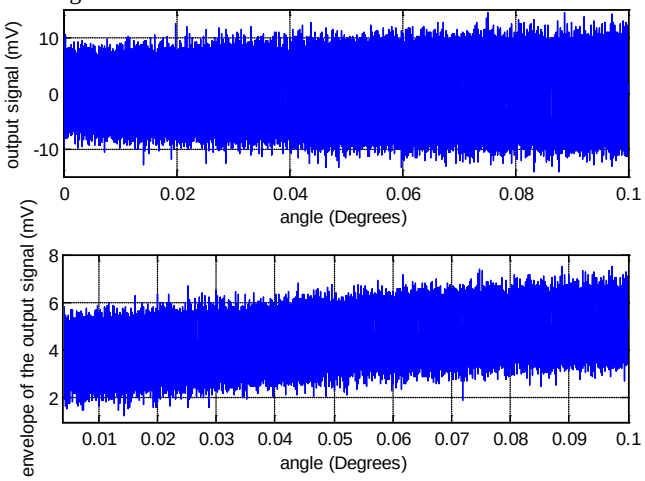

Figure 13: Measured signal (top) and its envelope (bottom), when the device is rotated at an angular rate of 0.1°/s. *At this low rotation rate, the device is capable of picking up signal proportional to the absolute angle of rotation.*

SUMMARY

A wafer-level microfabrication method for a symmetric dome-shaped resonator has been developed. The fabricated dome diaphragm is piezoelectrically actuated to vibrate in a four-node wine-glass mode, of which the shape change is sensed piezoelectrically. The micron-sized device shows a very large decay time constant (23 seconds) which is translated to a large Q factor (around 8.7 million), and compares very well with published results (Table 1). With the dome's soft boundary condition, the fabricated device has shown to be functional as a rate integrating gyroscope capable of detecting a sub-degree rotation as well as the direction of the rotation. It also works as an angular rate sensor with minimum detectable angular rate of around 0.1°/s. Currently, the minimum detectable angle and minimum detectable rate of rotation are limited by relatively high electromagnetic interference, which can be reduced substantially through a better packaging technique.

Table 1: Comparison of our device and some reported in literature.

		Dome size in diameter	Quality factor	Decay time constant	Sensitivity
Our device		1,500 µm	8.74×10^6	23 s	4.8385 mv/°/s
Reported results in literature	MEMS '12 [11]	5,000 µm	2.6×10^5	8 s	27.8 mv/°/s
	MEMS '12 [12]	1,200 µm	8,000	6 ms	Not reported
	JMEMS '12 [13]	1,000 µm	470	158 µs	2.1 mv/°/s

REFERENCES

[1] Gallacher, B.J., "Principles of a Micro-Rate Integrating Ring Gyroscope," Aerospace and Electronic Systems, IEEE Transactions on , vol.48, no.1, pp.658,672, Jan. 2012.

[2] Meyer, A. D.; Rozelle, D. M., "Milli-HRG inertial navigation system," Position Location and Navigation Symposium (PLANS), 2012 IEEE/ION , vol., no., pp.24,29, 23-26 April 2012.

[3] Dickinson, J.; Strandt, C.R., "HRG strapdown navigator," Position Location and Navigation Symposium, 1990. Record. The 1990's - A Decade of Excellence in the Navigation Sciences. IEEE PLANS '90., IEEE , vol., no., pp.110,117, 20-23 Mar 1990.

[4] C.H. Han and E.S. Kim, "Fabrication of dome-shaped diaphragm with circular clamped boundary on silicon substrate," *Micro Electro Mechanical Systems, 1999. MEMS '99. Twelfth IEEE International Conference on* , vol., no., pp.505-510, 17-21 Jan 1999.

[5] Prikhodko, I.P.; Zotov, S.A.; Trusov, A.A.; Shkel, A.M., "Microscale Glass-Blown Three-Dimensional Spherical Shell Resonators," *Microelectromechanical Systems, Journal of* , vol.20, no.3, pp.691,701, June 2011

[6] Cho, J.; Yan, J.; Gregory, J.A.; Eberhart, H.; Peterson, R.L.; Najafi, K., "High-Q fused silica birdbath and hemispherical 3-D resonators made by blow torch molding," Micro Electro Mechanical Systems (MEMS), 2013 IEEE 26th International Conference on , vol., no., pp.177,180, 20-24 Jan. 2013.

[7] H. Zhang; E.S. Kim, "Dome-shaped diaphragm microtransducers," Micro Electro Mechanical Systems, 1995, MEMS '95, Proceedings. IEEE , vol., no., pp.256, 29 Jan-2 Feb 1995.

[8] C.H. Han and E.S. Kim, "Simulation of Piezoelectric Dome-Shaped-Diaphragm Acoustic Transducers," Journal of Semiconductor Technology and Science, vol. 5, no. 1, pp. 17-23, 2005.

[9] Zotov, S.A.; Trusov, A.A.; Shkel, A.M., "High-Range Angular Rate Sensor Based on Mechanical Frequency Modulation," Microelectromechanical Systems, Journal of , vol.21, no.2, pp.398,405, April 2012.

[10] Gregory, J. A.; Cho, J.; Najafi, K., "Characterization and control of a high-Q MEMS inertial sensor using low-cost hardware," Position Location and Navigation Symposium (PLANS), 2012 IEEE/ION , vol., no., pp.239,247, 23-26 April 2012.

[11] Chan, M.L.; Fonda, P.; Reyes, C.; Xie, J.; Najar, H.; Lin, L.; Yamazaki, K.; Horsley, D.A., "Micromachining 3D hemispherical features in silicon via micro-EDM," Micro Electro Mechanical Systems (MEMS), 2012 IEEE 25th International Conference on , vol., no., pp.289,292, Jan. 29 2012-Feb. 2 2012.

[12] Sorenson, L.D.; Gao, X.; Ayazi, F., "3-D micromachined hemispherical shell resonators with integrated capacitive transducers," Micro Electro Mechanical Systems (MEMS), 2012 IEEE 25th International Conference on , vol., no., pp.168,171, Jan. 29 2012-Feb. 2 2012.

[13] Zotov, S.A.; Trusov, A.A.; Shkel, A.M., "Three-Dimensional Spherical Shell Resonator Gyroscope Fabricated Using Wafer-Scale Glassblowing," Microelectromechanical Systems, Journal of , vol.21, no.3, pp.509,510, June 2012.

CONTACT

*A. Vafanejad, tel: +1-818-515-2793; vafaneja@usc.edu

ULTRA-HIGH ASPECT-RATIO PDMS MICROPILLARS WITH SELF-ALIGNED MICROSPHERES FOR AIR-FLOW SENSING

Jungwook Paek and Jaeyoun Kim
Department of Electrical and Computer Engineering, Iowa State University, Ames, Iowa, USA

ABSTRACT

We developed a new technique that enables routine fabrications of high aspect-ratio PDMS micropillars. The key enabling factor is the adoption of the direct drawing technique incorporated with the *in situ* heating for simultaneous hardening and solidification of the PDMS micropillars. In addition, our technique allows self-aligned installation of highly reflective microspheres at the tips of the micropillars. Using the transparent PDMS micropillar as a flexible waveguide and the microsphere as a self-aligned reflector, we transformed the microsphere-tipped PDMS micropillars into all optically interrogated air-flow sensors and successfully demonstrated the air-flow sensing capability.

INTRODUCTION

Micropillars made of PDMS have seen rapid expansion in their application scope, from bio-mimetic dry adhesion [1] and surface wetting control [2] to cell mechanics studies [3]. The newest addition to their application list is mass flow transduction where PDMS micropillars with higher aspect ratios are preferred for their greater deformability, enabling highly sensitive transduction in a small form factor. Realizing high aspect ratio PDMS micropillars, however, is a difficult challenge, especially with the use of conventional, replica-molding-based fabrication techniques [4]. The main obstacle is the need to de-mold the PDMS micropillars after curing. Despite the efforts to improve the yield of the process [5], the failure rate increases inevitably with the aspect-ratio. Another source of difficulty is the inherently low Young's modulus, E_Y of PDMS (typically ~1 MPa) [6], which frequently leads to the collapse of the micropillar and then irreversible bonding to the substrate [7].

In this report, we present a new technique that enables routine fabrications of PDMS micropillars with aspect ratios higher than 40 [8]. The key enabling factor is the adoption of the direct drawing technique incorporated with the *in situ* thermal hardening for the realization of the high aspect-ratio PDMS micropillars, eliminating the de-molding process. To date, the direct drawing technique has been applied to polystyrene [9], PMMA [10], PTT [11], nylon [12], sucrose [13], polyurethane [14], SU-8 [15], and adhesives [16]. Its application to PDMS, however, has not been reported due mainly to the material's softness and slow solidification rate. We address the issues by incorporating *in situ* heating into the drawing process so that the micropillar gets simultaneously hardened and solidified during its formation. In addition, our technique allows self-aligned installation of highly reflective microspheres at the tips of the micropillars, leading to the realization of microsphere-tipped micropillars. Using the transparent PDMS micropillar as a flexible waveguide and the microsphere as a self-aligned reflector, we transformed the microsphere-tipped PDMS micropillars into all optically interrogated air-flow sensors and successfully demonstrated the air-flow sensing capability.

FABICATION OF PDMS MICROPILLARS

The PDMS MSMPs (microsphere-tipped micropillars) fabrication steps are depicted in Figure 1. We started out with the preparation of the drawing probe array. The microspheres were first assembled on a photo-lithographically patterned Su-8 grid and then transferred onto a piece of double-stick tape attached to a glass substrate shown in Figure 1a. We used two types of microspheres as the drawing probes: ~50 μm-diameter PMMA microspheres and ~58 μm-diameter Ag-coated hollow glass microspheres. The latter was more effective for increasing the levels of reflection and tip-visibility. We then flipped the microsphere array and attached it to a micro-manipulator. Also, a 25 μm PDMS layer was prepared and then pre-baked at 100°C on a hot plate. During the pre-bake, we lowered the microsphere array towards the PDMS thin film until they got separated by 50 μm. Upon completion of the pre-bake, we further lowered the microsphere array so that it can physically contact the PDMS thin film, as shown in Figure 1c. After 40 sec, we lifted the micro-manipulator, drawing PDMS micropillars as shown in Figure 1d. The temperature was maintained at 100°C throughout these steps for simultaneous solidification and hardening of the PDMS micropillars. Completed PDMS micropillars were then post-baked at 100°C for 2 hours and at room-temperature for 24 hours. After the post-bake, we further lifted the micro-manipulator so that the micropillars got elongated by 100%. The resulting tension induces gradual detachment of the microspheres from the double stick tape, leading to the realization of PDMS MSMPs as shown in Figure 1e.

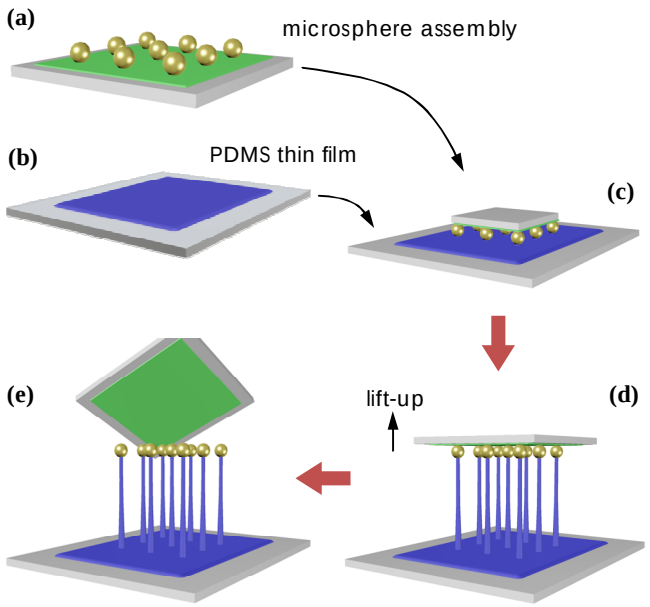

Figure 1. Fabrication flow (a) Microsphere assembly (b) PDMS thin film (c) After pre-baking of the PDMS thin film, the microsphere array physically contacted the PDMS thin film followed by an additional baking. (d) Directly drawing by lifting the microsphere array and the completed micropillars were then post-baked. (e) The double-stick tape was manually detached from the microspheres, completing the realization of the MSMPs

9781940470016/HH2014/$25©2014TRF
DOI 10.31438/trf.hh2014.106

At this step, the main cause of failure is insufficient curing of the PDMS micropillar which detaches the microsphere from the micropillar, rather than from the tape.

PHYSICAL CHARACTERISTICS OF PDMS MICROPILLARS

The direct drawing technique enabled routine fabrications of mm-scale PDMS micropillars with aspect-ratios > 40. Here, we defined the aspect-ratio as the ratio between h, the height and d_{ave}, the average of the top, middle and base diameters of the PDMS micropillar. The micropillar in Figure 2a was drawn with a 50 μm-diameter PMMA microsphere. With its h and d_{ave} at 1134 and 13.5 μm, respectively, the micropillar exhibits an aspect-ratio of 84. Such a high aspect-ratio was attainable for arrayed micropillars as well. The micropillars in the 4×4 array shown in Figure 2b were drawn with a matching array of 58 μm-diameter Ag-coated hollow glass microspheres. In average, they were 877.2 μm high and tapered with their diameter changing from 14.4 μm right underneath the microsphere to 29.8 μm at the base. With 20.8 μm in d_{ave}, their average aspect-ratio was 42. As pointed out above, capping the tip with a metallic microsphere greatly enhanced the micropillar's tip-visibility. Figure 2c shows the highest micropillar obtained so far. With its h and d_{ave} at 2400 and 21.3 μm, respectively, the aspect-ratio reached 112. To the best of our knowledge, this is the highest aspect-ratio reported for a vertical PDMS micropillar. Figure 2d shows the relation between h and d_{ave} of micropillars. Initially, the aspect-ratio increases with h. However, beyond h ~ 1.1mm, the increase in h induces a matching increase in the base diameter, saturating the aspect-ratio in the range of 70 ~ 110.

From the observations that the directly drawn PDMS micropillars can stand upright and support the weight of microspheres despite their thinness and high aspect-ratio, we conjectured that the *in situ* thermal hardening has indeed hardened PDMS. To quantify the impact of the *in situ* heating on PDMS hardening, we measured the PDMS micropillar's Young's modulus, E_Y based on the reference cantilever method [17] as shown in the inset of Figure 2e, in which a reference cantilever with known spring constant K_r is used to deflect the test cantilever and its spring constant K_t is estimated from the relation $K_t \cdot \delta_t = K_r \cdot \delta_r$, where δ_t and δ_r represent the deflection lengths of the test and reference cantilevers, respectively. For conically tapered beams, K and E_Y are related by $K = 3\pi \cdot E_Y \cdot d^4 \cdot T/(64 \cdot h^3)$ where T is the taper constant defined as d_{min}/d_{max} [18]. We chose a section of commercial PMMA fiber (E_Y ~ 3.0 GPa) as the reference cantilever and the two MSMPs in Table 1 were targeted for this characterization. From the results shown in Figure 2e, E_Y of MSMP-A and MSMP-B was calculated as 2.45 MPa and 2.31 MPa, respectively, which are higher than most E_Y values for bulk PDMS (~ 1 MPa). Therefore, we attribute the ~ 1 MPa increase in E_Y to the *in situ* thermal hardening incorporated into the direct drawing process so that the directly drawn microsphere-tipped PDMS micropillars can stand upright despite of their thinness and high aspect-ratio.

Table 1: Characteristics of the PDMS micropillars under test

	h [μm]	d_{ave} [μm]	Aspect Ratio
MSMP-A	800	19.8	40.4
MSMP-B	1600	22	72.7

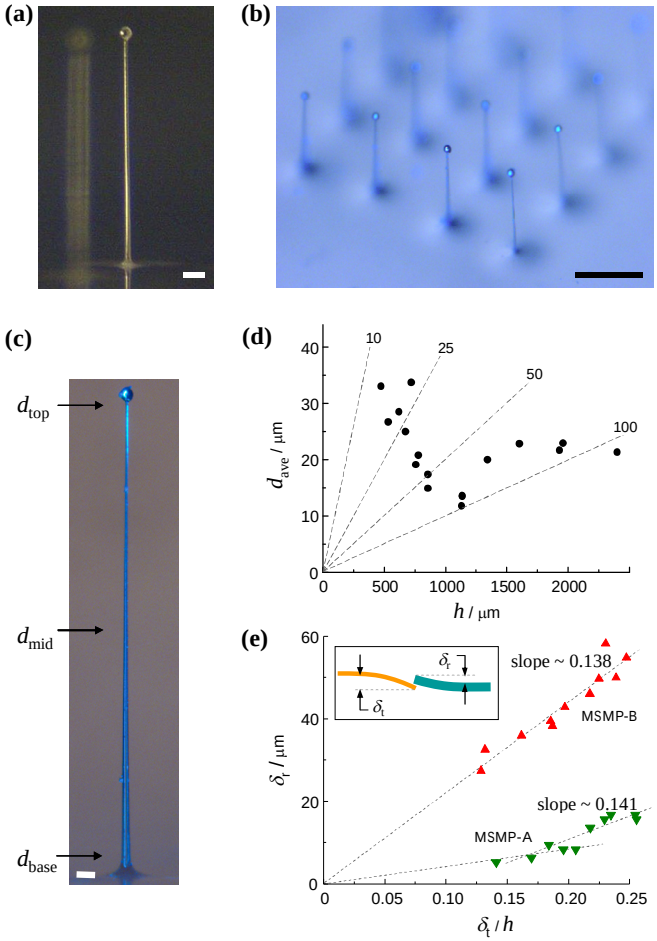

Figure 2. Optical micrographs of (a) a 1134 μm-high PDMS micropillar integrated with a 50 μm PMMA microsphere. Its aspect-ratio is 84. (Scale bar: 100 μm), (b) a 4×4 array comprising 877.2 μm-high micropillars integrated with 58 μm Ag-coated hollow glass microspheres. (Scale bar: 700 μm), and (c) the micropillar with the highest aspect-ratio of 112 (d_{top} = 9 μm, d_{mid} = 14 μm, d_{base} = 41 μm, and h = 2.4 mm, scale bar: 100 μm). (d) The average diameter d_{ave} of the micropillar plotted as a function of h. The dotted lines mark the aspect-ratios. (e) The results of the reference-cantilever method-based measurements. The inset outlines the setup. The dotted lines represent the results of linear fit with zero or non-zero x-intersection assumed.

BIO-INSPIRED ACOUSTIC SENSING

To demonstrate acoustic sensing capabilities of the PDMS MSMPs, we turned MSMP-A in Table 1 into an airflow sensor by adding the optical read-out setup as shown in Figure 3a. There, the PDMS micropillar functions as a flexible waveguide which deforms under airflows. The probe light enters the micropillar from the base and then gets reflected at the top facet back into the photodetector. The flow-induced bending of the micropillar reduces the reflection power through spoiled waveguiding and beam deflection. Critical to the success of the scheme is guaranteeing high-level reflection at the micropillar's top facet. We accomplish it by capping the micropillar with a Ag-coated microsphere and used its surface as the reflector. Figure 3b, c shows the MSMP-A's deformation in the absence and

presence of airflow, respectively. In the absence of an air-flow, the MSMP stays straight, producing maximal reflection. Upon contact with a constant airflow, it bends due to the fluidic drag force, which decreases the reflection.

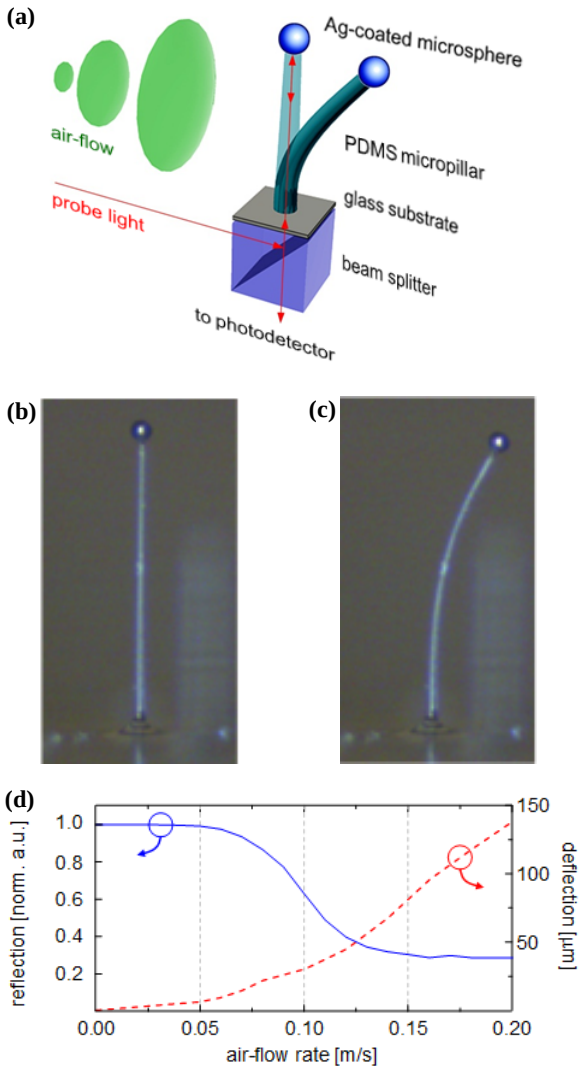

Figure 3. (a) A schematic diagram of an air-flow transducer configuration based on the MSMP (b) and (c) MSMP-A's deformation in response to the absence and presence of an air-flow, respectively. (d) The change in the reflectance as functions of the flow-rate. The deflection length was also plotted for convenience.

The change in the reflection levels is plotted in Figure 3d for MSMP-A as a function of the airflow rate. It exhibits a quasi-linear regime sandwiched between two slowly varying curved regimes. The onset of the first curved regime can be defined as the threshold velocity of the MSMP-based air-flow sensors. Figure 3d indicates that it was 0.07 m/sec for MSMP A. The curve also indicates that the decrease in the reflection saturates beyond a certain velocity, forming a flat pedestal at 29 % level. It is due mainly to the residual reflection at the air-glass interface, which is not affected by the airflow, and can be reduced with anti-reflection coating. In the quasi-linear regime, the optically retrieved reflection level can function as a good measure of the air-flow velocity. The data represent 10-measurement averages.

CONCLUSION

In conclusion, we demonstrated an optically interrogated air-flow sensor based on the PDMS micropillars with high aspect ratios ranging from 40 and 112. Due to the high aspect-ratio and the excellent flexibility of PDMS, the PDMS micropillars deform substantially under airflows, bringing in high sensitivity to small form-factors. The high aspect-ratio PDMS micropillars were fabricated by a new soft-lithography technique based on the combined utility of the *in situ* thermal hardening and the direct-drawing technique. Our scheme also allows self-aligned capping of the micropillar with microspheres. For this work, we exploited the feature as a way to realize highly reflecting top facets, so that we can interrogate the micropillars' deformation all-optically.

REFERENCES

[1] Sameoto, D. and Menon, C. "A low-cost, high-yield fabrication method for producing optimized biomimetic dry adhesives", *J. Micromech. Microeng.* **19,** 115002 (2009).

[2] Courbin, L., Denieul, E., Dressaire, E., Roper, M., Ajdari, A., and Stone, H. A. "Imbibition by polygonal spreading on microdecorated surfaces", *Nature Materials* **6,** 661-664 (2007).

[3] Tan, J. L., Tien, J., Pirone, D. M., Gray, D. S., Bhadriraju, K., and Chen, C. S. "Cells lying on a bed of microneedles: An approach to isolate mechanical force", *Proc. Natl. Acad. Sci. USA* **100,** 1484-1489 (2003).

[4] Große, S., Schröder, W., and Brücker, C. "Nano-newton drag sensor based on flexible micro-pillars", *Meas. Sci. Technol.* **17,** 2689-2697 (2006).

[5] Taylor, R. E., Kim, K., Sun, N., Park, S. J., Sim, J. Y., Fajardo, G., Bernstein, D., Wu, J. C., and Pruitt, B. L. "Sacrificial layer technique for axial force post assay of immature cardiomyocytes", *Biomed Microdevices* **15,** 171-181 (2013).

[6] Cheng, Q., Sun, Z., Meininger, G. A., and Almasri, "M. Note: Mechanical study of micromachined polydimethylsiloxane elastic microposts", *Rev. Sci. Instrum.* **81,** 106104 (2010).

[7] Roca-Cusachs, P., Rico, F., Martínez, E., Toset, J., Farré, R., and Navajas, D. "Stability of Microfabricated High Aspect Ratio Structures in Poly(dimethylsiloxane)", *Langmuir* **21,** 5542-5548 (2005).

[8] Paek, J. and Kim, J., "Microsphere-assisted fabrication of high aspect-ratio elastomeric micropillars and waveguides", *Nature Communications*, 5, 3324 (2014).

[9] Nain, A. S., Wong, J. C., Amon, C., and Sitti, M. "Drawing suspended polymer micro-nanofibers using glass micropipettes", *Appl. Phys. Lett.* **89,** 183105 (2006).

[10] Harfenist, S. A., Cambron, S. D., Nelson, E. W., Berry, S. M., Isham, A. W., Crain, M. M., Walsh, K. M., Keynton, R. S., and Cohn, R. W. "Direct Drawing of Suspended Filamentary Micro- and Nanostructures from Liquid Polymers", *Nano Lett.* **4,** 1931-1937 (2004).

[11] Xing, X., Wang, Y., and Li, B. "Nanofibers drawing and nanodevices assembly in poly(trimethylene terephthalate)", *Opt. Express* **16,** 10815-10822 (2008).

[12] Spina, G. L., Stefanini, C., Menciassi, A., and Dario, P. "A novel technological process for fabricating micro-tips for biomimetic adhesion", *J. Micromech. Microeng.* **15,** 1576-1587 (2005).

[13] Lee, J., Paek, J., and Kim, J. “Sucrose-based fabrication of 3D-networked, cylindrical microfluidic channels for rapid prototyping of lab-on-a-chip and vaso-mimetic devices”, *Lab Chip* **12,** 2638-2642 (2012).
[14] Lebel, L. L., Aissa, B., Khakani, M. A. E., and Therriault, D. “Ultraviolet-Assisted Direct-Write Fabrication of Carbon Nanotube/Polymer Nanocomposite Microcoils”, *Adv. Mater.* **22,** 592-596 (2010).
[15] Lee, K., Lee, H. C., Lee, D.-S., and Jung, H. “Drawing Lithography: Three-Dimensional Fabrication of an Ultrahigh-Aspect-Ratio Microneedle”, *Adv. Mater.* **22,** 483-486 (2010).
[16] Prakash, M. and Bush, J. W. M. “Interfacial propulsion by directional adhesion”, *Int. J. Non-Linear Mech.* **46,** 607-615 (2011).
[17] Gates, R. S. and Pratt, J. R. “Accurate and precise calibration of AFM cantilever spring constants using laser Doppler vibrometry”, *Nanotechnology* **23**, 375702 (2012).
[18] Sasoglu, F. M., Bohl, A. J., and Layton, B. E. “Design and microfabrication of a high-aspect-ratio PDMS microbeam array for parallel nanonewton force measurement and protein printing”, *J. Micromech. Microeng.* **17,** 623-632 (2007).

OMNI-DIRECTIONAL, SPECTRALLY SELECTIVE, WAFER-SCALE FABRICATED METALLIC-DIELECTRIC 2-D PHOTONIC CRYSTALS FOR HIGH TEMPERATURE ENERGY CONVERSION

J.B.Chou[1], A. Lenert[1], K. Smyth[1], E.N. Wang[1], and S.-G. Kim[1]*
[1]Massachusetts Institute of Technology, Cambridge, Massachusetts, USA

ABSTRACT

Two-dimensional metallic-dielectric photonic crystals (MDPhCs) as spectrally selective absorbers and emitters are a promising technology for efficient heat-to-electricity energy conversion in solar thermophotovoltaic (STPV) systems [1]–[4]. Previously demonstrated metallic air photonic crystals (MAPhCs) are only able to absorb incident light at ±30° to normal, and had non-CMOS/MEMS compatible fabrication [5]. Here, we present a wafer-scale fabricated selective absorber and emitter which are stable at high temperatures (1,000°C), possess omni-directional absorption measured up to 70°, contain tunable spectral control of absorption, and are polarization insensitive.

INTRODUCTION

One of the critical problems of traditional photovoltaic systems is their inability to efficiently store converted solar energy at low costs. The intermittent nature of solar energy renders photovoltaics incompatible with large scale grid level energy storage. However, STPV systems convert solar energy into thermal energy by means of a selective absorber where it can potentially be stored both efficiently and at low costs [6], [7]. When the energy is needed, the STPV system can then convert the thermal energy into electricity by means of a selective emitter and a photovoltaic device.

At the center of an STPV system lays the need for an efficient and robust selective absorber and emitter. Temperatures of STPV systems can reach as high as 1,000°C under concentrated solar energy. Previously demonstrated MAPhCs can serve as both selective absorbers and emitters and are able to survive high temperatures [2], [5], [8]. However, their limited angular absorption and non MEMS compatible fabrication techniques limit their performance and scalability. Plasmonic and metamaterial absorbers have yet to demonstrate high temperature stability and wafer-scale fabrication [9]–[12]. Thus, the MDPhC was originally developed to increase the high temperature stability of metallic nanostructures [13]. Here, we present a wafer-scale fabricated MDPhC by utilizing the sidewall lithography technique as shown in Fig. 1 [14]. The design, analysis, and fabrication of the MDPhC is presented. Measured Fourier transform infrared (FTIR) reflection spectrums demonstrate the wide-angle absorption. Scanning electron microscope (SEM) images demonstrate the robustness of the MDPhC after a high temperature exposure at 1,000°C for 24 hours.

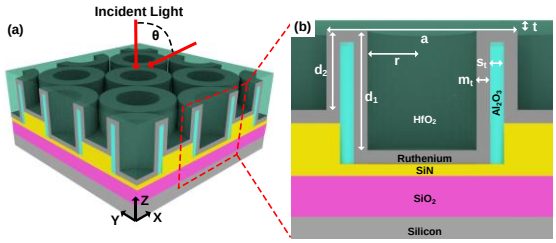

Figure 1: (a) Schematic of the MDPhC. (b) Cross-sectional schematic with period a, radius r, depths d_1, d_2, metal thickness m_t, Al_2O_3 thickness s_t, and top dielectric thickness t.

DESIGN

The MDPhC utilizes cylindrical cavity modes to define the absorption spectrum and cutoff wavelength λ_c [1], [15]. For incident light with wavelength < λ_c, light is coupled to the cavity modes where the increased lifetime allows for the light to be absorbed by the metal. For light with wavelength > λ_c, light is not allowed to couple into the cavity modes and is reflected away. According to Kirchoff's law, under thermal equilibrium the absorption spectrum is equivalent to the emission spectrum, and thus the MDPhC is capable of tuning both absorption and emission. By tuning the radius r and depths d_1 and d_2, the cutoff wavelength λ_c can be spectrally tuned. Optimal absorption of the cavity modes can be determined via Q-matching [16].

The spectral tuning of the cut-off wavelength λ_c is important for an efficient STPV system. A selective absorber optimally converts solar energy into heat by minimizing thermal radiative losses at wavelengths above the cutoff wavelength λ_c. A selective emitter optimally radiates towards a photovoltaic with a bandgap wavelength of λ_g. By tuning the cutoff wavelength to be equal to the bandgap, $\lambda_c = \lambda_g$, radiation above the bandgap wavelength, which cannot be converted into electron-hole pairs, is suppressed.

The omni-directional absorption is achieved with the dielectric filling inside the cavities which eliminates diffraction losses at oblique angles. The cavity modes can be tuned by the index n of the dielectric inside the cavity, wherein the cutoff wavelength scales with n. By shifting the cutoff wavelength beyond the period of the structure, diffraction grating losses no longer apply which allows for wide angle absorption [1].

FABRICATION

In our wafer-scale fabrication process shown in Figure 2, a 6" silicon wafer is first deposited with a 250 nm thick diffusion barrier composed of SiN and thermal SiO_2 to prevent the metal from diffusing into the silicon substrate at high temperatures. A 500 nm thick layer of sacrificial polysilicon layer is deposited via low-pressure chemical vapor deposition (LPCVD). A photolithographic stepper patterns resist on the polysilicon layer with an optimized checkerboard mask pattern to generate subwavelength gaps between the circular patterns, which is critical for optimal absorption in the MDPhCs. A sidewall lithography technique is used to define free-standing Al_2O_3 cylinders with a thickness of 40 nm [14], [17]–[19]. Ruthenium is then coated over the free-standing cylinders with conformal atomic layer deposition (ALD) with a thickness of 80 nm. We have also experimentally verified that sputtered W had the same conformal deposition as ALD, thus allowing for a wider variety of metals that can be successfully deposited at lower cost. A thick layer of HfO_2 is deposited via ALD followed by a chemical mechanical polishing (CMP) step to remove the excess HfO_2 and leave the exposed metallic-dielectric interface. SEM images of the final fabricated device as well as FIB created cross-section are shown in Figure 3. Due to slight variations across the large scale fabrication, the actual dimensions of the MDPhC unit cell can vary, thus the slight differences between images in Figure 3(a) and (b).

9781940470016/HH2014/$25©2014TRF
DOI 10.31438/trf.hh2014.107

Solid-State Sensors, Actuators and Microsystems Workshop
Hilton Head Island, South Carolina, June 8-12, 2014

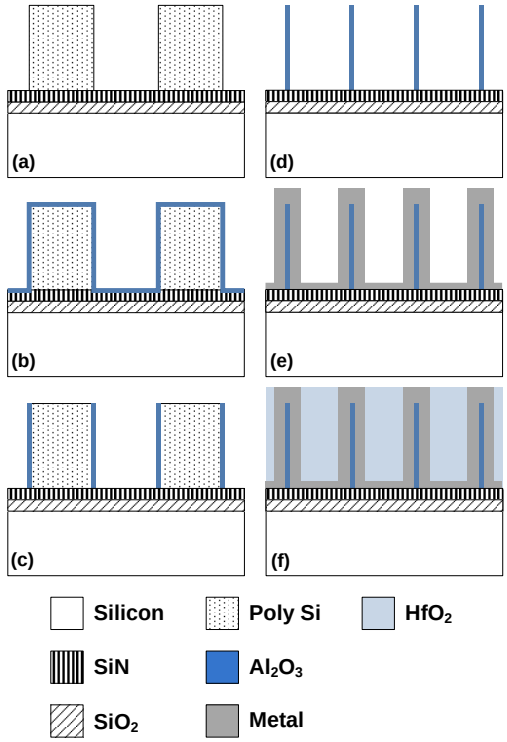

Figure 2: Schematic of the fabrication process. (a) Polysilicon layer is deposited and patterned on SiN and SiO_2. (b) ALD of Al_2O_3. (c) Anisotropic Cl_2 RIE. (d) Removal of polysilicon with XeF_2. (e) ALD of ruthenium. (f) ALD of HfO_2 followed by CMP to expose metal dielectric interface.

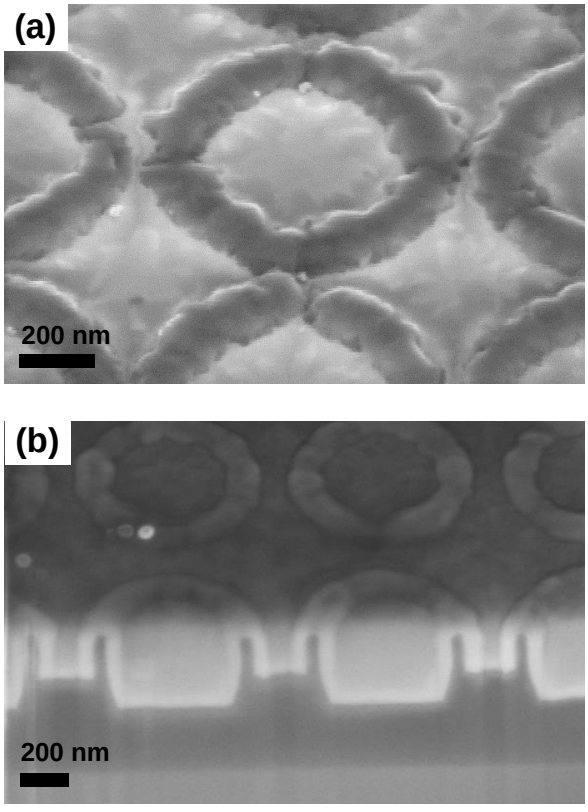

Figure 3: SEM images of the fully fabricated metallic dielectric photonic crystal: (a) top view and (b) angled cross-section view via FIB. The scale bars are 200 nm. The measured values are a=780 nm, r=600 nm, d_1=380 nm, d_2=200 nm, m_t=80 nm, s_t=40 nm, and t is estimated to be t=25 nm.

RESULTS

Reflection measurements, *R*, of the MDPhCs were performed in a Fourier transform infrared (FTIR) spectrometer. Subsequently, absorption is calculated as $\alpha_s = 1 - R - T$, where the transmission, *T*, is $T = 0$ due to the thickness of the metal layer. Since we are measuring the reflection at wavelengths greater than the period, diffractive reflections are nonexistent [1]. The absolute absorption is measured in reference to a commercial aluminum reference mirror with known reflection spectrums at 30°, 45°, 50°, 60°, and 70°.

The measured absorption spectrum of the MDPhC is shown in Figure 4(a) at angles up to 70°. Clearly the wavelength of the cut-off mode at 1.73 μm does not change with incident angle, indicative of a flat dispersion curve of a cavity mode. The amplitude of the cut-off mode does decrease slightly with incident angle and is consistent with simulations [1]. Previously published work reported significant absorption decline for incident angles greater than 30° due to diffraction losses [5]. Thus the improved angular performance of the MDPhC is experimentally confirmed. The distortions in the absorption spectra at approximately λ=2.7 μm and λ=4.25 μm are due to atmospheric absorptions. A slight absorption peak is observed at approximately 2.5 μm and is due to the gap mode created between the metallic cylinders. Not all devices had the gap mode as fabrication variation caused only some devices to have an observable gap mode.

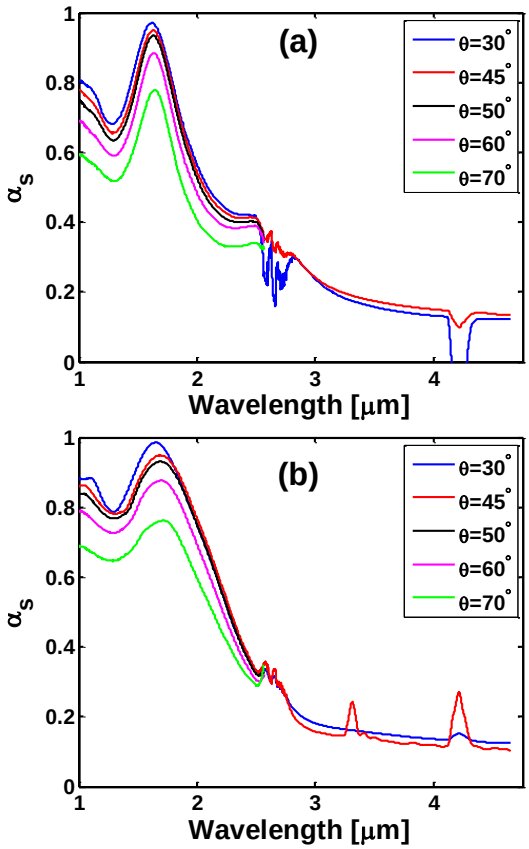

Figure 4: (a) Measured absorption spectrum of the MDPhC at various angles before the high temperature test. (b) Measured

absorption spectrum after the high temperature test at 1,000°C for 24 hrs in a 95% Ar and 5%H_2 environment.

To verify the high temperature stability of the MDPhC structures, the samples were placed in a furnace at 1,000°C for 24 hours in a 95% Ar and 5% H_2 environment to prevent oxidation. The measured absorption spectra of the same device shown in Figure 4(a) after the furnace test are shown in Figure 4(b). The linewidths of the cut-off mode have increased for the post-furnace samples, indicating to a lower Q mode. This may be attributed to annealing effects of the metal and dielectric or diffusion of the materials into each other. However, a larger Q smoothens out the absorption spectrum causing a more uniform absorption profile, although at the expense of a less steep cut-off. The wavelength of the cut-off mode remains relatively unchanged after the high temperature test which implies the structural integrity of the MDPhC is able to withstand the high temperature environment. The high temperature robustness is due to the HfO_2 filling which minimizes surface diffusion [13].

SEM Images of various MDPhC samples after the high temperature tests are shown in Figure 5. The MDPhC sample measured in Figure 4 is shown in Figure 5(a), where the metal surface appears to have a layer of dielectric coating the surface, indicated by the lack of contrast between the rings and the dielectric area. In comparison to Figure 3(a), the metal and dielectric show a strong contrast due to the conductive nature of the metal. The coating may be due to oxidation of the metal or a reflow of the HfO_2 over the metal surfaces. No physical damage to the MDPhC was observed for fully fabricated devices, which is significant due to the many different materials each with their own coefficients of thermal expansion.

Although no damage was observed within the MDPhC, outside of the MDPhC area crack and peeling effects were observed between the HfO_2 layer and the substrate, as shown in Figure 5(b). The crack propagation outside of the MDPhC area never permeated the actual lattice and can be seen bending at a 90° turn along the edge of the MDPhC. This shows the mechanical robustness of the MDPhC structure to high temperatures which is due to the high density of the periodic structure and the change of thickness in the MDPhC area.

For MDPhC structures with incomplete HfO_2 filling, cracks within the MDPhC were observed to occur along the lattice of the filling holes, as shown in Figure 5(c). Whether the cracks only exist on the HfO_2 layer or permeate further into the structure will require further investigation. Please note that due to the non-uniformity of the CMP process across a single wafer, a gradient of HfO_2 thicknesses remains on the top surface of a portion of the fabricated chipset. The device shown in Figure 5(c) is a chip with a relatively thick layer of HfO_2 remaining. Cracks were only observed in devices with thick HfO_2 layers, indicating the importance of removing the top dielectric layer for high temperature stability.

To test the structural durability of the MDPhC's for high frequency temperature fluctuations, the MDPhC samples were placed in a solar concentrator system with on/off pulses of length 1 minute each for up to 10 iterations. The maximum temperature reached during the "on" pulse was 900°C measured with a bonded thermocouple. No damage was observed for any of the samples measured. Thus only the long 24 hour high temperature tests were observed to cause change in the MDPhC samples.

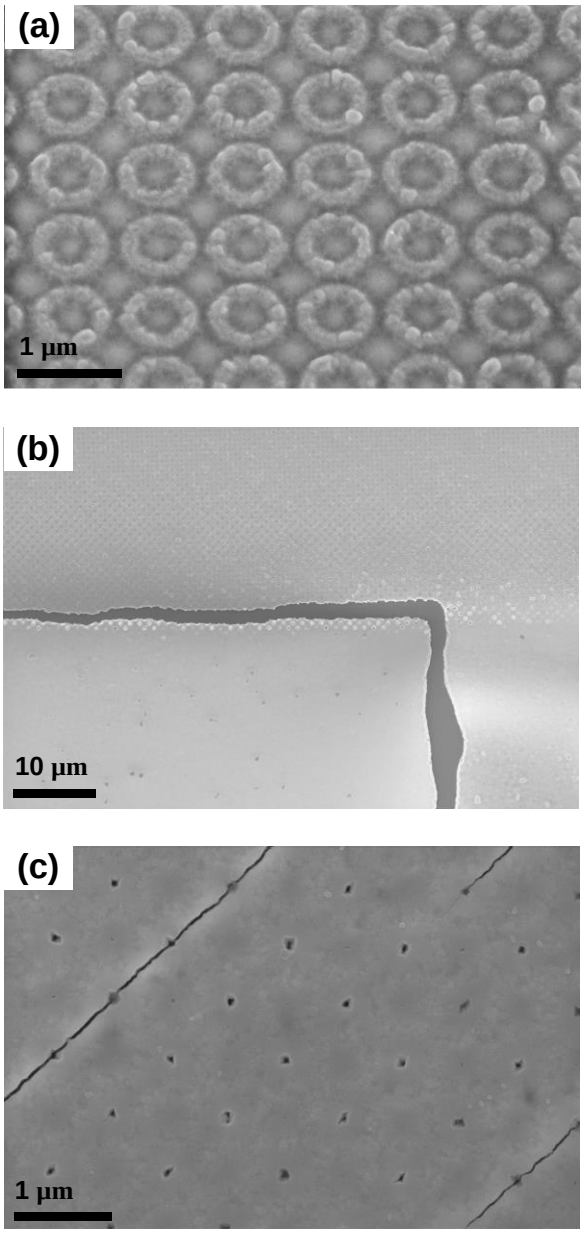

Figure 5: SEM images of the MDPhC after the high temperature tests. (a) Shows the sample measured in Figure 4 after the high temperature test. (b) The edge of the MDPhC is shown to be robust to crack propagation. (c) Inside the MDPhC lattice, cracks were only observed with samples with incomplete HfO_2 filling. For devices with complete filling, no cracks were observed.

CONCLUSION

We demonstrate a high temperature stable wide-angle absorber utilizing dielectric filled cavity modes. A multi-layer wafer-scale fabrication process has been demonstrated which can lead to low-cost and massively scalable STPV systems. The fabrication process may also be extended into a double sided absorber/emitter chip for a compact and thermally efficient solar energy conversion system. Future work is still needed in regards to optical simulations, visible light absorption, and high temperature emittance measurements. We hope that the wafer-scale fabricated MDPhC will make large strides in the solar and thermal energy conversion space.

This paper is based on the work supported as part of the Solid State Solar-Thermal Energy Conversion Center (S3TEC), an Energy Frontier Research Center funded by the U.S. Department of Energy, Office of Science, Office of Basic Energy Sciences under award DE-SC0001299/DE-FG02-09ER46577.

REFERENCES

[1] J. B. Chou, Y. X. Yeng, A. Lenert, V. Rinnerbauer, I. Celanovic, M. Soljačić, E. N. Wang, and S.-G. Kim, "Design of wide-angle selective absorbers/emitters with dielectric filled metallic photonic crystals for energy applications," *Opt. Express*, vol. 22, no. S1, pp. A144–A154, Jan. 2014.

[2] V. Rinnerbauer, S. Ndao, Y. Xiang Yeng, J. J. Senkevich, K. F. Jensen, J. D. Joannopoulos, M. Soljačić, I. Celanovic, and R. D. Geil, "Large-area fabrication of high aspect ratio tantalum photonic crystals for high-temperature selective emitters," *J. Vac. Sci. Technol. B Microelectron. Nanometer Struct.*, vol. 31, no. 1, pp. 011802 –011802–7, Jan. 2013.

[3] A. Lenert, D. M. Bierman, Y. Nam, W. R. Chan, I. Celanović, M. Soljačić, and E. N. Wang, "A nanophotonic solar thermophotovoltaic device," *Nat. Nanotechnol.*, vol. 9, no. 2, pp. 126–130, Feb. 2014.

[4] J. B. Chou, K. Smyth, and S.-G. Kim, "Low aspect ratio nanophotonic filled cavities with Q-matching for scalable thermophotovoltaic power conversion," in *2013 IEEE Photonics Conference (IPC)*, 2013, pp. 576–577.

[5] Y. X. Yeng, M. Ghebrebrhan, P. Bermel, W. R. Chan, J. D. Joannopoulos, M. Soljačić, and I. Celanovic, "Enabling high-temperature nanophotonics for energy applications," *Proc. Natl. Acad. Sci.*, vol. 109, no. 7, pp. 2280–2285, Feb. 2012.

[6] W. R. Chan, P. Bermel, R. C. N. Pilawa-Podgurski, C. H. Marton, K. F. Jensen, J. J. Senkevich, J. D. Joannopoulos, M. Soljačić, and I. Celanovic, "Toward high-energy-density, high-efficiency, and moderate-temperature chip-scale thermophotovoltaics," *Proc. Natl. Acad. Sci.*, vol. 110, no. 14, pp. 5309–5314, Apr. 2013.

[7] A. Datas, D. L. Chubb, and A. Veeraragavan, "Steady state analysis of a storage integrated solar thermophotovoltaic (SISTPV) system," *Sol. Energy*, vol. 96, pp. 33–45, Oct. 2013.

[8] H. Sai, H. Yugami, Y. Kanamori, and K. Hane, "Solar selective absorbers based on two-dimensional W surface gratings with submicron periods for high-temperature photothermal conversion," *Sol. Energy Mater. Sol. Cells*, vol. 79, no. 1, pp. 35–49, Aug. 2003.

[9] Y. Cui, K. H. Fung, J. Xu, H. Ma, Y. Jin, S. He, and N. X. Fang, "Ultrabroadband Light Absorption by a Sawtooth Anisotropic Metamaterial Slab," *Nano Lett.*, vol. 12, no. 3, pp. 1443–1447, Mar. 2012.

[10] C. Wu, B. Neuner, G. Shvets, J. John, A. Milder, B. Zollars, and S. Savoy, "Large-area wide-angle spectrally selective plasmonic absorber," *Phys. Rev. B*, vol. 84, no. 7, Aug. 2011.

[11] T. V. Teperik, F. J. García de Abajo, A. G. Borisov, M. Abdelsalam, P. N. Bartlett, Y. Sugawara, and J. J. Baumberg, "Omnidirectional absorption in nanostructured metal surfaces," *Nat. Photonics*, vol. 2, no. 5, pp. 299–301, May 2008.

[12] N. P. Sergeant, O. Pincon, M. Agrawal, and P. Peumans, "Design of wide-angle solar-selective absorbers using aperiodic metal-dielectric stacks," *Opt. Express*, vol. 17, no. 25, p. 22800, Nov. 2009.

[13] H.-J. Lee, K. Smyth, S. Bathurst, J. Chou, M. Ghebrebrhan, J. Joannopoulos, N. Saka, and S.-G. Kim, "Hafnia-plugged microcavities for thermal stability of selective emitters," *Appl. Phys. Lett.*, vol. 102, no. 24, pp. 241904–241904–5, Jun. 2013.

[14] T. J. Seok, A. Jamshidi, M. Eggleston, and M. C. Wu, "Mass-producible and efficient optical antennas with CMOS-fabricated nanometer-scale gap," *Opt. Express*, vol. 21, no. 14, pp. 16561–16569, Jul. 2013.

[15] J. D. Jackson, *Classical Electrodynamics Third Edition*, 3rd ed. Wiley, 1998.

[16] M. Ghebrebrhan, P. Bermel, Y. X. Yeng, I. Celanovic, M. Soljačić, and J. D. Joannopoulos, "Tailoring thermal emission via Q matching of photonic crystal resonances," *Phys. Rev. A*, vol. 83, no. 3, p. 033810, Mar. 2011.

[17] Y.-K. Choi, J. S. Lee, J. Zhu, G. A. Somorjai, L. P. Lee, and J. Bokor, "Sublithographic nanofabrication technology for nanocatalysts and DNA chips," *J. Vac. Sci. Technol. B Microelectron. Nanometer Struct.*, vol. 21, no. 6, pp. 2951–2955, 2003.

[18] D. C. Flanders and N. N. Efremow, "Generation of [less-than] 50 nm period gratings using edge defined techniques," *J. Vac. Sci. Technol. B Microelectron. Nanometer Struct.*, vol. 1, no. 4, pp. 1105–1108, 1983.

[19] X. Liu, X. Deng, P. Sciortino, M. Buonanno, F. Walters, R. Varghese, J. Bacon, L. Chen, N. O'Brie, and J. J. Wang, "Large Area, 38 nm Half-Pitch Grating Fabrication by Using Atomic Spacer Lithography from Aluminum Wire Grids," *Nano Lett.*, vol. 6, no. 12, pp. 2723–2727, Dec. 2006.

CONTACT

*J.B. Chou, jeffchou@mit.edu

POWERING BODY AREA NETWORKS USING THE BODY AS A TRANSMISSION MEDIUM

P. Wang[1], S. X. Li[1], C. A. Zorman[1], P. X.-L. Feng[1], and W. H. Ko[1]*
[1]Department of Electrical Engineering & Computer Science, Case School of Engineering,
Case Western Reserve University, Cleveland, OH 44106, USA

ABSTRACT

Body area networks (BAN) are an enabling technology for individually monitoring health or delivering care in a real-time, effective, and minimally obtrusive way. An ideal BAN requires both a high efficiency signal and power bus. Recent research shows promising signal transmission efficiency using the body as a transmission medium. However, these BAN systems require the sensor nodes to carry on-board power or use through-air transmitted power, whose utility is limited by the power transmission efficiency and/or distance. This paper reports an initial study to investigate, design and evaluate a through-body power transmission system that can distribute power to sensor nodes in the network. Our preliminary results show that it is feasible to distribute 0.5–1.0mW, at 50MHz, to sensor nodes over a distance of 40cm with ~18dB loss, which is ~10–100 times more efficient than through-air transmission. This result is instrumental for realizing a through-body signal and power bus for next generation BAN.

INTRODUCTION

The successful integration of MEMS with low power integrated circuits and wireless communication technologies has enabled rapid development of body area networks (BAN) for human health applications using the body as a transmission medium for signal bus [1]. As shown in Fig. 1, the ideal BAN needs an efficient power bus and signal bus for a central master station to interact with an array of sensor nodes wirelessly. However, these current systems require the sensors to carry on-board power or use through-air transmitted power [2]. On-board power has a lifetime limit while through-air transmitted power is limited by the transmission efficiency and the need for a nearby transmission station.

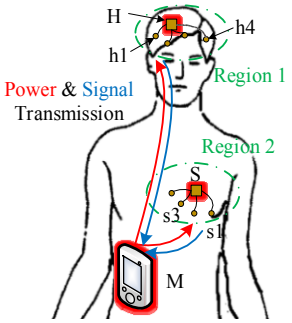

Figure 1: A body area sensor and power network.

It was predicted in 1997 [3] that a power and signal bus might be realized in a through-body medium. Recent reports [4] using computer simulation show the feasibility of powering the sensors wirelessly using the body as a transmission medium. However, these simulations have not been realized experimentally due to several challenges, such as electrode design, power transmission router selection, impedance matching, and low power sensor node electronics design.

This paper reports an initial study to investigate, design and evaluate a power transmission system for clinical applications that can distribute power to operate all sensor nodes in the network. First, we characterized and selected multiple potential routes for BAN signal and power transmission, such as from foot to head, abdomen to chest/head, wrist to chest/upper-arm etc. Second, we improved the design of a BAN electrode widely used for BAN communication [5], and characterized the impedance of this electrode. Third, we designed an impedance matching system based on the electrode properties. Finally, we demonstrated the feasibility of distributing 0.5–1.0mW, at 50MHz, to sensor nodes over a distance of 40cm with 18–23dB loss on the human body surface, which is ~10–100 times more efficient than through-air transmission. In addition, we also report our early stage implant-to-implant power transmission characterization in a vivo animal experiment, which is, to the best of our knowledge, the first published experimental data of in vivo implant power transmission that compares galvanic, capacitive, and coil coupling methods.

POWER DELIVERY PATH CHARACTERIZATION

Multiple potential routes were characterized for human and animal BAN signal and power transmission. These routes are needed for clinical and medical research purposes.

Measurement Setup

Transmission loss in a body area sensor network was studied using the configurations shown in Fig. 2. A network analyzer (4395A Agilent Inc.) was used for transmission loss measurements and balun (FTB-1-1 A15+, Mini-Circuits Inc.) was used for isolation. Both galvanic and capacitive coupling methods were evaluated. The transmitter (TX) and receiver (RX) terminals consisted of two electrodes (signal and ground). For galvanic coupling, the two electrodes were attached directly to the skin surface. For capacitive coupling, all signal electrodes were connected to skin and all ground electrodes were floating in air. The transmission routes and directions are shown in Fig. 2-c. The TX and RX electrodes were connected to the network analyzer. During this stage, we adapted the network analyzer to compensate for the mismatch between the electrode and body tissue, due to the

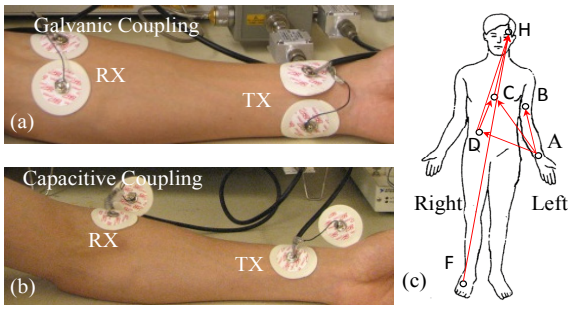

Figure 2: Photos of (a) galvanic and (b) capacitive coupling setups. (c) Transmission directions for S_{21} measurements are marked FH, DH, CH, AD, AC, and AB.

9781940470016/HH2014/$25©2014TRF
DOI 10.31438/trf.hh2014.108

Solid-State Sensors, Actuators and Microsystems Workshop
Hilton Head Island, South Carolina, June 8-12, 2014

difficulty of matching impedance over a wide frequency range.

On-Body Power Transmission Loss

With the test method shown in Fig. 2, we measured the human body area S_{21} versus frequency (10Hz–500MHz). The S_{21} characteristics are shown in Fig. 3-a, b and corresponding to the routing shown in Fig 2-c. The line marked "air" is the reference S_{21} with all electrodes in air at a distance of 15cm. For both galvanic and capacitive coupling, the S_{21} is insensitive to distance for frequencies between 40 and 60MHz. The lowest S_{21} values are -6dB (~380MHz) and -11dB for galvanic and capacitive coupling, respectively. Galvanic coupling at ~380MHz has a -6dB loss but varies more with distance. For capacitive coupling, the S_{21} has a peak at ~50MHz of ~-11dB, and differs from through-air transmission by as much as 70dB. Moreover, the S_{21} has a low sensitivity to a change in TX and RX distance from 15cm to 140cm, suggesting that capacitive coupling might be a feasible means of power distribution for a whole body BAN.

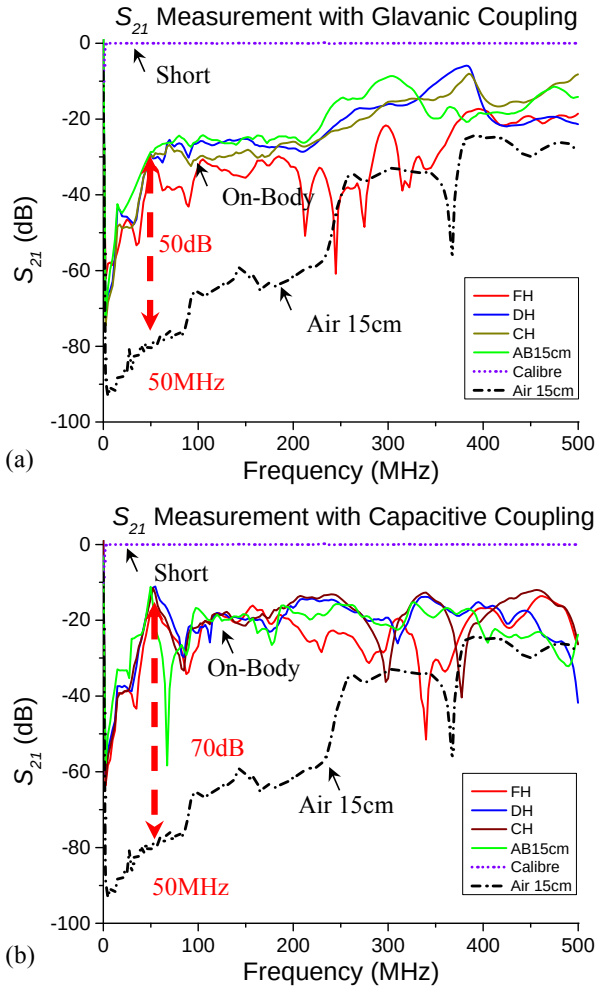

Figure 3: On-body S_{21} measurements for (a) galvanic and (b) capacitive coupling. The positions measured are shown in Fig. 2 (c). "Short" is a baseline with TX/RX shorted.

Implant Power Transmission Loss

In 2006, we demonstrated the feasibility of through-body signal and power transmission between implanted components in rabbit experiments [6]. In this study, a 5 month-old 8 lb rabbit was used for the experiment. The measurement was conducted with a function generator and oscilloscope. The selected routes are shown in Fig. 4-AB, CD, using a distance of 15 cm.

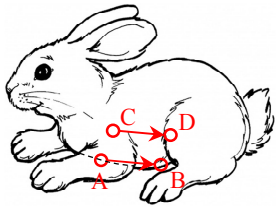

Figure 4: Route of rabbit experiment. AB: on surface skin from near Heart to stomach, and CD: implanted from near Heart to near stomach. Both AB and CD have a 15 cm distance.

The electrodes used are described in Table 1. Two types of electrodes were used including a 6 turn, a 0.9 cm^2 planar coil and an Ag/AgCl plate. For the Ag/AgCl electrode, 0.6 cm^2 and 0.9 cm^2 plates were used.

Table 1: Summary of electrodes used in the implant power transmission experiment.

Electrode	Type	Dimension
L2	Planar coil	6 turns, 0.9 cm^2
C1	Planar Ag/AgCl plate	0.9 cm^2
C2	Planar Ag/AgCl plate	0.6 cm^2

The measured S_{21} parameter is shown in Fig. 5. As before, we focus the analysis on the higher frequency range of the data set. The S_{21} at frequencies higher than 50Mhz might show a similar result when using balun for isolation, which is at a frequency range of 50–100MHz in this case. Within this frequency range, Fig. 5shows that all S_{21} curves have a peak near 86MHz. The C1 Ag/AgCl electrode has losses of 23dB and 31dB for on-skin and implant respectively. The larger Ag/AgCl (C1 than C2) electrode shows a 7 and 11dB less loss for on-body and implant respectively. The Ag/AgCl electrode (C1 implant) shows a 16dB less loss than the planar coil (L2 implant) with the same area at 86MHz.Although the grounding, impedance matching and isolation issues were not addressed due to the limited instrumental resources at that time, the reported S_{21} data still offer worthwhile information. For the balun isolation affect for frequencies below 50MHz according to Xu's experiment [7], and the transmission

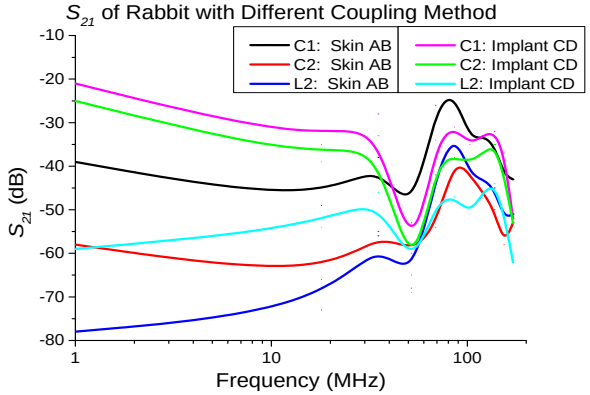

Figure 5: Comparison of measured S_{21} versus frequency for implanted and surface mounted electrodes in a rabbit model spaced 15 cm apart from heart to stomach. C1 is a 0.9 cm^2 electrode; C2 is a 0.6 cm^2 electrode; L1 is a 0.5 cm^2, 4 turn coupling coil; L2 is a 0.9 cm^2, 6 turn coupling coil.

loss at higher frequencies will be less if impedance was matched.

ON-BODY POWER TRANSMISSION

Electrode Types

Fig. 6 shows the diagram and dimension of the electrode designed for on-body power transmission. The design described in Ref.5 was adapted and improved by adding a matching network between the electrode and feed line and using a wide copper ribbon for connection. The matching network reduced the reflection coefficient Γ, and the wide ribbon reduced the high frequency impedance which is beneficial for power transmission.

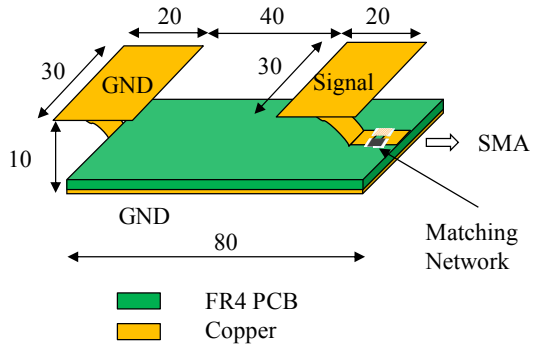

Figure 6: Diagram of the electrode for on body power transmission experiment. Fixed LC matching network was applied near the feed line connection. All dimensions are in mm.

Impedance Matching

In order to realize good impedance matching, we modified the electrode design of [5], by adding a matching network between the electrode and feed line and replacing the pillar with a wide ribbon copper (Fig. 6). Impedance matching is needed: i) to reduce the reflection between body tissue and wearable electronics; ii) to convert the received weak AC energy into a feasible DC supply.

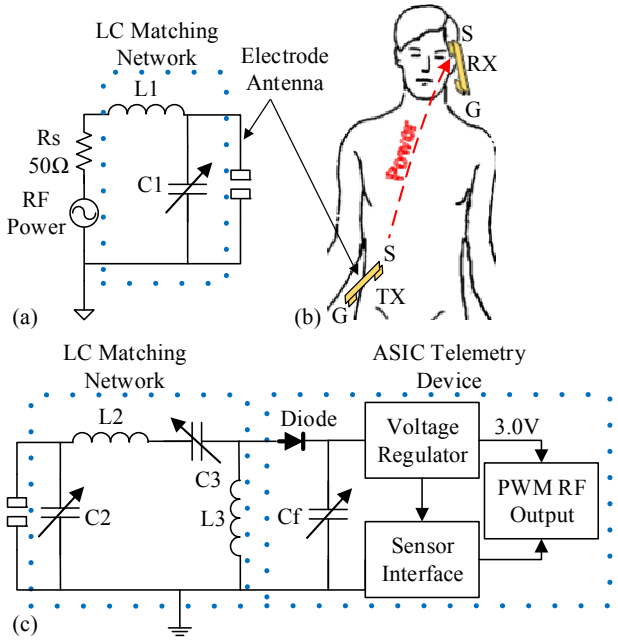

Figure 8: Circuit diagram of preliminary power distribution experiment; (a) TX; (b) Experiment setup for (a) and (c). TX and RX electrode pairs are configured to the abdomen and head by capacitive coupling; (c) Sensor node device.

We implemented the matching network in three steps: 1) matching the master station (chest) electrode to the 50Ω output RF function generator (AFG3252, Tektronix Inc.); 2) matching the receiver (i.e., head) electrode to a 50Ω transmission line; 3) matching the 50Ω transmission line to the low dropout rectifier with the load cascaded. Steps 2 and 3 can be merged to one step to reduce the mismatch due to the calculation error and stray electrical parameter. We separate step 2 and 3 for convenient RF measurement. The matching network in Fig. 8 was realized by the fixed passive LC component. The LC-type matching network was chosen for its relatively low Q, which is robust for two reasons: i) the proposed powering system adopts a narrow band frequency at 50MHz; ii) the human body impedance varies significantly, which increases the reflected power. The component values for matching a fixed AC load and DC load after the rectifier was calculated according to conjugate-image impedance theory [8] and the equivalent rectifier model [9, 10] respectively. The estimated reflected power is less than 1%, according to <0.1 reflection coefficients Γ (Fig. 9).

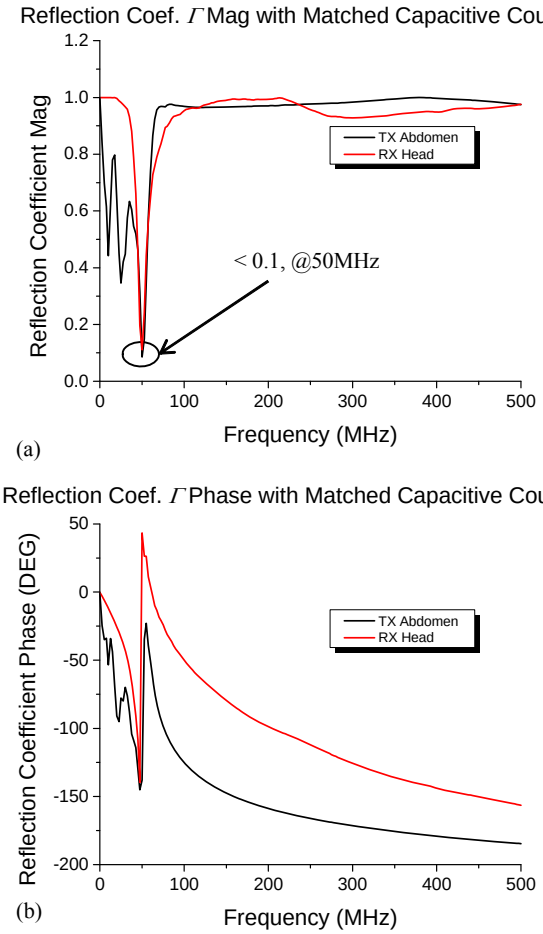

Figure 9: Impedance matching result, measured on the SMA feed point (Fig. 6) when electrode was coupled to human body capacitive. (a) and (b) are magnitude and phase of the reflection coefficient for TX/RX electrode placed on abdomen and head. All data comes from measurement after impedance matching.

Powering Actual Sensor Node Device

Using the configuration in Fig. 8, we investigated the possibility of a capacitive coupling-based distribution network to supply operating power from a master station to sensor nodes.

Measurements were made both with a fixed 10kΩ resistor load and an implantable blood pressure telemetry ASIC device (Fig. 8-c). The 10kΩ is an equivalent load to the ASIC device previously developed by our group that uses 200μA to charge a thin film battery [11]. The 50MHz, 50Ω output RF power source was at 18-23dBm. The coupling electrode is shown in Fig. 6. The distance from TX to RX electrodes was ~40cm. Balun was used to isolate the body from the instrument. LC networks were used for matching the 50Ω RF source, the body impedances (~100-i113Ω), the 10kΩ load and ASIC device rectifier input. The received voltage at 10kΩ load and output of ASIC device regulator can reach 3V, and the received power was ~0dBm (1mW), which is capable of charging a 50μAh lithium battery with 100μA current or to simultaneously power tens of 3μW pressure telemetry units. The estimated total transmission loss was ~18-23dB for the 10kΩ load and ASIC device respectively. The greater loss of the ASIC device as compared with the 10kΩ resistance load might be due to the loss on the diode stage, which can be improved by adding a voltage multiplier stage before the rectifier.

CONCLUSION

This paper reports an initial study to investigate, design and evaluate a power transmission system that can distribute power to operate all sensor nodes in the network. Several challenges are addressed for realizing power transmission using the body as a medium, such as electrode design, power transmission route selection, impedance matching, and low power sensor node electronics design. An example design was introduced to address these challenges. The preliminary result shows that it is feasible to distribute 0.5−1.0mW to sensor nodes over a distance of 40cm with an 18−23dB loss, which is ~10−100 times more efficient than through-air transmission. The preliminary implant experiment result also shows feasible power transmission with a loss of ~23dB. These results are helpful for realizing both a though-body medium signal and power bus for next generation BAN.

In the future, the utility and safety of the proposed powering system require the following key advancements. i) The system must be miniaturized for minimally intrusive health monitoring, with a tradeoff between maintaining high transmission efficiency and reducing the coupling ground area. ii) Ultra-low power sensor node devices are required reduce the power budget at power source within safety standards. For example, an 80μW sensor node requires only -20dBm power at the master station with a typical 20dB path loss; iii) Noise related issues, such as signal/noise ratio (SNR) and interference between powering path and signal transmission path must be addressed . Although not detailed here, we found the RF signal for the proposed powering system is pure in the frequency domain.

We are applying the proposed on-body power transmission method to power a 3−80μW ASIC RF transmitter (Fig. 8-c) that is integrated with a blood/ECG sensor using the through-body medium. The output pulse width modulation (PWM) carrier frequency will be tuned to 380MHz, which is the optimum frequency according to our power delivery path characterization. The signal transmission though-body medium is ongoing. The miniaturization of electrode and adaptive impedance matching will also be addressed in a future study. These works will be reported in future publication.

ACKNOWLEDGEMENTS

The authors would like to thank S.J.A. Majerus, Z.H. Wang for instrument support and discussing. Thank H.X. Zhang, Y.N. Cheng for animal experiment.

The financial and instrumental support of the study comes from NIH R-21-EB014442 and Louis Strokes Cleveland Medical Center of the Department of Veterans Affairs, the Advanced Platform Technology (APT) Center, and Case School of Engineering.

REFERENCES

[1] M. Seyedi, B. Kibret, D. T. H. Lai, and M. Faulkner, "A Survey on Intrabody Communications for Body Area Network Applications", *IEEE Transactions on Biomedical Engineering* **60**, 2067-2079 (2013).

[2] J. S. Besnoff, T. Deyle, R. R. Harrison, and M. S. Reynolds, "Battery-Free Multichannel Digital ECG Biotelemetry Using UHF RFID Techniques", *IEEE International Conference on RFID*, 4/30-5/2/13, Orlando, FL (2013), pp. 16-22.

[3] E. R. Post, M. Reynolds, M. Gray, J. Paradiso, and N. Gershenfeld, "Intrabody Buses for Data and Power", *The International Symposium on Wearable Computers*, 10/13-14/97, Cambridge, MA (1997), pp. 52-55.

[4] K. Ito, N. Haga, M. Takahashi, and K. Saito, "Evaluations of Body-Centric Wireless Communication Channels in a Range from 3 MHz to 3 GHz", *Proceedings of the IEEE* **100**, 2356-2363, (2012).

[5] F. Koshiji, K. Sasaki, D. Muramatsu, and K. Koshiji, "Input Impedance Characteristics of Wearable Transmitter Electrodes for Intra-Body Communication", *The 1st Global Conf. on Consumer Electronics*, 10/2-5/12, Makuhari Messe, Tokyo, Japan (2012), pp. 362-363.

[6] C. A. Zorman, D. J. Young, P. X.-L. Feng, and W. H. Ko, *Interal Technical Report* (included in NIH R21 proposal), Case Western Reserve University (2011).

[7] R. Y. Xu, H. J. Zhu, and J. Yuan, "Characterization and Analysis of Intra-Body Communication Channel", *Antennas and Propagation Society International Symposium*, 06/1-5/09, Charleston, SC (2009), pp. 1-4.

[8] S. Roberts, "Conjugate-Image Impedances", *Proceedings of the IRE* **34**, 198-204 (1946).

[9] J. P. Curty, N. Joehl, C. Dehollaini, and M. J. Declercq, "Remotely Powered Addressable UHF RFID Integrated System", *IEEE Journal of Solid-State Circuits* **40**, 2193-2202 (2005).

[10] J. P. Curty, N. Joehl, F. Krummenacher, C. Dehollaini, and M. J. Declercq, "A Model for μ-Power Rectifier Analysis and Design", *IEEE Transactions on Circuits and Systems I: Regular Papers* **52**, 2771-2779 (2005).

[11] P. Wang, D. Sun, S. J. A. Majerus, S. B. Lachhman, S. X. Li, M. S. Damaser, C. A. Zorman, P. X.-L. Feng, W. H. Ko, "Implantable Pressure Telemetry Device With Thin Film Micropackage", *Biomedical Engineering Society Annual Meeting*, 09/25-28/13, Seattle, WA (2013).

CONTACT

*W.H. Ko, Tel: +1-216-368-4081; Email: whk@case.edu

WAFER-LEVEL FABRICATION OF POWER INDUCTORS IN SILICON FOR COMPACT DC-DC CONVERTERS

Jiping Li[1], Victor Farm-Guoo Tseng[1], Zhiming Xiao[2], and Huikai Xie[1]*
[1]Department of Electrical and Computer Engineering, University of Florida, Gainesville, FL, USA
[2]Linear Technology Corporation, Milpitas, CA, USA

ABSTRACT

This paper reports the design, fabrication and characterization of a novel power inductor embedded inside a silicon substrate and fabricated at wafer level. Such power inductors in silicon (PIiS) fully explore the capability of forming high-aspect-ratio silicon molds by DRIE for large-cross-section copper winding plating (as thick as the silicon wafers) while also utilizing high-resistivity magnetic composites. By completely using electroplating processes to form the copper coils and vias, the contact resistance between conductive layers can be minimized, and the quality factor can be improved significantly. This process also provides surface mounting pads for a compact converter assembly. Square shaped spiral inductors ($3\times3\times0.83mm^3$) were successfully fabricated, achieving a large inductance (430 nH), low DC resistance (84 mΩ), and high quality factor (21) at 6 MHz. The fabricated inductors were also assembled with a TI TPS62621 buck converter IC, and an efficiency of 83% was achieved.

INTRODUCTION

DC-DC converters are voltage regulators widely used in portable electronics and office facilities, where bulky magnetic components or inductors are usually the largest single volume contributor. Using higher operation frequency is one approach to minimize the size of power converter modules with low power storage and inductance requirements, but at the price of more integration challenges such as substrate parasitics, coupling noise, and increased losses, which further prompt the compact integration of all components into a single package.

Power System in Packaging (PSiP) and Power System on Chip (PSoC) are two major approaches for passives integration in modern power systems operated at high frequency range (3-20 MHz). For PSiP, power inductors and other passive components are integrated off chip inside a package. Technologies such as co-packaged inductors, inductors on PCB, LTCC or magnetic substrates, and inductors by wire bonding are all PSiP examples [1-4]. They generally have larger dimensions compared to on-chip solutions. On the other hand, PSoC is a monolithic integration approach, mostly using MEMS technologies to form power inductors directly on chip. Researchers have reported on-chip inductors employing air cores, sputtered or electroplated magnetic cores, laminated magnetic cores, or composite cores [5-9]. PSoC approaches emphasize on wafer-level batch integration of power inductors, providing minimum sizes and compact interconnections. However, the integration of passives on power IC chips complicates the fabrication process and suffers from several technical challenges, for example, the difficulty of fabricating thick windings (>100μm) and thick magnetic cores, or incorporating high-resistivity low-hysteresis-loss core materials with sufficient permeability at high frequencies.

In PSoC approaches, in-silicon techniques have been well explored by using the bulk silicon substrate to improve the inductor performance, either for large cross section conductors or for large volume magnetic cores [9, 10]. This work reports a new micromachining process that can fabricate PIiS inductors with thick windings and high-quality magnetic cores at wafer level. A wafer-level integration process can be applied to monolithically bond the PIiS power inductor with IC circuitry and hence build a compact power module.

CONCEPT

Fully integrated power converter

To cope with all the challenges at this high switching frequency era and still take advantage of the high throughput of semiconductor processes, this work proposes a power converter module based on a PIiS inductor as shown in Fig. 1.

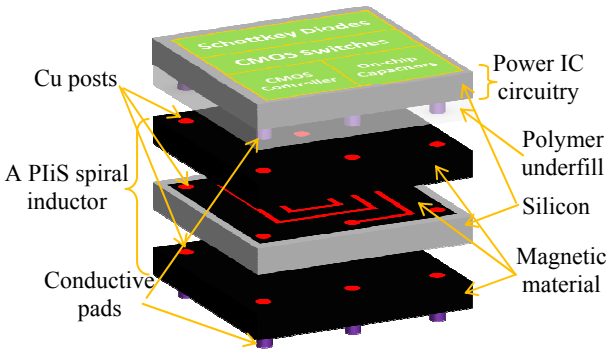

Figure 1: Concept of the fully integrated power converter with PIiS power inductor; 3D explosive view.

Major benefits of this PIiS design can be summarized as the following. (1) The substrate molded conductors can be electroplated as thick as the substrate (200-500 μm thickness). Forming a thick magnetic core is also possible by thoroughly replacing the lossy substrate with high-resistivity and polymer-bonded magnetic materials, hence enabling high current capability (>2A). (2) Closed or quasi-closed magnetic path is formed in the three device layers to avoid extra losses and electromagnetic interferences. (3) Through substrate copper plating provides TSVs and good thermal paths as well, leading to high-degree integration and compact packaging. (4) Polymer based dielectric materials that are regularly used in packaging are chosen as the passivation as well as stress buffering layers. (5) The whole fabrication flow can be done at low temperatures (<150°C) which is compatible with CMOS processes.

Compared to our prior work [9], one major improvement of the new process is using wafer-level plated copper posts instead of manually-placed solder balls for flip-chip bonding, which significantly reduces the contact resistances between conductive layers and increases the electrical contact reliability.

FABRICATION

Polymer-bonded magnetic

The magnetic material must have high resistivity and high permeability and can be applied at wafer level as well. Thus, a mixture of magnetic powders and polymer is employed. In this work, NiZn ferrite powders (FP350 from Powder Processing Technology, LLC, 89wt%) are first milled down from 10μm to 1-3μm size, and then mixed with PDMS (Sylgard 184 from Dow Corning, 11wt%). After curing in an oven at 120° C, this magnetic composite exhibits

9781940470016/HH2014/$25©2014TRF
DOI 10.31438/trf.hh2014.109

Solid-State Sensors, Actuators and Microsystems Workshop
Hilton Head Island, South Carolina, June 8-12, 2014

high resistivity, and the measured properties are as follows: ρ>2 GΩ·m, H_c=15 Oe, B_{sat} =0.2 T, and μ_r=8.

Process flow

As illustrated in Fig. 2, the device fabrication starts with a 2-inch, 280μm-thick silicon wafer. First, a 0.8 μm-thick SiO_2 layer is deposited on the backside for electrical isolation using plasma-enhanced chemical vapor deposition (PECVD). Next, a 1.0 μm-thick Cu seed layer is sputtered on the backside, and then the Cu thickness is increased to 40μm through Cu electroplating (Fig. 2(1)). This thickness is sufficient to withstand multiple polishing steps. Next, the silicon wafer is etched through with a slightly negative angle by deep reactive ion etch (DRIE). After a 1.0 μm conformal coating of PECVD SiO_2, an anisotropic reactive ion etch (RIE) exposes the Cu seed layer at the trench bottom and leaves the oxide on the trench sidewalls (Fig. 2(2)). Then, a Cu electroplating process fills the silicon trenches with Cu, and the over-plated parts are polished away (Fig. 2(3)). Subsequently, the silicon between the Cu windings is thoroughly removed by another DRIE etch, and the PDMS-bonded magnetic composite mixture is manually pressed into the newly formed trenches. Vacuum treatment is necessary to repel solvents and trapped air before curing the agent in an oven at 120ºC, and the overfilled magnetic composite is then polished away (Fig. 2(4)).

Another critical process is to fabricate tall Cu posts (>200μm) as the vias that can pass through the thick magnetic composites, which is accomplished by using multiple photoresist coatings, as shown in Fig. 2(5) and its intermediate steps). Fig. 3 is a photo of fabricated Cu posts. First, a 1.0 μm Cu/Cr seed layer is sputtered on the magnetic composite. Then, four layers of AZ9260 are spin coated and cured gradually to a total thickness of 80-85 μm. After exposure, this thick photoresist is developed in AZ 400K 1:2 for 6-7 minutes. Cu electroplating is then performed and slightly overfills the photoresist molds. This sequence of lithography and electroplating is then repeated until the Cu posts reach the desired height before removing the Cu/Cr seed layer.

PDMS-bonded magnetic composites are pressed and vacuum-pumped onto the wafer again, and the over filled part is polished away to expose the electroplated Cu posts (Fig. 2(6)). A 30-40 μm top Cu shield layer is pattered and electroplated (Fig. 2(7)). Then the above procedures are repeated on the backside to complete the PIiS inductor fabrication (Fig. 2 (8)).

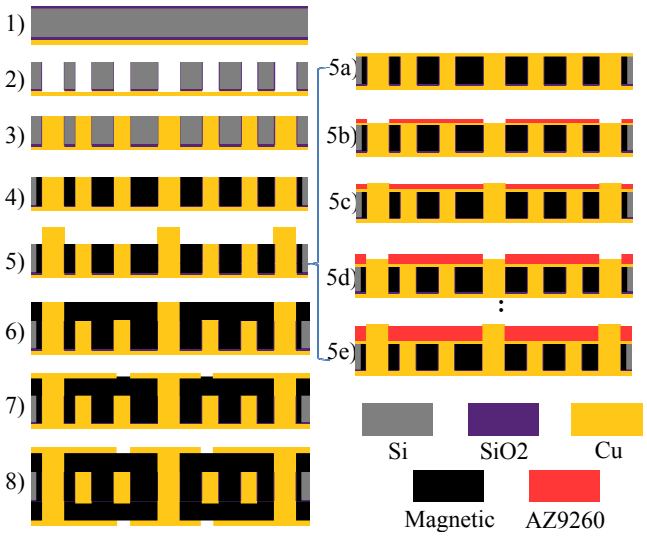

Figure 2: Cross-section view of the PIiS fabrication process.

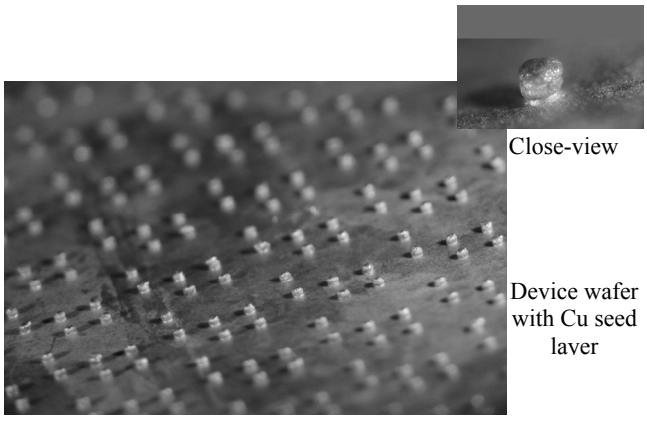

Figure 3: Side view of the Cu vias array on device wafer.

Discussion on fabrication issues

First, at step 5a) in Fig 2, the deposition of the Cu seed layer before the photolithography is needed to shield the thermal stresses originated from the magnetic material. Otherwise, cracks within the photoresist coating can be easily observed, with many bubbles appearing when coating another layer of photoresist, as shown in the photo in Fig. 4. For best interface adhesion between the seed layer and substrate, the wafer should be baked thoroughly for 5-6 minutes at around 110ºC to remove any remnant moisture before Cu/Cr sputtering. A 100-120Å Cr layer is sufficient for promoting good adhesion. Other thick photoresists (>200μm) such as SU8 are also applicable with only one layer of coating required, and the extra Cu seed layer can be eliminated to further improve the interface performance.

Second, air can be easily trapped between the Cu coils during the magnetic filling process, *e.g.,* steps 4), 6), and 8) in Fig. 2, and vacuum treatment is necessary to remove it before curing the PDMS-bonded magnetic composite. Multiple vacuum pumping cycles may be needed to ensure the air release. Fig. 5 shows one cross-section view of a fabricated 10-turn square spiral inductor with trapped air bubbles.

Third, the manual pressing process may cause the soft copper posts to become inclined or detached, as shown in Fig. 5. Therefore, careful control of the seed layer etching time is important to have a sufficient remaining Cu post diameter, as well as a large enough dimension design.

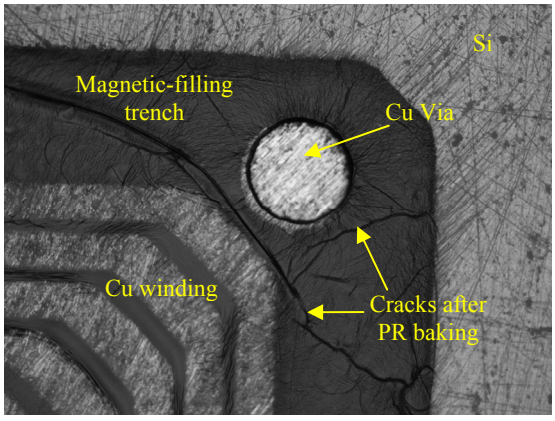

Figure 4: Top view of the stress accumulation problem after photoresist baking.

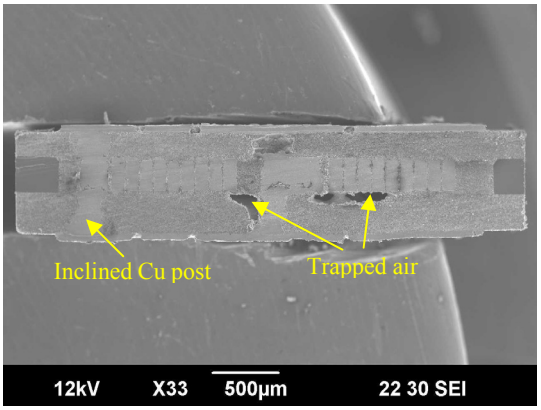

Figure 5: Cross-section view of a 10-turn PIiS power inductor with trapped air and inclined Cu post.

RESULTS

Inductor characterization

The PIiS inductors have been successfully fabricated and tested. Fig. 6 and 7 show the SEM pictures of the entire device and the cross section of a fabricated device. For this 10-turn square shaped spiral PIiS inductor, the thicknesses of the top magnetic core, copper winding and bottom magnetic core are 270 µm, 280 µm, and 200 µm, respectively. The measured inductance, Q and AC resistance of the PIiS inductor versus frequency are plotted in Fig. 8, where L=430 nH, R_{dc} =84 mΩ, R_{ac}=792 mΩ, and Q=21 at 6MHz.

Compared with our prior work [9], the newly fabricated square spiral inductor has a similar size (3 mm × 3 mm) but with much less resistance and higher inductance. Square spiral inductors are more area efficient than circular spiral ones. The magnetic layer is thicker on one side (270 µm vs 200 µm), which leads to higher inductance. For the lower resistance, there are several factors contributing to that. First, the windings are taller (280 µm vs 200 µm) than our previous circular design, and they are also become wider (around 5 µm) due to the undercut during the DRIE process. Second, electroplating Cu posts instead of placing solder balls reduces contact resistance between conductive layers significantly. Third, the resistivity of electroplated copper is lower than that of solder balls.

The PIiS is compared to other works in Table 1 and it has achieved low DC resistance, large inductance and high Q simultaneously.

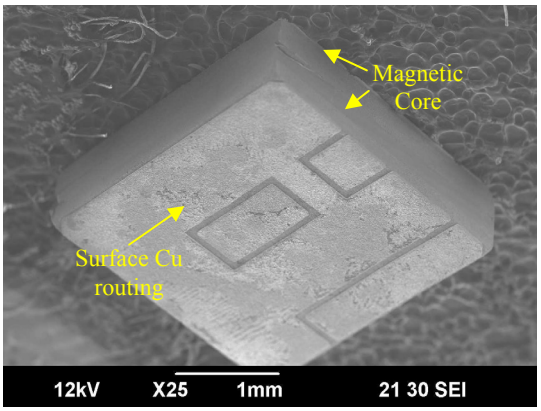

Figure 6: Side View of a 3×3×0.83mm^3 PIiS power inductor.

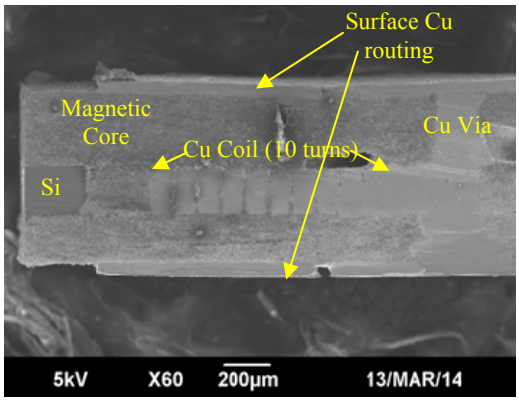

Figure 7: Cross-section view of a 10-turn PIiS power inductor.

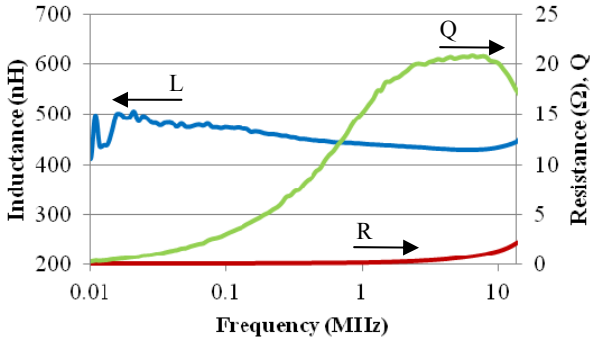

Figure 8: Inductance, Q and AC resistance verse frequency of a 10-turn PIiS power inductor.

Table 1: PIiS power inductor compared to other works with mm3-scale sizes..

Inductors	*Core*	*L (nH)*	*DCR (mΩ)*	*Q_{max}*	*Area (mm^2)*
This work	**NiZn+PDMS**	**430**	**84**	**20.8@6MHz**	**3×3**
Prior [9]	NiZn+PDMS	390	140	10@6MHz	3×3
On-Si [6]	FeCo	55	100	13.8@20MHz	3×3
On-Si [7]	NiFe	100	300	2.1@1MHz	4×1
In-Si [11]	SU8	60	399	17.5@70MHz	6×6
On-Si [5]	Air	130	695	15@160MHz	1×1

Converter performance

A PIiS has been bonded on a TI TPS62621 (600 mA, 6 MHz high-efficiency step-down converter) buck converter evaluation board, as shown in Fig. 9. The measured efficiencies versus load currents and temperatures are plotted in Figs. 10 and 11.

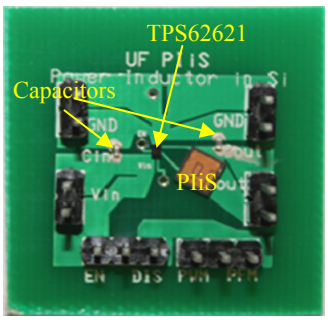

Figure 9: The TPS62621 buck converter evaluation board based on PIiS power inductor.

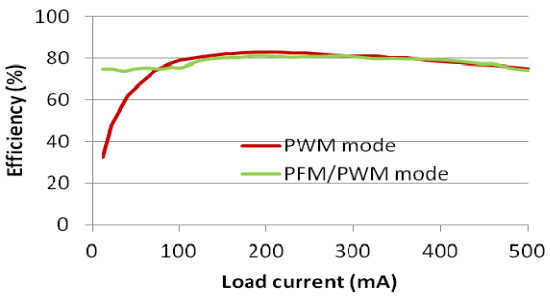

Figure 10: Efficiency vs. load current measurements (3.6/1.8V Vin/Vout).

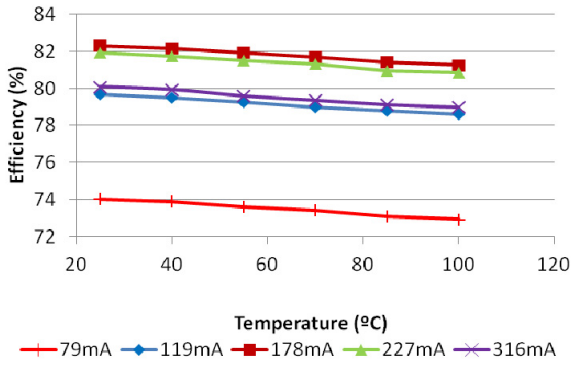

Figure 11: Efficiency vs. temperature measurements (3.6/1.8V Vin/Vout).

The buck converter module successfully delivered 600 mA at 1.8 V with an 83% maximum efficiency (PWM mode) at 6 MHz, which is comparable to commercial products and can be further improved with better packaging. The 3% loss reduction compared with our prior work is mainly benefited from the lower DC and AC resistances. A wide load current range (120-380 mA) for high efficiency (80-83%) was also observed.

For loss breakdown, at 3.6/1.8 V input/output voltage and 129/214 mA input/output current, the measured efficiency is 82.9% which corresponds to 79 mW total loss. The calculated inductor ripple current is 174.4 mA. Thus, the inductor's DC and AC losses are about 3.9 mW and 8 mW, respectively. The TPS62621 regulator has a rated efficiency of 90% which accounts for about 46.5 mW loss. Adding up these component losses, the module has a 58.4 mW power loss without considering the losses from core hysteresis, trace resistances on board, and capacitor parasitics.

CONCLUSION AND FUTURE WORK

Wafer-level integration of power inductors in silicon (PIiS) for high efficiency, high frequency, and compact DC-DC power converters has been successfully demonstrated. PIiS power inductors have been successfully fabricated with the IC-compatible, low-cost micromachining process. Through-substrate silicon trenches with an aspect ratio up to 20:1, obtained by DRIE, are used for Cu electroplating molds. After Cu electroplating and polishing, the Cu windings have the same thickness as the silicon substrate. Cu posts up to 270 μm, which pass through the thick magnetic composites, are also realized using a sequential plating process. Thus, the PIiS inductors simultaneously achieve low DC resistance (84 mΩ), large inductance (430 nH) and high Q (21).

The PIiS power inductor has been successfully assembled on a TI buck converter evaluation board and delivered 600 mA at 1.8V with an 83% maximum efficiency at 6 MHz. Furthermore, the surface Cu pads on the PIiS power inductors are well prepared for mounting other IC components. A fully integrated power converter can be implemented with size-matched PIiS inductors and IC regulators, and much higher power density and smaller size can be achieved.

ACKNOWLEDGEMENTS

The authors would like to thank Linear Technology Corporation for technical and funding supports, and Nanoscale Research Facility and Interdisciplinary Microsystems Group of the University of Florida for device fabrication and characterization. Travel support has been generously provided by the Transducers Research Foundation (TRF).

REFERENCES

[1] E. Waffenschmidt and J. A. Ferreira, "Embedded passives integrated circuits for power converters," in IEEE 33rd Annu. Power Electronics Specialists Conf.(pesc 02), 2002, pp. 12-17 vol.1.

[2] M. H. Lim, J. D. Van Wyk, F. C. Lee, and K. D. T. Ngo, "A Class of Ceramic-Based Chip Inductors for Hybrid Integration in Power Supplies," IEEE Trans. Power Electron., vol. 23, pp. 1556-1564, 2008.

[3] M. Wens and M. Steyaert, "A fully-integrated 0.18um CMOS DC-DC step-down converter, using a bondwire spiral inductor," in IEEE Custom Integrated Circuits Conf. (CICC 2008), 2008, pp. 17-20.

[4] Q. Li, M. Lim, J. Sun, A. Ball, Y. Ying, F. C. Lee, et al., "Technology roadmap for high frequency integrated DC-DC converter," in IEEE 6th Int. Power Electronics and Motion Control Conf. (IPEMC '09), 2009, pp. 1-8.

[5] C. D. Meyer, S. S. Bedair, B. C. Morgan, and D. P. Arnold, "Ultra-miniaturized power converter modules using micromachined copper scaffolds," IEEE Int. Conf. on Micro Electro Mechanical Systems (MEMS, Hilton Head), 2012.

[6] T. Liakopoulos, A. Panda, M. Wilkowski, A. Lotfi, K. H. Tan, L. Zhang, et al., "Introducing FCA, a new alloy for Power Systems on a chip and Wafer Level Magnetic applications," in 13th Int. Conf. on Electronic Packaging Technology and High Density Packaging (ICEPT-HDP), 2012, pp. 949-954.

[7] C. H. Ahn and M. G. Allen, "A comparison of two micromachined inductors (bar- and meander-type) for fully integrated boost DC/DC power converters," IEEE Trans. Power Electron., vol. 11, pp. 239-245, 1996.

[8] B. Orlando, R. Hida, R. Cuchet, M. Audoin, B. Viala, D. Pellissier-Tanon, et al., "Low-Resistance Integrated Toroidal Inductor for Power Management," IEEE Trans. Magn., vol. 42, pp. 3374-3376, 2006.

[9] M. Wang, J. Li, K. D. T. Ngo, and H. Xie, "A Surface-Mountable Microfabricated Power Inductor in Silicon for Ultracompact Power Supplies," IEEE Trans. Power Electron., vol. 26, pp. 1310-1315, 2011.

[10] D. Yao, et al., "Microfabricated V-Groove Power Inductors Using Multilayer Co-Zr-O Thin Films for Very-High-Frequency DC-DC Converters," IEEE Trans. Power Electron., vol. PP, pp. 1-1, 2011.

[11] X. Yu, et al., "Silicon-embedded 3D toroidal air-core inductor with through-wafer interconnect for on-chip integration," in IEEE 25th Int. Conf. on Micro Electro Mechanical Systems (MEMS), 2012, pp. 325-328.

CONTACT

*Jiping Li: jipingli@yahoo.com

HIGH OPTICAL Q, GHZ FSR LITHIUM-NIOBATE-ON-SILICON PHOTONIC RESONATORS

R. Wang and S. A. Bhave*
Cornell University, Ithaca, NY, USA

ABSTRACT

Lithium Niobate (LN or just "niobate") thin-film micro-photonic resonators have promising prospects in many applications including high efficiency electro-optic modulators, optomechanics and nonlinear optics. This paper presents micro-fabrication technology to achieve thin-film lithium niobate photonic resonators on a silicon platform. We fabricated a 400 μm radius niobate disk resonator that exhibits high intrinsic optical quality factor (Q) of 44,000, with 50 GHz free-spectral-range (FSR). Exploiting the high optical Q in the released free-standing photonic disks, we were able to optomechanically detect the radial mechanical vibration modes of a 150um radius disk resonator.

INTRODUCTION

The lack of inversion symmetry in the Lithium Niobate crystal exhibits itself via its characteristic strong piezoelectric effect, linear electro-optic effect, pyroelectric effect and photoelastic effect. The piezoelectric effect of bulk LN has found applications in surface acoustic wave devices in the RF community, while the fiber optics industry uses LN for manufacturing photonic modulators and optical frequency doublers taking advantage of its electro-optic effect.

Thin film LN is a promising platform for MEMS applications and chip-scale photonics applications. LN thin-film contour mode resonators have recently been demonstrated with low motional impedance, high mechanical Q and high electro-mechanical coupling factor, towards the goal of achieving large bandwidth RF filters. [1,2]. Chip-scale photonics has primarily focused on utilizing thin-film SOI for implementing monolithic yet inefficient modulators, isolators and optical delay elements. LN thin-film photonics have been attempted [3,4]. Due to the difficulty of achieving high quality anisotropic etching of LN, surface smoothing at close to melting point or slab waveguide with deposited high index guiding material were used to achieve low optical loss micro-photonic structures. In contrast, we present a micro-machining technology to realize thin film LN photonic resonators on a silicon platform. An ion mill anisotropic etching process, originally developed for RF MEMS applications, was used to define low optical loss photonic disks. Leveraging the strong cross-domain-coupling effects in LN, this platform can potentially be used to realize novel devices in chip-scale optomechanics.

MEMS FABRICATION TECHNOLOGY

There are two distinct fabrication challenges to fabricate the LN micro-photonic resonator on silicon substrate: 1. Achieving vertical side-wall and smooth surface profiles without mask residue, 2. Achieving clearance between the LN device and silicon substrate to enable efficient mode confinement.

MEMS niobate resonators to date have used either metal or silicon dioxide as a hard-mask to pattern the thin-film niobate [2,5]. However, any residue of metal or oxide left behind can interact with circulating photons causing optical absorption and scattering, which will significantly reduce the optical Q of the device. Acoustic waves in RF MEMS resonators have a wavelength of few microns to tens of microns. The acoustic waves are reflected by the anisotropic etching defined device boundaries forming high Q acoustic cavity. Therefore, the surface roughness of the sidewall profile has less impact on the mechanical Q of these devices, while the sidewall angle has a more important role. On the contrary, optical wavelength in LN optical devices ranges from several hundred nanometers to 2um, and the optical wave propagates along the etching defined device boundary. As a result, the surface roughness strongly affects the optical scattering loss. The angled sidewall is sometimes beneficial as it forces the optical mode profile to lie deep within the guiding material, thus reducing the scattering loss from the surface roughness. Our group has previously demonstrated LN contour-mode RF resonators [1] using 4 μm thick photo-resist as the mask with ion mill etching. The resist can then be easily rinsed off by acetone with sonication. If necessary, an additional O_2 plasma clean ensures that no residue is left behind. The Argon ion mill etching can be controlled to be self-balancing between etching and re-sputtering by carefully adjusting the ion beam incident angle, where the re-sputtering can act as an extra sidewall "protection" during the etching. With this process, we achieved sidewall angle of 87 degrees with <10nm surface roughness, thus meeting the requirement of a smooth vertical sidewall that is necessary for future integrated waveguide coupling of photons.

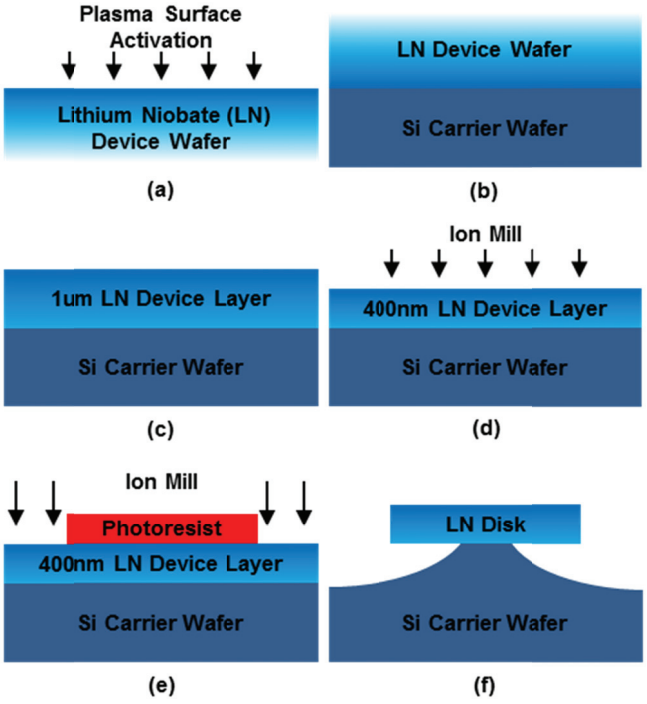

Figure 1: Fabrication process of the LN disk optical resonator: (a) Prepare the device wafer for bonding by plasma surface activation; (b) Direct bonding of the LN device wafer to Si carrier wafer; (c) Grounding the device wafer to 1um thickness; (d) Blank ion mill to reduce the LN film to 400nm for better index matching between LN and Silica optical fiber; (e) Ion mill with photoresist mask to define device geometry; (f) XeF_2 timed-etch release.

9781940470016/HH2014/$25©2014TRF
DOI 10.31438/trf.hh2014.110

Silicon has higher refractive index (3.4) than LN (2.3). So any light that couples into the niobate disk will leak into the silicon substrate. Using XeF_2 dry-etch to undercut the niobate disk resonator enables us to achieve >10 μm clearance between the niobate disk and silicon substrate, thereby enabling outstanding optical mode confinement in niobate and thus high optical Q. In addition, the free-standing disk structure will enable optomechanical interactions between the mechanical and photonic modes.

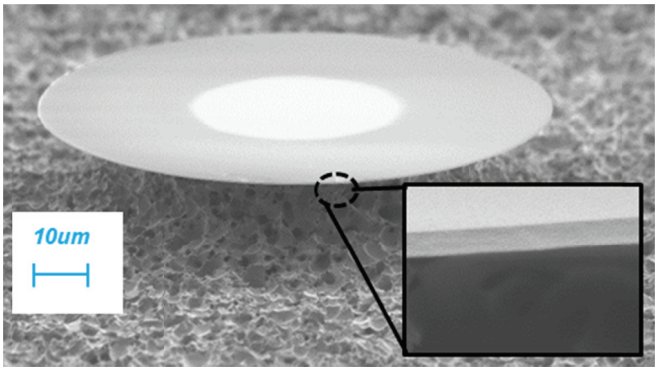

(a)

(b)

Figure 2: SEM of the LN resonators. (a) 40um radius LN optical resonator; Inset: Zoom-in view of the rim showing smooth side wall, which is crucial for high optical Q; (b) 500um radius LN resonator.

Fig. 1 shows the complete fabrication process leveraging these key MEMS processes. We start with a Z-cut white LN wafer. The bonding surface is activated by plasma (similar as in [6]). Then, the device wafer is flip-bonded to the Si handle wafer. The device wafer is ground down to 1um thickness. As will be discussed later, we perform optical tests on the LN disks using a tapered fiber, and one of the challenges for coupling light to LN disk resonators is the large refractive index mismatch between the LN disk and the silica fiber, where the refractive index of LN for infrared light is in the range of 2. 2~2.3, and the refractive index of the core for the SMF-28 single mode fiber is 1.45. Therefore, a blanket ion mill etching is used to further thin the device layer to 400nm to reduce the effective index of the optical mode in the disk resonator. Ideally a photonics designer could start with a thinner LN device thickness to avoid this ion mill etch step. Finally, the disk geometry is defined by Argon ion mill with photoresist mask, and the devices are released by timed XeF_2 etching. Fig. 2 shows the SEMs of LN disks with different radii. As the bonding process was performed at room temperature, no buckling or bending is observed in the released disks. The inset of Fig. 2(a) shows that the ion mill produced a smooth clean sidewall, which is crucial for high optical quality factor.

OPTICAL CHARACTERIZATION

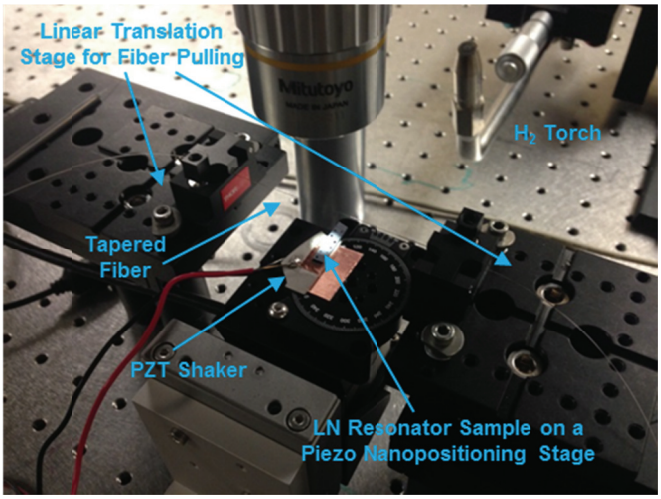

Figure 3: Optical characterization setup using a tapered fiber coupling to the LN disks.

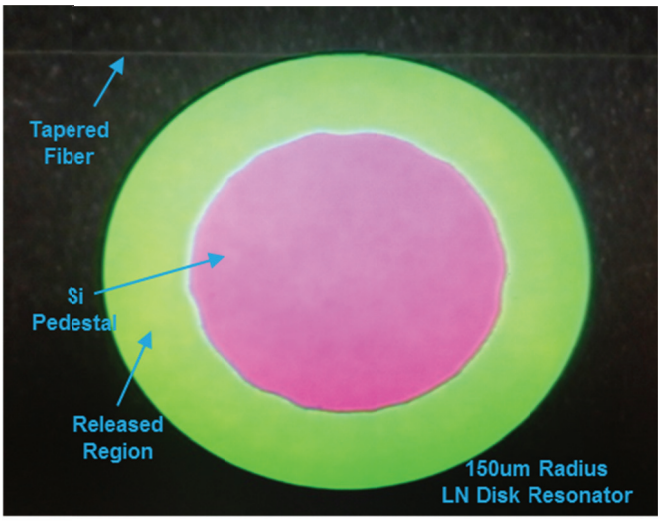

Figure 4: Microscope image of the tapered fiber coupling to a 150um radius LN disk.

We use a tapered optical fiber [7] to couple light from tunable near-IR laser (Santec TSL-510) to the niobate disk resonator. Fig. 3 shows the experimental setup. Due to the large index mismatch between the resonator optical mode and the effective refractive index of light in the tapered fiber, the taper is brought to physical contact with the LN disk rim to achieve efficient coupling (Fig. 4). A polarization controller is introduced to carefully adjust the light polarization in fiber such that it couples strongly with the photonic resonator. The transmitted optical signal is sent to a high-speed photodiode (Newport 1544A) and monitored on an Agilent

(DSO9404A) oscilloscope. By sweeping the wavelength of the input light, we measure the optical transmission spectrum and extract the optical parameters (quality factor, group index, optical propagation loss) by fitting the transmission dip to a Lorentzian [7].

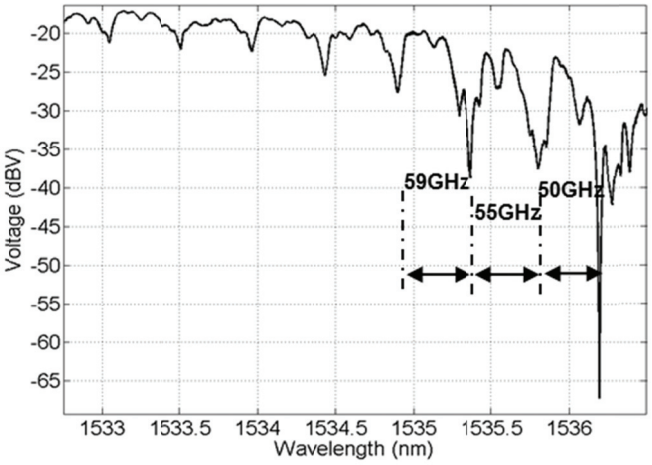

Figure 5: Broadband transmission spectrum of a 400um radius LN optical resonator, showing 50GHz FSR.

Fig. 5 shows the broad-band transmission spectrum of a 400 μm radius LN disk resonator. In the transmission measurement, less than 150uW of input optical power was used to ensure a linear response from the device. The resonator has an FSR of 50 GHz making it an exciting candidate for generating microwave frequency spaced optical frequency combs in a sub-1 mm^2 area. From the FSR, we estimate the group index to be 2.09. The high extinction for the optical resonance at 1536.19nm indicates that the mode is critically coupled. The extracted intrinsic optical Q is 44,000 corresponding to an optical propagation loss of 1.94dB/cm. This is the highest optical Q demonstrated in chip-scale LN disk resonators to date (Figure 6).

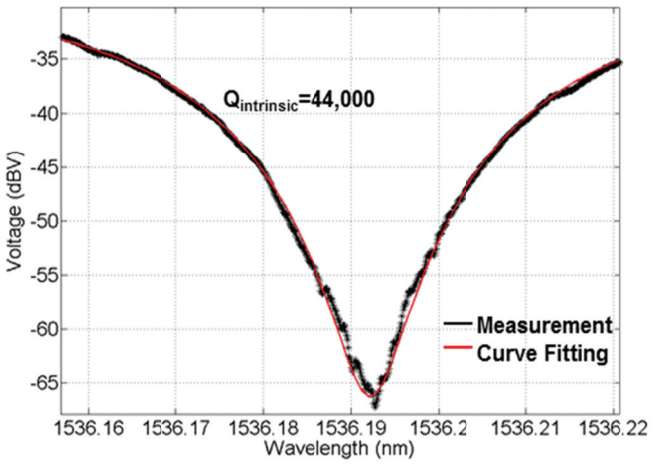

Figure 6: Zoom-in view of the transmission spectrum of the critically coupled dip (at 1536.193nm). Curve fitting of the dip to a Lorentzian yields an extracted intrinsic optical Q of 44,000.

OPTOMECHANICAL INTERACTION

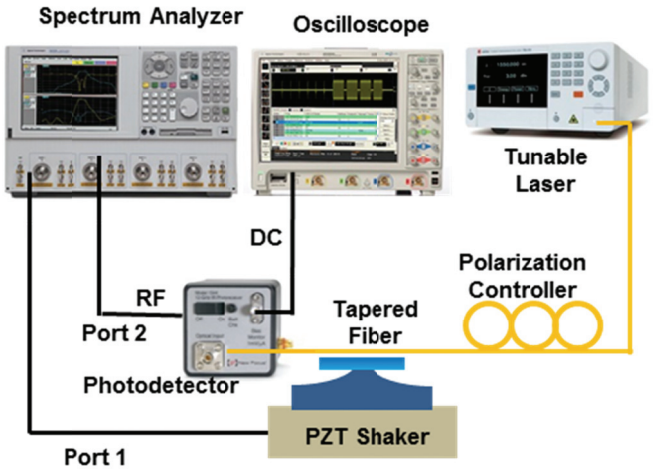

Figure 7: Schematic of the experimental setup for optomechanical sensing of disk vibration.

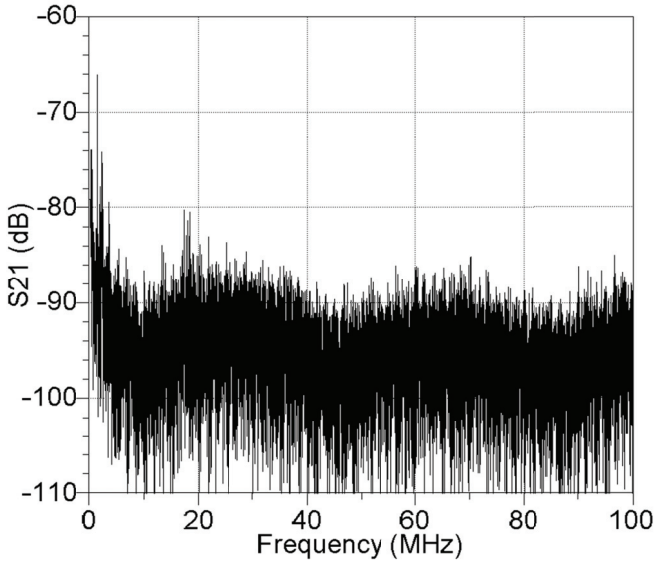

Figure 8: Background noise floor of the opto-mechanical transmission measurement, where the tapered fiber is not coupled to the LN disk resonator.

Fig. 7 shows the schematic of the experimental setup for optomechanical transduction. The LN disk resonator (150um radius) is mounted on a PZT shaker, which is excited by supplying an AC voltage from port 1 of an Agilent (N5230A) network analyzer. The RF output of the photodetector is connected to port 2 of the network analyzer, and the DC output is monitored on the oscilloscope to track the transmitted DC optical power. The laser wavelength is blue-detuned to a high optical Q, 1500.597nm resonance. When the actuation frequency of the PZT excited by port 1 of the network analyzer corresponds to a mechanical mode of the LN resonator, the acoustic energy couples from the PZT to

the LN disk. The resulting mechanical vibration of the disk causes modulation of the effective optical path length of the light propagating in the optical resonator cavity. As a result, the mechanical vibration of the disk is imprinted on the transmitted optical signal. By measuring the S_{21} parameter, we can characterize the mechanical resonance of the LN photonic disk resonator.

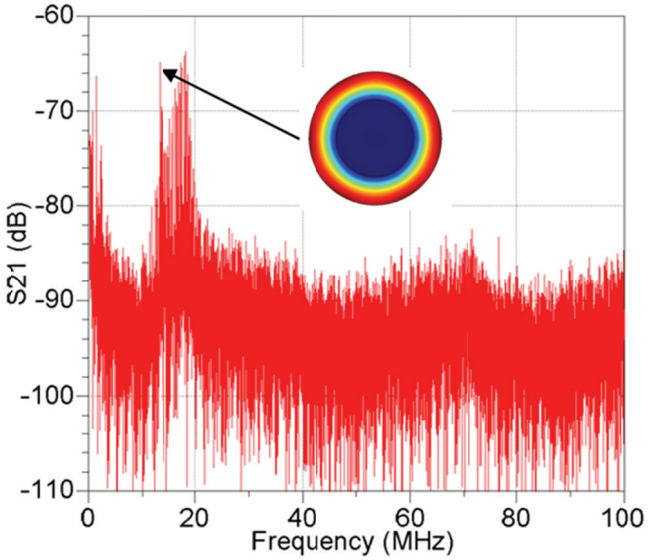

Figure 9: Opto-mechanical transmission measurement when the tapered fiber is coupled to the LN disk resonator (150um radius), showing a 13MHz peak corresponding to mechanical vibration of the radial breathing mode of the micro-disk. The low frequency peaks (below 5MHz) correspond to tapered fiber vibration modes, which are also observed in Fig. 8.

To improve the output signal strength, 10mW optical power is launched into the taper, and the network analyzer stimulus is set to 8dBm. The detuning of the laser wavelength is fine tuned to maximize the output signal. Fig. 8 shows the background noise floor when the taper is far away from the LN resonator, the low frequency peaks (below 5MHz) corresponds to the tapered fiber vibration modes. Fig. 9 shows the S_{21} parameter when the taper is coupled to the disk and the detuning of the laser wavelength is optimized for maximum transduction. The spectrum shows a peak at 13MHz, which corresponds to the fundamental radial breathing mode of the disk. The peaks near 18MHz are from the vibration modes of the laser cavity.

CONCLUSION

The MEMS-based fabrication technology presented in this work opens up new avenues to realize optical resonators, modulators, frequency doublers and frequency combs that leverage the multi-domain {RF, photonic, optomechanical} coupling in a monolithic LN-on-Silicon platform. The high refractive index of niobate enables us to achieve 50 GHz FSR, with a footprint 4× smaller than silica resonators [8]. In addition, we demonstrated optomechanical guided-light detection of mechanical vibration of the LN disk.

ACKNOWLEDGEMENT

The authors wish to thank Dr. Siddharth Tallur and Dr. Suresh Sridaran for proof-reading the manuscript, and the Transducer Research Foundation for generously providing the travel support. The described work was sponsored by the Charles Stark Draper Laboratory, and was performed in part at the Cornell NanoScale facility, a member of the National Nanotechnology Infrastructure Network, which is supported by the National Science Foundation (Grant ECCS-0335765).

REFERENCES

[1] R. Wang, S. Bhave and K. Bhattacharjee, "Thin-film high $k_t^2 \cdot Q$ multi-frequency lithium niobate resonators," MEMS 2013, pp. 165-168, 2013.

[2] S. Gong and G. Piazza, "Multi-Frequency Wideband RF Filters using High Electromechanical Coupling Laterally Vibrating Lithium Niobate MEMS Resonators," MEMS 2013, pp. 785-788, 2013.

[3] P. Rabiei, J. Ma, S. Khan, J. Chiles, and S. Fathpour, "Heterogeneous Lithium Niobate photonics on silicon substrates," Optics Express, vol. 21, pp. 25573-25581, 2013.

[4] C. Ying, C. Sones, A. Peacock, F. Johann, E. Soergel, R. Eason, M. Zervas, and S. Mailis, "Ultra-smooth lithium niobate photonic micro-structures by surface tension reshaping," Opt. Express, vol. 18, pp. 11508-11513, 2010.

[5] R. Olsson, et al., "A high electromechanical coupling coefficient SH0 Lamb wave lithium Niobate mircromechanical resonator and a method for fabrication", Sensors and Actuators A: Physical, vol. 209, pp. 183-190, 2014.

[6] D. Tulli, D. Janner, and V. Pruneri, "Room temperature direct bonding of $LiNbO_3$ crystal layers and its application to high-voltage optical sensing,", J. Micromech. Microeng., vol. 21, 2011.

[7] M. Cai, O. Painter and K. Vahala, "Observation of critical coupling in a fiber taper to silica-microsphere whispering gallery mode system," PRL 85, 74 (2000).

[8] J. Li, H. Lee, T. Chen and K. Vahala, "Low-pump-power, low-phase-noise, and microwave to millimeter-wave repetition rate operation in microcombs," PRL 109,233901 (2012).

CONTACT

*R. Wang, tel: +1-607-793-0877; rw364@cornell.edu

MULTI-RESONATOR APPROACH TO ELIMINATING THE TEMPERATURE DEPENDENCE OF SILICON-BASED TIMING REFERENCES

Vikram A. Thakar[*], *Zhengzheng Wu, Cesar Figueroa, and Mina Rais-Zadeh*
University of Michigan, Ann Arbor, USA

ABSTRACT

This work reports on a multi-resonator system capable of generating a temperature-stable frequency reference across a wide temperature range. The system involves the use of a minimum of three temperature-compensated oscillators having a slightly different turnover temperature. The oscillator output frequency undergoes frequency multiplication and mixing in two stages to achieve a temperature-stable frequency output. The sensitivity of the clock frequency is analyzed as a function of temperature induced measurement errors.

AlN-on-silicon ring resonators actuated piezoelectrically are proposed as the three frequency setting components. Their turnover temperature is controlled through the placement of oxide within the resonator volume. A total frequency shift of less than 10 ppm is estimated across the temperature range of -40 °C to 85 °C with this implementation.

INTRODUCTION

Timekeeping plays an important role in inertial navigation and modern communication systems. A temperature-stable frequency reference is an essential ingredient of such timing devices. Quartz-based oscillators have successfully fulfilled this need over the past few decades. As miniaturization leads to significant cost reduction, there has been a strong push to replace bulky quartz with micromachined silicon-based alternatives.

For all its merits as a mechanically robust material, moderately doped silicon suffers from a relatively large temperature-induced shift in its elastic modulus, which leads to an unacceptably large frequency fluctuation. To overcome this challenge, a number of approaches have been proposed and experimentally demonstrated [1], [2]. Passive compensation of silicon resonators has been achieved using silicon dioxide to negate the temperature dependence of silicon [3]. Due to the nature of the temperature coefficients, passive compensated silicon resonators demonstrate a parabolic temperature dependence of frequency, with the overall frequency shift limited to ~100 ppm across the industrial temperature range [4]. For more stable frequency references, the residual temperature sensitivity of silicon resonators can be actively compensated in a feedback loop with input from an on-chip temperature sensor [2].

Recently, we utilized the second-order temperature dependence of passively compensated silicon resonators to achieve a temperature-stable frequency output [5]. This approach makes use of three temperature-compensated resonators having distinct temperature compensation profiles in a multi-resonator system, as shown in Fig.1, to generate a temperature-stable frequency reference.

Using a simple analysis we showed that for three resonators with unique second-order temperature dependence we can achieve a temperature-insensitive clock signal [5]. In this work, we extend the analysis to look at the system sensitivity to measurement errors and resonator drift. We show that resonator drift has no impact on the temperature sensitivity of the clock output, but causes a constant shift in the output frequency over time. On the other hand, calibration-induced errors are shown to cause significant temperature sensitivity in the clock output. As a consequence, sufficient care must be taken during the initial one-time calibration to ensure a temperature-insensitive clock output.

CLOCK DESCRIPTION

Figure 1 shows a block diagram of the proposed temperature-insensitive clock. As seen from the schematic, the system utilizes three oscillators with different turnover temperatures, which is defined as the inflection point of the parabolic dependence of resonator frequency with temperature. The frequency of each oscillator can be written as

$$f_n = a_n T^2 + b_n T + c_n \tag{1}$$

Because of having different turnover temperatures, the three resonators have unique and non-zero coefficients a, b and c. These coefficients are calculated by measuring the resonator response as a function of temperature during a one-time calibration run. The output of the three oscillators undergoes frequency multiplication and mixing in two stages to achieve a final temperature-stable frequency reference. Stage I multiplication factors k_1 and k_3 are set so as to ensure a purely second-order frequency dependence on temperature. At the output of the first set of mixers we can write,

$$\begin{cases} f_{12} = (k_1 a_1 + a_2)T^2 + (k_1 b_1 + b_2)T + (k_1 c_1 + c_2) \\ f_{23} = (k_3 a_3 + a_2)T^2 + (k_3 b_3 + b_2)T + (k_3 c_3 + c_2) \end{cases} \tag{2}$$

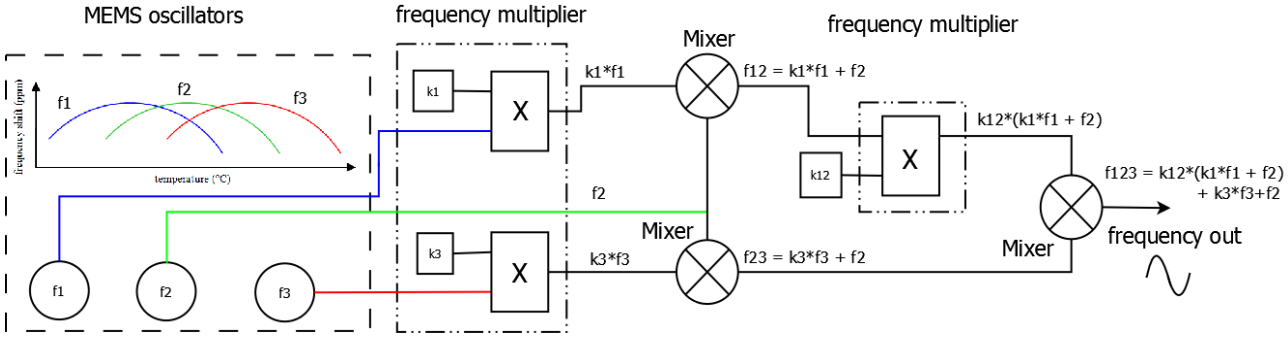

Figure 1: Algorithm for the multi-resonator temperature-stable clock. A minimum of three MEMS oscillators having different turnover temperatures are required in this implementation. The frequency multiplication is achieved using an n-fractional phase locked loop (PLL) while the frequency mixing is achieved using a mixer and a suitable filter.

9781940470016/HH2014/$25©2014TRF
DOI 10.31438/trf.hh2014.111

The above equation sets the multipliers k_1 and k_3; to remove the first-order dependence of frequency on temperature, we have

$$k_1 = -\frac{b_2}{b_1} \text{ and } k_3 = -\frac{b_2}{b_3}. \quad (3)$$

Thus, at the input of the second mixer, the two frequency signals have a pure second-order temperature dependence, which can be compensated using a similar approach. The multiplier k_{12} is determined such that the second-order term is canceled. The parameter k_{12} can then be estimated as

$$k_{12} = -\left[\frac{k_3 a_3 + a_2}{k_1 a_1 + a_2}\right] \quad (4)$$

and the output frequency can be written as

$$f_{123} = k_{12}k_1c_1 + (1 + k_{12})c_2 + k_3c_3 \, . \quad (5)$$

The equation for the output frequency is a combination of constants independent of temperature, and thus this system allows for the realization of a temperature-insensitive clock [5].

SENSITIVITY TO RESONATOR DRIFT

The effect of temperature-independent frequency drift can be captured in (1) by noting,

$$f_n = a_nT^2 + b_nT + (c_n + d_n), \quad (6)$$

where d_n is temperature-independent frequency drift for the nth resonator. Following the steps in the previous section the effect of individual resonator drift at the clock output can be written as,

$$(f_{123})_d = f_{123} + k_{12}k_1d_1 + (1 + k_{12})d_2 + k_3d_3 \, . \quad (7)$$

As can be noted from (7), since k_1, k_3 and k_{12} are invariant with temperature, the resultant frequency $(f_{123})_d$ is also independent of temperature but has a constant offset from the original calibrated output frequency.

SENSITIVITY TO MEASUREMENT ERRORS

Case 1: Non-uniform temperature distribution in measurement chamber

Considering that most low-frequency resonator measurements are performed in low-vacuum conditions, it is quite possible that the measurement chamber has some temperature non-uniformity. Since the temperature controller maintains the sensor at the set temperature rather than the actual resonator temperature, this implies the resonator may either lead or lag the sensor temperature depending on the nature of the non-uniformity. This can cause an error in the measurement during the calibration process, due to which we have

$$f'_n = a'_nT^2 + b'_nT + c'_n, \quad (8)$$

whereas the real temperature dependence is given using (1). For the purpose of this analysis we can split the measured individual coefficients a'_n, b'_n and c'_n into a real component and an error component. Then, we can express f'_n as,

$$f'_n = (a_{0n} + a_n)T^2 + (b_{0n} + b_n)T + (c_{0n} + c_n),$$

and

$$f'_n = f_n + f_{0n} \, . \quad (9)$$

Here, a_{0n}, b_{0n} and c_{0n} are the respective error components for the nth resonator while f_{0n} is the total frequency error for the nth resonator. Again, following the same steps from (1) to (5), we can express the effect of measurement error on the system output as,

$$f'_{123} = f_{123} + k_1k_{12}f_{01} + (1 + k_{12})f_{02} + k_3f_{03} \quad (10)$$

We should note here that f_{0n} values are temperature dependent and thus the clock output too has second-order temperature dependence.

Case 2: Temperature sensor calibration error

In this case, while we assume the resonator to be at temperature T, in reality it is operating at temperature T'. This would lead to a simplified case of (10) wherein the turnover temperature is incorrectly estimated by (T-T') but the shape of the frequency-temperature dependence (parabola) remains unchanged. In this case, we have no change in a_{0n} and we can write

$$f_{0n} = b_{0n}T + c_{0n} \, . \quad (11)$$

Equations (10) and (11) given above suggest that non-idealities during measurement of the individual resonators can significantly impact the temperature sensitivity of the clock output. This is graphically represented in Fig. 2. In Fig. 2(a) the expected nature of the temperature dependence of clock frequency with temperature errors is plotted. Fig. 2(b) plots the clock output in presence of a constant temperature sensor calibration error. Results suggest that proper care must be taken during the calibration run to ensure that these errors are minimized. Once properly calibrated a temperature-insensitive clock output can be obtained.

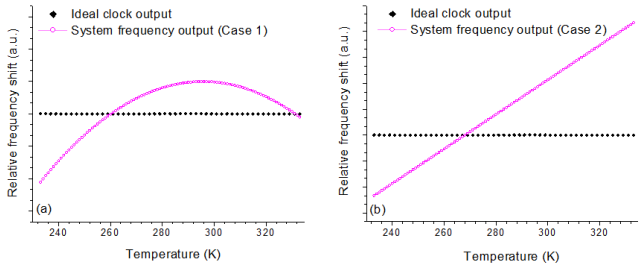

Figure 2: Graphical representation of the temperature dependence of the clock frequency output due to (a) temperature errors during measurement and (b) constant temperature sensor calibration error.

TEMPERATURE-COMPENSATED RESONATORS

For practical demonstration of the system, it is necessary to have a minimum of three resonators demonstrating unique temperature dependence of frequency. Here we choose to use a coupled-ring or 'dogbone' resonator for their suitable characteristics [6]. Figure 3 shows a schematic of the resonator and highlights the location of the silicon dioxide islands used to achieve the temperature compensation. By moving this oxide across the width of the ring we can achieve a fine control over the resonator turnover temperature [7].

Figure 4 plots the simulated turnover temperature as a function of 'edge' spacing and shows that the turnover temperature is a strong function of the location of oxide. Using this approach we can tune the turnover temperature from -20 °C to +80 °C through lithography variations across the same die. No process modifications are necessary to achieve these different temperature profiles. The fabrication process flow is shown in Fig. 5.

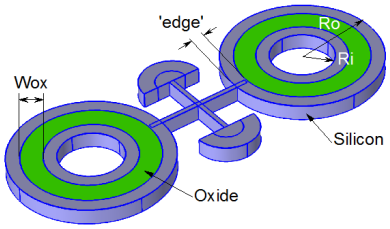

Figure 3: Schematic of a temperature-compensated coupled-ring or 'dogbone' resonator. By changing the spacing between the oxide island and the resonator boundary, we can control the turnover temperature.

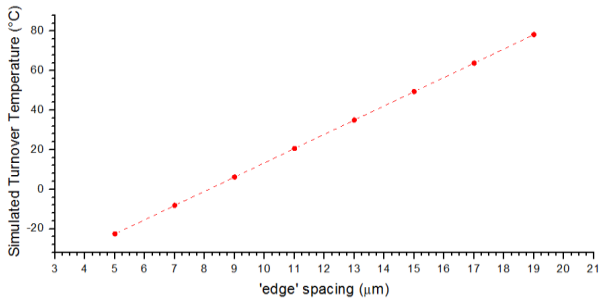

Figure 4: Simulated turnover temperature as a function of 'edge' spacing. By moving the oxide islands towards the center of the rings, the turnover temperature can be changed from -20 °C to +80 °C.

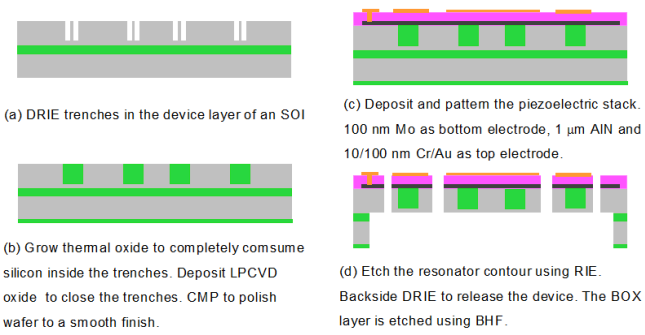

Figure 5: Process flow used to fabricate the 'dogbone' resonators [5].

Figure 6 shows two SEM images of a fabricated 'dogbone' resonator. The refilled oxide along with the 'edge' spacing can be clearly identified in Fig. 6(b). Figure 7 shows the measured frequency response of an uncompensated and a temperature-compensated ring resonator. A small degradation in the measured quality factor (Q) is noted due to the presence of the oxide islands.

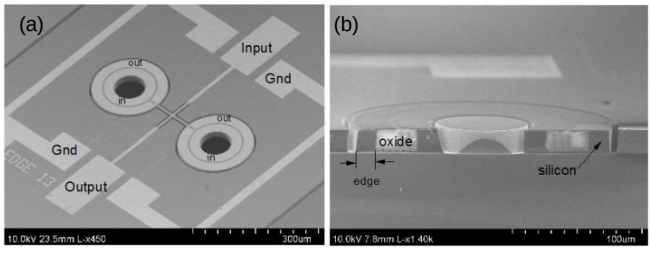

Figure 6: (a) Top SEM view of a fabricated coupled ring resonator. (b) Cross-section view showing the oxide islands within the silicon body.

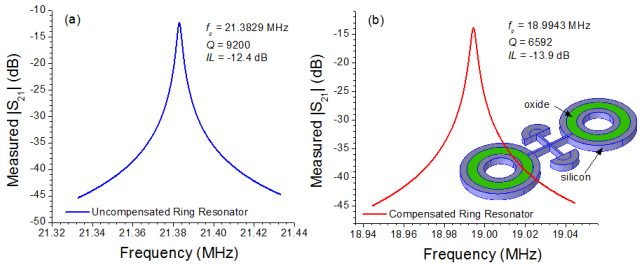

Figure 7: Measured frequency response of (a) an uncompensated and (b) a temperature-compensated ring resonator. The compensated ring resonator has an 'edge' spacing of 17 μm.

The temperature dependence of four temperature-compensated resonators is measured in a cryogenic probe station and is plotted in Fig. 8. Figure 8 includes two sets of measurements carried on the same devices. These results are utilized later to analyze the effect of measurement induced error on the clock output.

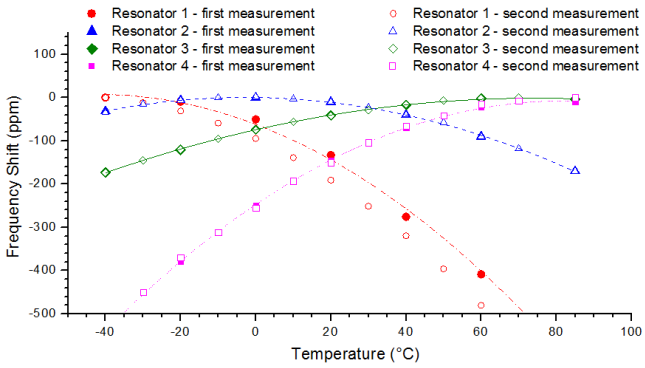

Figure 8: Measured frequency shift for four temperature-compensated ring resonators. All four resonators have the same volume of oxide but oxide trenches are placed 7 μm, 13 μm, 17 μm, and 19 μm from the edge. Refer to Fig. 3 and Fig. 6(b) for definition of 'edge'.

CLOCK OUTPUT

From the measured temperature induced frequency drift, we can extract using best fit to (1), the coefficients a, b and c for the four resonators. Table 1 summarizes these numbers for the resonators presented in Fig. 8 (first measurement).

Table 1. Extracted coefficients a, b and c for the best fit to first measurement of the four resonators shown in Fig. 8.

edge (μm)	Measured Turnover temperature (°C)	Fitted coefficients		
		a	b	c
7	-30	-0.000391	-73.704291	19,737,789
13	0	-0.190434	96.863662	19,561,079
17	65	-0.296843	203.868377	19,425,545
19	85	-0.663465	475.433541	19,251,377

Taking the extracted coefficients in Table 1 for Resonators 2, 3 and 4 from Fig. 8, we can calculate k_1 to be -0.4979, k_3 as -1.3202 and k_{12} as -0.9041. Using the extracted k numbers, the output of the proposed system can be estimated using (5) and is plotted in Fig. 9. In order to evaluate the applicability of the one-time calibration, the same devices are measured against temperature a second time with the result

plotted in Fig. 8 using hollow symbols. The three lines in Fig. 9 represent the ideal clock output (solid line - no symbol) assuming the measured data exactly lies along a second-order polynomial, estimated clock output (dotted line - circle) using the first measurement data and the estimated clock output (dash dot - diamond) using the second set of measured data in Fig. 8. For both measurement sets, the temperature sensitivity of frequency is less than 10 ppm across -40 ° C to 85 °C.

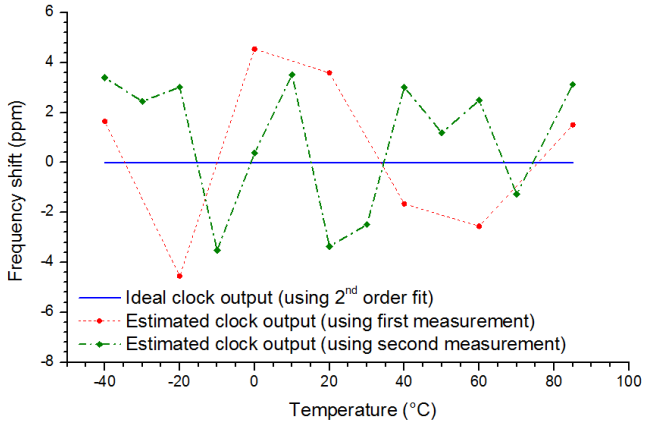

Figure 9: Relative frequency shift of the multi-resonator clock output (with Resonators 2, 3, and 4 in Fig. 8) in parts per million (ppm) as a function of temperature with first measurement (filled circles) and second measurement (filled diamonds). The estimated error of ~ 10 ppm is due to the resonator frequency deviating from the ideal parabolic dependence on temperature. The solid line (no symbols) represents the ideal clock output assuming no deviation from pure second-order temperature dependence for the three resonators.

In order to evaluate the effect of calibration on the output of the multi-resonator clock if the calibration is not performed properly, the same analysis is repeated using Resonators 1, 2 and 3. As shown in Fig. 8, during the second temperature sweep, Resonator 1 was seen to have a relatively large shift in its frequency-temperature relation indicating measurement induced errors. Figure 10 plots the estimated clock output using resonators 1, 2, and 3 as the frequency inputs. The k values for this estimation were calculated from the first measurement in Fig. 8 for the same three devices (k_1=-0.4751; k_3=1.3142; k_{12}=3.8657). As can be estimated from (10), the error in the two measurements for Resonator 1 leads to a second-order temperature dependence of the clock frequency output. Thus, achieving a temperature-stable clock output will necessitate use of stable resonators with repeatable frequency-temperature characteristics and a measurement setup capable of its accurate estimation.

CONCLUSIONS

We report on a novel approach to enable temperature-stable frequency references for potential applications in navigation and time keeping. This system consists of multiple temperature-compensated resonators each having a unique temperature dependence of frequency. The system is analyzed for its sensitivity to measurement errors and the effects of such errors on the clock output have been quantified.

AlN-based piezoelectrically actuated and temperature-compensated ring resonators are used as a proof of concept for the proposed system. Using the proposed algorithm, we showed the compensated clock has a total temperature induced frequency shift of ~ 10 ppm across a wide temperature range of -40 °C to +85 °C. Compared to the performance of the individual resonators we note a ~20× reduction in the total temperature induced frequency drift.

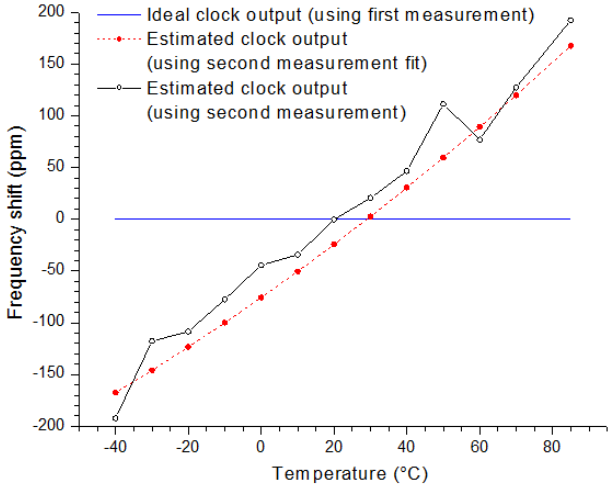

Figure 10: Relative frequency shift of the multi-resonator clock output (with Resonators 1, 2 and 3) in ppm as a function of temperature for three cases: (a) Ideal clock output using the fit to first measurement in Fig. 8. (b) Estimated clock output using the fit to second measurement. The error is due to the shift in the turnover characteristics of Resonator 1 between the first and second measurement. (c) Estimated clock output using the actual measured freqeuncy vs. temperature characteristics from the second measurement in Fig. 8.

ACKNOWLEDGEMENT

This work is supported by NASA under the Chip-Scale Precision Timing Unit project (Grant #NNX12AQ41G).) The authors acknowledge the support of the staff of the Lurie Nanofabrication Facility (LNF) at University of Michigan for their help with device fabrication.

REFERENCES

[1] R. Tabrizian, G. Casinovi and F. Ayazi, "Temperature-stable high-Q AlN-on-silicon resonators with embedded array of oxide pillars," *Hilton Head '10*, Hilton Head Island, SC, pp. 479-482, June 2010.

[2] H. Lee, A. Partridge, and F. Assaderaghi, "Low jitter and temperature stable MEMS oscillators," *IEEE IFCS*, Baltimore, MD, pp.1-5, May 2012.

[3] R. Melamud, *et al.*, "Temperature-compensated high-stability silicon resonators," *Appl. Phys. Lett.*, vol. 90, no. 24, pp. 244107, Jun. 2007.

[4] V. Thakar, Z. Wu, A. Peczalski, and M. Rais-Zadeh, "Piezoelectrically transduced temperature-compensated flexural-mode silicon resonators," *IEEE/ASME Journal of MEMS*, Vol. 22, No. 3, pp. 819-823, 2013.

[5] V. Thakar, Z. Wu, C. Figueroa and M. Rais-Zadeh, "A temperature-stable clock using multiple temperature-compensated micro-resonators," *IEEE IFCS '14*, Taiwan, accepted (in press).

[6] Z. Wu, *et al.*, "Piezoelectrically transduced high-Q silica micro resonators," *IEEE MEMS '13*, Taipei, Taiwan, pp.122-125, Jan. 2013.

[7] V. A. Thakar and M. Rais-Zadeh, "Temperature-Compensated piezoelectrically actuated Lamé-mode resonators," *IEEE MEMS '14*, San Francisco, pp. 214-217, Jan. 2014.

CONTACT

*Vikram Thakar, tel: +1-734-355-3480; thakar@umich.edu

NON-AXISYMMETRIC CORIOLIS VIBRATORY GYROSCOPE WITH WHOLE ANGLE, FORCE REBALANCE, AND SELF-CALIBRATION

A.A. Trusov[1], D.M. Rozelle[1], G. Atikyan[1], S.A. Zotov[2], B.R. Simon[2], A.M. Shkel[2], A.D. Meyer[1]
[1]Northrop Grumman Corporation, USA
[2]University of California, Irvine, USA

ABSTRACT

This paper presents detailed performance status and projections for the silicon MEMS Quadruple Mass Gyroscope (QMG) – a unique high Q, lumped mass, mode-symmetric Class II Coriolis Vibratory Gyroscope (CVG) with interchangeable whole angle, self-calibration, and force rebalance mechanizations. Analysis of a QMG sealed without getter with a Q-factor of 1e3 reveals an Angle Random Walk (ARW) of 0.02 deg/rt-hr limited only by the fundamental Mechanical-Thermal Noise (MTN). Propagation of a detailed noise model to a QMG sealed with getter at a Q-factor of 1e6 (previously demonstrated) showed better than Navigation Grade ARW of 0.001 deg/rt-hr. Combination of the very low ARW with the mode-symmetry enabled self-calibration substantiates the navigation grade performance capacity of the Si-MEMS QMG.

INTRODUCTION

Coriolis Vibratory Gyroscopes (CVGs) can be divided into two classes according to the nature of the two vibration modes involved, per the IEEE STD 1431 [1]. In the Class I, the two Coriolis force coupled modes are different. The main example of MEMS Class I CVG is the dual mass Tuning Fork Gyro (TFG), such as the Draper/Honeywell MEMS gyroscope and the majority of MEMS gyroscopes in the consumer electronics and automotive application space. Higher performance MEMS Class I CVGs, typically implemented as vacuum packaged high Q-factor dual mass tuning forks, have shown reasonable Angle Random Walk (ARW) and stability in low end (Honeywell) and medium performance (Northrop Grumman LITEF) tactical grade systems.

The classic dual TFG configuration offers several attractive features such as angular gain close to the maximal theoretical value of 1, increased modal mass and drive mode amplitude, and low dissipation of energy (Q>1e5, τ>1 second), Table I. However, the technology appears to have reached its fundamental limitation with bias uncertainty on the order of 1-10 deg/hr. Reduction of bias drift by 2-3 orders of magnitude would be necessary for these devices to approach gyrocompassing and navigation grade performance, which is highly unlikely, if not fundamentally impossible, with these mature architectures.

In the Class II CVG, the two modes are identical. Example configurations are the vibrating string, the vibrating prismatic (square) bar, the vibrating cylindrical and hemispherical shells, vibrating rings, and in fact the Foucault pendulum [1]. Unlike Class I devices, CVGs of the same-mode class can be operated in the whole-angle and self-calibration mechanizations. In the whole-angle mode, the Coriolis force resulting from input rotation is allowed to transfer energy freely between the two vibratory modes. The result (as in the Foucault pendulum) is that the change in the equivalent pendulum angle in any time interval is directly proportional to the total inertial angle the CVG has rotated through during that interval. The proportionality constant is called the angular gain, or Bryan's factor, of the CVG.

A unique enabling feature of Class II gyroscopes operated in rate measuring (or force rebalance) mode is the ability to arbitrarily place the drive-mode axis, or equivalently the pattern angle, by using proper controls. Detailed theoretical analysis predicts a change in the magnitude and polarity of the gyro bias as a function of drive axis orientation with respect to the fixed geometry of the gyro housing ("pattern angle"). By carouseling the pattern angle around the gyroscope structure, multiple error mechanisms are made observable, including frequency mismatch and misalignment, damping mismatch and misalignment, forcer and pickoff gain mismatch and misalignment, etc. Identification of these error sources through virtual carouseling (or a closely related technique called mode-reversal), enables the gyroscope system to self-calibrate bias and scale factor against device imperfections as well as variations of these imperfections throughout the lifetime of the instrument.

Table 1: Two classes of Coriolis Vibratory Gyroscopes.

IEEE STD 1431	Class I	Class II
Modal symmetry (not axial)	✘	✓
Whole angle, self calibraiton	✘	✓
Iimplementations	Lumpled masses	Ring, disk, shells in R&D
Angular gain, drive amplitude	✓	✘
Modal mass, time constant, Q	✓	✘
Examples	Draper/Honeywell TFG NG LITEF TFG	BAE/AIS/Goodrich/ UTC/ Silicon Sensing Vibrating Ring Gyro

Mature MEMS Class II CVGs are exemplified by the BAE/ AIS/ Goodrich/ UTC and Silicon Sensing vibrating ring gyroscope. While this Class II device is potentially capable of self-calibration, its performance is limited by relatively high ARW resulting from the low modal mass, low angular gain, and insufficient ringdown time constant. These fundamental limitations of existing micromachined Class II CVGs call for a new design paradigm, which is tailored to take advantage of the inherent strength of MEMS.

Since MEMS geometries are defined lithographically in a single step and do not require any assembly of parts, it is beneficial to pursue the use of complex mechanical designs with multiple moving parts in order to fulfill a dream device – a low cost batch micromachined silicon MEMS Class II CVG with stiffness and damping symmetry, Q-factors above 1 million and dissipation time constants of several minutes. Quadruple Mass Gyroscope (QMG), Figure 1, is a novel architecture [2] meeting these fundamental criteria with demonstrated low dissipation (Q>1e6 and τ>170 s when vacuum packaged with getter) and excellent modal symmetry (Δf<0.2 Hz, Δ(1/τ)<1e-4 Hz) [3,4].

This paper focuses on the performance analysis of a recently integrated fully closed loop, standalone gyro development system [5] using a QMG packaged without getter at a Q of 1e3 as well as detailed performance modeling and projections for the next generation, navigation grade system integrating a QMG transducer vacuum packaged with getter at a Q of 1e6.

9781940470016/HH2014/$25©2014TRF
DOI 10.31438/trf.hh2014.112

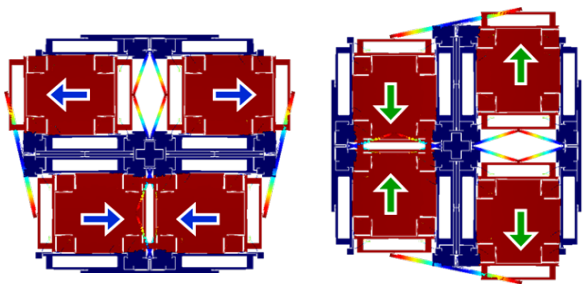

Figure 1: Quad Mass Gyroscope resonator FEM, showing the two identical mode-shapes characteristic of a Class II CVG. The QMG combines high angular gain, large drive amplitude, increased modal mass, and low dissipation advantages of MEMS tuning fork architectures with the mode-symmetry enabled stability, whole angle as well as self-calibration capabilities of Class II CVGs.

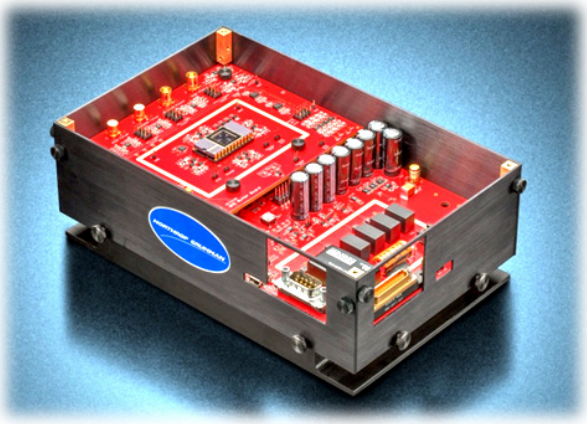

Figure 2: Photograph of the standalone CVG controls suite fully compatible with the DARPA PALADIN test platform. The bottom card is a flexible DSP/FPGA unit; the top card has analog signal conditioning. QMG in a ceramic DIP-24 with a glass lid is in the center of the top card. The system is adaptable to other CVGs through the top card interchange.

QUADRUPLE MASS GYROSCOPE TRANSDUCER

The optimal architecture of a high performance CVG comprises a mode-symmetric mechanical structure with a combination of very high Q-factor and decay time constant, high Coriolis coupling (angular gain), easy frequency tuning capability [6], and low cost batch manufacturing using established silicon MEMS processes. The QMG transducer, Figure 1, comprises four symmetrically decoupled tines synchronized into balanced anti-phase motion by outer and inner lever mechanisms, providing a unique combination of ultra-low energy dissipation due to the elimination of anchor loss and isotropy of both the resonant frequency and damping [2-5]. The use of anti-phase levers instead of conventional spring flexures enables a relatively low operational frequency of several kHz, while pushing parasitic in-phase modes to higher stiffness for common mode acceleration rejection [7].

STANDALONE GYROSCOPE SYSTEM

A fully closed loop and standalone turnkey electronics suite was developed to support experimental testing and performance analysis of the QMG, Figure 2. The suite integrates a packaged MEMS transducer with an analog signal conditioning card and a digital control card in a single unit compatible with DARPA Platform for Acquisition, Logging, and Analysis of Devices for

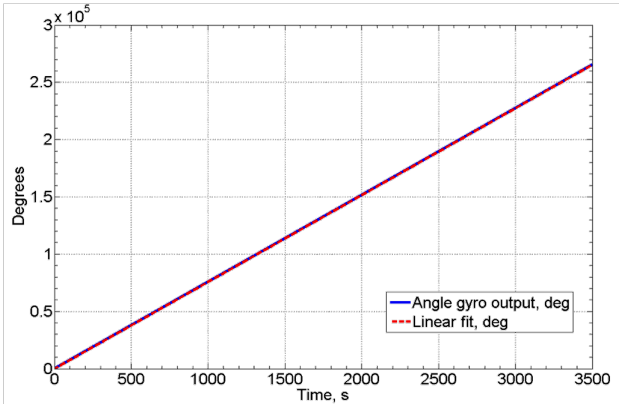

(a) Whole angle mechanization QMG output in degrees vs. time during a 100 deg/s rotation for 1 hour for a total of 0.3 million degrees, showing excellent linearity and stability.

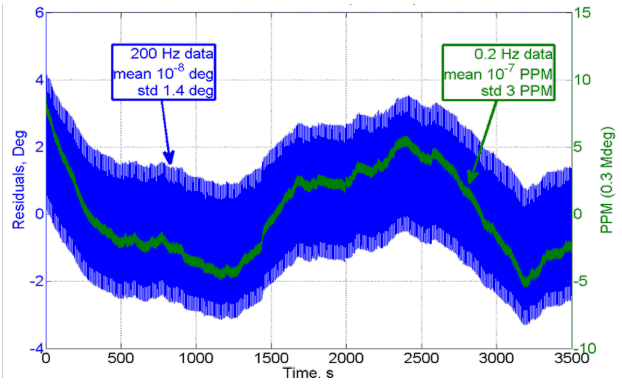

(b) Angle data linear fit residuals, showing 3 ppm stability.

Figure 3: Whole angle demonstration using a fully closed loop QMG. The gyroscope was rotated at a 100 deg/s rate for 1 hr, showing excellent 3 ppm scale factor stability despite low Q packaging without getter

Inertial Navigation (PALADIN). CVG control firmware running on the digital board implements the four primary servo loops: (1) drive amplitude, (2) drive frequency PLL, (3) sense Coriolis force rebalance, (4) sense quadrature. Additionally, the drive axis or the pattern angle can be (1) locked to a prescribed orientation for force rebalance operation, (2) allowed to precess in response to rotation for whole angle operation, or (3) commanded to slew at a prescribed rate for virtual carouseling or self-calibration.

WHOLE ANGLE AND SELF-CALIBRATION

A QMG with an operational frequency of 3047 Hz, as-fabricated frequency mismatch of 0.15 Hz, and a Q of 1e3 (vacuum sealed without getter) was integrated and characterized in all three mechanization modes: whole angle, self-calibration or virtual carouseling, and force rebalance rate mode. Switching between the modes is done by sending a command to the digital board through a computer GUI and does not require any hardware changes or adjustments.

To characterize operation of the whole angle mode, the gyroscope system was rotated at constant rates of ±100 deg/s for 1 hour. The data, shown in Figure 3, revealed a constant angular gain of 0.75 which agrees well with analytical modeling of the effect of the shuttle mass [3, 4]. Analysis of the linear fit to the angle data showed scale factor stability of 3 ppm, showcasing one of the inherent advantages of the whole angle mechanization of Class II

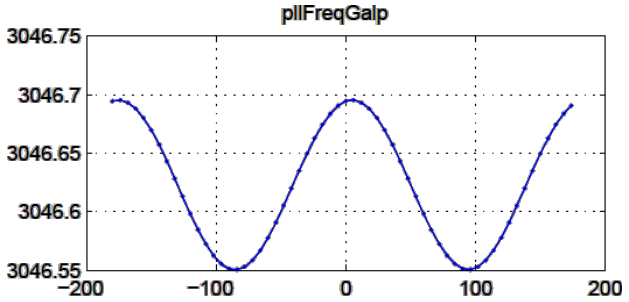

(a) Frequency in Hz vs. pattern angle in deg observing a 0.15 Hz native mismatch and nearly perfect alignment of axes.

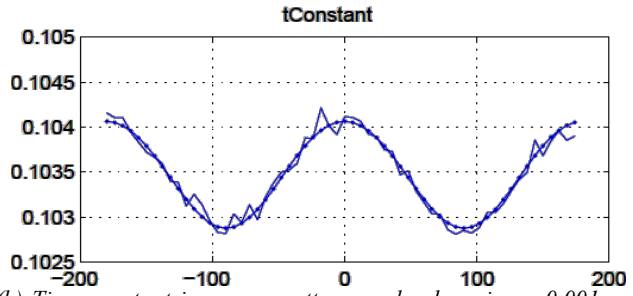

(b) Time constant in sec vs. pattern angle observing a 0.001 sec variation (Δ(1/τ) of 0.1 Hz), and perfect alignment of axes.

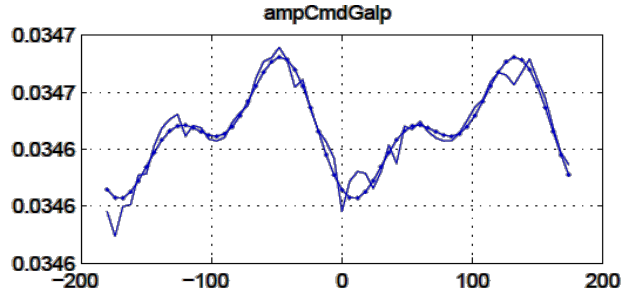

(c) Drive amplitude command vs. pattern angle observing second and fourth harmonic variation due to the imperfections in micromachined electrostatic forcers and pickoffs.

Figure 4: Demonstration of self-calibration using virtual carouseling of the Pattern Angle (PA). Mismatches and misalignments in frequency, damping, and gains are made observable as functions of pattern angle, enabling elimination of contributions to bias using D.D. Lynch models.

CVG. It should be noted that the gyroscope is successfully operated in whole angle mechanization despite the relatively low dissipation time constant of 0.1 seconds through closed loop energy control and pattern angle tracking.

Self-calibration is a closely related mechanization which uses virtual carouseling as opposed to Coriolis induced precession of the whole angle mode. Closed loop controlled slewing of the pattern angle is commanded and control signals in the gyroscope loops are observed as functions of the pattern angle, as illustrated in Figure 4. As a result virtual carouseling, mismatches and misalignments of stiffness and gains are identified in the nominally symmetric gyroscope. In addition, a ringdown measurement is automatically conducted at multiple equally spaced pattern angle orientations, making the damping mismatch and misalignment observable as well. The procedure allows self identification of these individual imperfections and enables elimination of their respective bias contributions using the math models developed by D.D. Lynch for Class II CVGs such as the HRG and the QMG.

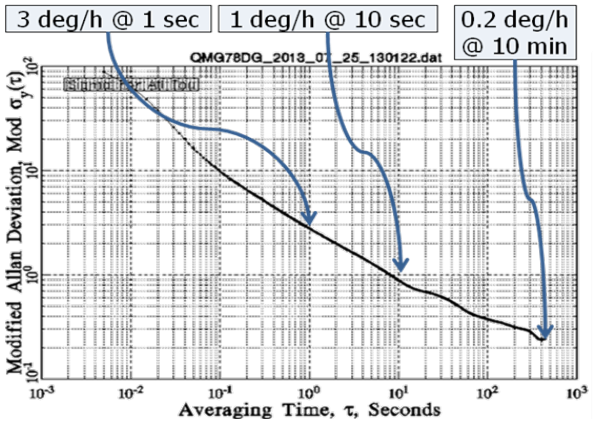

Figure 5: Modified Allan deviation of force rebalance operated QMG sealed without getter at a Q of 1e3 showing 0.05 deg/rt-hr ARW and 0.2 deg/hr bias instability. The gyroscope full scale is 1350 deg/s, providing a dynamic range of 147 dB by virtue of digital force rebalance.

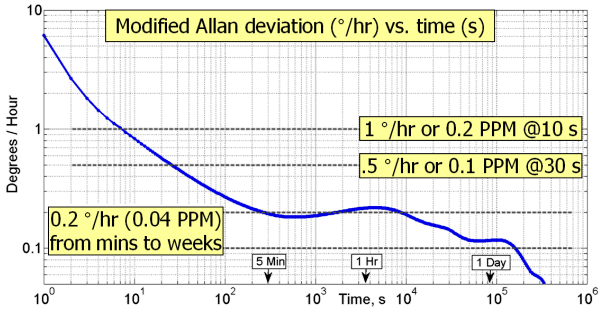

Figure 6: Modified Allan deviation in deg/hr vs. integration time in seconds. Half a month long in-run experiment demonstrating 0.2 deg/hr stability over several weeks using a QMG transducer packaged without getter at a Q of 1e3. Self-calibration against drifts using PLL and quadrature feedback loop command signals was employed.

FORCE REBALANCE RATE MODE

Experiments in the force rebalance rate measuring mode demonstrated a full scale of 1350 deg/s, a typical ARW of 0.02 to 0.05 deg/rt-hr, and a bias instability of 0.2 deg/hr or 0.05 ppm of the full scale, Figure 5. Characterization over power and temperature cycles showed excellent repeatability on the order of deg/hr, currently limited by the ARW imposed measurement accuracy. A half-month long in-run experiment was performed to assess the long term stability of the standalone gyro system, Figure 6. Self-calibration using the PLL and quadrature feedback loop command signals was employed [8,9]. The data demonstrates excellent stability of 0.2 deg/hr for integration times spanning from several minutes to several weeks (limited by the duration of the conducted experiment) with no discernible upward trend in the Allan deviation curve. This is attributed to the symmetry and mechanical stability of the QMG transducer as well as the advantages of digital closed loop gyro operation and self-calibration.

PERFORMANCE ANALYSIS AND PROJECTIONS

The gyro in-run performance and the effectiveness of self-calibration against long term drifts are limited by the gyro signal-to-noise ratio or the ARW. It is thus critical to investigate the ARW governing mechanisms in the current gyro and analyze their

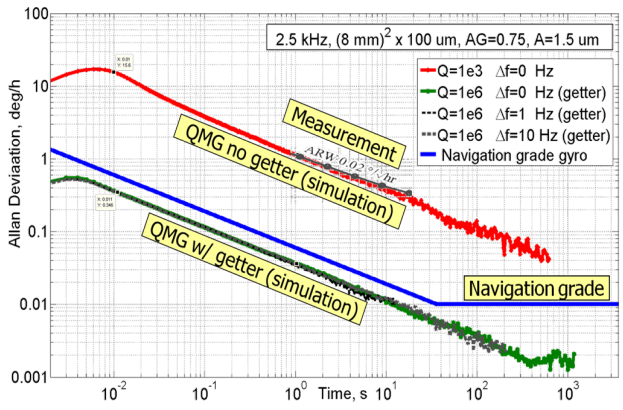

Figure 7: Mechanical-Thermal Noise in QMG, illustrating the effects of vacuum packaging, quality factor, frequency mismatch, and closed loop operation.

scaling in the future QMGs vacuum packaged with getter. The best ARW measured on the tested QMG transducer packaged without getter at a Q of 1e3 was on the order of 1 deg/hr/rt-Hz or 0.02 deg/rt-hr, Figure 7. Mechanical-Thermal Noise (MTN) is a known fundamental noise mechanism caused by the Brownian motion of the sense-mode appearing in the gyro output as ARW [10]. A detailed study of MTN scaling in the QMG as function of the quality factor and thus packaging conditions was conducted starting from the analytical formulas derived in [10] and verified and extended using direct numerical simulations of closed loop gyro dynamics with frequency mismatch imperfections under stochastic inputs. The MTN ARW for the gyroscope is

$$\frac{1}{\sqrt{4}}\frac{1}{A_G}\frac{1}{A}\sqrt{\frac{K_B T}{MQw}}\left(\frac{180}{\pi}\times 3600\right) \quad \text{deg/hr/rt-Hz,} \qquad (1)$$

Here, AG=0.75 is the gyro angular gain, A=1.5e-6 m is the drive mode amplitude, M=1.7e-6 kg is the modal mass of one tine, Q=1e3 to 1e6 is the sense-mode quality factor, and w=2*pi*2.5e3 is the sense-mode resonant frequency. Additionally, the $1/\sqrt{4}$ coefficient in front of the formulas is to account for the four statistically independent tines, T=300 K is the normal operating temperature, and KB is the Boltzmann constant.

To investigate the effect of frequency mismatch and Q on MTN ARW, a detailed Simulink model was developed and tested featuring a sense-mode dynamics, Coriolis and quadrature channels, demodulation, proportional-integral rebalance loops for both the Coriolis force and quadrature channels, a rate input, and wide bandwidth stochastic MTN force input. The gains of the sense-mode feedback loops were configured to provide a gyro measurement bandwidth on the order of 100-200 Hz independent of the open loop gyro Q factor. After each simulation run, a several hour long time history of the gyro output in deg/hr at a data rate of 1 kHz was produced and analyzed using Allan deviation, Figure 7.

The model was first executed for a QMG with a Q of 1e3 and a zero mismatch between the drive- and sense-mode frequencies. As the red curve in Figure 7 shows, the simulation outcome of 1 deg/hr/rt-Hz ARW is indistinguishable from both the theoretical prediction of ARW using (1) as well as the best measured data, shown as gray circles. This result validates the numerical simulation approach and reconfirms MTN limited performance of the current QMG packaged without getter at a Q of 1e3. In the following simulation runs the Q value was update to 1e6 representative of a getter packaged QMG, previously demonstrated in [11]. The frequency mismatch was set to 0 Hz, 1 Hz, and 10 Hz, shown as the green, black, and gray lines in Figure 7.

The simulation data reveals two very important observations. Firstly, the mismatch between drive- and sense-mode frequencies has no effect on MTN as long as the sense-mode dynamics is kept under Coriolis force feedback and quadrature nulling closed loop control. This allows very low noise operation of high Q MEMS gyros without requiring a perfect matching of resonant frequencies by virtue of feedback system. Secondly, operation of the current QMG at a Q of 1e6 using getter packaging is shown to yield a navigation grade ARW of 0.03 deg/hr/rt-Hz or 0.0005 deg/rt-hr. The 30 fold improvement of the ARW also translates into a proportional improvement in the gyro bias and scale factor self-calibration performance.

ACKNOWLEDGMENT

The authors thank Dr. Gunjana Sharma for help with MEMS fabrication, Philip R. Clark for the electronics design, James Pavell for help with test hardware design, and Mark R. Phillips for the software development. The MEMS gyroscope resonators were designed, fabricated, and packaged at the University of California, Irvine. The electronics design, DSP firmware and PC software development, integration, test, and analysis were performed at the Northrop Grumman Corporation Woodland Hills, CA campus in the Advanced Sensor and Instrument Development organization. This work was supported by DARPA Micro-PNT PASCAL project N66001-12-C-4035, program manager Dr. Robert Lutwak.

REFERENCES

[1] IEEE Standard "Specification Format Guide and Test Procedure for Coriolis Vibratory Gyros," IEEE Std 1431-2004 , vol., no., pp.1,78, Dec. 20 2004.

[2] A.A. Trusov, A.R. Schofield, A.M. Shkel, "Micromachined Tuning Fork Gyroscopes with Ultra-High Sensitivity and Shock Rejection," US Patent 8,322,213.

[3] A.A. Trusov, I.P. Prikhodko, S.A. Zotov, A.M. Shkel, "Low-Dissipation Silicon MEMS Tuning Fork Gyroscopes for Rate and Whole Angle Measurements," IEEE Sensors J., vol. 11, no. 11, pp. 2763-2770, Nov. 2011.

[4] I.P. Prikhodko, S.A. Zotov, A.A. Trusov, A.M. Shkel, "Sub-Degree-per-Hour Silicon MEMS Rate Sensor with 1 Million Q-Factor," Transducers 2011.

[5] A.A. Trusov, D.M. Rozelle, G. Atikyan, B.R. Simon, S.A. Zotov, A.M. Shkel, A.D. Meyer, "Force Rebalance, Whole Angle, and Self-Calibration Mechanization of Silicon MEMS Quad Mass Gyro," IEEE ISISS 2014.

[6] K. Shcheglov, "DRG - a High Performance MEMS Gyro," Joint Precision Azimuth Sensing Symposium 2010.

[7] B.R. Simon, A.A. Trusov, A.M. Shkel, "Anti-Phase Mode Isolation in Tuning-Fork MEMS Using a Lever Coupling Design," IEEE Sensors 2012.

[8] D.M. Rozelle, "The Hemispherical Resonator Gyro: From Wineglass to the Planets," 19th AAS/AIAA Space Flight Mechanics Meeting 2009.

[9] S.A. Zotov, B.R. Simon, G. Sharma, A.A. Trusov, A.M. Shkel, "Utilization of Mechanical Quadrature in Si-MEMS Gyro to Increase and Expand Long Term In-Run Bias Stability," IEEE ISISS 2014.

[10] R. Leland, "Mechanical-thermal noise in MEMS gyroscopes," IEEE Sensors J., vol. 5, no. 3, pp. 493–500, Jun. 2005.

[11] S.A. Zotov, A.A. Trusov, A.M. Shkel, "High-Range Angular Rate Sensor Based on Mechanical Frequency Modulation," IEEE/ASME JMEMS, vol. 21, no. 2, pp. 398-405, April 2012.

CONTACT

*A.A. Trusov, alex.trusov@gmail.com

POORER Q GIVES BETTER MASS SENSITIVITY: RECONSIDERING DYNAMIC RANGE IN OPTOMECHANICALY TRANSDUCED NEMS DEVICES

W.K. Hiebert[1,2], S.K. Roy[1,2], and V.T.K. Sauer[1,2]*
[1]National Institute for Nanotechnology, NRC Canada, Edmonton, Alberta, Canada
[2]University of Alberta, Edmonton, Alberta, Canada

ABSTRACT

We demonstrate that reduced mechanical quality factor can lead to improved frequency stability and mass sensitivity in a nano-optomechanical device. We measure the dynamic range and Allan deviation of frequency fluctuations in a phase-locked NEMS device at different pressures and quality factors, including at atmospheric pressure. As quality factor decreases, dynamic range increases and Allan deviation improves. Key to this improvement is that the dynamic range in vacuum and in 6 Torr pressure is limited only by the mechanical Duffing nonlinearity and the thermomechanical noise floor. This allows a fractional frequency stability of part per billion and a mass sensitivity in the zeptogram range for operation in 6 Torr pressure. These results open the door toward use of ultrasensitive NEMS devices in gas, liquid, and other low-Q environments.

INTRODUCTION

NEMS are well-known for achieving incredible results in terms of mass sensitivity with single molecule [1], even single Da sensitivity levels [2,3]. Transducing these tiny devices at all, let alone taking advantage of the full dynamic range (DR), is an extraordinary challenge [4]. Optomechanical transduction [5] has recently been shown to be very promising for conserving DR while size-down-scaling [6]. Particularly, it offers exquisite displacement sensitivity to nanomechanical motions, reaching into the attogram per root Hertz range [7]. This sensitivity level allows easily achieving thermal noise limited operation in a wide variety of conditions (high Q or low Q) and device size regimes. Further, the design freedom to tune optomechanical coupling strength allows full control over the linear operation range of the transduction. Together, these attributes make optomechanical readout perfectly suited for accessing the full intrinsic DR of NEMS devices.

This full intrinsic DR has seldom been accessed in state-of-the-art sized NEMS devices of sub-micron cross-sectional dimensions and few micron lengths. In such devices, while the upper end of the DR is often accessible (represented by the Duffing nonlinearity) [8], normally, the noise floor is set by instrumentation noise levels [4]. These levels remain unchanged during device size down-scaling or changes in Q-factor and pose a serious problem for transducing small, low-Q NEMS mechanical resonances. As mentioned above, this problem is obviated when transducing with optomechanics.

Using the platform of state-of-the-art optomechanical NEMS devices, we look at the dependence of DR and mass sensitivity on mechanical quality factor (Q) and measurement bandwidth. We find the surprising result that *poorer mechanical quality factor leads to better mass sensitivity* when the intrinsic DR is maximized. We confirm this experimental finding in deriving the DR dependence on Q. This result opens the door to ultrasensitive sensing in gas, liquid, or other low-Q environments.

BACKGROUND AND THEORY

The conventional picture of improving sensitivity with resonant micromechanical devices and the importance of DR was discussed in [4] (see Figure 1). In an ideal case, the resonator is driven close to a nonlinearity limit, such a Duffing nonlinearity

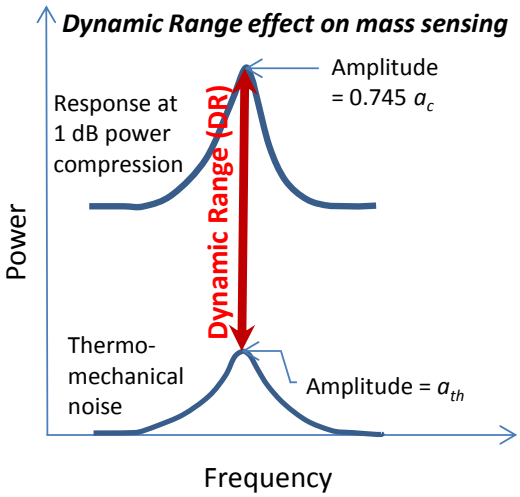

Figure 1. The intrinsic dynamic range of a resonant nanomechanical system. Upper limit is set by the onset of nonlinearity. Lower limit is set by the thermomechanical noise.

(specifically, to an amplitude where 1 dB power compression is observed) and the thermomechanical (TM) noise is resolvable. The DR represents the dB difference in power levels of these two extremes. The equation for the rms critical amplitude a_c at the top end of the range in doubly clamped beams is [9]:

$$a_c = \frac{\sqrt{2}\,d}{\sqrt{3Q\sqrt{3}}} \qquad (1)$$

where d is the thickness of the NEMS device in direction of motion and Q is the mechanical quality factor. The equation for the amplitude at the bottom end of the range a_{th} is the thermal noise:

$$a_{th} = {S_X}^{1/2}\Delta f^{1/2} = \left(\frac{4k_B TQ\Delta f}{M_{eff}{\omega_0}^3}\right)^{1/2} \qquad (2)$$

where k_b is Boltzmann's constant, T is the Temperature, Δf is measurement bandwidth, M_{eff} is the effective mass of the resonator, and ω_0 is 2π times the resonance frequency f. The DR in dB is defined explicitly as:

$$DR(dB) = 20\log\left(\frac{0.745a_c}{a_{th}}\right) \qquad (3)$$

The fractional frequency stability $\delta f/f$ (and mass sensitivity) improves when increasing DR according to the following relationship [4]:

$$\frac{1}{2}\frac{\delta m}{M_{eff}} = \frac{\delta f}{f} \approx \left(\frac{\Delta f}{Q\omega_0}\right)^{1/2} 10^{(-DR/20)} \qquad (4)$$

A closer examination of equations (1) to (4) reveals a very intriguing relationship. For the upper end of the DR the Duffing nonlinearity leads to a $Q^{-1/2}$ dependence of the critical amplitude (from (1)). On the bottom end of the DR, the displacement noise leads to a $Q^{+1/2}$ dependence (from (2)). Together, these relationships imply that *the DR can be **increased** at both ends by **reducing** the quality factor of the resonator*. Explicitly, if mass,

9781940470016/HH2014/$25©2014TRF
DOI 10.31438/trf.hh2014.113

temperature, and resonance frequency remain the same, substituting (1) and (2) into (3) implies:

$$DR(dB) = 20\log\left(\frac{\xi}{Q\,\Delta f^{1/2}}\right) \qquad (5)$$

where ξ is a constant. In essence, as long as more drive power is available, a poorer Q device can be driven to larger amplitude than a better Q one can. Similarly, the TM noise on resonance is suppressed in the poorer Q device compared with the better Q one, and this can be taken advantage of as long as enough transduction sensitivity is available to resolve the lower noise floor. When applying these findings to the $\delta f/f$ (or mass sensitivity) relationship (equation (4)), one finds that:

$$\delta m \propto Q^{1/2}\,\Delta f \qquad (6)$$

Amazingly, the mass sensitivity level becomes smaller (better) for poorer Q.

DEVICE FABRICATION AND EXPERIMENT

A racetrack resonator optical cavity structure is used to detect the nanomechanical motion of the doubly-clamped beam [10]. The 220 nm Silicon on Insulator devices are fabricated by a photonic foundry (IMEC) and NEMS devices are released by post-processing at the University of Alberta Nanofab. The NEMS are designed to be narrower than the photonic lines, facilitating a maskless release step wherein the NEMS are released without releasing the photonic elements. The NEMS are coupled laterally to the photonic elements and are contained in the same device layer. Further description of the fabrication can be found in [10]. A SEM picture of the device studied in this paper is shown in Fig. 2(a).

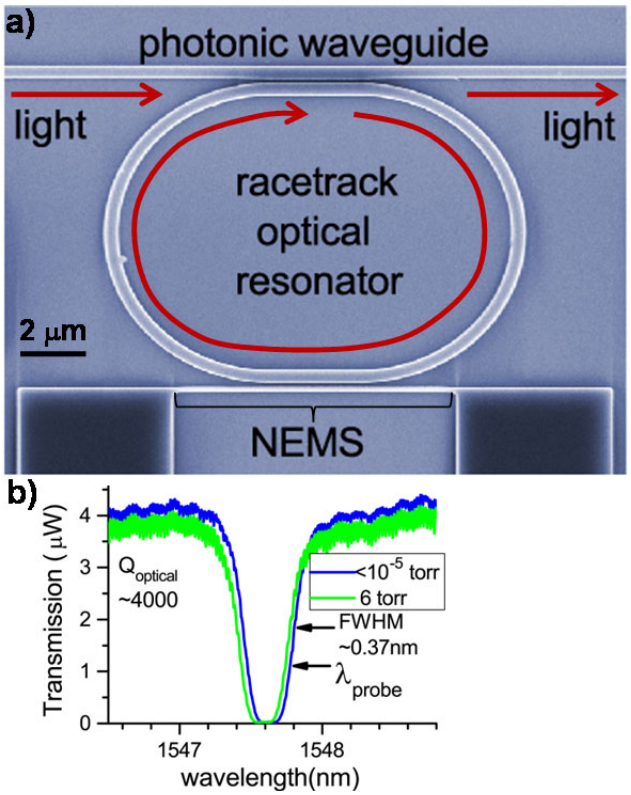

Figure 2. (a) Annotated scanning electron micrograph of the nano-optomechanical device of dimensions 8.75 μm x 160 nm x 220 nm. The gap between racetrack and NEMS is 130 nm. (b) Optical resonance at high vacuum and 6 Torr. The probe wavelength sits at a large slope in the transmission vs wavelength in order to transduce NEMS vibrations into optical power modulations.

The devices are driven by a sheer piezo actuating the chip and interrogated using a free-space confocal lens system to couple light to on-chip grating couplers [11]. NEMS motions are transduced by their interaction with the evanescent field of the light in the optical racetrack. Essentially, NEMS motion modulates the wavelength of the optical cavity resonance. Setting a laser probe wavelength on the steep side slope of an optical resonance translates that modulation into optical transmission power modulation (see Fig. 2(b)). This optical power modulation is read out by photodiode to ultimately give a voltage modulation that is directly proportional to the NEMS displacement. Further details of the experiment can be found in [6], [10], and [11].

RESULTS

In order to demonstrate the dependence of the dynamic range on Q (equation (5)), we measure the properties of the same device at different pressures. In particular, as we change the pressure from high vacuum (~10^{-5} Torr), to 6 Torr, to 760 Torr, the quality factor drops by two orders of magnitude. This method has the benefit of keeping all other parameters that could affect the result precisely identical. The primary results are displayed in Fig. 3.

At each pressure, the thermomechanical noise is measured and plotted on the same voltage axis (for a 1 Hz bandwidth). Of particular note is how the noise floor peak diminishes as the pressure increases (and the Q decreases). This is consistent with equation (2) and can be conceptually understood in the following way. The area under the TM resonance curve is conserved for a given Temperature. As the width of the resonance curve increases (i.e. Q decreases), the peak of the TM curve must drop in order to compensate. The TM curve is so wide by 760 Torr, it looks flat on the right most plot (the inset shows a wider field of view of the atmospheric TM noise). The reduction in Q from high vacuum to 6 Torr is about a factor of 3. This should imply a reduction of $\sqrt{3}$ in peak height. The actual peak height is reduced by a full factor of 3. Slight differences in displacement to voltage responsivity could explain part of this discrepancy. From 6 Torr to 760 Torr, Q_{TM} drops by 40x. We thus expect a drop in peak height by about 6x and this is what is observed.

The upper portion of Fig. 3 shows frequency sweeps of the resonance with increasing powers in order to find the limit of nonlinearity. For vacuum and 6 Torr, the nonlinearity is consistent with a Duffing nonlinearity. The 1 dB compression curve is noted in bold (red) in each case and $a_{crit} = 0.745\ a_c$ is marked. Again, of note here is how the value for a_{crit} increases moving from lower pressure to 6 Torr. A fit of Lorentzians to the critical sweep gives Q-factors for the two strongly driven cases. There are slight changes to the Q-factor in comparison to the TM noise derived Qs and the ratio is now around 2.4x. We thus expect an increase in a_{crit} of $\sqrt{2.4}$ or about 1.5x, and this is roughly what is observed.

Overall, the Q effects on the ends of the linear range lead to a 4x increase in the linear range or a 12 dB increase in the DR from 54 dB to 66 dB, when moving from high vacuum to 6 Torr.

The atmospheric pressure curve (right-hand side) of Fig. 3 has additional information to add to the story. The TM noise changes as expected compared to 6 Torr, however, the nonlinearity encountered is no longer a Duffing nonlinearity. Instead, a rather complex nonlinear response is evident at these very high drive powers in atmospheric pressure. More will be discussed about this in the context of Fig. 5. In any case, it is understandable that the trend of increasing a_{crit} no longer continues since other nonlinearities come into play before Duffing is encountered. It is important to note that the DR at atmospheric pressure is still better than that at high vacuum. This bodes very well for devices operating as gas sensors at atmospheric pressure.

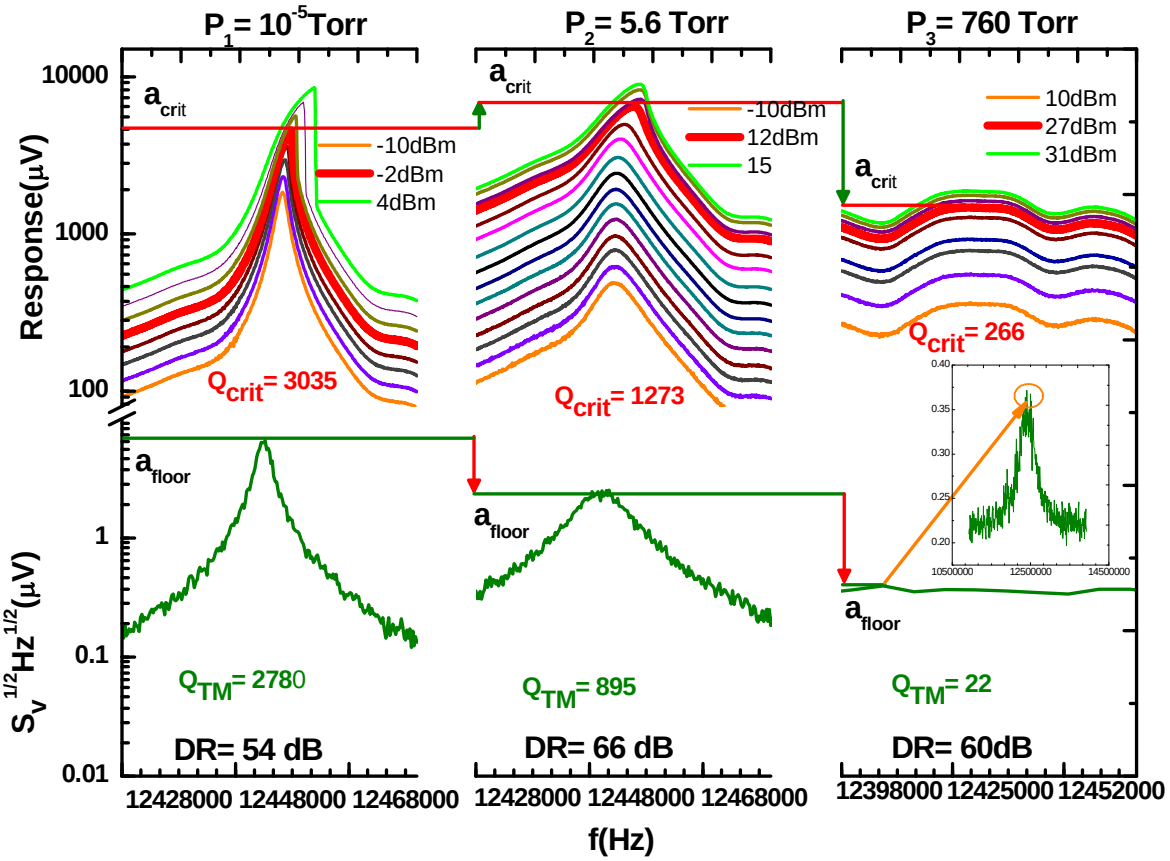

Figure 3. Summary of results on a single NEMS device operated at three different pressures (and different quality factors). Thermomechanical noise is resolved at small signal voltages in all three cases. The peak of the TM noise goes down with increasing pressure (decreasing Q). Responses to increasing drive powers are plotted at higher voltages. The thicker red plot highlights the responses for 1 dB signal compression and allows us to define a_{crit}. Duffing nonlinearities are reached for high vacuum and 6 Torr; a pressure induced nonlinearity is reached at atmospheric pressure.

Figure 4 shows how the increase in DR translates into improvement in fractional frequency stability and mass sensitivity. Allan deviation as a function of sampling time τ is plotted for two pressures (two values of Q) and two bandwidths. According to equation 6, we expect fluctuations to be proportional to both $\sqrt{Q}$ and bandwidth Δf. In both pressures the reduction of the bandwidth from 10 Hz to 2 Hz does indeed lead to a drop in the Allan deviation of approximately a factor of 5 as expected. The drop in Allan deviation of the right graph with respect to the left is roughly a factor of 2.5x. This is slightly more than the factor of $\sqrt{3}$ as expected from equation 6, but it is in the right expected direction and rough magnitude, and clearly demonstrates better performance in the lower Q case. This is an exciting development that could lead to better performance of NEMS mass sensors in gaseous environments. An estimation of the Allan deviation can also be made from equation (4). For 2 Hz, DR~54 dB, and Q~3000, a value of 6×10^{-9} is estimated. This is within a factor of 2 of the measured deviation at τ=0.5 s.

Furthermore, the mass sensitivity can be estimated from equation (4) with knowledge of the effective mass of the NEMS device. A mass axis has been added to the right side of the figure accordingly. The roughly part per billion value of the frequency stability at 5.6 Torr and 2 Hz bandwidth translates into a 1 zg noise level for the mass sensitivity of this particular device. This is state-of-the-art sensitivity for a top-down fabricated device, and is

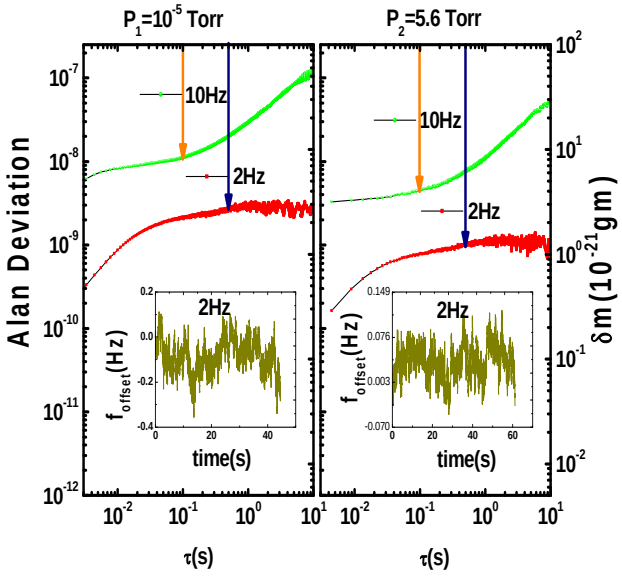

Figure 4. Allan deviation of NEMS frequency fluctuations at two different pressures and two different loop bandwidths. Insets: frequency fluctuations vs time for the 2 Hz cases. The low Q case (higher pressures) has better Allan deviation and mass sensitivity.

a state-of-the-art demonstration for any device subjected to gas damping.

Finally, we return to the prospect of atmospheric pressure sensing of mass by further investigating the atmospheric response in Fig. 5. From Fig. 3, Q_{crit} at 760 torr is 16 times higher than Q_{TM} at the same pressure. We elucidate this discrepancy by showing a 1MHz frequency span of the driven resonance mode in the right hand side of Fig. 5 for 2V driving power. Several peaks are evident around a highest central peak, each with its own phase change, the whole roughly taking on an envelope similar to the TM noise curve shape; it is as if the wider resonance peak has split into several, narrower, independent peaks. It was found that the position and shape of these peaks with their associated phases remains the same throughout all tested driving voltages, including up to 7 V. Furthermore each of the narrower peaks can be easily phase locked. From the phase data, we can estimate Q values by using the equation $\frac{d\phi}{df} = \frac{2Q}{f_{resonance}}$. The left part of Fig. 5 has Q calculated for the critical driving voltage in this way, as well as by Lorentz fitting the tallest peak. Both Q values (277, and 369) are similar and give us confidence in our assigning of an effective Q value of Q_{crit}=366 in Fig. 3.

We do not yet fully understand this partitioning of the atmospheric pressure peak into narrower pieces, but we do note that it could be used to advantage by allowing phase locking to a resonance that is essentially an order of magnitude sharper than would otherwise be the case.

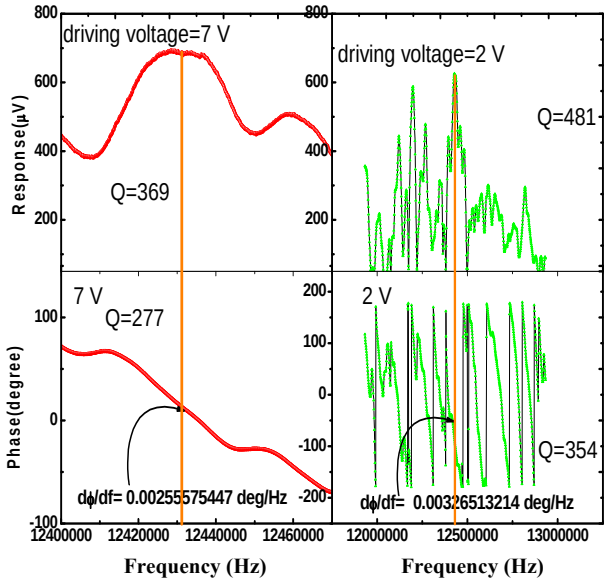

Figure 5: Magnitude and phase response of the device at 760 Torr for 7V (critical driving voltage, +27dBm) (left side) and for 2V (right side). The right side shows several peaks within a larger envelope over the 1 MHz span, each with a distinctive resonance phase change. The left side shows the consistency of assigning a high effective quality factor to a narrower resonance. Orange line is a guide for eye to show the quality factor calculated at center frequency.

CONCLUSIONS

We have used optomechanical transduction to investigate the full intrinsic dynamic range of a nano-optomechanical device at vacuum, 6 Torr, and atmospheric pressures. We looked at the dependence of dynamic range on quality factor and both measured and derived a relationship that sees the intrinsic DR increase as Q decreases, demonstrating DR of 54 dB, 66 dB and 60 dB at vacuum 6, Torr, and atmospheric pressure, respectively. Further, we have shown that reduction of Q leads to improved frequency stability and mass sensitivity and demonstrated a record zeptogram sensitivity level at 6 Torr pressure. Finally, we have shown an order of magnitude increase in effective quality factor at atmospheric pressure as well as an improvement in dynamic range compared to vacuum. These findings hold promise for use of resonant mechanical sensors in gas and liquid environments and also open the door to increased usage of any types of resonant mechanical systems in more diverse surroundings.

ACKNOWLEDGEMENTS

This work was supported by the National Institute for Nanotechnology (NINT), Alberta Innovates Technology Futures, the Natural Sciences and Engineering Research Council, Canada, the Canadian Institute for Advanced Research, and CMC Microsystems. The fabrication of the devices was facilitated through CMC Microsystems, and post processing was done at the University of Alberta NanoFab. Simulation software was provided by the Integrated Nanosystem Research Facility at the University of Alberta. SEMs were taken at the Electron Microscopy Facility at NINT.

REFERENCES

[1] A. K. Naik, M. S. Hanay, W. K. Hiebert, X. L. Feng, and M. L. Roukes, "Towards single-molecule nanomechanical mass spectrometry," *Nature Nanotechnology* **4,** 445 (2009).

[2] J. Chaste, A. Eicher, J. Moser, G. Ceballos, R. Rurali, and A. Bachtold, "A nanomechanical mass sensor with yoctogram resolution," *Nature Nanotechnology* **7,** 301 (2012).

[3] W. K. Hiebert, "Mass sensing Devices reach single proton limit," *Nature Nanotechnology*, **7**, 278 (2012).

[4] K. L. Ekinci, Y. T. Yang, and M. L. Roukes, "Ultimate limits to inertial mass sensing based upon nanoelectromechanical systems," *J. App. Phys.* **95**, 2682 (2004).

[5] M. Li, W. Pernice, C. Xiong, T. Baehr-Jones, M. Hochberg, and H. Tang, "Harnessing optical forces in integrated photonic circuits," *Nature* **456**, 480 (2009).

[6] V. T. K. Sauer, Z. Diao, M. R. Freeman, and W. K. Hiebert, "Optical racetrack resonator transduction of nanomechanical cantilevers," *Nanotechnology* **25**, 055202 (2014).

[7] M. Eichenfield, R. Camacho, J. Chan, K, J. Vahala, and O. Painter, "A picogram- and nanometer-scale photonic-crystal optomechanical cavity," *Nature* **444**, 67 (2009).

[8] X C. Zhang, E. B. Myers, J. E. Sader, and M. L. Roukes, "Nanomechanical torsional resonators for frequency-shit infrared thermal sensing," *Nano Letters* **13**, 1528 (2013).

[9] H. W. Ch. Postma, I. Kozinsky, A. Husain, and M. L. Roukes, "Dynamic range of nanotube- and nanowire-based electromechanical systems," *Appl. Phys. Lett.* **86**, 223105 (2005).

[10] V. T. K. Sauer, Z. Diao, M. R. Freeman, and W. K. Hiebert, "Nanophotonic detection of side-coupled nanomechanical cantilevers," *Appl. Phys. Lett.* **100**, 261102 (2012).

[11] Z. Diao, J. E. Losby, V. T. K. Sauer, J. N. Westwood, M. R. Freeman, and W. K. Hiebert, "Confocal scanner for highly sensitive photonic transduction of nanomechanical resonators," *Appl. Phys. Express* **6**, 065202 (2013).

CONTACT

*W.K. Hiebert, tel: +1-780-641-1708; Wayne.Hiebert@nrc.ca

Q OPTIMIZATION VIA QUARTER WAVE ACOUSTIC TRANSFORMERS IN THE BODY OF ALN CONTOUR-MODE RESONATORS

C. Cassella[1], M. Cremonesi[2], A. Frangi[2] and G. Piazza[1]
[1]Carnegie Mellon University, Pennsylvania, USA
[2]Politecnico of Milan, ITALY

ABSTRACT

This paper investigates the dependence of the quality factor in aluminum nitride contour mode resonators (CMRs) on the size of the inactive region between the resonator body and the lateral edges orthogonal to the main direction of vibration. Our work shows that an optimized length of this region exists and it is such that little energy leaks into the substrate through the supporting anchors. It turns out that the use of the optimum length makes the resonator inactive region behave as an equivalent λ/4 transformer. The reduction of the energy that is lost through the device anchors improves the device Q without substantial degradation of the electromechanical coupling, k_t^2. To validate this concept we built four different configurations of 207 MHz AlN CMRs, differing just in the length of the resonator inactive region, d (Fig. 1). An almost 40% improvement in the Figure of Merit, FoM, defined as the product between Q and k_t^2, was attained when d was varied from the minimum value we tested (~8 μm) to the equivalent acoustic quarter wavelength of the resonator inactive region (~11 μm).

INTRODUCTION

MicroElectroMechanical (MEM) resonators have been widely researched as they enable the implementation of stable frequency references and filtering functions through CMOS compatible fabrication processes. An important parameter of a MEM resonator performance is the quality factor, Q, an inverse measure of the energy lost in a passive component. A high Q is highly desirable to ameliorate the performance of both oscillators and filters. However, improving Q in MEM resonators requires a full understanding of the main loss mechanisms as well as the identification of the device parameters that can mitigate their impact.

AlN contour mode resonators (CMRs) have shown low motional resistance and moderate Q in the radio frequency bands. Previous studies have attempted to identify the main dissipation mechanisms affecting this resonator technology. In [3,5] it has been shown that the equivalent damping in AlN CMRs is mostly due to anchor loss and interfacial dissipation. Anchor loss refers to acoustic energy that is lost into the substrate through the supporting anchors. Interfacial dissipation is instead due to stress jumps at the interface between different materials in the resonator's body [2,4]. As shown in [3,5], anchor loss represents the main source of energy dissipation when the device resonance frequency is lower than 500 MHz. In contrast, interfacial dissipation [2,4] is the main source of energy lost when the device operates at frequencies greater than 500 MHz. Although the impact of the anchor geometry on the device Q was previously investigated [3], there is no understanding of how the length of the resonator inactive region, built between the edge of the active region and the closest stress-free boundary (d in Fig. 1), affects the device quality factor.

In this work we analyze the variation of Q with respect to d and we verify that it is possible to reduce anchor losses by designing d to be equal to the acoustic quarter wavelength of the resonator inactive region. In fact, in this scenario, each inactive region behaves as a λ/4 transformer, hence allowing the resonator active region to see a virtual fixed boundary condition along the anchors direction. As a consequence, the acoustic energy remains confined within the active region and no vibration leaks to the substrate through the supporting anchors.

To validate this new design approach, and to verify an analytical model that describes this phenomenon, four different configurations of 207 MHz AlN CMRs having different lengths, d, of the resonator inactive region were analyzed. An ad-hoc developed finite element code was also used to study the device performance as a function of d. The use of λ/4 transformers in 207 MHz AlN CMRs permitted to attain an almost 40% improvement of the device Q with respect to what is obtained when d is close to λ/5. No substantial variation of k_t^2 with respect to d was measured.

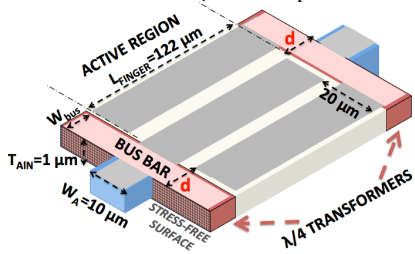

Figure 1: Schematic representation of the 207 MHz AlN CMRs analyzed in this work. Each region included between the edge of the active region and the closest anchor can be designed to act as a λ/4 transformer placed in the resonator body.

ALN CONTOUR-MODE RESONATORS

AlN CMRs are piezoelectric resonators that can excite longitudinal in-plane vibrations in an AlN plate. They are formed by a central active region and two inactive regions (Fig. 1). The active region corresponds to the area in which the electric field generates a mechanical strain through the AlN d_{31} coefficient. The inactive portions correspond to the areas placed between the edge of the active region and the anchors, where no direct piezoelectric excitation is present.

In this work we have used Lateral Field Excited (LFE) resonators, in which the active region is formed by a thin film of AlN sandwiched between two metal layers that are used to excite the electric field in the AlN film. The top metal layer is an interdigitated structure (IDT), where adjacent metal strips are connected to opposite voltage polarities. The bottom metal layer is a floating metal plate that is used to confine the electric field in the AlN body, hence attaining higher electromechanical coupling, k_t^2.

The inactive region is formed by a sequence of metal covered and uncovered regions and permits to bias each metal strip composing the top metal IDT.

As shown in [1] the resonance frequency of an AlN CMR can be computed as

$$f = \frac{1}{2W} \cdot \sqrt{\frac{E_p}{\rho_{eq}}} \qquad (1)$$

where E_p and ρ_{eq} are respectively the equivalent Young's modulus and mass density of the resonator stack.

9781940470016/HH2014/$25©2014TRF
DOI 10.31438/trf.hh2014.114

Solid-State Sensors, Actuators and Microsystems Workshop
Hilton Head Island, South Carolina, June 8-12, 2014

ANCHOR LOSSES

As shown in [3,5], anchor losses represent the main source of energy lost in AlN CMRs when their resonance frequency is lower than 500 MHz. This dissipation mechanism is due to the presence of stress along the anchors direction, at the interface between the supporting anchors and the AlN plate. In particular, when the stress is present at this interface, the anchors are strained, hence transfer energy from the resonator body to the substrate. This phenomenon makes the anchors behave as acoustic waveguides, which limit the maximum quality factor achievable by the device.

Different techniques have been investigated to reduce anchor losses in AlN CMRs. In [3] it has been shown that anchor losses can be reduced when the anchors show an internal resonance in a direction orthogonal to the main direction of propagation of the wave into the substrate. In particular, under these conditions, the flux of energy that would otherwise leak into the substrate is stored into the main mode of vibration, hence reducing the amount of energy lost and, therefore, increasing the resonator Q. In [7] it has been shown that anchor dissipations can be further reduced by creating etched slots in the body of AlN CMRs. In this work we show that anchor losses can be minimized by engineering the length of the resonator inactive region (d in Fig. 1). Although this approach has been validated in AlN CMRs its application can be extended to any similar resonator technology having Q limited by anchor dissipations.

λ/4 TRANSFORMERS – PRINCIPLE OF OPERATION

In this work we show that it is possible to use the acoustic properties of each resonator inactive region (Fig. 1) to limit the amount of energy that is released into the substrate through the device anchors.

Energy dissipation through the anchors is due to longitudinal waves propagating along the anchor direction and being originated by the contour-mode vibration through the AlN Poisson ratio.

To first order, we can express the displacement vector at a generic point, P, included in the resonator inactive region, as

$$\vec{u}_P = \int u_0 \cdot e^{j\vec{k}\cdot\vec{r}}\, d\vec{r} \tag{2}$$

where $\vec{k}$ is the wave vector and $\vec{r}$ is a vector connecting each infinitesimal point source forming the edge of the resonator active region to P. In Eq. (2) u_0 is the displacement value at each infinitesimal point source being part of the edge of the active region.

When the anchors include points at which $\vec{u}_P$ is non-zero, they let part of the acoustic energy that reaches them leak out of the resonator body, hence limiting the overall device Q.

According to Eq. (2) it is straightforward to note that it is possible to limit the amount of anchor dissipations by reducing u_0. This reduction can be achieved by forcing the edges of the active region to behave as nodal lines. This task can be accomplished by engineering each resonator inactive region to act as λ/4 acoustic transformers (Fig. 1). These transformers are capable of imposing virtual fixed boundaries (*i.e.* u_0 equal to zero) right at the edge of the resonator active region (Fig. 1-3). Consequently the displacement at the edge of the resonator finger connected to the anchors is also minimized, hence leading to a reduction of the acoustic energy incident on the anchors and, consequently, of the energy lost into the substrate.

For simplicity, assuming initially that the same materials compose both the resonator inactive and active regions, we can write the displacement at the edge of the active region as

$$u_0 = u_{in} - u_{in} \cdot \Gamma \cdot \cos(2kd) \tag{3}$$

where Γ is the reflection coefficient computed at the stress-free boundary, hence being equal to -1, and d is the length of the resonator inactive region. The negative sign in the second term of Eq. (3) is used to identify that the direction of the *incident* wave is opposite to the wave reflected by the stress-free boundary (*i.e.* the AlN sidewall).

As there is no energy reflected at the interface between the anchors and the resonator finger connected to them, the energy lost into the substrate is proportional to the product between force and displacement computed at each edge of this finger. Assuming the piezoelectric stress generated in this finger to be almost independent of d, the energy lost due to anchor dissipations, E_{lost}^{anc}, can be written as

$$E_{lost}^{anc} \propto (u_{in} + u_{in}\cos(2kd)) \tag{4}$$

This assumption can be adopted as the stress along the anchors direction is generated by the lateral stress in the resonator active region, and hence mostly depends on the resonator stiffness in the lateral direction. The resonator quality factor can then be written as

$$Q = \frac{E_{stored}}{E_{\text{var}} + E_{lost}^{anc}} = \frac{Q^{eff}}{(1 + \frac{E_{lost}^{anc}}{E_{\text{var}}})} \tag{5}$$

where E_{var} contains the energy that is lost through different dissipation mechanisms and Q^{eff} is the quality factor that would be achieved if the energy lost through the anchors were zero.
Assuming E_{var} to be independent of the dimensions of the resonator inactive region we can express Q as

$$Q = \frac{Q^{eff}}{(1 + \alpha \cdot (1 + \cos(2kd))} \tag{6}$$

where α indicates the amount of the resonator energy lost that is related to anchor dissipations. The variation of Q, normalized to Q^{eff}, with respect to d, for different values of α, is shown in Fig.2.

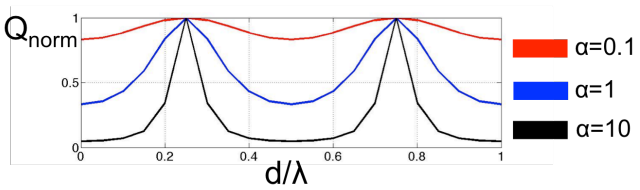

Figure 2: Variation of Q, normalized to Q^{eff} (Eq. 6), with respect to the ratio between the length of the resonator inactive region and the acoustic wavelength, for different values of α. The trend suggests that the bandwidth of each λ/4 transformer is inversely proportional to the value of α. No variation of the acoustic velocity between transformer and resonator active region is considered here.

As evident from Eq. (6), and as intuitively expected, the variation of the quality factor with respect to the distance, d, is strongly influenced by α. The higher the impact of anchor losses on Q, the greater the relevance of the size of d in setting the overall device Q. However the maximum quality factor is always achieved when d is equal to odd multiples of λ/4. This scenario corresponds to the case in which the edges of the active region are virtually clamped along the anchor direction.

λ/4 TRANSFORMERS – DESIGN CONSIDERATION

We analyzed the variation of Q with respect to the length of the resonator inactive region in 3-finger 207 MHz AlN CMRs. This analysis was done by varying the width of the two metal strips (one on each side of the resonator) that are used to connect the electrodes forming the top IDT to the proper voltage polarity (Fig. 1-3). This width, labeled as W_{bus},, is equivalent to $d - \lambda/10$, λ being equal to 40 µm at the frequency of interest. As in the actual design the resonator inactive region is formed by multiple sections (Fig. 3), each having a different acoustic velocity, we recurred to the transmission line theory to find the value of W_{bus} that maximizes the device Q. Each section forming the resonator inactive region was modeled as a transmission line having length equal to its actual size and characteristic impedance and propagation constant set by its acoustic property.

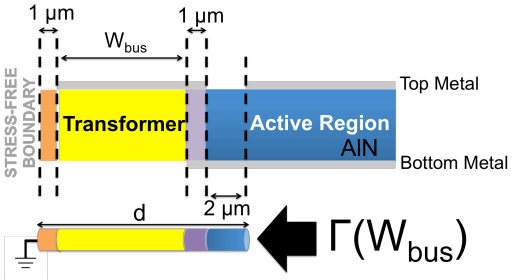

Figure 3: Cross-sectional schematic of the transformer under study. Each transformer is formed by four different sections characterized by different acoustic velocities. Both metal layers are made by platinum. Their thickness is about 0.1 µm. Both the active region and the transformers use the same AlN film having a thickness equal to 1 µm.

By looking at the reflection coefficient, Γ (Fig.1-3), defined as the ratio between incident and reflected waves at the edge of the active region, we found the value of W_{bus} that allows transforming the stress-free boundary into a fixed boundary. This value, W_{bus}^{opt}, corresponds to the size of the bus that makes the real part of Γ (Fig. 3) equal to 1 (Fig. 4). It is important to notice that the change in phase of the reflection coefficient observed by the lateral fingers (Fig. 1) is needed as it permits to virtually clamp the edge of the central finger connected to the anchor.

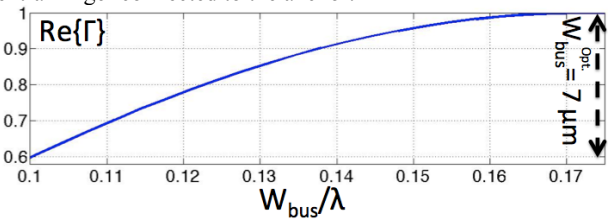

Figure 4: Real part of the reflection coefficient Γ as defined in Fig. 1 and Fig. 3. The presence of different sections in each transformer increases the size of the resonator inactive region that corresponds to λ/4 by a factor close to 10% with respect to the scenario in which the same acoustic velocity is assumed for both the resonator active and inactive regions.

DEVICE FABRICATION

In Fig. 5 we show the fabrication process we followed to build the devices we analyzed in this work. We first deposited 100 nm of platinum above 10 nm of titanium (Fig. 5-a). Afterwards we deposited 1 µm of AlN (Fig. 5-b) followed by the deposition of 100 nm of platinum (Fig. 5-c) top electrode. The etching of the AlN (Fig. 5-d), followed by the structural release (Fig. 7-e), completed the device fabrication.

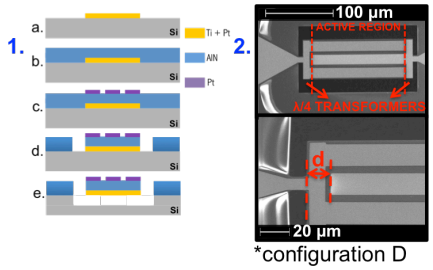

Figure 5: 1. Fabrication process for the AlN resonators built for this work: 2. SEM pictures of a tested device and zoomed in view of the transformer region.

EXPERIMENTAL RESULTS

To evaluate the variation of Q when W_{bus} approaches W_{bus}^{opt}, we built four different configurations of 207 MHz AlN CMRs differing just for the value of W_{bus} (Fig. 3). These 4 resonators were built with the optimum anchor width, W_A =10 µm (Fig. 1), which was found by measuring 36 resonators having W_A ranging from 10 to 60 µm.

W_{bus} was chosen to be 4, 5, 6 and 7 µm respectively in configurations A, B, C and D. We tested 6 devices for configuration A, 12 devices for configuration B, 6 devices for configuration C, and 6 devices for configuration D. All the devices were extracted from 3 chips belonging to the same wafer.

We report in Fig. 6 the average Q we measured for each configuration. Moreover, by using Eq. (6), in which Q^{eff} was set to be equal to the maximum average Q we measured, we were able to match closely the measured variation of Q with respect to W_{bus} by using a coefficient α equal to 1.5. The fact that the value of α that permits to match the experimental results is greater than one shows that anchor dissipations are greater than any other loss mechanism in 207 MHz AlN CMRs. However, this fact also proves that different dissipation mechanisms contribute significantly in limiting the quality factor achievable by this resonator technology operating in the Very High Frequency (VHF) range. It is important to clarify that, although Eq. (6) was formulated assuming that the resonator active region was formed by the same material than the transformers, it still can be used when the transformer topology is the one depicted in Fig. 3. This is possible since the magnitude of the reflection coefficient observed by the central finger looking at the anchors is approximately -30 dB and almost independent of W_{bus}.

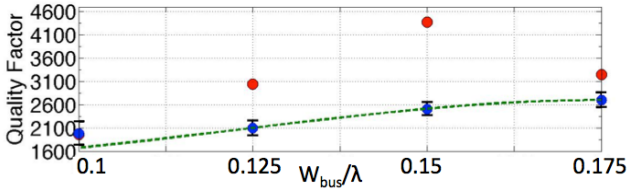

Figure 6: In blue: Averaged quality factor, Q, measured in configurations A, B, C and D. About 40% improvement of Q was measured going from configuration A (W_{bus}=4 µm) to configuration D (W_{bus}=7 µm) In red: Simulated Q by FEM analysis. The presence of metal covered areas in the inactive region was neglected. Because of this assumption the maximum Q is simulated at d equal to the equivalent resonator quarter-wave length. In green: analytical estimation of the resonator Q as a function of the ratio W_{bus}/λ. We speculate that the discrepancy between the analytical trend and the measured Q at W_{bus} equal to 4 µm is due to the presence of a spurious mode in the resonator inactive region that changes its transmission properties.

In Fig. 7 we report the best admittance we measured for each configuration we tested. Passing from configuration A to configuration D we observed a progressive slight reduction of k_t^2 motivated by the increased static capacitance due to the increase of W_{bus}. Moreover a reduction of the resonance frequency was also measured as W_{bus} was increased.

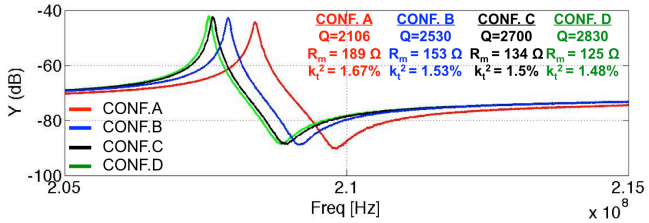

Figure 7: Best-measured admittance response for the four configurations analyzed in this work. Values of the motional resistance, R_m, and k_t^2 are also reported.

This fact is due to the larger value of the resonator effective mass as W_{bus} is increased. However the fact that the sensitivity of the resonance frequency with respect to W_{bus} decreases when W_{bus} approaches W_{bus}^{opt} represents a further indication that the displacement in the resonator inactive region, and consequently in the anchors, approaches zero in configuration D.

FEM ANALYSIS

In order to obtain a quantitative prediction of the overall quality factor, we assume the presence of both anchor and interface losses [3-7]. Anchor losses have been estimated by means of a robust Finite Element Method including absorbing boundary regions (PML) and simulating the dissipation of elastic waves scattered in the substrate through the anchors. Exploiting the symmetry of the devices, only 1/4-th of the resonators is discretized. Fig. 8 shows the geometrical model and the contour plot of the displacement field corresponding to the mechanical mode actuated.

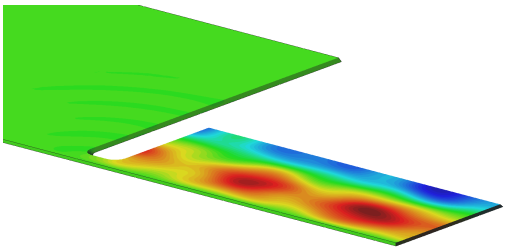

Figure 8: Model of 1/4th of the resonator. Contour plot of the displacement field corresponding to the mechanical mode actuated.

On the contrary, Fig. 9 presents the pattern of scattered elastic waves superposed to the finite element mesh adopted in the simulations; their smooth dissipation in the PML region validates the accuracy of the numerical model. The complex eigenfrequency Ω_0^2, corresponding to the activated mechanical mode, is computed and the quality factor due to anchor losses is estimated as:

$$Q_{anc} = \mathrm{Re}(\Omega_0^2) / \mathrm{Im}(\Omega_0^2) \tag{7}$$

Interface losses are described employing a phenomenological law implemented in the FEM model. Assuming a 1D extensional mode of vibration, it has been recently proposed that interface losses might be associated with the Cauchy stress jump $\Delta\sigma$ across the interfaces between different materials:

$$\Delta\sigma = \Delta E \frac{\partial u}{\partial x} \tag{8}$$

where u corresponds to the lateral acoustic displacement and ΔE is the discontinuity of Young modulus.

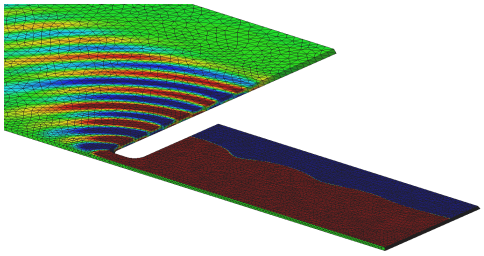

Figure 9: Pattern of scattered elastic waves and final dissipation in the PML region.

As previously formulated in [3-4,6], we postulate that the energy lost over one cycle T due to interfacial dissipation (E_{int}) at each interface S of the mechanical resonators is:

$$E_{\mathrm{int}} = \eta \int_S \int_0^T \left(\Delta\dot{\sigma}\right)^2 dt dS \tag{9}$$

where η is a material parameter.

The numerical results collected in Figure 6 reveal a strong sensitivity of the quality factor to W_{bus} and a good qualitative agreement with experimental data. It is worth stressing that, at present, simulations of anchor losses employ a homogenized resonator and do not represent the details of metallic interdigitated fingers. Since anchor losses are strongly sensitive to all the geometrical and material parameters, a more accurate model is expected to improve the predictive capabilities.

CONCLUSIONS

In this work, we provide theoretical and experimental demonstration of the dependence of the quality factor of AlN contour-mode resonators (CMRs) on the size of the resonator inactive region. We found that the optimization of this region permits to limit the amount of acoustic energy that leaks into the substrate through the device anchors and, consequently, maximizes Q. A 40% increase in the quality factor of 207 MHz AlN CMRs was measured when the size of the resonator inactive region was varied from λ/5 to λ/4, being λ the acoustic wavelength. This work also demonstrates that anchor loss is not the only significant dissipation mechanism that affects the quality factor in AlN CMRs operating in the Very High Frequency (VHF) range.

REFERENCES

[1] G. Piazza, P. J. Stephanou, A. P. Pisano, *Journal of MEMS*,vol. 15, no. 6, pp. 1406-1418, 2006.

[2] L.-W. Hung and C. T.-C. Nguyen, *Solid-State Sensor and Actuator Workshop*, pp. 463-466, 2010.

[3] J.Segovia, M.Cremonesi, C.Cassella, A.Frangi, G.Piazza, In *Solid-State Sensors, Actuators and Microsystems*, 2013 Transducers & Eurosensors XXVII: The 17th International Conference on (pp. 2473-2476). IEEE.

[4] C.Cassella, J.Segovia-Fernandez, G.Piazza, In *Solid-State Sensors, Actuators and Microsystems*, 2013 Transducers & Eurosensors XXVII: The 17th International Conference on (pp. 506-509). IEEE.

[5] A. Frangi, M. Cremonesi, A. Jaakkola, T. Pensala, *Sensors & Actuators: A Physical*, vol. 190, pp. 137-134, 2013.

[6] A. Frangi, A. Bugada, M. Martelo, P.T. Savadkoohi, *European Journal of Mechanics - A/Solids,* vol. 37, pp. 256-265, 2013.

[7] Cassella, C., Segovia-Fernandez, J., Piazza, G., Cremonesi, M., & Frangi, A., In Frequency Control Symposium (EFTF/IFC), 2013 Joint (pp. 926-929). IEEE.

SWITCHABLE ALUMINUM NITRIDE MEMS RESONATOR USING PHASE CHANGE MATERIALS

G. Hummel, Y. Hui, Z. Qian, and M. Rinaldi
Northeastern University, Boston, Massachusetts, USA

ABSTRACT

This paper reports on the first demonstration of a reconfigurable Aluminum Nitride (AlN) piezoelectric Micro Electro Mechanical Systems (MEMS) resonator using phase change material (PCM) based switchable electrodes, enabling switching and reconfiguration of a high quality factor (*Q~1400*) and high frequency (*~260MHz*) piezoelectric micro-acoustic resonator. This innovative design solution allows direct control and reconfigurability of the electrical coupling across the piezoelectric body of the device which enables effective ON/OFF switching of the acoustic resonance (*~18X* impedance variation at resonance) and reconfiguration of the device electromechanical coupling ($0\% < k_t^2 < 0.7\%$) and electrical capacitance ($258fF < C_0 < 340fF$) which can potentially lead to the implementation of filter architectures whose frequency, order, bandwidth, and roll-off can be dynamically reconfigured.

INTRODUCTION

In recent years the demand for highly reconfigurable radio frequency (RF) systems, capable of operating in the severely crowded and rapidly changing modern commercial and military spectral environment, at a reduced overall component count and with a reduced development cost compared to conventional multi-band radios, has been steadily growing. In this context, the implementation of high quality factor, *Q*, micro acoustic resonators with monolithically integrated switching and frequency reconfiguration functionalities will dramatically reduce loss associated with the filtering element enabling new radio architectures with enhanced spectrum coverage, whose implementation is currently prevented by the lack of such high performance and intrinsically reconfigurable components.

High Q MEMS resonant devices enable the implementation of low insertion loss filters in a very small form factor. Different MEMS resonator technologies based on electrostatic [1-2] or piezoelectric [3-4] transduction have been investigated. Among these, the piezoelectric Aluminum Nitride (AlN) contour-mode resonator (CMR) technology [3, 5, 6] has emerged as one of the most promising solutions in enabling the fabrication of multiple frequency and high performance resonators on the same silicon chip. Nevertheless, the current filtering solutions based on AlN micro acoustic resonant devices cannot be dynamically reconfigured to operate at different frequencies, orders, and bandwidths.

Switching of piezoelectric resonance in AlN contour-mode resonators has been recently demonstrated by integrating a MEMS capacitive switch over the AlN piezoelectric film [7]. This work can be considered the first demonstration of the monolithic integration of phase change material (PCM) RF switches with a MEMS resonator technology to implement switching and reconfiguration functionalities. In particular, switching and reconfiguration of a high quality factor (*Q~1400*) and high frequency (*~260MHz*) piezoelectric micro-acoustic resonator is demonstrated thanks to the unprecedented monolithic integration of PCM switches with the AlN piezoelectric MEMS resonator technology.

Phase change materials are chalcogenide materials that show a significant change in resistivity between the amorphous (OFF) and crystalline (ON) states. Reversible switching behavior can be achieved by applying low voltage pulses of proper duration (direct heating) across the PCM [9]. Due to this property, PCMs have been investigated for use as Radio Frequency (RF) switches [9]. IN this work, miniaturized ($2\times2\ \mu m^2$) $Ge_{50}Te_{50}$ PCM vias are employed as low loss (ON resistance < *5Ω*), high dynamic range (ON/OFF ratio *~10^7*), and low OFF-capacitance (*~40fF*) ohmic switches to control and reconfigure the electrical connections of the interdigital electrode employed to excite vibration in a piezoelectric resonator (Fig. 1, 2), enabling effective ON/OFF switching of the acoustic resonance (*~18X* impedance variation at resonance) and reconfiguration of the device electromechanical coupling ($0\% < k_t^2 < 0.7\%$) and electrical capacitance.

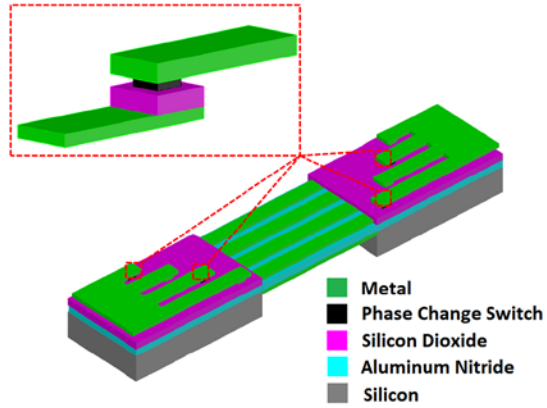

Figure 1: 3D representation of the switchable and reconfigurable resonator with closer view of an individual PCM via switch.

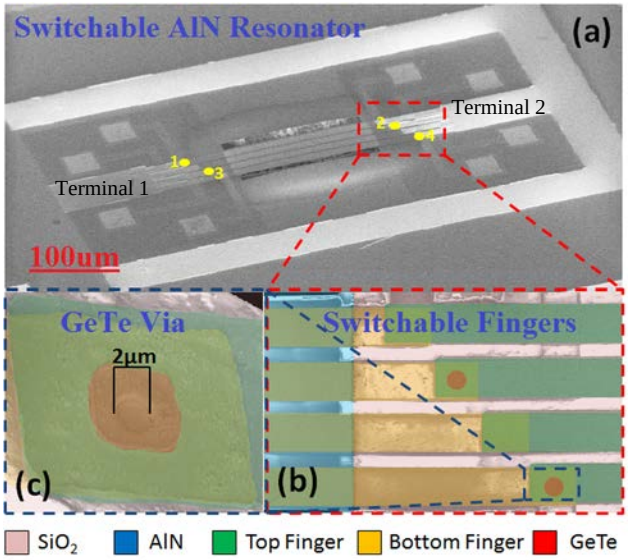

Figure 2: SEM Images of (a) the switchable and reconfigurable resonator (the locations of the PCM via switches utilized in this work are highlighted in gold), (b) close-up of phase change switches integrated into the fingers of the resonator, and (c) individual PCM via switch.

9781940470016/HH2014/$25©2014TRF
DOI 10.31438/trf.hh2014.115

This innovative technology has the potential to deliver a new class of monolithically integrated and highly reconfigurable RF components such as resonators, filters, and capacitors capable of achieving the highest level of programmability with the minimum possible effect on the performance (by minimizing the number of physically separated RF components), enabling new radio architectures with enhanced spectrum coverage. This new family of RF components can be fabricated with a relatively simple 6-mask fabrication process (instead of the 10-mask required for the capacitive switchable electrodes) and does not require the creation of a micro/nano scale gap between the resonator and the electrodes for the switching mechanism, which significantly reduces the complexity of the fabrication process.

Furthermore, thanks to the unique reversible switching behavior of PCMs, low voltages (1-2.5V compared to 35-40V in the electrostatic case) are required for switching and, differently from conventional MEMS capacitive switch technologies that have been integrated with AlN resonators previously [7], PCM switches do not need to be powered to maintain either state.

DESIGN AND FABRICATION

A conventional static contour-mode resonator is composed of an AlN film sandwiched between two metal electrodes (Fig. 1). When an alternating current (ac) signal is applied across the thickness T of the AlN film, a contour-extensional mode of vibration is excited through the equivalent d_{31} piezoelectric coefficient of AlN. Given the equivalent mass density, ρ_{eq}, and Young's modulus, E_{eq}, of the material stack that forms the resonator, the center frequency, f_0, of this laterally vibrating mechanical structure is set by the period, W, of the interdigital electrode patterned on top of the AlN plate and can be approximately expressed as:

$$f_0 = \frac{1}{2W}\sqrt{\frac{E_{eq}}{\rho_{eq}}} \quad (1)$$

For a given geometry of the AlN resonant micro-plate and period of the interdigital electrode, the equivalent electrical impedance of the device is set by the number of metal fingers, n, composing the interdigital electrode [5-7]. In particular, only the fraction of the device area covered by the metal fingers is effectively employed for transduction. Therefore, the device electrical static capacitance, C_0, and electromechanical coupling coefficient, k_t^2, are directly proportional to the number of metal fingers, n, composing the interdigital electrode employed to excite the higher order (n^{th}) contour-extensional mode of vibration in the AlN micro-plate.

In this work, an innovative design solution, that enables dynamic reconfiguration of the number of metal fingers composing the interdigital electrode employed to excite a higher order contour-extensional mode of vibration in an AlN resonant micro-plate, is introduced for the first time. This new approach allows direct control and reconfigurability of the electrical coupling across the piezoelectric body of the device, enabling effective ON/OFF switching of the acoustic resonance (OFF state corresponding to $n=0$) and reconfiguration of the device electromechanical coupling coefficient and electrical static capacitance.

The resonant core of this innovative device concept is composed of a *500 nm* thick AlN layer sandwiched between a bottom electrically floating plate electrode and a top interdigital electrode composed of $n=4$ metal fingers. Each metal finger completely covers the resonant body of the device extending up to the anchoring regions where it is overlapped by the electrical terminal of the resonator, but separated by a SiO_2 insulating layer. 4 miniaturized ($2\times2\ \mu m^2$) Phase Change Material (PCM) vias are monolithically integrated with the resonant structure and employed as low loss radio frequency (RF) switches to connect each of the 4 metal fingers forming the device interdigital electrode to the electrical terminals of the resonator through the SiO_2 insulating layer (Fig. 1, 2). $Ge_{50}Te_{50}$ is chosen to implement the PCM via switches due to its high ON/OFF ratio ($\sim10^6$) and low loss at radio frequencies [9]. The transition temperature (ON/OFF switching) of each PCM via is readily reached by passing current through the PC material itself (direct heating).

When all the vias are in the *OFF* state, the terminals of the device are ideally completely isolated (open circuit) and no electric field is coupled across the piezoelectric material (hence no resonance is excited). In practice, a high impedance path between the two terminals is formed through substrate parasitics (C_p, R_p, R_{pp}) and the capacitance and resistance associated with the combination of PCM via switches in the OFF state (C_{switch}, R_{switch}) (Fig. 3-a).

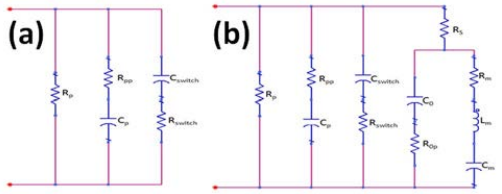

Figure 3: Equivalent circuit model of the device in the (a) OFF state, and (b) State 1 and State 2. C_p, R_p, and R_{pp} represent the parasitics. C_{switch} and R_{switch} are the capacitance/resistance associated with the combination of PCM via switches in the OFF state. R_S is the loss introduced by the combination of PCM vias in the ON state – note that R_S has minimal effect on resonator performance. C_0 and R_{0p} are static capacitance/resistance of the piezoelectric transducer. R_m, C_m, and L_m represent the motional branch of the resonator. All values used for these equivalent circuit elements are reported in Table 1.

When two vias (i.e. vias *1* and *4* in Figure 2) are in the *ON* state (*State 1*), only two fingers are connected to form the interdigital electrode with a polarity that uniquely matches the one of the strain field for the 4^{th} order contour-extensional mode of vibration of the plate. Therefore, a 4^{th} order contour-extensional mode of vibration is excited in the AlN micro-plate by means of a lateral field excitation scheme [5-6, 8]. Such configuration results in a relatively high impedance resonance due to the low values of device static capacitance, C_0, and electromechanical coupling coefficient, k_t^2, associated with the 2-finger top interdigital electrode configuration for which only a fraction of the device area (the one covered by the two metal fingers) is effectively employed for transduction.

Table 1: Values of the equivalent circuit elements for all the states as pictured in Figure 6. Note that the series resistance, R_S, introduced by the PCM vias has a minimal effect on the resonator performance. Values of parasitic components were extracted from the data using layout considerations. In the State 2 model, the malfunctioning PCM via 2 was considered to be OFF.

States	Equivalent Circuit Element Values										
	R_m	C_m	L_m	R_S	R_{0p}	C_0	R_{switch}	C_{switch}	C_p	R_{pp}	R_p
OFF	--	--	--	--	--	--	0Ω	69.232fF	75.768fF	47.095kΩ	48.04Ω
State 1	422.8Ω	1.0102fF	376.48μH	5Ω	5Ω	258.17fF	5Ω	86.092fF	75.768fF	47.095kΩ	48.04Ω
State 2	227.6Ω	1.9437fF	195.88μH	3.75Ω	5Ω	359.99fF	3.75Ω	106.79fF	75.768fF	47.095kΩ	48.04Ω

When three vias (i.e. vias *1*, *3*, and *4* in Figure 2) are in the *ON* state (corresponding to a 3-finger interdigital electrode configuration), the effective transduction area for 4^{th} order contour-extensional mode of vibration is increased resulting in larger values of device static capacitance, C_0, and electromechanical coupling coefficient, k_t^2, hence, lower impedance resonance. Maximum transduction area, C_0, and k_t^2, hence minimum impedance resonance, are achieved when all 4 vias are in the *ON* state, forming a 4-finger interdigital electrode with a polarity that uniquely matches the one of the strain field for the 4^{th} order contour-extensional mode of vibration of the plate. The values of C_0 and k_t^2, estimated by Finite Element Method (FEM) simulation using COMSOL Multiphysics, for the four possible device configurations are reported in Figure 4.

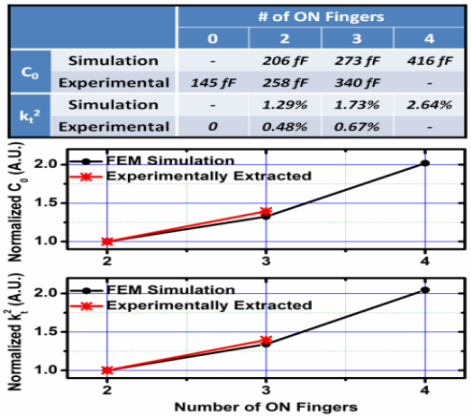

Figure 4: Comparison between Finite Element Method (FEM) simulated (COMSOL) and experimentally extracted values of C_0 and k_t^2 for the different possible device states.

The switchable resonator presented in this work was fabricated using a relatively simple 6-mask post-CMOS compatible fabrication process shown in Figure 5.

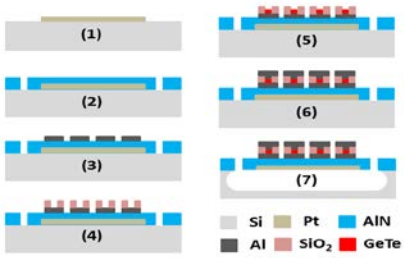

Figure 5: Device fabrication process. (1) Platinum electrode, (2) Aluminum nitride deposition and etch, (3) Aluminum fingers, (4) PECVD oxide deposition and etch, (5) Phase change material deposition, (6) Top Aluminum contact, (7) XeF_2 release.

The fabrication process began with a high resistivity Si substrate (resistivity > 10,000 Ω·cm). A *5nm/95nm* Titanium/Platinum (Ti/Pt) layer was sputter deposited and patterned with a lift-off process to form the bottom electrically floating electrode. Next, a high quality c-axis oriented *500nm* Aluminum Nitride (AlN) layer was sputter deposited on top of the Ti/Pt layer. Inductively Coupled Plasma (ICP) etching in Cl_2 based chemistry was used to open vias to the bottom Pt and define the dimensions of the micro-plate resonator. Next, sputter deposition was used to deposit a *100nm* layer of Aluminum (Al) which was patterned using lift-off to create the interdigital electrodes on top of the AlN micro-plate. Plasma Enhanced Chemical Vapor Deposition (PECVD) was used to deposit *300nm* of SiO_2 to form the insulation layer for the PCM switches. *2×2 um^2* vias were etched in the SiO_2 using ICP with CHF_3 based chemistry. DC Pulse Sputtering was used to deposit *100nm/10nm* of $Ge_{50}Te_{50}$/Ti in the vias and pattern using a lift-off process. A *100nm* Al film was deposited using sputter and patterned with lift-off to form the top probing pad and the top electrode of the PCM switches. Finally, Xenon Difluoride (XeF_2) isotropic etching was used to etch the Si substrate and create an air gap under the resonator, completely releasing the resonant structure.

EXPERIMENTAL RESULTS AND ANALYSIS

The electrical response of the fabricated switchable MEMS resonator was measured by an Agilent E5071C network analyzer after performing an open-short-load calibration on a standard substrate. The transition temperature, needed for *ON/OFF* switching of the PCM vias, was reached by passing current through the PC material itself (direct heating). *ON* state was achieved by applying a *300 μs* pulse with amplitude of *1 V* and a rise/fall time of *100 ns* while the *OFF* state was achieved by applying a *4 μs* pulse with amplitude of *2.5 V* and a rise/fall time of *5 ns*. The device was reconfigured to operate in 3 different states: *OFF* (all vias in the *OFF* state), *State 1* (vias *1* and *4* in the *ON* state), and *State 2* (all vias *1-4* in the *ON* state) (Fig. 6). Although all the PCM vias were turned *ON* in *State 2*, via *2* malfunctioned, showing a resistance of *~140MΩ*. Therefore, only 3 fingers (vias *1*, *3*, and *4*) were effectively connected to form the interdigital electrode.

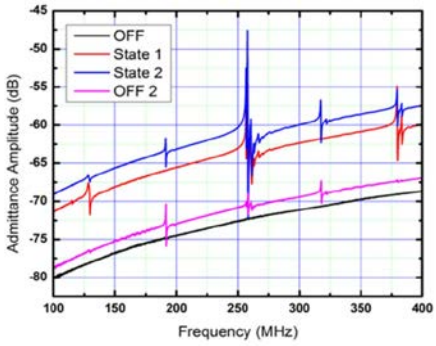

Figure 6: Measured admittance of the resonator in the OFF state (all the PCM vias OFF); State 1 (vias 1 and 4 ON); State 2 (all the vias ON); OFF 2 (all the vias OFF again). The difference between OFF and OFF 2 is believed to be due to imperfect re-amorphization of the PCM vias. In State 2, via 2 functioned imperfectly, connecting the metal finger to the terminal with a resistance of ~140MΩ. Therefore, only 3 fingers were effectively connected to form the interdigital electrode.

The measured responses of the device in the 3 different states were fitted to the equivalent circuits in Figure 3. The substrate parasitics (C_p, R_p, and R_{pp}) and the capacitance (C_{switch}) and resistance (R_{switch}), associated with the combination of PCM vias in the *OFF* state were extracted from the *OFF* state measurement (Fig. 3-a) while the remaining equivalent circuit components were extracted from *State 1* and *State 2* measurements (Fig. 3-b) (Being: R_S – the loss introduced by the combination of PCM vias in the *ON* state; C_0 and R_{0p} – static capacitance and resistance of the piezoelectric transducer; and R_m, C_m, and L_m – the motional branch of the resonator). The results of the fitting procedure are reported in Figures 7-8 and Table 1.

Values of *OFF* resistance larger than *~250MΩ*, *ON* resistance of *~5Ω* (*ON/OFF* ratio of *~10^7*) and OFF capacitance of *~40fF*, were extracted for the PCM vias.

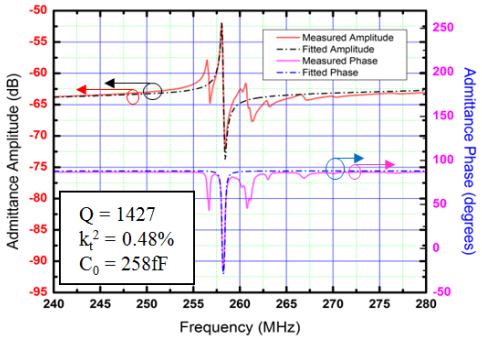

Figure 7: Measured admittance and circuit model fitting (Fig. 3-b, Table 1) of the fabricated resonator with PCM vias 1 and 4 in the ON state (State 1).

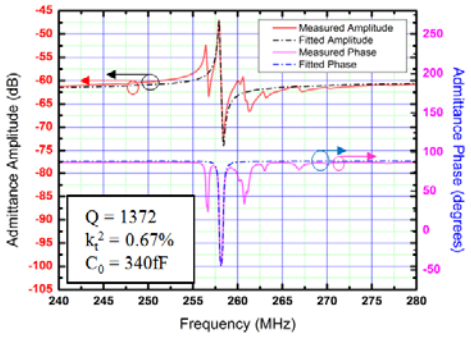

Figure 8: Measured admittance and circuit model fitting (Fig. 3-b, Table 1) of the fabricated resonator with the all 4 PCM vias in the ON state (State 2). Although all the PCM vias are turned ON, via 2 malfunctioned, showing a resistance of ~140MΩ. Therefore, only 3 fingers are effectively connected to form the interdigital electrode.

The values of C_0 and k_t^2 extracted from the measurements for each possible device configuration were compared with the ones estimated by FEM simulations (Fig. 4). Although a slight difference in absolute values is observed due to imperfections in the model and material coefficients used in the simulation, the experimentally recorded relative variations of C_0 and k_t^2, for different configurations of the top electrode, closely match the ones achieved by FEM simulations.

These experimental results clearly indicate that the proposed design solution enables not only effective *ON/OFF* switching of the acoustic resonance of the device (*~18X* impedance variation at resonance, C_{on}/C_{off} *~4* with parasitics, C_{on}/C_{off} *~7* without parasitics), but also tunability of the electrical capacitance ($258fF < C_0 < 340fF$) and reconfiguration of the device electromechanical coupling ($0\% < k_t^2 < 0.7\%$) (Figures 4, 6-8, Table 1) which can potentially lead to the implementation of filter architectures (exclusively based on AlN/PCM high performance resonators and capacitors) whose frequency, order, bandwidth, and roll-off can be dynamically reconfigured.

CONCLUSION

This paper reports on first demonstration of the monolithic integration of phase change material (PCM) RF switches with a MEMS resonator technology to implement switching and reconfiguration functionalities. A reconfigurable piezoelectric MEMS resonator using phase change material (PCM) based switchable electrodes was demonstrated. Miniaturized ($2\times2\ \mu m^2$) $Ge_{50}Te_{50}$ vias were employed as low loss (*ON* resistance < *5Ω*), high dynamic range (*ON/OFF* ratio *~10^7*), and low *OFF*-capacitance (*~40fF*) ohmic switches to control and dynamically reconfigure the number of metal fingers composing the interdigital electrode employed to excite a higher order contour-extensional mode of vibration in an AlN micro-plate. This innovative design solution allowed direct control and reconfigurability of the electrical coupling across the piezoelectric body of the device (by selecting the number of metal lines forming the electrode) enabling not only effective *ON/OFF* switching of the acoustic resonance (*~18X* impedance variation at resonance), but also reconfiguration of the device electromechanical coupling ($0\% < k_t^2 < 0.7\%$) and electrical capacitance ($258fF < C_0 < 340fF$) which can potentially lead to the implementation of filter architectures (exclusively based on AlN/PCM high performance resonators and capacitors) whose frequency, order, bandwidth, and roll-off can be dynamically reconfigured.

ACKNOWLEDGEMENTS

The authors would like to thank the staff of the George J. Kostas Nanotechnology and Manufacturing Facility, Northeastern University (Scott McNamara and David McKee) for their support in device fabrication. The authors would also like to acknowledge DARPA MTO for funding (Dr. William Chappell).

REFERENCES

[1] C. T.-C. Nguyen, “MEMS technology for timing and frequency control,” IEEE Trans. Ultrason. Ferroelectr. Freq. Control, vol. 54, no. 2, pp. 251–270, Feb. 2007.

[2] D. Weinstein and S. A. Bhave, “Internal dielectric transduction of a 4.5 GHz silicon bar resonator,” in IEEE Int. Electron Devices Meeting, Dec. 2007, pp. 415–418.

[3] G. Piazza, P. J. Stephanou, and A. P. Pisano, “Piezoelectric aluminum nitride vibrating contour-mode MEMS resonators,” J. Microelectromech. Syst., vol. 15, no. 6, pp. 1406–1418, Dec. 2006.

[4] R. Abdolvand, G. K. Ho, J. Butler, and F. Ayazi, “ZnO-on-nanocrystalline-diamond lateral bulk acoustic resonators,” in Proc. 20th IEEE Int. Conf. Micro Electro Mechanical Systems, Kobe, Japan, Jan. 2007, pp. 795–798.

[5] M. Rinaldi, C. Zuniga, C. Zuo, and G. Piazza, “Super High Frequency Two-Port AlN Contour-Mode Resonators for RF Applications”, IEEE Transactions on Ultrasonics, Ferroelectrics, and Frequency Control, vol. 57, n. 1, pg. 38-45, 2010.

[6] M. Rinaldi, C. Zuo, J. Van der Spiegel and G. Piazza, “Reconfigurable CMOS Oscillator based on Multi-Frequency AlN Contour-Mode MEMS Resonators”, IEEE Transactions on Electron Devices, vol. 58, issue 5, pg. 1281-1286, 2011.

[7] Nordquist, C.D.; Olsson, R.H.; Scott, S.M.; Branch, D.W.; Pluym, T.; Yarberry, V., "On/Off micro-electromechanical switching of AlN piezoelectric resonators," Microwave Symposium Digest (IMS), 2013 IEEE MTT-S International , vol., no., pp.1,4, 2-7 June 2013

[8] Piazza, Gianluca. "Chapter 2: Contour Mode Aluminum Nitride Piezoelectric MEMS Resonators and Filters." *MEMS-based Circuits and Systems for Wireless Communication*. Ed. Christian Enz and Andreas Kaiser. New York: Springer, 2013. 29-37. Print.

[9] Y. Shim, G. Hummel, and M. Rais-Zadeh, "RF switches using phase change materials," IEEE International Conference on Microelectromechanical Systems (MEMS’13), Taipei, Taiwan, pp. 237-240, Jan, 2013.

CONTACT

*G. Hummel, tel: +1-603-762-3014; hummel.gw@husky.neu.edu

VARIABLE THICKNESS DIAPHRAGM FOR A STRESS INSENSITIVE WIDEBAND PIEZOELECTRIC MICROMACHINED ULTRASONIC TRANSDUCER

Ofer Rozen[1], Stefon E. Shelton[1], André Guedes[2], and David A. Horsley[1]*
[1] University of California Davis, USA
[2] Chirp Microsystems, Inc., USA

ABSTRACT

A novel design for robust, air-coupled piezoelectric micromachined ultrasonic transducers (PMUTs) is presented. The design achieves a 10-fold reduction in the variation in fundamental frequency created by across-wafer residual stress gradients in the piezoelectric AlN layer. We realized this improvement by designing a thick-layered PMUT diaphragm with an 8 µm thick passive layer and a 375 µm radius. Simultaneously, we maintained the PMUT's wide bandwidth, required to achieve sufficient axial resolution in range measurement applications, by patterning wedge-shaped ribs that reduce the diaphragm's mass while enhancing stiffness. Compared to a traditional flat plate design with the same initial thickness, surface area, and center frequency, the ribbed designs are predicted to have twice the bandwidth and twice the sound pressure level – bandwidth product (SPL·BW).

INTRODUCTION

Despite the intensive study of micromachined ultrasonic transducers (MUTs) during the last 20 years, most designs adhere to clamped square and circular plates. The few attempts to modify this convention had different goals than this work. References [1-3] compared several configurations, targeted to achieve piston-like movement of a capacitive MUT (CMUT), in order to increase the output pressure and the device's active area. However, piezoelectric actuated transducers require a curvature mode shape in order to couple the electrical and the mechanical energy efficiently. For example, a prior study of a circular flexurally-suspended piezoelectric MUT (PMUT) [4] with a a piston-like mode shape, reveals an increased linear operating range at the cost of reducing the electromechanical coupling. Here, a reduced-mass/enhanced-stiffness design is demonstrated to improve the transducers' robustness to residual stress, increase their output pressure, and maintain a wide bandwidth.

Air coupled PMUT's can be used for range finding and gesture recognition applications [5-7]. Such applications require an array of identical PMUTs operating at a center frequency from 40-400 kHz, a fractional bandwidth greater than 5%, and center frequency variation between PMUTs within the same array that does not exceed the fractional bandwidth [6].

A micromachined ultrasonic transducer's dynamic response, namely its center frequency (ω) and bandwidth ($\Delta\omega$), is mainly determined by its mechanical resonance. In a constant-thickness diaphragm, these two parameters are dependent variables. If the diaphragm mechanics is modeled as a lumped second-order mass-spring-damper (m, k, b) system, they can be expressed as

$$\omega = \sqrt{k/m}, \qquad \Delta\omega = b/m \tag{1}$$

where the time-varying displacement of the diaphragm's center is its degree of freedom (DOF).

For a flat, constant-thickness plate, a reference design that we denote as design 0, the mass m_0, stiffness k_0 and damping b_0 are a functions of the plate surface area A_0 and thickness t_0:

$$m_0 \propto A_0 t_0, \qquad b_0 \propto A_0 \tag{2}$$

$$k_0 \propto \frac{t_0^3}{A_0}$$

Therefore, the frequency ω_0 and bandwidth $\Delta\omega_0$ are:

$$\omega_0 \propto \frac{t_0}{A_0} = \frac{t_0}{\pi a^2}, \qquad \Delta\omega_0 \propto \frac{1}{t_0} \tag{3}$$

where a denotes the diaphragm's radius. Residual stress in the thin film layers is known to result in variations in the effective stiffness of the diaphragm, which in turn results in changes in the frequency ω_0. A laminated diaphragm with a stressed AlN layer, will have a center frequency $\omega_{0,res}$ that is shifted relative to that of an unstressed diaphragm, ω_0, [8]

$$\left(\frac{\omega_{0,res}}{\omega_0}\right)^2 = \left[1 + \frac{a^2\,\sigma t_0}{\lambda_{01}^2 D}\right] \tag{4}$$

where σ is the average stress, D is the flexural rigidity, and λ_{01} is a constant defined by the vibration mode-shape of the diaphragm. Because $D \propto t_0^3$, (4) shows that the stress sensitivity of the center frequency, $S_\sigma \propto (a/t_0)^2$. Therefore, when comparing PMUTs with constant ω_0, the stress sensitivity scales inversely with thickness t_0. It is therefore possible to reduce the stress sensitivity by increasing the thickness. However, (3) shows that this approach has the undesirable effect of reducing the bandwidth $\Delta\omega_0$ by the same factor.

In order to separate the two variables we suggest patterning the diaphragm by selectively reducing its thickness. We denote the novel configuration as design 1, so its parameters mass m_1, stiffness k_1 and damping b_1 are functions of the new total diaphragm area A_1 and it maximum thickness t_1:

$$m_1 \propto (1-X)A_1 t_1, \qquad b_1 \propto A_1, \qquad k_1 \propto \frac{t_1^3}{A_1}(1-Y) \tag{5}$$

where X represents the mass reduction relative to the mass of a constant thickness plate with the same planar geometry, and Y represents the stiffness reduction relative to that of a plate with the same planar geometry.

Assuming that design 1 targets the same frequency as design 0, $\omega_1 = \omega_0$, the bandwidth can be adjusted by the mass reduction and thickness:

$$\Delta\omega_1 = \frac{1}{t_1(1-X)} \tag{6}$$

while the size of the new design is determined by both the change in stiffness and mass:

$$\frac{A_0}{t_0} = \frac{A_1\sqrt{(1-X)}}{t_1\sqrt{(1-Y)}} \tag{7}$$

As demonstrated by Equations (6-7), introducing X and Y adds two new design variables that broaden the design space.

To verify this approach, we fabricated patterned PMUTs using aluminum nitride (AlN) as the piezoelectric layer. We patterned wedge-shaped ribs that reduce the diaphragm's mass while enhancing its stiffness, in order to realize a design that is both robust to residual stress and has a wide bandwidth.

9781940470016/HH2014/$25©2014TRF
DOI 10.31438/trf.hh2014.116

DESIGN

We compare two flat PMUT designs (a thin design having a total thickness of 2 µm [8] and a thick design having a total thickness of 9 µm) to five patterned designs. Each patterned design has 8 radial ribs with 0, 5, 20, 35, and 45 degree rib angle, as shown in Figure 1. The ribbed and the flat thick PMUTs have a 1 µm AlN layer and 8 µm low-stress SiO_2 passive layer, while the thin flat PMUTs are composed of two 1 µm AlN layers. Each design has a nominal center frequency of approximately 200 kHz.

Table 1: Diaphragm design table

	Total thickness	***Diameter***
Ref [8]	2 µm	400 µm
Flat	9 µm	770 µm
Ribs	9 µm	750 µm

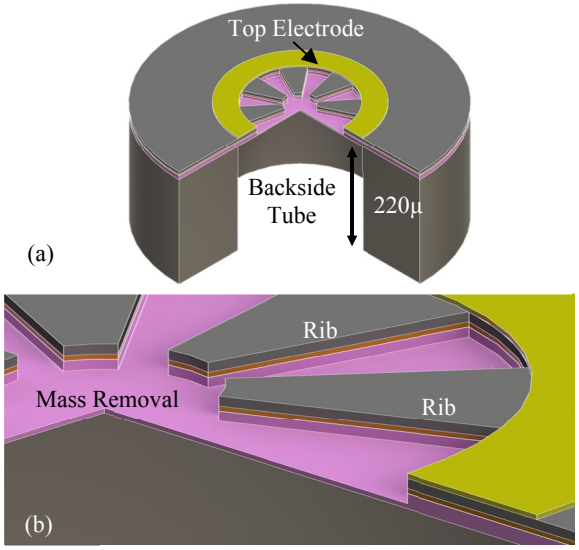

Figure 1: PMUT structure. (a) Reduced-mass/enhanced-stiffness configuration formed by etching a pattern of stiffening ribs into an AlN/SiO_2 unimorph diaphragm. The etched pattern removes mass from the diaphragm's center. (b) Zoom in on the rib structure.

The different PMUT configurations are spread across the wafer in a few repeating die layouts, depicted in Figure 2. Each die layout was duplicated at different positions on the wafer to allow determination of the across-wafer variation in transducer characteristics.

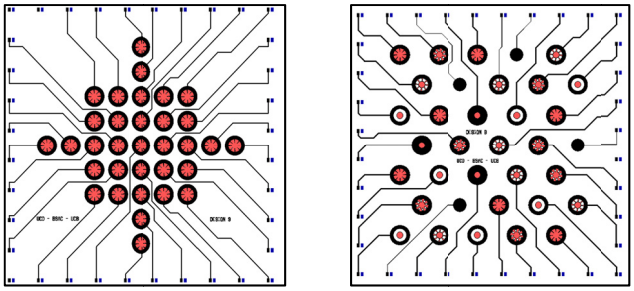

Figure 2: PMUT die layout. (a) 'Cross' die comprised of 36 identical elements. Both flat and 5° ribs cross dice were fabricated (b) 'Test' die comprised of 35 PMUTs of all different configurations. Both dice were duplicated at different positions on the wafer.

The stress sensitivity of the center frequency and the fractional bandwidth were simulated by finite element method (FEM). Stress sensitivity is found using a nonlinear eigenfrequency model at various residual stress levels. The center frequency and the fractional bandwidth were solved by a three dimensional axisymmetric piezo-acoustic model implemented in COMSOL.

As shown in Figure 3, it is possible to reduce the effect of stress on center frequency by increasing the thickness of the flat plate PMUT; however, this approach has the undesirable effect of reducing the bandwidth. The rib pattern, in contrast, reduces stress sensitivity without significantly reducing the bandwidth. The FEM indicates that the thick design reduces the sensitivity of the resonance frequency to residual stress by a factor of 10 compared to thin diaphragms with the same fundamental frequency. The simulations also indicate that the ribbed designs are expected to have twice the bandwidth and twice the sound pressure level – bandwidth product (SPL·BW) in comparison to the thick PMUT design.

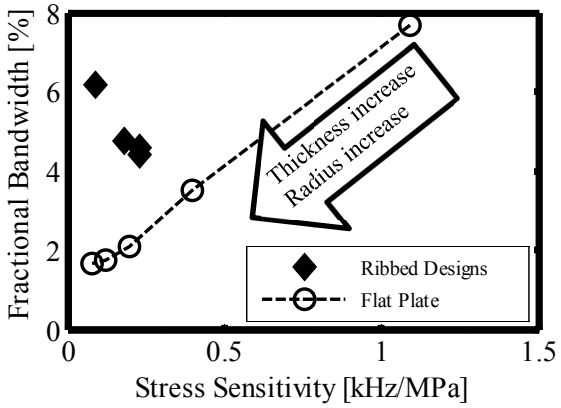

Figure 3: Stress sensitivity versus fractional bandwidth for 200 kHz PMUTs, found by FEM. The diamonds show five ribbed PMUT designs, with rib angle varying from 0°-45°, that have low stress sensitivity while also maintaining wide bandwidth.

FABRICATION

The process starts with a 150 mm silicon wafer with an 8 µm silicon dioxide layer on top. Then, Mo (150 nm)/AlN (1 µm) layers are deposited as the bottom electrode and active layer respectively. Then an Al top electrode is deposited and patterned and the bottom electrode via is opened by etching through the AlN. Next, the AlN, the bottom electrode and the SiO_2 structural layer are patterned using reactive-ion etching (RIE) into 3.5 µm deep ribs. Finally, the wafer is thinned to 220 µm by grinding and the membrane is released by etching the backside Si using deep reactive-ion etching (DRIE).

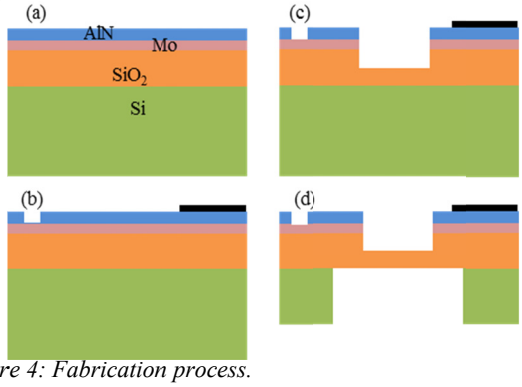

Figure 4: Fabrication process.

RESULTS

Wafer-level measurements of PMUT impedance versus frequency were collected using a semi-automated probe station. A representative frequency response is shown in Figure 5. The impedance data were fit with a Butterworth Van Dyke (BVD) model, allowing extraction of the motional impedance components (R_x, L_x, C_x) and electrical impedance components (R_s, C_0) as well as center frequency ($2\pi f = \omega$) and quality factor (Q), Figure 5. All the mean and standard deviation values reported are the robust values, found using Huber's M-estimation in JMP® 11.0.

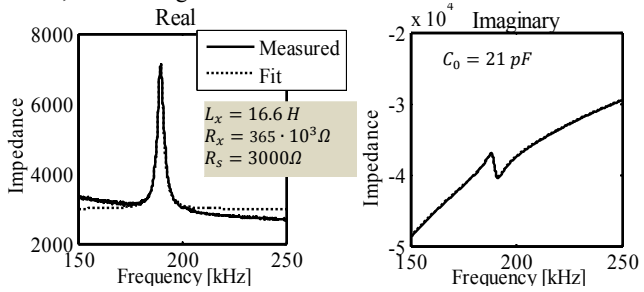

Figure 5: A typical frequency response. From the fit of the real part (left) the electric resistance and the mechanical serial equivalent R_x-L_x-C_x are found and transformed to the mechanical domain into the acoustic damping, effective mass and the stiffness of the diaphragm. From the imaginary part (right), the transducer capacitance C_0 is found.

The center frequency of a total 694 devices of different configurations is analyzed. For both flat and 5° ribs configurations, the histograms, Figure 6, show the center frequency distribution of all such devices. The variation in frequency for the ribbed configuration is half of that of the flat configuration.

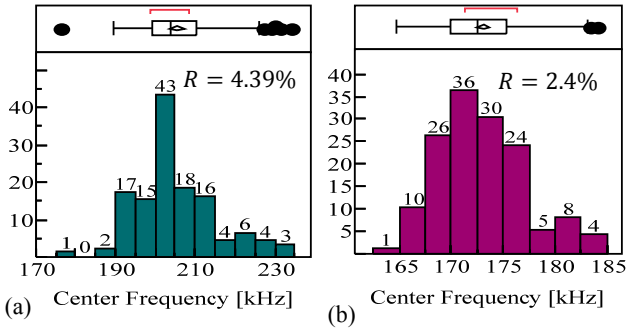

Figure 6: Center frequency histogram for (a) flat and (b) 5° ribs configurations measured at all points across the wafer. R is the robust standard deviation divided by the robust mean.

Results for all configurations were analyzed using the test dice and are shown in Figure 7. While the measured center frequency is higher the simulation's prediction, the differences between the configurations match well with the FEM results.

The simulations also indicated that the ribbed design's bandwidth would be twice that of the flat design. However, the wafer-level measurements indicate little difference in bandwidth for the flat and ribbed designs and both designs have a much higher Q than anticipated. This is due to the fact that the tube beneath each PMUT is not open to the air and is instead closed by the wafer chuck in probe-station measurements.

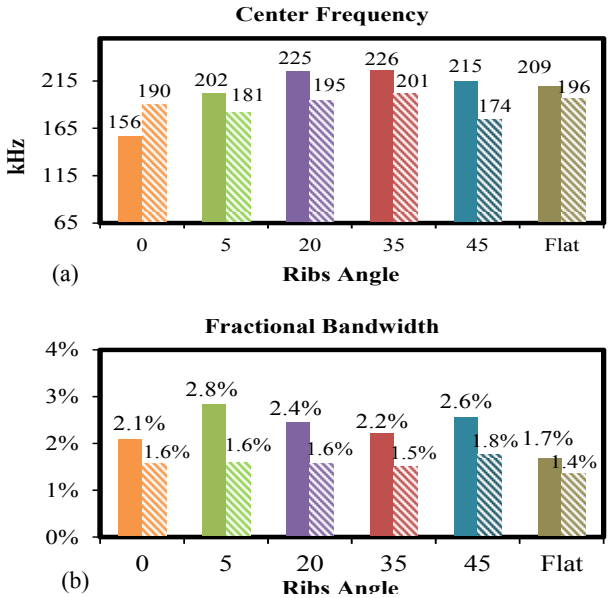

Figure 7: simulated (solid) and measured (hatched) (a) center frequency and (b) fractional bandwidth measured with a closed backside tube. (Simulated with an open backside tube)

Across-Die and Across-Wafer Matching of Center Frequency

A key performance metric is the variation of the PMUT center frequency from the average center frequency across each die and across each wafer. This variation is attributed to differences in PMUT geometry (diameter and film thickness) and residual stress. A wafer map of the mean and standard deviation of center frequency for the two cross dice (Fig. 2a) is shown in Figure 8.

The frequency variation of each design relative to the average frequency measured across the wafer $(\Delta f/\bar{f})$ is summarized in Table 2. While previous work [6] showed an across wafer variation of about 70%, the maximum variation measured in this work is only 8.1%, and the average variation of each design is 2.4%-4.9%.

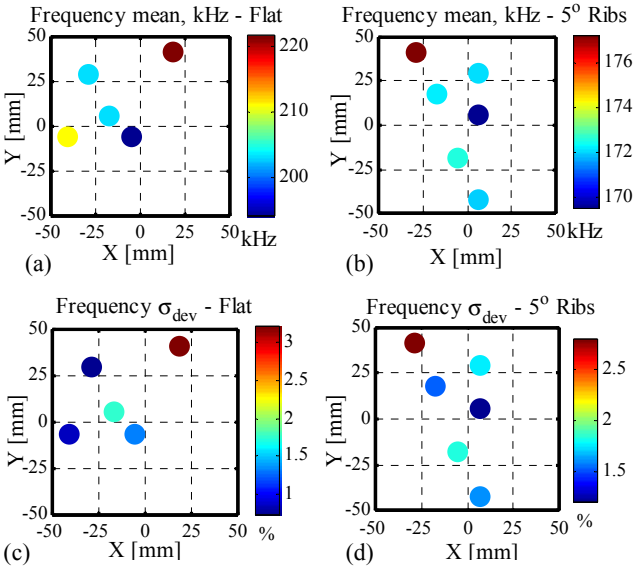

Figure 8: (a-b) Dice's robust mean center frequency and (c-d) robust standard deviation normalized by the mean center frequency, for flat and 5° ribs configuration. X and Y indicate the dice center position, relative to the mask center.

Table 2: Deviation of center frequency relative to wafer average.

Config.	*Minimum*	*Maximum*	*Average*	*N*
0°	3.1%	5.8%	4.2%	3
5°	2.9%	4.8%	3.8%	4
20°	3.3%	4.7%	4.1%	3
35°	2.8%	6.2%	4.0%	3
45°	0.6%	12%	2.4%	35
Flat	1.3%	8.1%	4.9%	35

The across-die variation of center frequency was analyzed for cross shaped arrays, each containing 36 PMUTs, as shown in Figure 2a. From Figure 9 it is clear that the die layout influences the frequency variation. PMUTs on the edge of the cross array are etched faster, have bigger radius and therefore lower frequency. This variation can be eliminated in future layouts by patterning dummy PMUTs around the array in order to maintain similar boundary conditions in the final DRIE step.

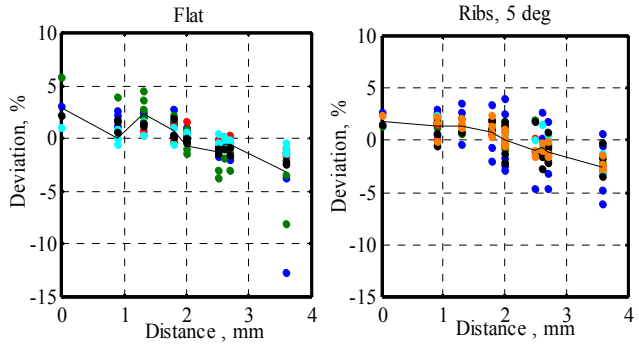

Figure 9: Center frequency deviation as a percentage of the die's mean frequency vs. distance of the PMUT from the center of the die. Different colors represent different dice. The solid line indicates the mean value at each location.

The across die variation robust statistics are shown in

Table 3. We are achieving low and robust variation, as the results are consistent across the wafer, improving the future manufacturing yield.

Table 3: *Deviation of center frequency relative to die average*

Config.	*Minimum*	*Maximum*	*Average*	*N*
5°	0.7%	3.2%	1.6%	5
Flat	1.2%	2.8%	1.8%	6

AlN Material Properties

The PMUT system can be modeled using a lumped parameter model [5]. Using the fitted model, the piezoelectric coefficient e_{31}, of the AlN and its dielectric constant ε_{11} can be extracted, Table 4, assuming a known geometry, density, Young modulus and Poisson ratio of all the layers.

Table 4: AlN material properties

	Literature [9]	*This work*
ε_{11}	*9.5*	*8.45*
e_{31}	*-0.58*	*-0.55*

CONCLUSIONS

We present a variable thickness diaphragm design that simultaneously improves several performance metrics. Six different configurations were compared, with center frequencies ranging between 190 kHz to 209 kHz. The across wafer variation in the center frequency of the ribbed designs is 4%, and their across die variation is 1.6%, 10 times better than previously fabricated flat thin configurations. Future work includes acoustic measurements of the pressure output as well as the frequency response in completely open backside conditions to verify the predicted bandwidth improvement of the rib design.

ACKNOWLEDGMENTS

The authors thank Ira Wygant, Wei Yan Shih, and Philippe Jansen at Texas Instruments for assistance with wafer-level test and data analysis. Devices were fabricated in the UC Berkeley Marvell Nanofabrication Laboratory.

Travel support has been generously provided by the Transducer Research Foundation.

REFERENCES

[1] Y. Huang, X. Zhuang, E. Hggstrom, A. S. Ergun, C. H. Cheng, and B. T. Khuri-Yakub, "Capacitive micromachined ultrasonic transducers with piston-shaped membranes: Fabrication and experimental characterization," in Trans. Ultrason., Ferroelect., Freq. Contr., vol. 56, pp. 136-145, 2009.

[2] A. Nikoozadeh and P. T. Khuri-Yakub, "CMUT with substrate-embedded springs for non-flexural plate movement," in IEEE Ultrason. Symp, 2010, pp. 1510-1513.

[3] B. C. Lee, A. Nikoozadeh, K. K. Park, and B. T. Khuri-Yakub, "Understanding CMUTs with Substrate-Embedded Springs," in IEEE Ultrason. Symp. , 2011, pp. 1008-1011.

[4] A. Guedes, S. Shelton, R. Przybyla, I. Izyumin, B. Boser, and D. A. Horsley, "Aluminum nitride pMUT based on a flexurally-suspended membrane," in Transducers, 2011, pp. 2062-2065.

[5] R. J. Przybyla, S. E. Shelton, A. Guedes, Izyumin, II, M. H. Kline, D. A. Horsley, et al., "In-Air Rangefinding With an AlN Piezoelectric Micromachined Ultrasound Transducer," IEEE Sensors J., vol. 11, pp. 2690-2697, Nov 2011.

[6] S. Shelton, A. Guedes, R. Przybyla, R. Krigel, B. Boser, and D. Horsley, "Aluminum Nitride Piezoelectric Micromachined Ultrasound Transducer Arrays," in Hilton Head, 2012, pp. 291-294.

[7] R. J. Przybyla, S. E. Shelton, A. Guedes, R. Krigel, D. A. Horsley, and B. E. Boser, "In-Air Ultrasonic Rangefinding and Angle Estimation Using an Array of AlN Micromachined Transducers," in Hilton Head, 2012, vol. 7, p. 3.

[8] S. Shelton, C. Mei-Lin, P. Hyunkyu, D. Horsley, B. Boser, I. Izyumin, et al., "CMOS-compatible AlN Piezoelectric Micromachined Ultrasonic Transducers," in IEEE Ultrason. Symp., 2009, pp. 402-405.

[9] A. V. Sotnikov, H. Schmidt, M. Weihnacht, E. P. Smirnova, T. Y. Chemekova, and Y. N. Makarov, "Elastic and piezoelectric properties of AlN and LiAlO2 single crystals," in Trans. Ultrason., Ferroelect., Freq. Contr. vol. 57, pp. 808-811, 2010.

CONTACT

*O. Rozen, tel: +1-530-219-8461; orozen@ucdavis.edu

BIO-INSPIRED ACOUSTIC SENSING WITH ULTRA-HIGH ASPECT-RATIO, MICROSPHERE-TIPPED PDMS MICROPILLARS

Jungwook Paek and Jaeyoun Kim
Department of Electrical and Computer Engineering, Iowa State University, Ames, Iowa, USA

ABSTRACT

The cricket's cercal acoustic receptors with their long and thin filiform hairs produce excellent performance in acoustic sensing, attracting numerous attempts to mimic them. However, their replication requires high aspect-ratio micropillars, which is a great difficulty when attempted with conventional micro-fabrication techniques and PDMS. Here, we present a new technique based on the direct drawing technique incorporated with the *in situ* heating, which enables the realization of PDMS micropillars with unprecedented aspect-ratios (40 ~112). Our scheme also allows self-aligned capping of the micropillars with microspheres. To validate the utility of the microsphere-tipped micropillar (MSMP), we transform it into all-optically interrogated acoustic sensors inspired by the filiform hairs.

INTRODUCTION

Nature is replete with tiny wind and sound sensors such as the cricket's cercal acoustic receptors shown in Fig.1 [1]. Using their thin and long filiform hairs, the receptors produce excellent performance in acoustic sensing, attracting numerous attempts to mimic them [2]. However, their replication requires high aspect-ratio micropillars, which is a great difficulty when attempted with conventional, replica-molding-based fabrication techniques and soft materials such as PDMS [3]. Here, we present a new technique, which enables the realization of PDMS micropillars with unprecedented aspect-ratios (40 ~112), through a combined utilization of direct drawing and *in situ* thermal hardening [4]. Our technique also allows automatic integration of multi-functional microspheres at the tips of the micropillars in a self-aligned fashion.

To validate the utility of the microsphere-tipped micropillar (MSMP), we configure it into all-optically interrogated airflow sensors inspired by the filiform hairs.

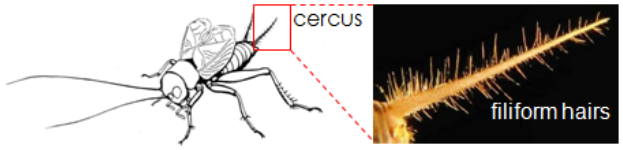

Figure 1: The cricket's cercus hosts a large number of filiform hairs as shown in the inset (from Ref. 1). They deform in response to airflows and generate signals for wind and sound reception.

MICROPILLAR FABRICATION

Steps for the PDMS MSMPs fabrication are depicted in Fig. 2. We prepared an array of 58μm-diameter Ag-coated hollow glass microspheres on a piece of double-stick tape as the drawing probe (Fig. 2a). Then we attached the array to a micromanipulator. Also, we spin-coated a thin layer of PDMS and pre-baked it on a hot plate at 100°C (Fig. 2b). During the pre-bake, we lowered the microsphere array towards the PDMS thin film until the separation was reduced to 50μm. After the pre-bake, we further lowered the array so that it can physically contact the PDMS film (Fig. 2c). After 40 sec, we lifted the micromanipulator, drawing PDMS micropillars (Fig. 2d). The completed PDMS micropillars were then post-baked at 100°C for 2 hours and cured at room temperature for 24 hours. Then we detached the microspheres from the tape, leading to the realization of the PDMS MSMPs (Fig. 2e). Fig. 3 shows fabricated high aspect-ratio MSMPs.

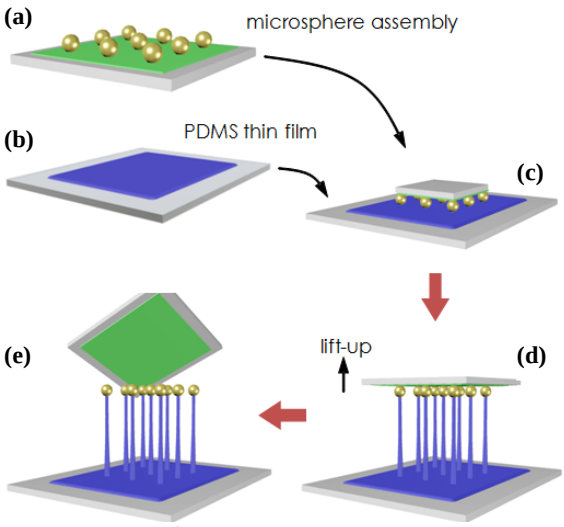

Figure 2:Fabrication flow (a) microsphere assembly (b) PDMS thin film (c) Contact between the microsphere array and PDMS thin film (d) Directly drawing PDMS micropillars (e) Detaching MSMPs from the tape

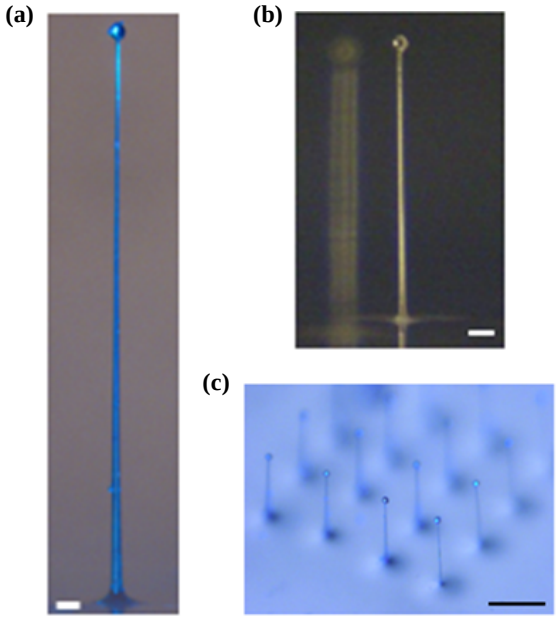

Figure 3: Optical micrographs of (a) PDMS micropillar with an aspect-ratio of 112 (scale bar: 100 μm)(b) PDMS micropillar with an aspect ratio of 84 (Scale bar: 100 μm) (c) 4×4 array comprising PDMS micropillars with an average aspect-ratio of 42 (Scale bar: 700 μm)

9781940470016/HH2014/$25©2014TRF
DOI 10.31438/trf.hh2014.117

BIO-INSPIRED ACOUSTIC SENSING

To demonstrate acoustic sensing capabilities of the PDMS MSMPs, we turn three MSMPs in Table 1 into mirror-coupled flexible waveguides incorporated with optical read-out interfaces. The micropillar functions as a flexible waveguide which deforms under airflows, and the microsphere as a self-aligned reflector which reports the micropillar's level of deformation as shown in Fig.4a. Fig.4b, c shows the MSMP-A's deformation in the absence and presence of airflow, respectively. In the former, the MSMP stays straight, producing maximal reflection. Upon contact with a constant airflow, it bends due to the fluidic drag force, which decreases the reflection. The change in the reflectance is also plotted in Fig. 5 for all three MSMPs as a function of the airflow rate. The results indicate that the reflectance is a good measure of the airflow rate.

Table 1: Characteristics of the PDMS micropillars under test

	Height (um)	Ave. diameter (um) (top, middle, base)	Aspect-ratio
MSMP-A	800	19.8	40.4
MSMP-B	1600	22	72.7
MSMP-C	2000	23	86.9

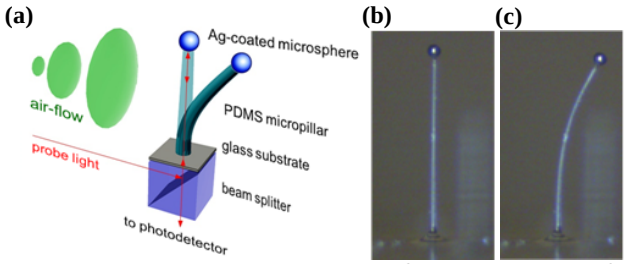

Figure 4: (a) The optical read-out setup for MSMP-based airflow sensing (b) and (c) MSMP-A's bending in response to the absence and presence of airflow, respectively

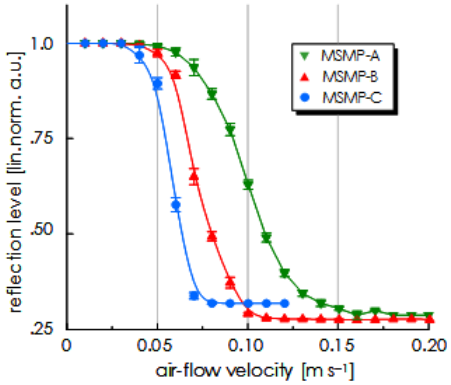

Figure 5: The change in the micropillar's reflection level as a function of the airflow velocity. The error bars represent the corresponding standard deviations.

We also investigated the utility of the MSMPs for sensing time-varying airflows, *i.e.*, sound-waves. Fig. 6a shows the optical reflection from MSMP-C responding to a sound-wave at 90 Hz with two identical dips per one temporal period. The shades in the plot represent one temporal period. The resulting generation of higher harmonics is evident in the Fourier transform of the 90 Hz response as shown in Fig. 6b, providing accurate information on the frequency of the sound-wave. MSMP-A and B generated similar reflection pattern. Fig. 6c shows how modulation-depth of the reflection output changes as a function of the excitation frequency over 60 ~ 200 Hz, showing 102 Hz and 93 Hz as the peak frequency of MSMP-B and C, respectively. Resonance at this low frequency range is difficult to obtain with cantilevers made of hard materials.

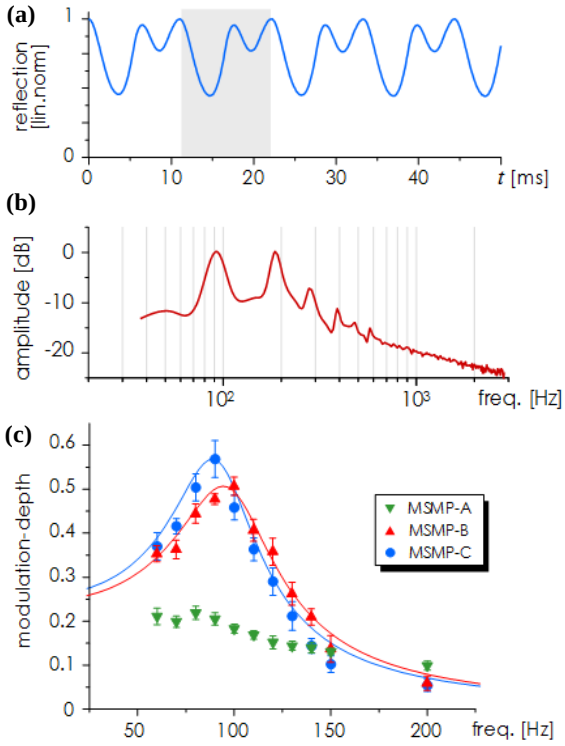

Figure 6: (a) Temporally changing reflections from MSMP-C in response to sound waves at 90 Hz (b) The amplitude portion of the Fourier transform of the 90 Hz output (c) The modulation-depth of the temporal responses from the three MSMPs as a function of the excitation frequency

CONCLUSION

We present a new soft-lithography technique which not only enables the realization of high aspect-ratio PDMS micropillars but also allows integration of multi-functional microspheres in a self-aligned fashion. Bio-inspired acoustic sensors we configured based on the micropillars exhibited high sensitivity at resonance frequencies close to 100 Hz.

REFERENCES

[1] Miller, J. P., Krueger, S., Heys, J. J. and Gedeon, T.,"Quantitative Characterization of the Filiform Mechanosensory Hair Array on the Cricket Cercus",*PLoS ONE*6, e27873 (2011)

[2] Dijkstra, M. *et al*,"Artificial sensory hairs based on the flow sensitive receptor hairs of crickets",*J. Micromech. Microeng.* 15, S132 (2005).

[3] Große, S., Schröder, W. and Brücker, C., "Nano-newton drag sensor based on flexible micro-pillars",*Meas. Sci. Technol.* 17, 2689 (2006).

[4] Paek, J. and Kim, J., "Microsphere-assisted fabrication of high aspect-ratio elastomeric micropillars and waveguides", *Nature Communications*, 5, 3324 (2014).

FLEXIBLE, TRANSPARENT, PRESSURE-SENSITIVE MICROFLUIDIC ARRAY FOR ARTIFICIAL TACTILE APPLICATIONS

R. Li, B. Nie, P. Digiglio and T. Pan
Micro-Nano Innovations (MiNI) Laboratory, Department of Biomedical Engineering,
Department of Electrical and Computer Engineering, University of California, Davis, California, USA

ABSTRACT

This paper reports the first effort to achieve large-area dynamic pressure mapping by a flexible and transparent microfluidic film, referred to as microflotronics, facilitating seamless integration with state-of-the-art microelectronics. The microflotronic devices offer a sensitivity of 0.45 kPa^{-1} and response time in millisecond range, which is at least an order of magnitude faster than that of its conventional solid-state counterparts. Several practical applications were successfully demonstrated, including surface topology mapping and dynamic blood pressure monitoring. The microflotronic devices offer an alternative approach to the solid-state pressure sensors, by offering an unprecedented sensitivity and ultrafast response time in a completely transparent, flexible and adaptive platform.

INTRODUCTION

Flexible pressure sensing has been a pertinent topic in both academic and industrial research over the past few years. For example, Javey's group utilized pressure sensitive rubber as the pressure sensing layer to modulate current in a thin-film transistor [1,2]. Bao's group utilized a hollow-sphere microstructure to perform resistive pressure sensing in conducting polymer film [3]. As a new innovative approach, we utilize a continuous microfluidic layer as the sensing element for large-area dynamic pressure mapping applications with an ultrahigh sensitivity of 0.45 kPa^{-1} in a compact, flexible, and transparent package as shown in Figure 1. Dissimilar to solid-state alternatives, the response time of the microflotronic device is in the millisecond range, which is at least an order of magnitude faster [1,3]. The overall device packaging can be as thin as 200µm with an optical transparency greater than 80%. The fabrication process of the device is fully compatible with the industrial-scale manufacturing of capacitive touchscreen devices and liquid-crystal displays.

Figure 1: Photographs of the microflotronic film 18 by 10 array with a 5×5mm² spatial resolution demonstrating ultra-flexibility and transparency.

METHODS

Operation Principle

Figure 2 illustrates the structural assembly of the microflotronic film which consists of flexible top and bottom polyethylene terephthalate (PET) membranes patterned with orthogonally aligned transparent indium-tin-oxide (ITO) microelectrode arrays, separated by mechanically supporting microstructures, between which is filled with a transparent microfluidic sensing layer. The impedance-based microflotronic sensing principle is demonstrated in Figure 3. The equivalent circuit of the microfluidic film was modeled to include the microfluidic film resistive element (R_L), the electrical double layer capacitance (C_{EDL}), and the parallel-plate capacitance (C_P). The force-sensing membranes experience deformation under external pressure, leading to displacement in the microfluidic volume which changes the capacitive and resistive values measured.

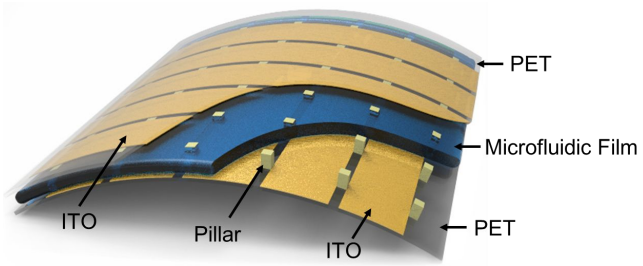

Figure 2: Schematic illustration of the microflotronic device structure, consisting of the top and bottom electrode layers with an orthogonally placed electrode array supported by a micropillar layer and filled with a microfluidic sensing layer.

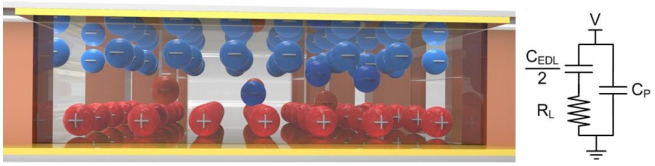

Figure 3: Cross-sectional sketch of the device sensing principle: ions in the microfluidic film accumulate at the liquid-electrode contacts which generate the EDL capacitances (C_{EDL}), liquid film is modeled as a resistor (R_L) and parallel plate capacitance (C_p) between the two electrodes.

Fabrication Process

First, the ITO electrodes were patterned using photolithography and wet etching. Then, UV patternable dielectric dry-film was laminated onto the substrate to form the micropillar array. Next, PDMS oligomer transfer and plasma-activated bonding was utilized to assemble the two electrode array films. Last, the working fluid was filled between the electrode films, and the inlet/outlet ports were sealed.

RESULTS

Characterization of Device Sensitivity

Figure 4a-c shows characterization results of the device sensitivity for different membrane thicknesses, spatial resolutions, and microfluidic layer heights. Specifically, the device sensitivity is evaluated as the relative resistance change ($\Delta R/R_0$) over the centralized pressure load (P).

Characterization of Response Time

Figure 4d-f summarizes the time-resolved experiment results to demonstrate the facilitated mechanical responses of DI

9781940470016/HH2014/$25©2014TRF
DOI 10.31438/trf.hh2014.118

water-filled and ethylene glycol (EG)-filled devices to 1Hz, 10Hz and 100Hz mechanical stimuli. Both microflotronic devices achieved a relaxation time in the millisecond range.

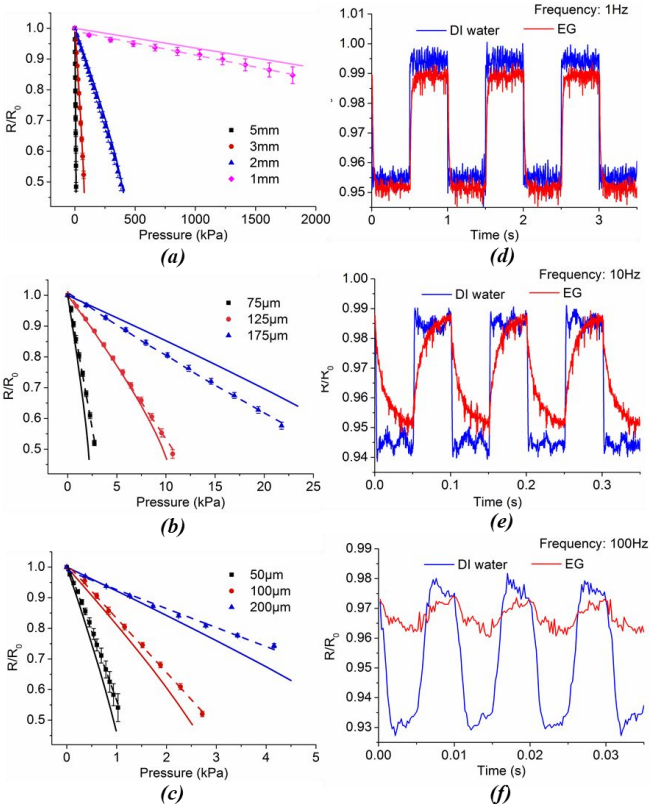

Figure 4: Experimental results (dots) with fitting curves (dash lines) against theoretical predictions (solid lines) of the microflotronic device sensitivity with different (a) spatial resolutions, (b) membrane thicknesses and (c) microfluidic layer heights. Mechanical response result under stimuli of (d) 1Hz, (e) 10Hz and (f) 100Hz.

Surface Topology Mapping

An 18 by 10 pixel array with a total surface area of 9×5 cm^2 was fabricated to demonstrate surface topology mapping capability. As shown in Figure 5, the pressure distribution of the letter-shaped polymeric stamp pressed onto the microflotronic film was clearly resolved.

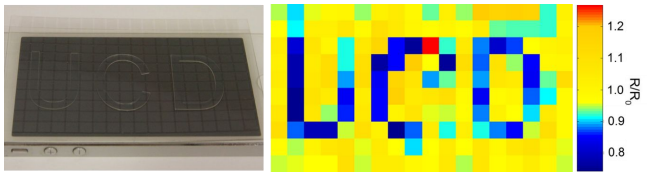

Figure 5: Result for polymeric stamp surface topology pressure mapping.

Radial Arterial Pressure Mapping

Unlike existing arterial tonometry systems [4], the proposed microflotronic film array offers not only real-time and continuous recording of the pulse pressure waveform, but also automatic pulse tracking that determines the optimal positions for pulse recording by analyzing the dynamic pressure distribution over the skin surface. Aligning the device on the wrist along the radial artery, the pressure variation under the 3 by 3 microflotronic array during one cardiovascular cycle was mapped as shown in Figure 6a. One recorded waveform gave an example of the signal acquired from the array. The optimal pulse tracking positions were determined based on the maximum pressure variations measured as shown in Figure 6b-d. By providing the dynamic pressure mapping result with ultrahigh sensitivity, the microflotronic device demonstrated its potential to automatically locate and resolve the arterial pulse waveforms with the delicate pressure events detected non-invasively.

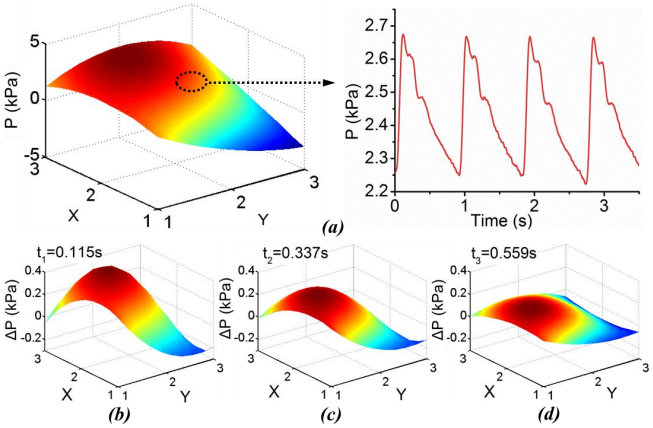

Figure 6: Non-invasive radial arterial pressure mapping. (a) Static pressure distribution on the 3 by 3 microflotronic array with three discrete radial artery waveforms recorded. During cardiovascular cycles, the consecutive pressure distribution maps on the skin surface were plotted at distinct physiological events: (b) systolic pressure peak t_1=0.115s, (c) dicrotic notch t_2=0.337s, and (d) diastolic runoff t_3=0.559s.

CONCLUSION

A flexible, transparent, pressure-sensitive film has been reported utilizing an embedded microfluidic sensing layer to achieve pressure and force mapping over various surface topologies. This novel microflotronic film offers a new flexible sensing interface that can be highly advantageous for emerging medical and electronic applications, such as health monitoring, medical prosthesis, 3D touchscreens, and human-machine interfaces, where device sensitivity, surface adaptability, and large-area mapping are all essential.

REFERENCES

[1] K. Takei, T. Takahashi, J. C. Ho, H. Ko, A. G. Gillies, P. W. Leu, R. S. Fearing and A. Javey, "Nanowire active-matrix circuitry for low-voltage macroscale artificial skin", Nature Materials 9(10), 821-826 (2010).

[2] C. Wang, D. Hwang, Z. B. Yu, K. Takei, J. Park, T. Chen, B. W. Ma and A. Javey, "User-interactive electronic skin for instantaneous pressure visualization", Nature Materials 12(10), 899-904 (2013).

[3] L. Pan, A. Chortos, G. Yu, Y. Wang, S. Isaacson, R. Allen, Y. Shi, R. Dauskardt and Z. Bao, "An ultra-sensitive resistive pressure sensor based on hollow-sphere microstructure induced elasticity in conducting polymer film", Nature communications 5(2014).

[4] G. Schwartz, B. C. Tee, J. Mei, A. L. Appleton, H. Wang, Z. Bao, "Flexible polymer transistors with high pressure sensitivity for application in electronic skin and health monitoring," Nature communications 4, 1859 (2013).

"GECKOFLUIDICS": A NEW CONCEPT IN REVERSIBLE BONDING OF MICROFLUIDIC CHANNELS

A. Wasay, and D. Sameoto*
Department of Mechanical Engineering, University of Alberta, Edmonton, Alberta, Canada

ABSTRACT

Reversibly sealed PDMS microfluidics are attractive because they solve the bonding challenges that are so difficult with rigid thermoplastics. Unfortunately, reversible bonding with PDMS is also problematic, because the channels cannot hold high pressures. In this work, we demonstrate a significant advancement through the application of gecko-inspired adhesives to strongly enhance polymer microfluidic reversible bonding and apply it with thermoplastic elastomers in a simple thermocompression molding process. This technique is applied to thermoplastic elastomers which have recently demonstrated great promise as a replacement material for PDMS in many microfluidic applications.

INTRODUCTION

Reversible microfluidic bonding with elastomer materials is easy, but typically very weak [1]. A strong, reversible bond may be considered a contradiction in terms, but is in fact achievable through the use of special contact geometries as employed in the field of gecko-inspired adhesives. Using a recently developed manufacturing method for thermoplastic elastomer dry adhesives [2], we demonstrate how these materials can be employed to turn any nearly flat surface into a microfluidic system with minimal effort.

For a typical reversible bonded channel in an elastomer based microfluidic system, a channel wall simply meets the bonded surface with a flat punch type contact tip at an angle of approximately 90°. This type of geometry is extremely vulnerable to stress concentrations at the contact edge which will cause much earlier adhesive failure than the theoretical strength possible via van der Waals forces [3]. An overhanging cap however strongly reduces the stress concentrations at the edge and can permit reversible adhesion of fibers approaching 1 MPa in axial loading. Through the design of a single "fiber" that is continuous around the perimeter of the desired channel shape, we can define a self-sealing gasket which will contain fluid. This gasket can be surrounded by further fibers to enhance the total adhesion and help make the rest of the surface more tolerant to defects and surface roughness. This mechanism strongly improves the total performance of the reversible bond.

FABRICATION

The fabrication steps are similar to those reported earlier for the fabrication of a master mold [4], and the thermocompression molding of a thermoplastic elastomer [2]. With the choice of an appropriate thermoplastic elastomer that will flow well at elevated temperatures, even highly interlocked features can be molded without large amounts of trapped gas. The "geckofluidics" concept has thus far been demonstrated with two types of styrene-ethylene-butylene-styrene (SEBS) elastomers, Kraton G1657 and G1645, but other materials could be used in future. Thermocompression molding time typically requires no more than a couple minutes total to produce the channels once the silicone mold is prepared. The molding is done using a Branson ultrasonic welder without application of ultrasonic energy, which can apply between 15-448lbs force on a pre-heated hotplate containing the silicone molds and elastomer pucks.

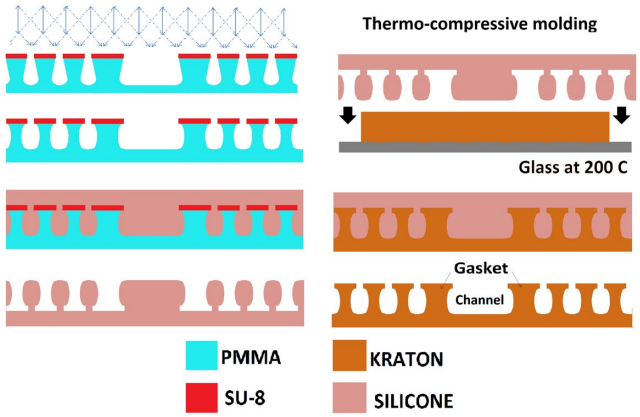

Figure 1: An SU-8 coated acrylic substrate is exposed with a semi-collimated 254 nm light and developed in solvent to produce a master mold with individual adhesive fibers and continuous features that serve as channel walls. Channels can range in depth from several to over 100 µm. A silicone negative (TC-5030 from BJB Enterprises) is cast from this master then demolded. The silicone negative is used for thermo-compression molding of Kraton G1657 or G1645 elastomer. Pellets of Kraton resin are first melted against a glass microscope slide on a hot plate at 200 °C, and then the silicone mold is placed on top. Once the mold and pellets are preheated, the silicone mold is pressed down for 30 seconds at variable force depending on the device size and desired thickness. After cooling and demolding, the elastomer geckofluidics can be peeled off the glass slide and are reversibly bonded to any relatively smooth surface.

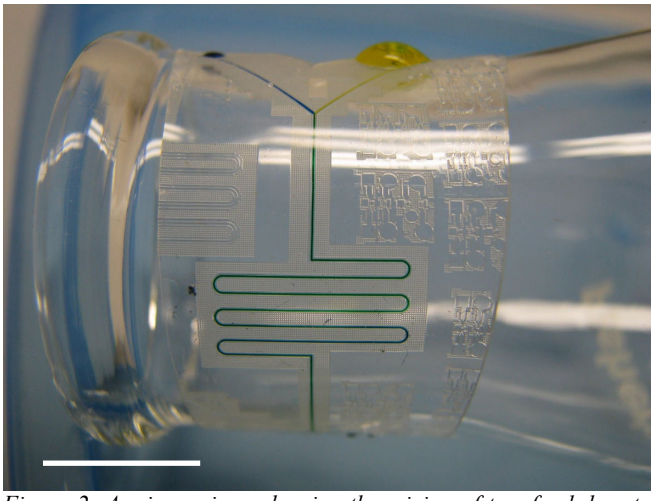

Figure 2: A micro-mixer, showing the mixing of two food dyes to produce a homogeneous blend. The whole design is attached reversibly and strongly to the neck of a clean Erlenmeyer flask demonstrating the versatility and flexibility of the technique. For example, in this case, gravity driven flow can assist in filling the channels of a micromixer while keeping large drops contained on the top surface. The scale bar is 1 cm.

9781940470016/HH2014/$25©2014TRF
DOI 10.31438/trf.hh2014.119

RESULTS

Once the microfluidics are demolded from the mold, they can have holes opened in SEBS reservoirs with a punch (Fig. 2-4), or be simply bonded like a sticker over through holes that are already drilled or cut into prepared substrates. For an initial proof of concept design, a polystyrene petri dish lid was sputtered with 20 nm of gold through a stencil to form electrodes to match the reservoirs of a capillary electrophoresis channel adapted from previous work [5] (Fig. 3). Wires were soldered to the gold electrodes with Field's metal. Future trials will be completed to compare with other recently reported work on SEBS electrokinetic applications [6]. Well-designed adhesive pillars permit extreme reversible peel strength of geckofluidics (Fig. 4). A rigid backing layer may be added to transfer load from the gaskets (Fig. 5) to the array of pillars and improve sealing against higher pressure.

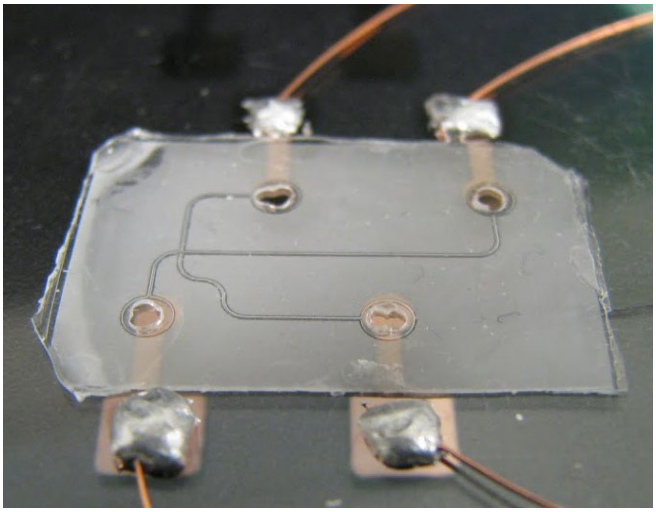

Figure 3: A capillary electrophoresis design adapted from other work [5] showing reversibly bonded channels on top of electrodes.

Figure 4: A demonstrative view of geckofluidics with dyed channels under a peeling load of 75 grams

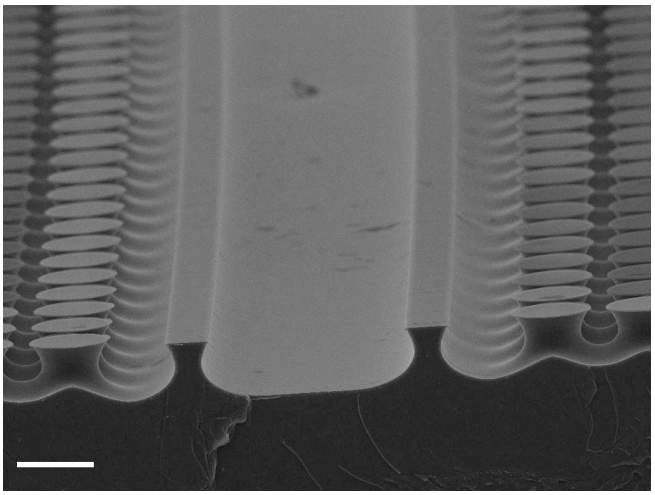

Figure 5: Scanning electron microscope image of SEBS pillars and gaskets for geckofluidics. Some debris is seen from the cutting process, but otherwise channels and cap surfaces are smooth for quality bonding and good imaging. Scale bar represents 100 µm.

CONCLUSIONS

We have demonstrated a novel and extremely effective fabrication technology for developing reversible bonded microfluidics with strong resistance to leakage and easy integration with electrodes. Because it can be bonded to any relatively smooth surface with minimal effort, it is a solution that could be integrated with CMOS or silicon MEMS with few modifications.

ACKNOWLEDGEMENTS

We would like to thank NSERC for financial support and CMC microsystems for test support through access to their microsystems integration platform (MIP).

REFERENCES

[1] J.C. McDonald, M.L. Chabinyc, S. Metallo, J. R. Anderson, A. D. Stroock, and G. M. Whitesides, "Prototyping of microfluidic devices in poly(dimethylsiloxane) using solid-object printing" Anal. Chem., **74**, 1537, (2002)

[2] W. Khaled, and D. Sameoto, "Manufacture of mushroom shaped dry adhesives by thermo-compression molding of thermoplastic elastomers", Proc. of the Adhesion Society, February 23-26, (2014). San Diego CA.

[3] G. Carbone, E. Pierro, and S. N. Gorb, "Origin of the superior adhesive performance of mushroom-shaped microstructured surfaces." Soft Matter, **7,** 5545 (2011)

[4] D. Sameoto and C. Menon, "Deep UV patterning of acrylic masters for molding biomimetic dry adhesives", J. Micromech. Microeng., **20,** 115037, (2010)

[5] Behnam, M.; Kaigala, G.V.; Khorasani, M.; Martel, S.; Elliott, D.G.; Backhouse, C.J., "Integrated circuit-based instrumentation for microchip capillary electrophoresis," Nanobiotechnology, IET, **4,** 91, (2010)

[6] M. D. Borysiak, E. Yuferova, and J. D. Posner, "Simple, Low-Cost Styrene-Ethylene/Butylene-Styrene Microdevices for Electrokinetic Applications", Anal. Chem **85,** 11700 (2013)

CONTACT

D. Sameoto, tel: +1-780-248-2052; sameoto@ualberta.ca

METAL-SU-8-GRAPHENE INTEGRATED CIRCUIT TECHNOLOGY FOR RIGID AND FLEXIBLE SUBSTRATES

H. Al-Mumen[1,2] and Wen Li[1]*
[1]Michigan State University, East Lansing, Michigan, USA
[2]University of Babylon, Babylon, Iraq

ABSTRACT

We have demonstrated in our previous work that SU-8 is effective and stable in ambient n-doping technique for graphene. In this paper we proposed a reliable technology for constructing graphene integrated circuits that can be used as an alternative to CMOS where graphene and SU-8 were used as replacements to silicon and oxide. In this work we selectively doped a graphene sheet and both n-type and p-type graphene FETs were fabricated on the same graphene sheet on a rigid and flexible substrates. E-beam lithography was used to pattern SU-8 resist and then selectively doped the SU-8 resist within the graphene sheet. The fabricated graphene transistors observed a high stability in air and at a wide range of temperatures.

INTRODUCTION

Graphene has attractive research interest since its discovery in 2004 [1] ; Geim and Novoselov receipt of the Nobel Prize in 2010. The ultrahigh electron mobility and cutoff frequency of graphene made it a candidate for future integrated circuits design. However, the lack of a reliable and practical technology for fabricating graphene circuits delayed the chance of transfer graphene circuits to the market.

It is well known that pristine graphene in always has a *p*-type property in ambient due to the oxygen that interact with the graphene edges [2]. However, Fabricating integrated circuits requires making both *n*-type and *p*-type graphene transistors monolithically on a single substrate. We have demonstrated in our previous work [3] that SU-8 is an effective and stable in ambient *n*-doping technique for graphene. We found out that the photo-acid generator (PAG), one of the SU-8 chemical components, is the n-doping source for graphene. The doping concentration can be controlled by controlling the amount of SU-8 chemical components (PAG, epoxy resin and cyclopentanone).

FABRICATION OF GRAPHENE CIRCUIT

One great benefit of using e-beam lithography to expose SU-8 [4] is the ability to selevtively pattern and *n*-dope a graphene sheet at the nanoscale feature size. First, graphene was transfer to a SiO_2/Si substrate. Three Ti/Au electrodes were constructed on the graphene sheet to form two transistors, via e-beam lithography, metal deposition, and the metal lift-off patterning. The SU-8 3005 was spin-coated on a SiO_2/Si substrate with a spin speed of 6000 rpm. Then, the substrate was soft-baked at 65 ^{0}C for 3 min and then at 95 ^{0}C for 3 min. JEOL 840 e-beam lithography instrument was used for selectively pattern the SU-8 resist within graphene sheet. The instrument operated at acceleration voltage of 35 kV, beam current of 25 pA and dose of 3 μC/cm^2. Then samples were developed by SU-8 developer for ~1 min, followed by immersion in isopropanol, and a rinse with DI water. Finally, samples were hard baked at 100 ^{0}C for 3 min. As schematically shown in Figure 1(a,b), The SU-8 coated graphene was an *n*-type region and the uncoated graphene was a *p*-type region. The two transistors shared a same back gate as an input voltage terminal (V_{in}). The source and drain contacts of the two transistors were connected together for use as an output voltage terminal (V_0), Figure 1 (c). We should mentioned that for preciously and selectively doping, a sacrificial layer, for example, PMMA resist is need to be deposited on the other parts of graphene sheet prior to patterning SU-8 to protect them from doping, which usually occur due to the effects of the impinging electrons during e-beam exposure (Figure 1 (d)).

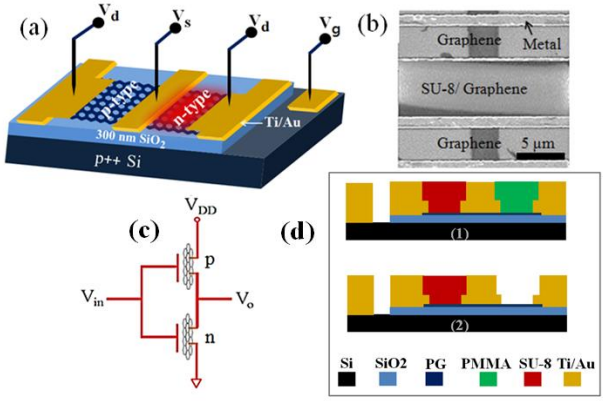

Figure.1 An integrated graphene inverter: (a) the schematic of the circuit fabrication; (b) the SEM image of the fabricated inverter; (c) the circuit layout and (d) Fabrication process.

CHARACTERIZATION OF GRAPHENE CIRCUIT

To verify the formation of the *n*-type and *p*-type transistors on the same graphene sheet, the transfer resistances R_p and R_n between the source and drain contacts of the individual FETs were measured as a function of the applied voltage V_{in} , as illustrated in Figure 2.

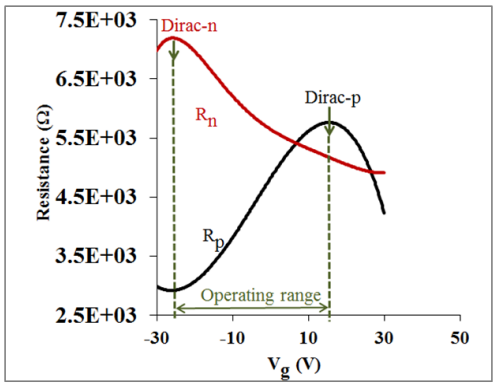

Figure 2: The transfer resistance (Rp and Rn).

The measured Dirac points of both the *p*-type and *n*-type graphene sheets were at -27 V and 17 V, respectively. By connecting *p*-type FETs to V_{DD} and *n*-type FET to the ground, a Dirac point splitting along the V_{in} axis and then the complementary configuration were achieved within the region of Dirac points. The voltage transfer characteristic of the fabricated inverter is given in Figure 3. The two FETs operated in the range between the Dirac points. Away

9781940470016/HH2014/$25©2014TRF
DOI 10.31438/trf.hh2014.120

from the Dirac points, the saturation of the output voltage V_0 resulted in the approximately constant ratio of R_n/R_p, when V_{in} < -27 V for the *n*-type FET and V_{in} > 17 V for the *p*-type FET. The voltage gain of the inverter was much less than 1, as determined by $A = dV_0/dV_{in}$. The small voltage gain of the fabricated inverter could be mainly due to the very small change of the transistor resistances around the Dirac points. The swing voltage of the inverter was 3 mV at V_{DD} = 10 mV. The threshold voltage (V_{TH}), which is the input voltage at the maximum voltage gain of the inverter, was approximately 5.6 mV (V_{in}=V_{TH}) and slightly greater than $V_{DD}/2$.

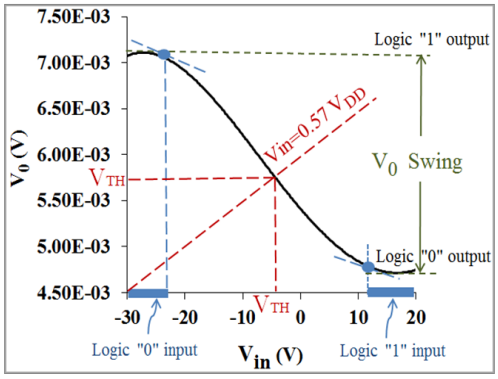

Figure 3: Voltage transfer characteristic, demonstrating a logic inverter function.

The ambient stability of n-type FET was studied by measuring the Vs-σ for 7 days of air exposure (Figure 4(a)) results showed no major change in the mobility of the charge carriers. The maximum carrier mobility was ~800 cm^2/Vs. The device was also stable at relatively wide range of temperature (Figure 4 (b)).

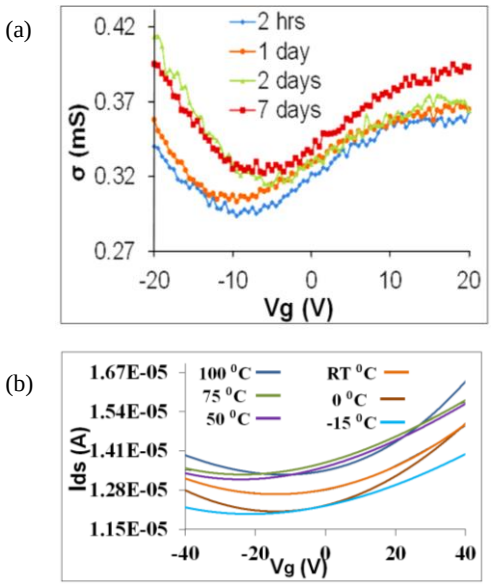

Figure 4. n-type FET chemical stability: (a) In ambeint for several days (b) At temperature variation.

Our developed metal-SU8-Graphene technology can also be applied in the development of flexible graphene transistors. The fabrication of transistor began with the deposition of a 10 µm Parylene layer on a silicon substrate, which was used as a mechanical carrier during the subsequence fabrication process. The graphene was transferred onto the Parylene surface and confirmed by Raman spectroscope (Figure 5(c)). Schematic of the device illustrated in Figure 5(a) and device after fabrication is illustrated in Figure 5(b). Figure 5(d) shows the flexibility test of Parylene based graphene circuits.

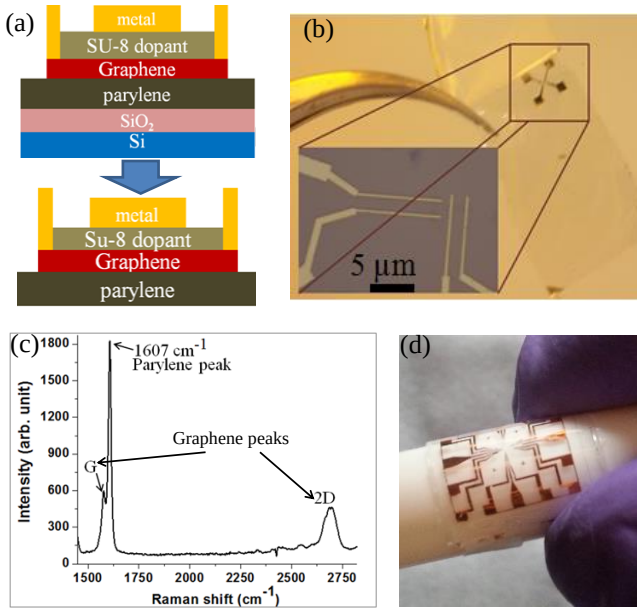

Figure 5. Flexible n-type graphene FET: (a) The overveiw of graphene-polymer layer structure; (b) A fabricated device; (c) Raman spectrum of graphene transferred on a Parylene substrate.(d) Demonstration of the device flexibility.

CONCLUSION

Doping a dedicated area within graphene sheet in a nanoscale feature size is a great achievement. It represents a practical method for Metal-SU-8-Graphene (MSG) integrated circuit technology. This technology can be applied for digital and analog circuits, as well. Furthermore, it can be used in the development of flexible graphene electronic circuits, which provides an enormous opportunity for future applications in, for example, biomedical systems.

REFERENCES

[1] K. S. Novoselov, A. K. Geim, S. V. Morozov, D. Jiang, Y. Zhang, S. V. Dubonos, I. V. Grigorieva, and A. A. Firsov, "Electric field effect in atomically thin carbon films", *Science* 306, 5696 , (2004).

[2] Jingwei Bai, Xing Zhong, Shan Jiang, Yu Huang, and Xiangfeng Duan, -"Graphene Nanomesh", Nature Nanotechnology, 5, 3, (2010).

[3] H. Al-Mumen, L. Dong and W. Li, "SU-8 doped and encapsulated n-type graphene nanomesh with high air stability", *Applied Physics Letters*, 113, 232113 (2013).

[4] Mirwais Aktary, Martin O. Jensen, Kenneth L. Westra, Michael J. Brett and Mark R. Freeman," High-resolution pattern generation using the epoxy novolak SU-8 2000 resist by electron beam lithography", *Journal of Vacuum Science & Technology B: Microelectronics and Nanometer Structures*, 21, L5, (2003).

CONTACT

*Wen Li, tel: +1-(517) 353-7832; wenli@egr.msu.edu.

MULTIFUNCTIONAL INTEGRATED SENSOR MONITORING

C.L. Roozeboom[1], B.E. Hill[1], V.A. Hong[1], C.H. Ahn[1], E.J. Ng[1], Y. Yang[1], M.A. Hopcroft[2], B.L. Pruitt[1]
[1]Stanford University, Stanford, California, USA
[2]Hewlett-Packard, Palo Alto, California, USA

ABSTRACT

We deploy multifunctional integrated sensors (MFISES) as a sensing platform in five applications and quantify their performance requirements for: weather stations, indoor climate control, parking monitoring, road activity monitoring, and chemical sensing. MFISES combines temperature, humidity, pressure, air speed, chemical gas, magnetic, and acceleration sensing in an encapsulated fabrication process to yield 2x2 mm sensor die. We compare the measurement resolution, range, and bandwidth of MFISES to application requirements to demonstrate the utility of integrated sensor platforms in a wide range of monitoring situations.

RESULTS AND DISCUSSION

The MFISES design enables a sensing platform engineered to meet target specifications from the literature, datasheets and our own experimental measurements for a number of multi-parameter sensing applications. This work expands an earlier report of the design and fabrication of MFISES [1] and presents MFISES applications in smart environmental and infrastructure monitoring. Integrating the sensor functions onto a single device enables reduction in the size and cost of the sensor components (Fig. 1). The transduction principle, tested range, measured resolution, and bandwidth or time constant data are presented in Table I.

Weather Station

We selected Oregon Scientific's WMR 100 Pro to benchmark weather center performance specifications (Table II) [2]. MFISES exceeds the performance requirements and can provide similar capabilities at a fraction of the size of the sensor system. One advantage of the WMR 100 is that its wind vane anemometer can be self-powered from the input energy of passing air. Whereas, MFISES uses a hot wire anemometer with sensitivity proportional to the temperature difference between the wire and air, which is inherently power dissipative.

Indoor climate control

Three important factors to measure in smart buildings to control the climate system are temperature, humidity, and room occupancy. For temperature and humidity measurements we chose the Analog Devices TMP36 temperature sensor [3] and the Honeywell HIH-4030 humidity sensor [4] as benchmark devices (Table II). One simple method to determine room occupancy is to detect the opening and closing of a door using a wall mounted accelerometer (Fig. 2a). For this application, we found the average acceleration amplitude for a door closing of 0.12 g ± 0.04 g with minimum and maximum amplitudes of 0.04 and 0.18 g.

MFISES exceeds the temperature and humidity specifications for indoor climate control and matches the range and resolution of benchmark commercial sensors. Using the *y*-axis accelerometer, MFISES could detect a minimum amplitude door event with a signal to noise ratio greater than 5. More extensive testing to measure accuracy limited by hysteresis, offset drift, linearity, and long term stability are underway.

TABLE II
Benchmark sensor performance specifications

Function	Range	Resolution	Accuracy
Oregon Scientific WMR 100 Pro weather station			
Temperature	-30 – 60 °C	0.1 °C	1 °C
Humidity	25 – 95 %RH	1 %RH	5 %RH
Pressure	70 – 105 kPa	0.1 kPa	1 kPa
Wind	0 – 56 m/s		3 m/s
TMP35 and HIH-4030			
Temperature	-40 – 125 °C	0.1 °C	2 °C
Humidity	0 – 100 %RH	0.5 %RH	3.5 %RH

Parking monitoring

Programs in San Francisco, CA, USA and Santander, Spain have implemented sensor networks to detect the presence of vehicles in parking spots using magnetometers [5]. Electromagnetic interference from trolley car wires and underground electrical cables has caused reliability issues [6], so additional devices such as proximity sensors or photodetectors are used to verify the magnetometer data. We experimentally measured the magnetic field changes for a mid-size sedan driving over a 3-axis YAS532 magnetometer placed underneath the vehicle (Fig. 2b). The steady state amplitude change of the magnetic field vector was 0.08 G with peaks of 0.4 G when the car

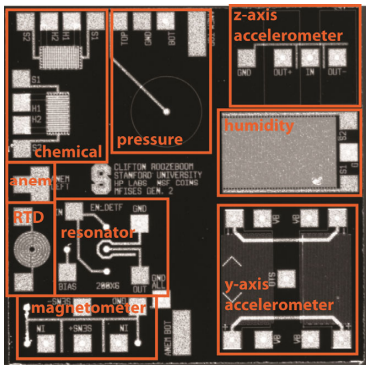

Figure 1: *MFISES die is 2x2 mm. Movable sensor elements are encapsulated and environmental sensors are open to ambient conditions.*

TABLE I
MFISES sensor performance specifications

Function	Sensor	Tested Range	Meas. Resol.	BW, time constant	Power
Temp.	Resonator	-30 – 60 °C	0.02 °C	-	Circuit: 380 mW
	Alum. RTD	-30 – 60 °C	0.03 °C	-	Sensor: 18 µW Circuit: 8.3 mW
Humidity	Polyimide capacitance	30 – 95 %RH	1 %RH	15 sec	Sensor: 2 µW Circuit: 280 mW
Pressure	Parallel plate capacitance	10 – 101 kPa	0.2 kPa	-	Sensor: 2 µW Circuit: 280 mW
Air speed	Hot wire anemometer	10 m/s	0.1 m/s	-	Sensor: 6.5 mW
Chemical	Carbon monoxide	-	-	5 min	Sensor: 18 nW Heater: 0.5 °C/mW
Magnetic	Lorentz force	-40 – 40 G	0.18 G	-	Sensor: 0.8 mW
Accel.	*y*-axis, comb finger cap.	-1 – 1 g	1.3 mg/rt-Hz	90 Hz	Sensor: 4 µW Circuit: 2.5 mW
	z-axis, teeter-totter cap.	-1 – 1 g	60 mg/rt-Hz	90 Hz	Sensor: 4 µW Circuit: 2.5 mW

9781940470016/HH2014/$25©2014TRF
DOI 10.31438/trf.hh2014.121

enters and exits the parking spot. For a single axis, we measured a maximum steady state change of 0.04 G in the axis aligned with the length of the vehicle. The MFISES magnetometer can detect the peaks of a vehicle entering and exiting, but the steady state value is below the resolution limit. Using a three-axis device would raise the minimum detection limit. Researchers have made devices in the same epi-seal fabrication process with the required specifications, but with a larger sensor footprint [11].

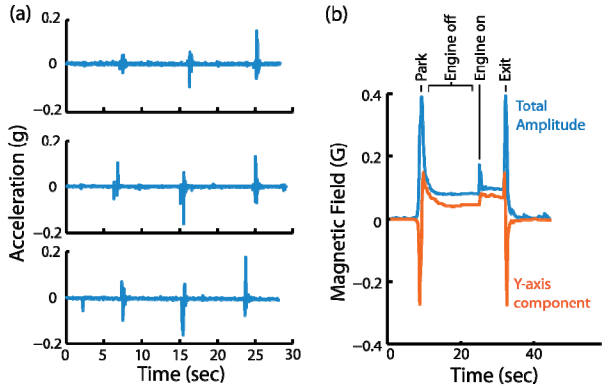

Figure 2: *(a) Accelerometer data for the closing and opening of three doors shows that a mounted wall accelerometer needs resolution better than 0.12 g to detect door events. (b) Experimental measurements of the change in amplitude of the magnetic field vector (blue line) and the change in the y-axis component (orange line) when a car drives into a parking spot, turns off the engine, turns on the engine, and drives away.*

Road activity monitoring

Current road activity monitoring systems count passing vehicles, measure their velocity, or classify them by weight using inductive coils at stop lights, radio frequency transmitter toll tags, traffic cameras, or piezoelectric cables. Here, we are interested in metrics for small-scale sensors placed on the roadside. Kim *et al.* installed a sensor network on structural elements of the Golden Gate Bridge [7] and Whelan *et al.* instrumented an abutment bridge [8]. Maximum measured accelerations were 10 mg sampled at 100 Hz. In our experiments, we placed an STMicro LSM330 accelerometer along an asphalt road and repeatedly drove a mid-size sedan past the sensor at speeds of 20 miles per hour. We were not able to detect the passing of the vehicle above the noise of the measurement. The measured MFISES *y*-axis accelerometer resolution is 1.3 mg/√Hz and theoretical limit is 0.4 mg/√Hz. With the current measurement setup we cannot measure 10 mg peaks in a 100 Hz bandwidth, but we are investigating how to reduce the parasitic capacitances likely causing the decreased resolution from the theoretical limit.

Chemical sensing

MFISES includes chemical sensing as a multi-parameter monitoring application not only because a chemical sensor system might monitor multiple contaminant gases, but also because many chemical sensors have large cross-sensitivities to temperature, humidity, and other gases [9]. A sensor system needs to measure these cross-dependent parameters to enable compensation in the measurement hardware or software. An example commercial carbon monoxide sensor, the Hanwei MQ-7, has a greater cross-sensitivity to hydrogen gas than to carbon monoxide and temperature and humidity cross-sensitivities of 0.8% full scale output/°C, and 0.4% full scale output/%RH [10].

MFISES demonstrates a platform for detection of chemical gases and compensation of gas sensor cross-sensitivities to temperature and humidity. We measure temperature and humidity at the level of commercial sensors and conducted a proof-of-concept measurement of carbon monoxide gas with MFISES surface heaters functionalized with tin oxide nanoparticles. Work is underway to assess the detection limit of MFISES.

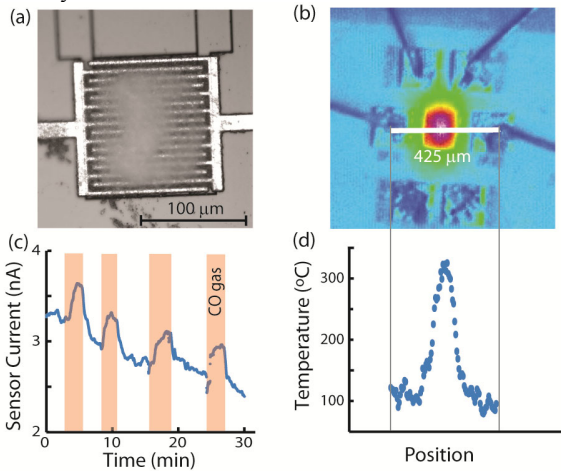

Figure 3: *(a) Microscope image of carbon monoxide sensor with tin oxide nanoparticle sensing film. (b) Infrared image of the heated chemical sensor. (c) Demonstration of detecting carbon monoxide gas. (d) Temperature profile of the infrared image.*

ACKNOWLEDGEMENTS

This work was supported by the Hewlett-Packard Labs Innovation Research Program, the NSF Center for Integrated Nanosystems (NSF ECCS-083281), Chevron Corporation through the Stanford Energy and Environment Affiliates Program, and Sandia National Labs' Excellence in Engineering Fellowship. Work was performed in part at the Stanford Nanofabrication Facility, a member of the NNIN, supported by NSF ECS-9731293, its lab members, and the industrial members of Stanford CIS.

REFERENCES

[1] C.L. Roozeboom, *et al*., "Multifunctional integrated sensor in a 2x2 mm epitaxial sealed chip operating in a wireless sensor node," *Proc. of 27th IEEE Intl. Conf. MEMS*, 2014, pp. 773-776.

[2] Oregon Scientific, "Advanced weather station with wireless sensor set and mounting package," WMR100N datasheet.

[3] Analog Devices, "Low voltage temperature sensors," TMP36 datasheet, 2010.

[4] Honeywell, "Humidity sensors," HIH-4030 datasheet, 2008.

[5] J. Wolff, *et al.*, "Parking monitor system based on magnetic field sensor" *IEEE Intelligent Transportation Systems Conf., 2006*, pp. 1275-1279, 2006.

[6] M. Albertson (2011, February). Critical vendor replaced before SFpark launch. [Online]

[7] S. Kim, *et al*. "Health monitoring of civil infrastructures using wireless sensor networks." *Info. Processing in Sensor Networks, 2007, 6th Inter. Symp. on*, 2007, pp. 254-263.

[8] M. J. Whelan, *et al*., "Real-time wireless vibration monitoring for operational modal analysis of an integral abutment highway bridge," *Engineering Structures*, vol. 31, pp. 2224-2235, 2009.

[9] K.J. Albert, *et al*.. "Cross-reactive chemical sensor arrays." *Chemical Reviews*, vol. 7, pp. 2595-2626, 2000.

[10] Hanwei Electronics, "MQ-7 gas sensor," MQ-7 datasheet.

[11] M. Li, *et al*., "Single-structure 3-axis Lorentz force magnetometer with sub-30 nT/rt-Hz resolution," *Proc. of 27th IEEE Intl. Conf. MEMS*, 2014, pp. 80-83.

ON-CHIP OPTOFLUIDIC RING RESONATOR SENSOR FOR MICRO-SCALE GAS CHROMATOGRAPHY

Kee Scholten,[1,5] Xudong Fan,[2,5] and Edward Zellers[1,3-5]*
[1]Applied Physics Program, University of Michigan, Ann Arbor, MI, USA 48109-1040
[2]Department of Biomedical Engineering, University of Michigan, Ann Arbor, MI, 48109- 2110
[3]Department of Environmental Health Sciences, Univ. of Michigan, Ann Arbor, MI, 48109-2029
[4]Department of Chemistry, University of Michigan, Ann Arbor, MI, 48109-1055
[5]Center for Wireless Integrated MicroSensing and Systems, Univ. of Michigan, Ann Arbor, MI, 48109-2121

ABSTRACT

The design, fabrication and preliminary performance assessment of a new vapor sensor comprising a *microfabricated* optofluidic ring resonator (μOFRR) and its application to micro-scale gas chromatographic (μGC) detection of volatile organic compounds (VOC) are presented. The μOFRR combines vapor sensing and fluidic transport functions in a micro-fabricated whispering gallery mode (WGM) resonator. The device also integrates on-chip fluidic-interconnection and fiber-optic probe alignment features. We demonstrate sub-second, sub-ng VOC detection and also couple the μOFRR to an upstream μGC column for rapid analysis of a simple VOC mixture.

INTRODUCTION

Advances in photonics have yielded a new class of (bio)chemical sensors adapted from WGM resonators [1], wherein shifts in resonant frequencies (λ_{WGM}) reflect analyte interactions with a sensitive interface layer. The optofluidic ring resonator (OFRR) merges sensing and fluidic transport into a single structure [2]: the evanescent components of WGMs, excited in the wall of a dielectric capillary by an external waveguide, extend into the interior of the OFRR, and changes in RI at the inner surface can cause a shift in λ_{WGM}. Previous iterations include heat-drawn glass capillaries with sorptive-polymer films [3,4], and self-rolled microtubes of semiconductor multi-layers [5]. Yet, devices reported to date have not had the small size, durability, precision fabrication, high Q-factors, and fluidic compatibility for integration into μGC systems suitable for multi-VOC analyses in environmental or clinical applications.

Here we unveil a 1st-generation μOFRR vapor sensor that improves upon prior OFRR designs and performs as well as, or better than, other microsensors used as GC/μGC detectors [6-8]. Our device integrates a PDMS-coated, SiO_x μOFRR cylinder (250-μm i.d., 1.2-μm wall; 85-μm tall), a microfluidic interconnection channel, capillary insertion port, and an optical-fiber alignment structure on a 2×2-cm Si chip (Fig. 1). High-Q (> 10^4) WGM resonances are excited in a centrally located quasi-toroidal mode-confinement expansion in the μOFRR by a 1550-nm laser via a fiber waveguide. This is a refinement of μOFRR test structures we have made [9], which lacked a complete fluidic pathway.

EXPERIMENTAL

μOFRR Fabrication

The μOFRR sensor was micromachined from Si. The resonator cylinder pre-form was made by through-wafer DRIE. An interim isotropic XeF_2 etch created a quasi-toroidal midsection expansion for mode confinement. Sidewalls were oxidized and HF-etched to reduce surface roughness before a final thermal oxidation step created the SiO_x μOFRR. The resonator was then partially released with a XeF_2 etch to a height of 85 μm.

Backside DRIE was used to create a tapered trench for capillary insertion, and a microfluidic channel connecting the capillary port and backside μOFRR aperture. A final frontside DRIE step created an optical-fiber alignment channel running laterally across the surface. Devices were diced into 2×2 cm chips.

An internal PDMS layer was deposited in the μOFRR by filling the resonator cavity with a toluene solution of PDMS and evaporating the solvent. The backside fluidic channels were sealed with a 2 × 2 cm Pyrex coverplate using UV curable glue. A short section of fused-silica capillary (250 μm i.d.) was sealed into the completed device for external fluidic connection.

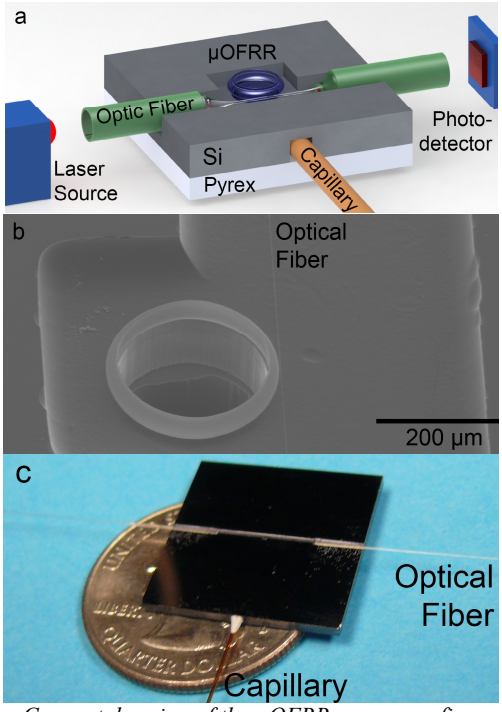

Fig. 1: a, Concept drawing of the μOFRR sensor configuration. b, SEM of μOFRR with tapered optical fiber (right) in contact with the quasi-toroidal expansion. c, Photo of the μOFRR sensor chip.

μOFRR Sensor Tests

WGM resonances were excited in the μOFRR wall by evanescently coupling a laser signal from a thinned optical fiber (~1 μm o.d.), placed in contact with the μOFRR expansion. The fiber was connected to a tunable 1550 nm laser source and an IR photoreciever. The laser wavelength was swept over a 375 pm range at 10 Hz while the transmitted signal was recorded.

The WGM was evident as a Lorentzian trough in the transmitted intensity. λ_{WGM} was defined as wavelength of minimum transmission and sensor response was defined as a shift in λ_{WGM} due to VOC exposure. Test atmospheres of benzene, toluene,

9781940470016/HH2014/$25©2014TRF
DOI 10.31438/trf.hh2014.122

ethylbenzene, m-xylene, and n-octane were created in Tedlar bags at 5 concentrations. VOC aliquots were collected in a 1-mL sample loop and injected into the µOFRR in dry air at 3 mL/min. This was repeated with m-xylene using a 5-µL sample loop to evaluate responses to transient exposures.

For µGC integration tests, the µOFRR was connected downstream from a 3×3cm chip containing a 3-m long PDMS-coated DRIE separation µcolumn. A 4-VOC mixture was injected (5-µL loop) into the µcolumn in dry air at 1.4 mL/min.

RESULTS AND DISCUSSIONS

All VOC exposures induced reversible red shifts in λ_{WGM}, with rapid steady-state responses for all VOCs (rise and fall times < 2.5 s and < 5.8 s, respectively). Fig. 2 presents calibration curves for the five individual vapors from steady-state responses. Sensitivity was defined as the slope of the calib. curve in pm/(mg/m^3), and limit of detection (LOD) was defined as 3σ/sensitivity, where σ is the std. deviation of the baseline. LODs ranged from 2.2 (benzene) to 22 mg/m^3 (ethylbenzene). The high sensitivity is attributed, in part, to the thin walls of the µOFRR, which increase the portion of the WGM probing the polymer film.

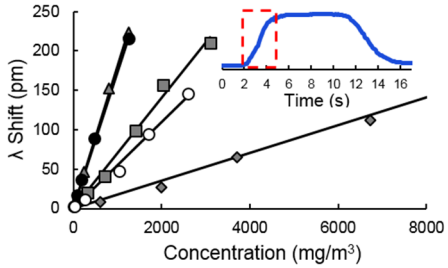

Fig. 2: Calibration curves for benzene (diamond), toluene (square), ethylbenzene (triangle), m-xylene (filled circle), and n-octane (unfilled circle) vapors. Inset shows the response profile to 700 mg/m^3 of toluene, while red square shows < 2.5 s rise time.

For transient exposures, peak height and peak area varied linearly ($R^2 > 0.997$) with injected mass. The calculated LOD of 49 pg is 10-1,000× lower than those of other microsensors adapted as µGC detectors [6,7] and ~100× lower than a polymer-coated capillary-based OFRR [4]. Fig. 3 shows the µOFRR response profile for 180-pg injection of m-xylene (FWHM = 0.71 s) compared to a similar injection for a commercial FID under the same conditions (FWHM = 0.60 s). This demonstrates the very low effective dead volume of the µOFRR which, combined with its rapid response time, is critical for a high-speed µGC detector.

Fig. 4 shows the separation/detection of four VOCs with a µGC column chip coupled to the µOFRR sensor. VOCs are easily separated in < 40 s and peaks are symmetric and sharp (FWHM = 0.33-1.17 s), reflecting excellent sensor response dynamics.

CONCLUSIONS

This is the first report of a microfabricated OFRR sensor and the first report of an on-chip optofluidic resonator for VOC sensing. Sensitivity is outstanding and response time is sufficient to capture very narrow peaks containing sub-ng quantities of vapor. This design reduces the size, increases structural integrity, and grants precise control of resonator dimensions, allowing for thinner walls and increased sensitivity, when compared to capillary drawn OFRRs. This is also the first report of an optofluidic resonator used to together with a µGC column. Results augur well for integration of the µOFRRs into µGC systems.

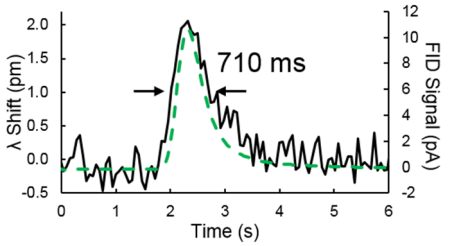

Fig. 3: Response profiles from the µOFRR (solid black line, left axis) for a 180-pg injection of m-xylene and the FID (dashed green line, right axis) for a ~500-pg injection of m-xylene; scaling of y axes facilitate comparison of full-width-at-half-maximum (FWHM).

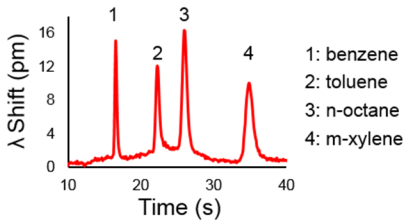

Fig. 4: Separation of benzene, toluene, n-octane and m-xylene using a µcolumn chip containing a 3-m long PDMS-coated channel at 63 °C and the (downstream) µOFRR sensor at 22 °C.

ACKNOWLEDGMENTS

We thank Mr. Will Collin for critical technical assistance with GC and µGC tests. This work was supported by NSF Grant ECCS 1128157. Devices were fabricated in the Lurie Nanofabrication Facility, a member of the NNIN supported by the NSF.

REFERENCES

[1] F. Vollmer, S. Arnold, "Whispering-Gallery-mode Biosensing: Label Free Detection Down to Single Molecules" *Nat. Meth.*, 5, 591 (2008).

[2] X. Fan, I. White, "Optofluidic Microsystems for Chemical and Biological Analysis" *Nat. Photon*, 5, 591 (2011).

[3] Y. Sun, S.I. Shopova, G. Frye-Mason, X. Fan, "Rapid Chemical-Vapor Sensing Using Optofluidic Ring Resonators" *Optics Lett.*, 33, 788 (2008).

[4] S. Shopova, et. al, "On-Column micro-GC Detection with Capillary-Based Optical Ring Resonators" *Anal. Chem*., 80, 2232 (2008).

[5] S.M. Harazim, et. al, "Lab-in-a-Tube: On-Chip Integration of Glass Optofluidic Ring Resonators for Label-Free Sensing Applications" *Lab Chip*, 12, 2649 (2012).

[6] M. Li., et. al, M. Roukes, "Nanoelectromechanical Resonator Arrays for Ultrafast, Gas-Phase Chromatographic Chemical Analysis" *Nano Lett,* 10, 3899 (2010).

[7] W. Collin, G. Serrano, L. Wright, H. Chang, N. Nunovero, E. T. Zellers, "Microfabricated Gas Chromatograph for Rapid, Trace-Level Determinations of Gas–Phase Explosive Marker Compounds" *Anal. Chem.,* 86, 655 (2014).

[8] S. Zampolli, et. al, "Real-Time Monitoring of Sub-ppb Concentrations of Aromatic Volatiles with a MEMS-Enabled Gas Chromatograph," Sens. Act. B - Chem., 141, 322 (2009).

[9] K. Scholten, X. Fan, E.T. Zellers, "Microfabricated Optofluidic Ring Resonator Structures" *App. Phys. Lett.,*99, 141108 (2011).

CONTACT

E. T. Zellers, tel: +1-734-936-0766; ezellers@umich.edu

REDUCTION OF ABLATION PLUME SHADING EFFECT FOR ULTRASHORT PULSED LASER MICROMACHINING OF SILICON

D. Blood[1], *T. Schmitz*[2], *and M. Sheplak*[1]
[1]University of Florida, Gainesville, Florida, USA
[2]University of North Carolina at Charlotte, Charlotte, North Carolina, USA

ABSTRACT

This paper presents the implementation of a novel technique for increasing the material removal rate (MRR) of silicon by a Nd:YAG ultrashort pulsed laser. During the machining process ablated material can interact with laser pulses to reduce the effective MRR. An analysis of the parameters affecting the ablated material-laser pulse interaction is explored, along with a technique for increasing the MRR by approximately 177% and decreasing the surface roughness (Ra) by approximately 65% over current machining techniques.

INTRODUCTION

Ultrashort pulsed lasers allow for single step processing of various materials in non-clean room environments [1]. They are advantageous for sensor and actuator fabrication due to their relatively minimal setup requirements, and minimal thermal load imparted into the surrounding workpiece [2]. The traditionally low MRR has thus far inhibited adoption of this technology in industrial applications. Recent increases in maximum laser power output have helped to increase the MRR; however, these advancements have also increased the significance of certain phenomena that negatively affect the machining process. One such phenomena is the ablation plume shading effect.

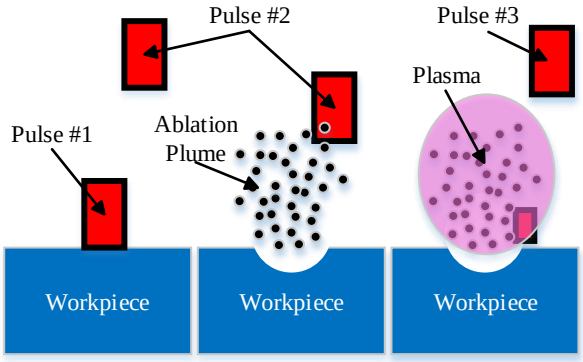

Figure 1: The process of forming plasma over the workpiece surface. First, pulse #1 impacts the workpiece (left). Then, ablated material is ejected (middle). Lastly, pulse #2 interacts with the weakly ionized molecules to form a plasma and the pulse intensity is decreased (right).

During the machining process ablated material is ejected out of the cut region [3]. This ejected material can interact with subsequent pulses, as seen in Fig. 1, to produce a plasma above the workpiece [4]. The plasma effectively shades the workpiece from the pulse by absorbing a fraction of the pulse's energy. This shading effect can cause a reduction in the MRR, and an increase in the surface roughness [5,6].

The two primary machining parameters of interest for the ablation plume shading effect are: (1) the pulse area overlap (PAO), and (2) the pulse repetition rate (PRR). A visualization of these parameters is shown in Fig. 2. The PAO affects the distance the plume must dissipate before the subsequent pulse reaches the workpiece, and the PRR affects the time the plume has to dissipate.

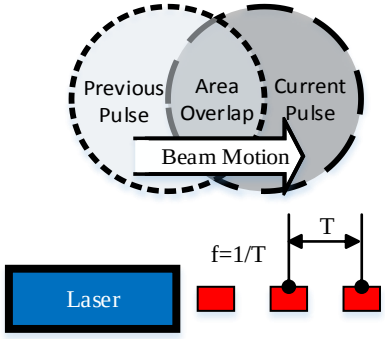

Figure 2: (Above) Visualization of the pulse area overlap, and (Below) the pulse period 'T' that can be used to calculate the pulse repetition rate 'f'.

EXPERIMENTAL PROCEDURE

To test the effects of these two parameters, several 100 µm squares were machined in <100> P-type silicon by a Coherent Talisker Ultra 355-4 laser with a nominal pulse duration of 10-15 picoseconds, and a wavelength of 355 nm. The results of these tests, shown in Fig. 3, reveal a decreasing trend in the average volume of material removed per pulse for an increasing PRR and an increasing PAO. While decreasing the PRR would reduce the shading effect, it also reduces the overall MRR. Also, decreasing the PAO results in an increase in the surface roughness; consequently, another solution

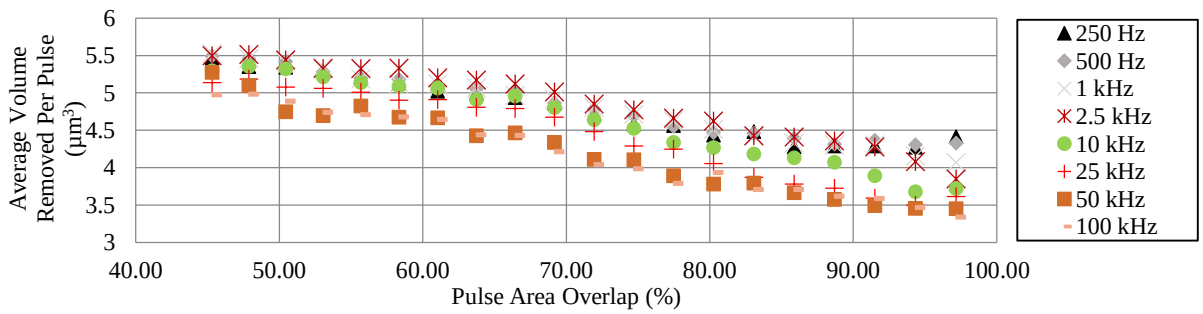

Figure 3: Demonstration that an increase in either the pulse area overlap or the pulse repetition rate results in a decrease in the MRR.

9781940470016/HH2014/$25©2014TRF
DOI 10.31438/trf.hh2014.123

Solid-State Sensors, Actuators and Microsystems Workshop
Hilton Head Island, South Carolina, June 8-12, 2014

is necessary to increase the MRR without affecting the quality of the feature.

In an attempt to reduce the effect of the ablation plume shading, various gases were blown over the workpiece surface. It was theorized that a gas flow would help remove the ablated material before the subsequent pulse could interact with the plume, and that a noble gas, in this case argon, would retard the plasma formation. The gases were blown through a 40 mm wide Lechler air nozzle, shown in Fig. 4, at a flow rate of 40 L/min, and at a distance of 12.7 mm from the workpiece surface. Gas flows oriented parallel and perpendicular to the cut direction, as shown in Fig. 5, were tested.

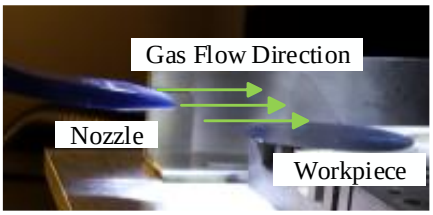

Figure 4: Setup for blowing gasses through a wide airflow nozzle over the silicon workpiece.

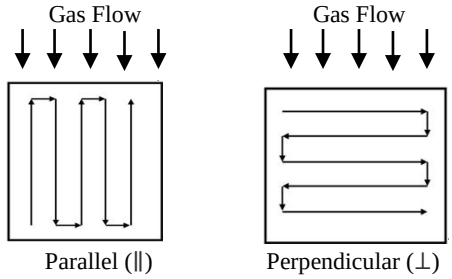

Figure 5: Visualization for the direction of gas flow for the two different cases. Lines inside of the squares represent the cut path of the laser.

RESULTS

Analyzing the results of the tests, shown in Fig. 6, reveals three points. First, the squares machined with a gas flow show greater cut depths for the same number of cut passes; effectively increasing the MRR. Second, the parallel gas flow shows a greater improvement in the cut depth compared to the perpendicular flow. Third, the flow of argon resulted in the largest depth of cut with a 177% increase over the stagnant machining environment at 19 cut passes.

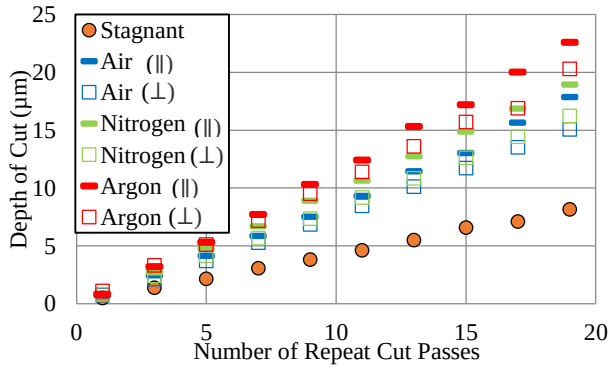

Figure 6: Experimental data validating the theory that gasses blowing over the workpiece can increase the MRR by decreasing the ablation plume shading effect.

In addition to increasing MRR, the surface roughness of the machined workpiece can also be improved with implementation of gas flow. Fig. 7 shows that at a cut depth of 8.16 µm the surface roughness (Ra) is 934 nm for the stagnant condition. With the gas flowing the surface roughness is reduced by approximately 65% to only 295 nm at a cut depth of 7.35 µm.

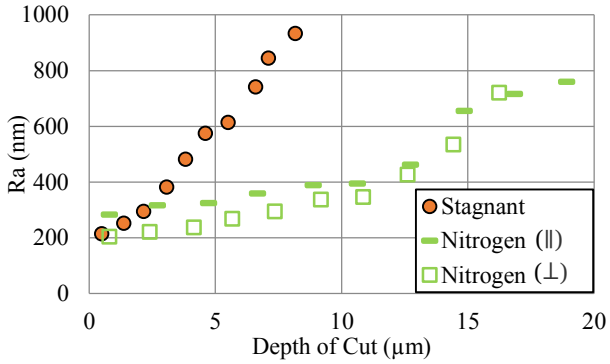

Figure 7: A comparison of the resulting surface roughness for three machining conditions. The presence of nitrogen flowing over the workpiece results in a relatively low surface roughness compared to a stagnant machining condition.

CONCLUSION

Ultrashort pulsed lasers allow for the machining of silicon in non-clean room environments with minimal setup. Recent advances in laser capabilities increase the potential maximum MRR; however, the ablation plume shading effect is reducing realized gains of these new lasers. While a decrease in the PRR or PAO reduces the effect of this shading, it also results in a lower overall MRR and an increase in the surface roughness. The implementation of a gas flow over the workpiece surface decreases the effect of the ablation plume shading by removing the ablated particles before the subsequent pulse could interact with the plume. Further investigation is necessary in order to optimize the effectiveness of this technique.

ACKNOWLEDGEMENT

The authors would like to thank the U.S. Department of Energy for their support (DE-FE0012370).

REFERENCES

[1] N.B. Dahotre, and S.P. Harimkar, *Laser Fabrication and Machining of Materials*, Springer Science + Business Media, LLC, New York, 2008.

[2] B.N. Chichkov, C. Momma, and S. Nolte, "Femtosecond, Picosecond, and Nanosecond Laser Ablation of Solids," Applied Physics A, 63, pp. 109-115, (1996).

[3] N. Rykalin, A. Uglov, and A. Kokora, *Laser Machining and Welding*, Pergamon Press Inc., New York, 1978.

[4] N. Dahotre, and A. Samant, *Laser Machining of Advanced Materials*, Leiden: Yalor & Francis Group, London, 2011.

[5] D. Bäuerle, *Laser Processing and Chemistry*, Springer Heidelberg Dordrecht, London, 2011.

[6] S. Amoruso, C. Altucci, and R. Bruzzese, "Study of the Plasma Plume Generated During Near IR Femtosecond Laser Irradiation of Silicon Targets", Applied Physics A, 79, 1377–1380 (2004).

CONTACT

*D. Blood, tel: +1-765-366-7835; DANIEL.BLOOD@UFL.EDU
*M. Sheplak, tel: +1-352-392-3983; SHEPLAK@UFL.EDU

RESONANT MEMS FOR HIGH RESOLUTION ATOMIC FORCE AND DISPLACEMENT MEASUREMENTS IN LIQUID

E. Mehdizadeh, M. Rostami, X. Guo, and S. Pourkamali
Department of Electrical Engineering, University of Texas at Dallas, Richardson, TX, USA

ABSTRACT

This work presents resonant microstructures capable of resolving subatomic features and/or measurement of atomic level forces in liquid media. It has previously been shown that forces in the micro- and nano-Newton range applied to laterally flexible extensional-mode micro-resonators lead to significant resonant frequency shifts [1]. In this work a similar principle has been applied to rotational mode disk resonators capable of maintaining relatively high quality factors in liquid. Preliminary results indicate about 10-fold improvement in combined displacement-force resolution in liquid compared to typical piezoresistive cantilevers. Using integrated comb-drive electrostatic actuators, displacement and force resolutions as high as 200fm and 1nN have been demonstrated. Using softer resonant structures or application of the force through a levering mechanism, force sensitivities in the pN range can be achieved while maintaining sub-nm spatial resolution.

INTRODUCTION

Sub-nanometer displacement and force measurements are an indispensable part of modern biological sciences including the study of cell mechanobiology, interaction forces within various biomolecules, nanomechanical properties of biological samples, monitoring of protein dynamics, and imaging biological samples in their native environments [2, 3]. To date, the most powerful tool to study biological systems is frequency-modulation atomic force microscopy (FM-AFM) utilizing optical lever. Due to significant quality factor drop of conventional AFM cantilevers in air and liquid (limited to 100 and 10, respectively), true atomic resolution imaging and force measurements in air and especially in liquid remain a formidable challenge [4]. Employing sophisticated instrumentation and readout electronics along with application of proper modifications within commercially available AFMs, subatomic displacement and force resolutions have been demonstrated in liquid. For instance, using small oscillation amplitude (0.16-0.33) of a ~40N/m cantilever, vertical resolution of 2-6pm has been shown [5]. Piezoresistive sensing, on the other hand, enables integration of sensing elements on the AFM cantilevers, significantly simplifying the experimental setup by eliminating the need for external sensing elements, precise system alignment and complex circuitry for operation [6]. However, such methods require complex fabrication processes and cannot compete with some of the conventional technologies in terms of sensitivity [7-9]. Taking advantage of high performance of microscale rotational mode disk resonators in liquid, this work presents an integrated, convenient (with fully electronic readout) and potentially transformative force-displacement measurement technique that can be deployed in various environments (vacuum, air, and liquid) with higher sensitivity.

DEVICE DESCRIPTION

Figure 1 illustrates SEM view of one of the test structures used in this work that is comprised of a disk resonator coupled to a comb-drive electrostatic actuator. The structures are fully made of single crystalline silicon and are fabricated on silicon-on-insulator (SOI) substrates with device and buried oxide layer thicknesses of 15µm and 5µm, respectively. The long narrow tangential beams on the two sides of the disk are responsible for both thermal actuation and piezoresistive detection of the resonator vibrations. Upon periodic electro-thermal excitation of the resonator with the appropriate frequency, the disk starts vibrating in its rotational resonance mode [10] (as depicted in the inset of Fig. 1). The comb drive actuator has 55 interdigitated electrode pairs separated by photolithography defined 2.3µm wide air-gaps and can simulate the effect of an external force applied to the resonant force sensor. The force from the actuator can slightly deform the resonator structure, and consequently change its effective mechanical stiffness and therefore resonance frequency.

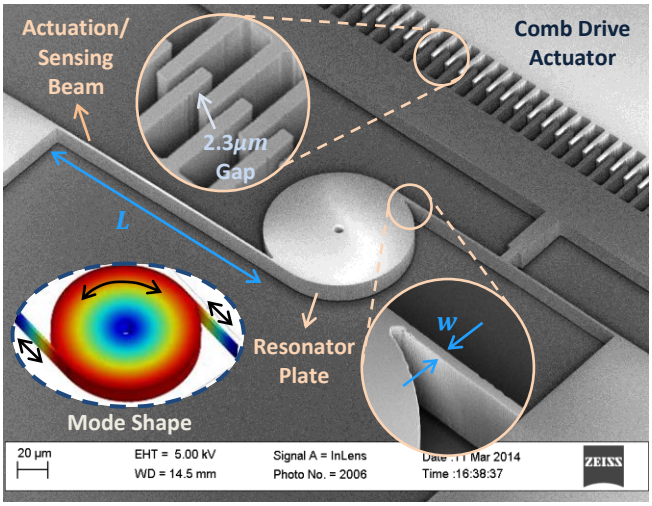

Figure 1: SEM view of a 2.3MHz in-plane disk resonant force-displacement sensor capable of operating in liquid. The inset on the bottom left depicts the finite element modal analysis of the rotational resonant mode of the disk structure.

RESULTS AND DISCUSSION

Resonant structures with different dimensions were tested in both air and xylene showing *Q* factors as high as ~4000 and ~80, respectively. Xylene, which is an organic nonconductive liquid, was used to allow application of relatively large actuation voltages to the electrostatic actuator. Figure 2 shows how the frequency response of the 2.3MHz resonator of Fig. 1 changes under constant bias current in both air and liquid, while increasing the external electrostatic force. The change in resonance frequency of the resonant force-displacement sensor of Fig. 1 as a function of the external force is illustrated in Fig. 3, showing force and displacement sensitivities of 0.88Hz/nN (0.38ppm/nN) and 21Hz/nm (9ppm/nm) in liquid. With a conservative frequency measurement accuracy of 1Hz this leads to force and displacement resolutions of 1nN and 40pm, respectively. Interestingly, the results show that sensitivities in liquid are ~2X larger than in air leading to 2-fold better force and displacement resolutions (ϵ_r=2.2 has been taken into account for Xylene). This is believed to be due to the increased effect of structural deformations on viscous damping. Table 1 summarizes the results obtained from a number of similar devices with different dimensions demonstrating

9781940470016/HH2014/$25©2014TRF
DOI 10.31438/trf.hh2014.124

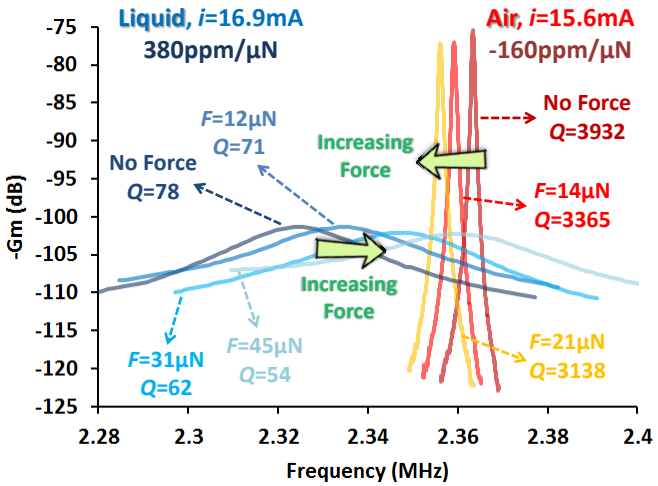

Figure 2: Measured frequency responses for the 2.3MHz thermal-piezoresistive resonator of Fig. 1 in air and xylene with different applied external forces. Red and blue plots refer to air and liquid testing conditions, respectively. The results indicate ~2X higher force-displacement sensitivities in liquid than in air. Dielectric constant of ϵ_r=2.2 for xylene has been used in electrostatic force calculations.

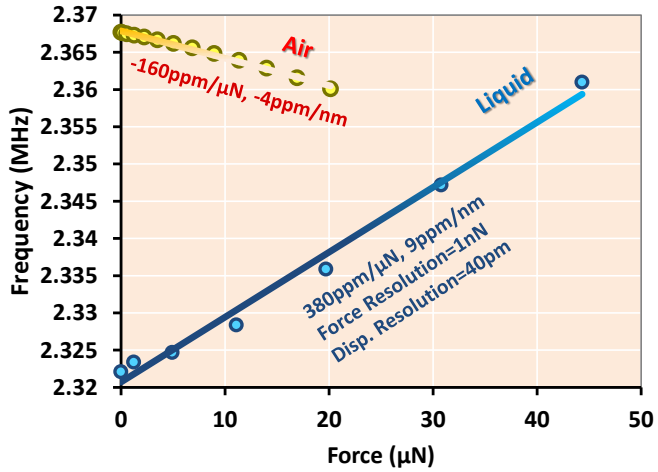

Figure 3: Measured frequency of the resonator of Fig. 1 as a function of the applied local force.

displacement and force resolutions as high as 200fm and 1nN. It should be noted that force resolution and displacement resolution of such sensors are directly related via the structural stiffness at the point where the external force is applied. Accordingly, force resolution can be improved at the expense of losing displacement resolution (by decreasing the structural stiffness at the point of force application) and vice versa. To have a fair comparison with other atomic force measurement techniques, therefore, resolution figure-of-merit (FOM) is defined as the force resolution-displacement resolution product. As shown in Figure 4, the proposed approach provides ~10X better FOM in liquid (40nN.pm) compared to typical piezoresistive cantilevers (400nN.pm) [7].

ACKNOWLEDGEMENT

This work has been supported by the National Science Foundation under award number #1056068.

Table 1: Summary of in-liquid measurement results obtained from devices with different dimensions (spotted in Fig. 4).

Device#	Dimensions (L×w)	Force Resolution	Stiffness (kN/m)	Displacement Resolution	FOM (nN.pm)
1	180µm×2µm	1nN	0.025	40pm	40
2	30µm×2µm	25nN	12.5	2pm	50
3	10µm×2µm	100nN	500	200fm	50

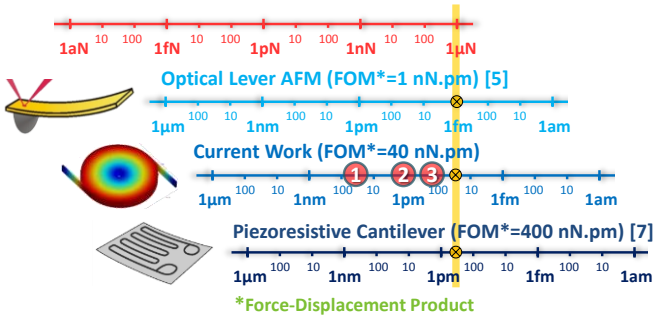

Figure 4: Comparison of current work performance with other approaches in terms of their FOM (force- displacement product). The blue and red axes represent force and displacement resolution, respectively. A blue cross-bar with a larger shift towards left depicts a better combined force/displacement performance (lower FOM). The numbers 1 to 3 show the force and displacement sensing performance of the three disk resonant sensors of Table 1.

REFERENCES

[1] E. Mehdizadeh, A. Hajjam, A. Rahafrooz, and S. Pourkamali, "Nano-precision force and displacement measurement using MEMS resonant structures," IEEE Sensors Conference (2013), pp. 1-4.

[2] S. Kasas *et al*, "Biological Applications of the AFM: From Single Molecules to Organs", Int J Imag Syst Tech, 8, 151(1997).

[3] A. Engel and D. J. Müller, "Observing single biomolecules at work with the atomic force microscope", Nature Structural & Molecular Biology, 7, 715 (2000).

[4] T. Fukuma *et al*, "Development of low noise cantilever deflection sensor for multi-environment frequency-modulation atomic force microscopy", Rev. Sci. Instrum. 76, 053704 (2005).

[5] T. Fukuma *et al*, "True atomic resolution in liquid by frequency-modulation atomic force microscopy", Appl. Phys. Lett. 87, 034101 (2005).

[6] A. A. Barlian *et al*, "Review: Semiconductor piezoresistance for microsystems," Proceedings of the IEEE, 97, 513 (2009).

[7] J. Polesel-Maris *et al*, "Piezoresistive cantilever array for life sciences applications", Journal of Physics: Conference Series, 61, 1 (2007).

[8] G. E. Fantner *et al*, "Use of self-actuating and self-sensing cantilevers for imaging biological samples in fluid", Nanotechnology, 20, 434003 (2009).

[9] J. C. Doll and B. L Pruitt, "High-bandwidth piezoresistive force probes with integrated thermal actuation", J. Micromech. Microeng. 22, 095012 (2012).

[10] A. Rahafrooz and S. Pourkamali, "Rotational Mode Disk Resonators for High-Q Operation in Liquid", IEEE Sensors Conference (2010), pp. 1071-1074.

CONTACT

E. Mehdizadeh, tel: +1-720-224-4714; exm124930@utdallas.edu

VIRUS-LIKE-PARTICLES FOR NEXT GENERATION MICRO/NANO-BIOSENSORS

X. Z. Fan[1], L. Naves[2], N. P. Siwak[1], A. Brown[3], J. Culver[2], and R. Ghodssi[1,3]*
[1]MEMS Sensors and Actuators Laboratory, Departments of Electrical and Computer Engineering, Institute for Systems Research, [2]Institute for Bioscience and Biotechnology Research,
[3]Fischell Department of Bioengineering,
University of Maryland, College Park, MD 20742, USA

ABSTRACT

A novel *Virus-like-particle* (VLP) bioreceptor layer has been integrated with an optical microdisk resonator platform for biosensing applications. This bioreceptor layer can be genetically programmed for selective binding. An optical microdisk resonator has been functionalized for antibody binding with this receptor, demonstrating resonant frequency shifts of (Δf_o) of 0.79 nm and 5.95nm after primary antibody binding and full enzyme linked immunosorbent assay (ELISA), respectively. These shifts are more than 300% higher compared to the non-specific binding of a control (non-conjugated) bioreceptor layer. The sensitivity of the optical resonator to detect primary antibody binding without the additional ELISA steps demonstrates the feasibility of this platform for rapid and simplified immunoassays on a chip.

INTRODUCTION

The detection and identification of biomolecules (e.g. antibodies, proteins, and peptides) are important for a wide range of biological sciences and bio-medical applications. The primary goals and challenges shared by all sensor systems are to achieve high sensitivity and selectivity. Recently, considerable research efforts have been focused toward developing miniaturized sensor microsystems by taking advantage of their small footprint, low power consumption, and easy read-out and integration schemes. While these microsystems also greatly benefit from the high sensitivity and reliability of microtransducers (e.g. bulk and surface acoustic waves, crystal microbalances, MEMS and optical resonators), they often lack the selectivity – the ability to recognize a specific target – because of challenges associated with expressing a functionalized receptor layer.

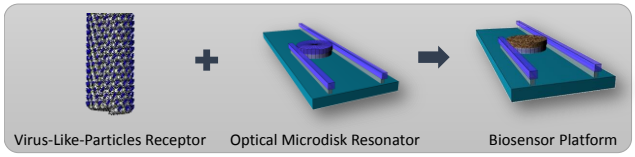

Figure 1. Schematic of the integration of VLP bioreceptor layer with an optical microdisk resonator to realize a biosensor system

The enabling technology in this work is a highly robust and genetically engineered bio-nanostructure called *Virus-like-particle* (VLP). VLPs are high-surface area biomolecules featuring a wide variety of genetically programmable functional groups [1-2]. These include cysteines that facilitate self-assembly onto various substrates and peptides with high affinity to target molecules. The expression of these highly selective VLP bioreceptors on the active surface of sensitive refractive index (RI) optical microresonators results in an ideal versatile platform for on-chip biosensing (Figure 1). The realization of this biosensor system was used to investigate and perform enzyme-linked immunosorbent assay (ELISA) for the detection of Flag antibody, using an established model antigen-antibody system. The ultra-high sensitivity of this sensor platform has the potential to recognize this immunoassay in a label-free manner, simplifying traditional ELISA procedures.

PRINCIPLE OF OPERATION

Figure 2 shows the overview schematic of the sensor system. An optical microdisk resonator is functionalized with the VLP layer to conduct antibody sensing via ELISA. The microdisk transducer is based on a change in the refractive index of the receptor layer upon the attachment of analytes on the surface of its optical resonant cavity. These types of sensors provide high sensitivity, and real-time measurement without labeling (e.g. fluorescent, enzyme indicator), requisites in both aqueous and dry conditions. A change in the surface condition of the resonator (cladding index) due to analyte binding onto this receptor layer will cause a change in effective RI (n_{eff}) of the sensor, inducing a measurable shift in resonant frequency (Δf_o). As a result, by acquiring the optical spectrum of the optical sensor and tracing its Δf_o, surfacing binding events can be monitored.

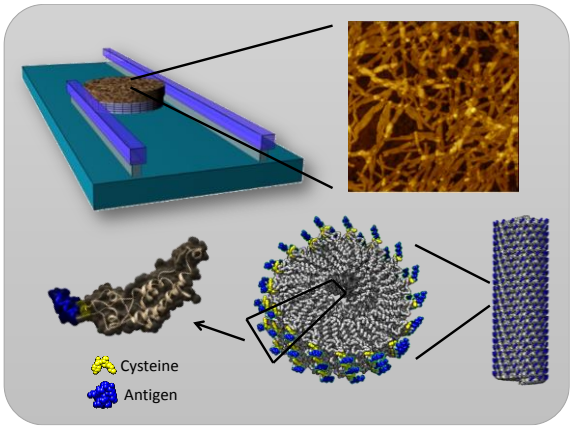

Figure 2. Schematic showing the expression of VLP on a microdisk resonator. The VLP nanostructure consists of identical CP subunits assembled into a helical formation. Each CP can be conjugated with a multitude of motifs, including cysteines (shown in yellow) and antigen peptides (shown in blue) used in this work.

We have developed the VLP bioreceptor layer for microscale selective sensing. Its selectivity may be tailored via genetic engineering. The VLP has a high aspect ratio nanotube structure formed from coat protein (CP) subunits. The VLP constructs were created in *E. Coli DH5 alpha* cells and expressed in *BL21* bacterial cells. Each CP was genetically mutated to allow for the self-assembly of viruses onto surfaces via a cysteine (*nCys*) conjugation. An additional VLP construct with a second peptide (*cFlag*) sequence (DYKDDDDK) is expressed for the binding of a specific antibody to the CP's outer surface.

The coating of the microdisk transducer surface with VLP-*nCys-cFlag* nanotubes via cysteine binding allows for a high surface area bioreceptor layer that expresses high affinity towards Flag antibodies. This model antigen-antibody binding system is investigated by performing ELISA on this sensor chip and monitoring the optical Δf_o induced by the attachment of the antibodies and the presence enzymatic activities.

9781940470016/HH2014/$25©2014TRF
DOI 10.31438/trf.hh2014.125

DESIGN AND METHODS

Figure 3 (a) shows the abridged fabrication process flow of the microdisk resonator. The 20 µm diameter and 340 nm thick silicon nitride on oxide microdisks were patterned using E-beam lithography. The 300 nm coupling gap and 600 nm wide waveguides extended to the edges of the chip and were optimized for system sensitivity. Reactive ion etching was used to transfer the resist pattern into an oxide mask and subsequently into the waveguide layer and was optimized for vertical and smooth sidewalls. The 3 mm wide chips were cleaved to ensure crystalline facets and minimal optical losses when light is coupled on to and off of the chip from lensed fibers. The fabricated microdisks were characterized using an IR tunable laser (1520-1620 nm).

Two types of VLPs were assembled on different microdisk resonator chips. VLP-*nCys-cFlag* was used to selectively bind to antibodies, and VLP-*nCys* (without the selective peptide) was used as a negative control to monitor unspecific bindings. Both chips underwent identical ELISA procedures by submerging the chip in solution, allowing for a sequential enzymatic binding of primary antibody (anti-Flag), secondary antibody, and enzymatic indicator assembly (schematically shown in Figure 3 (b)). The optical spectrum of each sensor chip was acquired under identical dehydrated conditions and the resonant frequency of the pre and post-ELISA of the two transducers were compared. Label-free immunoassays were conducted by introducing only primary antibody without secondary antibody and enzymatic indicator labeling. The selectivity of the bioreceptor layer was investigated against non-complementary antibodies (anti-HA and anti-His) as well as 5% non-fat milk solution, which contains a host of proteins and salts that can contribute to non-specific binding.

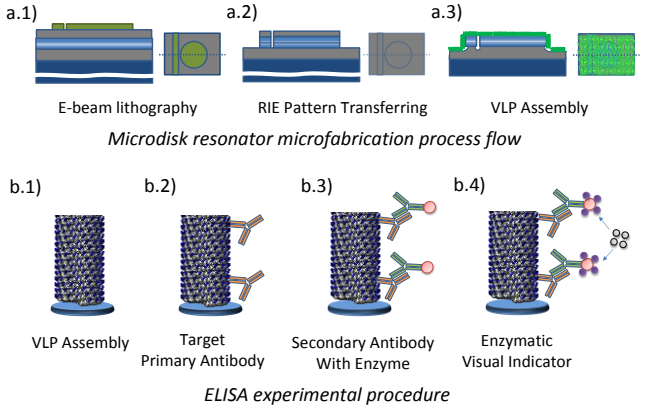

Figure 3. (a.1-3) An abridged schematic of the microdisk resonator fabrication process flow and (b.1-4) sequential steps of the ELISA experimental procedure conducted

RESULTS

The sensitivity of the transducer based on the stability and noise level of the device and setup over a period of 24 hours was 2.11pm. As seen from Figure 4, the assembly of the VLP-*nCys-cFlag* and VLP-*nCys* on microdisk resonators induced a Δf_o of 1.05±0.23 nm and 2.21±0.34 nm, respectively. The difference in wavelength shift is attributed to the difference in coverage density between the two strands of VLP, which was also confirmed by SEM (not shown here). This is most likely due to steric hindrance effects in the *VLP-nCys-cFlag* due to the additional peptide conjugated onto its surface. The full ELISA procedure shifted the resonant frequency by +5.95 nm (567%, with respect to receptor layer assembly) and -0.08nm (-4%) on VLP-*nCys-cFlag* and VLP-*nCys* coated sensor chips, respectively. The difference in the Δf_o indicates the selective bonding of Flag antibody to the genetically conjugated *cFlag* binding sites. Simplifying and truncating the ELISA process, label free detection of only the Flag antibody showed a Δf_o of +0.79 nm (51%). The selectivity of *VLP-nCys-cFlag* coated sensor chips were verified against non-complementary antibody HA and antibody His and both resulted in a negative shift in resonant frequency. The exposure to 5% non-fat milk also showed no unspecific binding to the receptor layer, showing a Δf_o of -0.03 nm (-7.1%). The sensor was, however, able to detect the positive presence of the antibody, Δf_o=+0.13 nm (34.8%), when the milk solution was mixed with Flag antibody at 1:1000 dilution. The negative shifts in resonant frequency are all associated with the rinsing and drying steps of the experimental procedure and were verified in an independent experiment.

The results presented here demonstrate the capability of a VLP-based receptor layer whose genetically programmable coat protein can display a multitude of unique binding motifs on transducer surfaces for target analytes. The sensitivity of the platform enabled, for the first time, utilization of VLP for label-free detection and simplification of the standard ELISA process and conduct, decreasing time and cost of immunoassays and creating new sensing opportunities.

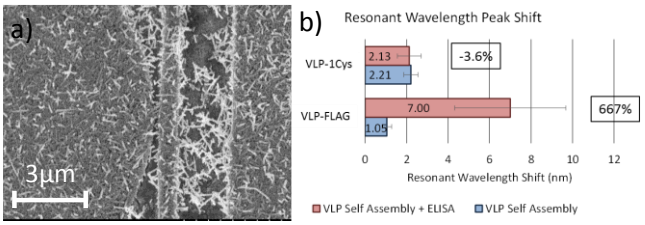

Figure 4. (a) A SEM image showing the assembly of VLPs on the surface of a micirodisk resonator (VLPs are metal coated for imaging). (b) Resonant frequency shift of pre- and post-ELISA on VLP-n1Cys and VLP-n1Cys-cFlag coated sensor chips.

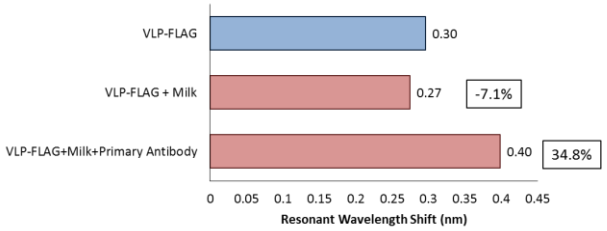

Figure 5. Resonant frequency shift of sensor chip after submersion in milk, -7.1%, and milk with primary Flag antibody, +34.8%, demonstrating the high selectivity of VLP-n1Cys-cFlag.

REFERENCES

[1] A. Brown, L. Naves, X. Wang, R. Ghodssi, and J. N. Culver, "Carboxylate Directed *In Vivo* Assembly of Virus-Like Nanorods and Tubes for the Display of Functional Peptides and Residues," *Biomacromolecules*, vol. 14, pp. 3123-3129, July 2013.

[2] X. Z. Fan, E. Pomerantseva, M. Gnerlich, A. Brown, K. Gerasopoulos, M. McCarthy, J. Culver, and R. Ghodssi, "*Tobacco mosaic virus*: a biological building block for micro/nano systems," *Journal of Vacuum Science and Technology A*, vol. 31, pp. 050815-1-24, August 2013 *Invited*

CONTACT

*Professor Reza Ghodssi: Tel.: +1 301 405 8158; E-mail: ghodssi@umd.edu

Author Index

Scroll to the author and select a **Blue** link to open a paper. After viewing the paper, use the bookmarks to the left to return to the beginning of the Author Index.

C

D

E

F

G

H

I

J

K

L

M

N

O

P

Q

R

S

T

V

W

X

Y

Z

Keyword Index

Scroll to the author and select a **Blue** link to open a paper. After viewing the paper, use the bookmarks to the left to return to the beginning of the Keyword Index.

D

E

F

G

H

I

J

K

L

M

N

O

P

Q

R

S

T

U

V

W

X

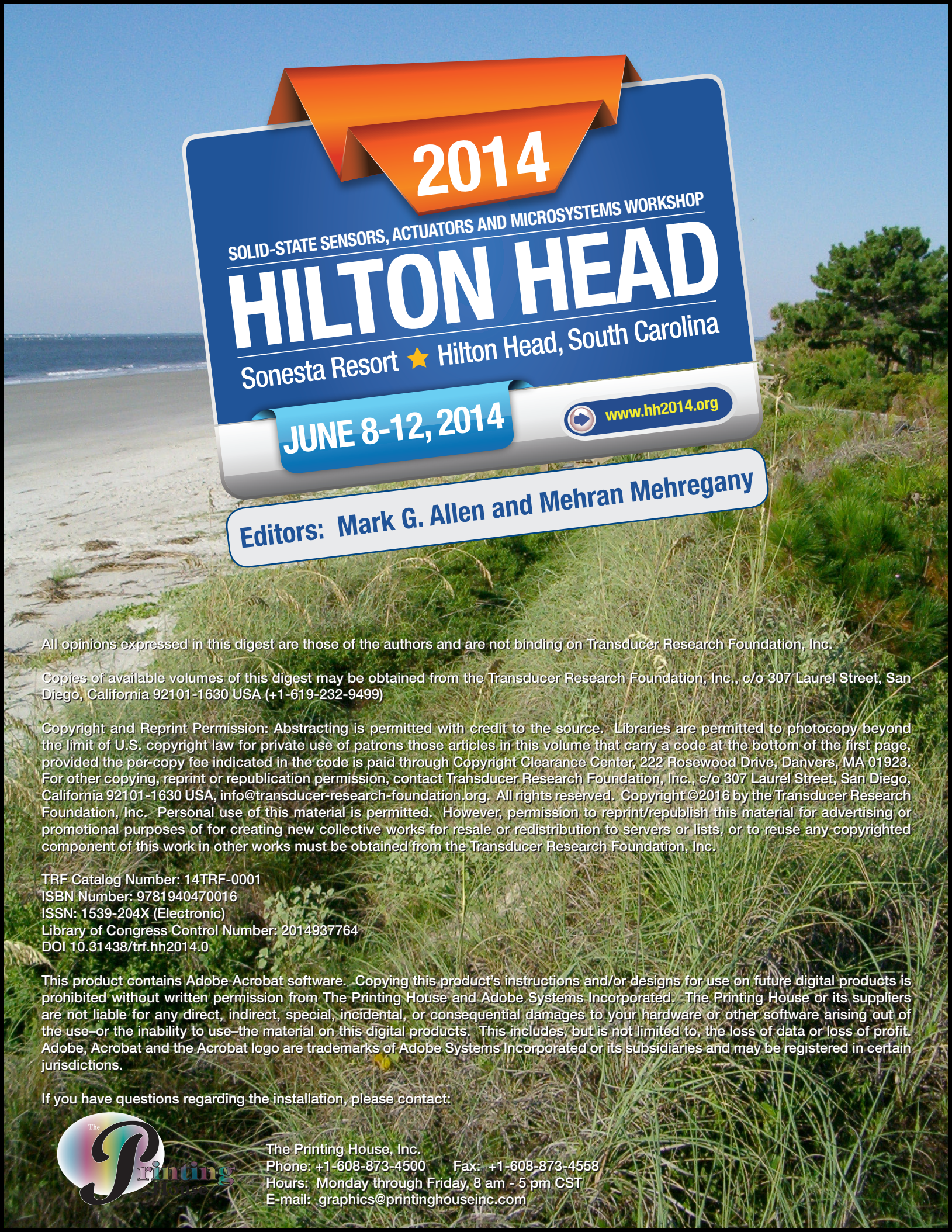

Copies of available volumes of this digest may be obtained from the Transducer Research Foundation, Inc., c/o 307 Laurel Street, San Diego, California 92101-1630 USA (+1-619-232-9499)

TRF Catalog Number: 14TRF-0001
ISBN Number: 9781940470016
ISSN: 1539-204X (Electronic)
Library of Congress Control Number: 2014937764
DOI 10.31438/trf.hh2014.0